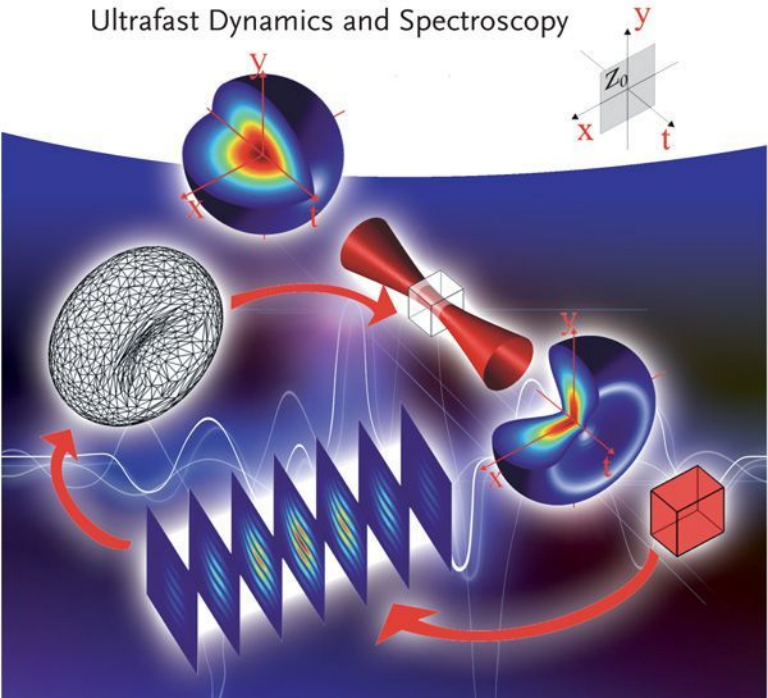


Thomas Schultz, Marc Vrakking

Attosecond and XUV Physics

Ultrafast Dynamics and Spectroscopy



Edited by

Thomas Schultz

Marc Vrakking

Attosecond and XUV Physics

Related Titles

Milonni, P.W., Eberly, J.H.

Laser Physics

2 Edition

2009

Print ISBN: 978-0-470-38771-9

Adobe PDF ISBN: 978-0-470-40970-1

ISBN: 978-0-470-40971-8

Weiner, A.

Ultrafast Optics

2009

Print ISBN: 978-0-471-41539-8

Adobe PDF ISBN: 978-0-470-47345-0

Adobe PDF ISBN: 978-0-470-47346-7

ePub ISBN: 978-1-118-21147-2

eMobi ISBN: 978-1-118-21305-6

Demtröder, W.

Molecular Physics

Theoretical Principles and Experimental Methods

2005

Print ISBN: 978-3-527-40566-4

ISBN: 978-3-527-61809-5

Adobe PDF ISBN: 978-3-527-61810-1

Hill, W.T., Lee, C.

Light-Matter Interaction

Atoms and Molecules in External Fields and Nonlinear Optics

2007

Print ISBN: 978-3-527-40661-6

ISBN: 978-3-527-61901-6

Adobe PDF ISBN: 978-3-527-61902-3

Happer, W., Jau, Y., Walker, T.

Optically Pumped Atoms

2010

Print ISBN: 978-3-527-40707-1

ISBN: 978-3-527-62950-3

Adobe PDF ISBN: 978-3-527-62951-0

Horn, A.

Ultra-fast Material Metrology

2009

Print ISBN: 978-3-527-40887-0

ISBN: 978-3-527-62792-9

Adobe PDF ISBN: 978-3-527-62793-6

Rafailov, E.U., Cataluna, M.A.,
Avrutin, E.A.

Ultrafast Lasers Based on Quantum Dot Structures Physics and Devices

2011

Print ISBN: 978-3-527-40928-0

ISBN: 978-3-527-63448-4

ePub ISBN: 978-3-527-63449-1

Adobe PDF ISBN: 978-3-527-63450-7

eMobi ISBN: 978-3-527-63451-4

Reiss, H.

Foundations of Strong-Field Physics

2013

Print ISBN: 978-3-527-41112-2

ISBN: 978-3-527-64920-4

eMobi ISBN: 978-3-527-64921-1

ePub ISBN: 978-3-527-64922-8

ePub ISBN: 978-3-527-64923-5

Edited by
Thomas Schultz
Marc Vrakking

Attosecond and XUV Physics

Ultrafast Dynamics and Spectroscopy

WILEY-VCH
Verlag GmbH & Co. KGaA

Editors**Dr. Thomas Schultz**

Max Born Institute
Div. A: Attosecond Physics
Max-Born-Strasse 2
12489 Berlin
Germany

Dr. Marc Vrakking

Max Born Institute
Max-Born-Strasse 2
12489 Berlin
Germany

All books published by **Wiley-VCH** are carefully produced. Nevertheless, authors, editors, and publisher do not warrant the information contained in these books, including this book, to be free of errors. Readers are advised to keep in mind that statements, data, illustrations, procedural details or other items may inadvertently be inaccurate.

Library of Congress Card No.:
applied for**British Library Cataloguing-in-Publication Data:**

A catalogue record for this book is available from the British Library.

**Bibliographic information published by the
Deutsche Nationalbibliothek**

The Deutsche Nationalbibliothek lists this publication in the Deutsche Nationalbibliografie; detailed bibliographic data are available on the Internet at <http://dnb.d-nb.de>.

© 2014 WILEY-VCH Verlag GmbH & Co. KGaA,
Boschstr. 12, 69469 Weinheim, Germany

All rights reserved (including those of translation into other languages). No part of this book may be reproduced in any form – by photoprinting, microfilm, or any other means – nor transmitted or translated into a machine language without written permission from the publishers. Registered names, trademarks, etc. used in this book, even when not specifically marked as such, are not to be considered unprotected by law.

Print ISBN 978-3-527-41124-5

ePDF ISBN 978-3-527-67767-2

ePub ISBN 978-3-527-67765-8

Mobi ISBN 978-3-527-67766-5

oBook ISBN 978-3-527-67768-9

Cover Design Adam-Design, Weinheim

Typesetting le-tex publishing services GmbH,
Leipzig

Printing and Binding Markono Print Media
Pte Ltd, Singapore

Printed in Singapore

Printed on acid-free paper

Contents

List of Contributors XIII

1	Attosecond and XUV Physics: Ultrafast Dynamics and Spectroscopy	1
	<i>Marc Vrakking</i>	
1.1	Introduction	1
1.2	The Emergence of Attosecond Science	2
1.2.1	Attosecond Pulse Trains and Isolated Attosecond Pulses	3
1.2.2	Characterization of Attosecond Laser Pulses	4
1.2.3	Experimental Challenges in Attosecond Science	5
1.2.4	Attosecond Science as a Driver for Technological Developments	6
1.3	Applications of Attosecond Laser Pulses	7
1.4	Ultrafast Science Using XUV/X-ray Free Electron Lasers	9
1.5	The Interplay between Experiment and Theory	11
1.6	Conclusion and Outlook	12
	References	13
	Part One Laser Techniques	17
2	Ultrafast Laser Oscillators and Amplifiers	19
	<i>Uwe Morgner</i>	
2.1	Introduction	19
2.2	Mode-Locking and Few-Cycle Pulse Generation	20
2.3	High-Energy Oscillators	23
2.4	Laser Amplifiers	25
	References	29
3	Ultrashort Pulse Characterization	37
	<i>Adam S. Wyatt</i>	
3.1	Motivation: Why Ultrafast Metrology?	37
3.1.1	Ultrafast Science: High-Speed Photography in the Extreme	38
3.2	Formal Description of Ultrashort Pulses	42
3.2.1	Sampling Theorem	45
3.2.2	Chronocyclic Representation of Ultrafast Pulses	46
3.2.3	Space-Time Coupling	46
3.2.4	Accuracy, Precision and Consistency	49

3.3	Linear Filter Analysis	51
3.4	Ultrafast Metrology in the Visible to Infrared	53
3.4.1	Temporal Correlations	53
3.4.2	Spectrography	55
3.4.3	Sonography	60
3.4.4	Tomography	60
3.4.5	Interferometry	63
3.5	Ultrafast Metrology in the Extreme Ultraviolet	73
3.5.1	Complete Characterization of Ultrashort XUV Pulses via Photoionization Spectroscopy	75
3.5.2	XUV Interferometry	81
3.6	Summary	85
	References	85
4	Carrier Envelope Phase Stabilization	95
	<i>Vincent Crozatier</i>	
4.1	Introduction	95
4.2	CEP Fundamentals	96
4.2.1	Time Domain Representation	96
4.2.2	Frequency Domain Representation	97
4.3	Stabilization Loop Fundamentals	99
4.3.1	The Noisy Source	99
4.3.2	Noise Detection	100
4.3.3	Open-Loop Noise Analysis	101
4.3.4	Feedback	102
4.3.5	Closed-Loop Noise Analysis	103
4.4	CEP in Oscillators	104
4.4.1	Oscillators Peculiarities	105
4.4.2	CEP Detection	107
4.4.3	Actuation	110
4.5	CEP in Amplifiers	115
4.5.1	Amplifier Peculiarities	116
4.5.2	CEP Detection	119
4.5.3	Actuation	123
4.5.4	Feedback Results	124
4.5.5	Parametric Amplification	126
4.6	Conclusion	129
	References	129
5	Towards Tabletop X-Ray Lasers	135
	<i>Philippe Zeitoun, Eduardo Oliva, Thi Thu Thuy Le, Stéphane Sebban, Marta Fajardo, David Ros, and Pedro Velarde</i>	
5.1	Context and Objectives	135
5.2	Choice of Plasma-Based Soft X-Ray Amplifier	137
5.2.1	Basic Aspects of High Harmonic Amplification	138
5.2.2	Basic Aspects of Plasma Amplifiers	140

5.3	2D Fluid Modeling and 3D Ray Trace	141
5.3.1	ARWEN Code	142
5.3.2	Model to Obtain 2D Maps of Atomic Data	143
5.4	The Bloch–Maxwell Treatment	149
5.5	Stretched Seed Amplification	157
5.6	Conclusion	170
	References	171

Part Two Theoretical Methods 177

6	Ionization in Strong Low-Frequency Fields	179
	<i>Misha Ivanov</i>	
6.1	Preliminaries	179
6.2	Speculative Thoughts	179
6.3	Basic Formalism	181
6.3.1	Hamiltonians and Gauges	181
6.3.2	Formal Solutions	182
6.4	The Strong-Field Approximation	184
6.4.1	The Volkov Propagator and the Classical Connection	185
6.4.2	Transition Amplitudes in the SFA	186
6.5	Strong-Field Ionization: Exponential vs. Power Law	189
6.5.1	The Saddle Point Approximation and the Classical Connection	190
6.6	Semiclassical Picture of High Harmonic Generation	195
6.7	Conclusion	198
	References	199
7	Multielectron High Harmonic Generation: Simple Man on a Complex Plane	201
	<i>Olga Smirnova and Misha Ivanov</i>	
7.1	Introduction	201
7.2	The Simple Man Model of High Harmonic Generation (HHG)	203
7.3	Formal Approach for One-Electron Systems	205
7.4	The Lewenstein Model: Saddle Point Equations for HHG	209
7.5	Analysis of the Complex Trajectories	214
7.6	Factorization of the HHG Dipole: Simple Man on a Complex Plane	221
7.6.1	Factorization of the HHG Dipole in the Frequency Domain	222
7.6.2	Factorization of the HHG Dipole in the Time Domain	224
7.7	The Photoelectron Model of HHG: The Improved Simple Man	227
7.8	The Multichannel Model of HHG: Tackling Multielectron Systems	231
7.9	Outlook	238
7.10	Appendix A: Supplementary Derivations	241
7.11	Appendix B: The Saddle Point Method	242
7.11.1	Integrals on the Real Axis	243
7.11.2	Stationary Phase Method	248
7.12	Appendix C: Treating the Cutoff Region: Regularization of Divergent Stationary Phase Solutions	250

7.13	Appendix D: Finding Saddle Points for the Lewenstein Model	251
	References	253
8	Time-Dependent Schrödinger Equation	257
	<i>Armin Scrinzi</i>	
8.1	Atoms and Molecules in Laser Fields	258
8.2	Solving the TDSE	259
8.2.1	Discretization of the TDSE	260
8.2.2	Finite Elements	263
8.2.3	Scaling with Laser Parameters	265
8.3	Time Propagation	266
8.3.1	Runge–Kutta Methods	267
8.3.2	Krylov Subspace Methods	268
8.3.3	Split-Step Methods	269
8.4	Absorption of Outgoing Flux	269
8.4.1	Absorption for a One-Dimensional TDSE	270
8.5	Observables	272
8.5.1	Ionization and Excitation	272
8.5.2	Harmonic Response	274
8.5.3	Photoelectron Spectra	275
8.6	Two-Electron Systems	278
8.6.1	Very Large-Scale Grid-Based Approaches	278
8.6.2	Basis and Pseudospectral Approaches	278
8.7	Few-Electron Systems	282
8.7.1	MCTDHF: Multiconfiguration Time-Dependent Hartree–Fock	283
8.7.2	Dynamical Multielectron Effects in High Harmonic Generation	285
8.8	Nuclear Motion	287
	References	290
9	Angular Distributions in Molecular Photoionization	293
	<i>Robert R. Lucchese and Danielle Dowek</i>	
9.1	Introduction	293
9.2	One-Photon Photoionization in the Molecular Frame	297
9.3	Methods for Computing Cross-Sections	302
9.4	Post-orientation MFPADs	304
9.4.1	MFPADs for Linear Molecules in the Axial Recoil Approximation	304
9.4.2	MFPADs for Nonlinear Molecules in the Axial Recoil Approximation	306
9.4.3	Breakdown of the Axial Recoil Approximation Due to Rotation	308
9.4.4	Breakdown of the Axial Recoil Approximation Due to Vibrational Motion	309
9.4.5	Electron Frame Photoelectron Angular Distributions	309
9.5	MFPADs from Concurrent Orientation in Multiphoton Ionization	310
9.6	Pre-orientation or Alignment, Impulsive Alignment	314
9.7	Conclusions	315
	References	315

Part Three	High Harmonic Generation and Attosecond Pulses	321
10	High-Order Harmonic Generation and Attosecond Light Pulses:	
	An Introduction	323
	<i>Anne L'Huillier</i>	
10.1	Early Work, 1987–1993	323
10.2	Three-Step Model, 1993–1994	325
10.3	Trajectories and Phase Matching, 1995–2000	328
10.4	Attosecond Pulses 2001	331
10.5	Conclusion	332
	References	335
11	Strong-Field Interactions at Long Wavelengths	339
	<i>Manuel Kremer, Cosmin I. Blaga, Anthony D. DiChiara, Stephen B. Schoun, Pierre Agostini, and Louis F. DiMauro</i>	
11.1	Theoretical Background	340
11.1.1	Keldysh Picture of Ionization in Strong Fields	340
11.1.2	Classical Perspectives on Postionization Dynamics	341
11.1.3	High-Harmonic Generation	342
11.1.4	Wavelength Scaling of High-Harmonic Cutoff and Attochirp	342
11.1.5	In-situ and RABBITT Technique	344
11.2	Mid-IR Sources and Beamlines at OSU	346
11.2.1	2- μm Source	346
11.2.2	3.6- μm Source	347
11.2.3	OSU Attosecond Beamline	347
11.3	Strong-Field Ionization: The Single-Atom Response	348
11.4	High-Harmonic Generation	350
11.4.1	Harmonic Cutoff and Harmonic Yield	350
11.4.2	Attochirp	352
11.4.3	In-situ Phase Measurement	352
11.4.4	RABBITT Method	355
11.5	Conclusions and Future Perspectives	356
	References	356
12	Attosecond Dynamics in Atoms	361
	<i>Giuseppe Sansone, Francesca Calegari, Matteo Lucchini, and Mauro Nisoli</i>	
12.1	Introduction	361
12.2	Single-Electron Atom: Hydrogen	362
12.3	Two-Electron Atom: Helium	365
12.3.1	Electronic Wave Packets	366
12.3.2	Autoionization: Fano Profile	371
12.3.3	Two-Photon Double Ionization	373
12.4	Multielectron Systems	380
12.4.1	Neon: Dynamics of Shake-Up States	381
12.4.2	Neon: Delay in Photoemission	384
12.4.3	Argon: Fano Resonance	386

12.4.4	Krypton: Auger Decay	388
12.4.5	Krypton: Charge Oscillation	390
12.4.6	Xenon: Cascaded Auger Decay	391
	References	393
13	Application of Attosecond Pulses to Molecules	395
	<i>Franck Lépine</i>	
13.1	Attosecond Dynamics in Molecules	395
13.2	State-of-the-Art Experiments Using Attosecond Pulses	397
13.2.1	Ion Spectroscopy	398
13.2.2	Electron Spectroscopy	402
13.2.3	Photo Absorption	404
13.3	Theoretical Work	405
13.3.1	Electron Dynamics in Small Molecules	405
13.3.2	Electron Dynamics in Large Molecules	406
13.4	Perspectives	413
13.4.1	Molecular Alignment and Orientation	413
13.4.2	Electron Delocalization between DNA Group Junction	414
13.4.3	Similar Dynamics in Water and Ice	416
13.4.4	More	416
13.5	Conclusion	416
	References	417
14	Attosecond Nanophysics	421
	<i>Frederik Süßmann, Sarah L. Stebbings, Sergey Zherebtsov, Soo Hoon Chew, Mark I. Stockman, Eckart Rühl, Ulf Kleineberg, Thomas Fennel, and Matthias F. Kling</i>	
14.1	Introduction	421
14.2	Attosecond Light-Field Control of Electron Emission and Acceleration from Nanoparticles	425
14.2.1	Imaging of the Electron Emission from Isolated Nanoparticles	426
14.2.2	Microscopic Analysis of the Electron Emission	429
14.3	Few-Cycle Pump-Probe Analysis of Cluster Plasmons	433
14.3.1	Basics of Spectral Interferometry	433
14.3.2	Oscillator Model Results for Excitation with Gaussian Pulses	435
14.3.3	Spectral Interferometry Analysis of Plasmons in Small Sodium Clusters	437
14.4	Measurements of Plasmonic Fields with Attosecond Time Resolution	439
14.4.1	Attosecond Nanoplasmionic Streaking	439
14.4.2	The Regimes of APS Spectroscopy	441
14.4.3	APS Spectroscopy of Collective Electron Dynamics in Isolated Nanoparticles	442
14.4.4	Attosecond Nanoscope	444
14.4.5	Experimental Implementation of the Attosecond Nanoscope	446
	Nanoplasmionic Field-Enhanced XUV Generation	449

14.5.1	Tailoring of Nanoplasmonic Field Enhancement for HHG	450
14.5.2	Generation of Single Attosecond XUV Pulses in Nano-HHG	452
14.6	Conclusions and Outlook	454
	References	455
Part Four Ultra Intense X-Ray Free Electron Laser Experiments 463		
15	Strong-Field Interactions at EUV and X-Ray Wavelengths 465	
	<i>Artem Rudenko</i>	
15.1	Introduction	465
15.2	Experimental Background	467
15.2.1	What Is a “Strong” Field?	467
15.2.2	Basic Parameters of Intense High-Frequency Radiation Sources	469
15.2.3	Detection Systems	471
15.3	Atoms and Molecules under Intense EUV Light	473
15.3.1	Two-Photon Single Ionization of Helium	473
15.3.2	Few-Photon Double Ionization of Helium and Neon	476
15.3.3	Multiple Ionization of Atoms	485
15.3.4	EUV-Induced Fragmentation of Simple Molecules	487
15.4	EUV Pump–EUV Probe Experiments	493
15.4.1	Split-and-Delay Arrangements and Characterization of the EUV Pulses	493
15.4.2	Nuclear Wave Packet Imaging in Diatomic Molecules	495
15.4.3	Isomerization Dynamics of Acetylene Cations	498
15.5	Experiments in the X-Ray Domain	499
15.5.1	Multiple Ionization of Heavy Atoms: Role of Resonant Excitations	500
15.5.2	Multiphoton Ionization of Molecules Containing High-Z Atoms	506
15.6	Summary and Outlook	510
	References	512
16	Ultraintense X-Ray Interactions at the Linac Coherent Light Source 529	
	<i>Linda Young</i>	
16.1	Introduction	529
16.1.1	Comparison of Ultrafast, Ultraintense Optical, and X-Ray Lasers	531
16.1.2	X-Ray Atom Interactions	533
16.2	Atomic and Molecular Response to Ultraintense X-Ray Pulses	536
16.2.1	Nonresonant High-Intensity X-Ray Phenomena	537
16.2.2	Resonant High-Intensity X-Ray Phenomena	540
16.3	Ultrafast X-Ray Probes of Dynamics	543
16.4	Characterization of LCLS Pulses	544
16.5	Outlook	546
	References	549
17	Coherent Diffractive Imaging 557	
	<i>Willem Boutu, Bertrand Carré, and Hamed Merdji</i>	
17.1	Introduction	557
17.2	Far-Field Diffraction	559

17.2.1	Optical Point of View	559
17.2.2	Born Approximation	561
17.2.3	Resolution	562
17.2.4	Comments on the Approximations	564
17.3	Source Requirements	565
17.3.1	Coherence	565
17.3.2	Signal-to-Noise Ratio	568
17.3.3	Dose	569
17.3.4	Different XUV Sources Comparison	572
17.4	Solving the Phase Problem	572
17.4.1	Oversampling Method	572
17.4.2	Basics on Iterative Phasing Algorithms	574
17.4.3	Implementations of Phase Retrieval Algorithms	577
17.5	Holography	583
17.5.1	Fourier Transform Holography	583
17.5.2	HERALDO	587
17.6	Conclusions	590
	References	592
	Index	599

List of Contributors

Pierre Agostini

The Ohio State University
Department of Physics
Columbus, OH 43210
USA

Roger Barlow

University of Huddersfield
Huddersfield
United Kingdom

Cosmin I. Blaga

The Ohio State University
Department of Physics
Columbus, OH 43210
USA

Willem Boutu

Centre d'Etudes de Saclay
Attophysics Group
Ultrafast Coherent Imaging Lab
CEA-SPAM, Bât. 522
91191 Gif-sur-Yvette
France

Francesca Calegari

Department of Physics
Politecnico di Milano
Institute of Photonics and
Nanotechnologies, IFN-CNR
Piazza L. da Vinci 32
20133 Milano
Italy

Bertrand Carré

Centre d'Etudes de Saclay
Attophysics Group
CEA-SPAM, Bât. 522
91191 Gif-sur-Yvette
France

Soo Hoon Chew

Physik Department
Ludwig-Maximilians-Universität
München
Am Coulombwall 1
85748 Garching
Germany

Vincent Crozatier

FASTLITE
Centre scientifique d'Orsay
Bât. 503
Plateau du Moulon, BP 45
91401 Orsay
France

Anthony D. DiChiara

The Ohio State University
Department of Physics
Columbus, OH 43210
USA

Louis F. DiMauro

The Ohio State University
Department of Physics
Columbus, OH 43210
USA

Danielle Dowek

Laboratoire des Collisions Atomiques et Moléculaires (UMR Université Paris-Sud et CNRS, 8625), Bât. 351 Université Paris-Sud 91405 Orsay Cedex France

Marta Fajardo

GoLP
Instituto de Plasmas e Fusão Nuclear
Laboratório Associado
Instituto Superior Técnico
Lisbon
Portugal

Thomas Fennel

Institut für Physik
Universität Rostock
Universitätsplatz 3
18051 Rostock
Germany

Misha Ivanov

Max Born Institute Berlin
Max-Born-Str. 2A
12489 Berlin
Germany

Ulf Kleineberg

Physik Department
Ludwig-Maximilians-Universität München
Am Coulombwall 1
85748 Garching
Germany

Matthias F. Kling

Physik Department
Ludwig-Maximilians-Universität München
Am Coulombwall 1
85748 Garching
Germany

Manuel Kremer

The Ohio State University
Department of Physics
Columbus, OH 43210
USA

Thi Thu Thuy Le

Laboratoire d'Optique Appliquée
ENSTA, CNRS
Ecole Polytechnique
Chemin de la Hunière
91671 Palaiseau
France

Franck Lépine

Université Lyon 1
ILM-Institut Lumière Matière
Domaine scientifique de la Doua
bâtiment Kastler
10 rue Ada Byron
69622 Villeurbanne CEDEX
France

Anne L'Huillier

Lund University
Department of Physics
PO Box 118
22100 Lund
Sweden

Robert R. Lucchese

Texas A&M University
Department of Chemistry
College Station, TX 77843-3255
USA

Matteo Lucchini

Department of Physics
Politecnico di Milano, Institute of Photonics and Nanotechnologies,
IFN-CNR
Piazza L. da Vinci 32
20133 Milano
Italy

Hamed Merdji

Centre d'Etudes de Saclay
 Attoptics Group
 Ultrafast Coherent Imaging Lab
 CEA-SPAM, Bât. 522
 91191 Gif-sur-Yvette
 France

Uwe Morgner

Leibniz Universität Hannover
 Institut für Quantenoptik
 Welfengarten 1
 30167 Hannover
 Germany

Mauro Nisoli

Department of Physics
 Politecnico di Milano, Institute of
 Photonics and Nanotechnologies,
 IFN-CNR
 Piazza L. da Vinci 32
 20133 Milano
 Italy

Eduardo Oliva

Laboratoire d'Optique Appliquée
 ENSTA, CNRS
 Ecole Polytechnique
 Chemin de la Hunière
 91671 Palaiseau
 France

David Ros

Université Paris-Sud
 Centre Laser de l'Université Paris Sud
 (EA.4127)
 Bât. 106
 91405 Orsay
 France

Artem Rudenko

Kansas State University
 Department of Physics
 J.R. Macdonald Laboratory
 116 Cardwell Hall
 Manhattan, KS 66506
 USA

Eckart Rühl

Freie Universität Berlin
 Institut für Chemie und Biochemie
 – Physikalische und Theoretische
 Chemie
 Takustr. 3
 14195 Berlin
 Germany

Giuseppe Sansone

Department of Physics
 Politecnico di Milano, Institute of
 Photonics and Nanotechnologies,
 IFN-CNR
 Piazza L. da Vinci 32
 20133 Milano
 Italy

Stephen B. Schouw

The Ohio State University
 Department of Physics
 Columbus, OH 43210
 USA

Stéphane Sebban

Laboratoire d'Optique Appliquée
 ENSTA, CNRS
 Ecole Polytechnique
 Chemin de la Hunière
 91671 Palaiseau
 France

Armin Scrinzi

LMU Munich
Arnold Sommerfeld Center
Theresienstrasse 37
80333 Munich
Germany

Olga Smirnova

Max Born Institute Berlin
Max-Born-Str.-2A
12489 Berlin
Germany

Sarah L. Stebbings

Physik Department
Ludwig-Maximilians-Universität
München
Am Coulombwall 1
85748 Garching
Germany

Mark I. Stockman

Department of Physics and Astronomy
Georgia State University
Atlanta, GA 30303
USA

Frederik Süssmann

Physik Department
Ludwig-Maximilians-Universität
München
Am Coulombwall 1
85748 Garching
Germany

Pedro Velarde

Universidad Politécnica de Madrid
Instituto de Fusion Nuclear
Madrid
Spain

Adam S. Wyatt

University of Oxford
Clarendon Laboratory
Keble Road
Oxford OX1 3RH
United Kingdom

Linda Young

Argonne National Laboratory
Argonne, IL 60439
USA

Philippe Zeitoun

Laboratoire d'Optique Appliquée
ENSTA, CNRS
Ecole Polytechnique
Chemin de la Hunière
91671 Palaiseau
France

Sergey Zherebtsov

Max-Planck Institut für Quantenoptik
Hans-Kopfermann-Str. 1
85748 Garching
Germany

1

Attosecond and XUV Physics: Ultrafast Dynamics and Spectroscopy

Marc Vrakking

1.1

Introduction

Scientific progress is tied to the observation and modeling of the world. Our ability to observe atomic and molecular matter requires tools beyond our natural senses. Following the development of X-ray techniques, it became possible in the twentieth century in biology and chemistry research to observe static structures, from the macroscopic scale down to the nanoscale and even beyond, with atomic resolution. However, many important material properties are not static, and involve elementary physical processes that occur on ultrafast time scales.

The natural time scale for the motion of atoms in molecules, and therefore for the making and breaking of chemical bonds, is in the femtosecond domain ($1\text{ fs} = 10^{-15}\text{ s}$). The observation of chemical or biological transformations therefore typically requires measurements with femtosecond time resolution. Such observations are only possible with correspondingly short light pulses, which then allow the photo-induced initiation of a process of interest using a short “pump” laser pulse, followed by a stroboscopic observation after a well-defined time delay, using an equally short “probe” pulse. In the last few decades, widely tunable femtosecond laser pulses were developed, allowing the emergence of femtosecond spectroscopy (“femtochemistry”) a research field that has meanwhile greatly enriched our understanding of physical, chemical and biological processes. This feat was recognized with the Nobel Prize in Chemistry that was awarded to Ahmed Zewail (Caltech) in 1999 [1].

Photochemical reactions studied by the methods of femtochemistry can commonly be described as making use of the Born–Oppenheimer approximation, where potential energy surfaces describe the energy of all electrons as a function of the atomic coordinates, as well as the resulting forces acting on the atoms. As the atoms move under the influence of these forces, the electrons adiabatically adapt until curve crossings are encountered, where the Born–Oppenheimer approximation breaks down and where the electronic structure may undergo drastic changes on time scales that are however still determined by the atomic motion.

Purely electronic motion, without involvement of atomic motion, can occur on much faster, attosecond time scales ($1\text{ as} = 10^{-18}\text{ s}$), as can be appreciated from the 152 attosecond orbital period of an electron in the Bohr model of atomic hydrogen. Until recently, direct measurements on these time scales were impossible. However, two new ultrafast, extreme ultraviolet (XUV)/X-ray sources, that is, high harmonic generation (HHG) and free-electron lasers (FELs) operating on the basis of self-amplified stimulated emission (SASE), have burst onto the scene in the last decade and are now beginning to provide unprecedented time-resolved access to processes reaching down into the attosecond domain.

It is against this background that the ATTOFEL Initial Training Network was established in 2009 as a training network within the FP7 Marie Curie Program of the European Commission. The acronym ATTOFEL stands for “Ultrafast dynamics using ATTOfemtosecond and XUV Free-Electron Laser sources”, expressing ATTOFEL’s goal of connecting the emerging attosecond and XUV/X-ray FEL scientific communities. ATTOFEL also aims to give scientific training, in the broadest sense, to early stage researchers in this emerging field. The book in front of you is a direct outcome of this training effort and covers material that was presented at an ATTOFEL summer school, organized on the island of Crete in May of 2011, supplemented by a number of additional chapters. In this book, leading scientists in the field of attosecond and XUV/X-ray FEL research provide a comprehensive introduction. The book is intended for new researchers entering the field, while at the same time providing a reference text for researchers that are already active in this research area.

1.2

The Emergence of Attosecond Science

In 2001, two independent research groups around Pierre Agostini at CEA Saclay and Ferenc Krausz at the TU Vienna showed almost simultaneously that attosecond XUV pulses can be created through HHG [2, 3]. These experiments were the result of a decade-long effort aimed towards understanding the dynamics of HHG, and culminating in the realization that HHG might be a viable way to produce attosecond pulses.

In HHG, an intense femtosecond laser, usually a femtosecond Ti:sapphire laser with a central wavelength around 800 nm, is focused on an atomic or molecular gas. As described by Anne L’Huillier in Chapter 10, it was discovered in the late 1980s that XUV radiation can then be produced at laser frequencies that are odd, and in some cases very high multiples of the driver laser frequency (hence the name “high harmonic generation”) [4, 5]. The explanation for the process was provided a few years later by Paul Corkum, who proposed a three-step mechanism starting with strong-field ionization of the target gas by the intense femtosecond laser, followed by acceleration of the released electron in the oscillatory electric field of the laser and, finally, a recombination of the accelerated electron with the ionized atom or molecule, where all the laser energy absorbed in order to ionize and accel-

erate the electron is released in the form of an energetic XUV or X-ray photon [6]. One of the early triumphs of the three-step model was its ability to explain the observed high-energy cutoff of HHG spectra given by $E_{\text{cutoff}} \approx \text{IP} + 3.2U_p$, where IP is the ionization potential of the target gas and U_p the ponderomotive energy, that is, the average kinetic energy of a free electron that is oscillating under the influence of a strong laser field. As Corkum showed using simple classical mechanics applied in the strong field approximation (i.e., neglecting the atomic potential once ionization has taken place, see Chapter 6 by Misha Ivanov), the maximum return energy of an electron that has left a target atom/molecule by tunnel ionization is equal to $3.17U_p$, in close agreement with the experimental observations.

The three-step model can also be used to rationalize why HHG leads to the formation of attosecond laser pulses. The initial ionization step is a highly nonlinear process that requires the absorption of a significant number of photons. Therefore, this process strongly favors the maxima of the oscillatory electric field of the laser, in particular at laser intensities where the tunneling picture applies. Consequently, electrons are not continuously being removed from the target atoms/molecules, but are formed in ultrashort bunches that have a duration much smaller than the optical period of the driving laser. The optical period of an 800 nm laser is only 2.7 fs long, and therefore the electron wave packet that is accelerated has a duration that is typically no more than a few hundred attoseconds long. Accordingly, the re-collision of the electron wave packet with its parent ion necessarily leads to attosecond laser pulses [7]. Of course, rationalizing that HHG ought to lead to the formation of attosecond pulses is one thing; to prove that it does is quite another matter, and this was the main accomplishment of the two aforementioned papers published in 2001 [2, 3].

1.2.1

Attosecond Pulse Trains and Isolated Attosecond Pulses

According to the three-step model, the attosecond pulse formation will occur twice during every intense enough cycle of the driving femtosecond laser pulse. In other words, using typical commercially available femtosecond laser pulses with a few tens of femtosecond duration, HHG will have the tendency to form an attosecond pulse train (APT), rather than an isolated attosecond pulse (IAP). This has had several important consequences.

First of all, performing attosecond pump–probe experiments with an APT intuitively seems very problematic. After all, if we use such a train in a pump–probe experiment (where the pump laser initiates the dynamics of interest and the probe laser makes a time-delayed observation of the evolving dynamics), then there is an uncertainty in the time delay between the pump and probe, since we do not know which attosecond pulse in the train has excited or probed the system. In the years since the first demonstration of APTs in HHG [2], attosecond scientists have learned how to deal with this problem, in particular by configuring experiments where the APTs are used in combination with a co-propagating near-infrared (NIR) laser field (typically a replica of the 800 nm femtosecond laser that was used to gen-

erate the APT). Rather than using the pulse envelope of the co-propagating 800 nm laser, the experiments use the optical cycle of this laser as a clock with attosecond time resolution. After all, 12 h on a normal clock correspond to only 2.7 fs on this “attoclock”! Given that the spacing between the attosecond pulses in the APT is exactly half the 800 nm optical period, all attosecond pulses experience the same 800 nm electric field (up to its sign), making time-resolved studies of electron dynamics on sub-fs time scales possible. For example, small time delays between the XUV-induced ionization of different argon atomic orbitals could be characterized in two-color XUV+NIR experiments using an APT [8]. Several examples of these types of experiments are discussed in this book, see, for example, Chapter 13 by Franck Lépine.

Secondly, very extensive efforts have been developed to tailor the HHG process in a manner that rejects all but one of the attosecond pulses that are produced, in order to be able to configure experiments with IAPs. A number of different routes towards the generation of IAPs have been taken [9], and work in this direction continues to this day [10]. The first successful demonstration by the team of Ferenc Krausz used the selection of cutoff harmonics generated in HHG with a very short (7 fs long) 800 nm driver pulse. When the duration of the 800 nm driver pulse is short enough, the highest energies (produced when U_p is highest) will only be produced during a single half-cycle of the driving laser pulse, thereby producing an IAP. In the years since the initial publication, this technique has been perfected, culminating in the reporting of 80 as IAPs in 2008 [11–16]. Alternatively, methods have been developed over the years that have relied on the use of a driving laser pulse with a time-varying polarization [17, 18], use of a two-color laser field [12], use of intensities that very rapidly increase and ionize the medium, leading to transient phase-matching [13], or using combinations of the above. One of the most recent developments has been the “attosecond lighthouse effect” where HHG is performed with a driver pulse with a time-varying wavefront tilt, leading to a situation where IAPs can be extracted from an APT because in the far field they move off in different directions [10, 19].

1.2.2

Characterization of Attosecond Laser Pulses

Somewhat different characterization methods have been developed for APTs and IAPs. A comprehensive overview of these methods is presented by Adam Wyatt in Chapter 3 of this book. The first characterization of APTs used the RABBITT (reconstruction of attosecond harmonic beating by interference of two-photon transitions) method [20], see also Chapter 10 by Anne L’Huillier, and Chapter 11 by Louis DiMauro. Here, a weak co-propagating NIR laser field (typically $\leq 2 \times 10^{11} \text{ W/cm}^2$) is used. In the measurement, interferences in two-color XUV+NIR photoelectron sidebands are used to characterize the relative phase of a comb of harmonics, providing a full characterization of the APT when combined with a measurement of the harmonic spectrum.

The characterization of IAPs generally relies on stronger NIR laser fields, and uses the principle of the attosecond streak camera [21]: depending on the delay be-

tween the IAP and a co-propagating, moderately strong (typically 10^{12} – 10^{13} W/cm²) NIR laser field, the photoelectrons resulting from ionization by the IAP will be up- or down-shifted. It has been shown that measuring a complete streaking trace, that is, a complete set of photoelectron spectra as a function of XUV-NIR delay, allows the full characterization of both the IAP [18] and the NIR laser pulse [13]. An example of a streaking measurement may be found in Chapter 12 by Giuseppe Sansone.

1.2.3

Experimental Challenges in Attosecond Science

Although the first experimental demonstration of the formation of an IAP was almost immediately followed by a remarkable demonstration of the use of attosecond techniques to measure the lifetime of highly excited atoms undergoing Auger decay (see [22], discussed in Chapter 12 by Giuseppe Sansone), the first few years after that were largely devoted to improvement of the attosecond pulse production and characterization techniques. To do so was necessary, since the experimental use of attosecond pulses poses a number of major challenges.

Given that attosecond pulses can only be synthesized using wavelengths with an optical period in the attosecond domain, the central wavelength of attosecond pulses is automatically in the XUV/X-ray range, where the development of highly reflective dispersive optics is extremely challenging. Moreover, since XUV radiation is absorbed by all materials, the experiments have to be entirely performed in vacuum. This creates challenges for the separation of the attosecond pulses from the NIR laser that has generated them and for the separation of the attosecond pulses generated via the “short” trajectory from those generated via the “long” trajectory (see Chapter 7 by Olga Smirnova and Misha Ivanov). Moreover, attosecond experiments pose extreme requirements on the stability of optical setups. When one considers that a light pulse travels a distance of 30 nm in 100 as and that in certain types of attosecond setups the “pump” and “probe” lasers travel along separate paths over a distance of several meters, then it becomes clear that active stabilization of optical beam paths is often an absolute necessity to retain the attosecond time resolution. Finally, the attosecond pulses obtained by HHG are typically very weak. The conversion efficiency from NIR to XUV is typically on the order of 10^{-6} in HHG, meaning that millijoule-level 800 nm driver pulses will only lead to nanojoule-level XUV/X-ray pulses. In the approaches used for the generation of IAPs, the efficiency is usually even lower. For this reason, the two color XUV-NIR experiments that were described above were up to now the only attosecond experiments possible. However, this is about to change. In the last few years, significant efforts have been undertaken to increase the pulse energy of attosecond pulses, and – in particular – the pulse energy of IAPs, in attempts to make IAP pump-IAP probe experiments possible [23]. Such experiments are extremely important, since they will allow more facile and reliable tracking of electronic motion over time delays exceeding the NIR optical period. Several laboratories have developed attosecond experiments on the basis of larger scale laser systems delivering 800 nm

pulses with several hundreds of millijoule pulse energy [24, 25]. With these systems IAPs with pulse energies in the 100 nJ range have recently been reported [25], which should be enough for IAP pump-IAP probe experiments. At the same time, as discussed by Uwe Morgner in Chapter 2, novel laser architectures like optical parametric chirped pulse amplification (OPCPA) are being introduced, that deliver 800 nm laser pulses with characteristics (in particular, with pulse durations) that are more favorable for generating IAPs than traditional Ti:sapphire lasers [26]. The first experiment using an IAP both to pump and probe attosecond dynamics has recently been published [27].

1.2.4

Attosecond Science as a Driver for Technological Developments

As can already be understood from the previous paragraph, the development of attosecond science is strongly dependent on developments in, especially, laser technology. Conversely, it may justifiably be stated that many current developments in laser technology are directly motivated by their utility in attosecond science.

At the time that the first attosecond experiments got underway, hollow core fiber compression for the generation of intense few-cycle laser pulses had been shown a few years earlier [28, 29]. Furthermore, the development of frequency combs, allowing the production of pulses with a stable carrier envelope offset (CEO) phase and a reproducible carrier envelope phase (CEP) had just been demonstrated for oscillator lasers producing low power (nanojoule-level) laser pulses [30, 31]. Both of these developments were vital for the development of attosecond science, since both of the methods that were conceived early on for the development of IAPs, that is, selection of cutoff harmonics [3, 32] and polarization gating in order to generate IAPs in the plateau region of high harmonic generation [18], required the availability of high power few-cycle CEP-stable driver pulses for the HHG. A key breakthrough came in 2003, when Baltuska *et al.* published the realization of the first CEP-stable driver laser for HHG, based on chirped pulse amplification (CPA) of the output of a CEP-stable oscillator [12]. This allowed, for the first time, the fully reproducible production of IAPs. Since then, stabilization of the carrier envelope phase has remained a key topic in attosecond science, and therefore this topic is discussed in detail in Chapter 4 by Vincent Crozatier, who furthermore discusses novel CEP stabilization schemes that have been developed in the last few years, which greatly improve the CEP quality [33].

As discussed in Chapter 2 by Uwe Morgner, attosecond science continues to stimulate laser development in a number of important directions. As already stated, the development of IAP pump-IAP probe experiments has motivated the implementation of higher power lasers in attosecond experiments, and a first Terawatt-class CEP-stable CPA Ti:sapphire laser has been reported in the literature [34]. Still, to reach the combination of pulse energies and pulse durations that are desirable for IAP production [26], a shift from Ti:sapphire-based CPA technology to OPCPA appears imminent and is already being actively pursued by a number of laser laboratories around the world. A major advantage of OPCPA is that

the sub-10 fs pulse durations that are a prerequisite for many of the IAP generation schemes can readily be obtained directly from the amplifier, benefitting from the large phase-matching bandwidth in a noncollinear optical parametric amplifier (NOPA). One of the main challenges is the development of suitable picosecond pump lasers for pumping the OPCPA. However, in the last few years a number of ytterbium-based systems have been reported with pulse characteristics that are fully adequate [35, 36], and first OPCPA-based attosecond experiments are likely to be performed very soon.

Another direction for OPCPA that is likely to become very important is the development of high repetition rate amplifier systems. Current Ti:sapphire lasers that are appropriate for use in attosecond science are largely limited to repetition rates ≤ 10 kHz, making it extremely challenging to implement detection schemes that rely on coincident detection of multiple particles from a single pump–probe event, such as the electron(s) and ion(s) formed in an ionization event (see Chapter 16 by Artem Rudenko). However, with attosecond experiments addressing increasingly complex systems, the needs for the implementation of such coincident detection schemes has grown substantially in the last few years. Using OPCPA, the development of CEP-stable, high repetition rate, few-cycle drivers that are developed for attosecond science has already been reported and we may anticipate the first pump–probe experiments on attosecond time scales soon [37, 38].

Finally, we would like to draw attention to the development of mid-infrared lasers motivated by attosecond science. As discussed in detail by Louis DiMauro in Chapter 11, the scaling of the photon energy of the attosecond pulses with U_p , allows a dramatic scaling with wavelength, given that $U_p = F_{\text{laser}}^2/4\omega_{\text{laser}}^2$ (a.u.), where F_{laser} is the peak electric field of the laser and $\omega_{\text{laser}} = 2\pi c/\lambda_{\text{laser}}$ is the laser frequency. In other words, the ponderomotive energy, and hence the photon energy achievable in HHG, scale quadratically with the laser wavelength. In principle, the efficiency of HHG at longer wavelength scales very unfavorably [39], but this can be overcome to a large extent using appropriate target and phase-matching geometries [40], providing a major impetus for the further development of mid-infrared, OPCPA-based driver lasers for HHG. In fact, the generation of keV X-rays by HHG using a 4 μm driver laser was recently demonstrated [41].

The usefulness of sophisticated, short pulse laser techniques in ultrafast pump–probe experiments is only as good as the characterization of the pulses. To this end, Chapter 3 by Adam Wyatt discusses in detail the wide range of available methods for pulse characterization at both the near-infrared driver wavelengths and in the XUV.

1.3

Applications of Attosecond Laser Pulses

One decade after the first demonstrations of attosecond laser pulses [2, 3], two-color attosecond pump–probe experiments have addressed electron dynamics in atomic [22, 42–45] and molecular physics [46–48], in surface science [49] and in

solid-state physics [50]. In addition, attosecond time scale dynamics has been inferred in a range of strong field laser-induced phenomena [51–54], paving the way to both current and future attosecond experiments.

Along the way, the arsenal of possible observables used in attosecond experiments has been significantly expanded. While many of the experimental implementations of attosecond pump–probe spectroscopy have used photoelectron-based measurements schemes developed for the characterization of attosecond laser pulses (i.e., RABBITT-like detection in the case of APTs and streaking in the case of IAPs), the technique of attosecond chronoscopy, that is, measuring atomic/molecular charge states as a function of delay, has been used for experiments involving multiple ionization, such as experiments where shake-up and/or Auger decay play a role [42, 55]. These experiments are discussed by Giuseppe Sansone in Chapter 12. Another technique that is discussed in this chapter is attosecond transient absorption spectroscopy (ATS), which is rapidly becoming the technique of choice in many attosecond laboratories around the world [43, 56]. In ATS, NIR-induced changes in the XUV transmission through a sample are measured. A major advantage of this method is that the time resolution that can be achieved in the pump–probe experiment and the energy resolution in the absorption measurement are not limited by a Fourier relationship, in other words very high spectral resolution (~ 20 meV) can be combined with very high time resolution (≤ 50 as).

In molecular systems, a main interest is in the attosecond time scale observation and control of intramolecular electronic processes such as charge transfer and charge migration. For this, measurements of charge asymmetries in fragment ion kinetic energy and angular distributions resulting from dissociative ionization have proven to be a useful method, allowing to visualize both coupling of electronic and nuclear degrees of freedom, and correlations in the optical response of multiple electrons [46]. In molecular systems, the development of attosecond experiments has sparked considerable theoretical interest. It has been proposed that attosecond time scale excitation of electronic coherences (e.g., by means of the ultrafast removal of an electron, thereby producing the molecular ion in a coherent superposition of ionic states [57–59]), may lead to migration of the hole in the electron density across the molecular frame, on time scales preceding any nuclear motion, and thereby possibly paving the way for novel control schemes for molecular reactivity [60]. First experiments have recently been performed that may be seen as first steps towards this perspective, which along with an overview of existing results are discussed in detail by Franck Lépine in Chapter 13.

Ionization by an XUV pulse is not the only way that a hole can be produced in the electron density of a molecular wave function. After all, as described by the three-step model, the process of HHG starts with an ionization process itself [6]. In the last few years, the production of multiple electronic states in atomic/molecular strong field ionization [61] in the course of HHG and correspondingly, the creation of rapidly moving holes in the electron density, has been intensively discussed. In fact, working alongside the attosecond science community relying on pump–probe spectroscopy using attosecond pulses, a second “dynamical imaging” research community has developed, where the process of HHG itself is studied in great detail.

Important successes of this work have been tomographic reconstruction of the orbitals that participate in the HHG process [62], the reconstruction of electronic wave packets that exist within HHG from the time that the photoelectron leaves the atom/molecule via tunneling, until the time of the laser-driven electron-ion recombination [63, 64], the extraction of molecular structural information from HHG experiments [65], and the quantitative extraction of the time when an electron exits from the tunneling barrier in a HHG experiment [66]. Against this background Olga Smirnova and Misha Ivanov discuss, in Chapter 7, the quantum-mechanical framework for a theoretical description of HHG, connecting the so-called simple man's model to more sophisticated methods that have been developed in the last few years. In doing so, they also address the role of multiple electrons in the HHG process.

Though not yet studied experimentally in attosecond pump–probe experiments, multielectronic (plasmonic) aspects are of the essence in experiments on nanoparticles and nanostructures that are discussed by Matthias Kling in Chapter 14. Nanoparticles and nanostructures allow both spatial and temporal tailoring of light fields on, respectively, nanometer length scales and (sub)-femtosecond time scales. In combination with the field enhancement effects that are intrinsic to these structures, this offers the promise of important implications in nanotechnology relevant to ultrafast computation and telecommunication. Already, plasmonic effects have been exploited in above threshold ionization (ATI) from nanoparticles [52] and nanoscale metal tips [53], and although very controversially discussed, in HHG from bowtie arrays [67] and three-dimensional metal nanostructures [68]. The possibility to visualize the nanoplasmonic field through streaking of photoelectrons is discussed in the chapter and is an active field of research.

1.4

Ultrafast Science Using XUV/X-ray Free Electron Lasers

As discussed in Section 1.2, one of the main challenges in attosecond science is the relatively low pulse energy, which makes it very challenging to perform attosecond pump-attosecond probe experiments. Moreover, although scaling of HHG techniques to keV photon energies has shown considerable progress in the last few years [41], the photon energies where HHG is used in pump–probe experiments so far tend to remain quite significantly below the energies required for the ionization of core shell electrons. For example, HHG in the “water window” region between the carbon K-edge at 284.2 eV (4.4 nm) and the oxygen K-edge at 543.1 eV (2.3 nm) [69] has been demonstrated, but has not yet been extensively exploited in experiments. These two limitations of HHG, the low pulse energy and the limited tuning range towards high photon energies, are overcome in dramatic fashion by the first SASE XUV/X-ray free-electron lasers (FELs) that have come into operation within the last decade. On these instruments, the interest in the use of XUV/X-ray light is not so much the short optical period that provides access to the generation of attosecond pulses, but the high pulse intensities and high photon

energies, the latter allowing the configuration of diffraction experiments, either using the XUV/X-ray photons directly, or using the XUV/X-ray photons to eject energetic photoelectrons with a short de Broglie wavelength, that can be used to extract structural information [70]. FELs provide unprecedented XUV/X-ray intensities, allowing studies of multiphoton ionization in this wavelength range for the first time.

As we observed in beginning of this introduction, X-ray techniques acquired a great prominence in the twentieth century as a tool for resolving structural information, the main implementation being X-ray diffraction from crystalline materials using synchrotron radiation. The development of XUV/X-ray FELs is driven to a considerable extent by the desire to be able to use X-ray diffraction techniques on systems that cannot be crystallized [71], with the added bonus of time resolution down into the femtosecond domain. Based on this motivation, intensive research efforts have gotten under way around the world to develop X-ray FELs, as well as the science that is made possible by them.

In Hamburg, the Tesla Test Facility (TTF) at DESY became the first operational XUV SASE FEL in 2000. TTF was used for pioneering experiments on Coulomb explosion of rare gas clusters [72], revealing novel ionization mechanisms that had not been observed in NIR-induced Coulomb explosions that had been intensively studied a decade earlier. In 2005, FLASH succeeded TTF as the world's first soft X-ray FEL user facility [73]. At FLASH, the first proof-of-principle experiments on coherent diffractive imaging were performed, showing that the technique can be implemented at FELs, and allowing the imaging of structures with sub-100 nm resolution before irreversible damage of the object under investigation set in [74–76]. Some of the early experiments at FLASH and the conceptual and theoretical framework underlying coherent diffractive imaging are discussed in detail by Willem Boutin in Chapter 17 of this book.

Beside the initial experiments on coherent diffractive imaging, FLASH was used to study the interaction of atoms and molecules with intense XUV light at a fundamental level. As explained in detail by Artem Rudenko in Chapter 15, ionization at high intensity by an XUV/X-ray FEL proceeds according to mechanisms that are radically different from the mechanisms that are at play at NIR wavelengths. For example, the ponderomotive energy, which plays such an important role in the description of NIR laser-induced HHG, is virtually absent at XUV/X-ray wavelengths. Accordingly, ionization processes are best described in a (multi)-photon picture. Besides studies of ionization processes, experiments were also performed at FLASH exploiting the femtosecond time resolution inherent in the source to monitor time-resolved molecular dynamics, and these experiments are discussed as well.

The year 2009 saw the commissioning of the Linac Coherent Light Source (LCLS) in Stanford, the world's first hard X-ray FEL, producing multi-mJ, femtosecond X-ray pulses down to 1.2 Ångström (10 keV) [77]. This soon led to major improvements in the resolution that could be achieved in coherent diffractive imaging experiments. First experiments on serial crystallography of nanocrystals were published in 2011, and showed how the accumulation of a large number of single-

shot diffraction patterns enabled retrieval of the structure of Photosystem I with 8 Å spatial resolution [78]. While these initial experiments were performed using a “moderate” photon energy of 1.8 keV, this result has since been improved upon, by using 9.4 keV hard X-ray photons, leading to a spatial resolution of just 2.1 Å [79].

LCLS allowed studies of X-ray laser-induced ionization at unprecedented intensities. These experiments, which are highly relevant for defining the conditions where coherent diffractive imaging experiments are possible, are discussed in detail in Chapter 16 by Linda Young, underscoring the greatly increased importance of inner shell and Auger processes in the ionization at X-ray wavelengths. She also discusses some of the other atomic and molecular physics pursued at LCLS shortly after it came on-line, including efforts to characterize the temporal properties of the LCLS beam.

Since 2011, the SACLAC hard X-ray FEL is operational in Japan [80]. Moreover, a number of additional hard X-ray FELs are planned around the world, including the European XFEL in Hamburg that is expected to generate first light in 2015, and the SwissFEL that is expected to come online in 2017. Extending the capabilities of FELs in the soft X-ray range, FERMI@ELETTRA came into operation just before the end of 2010 [81]. A special feature of this FEL is its seeded operation, thereby greatly improving the coherence properties of the source, as well as the synchronization of the FEL with external lasers, which is of crucial importance for pump-probe experiments. Seeding of hard X-ray FELs is also vitally important, and first results were recently obtained at LCLS [82].

Free-electron lasers are clearly “big machines” running at enormous costs and subject to considerable restrictions on the available beam time for individual users. For this reason, efforts to obtain high-energy XUV/X-ray pulses by alternative methods continue to this day. In Chapter 5, Philippe Zeitoun describes ongoing efforts aimed at developing tabletop X-ray lasers to a level where single-shot coherent diffractive imaging becomes possible. He reviews progress that has been achieved in recent years, including the operation of HHG-seeded tabletop X-ray lasers, and describes a roadmap for the development of an approximately 6 mJ, fully coherent X-ray laser, that is, even surpassing what can be achieved at an FEL today.

1.5

The Interplay between Experiment and Theory

The complexity of the atomic and molecular physics that is addressed by the attosecond pump–probe and FEL experiments described above is considerable. Therefore, this book also contains a number of chapters that are devoted to the theoretical methods that are vitally important for understanding the results of experiments that are being performed or that are likely to be performed shortly. The importance of Chapters 6 and 7 by Misha Ivanov and Olga Smirnova, explaining the fundamentals of strong field ionization and the theory underlying high harmonic generation, has already been explained in Sections 1.2 and 1.3. Complementing these chapters, Armin Scrinzi discusses several methods for numerically solving

the time-dependent Schrödinger equation (TDSE) in Chapter 8. He discusses in detail considerations that come into play when one seeks to numerically integrate the TDSE on a grid, as well as the development of a number of methods that deal with multielectron problems by working with a suitable “essential states” basis. An important example is the multiconfiguration time-dependent Hartree–Fock method (MCTDHF), which allows, for example, to assess the role of multielectron effects in HHG.

In view of their increasing importance in many pump–probe experiments, Robert Lucchese and Danielle Dowek discuss in Chapter 9 the formalism for calculating and evaluating photoelectron angular distributions (PADs) in atomic or molecular photoionization. They show how PADs can be completely described in terms of five angular functions, and describe methods that can be used to compute and measure these PADs, including the use of coincident photoelectron-fragment ion detection (leading to molecular frame photoelectron angular distribution (MF-PAD), respectively recoil frame photoelectron angular distribution (RFPAD) measurements), and the use of dynamically aligned or oriented molecular samples [83–86]. Using HHG and FEL sources and exploiting the short de Broglie wavelength of high-energy photoelectrons, novel methods for time-resolved femtochemistry may become possible that no longer rely on detailed knowledge of the potential energy surfaces of the molecules under investigation, but that allow the extraction of the time-dependent positions of all atoms through a measurement of holographic interferences [70]. We note that this type of structural information is not exclusively available in XUV-induced photoionization processes, but may also be available when energetic photoelectrons are generated by means of near-infrared or mid-infrared induced strong-field ionization, where first experiments have recently been performed illustrating the possibility of achieving attosecond time resolution [87, 88].

1.6 Conclusion and Outlook

Attosecond and XUV Physics, in the form of ground-breaking experimental work exploiting novel XUV/X-ray sources (both HHG and FELs), and in the form of novel theoretical and numerical methods, provides a new path towards understanding and controlling microscopic light-induced processes, that is, on atomic length scales and on time scales reaching down into the attosecond domain. In this book, mirroring the program of a summer school organized by the ATTOFEL network where the latest progress in this research field was presented, a range of internationally renowned specialists provide a snapshot of the current status of this extremely rapidly developing field. It is our hope that in the next few years, until its contents will be superseded by innovations that currently take place or will take place in laboratories around the world, this book will provide a valuable reference, introducing and inspiring scientists that want to acquaint themselves with this exciting field.

References

- 1 Zewail, A.H. (2000) Femtochemistry: Atomic-scale dynamics of the chemical bond using ultrafast lasers – (Nobel lecture). *Angew. Chem. Int. Edn.*, **39**, 2587.
- 2 Paul, P.M. *et al.* (2001) Observation of a train of attosecond pulses from high harmonic generation. *Science*, **292**, 1689.
- 3 Hentschel, M. *et al.* (2001) Attosecond metrology. *Nature*, **414**, 509.
- 4 McPherson, A. *et al.* (1987) Studies of multiphoton production of vacuum-ultraviolet radiation in the rare gases. *J. Opt. Soc. Am. B*, **4**, 595.
- 5 Ferray, M. *et al.* (1988) Multiple-harmonic conversion of 1064 nm radiation in rare gases. *J. Phys. B*, **21**, L31.
- 6 Corkum, P.B. (1993) Plasma perspective on strong-field multiphoton ionization. *Phys. Rev. Lett.*, **71**, 1994.
- 7 Agostini, P. and DiMauro, L.F. (2004) The physics of attosecond light pulses. *Rep. Progr. Phys.*, **67**, 813.
- 8 Klünder, K. *et al.* (2011) Probing single-photon ionization on the attosecond time scale. *Phys. Rev. Lett.*, **106**, 143002.
- 9 Krausz, F. and Ivanov, M. (2009) Attosecond physics. *Rev. Mod. Phys.*, **81**, 163.
- 10 Wheeler, J.A. *et al.* (2012) Attosecond lighthouses from plasma mirrors. *Nat. Photonics*, **6**, 828.
- 11 Kienberger, R. *et al.* (2002) Steering attosecond electron wave packets with light. *Science*, **297**, 1144.
- 12 Baltuska, A. *et al.* (2003) Attosecond control of electronic processes by intense light fields. *Nature*, **421**, 611.
- 13 Goulielmakis, E. *et al.* (2004) Direct measurement of light waves. *Science*, **305**, 1267.
- 14 Kienberger, R. *et al.* (2004) Atomic transient recorder. *Nature*, **427**, 817.
- 15 Goulielmakis, E. *et al.* (2007) Attosecond control and measurement: Lightwave electronics. *Science*, **317**, 769.
- 16 Goulielmakis, E. *et al.* (2008) Single-cycle nonlinear optics. *Science*, **320**, 1614.
- 17 Sola, I.J. *et al.* (2006) Controlling attosecond electron dynamics by phase-stabilized polarization gating. *Nat. Phys.*, **2**, 319.
- 18 Sansone, G. *et al.* (2006) Isolated single-cycle attosecond pulses. *Science*, **314**, 443.
- 19 Vincenti, H. and Quéré, F. (2012) Attosecond lighthouses: How to use spatiotemporally coupled light fields to generate isolated attosecond pulses. *Phys. Rev. Lett.*, **108**, 113904.
- 20 Muller, H.G. (2002) Reconstruction of attosecond harmonic beating by interference of two-photon transitions. *Appl. Phys. B*, **74**, S17.
- 21 Itatani, J. *et al.* (2002) Attosecond streak camera. *Phys. Rev. Lett.*, **88**, 173903.
- 22 Drescher, M. *et al.* (2002) Time-resolved atomic inner-shell spectroscopy. *Nature*, **419**, 803.
- 23 Sansone, G., Poletto, L., and Nisoli, M. (2011) High-energy attosecond light sources. *Nat. Photonics*, **5**, 656.
- 24 Tzallas, P. *et al.* (2007) Generation of intense continuum extreme-ultraviolet radiation by many-cycle laser fields. *Nat. Phys.*, **3**, 846.
- 25 Wu, Y. *et al.* (2013) Generation of high-flux attosecond extreme ultraviolet continuum with a 10 TW laser. *Appl. Phys. Lett.*, **102**, 201104.
- 26 Herrmann, D. *et al.* (2009) Generation of sub-three-cycle, 16 TW light pulses by using noncollinear optical parametric chirped-pulse amplification. *Opt. Lett.*, **34**, 2459.
- 27 Tzallas, P., Skantzakis, E., Nikolopoulos, L.A.A., Tsakiris, G.D., and Charalambidis, D. (2011) Extreme-ultraviolet pump–probe studies of one-femtosecond-scale electron dynamics. *Nat. Phys.*, **7**, 781.
- 28 Nisoli, M., DeSilvestri, S., Svelto, O. (1996) Generation of high energy 10 fs pulses by a new pulse compression technique. *Appl. Phys. Lett.*, **68**, 2793.
- 29 Nisoli, M. *et al.* (1997) Compression of high-energy laser pulses below 5 fs. *Opt. Lett.*, **22**, 522.
- 30 Reichert, J., Holzwarth, R., Udem, T., Hansch, T.W. (1999) Measuring the frequency of light with mode-locked lasers. *Opt. Commun.*, **172**, 59.

- 31** Telle, H.R. *et al.* (1999) Carrier-envelope offset phase control: A novel concept for absolute optical frequency measurement and ultrashort pulse generation. *Appl. Phys. B*, **69**, 327.
- 32** Kienberger, R. *et al.* (2002) Sub-femtosecond X-ray pulse generation and measurement. *Appl. Phys. B*, **74**, S3.
- 33** Koke, S. *et al.* (2010) Direct frequency comb synthesis with arbitrary offset and shot-noise-limited phase noise. *Nat. Photonics*, **4**, 462.
- 34** Gademann, G., Plé, F., Paul, P.-M., and Vrakking, M.J.J. (2011) Carrier-envelope phase stabilization of a terawatt level chirped pulse amplifier for generation of intense isolated attosecond pulses. *Opt. Express*, **19**, 24922.
- 35** Tummler, J., Jung, R., Stiel, H., Nickles, P.V., and Sandner, W. (2009) High-repetition-rate chirped-pulse-amplification thin-disk laser system with joule-level pulse energy. *Opt. Lett.*, **34**, 1378.
- 36** Metzger, T. *et al.* (2009) High-repetition-rate picosecond pump laser based on a Yb:YAG disk amplifier for optical parametric amplification. *Opt. Lett.*, **34**, 2123.
- 37** Krebs, M. *et al.* (2013) Towards isolated attosecond pulses at megahertz repetition rates. *Nat. Photonics*, **7**, 555.
- 38** Furch, F. *et al.* (2013) Carrier-envelope phase stable few-cycle pulses at 400 kHz for electron-ion coincidence experiments. *Opt. Express*, **21**, 22671–22682.
- 39** Tate, J. *et al.* (2007) Scaling of wave-packet dynamics in an intense mid-infrared field. *Phys. Rev. Lett.*, **98**, 013901.
- 40** Popmintchev, T. *et al.* (2009) Phase matching of high harmonic generation in the soft and hard X-ray regions of the spectrum. *Proc. Natl. Acad. Sci. USA*, **106**, 10516.
- 41** Popmintchev, T. *et al.* (2012) Bright coherent ultrahigh harmonics in the keV X-ray regime from mid-infrared femtosecond lasers. *Science*, **336**, 1287.
- 42** Uiberacker, M. *et al.* (2007) Attosecond real-time observation of electron tunnelling in atoms. *Nature*, **446**, 627.
- 43** Goulielmakis, E. *et al.* (2010) Real-time observation of valence electron motion. *Nature*, **466**, 739.
- 44** Schultze, M. *et al.* (2010) Delay in photoemission. *Science*, **328**, 1658.
- 45** Mauritsson, J. *et al.* (2010) Attosecond electron spectroscopy using a novel interferometric pump–probe technique. *Phys. Rev. Lett.*, **105**, 053001.
- 46** Sansone, G. *et al.* (2010) Electron localization following attosecond molecular photoionization. *Nature*, **465**, 763.
- 47** Kelkensberg, F. *et al.* (2011) Attosecond control in photoionization of hydrogen molecules. *Phys. Rev. Lett.*, **107**, 043002.
- 48** Neidel, C. *et al.* (2013) Probing time-dependent molecular dipoles on the attosecond time scale. *Phys. Rev. Lett.*, **111**, 033001.
- 49** Cavalieri, A.L. *et al.* (2007) Attosecond spectroscopy in condensed matter. *Nature*, **449**, 1029.
- 50** Schultze, M. *et al.* (2013) Controlling dielectrics with the electric field of light. *Nature*, **493**, 75.
- 51** Kling, M.F. *et al.* (2006) Control of electron localization in molecular dissociation. *Science*, **312**, 246.
- 52** Zherebtsov, S. *et al.* (2011) Controlled near-field enhanced electron acceleration from dielectric nanospheres with intense few-cycle laser fields. *Nat. Phys.*, **7**, 656.
- 53** Kruger, M., Schenk, M., Hommelhoff, P. (2011) Attosecond control of electrons emitted from a nanoscale metal tip. *Nature*, **475**, 78.
- 54** Schiffrin, A. *et al.* (2013) Optical-field-induced current in dielectrics. *Nature*, **493**, 70.
- 55** Uphues, T. *et al.* (2008) Ion-charge-state chronoscopy of cascaded atomic Auger decay. *New J. Phys.*, **10**, 025009.
- 56** Ott, C. *et al.* (2013) Lorentz meets Fano in spectral line shapes: A universal phase and its laser control. *Science*, **340**, 716.
- 57** Breidbach, J. and Cederbaum, L.S. (2005) Universal attosecond response to the removal of an electron. *Phys. Rev. Lett.*, **94**, 033901.
- 58** Breidbach, J. and Cederbaum, L.S. (2003) Migration of holes: Formalism, mechanisms, and illustrative applications. *J. Chem. Phys.*, **118**, 3983.

- 59** Remacle, F. and Levine, R.D. (2006) An electronic time scale in chemistry. *Proc. Natl. Acad. Sci. USA*, **103**, 6793.
- 60** Weinkauf, R., Schlag, E.W., Martinez, T.J., and Levine, R.D. (1997) Nonstationary electronic states and site-selective reactivity. *J. Phys. Chem. A*, **101**, 7702.
- 61** Boguslavskiy, A.E. *et al.* (2012) The multielectron ionization dynamics underlying attosecond strong-field spectroscopies. *Science*, **335**, 1336.
- 62** Itatani, J. *et al.* (2004) Tomographic imaging of molecular orbitals. *Nature*, **432**, 867.
- 63** Smirnova, O. *et al.* (2009) High harmonic interferometry of multi-electron dynamics in molecules. *Nature*, **460**, 972.
- 64** Haessler, S. *et al.* (2010) Attosecond imaging of molecular electronic wavepackets. *Nat. Phys.*, **6**, 200.
- 65** Kanai, T., Minemoto, S., and Sakai, H. (2005) Quantum interference during high-order harmonic generation from aligned molecules. *Nature*, **435**, 470.
- 66** Shafir, D. *et al.* (2012) Resolving the time when an electron exits a tunnelling barrier. *Nature*, **485**, 343.
- 67** Kim, S. *et al.* (2008) High-harmonic generation by resonant plasmon field enhancement. *Nature*, **453**, 757.
- 68** Park, I.Y. *et al.* (2011) Plasmonic generation of ultrashort extreme-ultraviolet light pulses. *Nat. Photonics*, **5**, 678.
- 69** (2009) X-RAY DATA BOOKLET. Center for X-ray Optics and Advanced Light Source, Lawrence Berkeley National Laboratory.
- 70** Krasniqi, F. *et al.* (2010) Imaging molecules from within: Ultrafast angstrom-scale structure determination of molecules via photoelectron holography using free-electron lasers. *Phys. Rev. A*, **81**, 033411.
- 71** Neutze, R., Wouts, R., van der Spoel, D., Weckert, E., and Hajdu, J. (2000) Potential for biomolecular imaging with femtosecond X-ray pulses. *Nature*, **406**, 752.
- 72** Wabnitz, H. *et al.* (2002) Multiple ionization of atom clusters by intense soft X-rays from a free-electron laser. *Nature*, **420**, 482.
- 73** Ackermann, W. *et al.* (2007) Operation of a free-electron laser from the extreme ultraviolet to the water window. *Nat. Photonics*, **1**, 336.
- 74** Chapman, H.N. *et al.* (2006) Femtosecond diffractive imaging with a soft-X-ray free-electron laser. *Nat. Phys.*, **2**, 839.
- 75** Chapman, H.N. *et al.* (2007) Femtosecond time-delay X-ray holography. *Nature*, **448**, 676.
- 76** Marchesini, S. *et al.* (2008) Massively parallel X-ray holography. *Nat. Photonics*, **2**, 560.
- 77** Emma, P. *et al.* (2010) First lasing and operation of an angstrom-wavelength free-electron laser. *Nat. Photonics*, **4**, 641.
- 78** Chapman, H.N. *et al.* (2011) Femtosecond X-ray protein nanocrystallography. *Nature*, **470**, 73.
- 79** Redecke, L. *et al.* (2013) Natively inhibited *trypanosoma brucei* cathepsin B structure determined by using an X-ray laser. *Science*, **339**, 227.
- 80** Pile, D. (2011) X-rays first light from SACLA. *Nat. Photonics*, **5**, 456.
- 81** Allaria, E. *et al.* (2012) Highly coherent and stable pulses from the FERMI seeded free-electron laser in the extreme ultraviolet. *Nat. Photonics*, **6**, 699.
- 82** Amann, J. *et al.* (2012) Demonstration of self-seeding in a hard-X-ray free-electron laser. *Nat. Photonics*, **6**, 693.
- 83** Rosca-Pruna, F. and Vrakking, M.J.J. (2001) Experimental observation of revival structures in picosecond laser-induced alignment of I₂. *Phys. Rev. Lett.*, **87**, 153902.
- 84** Stapelfeldt, H. and Seideman, T. (2003) Colloquium: Aligning molecules with strong laser pulses. *Rev. Mod. Phys.*, **75**, 543.
- 85** Ghafur, O. *et al.* (2009) Impulsive orientation and alignment of quantum-state-selected NO molecules. *Nat. Phys.*, **5**, 289.
- 86** Schröter, C., Kosma, K., and Schultz, T. (2011) CRASY: Mass- or electron-correlated rotational alignment spectroscopy. *Science*, **333**, 1011.
- 87** Huismans, Y. *et al.* (2011) Time-resolved holography with photoelectrons. *Science*, **331**, 61.
- 88** Blaga, C.I. *et al.* (2012) Imaging ultrafast molecular dynamics with laser-induced electron diffraction. *Nature*, **483**, 194.

Part One
Laser Techniques

2

Ultrafast Laser Oscillators and Amplifiers

Uwe Morgner

2.1

Introduction

Fifty years ago, in the early days of laser physics, scientists already recognized the tremendous potential of lasers for generating ultrashort light pulses with unique properties and applications. In the following decades, scientists and engineers invented the concepts of Q-switching and mode-locking, and, already in 1970, pulses with picosecond duration were created from dye lasers (see Figure 2.1) [1, 2]. In the late 1980s, an impressive development of solid-state laser materials created neodymium-doped crystals and explored the potential of chromium-doped mate-

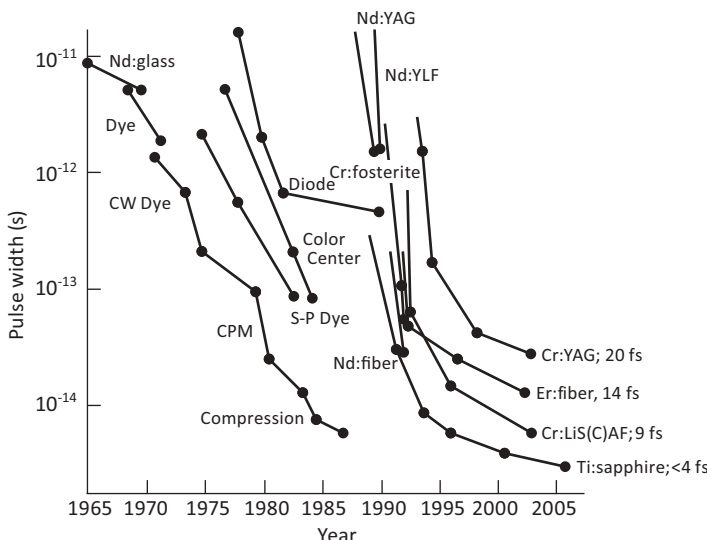


Figure 2.1 The steep decline of pulse durations directly obtained from laser oscillators from the beginning of laser physics to this day (extended from [5]).

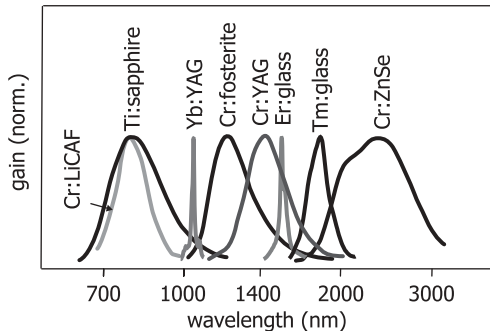


Figure 2.2 Overview of the gain spectra of important broadband solid-state laser materials.

rials. In the early 2000s, pulses emitted from Ti:sapphire oscillators reached durations of a few femtoseconds, close to the limit of a single optical cycle [3, 4].

In the meantime, a large number of broadband solid-state laser materials have been explored, covering the wavelength range from the near-UV to the near-infrared (see Figure 2.2). The most prominent laser material for the generation of femtosecond pulses in the few-cycle range is still Ti:sapphire, which offers a large gain bandwidth, large heat conductivity, and a readily available high crystal quality [6–9]. For high-power laser light generation, Yb-doped materials became the most important gain media due to the availability of high brightness semiconductor pump lasers and a small quantum defect [10–17].

This book chapter shall give a brief overview of current laser technology for the generation of ultrashort and high-energy femtosecond laser pulses. Considering the extraordinary extent of this research area, this chapter can only highlight some selected topics and must refer to recent review papers for details. The emphasis here is laid on sources of laser light for strong-field science, for high harmonic generation, and for the generation of attosecond pulses. Thus, after a brief overview of few-cycle pulse generation and laser oscillators, different amplification concepts will be introduced and the current literature will be referenced.

2.2

Mode-Locking and Few-Cycle Pulse Generation

For the production of ultrashort laser pulses, the phases of all frequency components in a laser pulse must be locked. The general principle of mode-locking is sketched in Figure 2.3. The resonator determines the longitudinal modes by imposing the constraint that an integer number of wavelengths has to fit into the cavity length. If the modes are spectrally equidistant and excited in phase, they interfere constructively at exactly one position inside the resonator and form a short pulse. The pulse duration is inversely proportional to the number of excited and phase coherent modes. The equidistance of modes, and therefore the achievable pulse duration, is a matter of cavity dispersion management. The generation of *few-cycle pulses*

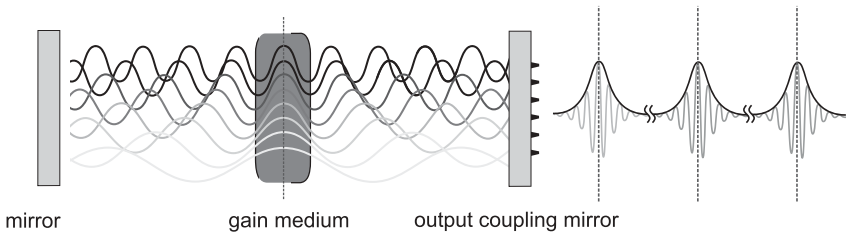


Figure 2.3 The mode-locking principle. The coherent superposition of equidistant longitudinal resonator modes results in a periodic pulse train of ultrashort laser pulses.

was enabled in the 1990s with the development of sophisticated dispersion compensation technology, most notably the dispersive mirror concepts [18–27]. This led to the shortest pulses directly from laser oscillators [3, 4, 28–32] with nJ pulse energies. The predominant mode-locking mechanism for few-cycle pulse generation, directly from the oscillator, is Kerr lens mode-locking (KLM), where nonlinear Kerr self-focusing discriminates the short pulses from the longer low-intensity background.

Nonzero dispersion in the cavity results in a difference between group- and phase-velocity of the propagating pulse, giving rise to a pulse-to-pulse shift $\Delta\phi$ of the carrier envelope offset phase (CEO phase, see Figure 2.4) between subsequent pulses with repetition rate f_{rep} [33–37]. This pulse-to-pulse shift defines the offset frequency $f_{\text{CEO}} = \Delta\phi/2\pi \cdot f_{\text{rep}}$, so that each tooth of the comb f_m has a frequency that is defined by an integer number m via $f_m = f_{\text{CEO}} + m \cdot f_{\text{rep}}$. These simple relations between repetition rate and optical frequency allow the syn-

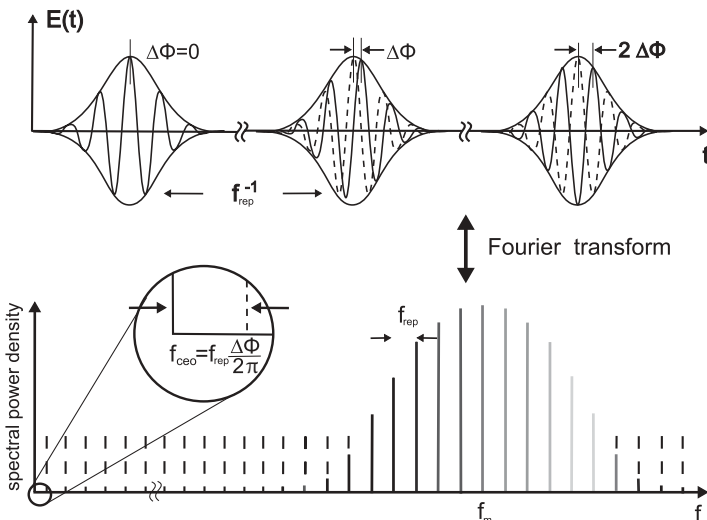


Figure 2.4 The phase $\Delta\phi$ between the carrier peak and the envelope peak (carrier envelope offset phase, CEO phase) shifts from pulse to pulse. This shift defines the offset frequency f_{CEO} of the mode comb.

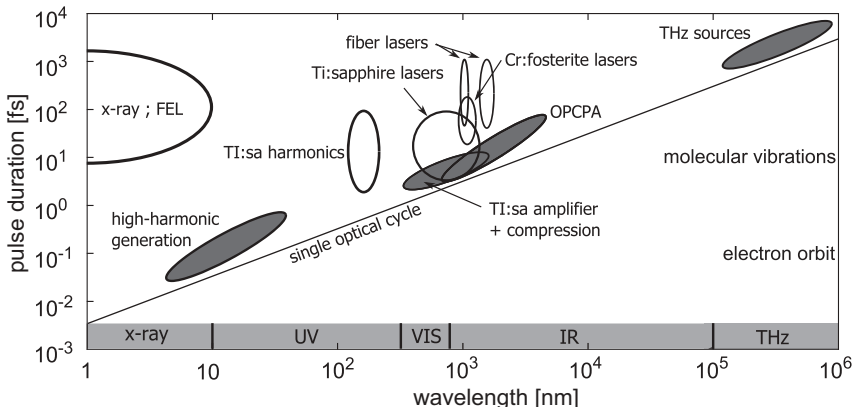


Figure 2.5 Coherent light pulses in the few-cycle regime from different sources. The diagonal represents the single-cycle pulse.

chronization of rather low-frequency clocks with the high frequencies of optical waves. The frequency comb technique therefore revolutionized precision frequency metrology [38]. The carrier envelope phase plays a significant role in attosecond science, defining the temporal position and the strength of the major field oscillation.

The high-energy regime has been explored by chirped pulse amplification (CPA) concepts [39] (see also Figure 2.10), where nonlinear damage of the amplifying gain medium is avoided by dispersive stretching of the pulse duration beforehand, for example, by a grating sequence. After amplification the high-energy pulse is then recompressed with the opposite dispersion to a Fourier-limited short pulse. For the generation of few-cycles, the high-energy pulses are spectrally broadened by self-phase modulation in gas filled capillaries [40–45] or filaments [46–48]. Filaments are self-guiding light ducts in gas where defocusing due to diffraction and plasma formation is balanced by nonlinear self-focusing, leading to a high-intensity channel much longer than the Rayleigh length of the beam [49–51]. Based on dispersive mirrors as well as on other adaptive techniques such as the DAZZLER [52] or 4-f LCD-based schemes [53–57], the output reached the single-cycle limit (2.7 fs at 800 nm [43]). Figure 2.5 summarizes the state-of-the-art regarding pulse durations of different laser light sources.

The abovementioned laser technology has been very successful in the visible and near-IR spectral range. In the long-wavelength range, based on methods such as optical rectification or photoconductive switches, the single-cycle THz pulse is standard technology [59–61]. On the short wavelength side, the shortest pulses – attosecond pulses – have been generated by high harmonic generation in the XUV. For an overview, see the following papers and the remainder of this book [62–68].

We see in Figure 2.5 that there are significant gaps in the mid and far-IR spectral range as well as in the UV, with no few-cycle sources available yet. In the IR the approaches are based on materials such as Cr:ZnSe or novel nonlinear crystals for

parametric amplification [69, 70]. Below 300 nm no broadband amplifying medium is available yet. There are two main approaches for ultrashort pulse generation in this region: via ultrabroadband frequency conversion of few-cycle NIR pulses [71–75] or pulse compression directly in the UV [76, 77]. However, real few-cycle pulses in the UV could only be generated via harmonic generation in gas jets [78–80].

2.3 High-Energy Oscillators

The pulse energy scaling of femtosecond laser oscillators made rapid progress, over many orders of magnitude, over the past few years, as visualized in Figure 2.6. The data highlights the technology transition from Ti:sapphire to ytterbium-based oscillators for high-energy pulse generation with high repetition rates. We are thus tempted to formulate the following scaling law for mode-locked laser oscillators: *every five years the pulse energy increases by an order of magnitude*. Accordingly, millijoule pulses directly from a mode-locked oscillator can be expected in 2017.

During the last decade, all world record results for single-pulse energies from oscillators have been obtained by thin-disk laser concepts. The thin gain medium allows a one-dimensional, homogeneous heat flow, drastically reducing the thermal gradients inside the gain medium as compared to end-pumped bulk crystals [81]. Beyond the improved thermal management, the low quantum defect of Yb-doped crystals and major progress in InGaAs semiconductor pump laser technology supplied the key technologies for improving pulse energy scaling. Also, the thin crystals and the possibility to use large beam geometries reduces nonlinearities. Details about the latest technologies can be found in [58, 82–86]. The abovementioned ad-

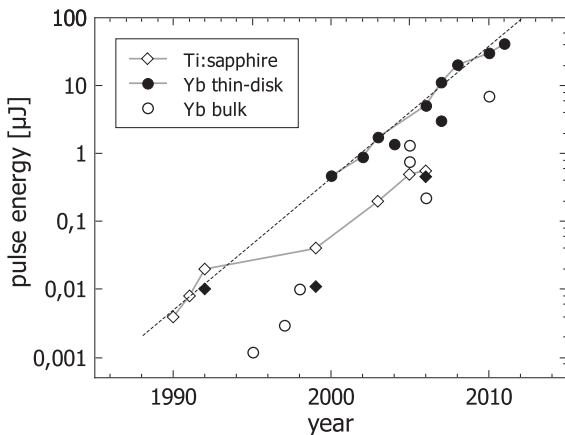


Figure 2.6 Evolution of high-energy femtosecond laser oscillators during the last two decades (compare with, e.g., [58]).

vantages of a thin-disk gain medium have also proven their usefulness for generation of high average power from Yb-based oscillators.

Figure 2.7 summarizes the achievements of high-power femtosecond oscillators for different host materials, which are mainly responsible for the available spectral bandwidth and thermal properties of the disk. The tungstates (Yb:KYW, Yb:KL_uW) suffer from poor crystal qualities, whereas the sesquioxides (e.g., Yb:Lu₂O₃) offer excellent thermomechanical properties, a good thermal conductivity, and a comparably broad amplification bandwidth [87]. They are well suited for extracting high average powers; the latest results have been published in [86, 88–90]. These lasers are mode-locked by semiconductor saturable absorber mirrors (SESAM). The design principle of a SESAM is sketched in Figure 2.8: a quantum film of absorbing material is located at the field maximum of the standing wave inside a reflecting mirror. Low pulse energies excite the electrons of the quantum layer and suffer loss,

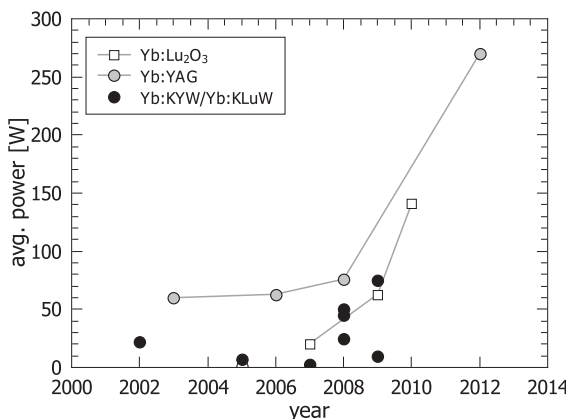


Figure 2.7 The development of thin-disk ultrafast oscillators in terms of average power for different ytterbium-doped materials.

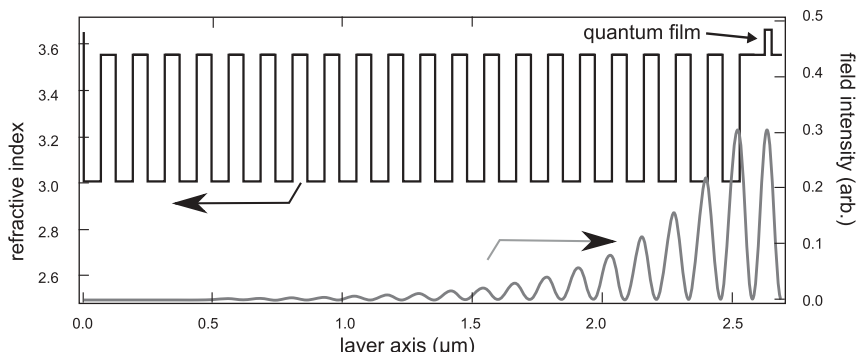


Figure 2.8 The semiconductor saturable absorber mirror consists of a quarter wave highly reflecting mirror made of alternating transparent layers with high and low index of refraction

(e.g., GaAs and AlAs). A small quantum film in the front of the mirror made of an absorbing semiconductor material (e.g., InGaAs) defines the saturable absorption.

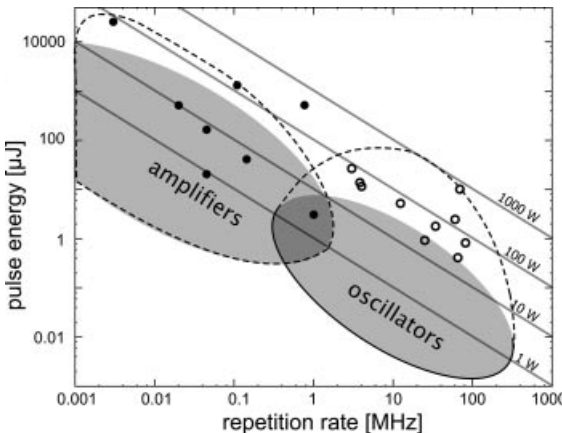


Figure 2.9 Overview of ultrafast high-energy laser sources with femtosecond pulse duration. The gray shaded areas are typical regimes of oscillators and amplifiers. The areas surrounded by dashed lines visualize the

trend of up-to-date systems towards higher average powers; the dots are specific systems (filled dots: amplifier systems; open dots: oscillators) (compare with, e.g., [58]).

whereas higher pulse energies saturate the absorption and see a larger reflectance. The details about absorber technology are reviewed in [91, 92].

Pulse energies can be scaled up by many orders of magnitude using postamplification at a lower repetition rate while keeping the average power constant. Figure 2.9 highlights the typical areas of operation of mode-locked oscillators and amplifier systems. The dots represent specific state-of-the-art laser systems. The intensity in the focus of a commercial university lab sized laser system can nowadays reach 10^{18} W/cm^2 , easily reaching the regime of relativistic optics [93]. Meanwhile, large specialized industry provides standard and customized high-energy laser systems for the vast number of applications in engineering, physics, chemistry, and life sciences.

2.4

Laser Amplifiers

The basic principle of a laser amplifier system is sketched in Figure 2.10. The repetition rate of a pulse train from a short-pulse laser oscillator is reduced by an electrooptic or acoustooptic pulse picker. To avoid nonlinear damage in the amplifier, the pulses are stretched to pulse durations many orders of magnitude longer than the Fourier limit. The stretcher can be constructed by a grating sequence, a fiber line, a chirped fiber-Bragg grating (CFBG [94]), a chirped-volume Bragg grating (CVBG [95]), or chirped mirrors. Behind the power amplifier, the high-energy pulses are recompressed to the Fourier limit by optical elements with opposite dispersion. This concept is referred to as CPA [39].

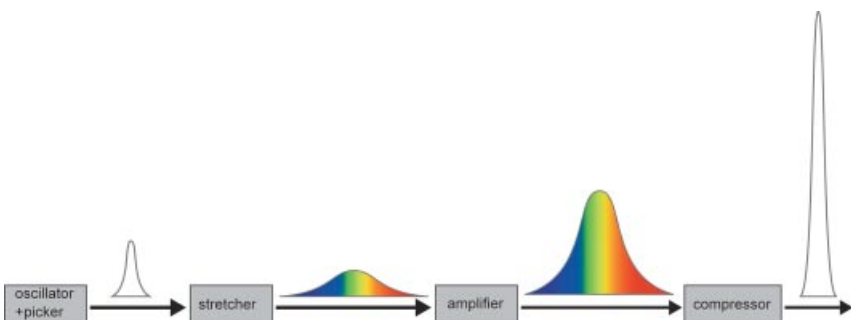


Figure 2.10 Principle of chirped pulse amplification.

The laser amplifier concepts are categorized into single-pass fiber amplifiers, multipass, regenerative, and parametric amplifiers.

- The *fiber amplifier* is the ideal candidate for high average power amplification. Due to the hardly avoidable nonlinearities caused by the long propagation in the fibers, peak intensities have to be reduced by CPA techniques and by novel fiber designs with large mode field diameters. The technology for Yb-doped fiber amplifiers is well developed and high-power InGaAs pump diodes are available. With the emergence of dielectric gratings for the compression of pulses with high average powers, fiber amplifier-based systems are now rather close to the kW-level with pulse durations in the hundreds of femtoseconds to picoseconds range. Recent state-of-the-art is published in [96–102].
- The *multipass amplifier* is currently the system employed for most strong-field experiments. Due to the large emission cross-section and the large amplification bandwidth, commercial tabletop multipass Ti:sapphire CPA systems generate femtosecond pulses in the multi-mJ range and in many cases with carrier envelope phase stabilization. (For details of the CEP and its relevance, I refer the reader to Chapter 4.) These systems are the workhorses for attosecond science, but suffer from expensive (and low performance) pump lasers in the green spectral range. The current state of multipass amplifier technology is documented in [103, 104]. To overcome the shortcomings of green pump laser technology and to explore the benefits of high-power/high-brightness pump diodes, directly diode-pumped Yb-doped materials for multipass amplification are the subject of current investigations. These approaches combine high average powers with low nonlinearities. The latest developments are documented in [105, 106].
- The *regenerative amplifier* is the traditional amplification scheme for directly diode-pumped low gain materials such as Yb-based crystals since the number of passes through the gain medium is flexible. It is closely related to *cavity dumping*. The principles are presented in Figure 2.11. In Figure 2.11a, a standard passively mode-locked laser oscillator is sketched. The repetition rate of the pulse train is defined by the resonator length. Figure 2.11b illustrates a cavity-dumped mode-locked oscillator. With no output coupling mirror, the repetition rate is de-

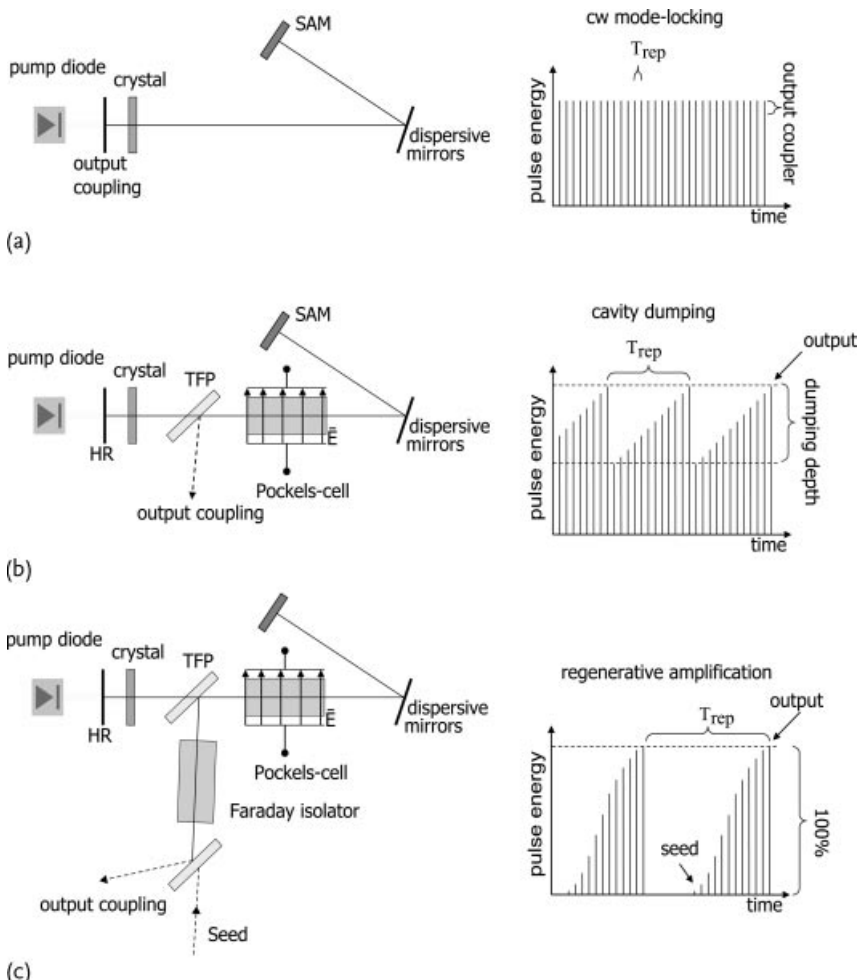


Figure 2.11 Dynamic output coupling: cw-mode-locking (a), cavity-dumping (b), regenerative amplification (c). TFP = thin-film polarizer, SAM = saturable absorber mirror.

fined by the external electronics and can be varied over large ranges. Substantial amounts of intracavity pulse energy can be extracted by a transient polarization rotation imposed by a Pockels cell in front of a polarizing beam splitter. Unfortunately, the average power drops with decreasing repetition rate. Latest results are published in [107, 108]. The regenerative amplifier (Figure 2.11c) relies on 100% dumping and requires a seed source. Here, the average power is constant over large ranges of repetition rates and pulse energies can be easily scaled. Recent results from directly diode-pumped schemes are published in [109–114].

- *Parametric amplification* of ultrashort light pulses employs second-order difference frequency mixing schemes and benefits from reduced thermal load on the amplification crystal due to the all-optical amplification process (see Fig-

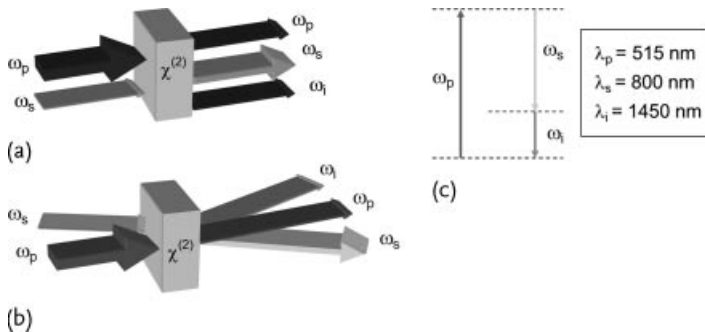


Figure 2.12 Collinear (a) and noncollinear (b) optical parametric amplification (OPA, NOPA). The term “p” denotes “pump,” “s” denotes “signal” and “i” denotes “idler.” Ener-

gy level diagram showing the creation of one signal photon and one idler photon from one pump photon (c).

ure 2.12). As parametric amplification is a nonresonant $\chi^{(2)}$ effect, the upper state lifetime is practically zero. In contrast to the genuine laser amplification schemes, the quantum defect between pump and signal does not remain in the medium, but leaves the crystal as optical radiation (idler, term scheme, see Figure 2.12c). Amplification occurs only within the duration of the pump pulse, imposing strict requirements on the temporal overlap between the pump and the signal pulses.

The amplification bandwidth is determined by the phase matching of the three interacting waves. Figure 2.13 gives a typical example of phase-matched signal wavelength versus crystal angle in BBO. It reveals that the bandwidth can be drastically increased by a noncollinear beam geometry with an angle of $\alpha = 2.4^\circ$ between incident pump and signal. This is the “magic angle” valid for 515 nm pump wavelength; in case of a blue pump beam at 400 nm the optimum noncollinear angle increases to $\alpha = 3.7^\circ$ (see Figure 2.12b). Employing the second or third harmonic of the abovementioned directly pumped solid-state pump sources, noncollinear parametric amplification is ideally suited for the generation of few-cycle pulses with high energies and high repetition rates.

The literature proves the versatility of the OPA concept: pulse durations below 5 fs and pulse energies on the joule scale have been demonstrated. An overview and recent results are published in [115–123]. The advantages of parametric amplification schemes have been broadly recognized and within the next few years we will witness optical parametric chirped pulse amplification (OPCPA) technology slowly replacing the Ti:sapphire amplifier systems in strong-field science labs around the world.

After 50 years of research on pulsed laser sources, laser science has reached the limit of the single-cycle pulse duration, and the power and energy performance of commercial and custom systems is steadily increasing. With further progress in pump diode technology, advanced optical components, and novel concepts such as the coherent combination of short pulses from multiple amplification stages [122,

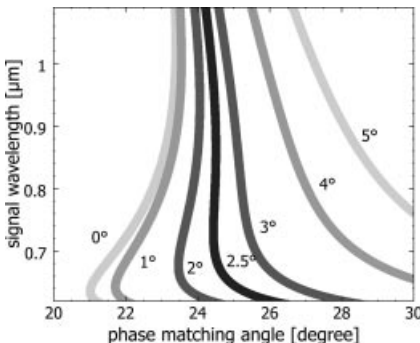


Figure 2.13 Phase matching for collinear ($\alpha = 0^\circ$) and noncollinear parametric amplification in BBO (pump wavelength 515 nm).

124–127], no fundamental limit in power scaling is in view. Last but not least, development of waveform synthesizers broke the single-cycle limit, allowing artificial pulse shaping of octave-spanning pulses with durations below 2 fs [128]. For the foreseeable future, the laser will continue to deliver enabling technologies for a wide field of science.

The author acknowledges the contributions of Marcel Schultze, Moritz Emons, Guido Palmer, and Maike Lieser.

References

- 1 Glenn, W.H., Brienza, M.J., and De Maria, A.J. (1968) Mode locking of an organic dye laser. *Appl. Phys. Lett.*, **12**, 54–56.
- 2 Smith, P.W. (1970) Mode-locking of lasers. *Proc. IEEE*, **58**, 1342–1356.
- 3 Ell, R., Morgner, U., Kärtner, F., Fujimoto, J., Ippen, E., Scheuer, V., Angelow, G., Tschudi, T., Lederer, M., Boiko, A., and Luther-Davies, B. (2001) Generation of 5 fs pulses and octave-spanning spectra directly from a Ti:sapphire laser. *Opt. Lett.*, **26**, 373–375.
- 4 Binhammer, T., Rittweger, E., Morgner, U., Ell, R., and Kärtner, F.X. (2006) Spectral phase control and temporal superresolution toward the single-cycle pulse. *Opt. Lett.*, **31**, 1552–1554. <http://dx.doi.org/10.1364/OL.31.001552>.
- 5 Haus, H. (2000) Mode-locking of lasers. *IEEE J. Sel. Top. Quantum Electron.*, **7**, 1173–1185.
- 6 Joyce, R.R. and Richards, P.L. (1969) Far-infrared spectra of Al_2O_3 doped with Ti, V, and Cr. *Phys. Rev.*, **179** (2), 375–380.
- 7 Moulton, P. (1982) Ti-doped sapphire: a tunable solid-state laser. *Opt. News*, **8** (6), 9.
- 8 Moulton, P.F. (1986) Spectroscopic and laser characteristics of Ti: Al_2O_3 . *J. Opt. Soc. Am. B*, **3** (1), 125, <http://dx.doi.org/10.1364/JOSAB.3.000125>, printed.
- 9 Albers, P., Stark, E., and Huber, G. (1986) Continuous-wave laser operation and quantum efficiency of titanium-doped sapphire. *J. Opt. Soc. Am. B*, **3** (1), 134, <http://dx.doi.org/10.1364/JOSAB.3.000134>, printed.
- 10 Hoenninger (1999) Ultrafast ytterbium-doped bulk lasers and laser amplifiers. *Appl. Phys. B*, **69**, 3–17.

- 11** Krupke, W.F. (2000) Ytterbium solid-state lasers – the first decade. *IEEE J. Sel. Top. Quantum Electron.*, **6**, 1287–1296.
- 12** Schmidt, A., Rivier, S., Petrov, V., Griebner, U., Han, X., Cano-Torres, J.M., García-Cortés, A., Serrano, M.D., Cascales, C., and Zaldo, C. (2008) Continuous-wave tunable and femtosecond mode-locked laser operation of Yb:NaY(MoO₄)₂. *J. Opt. Soc. Am. B* **25** (8), 1341–1349, <http://dx.doi.org/10.1364/JOSAB.25.001341>.
- 13** Schmidt, B.E., Unrau, W., Mirabal, A., Li, S., Krenz, M., Wöste, L., and Siebert, T. (2008) Poor man's source for sub 7 fs: a simple route to ultrashort laser pulses and their full characterization. *Opt. Exp.*, **16**, 18910–18921.
- 14** Huber, G., Kränkel, C., and Petermann, K. (2010) Solid-state lasers: status and future (invited). *J. Opt. Soc. Am. B*, **27** (11), B93–B105, <http://dx.doi.org/10.1364/JOSAB.27.000B93>.
- 15** Schmidt, A., Petrov, V., Griebner, U., Peters, R., Petermann, K., Huber, G., Fiebig, C., Paschke, K., and Erbert, G. (2010) Diode-pumped mode-locked Yb:LuScO₃ single crystal laser with 74 fs pulse duration. *Opt. Lett.*, **35** (4), 511–513, <http://dx.doi.org/10.1364/OL.35.000511>.
- 16** Yoshida, A., Schmidt, A., Zhang, H., Wang, J., Liu, J., Fiebig, C., Paschke, K., Erbert, G., Petrov, V., and Griebner, U. (2010) 42-fs diode-pumped Yb:Ca₂YO(BO₃)₃ oscillator. *Opt. Exp.*, **18** (23), 24325–24330, <http://dx.doi.org/10.1364/OE.18.024325>.
- 17** Druon, F., Ricaud, S., Papadopoulos, D.N., Pellegrina, A., Camy, P., Doualan, J.L., Moncorgé, R., Courjaud, A., Mottay, E., and Georges, P. (2011) On Yb:CaF₂ and Yb:SrF₂: review of spectroscopic and thermal properties and their impact on femtosecond and high power laser performance. *Opt. Mater. Express*, **1** (3), 489–502, <http://dx.doi.org/10.1364/OME.1.000489>.
- 18** Szipöcs, R., Ferencz, K., Spielmann, C., and Krausz, F. (1994) Chirped multi-layer coatings for broadband dispersion control in femtosecond lasers. *Opt. Lett.*, **19**, 201–203.
- 19** Szipöcs, R. and Koházi-Kis, A. (1997) Theory and design of chirped dielectric laser mirrors. *Appl. Phys. B*, **65**, 115.
- 20** Tempea, G., Yakovlev, V., Bacovic, B., Krausz, F., and Ferencz, K. (2001) Tilted-front-interface chirped mirrors. *J. Opt. Soc. Am. B*, **18**, 1747–1750, <http://dx.doi.org/10.1364/JOSAB.18.001747>.
- 21** Pervak, V., Ahmad, I., Trubetskoy, M., Tikhonravov, A., and Krausz, F. (2009) Double-angle multilayer mirrors with smooth dispersion characteristics. *Opt. Exp.*, **17** (10), 7943–7951.
- 22** Kärtner, F.X., Matuschek, N., Schibli, T., Keller, U., Haus, H.A., Heine, C., Morf, R., Scheuer, V., Tilsch, M., and Tschudi, T. (1997) Design and fabrication of double-chirped mirrors. *Opt. Lett.*, **22** (11), 831–833, <http://ol.osa.org/abstract.cfm?URI=ol-22-11-831>, printed.
- 23** Kärtner, F.X., Morgner, U., Ell, R., Schibli, T., Fujimoto, J.G., Ippen, E.P., Scheuer, V., Angelow, G., and Tschudi, T. (2001) Ultrabroadband double-chirped mirror pairs for generation of octave spectra. *J. Opt. Soc. Am. B*, **18** (6), 882–885, <http://dx.doi.org/10.1364/JOSAB.18.000882>.
- 24** Laude, V. and Tournois, P. (1999) Chirped-mirror-pairs for ultrabroadband dispersion control, in *Conf. Lasers Electroopt.*, Optical Society of America, OSA, Washington, DC, pp. 187–188.
- 25** Matuschek, N., Gallmann, L., Sutter, D., Steinmeyer, G., and Keller, U. (2000) Back-side coated chirped mirrors with ultra-smooth broadband dispersion characteristics. *Appl. Phys. B*, **71**, 509–522.
- 26** Matuschek, N., Kärtner, F., and Keller, U. (1999) Analytical design of double-chirped mirrors with custom tailored dispersion characteristics. *IEEE J. Quantum Electron.*, **QE 35**, 129–137.

- 27 Steinmeyer, G. (2003) Brewster-angled chirped mirrors for high-fidelity dispersion compensation and bandwidths exceeding one optical octave. *Opt. Eng.*, **11**, 2385–2396.
- 28 Chudoba, C., Fujimoto, J., Ippen, E., Haus, H., Morgner, U., Kärtner, F., Scheuer, V., Angelow, G., and Tschudi, T. (2001) All-solid-state Cr:forsterite laser generating 14 fs pulses at 1.3 μm. *Opt. Lett.*, **26**, 292–294.
- 29 Ripin, D., Kärtner, F., Chudoba, C., Morgner, U., Gopinath, J., Fujimoto, J.G., Ippen, E.P., Scheuer, V., Angelow, G., and Tschudi, T. (2002) Generation of 20 fs pulses by a prismless Cr⁴⁺:YAG laser. *Opt. Lett.*, **27**, 61–63.
- 30 Wagenblast, P., Ell, R., Morgner, U., Grawert, F., and Kärtner, F. (2003) Diode-pumped 10-fs Cr³⁺:LICAF laser. *Opt. Lett.*, **28**, 1713–1715.
- 31 Wagenblast, P., Morgner, U., Grawert, F., Kärtner, F., Scheuer, V., Angelow, G., and Lederer, M. (2002) Generation of 10-fs pulses from a Kerr-lens mode locked Cr³⁺:LICAF laser oscillator using third order dispersion compensating double chirped mirror. *Opt. Lett.*, **27**, 1726–1728.
- 32 Morgner, U., Kärtner, F.X., Cho, S.H., Chen, Y., Haus, H.A., Fujimoto, J.G., Ippen, E.P., Scheuer, V., Angelow, G., and Tschudi, T. (1999) Sub-two-cycle pulses from a Kerr-lens mode-locked Ti:sapphire laser. *Opt. Lett.*, **24**, 411–413.
- 33 Xu, L., Spielmann, C., Poppe, A., Brabec, T., Krausz, F., and Hänsch, T.W. (1996) Route to phase control of ultrashort light pulses. *Opt. Lett.*, **21** (24), 2008–2010, <http://dx.doi.org/10.1364/OL.21.002008>, printed.
- 34 Telle, H., Steinmeyer, G., Dunlop, A., Stenger, J., Sutter, D., and Keller, U. (1999) Carrier-envelope offset phase control: A novel concept for absolute optical frequency measurement and ultrashort pulse generation. *Appl. Phys. B*, **69** (4), 327–332, <http://dx.doi.org/10.1007/s003400050813>.
- 35 Jones, D.J., Diddams, S.A., Ranka, J.K., Stentz, A., Windeler, R.S., Hall, J.L., and Cundiff, S.T. (2000) Carrier-envelope phase control of femtosecond mode-locked lasers and direct optical frequency synthesis. *Science*, **288** (5466), 635–639, <http://www.sciencemag.org/cgi/content/abstract/288/5466/635>, printed.
- 36 Apolonski, A., Poppe, A., Tempea, G., Spielmann, C., Udem, T., Holzwarth, R., Hänsch, T., and Krausz, F. (2000) Controlling the phase evolution of few-cycle light pulses. *Phys. Rev. Lett.*, **85**, 740–743.
- 37 Morgner, U., Ell, R., Metzler, G., Schibli, T.R., Kärtner, F.X., Fujimoto, J.G., Haus, H.A., and Ippen, E.P. (2001) Nonlinear optics with phase-controlled pulses in the sub-two-cycle regime. *Phys. Rev. Lett.*, **86**, 5462–5465.
- 38 Weiner, A. (2009) *Ultrafast Optics*, John Wiley & Sons, Inc.
- 39 Strickland, D. and Mourou, G. (1985) Compression of amplified chirped optical pulses. *Opt. Commun.*, **55** (6), 447–449, <http://www.sciencedirect.com/science/article/B6TVF-46JGW3M-1BX/2/e5f83949f08c6e26c541eff02c32fa1>.
- 40 Nisoli, M., De Silvestri, S., and Svelto, O. (1996) Generation of high energy 10 fs pulses by a new pulse compression technique. *Appl. Phys. Lett.*, **68** (20), 2793–2795.
- 41 Nisoli, M., Stagira, S., De Silvestri, S., Svelto, O., Sartania, S., Cheng, Z., Lenzner, M., Spielmann, C., and Krausz, F. (1997) A novel-high energy pulse compression system: generation of multi-gigawatt sub-5-fs pulses. *Appl. Phys. B*, **65**, 189–196.
- 42 Suda, A., Hatayama, M., Nagasaka, K., and Midorikawa, K. (2005) Generation of sub-10-fs, 5-mJ-optical pulses using a hollow fiber with a pressure gradient. *Appl. Phys. Lett.*, **86**, 111116.
- 43 Matsubara, E., Yamane, K., Sekikawa, T., and Yamashita, M. (2007) Generation of 2.6 fs optical pulses using induced-phase modulation in a gas-filled hollow fiber. *J. Opt. Soc. Am. B*, **24** (4), 985–989.
- 44 Bohman, S., Suda, A., Kaku, M., Nurhuda, M., Kanai, T., Yamaguchi, S., and Midorikawa, K. (2008) Generation of 5 fs, 0.5 TW pulses focusable to rela-

- tivistic intensities at 1 kHz. *Opt. Exp.*, **16** (14), 10684–10689.
- 45** Nagy, T., Pervak, V., and Simon, P. (2011) Optimal pulse compression in long hollow fibers. *Opt. Lett.*, **36** (22), 4422–4424, <http://dx.doi.org/10.1364/OL.36.004422>.
- 46** Hauri, C.P., Kornelis, W., Helbing, F.W., Couairon, A., Mysyrowicz, A., Biegert, J., and Keller, U. (2004) Generation of intense carrier-envelope phase-locked few-cycle laser pulses through filamentation. *Appl. Phys. B*, **79**, 673–677.
- 47** Zair, A., Guandalini, A., Schapper, F., Holler, M., Biegert, J., Gallmann, L., Couairon, A., Franco, M., Mysyrowicz, A., and Keller, U. (2007) Spatio-temporal characterization of few-cycle pulses obtained by filamentation. *Opt. Exp.*, **15** (9), 5394–5404, <http://dx.doi.org/10.1364/OE.15.005394>.
- 48** Schulz, E., Binhammer, T., Steingrube, D., Rausch, S., Kovacev, M., and Morgner, U. (2009) Intense few-cycle laser pulses from self-compression in a self-guiding filament. *Appl. Phys. B*, **95** (2), 269–272.
- 49** Couairon, A. and Mysyrowicz, A. (2007) Femtosecond filamentation in transparent media. *Phys. Rep.*, **441** (2–4), 47–189, <http://www.sciencedirect.com/science/article/B6TVP-4N0HJBX-1/2/94b551a9e5a24405be3cd4b0758bb9ec>.
- 50** Bergé, L., Skupin, S., Nuter, R., Kasparian, J., and Wolf, J. (2007) Ultrashort filaments of light in weakly ionized, optically transparent media. *Rep. Prog. Phys.*, **70**, 1633.
- 51** Chin, S. (2010) *Femtosecond Laser Filamentation*, vol. 55, Springer Verlag.
- 52** Verluse, F., Laude, V., Cheng, Z., Spielmann, C., and Tournois, P. (2000) Amplitude and phase control of ultrashort pulse by use of an acousto-optic programmable device. *Opt. Lett.*, **25**, 575.
- 53** Weiner, A., Heritage, J., and Kirschner, E. (1988) High-resolution femtosecond pulse shaping. *J. Opt. Soc. Am.*, **5**, 1563.
- 54** Yelin, D., Meshulach, D., and Silberberg, Y. (1997) Adaptive femtosecond pulse compression. *Opt. Lett.*, **22**, 1793–1795.
- 55** Baumert, T., Brixner, T., Seyfried, V., Strehle, M., and Gerber, G. (1997) Femtosecond pulse shaping by an evolutionary algorithm with feedback. *Appl. Phys. B*, **65**, 779–782.
- 56** Weiner, A. (2000) Femtosecond pulse shaping using spatial light modulators. *Rev. Sci. Instrum.*, **71**, 1930–1960.
- 57** Binhammer, T., Rittweger, E., Ell, R., F.X.Kartner, and Morgner, U. (2005) Prism-based pulse shaper for octave spanning spectra. *IEEE J. Quantum Electron.*, **41** (12), 1552–1557.
- 58** Südmeyer, T., Marchese, S.V., Hashimoto, S., Baer, C.R.E., Gingras, G., Witzel, B., and Keller, U. (2008) Femtosecond laser oscillators for high-field science. *Nat. Photonics*, **2** (10), 599–604.
- 59** Siegel, P. (2002) Terahertz technology. *IEEE Trans. Microwave Theory Tech.*, **50** (3), 910–928.
- 60** Federici, J.F., Schultkin, B., Huang, F., Gary, D., Barat, R., Oliveira, F., and Zimdars, D. (2005) Thz imaging and sensing for security applications – explosives, weapons and drugs. *Semicond. Sci. Technol.*, **20**, 266–280.
- 61** Schneider, A., Neis, M., Stillhart, M., Ruiz, B., Khan, R.U.A., and Günter, P. (2006) Generation of terahertz pulses through optical rectification in organic dast crystals: theory and experiment. *J. Opt. Soc. Am. B*, **23** (9), 1822–1835.
- 62** Mairesse, Y., de Bohan, A., Frasin-ski, L.J., Merdji, H., Dinu, L.C., Monchicourt, P., Breger, P., Kovačev, M., Taieb, R., Carré, B., Muller, H.G., Agostini, P., and Salières, P. (2003) Attosecond synchronization of high-harmonic soft X-rays. *Science*, **302** (5650), 1540–1543, <http://www.sciencemag.org/content/302/5650/1540.abstract>.
- 63** Tzallas, P., Charalambidis, D., Papadogiannis, N.A., Witte, K., and Tsakiris, G.D. (2003) Direct observation of attosecond light bunching. *Nature*, **426** (6964), 267–271, <http://dx.doi.org/10.1038/nature02091>.
- 64** Remetter, T., Johnsson, P., Mauritsson, J., Varju, K., Ni, Y., Lepine, F., Gustafsson, E., Kling, M., Khan, J., Lopez-Martens, R., Schafer, K.J., Vrakking, M.J.J., and L'Huillier, A. (2006) At-

- tosecond electron wave packet interferometry. *Nat. Phys.*, **2** (5), 323–326, <http://dx.doi.org/10.1038/nphys290>.
- 65** Goulielmakis, E., Schultze, M., Hofstetter, M., Yakovlev, V.S., Gagnon, J., Uiberacker, M., Aquila, A.L., Gulliksson, E.M., Attwood, D.T., Kienberger, R., Krausz, F., and Kleineberg, U. (2008) Single-cycle nonlinear optics. *Science*, **320** (5883), 1614–1617, <http://www.sciencemag.org/cgi/content/abstract/320/5883/1614>.
- 66** Thormann, I., Bahabad, A., Liu, X., Trebino, R., Murnane, M.M., and Kapteyn, H.C. (2009) Characterizing isolated attosecond pulses from hollow-core waveguides using multi-cycle driving pulses. *Opt. Exp.*, **17**, 4611–4633, <http://dx.doi.org/10.1364/OE.17.004611>.
- 67** Ferrari, F., Calegari, F., Lucchini, M., Vozzi, C., Stagira, S., Sansone, G., and Nisoli, M. (2010) High-energy isolated attosecond pulses generated by above-saturation few-cycle fields. *Nat. Photonics*, **4**, 875–879.
- 68** Gilbertson, S., Khan, S.D., Wu, Y., Chin, M., and Chang, Z. (2010) Isolated attosecond pulse generation without the need to stabilize the carrier-envelope phase of driving lasers. *Phys. Rev. Lett.*, **105** (9), 093902.
- 69** Bernhardt, B., Sorokin, E., Jacquet, P., Thon, R., Becker, T., Sorokina, I.T., Picque, N., and Hänsch, T.W. (2010) Mid-infrared dual-comb spectroscopy with 2.4 μm Cr(2+):ZnSe femtosecond lasers. *Appl. Phys. B*, **100** (1, SI), 3–8.
- 70** Vodopyanov, K.L., Sorokin, E., Sorokina, I.T., and Schunemann, P.G. (2011) Mid-IR frequency comb source spanning 4.4–5.4 μm based on subharmonic GaAs optical parametric oscillator. *Opt. Lett.*, **36** (12), 2275–2277.
- 71** Durfee, C., Backus, S., Kapteyn, H., and Murnane, M. (1999) Intense 8-fs pulse generation in the deep ultraviolet. *Opt. Lett.*, **24** (10), 697–699.
- 72** Baum, P., Lochbrunner, S., and Riedle, E. (2004) Generation of 7-fs ultraviolet pulses: achromatic phase matching and chirp management. *Appl. Phys. B*, **79**, 1027–1032.
- 73** Fuji, T., Horio, T., and Suzuki, T. (2007) Generation of 12 fs deep-ultraviolet pulses by four-wave mixing through filamentation in neon gas. *Opt. Lett.*, **32**, 2481–2483.
- 74** Beutler, M., Ghotbi, M., Noack, F., Brida, D., Manzoni, C., and Cerullo, G. (2009) Generation of high-energy sub-20 fs pulses tunable in the 250–310 nm region by frequency doubling of a high-power noncollinear optical parametric amplifier. *Opt. Lett.*, **34** (6), 710–712.
- 75** Kida, Y., Liu, J., Teramoto, T., and Kobayashi, T. (2010) Sub-10 fs deep-ultraviolet pulses generated by chirped-pulse four-wave mixing. *Opt. Lett.*, **35** (11), 1807.
- 76** Nagy, T. and Simon, P. (2009) Generation of 200-μJ, sub-25-fs deep-UV pulses using a noble-gas-filled hollow fiber. *Opt. Lett.*, **34** (15), 2300–2302.
- 77** Ghotbi, M., Trabs, P., and Beutler, M. (2011) Generation of high-energy, sub-20-fs pulses in the deep ultraviolet by using spectral broadening during filamentation in argon. *Opt. Lett.*, **36** (4), 463–465, <http://dx.doi.org/10.1364/OL.36.000463>.
- 78** Graf, U. et al. (2008) Intense few-cycle light pulses in the deep ultraviolet. *Opt. Exp.*, **16** (23), 18956–18963.
- 79** Bothschafter, E., Schiffrian, A., Yakovlev, V., Azzeer, A., Krausz, F., Ernststorfer, R., and Kienberger, R. (2010) Collinear generation of ultrashort UV and XUV pulses. *Opt. Exp.*, **18** (9), 9173–9180.
- 80** Reiter, F., Graf, U., Schultze, M., Schweinberger, W., Schröder, H., Karpowicz, N., Azzeer, A.M., Kienberger, R., Krausz, F., and Goulielmakis, E. (2010) Generation of sub-3 fs pulses in the deep ultraviolet. *Opt. Lett.*, **35** (13), 2248.
- 81** Giesen, A. and Speiser, J. (2007) Fifteen years of work on thin-disk lasers: Results and scaling laws. *IEEE J. Sel. Top. Quantum Electron.*, **13**, 598–609.
- 82** Südmeyer, T., Kränkel, C., Baer, C.R.E., Heckl, O.H., Saraceno, C.J., Golling, M., Peters, R., Petermann, K., Huber, G., and Keller, U. (2009) High-power ultrafast thin disk laser oscillators and their

- potential for sub-100-femtosecond pulse generation. *Appl. Phys. B*, **97** (2), 281–295.
- 83** Südmeyer, T., Baer, C.R.E., Kränkel, C., Saraceno, C.J., Heckl, O.H., Golling, M., Peters, R., Petermann, K., Huber, G., and Keller, U. (2011) Power-scaling of femtosecond thin disk lasers. Advances in Optical Materials, OSA Technical Digest (CD), Optical Society of America, paper ATuC1, <http://dx.doi.org/10.1364/ASSP.2011.ATuC1>.
- 84** Neuhaus, J., Bauer, D., Zhang, J., Killi, A., Kleinbauer, J., Kumkar, M., Weiler, S., Guina, M., Sutter, D.H., and Dekorsy, T. (2008) Subpicosecond thin-disk laser oscillator with pulse energies of up to 25.9 microjoules by use of an active multipass geometry. *Opt. Exp.*, **16**, 20530–20539.
- 85** Bauer, D., Zawischa, I., Sutter, D., Killi, A., and Dekorsy, T. (2012) Mode-locked Yb:YAG thin-disk oscillator with 41 μJ pulse energy at 145 W average infrared power and high power frequency conversion. *Opt. Exp.*, **20** (9), 9698–9704.
- 86** Saraceno, C., Emaury, F., Heckl, O., Baer, C., Hoffmann, M., Schriber, C., Golling, M., Südmeyer, T., and Keller, U. (2012) 275 W average output power from a femtosecond thin disk oscillator operated in a vacuum environment. *Opt. Exp.*, **20** (21), 23535–23541.
- 87** Peters, R., Kränkel, C., Petermann, K., and Huber, G. (2008) Crystal growth by the heat exchanger method, spectroscopic characterization and laser operation of high-purity Yb:Lu₂O₃. *J. Cryst. Growth*, **310** (7–9), 1934–1938.
- 88** Palmer, G., Schultze, M., Siegel, M., Emons, M., Bünting, U., and Morgner, U. (2008) Passively mode-locked Yb:KLu(WO₄)₂ thin-disk oscillator operated in the positive and negative dispersion regime. *Opt. Lett.*, **33** (14), 1608–1610, <http://dx.doi.org/10.1364/OL.33.001608>.
- 89** Baer, C.R.E., Kränkel, C., Saraceno, C.J., Heckl, O.H., Golling, M., Suedmeyer, T., Peters, R., Petermann, K., Huber, G., and Keller, U. (2009) Femtosecond Yb:Lu₂O₃ thin disk laser with 63 W of average power. *Opt. Lett.*, **34** (18), 2823–2825.
- 90** Baer, C., Heckl, O., Saraceno, C., Schriber, C., Kränkel, C., Südmeyer, T., and Keller, U. (2012) Frontiers in passively mode-locked high-power thin disk laser oscillators. *Opt. Exp.*, **20** (7), 7054–7065.
- 91** Keller, U., Weingarten, K., Kärtner, F., Kopf, D., Braun, B., Jung, I., Fluck, R., Honninger, C., Matuschek, N., and Aus der Au, J. (1996) Semiconductor saturable absorber mirrors (sesam's) for femtosecond to nanosecond pulse generation in solid-state lasers. *IEEE J. Sel. Top. Quantum Electron.*, **2** (3), 435–453.
- 92** Keller, U. (2010) Ultrafast solid-state laser oscillators: a success story for the last 20 years with no end in sight. *Appl. Phys. B*, **100**, 15–28, <http://dx.doi.org/10.1007/s00340-010-4045-3>.
- 93** Mourou, G.A., Tajima, T., and Bulanov, S.V. (2006) Optics in the relativistic regime. *Rev. Mod. Phys.*, **78**, 309–371.
- 94** Kashyap, R., Froehlich, H.G., Swanton, A., and Armes, D.J. (1996) 1.3 m long super-step-chirped fibre Bragg grating with a continuous delay of 13.5 ns and bandwidth 10 nm for broadband dispersion compensation. *Electron. Lett.*, **32**, 1807–1809.
- 95** Liao, K., Cheng, M., Flecher, E., Smirnov, V.I., Glebov, L.B., and Galvanauskas, A. (2007) Large-aperture chirped volume Bragg grating based fiber CPA system. *Opt. Exp.*, **15**, 4876–4882.
- 96** Buckley, J.R., Clark, S.W., and Wise, F.W. (2006) Generation of ten-cycle pulses from an ytterbium fiber laser with cubic phase compensation. *Opt. Lett.*, **31** (9), 1340–1342, <http://ol.osa.org/abstract.cfm?URL=ol-31-9-1340>.
- 97** Kobtsev, S., Kukarin, S., and Fedotov, Y. (2008) Ultra-low repetition rate mode-locked fiber laser with high-energy pulses. *Opt. Express*, **16** (26), 21936–21941, <http://dx.doi.org/10.1364/OE.16.021936>.
- 98** Eidam, T., Hanf, S., Seise, E., Andersen, T.V., Gabler, T., Wirth, C.,

- Schreiber, T., Limpert, J., and Tünnermann, A. (2010) Femtosecond fiber CPA system emitting 830 W average output power. *Opt. Lett.*, **35** (2), 94–96, <http://dx.doi.org/10.1364/OL.35.000094>.
- 99** Mortag, D., Wandt, D., Morgner, U., Kracht, D., and Neumann, J. (2011) Sub-80-fs pulses from an all-fiber-integrated dissipative-soliton laser at 1 μm. *Opt. Exp.*, **19** (2), 546–551, <http://dx.doi.org/10.1364/OE.19.000546>.
- 100** Eidam, T., Rothhardt, J., Stutzki, F., Jansen, F., Hädrich, S., Carstens, H., Jauregui, C., Limpert, J., and Tünnermann, A. (2011) Fiber chirped-pulse amplification system emitting 3.8 GW peak power. *Opt. Exp.*, **19** (1), 255–260, <http://www.opticsexpress.org/abstract.cfm?URI=oe-19-1-255>.
- 101** Stutzki, F., Jansen, F., Eidam, T., Steinmetz, A., Jauregui, C., Limpert, J., and Tünnermann, A. (2011) High average power large-pitch fiber amplifier with robust single-mode operation. *Opt. Lett.*, **36** (5), 689–691.
- 102** Limpert, J., Stutzki, F., Jansen, F., Otto, H., Eidam, T., Jauregui, C., and Tünnermann, A. (2012) Yb-doped large-pitch fibres: effective single-mode operation based on higher-order mode delocalisation. *Light: Sci. Appl.*, **1** (4), e8.
- 103** Muller, D., Backus, S., Read, K., Murnane, M., and Kapteyn, H. (2005) Cryogenic cooling multiplies output of Ti:sapphire output. *Laser Focus World*, **41** (10), 65–68.
- 104** Anderson, A., Luecking, F., Prikoszovits, T., Hofer, M., Cheng, Z., Neacsu, C.C., Scharrer, M., Rammler, S., Russell, P.S.J., Tempea, G., and Assion, A. (2011) Multi-mJ carrier envelope phase stabilized few-cycle pulses generated by a tabletop laser system. *Appl. Phys. B*, **103** (3), 531–536.
- 105** Pugzlys, A., Andriukaitis, G., Baltuska, A., Su, L., Xu, J., Li, H., Li, R., Lai, W.J., Phua, P.B., Marcinkevicius, A., Fermann, M.E., Giniunas, L., Danielius, R., and Alisauskas, S. (2009) Multi-mJ, 200-fs, CW-pumped, cryogenically cooled, Yb,Na:CaF₂ amplifier. *Opt. Lett.*, **34** (13), 2075–2077.
- 106** Russbueldt, P., Mans, T., Hoffmann, H., and Poprawe, R. (2011) 1100 W Yb:Yag femtosecond innoslab amplifier, in *SPIE LASER*, International Society for Optics and Photonics, pp. 79120R–79120R.
- 107** Wegner, U., Meier, J., and Lederer, M.J. (2009) Compact picosecond mode-locked and cavity-dumped Nd:YVO₄ laser. *Opt. Eng.*, **17** (25), 23098–23103.
- 108** Palmer, G., Schultze, M., Emons, M., Lindemann, A.L., Pospiech, M., Steingrube, D., Lederer, M., and Morgner, U. (2010) 12 MW peak power from a two-crystal Yb:KYW chirped-pulse oscillator with cavity-dumping. *Opt. Exp.*, **18** (18), 19095–19100, <http://dx.doi.org/10.1364/OE.18.019095>.
- 109** Buenting, U., Sayinc, H., Wandt, D., Morgner, U., and Kracht, D. (2009) Regenerative thin disk amplifier with combined gain spectra producing 500 μJ sub 200 fs pulses. *Opt. Exp.*, **17**, 8046–8050.
- 110** Calendron, A.L., Wentsch, K., Meier, J., and Lederer, M.J. (2009) High power and high energy Yb:KYW regenerative amplifier using a chirped volume bragg grating, in *Conf. Lasers Electroopt. International Quantum Electronics Conference*, Optical Society of America, p. CFD2, <http://dx.doi.org/10.1364/OL.34.002123>.
- 111** Metzger, T., Schwarz, A., Teisset, C.Y., Sutter, D., Killi, A., Kienberger, R., and Krausz, F. (2009) High-repetition-rate picosecond pump laser based on a Yb:YAG disk amplifier for optical parametric amplification. *Opt. Lett.*, **34** (14), 2123–2125, <http://dx.doi.org/10.1364/OL.34.002123>.
- 112** Buettner, A., Buenting, U., Wandt, D., Neumann, J., and Kracht, D. (2010) Ultrafast double-slab regenerative amplifier with combined gain spectra and intracavity dispersion compensation. *Opt. Exp.*, **18** (21), 21973–21980.
- 113** Ricaud, S., Druon, F., Papadopoulos, D.N., Camy, P., Doualan, J., Moncorge, R., Delaigue, M., Zaouter, Y., Courjaud, A., Georges, P., and Mottay, E. (2010)

- Short-pulse and high-repetition-rate diode-pumped Yb:CaF₂ regenerative amplifier. *Opt. Lett.*, **35** (14), 2415–2417.
- 114** Takeuchi, Y., Kawanaka, J., Yoshida, A., Yasuhara, R., Kawashima, T., Kan, H., and Miyanaga, N. (2011) Sub-kHz cryogenic Yb:YAG regenerative amplifier by using a total-reflection active mirror. *Appl. Phys. B*, **104** (1), 29–32.
- 115** Cerullo, G. and De Silvestri, S. (2003) Ultrafast optical parametric amplifiers. *Rev. Sci. Instrum.*, **74**, 1–18.
- 116** Adachi, S., Ishii, N., Kanai, T., Kosuge, A., Itatani, J., Kobayashi, Y., Yoshitomi, D., Torizuka, K., and Watanabe, S. (2008) 5-fs, multi-mJ, CEP-locked parametric chirped-pulse amplifier pumped by a 450-nm source at 1 kHz. *Opt. Exp.*, **16**, 14341–14352.
- 117** Moses, J., Huang, S.W., Hong, K.H., Mücke, O.D., Falcão-Filho, E.L., Benedick, A., Ilday, F.Ö., Dergachev, A., Bolger, J.A., Eggleton, B.J., and Kärtner, F.X. (2009) Highly stable ultrabroadband mid-IR optical parametric chirped-pulse amplifier optimized for superfluorescence suppression. *Opt. Lett.*, **34**, 1639–1641.
- 118** Tavella, F., Willner, A., Rothhardt, J., Hädrich, S., Seise, E., Düsterer, S., Tschentscher, T., Schlarb, H., Feldhaus, J., Limpert, J., Tünnermann, A., and Rossbach, J. (2010) Fiber-amplifier pumped high average power few-cycle pulse non-collinear OPCPA. *Opt. Exp.*, **18** (5), 4689–4694, <http://www.opticsexpress.org/abstract.cfm?URL=oe-18-5-4689>.
- 119** Schultze, M., Binhammer, T., Steinmann, A., Palmer, G., Emons, M., and Morgner, U. (2010) Few-cycle OPCPA system at 143 kHz with more than 1 μJ of pulse energy. *Opt. Exp.*, **18** (3), 2836–2841, <http://www.opticsexpress.org/abstract.cfm?URL=oe-18-3-2836>.
- 120** Herrmann, D., Tautz, R., Tavelia, F., Krausz, F., and Veisz, L. (2010) Investigation of two-beam-pumped noncollinear optical parametric chirped-pulse amplification for the generation of few-cycle light pulses. *Opt. Exp.*, **18** (5), 4170–4183, <http://dx.doi.org/10.1364/OE.18.004170>.
- 121** Hädrich, S., Demmler, S., Rothhardt, J., Jocher, C., Limpert, J., and Tünnermann, A. (2011) High-repetition-rate sub-5-fs pulses with 12 GW peak power from fiber-amplifier-pumped optical parametric chirped-pulse amplification. *Opt. Lett.*, **36** (3), 313–315, <http://dx.doi.org/10.1364/OL.36.000313>.
- 122** Harth, A., Schultze, M., Lang, T., Binhammer, T., Rausch, S., and Morgner, U. (2012) Two-color pumped opcpa system emitting spectra spanning 1.5 octaves from vis to NIR. *Opt. Exp.*, **20** (3), 3076–3081.
- 123** Lang, T., Harth, A., Matyschok, J., Binhammer, T., Schultze, M., and Morgner, U. (2013) Impact of temporal, spatial and cascaded effects on the pulse formation in ultra-broadband parametric amplifiers. *Opt. Exp.*, **21** (1), 949–959.
- 124** Sabourdy, D., Kermene, V., Desfarges-Berthelemot, A., Lefort, L., Barthelemy, A., Even, P., and Pureur, D. (2003) Efficient coherent combining of widely tunable fiber lasers. *Opt. Exp.*, **11** (2), 87–97.
- 125** Augst, S., Ranka, J., Fan, T., and Sanchez, A. (2007) Beam combining of ytterbium fiber amplifiers. *J. Opt. Soc. Am. B*, **24** (8), 1707–1715.
- 126** Seise, E., Klenke, A., Breitkopf, S., Plötner, M., Limpert, J., and Tünnermann, A. (2011) Coherently combined fiber laser system delivering 120 μJ femtosecond pulses. *Opt. Lett.*, **36** (4), 439–441.
- 127** Manzoni, C., Huang, S.W., Cirmi, G., Farinello, P., Moses, J., Kärtner, F.X., and Cerullo, G. (2012) Coherent synthesis of ultra-broadband optical parametric amplifiers. *Opt. Lett.*, **37** (11), 1880–1882, <http://ol.osa.org/abstract.cfm?URL=ol-37-11-1880>.
- 128** Wirth, A., Hassan, M., Grguraš, I., Gagnon, J., Moulet, A., Luu, T., Pabst, S., Santra, R., Alahmed, Z., Azzeer, A. et al. (2011) Synthesized light transients. *Science*, **334** (6053), 195–200.

3

Ultrashort Pulse Characterization

Adam S. Wyatt

3.1

Motivation: Why Ultrafast Metrology?

The measurement process is fundamental in any experiment: without the ability to make a measurement, it is impossible to learn about the system under study. Since the electric field is a fundamental entity in Maxwell's theory, complete knowledge of the input, scattered, and radiated fields is required to extract the maximum information about an *optical* experiment.

In ultrafast optics, a key parameter of any experiment is the pulse duration, or more generally the exact time-dependent electric field. The pulse duration determines the temporal resolution of dynamical measurements and, for a given fluence, the peak intensity in strong-field experiments (shorter pulses have higher peak intensities). Since the pulse duration and shape is a key parameter in the characteristics of ultrashort pulses, it is necessary to perform ultrafast metrology from the start. The most advanced ultrafast experiments often require the most advanced laser sources; these sources need to be optimized to deliver the maximum energy, power, or intensity at a given central wavelength, bandwidth or pulse duration. Optimum performance can only be obtained through temporal characterization of the output pulses, or even complete space-time characterization of the pulses.

Since ultrashort pulses are, by definition, faster than any current electronic detector, it is not possible to perform direct measurements of the temporal intensity. In general it is possible to consider detectors to be time-integrating, simply measuring the average power incident on the detector. Thus it is necessary to utilize more elaborate schemes for measuring the temporal intensity profile. These schemes are based on measuring the spectral intensity and phase of the field, thus allowing a Fourier transform to obtain the temporal intensity and phase. In this tutorial, I shall describe a general framework for ultrafast metrology, and then outline a few of the most common methods within this framework.

This chapter is organized as follows: Section 3.1.1 outlines the motivation for ultrafast metrology in more detail and describes a few cartoon examples of how it

can be applied to study dynamical systems; Section 3.2 formally outlines what one wishes to measure, as well as some commonly used methods to describe ultrashort pulses; Section 3.3 describes a general framework for ultrafast metrology that can be used to understand the capabilities and limitations of any technique. This helps to visualize how existing methods can be extended to new regimes of operation; Section 3.4 details a wide variety of characterization schemes to measure ultrashort pulses in the infrared (IR), visible (vis) and ultraviolet (UV) spectral regions, where it is possible to make use of electro-optic modulators and nonlinear interactions, including the two most commonly used techniques of FROG (Section 3.4.2.1) and SPIDER (Section 3.4.5.2) – acronyms are explained in the relevant sections; and Section 3.5 outlines the most commonly used methods for characterizing extreme ultraviolet (XUV) pulses with durations ranging from femtoseconds to attoseconds, as well as several methods that have been proposed or demonstrated under limiting conditions.

The purpose of this tutorial is to provide a relatively unbiased outline of commonly used, and not so commonly used methods for characterizing ultrashort light pulses. For each method, I shall provide a nonexhaustive list of references describing experimental demonstrations of the method. Where appropriate, I will highlight currently known advantages and disadvantages of each technique in order to aid readers to isolate the most appropriate methods for their application. It is important to note that each method has its own advantages and that the true capabilities depend strongly on the nature of the pulse being characterized, on the exact variant of the technique used, and on the expertise of the user.

3.1.1

Ultrafast Science: High-Speed Photography in the Extreme

The method of high-speed photography was first demonstrated by Eadweard Muybridge in 1878 with his “Horse in motion”: for the first time it was possible to determine whether all four hooves of a horse simultaneously leave the ground when the horse gallops. Human observers could not resolve this question before. Muybridge’s achievement was possible through advancements in three key areas: (1) synchronization between the observed dynamical process and the measurement (via the use of trip wires), (2) gating the acquisition to limit the exposure time (via the use of fast mechanical shutters) and (3) improved detector sensitivity (improved film technology that could acquire the image in the short acquisition time). Synchronization is essential to ensure that the image is captured at the correct time; if averaging over multiple acquisitions, it is essential to ensure that the synchronization jitter is less than the temporal resolution. Gating is necessary to ensure that the system appears to be frozen during the exposure time of the detector; this is typically achieved by electronically gating the detector, or by illuminating the sample with a short flash. The shortest temporal resolution is now achieved via the use of gating with ultrashort laser pulses. Finally, the detection system needs to be sensitive enough to capture the image within the limited exposure time.

3.1.1.1 Time-Resolved Spectroscopy

A modern equivalent of Muybridge's experiment forms the basis of femtoscience and attoscience and is the so-called time-resolved spectroscopy (TRS), typically in the form of a pump-probe experiment. In such an experiment, a dynamical system is driven by a pump (usually a laser pulse) and then probed by a short laser pulse some time later. By scanning the delay between the pump and probe, a movie of the dynamics can be acquired, similar to a flick book, in order to measure how the system relaxes back into equilibrium [1]. In transient absorption spectroscopy (TAS), the absorption of specific wavelengths of light are measured as a function of the pump-probe delay [2–4], as shown in Figure 3.1a. The temporal resolution is then given by the interaction time of the probe with the system.

Time-resolved fluorescence spectroscopy (TRFS) is another common approach. In this case, the fluorescence emitted from an excited system is temporally gated and spectrally filtered as a function of the delay after pumping the system [5–7], see Figure 3.1b. The temporal resolution is then determined by the detection mechanism: electronic shuttering can provide sub-nanosecond resolution, streak cameras [8] offer sub-picosecond resolution, while optical gating provides the shortest temporal resolution, currently at tens of attoseconds.

Most forms of TRS assume that the optical pulses used to probe/gate the system are much shorter than the time scale of the dynamics of interest. It is necessary to characterize the probe/gate pulses to ensure that this assumption is correct. As the sources become more advanced, pushing the boundaries in terms of pulse duration, intensity and central wavelength, the information required to optimize the source becomes more complex and the requirements placed on the metrology devices become more demanding.

Figure 3.2a represents a cartoon for a model system and indicates how this system could be investigated using time-resolved spectroscopy. I shall use the example of a diatomic molecule, but the concepts can be applied to more general systems: the energy of the system (vertical axis) is plotted against internuclear separation along the horizontal axis. The curved lines are the electronic potential curves for the ground state, first excited state, and the ion. Initially, all molecules are in the ground state at some large internuclear separation. The molecules are then excited by a broadband pulse, resonant with the first excited state. Since the pulse is broad-

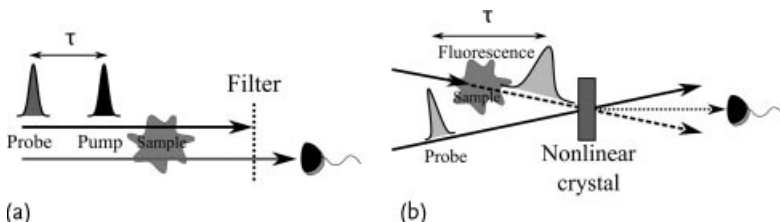


Figure 3.1 Cartoons of different time-resolved spectroscopy experiments. Transient absorption spectroscopy: the absorption of the ultra-short probe is measured as a function of

the pump-probe delay, τ (a). Time-resolved fluorescence spectroscopy: the fluorescence is temporally gated by an ultrafast pulse and then spectrally resolved (b).

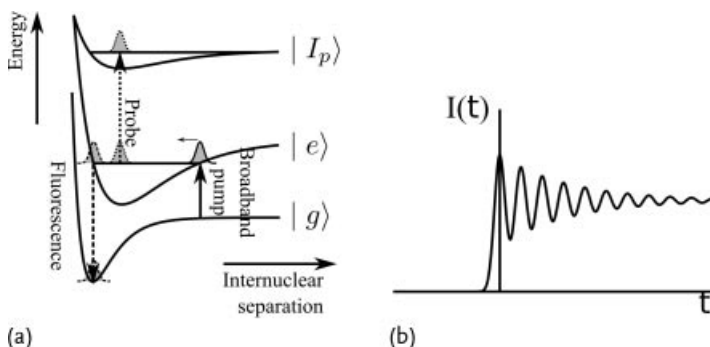


Figure 3.2 A model system based on a diatomic molecule for performing time-resolved spectroscopy. Energy level diagram of the molecule as a function of internuclear separation (a). The potential curves for three different electronic states are shown: ground state, $|g\rangle$, excited state, $|e\rangle$ and singly ionized state, $|I_p\rangle$. Excitation from a broadband pump can excite multiple excitation levels, generating an excited state vibrational wave packet

that will oscillate in the electronic potential. This wave packet can be probed either with an ionizing pulse or by spectrally and temporally resolving the fluorescence at the inner turning point. An example pump-probe signal for this system (b). The decay in the oscillation amplitude could be due to population decay, anharmonicity in the electronic potential (which could exhibit revivals), or from decoherence through interactions with the environment.

band, this will excite multiple vibrational and rotational levels, thus creating a wave packet in the excited state. This wave packet will then oscillate in the potential; the oscillation corresponds to a molecular vibration. The system can be probed in two ways. The first way utilizes the fact that there is a relatively good Franck–Condon overlap with the ground state at the inner turning point. Thus, some molecules will decay into the ground state, spontaneously emitting fluorescence with a photon energy equal to the ground-excited state separation at that internuclear separation. If this fluorescence is spectrally and temporally resolved, the measurement would provide an oscillating intensity similar to that shown in Figure 3.2b.

Alternatively, one may ionize the molecules with a high frequency pulse and then detect the number of ions formed [9]. At a specific internuclear separation, the ionizing pulse spectrum can match the energy separation between excited and ionic state and a high ionic yield will only occur when the oscillating wave packet crosses that internuclear separation. Thus, one would also obtain a trace similar to Figure 3.2b. Depending on the potential energy curve of the molecule, excitation can be to or from inner or outer turning points [10], or to and from nonturning points [11, 12], although typically the Frank–Condon overlap is largest when transferring the population between turning points.

Many electronic potential curves exist in a real system and the population can be transferred between many different pairs of levels. In some cases, there may not be a single position with pronounced wavelength selectivity. There is also a fundamental limit resulting from the time-bandwidth theorem, which states that the product between the pulse duration and the spectral bandwidth is at least on the order of unity: the narrower the bandwidth, the longer the pulse. For longer

pulses, the wave packet will move during the interaction time, blurring out the dynamics. However, using a shorter pulse will require a larger bandwidth and thus may interact with more energy levels, reducing the wavelength selectivity.

3.1.1.2 Coherent Control

There is a logical step from observing a dynamical process to the attempt of controlling the process by optimization (either maximization or minimization) of the population transfer to a particular final state via coherent excitation with electromagnetic pulses. A classic example is the pump-dump scheme [13–15]: the system is excited by a broadband optical pulse, resulting in an excited state wave packet. This wave packet will then evolve depending on the shape of the excited state potential. At some later point, a dump pulse transfers the population to the desired final state, for example the ground vibrational state of the molecule in Figure 3.2 [16–18]. The pulse shapes found by optimizing a dynamical process in a real system tend to be very complex and usually exhibit multiple pulses, centered at different central wavelengths, and arriving at different times [19]. Such complex pulse shapes are intuitively expected, since it is necessary to transfer population to multiple states and to ensure destructive interference between excitation pathways that lead to undesired final states. To understand the coherent control process, it is necessary to fully characterize the optimal pulse used in the experiment. Due to the complexity of the pulses, this requires the most advanced pulse characterization techniques or a combination of different methods. Another experiment, similar to coherent control, is to distinguish between different species by observing the pulse shape that optimally transfers the population to a desired state [20].

3.1.1.3 A General Dynamical Optical Experiment

Many pump-probe experiments utilize near-Fourier-limited probe pulses at a well-defined time. However, it is also possible to utilize longer probe pulses with a duration that is comparable to the time scale of the dynamics being observed, but with a precisely known pulse shape. By accurately and precisely measuring changes in the pulse shape, it is possible to extract information about the dynamics of the system. A simple example, commonly used in experiments, is the use of a linearly chirped ultrabroadband pulse. Acting as the probe, the pulse duration spans the total duration of the dynamics being studied [21, 22]. Since the frequencies are linearly mapped in time, it is possible to directly measure the response of the system as a function of time by measuring the change in the intensity of each frequency with a spectrometer. This scheme requires that the wavelength dependence of the detector and system response is taken into account, although, if the probe pulse is far detuned from any resonances relative to the pulse bandwidth, then the system response is approximately flat. For this method to be accurate, it is necessary to fully characterize the chirp rate. For extremely large bandwidths, it may not be possible to exactly linearly chirp the pulse. This results in a nonlinear mapping of time to frequency, placing even more importance on accurately determining the chirp rate.

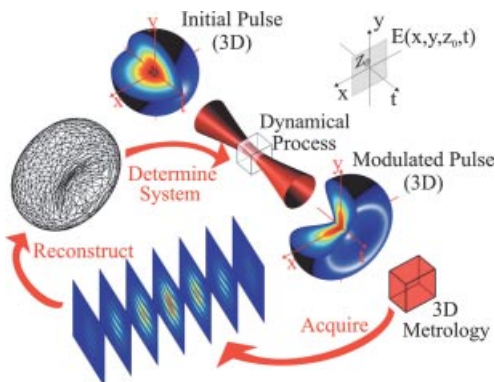


Figure 3.3 Cartoon of the most general optical experiment to determine some time-nonstationary system. To fully determine the dynamics of the system, one would need to know the electric field on the boundary to that

system. For ultrashort pulses, this can be determined by fully characterizing, in space and time, the incident and emergent fields at the entrance and exit planes, respectively.

Accurate and precise ultrafast metrology is very important in measuring and understanding nonlinear phenomena, since relatively small changes in the pulse shape (either spatial, temporal, or both) can lead to quite different dynamics, especially in strong-field physics. Figure 3.3 demonstrates the general principle of how to determine the dynamics of a nonlinear interaction. By measuring the full space-time field for both the incoming pulse and the modulated pulse after the interaction, the extra degrees of freedom can provide improved precision and accuracy for determining the dynamics of the process [23]. Such an experiment can even track specific dynamics of interest in the measured data that cannot be identified by measuring the temporal evolution alone [24].

3.2

Formal Description of Ultrashort Pulses

In this section I shall formally outline the mathematical and physical descriptions of ultrashort pulses. The objective of ultrafast metrology is not to determine how the electric field changes inside the medium of interest – this is the goal of the ultrafast scientist. Instead, ultrafast metrology reconstructs the electric field at some point or plane transverse to the direction of propagation. Typically, the location of this point or plane differs from the location of the experiment and therefore the user is required to determine the electric field at the entrance or exit of the system under study. Under these restrictions, it is only necessary to consider linear optics and to neglect the magnetic field for the purpose of defining the ultrashort pulse at the entrance/exit of the system. The electric field, magnetic field, and nonlinear polarization can then be uniquely determined from the electric field on the boundary of the system, where linear optics are valid.

In a homogeneous isotropic linear medium, all electric field polarizations are decoupled, thus it is sufficient to describe the electric field according to Maxwell's scalar wave equation:

$$\left[\nabla^2 - \frac{n^2}{c^2} \frac{\partial^2}{\partial t^2} \right] \xi = 0, \quad (3.1)$$

where n is the refractive index of the medium, c is the speed of light (in vacuum) and ξ is the real electric field in a given polarization. A particular solution of interest to this equation is that of a plane wave,

$$\xi = \xi_0 \cos(\mathbf{k} \cdot \mathbf{r} - \omega t + \phi), \quad (3.2)$$

where \mathbf{k} is the wave vector (denoting the phase velocity and direction of propagation), ω is the frequency¹⁾ and ξ_0 is the amplitude of oscillation. Such a solution is neither a general solution, nor is it a physical solution since it extends over all space and time. A physical (and general) field can be obtained by summing over all wave vectors and frequencies. Since the wave vector is constrained, $|\mathbf{k}|^2 = k_x^2 + k_y^2 + k_z^2 = (n\omega/c)^2$ (setting \hat{z} to be the optical axis), the general solution located at a plane z relative to a reference plane z_0 can be defined as

$$\begin{aligned} \xi(\mathbf{r}, t) = 2\Re \left\{ \iiint \left| \tilde{E}(\mathbf{k}_\perp, \omega, z_0) \right| e^{i\tilde{\phi}(\mathbf{k}_\perp, \omega, z_0)} \right. \\ \times \exp \left[i\sqrt{|\mathbf{k}|^2 - k_x^2 - k_y^2}(z - z_0) \right] e^{ik_x x} e^{ik_y y} e^{-i\omega t} dk_x dk_y d\omega \left. \right\}. \end{aligned} \quad (3.3)$$

For convenience in linear optics, it is only necessary to consider the positive frequencies, corresponding to forward propagating waves, thus Eq. (3.3) reduces to the analytic solution given by the Fourier transform over all angles of propagation and frequencies,

$$\begin{aligned} E(\mathbf{r}, t) &= \mathcal{F}_{k_x \rightarrow x} \left\{ \mathcal{F}_{k_y \rightarrow y} \left\{ \mathcal{F}_{\omega \rightarrow t}^{-1} \left\{ \tilde{E}(\mathbf{k}_\perp, \omega, z_0) e^{ik_z \Delta z} \right\} \right\} \right\} \\ \xi(\mathbf{r}, t) &= 2\Re \{ E(\mathbf{r}, t) \} \end{aligned} \quad (3.4)$$

where $\Delta z = z - z_0$ and E is the analytic signal. In nonlinear optics, it is necessary to consider both positive and negative frequency components (e.g., the third-order polarization can be decomposed into two contributing factors: E^3 and $E|E|^2$, resulting in third harmonic generation and self-phase modulation/optical Kerr lensing respectively).

The analytic signal, $E(\mathbf{r}, t)$, is a complex entity, the magnitude of which is proportional to the square root of the temporal intensity. The Fourier transform of the analytic signal determines the spectral amplitude, $\tilde{E}(\mathbf{k}_\perp, \omega, z)$, a complex entity whose magnitude is proportional to the square root of the spectral intensity.

1) Unless specifically stated otherwise, I shall use the term frequency to mean angular frequency.

It may be convenient, but not necessary or always useful, to decompose the spectral ($\tilde{\phi}(\omega)$) and temporal ($\phi(t)$) phase functions into their Taylor coefficients (for simplicity I shall neglect the spatial degree of freedom):

$$\begin{aligned}\phi(t) = \phi_0 + \frac{\partial\phi(t_0)}{\partial t}(t - t_0) + \frac{\partial^2\phi(t_0)}{\partial t^2}(t - t_0)^2 \\ + \sum_{n=3}^{\infty} \frac{\partial^n\phi(t_0)}{\partial t^n}(t - t_0)^n\end{aligned}\quad (3.5)$$

$$\begin{aligned}\tilde{\phi}(\omega) = \tilde{\phi}_0 + \frac{\partial\tilde{\phi}(\omega_0)}{\partial\omega}(\omega - \omega_0) + \frac{\partial^2\tilde{\phi}(\omega_0)}{\partial\omega^2}(\omega - \omega_0)^2 \\ + \sum_{n=3}^{\infty} \frac{\partial^n\tilde{\phi}(\omega_0)}{\partial\omega^n}(\omega - \omega_0)^n.\end{aligned}\quad (3.6)$$

Each of the first three terms in the expansion can be associated with an intuitive physical entity. The absolute temporal and spectral phase in Eq. (3.5) is known as the *carrier envelope phase* (CEP) and relates (in simple pulse shapes) the offset between the peak electric field and the peak of the intensity envelope. The linear temporal phase term gives rise to the instantaneous frequency, $\omega_{\text{inst}}(t) = \omega_0 + \partial\phi(t)/\partial t$, and the quadratic term the (linear) chirp, since it quantifies the rate of change in the instantaneous frequency. The linear spectral phase term is the *group delay* (GD) of the pulse, $\tau_{\text{GD}}(\omega) = \partial\tilde{\phi}(\omega)/\partial\omega$. For simple pulse shapes, this is the delay of the peak in the intensity envelope. The third term is the *group delay dispersion* (GDD) and determines the (linear) stretch of the pulse resulting from dispersion. These terms are shown in Figure 3.4a. The rate of change of the CEP from pulse to pulse in a pulse train gives rise to the *carrier envelope offset* (CEO) and results in the frequency comb being offset from zero frequency (DC), as shown in Figure 3.4b.

It should be noted that all self-referencing methods described later in Section 3.4 cannot measure the CEP or GD of the pulse. The latter is trivially obvious, since the GD is not defined for a pulse in isolation – one requires a reference time to be delayed from. It is possible to measure the CEO via an f-to-2f interferometer (or equivalent) and then to stabilize the CEO of a laser (see Chapter 4) [25–28]. However, this does not define the CEP of the individual pulses, but rather the CEP phase slip from one pulse to the next (or, more usually, to the fourth pulse). The CEP can be varied via a number of techniques: applying an offset to a CEO stabilization feedback system, using a phase modulator, or transmission through a variable amount of glass, such that the dispersion results in a different group and phase velocity (e.g., fused silica introduces approximately 0.12 rad/ μm CEP phase shift at 750 nm). The CEP can be measured by processes that are sensitive to the electric field and not the intensity, for example via high harmonic generation [29, 30], stereo above-threshold ionization [31], photoelectron emission from metal surfaces [32, 33], or terahertz-emission spectroscopy [34].

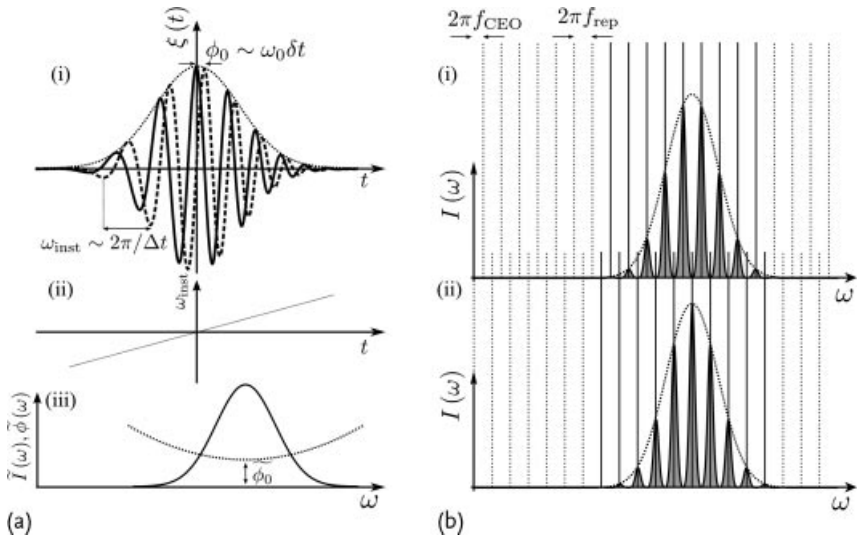


Figure 3.4 (a) Physical meaning of phase terms in Eqs. (3.5)–(3.6): (i) CEP (absolute phase) and instantaneous frequency, (ii) chirp (change in instantaneous frequency) and (iii) spectral phase (Δt – optical period). (b) Frequency comb with (i) $\phi_{\text{CEO}} = \pi$ and (ii) $\phi_{\text{CEO}} = 0$.

3.2.1

Sampling Theorem

The sampling theorem states that for a pulse with compact support T , the spectrum needs to be sampled at a rate $\delta\omega = 2\pi/T$. Conversely, for a band-limited pulse with total bandwidth B , the required temporal sampling rate is given by $\delta t = 2\pi/B$. Combining these two equations leads to a definition of the *time-bandwidth product* (TBP), $N_{\text{dB}} = BT/2\pi$, that is a useful measure to indicate the *pulse complexity*, which defines the minimum number of points N required to sufficiently sample the analytic function. It should be noted that it is impossible for a pulse to have both compact support and be band-limited simultaneously. Therefore, it is necessary to choose the dynamic range, determined to be the ratio of the peak intensity to the noise floor; I shall quote the dynamic range in dB as a numeric subscript in the pulse complexity. The choice of the dynamic range depends strongly on the application. For example, in high harmonic generation with a peak intensity of $I_0 \lesssim 10^{15} \text{ W cm}^{-2}$, a dynamic range of 30 dB should suffice. If the peak laser intensity increases further, for example, $I_0 > 10^{18} \text{ W cm}^{-2}$, it is necessary to measure the pulse with an even higher dynamic range, since a comparatively small pre-pulse may still have sufficient intensity to field-ionize the medium and thus change the dynamics of the process, or the amplified spontaneous emission background could fully ionize the sample before the main pulse arrives.

3.2.2

Chronocyclic Representation of Ultrafast Pulses

As described in Section 3.2, the gradient of the temporal phase determines the instantaneous frequency as a function of time; this implies the possibility to describe ultrafast pulses via a time-frequency distribution. A commonly used distribution is the chronocyclic Wigner distribution [35], defined as

$$W(t, \omega) = \frac{1}{2\pi} \int \left\langle E\left(t + \frac{t'}{2}\right) E^*\left(t - \frac{t'}{2}\right) \right\rangle e^{i\omega t'} dt' . \quad (3.7)$$

The Wigner distribution, used extensively in quantum optics, is useful in describing the action of devices and the nonlinear propagation of ultrashort pulses. The Wigner distribution is always real, but not necessarily positive – negativity is a sign of interference of a frequency located at multiple times (e.g., cubic phase or a double pulse). The marginals (Eqs. (3.8) and (3.9)) of the Wigner distribution give the spectral and temporal intensities (and, therefore, are always positive)

$$\tilde{I}(\omega) = \int W(t, \omega) dt \quad (3.8)$$

$$I(t) = \frac{1}{2\pi} \int W(t, \omega) d\omega . \quad (3.9)$$

Example Wigner distributions and marginals are shown in Figure 3.5.

3.2.3

Space-Time Coupling

The description of optical pulses so far has only considered temporal field distributions, neglecting any spatial distribution. This is sufficient, provided the pulse is factorable in space and time, that is, the temporal profile is independent of position:

$$E(t, \mathbf{r}) = E_{\text{time}}(t) E_{\text{space}}(\mathbf{r}) . \quad (3.10)$$

In practice, Eq. (3.10) is not always satisfied, as the temporal evolution of the field may depend on position; the pulse is said to exhibit space-time coupling (STC). Equation (3.10) also implies, when considering the complex amplitudes, that if a pulse does not exhibit STC then it must be possible to write the pulse in a factorizable form in any combination of temporal–frequency and spatial-angular representations. Thus, STC also exists when there is a spatial or angular dependence on the pulse spectrum, or the spectral phase, or both, leading to eight types of space-time coupling [36] (four amplitude and four phase spatio-temporal distortions). STC is often used to perform temporal shaping of optical pulses, for example, in a 4-f pulse shaper and in chirped pulse amplifier systems [37, 38]. However, STC can also arise due to misalignment of optical setups, from propagation of large bandwidth pulses or from nonlinear effects. Although STC can arise in a complicated form, it is useful to consider first-order STC.

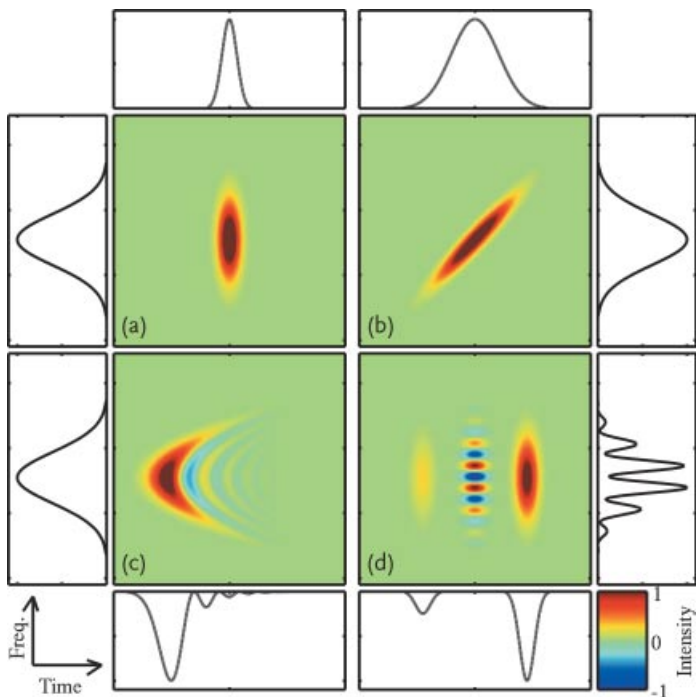


Figure 3.5 Example chronocyclic Wigner distributions (images: negative values in black, positive in white, zero in gray) and marginals (spectral intensity as solid line, temporal in-

tensity as dashed line) for Fourier-limited pulse (a), quadratic phase (linear chirp) (b), cubic phase (c) and a double pulse (d).

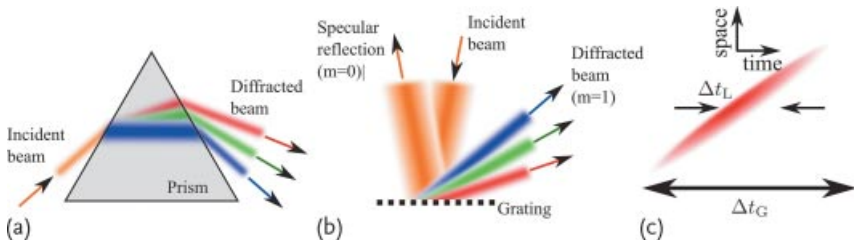


Figure 3.6 Angular dispersion (i.e., frequency-dependent propagation direction) generated from a prism (a) and grating (b). Pulse front tilt (i.e., spatially dependent group delay) as a result of angular dispersion (c).

3.2.3.1 Angular Dispersion

Angular dispersion (AD) occurs when there exists a frequency-dependent propagation direction, typically generated from prisms or gratings as shown in Figure 3.6a,b. AD is also equivalent to *pulse front tilt* (PFT): the arrival time of the pulse varies as a function of position and is shown in Figure 3.6c.

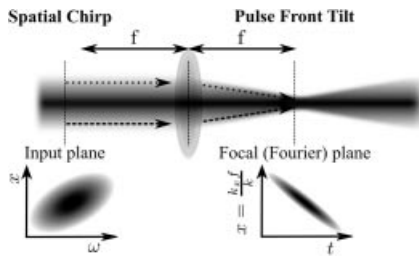


Figure 3.7 A collimated beam that exhibits spatial chirp (i.e., a spatially dependent carrier frequency) will exhibit pulse front tilt at the focal plane of a lens, since the angular distribution is mapped to space due to the Fourier transform property of the lens.

Pulse front tilt is generally detrimental to time-resolved spectroscopy as it creates temporal smearing in spatially integrated measurements. This is because the arrival time of the probe at the sample is less well defined if the measurement is averaged over the spatial profile of the beam. Angular dispersion normally arises from an improperly aligned prism or grating stretchers/compressors or from transmission through a wedged optic.

3.2.3.2 Spatial Chirp

Spatial chirp occurs when the central wavelength changes as a function of position and often arises from chirped pulse amplified systems due to improper alignment of prism or grating stretchers/compressors. Spatial chirp in a collimated beam results in pulse front tilt when the beam is focused to a spot, see Figure 3.7. Each frequency will have a different mean tilt due to passing the focusing optic at different spatial position and thus the pulse will exhibit angular dispersion at the focus. Nonlinear spatial chirp is also present in high harmonic generation and needs to be measured and reduced to obtain the optimal pulse for time-resolved spectroscopy.

3.2.3.3 Focusing of a Short Optical Pulse

When a short pulse is focused by a lens, portions of the wavefront at the edge of the lens will experience a different thickness of material than the portions at the center of the lens and, thus, will experience different dispersion and group delays, see Figure 3.8. Portions of the wavefront that traverse the lens near the edge will arrive at the focus before portions that traverse the lens through the center. The group front of the beam will no longer be a spherical wave centered at the focus. The apparent pulse duration at the focus can therefore be dramatically larger than the effective duration of each ray. This phenomenon was first pointed out by Bor, using simple ray tracing calculations [39].

As an example, a singlet lens made of BK7 with a focal length of 10 cm will introduce a 50 fs delay between the paraxial ray and a ray 1 cm off-axis. This is obviously significant for short, few-cycle pulses. This phenomenon can also be described in the frequency domain as *chromatic aberration* (i.e., a frequency-dependent focal length and mode size). An achromat, optimized for the correct wavelength,

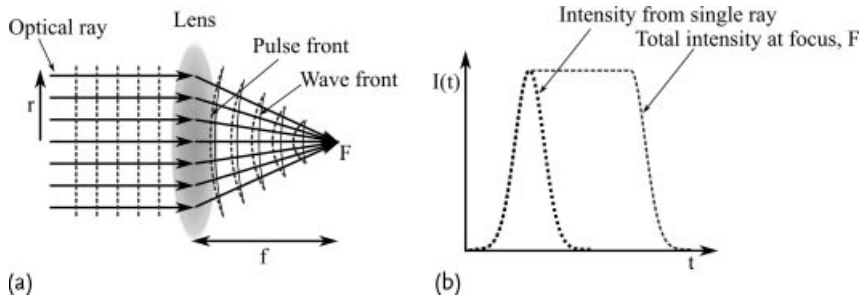


Figure 3.8 Increase in the duration of an ultrashort pulse due to a lens. A singlet lens focuses a collimated beam at F (a). The pulse front does not coincide with the spherical wavefront and thus the temporal intensity will be considerably longer at the focus than before the lens (b).

can reduce this group delay. However, the pulse will also experience GDD due to the material itself. This will result in the pulse stretching in time due to material dispersion alone, which is also significant for few-cycle pulses. For example, a bandwidth-limited 10 fs pulse centered at 800 nm is stretched by a factor of four when traversing 3 mm of BK7 glass (i.e., at the center of a thin lens). The dispersion at the edge of the lens is smaller, resulting in STC. This dispersion effect is considerably less than the STC introduced by the difference in the group and phase delay.

3.2.3.4 Frequency-Dependent Mode Size

A pulse can also exhibit STC from diffraction alone, since diffraction is wavelength dependent, resulting in a *frequency-dependent mode size* (FDMS). This effect is only noticeable for a bandwidth that is at least octave spanning (i.e., few-cycle pulses). Figure 3.9 illustrates this phenomenon for a few-cycle pulse upon propagation in free space and subsequent recollimation by a spherical mirror. The initial pulse can be written in the form given in Eq. (3.10).

The carrier frequency decreases as a function of the radial coordinate, a result of the frequency-dependent diffraction. A further effect, that is less obvious, is that the root mean square pulse duration is also radially dependent. This would have a significant effect in a spatially integrated linear time-nonstationary optical experiment, but has less significance in an optically nonlinear experiment.

3.2.4

Accuracy, Precision and Consistency

The performance of any metrology device can be quantified by three different parameters. *Accuracy* is a measure of how well the reconstructed field matches the physical field which is measured. Inaccuracies are often a result of *systematic* errors. Since the physical field can only be obtained through measurement, the accuracy can only be quantified via simulation of the device and comparison with reconstructions of the same pulse from multiple independent devices. *Precision* is

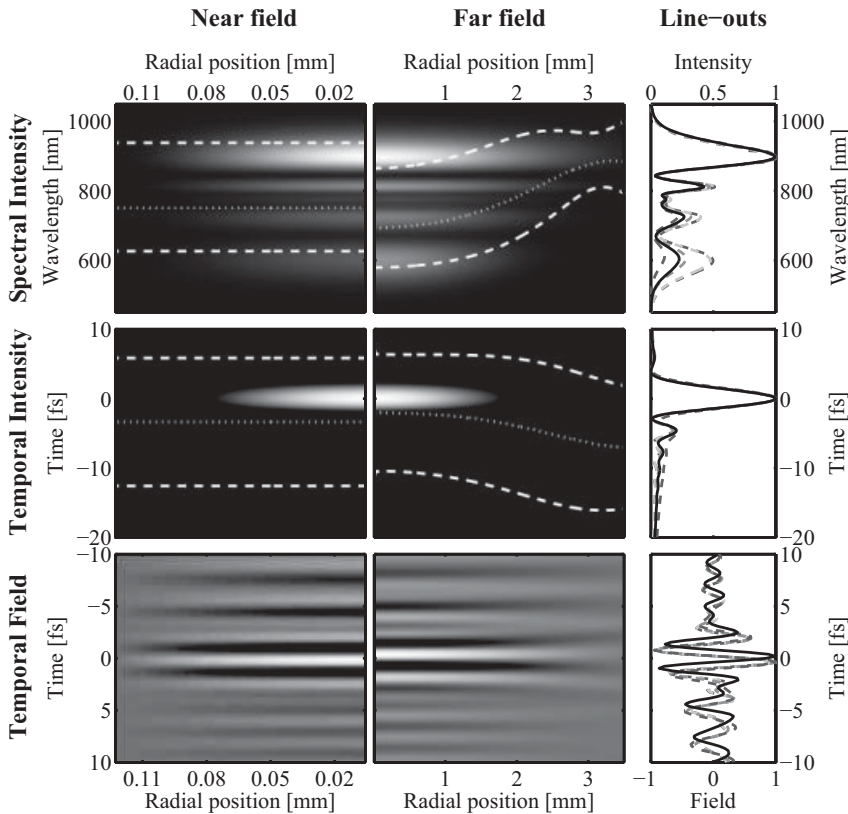


Figure 3.9 Space-time coupling of an octave spanning pulse due to a frequency-dependent mode size resulting from propagation in free space. The pulse is generated via a simulation of the output of a 250 μm diameter hollow fiber pulse compressor [40] and the output mode is assumed to have zero space-time coupling. The fiber output is numerically propagated 750 mm, collimated by a spherical mirror (astigmatism neglected) and propagated a further 750 mm. The near field (exit face of fiber), far field (after propagation and collimation) and line-out from near field (solid black) and far field (dashed gray) in columns are shown. The three rows show the spectral

intensity, temporal intensity and real temporal field. Dotted lines mark the intensity centroid position, dashed lines mark plus/minus one standard deviation. Note that the far field has a $\pi/2$ phase shift due to the Gouy phase. The pulse spectrum is blue-shifted near the center of the beam in the far field compared to the near field. The spectrum red-shifts with a decreasing bandwidth away from the center, consistent with the fact that longer wavelengths diffract more. The arrival time of the peak intensity is constant with radial position, but the mean arrival time and root mean square duration of the pulse varies across the beam.

a measure of the dispersion between multiple reconstructions of the same pulse. Imprecision is often a result of *random* errors. If a reliably reproducible pulse is available, the precision can be determined from multiple measurements of the same pulse. However, redundancy in the data can also be used to measure precision from a single measurement, thereby avoiding shot-to-shot instabilities. Consis-

tency is here defined to be a measure of the difference between the measured data and data simulated from the reconstructed field. Iterative routines often strive to maximize consistency. But although poor consistency implies poor accuracy, good consistency does not necessarily imply good accuracy.

3.3

Linear Filter Analysis

Different characterization methods encode information about the pulse in different ways and therefore require quite different inversion protocols. The general protocol required for a given device can be made clear by working with linear transformations. This allows for the categorization of different methods and provides a catalogue of currently available technologies. This methodology becomes even more useful when it is necessary to operate in new regimes and therefore new devices are sought. Although the processes involved in these new regimes may appear quite different, the concepts involved (and the inversion routines employed) would be the same as in existing regimes.

The necessary and sufficient conditions that must be satisfied to completely characterize an ultrashort pulse can be determined from a general theory based on manipulating the pulses via a set of linear filters [41, 42]. This implies that it is possible to fully characterize ultrashort pulses utilizing purely linear optics, a fact that was only recently appreciated [41, 43]. In practice, however, many methods make use of nonlinear optics since it is difficult to construct linear devices suitable for pulses with durations of several hundred femtoseconds or less. Nonlinear optics often increases the complexity of the inversion routine, sometimes requiring an iterative inversion routine. However, as will be seen, nonlinear methods can often be formulated in terms of linear filters. By expressing an optical interaction in terms of linear filters, it becomes clear how to characterize the ultrashort pulse by utilizing a metrological scheme that is based on the same set of filters.

Since the pulse spectrum can be measured straightforwardly with a spectrometer, we remain with the issue of determining the spectral phase. Although some methods also return the spectrum, it is wise to compare this to an independent spectral measurement, since this provides a most basic accuracy check.

A linear filter is one in which the output field depends linearly on the input field:

$$E_{\text{out}}(t) = \int H(t, t') E_{\text{in}}(t') dt', \quad (3.11)$$

$$\tilde{E}_{\text{out}}(\omega) = \int \tilde{H}(\omega, \omega') \tilde{E}_{\text{in}}(\omega') d\omega'.$$

One can decompose the filters into two types: time-stationary (frequency-nonstationary), H_S (Eq. (3.12)) and frequency-stationary (time-nonstationary), H_N

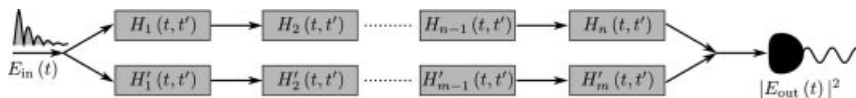


Figure 3.10 Pulse characterization methods can be decomposed into an array of linear filters placed in series or in parallel.

Table 3.1 Basic linear filters used for ultrafast metrology: all filters in general can be described as a combination of these filters.

Type	Time	Frequency
Gate/filter	$N^a(t - \tau; \tau_g) = -((t - \tau)/\tau_g)^2$ $\sim \delta(t - \tau)$	$\tilde{S}^a(\omega - \Omega; \Gamma) = e^{-(\omega - \Omega)/\Gamma^2}$ $\sim \delta(\omega - \Omega)$
Linear phase	$N_1^P(t; \psi^{(1)}) = e^{i\psi^{(1)}t}$	$\tilde{S}_1^P(\omega; \phi^{(1)}) = e^{i\phi^{(1)}\omega}$
Quadratic phase	$N_2^P(t - \tau; \psi^{(2)}) = e^{i\psi^{(2)}/2(t-\tau)^2}$	$\tilde{S}_2^P(\omega - \Omega; \phi^{(2)}) = e^{i\phi^{(1)}/2(\omega - \Omega)^2}$

(Eq. (3.13)).²⁾

$$H_S = S(t - t') \longleftrightarrow \tilde{H}_S = \tilde{S}(\omega') \delta(\omega - \omega') \quad (3.12)$$

$$H_N = N(t') \delta(t - t') \longleftrightarrow \tilde{H}_N = \tilde{N}(\omega - \omega'), \quad (3.13)$$

where \longleftrightarrow denotes a Fourier transform. These filters can be arranged in series or in parallel, as shown in Figure 3.10, whose output would be given by $E_{\text{out}}(t) = \{\int \dots \int H_n H_{n-1} \dots H_2 H_1 + \int \dots \int H'_m H'_{m-1} \dots H'_2 H'_1\} E_{\text{in}}(t')$. The basic requirements for complete characterization are quite straightforward: a time-nonstationary filter (i.e., a fast shutter or phase modulator), a spectrometer or dispersive element, and one or two beam-splitters.

The linear filters can be broken down further into a set of three stationary and three nonstationary filters:³⁾ a fast shutter or spectral filter, a linear temporal or spectral phase filter (i.e., a spectral shift or time delay, respectively), and a quadratic temporal or spectral phase filter (i.e., frequency modulation and linear chirp, respectively). The forms of these filters are described in Table 3.1.

Walmsley *et al.* [44] showed that a sufficient and necessary condition for ultrafast metrology is the use of both, a time stationary and time nonstationary filter. Since, when dealing with ultrafast pulses, all detectors are time integrating, the last filter must be an amplitude filter. Therefore, there are only four basic characterization categories: either a phase or amplitude nonstationary filter followed by an amplitude stationary filter, or an amplitude or phase stationary filter followed by an amplitude nonstationary filter.

2) I will use S to denote time-stationary and N to denote time-nonstationary filters.

3) I forthwith omit the word “time,” i.e., time-stationary and time-nonstationary become stationary and nonstationary, respectively.

3.4

Ultrafast Metrology in the Visible to Infrared

3.4.1

Temporal Correlations

3.4.1.1 Field Autocorrelation

The *field autocorrelation*, $A(\tau)$ of a pulse is the time-integrated interference of a pulse and a time-delayed version of itself, formally described by Eq. (3.14). This forms the basis of *Fourier transform spectroscopy* (FTS) [45, 46]. It is relatively straightforward to show that the Fourier transform of the field autocorrelation is equal to the pulse spectral intensity, $|\tilde{E}(\omega)|^2$, and therefore does not contain any information on the pulse spectral phase:

$$\begin{aligned} A(\tau) &= \int E(t) E^*(t - \tau) dt \\ &= \mathcal{F}_{\omega \rightarrow t}^{-1} \left\{ |\tilde{E}(\omega)|^2 \right\}. \end{aligned} \quad (3.14)$$

The field autocorrelation is useful for measuring the spectrum with high resolution and dynamic range with a single detector and can be achieved experimentally by measuring the intensity of the output of a Michelson interferometer as a function of the delay between the two pulses. The intensity signal is given by

$$\begin{aligned} I_m(\tau) &= \int |E(t) + E(t - \tau)|^2 dt \\ &= 2 \int I(t) dt + 2\Re \left\{ \int E(t) E^*(t - \tau) dt \right\}. \end{aligned} \quad (3.15)$$

Simulations of example signals are shown in Figure 3.11c.

3.4.1.2 Second-Order Autocorrelation

If the output of the interferometer is up-converted in a crystal with $\chi^{(2)}$ nonlinearity, then it is possible to perform an *interferometric autocorrelation*, provided there is sufficient intensity. The measured signal (see Figure 3.11d) is given by

$$\begin{aligned} I_{AC}(\tau) &= \int |E(t) + E(t - \tau)|^4 \\ &= 2 \int I^2(t) dt + 2\Re \left\{ \int [E(t) E^*(t - \tau)]^2 dt \right\} \\ &\quad + 4\Re \left\{ \int I(t) E(t) [E^*(t - \tau) + E^*(t + \tau)] dt \right\} \\ &\quad + 4 \int I(t) I(t - \tau) dt. \end{aligned} \quad (3.16)$$

The frequency of the fringes in the measured signal are equal to the central wavelength of the test pulse and therefore provide a quick calibration of the tempo-

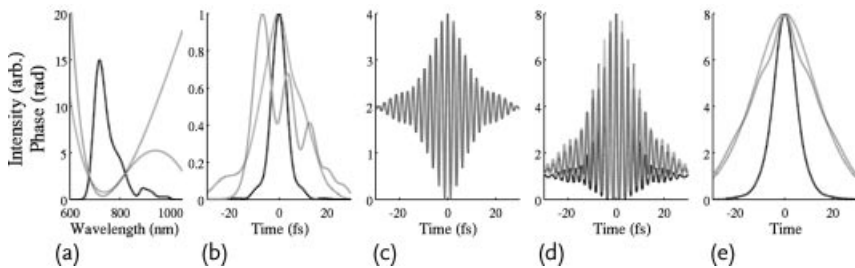


Figure 3.11 Simulated examples of temporal correlations. Spectral intensity (dotted black) and two different spectral phases (gray) used to simulate various temporal autocorrelations (a). Temporal intensity (gray) of pulses in (a), including the temporal intensity corresponding to the Fourier transform-limited pulse, that is, Fourier transform of spectral amplitude only (dotted black) (b). The field (c), interferometric (d) and intensity autocorrelations (e), respectively, of pulses in (b). All

pulses have the same spectrum and thus the same field autocorrelation (c). Notice that the intensity autocorrelation easily identifies the approximate pulse duration but cannot easily distinguish between very different pulse shapes. Phase information is encoded in the fringe pattern of the interferometric autocorrelation (d), but very high signal-to-noise ratio is required to enable an adequate reconstruction of the spectral phase.

ral axis. The interferometric autocorrelation does contain phase information, but as the complexity of the pulse increases, structure in the measured trace “washes” out. Therefore, it is not the ideal measurement device: the more “information” there is to obtain from the pulse, the less “information” is contained in the measured signal. The ratio of the peak to the background should be 8 : 1 and is often used as quick consistency check.

If the beams cross noncollinearly in the crystal, the measured signal will be given by only the last term in Eq. (3.16), giving rise to an *intensity autocorrelation*, Figure 3.11e. The intensity autocorrelation is easier to measure, since it does not require interferometric stability. Although the intensity autocorrelation does not contain any phase information directly, it is possible to invert the signal provided additional constraints are applied (e.g., measured spectrum, nonnegative spectrum, known compact support) [47, 48]. However, many different pulse shapes lead to similar intensity autocorrelations and very high signal-to-noise ratio (SNR) and simple pulse shapes are required to provide a good reconstruction.

Although autocorrelations are not ideal for providing the exact pulse shape, they are very useful due to their simplicity and allow easy estimation of the pulse duration and, for example, aid the optimization of compressors in amplified systems. They can also be used as a consistency check for more complete measurement devices. Misalignment of the autocorrelator can create errors in the reconstructed pulse duration estimate, often reducing the measured value with respect to the real value. Other effects, such as the spatial profile or space-time coupling can also lead to erroneous results.

3.4.1.3 Cross-Correlation

If the two pulses crossing in a nonlinear crystal are not identical, then the measurement is called a *cross-correlation*. This technique is often employed when one of the pulses is known to be significantly shorter than the other; the shorter pulse can then be approximated as a temporal delta-function and can be used to sample the intensity of the longer pulse. Third-order cross-correlation is often employed to measure the contrast ratio of ultrahigh intensity pulses on long time scales and with very high dynamic range. This method was used, for example, to measure amplified spontaneous emission over hundreds of picoseconds [49].

3.4.1.4 Electro-optic Sampling

Electro-optic sampling (EOS) is a method based on the electro-optic effect and can be used to measure ultrafast pulses with picosecond resolution [50] or for measuring the electric field (not intensity) of a low-frequency test field via a cross-correlation with a higher frequency gate pulse. The gate pulse duration must be less than the period of the test field, for example, to measure fields in the terahertz spectral frequency range [51]. In this case, it is possible to obtain the pulse spectral intensity and phase, including the CEP, since the complete field is measured. Usually the gate field is considered to be a delta function as compared to the oscillation period of the test field. This does not necessarily need to be the case, see, for example, Section 3.5.1.8, where a variant of EOS is used to reconstruct XUV attosecond pulses “mixed” with an IR field.

3.4.2

Spectrography

The general principle of spectrography is to temporally gate the test pulse and then spectrally resolve the gated pulse. Thus, the device consists of an amplitude non-stationary filter (fast shutter), followed by an amplitude stationary filter (spectrometer), as shown in Figure 3.12. Such a method can be considered as very intuitive: as the gate is scanned through the test pulse, the central wavelength of the gated pulse will follow the instantaneous frequency. Ideally, one would like to obtain maximum temporal resolution by using the fastest gate possible. However, the time-bandwidth theorem dictates that the bandwidth of the gated function is inversely proportional to its time duration. Therefore, the optimal gate duration is approximately equal to the inverse of the test-pulse bandwidth, in order to prevent “spectral blurring.” For femtosecond pulses, the only object that satisfies this condition is the pulse itself and therefore spectrographic methods are typically based on nonlinear interactions.

3.4.2.1 Frequency-Resolved Optical Gating

Frequency-resolved optical gating (FROG) is a spectrographic method for measuring ultrafast pulses in the ultraviolet (UV), visible (vis.) and infrared (IR) with pulse durations ranging from a few femtoseconds up to hundreds of picoseconds [52–54]. There are numerous experimental implementations that differ in the nonlinear

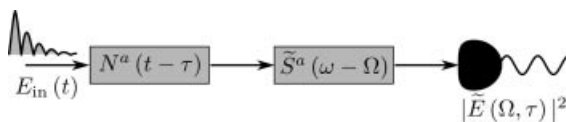


Figure 3.12 Linear filter combination required to perform spectrography: an amplitude non-stationary filter (temporal gate), followed by an amplitude stationary filter (spectrometer). In the case of FROG, the gate is formed by the

pulse itself (equivalent to a series of amplitude nonstationary filters with varying phase), therefore the measured signal requires an iterative inversion routine to recover the pulse shape.

process used, or in the method of generating the “gate” and “probe” (test) pulses. In all cases, the measured signal can be written as

$$I(\omega, \tau) = \left| \int P(t) G(t - \tau) e^{i\omega t} dt \right|^2 \quad (3.17)$$

where τ is the delay between the “probe” P and “gate” G , and ω is the frequency axis of the spectrometer. The functional form of the probe and gate is determined by the nonlinear process and is described mathematically in Eqs. (3.18a)–(3.18e). The most commonly used geometry is that of *second harmonic generation* (SHG) FROG, Eq. (3.18a), since this typically has the highest efficiency, see Figure 3.13 [55]. However, the measured trace is symmetric about the delay axis, thus resulting in a direction of time ambiguity, that is, $I_{SHG}[\omega, \tau; E(t)] = I_{SHG}[\omega, \tau; E(-t)]$. This ambiguity can be resolved by an additional measurement of the test pulse after adding known dispersion (e.g., passing through a glass slide before the device) or adding a dispersive element in one arm of the interferometer to break the symmetry (note that simply attenuating one beam is not sufficient) [56].

Alternatively one can use the third-order polarizability of optical materials to provide five alternative geometries: *polarization gating* (PG), *self-diffraction* (SD), *transient grating* (TG) in two geometries [57] and *third harmonic generation* (THG) [58]; the gate functions are given in Eqs. (3.18b), (3.18c), (3.18d) and (3.18e) respectively. These methods often have lower efficiency than SHG frog, due to the lower nonlinear polarizability. However, since phase matching is not an issue in PG-, TG- and SD-FROG, thicker materials can be used and detection occurs at the fundamental wavelength, which may have higher detection efficiency. This can partially compensate the lower nonlinearity compared to SHG-FROG. In all cases, the symmetry of the process is broken and there is no direction of time ambiguity (except for the

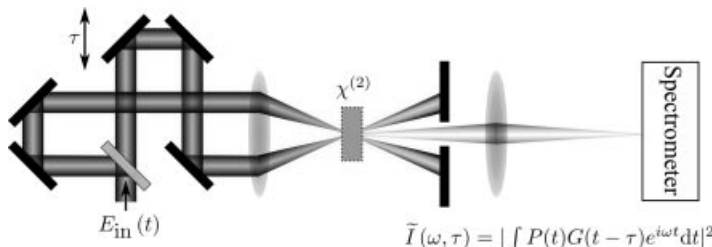


Figure 3.13 Schematic of SHG FROG setup.

sign of linear chirp in THG-FROG for symmetric pulses).

$$\text{SHG: } P(t) = E(t) \quad G(t) = E(t) \quad (3.18\text{a})$$

$$\text{PG: } P(t) = E(t) \quad G(t) = |E(t)|^2 \quad (3.18\text{b})$$

$$\text{SD: } P(t) = E^2(t) \quad G(t) = E^*(t) \quad (3.18\text{c})$$

$$\begin{aligned} \text{TG: } P_1(t) &= |E(t)|^2 & G_1(t) &= E^*(t) \\ P_2(t) &= E^2(t) & G_2(t) &= E^*(t) \end{aligned} \quad (3.18\text{d})$$

$$\text{THG: } P(t) = E^2(t) \quad G(t) = E(t) . \quad (3.18\text{e})$$

FROG is a widely used technique and has been developed into commercial products suitable to measure pulses in many different regimes. Due to its common use, versatility, and broad range of applications, the inversion algorithms shall be discussed in more detail.

3.4.2.2 Spectrography Inversion Algorithm

Since the gate function used is a function of the incident field itself, the test pulse is reconstructed via an iterative inversion routine. There are many algorithms available, all of which employ the same strategy that is based on the Gerchberg–Saxton [59] routine:

- 1) Initial guesses of the probe and gate fields are generated (e.g. using the pulse spectrum with random phase).
- 2) The gating process is simulated.
- 3) The spectral intensity of the simulated trace is replaced by the square root of the measured intensity.
- 4) A temporal constraint is applied and the next iteration of the probe and gate fields is extracted.

The inversion routine for FROG is shown in Figure 3.14. Since it is a two-dimensional phase retrieval problem, it is known to have a unique solution, unlike the one-dimensional phase retrieval problem of the intensity autocorrelation [60, 61]. FROG requires an iterative algorithm to reconstruct one-dimensional information of length $2N$ from a two-dimensional dataset of length N^2 , where N is the number of sample points in one dimension of the FROG trace. It is therefore not the most efficient method in terms of the information to data ratio. However, the redundancy can be used to check the alignment of the device and to estimate the precision of the measurement; it therefore helps to ensure a robust reconstruction in the presence of noise [62].

One deconvolution method for reconstructing the electric field from a FROG trace is called *principle component generalized projection algorithm* (PCGPA)[63–66]. Although other methods exist [67–69], the PCGPA tends to be widely used because it is independent of the type of FROG used, as it reconstructs both the gate and probe pulse simultaneously and allows rapid convergence for real-time reconstruction.

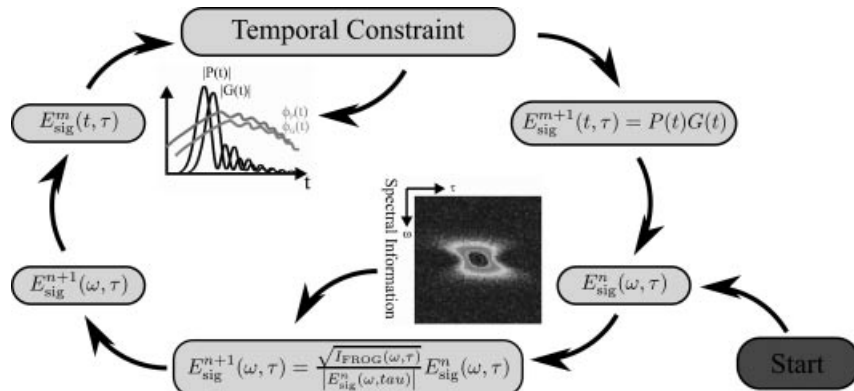


Figure 3.14 Schematic of a typical iterative FROG algorithm. The algorithm is seeded with an initial guess for the test (probe) pulse, $P(t)$, and gate, $G(t)$, fields, usually derived from noise or a previous reconstruction. The algorithm switches between the frequency and time domains. In the frequency domain, the

amplitude of the signal function is replaced by the square root of the measured FROG trace. A constraint based on the form of the signal field is applied in the time domain and the resulting probe and gate fields are used as the seeds for the next iteration.

In the PCGPA, the temporal constraint comes from the fact that, after some row rotations, the signal field can be written in terms of the outer product of the gate and probe fields. This outer product can then be inverted using a *singular value decomposition* (SVD) to determine the gate and probe. Additional constraints can also be applied, such as symmetrizing the signal field in SHG-FROG to ensure that the gate and probe are identical.

An important issue in measuring the spectrogram is that the temporal and spectral resolutions are constrained with respect to each other by the sampling theorem. This condition is rarely satisfied experimentally and it is necessary to perform interpolation on the measured data before processing it. Incorrect sampling leads to very inaccurate reconstructions, typically highlighted by a larger than normal FROG error, poor convergence or quite different reconstructed fields if the algorithm is run with different seed fields. In addition, it may also be necessary to filter the data (e.g., remove noise, background signal, etc.), or to symmetrize the measured trace (for SHG-FROG).

The algorithm is seeded with initial guesses for the probe and gate fields. These can be derived from uniform noise, a noisy Gaussian, or even a previous reconstruction. The latter case improves the speed of the convergence, provided the reconstructed pulse only differs slightly from the seed pulse. However, it can be difficult for the routine to move out of a local minimum if the pulse differs significantly and, thus, it is usual to apply noise to the seed to help prevent stagnation.

The performance of the inversion routine is measured by the FROG error. This is defined as

$$\sigma_n^{\text{FROG}} = \frac{1}{N} \sqrt{\sum_{i=1}^N \sum_{j=1}^N [I_{\text{Meas}}(\omega_i, \tau_j) - I_n(\omega_i, \tau_j)]^2}. \quad (3.19)$$

The measured FROG trace is given by $I_{\text{Meas}}(\omega_i, \tau_j)$ and the n th iteration of the reconstructed FROG trace is given by $I_n(\omega_i, \tau_j)$, where the subscripts i, j represent the pixel number. Typical values of σ^{FROG} are 0.1 or lower. However, the definition of the FROG error used above depends on the sampling rate. It is therefore difficult to compare the accuracy of the FROG routine with that of other methods (or different FROG configurations), unless the sampling grid and the span of the time and frequency axes are known. Low values for the FROG error can only be obtained if the FROG trace corresponds to one calculated from a physical field, that is, systematic errors result in a high FROG error. However, the opposite is not true: a high FROG error does not imply a systematic error. High FROG errors can also be a result of noise, from stagnation of the iterative algorithm at a local minimum, or from the measurement of an ensemble of incoherent pulses [70]. As the reconstruction is a global routine, it can be difficult to determine the source of large FROG errors.

3.4.2.3 GRENOUILLE

Grating-eliminated no-nonsense observation of ultrafast incident laser-light electric fields (GRENOUILLE) is a simplified version of SHG-FROG that uses a Fresnel bi-prism to eliminate the need for an interferometer and a thick crystal to remove the need for a spectrometer [71–73]. This enables a completely collinear geometry with few optics, significantly reducing the device cost and simplifying alignment. The concept is shown in Figure 3.15. The temporal scan is performed by mapping time to space, using the bi-prism to split a beam into two copies that converge in the

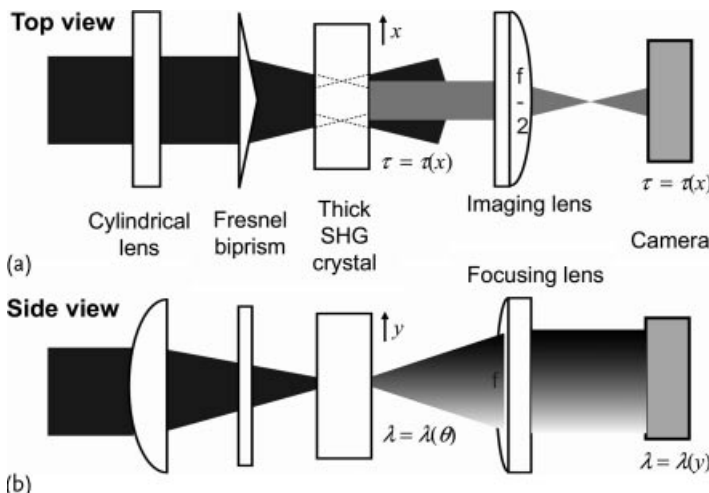


Figure 3.15 Experimental configuration for GRENOUILLE. Top view shows the time-to-space mapping, which is performed via a Fresnel bi-prism and one-to-one imaging of the crystal onto the 2D sensor (a). The side view

shows that the autocorrelation is spectrally resolved by “tight” focusing into a thick crystal and then Fourier transforming the image onto the sensor via f -to- f “imaging” (b). Figure courtesy of Professor Rick Trebino.

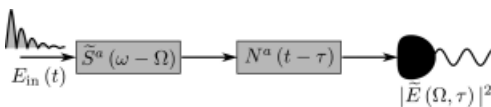


Figure 3.16 Linear filter combination required to perform sonography: an amplitude stationary filter (spectral filter) followed by an amplitude nonstationary filter (temporal gate).

The gate is typically achieved via the use of a nonlinear interaction to achieve the required temporal resolution.

nonlinear crystal. The relatively thick crystal (a few millimeters or more) results in a narrow phase-matching function compared to the pulse bandwidth; the central frequency of the phase-matching function depends on the angle of propagation of the pulse with respect to the crystal axis. Therefore, in the transverse spatial axis orthogonal to the time-to-space mapping, the beam is “tightly” focused into the crystal to generate a range of angles of propagation. The crystal is imaged onto a 2D sensor (i.e., 2f-to-2f) in the time-to-space axis to preserve the mapping, but is spatially Fourier transformed (f-to-f) in the orthogonal transverse spatial axis to map the angular dispersion resulting from the thick crystal to different spatial locations on the sensor. The bandwidth that can be measured (and therefore the minimum pulse duration) is limited by the range of angles traversing the crystal. This can be increased to enable measurement of 10–20 fs pulses by angle dithering the crystal or tight focusing [74, 75]. In addition to simplifying the device, GRENOUILLE enables the measurement of first-order space-time coupling (i.e., angular dispersion and spatial chirp) [76, 77]. Due to its simplicity and low cost, this is one of the most widely used devices for the characterization of ultrashort pulses.

3.4.3

Sonography

A conceptually similar approach to spectrography is that of *sonography*, in which the order of the filters is swapped as compared to spectrography. Thus, the test pulse is spectrally filtered (amplitude stationary filter) and then temporally resolved (amplitude nonstationary filter), see Figure 3.16. This can be achieved, for example, by spectrally filtering the pulse and then using frequency up-conversion with the unfiltered pulse in a nonlinear crystal [78]. Since sonography is often more technically challenging to implement than its spectrographic cousin, it is not as widely used, although the measured signal and inversion algorithm is similar to spectrography [66, 79].

3.4.4

Tomography

The method of *chronocyclic tomography* is based on measuring projections of rotated Wigner distributions of the pulse (ensemble) onto the spectral axis, see Figure 3.17a. The rotations are performed via temporal and spectral quadratic phase filters; the projection operation is achieved by an amplitude stationary fil-

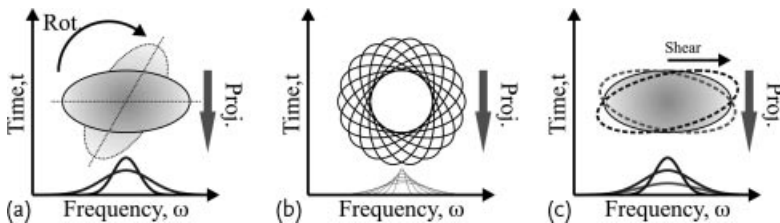


Figure 3.17 Schematic of chronocyclic tomography via rotations of the Wigner distribution of the pulse. The original Wigner distribution in time-frequency space is shown as a horizontal oval (a). The rotated distribution, achieved by applying a quadratic temporal and spectral phase, is shown as a lighter oval oriented at an angle to the figure axes. The projections of the two distributions are shown beneath; in this case the rotated distribution

has a much narrower spectrum. Multiple rotations of the Wigner distribution and their projections onto the frequency axis (b): a complete and unambiguous reconstruction of the pulse (except for the absolute phase) is possible via an inverse Radon transform. Two small shears of the Wigner distribution along the frequency axis, achieved with quadratic temporal phase only (c); the projections onto the frequency axis are shown beneath.

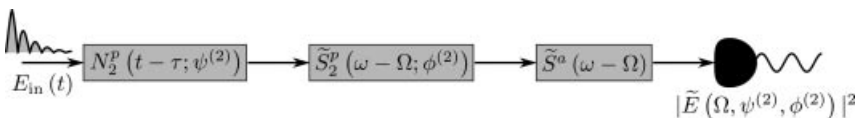


Figure 3.18 Linear filter combination required to perform complete tomography: a quadratic phase nonstationary and stationary filter, followed by a stationary amplitude filter (or alternatively an nonstationary amplitude fil-

ter). The purpose of the phase filters is to rotate the Wigner distribution, whereas the amplitude filter measures the marginal of the Wigner distribution, in this case along the spectral axis.

ter followed by a time-integrating detector (i.e., a spectrometer), as outlined in Figure 3.18. In contrast to spectrographic methods, tomography methods utilize a direct inversion algorithm. The most thorough method projects rotations up to 2π and then performs an inverse Radon transform on all projections, see Figure 3.17b [80]. Due to bandwidth constraints, this technique has only been demonstrated for picosecond pulses. However, since the method can be accomplished using purely linear optics, the high sensitivity may lead to applications, for example, in telecommunications.

The quadratic spectral phase can be obtained by the use of a dispersive delay line. The temporal phase is applied via an electro-optic phase modulator, driven sinusoidally at radio frequencies (RF). If the pulse is short as compared to the RF period, and aligned with the peak (or trough) of the modulation, then the phase can be approximated as a quadratic modulation. However, it is clear that such an implementation is limited by the device performance. For subpicosecond pulses, the quadratic chirp would stretch the pulse to a duration outside the usable window of the phase modulator. Longer pulses are limited by the spectral resolution of the spectrometer. However, such a method is able to reconstruct fairly complicated pulses (e.g., a double pulse pair) that are difficult to measure with other techniques.

3.4.4.1 Simplified Chronocyclic Tomography

Chronocyclic tomography requires many rotations in order to reconstruct the Wigner function of the pulse in question. In addition, it is necessary to apply relatively large quadratic phases in both the temporal and spectral domains. If the pulses in the ensemble are coherent, then it is possible to simplify the process such that only two rotations and the original spectrum (corresponding to no rotation) are needed [81, 82]. In fact, it is possible to fully reconstruct a coherent field by performing two small shears of the Wigner distribution along the spectral dimension. The concept is shown schematically in Figure 3.17c. If the projection of a sheared distribution onto the spectral axis is given by

$$I_\psi(\omega) = \int W(t, \omega - \psi t) dt, \quad (3.20)$$

where ψ is the size of the temporal phase modulation such that $E(t) \rightarrow E(t) \exp(i\psi/2t^2)$, then it is possible to reconstruct the electric field by integration of

$$\begin{aligned} \frac{\partial I_\psi}{\partial \psi} &= -\frac{\partial}{\partial \omega} \left(I \frac{\partial \phi}{\partial \omega} \right) \\ &\simeq \frac{I_{+\psi} - I_{-\psi}}{2\psi}. \end{aligned} \quad (3.21)$$

Here, $I_{+\psi}$ and $I_{-\psi}$ correspond to the projections of the Wigner distributions onto the spectral axis for a small shear, $\psi \ll 1$, in the positive or negative direction, respectively. The original spectrum of the pulse with no modulation present is given by I . Similar to full tomography, this method still suffers from the limited availability of phase modulators with sufficient bandwidth for subpicosecond pulses.

3.4.4.2 Time Lens

A simplified extension to chronocyclic tomography for a coherent pulse train is a measurement of the temporal intensity by a 90° rotation of the Wigner distribution, followed by a measurement of the resulting spectral intensity. The concept obtains its name from the analogy of a lens in the spatial domain, whereby a lens acts as a Fourier transform operator. The quadratic temporal and spectral phases act to replace the lens and diffraction in conventional spatial imaging [83, 84]. Note that any deviation from perfect quadratic phases (e.g., for broadband pulses) acts as an aberration. The pulse shape can be reconstructed using the same Gerchberg–Saxton routine used in the spatial domain [59]. This method is limited by the availability of sufficient phase modulators that can apply pure quadratic phases with sufficient bandwidth for femtosecond pulses. It is also possible to utilize nonlinear interactions, such as self-phase modulation (SPM) and cross-phase modulation (XPM), although the phase modulations depend on the input field and the measured spectrum does not correspond to the marginal of an exact rotation, therefore requiring more advanced iterative reconstruction algorithms that can deal with nonquadratic phase transformations [85–88].

3.4.5

Interferometry

Interferometry is the process in which phase information is directly encoded onto the intensity pattern via spatially overlapping two beams on the same detector, such that the difference in phase between the two beams at each pixel is encoded onto the measured *interferogram* [89, 90]. Typically, for broadband pulses, the interference pattern is spectrally resolved using a spectrometer and the spectral phase is reconstructed. Usually, but not necessarily, a rapidly varying phase difference, denoted as a *carrier phase*, is applied to impart fringes onto the interferogram with a known spacing. The phase difference between the two pulses is then encoded as a modulation in the nominal fringe spacing, and can be extracted using the Takeda algorithm [91] (see Section 3.4.5.1). The carrier can be in the spatial domain (via applying a tilt to one of the beams), spectral domain (via a time delay), angular domain (via a lateral displacement), or temporal domain (via a spectral shift). Alternatively, an absolute phase shift can be added to one beam and then modulated as multiple acquisitions are made, resulting in *phase-shifting interferometry*. Interferometric measurements can be decomposed into two types: *test plus reference* or *self-referencing*. In the former, the reference can be a filtered version of the pulse (e.g., spatially filtering the beam will produce a reference beam with a flat or spherical wavefront), or a pulse previously measured with a self-referenced technique. However, it is necessary to have a reference with a bandwidth and spatial extent that fully covers the test pulse.

3.4.5.1 Spectral Interferometry

Figure 3.19a shows two time-delayed pulses that are combined collinearly on a beam-splitter. The measured interferogram in Figure 3.19b can be written as

$$\begin{aligned} S(\omega) &= |E_{\text{TP}}(\omega) + E_{\text{Ref}}(\omega)e^{i\omega\tau}|^2 \\ &= |E_{\text{TP}}(\omega)|^2 + |E_{\text{Ref}}(\omega)|^2 \\ &\quad + 2|E_{\text{TP}}(\omega)||E_{\text{Ref}}(\omega)|\cos[\phi_{\text{TP}}(\omega) - \phi_{\text{Ref}}(\omega) - \omega\tau] \\ &= I_{\text{TP}}(\omega) + I_{\text{Ref}}(\omega) + \sqrt{I_{\text{TP}}(\omega)I_{\text{Ref}}(\omega)}[e^{i\Delta\phi(\omega)}e^{i\omega\tau} + \text{c.c.}] , \end{aligned} \quad (3.22)$$

where τ is the delay between the test pulse (TP) and reference pulse (Ref), I is the intensity, ϕ the phase and E the analytic signal. To extract the phase difference, the measured interferogram is Fourier transformed into the pseudo time-domain:

$$\tilde{S}(\tilde{t}) = \tilde{I}^{\text{DC}}(\tilde{t}) + \tilde{I}^{\text{AC}}(\tilde{t} - \tau) + \tilde{I}^{-\text{AC}}(\tilde{t} + \tau) , \quad (3.23)$$

resulting in three peaks corresponding to the “DC” term and two “AC” sidebands, in analogy to radio frequency modulation (see Figure 3.19c):

$$\tilde{I}^{\text{DC}}(\tilde{t}) = \mathcal{F}_{\omega \rightarrow \tilde{t}}\{I_{\text{TP}}(\omega) + I_{\text{Ref}}(\omega)\} \quad (3.24)$$

$$\tilde{I}^{\pm\text{AC}}(\tilde{t}) = \mathcal{F}_{\omega \rightarrow \tilde{t}}\left\{\sqrt{I_{\text{TP}}(\omega)I_{\text{Ref}}(\omega)}e^{\pm i\Delta\phi(\omega)}e^{\pm i\omega\tau}\right\} . \quad (3.25)$$

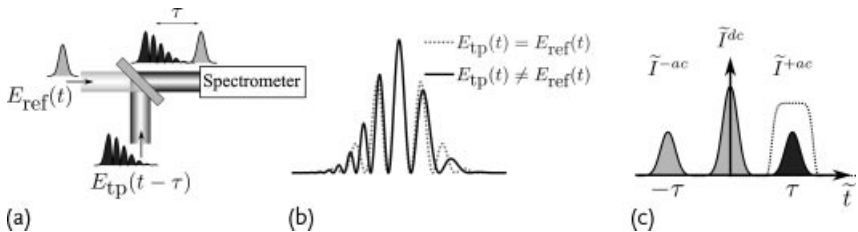


Figure 3.19 Concept of spectral interferometry: two time-delayed pulses interfere on a spectrometer (a). Measured interferograms when both pulses are identical (dotted line), resulting in fringes spaced by $2\pi/\tau$, or non-identical (solid line), resulting in nonuniform fringe spacing (b). The spectral phase differ-

ence is encoded as a modulation in the fringe spacing from the nominal $2\pi/\tau$ fringe spacing. Fourier transform of (b), resulting in a central “DC” term and two “AC” sidebands, of which one sideband is filtered and inverse Fourier transformed to extract the phase of the interferogram (c).

One of the AC sidebands is selected and Fourier transformed back to the spectral domain to give the interferometric (last) term in Eq. (3.22). Taking the argument of this function and subtracting the carrier phase term (obtained from a calibration trace) reveals the phase difference between the two pulses. The magnitude of the AC term can be used to obtain the pulse spectrum. Alternatively, the spectrum from both pulses can be taken from a quadratic equation involving both the DC and AC intensities. This method can be used to measure the dispersion introduced by a sample [92], or to completely characterize a weak or complex pulse by referencing against a simple strong pulse that has been fully characterized by any complete characterization device [93]. *Temporal analysis by dispersing a pair of light electric fields* (TADPOLE) is a technique that enables the characterization of an unknown pulse by spectral interferometry with a reference that has been characterized using a self-referencing technique. Note that the method used to characterize the reference pulse is arbitrary, but any inaccuracies in the reference will affect the reconstruction of the unknown pulse.

3.4.5.2 Spectral Phase Interferometry for Direct Electric Field Reconstruction

Spectral phase interferometry for direct electric field reconstruction (SPIDER) is a self-referencing interferometric technique for complete temporal characterization of optical pulses based on spectral shearing interferometry (SSI) [94–96]. The simple concept allows extraction of the one-dimensional spectral phase of a pulse from a one-dimensional dataset.

In spectral shearing interferometry, the objective is to interfere two spectrally sheared copies of the test pulse (TP), thus the spectral phase at one frequency is referenced to the spectral phase at a different frequency, separated by the spectral shift (shear) Ω . In conventional SPIDER, this is achieved by sum frequency generation (SFG) of two time-delayed copies of the TP with a highly chirped pulse. The latter is derived from a highly stretched copy of the TP. The form of the interferogram is similar to Eq. (3.22), except $E_{\text{Ref}}(\omega) = E_{\text{TP}}(\omega - \Omega)$; the interferometric

term is thus given by Eq. (3.26). The carrier phase is removed from a calibration trace, taken by measuring the spectrum of the two time-delayed, non frequency-shifted replicas of the TP. During the SFG process, each TP experiences a different quasi-monochromatic frequency shift from the chirped pulse, due to the time delay. The time delay also introduces a carrier phase term which allows extraction of the SPIDER phase, Eq. (3.27), via the Takeda algorithm [91]. The experimental concept is shown in Figure 3.20. Type II SFG is used, since it is necessary to up-convert the full TP bandwidth with only a narrow bandwidth, Ω , from the ancillary (chirped) pulse. Therefore, a thicker crystal can be used for the same spectral bandwidth, as compared to the type I configuration typically used in SHG-FROG.

$$D(\omega) = E^*(\omega - \omega_{CP}) E(\omega - \omega_{CP} - \Omega) \quad (3.26)$$

$$\begin{aligned} \theta(\omega) &= \arg[D(\omega + \omega_{CP})] \\ &= \phi_{TP}(\omega - \Omega) - \phi_{TP}(\omega). \end{aligned} \quad (3.27)$$

There are two commonly used algorithms to reconstruct the TP spectral phase from the SPIDER phase. The first is based on the fact that, for a small shear, the SPIDER phase is equivalent to a finite difference of the TP phase and therefore is approximately equal to the gradient of the spectral phase scaled by the spectral shear, that is, $\theta(\omega) \approx \Omega \partial \phi_{TP}(\omega) / \partial \omega$. The TP spectral phase is thus calculated by cumulative integration of the SPIDER phase divided by the spectral shear. The accuracy of this method depends on the method of integration; typically the trapezoidal rule is used:

$$\phi_{TP}\left(\omega_N - \frac{\Omega}{2}\right) \approx - \sum_{n=0}^N \frac{\omega_{n+1} - \omega_n}{2\Omega} [\theta(\omega_n) + \theta(\omega_{n+1})]. \quad (3.28)$$

This method can accurately recover the GDD and third-order phase; accuracy for higher orders can be improved by decreasing the magnitude of the shear [97]. Alternative, but more complex inverse finite difference schemes can accurately measure higher-order Taylor coefficients for the spectral phase [97].

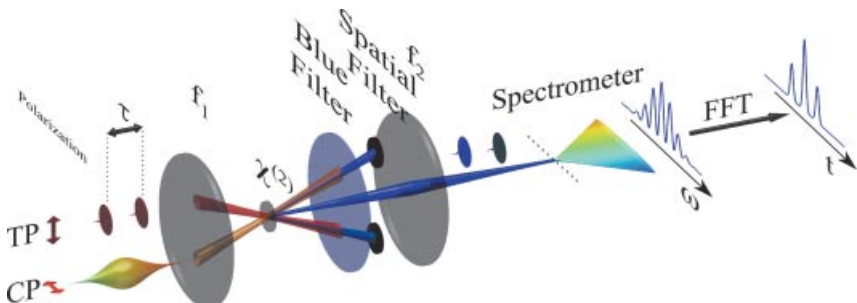


Figure 3.20 Experimental configuration for conventional SPIDER. Type II sum frequency generation between a highly chirped ancillary with two time-delayed replicas results in two spectrally sheared signal pulses, centered near

twice the frequency of the test pulse. The signal pulses are spatially and spectrally filtered and imaged from the crystal to the entrance slit of a spectrometer.

The second commonly used algorithm to reconstruct the TP spectral phase is an exact method based on concatenation: cumulative integration of the SPIDER phase sampled at a rate equal to the spectral shear as in Eq. (3.29).

$$\phi_{\text{TP}}(\omega) = \begin{cases} -\sum_{n=1}^N \theta(\omega_0 + n\Omega) & \text{if } \Omega > 0 \\ \sum_{n=0}^{N-1} \theta(\omega_0 + n|\Omega|) & \text{if } \Omega < 0 \end{cases} \quad (3.29)$$

This method results in a reconstructed phase that is sampled on an evenly spaced frequency grid with a sampling resolution equal to the spectral shear. The reconstructed phase is, in principle, exact, provided $\Omega \leq 2\pi/T$ where T is the compact support. Inaccuracies can result from interpolation of the unevenly spaced SPIDER phase (the sampling defined by the spectrometer) onto the evenly spaced reconstruction grid.

Increasing the magnitude of the spectral shear results in larger measured phase differences and therefore higher measured signal-to-noise ratio for the SPIDER phase. Thus it is optimal to use the largest magnitude shear that satisfies the sampling theorem. It is possible to check for under-sampling (i.e., too large shear) directly from the measured data, thus it is not necessary to know the compact support *a priori* [98].

SPIDER has several positive features: (1) the reconstruction is direct, enabling real-time reconstructions with modest computing power [99] and the ability to perform an analytic analysis of the accuracy, precision, and consistency of the reconstruction [97, 98]; (2) the phase is encoded in fringes, thus the reconstruction of the spectral phase is unaffected by the response function of the crystal and detector (given sufficient SNR) and the method is robust against noise: the Fourier filtering routine aids in reducing the effects of noise, and a low bit depth camera can be used to obtain high accuracy results [100, 101]; (3) the reconstruction is local, that is, the precision of the spectral phase at a given frequency is proportional to the SNR at that frequency [98]; (4) the one-dimensional electric field function is encoded in a one-dimensional measured trace, providing efficient data encoding and reducing the amount of data acquired, allowing spatially resolved measurements to be used to directly measure arbitrary space-time coupling [102, 103].

SPIDER also contains redundancy in its data and allows estimates of the precision and consistency of the reconstruction directly from the measured data. SPIDER was used to characterize a large variety of pulses, ranging from several femtoseconds [104, 105] to tens of picoseconds [106, 107], and from the ultraviolet [108, 109] to the mid infrared [110]; it is only limited by the availability of a second-order nonlinearity at the pulse wavelength and by the requirement for sufficient resolution and sensitivity of the detector.

Conventional SPIDER does exhibit some negative features: (1) the spectrum needs to be oversampled to resolve the AC sidebands and thus requires a high-resolution spectrometer; (2) it is sensitive to the interpulse delay, thus requiring a very accurate and precise calibration [111]; (3) replicas of the test pulse are required, which can become problematic for large bandwidth pulses; (4) the shear and carrier phase are coupled via the interpulse delay and ancillary chirp, limiting

the range of usable shears with any given setup; and (5) the traces are unintuitive, requiring a complete reconstruction. The latter issue is not a major problem, since the reconstruction is simple, direct, and very fast. Nevertheless, it is impossible to qualitatively check the reconstruction against the measured data. However, this can be achieved using the methods described in [98].

3.4.5.3 Spatially Encoded Arrangement for SPIDER

In light of the issues highlighted with the conventional SPIDER in Section 3.4.5.2, a variation was developed based on interfering two tilted spectrally sheared replicas at zero delay, known as spatially encoded arrangement (SEA-) SPIDER. The SEA-SPIDER concept is shown in Figure 3.21 [105, 112]. Since there are no spectral fringes, the interferogram can be sampled spectrally at the Shannon limit; the spatial dimension needs to be oversampled to resolve the spatial fringes, but this is typically not an issue. Since only a single copy of the test pulse is required, no distortion is introduced to the test pulse (other than dispersion due to air), thus making the device *zero additional phase* (ZAP) [109]. Due to the carrier phase being in the spatial dimension, it is now possible to vary the shear by changing the delay between the two ancillaries without adjusting the carrier phase, thus requiring a single calibration trace. In fact, by performing measurements at two different time delays, a homodyne measurement [113] is performed, thus eliminating the need for a calibration trace or a guaranteed zero delay between the two signal pulses. All these advantages make SEA-SPIDER ideally suited to the measurement of few-cycle or complex pulses.

In the absence of space-time coupling, SEA-SPIDER interferograms are very intuitive: the gradient of the spectral phase is mapped directly in the contours of the fringes, as shown in Figure 3.22. Thus it is possible to roughly optimize the compression of a pulse without the need for a complete reconstruction and qualitative consistency checks between the measured and reconstructed fields are possible.

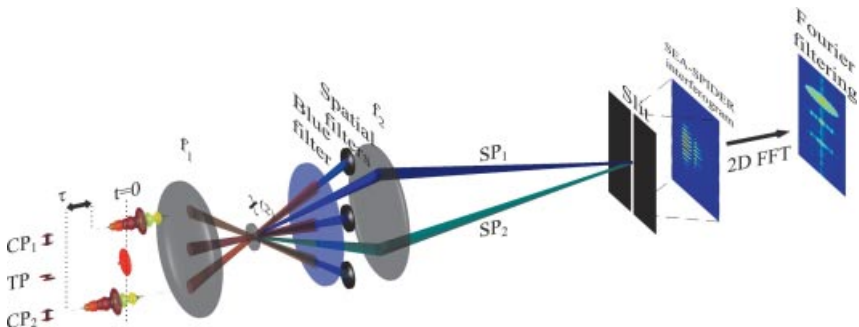


Figure 3.21 SEA-SPIDER concept: a single replica of the TP is up-converted with two time-delayed, highly chirped ancillaries in a $\chi^{(2)}$ nonlinear crystal with a type II non-collinear geometry. The two signal pulses are spatially and spectrally filtered and imaged

onto the entrance slit of an imaging spectrometer. The delay between the two ancillaries generates the spectral shear. The tilt between the two pulses results in spatial fringes and allows extraction of the SPIDER phase.

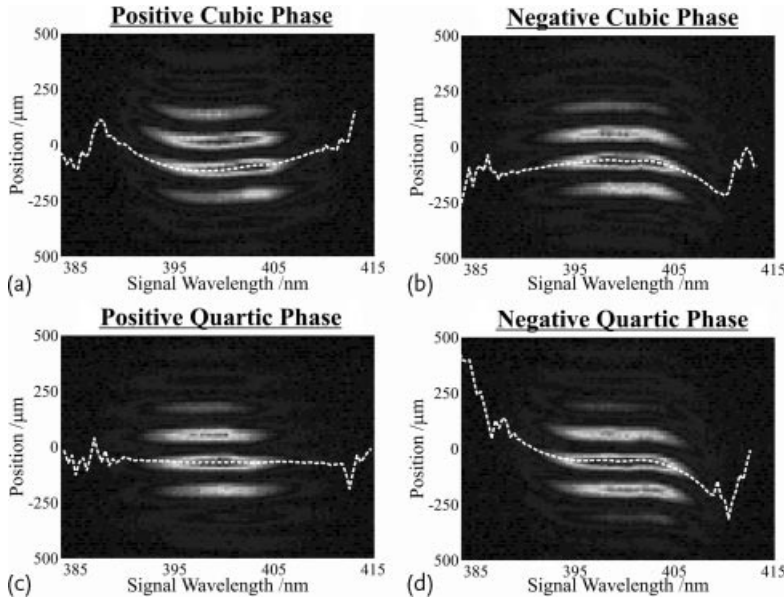


Figure 3.22 Intuitive SEA-SPIDER interferograms of a chirped pulse amplifier with different amounts of known dispersion: positive cubic (a), negative cubic (b), positive quartic (c) and negative quartic phase (d). The contours of the fringes directly map out the gradient of the spectral phase (i.e., the frequency chirp).

The dashed lines correspond to the contours of the fringes and are equal to the SPIDER phase extracted from the Takeda algorithm. The phase applied in (c) was limited by the shaper and can be seen if a different aspect ratio is used.

3.4.5.4 Multiple Spectral Shearing Interferometry

The two constraints for a spectral shearing measurement are the following:⁴⁾ (1) that the shear, and hence the spectral sampling, must satisfy the sampling theorem and (2) that the spectrometer must have sufficient resolution to sample the interferogram. The two conditions are, in principle, sufficient to allow reconstruction of any pulse whose compact support is less than $2\pi/\Omega$. In practice, the measured interferogram will be degraded by noise. When the magnitude of the interferometric signal at a given frequency is reduced the relative noise on the SPIDER phase increases at that frequency. Since the reconstructed phase is found by integrating or concatenating the SPIDER phase, errors in the reconstructed phase can occur due to the accumulation of noise across the spectrum.

The accumulation of noise becomes problematic for complex pulses with a large bandwidth: a small shear is required to sufficiently sample the pulse, resulting in a large accumulated spectral error across the bandwidth due to the large number of sampling points. This problem is most pronounced when the spectral intensity approaches zero. If the bandwidth of the spectral null is wider than the required

4) The following principles can be generalized to all forms of shearing interferometry; I shall restrict the arguments to spectral shearing interferometry for clarity.

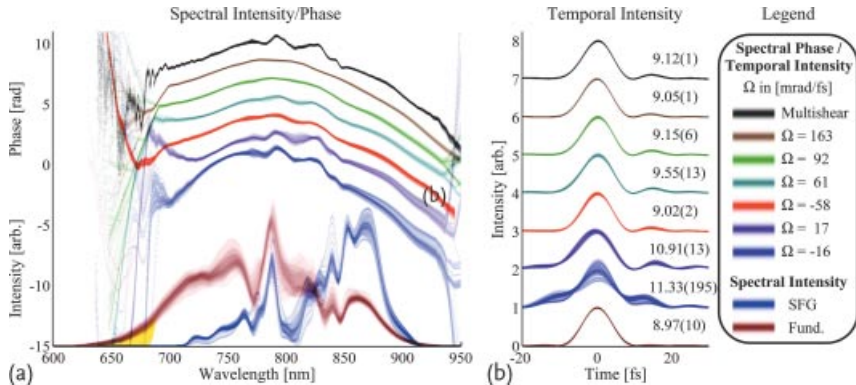


Figure 3.23 Spectral and temporal reconstructions; the intensity of the line reflects the probability that the phase or intensity has the corresponding value. Spectral intensity and phase (a). The phases have been offset from each other for clarity (the magnitude of the shear increases with the offset, with the top-most spectral phase corresponding to reconstructions from the multishearing algorithm). The SP spectrum has been shifted in wave-

length to overlap with the fundamental. Temporal intensity reconstructions and FWHM pulse durations after phase compensation, i.e., the GDD between the measurement and experiment was calculated and subtracted before reconstructing the temporal intensity (b); the color scheme is the same as in (a). The Fourier transform-limited temporal profile (dark red) is calculated from the fundamental spectrum.

spectral shear, or if the accumulated phase noise across a spectral region is larger than π , then the relative phase between the disjoint spectral regions will be undefined, resulting in a significant error in the reconstructed temporal phase. This can be seen in Figure 3.23 by the loss of precision in the reconstructed spectral phase corresponding to measurements from a small spectral shear, resulting in a large variation in the reconstructed temporal intensity profile. As the magnitude of the shear is increased, the precision improves and the global phase is accurately reconstructed. However, the coarser sampling means that the fine phase structure is “washed out,” reducing the accuracy in determining the contrast ratio of the pulse and the peak intensity (further details can be found in [114]).

Fortunately there is a simple solution to these problems: performing multiple measurements with different sized shears to improve both the accuracy and precision: a small shear can be used to ensure that the spectral phase is sampled with sufficient resolution and a large shear can be used to bridge any spectral nulls, thus ensuring accurate reconstructions. Precision is improved since the large shear reduces the number of integration points and, thus, the accumulation of errors across the bandwidth. Additionally, the combination of multiple shears over-determines the spectral phase at any given frequency and a weighted average of the phase at that frequency can be determined.

Once the SPIDER phase has been measured for a number of different shears, the optimal TP spectral phase, with minimal error between the SPIDER phase extracted from the measured data and that determined from the optimal reconstructed phase, must be evaluated. This could be achieved via a nonlinear minimization or

maximum likelihood estimation algorithm. A more elegant solution, based on linear algebra, was developed by Austin and co-workers [115], enabling a direct (non-iterative) inversion. The method is based on the fact that Eq. (3.27) can be written as a matrix equation

$$\begin{bmatrix} \theta_1 \\ \theta_2 \\ \theta_3 \\ \vdots \\ \theta_N \end{bmatrix} = \begin{bmatrix} -1 & 0 & \dots & & \\ 1 & -1 & 0 & \dots & \\ 0 & 1 & -1 & 0 & \dots \\ & & \ddots & \ddots & \\ & \dots & 0 & 1 & -1 \end{bmatrix} \begin{bmatrix} \phi_0 \\ \phi_1 \\ \phi_2 \\ \vdots \\ \phi_{N-1} \end{bmatrix} \quad (3.30)$$

$$\boldsymbol{\theta} = \mathbf{d}\boldsymbol{\phi}, \quad (3.31)$$

where $\phi_n = \phi(\omega_0 + n\Omega)$ is the sampled reconstructed phase, $\theta_n = \phi(\omega_0) - \phi(\omega + n\Omega)$ is the sampled SPIDER phase, $\phi(\omega_0) = 0$ is the boundary condition and \mathbf{d} is the shearing matrix relating the TP spectral phase to the SPIDER phase. Equation (3.31) has a unique solution that is identical to the concatenation formula of Eq. (3.29).

The principle is then to extend the concept as an over-determined matrix equation

$$\mathbf{W}\boldsymbol{\theta} = \mathbf{WD}\boldsymbol{\phi}, \quad (3.32)$$

where $\boldsymbol{\phi} = [\phi_0; \phi_1; \dots; \phi_{N-1}]$ is the reconstructed spectral phase, sampled with a resolution equal to the smallest magnitude shear, that is, $\phi_n = \phi(\omega_0 + n|\Omega_0|)$, such that each shear is an integer multiple of the smallest shear, $|\Omega_{s=1\dots S-1}| = a_s\Omega_0$ (with a_s an integer); $\boldsymbol{\theta} = [\boldsymbol{\theta}(\Omega_0); \boldsymbol{\theta}(\Omega_1); \dots; \boldsymbol{\theta}(\Omega_{S-1})]$ is a vector of measured SPIDER phases generated by concatenating the SPIDER phase vectors for each individual shear measurement; $\mathbf{D} = [\mathbf{d}(\Omega_0); \mathbf{d}(\Omega_1); \dots; \mathbf{d}(\Omega_{S-1})]$ is a rectangular matrix generated by the concatenation of the individual shearing matrices $\mathbf{d}(\Omega_s)$, similar to Eq. (3.30) but taking into account the fixed sampling grid and the value of the shear for each matrix; and $\mathbf{W} = [\mathbf{w}(\Omega_0); \mathbf{w}(\Omega_1); \dots; \mathbf{w}(\Omega_{S-1})]$ is a rectangular weighting matrix generated from concatenation of the diagonal weighting matrices $\mathbf{w}(\Omega_s) = \text{diag}[\boldsymbol{\theta}(\Omega_s)]$, since the problem is now over-determined and thus it is necessary to use a weight that is proportional to the SNR to ensure a robust reconstruction.

The algorithm can be generalized to include interpolation of the measured data and to extend it to multiple dimensions, see [114, 116] for further details. It is important to note that combining measurements from suitably sized shears improves the precision by an amount more than can be achieved by simply averaging the same number of interferograms with a fixed shear, see [115].

An additional advantage gained by using multiple shears is that it is possible to test the consistency of the different shear measurements to check for any inaccuracies in the measured data, as demonstrated in Figure 3.24. The small regions of undefined phase (e.g., near a wavelength of 400 nm) result from a null in the measured amplitude (not plotted for clarity). The agreement between the measured

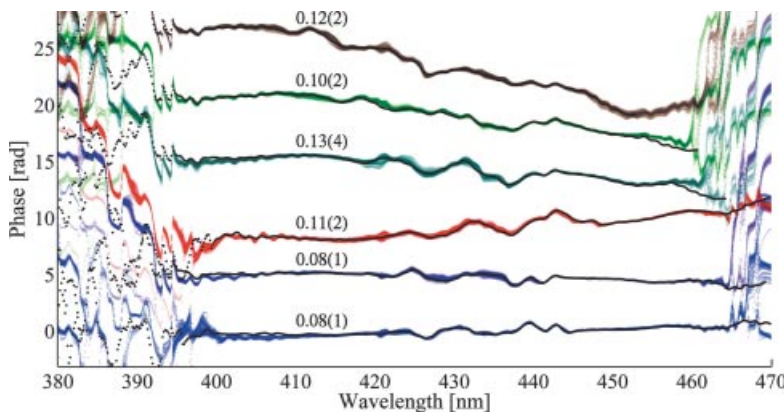


Figure 3.24 Extracted SPIDER phases for different shear measurements. The intensity of each line represents the probability distribution calculated from 100 measurements for each individual shear. For each shear, the SPIDER phase has also been calculated using the TP spectral phase, reconstructed via

the multishear algorithm (superimposed as a black line). The root mean square phase error between the measured and reconstructed SPIDER phase for each shear is written above each measurement. The SPIDER phases have been offset for clarity.

SPIDER phases and the SPIDER phases calculated from the reconstructed spectral phase is excellent, indicating an accurate reconstruction. The fine modulations in the measured SPIDER phases are also reproduced exactly, indicating that they are physically present in the measured pulse and are not an artifact arising from noise or other effects. Further examples of the merits of multishearing interferometry are described in [114–117].

3.4.5.5 Long-Crystal SPIDER

Another ridiculous acronym for interferometric geometrically simplified noniterative electric field extraction (ARAIGNEE), or sometimes called long crystal (LX-) SPIDER, is a simplified version that utilizes the phase-matching properties of a thick crystal to remove the need for an ancilla [118]. For Ti:Sapphire pulses (centered near 800 nm), Type II sum frequency generation in KDP has the property that a large bandwidth from the o-ray will phase-match with a very narrow bandwidth of the e-ray, due to group-velocity matching between the fundamental o-ray and up-converted e-ray and group-velocity mismatch between the o-ray and the fundamental e-ray (Figure 3.25b). The frequency from the fundamental e-ray can be selected simply by angle-tuning the propagation through the crystal. Therefore, propagating two tilted beams centered near 830 nm through a thick KDP crystal results in two frequency shifted replicas of the fundamental pulse.

There are a few subtleties involved in utilizing the long crystal for performing spectral shearing interferometry. The first is that the o-ray and e-ray temporally walk-off from each other. Therefore, the e-ray is predelayed with respect to the o-ray by passing the pulse through a quartz plate (approximately 1 cm), rotated at 45° to the test pulse polarization. It is necessary to ensure that the predelay tem-

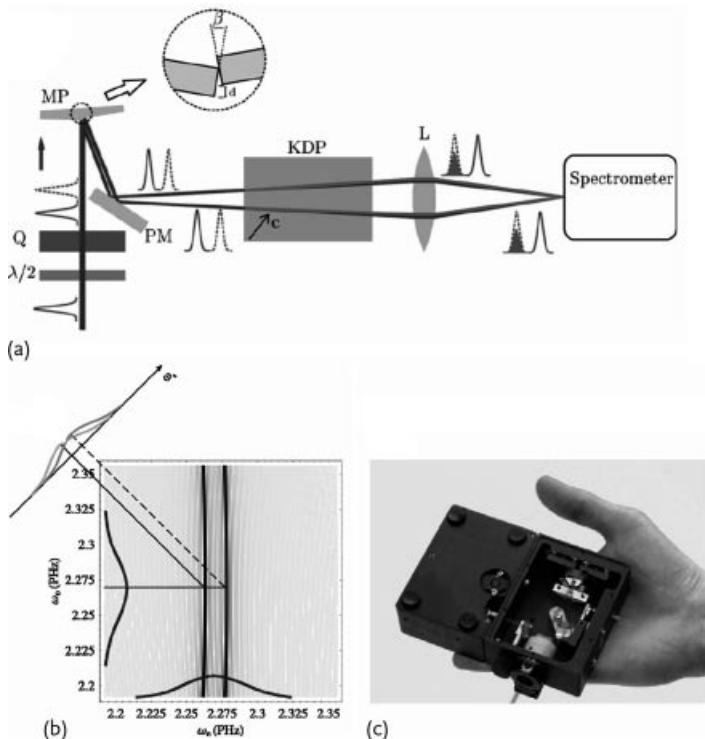


Figure 3.25 Experimental configuration for ARAIGNEE (a). Phase-matching plot for two different propagation angles through the KDP (b). Photograph of the device (c), coupled to a commercial spectrometer (Ocean Optics USB2000). Courtesy of Ian Walmsley.

porally separates the two polarizations, but that the crystal is thick enough to allow the two polarizations to fully walk-through each other so that they emerge completely separated in time, but with the opposite delay. It is also necessary to calibrate and remove the spectral phase added by the sum-frequency generation process. The spectral phase can be determined by the central wavelength of the pulse, bandwidth, crystal thickness, and angle through the crystal [119]. A split-mirror (Figure 3.25a) is used to generate two tilted beams with a temporal offset. If the test-pulse exhibits space-time coupling, then one can use a Michelson style interferometer. Alternatively, the space-time coupling can be characterized by spatially resolving the interference pattern (in the direction of the tilt). The sheared signal pulses are spectrally filtered and interfered on a spectrometer. A calibration of the delay is performed by interfering the fundamental beams in one polarization axis.

3.4.5.6 Other Spectral Shearing Interferometry Methods

In addition to SPIDER and its variants, there exists a number of other methods that utilize spectral shearing interferometry to completely characterize the spectral

phase. *Two-dimensional spectral shearing interferometry* (2DSI) up-converts a single copy of the TP with two collinear time-delayed highly chirped ancillary pulses [120]. Small changes in the delay between the two ancillaries results in a change in the relative phase of the two spectrally sheared signal pulses, thus producing fringes via phase-shifting interferometry [121]. *Spectral interferometry resolved in time* (SPIRIT) is to SPIDER as sonography is to spectrography: the beat pattern resulting from the interference of two laterally displaced spatially chirped replicas of the test pulse is temporally gated to obtain an interference pattern that is identical to that observed in SPIDER [122].

3.4.5.7 Measuring Space-Time Coupling with Interferometry

Unlike spectrographic, sonographic, and tomographic methods that encode the information in two dimensions, interferometry encodes the spectral information in a single dimension, thus it is possible to use the other dimension of a two-dimensional detector to encode spatial information about the pulse [123, 124]. To completely measure space-time coupling in both SPIDER and SEA-SPIDER, it is necessary to ensure that the test pulse up-converts with a flat wavefront that does not change with frequency. It is therefore necessary to perform spatial filtering on the ancilla(s), as well as chirping [125]. One may combine a SPIDER measurement with a lateral shearing measurement (i.e., the spatial equivalent of spectral shearing interferometry) [102, 103]. Even if the ancilla is not spatially filtered, it is possible to measure the temporal profile at every spatial position without knowledge of the relative group delay [126, 127].

3.5

Ultrafast Metrology in the Extreme Ultraviolet

Metrology for extreme ultraviolet (XUV) femtosecond and attosecond pulses is much more difficult than in the UV, visible, or IR. Available optics and methods of detection are highly limited in the XUV spectral range. For example, there is no good nonlinear medium for this wavelength when we account for the typically low intensity of these pulses, thus preventing the direct transfer of techniques used in the visible to the XUV. Since a sufficient, and necessary, condition for ultrashort pulse characterization is a time-nonstationary filter with a response time comparable to the pulse duration under study, plus a time-stationary filter, extreme ultraviolet pulses can be characterized by photoionization in the presence of a strong, relatively low-frequency field. As will be shown, the low-frequency field acts as a temporal phase modulator, thus opening up the possibility to use similar characterization methods as shown in the previous section, even though the physical process is very different.

An alternative method for the complete characterization of XUV femtosecond and attosecond pulses is to utilize the pulse generation process itself as the time-

nonstationary filter. Currently, there exist two approaches to achieve this, the first is to generate two sources of high harmonic generation (HHG), driven by two frequency shifted driving pulses; since the output field contains harmonics of the driving field, the harmonics themselves will be frequency shifted and spectral shearing interferometry can thereby be extended into the XUV. Alternatively, one may drive the HHG process with two (or more) fields. The secondary field acts as a perturbation to the system and can provide temporal information on the emitted field.

The method of two-color photoionization can be seen as more general, since it measures the XUV pulses after the generation process and is independent of the generation method. Photoionization methods cannot measure space-time coupling in the field and could possibly lead to erroneous interpretation of dynamical measurements. Sensitivity is also not as high as direct detection. As will be shown, the photoelectron and photoion spectrum depends on the angle of detection and space-charge effects limit the number of ions or electrons that can be detected. However, improvements in detection and laser technology have significantly improved detection efficiency and repetition rates, thus reducing the total acquisition time for an experiment. Improvements in the understanding of the emission spectrum has provided new inversion algorithms, extending the regime of applicability of such techniques.

The method of modifying the XUV generation process with a second field is dependent on the generation process and the models used to describe it. However, since the emitted field is detected directly, the sensitivity is vastly increased, even enabling single-shot acquisition, and the measurement of space-time information. This could be used to directly measure space-time coupling in the field [24, 128], observe spatially dependent processes [30], or to map time to space to perform a pump-probe measurement in a single shot. Additionally, direct XUV detection is much less expensive and requires less expertise than photoionization, thus it could open the research field to non specialists. The major downside to direct XUV detection is that the complexity is moved from the XUV detection to the control of the driving field, which is a difficult task due to the need to work with extremely short pulse duration and high-intensity pulses, which is the current bottleneck in these approaches.

It is important to note that photoionization is currently the only method that has been demonstrated experimentally to characterize both attosecond pulse trains and isolated attosecond pulses. These methods are much more mature than direct detection techniques. For the latter, there is still much more work to be done to truly harness its potential. Another important point is that developments in metrology lead to new techniques in extracting information in dynamical experiments. Since the two detection methods are based on entirely different physical processes, the exact information that they provide is quite different and they can potentially compliment each other to provide complete information about the system.

3.5.1

Complete Characterization of Ultrashort XUV Pulses via Photoionization Spectroscopy

3.5.1.1 XUV Autocorrelation

Intensity autocorrelation is arguably the simplest temporal characterization method and is conceptually the same for XUV pulses and for optical pulses. However, due to the short wavelength of the light being characterized (sub-100 nm), neither beam-splitters (in the traditional sense) nor nonlinear crystals exist. To generate two replicas of the XUV light, it is necessary to: (1) produce two identical sources, (2) spatially split the beam in two or (3) use a grating in a double pass configuration to act as a beam-splitter [129]. The first method is hard to implement due to the high nonlinearity of the generation process and the high field intensities required for each source. The second method is sensitive to space-time coupling, which is known to exist in HHG. The latter method is inefficient and geometrically complicated. For the nonlinear medium, it is necessary to ensure the absence of resonances in the spectral region of interest.

It is possible to perform an intensity autocorrelation (see Figure 3.26) on the low-order harmonics: up to harmonics 7–9 [130–132] and harmonics 8–14 from solid targets [133]. The weak intensity and high photon energy of the XUV field results in a low cross-section for the two-photon ionization process, resulting in an extremely low signal-to-background value. This technique is only likely to be viable for the lowest-order harmonics, but can provide insight into new dynamics in this wavelength regime due to the simplicity of the method, see [134] for an example.

3.5.1.2 Theory of XUV Photoionization in a Laser Field

If XUV photoionization is performed in the presence of an intense, relatively low-frequency dressing field, the dressing field can act as a temporal phase modulator, thus providing the time-nonstationary filter required for complete characterization of the XUV field. The form of the filter depends on the XUV pulse duration relative to the period of the IR field and the timing of the XUV arrival with respect to the phase of the IR field. This leads to a variety of characterization methods [135–137].

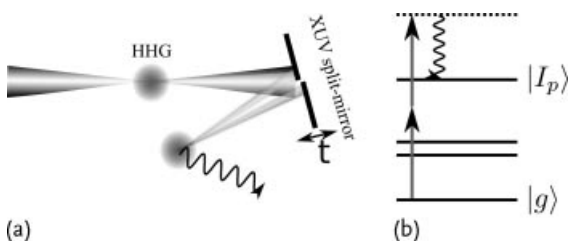


Figure 3.26 Experimental setup for XUV autocorrelation (a): two time-delayed XUV replicas are generated via a split multilayer XUV mirror and the yield of two-photon ionization is mea-

sured. Energy level diagram of the process (b): it is necessary to ensure that there are no internal single-photon absorption resonances for the harmonics of interest.

Considering the ionization of an atom from the XUV field alone, under the single active electron approximation, the transition amplitude, a_ν , from the ground state to the final continuum state $|\nu\rangle$ can be calculated via first-order perturbation theory. For sufficiently large times compared to the XUV pulse duration,

$$a_\nu = -i \int d_\nu(t) \cdot \xi_{\text{XUV}}(t) e^{i(|\nu|^2/2 + I_p)t} dt, \quad (3.33)$$

where $\xi_{\text{XUV}}(t)$ is the XUV field, $|\nu|^2/2$ is the energy of the final continuum state, d_ν is the dipole matrix element for the transition and IP is the ionization potential, in atomic units. Equation (3.33) shows that the electron velocity distribution is the Fourier transform of the product of the temporal XUV field with the temporal response of the ionizing medium and therefore the electron spectrum is the convolution of the XUV spectrum with the spectral response of the ionizing medium. Using known or calculated ionization cross-sections, it is possible to deconvolve the dependence of $|d_\nu|$ on ν to obtain the XUV spectrum.

It is also necessary to correct for the phase of the dipole element when performing temporal characterization. Yakovlev and co-workers [138] have formally shown how to fully take into account the effect of the ionizing medium and how it is possible to learn about the dynamics of the ionizing medium using photoionization (highlighting how metrology developments can lead to new understanding).

Using the strong-field approximation (SFA), it is possible to calculate the electron velocity distribution in the presence of both the XUV and low-frequency field. As the XUV photon energy is much larger than the ionization potential (i.e., $\omega_{\text{XUV}} \gg I_p$), the SFA is satisfied for even moderate IR intensities. The probability amplitude for a transition to the final state $|\nu\rangle$ is given by Quere and co-workers [136, 137],

$$a_\nu = -i \int d_\nu(t) \cdot \xi_{\text{XUV}}(t - \tau) \exp \left\{ i \left[I_p t - \int_t^\infty \frac{[\nu(t') + A(t')]^2}{2} dt' \right] \right\} dt, \quad (3.34)$$

where τ is the delay between the IR and XUV fields and $p(t) = \nu + A(t)$ is the instantaneous canonical momentum of the free electron in the vector potential $A(t)$. Note that in the absence of the IR field, Eq. (3.34) reduces to Eq. (3.33).

Equation (3.34) offers an intuitive picture: the ionization occurs with a probability proportional to the XUV field strength, followed by classical electron motion in the presence of the IR field, resulting in a phase shift and, thus, a change in the energy of the electron. This can be made more clear by rearranging Eq. (3.34) to obtain

$$a_\nu(\Omega, \tau) = -i \int [\chi(t, \tau) e^{i\Phi(t)}] e^{i\Omega t} dt \quad (3.35)$$

$$\chi(t, \tau) = d_\nu(t) \cdot \xi_{\text{XUV}}(t - \tau) \quad (3.36)$$

$$\Phi(t) = - \int_t^\infty \left[\nu \cdot A(t') + \frac{A^2(t')}{2} \right] dt', \quad (3.37)$$

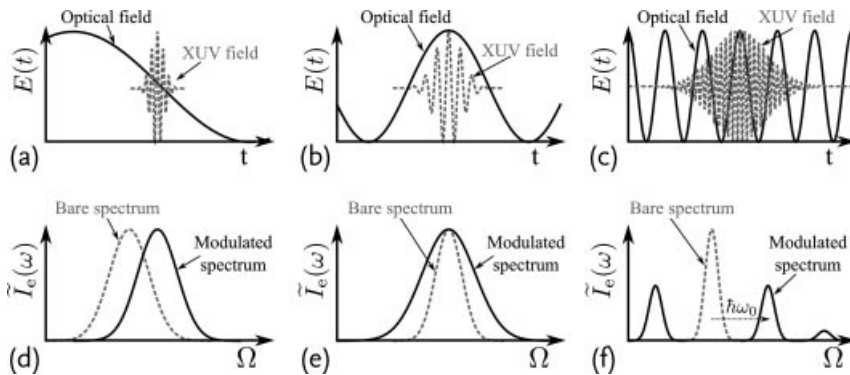


Figure 3.27 Time-dependent XUV (dashed gray) and optical dressing (solid black) fields for three different relative pulse durations and delays (a–c). Original XUV photoelectron spectrum (dashed gray) and modulated spectrum (solid black) as a result of photoionization in the presence of the dressing field (d, e) for the scenarios depicted in parts (a–c). In (a), the XUV pulse is much shorter than the optical period and coincides with the zero crossing of the optical field, resulting in a spectrally sheared photoelectron spectrum, cf. (d); the spectral shear being proportional to the optical field strength and frequency.

In (b), the XUV field is approximately half the optical period and coincides with a peak (minimum) of the optical field resulting in a spectral broadening (narrowing), cf. (e); the amount of broadening is proportional to the optical field strength, XUV pulse duration and the square of the optical frequency. In (c), the XUV field is much longer than an optical period, resulting in sidebands, cf. (f); the separation of the sidebands is proportional to the optical frequency, the strength and number of sidebands is determined by the optical field strength.

where $\Omega = |\mathbf{v}|^2/2 + I_p$ and $\Phi(t)$ is the phase accumulated by the electron (i.e., the *classical action*). Thus the IR laser acts as a temporal phase modulator for the XUV field. Due to the scalar product in Eq. (3.37), the phase modulation is dependent on the angle of detection of the emitted electrons relative to the polarization of the IR field. It is also clear from Eq. (3.35) that it is not the envelope of the IR field, but the electric field itself that acts as the time-nonstationary filter, and thus provides the subfemtosecond temporal resolution required to resolve attosecond dynamics.

The effect of phase modulation on the photoelectron spectrum is dependent on the duration of the XUV field, relative to the period of the IR field, giving rise to three regimes of operation: the XUV field can be (1) much shorter than, (2) comparable to or (3) much longer than the optical period of the low-frequency field. These three scenarios are depicted in Figure 3.27, along with the effect this has on the photoelectron spectrum.

3.5.1.3 Attosecond Spectral Shearing Interferometry

If the XUV pulse is much shorter than the optical period of the dressing laser field, as depicted in Figure 3.27a,d, then it is possible to perform attosecond spectral shearing interferometry – one method of implementing SPIDER via photo-electron spectroscopy (PES) [139]. The method is conceptually simple: two time-delayed replicas of the XUV pulse are temporally aligned with adjacent zeros of the

low-frequency electric field. The delay between the two XUV pulses will generate fringes in the PE spectrum and allows one to extract the phase between them via a Fourier filtering routine. The dressing laser field will cause the two PE velocity distributions to spectrally shift in opposite directions, thus generating the spectral shear required for SPIDER.

This technique has many of the advantages associated with spectral shearing interferometry: excellent robustness to noise, simple and direct phase retrieval algorithm, and acquisition of a 1D dataset. It is necessary to synchronize the timing of the IR and XUV fields with interferometric stability. However, it is possible to use the same IR field that generated the harmonics for the spectral shearing routine, thus ensuring that they are phase locked. Finally, the range of pulse durations is limited by the requirement that the dressing laser electric field must vary linearly with time over the XUV pulse duration. However, it is possible to use a longer wavelength dressing field if necessary (or utilize the approach in Section 3.5.1.7). It can be very difficult to generate two identical copies of the XUV field that are separated by half an optical period. This technique also suffers from the disadvantage of requiring a high-resolution PE spectrometer, which is currently the limiting factor in the experimental demonstration of this method. It is possible to delay the two harmonic pulses by an odd integer multiple of half-cycles, but this increases the spectrometer resolution requirements even further.

3.5.1.4 Attosecond Streak Camera

If the duration of the XUV pulse is comparable to the dressing laser period, then the spectral shift acting on the photoelectron velocity distribution will become time dependent. If the XUV pulse is timed to coincide with the peak of the electric field, as depicted in Figure 3.27b,e, then the phase modulation will be approximately quadratic in time. This will result in a linear stretch (or streaking) of the photoelectron spectrum. Comparison of the spectral width with and without the streaking allows one to estimate the XUV pulse duration. This method, known as the *attosecond streak camera*, has the advantage of being experimentally simple to implement but it is necessary to ensure synchronization of the timing of the XUV and dressing laser fields [140]. Thus the fundamental field used to generate the harmonics is often used as the dressing field.

3.5.1.5 XUV Simplified Chronocyclic Tomography

XUV simplified chronocyclic tomography (XUV-SCT) can be considered as an extension of the attosecond streak camera to unambiguously characterize the XUV field using a direct routine [137]. The method works as described in Section 3.4.4.1: two independent photoelectron spectra are obtained with the XUV field timed to coincide with the peak and the trough of the electric field. This corresponds to positive and negative quadratic temporal phases. Combined with the unmodulated photoelectron spectrum, the data allows one to recover the XUV spectral phase. It is necessary to ensure that the phase added in the modulated spectra is equal in magnitude, of opposite sign, and quadratic in nature. This requires the dressing field to contain many cycles to ensure that the envelope of the pulse does not

affect the modulation. The optical period of the dressing field sets a limit on the maximum pulse duration that can be measured. So far, no experimental demonstration has been performed, most likely since this technique has been superseded by FROG-CRAB (Section 3.5.1.8).

3.5.1.6 RABITT

If the XUV pulse is much longer than the dressing field period, then sidebands will occur in the PE spectrum as depicted in Figure 3.27c,f. If the dressing field is the same that is used to generate the harmonics, then the sideband will consist of a contribution from each adjacent harmonic, resulting in interference, see Figure 3.28. If the sideband intensity is measured as a function of the delay between the XUV and dressing laser fields, the sidebands will appear modulated with a period equal to twice the phase of the dressing laser field and with a relative offset equal to the phase difference between the adjacent harmonics, that is,

$$I_q \sim A \cos(2\phi_{\text{IR}} + \phi_{q-1} - \phi_{q+1}), \quad (3.38)$$

where I_q is the intensity at the even harmonic (i.e., sideband) q , ϕ_{IR} is the phase of the IR dressing laser, $\phi_{q\pm 1}$ are the phases of the adjacent harmonics. By measuring the phase offset for many sidebands, it is possible to obtain the phase difference between multiple harmonics and thus determine whether they are phase locked. This technique offered the first experimental verification of attosecond bursts and is called *resolution of attosecond beating by interference of two-photon transitions* (RABITT) [141, 142]. This technique is not suitable for isolated attosecond pulses, as it only gives the phase difference between adjacent harmonics. This is enough information to obtain the duration of individual pulses in a pulse train, but not to determine the intensity envelope of the pulse train. RABITT is a commonly used technique for studying attosecond pulse trains and has, for example, been used to characterize XUV multilayer mirrors [143].

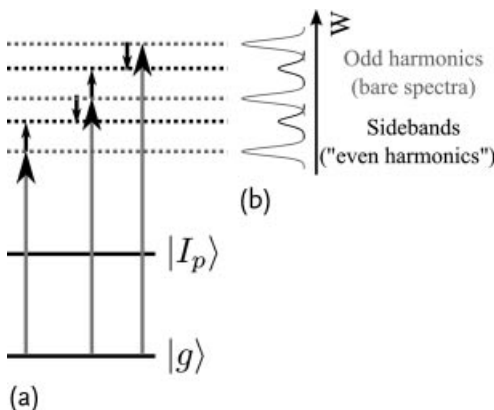


Figure 3.28 Energy level diagram for RABITT (a) and resulting photoelectron spectrum (b) at a given delay between the XUV and an optical field. Due to the interference of the two pathways, the sidebands will be modulated as a function of this delay. The phase of the fringes depends on the relative phase of the adjacent harmonics.

3.5.1.7 X-SPIDER

Another form of XUV-SSI, similar to the RABITT technique described above, can be used for XUV pulses that are long compared to the period of the dressing laser field [137]. In this case, two time-delayed XUV pulse replicas are used to ionize a gas in the presence of a chirped dressing field. The dressing field will cause sidebands to form in the photoelectron spectra of each individual XUV pulse. The frequency of the sideband is determined by the instantaneous frequency of the dressing field. This method can be considered as a direct implementation of conventional SPIDER for PES, except that the SPIDER signal is encoded in sidebands of a photoelectron spectrum. This method has the same advantages and disadvantages as the attosecond spectral shearing technique in Section 3.5.1.3, except that it works in a slightly different parameter range. As with Section 3.5.1.3, the requirement of a high-resolution photoelectron spectrometer is currently the bottleneck to a successful demonstration of this technique.

3.5.1.8 FROG-CRAB

The PES techniques described above rely on a specific relationship between the duration (timing) of the XUV field relative to the period (phase) of the dressing laser field. It is possible to completely characterize the XUV field without knowledge about the relative pulse durations and delays via *frequency-resolved optical gating for complete reconstruction of attosecond bursts* (FROG-CRAB) [144]. The method is completely analogous to conventional FROG in the optical domain, except that the gate function is a phase filter instead of an amplitude filter. This offers the bonus of measuring the electric field of the optical pulse. Thus, Eq. (3.35) is equivalent to a spectrogram where

$$P(t) = d_v(t) \cdot \xi_{\text{XUV}}(t - \tau) \quad (3.39\text{a})$$

$$G(t) = e^{i\Phi(t)}. \quad (3.39\text{b})$$

Using this method, it is not only possible to obtain the XUV field, but also the dressing laser field via, for example, the PCGPA deconvolution algorithm (Section 3.4.2.2). Technically, the reconstructed probe is equal to the convolution of the XUV field with the spectral response of the medium. Initial experiments utilized attosecond pulses that were relatively long in duration as compared to the response time of the medium (i.e., the spectral response is largely flat over the bandwidth of the XUV pulse). However, as the pulse duration decreases and the pulse bandwidth increases, the effects of the ionizing medium become more important. Other limits of validity of FROG-CRAB are set by the size of the phase modulation that can be applied, the resolution of the photoelectron spectrometer and the range of travel for the stage used to scan the delay between the gate (i.e., dressing laser) and probe (i.e., XUV) fields. FROG-CRAB has been used to completely characterize isolated attosecond pulses [145], attosecond pulse trains [146, 147], and to measure NIR fields [148], and even terahertz fields [149]. Recent advances allowed the characterization of even shorter pulses. Gagnon and co-workers [138, 150] have shown how to account for the ionizing medium response and Chini and co-workers [151]

generalized the streaking method in a technique called *phase retrieval by omega oscillation filtering* (PROOF). PROOF is related to both FROG-CRAB and RABITT. These advances enable FROG-CRAB to be extended to the measurement of pulses approaching the atomic unit of time (24 as).

3.5.2 XUV Interferometry

3.5.2.1 XUV SPIDER for HHG

One of the underlying features of HHG is that the spectrum consists of peaks centered around the odd harmonics of the driving field, corresponding to the emission and recollision of electrons every half-cycle of the laser field in an antisymmetric fashion. Thus, it is reasonable to assume that if one were to shift the central frequency of the driving laser by an amount $\delta\omega \ll \Delta\omega$, where $\Delta\omega$ is the bandwidth of the drive pulse, then the harmonics should shift in frequency by an amount $\Omega = n\delta\omega$, where n is the harmonic number. It therefore seems possible to shift the harmonic frequency by simply driving with a slightly frequency shifted replica of the IR field. This process is a direct consequence of conservation of energy. Simulations using the time-dependent Schrödinger equation (TDSE) have indeed shown that this is quantitatively the case [152]. This then allows for the possibility of performing SSI on XUV attosecond pulses by driving HHG with two spectrally sheared driving fields. One difference between optical SPIDER and XUV SPIDER is that the spectral shear is not constant, but a linear function of frequency since $\phi_1(n\omega_{01}) = \phi_2(n\omega_{02})$, where n is the fractional harmonic number, thus

$$\Omega = \frac{\delta\omega}{\omega_{01}}\omega, \quad (3.40)$$

where $\delta\omega = \omega_{02} - \omega_{01}$ and the phase is reconstructed for pulse 1, that is, $\phi_1(n\omega_{01})$.

Numerical simulations based on the resolution of the 3D TDSE for the single atom response in cylindrical coordinates in argon ($I_p = 0.581$ a.u.) calculated the HHG from a 30 fs driving pulse. The simulation showed that harmonics in the cut-off region are sheared replicas for small shears in the driving pulse ($\lesssim 0.5\%$), see Figure 3.29a. As a result of the intensity-dependent dipole phase, the harmonics are individually negatively chirped, and the harmonic train itself is also negatively chirped. The scaling of the shear, as defined by Eq. (3.40), can be verified by rescaling the frequency axis by the central frequency of the driving laser, as shown in Figure 3.29b, where the harmonics are plotted against the fractional harmonic number.

The measurement of attosecond pulse trains requires the measurement of the spectral phase across individual harmonics and, more importantly, the relative phase between adjacent harmonics. In general, the spectral intensity in individual harmonics from multicycle driving pulses is too low to enable concatenation of the spectral phase between harmonics, thus preventing the measurement of the relative phase of adjacent harmonics. An alternative approach, yet to be explored, is the possibility to utilize multiple spectral shearing interferometry (Section 3.4.5.4)

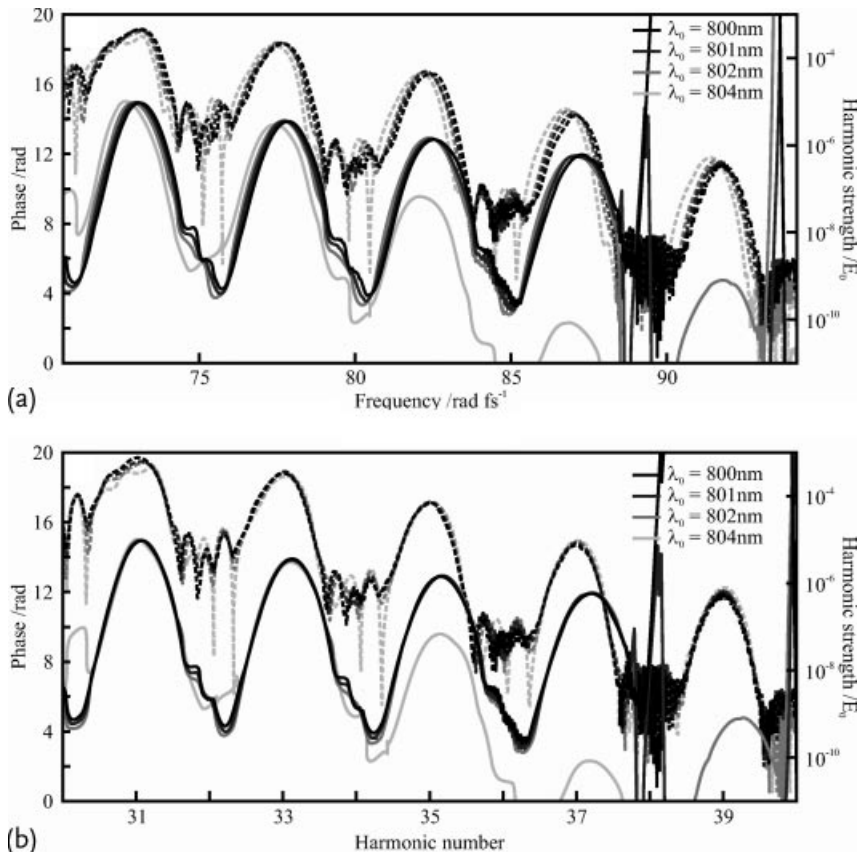


Figure 3.29 Numerical simulation of HHG spectrum (dashed, log scale) and phase (solid) for slightly different driving frequencies. Numerical artifacts cause the relative phase offset between the highest harmonics for the

longest wavelength. Results plotted against the frequency of the emitted harmonics (a). Results plotted against fractional harmonic number, that is, $n_i = \omega/\omega_0$; (b).

to enable attosecond pulse train characterization via XUV-SSI. When the driving pulse duration decreases to the point that the pulse duration is only a few optical cycles long (and the pulse bandwidth is a large fraction of its central frequency), it is not clear that the HHG spectrum is sheared as the central frequency of the driving pulse is sheared. Thus, it is not immediately clear how to measure an isolated attosecond pulse, since this is typically generated from a few-cycle pulse. One approach could be to interfere an attosecond pulse train with an isolated attosecond pulse (i.e., a harmonic comb with a continuum) and then to continuously shear the attosecond pulse train (i.e., shear the multicycle driving pulse) covering the full continuous spectrum of the isolated attosecond pulse. The possibilities afforded by multiple spectral shearing interferometry have yet to be fully explored, but this could be a viable route to enable XUV-SSI of attosecond pulse trains and isolated attosecond pulses.

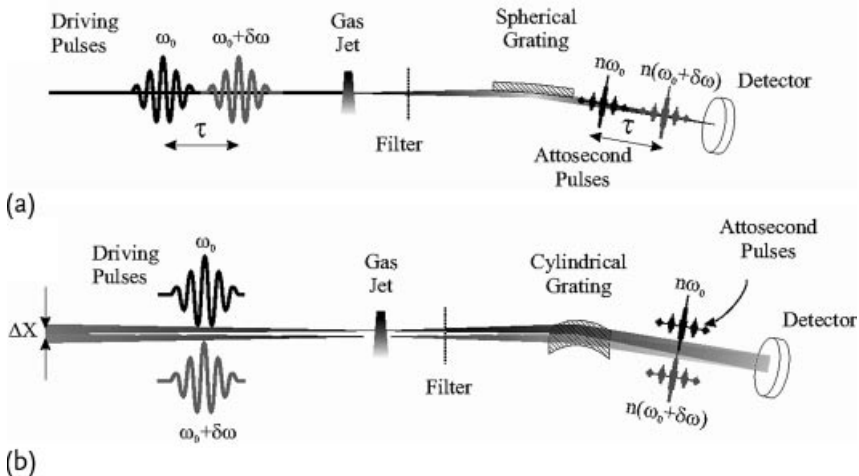


Figure 3.30 Schematic of the experimental setup for performing XUV SPIDER. Spectrally encoded XUV-SPIDER (a) – a temporal delay between the driving pulses generates tem-

porally delayed harmonics and thus spectral fringes. Spatially encoded XUV-SPIDER (b) – a spatial displacement between the driving pulses leads to spatial fringes due to diffraction.

There are two basic geometries for performing XUV-SPIDER: (1) spectrally encoded and (2) spatially encoded, as depicted in Figure 3.30a,b, respectively. The former requires a temporal delay between the two driving fields, and thus generates spectral fringes in the harmonic spectrum. The latter requires two spatially separated sources of harmonics, which are then interfered on a spatially resolved spectrometer in the far-field. There are inherent advantages and disadvantages for each technique.

Spectrally encoded XUV-SPIDER The delay between two IR pulses needs to be sufficient to avoid temporal overlap of the two pulses and to ensure that the spectral fringes have sufficient periodicity to enable extraction of the sidebands in the Fourier domain (Figure 3.30a). However, the separation also needs to be small enough that it is possible to resolve the fringes with the spectrometer. The advantage of this technique is that the two pulses will experience the same gas density and thus the same dispersion after their generation, providing that gas ionization remains negligible. Producing the two sheared driving pulses can be technically simple for this geometry, for example using a pulse shaper. However, it is necessary to note that the first pulse may cause ionization, which will affect the succeeding pulse, thus limiting the peak intensity and therefore the maximum harmonic frequency, as shown by the simulation results in Figure 3.31.

Another disadvantage of the spectrally encoded XUV-SPIDER is the requirement of high spectral resolution, which is very difficult to achieve. For example, a typical XUV spectrometer provides sufficient resolution to sample fringes due to a delay of 10–100 fs at a photon energy of ~ 100 eV, which is only barely suitable to ensure

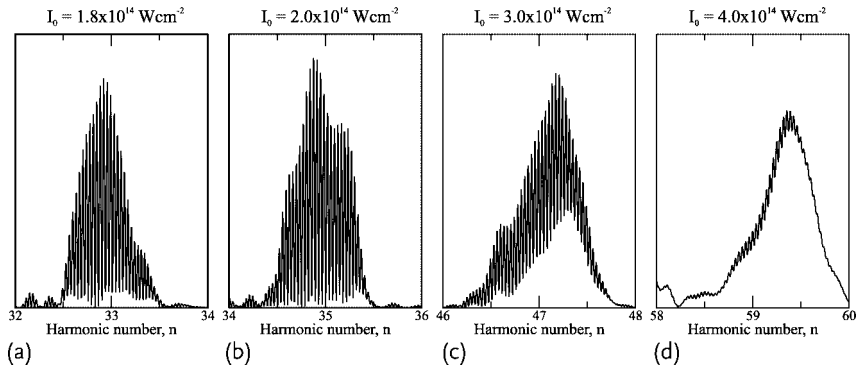


Figure 3.31 Simulation of spectrally encoded XUV-SPIDER traces for different driving intensities. As the intensity increases, ionization results in a decreasing fringe contrast. For $I_0 \lesssim 2.0 \times 10^{14} \text{ W cm}^{-2}$ in argon, the effect of

the preceding pulse on the medium remains negligible. The harmonic depicted is from the cutoff region, hence the harmonic number shown increases with intensity.

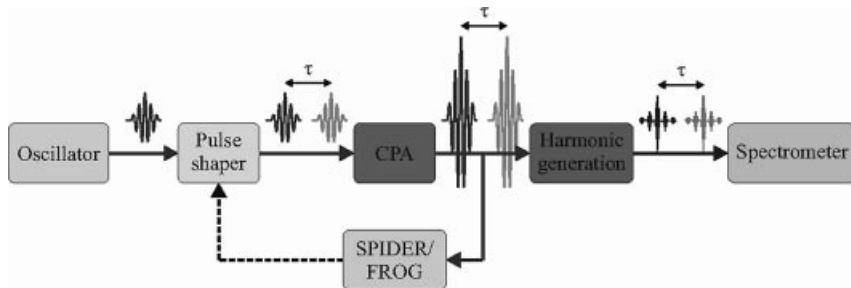


Figure 3.32 Schematic of a spectrally encoded XUV-SPIDER, using a pulse shaper integrated into a CPA system.

the two time-delayed driving pulses do not interfere if they are clean from any pre- or postpulses and extended pedestals.

Mairesse and co-workers [153] experimentally implemented an XUV-SPIDER, utilizing an all-optical setup (see Figure 3.32) to measure harmonic 11, generated from 50 fs pulses. The measured XUV pulse duration was 22 fs and was reduced to 13 fs when using polarization gating.

Spatially encoded arrangement for XUV-SPIDER Two spatially separated sources of harmonics are propagated to the far-field, where they overlap to generate spatial fringes due to diffraction (Figure 3.30b). Since the fringes are in the spatial domain, the spectrum can be sampled at the sampling limit, thus preventing the need for an extremely high-resolution spectrometer. Additionally, there is no limit on the maximum intensity of the driving pulses, since the two pulses propagate through different regions of the gas jet.

In practice, it is very difficult to ensure that the focusing conditions are identical for both driving pulses to guarantee the generation of two identical, but spectrally shifted, harmonics. Ideally, one pulse should pass through a “frequency shifter” – this can be either a linear temporal phase modulator or a time-stationary pulse shaper, combined with a complete pulse characterization device to measure and control the output of the pulse shaper. The harmonics from this shaped beam interfere with the harmonics from the unshaped pulse. The unshaped pulse is to act as a local oscillator and the SPIDER measurement is achieved by two interference measurements, each performed with a different frequency shift applied to the shaped pulse. The phase of the local oscillator is irrelevant and it is only necessary to ensure its harmonic spectrum overlaps the harmonic spectrum from the frequency shifted pulse. Such a geometry should: (1) ensure equal focusing conditions for the two sheared driving pulses; (2) remove the need to calibrate the temporal delay between the pulses and (3) eliminate errors due to space-time coupling in the beam. This geometry has not yet been demonstrated due to the difficulty in building a frequency shifter suitable for high-power few-cycle pulses, that is, one with sufficient bandwidth and output power. However, a suitable pulse shaper is now available [154, 155] and experimental demonstration of this method should be possible. Alternatively, one could attempt to frequency shift the driving field through nonlinear optics, such as ionization blue-shifting [156].

3.6 Summary

A wide variety of methods exist for determining the complete pulse shape of optical pulses. As technologies have improved, the demands placed on metrological methods have increased, resulting in improvements in existing characterization methods and the development of new ones. However, the general principles involved can generally be broken down into a few categories, based on the order and types of linear filters that can be used to describe the method. The developments in metrology have led to a breakthrough in the understanding of nonlinear optics and generated new tools for science and technology, promising unprecedented access to the natural world at the shortest time scales observable. It is clear that as ultrafast science continues to evolve, so will the metrological tools.

References

- 1** Fleming, G. (1986) *Chemical Applications of Ultrafast Spectroscopy*, Oxford University Press, New York.
- 2** Misewich, J., Glownia, J., Rothenberg, J., and Sorokin, P. (1988) Subpicosecond UV kinetic spectroscopy: Photolysis of thallium halide vapors. *Chem. Phys. Lett.*, **150** (6), 374–379.
- 3** Rosker, M., Dantus, M., and Zewail, A. (1988) Femtosecond real-time probing of reactions. I. The technique. *J. Chem. Phys.*, **89**, –6113.

- 4 Zewail, A. (1988) Laser femtochemistry. *Science*, **242** (4886), 1645–1653.
- 5 Cundall, R. and Dale, R. (1983) *Time-resolved Fluorescence Spectroscopy in Biochemistry and Biology*, Plenum Press.
- 6 Diamandis, E. (1988) Immunoassays with time-resolved fluorescence spectroscopy: principles and applications. *Clin. Biochem.*, **21** (3), 139–150.
- 7 Kowalczyk, P., Radzewicz, C., Mostowski, J., and Walmsley, I. (1990) Time-resolved luminescence from coherently excited molecules as a probe of molecular wave-packet dynamics. *Phys. Rev. A*, **42** (9), 5622–5626.
- 8 Ito, H., Yokoyama, H., Murata, S., and Inaba, H. (1981) Generation of picosecond optical pulses with highly RF modulated AlGaAs DH laser. *IEEE J. Quantum Electron.*, **17** (5), 663–670.
- 9 McCabe, D.J., England, D.G., Martay, H.E.L., Friedman, M.E., Petrovic, J., Dimova, E., Chatel, B., and Walmsley, I.A. (2009) Pump-probe study of the formation of rubidium molecules by ultrafast photoassociation of ultracold atoms. *Phys. Rev. A*, **80**, 033404.
- 10 Berg, L.E., Beutter, M., and Hansson, T. (1996) Femtosecond laser spectroscopy on the vibrational wave packet dynamics of the $A^1 \sum_{3-4}^+$ state of NaK. *Chem. Phys. Lett.*, **253** (3–4), 327–332, doi:10.1016/0009-2614(96)00206-0.
- 11 Papanikolas, J.M., Williams, R.M., Kleiber, P.D., Hart, J.L., Brink, C., Price, S.D., and Leone, S.R. (1995) Wave-packet dynamics in the $Li_2E(^1\sum_g^+)$ shelf state: Simultaneous observation of vibrational and rotational recurrences with single rovibronic control of an intermediate state. *J. Chem. Phys.*, **103** (17), 7269–7276, doi:10.1063/1.470301.
- 12 Amitay, Z., Ballard, J.B., Stauffer, H.U., and Leone, S.R. (2001) Phase-tailoring molecular wave packets to time shift their dynamics. *Chem. Phys.*, **267** (13), 141–149, doi:10.1016/S0301-0104(01)00217-8.
- 13 Rice, S.A. and Zhao, M. (2000) *Optical Control of Molecular Dynamics*, John Wiley & Sons, New York.
- 14 Shapiro, M. and Brumer, P. (2003) *Principles of the Quantum Control of Molecular Processes*, Wiley-VCH Verlag GmbH.
- 15 Kühn, O. and Wöste, L. (2007) *Analysis and Control of Ultrafast Photoinduced Reactions*, Springer Series in Chemical Physics, vol. 87, Springer.
- 16 Niikura, H., Legare, F., Hasbani, R., Bandrauk, A.D., Ivanov, M.Y., Villeneuve, D.M., and Corkum, P.B. (2002) Sub-laser-cycle electron pulses for probing molecular dynamics. *Nature*, **417** (6892), 917–922.
- 17 Brown, B.L. and Walmsley, I.A. (2006) Analysis of some intuitive approaches to the coherent control of state-selected ultracold molecules. *J. Phys. B*, **39** (19), S1055–S1075.
- 18 Martay, H.E.L., McCabe, D.J., England, D.G., Friedman, M.E., Petrovic, J., and Walmsley, I.A. (2009) Demonstrating coherent control in $^{85}\text{Rb}_2$ using ultrafast laser pulses: A theoretical outline of two experiments. *Phys. Rev. A*, **80**, 033403.
- 19 Prokhorenko, V., Nagy, A., Waschuk, S., Brown, L., Birge, R., and Miller, R. (2006) Coherent control of retinal isomerization in bacteriorhodopsin. *Science*, **313** (5791), 1257–1261.
- 20 Petersen, J., Mitrić, R., Bonačić-Koutecký, V., Wolf, J.P., Roslund, J., and Rabitz, H. (2010) How shaped light discriminates nearly identical biochromophores. *Phys. Rev. Lett.*, **105**, 073003.
- 21 Baker, S., Robinson, J.S., Haworth, C.A., Teng, H., Smith, R.A., Chirila, C.C., Lein, M., Tisch, J.W.G., and Marangos, J.P. (2006) Probing proton dynamics in molecules on an attosecond time scale. *Science*, **312** (5772), 424–427.
- 22 Niikura, H., Legare, F., Hasbani, R., Ivanov, M.Y., Villeneuve, D.M., and Corkum, P.B. (2003) Probing molecular dynamics with attosecond resolution using correlated wave packet pairs. *Nature*, **421** (6925), 826–829.
- 23 Piredda, G., Dorrer, C., Williams, E.M.K., Walmsley, I.A., and Boyd, R.W. (2005) Measurement of the intensity-dependent refractive index using complete spatio-temporal pulse characterization. *J. Nonlinear Opt. Phys. Mater.*, **14** (1), 9–20.

- 24** Kim, K.T., Zhang, C., Shiner, A.D., Kirkwood, S.E., Frumker, E., Gariety, G., Naumov, A., Villeneuve, D.M., and Corkum, P.B. (2013) Manipulation of quantum paths for space-time characterization of attosecond pulses. *Nat. Phys.*, **9** (3), 159–163.
- 25** Telle, H.R., Steinmeyer, G., Dunlop, A.E., Stenger, J., Sutter, D.H., and Keller, U. (1999) Carrier-envelope offset phase control: A novel concept for absolute optical frequency measurement and ultrashort pulse generation. *Appl. Phys. B*, **69** (4), 327–332.
- 26** Jones, D., Diddams, S., Ranka, J., Stentz, A., Windeler, R., Hall, J., and Cundiff, S. (2000) Carrier-envelope phase control of femtosecond mode-locked lasers and direct optical frequency synthesis. *Science*, **288** (5466), 635–639.
- 27** Helbing, F.W., Steinmeyer, G., and Keller, U. (2003) Carrier-envelope offset phase-locking with attosecond timing jitter. *IEEE J. Sel. Top. Quantum Electron.*, **9** (4), 1030–1040.
- 28** Baltuška, A., Uiberacker, M., Goulielmakis, E., Kienberger, R., Yakovlev, V., Udem, T., Hänsch, T., and Krausz, F. (2003) Phase-controlled amplification of few-cycle laser pulses. *IEEE J. Sel. Top. Quantum Electron.*, **9** (4), 972–989.
- 29** Baltuška, A., Udem, T., Uiberacker, M., Hentschel, M., Goulielmakis, E., Gohle, C., Holzwarth, R., Yakovlev, V.S., Scrinzi, A., Hänsch, T.W., and Krausz, F. (2003) Attosecond control of electronic processes by intense light fields. *Nature*, **421** (6923), 611–615.
- 30** Haworth, C.A., Chipperfield, L.E., Robinson, J.S., Knight, P.L., Marangos, J.P., and Tisch, J.W.G. (2007) Half-cycle cutoffs in harmonic spectra and robust carrier-envelope phase retrieval. *Nat. Phys.*, **3** (1), 52–57.
- 31** Kakehata, M., Kobayashi, Y., Takada, H., and Torizuka, K. (2002) Single-shot measurement of a carrier-envelope phase by use of a time-dependent polarization pulse. *Opt. Lett.*, **27** (14), 1247–1249.
- 32** Lemell, C., Tong, X.M., Krausz, F., and Burgdörfer, J. (2003) Electron emission from metal surfaces by ultrashort pulses: Determination of the carrier-envelope phase. *Phys. Rev. Lett.*, **90**, 076403.
- 33** Apolonski, A., Dombi, P., Paulus, G.G., Kakehata, M., Holzwarth, R., Udem, T., Lemell, C., Torizuka, K., Burgdörfer, J., Hänsch, T.W., and Krausz, F. (2004) Observation of light-phase-sensitive photoemission from a metal. *Phys. Rev. Lett.*, **92**, 073902.
- 34** Kresz, M., Löffler, T., Thomson, M.D., Dorner, R., Gimpel, H., Zrost, K., Ergler, T., Moshammer, R., Morgner, U., Ullrich, J., and Roskos, H.G. (2006) Determination of the carrier-envelope phase of few-cycle laser pulses with terahertz-emission spectroscopy. *Nat. Phys.*, **2** (5), 327–331.
- 35** Paye, J. (1992) The chronocyclic representation of ultrashort light pulses. *IEEE J. Quantum Electron.*, **28** (10), 2262–2273.
- 36** Akturk, S., Gu, X., Gabolde, P., and Trebino, R. (2005) The general theory of first-order spatio-temporal distortions of gaussian pulses and beams. *Opt. Express*, **13** (21), 8642–8661.
- 37** Walmsley, I., Waxer, L., and Dorrer, C. (2001) The role of dispersion in ultrafast optics. *Rev. Sci. Inst.*, **72** (1), 1–29.
- 38** Weiner, A.M. (2000) Femtosecond pulse shaping using spatial light modulators. *Rev. Sci. Inst.*, **71** (5), 1929–1960.
- 39** Bor, Z. (1988) Distortion of femtosecond laser-pulses in lenses and lens systems. *J. Mod. Opt.*, **35** (12), 1907–1918.
- 40** Frank, F., Arrell, C., Witting, T., Okell, W.A., McKenna, J., Robinson, J.S., Haworth, C.A., Austin, D., Teng, H., Walmsley, I.A., Marangos, J.P., and Tisch, J.W.G. (2012) Invited review article: Technology for attosecond science. *Rev. Sci. Inst.*, **83** (7), 071101, doi:10.1063/1.4731658.
- 41** Wong, V. and Walmsley, I.A. (1994) Analysis of ultrashort pulse-shape measurement using linear interferometers. *Opt. Lett.*, **19** (4), 287–289.
- 42** Wong, V. and Walmsley, I.A. (1995) Linear filter analysis of methods for ultrashort-pulse-shape measurements. *J. Opt. Soc. Am. B*, **12** (8), 1491–1499.
- 43** Dorrer, C. and Kang, I. (2008) Linear self-referencing techniques for short-

- optical-pulse characterization invited. *J. Opt. Soc. Am. B*, **25** (6), A1–A12.
- 44** Walmsley, I.A. and Wong, V. (1996) Characterization of the electric field of ultrashort optical pulses. *J. Opt. Soc. Am. B*, **13** (11), 2453–2463.
- 45** Bell, R. (1972) *Introductory Fourier Transform Spectroscopy*, Academic Press.
- 46** Saptari, V. (2003) *Fourier Transform Spectroscopy Instrumentation Engineering*, SPIE Publications.
- 47** Peatross, J. and Rundquist, A. (1998) Temporal decorrelation of short laser pulses. *J. Opt. Soc. Am. B*, **15** (1), 216–222.
- 48** Nicholson, J.W., Jasapara, J., Rudolph, W., Omenetto, F.G., and Taylor, A.J. (1999) Full-field characterization of femtosecond pulses by spectrum and cross-correlation measurements. *Opt. Lett.*, **24** (23), 1774–1776.
- 49** Luan, S., Hutchinson, M., and Smith, R. (1993) High dynamic range third-order correlation measurement of picosecond laser pulse shapes. *Meas. Sci. Technol.*, **4** (12), 1426–1429.
- 50** Valdmanis, J., Mourou, G., and Gabel, C. (1982) Picosecond electro-optic sampling system. *Appl. Phys. Lett.*, **41**, 211.
- 51** Wu, Q. and Zhang, X. (1995) Free-space electro-optic sampling of terahertz beams. *Appl. Phys. Lett.*, **67**, 3523.
- 52** Kane, D.J. and Trebino, R. (1993) Characterization of arbitrary femtosecond pulses using frequency-resolved optical gating. *IEEE J. Quantum Electron.*, **29** (2), 571–579.
- 53** Trebino, R., DeLong, K.W., Fittinghoff, D.N., Sweetser, J.N., Krumbiegel, M.A., Richman, B.A., and Kane, D.J. (1997) Measuring ultrashort laser pulses in the time-frequency domain using frequency-resolved optical gating. *Rev. Sci. Inst.*, **68** (9), 3277–3295.
- 54** Trebino, R. (2002) *Frequency-Resolved Optical Gating: The Measurement of Ultrashort Laser Pulses*, Springer.
- 55** Delong, K.W., Trebino, R., Hunter, J., and White, W.E. (1994) Frequency-resolved optical gating with the use of 2nd-harmonic generation. *J. Opt. Soc. Am. B*, **11** (11), 2206–2215.
- 56** Zeek, E., Shreenath, A.P., O’Shea, P., Kimmel, M., and Trebino, R. (2002) Simultaneous automatic calibration and direction-of-time removal frequency-resolved optical gating. *Appl. Phys. B*, **74**, S265–S271.
- 57** Sweetser, J.N., Fittinghoff, D.N., and Trebino, R. (1997) Transient-grating frequency-resolved optical gating. *Opt. Lett.*, **22** (8), 519–521.
- 58** Tsang, T., Krumbiegel, M.A., DeLong, K.W., Fittinghoff, D.N., and Trebino, R. (1996) Frequency-resolved optical-gating measurements of ultrashort pulses using surface third-harmonic generation. *Opt. Lett.*, **21** (17), 1381–1383.
- 59** Gerchberg, R. (1972) A practical algorithm for the determination of phase from image and diffraction plane pictures. *Optik*, **35**, –237.
- 60** Barakat, R. and Newsam, G. (1984) Necessary conditions for a unique solution to two-dimensional phase retrieval. *J. Math. Phys. (NY)*, **23**, 3190–3193.
- 61** Millane, R. (1990) Phase retrieval in crystallography and optics. *J. Opt. Soc. Am. A*, **7** (3), 394–411.
- 62** Kane, D.J., Omenetto, F.G., and Taylor, A.J. (2000) Convergence test for inversion of frequency-resolved optical gating spectrograms. *Opt. Lett.*, **25** (16), 1216–1218.
- 63** Kane, D.J. (1998) Real-time measurement of ultrashort laser pulses using principal component generalized projections. *IEEE J. Sel. Top. Quantum Electron.*, **4** (2), 278–284.
- 64** Kane, D.J. (1999) Recent progress toward real-time measurement of ultrashort laser pulses. *IEEE J. Quantum Electron.*, **35** (4), 421–431.
- 65** Kane, D.J., Weston, J., and Chu, K.C.J. (2003) Real-time inversion of polarization gate frequency-resolved optical gating spectrograms. *Appl. Opt.*, **42** (6), 1140–1144.
- 66** Kane, D.J. (2008) Principal components generalized projections: a review invited. *J. Opt. Soc. Am. B*, **25** (6), A120–A132.
- 67** Delong, K.W., Fittinghoff, D.N., Trebino, R., Kohler, B., and Wilson, K. (1994) Pulse retrieval in frequency-resolved optical gating based on the method of gen-

- eralized projections. *Opt. Lett.*, **19** (24), 2152–2154.
- 68** Delong, K.W. and Trebino, R. (1994) Improved ultrashort pulse-retrieval algorithm for frequency-resolved optical gating. *J. Opt. Soc. Am. A*, **11** (9), 2429–2437.
- 69** Krumbiegel, M.A., Ladera, C.L., DeLong, K.W., Fittinghoff, D.N., Sweetser, J.N., and Trebino, R. (1996) Direct ultrashort-pulse intensity and phase retrieval by frequency-resolved optical gating and a computational neural network. *Opt. Lett.*, **21** (2), 143–145.
- 70** Ratner, J., Steinmeyer, G., Wong, T.C., Bartels, R., and Trebino, R. (2012) Coherent artifact in modern pulse measurements. *Opt. Lett.*, **37** (14), 2874–2876.
- 71** O’Shea, P., Kimmel, M., Gu, X., and Trebino, R. (2001) Highly simplified device for ultrashort-pulse measurement. *Opt. Lett.*, **26** (12), 932–934.
- 72** O’Shea, P., Akturk, S., Kimmel, M., and Trebino, R. (2004) Practical issues in ultra-short-pulse measurements with “Grenouille”. *Appl. Phys. B*, **79** (6), 683–691.
- 73** Gu, X., Akturk, S., Shreenath, A., Cao, Q., and Trebino, R. (2004) The measurement of ultrashort light pulses – simple devices, complex pulses. *Opt. Rev.*, **11** (3), 141–152.
- 74** O’Shea, P., Kimmel, M., Gu, X., and Trebino, R. (2000) Increased-bandwidth in ultrashort-pulse measurement using an angle-dithered nonlinear-optical crystal. *Opt. Express*, **7** (10), 342–349.
- 75** Akturk, S., Kimmel, M., O’Shea, P., and Trebino, R. (2004) Extremely simple device for measuring 20-fs pulses. *Opt. Lett.*, **29** (9), 1025–1027.
- 76** Akturk, S., Kimmel, M., O’Shea, P., and Trebino, R. (2003) Measuring pulse-front tilt in ultrashort pulses using grenouille. *Opt. Express*, **11** (5), 491–501.
- 77** Akturk, S., Kimmel, M., O’Shea, P., and Trebino, R. (2003) Measuring spatial chirp in ultrashort pulses using single-shot frequency-resolved optical gating. *Opt. Express*, **11** (1), 68–78.
- 78** Cormack, I., Sibbett, W., and Reid, D. (2001) Rapid measurement of ultrashort-pulse amplitude and phase from a two-photon absorption sonogram trace. *J. Opt. Soc. Am. B*, **18** (9), 1377–1382.
- 79** Reid, D. (1999) Algorithm for complete and rapid retrieval of ultrashort pulse amplitude and phase from a sonogram. *IEEE J. Quantum Electron.*, **35** (11), 1584–1589.
- 80** Beck, M., Raymer, M.G., Walmsley, I.A., and Wong, V. (1993) Chronocyclic tomography for measuring the amplitude and phase-structure of optical pulses. *Opt. Lett.*, **18** (23), 2041–2043.
- 81** Dorrer, C. and Kang, I. (2003) Complete temporal characterization of short optical pulses by simplified chronocyclic tomography. *Opt. Lett.*, **28** (16), 1481–1483.
- 82** Kang, I. and Dorrer, C. (2005) Highly sensitive differential tomographic technique for real-time ultrashort pulse characterization. *Opt. Lett.*, **30** (12), 1545–1547.
- 83** Kolner, B.H. and Nazarathy, M. (1989) Temporal imaging with a time lens. *Opt. Lett.*, **14** (12), 630–632, doi:10.1364/OL.14.000630.
- 84** Mouradian, L., Louradour, F., Messager, V., Barthelemy, A., and Froehly, C. (2000) Spectro-temporal imaging of femtosecond events. *IEEE J. Quantum Electron.*, **36** (7), 795–801.
- 85** Nibbering, E.T.J., Franco, M.A., Prade, B.S., Grillon, G., Chambaret, J.P., and Mysyrowicz, A. (1996) Spectral determination of the amplitude and the phase of intense ultrashort optical pulses. *J. Opt. Soc. Am. B*, **13** (2), 317–329, doi:10.1364/JOSAB.13.000317.
- 86** Franco, M., Lange, H., Ripoche, J.F., Prade, B., and Mysyrowicz, A. (1997) Characterization of ultra-short pulses by cross-phase modulation. *Opt. Commun.*, **140**, 331–340, doi:10.1016/S0030-4018(97)00201-0.
- 87** Lange, H., France, M., Ripoche, J., Prade, B., Rousseau, P., and Mysyrowicz, A. (1998) Reconstruction of the time profile of femtosecond laser pulses through cross-phase modulation. *IEEE J. Sel. Top. Quantum Electron.*, **4** (2), 295–300, doi:10.1109/2944.686735.
- 88** Ferreiro, J.J., de la Fuente, R., and López-Lago, E. (2001) Characteriza-

- tion of arbitrarily polarized ultrashort laser pulses by cross-phase modulation. *Opt. Lett.*, **26** (13), 1025–1027, doi:10.1364/OL.26.001025.
- 89** Froehly, C., Lacourt, A., and Vienot, J. (1973) Notions de réponse impulsionnelle et de fonction de transfert temporelles des pupilles optiques, justifications expérimentales et applications. *Nouv. Rev. Opt.*, **4**, 183–196.
- 90** Dorrer, C. and Joffre, M. (2001) Characterization of the spectral phase of ultrashort light pulses. *Comptes Rendus – Phys. Astrophys. Ser. IV*, **2** (10), 1415–1426.
- 91** Takeda, M., Ina, H., and Kobayashi, S. (1982) Fourier-transform method of fringe-pattern analysis for computer-based topography and interferometry. *J. Opt. Soc. Am.*, **72** (1), 156–160.
- 92** Piasecki, J., Colombeau, B., Vampouille, M., Froehly, C., and Arnaud, J.A. (1980) Nouvelle méthode de mesure de la réponse impulsionnelle des fibres optiques. *Appl. Opt.*, **19** (22), 3749–3755.
- 93** Fittinghoff, D.N., Bowie, J.L., Sweetser, J.N., Jennings, R.T., Krumbiegel, M.A., DeLong, K.W., Trebino, R., and Walmsley, I.A. (1996) Measurement of the intensity and phase of ultraweak, ultrashort laser pulses. *Opt. Lett.*, **21** (12), 884–886.
- 94** Iaconis, C. and Walmsley, I.A. (1998) Spectral phase interferometry for direct electric-field reconstruction of ultrashort optical pulses. *Opt. Lett.*, **23** (10), 792–794.
- 95** Walmsley, I.A. (2004) Characterization of ultrashort optical pulses in the few-cycle regime using spectral phase interferometry for direct electric-field reconstruction. *Few-Cycle Laser Pulse Generation and Its Applications*, Topics in Applied Physics, vol. 95, pp. 265–291.
- 96** Walmsley, I. and Dorrer, C. (2009) Characterization of ultrashort electromagnetic pulses. *Adv. Optics Photon.*, **1** (2), 308–437.
- 97** Dorrer, C. and Walmsley, I.A. (2002) Accuracy criterion for ultrashort pulse characterization techniques: application to spectral phase interferometry for direct electric field reconstruction. *J. Opt. Soc. Am. B*, **19** (5), 1019–1029.
- 98** Dorrer, C. and Walmsley, I. (2002) Precision and consistency criteria in spectral phase interferometry for direct electric-field reconstruction. *J. Opt. Soc. Am. B*, **19** (5), 1030–1038.
- 99** Shuman, T.M., Anderson, M.E., Broome, J., Iaconis, C., Waxer, L., and Walmsley, I.A. (1999) Real-time spider: ultrashort pulse characterization at 20 Hz. *Opt. Express*, **5** (6), 134–143.
- 100** Dorrer, C. (1999) Influence of the calibration of the detector on spectral interferometry. *J. Opt. Soc. Am. B*, **16** (7), 1160–1168.
- 101** Anderson, M.E., de Araujo, L.E.E., Kosik, E.M., and Walmsley, I.A. (2000) The effects of noise on ultrashort-optical-pulse measurement using spider. *Appl. Phys. B*, **70**, S85–S93.
- 102** Dorrer, C., Kosik, E.M., and Walmsley, I.A. (2002) Spatio-temporal characterization of the electric field of ultrashort optical pulses using two-dimensional shearing interferometry. *Appl. Phys. B*, **74**, S209–S217.
- 103** Dorrer, C., Kosik, E.M., and Walmsley, I.A. (2002) Direct space-time characterization of the electric fields of ultrashort optical pulses. *Opt. Lett.*, **27** (7), 548–550.
- 104** Gallmann, L., Sutter, D.H., Matuschek, N., Steinmeyer, G., Keller, U., Iaconis, C., and Walmsley, I.A. (1999) Characterization of sub-6-fs optical pulses with spectral phase interferometry for direct electric-field reconstruction. *Opt. Lett.*, **24** (18), 1314–1316.
- 105** Wyatt, A.S., Walmsley, I.A., Stibenz, G., and Steinmeyer, G. (2006) Sub-10 fs pulse characterization using spatially encoded arrangement for spectral phase interferometry for direct electric field reconstruction. *Opt. Lett.*, **31** (12), 1914–1916.
- 106** Wemans, J., Figueira, G., Lopes, N., and Cardoso, L. (2006) Self-referencing spectral phase interferometry for direct electric-field reconstruction with chirped pulses. *Opt. Lett.*, **31** (14), 2217–2219.
- 107** Bromage, J., Dorrer, C., Begishev, I.A., Usechak, N.G., and Zuegel, J.D. (2006) Highly sensitive, single-shot characteri-

- zation for pulse widths from 0.4 to 85 ps using electro-optic shearing interferometry. *Opt. Lett.*, **31** (23), 3523–3525.
- 108** Londero, P., Anderson, M.E., Radzewicz, C., Iaconis, C., and Walmsley, I.A. (2003) Measuring ultrafast pulses in the near-ultraviolet using spectral phase interferometry for direct electric field reconstruction. *J. Mod. Opt.*, **50** (2), 179–184.
- 109** Baum, P., Lochbrunner, S., and Riedle, E. (2004) Zero-additional-phase spider: full characterization of visible and sub-20-fs ultraviolet pulses. *Opt. Lett.*, **29** (2), 210–212.
- 110** Ventalon, C., Fraser, J.M., Likforman, J.P., Villeneuve, D.M., Corkum, P.B., and Joffre, M. (2006) Generation and complete characterization of intense mid-infrared ultrashort pulses. *J. Opt. Soc. Am. B*, **23** (2), 332–340, doi:10.1364/JOSAB.23.000332.
- 111** Birge, J.R. and Kärtner, F.X. (2008) Analysis and mitigation of systematic errors in spectral shearing interferometry of pulses approaching the single-cycle limit. *J. Opt. Soc. Am. B*, **25** (6), A111–A119.
- 112** Kosik, E.M., Radunsky, A.S., Walmsley, I.A., and Dorrer, C. (2005) Interferometric technique for measuring broadband ultrashort pulses at the sampling limit. *Opt. Lett.*, **30** (3), 326–328.
- 113** Dorrer, C., Londero, P., and Walmsley, I.A. (2001) Homodyne detection in spectral phase interferometry for direct electric-field reconstruction. *Opt. Lett.*, **26** (19), 1510–1512.
- 114** Wyatt, A.S., Grün, A., Bates, P.K., Chalus, O., Biegert, J., and Walmsley, I.A. (2011) Accuracy measurements and improvement for complete characterization of optical pulses from nonlinear processes via multiple spectral-shearing interferometry. *Opt. Express*, **19** (25), 25355–25366, doi:10.1364/OE.19.025355.
- 115** Austin, D., Witting, T., and Walmsley, I. (2009) High precision self-referenced phase retrieval of complex pulses with multiple-shearing spectral interferometry. *J. Opt. Soc. Am. B*, **26** (9), 1818–1830.
- 116** Wyatt, A.S., Biegert, J., and Walmsley, I.A. (2012) Generalized multishearing interferometry for the complete multidimensional characterization of optical beams and ultrashort pulses, in *CLEO: Science and Innovations*, Optical Society of America, p. CF1L.6.
- 117** Austin, D., Witting, T., and Walmsley, I. (2010) Resolution of the relative phase ambiguity in spectral shearing interferometry of ultrashort pulses. *Opt. Lett.*, **35** (12), 1971–1973.
- 118** Radunsky, A.S., Walmsley, I.A., Gorza, S.P., and Wasylczyk, P. (2007) Compact spectral shearing interferometer for ultrashort pulse characterization. *Opt. Lett.*, **32** (2), 181–183.
- 119** Gorza, S., Radunsky, A., Wasylczyk, P., and Walmsley, I. (2007) Tailoring the phase-matching function for ultrashort pulse characterization by spectral shearing interferometry. *J. Opt. Soc. Am. B*, **24** (9), 2064–2074.
- 120** Birge, J., Ell, R., and Kärtner, F. (2006) Two-dimensional spectral shearing interferometry for few-cycle pulse characterization. *Opt. Lett.*, **31** (13), 2063–2065.
- 121** Malacara, D. (ed.) (2007) *Optical Shop Testing*, Wiley-Interscience.
- 122** Messager, V., Louradour, F., Froehly, C., and Barthelemy, A. (2003) Coherent measurement of short laser pulses based on spectral interferometry resolved in time. *Opt. Lett.*, **28** (9), 743–745.
- 123** Tanabe, T., Tanabe, H., Teramura, Y., and Kannari, F. (2002) Spatiotemporal measurements based on spatial spectral interferometry for ultrashort optical pulses shaped by a fourier pulse shaper. *J. Opt. Soc. Am. B*, **19** (11), 2795–2802.
- 124** Dorrer, C. and Walmsley, I.A. (2002) Simple linear technique for the measurement of space-time coupling in ultrashort optical pulses. *Opt. Lett.*, **27** (21), 1947–1949.
- 125** Wyatt, A. and Walmsley, I. (2009) Analysis of space-time coupling in sea-spider measurements, in *Lasers and Electro-Optics 2009 and the European Quantum Electronics Conference*, CLEO Europe – EQEC 2009, pp. 1.
- 126** Zair, A., Guandalini, A., Schapper, F., Holler, M., Biegert, J., Gallmann, L., Couairon, A., Franco, M., Mysyrowicz, A., and Keller, U. (2007) Spatio-temporal

- characterization of few-cycle pulses obtained by filamentation. *Opt. Express*, **15** (9), 5394–5404.
- 127** Witting, T., Frank, F., Arrell, C.A., Okell, W.A., Marangos, J.P., and Tisch, J.W.G. (2011) Characterization of high-intensity sub-4-fs laser pulses using spatially encoded spectral shearing interferometry. *Opt. Lett.*, **36** (9), 1680–1682.
- 128** Austin, D.R., Witting, T., Arrell, C.A., Frank, F., Wyatt, A.S., Marangos, J.P., Tisch, J.W., and Walmsley, I.A. (2011) Lateral shearing interferometry of high-harmonic wavefronts. *Opt. Lett.*, **36** (10), 1746–1748.
- 129** Goulielmakis, E., Nersisyan, G., Papadogiannis, N., Charalambidis, D., Tsakiris, G., and Witte, K. (2002) A dispersionless michelson interferometer for the characterization of attosecond pulses. *Appl. Phys. B*, **74** (3), 197–206.
- 130** Kobayashi, Y., Sekikawa, T., Nabekawa, Y., and Watanabe, S. (1998) 27-fs extreme ultraviolet pulse generation by high-order harmonics. *Opt. Lett.*, **23** (1), 64–66.
- 131** Sekikawa, T., Kosuge, A., Kanai, T., and Watanabe, S. (2007) Attosecond pulse characterization by xuv nonlinear optics, in *Ultrafast Optics V*, Springer Series in Optical Sciences, vol. 132 (eds S. Watanabe and K. Midorikawa), Springer, New York, pp. 27–31, doi:10.1007/978-0-387-49119-6_3.
- 132** Tzallas, P., Charalambidis, D., Papadogiannis, N.A., Witte, K., and Tsakiris, G.D. (2003) Direct observation of attosecond light bunching. *Nature*, **426** (6964), 267–271.
- 133** Nomura, Y., Hörlein, R., Tzallas, P., Dromey, B., Rykovanov, S., Major, Z., Osterhoff, J., Karsch, S., Veisz, L., Zepf, M. et al. (2008) Attosecond phase locking of harmonics emitted from laser-produced plasmas. *Nat. Phys.*, **5** (2), 124–128.
- 134** Skantzakis, E., Tzallas, P., Kruse, J.E., Kalpouzos, C., Faucher, O., Tsakiris, G.D., and Charalambidis, D. (2010) Tracking autoionizing-wave-packet dynamics at the 1-fs temporal scale. *Phys. Rev. Lett.*, **105**, 043902.
- 135** Itatani, J., Quere, F., Yudin, G.L., and Corkum, P.B. (2004) Methods for measuring attosecond X-ray pulses with a strong laser field. *Laser Phys.*, **14** (3), 344–353.
- 136** Quere, F., Mairesse, Y., and Itatani, J. (2005) Temporal characterization of attosecond XUV fields. *J. Mod. Opt.*, **52** (2–3), 339–360.
- 137** Kosik, E.M., Corner, L., Wyatt, A.S., Cormier, E., Walmsley, I.A., and Dimaruro, L.F. (2005) Complete characterization of attosecond pulses. *J. Mod. Opt.*, **52** (2–3), 361–378.
- 138** Yakovlev, V.S., Gagnon, J., Karpowicz, N., and Krausz, F. (2010) Attosecond streaking enables the measurement of quantum phase. *Phys. Rev. Lett.*, **105**, 073001, doi:10.1103/PhysRevLett.105.073001.
- 139** Quere, F., Itatani, J., Yudin, G.L., and Corkum, P.B. (2003) Attosecond spectral shearing interferometry. *Phys. Rev. Lett.*, **90** (7), 073902.
- 140** Itatani, J., Quere, F., Yudin, G.L., Ivanov, M.Y., Krausz, F., and Corkum, P.B. (2002) Attosecond streak camera. *Phys. Rev. Lett.*, **88** (17), 173903.
- 141** Paul, P., Toma, E., Breger, P., Mullot, G., Auge, F., Balcou, P., Muller, H., and Agostini, P. (2001) Observation of a train of attosecond pulses from high harmonic generation. *Science*, **292** (5522), 1689–1692.
- 142** Muller, H. (2002) Reconstruction of attosecond harmonic beating by interference of two-photon transitions. *Appl. Phys. B*, **74**, 17–21.
- 143** Bourassin-Bouchet, C., Diveki, Z., de Rossi, S., English, E., Meltschakov, E., Gobert, O., Guénot, D., Carré, B., Delmotte, F., Salières, P., and Ru-chon, T. (2011) Control of the attosecond synchronization of XUV radiation with phase-optimized mirrors. *Opt. Express*, **19** (4), 3809–3817, doi:10.1364/OE.19.003809.
- 144** Mairesse, Y. and Quere, F. (2005) Frequency-resolved optical gating for complete reconstruction of attosecond bursts. *Phys. Rev. A*, **71** (1), 011401.
- 145** Sansone, G., Benedetti, E., Calegari, F., Vozzi, C., Avaldi, L., Flammmini, R., Polletto, L., Villoresi, P., Altucci, C., Velotta, R., Stagira, S., De Silvestri, S., and

- Nisoli, M. (2006) Isolated single-cycle attosecond pulses. *Science*, **314** (5798), 443–446.
- 146** Thomann, I., Gregonis, E., Liu, X., Trebino, R., Sandhu, A.S., Murnane, M.M., and Kapteyn, H.C. (2008) Temporal characterization of attosecond wave forms in the sub-optical-cycle regime. *Phys. Rev. A*, **78**, 011806, doi:10.1103/PhysRevA.78.011806.
- 147** Kim, K.T., Ko, D.H., Park, J., Tosa, V., and Nam, C.H. (2010) Complete temporal reconstruction of attosecond high-harmonic pulse trains. *New J. Phys.*, **12** (8), 083019.
- 148** Witting, T., Frank, F., Okell, W.A., Arrell, C.A., Marangos, J.P., and Tisch, J.W.G. (2012) Sub-4-fs laser pulse characterization by spatially resolved spectral shearing interferometry and attosecond streaking. *J. Phys. B*, **45** (7), 074 014.
- 149** Schütte, B., Frühling, U., Wieland, M., Azima, A., and Drescher, M. (2011) Electron wave packet sampling with laser-generated extreme ultraviolet and terahertz fields. *Opt. Express*, **19** (20), 18833–18841, doi:10.1364/OE.19.018833.
- 150** Gagnon, J., Goulielmakis, E., and Yakovlev, V. (2008) The accurate frog characterization of attosecond pulses from streaking measurements. *Appl. Phys. B*, **92**, 25–32, doi:10.1007/s00340-008-3063-x.
- 151** Chini, M., Gilbertson, S., Khan, S.D., and Chang, Z. (2010) Characterizing ultrabroadband attosecond lasers. *Opt. Express*, **18** (12), 13006–13016, doi:10.1364/OE.18.013006.
- 152** Cormier, E., Walmsley, I.A., Kosik, E.M., Wyatt, A.S., Corner, L., and DiMauro, L.F. (2005) Self-referencing, spectrally, or spatially encoded spectral interferometry for the complete characterization of attosecond electromagnetic pulses. *Phys. Rev. Lett.*, **94** (3), 033905.
- 153** Mairesse, Y., Gobert, O., Breger, P., Merdji, H., Meynadier, P., Monchicourt, P., Perdrix, M., Salieres, P., and Carre, B. (2005) High harmonic xuv spectral phase interferometry for direct electric-field reconstruction. *Phys. Rev. Lett.*, **94** (17), 173903.
- 154** Matsubara, E., Yamane, K., Sekikawa, T., and Yamashita, M. (2007) Generation of 2.6 fs optical pulses using induced-phase modulation in a gas-filled hollow fiber. *J. Opt. Soc. Am. B*, **24** (4), 985–989.
- 155** Rausch, S., Binhammer, T., Harth, A., Krtner, F.X., and Morgner, U. (2008) Few-cycle femtosecond field synthesizer. *Opt. Express*, **16** (22), 17410–17419.
- 156** Verhoeft, A.J., Mitrofanov, A., Zheltikov, A., and Baltuška, A. (2009) Plasma-blueshift spectral shear interferometry for characterization of ultimately short optical pulses. *Opt. Lett.*, **34** (1), 82–84.

4**Carrier Envelope Phase Stabilization**

Vincent Crozatier

4.1**Introduction**

Since the early 1990s, femtosecond laser development has succeeded to reduce optical pulses to a point where the electric field oscillates only a few cycles under the envelope. In such pulses, the relative position of the field maximum with respect to the maximum of the envelope becomes important. This relative position is commonly called the carrier envelope phase (CEP).

Few-cycle pulses with a stable and controllable CEP are fundamental in several fields of physics, including frequency combs in metrology [1] and any experiment sensitive to the electric field, for example, experiments in attosecond physics [2]. The two topics of frequency combs and attosecond physics have different definitions of the CEP and also have different requirements regarding CEP stabilization. An important difference lies in the source type. In frequency combs, the source is usually a broadband, high repetition rate, and stable oscillator, the comb being the oscillator discrete output spectrum. Attosecond physics experiments, on the other hand, are based on the highly nonlinear interaction between a single amplified pulse and a gaseous or solid medium.

In this chapter, we will give a review of the different techniques to monitor and stabilize the CEP. We will start with fundamental points regarding CEP, before introducing basic notions of stabilization loops. Sections 4.3 and 4.4 will focus on the CEP in oscillators and amplifiers, respectively. In both cases, we will detail the peculiarities of the systems, the different methods to measure the CEP, and describe how to stabilize it. Understanding noise spectra will be emphasized throughout this chapter.

4.2

CEP Fundamentals

An optical pulse emitted by a femtosecond laser can be expressed in the time domain as

$$E(t) = \text{Re}\{A(t) \exp(-i\omega_c t)\}, \quad (4.1)$$

where $A(t)$ is the complex pulse envelope, ω_c the optical carrier angular frequency, and Re represents the real part. The envelope contains both amplitude and phase variations:

$$A(t) = |A(t)| \exp(i\phi(t)). \quad (4.2)$$

When propagating, the carrier frequency experiences the *refractive* index n , while the pulse envelope experiences the *group* index n_G , defined as:

$$n_G = n + \omega \frac{\partial n}{\partial \omega} = n - \lambda \frac{\partial n}{\partial \lambda}. \quad (4.3)$$

Although both indices are linked through Eq. (4.3), they may evolve independently for reasons that we will discuss later. The direct consequence is a variation of the carrier envelope phase.

4.2.1

Time Domain Representation

The CEP can be easily pictured in the time domain, as shown in Figure 4.1.

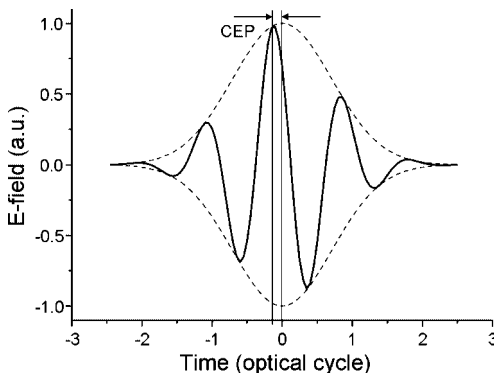


Figure 4.1 Few-cycle pulse. The dashed line represents the Gaussian-shaped envelope, whereas the continuous line represents the oscillating field within the envelope.

When referencing the envelope extremum relative to $t = 0$, the CEP can be simply expressed as

$$\phi_{\text{CEP}} = \omega_c \cdot \tau, \quad (4.4)$$

where τ is the delay of the oscillation maximum with respect to the envelope extremum. To contain the CEP in a $]-\pi; \pi]$ window, τ should be contained in a time window of $]-\pi/\omega_c; \pi/\omega_c]$.

However, this definition of the CEP may be very confusing. When the pulse is very short, that is, a few optical cycles long, then its spectral support becomes a significant fraction of the optical frequency. Distortions rapidly arise in very broad spectra and the pulse envelope may not be as smooth as pictured in Figure 4.1. The very notion of carrier frequency is also ambiguous. To address these issues, the frequency domain gives another point of view.

4.2.2

Frequency Domain Representation

4.2.2.1 Single Pulse

Going back to the single-pulse expression in Eq. (4.1), what does the envelope term really correspond to? The complex representation includes both a modulus and a phase, as written in Eq. (4.2). Fourier transforming the envelope leads to the spectral amplitude $|A(\omega)|$ and phase $\phi(\omega)$. The latter can be developed in a Taylor series around the carrier frequency ω_c :

$$\phi(\omega) = \phi(\omega_c) + \left. \frac{\partial \phi}{\partial \omega} \right|_{\omega_c} (\omega - \omega_c) + \frac{1}{2} \left. \frac{\partial^2 \phi}{\partial \omega^2} \right|_{\omega_c} (\omega - \omega_c)^2 + \dots \quad (4.5)$$

The carrier frequency should be defined with care, following the center of gravity of the intensity spectrum $I(\omega)$:

$$\omega_c = \frac{\int \omega I(\omega) d\omega}{\int I(\omega) d\omega}. \quad (4.6)$$

The CEP being the phase difference between the carrier and the envelope, it can be defined in the spectral domain as:

$$\phi_{\text{CEP}} = \phi(\omega_c) - \left. \frac{\partial \phi}{\partial \omega} \right|_{\omega_c} (\omega_c). \quad (4.7)$$

Using the phase Taylor development isolates the CEP expression from the other polynomial coefficients. However, more complex phase distortions are not taken into account here. Finally, the spectral domain leads to clearer insight into the pertinent parameters of CEP.

4.2.2.2 Pulse Train

If we now consider oscillators, they produce short pulses of duration δt , with a repetition rate f_{rep} (see Figure 4.2). From one pulse to the next, the CEP evolves

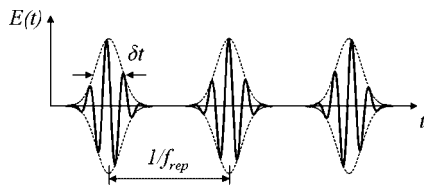


Figure 4.2 Pulse train emitted by an oscillator.

randomly, due to the variations of the carrier phase and the envelope phase in the laser cavity, as we will discuss later on.

Mathematically, the pulse train emission is the convolution between a single pulse, as in Eq. (4.1), and a comb of Dirac functions evenly spaced by $1/f_{\text{rep}}$. In order to take into account the CE phase variations $\delta\phi_{\text{CEP}}$ from pulse to pulse, an extra phase term is added [3]:

$$E_{\text{train}}(t) = E(t) \otimes \sum_n \delta\left(t - \frac{n}{f_{\text{rep}}}\right) \cdot e^{n\delta\phi_{\text{CEP}}} . \quad (4.8)$$

Moving to the frequency domain, the pulse train spectrum (see Figure 4.3) is now the product between the spectral amplitude $|A(\omega)|$ centered at ω_c and a frequency comb of Dirac functions evenly spaced by f_{rep} :

$$|E_{\text{train}}(\omega)| = |A(\omega - \omega_c)| \cdot \sum_n \delta(\omega - 2\pi n f_{\text{rep}} - \delta\phi_{\text{CEP}} f_{\text{rep}}) . \quad (4.9)$$

This is the common description of the frequency comb, widely used in metrology and spectroscopy. The comb acts as a frequency ruler, whose teeth are the modes of the oscillator. A closer look at the sum term shows that the oscillator modes ν_n are not precisely located at $n f_{\text{rep}}$, but are offset by a frequency f_0 , which can be defined as:

$$f_0 = \frac{\delta\phi_{\text{CEP}}}{2\pi} f_{\text{rep}} . \quad (4.10)$$

The frequency f_0 is usually called the offset frequency. In this case, the carrier envelope phase is referred to as the carrier envelope *offset* (CEO). One should note that the phase term $\delta\phi_{\text{CEP}}$ in Eq. (4.10) is not the absolute CEP, but its pulse-to-pulse variation. The value of f_0 actually tells us about the slip rate of the CEP from one pulse to the next.

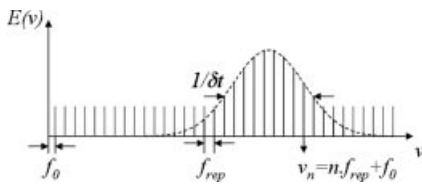


Figure 4.3 Oscillator pulse train spectrum.

We will revisit these issues later and remain with the insight that the frequency domain offers another picture of the problem. The offset frequency is easily observable, but does not yield the absolute value of the CEP.

4.3 Stabilization Loop Fundamentals

As already mentioned, high-energy few-cycle pulses are commonly used in attosecond physics and corresponding experimental results are very sensitive to the electric field. Stabilizing the CEP is therefore fundamental in obtaining reproducible results. This stabilization issue is particularly crucial when the detected signal level is low, and thus requires integration over several shots. We shall now focus on key issues for CEP stabilization.

The functional block diagram of a stabilization loop is pictured in Figure 4.4. It can be divided into four primary elements:

- a noisy source
- a noise detection device
- a loop filter
- an actuator to close the stabilization loop.

4.3.1 The Noisy Source

In our case, the source is the laser chain, delivering high-energy, few-cycle optical pulses. This source can be divided into two parts: an oscillator delivering low-energy pulses at a high repetition rate (typically several nJ at 80 MHz); and a complex amplification system working at a lower repetition rate (typically mJ pulse energy at 1–10 kHz).

The repetition rate is a first major issue. The Shannon–Nyquist theorem states that no frequency larger than half of the system repetition rate can be measured. We will later see the consequences of this theorem. However, we can already infer that the stabilization loop bandwidth and performance will be highly dependent on the repetition rate.

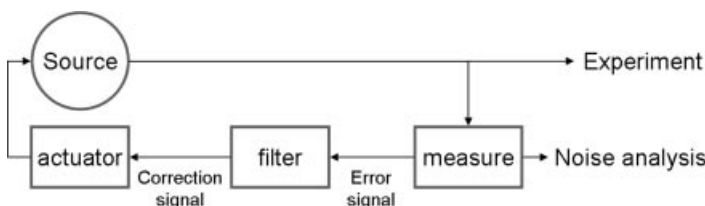


Figure 4.4 Functional block diagram of a stabilization loop.

Next we consider the noise sources and try to understand their influence. Noise sources may be external (temperature variations, air flows ...) or internal (mode-locking in oscillators, stretching/compression in amplifiers ...). When the noise origin is well targeted, it may be possible to reduce the perturbation by so-called passive stabilization. For instance, air flows can be prevented using enclosures.

The basic question is of course: how can we know where the noise comes from, and what is its impact? To answer the question, a noise detection system is required.

4.3.2

Noise Detection

Noise detection is the first step towards noise analysis and suppression. The noise describes all the variations from a stable reference. This reference can be external or self-created. The comparison output is denoted as the error signal $\epsilon(t)$.

The demands on a good phase detector are manifold. It should be easy to implement, yield a high signal-to-noise ratio (SNR) and offer a fast response. Last but not least, the detector should be independent from additional fluctuations. In the case of the phase measurement of an optical pulse, amplitude variations should not induce phase variations. In other words, there should be no phase-amplitude coupling, or AM/PM coupling (amplitude modulation/phase modulation). This uncoupling is by far the most difficult criterion to fulfill.

The error signal $\epsilon(t)$ naturally gives insight into the noise sources. A first analysis without stabilization (open loop) can be very fruitful. A common way to read a noise figure consists of computing the phase noise power spectral density (PSD) $S_\phi(f)$:

$$S_\phi(f) = \frac{1}{T_{\text{int}}} \left| \int \epsilon(t) e^{-2\pi i f t} dt \right|^2, \quad (4.11)$$

where T_{int} is the integration time. In the case of phase noise, units are rad^2/Hz , and can be converted to dB/Hz. Taking the square root of Eq. (4.11) leads to units of $\text{rad}/\text{Hz}^{1/2}$. Computing the PSD is not as easy as it seems. A proper way to do it is the following: one starts from a sampled error signal $\epsilon(t)$, with a sampling period δt , and a number of samples N . The full time window is T_{int} , which is the product $N \delta t$. Next, the fast Fourier transform (FFT) of $\epsilon(t)$ is computed. The FFT $\epsilon(f)$ should contain N points as well, spreading over $-f_s/2$ to $f_s/2$, where $f_s = 1/\delta t$ is the sampling frequency. The power spectrum of the signal is $S_\epsilon(f) = (\epsilon(f)/N)^2$. Further dividing $S_\epsilon(f)$ by the time window T_{int} leads to the power spectral density. The PSD spreading from $-f_s/2$ to $f_s/2$ is called *double-sided* PSD. As the error signal $\epsilon(t)$ is real, the FFT should fulfill $\epsilon(-f) = \epsilon^*(f)$ and only the positive frequency part of the FFT is relevant. The *single-sided* PSD, corresponding to the real power spectrum, is $2S_\epsilon(f)$, and spreads from DC to $f_s/2$.

The noise PSD plots the noise spectral distribution. A PSD value at a frequency f tells the amount of noise within a bandwidth of 1 Hz. It is usually plotted in log vs. log scale, because a large bandwidth (from mHz up to MHz) and a large PSD

amplitude is analyzed. This log vs. log plot may be quite confusing, as we will see in an example later on. Common kinds of noise are the following:

- White noise: constant level of noise, independent of the frequency. White noise is noncorrelated noise.
- $1/f^n$ noise: usual technical noise. In the log vs. log standard plot, it corresponds to a decreasing noise value for increasing measurement frequency, with a $-n$ slope. Unlike white noise, $1/f^n$ noise is correlated.
- Spikes: sharp lines in the noise figure. Most of the time, the spikes stem from electrical parasitic modulations (line, switching supplies, etc.).

The PSD is not only a very instructive way to analyze noise, but it can also tell the amount of jitter. The root mean square phase jitter is simply the result of the integrated phase PSD:

$$\Delta\phi_{\text{CEP}}^{\text{rms}} = \sqrt{\int_{1/T_{\text{int}}}^{f_{\max}} S_{\phi}(f) df} . \quad (4.12)$$

One usually integrates from the maximum frequency, either $f_s/2$ or f_s (depending on the single- or double-sided computation, respectively), down to the desired integration time T_{int} . The amount of jitter computed with Eq. (4.12) should equal the standard deviation of the time-domain error signal, according to Parsevals theorem: the energy must be the same in the time domain and the frequency domain. It is also worth noting that, when considering a large number of samples (typ. $> 10\,000$) with a Gaussian noise distribution, the peak-to-peak jitter (5–95% of the distribution) is roughly 6 times the root mean square jitter.

4.3.3

Open-Loop Noise Analysis

As an example of noise analysis, we use the results published in [4], in which the authors stabilize the CEP of a 3 kHz Ti:Sa amplifier. Figure 4.5 shows a time record of the open-loop error signal. The gray and black lines are obtained simultaneously using two detection schemes (gray is single shot, black is integrated over 15 shots with further computation time). The phase randomly evolves, but shows continuous behavior within $]-\pi; \pi]$. The absence of phase jumps justifies an analysis in the Fourier domain.

Figure 4.6 plots the open-loop PSD of a 10 minute error signal record, with single-shot detection. The overall integration time leads to a spectral resolution of 1.67 mHz, while the single-shot operation at 3 kHz leads to a 1.5 kHz analysis bandwidth (Shannon–Nyquist theorem). The bandwidth-to-resolution ratio is 10^6 and it makes sense to plot the PSD in log scale, at least in the frequency scale. The PSD is expressed in rad/Hz $^{1/2}$ and shows several orders of magnitude variations, therefore a log scale was used for the y axis, too.

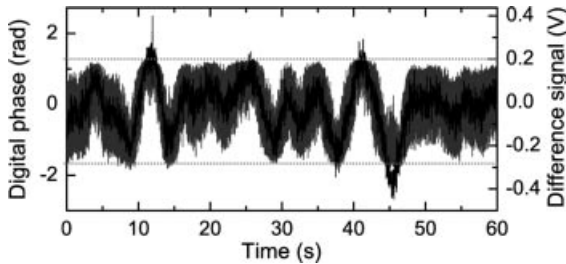


Figure 4.5 Open-loop error signal from [4].

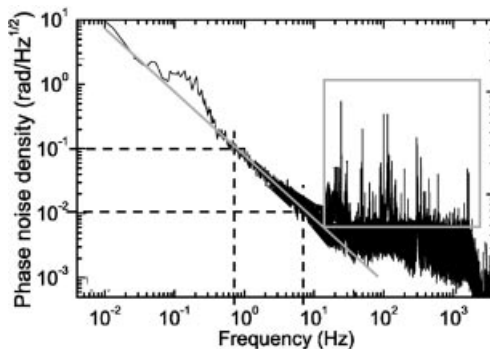


Figure 4.6 Open-loop PSD from [4]. See text for illustration details.

This open-loop PSD is an excellent illustration of the noise described in Section 4.3.2. The gray line highlights the typical low-frequency $1/f$ noise, up to 10 Hz. Note the dashed lines: the noise decreases by one order of magnitude while the frequency increases by one order of magnitude. Then the PSD slowly tends to white noise. The authors attribute the large bump around 0.1 Hz to the amplifier cooling system. The spikes in the box are either electrical or mechanical perturbations. A way to distinguish their origin is the Q-factor of the peaks. The very sharp lines are electrical (locate the line leakage at 50 Hz and its harmonics), while mechanical and acoustic disturbances exhibit a wider resonance (see for instance the bumps around 20 and 120 Hz).

4.3.4 Feedback

Once the error signal is captured, one has to find a way to use it to perform feedback. This is the role of the actuator, which can employ any physical means to control the parameter to stabilize. Multiple actuation concepts exist and the selection criteria involves speed, linearity, reproducibility (no hysteresis), and of course the ease of implementation.

But in order to feed the actuator the proper input, an important step is the conditioning of the error signal $\epsilon(t)$ into a correction signal $c(t)$. This is the role of the loop filter. First, a gain or attenuation is required in order to match the sensitivities

of the noise detection and the actuation. Second, one needs to shape the spectral response of the correction signal, for example, by adding gain at low frequency to prevent slow drifts, or attenuating the high-frequency response to get a stable feedback. This filter tailoring is the core of the stabilization loop and finely depends on all the other element characteristics, and the required performance [5].

Finally, it is often desirable to get two feedback loops for a single system: one with a fast response to get a high-frequency feedback; a second with a slower response to compensate for drifts and to ensure robust stabilization over the long term. This is typically the case for CEP in ultrafast amplified laser chains. The oscillator is first stabilized (sometimes itself with two loops) to take advantage of the large repetition rate and thus get a large bandwidth feedback. Then the drifts induced by the amplifier are corrected with a slower loop. This dual loop operation, however, requires some precautions. Particularly, the two loops must be completely independent. This is usually the case for the detection and the filter, because of the different pulse parameters (energy, repetition rate), but it should also be the same for the actuation, otherwise crosstalk between the fast and slow correction signals may cause instabilities and eventually unlocking.

4.3.5

Closed-Loop Noise Analysis

Let us go back to the PSD example of Section 4.3.3, on the 3 kHz ultrafast amplifier of [4]. The authors have two different feedback loops, using two detection schemes. As already mentioned, one is single shot, while the other needs a 5 ms integration to get proper optical signal detection. In the single-shot case, the error filtering is immediate, offering the largest achievable feedback bandwidth. In the slow detection case, the phase error processing takes 20 ms, which limits the loop time to 25 ms. In other words, the maximum loop bandwidth is 40 Hz. The analysis of the error signal in both cases is pictured in Figure 4.7.

The blue curve is the open-loop PSD of Figure 4.6. The gray curve is obtained with the slow feedback scheme. The feedback suppresses the typical $1/f$ noise,

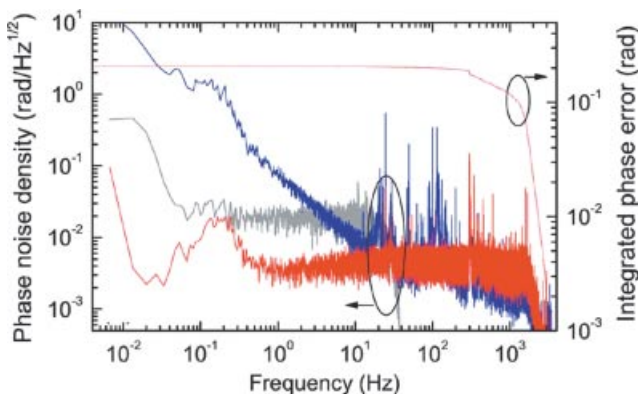


Figure 4.7 Closed-loop PSDs from [4]. See text for details.

and the residual noise is white, around $30 \text{ mrad}/\text{Hz}^{1/2}$ over a 20 Hz bandwidth. The fast roll-off between 20 and 40 Hz is symptomatic of the finite feedback bandwidth. The red curve is the residual PSD plot using the single-shot detection scheme. The feedback is much faster (see the roll-off around 1.5 kHz), limited by the repetition rate of the amplifier. Increasing the bandwidth reduces the residual white noise level down to $8 \text{ mrad}/\text{Hz}^{1/2}$. Note as well that the spikes in the 10–100 Hz window are efficiently suppressed by the loop. Only spikes above 300 Hz are still present. One can therefore wonder if these spikes are caused by feedback electronics noise.

The dotted red curve represents the integrated phase jitter of the fast feedback system. When integrated over the full analysis window, the jitter is 210 mrad. Reading this curve from right to left, one can see that most of the jitter is due to high-frequency noise. Remember, the PSD plot is depicted on a log scale: as the noise is white, the contribution of the 1–2 kHz band is the same as the contribution of the rest of the plot. Note the jump in the phase jitter due to the 300 Hz spike: even a sharp line rapidly contributes (here typically 25 mrad) to the total phase jitter if located at a high frequency. This motivates the quest for fast feedback.

As a comparison, the integrated phase jitter of the slow feedback loop error signal is only 115 mrad. This seems surprising as the noise level of the slow system is much larger than the noise level of the fast system. This result is actually an artifact of the slow detection bandwidth. Taking a closer look at the gray plot, there is no noise after the loop bandwidth, that is, above 40 Hz. From the detection point of view, this is normal: as the detection cannot go faster than 40 Hz, noise occurring at higher frequencies is ignored. However, from the user point of view, this is completely wrong! The open-loop PSD clearly shows noise between 40 Hz and 3 kHz. Besides, the noise in this region is significant: the noise level is still high, and the numerous spikes above 50 Hz contain an important amount of noise. The real slow loop noise should then follow the gray line up to the loop feedback (40 Hz), and then follow the blue line up to 3 kHz. In this case, the integrated phase jitter should be much larger than 115 mrad and even larger than the fast loop jitter of 210 mrad.

4.4

CEP in Oscillators

CEP stabilized oscillators are key instruments in two experimental fields. First, frequency combs are powerful tools in metrology [1], frequency synthesis [6], and spectroscopy [7]. The frequency domain representation is well established and generally both the offset frequency f_0 and the repetition rate f_{rep} are stabilized [8]. On the other hand, CEP-stable oscillators are a prerequisite to get amplified CEP-stable pulses. It is worth noticing that the CEP stabilization in oscillators has been jointly developed in the metrology (JILA in Boulder) and the high-energy communities (ETH in Zürich, MPQ in Garching). In this section, we will focus on the CEP in oscillators: where the noise comes from, how to measure the CEP, and ways to stabilize it.

4.4.1

Oscillators Peculiarities

Femtosecond oscillators are peculiar lasers. Of course, they are lasers: there is a gain medium in a resonant cavity, with an appropriate pumping system. But femtosecond pulse generation relies on the mode-locking process, which occurs under precise circumstances. When considering the CEP, all these peculiarities have effects, which we will study in this section.

4.4.1.1 Gain Medium

Various gain media are employed in ultrashort lasers (see Chapter 2). Erbium- [9] and ytterbium-doped [10] materials are candidates but produce long pulses (typically 100 fs). Shortening these pulses down to a few cycles requires spectral broadening. Moreover, millijoule amplification in this few-cycle regime is not trivial. For these reasons, Ti:Sa crystals are preferred when the CEP matters. The physical properties and dynamics of this crystal are well known [11]. The gain is large over a broad emission bandwidth, the latter typically covering at least 700–900 nm. Very short mode-locked pulses are obtained through the Kerr effect. Sub-10 fs oscillators are commercially available and even octave-spanning spectra can be routinely generated.

Pumping the gain medium remains an important issue when the CEP matters. The Kerr lens mode-locking is highly dependent on the intensity in the gain medium. As the Kerr effect implies changes of the refractive index, it affects the CEP. If the pump power fluctuates, small intensity fluctuations appear, which translate into CEP noise. The phase-amplitude coupling mechanisms have been discussed [8, 12, 13], especially the pump intensity noise transfer into CEP noise [5, 14]. The mechanisms are rather complex and depend critically on the laser parameters (mode-locking, repetition rate) [13].

4.4.1.2 Cavity

The pulse repetition rate f_{rep} of an oscillator is solely defined by the cavity length L :

$$f_{\text{rep}} = \frac{c}{2L}. \quad (4.13)$$

L may vary from 10 m down to tens of centimeters. Short cavities exhibit a high repetition rate and modal gain, but offer only a low pulse energy, because of the small storage time. They are of interest in metrology, because several stable microwave references exist in the GHz range which can be used to stabilize f_{rep} . Moreover, they are intrinsically more stable with respect to mechanical noise. However, longer cavities are more practical in amplified systems. The smaller repetition rate facilitates pulse picking and amplifier seeding, the latter because the energy per pulse is larger. In this case, typical repetition rates are around 80 MHz.

Good Kerr lens mode-locking conditions occur when pulses are short in the gain medium. This requires intracavity dispersion compensation. Dispersion compensation historically started with prism pairs, enabling straightforward actuation [15].

Nevertheless, prism pairs suffer from several drawbacks, including beam pointing stability and, to a lesser extent, self-steepening effects [16]. Development of chirped mirror technology progressively offered a more stable solution for intracavity dispersion compensation, particularly in sub-10 fs oscillators [17]. Chirped mirrors are now widespread in ultrafast oscillators.

4.4.1.3 CEP Noise in Oscillators

As already pointed out in Section 4.2, the CEP is the result of the relative variations between the phase index and the group index. In oscillators, it can be reduced to the relative variation from one pulse to the other, or in other words, the relative variation per round trip [18]. This situation makes the CEP variations small and thus allows stabilization.

The discussion in the last paragraphs showed how the different elements in an oscillator create CEP noise. In short, one can distinguish elementary external noise sources, such as temperature and air pressure changes, and mechanical vibrations. These sources are sorted by increasing noise bandwidth; mechanical vibrations typically occur with frequencies up to hundreds of Hz. Proper engineering can improve the intrinsic stability, for example, using a shielded box and a monolithic cavity design, which is typically the case in commercial systems. Faster noise stems from intensity noise of the pump laser. Although single longitudinal mode, low-intensity noise pump sources exist, even small perturbations from the power supply are converted into CEP noise.

Figure 4.8 shows the typical CEP noise PSD of a free running oscillator. Details in the manuscript emphasize the careful oscillator design, which nevertheless does not prevent the presence of noise. One can clearly see the typical technical noises across the analysis bandwidth (244 μ Hz to 102.4 kHz). The noise can then be considered as well detected. The $1/f$ noise lies above 1 kHz (see dotted line), while at lower frequency one rather sees $1/f^2$ noise (see dashed line). One can also notice the structured part in the 100–1000 Hz band. As we will see in this chapter, this noise shape is always present in PSDs. This is the typical signature of pump laser intensity noise, transferred to the CEP.

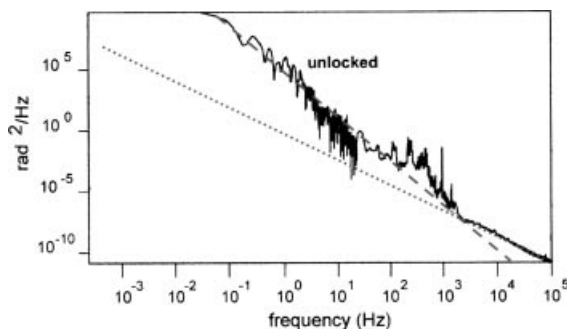


Figure 4.8 Typical oscillator open-loop PSD. Figure courtesy of T. M. Fortier and S. T. Cundiff.

4.4.2

CEP Detection

Equation (4.10) shows that detection of the offset frequency f_0 gives insight into the pulse-to-pulse fluctuations of the CEP. However, it must be pointed out that f_0 does *not* yield the absolute CEP value. The question remains: how can f_0 be measured? The most common detection scheme is the $f - 2f$ interferometer [19]. It has been extensively studied and we will devote a larger section to it. We will also mention other methods that have been proposed and demonstrated experimentally.

4.4.2.1 $f - 2f$ Interferometer

As described in Section 4.2.2, the spectrum of a femtosecond pulse train emitted by an oscillator is composed by isolated modes ν_n under the broad emission spectrum of the laser. The n th mode can be expressed using the following equation:

$$\nu_n = f_0 + n f_{\text{rep}} . \quad (4.14)$$

The basic idea of the $f - 2f$ interferometer is to create interferences between two modes of the oscillator spectrum in order to extract f_0 , as pictured in Figure 4.9. For that purpose, one can start from an octave spanning spectrum, containing both the n th mode and the $2n$ th mode. If the laser spectrum is not broad enough to spread over an octave, spectral broadening in a microstructured fiber can solve the problem [20]. The octave spanning spectrum contains both a “red part” at ν_n and a “blue part” at ν_{2n} . The red part can be frequency doubled using a nonlinear crystal, leading to an additional $2\nu_n$ frequency:

$$2\nu_n = 2f_0 + 2n f_{\text{rep}} . \quad (4.15)$$

Part of this doubled frequency spectrum lies in the same spectral region as the fundamental ν_{2n} frequency. With a spatial and temporal overlap of these two frequencies, one can detect a beat note at frequency f_b , using any integrating photodetector (photodiode, photomultiplier tube):

$$f_b = 2\nu_n - \nu_{2n} = 2f_0 + 2n f_{\text{rep}} - (f_0 + 2n f_{\text{rep}}) = f_0 . \quad (4.16)$$

This method is elegant, and seems easy to implement at first sight: a typical setup is sketched in Figure 4.10. Yet, several issues must be considered.

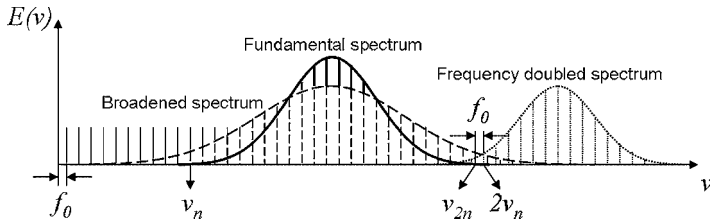


Figure 4.9 $f - 2f$ spectra. The fundamental spectrum is broadened sufficiently to overlap with the frequency doubled spectrum. Interferences can be observed at frequencies where both spectra overlap.

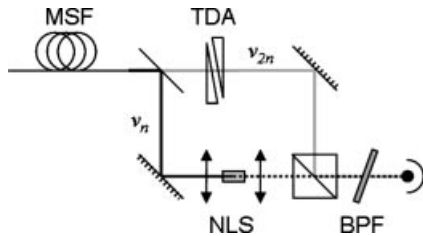


Figure 4.10 Typical $f - 2f$ setup. MSF: micro-structured fiber for octave spanning spectrum; NLS: nonlinear stage for $2\nu_n$ generation; TDA: time delay adjust for temporal overlapping of the ν_{2n} and $2\nu_n$ spectral components; BPF: bandpass filter for the beat note detection.

4.4.2.2 Key Parameters

The first requirement to get proper $f - 2f$ interferometry is the octave spanning spectrum. Starting from a standard oscillator, the spectrum must be broadened to spread over an octave. This is commonly achieved with micro-structure optical fibers (MSF) [20], with zero group velocity dispersion. The short pulse remains short while propagating along the fiber and allows for nonlinear processes along a long interaction length. In order to get the desired effect, the fiber length must be adjusted to the pulse peak power: the smaller the peak power, the longer the fiber. However, one can wonder if the continuum generation actually preserves the CEP or if it adds noise.

Regarding the continuum generation, the fiber output pulse exhibits a different CEP value as compared to the input pulse, because of residual dispersion and nonlinear wave mixing. Nevertheless, CEP drifts are conserved during the propagation [21]. Although the MSF does not blur the CEP, extra noise appears through different types of fluctuations. Continuum generation in MSF is sensitive to polarization [22], peak power [23], and optical bandwidth [24]. Fluctuations affecting these parameters at the output of an oscillator are negligible. But peak power variations inside the fiber may be induced by coupling efficiency variations. Indeed, MSF core diameters are typically a few microns at 800 nm, which makes the coupling a difficult task, and very sensitive to beam pointing. The best way to prevent coupling efficiency noise is actually to get rid of the MSF, that is, working with an octave spanning oscillator.

The second source of instabilities concerns the spatio-temporal overlap of the f and $2f$ components. Residual dispersion of the optical components in the setup (including the MSF and the frequency doubling crystal) must be compensated, so that the spectral heterodyning can be detected on a photodiode. The group delay between the fundamental blue part and the doubled red part can be removed using an interferometer with a delay stage in one arm. The first demonstrations of $f - 2f$ used Mach-Zehnder interferometers (for instance, see [25], and Figure 4.10), which are not easily miniaturized. Such interferometers are thus sensitive to acoustic noise, air flows and temperature changes, all of which directly impinge the CEP error signal. Michelson interferometers [26] can be used as an alternative, although they are not much smaller (see Figure 4.11a). The added interferometer noise can

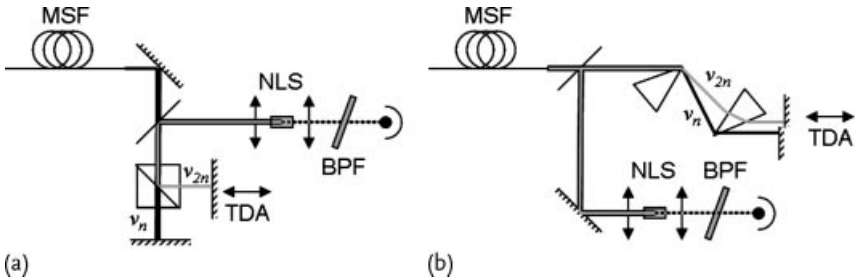


Figure 4.11 Typical $f - 2f$ setup using a Michelson interferometer (a), or a common-path interferometer (b). MSF: micro-structure fiber; NLS: nonlinear stage; TDA: time delay adjust; BPF: bandpass filter.

be eliminated at first order by implementing common-path interferometers using standard prisms [27, 28] (see Figure 4.11b) or Wollaston prisms [29]. Both interferometer types demonstrated improved noise immunity. It is also possible to stabilize the interferometer with an external reference CW laser [30].

Of course, the most robust $f - 2f$ setup uses neither a MSF nor an interferometer. This can be possible working with periodically poled nonlinear crystals (PPLN crystals) and short pulses [31]. In this special case, PPLN provides both, the extra spectral broadening required and the nonlinear stage, combining two steps in one. Moreover, a simple dichroic mirror achieves the pick up for the detection. The major drawbacks concern the low photorefractive damage threshold of the PPLN crystal and the short pulse required (typically sub-7 fs). This scheme has been also demonstrated in ZnO layers [32], but with a poorer efficiency.

Other aspects are fundamental, such as the beat note signal quality. Common SNR values at the detection level are 30–40 dB, measured with a spectrum analyzer with a 100 kHz resolution bandwidth. It is important to note that the measurement of f_0 leads to the CEP slip rate from pulse to pulse, not to the CEP value itself. In the case of frequency combs, f_0 can further be compared to any frequency reference (e.g., an atomic clock). As a matter of fact, the aim of metrology is to control the absolute position of the comb teeth ν_n . When injection in an amplifier matters, one is rather focused on the CEP slip rate: it must be kept constant in order to ensure that every amplified pulse will exhibit a predictable CEP. In this case, f_0 is compared to a fraction of the repetition rate, so as to fulfill the condition

$$f_0 = \frac{\delta\phi_{\text{CEP}}}{2\pi} f_{\text{rep}} = \frac{f_{\text{rep}}}{N}. \quad (4.17)$$

Therefore, one pulse every N has the same CEP. Most often N is small (typically 4), so that f_0 lies around 20 MHz.

4.4.2.3 Other Methods

Quantum interferences in semiconductors It has been proposed to excite a semiconductor sample (e.g., LT-GaAs) with a broadband oscillator pulse train [33]. Single- and two-photon absorption pathways interfere in the sample. The interfer-

ences are sensitive to the relative phase between components at ν_n and ν_{2n} and provide a photocurrent. The magnitude and direction of the latter gives access to the offset frequency f_0 and therefore to the CEP slip rate. This scheme does not require the nonlinear stage or the interferometer, easing the setup implementation and improving the intrinsic stability. However, the sensitivity is poor, even with rather large optical power on the sample.

Spectrally and spatially resolved interferometry Standard interferometry can also be a way to access the CEP. The most straightforward method consists of building an interferometer with an arm unbalance equal to the oscillator cavity length [12]. But usually the reference interferometer is not more stable than the oscillator cavity.

A more subtle method combines a Mach–Zehnder interferometer, a ring resonator and a spectrograph [34]. We first consider the interference pattern of a broadband spectrum generated by a Mach–Zehnder interferometer, with a slight angular mismatch. The output signal exhibits both a spectral and spatial dependence. If a ring resonator is inserted in one arm of the interferometer, the output signal now represents the interferences between the pulse propagating in the normal arm, and the interference of the subsequent pulses trapped in the resonator ring. The resonator ring provides an average of the subsequent pulse phase. Therefore the complete interference pattern visibility depends on the pulse CEP. The overall system is rather complex, and the CEP retrieval is nontrivial: it requires computer-based processing to acquire a spectrograph picture and extract the phase. This solution is inherently slow and less accurate as compared to standard $f - 2f$ schemes. However, most of the limitations of the $f - 2f$ scheme (octave spanning spectrum, high peak power) are overcome.

4.4.3

Actuation

In the previous section, the detection of the offset frequency f_0 has been discussed. This frequency tells us about the CEP slip rate from one pulse to the other, but does not reflect the absolute CEP value of the pulse. Stabilizing this frequency still ensures a constant CEP slip rate, and so allows for further CEP stabilization. The question is now how to stabilize f_0 .

There are two ways to do it. The first method, by far the most common, relies on a phase-locked loop (PLL) design. The elements discussed in Section 4.3 are needed, especially the actuation, to close a feedback loop with the laser. Another method uses the so-called feed-forward scheme, which has been recently introduced and gave very promising results.

4.4.3.1 Feedback

In order to stabilize the offset frequency f_0 , one needs to isolate its noise. This can be typically done by mixing this frequency with an external frequency reference. The beat note signal $B(t)$ measured at the $f - 2f$ setup output can be written as:

$$B(t) = B_0 \sin(2\pi f_0 t + \phi), \quad (4.18)$$

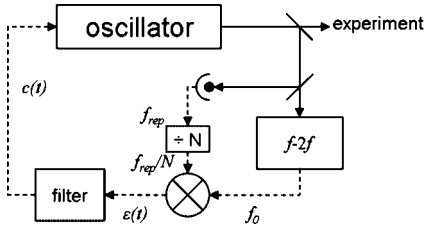


Figure 4.12 PLL-based CEP stabilization of an oscillator, with a self-reference.

where B_0 is the signal amplitude, and ϕ the phase noise affecting the beat note. As already discussed in Section 4.4.2.2, the reference can be the oscillator repetition rate f_{rep} , or a fraction of it, f_{rep}/N . The associated signal $R(t)$ can be expressed as:

$$R(t) = R_0 \cos \left(2\pi \frac{f_{\text{rep}}}{N} t \right). \quad (4.19)$$

Mixing these signals leads to a signal containing two oscillating terms, at $f_0 \pm f_{\text{rep}}/N$. Filtering out the sum term, the remaining signal is:

$$\epsilon(t) = \frac{B_0 R_0}{2} \sin \left(2\pi \left(f_0 - \frac{f_{\text{rep}}}{N} \right) t + \phi \right). \quad (4.20)$$

When f_0 and f_{rep}/N are equal, and ϕ is small, $\epsilon(t)$ is directly proportional to the phase noise ϕ and thus can be used as an error signal. Further filtering of this signal leads to a correction signal $c(t)$ that can be applied to an actuator. This is the typical scheme of a PLL, as pictured in Figure 4.12.

The possible feedback points in oscillators are limited, because of the nature of the CEP: the actuation must affect the relative shift between the group and phase delays inside the oscillator cavity. So far, only three methods have been demonstrated.

The first solution consists of moving the end mirror in a prism-based cavity. It implies working with a prism pair dispersion line in the cavity. Although this situation was common in the early years of CEP stabilization, the reign of chirped mirrors has made this implementation more scarce now. Figure 4.13 shows how the actuation works. As the spectral components are spatially dispersed on the mirror, turning the mirror around the vertical axis (out of the picture plane) causes a group delay. As long as the rotation angle is small, one can assume that the group delay variation is linear and the cavity length variation is negligible. Otherwise, a

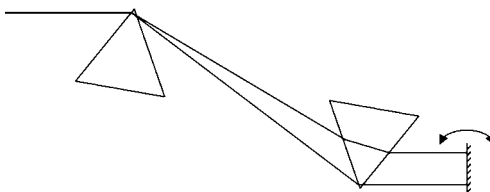


Figure 4.13 End mirror swiveling in a prism pair dispersion line.

parasitic coupling on f_{rep} would exist, disturbing the phase delay and the reference for demodulation. This scheme allows for a quiescent pump. On the other hand, the prism pair may degrade the mechanical stability of the cavity and piezo actuators are well known to suffer from hysteresis, nonlinearities and low bandwidth (up to 20 kHz with special care) [15].

The second solution uses a pair of wedges, which allows for a slight modification of material dispersion in the beam path [35]. This setup can be implemented inside or outside the cavity. A combination of different materials can make this solution isochronic (constant group delay) or isodispersive (constant group delay dispersion) [36]. However, this wedge pair introduces spatial chirp that can only be removed at the expense of a second wedge pair. The method also relies on a mechanical actuation.

The third solution, not the least, is pump power modulation. In Section 4.4.1.1, we discussed the coupling between the pump intensity and the CEP drift. The same physical mechanism leading to this parasitic coupling can be used as an actuation to control the CEP. This idea was discussed as soon as the coupling was observed [12] and demonstrated a few years later [25]. One just inserts an electro- or acoustooptic modulator into the pump beam in a noise-eater configuration. The main benefit of this setup is the fast bandwidth that is achievable, limited by the relaxation dynamics of the gain medium (μ s time scale in Ti:Sa lasers [11]). The potential bandwidth is up to hundreds of kHz [5]. Moreover, the cavity remains very stable, as no mechanical action or movement is required. However, the actuation mechanism intrinsically creates parasitic intensity modulations and the locking range is limited. Long-term stabilization usually needs a slow loop, which can be implemented with a wedge pair, or temperature control [37].

4.4.3.2 Examples of Feedback Results

Figure 4.14 shows the performance of a stabilization loop using a standard Mach-Zehnder interferometer-based $f - 2f$ setup, with a prism line feedback [15]. The frequency analysis is performed on a 244 μ Hz to 102.4 kHz bandwidth. Two $f - 2f$ setups are used: one for feedback and a second for noise analysis. Comparing the error signal from both interferometers gives slightly different results, especially at low frequency (below 10 Hz). When analyzing the error signal used in the feedback loop, this signal includes both the real CEP noise plus the noise introduced by the $f - 2f$ interferometer itself. This is called *in-loop* analysis. This analysis is self-biased, as the CEP noise and CEP detection noise are entangled. If the loop works well, the error signal will remain stable with a mean value of zero, even if it includes some extra noise independent on the CEP.

On the other hand, *out-of-loop* error analysis includes the remaining CEP noise from the oscillator, plus additive noise from the feedback *and* the analysis $f - 2f$ interferometers. If the feedback error signal includes interferometer noise, the ambiguity is resolved. The noise level is higher, leading to degraded, but more objective performance, as the parasitic noise introduced by the phase detector is doubled. The noise increase is mainly located at low frequency, as the added noise is mechanical.

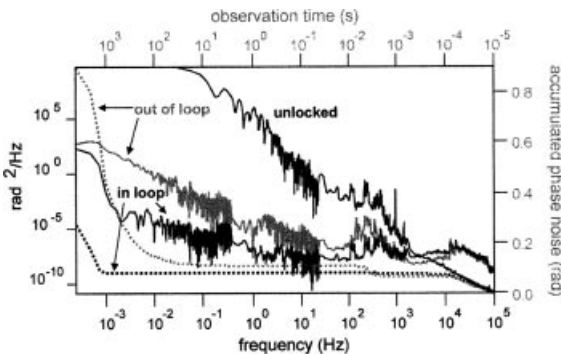


Figure 4.14 Oscillator PSD in open and closed loop, figure courtesy of T. M. Fortier and S. T. Cundiff. Shown are the in-loop (black line) and out-of-loop (gray line) measurements.

Figure 4.14 clearly emphasizes this effect. In the 10 Hz to 102.4 kHz bandwidth, noise figures are almost the same, that is, showing white noise. Spikes in the 100–1000 Hz window are not compensated for. Extra noise above 10 kHz is introduced because of the feedback loop, peaks and roll off indicate the bandwidth of the system. At frequencies below 100 mHz, the PSD curves diverge, because the out-of-loop analysis shows additional mechanical noise. The integrated phase noise shows this effect: both analysis exhibit typical 100 mrad phase jitter from 102.4 kHz down to 100 Hz. This level remains the same with the in-loop integration, but the out-of-loop integration slowly increases from 100 Hz and eventually reaches 700 mrad at 1 mHz!

Figure 4.15 now shows the CEP noise PSD out of a stabilization loop, using a monolithic PPLN $f - 2f$ setup, with pump laser feedback [38]. The analysis is out-of-loop, on a 200 μ Hz–35 MHz bandwidth. The upper value is limited by the oscillator repetition rate (analysis up to $f_{\text{rep}}/2$). One can observe white noise in the 1 Hz–30 kHz bandwidth, with the usual spikes at hundreds of Hz. Again, the peak and roll off tell us about the loop bandwidth. It is interesting to note the large noise level introduced by the loop: three orders of magnitude as compared to the detection noise floor. Below 1 Hz, $1/f$ -like noise arises. It can be attributed to the detection, as indicated by the dashed line.

Considering now the integrated jitter, one can see several jumps. First, the integrated phase jitter down to 100 kHz is 65 mrad (timing jitter of 27 as for an optical cycle period of 2.7 fs at 800 nm). As the noise level is limited by the detection, it clearly gives an ultimate performance of the system. Then the loop noise floor raises the jitter up to 80 mrad (down to 1 kHz). Finally, the technical spikes increase the phase noise up to 100 mrad, but the noise then remains stable down to the full integration bandwidth. This analysis is very fruitful, as it highlights the different contributions of the loop: detection noise floor, loop noise floor, and residual noise that is not compensated for.

To compare these results to the ones of [15] and Figure 4.14, the analysis bandwidth should be matched. Reducing the integration bandwidth to 100 kHz (i.e., ignoring the high-frequency noise contribution), the phase jitter is 72 mrad, one

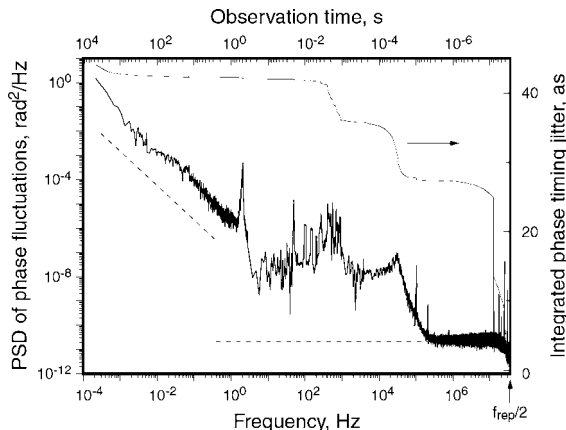


Figure 4.15 Oscillator PSD in closed loop from [38]. Detection noise level (dashed line) and integrated jitter (solid line) shown.

order of magnitude better than in Figure 4.14! The reasons are twofold: a better mechanical stability of the monolithic $f - 2f$ setup as compared to the “classical” one (no Mach–Zehnder interferometer, no MSF), and a lower noise level in the loop bandwidth. It is worth noting that 3 years occurred between the two works of [15] and [38], showing the major interest and efforts devoted to CEP stabilization in oscillators.

4.4.3.3 Feed-Forward

An alternative to feedback is the so-called “feed-forward” method [39]. Instead of closing a loop with an intracavity actuator, feed-forward schemes work with an external acoustooptic frequency shifter. When a laser beam at frequency ν is diffracted by a frequency shifter, fed with an acoustic frequency f_{ac} , its frequency is shifted by the Doppler effect to $\nu \pm f_{\text{ac}}$. The shift sign depends on the order of diffraction (± 1). In the case of a frequency comb emitted by an oscillator, the comb modes at ν_n will all be shifted at $\nu_n \pm f_{\text{ac}}$. Using Eq. (4.14), one can write the diffracted modes in the -1 order as:

$$\nu_n - f_{\text{ac}} = n f_{\text{rep}} + f_0 - f_{\text{ac}} . \quad (4.21)$$

As a consequence, if one can make $f_0 = f_{\text{ac}}$, the output frequency comb can be stabilized. This situation is easily achieved, measuring f_0 with a $f - 2f$ setup, amplifying it and feeding the shifter with this frequency.

This feed-forward method has several advantages as compared to standard feedback schemes. First, it leaves the oscillator quiescent. It can be made highly stable, and the pump is no more modulated. The latter could be even intensity stabilized in order to get rid of the parasitic phase-amplitude coupling. The second advantage concerns the achievable bandwidth. It is no more limited by the gain medium as in pump modulation feedback, but only by the propagation time of the acoustic wave in the frequency shifter. This can be made as short as 1 μ s, or even less, taking care

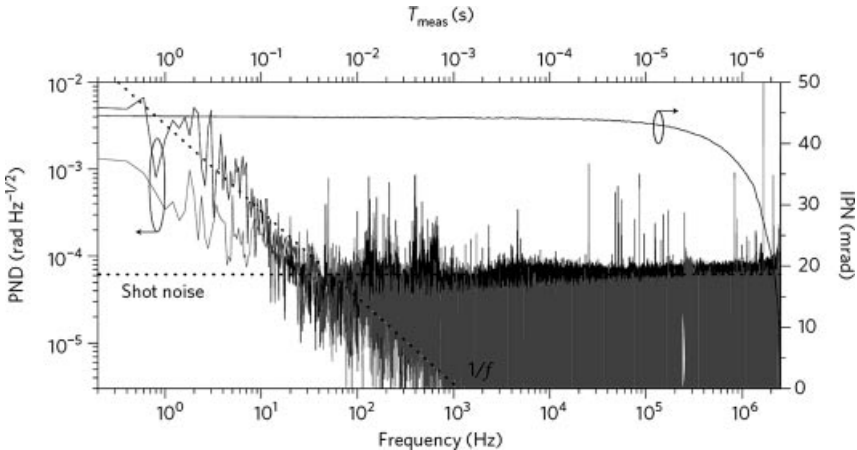


Figure 4.16 Oscillator PSD using the feed-forward scheme (black line), from [39]. Full system detection noise level also shown (gray line).

on the interaction zone. Last but not least, the scheme works without demodulation and baseband filtering of the error signal: feeding the measured offset frequency to the frequency shifter is enough, which eases the implementation. The first demonstration also almost showed a shot noise-limited signal-to-noise ratio, which is not the case in other setups (see for instance Figure 4.15). Although the noise floor is a bit higher than in the case of [38], the integrated noise on a 0.1 Hz–2.5 MHz frequency window is as low as 45 mrad (see Figure 4.16).

There are, however, drawbacks. The CEP-stabilized beam is the diffracted one. The diffraction efficiency is limited, although it can be made rather high at 800 nm (typically >70%). The main problem lies in the acoustooptic crystal cut, which introduces a prism effect for the diffracted beam. Because of the broadband nature of the oscillator spectrum, the diffracted beam has an angular chirp. It can be converted into a spatial chirp, or even removed, using proper beam shaping optics. Finally, the frequency shifter has a finite bandwidth. If the offset frequency drifts away from this bandwidth, then the diffraction efficiency decreases, limiting thus the compensation capability of the method. A slow feedback system should prevent this long-term drift.

4.5

CEP in Amplifiers

In high-field physics experiments, for instance for attosecond pulse generation, a millijoule few-cycle pulse interacts with a gaseous or solid medium to generate XUV pulses. The spectrum of this generation not only depends on the duration and the energy of the incoming pulse, but also on the CEP. All along the amplification chain, the CEP of the pulses fluctuates. In this section, we will detail the noise sources, how to measure the CEP noise and how to remove it.

4.5.1

Amplifier Peculiarities

In order to get the required pulse characteristics in terms of energy, duration and central wavelength, several steps are required. Figure 4.17 shows the typical chirped pulse amplification (CPA) scheme. We will now discuss each of these steps.

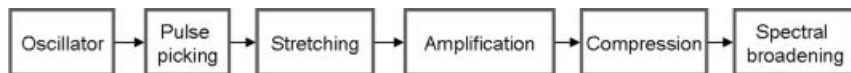


Figure 4.17 Typical amplification steps for millijoule few-cycle pulses.

4.5.1.1 Pulse Picking

Starting from a low-energy (nJ), high repetition rate (70–100 MHz) oscillator, the very first step consists of reducing the repetition rate, so as to get high-energy pulses at a limited average power. This slowing down has fundamental effects on the CEP. As we rapidly mentioned in Section 4.3.1, the repetition rate has an impact on the noise detection. The repetition rate of the laser defines an upper sampling rate for any observation. In other words, nothing faster than half the pulse period can be measured. A straightforward consequence concerns the measurement and feedback bandwidth, which will be limited by the repetition rate of the amplifier. Precisely, it cannot be larger than the repetition rate divided by 2, because of aliasing. Half of the sampling frequency is usually called the Nyquist frequency and the bandwidth from 0 up to this Nyquist frequency is referred to as the Nyquist zone or band.

The second effect, illustrated in Figure 4.18 from [40], is more vicious. Here, the authors measure the CEP from an oscillator both with a fast (35 MHz) and a slow (5 kHz) sampling rate. The respective PSDs (dashed line and gray line) are plotted on the same frequency range of 0.2 Hz–2.5 kHz. From 0.2 to 2 Hz, both PSDs follow a $1/f$ -like noise. While the slowly sampled signal exhibits a white noise level at $7 \cdot 10^{-6} \text{ rad}^2/\text{Hz}$, the fast sampled PSD still follows the $1/f$ trend up to 40 Hz, reaching a white noise level below $10^{-8} \text{ rad}^2/\text{Hz}$. The question arises: why does the noise level increase when the sampling rate decrease?

Let us consider the problem from Nyquist's point of view: the oscillator delivers pulses at 70 MHz; its Nyquist frequency is therefore 35 MHz. If the oscillator CEP is now sampled at 5 kHz, then the Nyquist zone shrinks to 2.5 kHz, that is, by roughly four orders of magnitude. Moreover, the noise at frequencies higher than 2.5 kHz cannot be seen by the measurement device. However, this high-frequency noise still exists. The question thus becomes, what happens to the noise spectral region above 2.5 kHz?

The right way to answer the question is the following: the amount of CEP jitter between two pulses sampled at 5 kHz can be determined simply by considering that the integration time in Eq. (4.12) is the pulse sampling period. A single point of

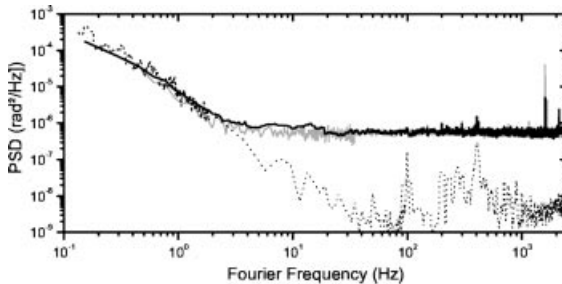


Figure 4.18 Oscillator CEP noise PSD derived with a 35 MHz (dashed line) and a 5 kHz (gray line) sampling rate, from [40]. Black line shows the computed PSD with aliasing effect.

the PSD obtained at 5 kHz sampling rate includes the oscillator noise from 2.5 kHz to 35 MHz, explaining the higher noise level at low sample frequency. Given the square root in Eq. (4.12), the noise level increase scales with the square root of the sampling rates ratio, here ≈ 100 : this corresponds to the two orders of magnitude between the white noise levels of the fast and slowly sampled PSD. The exact derivation of this aliasing effect is described in [40]: when it is taken into account, the fast sampled error PSD can be corrected to match the slowly sampled PSD (black line) in Figure 4.18.

As a consequence, reducing the pulse repetition rate in amplifiers intrinsically raises the noise level, so that all the high-frequency noise of the oscillator CEP is taken into account in the amplifier CEP. The practical impacts of this aliasing effect are twofold. First and foremost, the performance of the amplifier stabilization is bounded by the performance of the oscillator. This explains why there are still efforts on oscillator CEP stabilization. Second, increasing the repetition rate of the amplifier not only permits to increase the potential bandwidth of the servo-loop, but also reduces the integration bandwidth of the CEP noise transfer from the oscillator, or, in other words, the white noise level.

Finally, it should be noted that the amplifier repetition rate is obtained by dividing the oscillator repetition rate. The divider integer P must be a multiple of the integer N that satisfies the condition Eq. (4.17), so that the picked pulses exhibit the same average CEP. Otherwise there is no use in trying to stabilize the CEP of the pulse after amplification.

4.5.1.2 Pulse Stretching and Compression

In the case of CPA, two steps must be taken to allow a large amplification factor: the stretching and compression of the pulse. These two steps consist of managing the pulse dispersion with opposite signs and values matched as close as possible. Speaking of pulse dispersion means handling group velocities. Although the CEP definition in a stretched pulse is not very clear, it seems evident that the stretching/compression steps induce CEP drifts, whatever their implementation is.

Among the CEP issues in dispersion management systems, one can think of mechanical stability and associated beam pointing effects, just like in oscillators.

Therefore, the same idea applies: the bulkier, the better. If the pulse energy is small ($< \text{mJ}$), stretching durations of 10 ps may be enough. In this case, a block of glass as a stretcher and a prism pair or chirped mirrors for compression are good choices. This implementation led to the first demonstration of CEP stabilization in an amplifier [21]. When larger energies are aimed at, one must use grating-based systems which are more sensitive to external perturbations [41–43]. Although the impact is sufficiently small to be corrected, the quest for highly dispersive devices with so-called CEP compatibility is currently a hot topic.

4.5.1.3 Amplification

There are three ways to amplify ultrashort pulses:

- regenerative amplification
- multipassage amplification
- parametric amplification.

The two first ways are performed through laser amplification, using the same kind of crystal as the oscillator (titanium-, or ytterbium-doped crystals). The net gain per pass is rather small, and thus one needs many passes (typically > 10) to reach mJ energies from nJ oscillator pulses. This leads to large footprint systems, which are sensitive to mechanical noise. Moreover, the pump laser influence may be dramatic in terms of timing jitter and energy stability, especially when the B integral in the amplifier is large [44]. These points are intrinsically improved using diode-pumped solid-state lasers with high repetition rate. Finally, when dealing with large energies and high repetition rate, one must take into account the thermal load inside the amplification crystal. Heat is brought by the pumping laser energy and is partially removed by the amplified pulse. Cryo-cooling is usually a way to ensure good thermal equilibrium [45] and prevent thermal lens distortion. However, the cryo-cooler needs a compressor that induces large vibrations, even if it is away from the optical table [46].

Optical parametric amplification (OPA) is based on nonlinear interaction. This presents several interesting points. First, the net gain can be very large over a broad bandwidth: hundreds of μJ are reached within a couple of passes. Further energies may require optical chirped pulse parametric amplification (OPCPA). Second, the spectral region of the amplified pulse can be tuned, especially towards the infrared, which is known to be more attractive for attosecond pulse generation (see Chapter 10). Last but not least, the nonlinear interaction can make the amplification intrinsically CEP-stable. We shall discuss this method further in this chapter (Section 4.5.5).

4.5.1.4 Spectral Broadening

In the typical case of CPA lasers, the gain narrowing in the amplifier limits the output optical bandwidth. Although ways to fight against gain narrowing exist, delivering sub-15 fs pulses at the mJ level remains a tour de force. In any case, few-cycle pulses are not directly available at the amplifier output. A final step is therefore needed to perform spectral broadening. This is commonly achieved in

a hollow-core fiber, filled with noble gas [47], or through filamentation [48]. These implementations have been refined to reach impressive efficiency and energy scalability. Moreover, these effects preserve the CEP [2, 49], as long as the input energy is stable.

4.5.1.5 CEP Noise in Amplifiers

The long route of femtosecond pulse amplification creates many CEP noise inputs. These are mainly low-frequency noises, induced by mechanical displacements, temperature changes, and air turbulences in the pulse path [44]. In order to improve the passive stabilization, several rules must be followed [50]:

- Start with a low-CEP noise oscillator, as its noise figure will be the bottom line performance of the amplifier.
- Increase the repetition rate of the amplifier, so as to increase accordingly the potential detection bandwidth and limit the aliasing impact.
- Design the stretcher and the compressor to be as small and monolithic as possible.
- Get an energy-stable pump laser.
- Isolate any cryo- or liquid-cooled apparatus from the optical table.

4.5.2

CEP Detection

As for oscillators, $f - 2f$ interferometers are frequently used to measure the CEP of amplified pulses. The scheme is adapted to high-energy isolated pulses, as we will see. Due to the varied use of few-cycle pulses, several other methods have been proposed to measure the CEP, some of which can be seen as small-size physical experiments.

4.5.2.1 $f - 2f$ Interferometer

The basic principle of $f - 2f$ interferometers consists of comparing the phase of the wings of short pulse broadband spectra. In oscillators, the pulse train creates a discrete spectrum composed of modes. The detection of the CEP is achieved by the detection of the offset frequency, which can be done using a single-point detector (e.g., a photodiode). In amplifiers, the pulses are no more emitted in high repetition rate manner: the mode representation is no longer valid. The spectrum is continuous and so the offset frequency cannot be easily detected. However, CEP can be retrieved using the same basic elements of $f - 2f$ interferometers, as pictured in Figure 4.19: spectral broadening, frequency doubling, and group delay between the fundamental and frequency-doubled pulses [21, 51].

Let us consider an amplified pulse with a CEP ϕ_{CEP} . First, one needs an octave spanning spectrum. Given the large energy available in the amplified pulse, the continuum can be obtained directly in a sapphire plate, removing the need for an optical fiber. The continuum generation yields the electric field:

$$E_{\text{WLG}}(\omega) = \sqrt{I_{\text{WLG}}(\omega)} \exp(i\phi_{\text{WLG}}(\omega) + \phi_{\text{CEP}}), \quad (4.22)$$

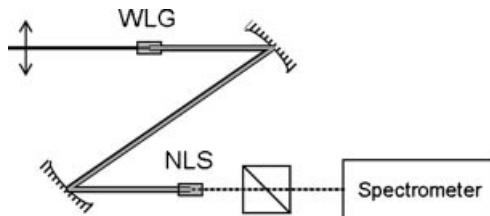


Figure 4.19 Typical $f - 2f$ setup for amplified pulses. WLG: white light generation; NLS: nonlinear stage.

where $I_{\text{WLG}}(\omega)$ is the pulse intensity and $\phi_{\text{WLG}}(\omega)$ is the spectral phase added through white-light generation. The pulse is further focused in a nonlinear crystal so as to create a frequency doubled pulse. The pulse after this nonlinear stage can be described as follows:

$$E_{\text{SHG}}(\omega) = \sqrt{I_{\text{SHG}}(\omega)} \exp(i\phi_{\text{SHG}}(\omega) + 2\phi_{\text{CEP}}), \quad (4.23)$$

with an intensity $I_{\text{SHG}}(\omega)$ and an additional phase ϕ_{SHG} , including both the phase of the nonlinear crystal itself and the frequency doubling of the white light phase $\phi_{\text{WLG}}(\omega)$. The second harmonic consequently exhibits a global phase $\phi_{\text{SHG}}(\omega) + 2\phi_{\text{CEP}}$.

Suppose now the fundamental and frequency-doubled pulses are separated by a time delay τ . When the pulses interfere on the detector, the resulting signal is

$$\begin{aligned} I_{\text{TOT}}(\omega) &= I_{\text{WLG}}(\omega) + I_{\text{SHG}}(\omega) \\ &+ \sqrt{I_{\text{WLG}}(\omega)I_{\text{SHG}}(\omega)} \cos(\phi_{\text{SHG}}(\omega) - \phi_{\text{WLG}}(\omega) + \omega\tau + \phi_{\text{CEP}}). \end{aligned} \quad (4.24)$$

Detecting this signal with a spectrometer around the spectral region of overlap between the fundamental and frequency-doubled pulses, one can observe spectral fringes, with a frequency $1/\tau$. The phase of the fringes includes the CEP ϕ_{CEP} of the input pulse. Performing Fourier analysis of this interferogram around τ leads to the CEP of the pulse. One can understand that this method is still very straightforward. Some of the drawbacks of $f - 2f$ for oscillators disappear:

- The continuum is generated in a sapphire plate instead of a photonic crystal fiber. This removes the beam pointing issue and the associated parasitic noise detection.
- The intrinsic group delay induced by the white-light generation and the frequency doubling stage becomes the key for the CEP retrieval. In the case of oscillators, it must be canceled to get temporal overlap between the pulses to get the oscillating part at f_0 . There is no more need for an interferometer here, which makes this setup more stable.

In other words, the two major contributions of parasitic noise in the CEP retrieval for oscillators do not exist for amplifiers. A good point for this scheme is also the low energy required (typically around the μJ level).

However, some drawbacks remain. First and foremost, the $f - 2f$ interferometers do not lead to the absolute value of the CEP. The phase retrieved by the Fourier analysis is the sum of the CEP and the phase associated with the white light and second harmonic generation. The latter are assumed to remain constant in the set-up, and only the CEP is supposed to vary. Second, the continuum generation still suffers from phase-amplitude coupling. This is not due to fiber coupling efficiency, but simply to the energy fluctuations of the amplified pulses. These variations are known to shrink when the repetition rate increases (due to both the pump energy stability and the thermal effects in the amplifier). Coupling values of 10 mrad/nJ for the input pulse of $f - 2f$ interferometer have been measured [21]. The corresponding reference also discussed the side effects of the continuum and second harmonic generation.

One can also question the single-shot capability of the scheme. As we discussed, the interference pattern is detected with a spectrometer and the Fourier analysis is performed by a computer. A practical consideration of the time scales is useful: it takes a few milliseconds just to read a standard 2048-points spectrum, which directly prevents single-shot CEP retrieval for kHz amplifiers. Adding the Fourier analysis time (several ms), real implementations require at least 10 ms, therefore limiting the loop bandwidth to 100 Hz. There are, however, ways to circumvent the problem working either with single-point detection [4], or embedded phase processing on the spectrometer.

4.5.2.2 Above-Threshold Ionization

Above threshold ionization (ATI), is a physical phenomenon in which an atom absorbs more photons than necessary for its ionization. This easily happens with intense femtosecond pulses (see Chapters 6 and 11). In the case of few-cycle pulses, the photoelectron emission is very sensitive to the CEP, as electrons follow the electric field oscillations. If the pulse is linearly polarized, then the electrons are emitted in the polarization plane, in directions perpendicular to the propagation axis of the pulse. Detecting the number of electrons emitted to the left and right side allows a direct analysis of the absolute phase of the pulse. This method is known as stereo-ATI [52] and has been improved in order to get high precision, single-shot detection of the CEP [53]. The laser pulse interacts with Xenon gas in a vacuum chamber (see Figure 4.20). The lateral detection of photoelectrons is performed with two time-of-flight spectrometers. The detected spectra are separated in two bands, which are separately processed for CEP extraction.

This scheme has strong advantages with respect to the $f - 2f$ interferometer. First, it is based on a physical phenomenon that is intrinsically sensitive to the absolute CEP value. Its extraction is quite straightforward and relies on electronics-only processing. The CEP detection is very sensitive (up to $\pi/300$) and can be single shot, even for multi-kHz amplifiers. In addition, the phase distribution can be directly observed on an oscilloscope with a radial figure. Finally, the setup is non intrusive, as the interaction with gas is almost free from dispersion and absorption.

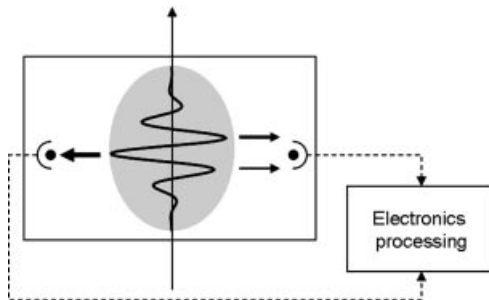


Figure 4.20 Stereo-ATI setup. Atomic ionization in a strong few-cycle pulse leads to right-left asymmetries of photoelectron emission, which are directly related to the CEP. The gray zone is the interaction chamber.

Nevertheless, the setup needs a vacuum chamber and two time-of-flight detection systems. The cost and footprint of such a system are much more important than in a simple $f - 2f$ interferometer. In addition, the pulse requirements are quite stringent: typically tens of μJ are required in a pulse duration of less than 7 fs.

4.5.2.3 Other Methods

Other CEP measurement schemes have been published. Just like stereo-ATI, all of them are derived from larger experimental systems, so as to only measure the CEP. Surface photoelectron emission [54], terahertz-emission spectroscopy [55], and half-cycle cutoffs in high harmonic spectra [56] are examples of such propositions. Detailing the way these schemes work would take too much room; we shall therefore give only a brief description of them.

Multiphoton-induced surface photoemission Experiments have been conducted to focus a very short pulse (sub-8 fs) on a gold photocathode. With sufficient light peak intensity ($10^{12}\text{--}10^{13} \text{ W/cm}^2$), electrons are emitted from the metal surface of the cathode. The electrons are amplified in a multiplier tube and the time-averaged current shows a dependence on the pulse CEP. This system can be used with very low energy (the experiments in [54] are performed with unamplified pulses) and the setup is rather small. On the other hand, the effect shows a significant dependence on the pulse duration, and offers only a poor precision.

Terahertz-emission spectroscopy Focusing a high-energy pulse in ambient air creates a plasma. During this photoionization, THz generation occurs through four-wave mixing and the intensity of the THz emission depends on the pulse CEP. In this scheme, the setup is very simple. No vacuum is required, and off-the-shelf THz measurement devices are used. Single-shot detection seems easy to achieve. But the ionization, requires high energy (tens of μJ), and very short pulses (sub-8 fs).

Half-cycle cutoff in high harmonic spectra The role of CEP in high harmonic generation is fundamental. Analyzing the high harmonic spectra should thus offer a good opportunity to observe the CEP. Within half an optical cycle, electrons are freed and can produce harmonics by recollision with the atom. Spatially resolved spectra analysis can provide the pulse CEP, with a rather good precision. However, the experimental setup is large, and single-shot capability seems hard to manage because large pulse energies are required and the CEP retrieval algorithm is complex.

These three examples show that, although several CEP sensitive physical effects exist, it remains a challenge to exploit them in order to get fast, precise and robust access to the CEP.

4.5.3

Actuation

Actuation points in amplifiers are manifold. Historically, it started by combining the error signals from the amplifier and the oscillator on the oscillator pump laser [2, 21]. This scheme is still employed in many systems, although this situation is far from ideal for two reasons. First, closing two feedback loops with different phase noise origins and bandwidth at a single point is not recommended. The crosstalk between both stabilization loops tends to degrade the performance of the overall system. Second, the oscillator pump actuation is known to exhibit a rather small correction window and the slow, but large drift induced by the amplifier can rapidly move the CEP out of this window.

As the CEP is the difference between the group index and the phase index, one can think of tuning either both parameters, or one of them while leaving the second constant. Dispersion management systems with a mechanical actuator are often encountered. Displacement of gratings in the stretcher [57] or the compressor [58, 59] have been demonstrated and, in the case of bulk stretching, mechanical solutions also exist [36, 50]. However, piezo-electric transducers are slow and suffer from nonlinearities and hysteresis. As the speed depends on weight of the optical mount, the limitation is stronger in grating-based devices, especially in compressors. Finally, side effects on the high-order dispersion are supposed to occur.

External components such as pulse shapers can be used to close the feedback loop. $4f$ -lines [60] do not seem to be interesting candidates because of their large footprint and the slow response of spatial light modulators [61]. Speed and linearity issues can be solved using acousto- or electrooptical components. The acoustooptical programmable dispersive filter [62, 63] is a pulse-shaper based on a longitudinal acoustooptical interaction. The spectral amplitude and phase of the acoustic waveform directly impinges on the spectral amplitude and phase of the broadband optical pulse. Leaving the programmed dispersion while shifting the acoustic absolute phase allows for shifting the optical pulse CEP [46, 64]. The acoustic phase can be changed for every trigger event, up to the maximum refreshing rate of the device (tens of kHz), together with an excellent precision. Electrooptical modulation has recently been proposed to control the CEP [65]. The electrooptic effect is known to

be fast and precise and this scheme could prove to be a good candidate, providing the high voltage biasing of the electrooptic crystal is not noisy.

Finally, with the CEP being highly sensitive to pulse energy stability, both in the amplifier and the detection, it has been demonstrated that a stabilization loop on the seed energy tends to improve the CEP stability of the amplifier [66].

4.5.4

Feedback Results

The system comparison or even performance analysis of an amplifier is not as easy as for oscillators. A first reason concerns the measurement. Although $f - 2f$ schemes with a Fourier analysis are the most encountered measurement methods, the spectrometer setting (integration and/or average) and the computer capability hugely change the results. Among the cited references in this chapter, integration varies from one shot [64] to 50 [61]. Furthermore, the loop bandwidth or processing time are almost never mentioned. It seems that reducing the Fourier processing time below 60 ms is a hard task, even when the spectrometer can handle single-shot detection [64]. In-loop CEP time charts offer the only comparison figures but the time frame can vary from minutes up to hours. As a rule of thumb, typical amplifiers deliver several mJ, sub 30 fs pulses, with < 200 mrad root mean square stability over a few Hz bandwidth [50, 59, 61]. In these conditions, it is worth noting that the actuation bandwidth is not a relevant criterion, as the CEP detection/processing speed is very low (\ll kHz) in conventional $f - 2f$ interferometers.

However, single shot CEP extraction schemes are under study [4, 53]. No single-shot feedback has been performed so far, as the first demonstration of single-shot detection and the availability of fast feedback actuators occurred almost simultaneously. Interestingly, the two single-shot detection systems of [4] and [53] have monitored the same laser, delivering 25 fs, mJ pulses at 3 kHz. Figure 4.21 shows results of these devices.

In [4], the phase detection is based on a standard $f - 2f$ interferometer. Instead of processing the spectrum with a classical spectrometer and a computer,

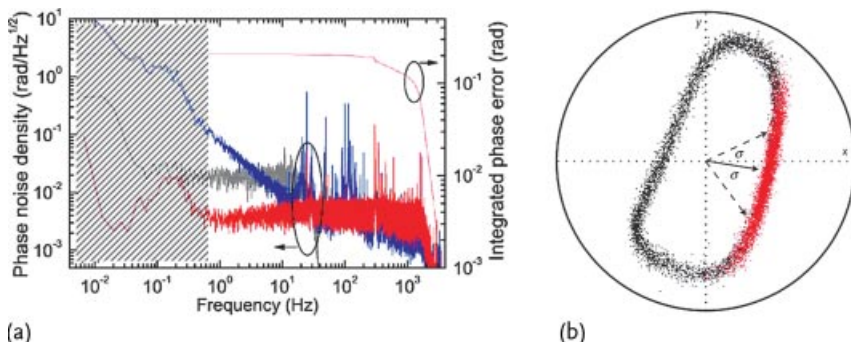


Figure 4.21 Comparison of single-shot detection schemes using a $f - 2f$ interferometer with direct electronic phase processing (a) [4] and using the stereo-ATI device (b) [53].

the optoelectronic detector consists only of two single-point photodetectors (photomultiplier tubes), which see two points within the interferogram. A basic analog processing further extracts the interferogram phase. As the phase can be computed at every laser pulse, a conventional noise PSD analysis can be performed. The results are plotted in Figure 4.21a. This PSD plot is, to the author's knowledge, the only PSD plot ever published for a CEP-stabilized amplified system. The interpretation of these results has already been discussed in Section 4.3.5. We should just remind the reader that the gray line is the in-loop PSD of the stabilized system using a standard slow detection $f - 2f$ and the red line is the in-loop PSD of the same system, stabilized with a single-shot detection $f - 2f$. The respective computed jitters over the feedback bandwidth are 115 mrad and 210 mrad.

On the other hand, Figure 4.21b plots the phase extracted by the single-shot stereo-ATI of [53]. In this case, the plot is almost angular, so that the phase variation is very easy to read. The black points represent the phase evolving around 2π radians, and the red points correspond to the phase distribution of 4500 consecutive shots of the stabilized laser using a conventional slow $f - 2f$ interferometer. The standard deviation of the distribution is 278 mrad.

In order to compare the results of Figure 4.21a,b, we must first set the same analysis window. As in both cases the detection is single shot, the upper frequency of Figure 4.21a remains 1.5 kHz (the Nyquist frequency of the 3 kHz laser repetition rate). Regarding the integration time, the ATI plot is limited to 4500 shots, that is, a 1.5 s long time window. The lower frequency of the PSD of Figure 4.21a should be 0.6 Hz: the shaded region of the PSD plot must then be ignored. As most jitter comes from high-frequency noise, this should allow the comparison of system jitter.

There is however a problem. In the case of Figure 4.21b, stereo-ATI is used to monitor the results of the conventional slow spectrometer (out-of-loop analysis). In the case of Figure 4.21a, we can interpret the in-loop results either with a conventional slow spectrometer, or with the single-shot detector. We unfortunately miss the monitoring of the conventional system with a single-shot detector. Luckily, the authors of [53] performed averaging up to 25 shots. The analysis upper frequency is reduced to 60 Hz, which is almost comparable to the feedback bandwidth obtained for the gray line of Figure 4.21a. Under these conditions, the standard deviation measured by the stereo-ATI is only 110 mrad, which is comparable to the 115 mrad of the in-loop jitter of Figure 4.21a.

We now have a comparison point between the two systems: the jitter on a 0.6–60 Hz integration bandwidth is 110 mrad. In Section 4.3.5, we discussed this value, saying that this rather flattery performance should be weighted by the small integration bandwidth with respect to the amplifier repetition rate. The result of the stereo-ATI device corroborates this inference. The real jitter of the slow stabilization over the full integration bandwidth (i.e., up to the real repetition rate of the laser) increases to 278 mrad. This illustrates an important discussion point of phase stabilization loops: what is the jitter and what is the integration bandwidth? Last, the jitter can be slightly reduced with an increase of the feedback bandwidth

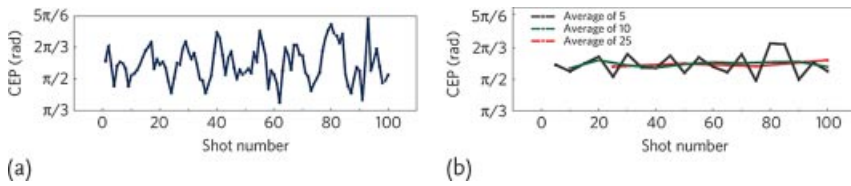


Figure 4.22 Effect of averaging, from [53].

and proper error signal filtering: the stabilization of the amplifier with the single-shot system yields a jitter of 210 mrad.

At this stage of discussion, the reader should be warned that the loop performance improvement relies on different parameters. As mentioned, it seems important that both the detection and the actuator can work in the single-shot mode: in this case, the loop bandwidth is solely limited by the error signal filtering stage, which can be engineered with as much freedom as possible. The second fundamental point concerns the overall detection noise level. Of course, when the white noise floor is reached at low frequencies, it is of no use to increase the loop bandwidth, as the error signal contains a large amount of noise, especially at high frequencies. Regarding the CEP detection schemes state-of-the-art, this noise issue seems to be the major point, where future efforts could improve stabilization. However, single-shot detection still remains the only way to make proper noise frequency analysis, just as presented in [4]. And finally, if one had both, low-noise single-shot detection and high bandwidth actuation, the last step of the loop filter design would need high care to get the best performance.

Going back to the system comparison, the authors of [53] show a very clear effect of averaging, or in other words high-frequency noise blindness. Figure 4.22a shows a number of consecutive points measured with stereo-ATI on the stabilized system. The trace clearly shows oscillations with a period of 10 to 15 shots, that is, noise frequencies between 200 and 300 Hz. This roughly corresponds to the spikes one can see in the open-loop PSD of Figure 4.21a (blue line). If one averages over 5 shots (see black line of Figure 4.22a), then the oscillation amplitude is reduced. In this case, the standard deviation of 4500 shots is only 195 mrad: 30% of the noise has been removed! This averaging corresponds to ignoring the spectral noise of Figure 4.21a above 600 Hz. Looking at the integrated phase error, one can see that this very part of the noise spectrum contributes mostly to the system jitter. Increasing the averaging to 10, and eventually 25 shots, further reduces the noise standard deviation down to 140 and 110 mrad, respectively, as the oscillation frequency is faster than the averaging rate.

4.5.5

Parametric Amplification

Optical parametric amplification remains a special case, as we briefly discussed in Section 4.5.1.3. The all-optical setup, with large gain over a tunable broad bandwidth makes it very attractive. This scheme can be made CEP self-stabilized. This

self-stabilization idea stems from conservation laws between the three waves interacting in the parametric amplification: the pump, the signal, and the idler. The simplified energy and phase conservation laws can be written as [67]

$$\omega_P = \omega_S + \omega_I \quad \phi_P = \phi_S + \phi_I + \frac{\pi}{2}, \quad (4.25)$$

where ω_i and ϕ_i , respectively, stand for the angular frequency and phase, and the index P, S, I stand for the pump, the signal and the idler, respectively.

Of course, the phase conservation law is of primary interest in the case of generating CEP-stable pulses. Several ways can be implemented, taking advantage of different elements of the parametric amplification.

4.5.5.1 White Light Seeding

One can note that the idler is actually generated through difference frequency generation (DFG). Focusing on the phase conservation law of Eq. (4.25), the idler phase is the difference between the pump and the signal phase. As a consequence, if the pump and the signal are derived from the same initial pulse, that is, with the same original phase ϕ_0 , then the pump and signal phases cancel out, leaving the idler phase free from fluctuations. The first method to get self-stable CEP pulses consists of seeding the OPA with a white-light continuum, as sketched in Figure 4.23. A pulse emitted by a standard CPA laser chain is divided into two arms. One, with high energy, acts as the pump; the second is focused in a sapphire or CaF₂ plate to generate a continuum, and further acts as a broadband seed.

As both pulses are emitted from the same source, and assuming that the white light generation preserves the optical phase (as discussed in Section 4.5.2.1), one can write $\phi_P = \phi_0$ and $\phi_S = \phi_0 + \phi_{WLG}$. The idler pulse generated in the parametric amplification has a constant phase: $\phi_I = \phi_P - \phi_S - \pi/2 = -\phi_{WLG} - \pi/2$. It is worth noticing that frequency doubling the output pulse of the CPA can create a self-stabilized idler with the same frequency as the CPA. This is a (lossy) way to get CEP-stable pulses at 800 nm.

An important drawback of the scheme is the angular chirp of the generated idler. Amplification of few-cycle pulses requires broad gain bandwidth. The latter can be reached in parametric amplification either in a noncollinear geometry (NOPA), or in type I interaction at degeneracy [68]. In both cases, the arrangement is not collinear: in an intrinsic way in the NOPA, and in order to avoid signal-idler interferences in the type I interaction. The consequence is an angular dispersion of the idler beam, which is difficult to compensate. Another way to circumvent the chirp problem is by generating a narrow-band CEP-stable idler pulse and manage, in different stages, the amplification and spectral broadening. The broadening can be performed prior to the amplification [69] or after [70].

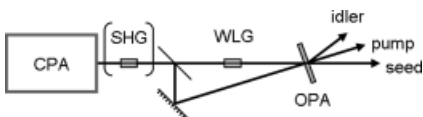


Figure 4.23 White-light seeded OPA. SHG: second harmonic generation; WLG: white light generation.

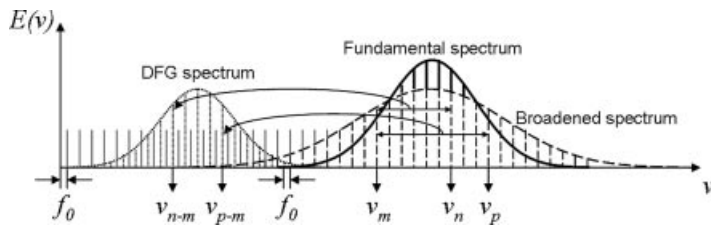


Figure 4.24 0 – f spectra for self-stabilization using DFG.

4.5.5.2 Intrapulse Self-Stabilization

A very elegant way to provide CEP-stable pulses is by using difference frequency generation (DFG). The concept is called the $0 - f$ method, as opposed to the $f - 2f$ scheme. This method can be used in oscillators [71], or in OPAs [72] and OPCPAs [73]. The idea is to perform DFG between spectral components within the pulse (Figure 4.24). Considering the case of a broadband comb spectrum with v_n and v_m components, as defined with Eq. (4.14), and with $v_n > v_m$, the DFG writes $v_n - v_m = (n - m)f_{\text{rep}}$, which is independent of f_0 . With this self-stabilization scheme, the resulting spectrum is free from CEP fluctuations, without any active feedback.

This scheme is very easy to implement. It is especially popular for stabilizing OPA seeding pulses. The DFG naturally increases the central wavelength of the spectrum, which can be suited for OPAs working in the infrared. However, the DFG tends to reduce the pulse bandwidth. The efficiency is rather low and therefore needs a preamplification stage to compensate for the losses.

4.5.5.3 Results

The comparison of results is a very delicate matter, for the same reasons as explained in Section 4.5.4. Although most of CEP characterizations are performed with $f - 2f$ interferometers, the details concerning the spectrometer integration and the analysis speed are not always reported. Actually, no long-term analysis has been performed: references usually only show the CEP stability over seconds or minutes. The intrinsic self-stabilization of DFG ensures a robust lock. Stability around 200 mrad root mean square in single-shot interferograms are typical results.

Considering the self-stabilization concepts, one could imagine reaching very high stability. Several sources of noise remain in the OPA [69]. First, the parametric amplification is based on a nonlinear instantaneous effect. Any fluctuations in the pump or the seed source energies or beam pointing induce CEP jitter. When the white light seeding scheme is envisaged, the seed and the pump pulses must be synchronized. This is usually performed with a delay line between the pump path and the seed path. But any path length difference will cause CEP variation. From this point of view, the intrapulse DFG is a more robust setup. Of course, the detection apparatus remains an extra-CEP noise source.

4.6 Conclusion

Since the first observation of CEP in oscillators in 1996 [12] and the pioneering work towards stabilization [6, 35], less than 20 years have passed. Within the past 10 years, large efforts have led to the understanding of noise sources and underlying physical mechanisms, the improvement of the measurement, and the implementation of efficient correction schemes. A 100 mrad stability over a broad bandwidth can now be achieved [38] and new ideas are still emerging [39]. Broad bandwidth, detection noise-limited feedback loops may be designed in the near future, probably enabling sub- $\pi/100$ CEP stability.

Soon after the oscillators become stabilized, efforts will then focus on amplifiers [2]. The room for technological improvement is still large, as attested to by the recent work on the CEP measurement schemes and the feedback actuation points. Low-noise detection and multi-kHz amplifier systems (so as to reduce the impact of aliasing) are the next technological keys for efficient stabilization loops. It can be foreseen that sub-100 mrad CEP stability on a shot-to-shot basis may be reached.

Apart from technical considerations, another interesting point of the CEP-based technologies is the rapid knowledge transfer from labs to companies. Over the past 15 years, many concepts were transferred from fundamental science laboratories to industry and enabled commercial turn-key systems, able to deliver CEP-stable sub-10 fs pulse oscillators, coupled to multi-mJ, multi-kHz amplifiers [50].

References

- 1 Udem, T., Holzwarth, R., and Hansch, T. (2002) Optical frequency metrology. *Nature*, **416** (6877), 233–237.
- 2 Baltuska, A., Udem, T., Uiberacker, M., Hentschel, M., Goulielmakis, E., Gohle, C., Holzwarth, R., Yakovlev, V., Scrinzi, A., Hansch, T., and Krausz, F. (2003) Attosecond control of electronic processes by intense light fields. *Nature*, **421** (6923), 611–615.
- 3 Cundiff, S. (2002) Phase stabilization of ultrashort optical pulses. *J. Phys. D*, **35** (8), R43–R59.
- 4 Koke, S., Grebing, C., Manschwetus, B., and Steinmeyer, G. (2008) Fast f -to- $2f$ interferometer for a direct measurement of the carrier-envelope phase drift of ultrashort amplified laser pulses. *Opt. Lett.*, **33** (21), 2545–2547.
- 5 Matos, L., Mucke, O., Chen, J., and Kartner, F. (2006) Carrier-envelope phase dynamics and noise analysis in OCTAVE-spanning Ti:Sapphire lasers. *Opt. Express*, **14** (6), 2497–2511.
- 6 Jones, D., Diddams, S., Ranka, J., Stentz, A., Windeler, R., Hall, J., and Cundiff, S. (2000) Carrier-envelope phase control of femtosecond mode-locked lasers and direct optical frequency synthesis. *Science*, **288** (5466), 635–639.
- 7 Schiller, S. (2002) Spectrometry with frequency combs. *Opt. Lett.*, **27** (9), 766–768.
- 8 Cundiff, S., Ye, J., and Hall, J. (2001) Optical frequency synthesis based on mode-locked lasers. *Rev. Sci. Instrum.*, **72** (10), 3749–3771.
- 9 Washburn, B., Diddams, S., Newbury, N., Nicholson, J., Yan, M., and Jorgensen, C. (2004) Phase-locked, erbium-fiber-laser-based frequency comb in the near infrared. *Opt. Lett.*, **29** (3), 250–252.
- 10 Meyer, S.A., Squier, J.A., and Diddams, S.A. (2008) Diode-pumped Yb:KYW

- femtosecond laser frequency comb with stabilized carrier-envelope offset frequency. *Eur. Phys. J. D.*, **48** (1), 19–26.
- 11** Moulton, P. (1986) Spectroscopic and laser characteristics of Ti:Al₂O₃. *J. Opt. Soc. Am. B*, **3** (1), 125–133.
- 12** Xu, L., Spielmann, C., Poppe, A., Brabec, T., Krausz, F., and Hansch, T. (1996) Route to phase control of ultrashort light pulses. *Opt. Lett.*, **21** (24), 2008–2010.
- 13** Holman, K., Jones, R., Marian, A., Cundiff, S., and Ye, J. (2003) Intensity-related dynamics of femtosecond frequency combs. *Opt. Lett.*, **28** (10), 851–853.
- 14** Witte, S., Zinkstok, R., Hogervorst, W., and Eikema, K. (2004) Control and precise measurement of carrier-envelope phase dynamics. *Appl. Phys. B*, **78** (1), 5–12.
- 15** Fortier, T., Jones, D., Ye, J., and Cundiff, S. (2003) Highly phase stable mode-locked lasers. *IEEE J. Sel. Top. Quantum Electron.*, **9** (4), 1002–1010.
- 16** Helbing, F., Steinmeyer, G., Stenger, J., Telle, H., and Keller, U. (2002) Carrier-envelope-offset dynamics and stabilization of femtosecond pulses. *Appl. Phys. B*, **74** (Suppl. S), S35–S42.
- 17** Stingl, A., Lenzner, M., Spielmann, C., Krausz, F., and Szipocs, R. (1995) Sub-10-fs mirror-dispersion-controlled Ti-sapphire laser. *Opt. Lett.*, **20** (6), 602–604.
- 18** Helbing, F., Steinmeyer, G., and Keller, U. (2003) Carrier-envelope offset phase-locking with attosecond timing jitter. *IEEE J. Sel. Top. Quantum Electron.*, **9** (4), 1030–1040.
- 19** Telle, H., Steinmeyer, G., Dunlop, A., Stenger, J., Sutter, D., and Keller, U. (1999) Carrier-envelope offset phase control: A novel concept for absolute optical frequency measurement and ultrashort pulse generation. *Appl. Phys. B*, **69** (4), 327–332.
- 20** Ranka, J., Windeler, R., and Stentz, A. (2000) Visible continuum generation in air-silica microstructure optical fibers with anomalous dispersion at 800 nm. *Opt. Lett.*, **25** (1), 25–27.
- 21** Baltuska, A., Uiberacker, M., Goulielmakis, E., Kienberger, R., Yakovlev, V., Udem, T., Hansch, T., and Krausz, F. (2003) Phase-controlled amplification of few-cycle laser pulses. *IEEE J. Sel. Top. Quantum Electron.*, **9** (4), 972–989.
- 22** Zhu, Z. and Brown, T. (2004) Experimental studies of polarization properties of supercontinua generated in a birefringent photonic crystal fiber. *Opt. Express*, **12** (5), 791–796.
- 23** Fortier, T., Ye, J., Cundiff, S., and Windeler, R. (2002) Nonlinear phase noise generated in air-silica microstructure fiber and its effect on carrier-envelope phase. *Opt. Lett.*, **27** (6), 445–447.
- 24** Washburn, B. and Newbury, N. (2004) Phase, timing, and amplitude noise on supercontinua generated in microstructure fiber. *Opt. Express*, **12** (10), 2166–2175.
- 25** Poppe, A., Holzwarth, R., Apolonski, A., Tempea, G., Spielmann, C., Hansch, T., and Krausz, F. (2001) Few-cycle optical waveform synthesis. *Appl. Phys. B*, **72** (3), 373–376.
- 26** Fortier, T., Bartels, A., and Diddams, S. (2006) Octave-spanning Ti:Sapphire laser with a repetition rate > 1 ghz for optical frequency measurements and comparisons. *Opt. Lett.*, **31** (7), 1011–1013.
- 27** Jones, D., Fortier, T., and Cundiff, S. (2004) Highly sensitive detection of the carrier-envelope phase evolution and offset of femtosecond mode-locked oscillators. *J. Opt. Soc. Am. B*, **21** (5), 1098–1103.
- 28** Grebing, C., Koke, S., Manschwetus, B., and Steinmeyer, G. (2009) Performance comparison of interferometer topologies for carrier-envelope phase detection. *Appl. Phys. B*, **95** (1), 81–84.
- 29** Tsatourian, V., Margolis, H.S., Marra, G., Reid, D.T., and Gill, P. (2010) Common-path self-referencing interferometer for carrier-envelope offset frequency stabilization with enhanced noise immunity. *Opt. Lett.*, **35** (8), 1209–1211.
- 30** Moon, E., Li, C., Duan, Z., Tackett, J., Corwin, K.L., Washburn, B.R., and Chang, Z. (2006) Reduction of fast carrier-envelope phase jitter in femtosecond laser amplifiers. *Opt. Express*, **14** (21), 9758–9763.

- 31** Fuji, T., Rauschenberger, J., Apolonski, A., Yakovlev, V., Tempea, G., Udem, T., Gohle, C., Hansch, T., Lehnert, W., Scherer, M., and Krausz, F. (2005) Monolithic carrier-envelope phase-stabilization scheme. *Opt. Lett.*, **30** (3), 332–334.
- 32** Mucke, O., Tritschler, T., Wegener, M., Morgner, U., and Kartner, F. (2002) Determining the carrier-envelope offset frequency of 5-fs pulses with extreme nonlinear optics in ZnO. *Opt. Lett.*, **27** (23), 2127–2129.
- 33** Roos, P., Li, X., Smith, R., Pipis, J., Fortier, T., and Cundiff, S. (2005) Solid-state carrier-envelope phase stabilization via quantum interference control of injected photocurrents. *Opt. Lett.*, **30** (7), 735–737.
- 34** Osvay, K., Goerbe, M., Grebing, C., and Steinmeyer, G. (2007) Bandwidth-independent linear method for detection of the carrier-envelope offset phase. *Opt. Lett.*, **32** (21), 3095–3097.
- 35** Apolonski, A., Poppe, A., Tempea, G., Spielmann, C., Udem, T., Holzwarth, R., Hansch, T., and Krausz, F. (2000) Controlling the phase evolution of few-cycle light pulses. *Phys. Rev. Lett.*, **85** (4), 740–743.
- 36** Grebing, C., Goerbe, M., Osvay, K., and Steinmeyer, G. (2009) Isochronic and isodispersive carrier-envelope phase-shift compensators. *Appl. Phys. B*, **97** (3), 575–581.
- 37** Yun, C., Chen, S., Wang, H., Chini, M., and Chang, Z. (2009) Temperature feedback control for long-term carrier-envelope phase locking. *Appl. Opt.*, **48** (27), 5127–5130.
- 38** Rauschenberger, J., Fuji, T., Hentschel, M., Verhoef, A., Udem, T., Gohle, C., Hansch, T., and Krausz, F. (2006) Carrier-envelope phase-stabilized amplifier system. *Laser Phys. Lett.*, **3** (1), 37–42.
- 39** Koke, S., Grebing, C., Frei, H., Ander-son, A., Assion, A., and Steinmeyer, G. (2010) Direct frequency comb synthesis with arbitrary offset and shot-noise-limited phase noise. *Nat. Photonics*, **4** (7), 462–465.
- 40** Gohle, C., Rauschenberger, J., Fuji, T., Udem, T., Apolonski, A., Krausz, F., and Hansch, T. (2005) Carrier envelope phase noise in stabilized amplifier systems. *Opt. Lett.*, **30** (18), 2487–2489.
- 41** Kakehata, M., Fujihira, Y., Takada, H., Kobayashi, Y., Torizuka, K., Homma, T., and Takahashi, H. (2002) Measurements of carrier-envelope phase changes of 100-hz amplified laser pulses. *Appl. Phys. B*, **74** (Suppl. S), S43–S50.
- 42** Thomann, I., Gagnon, E., Jones, R., Sandhu, A., Lytle, A., Anderson, R., Ye, J., Murnane, M., and Kapteyn, H. (2004) Investigation of a grating-based stretcher/compressor for carrier-envelope phase stabilized fs pulses. *Opt. Express*, **12** (15), 3493–3499.
- 43** Chang, Z. (2006) Carrier-envelope phase shift caused by grating-based stretchers and compressors. *Appl. Opt.*, **45** (32), 8350–8353.
- 44** Chen, X., Canova, L., Malvache, A., Julian, A., Lopez-Martens, R., Durfee, C., Papadopoulos, D., and Druon, F. (2010) 1-mJ, sub-5-fs carrier-envelope phase-locked pulses. *Appl. Phys. B*, **99** (1–2), 149–157.
- 45** Zavelani-Rossi, M., Lindner, F., Le Blanc, C., Cheriau, G., and Chambaret, J. (2000) Control of thermal effects for high-intensity Ti:Sapphire laser chains. *Appl. Phys. B*, **70** (Suppl. S), S193–S196.
- 46** Fordell, T., Miranda, M., Persson, A., and L’Huillier, A. (2009) Carrier-envelope phase stabilization of a multi-millijoule, regenerative-amplifier-based chirped-pulse amplifier system. *Opt. Express*, **17** (23), 21091–21097.
- 47** Nisoli, M., DeSilvestri, S., Svelto, O., Szipocs, R., Ferencz, K., Spielmann, C., Sartania, S., and Krausz, F. (1997) Compression of high-energy laser pulses below 5 fs. *Opt. Lett.*, **22** (8), 522–524.
- 48** Hauri, C., Kornelis, W., Helbing, F., Heinrich, A., Couairon, A., Mysyrowicz, A., Biegert, J., and Keller, U. (2004) Generation of intense, carrier-envelope phase-locked few-cycle laser pulses through filamentation. *Appl. Phys. B*, **79** (6), 673–677.
- 49** Guandalini, A., Eckle, P., Anscombe, M., Schlup, P., Biegert, J., and Keller,

- U. (2006) 5.1 fs pulses generated by filamentation and carrier envelope phase stability analysis. *J. Phys. B*, **39** (13), S257–S264.
- 50** Anderson, A., Luecking, F., Prikovitz, T., Hofer, M., Cheng, Z., Neacsu, C.C., Scharrer, M., Rammller, S., Russell, P.S.J., Tempea, G., and Assion, A. (2011) Multi-mJ carrier envelope phase stabilized few-cycle pulses generated by a tabletop laser system. *Appl. Phys. B*, **103** (3), 531–536.
- 51** Kakehata, M., Takada, H., Kobayashi, Y., Torizuka, K., Fujihira, Y., Homma, T., and Takahashi, H. (2001) Single-shot measurement of carrier-envelope phase changes by spectral interferometry. *Opt. Lett.*, **26** (18), 1436–1438.
- 52** Paulus, G., Grasbon, F., Walther, H., Viloresi, P., Nisoli, M., Stagira, S., Priori, E., and De Silvestri, S. (2001) Absolute-phase phenomena in photoionization with few-cycle laser pulses. *Nature*, **414** (6860), 182–184.
- 53** Wittmann, T., Horvath, B., Helml, W., Schaetzel, M.G., Gu, X., Cavalieri, A.L., Paulus, G.G., and Kienberger, R. (2009) Single-shot carrier-envelope phase measurement of few-cycle laser pulses. *Nat. Phys.*, **5** (5), 357–362.
- 54** Apolonski, A., Dombi, P., Paulus, G., Kakehata, M., Holzwarth, R., Udem, T., Lemell, C., Torizuka, K., Burgdorfer, J., Hansch, T., and Krausz, F. (2004) Observation of light-phase-sensitive photoemission from a metal. *Phys. Rev. Lett.*, **92** (7).
- 55** Kress, M., Löffler, T., Thomson, M., Dorner, R., Gimpel, H., Zrost, K., Erbler, T., Moshammer, R., Morgner, U., Ullrich, J., and Roskos, H. (2006) Determination of the carrier-envelope phase of few-cycle laser pulses with terahertz-emission spectroscopy. *Nat. Phys.*, **2** (5), 327–331.
- 56** Haworth, C.A., Chipperfield, L.E., Robinson, J.S., Knight, P.L., Marangos, J.P., and Tisch, J.W.G. (2007) Half-cycle cutoffs in harmonic spectra and robust carrier-envelope phase retrieval. *Nat. Phys.*, **3** (1), 52–57.
- 57** Li, C., Moon, E., and Chang, Z. (2006) Carrier-envelope phase shift caused by variation of grating separation. *Opt. Lett.*, **31** (21), 3113–3115.
- 58** Li, C., Mashiko, H., Wang, H., Moon, E., Gilbertson, S., and Chang, Z. (2008) Carrier-envelope phase stabilization by controlling compressor grating separation. *Appl. Phys. Lett.*, **92** (19).
- 59** Lee, J.H., Lee, Y.S., Park, J., Park, J.J., Kim, D. S. and Yu, T.J., and Nam, C.H. (2009) Implementation of the direct locking method for long-term carrier-envelope-phase stabilization of a grating-based kHz femtosecond laser. *Appl. Phys. B*, **96** (2–3), 287–291.
- 60** Weiner, A., Heritage, J., and Kirschner, E. (1988) High-resolution femtosecond pulse shaping. *J. Opt. Soc. Am. B*, **5** (8), 1563–1572.
- 61** Wang, H., Chini, M., Wu, Y., Moon, E., Mashiko, H., and Chang, Z. (2010) Carrier-envelope phase stabilization of 5-fs, 0.5-mJ pulses from adaptive phase modulator. *Appl. Phys. B*, **98** (2–3), 291–294.
- 62** Tournois, P. (1997) Acousto-optic programmable dispersive filter for adaptive compensation of group delay time dispersion in laser systems. *Opt. Commun.*, **140** (4–6), 245–249.
- 63** Verluijs, F., Laude, V., Cheng, Z., Spielmann, C., and Tournois, P. (2000) Amplitude and phase control of ultrashort pulses by use of an acousto-optic programmable dispersive filter: pulse compression and shaping. *Opt. Lett.*, **25** (8), 575–577.
- 64** Forget, N., Canova, L., Chen, X., Jullien, A., and Lopez-Martens, R. (2009) Closed-loop carrier-envelope phase stabilization with an acousto-optic programmable dispersive filter. *Opt. Lett.*, **34** (23), 3647–3649.
- 65** Govert, O., Paul, P.M., Hergott, J.F., Tcherbakoff, O., Lepetit, F., Oliveira, P.D., Viala, F., and Comte, M. (2011) Carrier-envelope phase control using linear electro-optic effect. *Opt. Express*, **19** (6), 5410–5418.
- 66** Wang, H., Li, C., Tackett, J., Mashiko, H., Nakamura, C.M., Moon, E., and Chang, Z. (2007) Power locking of high-repetition-rate chirped pulse amplifiers. *Appl. Phys. B*, **89** (2–3), 275–279.

- 67** Baltuska, A., Fuji, T., and Kobayashi, T. (2002) Controlling the carrier-envelope phase of ultrashort light pulses with optical parametric amplifiers. *Phys. Rev. Lett.*, **88** (13).
- 68** Cerullo, G. and De Silvestri, S. (2003) Ultrafast optical parametric amplifiers. *Rev. Sci. Inst.*, **74** (1, Part 1), 1–18.
- 69** Cirmi, G., Manzoni, C., Brida, D., De Silvestri, S., and Cerullo, G. (2008) Carrier-envelope phase stable, few-optical-cycle pulses tunable from visible to near IR. *J. Opt. Soc. Am. B*, **25** (7), B62–B69.
- 70** Schmidt, B.E., Shiner, A.D., Lassonde, P., Kieffer, J.C., Corkum, P.B., Vileneuve, D.M., and Legare, F. (2011) CEP stable 1.6 cycle laser pulses at 1.8 μm . *Opt. Express*, **19** (7), 6858–6864.
- 71** Fuji, T., Apolonski, A., and Krausz, F. (2004) Self-stabilization of carrier-envelope offset phase by use of difference-frequency generation. *Opt. Lett.*, **29** (6), 632–634.
- 72** Vozzi, C., Calegari, F., Benedetti, E., Gasilov, S., Sansone, G., Cerullo, G., Nisoli, M., De Silvestri, S., and Stagira, S. (2007) Millijoule-level phase-stabilized few-optical-cycle infrared parametric source. *Opt. Lett.*, **32** (20), 2957–2959.
- 73** Gu, X., Marcus, G., Deng, Y., Metzger, T., Teisset, C., Ishii, N., Fuji, T., Baltuska, A., Butkus, R., Pervak, V., Ishizuki, H., Taira, T., Kobayashi, T., Kienberger, R., and Krausz, F. (2009) Generation of carrier-envelope-phase-stable 2-cycle 740- μJ pulses at 2.1- μm carrier wavelength. *Opt. Express*, **17** (1), 62–69.

5

Towards Tabletop X-Ray Lasers

Philippe Zeitoun, Eduardo Oliva, Thi Thu Thuy Le, Stéphane Sebban, Marta Fajardo, David Ros, and Pedro Velarde

5.1

Context and Objectives

Short pulses in the X-ray regime offer unique opportunities for the study of ultrafast processes in biology, chemistry and physics. The absorption of X-rays can occur with high spectral selectivity for direct chemical or physical analysis, the very low diffraction limit of X-rays is useful for imaging and physical analysis, and the short wavelength supports extremely short pulses in the attosecond ($1\text{ as} = 10^{-18}\text{ s}$) and even zeptosecond ($1\text{ zs} = 10^{-21}\text{ s}$) range [1, 2]. Over the past few years, X-ray sources have reached higher and higher intensities by either reducing the pulse duration and the size of the focal spot, or by increasing the energy available in the generating process.

The availability of X-ray pulses with ultrahigh intensity has opened new avenues for nonlinear physics and ultrafast imaging (see Chapter 17). A major concern in the field of ultrafast imaging is the danger of sample decomposition due to ionization by X-rays before the diffraction image (2D or 3D) is acquired. A theoretical study by Neutze *et al.* proposed that the ideal light source for this type of imaging should have about 10^{12} photons in a fully coherent pulse with 5 fs duration or less, and with 12 keV photon energy [3]. For soft X-ray imaging (typically 30 eV to 1 keV photon energy), the parameters differ significantly. This energy range corresponds to wavelengths from 30 nm down to 1 nm, allowing experiments with diffraction-limited resolution of a few nanometers. Unlike the case discussed by Neutze, diffraction will not occur on molecular electrons but on nanoscale structures or sample structural variation. The bulk matter structure does not evolve as fast as molecular electrons, which often acquire relativistic speed. The relevant time scales are therefore defined by the speed of sound, typically 10^4 ms^{-1} for the density and temperature under consideration. To reach a target spatial resolution of 1 nm, the soft X-ray pulse duration should be on the order of 100 fs to prevent blurring during image exposure at the irradiation levels considered.

Soft X-rays are often absorbed by the sample, reducing the signal flux at the detector. Hence the experiments require a high energy per pulse. To find an es-

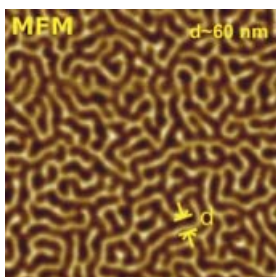


Figure 5.1 False color image of a magnetic system. The variation of color indicates a change on spin orientation. The image has been achieved with magnetic force microscope.

timate of the required threshold energy, we consider two experiments. Mancuso *et al.* [4] imaged algae by coherent diffraction. With a single-shot ($15 \mu\text{J}$ pulse energy), the signal was only strong enough for low diffraction angles, that is, to resolve large structural features between 650 and 1200 nm. To achieve a 230 nm resolution, Mancuso averaged 1500 shots, equivalent to a total energy of about 15 to 20 mJ on the sample. At the Laboratoire d'Optique Appliquée,¹⁾ we achieved coherent diffraction on magnetic samples. The magnetic samples show aligned 65 nm domains, as evident from the magnetic force microscope displayed in Figure 5.1.

The soft X-ray source used in our experiments produced 20 nm radiation through high harmonic generation with intense 35 fs, 8 mJ, 800 nm laser pulses at 1 kHz repetition rate (Figure 5.2). To achieve an image contrast sufficient for recovering the parameters of the sample, an integrated X-ray energy of about 1 mJ was used (about 10^6 shots). The resulting diffraction image displayed structure due to the alignment of the magnetic domains and confirms the aforementioned considerations: An ideal source for soft X-ray imaging should emit a pulse of about

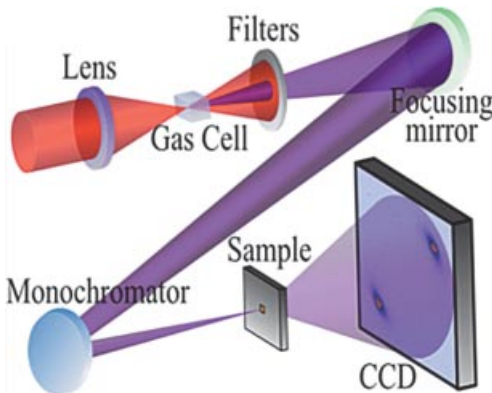


Figure 5.2 Schematic representation of the diffraction experiment on magnetic samples. The 800 nm laser pulses (red beam) generated high harmonics (purple beam). A diffraction image is acquired on a CCD behind the sam-

ple. The image displayed on the CCD shows a real experimental result, with two spots of diffraction due to the alignment of the magnetic domains.

1) In collaboration with LCPMR-Paris, France, and CEA- Gif/Yvette, France.

100 fs duration containing about 1–10 mJ of spatially coherent photons. Note that for holography, temporal coherence is also required.

Currently, three classes of soft X-ray sources ($\lambda = 4\text{--}50\text{ nm}$) have the potential to produce the high energy per pulse required for single femtosecond shot imaging: free-electron lasers (FEL), plasma-based soft X-ray lasers (PBSXRL), and high harmonic generation (HHG). Among these sources, PBSXRL routinely demonstrate extreme pulse energies of up to 10 mJ [5]. FEL and HHG sources reach several 10 μJ and a number of microjoule, respectively [6, 7], several orders of magnitude below the value required for single-shot nanometer resolution imaging.

PBSXRL reach the required energy level, but only when running in the so-called amplification of spontaneous emission mode (ASE). This regime consists of amplifying the stochastic self-emission of the plasma. In the absence of a system ensuring spatial mode selection (spatial filter or optical cavity), the output beam is highly divergent ($>10\text{ mrad}$), weakly coherent and does not exhibit any commensurable polarization. Furthermore, reduction of the pulse duration is not an easy process, since the pulse duration is governed by complex hydrodynamics. Today, the shortest ASE plasma-based soft X-ray laser emits pulses of 2 ps [8]. The PBSXRL sources are therefore not overly attractive for coherent imaging or for many other applications in nonlinear physics that are concurrently developed with FEL or HHG technology.

Seeding plasma sources with coherent X-ray pulses may hold great promise, but only a number of experiments and theoretical studies have been performed on seeding plasma sources. The seeding and amplification of high harmonics in a plasma was demonstrated by Zeitoun *et al.* [9]. The resulting pulses from both, solid and gas amplifiers, were fully coherent in space and in time, showed low divergence, and were fully polarized. However, the output energy of the amplified pulses was limited to below about 1 μJ with a pulse duration of about 1 ps [10–12]. Other studies have been performed with plasmas emitting about 1–10 μJ of ASE [13]. Current short pulse PBSXRL, when forced into space and time coherence by seeding, therefore do not seem to compete well with other soft X-ray sources. A solution for keeping the optical and temporal properties of HHG during amplification in plasma is required to create pulses with mJ or more energy.

5.2

Choice of Plasma-Based Soft X-Ray Amplifier

Plasma-based soft X-ray lasers represent a diverse family. Plasma may be created either by electrical discharge, infrared (visible) lasers, or X-ray free-electron lasers.

Electrical discharge soft X-ray lasers offer the potential for tabletop, high repetition rate (10 Hz or more) sources, but to date, only systems for a single wavelength (46.9 nm) exist [14]. This is a severe limiting factor and thus we will not further consider electrical discharge lasers in this chapter. X-ray free-electron lasers recently demonstrated their ability to pump soft X-ray lasers at several wavelengths [15].

However, the output is limited at a few microjoule, far below the requirement of single-pulse coherent imaging discussed here.

Soft X-ray lasers pumped by optical lasers were demonstrated with gas, liquid and solid targets, and with wavelengths ranging from 3 to 60 nm [16–18] and repetition rate up to 100 Hz [11, 19]. To determine the possibilities of this approach, we need to consider the plasma for each case and address whether they offer the possibility to reach millijoule energy levels in pulses of 100 fs duration. Towards this end, this chapter will describe in-depth studies using a number of different models. Some general trends can be considered thanks to rules validated in other types of lasers, operating in the infrared to visible and UV spectral range. Prior to considering these rules, we would like to recall some basic aspects of high harmonic amplification processes.

5.2.1

Basic Aspects of High Harmonic Amplification

The conceptual geometry for seeded plasma amplification is displayed in Figure 5.3. For a homogeneous plasma amplifier of length L , the output intensity is given by the incoherent sum of the amplified seed and the amplified self-emission (ASE):

$$I_{\text{out}}(\nu, t) = I_{\text{in}}(\nu, t)(e^{G(\nu, t)L} - 1) + \frac{j(\nu, t)}{G(\nu, t)}(e^{G(\nu, t)L} - 1), \quad (5.1)$$

where $G(\nu, t)$ is the spectrotemporal gain coefficient (“gain”) and $j(\nu, t)$ is the emissivity (a parameter characterizing the level of self-emission).

For laser-driven soft X-ray lasers, the self-emission is incoherent in space and often results in long pulses (ps to 100s of ps). This corresponds to spurious emission. Multiple efforts are required to reduce self-emission to a negligible level.

For a first-order approximation for seeded plasma amplification, we may consider only the first term in Eq. (5.1), meaning that the seed intensity is an order of magnitude higher than the plasma self-emission intensity. Currently, seeding experiments are all set using optics to focus the seed on the plasma entrance. In that case, this assumption is fulfilled. We note that increasing the plasma length will exponentially increase the output intensity. At some high intensity (the level

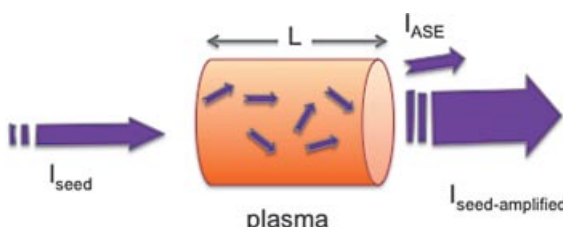


Figure 5.3 Schematic representation of the seeding geometry. The output beam consists of amplified seed and the stochastic self-emission of the plasma.

depends on the lasing medium), the system will saturate. The density of energy stored in the medium is comparable to that of the amplified wave. The rising part of the pulse will be amplified, while the tail will encounter a medium with reduced population inversion (i.e., reduced gain). The exponential regime is called amplification in the small signal regime. Taking saturation into account, the gain G is given by the formula:

$$G(\nu, t) = \frac{G_0(\nu, t)}{1 + \frac{I(\nu, t)}{I_{\text{sat}}}}, \quad (5.2)$$

where I_{sat} is the saturation intensity corresponding to $G = G_0/2$.

For intensities far above the saturation intensity, the amplification is growing linearly with the plasma length. This is the deep saturation regime.

By integrating both sides of Eq. (5.1) over time, we obtain the same type of evolution for the fluence (i.e., surface density of energy). Equation (5.2) might be rewritten by substituting $I(\nu, t)$ with $F(\nu, t)$. The saturation fluence F_{sat} is given by:

$$F_{\text{sat}}(\nu) = h \frac{\nu}{\sigma(\nu)}. \quad (5.3)$$

Here, ν is the soft X-ray laser central frequency and σ is the stimulated emission cross-section given by:

$$\sigma(\nu) = \frac{\lambda^2}{8\pi} A_{21} \frac{\beta}{\Delta\nu}, \quad (5.4)$$

where A_{21} is Einstein's coefficient for the laser transition, $\Delta\nu$ is the full width half maximum value of the spectral width, and β is a parameter depending on the spectral profile with $\beta = (2\sqrt{\ln 2})/\sqrt{\pi}$ for a Gaussian profile and $\beta = 2/\pi$ for a Lorentzian profile.

Two avenues allow us to reach very high pulse energies. The first is by an increase of the plasma length. From Eq. (5.2), we observe that this solution is efficient before and near saturation. When the system is deeply saturated, the output energy increases nearly linearly with length. A high pumping energy is therefore required. The second consists of increasing the plasma cross-sectional surface, so as to keep the system always near saturation. Amplification remains strong and thus one may extract more energy from the same pump energy. The second avenue is explored here and corresponding results are presented below.

It is worth noting that we may also increase the saturation fluence by reducing the stimulated emission cross-section. The easiest solution consists of optimizing the plasma conditions so as to lead to significant enhancement of the lasing spectral width (Eq. (5.4)). This strategy is particularly interesting, since the production of short pulses, by using seeding techniques, requires a soft X-ray laser with a spectral width as large as possible. Indeed, the seed being high harmonics from infrared lasers have most often a duration of tens of femtoseconds, two to three orders of magnitude shorter than ASE soft X-ray lasers. In this particular seeding regime, the output pulse is always at the Fourier limit. Note that pulse broadening

due to the high harmonic spectral phase is assumed to be negligible. This point will be discussed in more details at the end of this chapter.

The link between fluence, spectral width and pulse duration has often been verified with visible or infrared lasers. Gas lasers, due to their very narrow spectral width, are known to have much lower saturation fluence than solid-state lasers and they support amplification of pulses with much longer duration than solid-state lasers. Therefore, our search will be mainly oriented towards the use and optimization of X-ray amplifiers created from interaction of an intense pump laser with a solid target.

5.2.2

Basic Aspects of Plasma Amplifiers

In the following, we recount some basic knowledge on plasma amplifiers, which will be useful for the rest of this chapter. To date, only the so-called collisional scheme has demonstrated saturation. Pumping of the plasma medium occurs by energy transfer during collisions between the plasma free electrons and the lasing ions. To increase the pumping rate, and thus the gain, the plasma has to be dense and hot. To extract a high amount of energy, the lasing ions have to be the predominant species inside the plasma (at least at the time of seeding the high harmonic). This implies using very stable ions, which cannot be over-ionized easily. Such ions must have the highest possible ionization potentials and follow closed shell isoelectronic sequences. Therefore the electronic structure of those ions resembles helium (2 bound electrons), neon (10 electrons), or particles with closed subshells such as nickel (28 electrons), or palladium (56 electrons). Helium-like ions require extreme pumping intensities and lasing has never been demonstrated for such ions.

Considering the so-called collisional scheme, specialists often discriminate two regimes, respectively called quasi-steady-state (QSS) and transient collisional electron pumping (TCE). To understand the difference between the two regimes, we have to consider once again the pumping process. While pumping the plasma with nanosecond to sub-ns lasers, the hydrodynamic time scale is around 100 ps (variation in density or temperature), while the collisions between lasing ions occur in the 1–10 ps time range. Therefore, the ion population is always close to local thermodynamic equilibrium.²⁾ In this case, population inversion cannot be strong. Highest gains achieved in the QSS regime are on the order of a few units per centimeter, requiring long plasmas of several centimeters to achieve saturation³⁾ [20–23]. Also, the laser energy transferred as kinetic energy onto the free electrons is only partially available for pumping the ions: most energy is absorbed by ionization, plasma expansion, thermal loss by heat conduction, and radiative losses. All these processes are relatively slow, but due to the long pump laser duration, they

- 2) Population inversion intrinsically requires that the atoms or ions are removed from their thermodynamic equilibrium.
- 3) It is generally admitted that saturation arises for a $G \times L$ product of about 18 for collisional scheme.

compete strongly with ion pumping. Consequently, QSS soft X-ray lasers consume high amounts of pump energy.

TCE is an interesting regime, where a long pulse of moderate energy ionizes the plasma at, or slightly below the lasing stage. Population inversion is not, or only weakly created. A second, short pulse (1–10 ps) then interacts with the pre-formed plasma. The second pulse energy is instantaneously transferred to the free electrons and induces very strong pumping. During a short time of about a few picoseconds, the ions are not over-ionized, placing the plasma very far from thermal equilibrium [24]. Gains in this regime can be extremely high, ranging from 50 to 100 per centimeter of plasma medium [25–28]. Saturation is achievable for millimeter long plasmas [29, 30]. Due to the speed of the pumping, thermal conduction and radiation or kinetic losses are minimized. The transient regime requires much lower pumping energy than QSS for reaching saturation, typically 1 J for TCE [25] as compared to several 100 J for QSS [20, 31, 32].

The most natural choice of amplifier would be the transient scheme, which can be constructed in a tabletop setup. However, at this stage, we did not clarify the capacity of either scheme to produce multi-mJ pulse energies in a femtosecond pulse.

In conclusion from this introductory part, we separated the pumping schemes in two classes, depending on the pump laser duration [33, 34]. Typically, for lasers longer than a few tens of picoseconds, the plasma evolved slowly and the atomic populations are placed in the so-called quasi-steady-state (near local thermodynamic equilibrium). The amplification coefficient is rather low, ranging at a few units per cm. For pump pulses shorter than tens of ps, the plasma is far from LTE, leading to very high gain of several tens to 100s per cm of plasma. We also observed that for reaching our goal of 10 mJ in a 100s fs soft X-ray laser, both the amplification region cross-section and the soft X-ray laser line width have to be maximized through hydrodynamic tailoring.

5.3

2D Fluid Modeling and 3D Ray Trace

The interaction of intense lasers with a solid target is rather complex and often driven by hydrodynamic behavior. From now to the end of this chapter, we will concentrate on pump lasers with pulse durations of 1 ps or more. In that regime, the laser radiation is mainly absorbed by inverse Bremsstrahlung, by accelerating the free electrons in the field of the laser photons in the vicinity of plasma ions. At intensities typically used for pumping a soft X-ray laser, below $10^{15} \text{ W cm}^{-2}$ for shorter pulses and below $10^{14} \text{ W cm}^{-2}$ for longer pulses, we may neglect parametric instabilities (energy transfer from the laser to plasma waves) or resonant absorption.

5.3.1

ARWEN Code

Our major tool for this study is the ARWEN code [35]. This code has been used in several fields, such as those involving inertial confinement fusion [36], laboratory astrophysics [36], and plasma-based seeded soft-X-ray lasers [37, 38], and thus has been thoroughly benchmarked. The postprocessing of ARWEN data aiming to extract small-signal gain and saturation fluence is done with a simple atomic level model developed at the LOA/LIXAM laboratories [38, 39]. The ARWEN code is a 2D hydrodynamic code, incorporating radiation transport, that was developed at the Instituto de Fusión Nuclear of the Universidad Politécnica de Madrid, Spain. The equations solved are those of radiation hydrodynamics with thermal conduction.

$$\frac{\partial \rho}{\partial t} + \nabla(\rho u) = 0 \quad (5.5)$$

$$\frac{\partial \rho u}{\partial t} + \nabla(\rho uu) = -\nabla(P_m + P_r) \quad (5.6)$$

$$\frac{\partial \rho E_m}{\partial t} + \nabla[\rho E_m u + (P_m + P_r)u] = S_E + \nabla q_c + \nabla q_r \quad (5.7)$$

$$\Omega \nabla I + k I = \varepsilon \quad (5.8)$$

$$\nabla q_c = -\nabla k_e \nabla T \quad (5.9)$$

$$\nabla q_r = \int (k I - \varepsilon) d\nu \quad (5.10)$$

$$E_r = \frac{1}{c} \int I d\Omega d\nu \quad (5.11)$$

$$P_r = \frac{1}{3} E_r \quad (5.12)$$

Here, ρ is the density, u is the velocity vector, P_m and P_r are, respectively, the matter and radiation pressure tensors, E_m is the energy of the matter, S_E is the laser energy source, q_c and q_r are, respectively, the heat flux due to conduction and radiation, c is the speed of light, I is the radiation intensity, Ω is the solid angle, k and ε are, respectively, the opacity and the emissivity of the medium, k_e is the thermal conductivity, ν is the frequency of the radiation, and E_r is the energy of the radiation field. The Navier–Stokes equations, Eqs. (5.5)–(5.7) are solved with an Eulerian scheme, using a high-order Godunov type method with an approximate Riemann solver [40]. Flux-limited thermal electron conduction, Eq. (5.9), and radiation transport, Eqs. (5.8) and (5.10), are treated with multigrid [41] and Sn multigroup methods [42, 43], respectively. Matrix-free solvers for thermal conduction are available in the new version of the code. Laser energy deposition is treated with a simple model, as explained later. The laser energy is treated as a source term for Eq. (5.9). Planar and cylindrical geometries are available.

Equations of state necessary for calculating the plasma evolution are obtained from the QEOS code [44]. The equation of state and the multipliers are adjusted

to fit experimental data such as the Hugoniot curves. Opacities are computed with the JIMENA code [45], also developed at the Instituto de Fusión Nuclear.

The ARWEN code and all its packages are based on the adaptive mesh refinement (AMR) technique [46, 47]. In plasma hydrodynamic simulations, it is common to have small zones where high resolution is needed to describe shock waves or high-energy zones, whereas the majority of the computational domain is well resolved with coarser grids. The AMR technique creates patches of finer grids where they are needed, producing a uniform numerical error and saving computational time. The structure of levels and grids is created and controlled by the C++ library BoxLib [CCSE]. The output of the code is in read-write memory (rwm) and also a standard Hierarchical Data Format (HDF) format to facilitate postprocessing with other codes. We postprocess using an atomic model as described below; other codes, such as SHADOX [48], exist to model the injection and amplification of radiation in the plasma.

5.3.2

Model to Obtain 2D Maps of Atomic Data

The hydrodynamic parameters obtained from ARWEN were postprocessed [38, 49] to obtain 2D maps of atomic data in the small-signal gain regime, and to determine the saturation fluence. This postprocessing was done with a simple three-level atomic model that computed the gain and saturation fluence on the $2p_{1/2}^5 3s_{1/2}$, $J = 1 \rightarrow 2p_{1/2}^5 3p_{1/2}$, $J = 0$ neon-like Fe¹⁶⁺ transition, occurring at $\lambda = 25.5$ nm (see Figure 5.4). This calculation slightly overestimated the gain [50].

In our model, we postulate that the lower level $1s^2 2s^2 2p^6$ is much more populated than the other two levels. There is a forbidden transition between the lower level and an upper lasing level $1s^2 2s^2 2p^5 3p_{1/2}(J = 0)$. The lower lasing level $1s^2 2s^2 2p^5 3s_{1/2}(J = 1)$ depopulates quickly toward the fundamental level, creating a population inversion between the two lasing levels by collisional excitation, as shown by Witten *et al.* [52]. This phenomenon was confirmed later by Goldstein *et al.* [53], demonstrating that collisional excitation is the dominant process

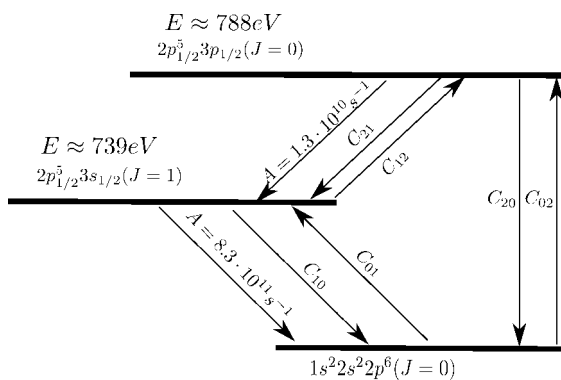


Figure 5.4 Simplified Grotrian scheme and transitions obtained from [51] for Ne-like Fe.

for populating the laser levels at the high temperatures that typically exist in these plasmas [25]. The objective of the model is to compute the small-signal gain coefficient $g_0 (\nu = \nu_0)$ and the saturation fluence $F_{\text{sat}}(\nu = \nu_0)$ at the lasing line central frequency ν_0 . For simplicity of notation, we will later use $g_0(0)$ and $F_{\text{sat}}(0)$, with

$$g_0(\nu = \nu_0) = \left(N_2 - \frac{\gamma_2}{\gamma_1} N_1 \right) \sigma_{\text{stim}}(\nu = \nu_0) \quad (5.13)$$

$$F_{\text{sat}}(\nu = \nu_0) = \frac{h\nu_0}{\sigma_{\text{stim}}(\nu = \nu_0)}. \quad (5.14)$$

In these formulas, N_i and γ_i are the population and degeneracy of the i th level of the transition and σ_{stim} is the stimulated emission cross-section, respectively. These last four values are computed at the line center. The populations of the levels are computed by solving the stationary rate equations of our three-level model,

$$\frac{dN_i}{dt} = \sum_j C_{ij} n_e N_j + \sum_j A_{ij} N_i \quad (5.15)$$

$$\frac{dN_i}{dt} = 0, \quad (5.16)$$

where C_{ij} are the collisional excitation rates between levels i and j , A_{ij} are the spontaneous emission and absorption coefficients, N_i are the populations of the corresponding levels i , and n_e is the electron density. The plus or minus sign is included in the coefficients, describing the effect of the transition (populating or depopulating level i). The upper (numbered 2) and lower (numbered 1) lasing levels are $2p_{1/2}^5 3p_{1/2} J = 0$ and $2p_{1/2}^5 3s_{1/2} J = 1$, respectively. The fundamental level (numbered 0) is $2p^6 J = 0$. The mechanisms taken into account in our model are collisional excitation between the fundamental and the two lasing levels ($0 \rightarrow 2$, $0 \rightarrow 1$), collisional deexcitation, and radiative transitions ($2 \rightarrow 1$, $1 \rightarrow 0$). Electron collisional rates are Van Regemorter's rates [54], which depend on the electron temperature, computed as explained above, and electron density, also given by our code. The rates are calculated assuming that the electrons have a Maxwellian distribution of velocities,

$$C_{ij} \approx 1.6 \times 10^{-5} \frac{f_{ij} \langle g \rangle}{\Delta E_{ij} \cdot \sqrt{k T_e}} e^{-\Delta E_{ij} / k T_e} \quad (5.17)$$

$$C_{ji} = \frac{\gamma_i}{\gamma_j} C_{ij} e^{-\Delta E_{ij} / k T_e}, \quad (5.18)$$

where f_{ij} is the oscillator strength, $\langle g \rangle$ is the Gaunt factor (assumed to be $\langle g \rangle = 0.2$), ΔE_{ij} is the difference of energy between levels i and j , k is Boltzmann's constant, and T_e is the electron temperature. The stimulated emission cross-section is computed as follows:

$$\sigma_{\text{stim}}(\nu) = \Phi(\nu) \frac{\lambda^2}{8\pi} A_{21}, \quad (5.19)$$

where A_{21} is Einstein's coefficient of the $2 \rightarrow 1$ transition and $\Phi(\nu)$ is the spectral line profile. We assume only a Doppler profile. Neglecting collisional broadening

reduces the profile width, artificially augmenting the gain and underestimating the saturation fluence [55], as shown by Koch and co-workers [56]. The Doppler effect is the principal mechanism of line broadening. In addition to this, we computed the value of the gain at the center of the line profile. Then, the peak Doppler value is

$$\Phi_D(0) = \lambda \left(\frac{m}{2\pi k T_i} \right)^{1/2}, \quad (5.20)$$

where m is the atomic mass of the lasing ions, k is Boltzmann's constant, and T_i is the ion temperature. These simulations of transient collisional excitation pumping, using a combination of a long nanosecond pulse and a short picosecond pulse, were performed with a single-temperature hydrodynamic version of the ARWEN code. During the interaction of the long pulse with the plasma, both electron and ion fluids have enough time to thermalize through collisions. This assumption has been validated in several experiments and in the modeling of plasmas heated with nanosecond pulses [53, 57, 58]. However, the peak gain appears only after interaction with the picosecond pulse, when the electron temperature has been dramatically increased, while the ion temperature still remained nearly unchanged. Consequently, we calculated the gain at the instant of the peak value using the ion temperature before the interaction with the short pulse and the electron temperature as the value given by ARWEN at the moment of the pulse interaction.

Although ARWEN has been thoroughly benchmarked previously, we decided to check it again for soft X-ray laser conditions, accounting for our target geometry, the relevant pump lasers and so on. For this purpose, we used the only carefully detailed seeding experiment with a solid amplifier performed so far. We use the data from the seeded experiment, as opposed to the results from the multiple other experiments performed over more than 30 years, because we need to obtain a good experimental estimate of the gain, the saturation fluence and the output energy. Using ASE soft X-ray lasers, the duration of the soft X-ray pulse is given mainly by the plasma hydrodynamics. As long as the pumping conditions are right (high electron density and temperature, and the appropriate level of ionization) the plasma will amplify the spontaneous emission. ARWEN and our gain calculation postprocessor do not yet take into account the possibility to amplify several independent waves. Direct comparison with ASE soft X-ray lasers may therefore induce mistakes by orders of magnitude. However, using an ultrafast seed, the soft X-ray laser is, based on the zero-order approximation, emitting only one wave. We will see later (Section 5.4) that this assumption has to be slightly reconsidered for very intense seed pulses.

Figure 5.5 shows the plasma electron density and gain modeled by ARWEN, using the parameters of the experiment reported by Wang *et al.* [13]. The gain reached a maximum value of 61 per cm, to be compared with 60 per cm measured by Wang *et al.* The surface of the gain zone is rather small (cf. [38, 49]), due to a very strong plasma expansion along the target surface. This flow induces a fast drop of density and temperature, and thereby a reduction of the collisional pumping. We notice

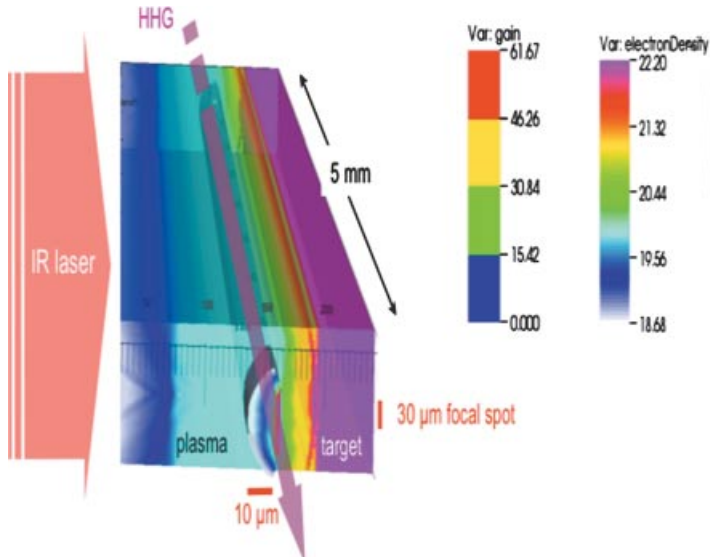


Figure 5.5 Electron density and gain maps in false colors for a plasma as described by Wang *et al.* [13].

that the plasma extension along the target surface is more than twice the focal line width.

We also calculate the saturation fluence that allows us to estimate the output energy. The value of the saturation fluence of 1.3 mJ/cm^2 is in good agreement with the experiment (1.8 mJ/cm^2). The only assumption we have to introduce at this step of benchmarking is the level of saturation achieved during the experiment. We assumed that Wang *et al.* reached about 10 times the saturation energy, leading to an assumed energy of about 60 nJ, as compared to 75 nJ measured during the experiment. In conclusion, our model agrees well with the different key data measured by Wang *et al.* The very strong lateral plasma flow in our model seems to be highly detrimental for generating a large gain zone and thus a high output energy.

We thus conducted a study aiming to reduce the plasma flow by increasing the lateral width of the IR laser focal line. We changed the focal line width from $20 \mu\text{m}$, narrower than in the experiment of Wang *et al.*, to values up to 2 mm . Figure 5.6 shows the modeled plasma electron density and gain. Due to plasma flow, the plasma width for a narrow focal line (up to $50 \mu\text{m}$) is twice as large as the width of the focal line. For large focal lines, the plasma width is only a few percent larger than the focal line. This reduction of the lateral plasma flow induces an enhancement (by a factor of 6) of the gain zone along the horizontal direction. Also, the gain rises from 13 per cm for a $20 \mu\text{m}$ focal spot to 130 per cm for a line focus wider than $100 \mu\text{m}$. Such favorable properties stem from an enhancement of both, the electron density and temperature. Finally, we observed only weak changes in the saturation fluence in the range from 2.2 to 2.6 mJ/cm^2 .

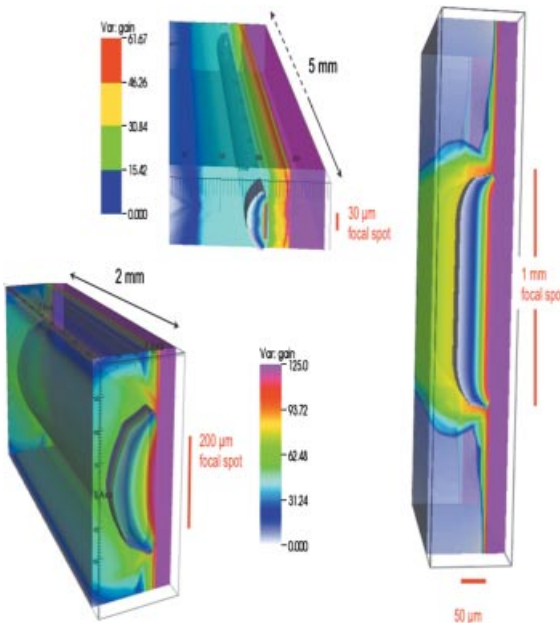


Figure 5.6 Electron density and gain maps, in false colors, for plasmas created with focal widths varying from 20 μm to 2 mm.

These results raise an important issue. Assuming that it is possible to seed every plasma at the same fluence, the length to achieve gain saturation is much shorter for large plasmas thanks to the enhanced gain. Consequently, the enlargement of the line width does not require an increase of pump energy. Furthermore, the enhancement of the gain surface by orders of magnitude allows to extract much more energy for large than narrow plasmas. Considering the issue of pump energy, we estimated the pumping efficiency, that is, the output energy/pump energy, for the different plasmas (Table 5.1). The table clearly shows the change in plasma hydrodynamics. For plasmas narrower than 30 μm , the pumping efficiency is rather low (up to 80 nJ/J), but increases quickly with the plasma width up to 1.1 $\mu\text{J/J}$ for 100 μm width, and saturates at values around 1.7 $\mu\text{J/J}$ for larger plasmas.

Considering that deeply saturated soft X-ray lasers are running typically at 10 times the saturation energy [13], we estimated the output energy at about 22 μJ for 1 mm wide focal width. Although this result represents a breakthrough as compared to existing soft X-ray lasers (output $\leq 1 \mu\text{J}$), it is still far from our goal to reach several mJ. We thus model larger plasmas up to 2 mm width. The result is displayed in Figure 5.7. Again, the plasma is very homogeneous, with nearly no lateral expansion and a very large gain zone. At first glance, it seems an interesting solution to increase the focal width as much as possible for reaching mJ soft X-ray laser pulses (i.e., the pump laser energy should be high enough to keep the pump intensity at its nominal level). However, the plasma vertical extension will generate a spurious effect already observed on Ti:Sa lasers: transverse lasing.

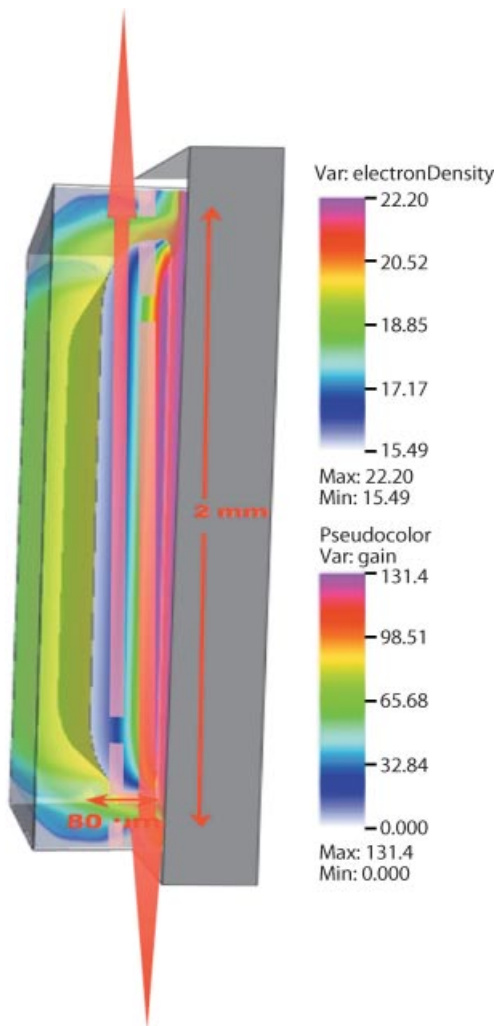


Figure 5.7 Plasmas wide enough (2 mm in this case) will saturate and develop transverse lasing.

With a gain of about 130 per cm and a transverse amplification length of $\Delta y = 2 \text{ mm}$, the gain-length product can be as high as 26. However, it is commonly observed that soft X-ray lasers saturate at a gain-length product of about 18. Thus, self-emission emitted from one side of the plasma will be amplified along the Y direction and can extract most of the energy stored near the other side. Considering 18 as the saturation gain-length, the transverse lasing will be problematic for plasmas larger than 1.4 mm.

One possible solution consists of reducing the pumping intensity, so as to decrease the gain. A reduction by 50% of the pump energy in the short pulse halves

Table 5.1 Width of the plasma, energy of the plasma-inducing nanosecond laser (E_{in}^{ns}), length of the gain zone (L_y), gain, saturation fluence (F_{sat}), saturation energy (E_{sat}), available energy in the population inversion (E_{avail}), output energy (E_{out}), pumping efficiency (Eff).

Width (μm)	E_{in}^{ns} (J)	E_{in}^{ps} (J)	L_y (mm)	Gain (cm ⁻¹)	F_{sat} (mJ/cm ²)	E_{sat} (μJ)	E_{avail} (μJ)	e_{out} (μJ)	Eff (μJ/J)
20	0.75	1.75	13	13	2.2	1×10^{-3}	0.017	0.01	4×10^{-3}
30	0.24	0.56	6	60	2.3	6×10^{-3}	0.25	0.06	8×10^{-2}
50	0.3	0.7	11	80	2.4	6×10^{-2}	6	0.6	0.6
75	0.33	0.77	13	110	2.5	0.11	16	1.1	1.0
100	0.39	0.91	12	124	2.5	0.15	22	1.5	1.1
150	0.57	1.33	16	126	2.6	0.31	65	3.1	1.6
200	0.78	1.82	17	126	2.6	0.46	97	4.6	1.8
1000	4.0	9.2	16	126	2.6	2.2	447	22	1.7

the gain. In that case, the 2 mm large plasma does not generate too strong transverse lasing. With this condition, we estimate the total output energy to be around 44 μJ.

In conclusion, we numerically studied the hydrodynamic behavior of plasmas created by the so-called transient collisional electron pumping scheme. We clarified the reason for anomalously low energies achieved by seeding plasma created from a solid [13] as compared to a gas amplifier [9]. Based on these findings, we explore the path towards amplifiers able to generate millijoule level seeded soft X-ray lasers. It appears that with a saturation fluence of about 2 mJ/cm² and an amplifier surface of about 8×10^{-4} cm⁻², the output energy remains far below our goal of 10 mJ.

5.4

The Bloch–Maxwell Treatment

The hydrodynamic simulations presented in the previous section give valuable information about the temporal evolution of the plasma and several parameters of interest, such as the electron density and temperature. As explained, the gain and saturation fluence are directly related with these parameters and can be computed from these simulations. Nevertheless, the energy that can be extracted can only be roughly guessed from the saturation fluence [38, 49]. Furthermore, there is no information on the spatial and temporal profile of the output XUV beam, nor about the coupling between the XUV radiation and the plasma (i.e., refraction and saturation).

It is therefore necessary to model the amplification of the XUV radiation along the plasma amplifier. Due to the different time scales involved in the process, from tens of femtoseconds (HHG pulse duration), to picoseconds (plasma response), a full time-dependent model is needed. The propagation of the electric field through-

out the plasma is deduced from the Maxwell wave equation particularized in plasma,

$$\Delta E - \frac{1}{c} \frac{\partial^2 E}{\partial t^2} - \frac{\omega_p^2}{c^2} E = \mu_0 P , \quad (5.21)$$

where ω_p is the plasma frequency. For the sake of simplicity, a one-dimensional model will be used, neglecting the transverse Laplacian and retaining the spatial derivatives on the z coordinate only. With this simplification, we lose the capacity of studying refraction and diffraction effects, but the solving of the equations is significantly simplified. Assuming the XUV field is monochromatic, the z component of the electric field can be written as $E_z = \Re[E e^{(-i\omega_0 t + ikz)}]$, where ω_0 is the frequency of the electric field and k its wave number. E is a slowly varying function of space and time (the so-called envelope function). Polarization can be expressed in a similar way. Introducing these functions in the wave equation and neglecting second-order derivatives of the electric field envelope function and first-order derivatives of the polarization envelope function (the so-called slowly varying envelope approximation) we obtain a first-order advection equation for the electric field:

$$\frac{2i\omega_0}{c^2} \left(\frac{\partial E}{\partial t} + c \frac{\partial E}{\partial z} \right) = -\frac{\omega_0}{c^2} \left(-\frac{\omega_p^2}{\omega_0^2} E + \mu_0 c^2 P \right) . \quad (5.22)$$

The numerical solution of this equation is simplified in the reference frame of the photon, using the reduced time $\tau = t - z/c$ and the coordinate change $\xi = c\tau$. With all these approximations, the second-order partial derivative equation is reduced to a first-order ordinary derivative equation, solvable by standard Runge–Kutta methods:

$$\frac{\partial E}{\partial \xi} = \frac{i\omega_0}{2c} \left[\mu_0 c^2 P - \left(\frac{\omega_p^2}{\omega_0} \right) E \right] . \quad (5.23)$$

This equation describes the electric field propagation through the plasma, amplification by the polarization density, and damping by the free-electron current. As usual, a constitutive relation for the polarization is needed. The polarization density is given by $P = Tr(\rho d)$, where d is the density operator and d is the atomic electric dipole. The temporal variation of the matrix elements of the density operator is given by the Bloch equation, particularized in the dipole approximation,

$$i\hbar \frac{\partial \rho}{\partial t} = [H, \rho] , \quad (5.24)$$

$$H = H_A - \mathbf{d} \cdot \mathbf{E} , \quad (5.25)$$

where H_A is the atomic Hamiltonian in absence of the electric field.

Neglecting the second-order (Zeeman) coherences [59] and assuming the light is linearly polarized, the nondiagonal matrix-element follows the equation:

$$\frac{\partial \rho_{21}}{\partial \tau} = -\gamma \rho_{21} + \frac{iE}{\hbar} z_{21}(N_2 - N_1) . \quad (5.26)$$

In this equation γ is the depolarization rate due to collisions and N_1 , N_2 are the populations of the upper and lower levels of the transition (diagonal terms), respectively. The equation for the polarization density is obtained by multiplying the former equation by the dipole matrix element. A stochastic source term Γ [60] is added to account for spontaneous emission. This term is properly normalized to obtain the correct Lorentzian line profile of the soft X-ray field [61]:

$$\frac{\partial P}{\partial \tau} = \Gamma - \gamma P - \frac{iz_{21}^2}{\hbar} E(N_2 - N_1). \quad (5.27)$$

Finally, the populations are computed using standard rate equations coupled with the electric field:

$$\frac{\partial N_2}{\partial \tau} = \sum_k C_{k2} N_k + \Im(E \cdot P) \frac{1}{2\hbar} \quad (5.28)$$

$$\frac{\partial N_1}{\partial \tau} = \sum_k C_{k1} N_k + \Im(E \cdot P) \frac{1}{2\hbar}. \quad (5.29)$$

The populations of the levels are coupled via electron collisional (de)excitation rates C_{ij} and radiative deexcitation rates (included in the C_{ij} coefficients). This set of equations is known as the Maxwell–Bloch equations and allows to study several processes required to understand the amplification of soft X-ray radiation in a plasma, such as Rabi oscillations or amplification of a noisy signal (ASE) mixed with a nonrandom signal (seed HHG).

With this model, the spatio-temporal evolution of the HHG seed throughout the plasma can be studied. As a benchmark of the code, the experiment performed by Wang *et al.* [13] is modeled. The model is based on a plasma created by a laser focused on a $4\text{ mm} \times 30\text{ }\mu\text{m}$ focal line, creating a gain cross-sectional area of about $4 \times 10^{-6}\text{ cm}^2$, as given by our hydrodynamic code (Section 5.2). The seed pulse is 20 fs FWHM with 50 pJ of energy. As this seed is much more intense than the ASE, the plasma is immediately polarized coherently.

This long-lasting polarization (Figure 5.8) generates and amplifies a wake following the HHG pulse. The duration of the wake, defined as the time interval containing half the total energy of the beam, increases in the first millimeters of the amplifier. For longer distances, the interaction between the electric field and the atomic populations starts developing Rabi oscillations, saturating the gain, and reducing the duration of the wake. At 4 mm, the typical structure of the beam is fully developed: a barely amplified HHG pulse and a wake presenting Rabi oscillations and polarization decay [62–64]. After 4 mm, ASE starts to become important. The total energy contained in the beam is 100 nJ after 4 mm (in good agreement with experiments, as refraction effects are not taken into account). This energy is completely contained in the wake, whereas the seeded HHG pulse (140 pJ) is mixed with the ASE, which starts to develop (50 pJ).

A detailed study of how the plasma is polarized by the HHG pulse will be useful to understand the dynamics of the system. An exact solution of the polarization

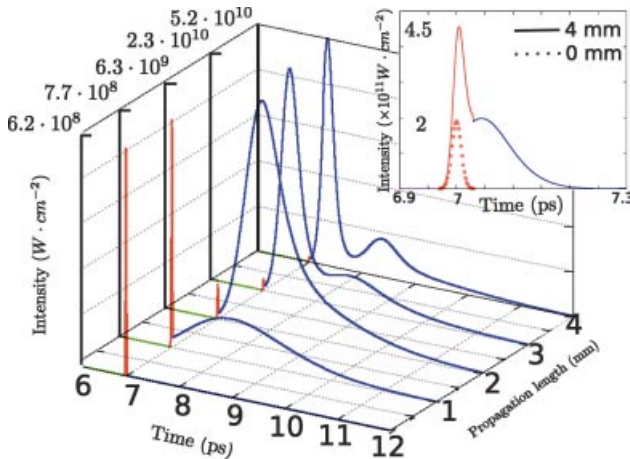


Figure 5.8 Temporal profile of the intensity of a 20 fs, 50 pJ seeded HHG beam at different locations along the plasma amplifier with $N_e = 1.2 \times 10^{20} \text{ cm}^{-3}$ and $T_e = 550 \text{ eV}$. The

colors represent the ASE (green), HHG (red) and wake (blue). The inset shows the temporal profile of the intensity when the seeding equals 15 nJ.

equation at the entrance of the plasma ($z = 0$) can be found assuming the populations are constant during the action of the electric field (which is a good approximation since the duration of the HHG is 20 fs and the populations evolve much slower). This solution can be factorized in three terms $P = P_0 \cdot P_1 \cdot P_2$, which for an electric field with a Gaussian distribution of standard deviation (related to the FWHM duration of the HHG pulse) can be written as,

$$P_0 = -\frac{iz_{21}^2}{\hbar} E_0 (N_2 - N_1) e^{\gamma^2 \sigma^2 / 2} \sigma \sqrt{2\pi} \quad (5.30)$$

$$P_1 = -\frac{1}{\sigma \sqrt{2\pi}} \int_{-\infty}^{\infty} e^{-(t-t_{\text{cent}}-\gamma \sigma^2)^2/(2\sigma^2)} d\tau \quad (5.31)$$

$$P_2 = \begin{cases} e^{-\gamma(t-t_{\text{cent}})} & t \geq t_{\text{cent}} \\ 1 & \text{otherwise} \end{cases}, \quad (5.32)$$

where t_{cent} is the time of the maximum seed intensity and E_0 is the electric field at that time.

Both terms P_1 and P_2 are normalized to unity (i.e., their maximum value is one) and the numerical value of the polarization is given by P_0 . Polarization is created by the electric field and thus the rising time is given by P_1 , whereas the decay time, due to collisions, is given by P_2 . This rising time has the same characteristic time as the seed and follows the electric field with a delay depending on the integral of the electric field (P_1). On the other hand, the depolarization characteristic time depends only on the plasma properties. In the studied case of a 20 fs HHG seeded in a plasma with $N_e = 1.2 \times 10^{20} \text{ cm}^{-3}$ and $T_e = 550 \text{ eV}$, the two characteristic times

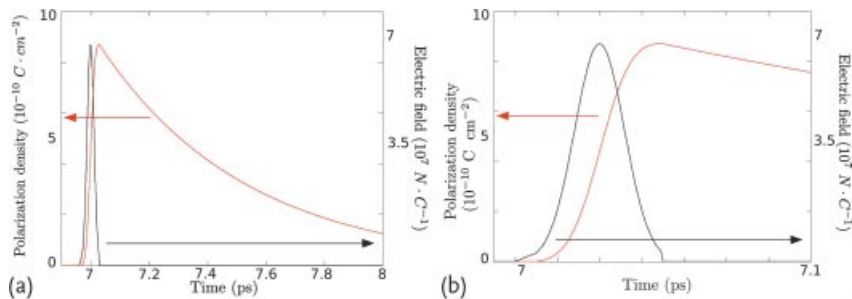


Figure 5.9 Electric field (black) and computed polarization (red) at $z = 0$ mm of a 50 pJ, 20 fs HHG seeded in a plasma with $N_e = 1.2 \times 10^{20} \text{ cm}^{-3}$ and $T_e = 550 \text{ eV}$. The full model (a) and a zoom on the early instants of seeding (b) are shown.

are $\sigma = 9 \text{ fs}$ and $\gamma^{-1} = 500 \text{ fs}$. The depolarization time is an order of magnitude greater than the rising time.

This difference of scale explains the fact that only the wake and not the HHG is strongly amplified. As shown in Figure 5.9, the seed electric field induces the polarization but due to the intrinsic delay, the HHG is barely amplified, as the polarization is still small during their presence. The maximum of the polarization is achieved when the electric field reaches zero and then decays slowly, developing the long-lasting picosecond wake.

Thus, in order to obtain a short and intense pulse, it is necessary to enhance the matching between the electric field and the polarization. This may be achieved by increasing the rise time and by shortening the duration of the pulse, thereby reducing the polarization decay time. Seeding with longer HHG pulses increases the rising time and, in addition to this, augments the polarization value as shown in Eq. (5.31). The polarization decay time can be shortened by increasing the electron density, and thus increasing the collisions that depolarize the medium. As explained, wider plasmas present a denser gain zone, hence, seeding long HHG pulses (hundreds of fs) in these wide, dense plasmas is optimal. With this consideration in mind, a $100 \mu\text{m} \times 4 \text{ mm}$ plasma, seeded with a 1.5 nJ, 200 fs HHG pulse is studied. The gain cross-sectional area is now $6 \times 10^{-5} \text{ cm}^{-2}$ and the electron density and temperature are $N_e = 2.2 \times 10^{20} \text{ cm}^{-3}$ and $T_e = 531 \text{ eV}$. As expected, the electric field matches much better the induced polarization (Figure 5.10a) and the decay time is shorter. The amplification dynamics are completely different now. The HHG seed is directly coupled with the polarization from the beginning of the plasma, forcing the amplification of the HHG pulse itself, as shown in Figure 5.10b. A shorter wake is still observed and Rabi oscillations are developed between 3 and 4 mm. Due to the higher cross-sectional area, ASE already appears before the HHG pulse at 4 mm. The amplified beam exhibits best properties between 2 and 3 mm, with a pulse duration of about 240 fs and an energy of about 1 μJ (of a total of 1.5 μJ).

Seeding at higher energies allows the HHG to saturate the plasma earlier and inhibits the wake. As an example, a 15 nJ, 200 fs HHG seeded in the former plasma has an energy of 1.5 μJ (of a total of 1.7 μJ) in a 2.5 mm long plasma. The duration

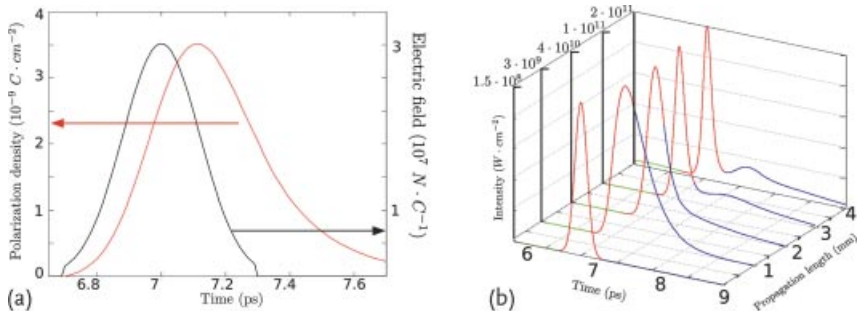


Figure 5.10 Electric field (black) and computed polarization (red) at $z = 0$ mm of a 1.5 nJ, 200 fs HHG (a). Temporal profile of the intensity of the same seeded HHG beam at different parts of the plasma amplifier (b). The col-

ors represent the ASE (green), HHC (red) and wake (blue). In both cases the electron density and temperature are $N_e = 2.2 \times 10^{20} \text{ cm}^{-3}$ and $T_e = 531 \text{ eV}$.

of the beam is 140 fs, as the saturation shortens the HHG and the pulse consists only of the HHG itself, with ASE and wake being negligible [65].

In conclusion, seeding wider plasmas not only allows to extract more energy, as explained in previous sections, but enhances the matching between electric field and plasma polarization, increases the energy, and reduces the duration of the output pulse. The next logical step towards obtaining tens of microjoules would be to study seeding wider (1 mm) plasmas [38, 49]. Nevertheless, the seeding of these bigger plasmas raises new problems, as the strong ASE signal is now strong enough to compete with the HHG signal. As the origin of ASE is the amplification of stochastic noise, the resulting beam will lack spatial coherence. In order to overcome the ASE and to favor the amplification of the seed, a careful modeling of the amplification process is needed.

As Kim *et al.* discussed [64], adjusting the injection time may help the coherent seed to dominate the output beam. As an example, we show the output beam of a $4 \times 1 \text{ mm}^2$ plasma seeded with a 100 nJ, 200 fs HHG in Figure 5.11. It is clearly

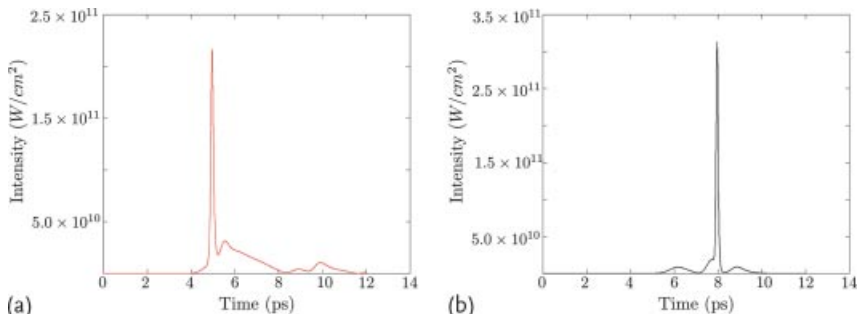


Figure 5.11 Output beam of a $4 \times 1 \text{ mm}^2$ plasma seeded with a 100 nJ, 200 fs HHG. The beam exhibits the classical temporal structure of an intense HHG pulse, Rabi oscilla-

tions, and coherent decay (wake), surrounded by ASE. The seeding time is 2 ps before the maximum value of gain (a) and 1 ps after the maximum value (b).

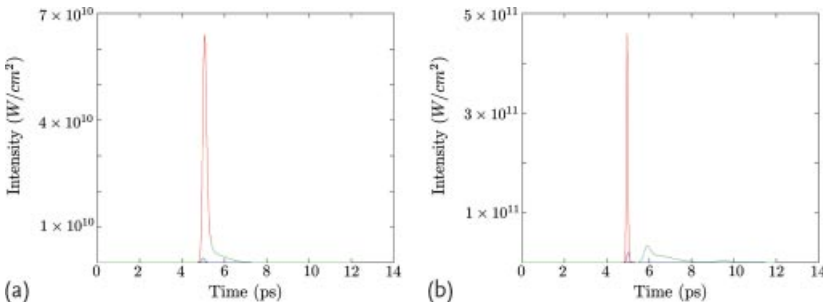


Figure 5.12 Output beam of a 2 mm (length) \times 1 mm (width) plasma seeded with a 100 nJ, 200 fs HHG pulse (a). Output beam of a 4 mm (length) \times 1 mm (width) plasma seeded

with a 2.2 μ J, 200 fs HHG pulse (b). The seed is depicted in blue, the HHG pulse in red, and the wake and ASE in green.

seen that adjusting the seeding time has a strong impact on the output beam temporal profile. When seeding occurs early (Figure 5.11a), the structure composed of HHG and wake (from 5 to 8 ps) is completely developed and clearly differentiated from the ASE, which appears before the HHG and after the wake (after 9 ps). On the other hand, when seeding occurs later, the ASE is strong enough to mask this structure and only the intense spike is observed. Nevertheless, from Figure 5.11b and 5.11a, it is clear that optimizing the seeding time is not sufficient to destroy the ASE signal nor the wake. The output pulse always has complicated temporal structures, preventing the extraction of single short and intense pulses (100 fs or less).

There are several strategies to get rid of the wake and ASE obtaining a short, energetic, single pulse. First of all, it is clear that seeding earlier is better than later as explained in [64]. As the ASE and wake need some millimeters of plasma to develop, shortening the plasma shall inhibit these structures at the cost of decreasing the output power. Another strategy consists of seeding at higher intensities. In this case, the HHG will saturate the plasma, destroying the population inversion and thus preventing the development of the ASE and wake. In Figure 5.12 the output pulse obtained with both strategies is shown.

It is clear that, although the output pulse is improved with each of these strategies, none of the beams is optimal for applications. When the length of the plasma is reduced (Figure 5.12a), the wake is still developed and reducing the length of the plasma further would be impractical, as the HHG pulse would not be amplified sufficiently. Seeding at higher energies (Figure 5.12b), as expected, saturates the amplifier and prevents the wake and ASE to appear after the HHG pulse. Nevertheless, as the gain duration on this kind of plasma has a duration of several picoseconds, the population inversion is recovered some picoseconds after the HHG and the wake and ASE appear later in the beam.

As these two strategies work relatively well, but are not enough to obtain an optimized beam, it is logical to try combining both and seed a short (less than 2 mm), wide (1 mm) plasma with an intense (greater than 1 μ J, 200 fs), structure-free HHG beam. The combination of these techniques should combine all advantages, while

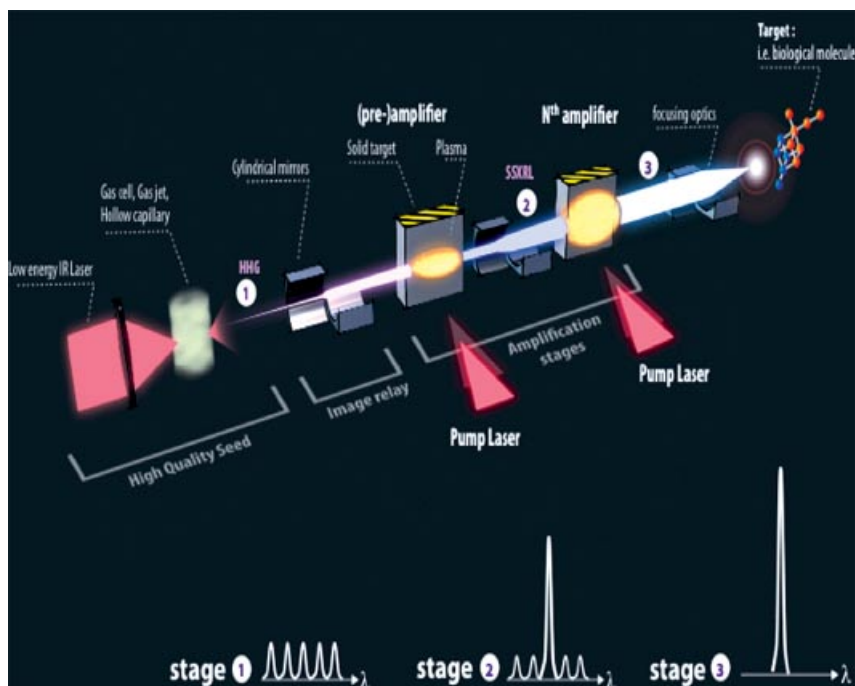


Figure 5.13 Artistic view of a multistage amplification chain working in the soft X-ray range. The seed is HHG source.

the drawback of losing amplification power by shortening the plasma is overcome by seeding at higher energy.

Nowadays, common HHG sources provide tens of nJ, which is clearly insufficient to directly seed these plasmas. Plasma-based soft X-ray lasers easily achieve this energy, but the resulting beam is not coherent. The optimal source to seed these wide plasmas would be another plasma, narrower ($100\text{ }\mu\text{m}$), directly seeded with HHG pulses (Figure 5.13). This preamplifier stage must augment the energy of the seed from several tens of nanojoules to $1\text{--}2\text{ }\mu\text{J}$, while maintaining the duration of the pulse ($\sim 150\text{ fs}$). In addition to this, the output beam of the preamplifier must present a structure free of ASE or wake, as these undesirable features would be strongly amplified in the 1 mm plasma of the main amplifier. The pulse described earlier in this section is ideal in terms of energy, duration and temporal structure to seed wide, dense plasmas.

As shown in Figure 5.14, the 50 nJ , 200 fs beam is amplified in a $2.5\text{ mm} \times 100\text{ }\mu\text{m}$ preamplifier. As this plasma is short and the seed is intense enough, the beam does not develop the wake and the ASE cannot appear. Saturation effects reduce the duration of the pulse to 130 fs . This $1.6\text{ }\mu\text{J}$, 130 fs pulse is seeding the main amplifier and, as explained, the intense beam saturates the medium and the wake cannot appear. In addition to this, as the medium is short, ASE will not

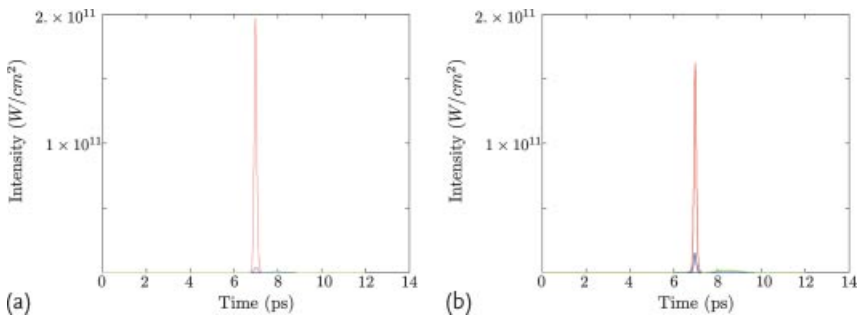


Figure 5.14 Seed beam (50 nJ, 200 fs, blue) and amplified beam (1.6 μ J, 130 fs, red) for a 2.5 mm \times 100 μ m preamplifier plasma (a). This beam is seeded in the 1.5 mm \times 1 mm main amplifier (b). The resulting beam has an energy of 15 μ J in a 120 fs pulse (red).

be developed and the coherent seeded beam will completely dominate the 15 μ J, 120 fs beam.

In conclusion, tens of microjoules in \sim 120 fs, coherent pulses can be routinely obtained seeding short, wide plasmas (1.5 mm \times 1 mm). Nevertheless, these optimal output beams need a carefully optimized seed, strong enough to overcome ASE and prevent the wake to appear. In addition to this, the temporal structure of the seed must not present deleterious structures (ASE or wake), as they will be strongly amplified and thus increase the duration of the pulse.

The optimal source to seed these plasmas would be another narrow plasma (2.5 mm \times 100 μ m), directly seeded with HHG pulses. This preamplifier must be seeded with a HHG source whose duration matches the characteristic depolarization time of the plasma (i.e., the inverse of the electron-ion collision frequency). In this case, the output beam of the preamplifier will be optimal to seed a main amplifier, obtaining a fully coherent, 15 μ J, 120 fs beam.

5.5 Stretched Seed Amplification

In Sections 5.3 and 5.4 we used two independent approaches for calculating the maximum output energy achievable with realistic parameters for transiently pumped seeded soft X-ray lasers. In both cases, we concluded that enlarging the plasma width is the only solution for increasing the output energy. For plasmas as large as 1 mm, the maximum output energy will be in the 10–20 μ J range. Our modeling shows that 2 mm plasmas may deliver about 40 μ J, but with considerable complexity of managing the transverse lasing. Although experimental demonstration of such an energetic ultrashort pulse (120 fs duration) will be a remarkable breakthrough, the energy remains far below the required level of 1 to 10 mJ for single-shot imaging of complex nanoobjects. Another class of amplifier has to be considered, namely QSS. This motivates us to study the very first seeding experiment achieved by Ditmire and collaborators [66]. These QSS X-ray lasers

demonstrate the highest number of photons per pulse, up to 10^{15} , corresponding to an energy of 10 mJ [32]. This compares favorably with existing soft X-ray FELs that emit a maximum of 10^{13} photons per pulse [6, 67].

Modeling a seeding experiment for this kind of amplifier remains a tricky issue. The relevant time scales range from a few femtoseconds for the seed electric field to picoseconds for the atomic processes and hundreds of picoseconds or even nanoseconds for the plasma hydrodynamics. Also, description of the ASE has to be particularly accurate, since Ditmire and collaborators observed that the ASE was orders of magnitude stronger than the amplified seed. A clear understanding of the Ditmire experiment [66] is required to achieve our goal for generating an ASE-free, 100 fs, 10 mJ soft X-ray pulse. First, we tested our Maxwell–Bloch code to model this experiment. Our code, DeepOne, can give precise insight in the process of seeding QSS plasmas with the hope to clarify the path for moving from ASE-dominant to ASE-free, seeded soft X-ray lasers.

All seeding experiments apart from that described by Ditmire [66] exhibit ASE at negligible levels. From our extensive modeling of the TCS scheme (Section 5.4), we observed that ASE starts to have a nonnegligible contribution for large plasmas, about 1 mm wide. Even for such plasmas, ASE is not dominant. In the Ditmire experiment, the focal width for generating the plasma was about 200 μm wide and we would expect to observe some ASE, but not the measured ASE with a 1000-fold stronger energy as compared to the amplified seed. Also, considering the time-resolved signal (Figure 5.15a) it is striking to observe that ASE remains at a very strong level of intensity after amplification of the seed. Considering a classical laser, one would expect to have ASE prior to amplification of the seed. Later, due to gain saturation by the seed, ASE should drop to very low levels (Figure 5.15b). Such behavior has been observed in all our previous modeling, independent of the plasma size (Section 5.4). We must understand the peculiar behavior of seeded QSS plasmas, where the cumulated emission contains strong ASE, to move towards mJ energy amplified HHG pulses.

The most obvious issue to be investigated is the seeding intensity. In the modeling of transient pumping, we observed the crucial role of seeding intensity to extract energy from the plasma. In the Ditmire experiment [66], the seeding intensity was rather low (low energy, low geometrical coupling between the seed and the gain region, long pulse duration), with the drawback that saturation was probably not reached. We modeled the experiment exactly, as well as another case with a seed intensity 1000 times higher (higher energy, 100% coupling, shorter pulse duration). The results are displayed in Figure 5.16a,b.

The model in Figure 5.16a agrees well with the experiment: (1) ASE develops strongly before, but also after the propagation of the seed; (2) the stochastic character of the ASE is clearly visible by the presence of many spikes with variable intensities; (3) the low resolution of the streak camera increases significantly both the ASE spikes and seed duration; (4) the seeded XRL reaches an energy of about 11 μJ and the ASE reaches 5 mJ.

Increasing the seed intensity by a factor of 1000 (Figure 5.16b) changes the ratio between ASE and amplified seed intensities, indicating that the gain in Ditmire's

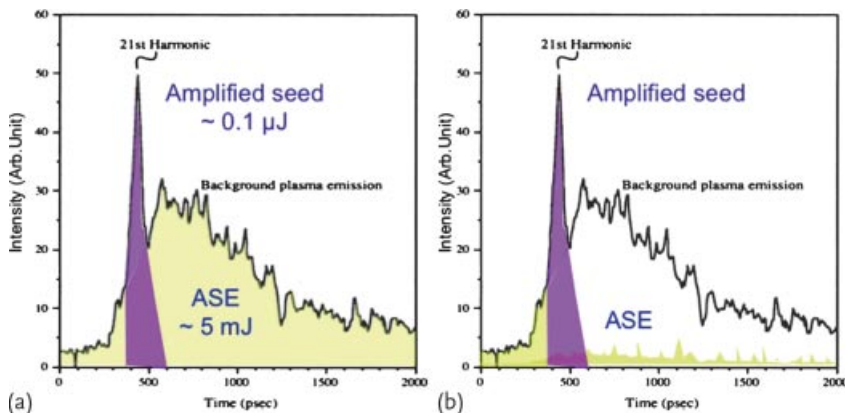


Figure 5.15 Experimental intensity of the seeded HHG and ASE for Ditmire's experiment (a) and expected result if the amplifier had a classical behavior (b) (the seed saturates completely the amplifier).

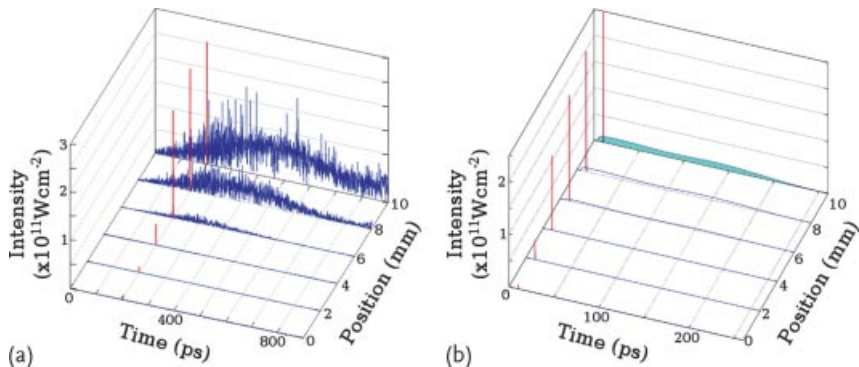


Figure 5.16 Modeling of Ditmire's experiment (a) and a comparable experiment with high intensity seed (b). In the latter case, the result is averaged over time, suppressing the spikes characteristic of ASE.

experiment was not deeply saturated. However, the seed output energy increases by less than a factor of 2, to $20 \mu\text{J}$, while the ASE energy remains at 5 mJ . The latter seems to contradict the previous conclusion that Ditmire's experiment was not running in deep saturation. To clarify this issue, we study the temporal evolution of the gain at two locations along the plasma column, corresponding to different levels of amplification (Figure 5.17). At a location $z = 4 \text{ mm}$ (Figure 5.17a), we observe a strong amplification of the seed (900-fold), characteristic of unsaturated, exponential gain. ASE is not visible, although present at very low intensity. We may observe that the seed pulse induces a very sharp and strong drop of the gain down to nearly 0 per cm, but only for a very short time. For the remaining time, the gain remains unperturbed by the seed. This observation shows that a very intense seed pulse is not sufficient for extracting the energy stored in the plasma.

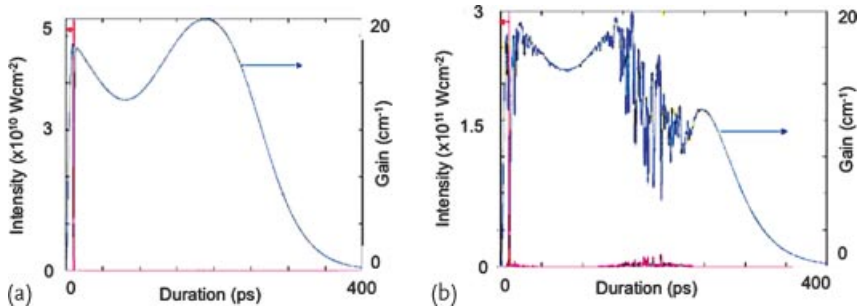


Figure 5.17 Gain (blue) and intensity (seed) for Ditmire's experiment at 4 mm (a) and 5 mm (b). Note that the intensity scales are different.

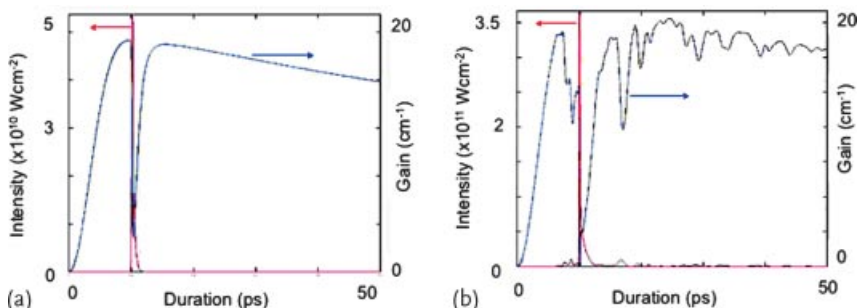


Figure 5.18 Gain (blue) and intensity (red) for Ditmire's experiment at 4 mm (a) and 6 mm (b) zoomed on time. Note that the vertical intensity scales are different.

Considering the time evolution of the gain for position $z = 5$ mm along the plasma column (Figure 5.17b), we observe a weak amplification of the seed (less than a factor of 2 gain, as compared to the location $z = 4$ mm). This is characteristic of deep saturation. We also observe the rise of ASE before and after the seed. At this position, ASE is strong enough to reduce the gain and is reaching saturation for the strongest spikes. Here, we observe the cause for strong ASE after seed amplification.

The presence of unperturbed gain after the saturated seed was not expected, so we zoom into the gain temporal evolution just around the seed, for both locations (Figure 5.18a,b). At $z = 4$ mm, we observe a strong drop of gain to about 3 per cm, revealing deep saturation followed by fast rise of the gain on a time scale of 2 ps (Figure 5.18a). One can also note the development of a weak and short duration wake in the tail of the seed pulse. At $z = 6$ mm, ASE develops before and after the seed with the effect of reducing the gain (Figure 5.18b). Clearly, it is the very fast regeneration of the gain that enables ASE to develop. It shows also that the mJ energy level is not reached due to the unique combination of long gain duration and ultrafast regeneration. *The energy is stored in time and not in space.*

Based on this conclusion, one may understand that extracting the stored energy relies in forcing the lasing ions to amplify only the seed and not spontaneous emis-

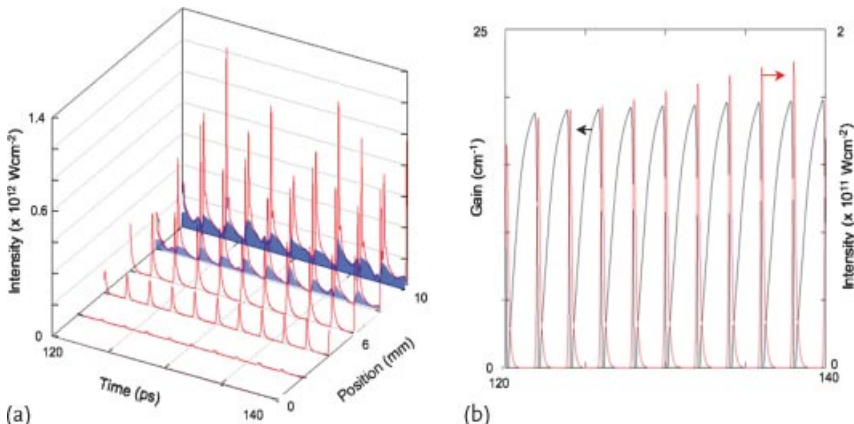


Figure 5.19 Intensity of ASE (blue) and 100 HHG pulses (red), seeded in a QSS plasma and shown at different positions (a). Gain (blue) and HHG intensity (red) at a position of 4 mm (b). Only 20 ps are depicted in both cases.

sion for the complete duration of gain. Several solutions can be considered and will be studied with our Maxwell–Bloch code. For the best concepts that emerge, we will also study possibilities for their implementation.

Since the gain recovers after about 2 ps, a conceptually simple solution consists of seeding a train of femtosecond pulses with a time delay of about 2 ps between the pulses. The number of pulses is chosen to match the total gain duration. In Figure 5.19, we display a zoom in the temporal evolution of the soft X-ray laser intensity (Figure 5.19a) and gain (Figure 5.19b) for the pulse train. The ASE is still amplified, but not at a strong level, while the seed pulses reach very high intensities up to $1.4 \times 10^{12} \text{ W cm}^{-2}$. Each pulse has a duration of 150 fs, equal to the case of single-pulse seeding. We observed that the system is well driven by the seed. This conclusion is confirmed by (Figure 5.19b), where the gain drops to near zero due to the seed intensity. As soon as gain recovers to its initial value, another seed pulse is strongly amplified and reduces the gain again. The total energy contained in the pulse train amplified in nearly⁴⁾ the same plasma as before (Figure 5.19a) reaches 7 mJ, that is, 300 times more than the optimized case for Ditmire's experiment. ASE appears at an energy level as high as 1 mJ. However, for extracting these 7 mJ from the plasma, we seed a train of about 100 coherent pulses. Generating such a pulse train will be very challenging. One solution may exist by trapping one or several femtosecond infrared pulses in a cavity, where a gas jet or gas cell is placed. HHG pulses are emitted at each round-trip by interaction of the intense IR pulse with gas. However, there is no technique to resynchronize all the pulses contained in the train to generate a single 150 fs pulse containing a fraction of the 7 mJ energy of the pulse train. We would like to note that such a source of pulse trains would

4) We considered here the plasma used by Rus *et al.* [32] (zinc at 21.2 nm), which demonstrated the highest energy per pulse at 10 mJ. Ditmire and collaborators achieved about 5 mJ per pulse but for a plasma width two times narrower.

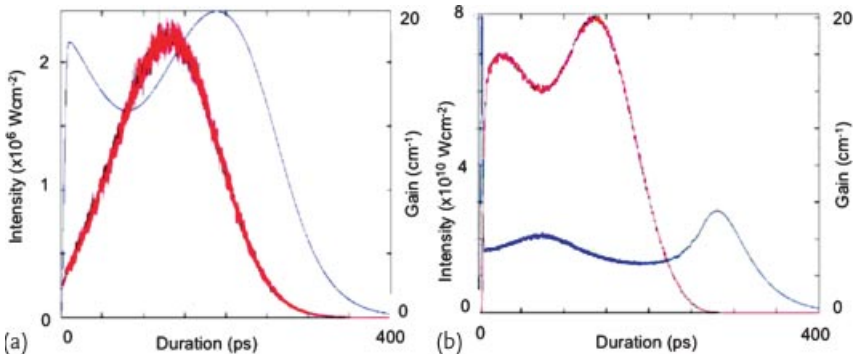


Figure 5.20 Gain (blue) and intensity (red) for a 200 ps HHG pulse seeded in the same plasma as above. Shown is the situation at the beginning of the plasma (a) and 4 mm (b).

find multiple applications, such as coherent nanoimprint [5], or coherent imaging of slowly evolving phenomena (e.g., plasmas created by nanosecond lasers for inertial confinement fusion or laboratory astrophysics).

We next consider the possibility of seeding a single Gaussian 200 ps pulse. To keep the intensity above the spontaneous emission level, we increased the seed pulse energy to 0.1 μJ . Results of the model are shown in Figure 5.20. At the very beginning of the plasma (Figure 5.20a), spontaneous emission is visible superimposed to the coherent seed pulse. The gain is unperturbed. The temporal structure is given from the balance between pumping and atomic processes. At $z = 4 \text{ mm}$ (Figure 5.20b), the seed is strongly amplified. ASE is very weak, demonstrating the efficiency of seeding a long coherent pulse. As soon as the seed interacts with lasin ions, the gain drops nearly instantaneously from 20 per cm down to 3 per cm and rises to its normal value at the end of the seed pulse ($T \sim 300 \text{ ps}$), where seed intensity is very low. The output energy is thus distributed in 8 mJ for the coherent pulse and 0.1 mJ for the ASE. It is interesting to note that the use of a continuous wave, instead of a discrete pulse train, is very beneficial for limiting spontaneous emission amplification.

Although the seed/ASE energy ratio has been well improved as compared to seeding with a single short pulse or a multipulse train, ASE remains at nonnegligible values in the present configuration. We thus studied the case of a much stronger seed, having an initial energy of 10 μJ , while keeping the seed pulse duration at 200 ps. The result is displayed in Figure 5.21. In this case, the spontaneous emission spikes are barely visible at the plasma entrance (Figure 5.21a) or at $z = 4 \text{ mm}$ (Figure 5.21b). The amplifier is therefore dominantly driven by the coherent seed. The coherent energy rises up to 12 mJ, while the ASE drops down to a few μJ . The seed/ASE energy ratio moves from 10^{-3} for Ditmire's case, to 7 for the pulse train and 2000 for the 10 μJ continuous seed.

Considering the implementation of such a long seed, we would like to stress an important issue. Seeding is interesting only if the output beam has an improved optical quality or a shorter duration than the ASE. Whatever the pulse duration of the seed, it has to be spatially fully coherent and, if possible, polarized. To date,

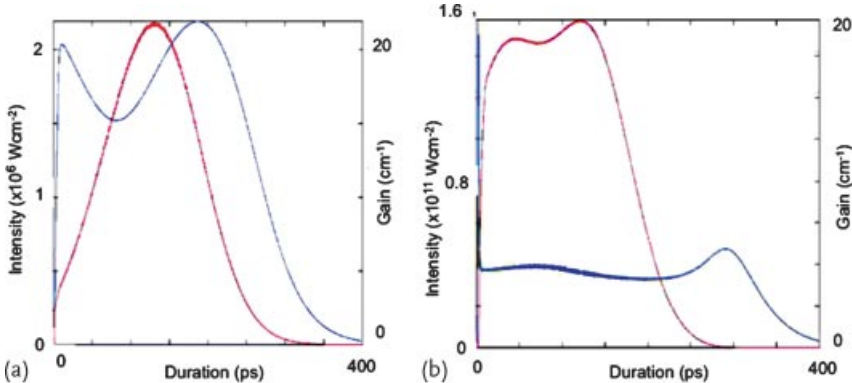


Figure 5.21 Gain (blue) and intensity (red) for a $10 \mu\text{J}$ 200 ps HHG pulse, seeded in the same plasma as above. We show the situation at the beginning of the plasma (a) and at 4 mm (b).

only free-electron lasers and high harmonics of a laser demonstrated full spatial coherence. Although it is possible to seed a plasma with FEL radiation, we will not consider this issue.

High harmonics from a laser have never been produced with pump laser durations longer than a few picoseconds. Indeed, the process of high harmonic generation requires a pulse intensity above several 10^{14} W/cm^2 to be efficient. However, at such intensities, gases are ionized and thereby deteriorate the phase-matching between high harmonic and the pump laser. A solution has been found by reducing the pump laser duration down to tens of femtoseconds and below. Consequently, we doubt that 200 ps high harmonic pulses might be produced directly with a 100 ps infrared laser. Consequently, we explore the possibility of generating intense femtosecond high harmonics and then stretch them to the nominal duration prior to amplification.

Before describing the stretcher, we would like to consider a key issue. As noted before, long (~ 200 ps), spatially coherent soft X-ray pulses have some niche of interest. However, our main goal is to generate high energy ($>\text{mJ}$), femtosecond pulses. This implies that the pulse has to be compressed after amplification. At our level of study, the only viable solution we found is an extrapolation of the chirped pulse amplification method [68] into the soft X-ray range. In this technique, the different spectral components are separated in time by a grating pair, then amplified and recompressed by a similar grating pair. Such a system requires the use of a temporally coherent and phase-locked seed for the compression stage. High harmonic generation pulses are temporally coherent and phase locked [1].

We would like to remind the reader that the intensity $I(t)$ of a pulse, compressed by a perfect grating pair, is given by the following formula:

$$I(z, t) = \left| \int_0^\infty E(z, \nu) e^{-2i\pi\nu t d\nu} \right|^2, \quad (5.33)$$

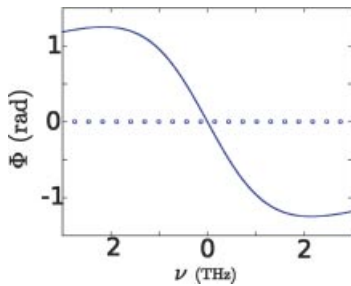


Figure 5.22 Spectral phase of the HHG before (circles) and after passing through a 1 cm amplifier (plain line).

with

$$E(z, \nu) = E_0(z, \nu) e^{-i\varphi(z=0, \nu)} e^{-i\varphi(z, \nu)}, \quad (5.34)$$

where $E(z, \nu)$ is the electric field at location z and at the frequency ν and ϕ is the spectral phase at the plasma entrance $z = 0$ (i.e., seed phase) and after amplification ($z \neq 0$).

Several previous studies measured the high harmonic spectral phases to vary by about 0.1 fs between two consecutive high harmonics [69]. Since the spectral width of the soft X-ray laser is much narrower than the spectral separation between two harmonics, we may assume the high harmonic intrinsic phase to be negligible.

When amplifying a large bandwidth pulse, the different spectral components do not propagate at the same speed inducing a spectral phase deformation. Considering only the Doppler broadening, the phase acquired at the frequency, ν , is given by:

$$\varphi(z, t) = \frac{-\left(\frac{\nu - \nu_0}{\Delta\nu}\right)}{1 + \left[\frac{2(\nu - \nu_0)}{\Delta\nu}\right]^2} \sigma_e G L, \quad (5.35)$$

where $\Delta\nu$ is the spectral width at half maximum and ν_0 is the central frequency.

Figure 5.22 displays the spectral phase, considering the zinc amplifier [32], and a propagation length of 10 mm. The total phase slightly exceeds 2 rad. Only constant and linear phases do not enlarge or modify the pulse duration, meaning that amplification will increase the pulse duration above the Fourier limit (in that case 130 fs, as demonstrated before).

Stretching the pulse with a grating pair separates the spectral components in time. Since the gain in plasmas is not constant in time, the relative intensity of the different spectral components is modified after amplification. We modified our Maxwell–Bloch model accordingly, to consider the seed not as a single frequency but as a large frequency pulse with spectrotemporal stretch. At this step, we convolved the gain at the line center, given by DeepOne, with the lasing line shape assuming a realistic stretch factor (duration of the pulse). Note that we may also modify the instant when the central wavelength arrives. A full calculation is displayed in Figure 5.23.

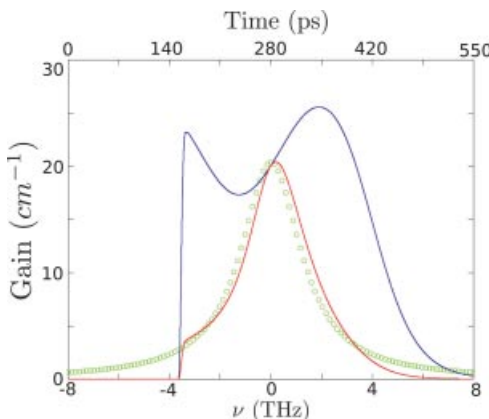


Figure 5.23 Unmodified spectral gain (blue), spectral Lorentzian line shape (green) and convoluted spectral gain (red).

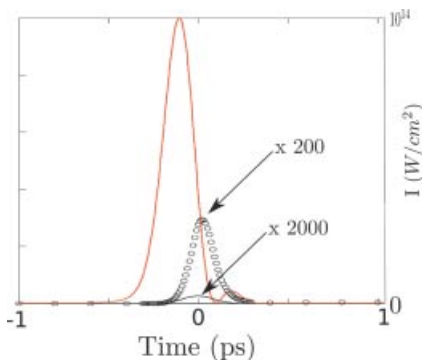


Figure 5.24 HHG intensity seeded in a preamplifier (black line), output intensity of the preamplifier (black dots) and output intensity of a main amplifier after compression. The pulse is asymmetric due to the asymmetries in the spectral gain.

In Figure 5.24, we show the intensity at a preamplifier and a main amplifier entrance, as well as the intensity calculated at the output of the main amplifier considering all the above issues. We observe the generation of a weak postpulse containing 3% of the total energy. It is interesting to note that the asymmetry of the spectral gain, due to the seed timing, induces a forward shift of the amplified pulse as compared to the seed. The main pulse duration is 230 fs, longer than in the case of a single short seed pulse. Nevertheless, we demonstrated that 12 mJ, 230 fs pulses are achievable. This is a formidable leap forward in the race towards ultrahigh intensities and towards single-shot femtosecond imaging.

In the visible spectral range, stretching and compression of laser pulses is performed with prisms and gratings. However, in the soft X-ray regime, absorption by any material is strong and it is barely realistic to consider refractive optics. This leaves gratings as a possible option. In general, X-ray gratings have diffrac-

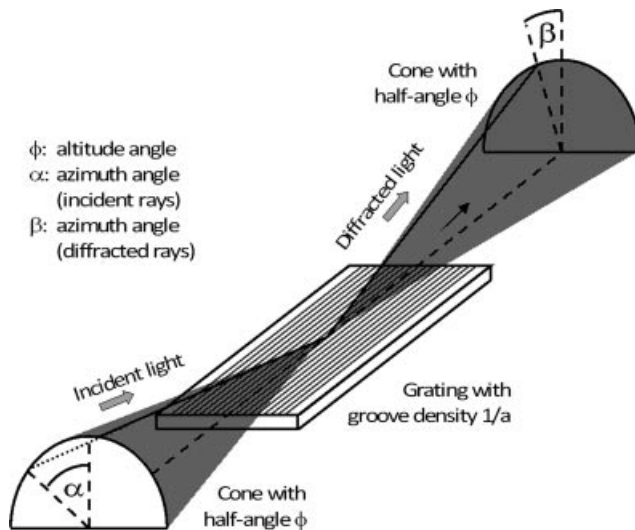


Figure 5.25 Geometry of the off-axis diffraction gratings with definition of the angles. Image from [70].

tion efficiencies, in the first or second orders, of about 10–20%. A classical compressor composed of two parallel gratings will thus have a throughput of 1 to 4%. Such a very low transmission is a major limitation of stretched seed amplification schemes: most of the energy gained by the last amplifier is lost on the gratings. Recently, different groups proposed and experimentally tested a new geometry, called off-axis or conical diffraction. This solution resulted in diffraction efficiencies up to 70% around 20 nm [70]. More precisely, these groups claimed that diffraction efficiency may achieve the value of specular reflection. In their experiment, they used gold coatings, which have a typical efficiency of about 70%. However, for wavelengths in the 10 nm range, carbon (often diamond-like) shows reflectivity up to 95%. A corresponding compressor might then reach an efficiency of about 50% when using gold coating, or up to 80% when using carbon coating.

Considering the use of such off-axis gratings for stretcher and compressor is not trivial, since few studies have been performed so far. Such gratings are mainly used for spatial telescopes as monochromator (one grating) or as low-dispersion monochromator (two gratings) in combination with high harmonic generation. We fully studied the stretcher and compressor geometry based on Martinez's seminal article [71]. Here we give only the main results.

The diffraction equation of an off-axis grating is given by

$$\sin \phi \times (\sin \theta + \sin \theta') = n \frac{\lambda}{a}, \quad (5.36)$$

where θ and θ' are the incident and diffracted angles and ϕ is the off-axis incident angle, also called altitude angle. The general geometry is given in Figure 5.25.

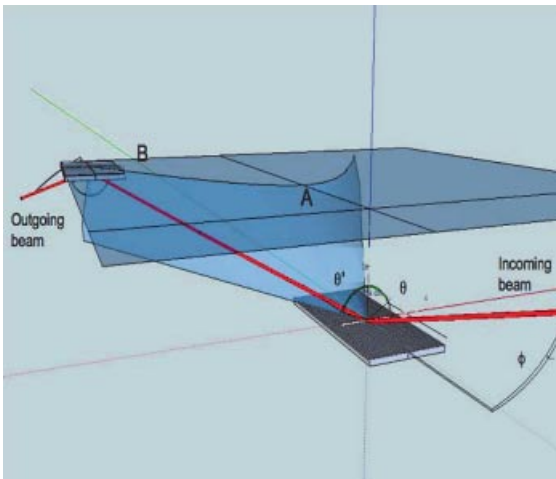


Figure 5.26 Artistic view of a stretcher based on off-axis diffraction. The blue cone represents the full diffraction, considering all ϕ and θ angles. Point A is the region of low dispersion and point B is the region of high dispersion.

Considering every angle ϕ and θ , the diffracted wave covers a cone (Figure 5.26). The region of the cone covered by a collimated beam, such as the soft X-ray laser, depends on the incidence angles ϕ and θ . The part near the top of the cone (point A) has a low stretch factor, since the dispersion is mainly perpendicular to the light propagation, while parts near B may have strong dispersion. We will choose this region by choosing the appropriate incidence angles and placing the second grating accordingly.

It is interesting to remark that Eq. (5.36) can be modified to

$$\sin \theta + \sin \theta' = n \frac{\lambda}{a'}, \quad (5.37)$$

with the equivalent groove spacing $a' = a \times \sin \phi$.

This equation corresponds to classical diffraction with a grating of smaller line pitch, given by $a \times \sin \phi$. This remark raises two major conclusions (verified by full diffraction calculations).

The diffraction efficiency is maximal for a grating with a line pitch equal 0.7λ . Considering the spectral range of soft X-ray plasma amplifiers (4–50 nm typically) and classical gratings, this would require the use of a nanometer pitch grating, which are not commercially available. However, for an altitude angle of about 10° , a commercially available 5000 lines/mm grating (200 nm pitch) works like a 29 000 lines/mm grating, that is, 35 nm pitch. For $f = 5^\circ$, the equivalent grating is 57 000 lines/mm (17 nm pitch).

Based on the analogy with equivalent gratings, we verified that the second and third dispersion orders, Φ'' and Φ''' , are modified from the classical value (see [71]

Table 5.2 Typical parameters for different stretcher and compressor geometries based on conical diffraction.

λ_0 (nm)	$\Delta\lambda$ (nm)	Φ (°)	Θ (°)	Groove per mm	Inte- grating distance (m)	Beam length on first grating (mm)	Beam length on second grating (mm)	Stretched duration (ps)	Fourier- limited duration (fs)
21	0.005	19.3	69.22	1000	1200	1.1	270	207	139
id	id	id.3	68.7	1000	120	id	30	20.4	id
id	id	id	66.4	id	id	id	3	2	id
13	0.002	19.21	53.12	5000	1200	1.28	280	197	134
4	0.0005	18.4	69.33	5000	1200	1.11	320	213	51

for example) according to the following formula:

$$\Phi_{\text{off-axis}}'' = \frac{\Phi''}{\sin \phi} \quad (5.38)$$

$$\Phi_{\text{off-axis}}''' = \Phi''' \times \sin \phi . \quad (5.39)$$

Small ϕ correspond to the part of the cone far from point A, where dispersion is achieved nearly parallel to the diffracted wave propagation axis, inducing a very strong temporal delay ϕ'' between the spectral components.

Stretcher and compressor have to be treated independently. Indeed, to stretch a pulse with gratings, a negative distance between the gratings is required, which is obtained by imaging the first grating on the back of the second grating. The image can be generated with any magnification. At this step of our work, we consider only a magnification of 1. Compressors are based on two parallel gratings with a positive distance between them, requiring no additional optics. Examples of geometries are given in Table 5.2.

Finally, we would like to present two versions of the full amplification chains including amplification using X-ray CPA, based on all the developments and modeling we have done so far. Figure 5.27 displays the full setup including a high-energy pump laser (100 J class). Currently, these lasers have a low repetition rate, except for the Mercury laser (65 J at 10 Hz) [72, 73]. However, several groups and firms actively work to improve the repetition rate of other high-energy lasers. Thanks to the development of the extreme light infrastructure (ELI) in Europe within the next few years, 100 J commercially available lasers are expected to deliver about 1 shot every minute. On the 5–7 year time frame, 1–10 Hz lasers are expected. As explained throughout this chapter, it is crucial to keep the seeding intensity at a relatively high level (about 10^6 to 10^8 W cm^{-2}) for coherently driving the amplifier. This means that a preamplifier(s) has to be used. For the case of 200 ps stretched seed duration, a 10 μJ seed is necessary, requiring two plasma preamplifiers (see Part 3). However, stretching the HHG seed from typically 20–200 fs up to 200 ps

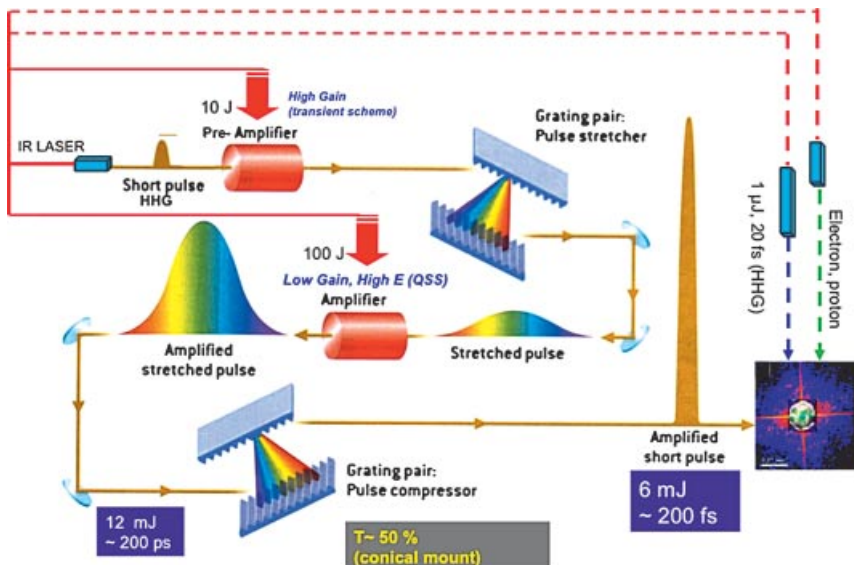


Figure 5.27 Schematic representation of the full X-ray CPA architecture using both QSS and TCE amplifiers. A single infrared laser generates the HHG seed (left) that is injected in the first plasma created by the IR laser, then the amplified HHG is stretched on a grating pair and send for further amplification in a plasma created by the IR laser and finally send

to a grating pair for compression. On the right we display a typical diffraction image from a nanoobject. Using multi-PW lasers, some of the IR energy may be used to generate HHG around $1\mu\text{J}$ (blue dotted arrow) or a relativistic electron bunch to excite the sample. Since each beam is generated from the same laser, they are jitter-free.

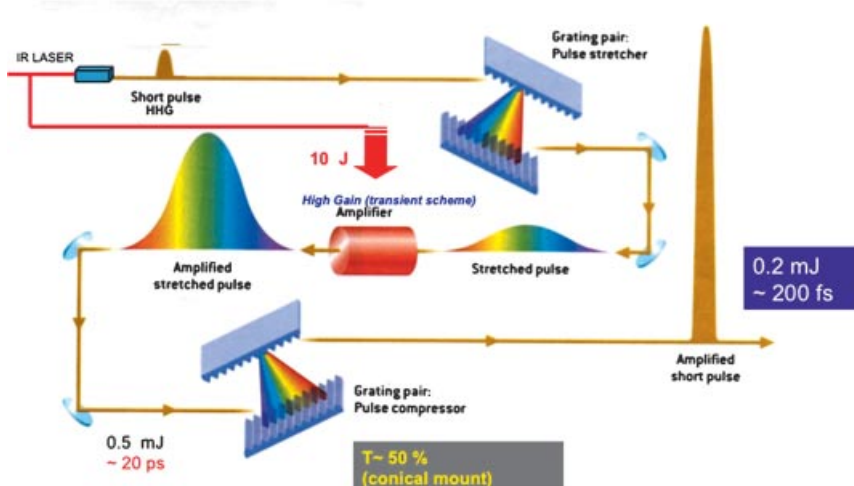


Figure 5.28 Schematic representation of the downscaled version of a X-ray CPA soft X-ray laser. This scheme can be operated with a 10 J, 10 Hz pump laser.

induces a dramatic intensity loss. From our modeling (not displayed), we conclude that this loss is too strong for seeding the preamplifier and keeping a high-quality output. However, all amplifiers are coherently driven when a 75 or 100 μm wide preamplifier is seeded and the output pulse is stretched afterwards to seed the latter stages. Finally, we would like to note that with a reasonable enhancement of the total pump-energy (few tens of joules), one may generate electron or hadrons (ions or protons) or other X-ray beams. If every pulse is synchronized without jitter, breakthrough experiments can be imagined, such as pump-probe schemes with the probe using a coherent single-shot flash imaging. Such experiments would have large implications for the fields of biology, medicine, and material science.

The second version we studied is a downscaled X-ray CPA amplifier scheme. In this case, we consider a pump laser delivering several tens of joules. With such a low energy, a QSS plasma cannot be pumped and the full chain is based on transient pumping. A particular requirement will be to use a short pulse with a pulse duration of about 10–20 ps in order to have a sufficiently long gain lifetime. The HHG pulse will be then stretched to “only” 10–20 ps, limiting the intensity drop. In that case, seeding the plasma after stretching the HHG pulse is feasible. The architecture is displayed in Figure 5.28.

5.6 Conclusion

In this chapter, we have shown that, despite important recent breakthroughs, existing soft femtosecond X-ray sources with energies of about 10 to 100 μJ lack photons for recording single-shot images by coherent diffraction or holography. This holds true for absorbing or highly scattering living or inert samples. Sources that deliver several mJ pulse energy in a single pulse must be developed to fulfill this goal.

We numerically studied different paths for achieving such extreme bursts of light. Amplification of existing fully coherent sources in a plasma amplifier seems to be the most viable solution. With our newly developed model DeepOne, we demonstrated that plasmas created by the so-called transient collisional excitation scheme will not deliver coherent pulses with an energy exceeding 40 μJ in 120 fs.

We thus worked out an alternative seeding experiment that used plasma created by the so-called quasi-steady-state scheme. We showed that direct seeding, using a 100 fs pulse, also limits the achievable energy to several tens of μJ . Therefore, we proposed to either amplify a pulse train (7 mJ output over 100 pulses), or to use a new concept called stretched seed amplification to obtain up to 12 mJ pulse energy. With resynchronizing 100 pulses being barely feasible, we concentrated on the second scheme. By stretching a high harmonic pulse with a grating pair, it is possible to generate a 200 ps pulse and thus amplify it efficiently in QSS plasma. The pulse can be recompressed by a grating pair to near the Fourier limit (215 fs), thanks to the phase-locked characteristic of high harmonics. Using off-axis diffraction, losses on grating can be minimized, promising a 6 mJ, 215 fs, fully coherent pulse.

X-ray CPA can be easily downscaled with a plasma amplifier that has gain lasting about 10 ps. In that case, a 10 Hz, few-joule laser can pump the plasma. Also, our work on plasma tailoring (Section 5.3) for transient pumping led us to believe that doing the same optimization on QSS soft X-ray lasers will allow to increase the output energy by at least a factor of 10, leading to 0.1 J fully coherent soft X-ray lasers.

The X-ray CPA process can also be used to enhance the output energy of seeded soft X-ray free-electron lasers. In that case, the amplifying medium will be the free electron and no longer the plasma. Seeding has been done at the fundamental wavelength of the Free-electron laser [74]. In that case the stretcher and compressor will follow the design showed above. Seeding can also be done at high wavelengths with lasing on the seed harmonics [75]. In that case, the stretcher will correspond to a classical mount.

Acknowledgments

Authors would like to thank J. Gauthier, G. Lambert, K. Cassou, M. Pitman, M. Marty, G. Chériaux, H. Merdji, V. Cebban, G. Mourou for fruitful discussions. The work has been partially supported by NEST-Adventure TUIXS EC Sixth Framework Programme, SFINX-LASERLAB EC Seventh Framework Programme under grant agreement no. 228334 and the SHYLAX project from RTRA-Triangle de la Physique.

References

- 1 Paul, P.M., Toma, E.S., Breger, P., Mullot, G., Auge, F., Balcou, P., Muller, H.G., and Agostini, P. (2001) Observation of a Train of Attosecond Pulses from High Harmonic Generation. *Science*, **292**, 1689.
- 2 Kaplan, A.E. and Shkolnikov, P.L. (2002) Lasetron: A Proposed Source of Powerful Nuclear-Time-Scale Electromagnetic Bursts. *Phys. Rev. Lett.*, **88**, 074801.
- 3 Neutze, R., Wouts, R., van der Spoel, D., Weckert, E., and Hajdu, J. (2000) Potential for biomolecular imaging with femtosecond X-ray pulses, *Nature*, **406**, 752.
- 4 Mancuso, A.P., Gorniak, T., Staier, F., Yefanov, O.M., Barth, R., Christophis, C., Reime, B., Gulden, J., Singer, A., Pettit, M.E., Nisius, T., Wilhein, T., Gutt, C., Grubell, G., Guerassimova, N., Treusch, R., Feldhaus, J., Eisebitt, S., Weckert, E., Grunze, M., Rosenhahn, A., and Vartanyants, I.A. *et al.* (2010) Coherent imaging of biological samples with femtosecond pulses at the free-electron laser FLASH. *N. J. Phys.*, **12**, 035003.
- 5 Mocek, T., Rus, B., Kozlová, M., Polan, J., Homer, P., Juha, L., Hájková, V., and Chalupský, J. (2008) Single-shot soft X-ray laser-induced ablative microstructuring of organic polymer with demagnifying projection. *Opt. Lett.*, **33**, 10, 1087.
- 6 Ackermann, W., Asova, G., Ayvazyan, V., Azima, A., Baboi, N., Bähr, J., Balandin, V., Beutner, B., Brandt, A., Bolzmann, A. *et al.* (2007) Operation of a free-electron laser from the extreme ultraviolet to the water window. *Nat. Photonics*, **1**, 341.
- 7 Takahashi, E., Nabekawa, Y., Nurhuda, M., and Midorikawa, K. (2003) Generation of high-energy high-order harmon-

- ics by use of a long interaction medium. *J. Opt. Soc. Am. B*, **20**, 1, 58.
- 8** Klisnick, A., Kuba, J., Ros, D., Smith, R., Jamelot, G., Chenaïs-Popovics, C., Keenan, R., Topping, S.J., Lewis, C.L.S., Strati, F., Tallents, G.J., Neely, D., Clarke, R., Collier, J., MacPhee, A.G., Bortolotto, F., Nickles, P.V., and Janulewicz, K.A. *et al.* (2002) Demonstration of a 2-ps transient X-ray laser. *Phys. Rev. A*, **65**, 033810.
- 9** Zeitoun, P., Fairve, G., Sebban, S., Mocck, T., Hallou, A., Fajardo, M., Aubert, D., Balcou, P., Burg, F., Douillet, D., Kazamias, S., de Lachèze-Murel, G., Lefrout, T., le Pape, S., Mercere, P., Merdji, H., Morlens, A.S., Rousseau, J.P., and Valentin, C. *et al.* (2004) A high-intensity highly coherent soft X-ray femtosecond laser seeded by a high harmonic beam. *Nature*, **431**, 426.
- 10** Mocck, T., Sebban, S., Maynard, G., Zeitoun, P., Fairve, G., Hallou, A., Fajardo, M., Kazamias, S., Cros, B., Aubert, D., de Lachèze-Murel, G., Rousseau, J., and Dubau, J. (2005) Absolute time-resolved X-Ray laser gain measurement. *Phys. Rev. Lett.*, **95**, 19–22.
- 11** Wang, Y., Larotonda, M.A., Luther, B.M., Alessi, D., Berrill, M., Shlyaptsev, V.N., and Rocca, J.J. (2005) Measurement of 1-ps soft-X-ray laser pulses from an injection-seeded plasma amplifier. *Phys. Rev. A* **72**, 053807.
- 12** Ecker, B., Oliva, E., Aurand, B., Hochhaus, D., C., Neumayer, P., Zhao, H., Zielbauer, B., Cassou, K., Daboussi, S., Guilbaud, O., Kazamias, S., Le, T.T.T., Ros, D., Zeitoun, P., and Kuehl, T. *et al.* (2012) Gain lifetime measurement of a Ni-like Ag soft X-ray laser. *Opt. Exp.*, **20** (23), 25391–25399.
- 13** Wang, Y., Granados, E., Pedaci, F., Alessi, D., Luther, B., Berrill, M., and Rocca, J.J. (2008) Phase-coherent, injection-seeded, table-top soft-X-ray lasers at 18.9 nm and 13.9 nm. *Nat. Photonics*, **2**, 94.
- 14** Rocca, J.J., Clark, D.P., Chilla, J.L.A., and Shlyaptsev, V.N. (1996) Energy extraction and achievement of the saturation limit in a discharge-pumped table-top soft X-ray amplifier. *Phys. Rev. Lett.*, **77**, 1476.
- 15** Rorhinger, N., Ryan, D., London, R.A., Purvis, M., Albert, F., Dunn, J., J.D. Bozek, Bostedt, C., Graf, A., Hill, R., Hau-Riege, S.P., and Rocca, J.J. (2012) Atomic inner-shell X-ray laser at 1.46 nanometres pumped by an X-ray free-electron laser. *Nature*, **481**, 488.
- 16** Jaeglé, P., Jamelot, G., Carillon, A., Sureau, A., and Dhez, P. (1974) Super radiant line in the soft X-ray range. *Phys. Rev. Lett.*, **33**, 18, 1070.
- 17** MacGowan, B.J., Da Silva, L.B., Fields, D.J., Keane, C.J., Koch, J.A., London, R.A., Matthews, D.L., Maxon, S., Mrowka, S., Osterheld, A.L., Scofield, J.H., Shimkaveg, G., Trebes, J.E., and Walling, R.S. (1992) Short wavelength X-ray laser research at the Lawrence Livermore National Laboratory. *Phys. Fluids*, **4**, 7.
- 18** Daido, H., Ninomiya, S., Imani, T., Kodama, R., Takagi, M., Kato, Y., Murai, K., Zhang, J., You, Y., and Gu, Y. (1996) Nickel-like soft-X-ray lasing at the wavelengths between 14 and 7.9 nm. *Opt. Lett.*, **21** (13), 958.
- 19** J. Tiemann, Jung, R., Stiel, H., Nickles, P.V., and Sandner, W., (2009) 10-Hz grazing-incidence pumped Ni-like Mo X-ray laser. *Opt. Lett.* **34** (9), 1378.
- 20** Matthews, D.L., Hagelstein, Rosen, E., M.J., Ceglio, N.M., Hazi, A.U., Medecki, H., MacGowan, B.J., Trebes, J.E., Whitten, B., Campbell, E.M., Hatcher, C.W., Hawryluk, Kaufman, Pleasance, L.D., Rambach, G., Scofield, J.H., Pleasance, L.D., and Waver, T.A. *et al.* (1985) Demonstration of soft X-ray amplifier. *Phys. Rev. Lett.*, **54**, 2, 110.
- 21** Rosen, E., Hagelstein, P.L., Matthews, D.L., Campbell, E.M., Hazi, A.U., Whitten, B.L., MacGowan, B.J., Turner, R.E., and Lee, R.W. (1985) Exploding-Foil Technique for Achieving a Soft X-Ray Laser. *Phys. Rev. Lett.*, **54**, 2, 106.
- 22** Rus, B., Carillon, A., Dhez, P., Jaeglé, P., Jamelot, G., Klisnick, A., Nantel, M., and Zeitoun, P. (1997) Efficient, high-brightness soft X-ray laser at 21.2 nm. *Phys. Rev. A*, **55**, 3858.
- 23** Sebban, S., Daido, H., Sakaya, N., Kato, Y., Murai, K., Tang, H., Gu, Y., Huang, G., Wang, S., Klisnick, A., Zeitoun, P.,

- Koike, F., and Takenaka, H., (2000) Full characterization of a high-gain saturated X-ray laser at 13.9 nm. *Phys. Rev. A*, **61**, 4.
- 24** Nilsen, J., Li, Y., and Dunn, J., (2000) Modeling picosecond-laser-driven neon-like titanium X-ray laser experiments. *J. Opt. Soc. Am. B*, **17** (6), 1084.
- 25** Nickles, P.V., Shlyaptsev, V.N., Kalashnikov, M., Schnürer, M., Will, I., and Sandner, W., (1997) Short Pulse X-Ray Laser at 32.6 nm Based on Transient Gain in Ne-like Titanium. *Phys. Rev. Lett.*, **78**, 2748.
- 26** Decker, C.D. and London, R.A. (1998) Designs for a compact Ni-like-tungsten X-ray laser. *Phys. Rev. A*, **57** (2), 1395.
- 27** Klisnick, A., Zeitoun, P., Ros, D., Carillon, A., Fourcade, P., Hubert, S., Jamelot, G., Lewis, C.L.S., Mac Phee, A.G., O'Rourke, R.M.N., Keenan, R., Nickles, P.V., Janulewicz, K., Kalashnikov, M., Warwick, J., Chanteloup, J.-C., Migus, A., Salmon, E., Sauteret, C., and Zou, J.P. *et al.* (2000) Transient pumping of a Ni-like Ag X-ray laser with a subpicosecond pump pulse in a traveling-wave irradiation geometry. *J. Opt. Soc. Am.*, **17**, 1093.
- 28** Lin, J.Y., Tallents, G.J., MacPhee, A.G., Demir, A., Lewis, C.L.S., O'Rourke, R.M.N., Pert, G.J., Ros, D., and Zeitoun, P. (1999) Travelling wave chirped pulse amplified transient pumping for collisional excitation lasers. *Opt. Comm.*, **166** (1–6), 211–218.
- 29** Li, Y., Dunn, J., Nilsen, J., Barbee Jr., T.W., Osterheld, A.L., and Shlyaptsev, V.N. (2000) Saturated tabletop X-ray laser system at 19 nm. *J. Opt. Soc. Am. B*, **17** (6), 1098.
- 30** Keenan, R., Dunn, J., Patel, P.K., Price, D.F., Smith, R.F., and Shlyaptsev, V.N. (2005) High-Repetition-Rate Grazing-Incidence Pumped X-Ray Laser Operating at 18.9 nm. *Phys. Rev. Lett.*, **94**, 103901.
- 31** Rus, B., Carillon, A., Gauthe, B., Goedtkindt, P., Jaegle, P., Jamelot, G., Klisnick, A., Sureau, A., and Zeitoun, P. (1994) Observation of intense soft X-ray lasing at the $J = 0$ to $J = 1$ transition in neonlike zinc. *J. Opt. Soc. Am. B*, **11** (4), 564
- 32** Rus, B., Mocek, T., Prag, A.R., Kozlova, M., Jamelot, G., Carillon, A., Ros, D., Joyeux, D., and Phalippou, D., (2002) Multimillijoule, highly coherent X-ray laser at 21 nm operating in deep saturation through double-pass amplification. *Phys. Rev A*, **66**, 063806.
- 33** Daido, H. (2002) Review of soft X-ray laser researches and developments. *Rep. Prog. Phys.*, **65**, 1513–1576.
- 34** Tallents, G.J. (2003) The physics of soft X-ray lasers pumped by electron collisions in laser plasmas. *J. Phys. D*, **36**, R259–R276.
- 35** Ogando, F. and Velarde, P., (2001) Development of a radiation transport fluid dynamic code under AMR scheme. *J. Quant. Spectrosc. Radiat. Transf.*, **71**, 541.
- 36** Velarde, P., García-Senz, D., Bravo, E., Ogando, F., Relaño, A., García, C., and Oliva, E. (2006) Interaction of supernova remnants: From the circumstellar medium to the terrestrial laboratory. *Phys. Plasmas*, **13**, 092901.
- 37** Cassou, K., Zeitoun, P., Velarde, P., Roy, F., Ogando, F., Fajardo, M., Faivre, G., and Ros, D. (2006) Transverse spatial improvement of a transiently pumped soft-X-ray amplifier. *Phys. Rev. A*, **74**, 045802.
- 38** Oliva, E., Zeitoun, P., Fajardo, M., Velarde, P., Cassou, K., Ros, D., and Sebban, S. (2009) Optimization of soft X-ray amplifier by tailoring plasma hydrodynamics. *Opt. Lett.*, **34**, 2640.
- 39** Cassou, K., Kazamias, S., Ros, D., Plé, F., Jamelot, G., Klisnick, A., Lundh, O., Lindau, F., Persson, A., Wahlström, C.-G., de Rossi, S., Joyeux, D., Zielbauer, B., Ursescu, D., and Kühl, T. *et al.* (2007), Optimization toward a high-average-brightness soft-X-ray laser pumped at grazing incidence. *Opt. Lett.*, **32**, 139.
- 40** Colella, P. and Glaz, H.M. (1985) Local adaptive mesh refinement for shock hydrodynamics. *J. Comput. Phys.*, **59**, 264.
- 41** Ewing, R.E. (1987) *Multigrid Methods*, (ed. S.F. McCormick) In *Multigrid Methods*. SIAM, Philadelphia, Pennsylvania.

- 42** Chandrasekhar, S. (1960) *Radiative Transfer*, Dover Publications, New York.
- 43** Lathrop, K.D. (1966) Use of discrete-ordinates methods for solution of photon transport problems. *Nucl. Sci. Eng.*, **24**, 381.
- 44** More, R.M., Warren, K.H., Young, D.A., and Zimmerman, G.B. (1988) A new quotidian equation of state (QEOS) for hot dense matter. *Phys. Fluids*, **31**, 3059.
- 45** Minguez, E. and Falquina, R. (1992) Analysis of atomic physics models for gold plasmas in local thermodynamic equilibrium. *Laser Part. Beams*, **10**, 651.
- 46** Berger, M.J. and Colella, P. (1989) Local adaptive mesh refinement for shock hydrodynamics. *J. Comput. Phys.*, **82**, 64.
- 47** Rendleman, C.A., Beckner, V.E., Lijewski, M., Crutchfield, W., and Bell, J.B., (2000) Parallelization of structured, hierarchical adaptive mesh refinement algorithms. *Comput. Vis. Sci.*, **3**, 147.
- 48** Le Pape, S. and Zeitoun, P., (2002) Modeling of the influence of the driving laser wavelength on the beam quality of transiently pumped X-ray lasers. *Opt. Commun.*, **219**, 323.
- 49** Oliva, E., Zeitoun, P., Velarde, P., Fajardo, M., Cassou, K., Ros, D., Sebban, S., Portillo, D. and Le Pape, S., (2010) Hydrodynamic study of plasma amplifiers for soft-X-ray lasers: a transition in hydrodynamic behavior for plasma columns with widths ranging from 20 μm to 2 mm. *Phys. Rev. E*, **82**, 056408.
- 50** Li, Y., Preztler, G.P., Lu, P., Fill, E., and Nilsen, J. (1997) Study of Ne- and Ni-like X-ray lasers using the prepulse technique. *Phys. Plasmas*, **4**, 479.
- 51** Shirai, T. and Funatake, Y. (1990) *Spectral Data and Grotrian Diagrams for Highly Ionized Iron, Fe VIII–XXVI*, **19** (1), 127–275.
- 52** Whitten, B.L., Hazi, A.U., Chen, M.H., and Hagelstein, P.L. (1986) Effect of dielectronic recombination on the kinetics of neonlike selenium. *Phys. Rev. A*, **33**, 2171.
- 53** Goldstein, W.H., Whitten, B., Hazi, A.U., and Chen, M.H. (1987) Mechanisms for creating population inversion in Ne-like ions. *Phys. Rev. A*, **36**, 3607.
- 54** Van Regemorter, H. (1962) Rate of collisional excitation in stellar atmospheres. *Astrophys. J.*, **136**, 906.
- 55** Whittaker, D.S., Fajardo, M., Zeitoun, P., Gautier, J., Oliva, E., Sebban, S., and Velarde, P. (2010) Producing ultrashort, ultraintense plasma-based soft-X-ray laser pulses by high-harmonic seeding. *Phys. Rev. A*, **81**, 043836.
- 56** Koch, J.A., Mc Gowan, B.J., Da Silva, L.B., Matthews, D.L., Underwood, J.H., Batson, P.J., Lee, R.W., London, A., and Mrwoka, S. (1994) Experimental and theoretical investigation of neonlike selenium X-ray laser spectral linewidths and their variation with amplification. *Phys. Rev. A*, **50**, 2.
- 57** Aliverdiev, A., Batani, D., Dezelian, R., Vinci, T., Benuzzi-Mounaix, A., Koenig, M., and Malka, V. (2008) Coronal hydrodynamics of laser-produced plasmas. *Phys. Rev. E*, **78**, 046404.
- 58** Fajardo, M., Audebert, P., Renaudin, P., Yashiro, H., Shepherd, R., Gauthier, J.C., and Chenais-Popovics, C. (2001) Study of the Ion-Distribution Dynamics of an Aluminum Laser-Produced Plasma with Picosecond Resolution. *Phys. Rev. Lett.*, **86** (7), 1231.
- 59** Sureau, A. and Holden, P.B. (1995) From amplification of spontaneous emission to saturation in X-ray lasers: A Maxwell–Bloch treatment. *Phys. Rev. A*, **52**, 3110.
- 60** Chandrasekhar, S. (1943) Stochastic Problems in Physics and Astronomy. *Rev. Mod. Phys.*, **15**, 1–89.
- 61** Larroche, O., Ros, D., Klisnick, A., Sureau, A., Möller, C., and Guennou, H. (2000) Maxwell–Bloch modeling of X-ray-laser-signal buildup in single- and double-pass configurations. *Phys. Rev. A*, **62**, 043815.
- 62** Al'miev, I.R., Larroche, O., Benredjem, D., Dubau, J., Kazamias, S., Moller, C., and Klisnick, A. (2007) Dynamical description of transient X-ray lasers seeded with high-order harmonic radiation through Maxwell–Bloch numerical simulations. *Phys. Rev. Lett.*, **99**, 123902.
- 63** Kim, C.M., Janulewicz, K.A., Kim, H.T., and Lee, J. (2009) Amplification of a high-order harmonic pulse in an active

- medium of a plasma-based X-ray laser. *Phys. Rev. A*, **80**, 053811.
- 64** Kim, C.M., Janulewicz, K.A., Kim, H.T., and Lee, J. (2010) Coherent amplification of an ultrashort pulse in a high- and swept-gain medium. *Phys. Rev. Lett.*, **104**, 053901.
- 65** Oliva, E., Zeitoun, P., Fajardo, M., Lambert, G., Ros, D., Sebban, S., and Vellarde, P. (2011) Comparison of natural and forced amplification regimes in plasma-based soft-X-ray lasers seeded by high-order harmonics. *Phys. Rev. A*, **84**, 013811.
- 66** Ditmire, T., Hutchinson, M.H.R., Key, M.H., Lewis, C.L.S., McPhee, A., Mercer, I., Neely, D., Perry, M.D., Smith, R.A., Wark, J.S., and Zepf, M. (1995) Amplification of XUV harmonic in a gallium amplifier. *Phys. Rev. A*, **51**, 6.
- 67** Emma, P., Akre, R., Arthur, J., Bionta, R., Bostedt, C., Bozek, J., Brachmann, A., Bucksbaum, P., Coffee, R., Decker, F.-J., Ding, Y., Dowell, D., Edstrom, S., Fisher, A., Frisch, J., Gilevich, S., Hastings, J., Hays, G., Hering, P., Huang, Z., Iverson, R., Loos, H., Messerschmidt, M., Miahnahri, A., Moeller, S., Nuhn, H.-D., Pile, G., Ratner, D., Rzepiela, J., Schultz, D., Smith, T., Stefan, P., Tompkins, H., Turner, J., Welch, J., White, W., Wu, J., Yocky, G., and Galayda, J. *et al.* (2010) First lasing and operation of an angstrom-wavelength free-electron laser. *Nat. Photonics*, **4**, 641.
- 68** Strickland, D. and Mourou, G. (1985) Compression of amplified chirped optical pulses. *Opt. Comm.*, **56**, 219.
- 69** Morlens, A.-S., Gautier, J., Rey, G., Caumes, J.-P., Kos-Rosset, M., Merdji, H., Kazamias, S., Cassou, K., Fajardo, M., and Zeitoun, P. (2006) Design and characterization of extreme-ultraviolet broadband mirrors for attosecond science. *Opt. Lett.*, **31**, 1558.
- 70** Pascolini, M., Bonora, S., Giglia, A., Mahne, N., Nannarone, S., and Poletto, L. (2006) Gratings in a conical diffraction mounting for an extreme-ultraviolet time-delay-compensated monochromator. *Appl. Opt.*, **45** (14), 3253.
- 71** Martinez, O.E. (1987) 3000 times grating compressor with positive group velocity dispersion: Application to fiber compensation in 1.3–1.6 μm region. *IEEE Quantum Electron.*, **QE-23** (1), 59.
- 72** Bibeau, C., Beach, R.J., Bayramian, A., Chanteloup, J.C., Ebbers, C.A., Emanuel, M.A., Kanz, V.K., Orth, C.D., Rothenberg, J.E., Schaffers, K.I., Skidmore, J.A., Smith, L.K., Sutton, S.B., Zapata, L.E., Payne, S.A., and Powell, H.T. (2000) The Mercury laser: a diode-pumped, gas-cooled Yb:S-FAP solid-state laser. Proceedings of CLEO 2000, IEEEExplore, 49.
- 73** Bayramian, A.J., Armstrong, J.P., Beer, G., Campbell, R., Cross, R., Erlandson, A., Freitas, B., Menapace, J., Molander, W., Perkins, L.J., Schaffers, K., Siders, C., Sutton, S., Tassano, J., Telford, S., Ebbers, C.A., Caird, J., and Barty, C.P.J. *et al.* (2009) Compact, efficient laser systems required for laser inertial fusion energy. *Fusion Sci. Technol.*, **56**, 295.
- 74** Lambert, G., Hara, T., Garzella, D., Tanikawa, T., Labat, M., Carre, B., Kitamura, H., Shintake, T., Bougeard, M., Inoue, S., Tanaka, Y., Salieres, P., Merdji, H., Chubar, O., Gobert, O., Tahara, K., and Couprie, M.-E. *et al.* (2008) Injection of harmonics generated in gas in a free-electron laser providing intense and coherent extreme-ultraviolet light. *Nat. Phys.*, **4**, 296–300.
- 75** Allaria, E., Appio, R., Badano, L., Barletta, W.A., Bassanese, S., Biedron, S.G., Borga, A., Busetto, E., Castronovo, D., Cinquegrana, P., Cleva, S., Cocco, D., Cornacchia, M., Craievich, P., Cudin, I., D'Auria, G., Dal Forno, M., Danailov, M.B., De Monte, R., De Ninno, G., Delgiusto, P., Demidovich, A., Di Mitri, S., Diviacco, B., Fabris, A., Fabris, R., Fawley, W., Ferianis, M., Ferrari, E., Ferry, S., Froehlich, L., Furlan, P., Gaio, G., Gelmetti, F., Giannessi, L., Giannini, M., Gobessi, R., Ivanov, R., Karantzoulis, E., Lonza, M., Lutman, A., Mahieu, B., Milloch, M., Milton, S.V., Musardo, M., Nikolov, I., Noe, S., Parmigiani, F., Penco, G., Petronio, M., Pivetta, L., Predonzani, M., Rossi, F., Rumiz, L., Salom, A., Scafuri, C., Serpico, C., Sigalotti, P., Spampinati, S., Spezzani, C., Svandrlík, M., Svetina, C., Tazzari, S., Trovo,

- M., Umer, R., Vascotto, A., Veronese, M., Visintini, R., Zaccaria, M., Zangrandi, D., and Zangrandi, M. *et al.* (2012) Highly coherent and stable pulses from the FERMI seeded free-electron laser in the extreme ultraviolet. *Nat. Photonics*, **6**, 699.
- 76** Oliva, Fajardo, M., Li, L., Pittman, M., Le, T.T.T., Gautier, J., Lambert, G., Velarde, P., Ros, D., Sebban, S., and Zeitoun, P. (2012) A proposal for multi-tens of GW fully coherent femtosecond soft X-ray lasers. *Nat. Photonics*, **6**, 764–767.

Part Two
Theoretical Methods

6

Ionization in Strong Low-Frequency Fields

Misha Ivanov

6.1

Preliminaries

When the laser field is weak, perturbation theory allows us to understand and describe almost everything. But what do you do when perturbation theory is no longer applicable? This is definitely the case in many strong-field processes. Take for example high harmonic generation, where many tens of harmonics have the same intensity – and perturbation theory would require higher-order terms to be smaller and smaller.

In such situations one has to resort to nonperturbative methods where the laser field is included as fully as possible. Fortunately, in strong fields a different kind of perturbation theory seems very reasonable: if the field is strong, why don't we include it exactly and treat the potential of the field-free system as a perturbation? This is exactly the idea behind the strong-field approximation (SFA) championed by H. Reiss, which will be introduced in this chapter after a brief description of the so-called strong-field S-matrix.

6.2

Speculative Thoughts

Everywhere below I will use atomic units, where $\hbar = m_e = e = 1$, m_e being the electron mass and e the positron charge. I will also restrict most of the discussion to the case of a low-frequency (infrared, IR) laser field and a single active electron.

Let us start with the time-dependent Schrödinger equation (TDSE):

$$i|\Psi\rangle_t = \hat{H}(t)|\Psi\rangle. \quad (6.1)$$

Had there been no hat above $H(t)$, we would have had no trouble solving this equation:

$$|\Psi(t)\rangle = e^{-i\int_{t_i}^t \hat{H}(t')dt'}|\Phi_i\rangle. \quad (6.2)$$

Here Φ_i is the initial state of the system at the initial moment of time t_i .

Of course, life is not that simple: the exponent has an operator in it. The exponential operator $\hat{U}(t, 0) = \exp[-i \int_{t_i}^t \hat{H}(t') dt']$ is called the propagator. How does one understand it? The mathematically correct way to understand it is to break the whole time-interval from t_i to t into N little intervals Δt centered around t_n , with index n running from $n = 1$ to $n = N$ and t_n changing from $t_1 = t_i + \Delta t/2$ to $t_N = t - \Delta t/2$. With $N \rightarrow \infty$, the Hamiltonian does not change within each time-interval. Then, the propagator from t_i to t corresponds to $N \rightarrow \infty$ successive steps

$$e^{-i \int_{t_i}^t \hat{H}(t') dt'} |\Phi_i\rangle \rightarrow \lim_{N \rightarrow \infty} e^{-i \hat{H}(t_N) \Delta t} \dots e^{-i \hat{H}(t_2) \Delta t} e^{-i \hat{H}(t_1) \Delta t} |\Phi_i\rangle \quad (6.3)$$

applied from right to left to the initial state $|\Phi_i\rangle$ and this is symbolically written as

$$e^{-i \int_{t_i}^t \hat{H}(t') dt'} |\Phi_i\rangle \rightarrow \hat{T} \lim_{N \rightarrow \infty} \prod_{n=1}^N e^{-i \hat{H}(t_n) \Delta t} |\Phi_i\rangle = \hat{T} e^{-i \int_{t_i}^t \hat{H}(t') dt'} |\Phi_i\rangle, \quad (6.4)$$

where \hat{T} is the time-ordering operator, which ensures that the terms in the product are arranged in correct time-order, with later times coming after earlier times. I will drop the symbol \hat{T} from now on, to simplify notations.

Our goal is to find a way to deal with this propagator. A tempting substitution is to replace

$$\exp \left[-i \int_{t_i}^t \hat{H}(t') dt' \right] \rightarrow \exp \left[-i \int_{t_i}^t E(t') dt' \right], \quad (6.5)$$

where E is the energy. Of course, this is not generally correct because different spatial parts of the initial wavefunction will evolve differently, in particular with different energy. The only case where this substitution works is for stationary eigenstates, where the energy is the same at all points in space. Otherwise, the phase must be coordinate-dependent, which will also lead to changing the state from Φ_i to something else.

Intuitively, recalling the time-independent semiclassical approximation that one can find in any quantum mechanics textbook, one should expect that this spatial phase, accumulated during the propagation, should include $\int p(x) dx$. When added to the temporal phase accumulated during the same propagation, $-\int E(\tau) d\tau$, the overall phase is nothing but the complete classical action S_F (the subscript “F” stands for “full”). The idea of substituting

$$\exp \left[-i \int_{t_i}^t \hat{H}(t') dt' \right] \rightarrow \exp[i S_F(x, t)] \quad (6.6)$$

is rooted in the Feynman’s path formulation of quantum mechanics and is a basis for approximate semiclassical propagators. We will now see how this idea emerges from the quantum analysis of the strong-field dynamics.

6.3

Basic Formalism

6.3.1

Hamiltonians and Gauges

Let us return to the time-dependent Schrödinger equation,

$$i|\Psi\rangle_t = \hat{H}(t)|\Psi\rangle = [\hat{H}_0 + \hat{V}(t)]|\Psi\rangle . \quad (6.7)$$

Here $V(t)$ describes the interaction with the laser field and H_0 is the field-free Hamiltonian. I will assume that the wavelength of light is much bigger than the size of our quantum system, and so I will use the dipole approximation, which means that the spatial dependence of the electromagnetic field across the size of the system is ignored.

In the dipole approximation, the laser-system interaction can be written in the so-called length gauge as $\hat{V} = -\hat{\mathbf{d}}F(t)$, with $\hat{\mathbf{d}} = q\hat{\mathbf{r}}$ the dipole operator. The Hamiltonian has the form

$$\hat{H}_{LG}(t) = \frac{\hat{\mathbf{p}}^2}{2m} + U(\mathbf{r}) - \hat{\mathbf{d}}F(t) = \frac{\hat{\mathbf{p}}^2}{2m} + U(\mathbf{r}) + \hat{\mathbf{r}}F(t) . \quad (6.8)$$

Here $\hat{\mathbf{p}}$ is the momentum operator, $U(r)$ is the interaction potential between the ionizing active electron and the ionic core. The mass of the electron is $m = 1$ in the atomic units which are used everywhere below. The electron charge $q = -e = -1$ in the same units.

There are two more approximations here. The first is to describe the laser field classically – this is fine given large number of photons (high intensity). The second is to use the single active electron approximation in Eq. (6.8).

Before we proceed further, let me stress that the length form of the interaction is approximate and can only be used in the dipole approximation. There is another gauge that is often used in treating the laser-matter interaction, the so-called velocity gauge. This one is general and works beyond the dipole approximation. The Hamiltonian in the velocity gauge is

$$\hat{H}_{VG}(t) = \frac{[\hat{\mathbf{p}} - q\mathbf{A}]^2}{2m} + U(\mathbf{r}) = \frac{[\hat{\mathbf{p}} + \mathbf{A}]^2}{2m} + U(\mathbf{r}) , \quad (6.9)$$

where in the last line $q = -1$ was used and the vector potential \mathbf{A} is defined as

$$\mathbf{F}(t) = -\frac{\partial \mathbf{A}(t)}{\partial t} . \quad (6.10)$$

These two forms of the Hamiltonian are equally good, meaning that one can go from the TDSE in the velocity form to the TDSE in the length form by a unitary transformation

$$\Psi_{LG}(t) = e^{-iq\hat{\mathbf{A}}(t)}\Psi_{VG}(t) = e^{i\hat{\mathbf{r}}\mathbf{A}(t)}\Psi_{VG}(t) \quad (6.11)$$

and the corresponding transformation of the Hamiltonian, which the reader is welcome to try to derive. All observable quantities are invariant under this unitary gauge transformation – that is, as long as the TDSE is solved exactly, and as long as the dipole approximation is acceptable.

From now on I will stick to the length gauge and I will drop the subscript LG from H_{LG} .

6.3.2

Formal Solutions

The discussion below applies equally to both the length and the velocity gauge, or any other gauge. We have already seen the formal solution of the TDSE

$$i|\Psi\rangle_t = \hat{H}(t)|\Psi\rangle \quad (6.12)$$

which is

$$|\Psi(t)\rangle = e^{-i \int_{t_i}^t \hat{H}(\tau) d\tau} |\Phi_i\rangle = \hat{U}(t, t_i) |\Phi_i\rangle. \quad (6.13)$$

Evaluating the exponential operator $\hat{U}(t, t_i)$ is a tedious task, no easier than solving the TDSE. However, we will find good use to this formal solution very shortly.

Let us rewrite Eq. (6.1) in a slightly different form,

$$i|\Psi\rangle_t = \hat{H}_0|\Psi\rangle + \hat{V}|\Psi\rangle. \quad (6.14)$$

What I have done here is broken the full Hamiltonian H into two parts – $H = H_0 + V$. Often, H_0 is taken as the field-free Hamiltonian and $V(t)$ is taken as the interaction with the laser field – this is what I have done here. However, I could have broken H into any other pair, for example $H = H_V + U$ where

$$\hat{H}_V = \frac{\hat{p}^2}{2} + \hat{V}(t) \quad (6.15)$$

describes the interaction of a free electron with the laser field and U is the potential of the ionic core. The separation of the Hamiltonian $H(t)$ into two parts is known as “partitioning” of the Hamiltonian.

Our immediate goal is to relate the solution for the full Hamiltonian H to the solution for the Hamiltonian H_0 , the latter presumably known. Let us write the TDSE with the Hamiltonian H_0

$$i|\Psi^{(0)}\rangle_t = \hat{H}_0|\Psi^{(0)}\rangle. \quad (6.16)$$

Its formal solution is

$$|\Psi^{(0)}\rangle = e^{-i \hat{H}_0 t} |\Psi(t=0)\rangle = e^{-i \hat{H}_0 t} |\Phi_i\rangle \quad (6.17)$$

where $|\Phi_i\rangle$ is the same initial state of the system as above in Eq. (6.13) and the index (0) means that this solution applies to the Hamiltonian H_0 .

What is the relationship between $\Psi(t)$ and $\Psi^{(0)}(t)$? Direct substitution into the TDSE Eq. (6.1) shows that its exact solution can be written as

$$\begin{aligned} |\Psi(t)\rangle &= |\Psi^{(0)}(t)\rangle + |\Delta\Psi(t)\rangle = e^{-i\hat{H}_0 t}|\Phi_i\rangle + |\Delta\Psi(t)\rangle \\ |\Delta\Psi(t)\rangle &= -i \int_{t_i}^t dt' e^{-i \int_{t'}^t \hat{H}(\tau)d\tau} \hat{V}(t') e^{-i\hat{H}_0(t'-t_i)}|\Phi_i\rangle. \end{aligned} \quad (6.18)$$

Try to substitute this into the TDSE and check that it does indeed work.

Let's see where we have come. We started with a single exponential operator in Eq. (6.13) and we replaced it with an integral over exponential operators taken from all times t' . Let's be frank: Eq. (6.18) does not look very inviting. However, it is this general – and exact – expression where interesting approximations can be explicitly tried, sometimes based on rigorous math and sometimes based on physical reasoning.

Let us look at the physics behind the expression Eq. (6.18). The system starts in the state $|\Phi_i\rangle$. During the time-interval before some moment t' it evolves without interacting with the laser field, as if the field was not there. This may look weird, but one cannot argue with the exact expression. Besides, it is very convenient: if the initial state is an eigenstate of the Hamiltonian H_0 with energy E_i , all this evolution does is accumulates the phase due to the energy, $\exp[-iE_i(t' - t_i)]$.

This quiet evolution ends at a moment t' when the system is kicked by the instantaneous laser field $V(t')$. To which state the transition occurs at this moment is anybody's guess. It is called a virtual transition and it can go anywhere – the energy conservation law need not be satisfied until the interaction is over. The single dipole operator hiding behind $\hat{V} = \hat{r}F$ can induce single-photon transitions to the continuum states even when the photon energy is much less than the binding energy (ionization potential) IP. Such transitions do not yet mean that the electron has become free – only that it is transiently populating continuum states and may become free at some point when (or if) this virtual population becomes real, that is, satisfying the energy conservation law.

From the moment t' to the moment of observation t , the evolution is under the action of the full Hamiltonian, including both the laser field and the field-free potential.

If we are interested in finding the transition amplitude from the initial field-free state Φ_i to some final state Ψ_f , then at the moment of observation the wavefunction must be projected onto the state of interest, Ψ_f . If we are interested in ionization and our initial state is a bound state, then the final (continuum) state must be orthogonal to the initial state. Then the projection of $\Psi^{(0)}(t)$ onto Ψ_f is zero, and the transition amplitude a_{fi} is

$$\begin{aligned} a_{fi}(t) &= \langle \Psi_f | \Psi(t) \rangle = \langle \Psi_f | \Delta\Psi(t) \rangle \\ &= -i \int_{t_i}^t dt' \langle \Psi_f | e^{-i \int_{t'}^t \hat{H}(\tau)d\tau} V(t') e^{-i\hat{H}_0(t'-t_i)} |\Phi_i\rangle. \end{aligned} \quad (6.19)$$

This expression is often referred to as the strong-field S-matrix, as it is similar to the time-dependent treatment of scattering problems. It is exact. No approximations have been made yet. Now let's turn to approximations.

6.4

The Strong-Field Approximation

Let us think about the physics of the situation in the strong low-frequency field. “Low frequency” means “compared with the characteristic response frequency” of the system – the inverse of the excitation frequency. For most systems of interest it is in the deep UV, so that the response time is a few atomic units, or about 100 as. Thus, the interaction with the IR field would be in the low-frequency regime.

While the electron is in the initial – ground – state, not much is happening until it manages to escape to the continuum at some t' , which could be pretty much any instant of time. At this point in time the strong field takes the electron over and it starts to oscillate in the field, possibly scattering on the parent ion. Can we put this physical picture into the mathematical terms? Or, rather, can we use this picture to do something to the formal expressions for the amplitude a_{fi} ?

Once we realize that the ground state and the continuum are the two main participants in the dynamics, the plan is rather clear. Indeed, in Eqs. (6.18) and (6.19) first the electron sits in the ground state until the moment t' , at which point the laser field $V(t')$ kicks it, and we assume that this kick promotes the electron to the continuum. Now, while in the continuum, the electron is dominated by the laser field. Therefore, instead of the exact propagator

$$\exp\left(-i \int_{t'}^t \hat{H}(\tau) d\tau\right)$$

we will use an approximate propagator that includes the laser field fully and exactly but completely ignores the field-free potential of the system,

$$a_{fi}(t) \sim -i \int dt' \langle \Psi_f | e^{-i \int_{t'}^t \hat{H}_V(\tau) d\tau} V(t') e^{-i \hat{H}_0(t'-t_i)} | \Phi_i \rangle \quad (6.20)$$

where H_V is given by Eq. (6.15). This is the essence of the strong-field approximation. One of the main reasons to make this approximation – completely neglect the atomic (or molecular) potential in the continuum – is that the propagator for the free electron in the laser field

$$U_V(t, t') = e^{-i \int_{t'}^t \hat{H}_V(\tau) d\tau} \quad (6.21)$$

is known exactly. It is called the Volkov propagator. It corresponds to solving the TDSE for the Hamiltonian $H_V(t)$, which in the length gauge is

$$\hat{H}_V(t) = \frac{\mathbf{p}^2}{2} + x F(t), \quad (6.22)$$

with x being the polarization direction of the laser field.

6.4.1

The Volkov Propagator and the Classical Connection

To understand how the Volkov propagator acts on the electron in the laser field, let us see how it would act on the plane wave $\exp(i\mathbf{k}\mathbf{r})$, which describes the free electron which has the kinetic momentum \mathbf{k} along the laser polarization. For simplicity, we will restrict the analysis below to this single dimension, and then generalize to the 3D case.

All the free electron does in the laser field is oscillate. Classically, if at time t' the electron has kinetic momentum $k' = k(t')$ (kinetic momentum $k(t') = mv(t')$ is proportional to the instantaneous velocity), then its kinetic momentum at any other time is

$$\mathbf{k}(t) = \mathbf{k}(t') - \mathbf{A}(t') + \mathbf{A}(t). \quad (6.23)$$

In other words,

$$\mathbf{k}(t) - \mathbf{A}(t) = \mathbf{k}(t') - \mathbf{A}(t') = \mathbf{p} = \text{const}. \quad (6.24)$$

The conserved quantity \mathbf{p} is called the canonical momentum.

This purely classical picture shows up when we apply the quantum Volkov propagator to the plane wave with the kinetic momentum k' at the moment t' :

$$e^{-i \int_{t'}^t \hat{H}_V(\tau) d\tau} |\mathbf{k}'\rangle = e^{-i \int_{t'}^t E(\tau) d\tau} |\mathbf{k}\rangle. \quad (6.25)$$

Here the plane waves $|\mathbf{k}\rangle$, $|\mathbf{k}'\rangle$ have different momenta related by Eq. (6.23), and the instantaneous kinetic energy is

$$\begin{aligned} E(\tau) &= \frac{1}{2}[\mathbf{k} - \mathbf{A}(t) + \mathbf{A}(\tau)]^2 = \frac{1}{2}[\mathbf{k}' - \mathbf{A}(t') + \mathbf{A}(\tau)]^2 \\ \mathbf{k} &= \mathbf{k}' - \mathbf{A}(t') + \mathbf{A}(t). \end{aligned} \quad (6.26)$$

In terms of the conserved canonical momentum \mathbf{p} , which is also equal to the kinetic momentum of the electron after the laser field is switched off, the result can be rewritten as

$$e^{-i \int_{t'}^t \hat{H}_V(\tau) d\tau} |\mathbf{p} + \mathbf{A}(t')\rangle = e^{-i \int_{t'}^t E(\tau) d\tau} |\mathbf{p} + \mathbf{A}(t)\rangle. \quad (6.27)$$

Thus, the coordinate part of the wavefunction has been changed, but the temporal phase added is the same for all coordinates because the interaction (the laser field) is homogeneous. This is the only reason we could replace the Hamiltonian operator in the exponent with the energy.

The result above is exact and can be obtained in many ways. Let me now derive it using the classical action and the semiclassical approach. While this route is not the simplest, it gives you a very clear feeling for the quantum-classical connection. For simplicity of notation, let me assume that the motion is one-dimensional, parallel to the laser field polarization. Generalizing to 3D is easy and a good exercise.

Our initial condition, the plane wave $\Psi(x, t') \propto \exp(i k' x)$ at the moment t' , has the nice semiclassical form $\Psi(x, t') \propto \exp(i S)$ with the initial condition for the action $S_F(k', x, t = t', t') = k' x$. Let us look for the solution of the TDSE in the form

$$\begin{aligned}\Psi(x, t) &= e^{i S_F(k', x, t, t')} \\ S_F(k', x, t', t') &= k' x.\end{aligned}\quad (6.28)$$

The many arguments in S_F denote the initial momentum, the initial time, and the coordinate x at the moment t . The subscript “F” stands for “full” – it stresses that we have full classical action that depends on initial and running times, coordinates, and momenta. The reason to use this notation will become clear later, when a part of S_F will be denoted as S , following the tradition that has (unfortunately) entrenched itself in the strong-field community and leads to some confusion when the component S of the full action S_F is referred to as the classical action.

Substituting this expression into the TDSE for the free electron in the laser field yields exact equation for the action

$$-\frac{\partial S_F}{\partial t} = \frac{1}{2} \left[\frac{\partial S_F}{\partial x} \right]^2 + x F(t) - \frac{i}{2} \frac{\partial^2 S_F}{\partial x^2}. \quad (6.29)$$

This equation differs from the classical Hamilton–Jacobi equation for the action due to the presence of the last term, which involves the second-order spatial derivative. It coincides with the Hamilton–Jacobi equation if this term is equal to zero. This is precisely the case for potentials that depend on x linearly, which allows for solutions that also linearly depend on x .

Exact solution of Eq. (6.29), subject to the initial conditions above, is

$$\begin{aligned}S_F &= k' x + [A(t) - A(t')]x - \frac{1}{2} \int_{t'}^t d\tau [k' - A(\tau)]^2 \\ &= k(t)x - \frac{1}{2} \int_{t'}^t d\tau k^2(\tau)\end{aligned}\quad (6.30)$$

and is identical to the classical action for the free electron in the laser field.

6.4.2

Transition Amplitudes in the SFA

Let the system start at the moment t_i in the ground state $\Phi_i \equiv \Phi_g$ with the energy $E_g = -IP$ (and hence $\exp(-i \hat{H}_0(t' - t_i)) = \exp(+iIP(t' - t_i))$). The amplitude to find the system with the momentum k at the time t , according to the general equation (Eq. (6.19)), is

$$a(k, t) = -i \int dt' \langle k | e^{-i \int_{t'}^t \hat{H}(\tau) d\tau} V(t') e^{i \hat{I}_P(t' - t_i)} | \Phi_g \rangle. \quad (6.31)$$

In the SFA, we replace the exact propagator between t' and t with the Volkov propagator,

$$a(\mathbf{k}, t) = -i \int_{t_i}^t dt' \langle \mathbf{k} | e^{-i \int_{t'}^t \hat{H}_V(\tau) d\tau} V(t') e^{i \hat{I}_P(t' - t_i)} | \Phi_g \rangle. \quad (6.32)$$

Now we use the fact that we have just learned how to propagate the plane wave in the laser field, and apply this knowledge to the “bra”:

$$\langle \mathbf{k} | e^{-i \int_{t'}^t \hat{H}_V(\tau) d\tau} = e^{-i \int_{t'}^t E(\tau) d\tau} \langle \mathbf{k} + \mathbf{A}(t') - \mathbf{A}(t) | = e^{-i \int_{t'}^t E(\tau) d\tau} \langle \mathbf{k}(t') | \quad (6.33)$$

with the instantaneous kinetic energy

$$E(\tau) = \frac{1}{2} [\mathbf{k} - \mathbf{A}(t) + \mathbf{A}(\tau)]^2 = \frac{1}{2} [\mathbf{k}' - \mathbf{A}(t') + \mathbf{A}(\tau)]^2. \quad (6.34)$$

The SFA expression for the amplitude to find the system with the momentum $|\mathbf{k}\rangle$ at an instant t becomes

$$a_{\mathbf{k}}(t) = -i \int_{t_i}^t dt' e^{-i \int_{t'}^t E(\tau) d\tau + i \text{IP}(t' - t_i)} \langle \mathbf{k} + \mathbf{A}(t') - \mathbf{A}(t) | V(t') | \Phi_g \rangle, \quad (6.35)$$

where

$$E(\tau) = \frac{1}{2} [\mathbf{k} - \mathbf{A}(t) + \mathbf{A}(\tau)]^2 \quad (6.36)$$

since we have fixed the momentum \mathbf{k} at the instant t .

In the literature, the \mathbf{k}, t, t' -dependent phase of this integral,

$$S(t, t', \mathbf{k}) = \frac{1}{2} \int_{t'}^t d\tau [\mathbf{k} - \mathbf{A}(t) + \mathbf{A}(\tau)]^2 - \text{IP}t' \quad (6.37)$$

is often referred to as the classical action of the free electron in the laser field. It is a stretch of the term, since it also includes the $-\text{IP}t'$, and misses the coordinate-dependent part. Often you will find it written in terms of the canonical momentum $\mathbf{p} = \mathbf{k} - \mathbf{A}(t)$, which is the conserved quantity and will stay unchanged at all times – that’s within the SFA, of course. In this case the phase will look like

$$S(t, t', \mathbf{p}) = \frac{1}{2} \int_{t'}^t d\tau [\mathbf{p} + \mathbf{A}(\tau)]^2 - \text{IP}t'. \quad (6.38)$$

In terms of action and the canonical momentum \mathbf{p} , the SFA transition amplitude is

$$a_{\mathbf{p}}(t) = -i \int_{t_i}^t dt' e^{-i S(t, t', \mathbf{p}) - i \text{IP}t_i} \langle \mathbf{p} + \mathbf{A}(t') | V(t') | g \rangle. \quad (6.39)$$

In the future, if and when you come across such expressions, pay special attention to the meaning of the momentum – is it canonical or kinetic.

Equations (6.35) and (6.39) are intuitive and clear. The electron sits in the ground state until t' when it makes a (at this point still virtual) transition to the continuum. Then the electron moves in the laser field, converting the virtual transition into real and oscillating – as the free electron should. It accumulates the phase given by the integration of its instantaneous energy $E(\tau)$, performed between the moment t' and the moment of observation t . The electron finishes with the canonical momentum \mathbf{p} , which dictates the initial kinetic momentum that the electron populates at t' , $\mathbf{k} = \mathbf{p} + \mathbf{A}(t')$.

There are several major problems with this result, all stemming from the main approximation of the theory – to neglect the effect of the Coulomb potential.

- 1) During the transition to the continuum the electron will be liberated differently if we include its interaction with the atomic core. After all, if it has to tunnel through the barrier, the shape of this barrier is important – and it is heavily affected by the binding potential. Thus, the ionization amplitude will be different. This problem can be corrected by incorporating the effect of the Coulomb tail into the electron action.
- 2) The propagation in the continuum is also different: the electron not only oscillates in the laser field, it can also scatter off the atomic core. This is not present in the SFA formalism, but can be included additionally: the SFA result can be considered as the first term in a perturbative expansion, with the atomic potential being a perturbation. The corresponding new terms are often referred to as SFA2, and have been derived and analyzed by M. Lewenstein *et al.*, see [1].
- 3) The Volkov propagator is sensitive to the gauge. The formalism in this chapter is written in the length gauge. In the velocity gauge, where $\hat{V} = \hat{\mathbf{p}}\mathbf{A} + \mathbf{A}^2/2$, the plane wave state $|\mathbf{p}\rangle$ with canonical momentum \mathbf{p} stays the same between t' and t . This is simply because in the velocity gauge \mathbf{p} refers to *canonical*, not *kinetic* momentum, and in the laser field the *canonical* momentum of the free electron is a constant of motion. This does not lead to any problems in the exact theory – that is, if the electron was indeed free at all times. But in the approximate theory this is not the case – the initial field-free ground state is not a state of the free electron. *As a result, the SFA is not gauge invariant, which is bad news for a theory.*

However, the good news is that the gauge problem directly affects only the preexponential terms in the amplitude, and keeps the major piece – which is the fast oscillating exponent – intact. So with the exponential part we are more-or-less safe, at least as far as gauges go.

- 4) Finally, by using the plane waves as continuum states, we have selected a basis which is not orthogonal to the initial state of the system. In other words, in addition to all other problems our basis set is also overcomplete: it includes all plane waves that already make up a complete basis *plus* the extra bound state. The preexponential factor which includes the bound-free transition matrix elements suffers greatly – but the key exponential dependence stays the same.

To summarize, SFA is wrong in many ways and it violates almost every rule in the theory book. But the physical picture that stands behind it is intuitive, clear, and compelling. As a result, the SFA is used very widely, and it works very well for gaining qualitative and – with proper modifications along the lines described in [2] and further developed in [3] – even quantitative insight into the physics of intense laser-matter interaction.

6.5

Strong-Field Ionization: Exponential vs. Power Law

Let us now use it to look at the dynamics of strong-field ionization, and see how the exponential dependence on the laser field strength, typical for tunneling, turns into a power law dependence commonly associated with multiphoton ionization.

Up to the global phase factor $e^{i\text{IP}(t-t_i)}$, the SFA probability amplitude of populating the field-free continuum state labeled by the canonical momentum $|\mathbf{p}\rangle$ is

$$\begin{aligned} a_p(t) &= -i \int_{t'}^t dt' e^{-iS(t,t',\mathbf{p})} \langle \mathbf{p} + \mathbf{A}(t') | V(t') | g \rangle \\ S(t, t', \mathbf{p}) &= \frac{1}{2} \int_{t'}^t d\tau [\mathbf{p} + \mathbf{A}(\tau)]^2 + \text{IP}(t - t') . \end{aligned} \quad (6.40)$$

Let us assume that the field is linearly polarized, $\mathbf{F} \cos \omega t$. Then the vector potential is

$$A_{\parallel} = -\frac{F}{\omega} \sin \omega t = -v_0 \sin \omega t \quad A_{\perp} = 0 . \quad (6.41)$$

Then, keeping only exponential accuracy, we obtain

$$a_p(t) \sim \int_{-\infty}^t dt' \exp(-iS(\mathbf{p}, t, t')) , \quad (6.42)$$

where

$$S(\mathbf{p}, t, t') = \left(\text{IP} + \frac{1}{2} p_{\perp}^2 \right) (t - t') + \frac{1}{2} \int_{t'}^t d\tau [p_{\parallel} - v_0 \sin \omega \tau]^2 \quad (6.43)$$

is commonly refereed to in the literature as the action integral (even though, rigorously speaking, it is not quite that), v_{\parallel} and v_{\perp} are the velocity components parallel and perpendicular to \mathbf{F} and $v_0 = F/\omega$ is the velocity amplitude of electron oscillations.

You already see that having nonzero perpendicular momenta is like increasing IP. Hence, for now p_{\perp} can be set to zero. If we are interested in the probabilities

of populating nonzero p_{\perp} , all we need to do is take the formula for $p_{\perp} = 0$ and replace IP with $\text{IP} + p_{\perp}^2/2$.

This expression is the standard SFA expression for the ionization amplitudes. The next step is to evaluate the integral.

6.5.1

The Saddle Point Approximation and the Classical Connection

To evaluate the integral, we need to understand what the phase $S(\mathbf{p}, t, t')$ does in this integral. The best way to approach this is to rewrite S in terms of dimensionless variables: let us pull v_0 out of the brackets of Eq. (6.43), and also introduce phase $\phi = \omega\tau$ as a new dimensionless integration variable:

$$S(\mathbf{p}, t, t') = \frac{\text{IP}}{\omega}(\omega t - \omega t') + \frac{v_0^2}{2\omega} \int_{\omega t'}^{\omega t} d\phi [u - \sin \phi]^2 , \quad (6.44)$$

where the dimensionless momentum is $u = p_{\parallel}/v_0$.

We see that there are two important parameters in the phase – $N = \text{IP}/\omega$ and

$$\frac{v_0^2}{2\omega} = 2 \frac{U_p}{\omega} = 2Z , \quad (6.45)$$

where $U_p = F^2/4\omega^2$ is the ponderomotive energy – the laser-cycle-average kinetic energy of the oscillating electron, and Z is known as the Reiss parameter. The number $N = \text{IP}/\omega$ tells us roughly how many photons are required for ionization.

In strong low-frequency fields both parameters are very large, meaning that the phase is changing very rapidly with time. For example, at intensities around 10^{14} W/cm^2 and for $\omega = 1.56 \text{ eV}$, which corresponds to the laser wavelength of 800 nm, the characteristic value of the second term in the phase, over one laser cycle, is about 10π , which is a very large phase change over one laser cycle.

This is very good news. If the phase is large and oscillates quickly, we can use the saddle point method to calculate the integral.

The saddle point method proceeds as follows. First, one looks for the values of the integration variable t' where the phase of the integrand is stationary, that is, the derivative with respect to t' is zero. In our case we have

$$S(\mathbf{p}, t, t') = \text{IP}(t - t') + \frac{v_0^2}{2} \int_{t'}^t d\tau [u - \sin \omega\tau]^2$$

$$\frac{\partial S(\mathbf{p}, t, t')}{\partial t'} = -\text{IP} - \frac{v_0^2}{2} [u - \sin \omega t']^2 = 0 . \quad (6.46)$$

Solving this equation is the key component of the calculation, and we shall turn to it shortly. Once we find the stationary point t'_{in} which satisfies the above equation, we can move to the second step. (I will explain the subscript “in” shortly.)

To make notations simpler, I will drop the arguments \mathbf{p} and t from $S(\mathbf{p}, t, t')$, keeping only t' . The second step of the calculation is to expand $\exp(-iS(t'))$ in Taylor series around the stationary phase point t'_{in} . Since the first derivative w.r.t t' at this point is zero, the second derivative S'' is kept and the integral becomes

$$\int dt' e^{-iS(t')} \simeq e^{-iS(t'_{\text{in}})} \int dt' e^{-iS''(t'_{\text{in}})/[2(t' - t'_{\text{in}})^2]}. \quad (6.47)$$

Now one uses the fact that the phase changes quickly and changes a lot. Hence, the integral converges quickly and the limits of integration with respect to $\xi = t' - t'_{\text{in}}$ in the vicinity of the stationary point are extended to $\pm\infty$. The integral is then well known, and the answer is

$$\int dt' e^{-iS(t')} \simeq e^{-iS(t'_{\text{in}})} \sqrt{2 \frac{\pi}{i S''(t'_{\text{in}})}}. \quad (6.48)$$

The preexponential factor is not important at this stage, since we have already dropped many preexponential terms when writing the amplitude as in Eq. (6.40). Moreover, the preexponential term one finds in the SFA is quantitatively wrong. It is the exponential dependence that gives the qualitative insight we are looking for.

There could be many stationary phase points, and one needs to sum the contributions from all of them, so the full answer is

$$\int dt' e^{-iS(t')} \sim \sum_{t'_{\text{in}}} e^{-iS(t'_{\text{in}})}. \quad (6.49)$$

Each stationary phase point corresponds to an ionization burst that leads to the specific final momentum u (in dimensionless units) at the detector.

The phase $S(t'_{\text{in}})$ has real and imaginary parts, so let us write

$$S(\mathbf{p}, t, t'_{\text{in}}) = \Re S(\mathbf{p}, t, t'_{\text{in}}) - i\sigma(\mathbf{p}, t, t'_{\text{in}}). \quad (6.50)$$

In a long laser pulse where all cycles are the same, different stationary points t'_{in} separated by an integer number of laser cycles yield the same imaginary part. Thus, the sum of the contributions of all stationary points to the total ionization amplitude is:

$$a(\mathbf{p}, t) \propto e^{-\sigma(\mathbf{p})} \sum_{t'_{\text{in}}} \exp[-i\Re S(\mathbf{p}, t, t'_{\text{in}})]. \quad (6.51)$$

In a long laser pulse, where many cycles are the same, and many ionization bursts are identical, the interference of many stationary phase points separated by an integer number of laser cycles leads to minima and maxima in the electron spectra. Since the ionization bursts repeat every laser cycle, they form a train of electron wave packets with the laser cycle being the “repetition rate” in the train. In the energy domain, this train leads to peaks separated by the photon energy. The maxima are nothing but the above-threshold ionization (ATI) peaks.

Now, having understood the time-domain picture of strong-field ionization for many laser cycles, let us finally turn to the contribution from a single stationary point, that is, from a single ionization burst that produces electrons with the canonical momentum $p = v_0 u$. To find the ionization rate for each value of $p = v_0 u$, we will need to do as follows.

First, we need to solve the stationary point equation (6.46)

$$\begin{aligned} \frac{v_0^2}{2} [u - \sin \omega t']^2 &= -\text{IP} \\ [u - \sin \omega t']^2 &= -\frac{\text{IP}}{2 U_p} = -\gamma^2, \end{aligned} \quad (6.52)$$

where γ is the Keldysh parameter, and find the stationary point t'_{in} . It is clear that the solutions of this equation are complex-valued: no real-valued t' can give negative square, and we should look for the complex solutions $t'_{\text{in}} = t'_{\text{out}} + i\tau_T$.

Second, we need to calculate the value of the phase S at this point, and then find the imaginary part of this phase $\sigma(p)$ which will give us the corresponding rate,

$$\Gamma(p) \propto e^{-2\sigma(p)}. \quad (6.53)$$

This expression is written with only exponential accuracy, and it is a standard semi-classical expression for the transmission probability – but written for the time-dependent and not for the time-independent problem.

What is the meaning of Eq. (6.52) and these complex times? The left-hand side of the equation is the kinetic energy of the electron. The kinetic energy has negative value when the particle enters the classically forbidden region as it tunnels from the binding potential well through the barrier created by the oscillating electric field.

Appropriately, the velocity under the barrier is imaginary,

$$u - \sin \omega t' = \pm i\gamma. \quad (6.54)$$

Since the motion under the barrier occurs with imaginary velocity, it must proceed in imaginary time, so that the product of velocity and time (distance) has a chance of being real, or at least having a growing real part, allowing the electron to come out of the barrier. The associated semiclassical trajectory enters the classically forbidden region at $t'_{\text{in}} = t'_{\text{out}} + i\tau_T$. As we move along the imaginary time axis from $t' = t'_{\text{in}} = t'_{\text{out}} + i\tau_T$ towards $t' = t'_{\text{out}}$ on the real time axis, decreasing the imaginary part from $i\tau_T$ to zero and keeping the real part t'_{out} fixed, the associated electron trajectory

$$x(t') = \int_{t'_{\text{in}}}^{t'} d\tau v_0 [u - \sin \omega \tau] \quad (6.55)$$

evolves towards the exit point of the barrier. Which of the two signs on the left-hand side of Eq. (6.54) should we take? The decision must ensure that the semiclassical

transmission amplitude $\exp(-\sigma(p))$ is exponentially small and not exponentially large, dictating that τ_T is positive, and hence we write

$$u - \sin[\omega t'_{\text{out}} + i\omega\tau_T] = -i\gamma . \quad (6.56)$$

Equation (6.56) can be solved for any u , but for the moment I will limit the discussion to $u = 0$. The reason is simple: these values dominate the overall ionization rate, integrated over all $u = p/v_0$. Indeed, we will see very quickly that for $u = 0$ the complex time $t'_{\text{in}} = t'_{\text{out}} + i\tau_T$ has $t_{\text{out}} = 0$. Thus, for $u = 0$ the electron emerges from the classically forbidden region, where it has been traveling in complex (imaginary) time, at the maxima of the instantaneous electric field $F \cos \omega t_{\text{out}} = F$. This is precisely when the strong-field ionization is peaked. Thus, the rate for $u = 0$ corresponds to the rate at the peaks of the field, and it will dominate the total, cycle-averaged, ionization rate. With exponential accuracy, this is all we need to know.

Our equation becomes

$$\sin \omega(i\tau_T) = i\gamma \quad (6.57)$$

or

$$\sinh(\omega\tau_T) = \gamma . \quad (6.58)$$

Remembering that

$$\sinh(\omega\tau_T) \equiv \frac{e^{\omega\tau_T} - e^{-\omega\tau_T}}{2} \quad (6.59)$$

and denoting $\exp(\omega\tau_T) = z$, we find the quadratic equation

$$z - \frac{1}{z} = 2\gamma \quad (6.60)$$

with the solution

$$\begin{aligned} z &= \gamma + \sqrt{\gamma^2 + 1} \\ \omega\tau_T &= \ln[\gamma + \sqrt{\gamma^2 + 1}] . \end{aligned} \quad (6.61)$$

Let us now look at the two limits of this expression. For $\gamma \ll 1$ we have

$$\tau_T = \frac{\gamma}{\omega} . \quad (6.62)$$

This expression gives a clear meaning to the γ parameter in terms of the imaginary “tunneling time” τ_T : small γ means that during tunneling the barrier has no time to move, $\omega\tau_T \ll 1$. Once we find the stationary phase point, we can now calculate the corresponding action integral:

$$S(\mathbf{p}, t, t') = \text{IP}(t - i\tau_T) + \frac{v_0^2}{2} \int_{i\tau_T}^0 d\tau [\sin \omega\tau]^2 + \frac{v_0^2}{2} \int_0^t d\tau [\sin \omega\tau]^2 . \quad (6.63)$$

We note that by introducing the new integration variable $\tau = i\xi$ the integral term can be rewritten as

$$\int_{i\tau_T}^0 d\tau [\sin \omega \tau]^2 = i \int_0^{\tau_T} d\xi \sinh^2(\omega \xi) \quad (6.64)$$

and hence the imaginary part $\sigma = -\Im S$ is

$$\sigma = \text{IP}\tau_T - \frac{F^2}{2\omega^2} \int_0^{\tau_T} d\xi \sinh^2(\omega \xi). \quad (6.65)$$

Exercise

Calculate the remaining integral and show that in the limit $\gamma \ll 1$ this rate is given by the exact analogue of a DC tunneling exponent:

$$\Gamma \propto \exp \left[-\frac{4}{3} \text{IP}\tau_T \right] = \exp \left[-\frac{2}{3} \frac{[2\text{IP}]^{3/2}}{F} \right]. \quad (6.66)$$

Let us now look at the opposite limit of very large $\gamma \gg 1$. The integral we need to calculate and the imaginary part of the action are given by the same general expression as before,

$$\sigma = \text{IP}\tau_T - \frac{F^2}{2\omega^2} \int_0^{\tau_T} d\xi \sinh^2(\omega \xi) \quad (6.67)$$

but now

$$\tau_T = \frac{1}{\omega} \ln[\gamma + \sqrt{\gamma^2 + 1}] \approx \frac{1}{\omega} \ln(2\gamma). \quad (6.68)$$

Exercise

Calculate the integral and show that in the limit $\gamma \gg 1$ this rate is given by the expression familiar from the time-dependent perturbation theory for the multiphoton ionization process:

$$\Gamma \propto F^{2\text{IP}/\omega} \propto I^{\text{IP}/\omega}. \quad (6.69)$$

Finally, do the calculation for the general case of arbitrary γ and derive the general expression for the ionization rate

$$\Gamma \propto \exp \left[-\frac{F^2}{\omega^3} \left[\left(\gamma^2 + \frac{1}{2} \right) \omega \tau_T - \frac{1}{4} \sinh(2\omega \tau_T) \right] \right], \quad (6.70)$$

where $\omega \tau_T = \ln[\gamma + \sqrt{\gamma^2 + 1}] = \text{Arcsh}(\gamma)$.

6.6

Semiclassical Picture of High Harmonic Generation

Now let us see how the SFA theory can be applied to such a highly nonperturbative phenomenon as the generation of very high harmonics of intense incident radiation.

First, let us recall where these harmonics come from. For an experimentalist, they come from a little gas jet sitting in a vacuum chamber and irradiated by a laser. For a theorist, harmonics come from the Fourier components of laser-induced polarization $P(t)$ in the gas,

$$P(t) = n_0 d(t) = n_0 \langle \Psi(t) | d | \Psi(t) \rangle , \quad (6.71)$$

where n_0 is the number density. All we need is $\Psi(t)$, the wavefunction we already know from the SFA theory,

$$\Psi(t) = a_g(t) |\Phi_g\rangle + \int d\mathbf{k} |\mathbf{k}\rangle a_{\mathbf{k}} , \quad (6.72)$$

where $|g\rangle$ is the ground state. Using the SFA expressions for the amplitudes $a_k(t)$, and assuming that the ionization is not too strong and hence most of the amplitude always resides in the ground state, hence $a_g \approx \exp[+iIP(t - t_i)]$, we get

$$d(t) = -i \int dt' \int d\mathbf{k} \langle \Phi_g | d | \mathbf{k} \rangle e^{-i \int_{t'}^t E(t'') dt'' - iIP(t-t')} \\ F \cos \omega t' (\mathbf{k} + A(t') - A(t)) |d| \Phi_g \rangle + c.c. \quad (6.73)$$

This rather lengthy and cumbersome expression can be simplified quite a bit if we do three things:

- 1) Recall that the preexponential factors are wrong anyway and drop them.
- 2) Recall that the exponential dependence on k is quadratic and hence the integral over $d\mathbf{k}$ is from a Gaussian function.
- 3) Recall that the integration of Gaussians, even with very involved quadratic expressions, can be easily performed once we find the points at which the phase of the exponent is stationary with respect to all the integration variables.

Before doing that, I will add a third integral into this already involved expression. I want a specific Fourier component of the dipole, at a frequency Ω :

$$d(\Omega) \sim -i \int dt \int dt' \int d\mathbf{k} e^{-i \int_{t'}^t E(t'') dt'' - iIP(t-t') + i\Omega t} , \quad (6.74)$$

where I dropped all matrix elements, and also left only the positive Ω part of the spectrum. This $d(\Omega)$ is the harmonic response of a single atom.

The triple integral (actually, fivefold if you count that there are three integrals over the momentum) is very transparent and logical. The electron can be promoted

to the continuum at any time t' – thus the integral over t' . It can emit a photon with frequency Ω at any moment t – thus the integral over t . In principle, it can be in any state $|k\rangle$ at the moment of emission – thus the integral over dk . The $\exp(+i\Omega t)$ corresponds to the emission of the photon Ω , while the rest of the phase is related to the electron absorbing (changing) energy while moving in the continuum. The energy is measured from the ground state (thus the IP part), which is logical since the harmonic emission concludes in the ground state.

Let us look at the phase in this integral: is it fast oscillating or not? If the phase accumulation is many π over one cycle of the driving field, that would be fast. This is indeed the case when

$$U_p = \frac{F^2}{4}\omega^2 \gg \omega , \quad (6.75)$$

where U_p is the so-called ponderomotive energy – the average energy of free-electron oscillations in the laser field. Since the phase

$$\begin{aligned} \Theta(t, t', p) &= \int_{t'}^t E(\tau)d\tau + \text{IP}(t - t') - \Omega t \\ &= \int_{t'}^t d\tau \frac{1}{2}[p + A(\tau) - A(t)]^2 + \text{IP}(t - t') - \Omega t \end{aligned} \quad (6.76)$$

is oscillating fast, let us look for its stationary points. The phase depends on all three integration variables. Hence, we have to find first derivatives with respect to all these three variables and find those points where all are equal to zero. Calculating the partial derivatives of Θ , we obtain the following conditions:

$$\begin{aligned} \int_{t'}^t d\tau [k + A(\tau) - A(t)] &= 0 \\ \frac{1}{2}[k + A(t') - A(t)]^2 + \text{IP} &= 0 \\ \frac{1}{2}k^2 + \text{IP} &= \Omega . \end{aligned} \quad (6.77)$$

These equations can be rewritten in a very transparent form:

$$\begin{aligned} x(t) &= x(t') \\ \frac{1}{2}k^2(t') + \text{IP} &= 0 \\ \frac{1}{2}k^2(t) + \text{IP} &= \Omega . \end{aligned} \quad (6.78)$$

The first condition says that, in order to emit the photon, the electron must come back to the same spot from where it left as it started to tunnel out. Making a very reasonable assumption that the electron departed from the core, we see that the electron must come back to the same core of the same parent ion, after oscillating in the laser field.

The second condition is already familiar to us. It cannot be satisfied classically, and describes tunneling. The corresponding moment $t' = t'_{\text{in}}$ is the moment when the electron enters the classically forbidden region, just like in the case of ionization which we have considered above. Its imaginary part τ_T determines the tunneling time, and its real part t'_{out} is determined by the condition

$$\mathbf{k}(t_{\text{out}}) = \mathbf{k}(t) + \mathbf{A}(t_{\text{out}}) - \mathbf{A}(t) \approx 0 \quad (6.79)$$

in the limit of large U_p , when $\gamma^2 \equiv \text{IP}/2U_p \ll 1$.

The third condition is nothing but the energy conservation law for the emission of the harmonic photon Ω .

So now we have a simple classical physical picture emerging from the fivefold integral. This picture is of an electron tunneling out and appearing in the continuum at some time t_{out} . It emerges from under the barrier with nearly zero velocity. Then it moves in the laser field until it comes back to the same parent ion. Here, it converts its instantaneous kinetic energy $\mathbf{k}^2(t)/2$ into a photon by recombining into the ground state. The photon energy is $\Omega = \mathbf{p}^2(t)/2 + \text{IP}$.

The most important result that follows from the classical equations and its quantum counterpart for harmonic generation is that the maximum electron energy at the return scales with U_p as $3.17 U_p$. One can easily check it by taking different possible moments of birth t_{out} , setting classical initial conditions to zero (both position and velocity) and finding the instantaneous kinetic energy at the moment of return t , defined as the moment when the electron coordinate is equal to zero again. The upper limit on the energy at the moment of return implies that classically harmonic spectra cannot extend beyond the cutoff at $\text{IP} + 3.17 U_p$. Quantum mechanically, harmonics at higher energies are still possible – but require complex t to satisfy the energy conservation law. As the stationary phase point for t -integral moves into the complex plane, the contribution dies out exponentially.

Turning back to the quantum analysis, once we know the stationary phase points that satisfy the equations above, we can easily find the answer for the full integral. In the limit $\gamma^2 \ll 1$, the five-fold integral reduces to the product of three amplitudes for ionization (tunneling), propagation, and recombination:

$$d(\Omega) \propto A_{\text{rec}}(t(\Omega)) A_{\text{prop}}(t_{\text{out}}(t) \rightarrow t) A_{\text{ion}}(t_{\text{in}} \rightarrow t_{\text{out}}(t)) . \quad (6.80)$$

This factorized form of the expression for the induced dipole $d(\Omega)$ appears as a natural consequence of the saddle point method, which implies that the result is proportional to the integrand taken at the stationary point. The ionization amplitude is given by the imaginary part of the phase, $\exp(-\sigma)$, just like for ionization. It corresponds to the time-integral for the phase $S(k, t, t')$ from $t' = t_{\text{in}}$ to t_{out} . The propagation amplitude arises from the momentum integral and depends on t, t' . It contains the next component of the factor $\exp(-iS(k, t, t'))$, which corresponds to the integral from $t' = t_{\text{out}}$ to t . It also contains the factor $(t - t_{\text{in}})^{-3/2}$, which describes the spreading of the continuum wave packet and results from integration over the momenta k . The recombination amplitude is given by the transition dipole between the continuum state with momentum $k(t)$ and the ground state.

More detailed discussion of this factorization, and of the theory of high harmonic generation is presented in the next Chapter 7.

6.7

Conclusion

Any attempt to develop tractable analytical theory has to confront reality. And the reality is such that nine times out of ten perturbation theory of some sort is the only tractable approach. The strong-field approximation is an approximation to the strong-field S-matrix, with the binding potential treated as perturbation for the continuum motion of the electron. It has many drawbacks and “wrongs” that fly right into the face of any rigorous quantum theory, and it continues to amaze me that one of the key original papers – that by L. V. Keldysh from 1965 [4, 5] – was published in such a puritan journal as the *Journal of Experimental and Theoretical Physics*. Fortunately, the SFA gets most of the basic physics right, providing an excellent basis for understanding the fundamentals of strong-field processes. Moreover, it can be modified and turned into a quantitatively accurate theory, see [2, 3, 6] and Chapter 7 of this book.

Importantly, the SFA allows us to see simple classical pictures that underlie the seemingly very complex strong-field dynamics. This classical picture is due to P. Corkum and F. Brunel [7–10], and it was predicated by the quantum insight developed by M. Kuchiev [11, 12] and by the key numerical results of K. Schafer, J. Krause and K. Kulander [13]. By now, the new students in the field begin with the simple classical picture, taking it for granted. It is, however, important to know how this picture emerged from the combination of quantum and classical analysis and the experimental results. I strongly recommend to begin with the papers of F. Brunel [8–10] and M. Kuchiev [11, 12] and K. Schafer *et al.* [13], then turning to the seminal paper by P. Corkum [7].

In addition to the SFA [4, 5, 14–17], a more accurate but technically more complicated approach was developed in the 1960s by V. S. Popov, A. M. Perelomov and M. V. Terentév – the so-called PPT theory [18–25]. Finally, I must mention the effective range theory (ERT) of M. Frolov, N. Manakov, and A. Starace [26–28], which grew out of the earlier work of L. Rapoport, N. Manakov, and B. Zon. It is essentially exact for the short-range binding potentials (such as those of negative ions). It also shows that the PPT theory, when applied to the short-range potentials, is almost exact – the only thing it is missing is the Stark shift of the ground state. Unlike the SFA, the ERT and the PPT are gauge-invariant.

The insight gained from these theories is instrumental in turning the approximate SFA models into quantitatively accurate ones. The corresponding ideas were suggested in [2] and very successfully used by T. Brabec, F. Krausz, and V. Yakovlev already in late 1990s and early 2000s to describe experiments on high harmonic generation and the production of attosecond pulses in atomic gases (see, e.g., [6]). The version known as the quantitative rescattering theory, developed by C.D. Lin, T. Morishita and co-workers has been very successful in describing many aspects

of strong-field experiments in molecules [3]. It shows how well one can do when armed with clear understanding of the basic underlying physical mechanisms. For example, in the case of high harmonic generation, the approximate SFA expression can become quantitatively accurate by substituting the correct ionization amplitudes and proper recombination dipoles, which take into account the structure of the atom or molecule.

References

- 1 Lewenstein, M., Kulander, K.C., Schafer, K.J., and Bucksbaum, P.H. (1995) Rings in above-threshold ionization: A quasi-classical analysis. *Phys. Rev. A*, **51**, 1495–1507, doi:10.1103/PhysRevA.51.1495.
- 2 Ivanov, M.Y., Brabec, T., and Burnett, N. (1996) Coulomb corrections and polarization effects in high-intensity high-harmonic emission. *Phys. Rev. A*, **54**, 742–745, doi:10.1103/PhysRevA.54.742.
- 3 Lin, C.D., Le, A.T., Chen, Z.J., Morishita, T., and Lucchese, R. (2010) Strong-field rescattering physics-self-imaging of a molecule by its own electrons. *J. Phys. B*, **43** (12), 122001.
- 4 Keldysh, L.V. (1964) *Zh. Eksp. Teor. Fiz.*, **47**, 1945, (in Russian).
- 5 Keldysh, L.V. (1965) Ionization in field of a strong electromagnetic wave. *Soviet Phys. JETP-USSR*, **20** (5), 1307.
- 6 Brabec, T. and Krausz, F. (2000) Intense few-cycle laser fields: Frontiers of nonlinear optics. *Rev. Mod. Phys.*, **72**, 545–591, doi:10.1103/RevModPhys.72.545.
- 7 Corkum, P.B. (1993) Plasma perspective on strong field multiphoton ionization. *Phys. Rev. Lett.*, **71**, 1994–1997, doi:10.1103/PhysRevLett.71.1994.
- 8 Brunel, F. (1987) Not-so-resonant, resonant absorption. *Phys. Rev. Lett.*, **59**, 52–55, doi:10.1103/PhysRevLett.59.52.
- 9 Corkum, P.B., Burnett, N.H., and Brunel, F. (1989) Above-threshold ionization in the long-wavelength limit. *Phys. Rev. Lett.*, **62**, 1259–1262, doi:10.1103/PhysRevLett.62.1259.
- 10 Brunel, F. (1990) Harmonic-generation due to plasma effects in a gas undergoing multiphoton ionization in the high-intensity limit. *J. Opt. Soc. Am. B*, **7** (4), 521–526.
- 11 Kuchiev, M.Y. (1987) Atomic antenna. *Pisma Zh. Eksp. Teor. Fiz.*, **45**, 319, (in Russian).
- 12 Kuchiev, M.Y. (1987) Atomic antenna. *JETP Letters*, **45** (7), 404–406.
- 13 Krause, J.L., Schafer, K.J., and Kulander, K.C. (1992) High-order harmonic generation from atoms and ions in the high intensity regime. *Phys. Rev. Lett.*, **68**, 3535–3538, doi:10.1103/PhysRevLett.68.3535.
- 14 Faisal, F.H.M. (1973) Multiple absorption of laser photons by atoms. *J. Phys. B*, **6** (4), L89–L92.
- 15 Reiss, H.R. (1980) Effect of an intense electromagnetic field on a weakly bound system. *Phys. Rev. A*, **22**, 1786–1813, doi:10.1103/PhysRevA.22.1786.
- 16 Becker, A. and Faisal, F.H.M. (2005) Intense-field many-body s-matrix theory. *J. Phys. B*, **38** (3), R1–R56.
- 17 Becker, W., Lohr, A., and Kleber, M. (1995) Light at the end of the tunnel – 2-step and 3-step models in intense-field laser-atom physics. *Quantum Semiclass. Opt.*, **7** (3), 423–448.
- 18 Perelomov, A.M., Popov, V.S., and Terentev, M.V. (1966) *Zh. Eksp. Teor. Fiz.*, **50**, 1393.
- 19 Perelomov, A.M., Popov, V.S., and Terentev, M.V. (1966) Ionization of atoms in an alternating electric field. *Soviet Phys. JETP-USSR*, **23** (5), 924.
- 20 Perelomov, A.M., Popov, V.S., and Terentev, M.V. (1966) *Zh. Eksp. Teor. Fiz.*, **51**, 309.
- 21 Perelomov, A.M., Popov, V.S., and Terentev, M.V. (1967) Ionization of atoms in an alternating electric field. 2. *Soviet Phys. JETP-USSR*, **24** (1), 207.
- 22 Perelomov, A.M. and Popov, V.S. (1967) *Zh. Eksp. Teor. Fiz.*, **52**, 514.

- 23** Perelomov, A.M. and Popov, V.S. (1967) Ionization of atoms in an alternating electrical field. 3. *Soviet Physics JETP-USSR*, **25** (2), 336.
- 24** Popov, V.S., Kuznetsov, V.P., and Perelomov, A.M. (1967) *Zh. Eksp. Teor. Fiz.*, **53**, 331.
- 25** Popov, V.S., Kuznetsov, V.P., and Perelomov, A.M. (1968) Quasiclassical approximation for nonstationary problems. *Soviet Phys. JETP-USSR*, **26** (1), 222.
- 26** Frolov, M.V., Manakov, N.L., Pronin, E.A., and Starace, A.F. (2003) Model-independent quantum approach for intense laser detach-
ment of a weakly bound electron. *Phys. Rev. Lett.*, **91**, 053003, doi:10.1103/PhysRevLett.91.053003.
- 27** Frolov, M.V., Manakov, N.L., and Starace, A.F. (2008) Effective-range theory for an electron in a short-range potential and a laser field. *Phys. Rev. A*, **78**, 063418, doi:10.1103/PhysRevA.78.063418.
- 28** Frolov, M.V., Manakov, N.L., Sarantseva, T.S., and Starace, A.F. (2011) Analytic confirmation that the factorized formula for harmonic generation involves the exact photorecombination cross section. *Phys. Rev. A*, **83**, 043416, doi:10.1103/PhysRevA.83.043416.

7

Multielectron High Harmonic Generation: Simple Man on a Complex Plane

Olga Smirnova and Misha Ivanov

7.1

Introduction

Attosecond science has emerged with the discovery of coherent electron-ion collisions induced by a strong laser field, usually referred to as “recollisions” [1]. This discovery was initiated by the numerical experiments of K. Schafer, J. Krause and K. Kulander (see [2]). The work [1] drew on the concepts developed by F. Brunel and colleagues [3–5]. It has also been predicated by the concept of the “atomic antenna” [6] developed by M. Kuchiev. With the benefit of hindsight, we now see the “atomic antenna” [6] as the earliest quantum counterpart of the classical picture developed by [1, 7].¹⁾

The classical picture of strong-field-induced ionization dynamics is summarized as follows. Once ionization removes an electron from an atom or a molecule, this electron finds itself in the strong oscillating laser field. Newton’s equations of motion show that, within one or a few cycles after ionization, the oscillating electron can be driven back by the laser field to reencounter the parent ion. During this reencounter, referred to as recollision, the electron can do many things: scatter elastically (diffract), scatter inelastically (excitation or ionization of the parent ion), or radiatively recombine with the ion. It is this latter process that we will focus on here. The classical picture is usually referred to as the three-step model, or the simple man model.²⁾

1) While the quantum vision of [6] has predicated the classical picture, at that time it lacked the striking clarity and transparency of the classical model [1], which linked several key – and seemingly disparate – strong-field phenomena, like high harmonic generation, production of very high-energy electrons, and extreme efficiency of double ionization. The history of this discovery and of its impact on nonlinear optics and technology are rich and interesting in their own right. Some

of it is recounted, from a more historical perspective, in Chapter 10. Our purpose here is different – we simply urge the reader to read the papers [3–6, 8], as well as a seemingly unrelated paper [9].

2) As far as one of us (M.I.) can remember, the latter term has been used by K. Kulander, K. Schafer and H.-G. Muller, who have largely contributed to the development of this classical model.

If the recombination occurs at the exact same state from which the electron left, then the phase of the emitted radiation is the same from one atom to another, leading to the generation of coherent radiation in the medium. This process is known as high harmonic generation (HHG). It can produce many tens to hundreds of eV-broad coherent spectra and has two crucial applications. First, high harmonic emission is used to generate attosecond pulses of light (see, e.g., [10]), which can then be used in time-resolved pump-probe experiments. Second, the ultrabroad coherent harmonic spectrum carries attosecond information about the underlying nonlinear response of the medium, which can be extracted. The second direction is the subject of high harmonic spectroscopy (see, e.g., [11–14]) – an emerging imaging technique with the potential to combine sub-angstrom spatial and attosecond temporal resolution.

In the language of nonlinear optics, high harmonic generation is a frequency up-conversion process that results from the macroscopic response of the medium. The nonlinear polarization is induced in the medium by (1) the response of the atoms and the molecules, (2) the response of the free electrons, (3) the response of the guiding medium. Here we focus on the theory of the single atom or single molecule response. The description of macroscopic propagation effects, which determine how coherent radiation from different atoms or molecules add together, can be found in [15].

From the famous simple man model to the recent multichannel model, we will try to guide the reader through several landmarks in our understanding of high harmonic generation. We hope to provide recipes and insight for modeling the harmonic response in complex systems. The chapter includes the following sections:

- 7.2 The *Simple Man Model* of High Harmonic Generation (HHG)
- 7.3 Formal Approach for One-Electron Systems
- 7.4 *The Lewenstein Model*: Saddle Point Equations for HHG
- 7.5 Analysis of Complex Trajectories
- 7.6 Factorization of the HHG Dipole: Simple Man on a Complex Plane
- 7.7 *The Photoelectron Model* of HHG: The Improved Simple Man
- 7.8 *The Multichannel Model* of HHG: Tackling Multielectron Systems
- 7.9 Outlook
- 7.10 Appendix A: Supplementary Derivations
- 7.11 Appendix B: The Saddle Point Method
- 7.12 Appendix C: Treating the Cutoff Region: Regularization of Divergent Stationary Phase Solutions
- 7.13 Appendix D: Finding Saddle Points for the Lewenstein Model

Atomic units $\hbar = m = e = 1$ are used everywhere, unless specified otherwise.

7.2

The Simple Man Model of High Harmonic Generation (HHG)

Experiments in the 1980s and the early 1990s yielded an astounding result: shaken with sufficiently intense infrared laser radiation, the atomic medium was found to up-convert the frequency of the driving infrared laser light by up to two orders of magnitude (see, e.g., [16, 17]). The observed harmonic spectrum formed a long plateau, with many harmonic orders, followed by a sharp cutoff. This observation has to be placed in the context of what has been routinely seen in traditional nonlinear optics: in the absence of resonances, the nonlinear response would decrease dramatically with increasing harmonic order, and the harmonic numbers would hardly ever reach double digits, let alone form a plateau extending beyond $N = 101$.

To generate very high harmonics of the driving frequency, the atom has to absorb lots of photons. Generation of harmonics with numbers like $N = 21, \dots, 31, \dots$, and so on means that at least that many photons ($21, \dots, 31, \dots$) had to be absorbed by the atom.

The minimal amount of photons required for ionization is $N_0 = \text{IP}/\omega$, where IP is the ionization potential and ω is the infrared laser frequency. For $\text{IP} \sim 12\text{--}15\text{ eV}$ and an 800 nm driving IR laser field (the standard workhorse in many HHG experiments), $N_0 \sim 10$. One would have thought that once ten or so photons are absorbed, the electron should be free. And since it is well known that a free electron should not absorb any more photons, the emission should stop around $N = 11$ or so, in stark contrast with experimental observations.

Why and how many additional photons are absorbed? What is the underlying mechanism? The liberated electron oscillates in the laser field, and its instantaneous energy can be very high. Can this instantaneous electron energy be converted into the harmonic photons? Where is the source of nonlinearity, if the free electron oscillates with the frequency of the laser field?

The physical picture that clearly answered these questions is the classical three-step model. It is simple, remarkably accurate, and is also intrinsically subcycle: within one optical period, an electron is (1) removed from an atom or molecule, (2) accelerated by the oscillating laser field, and (3) driven back to recollide with the parent ion. This picture connects the key strong-field phenomena: above-threshold ionization, nonsequential double ionization, and high harmonic generation. It reveals the source of nonlinearity in HHG: the recombination of the accelerated electron with the ion.

How can one check that this mechanism is indeed responsible for HHG? The key thing to test is whether or not this picture explains the cutoff of the harmonic spectra, that is, the highest harmonic order that can be efficiently produced. Numerically, the empirical cutoff law was found to be $\Omega_{\max} = \text{IP} + 3U_p$ [18], where U_p is the cycle-averaged energy of the electron's oscillatory motion in the laser field. To calculate the classical cutoff, we should calculate the maximal instantaneous energy of the returning electron, but to do so we need to know the initial conditions for the electron just after ionization. These conditions are specified within the three-step

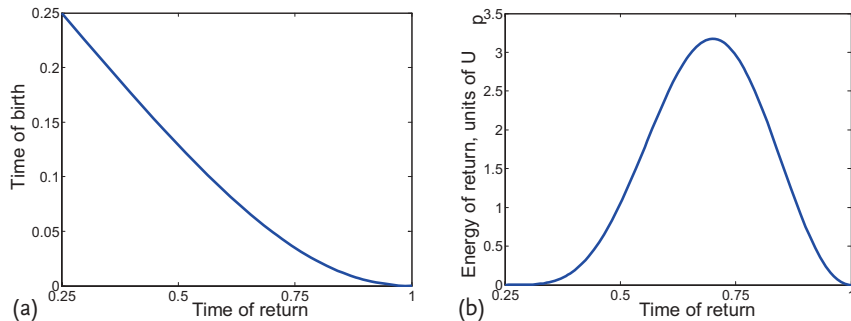


Figure 7.1 Window of classical “birth” times and the return energy. Time of birth vs. time of return (a). Energy of the electron at the time of return (b).

(simple man) model of HHG, which makes the following assumptions:

- SM1: The electron is born in the continuum at any time within the laser cycle.
- SM2: The electron is born near the ionic core (i.e., near the origin of the reference frame) with zero velocity.
- SM3: If the electron returns to the ionic core (origin), its instantaneous energy at the moment of return is converted into the harmonic photon.

The pull of the ionic core on the liberated electron is neglected in the model, which is not unreasonable considering the very large excursions that the electron makes in the strong infrared laser field. The possibility that the electron returns to the core is dictated by the phase of the laser field at which it is launched on its classical orbit, and the time-window for the returning trajectories – the range of the “birth” times t_B – shown in Figure 7.1.

The calculation is done as follows: for each t_B , we find the time of return t_R to the electron’s original position (Figure 7.1a) and the energy at the moment of return (Figure 7.1b). The assumption that the strong laser field dominates the electron’s motion after ionization simplifies our calculations. Once the ionic core potential is neglected, the kinetic momentum (velocity) at the time of birth t_B can be written as $\mathbf{k}(t_B) = \mathbf{p} + \mathbf{A}(t_B)$, where \mathbf{p} is the canonical momentum of the electron and $\mathbf{A}(t)$ is the vector potential of the laser field, which is related to the electric field $\mathbf{F}(t)$ as $\mathbf{F}(t) = -\partial \mathbf{A}/\partial t$. The condition $\mathbf{k}(t_B) = 0$ (SM2) specifies $\mathbf{p} = -\mathbf{A}(t_B)$. Therefore, the electron kinetic momentum at all later times t is $\mathbf{k}(t) = -\mathbf{A}(t_B) + \mathbf{A}(t)$ and the electron energy at the time of return is

$$E_{\text{ret}}(t_R) = \frac{\mathbf{k}^2(t_R)}{2} = \frac{(\mathbf{A}(t_B) - \mathbf{A}(t_R))^2}{2} .$$

The zero displacement of the electron from the time of birth, t_B , to the time of return, t_R , (SM3) defines the return time t_R :

$$\int_{t_B}^{t_R} dt (\mathbf{A}(t) - \mathbf{A}(t_B)) = 0 . \quad (7.1)$$

According to this model, the maximal return energy is about $3.17 U_p$, where $U_p = F^2/4\omega^2$ and F is the electric field amplitude (see Figure 7.1). Then the maximum energy of the emitted harmonic photon is $3.17 U_p + IP$, where IP is the binding energy of the ground state to which the electron recombines, is in excellent agreement with the empirical cutoff law found numerically [2].

The formal quantum approach considered in the next section will first take us away from the simple classical model. However, just like the recolliding electron revisits the ion, we will revisit the simple man model several times in this chapter, refining it at each step.

7.3

Formal Approach for One-Electron Systems

The response of an individual atom or a molecule $\mathbf{P}(\mathbf{r}, t) = n \mathbf{D}(t)$ is proportional to the induced dipole $\mathbf{D}(t)$:

$$\mathbf{D}(t) = \langle \Psi(t) | \hat{\mathbf{d}} | \Psi(t) \rangle , \quad (7.2)$$

where n is the number density, $\hat{\mathbf{d}}$ is the dipole operator, and $\Psi(t)$ is the wavefunction of the system obtained by solving the time-dependent Schrödinger equation (TDSE) with the Hamiltonian $\hat{H}(t)$:

$$i \frac{\partial \Psi(t)}{\partial t} = \hat{H}(t) \Psi(t) . \quad (7.3)$$

We will first focus on the single active electron approximation (see Section 7.8 for the multielectron case). This approximation assumes that only one electron feels the laser field – the one that is liberated via strong-field ionization and subsequently recollides with the parent ion. All other electrons are frozen in the ion, unaffected by the laser field. The Hamiltonian of our system in the single active electron approximation is

$$\hat{H}(t) = \frac{\hat{\mathbf{p}}^2}{2} + U(\hat{\mathbf{r}}) + \hat{V}_L(t) , \quad (7.4)$$

where $\hat{\mathbf{p}} = -i\nabla_{\mathbf{r}}$ is the momentum operator, $U(\hat{\mathbf{r}})$ describes the interaction of the electron with the ionic core, and $\hat{V}_L(t)$ describes the interaction between the electron and the laser field. In the dipole approximation and in the length gauge, $\hat{V}_L(t) = -\hat{\mathbf{d}} \cdot \mathbf{F}(t) = \hat{\mathbf{r}} \cdot \mathbf{F}(t)$ (see Chapter 6 to learn about different gauges or read Section 2.2.4 in the excellent book [19] for a more detailed discussion).

Formally, the solution of the Schrödinger equation (7.3) can be written in the integral form (see, e.g., [20] for a simple derivation):

$$|\Psi(t)\rangle = -i \int_{t_0}^t dt' \hat{U}(t, t') \hat{V}_L(t') \hat{U}_0(t', t_0) |g\rangle + \hat{U}_0(t, t_0) |g\rangle , \quad (7.5)$$

where the ket-vector $|g\rangle$ represents the wavefunction of the electron in the ground state at initial time $t = t_0$, $\hat{U}(t, t')$ is the full propagator, while $\hat{U}_0(t', t_0)$ is the field-free propagator. The propagators are the operators that describe the time evolution of the wavefunction. The propagator $\hat{U}_0(t', t_0)$ governs the electron dynamics from time t_0 to time t' without the laser field, and is determined by the following equations:

$$i \frac{\partial \hat{U}_0(t, t_0)}{\partial t} = \hat{H}_0 \hat{U}_0(t, t_0) , \quad (7.6)$$

$$\hat{U}_0(t_0, t_0) = 1 , \quad (7.7)$$

$$\hat{H}_0 = \frac{\hat{\mathbf{p}}^2}{2} + U(\hat{\mathbf{r}}) . \quad (7.8)$$

Symbolically, the solution of Eq. (7.6) can be written in the compact form

$$\hat{U}_0(t', t_0) = e^{-i \int_{t_0}^{t'} \hat{H}_0(\xi) d\xi} , \quad (7.9)$$

where the integral is *time-ordered*, that is, the contribution of later times to the evolution follows the contribution of the earlier times.

The full propagator $\hat{U}(t, t')$ governs the electron dynamics from time t' to the observation time t , driven by the combined action of the laser field and of the ionic core potential $U(\hat{\mathbf{r}})$. It is given by

$$i \frac{\partial \hat{U}(t, t')}{\partial t} = \hat{H} \hat{U}(t, t') , \quad (7.10)$$

$$\hat{U}(t, t') = 1 , \quad (7.11)$$

$$\hat{U}(t', t') = e^{-i \int_{t'}^t \hat{H}(\xi) d\xi} . \quad (7.12)$$

where the integral in the symbolic exponential expression is time-ordered. The propagation without the laser field is straightforward. Denoting the ground state energy $E_g = -\text{IP}$ (ionization potential) and the stationary ground state wavefunction $\Psi_g(\mathbf{r}) = \langle \mathbf{r} | g \rangle$, we have:

$$\Psi_g(\mathbf{r}, t') = U_0(t', t_0) \Psi_g(\mathbf{r}) = e^{i\text{IP}(t' - t_0)} \Psi_g(\mathbf{r}) . \quad (7.13)$$

The full propagator $\hat{U}(t, t')$, on the other hand, is just as hard to find as the solution of the original Eq. (7.3). The advantage of the integral expression Eq. (7.5) is that making meaningful approximations is technically easier and physically more transparent.

Remembering that the laser field is strong, we can try to neglect the ionic potential in the full propagator. In this case the electron is free from time t' to time t . Its motion is only affected by the laser field and is described by the Hamiltonian $\hat{H}_V(t) = \hat{\mathbf{p}}^2/2 + \hat{V}_L(t)$. The corresponding approximation is called the strong-field

approximation (SFA), and the propagator corresponding to $\hat{H}_V(t)$ is often called the Volkov propagator. The main advantage of the SFA is that the Volkov propagator can be found analytically. In the length gauge used here, the result of acting with the Volkov propagator $\hat{U}_V(t, t')$ on the plane wave with kinetic momentum $\mathbf{k}(t') = \mathbf{p} + \mathbf{A}(t')$ is

$$\begin{aligned}\hat{U}_V(t, t')|\mathbf{p} + \mathbf{A}(t')\rangle &= e^{-iS_V(\mathbf{p}, t, t')}|\mathbf{p} + \mathbf{A}(t)\rangle, \\ \langle \mathbf{r} | \mathbf{p} + \mathbf{A}(t) \rangle &= \frac{1}{(2\pi)^{3/2}} e^{i[\mathbf{p} + \mathbf{A}(t)] \cdot \mathbf{r}}, \\ S_V(\mathbf{p}, t, t') &= \frac{1}{2} \int_{t'}^t d\xi [\mathbf{p} + \mathbf{A}(\xi)]^2.\end{aligned}\quad (7.14)$$

That is, the plane wave with the kinetic momentum $\mathbf{k}(t') = \mathbf{p} + \mathbf{A}(t')$ turns into a plane wave with the kinetic momentum $\mathbf{k}(t) = \mathbf{p} + \mathbf{A}(t)$ and accumulates the phase $S_V(\mathbf{p}, t, t')$ on the way.

The relations in Eq. (7.14) define the Volkov function

$$\Psi_p^V(\mathbf{r}, t; t') = \frac{1}{(2\pi)^{3/2}} e^{-iS_V(\mathbf{p}, t, t')} e^{i[\mathbf{p} + \mathbf{A}(t)] \cdot \mathbf{r}}.$$

Formally, the Volkov function is an eigenstate of the time-periodic Hamiltonian. It provides the quantum-mechanical description of the behavior of the free electron in the laser field. The coordinate part of the Volkov function is a plane wave, and these plane waves form a complete basis at each moment of time:

$$\hat{1} = \int d\mathbf{p} |\mathbf{p} + \mathbf{A}(t)\rangle \langle \mathbf{p} + \mathbf{A}(t)|. \quad (7.15)$$

Within the SFA, Eq. (7.5) takes the form

$$|\Psi(t)\rangle = -i \int_{t_0}^t dt' \hat{U}_V(t, t') \hat{V}_L(t') \hat{U}_0(t', t_0) |g\rangle + \hat{U}_0(t, t_0) |g\rangle, \quad (7.16)$$

and can be solved analytically. The first term describes the interaction with the laser field, including ionization, the second term describes the field-free evolution of the nonionized part of the wavefunction.

Thus, it is natural to associate t' with the time when ionization is initiated: before t' the electron is bound, after t' the electron becomes excited and, within the SFA, free. Substituting Eq. (7.16) into Eq. (7.2) yields:

$$D(t) \simeq -i \langle \hat{U}_0(t, t_0) g | \hat{\mathbf{d}} | \int_{t_0}^t dt' \hat{U}_V(t, t') \hat{V}_L(t') \hat{U}_0(t', t_0) |g\rangle + \text{c.c.} \quad (7.17)$$

Here we have assumed that there is no permanent dipole in the ground state and that the contribution of the continuum-continuum transitions to the dipole is negligible. The latter assumption is fine as long as ionization is weak. Thus, the dipole

in Eq. (7.17) is evaluated between the bound and the continuum components of the same wavefunction.

The propagator $\hat{U}_V(t, t')$ is known when it acts on the Volkov states. Thus, we introduce the identity operator resolved on the Volkov states, Eq. (7.15), into Eq. (7.17):

$$\begin{aligned} D(t) &= -i \langle g | \hat{d} | \int_{t_0}^t dt' e^{i\text{IP}(t'-t)} \\ &\quad \times \int d\mathbf{p} U_V(t, t') |\mathbf{p} + A(t')\rangle \langle \mathbf{p} + A(t') | \hat{V}_L(t') | g \rangle + \text{c.c.} \end{aligned} \quad (7.18)$$

Finally, remembering that $\hat{V}_L(t) = -\hat{\mathbf{d}} \cdot \mathbf{F}(t)$, we rewrite Eq. (7.18) in the compact form:

$$D(t) = i \int_{t_0}^t dt' \int d\mathbf{p} \mathbf{d}^*(\mathbf{p} + A(t)) e^{-iS(\mathbf{p}, t, t')} \mathbf{F}(t') \mathbf{d}(\mathbf{p} + A(t')) + \text{c.c.}, \quad (7.19)$$

where we have introduced the dipole matrix elements $\mathbf{d}(\mathbf{p} + A(t))$ of the transitions between the ground state and the plane wave continuum,

$$\mathbf{d}(\mathbf{p} + A(t)) \equiv \langle \mathbf{p} + A(t) | \hat{d} | g \rangle. \quad (7.20)$$

The phase

$$S(\mathbf{p}, t, t') \equiv \frac{1}{2} \int_{t'}^t [\mathbf{p} + A(\tau)]^2 d\tau + \text{IP}(t - t') \quad (7.21)$$

is often referred to as action, and we will use this term below, even though, strictly speaking, it is only the energy part of the full classical action.

It is convenient to rewrite Eq. (7.19) for the harmonic dipole $D(t)$ by evaluating the integral over t' by parts (see, e.g., [21, 22] and Appendix 7.10):

$$\int_{t_0}^t dt' e^{-iS(\mathbf{p}, t, t')} \mathbf{F}(t') \mathbf{d}(\mathbf{p} + A(t')) = \int_{t_0}^t dt' e^{-iS(\mathbf{p}, t, t')} \Upsilon(\mathbf{p} + A(t')), \quad (7.22)$$

$$\Upsilon(\mathbf{p} + A(t')) = \left[\frac{(\mathbf{p} + A(t'))^2}{2} + \text{IP} \right] \langle \mathbf{p} + A(t') | g \rangle, \quad (7.23)$$

where $\langle \mathbf{p} + A(t) | g \rangle$ is a Fourier transform of the ground state $|g\rangle$, $\Upsilon(\mathbf{p})$ reflects the dependence of ionization step on the angular structure of the ground state. Equation (7.19) takes the following form:

$$D(t) = i \int_{t_0}^t dt' \int d\mathbf{p} \mathbf{d}^*(\mathbf{p} + A(t)) e^{-iS(\mathbf{p}, t, t')} \Upsilon(\mathbf{p} + A(t')) + \text{c.c.} \quad (7.24)$$

The harmonic spectrum $I(N\omega)$ can be obtained from the Fourier transform of $D(t)$:

$$I(N\omega) \propto (N\omega)^4 |D(N\omega)|^2 ,$$

$$D(N\omega) = \int dt e^{iN\omega t} D(t) . \quad (7.25)$$

Note that $S(\mathbf{p}, t, t')$ is large and the integrand is a highly oscillating function, which is an advantage for the analytical evaluation of this integral. The analytical approach [23] is based on the saddle point method (see Appendix 7.11), which is the mathematical tool for evaluating integrals from fast-oscillating functions. It provides the physical picture of high harmonic generation as a three-step process involving ionization, propagation and recombination [24]. It also supplies the time-energy mapping [11, 12] crucial for attosecond imaging, and it is the basis for the extension of the above approach beyond the SFA and beyond the single active electron approximation (see, e.g., [13]).

Let us now focus on the analytical saddle point approach to HHG.

7.4

The Lewenstein Model: Saddle Point Equations for HHG

The goal of this section is to evaluate the integral equations ((7.24) and (7.25)) using the saddle point method (see Chapter 6 and Appendix 7.11). We need to find saddle points for all three integration variables t' , t and \mathbf{p} , that is, points where the rapidly changing phase of the integrand has zero derivatives with respect to all integration variables.

There are two ways to deal with the integrals Eqs. (7.24) and (7.25). First, one can treat them as multidimensional integrals, that is, one finds the saddle points for all the integration variables “in parallel,” and then one follows the multidimensional saddle point approach to deal with the whole multidimensional integral “at once.”

One can also take a different route and evaluate the multiple integrals Eqs. (7.24) and (7.25) step by step, sequentially. First, we find the saddle points t_i for the integral over t' from the saddle point equation:

$$\frac{dS}{dt'} \equiv \frac{\partial S(t', \mathbf{p}, t)}{\partial t'} = 0 , \quad (7.26)$$

where the phase S is given by Eq. (7.21). We then evaluate the integral over t' treating it as a one-dimensional integral, with \mathbf{p} and t entering as fixed parameters.

Next, we move to the integral over \mathbf{p} . Dealing with its saddle points, we should keep in mind that the saddle points of the previous integral $t' = t_i \equiv t_i(\mathbf{p}, t)$ depend on \mathbf{p} : $\partial t_i / \partial p_\alpha \neq 0$, $\alpha = x, y, z$.

Fortunately, thanks to Eq. (7.26), the explicit dependence of $t_i(\mathbf{p}, t)$ on \mathbf{p} does not affect the position of the saddle points for the \mathbf{p} -integral:

$$\frac{dS(t_i, \mathbf{p}, t)}{dp_\alpha} \equiv \frac{\partial S(t_i, \mathbf{p}, t)}{\partial p_\alpha} + \frac{\partial S(t_i, \mathbf{p}, t)}{\partial t_i} \frac{dt_i}{dp_\alpha} = \frac{\partial S(t_i, \mathbf{p}, t)}{\partial p_\alpha} = 0 . \quad (7.27)$$

Note that the integral over \mathbf{p} is multidimensional, which leads to a slightly different form of the preexponential factor (prefactor) involving the Hessian (see Appendix 7.11).

Finally, we deal with the integral over t . Here, again, the saddle points $\mathbf{p}_s(t_i, t)$ depend on t : $\partial p_{s,a}/\partial t \neq 0$. But once again the explicit dependence of $\mathbf{p}_s(t_i, t)$ on t does not affect the position of the saddle points thanks to Eq. (7.27):

$$\frac{dS(t_i, \mathbf{p}_s, t)}{dt} \equiv \frac{\partial S(t_i, \mathbf{p}_s, t)}{\partial t} + \frac{\partial S(t_i, \mathbf{p}_s, t)}{\partial p_a} \frac{dp_a}{dt} = \frac{\partial S(t_i, \mathbf{p}_s, t)}{\partial t} = 0. \quad (7.28)$$

The fact that both routes yield the same saddle point equations is, of course, not surprising – one should not get different answers depending on how the integral is evaluated.

Using Eq. (7.21), we obtain the explicit form of Eqs. (7.26)–(7.28), which define the saddle points t_i, \mathbf{p}_s, t_r :

$$\frac{[\mathbf{p}_s + \mathbf{A}(t_i)]^2}{2} + \text{IP} = 0, \quad (7.29)$$

$$\int_{t_i}^{t_r} [\mathbf{p}_s + \mathbf{A}(t')] dt' = 0, \quad (7.30)$$

$$\frac{[\mathbf{p}_s + \mathbf{A}(t_r)]^2}{2} + \text{IP} = N\omega. \quad (7.31)$$

Here, \mathbf{p}_s is the electron drift (canonical) momentum, $\mathbf{k}_s(t) = \mathbf{p}_s + \mathbf{A}(t)$ is the kinetic momentum (the instantaneous electron velocity, up to the electron mass). The trajectories that satisfy Eqs. (7.29)–(7.31) are known as quantum orbits, see for example [25–27].

Equation (7.30) requires that the electron returns to the parent ion – the prerequisite for recombination. Indeed, the time integral of the electron velocity yields the electron displacement from t_i to t_r . Thus, Eq. (7.30) dictates that the displacement is equal to zero.

Whereas Eq. (7.31) describes energy conservation during recombination, Eq. (7.29) describes tunneling (see Chapter 6). It shows that the electron's kinetic energy at t_i is negative, its velocity $\mathbf{k}_s(t_i) = \mathbf{p}_s + \mathbf{A}(t_i)$ is complex, and hence $t_i = t'_i + t''_i$ is also complex – the hallmarks of the tunneling process.

The time t_i can be identified with the moment when the electron *enters the barrier*, see Figure 7.2. Its *real part* will then correspond to the time when the electron *exits the barrier*. The origin of this concept will be explained in the next section.

The electron displacement during this “under-the-barrier” motion from t_i to its real part $\Re(t_i)$ is, in general, complex. Whether we like it or not, it yields a complex coordinate of “exit” $\mathbf{r}_{\text{ex}} = \mathbf{r}'_{\text{ex}} + i\mathbf{r}''_{\text{ex}}$ at $\Re(t_i) \equiv t'_i$ (see, e.g., [28]):

$$\int_{t_i}^{t'_i} [\mathbf{p} + \mathbf{A}(t')] dt' = \mathbf{r}'_{\text{ex}} + i\mathbf{r}''_{\text{ex}}. \quad (7.32)$$

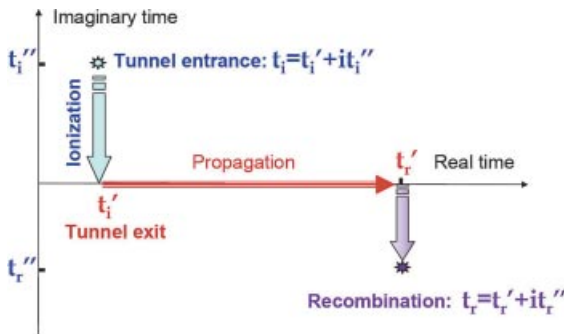


Figure 7.2 Contour of the time integration in the action S . Ionization occurs from the complex time t_i to the real time t_i' .

As a result, Eqs. (7.30) and (7.31) cannot be satisfied unless \mathbf{p} or t_r are complex. Indeed, t_r must be complex to compensate for the imaginary displacement accumulated under the barrier. However, the energy conservation condition in Eq. (7.31) dictates that $\mathbf{k}_s(t_r) = \mathbf{p}_s + \mathbf{A}(t_r)$ is real at the moment of recombination. Therefore \mathbf{p}_s must also be complex to compensate for the imaginary part of $\mathbf{A}(t_r)$.

Thus, we are forced to conclude that, in contrast to the classical trajectories of the simple man model, the quantum orbits are trajectories with complex canonical momenta, complex velocities, and complex displacements. These trajectories evolve in complex time. The only quantity that is required to be real is the one we measure – the energy of the emitted photon, see Eq. (7.31). Later in this chapter, we will see when and how one can replace these trajectories with a different set of trajectories that do not involve complex canonical momenta and therefore better correspond to the classical picture. But for the moment, let us deal with what we've got.

For a linearly polarized field, it is convenient to rewrite Eqs. (7.29)–(7.31) in terms of electron momenta parallel, $p_{s,\parallel}$, and perpendicular, $p_{s,\perp}$, to the polarization vector of the laser field:

$$\frac{[p_{s,\parallel} + A(t_i)]^2}{2} + I_{p,\text{eff}} = 0 , \quad (7.33)$$

$$\int_{t_i}^{t_r} [p_{s,\parallel} + A(t')] dt' = 0 , \quad \int_{t_i}^{t_r} p_{s,\perp} dt' = 0 , \quad (7.34)$$

$$\frac{[p_{s,\parallel} + A(t_r)]^2}{2} + I_{p,\text{eff}} = N\omega , \quad (7.35)$$

where we have introduced an “effective” ionization potential: $I_{p,\text{eff}} = \text{IP} + p_{s,\perp}^2/2$. Equations (7.34) dictate that the stationary perpendicular canonical momentum is equal to zero for the linearly polarized field, $p_{s,\perp} = 0$ and hence $I_{p,\text{eff}} = \text{IP}$. Then,

Eqs. (7.33)–(7.35) reduce to:

$$\frac{[p_{s,\parallel} + A(t_i)]^2}{2} + \text{IP} = 0 , \quad (7.36)$$

$$\int_{t_i}^{t_r} [p_{s,\parallel} + A(t')] dt' = 0 , \quad (7.37)$$

$$\frac{[p_{s,\parallel} + A(t_i)]^2}{2} + \text{IP} = N\omega . \quad (7.38)$$

Separating the real and the imaginary parts in Eqs. (7.36)–(7.38), we obtain six equations for six unknowns: $t_i = t'_i + it''_i$, $t_r = t'_r + it''_r$, $p_{s,\parallel} = p' + ip''$. Our goal is to solve these equations for each harmonic order N . Here is one way to do it, which we find simple and visually appealing.

First, we use Eqs. (7.36) and (7.38) to express all variables via the real, t'_r , and the imaginary, t''_r , return times. This can be done analytically. Second, we substitute the result into the real part and the imaginary part of Eq. (7.37):

$$F_1(N, t'_r, t''_r) = \Re \left[\int_{t_i}^{t_r} [p_{s,\parallel} + A(t')] dt' \right] = 0 , \quad (7.39)$$

$$F_2(N, t'_r, t''_r) = \Im \left[\int_{t_i}^{t_r} [p_{s,\parallel} + A(t')] dt' \right] = 0 . \quad (7.40)$$

Third, we solve Eqs. (7.39) and (7.40) to find the only two remaining unknowns: the real, t'_r , and the imaginary, t''_r , return times. While Eqs. (7.39) and (7.40) cannot be solved analytically, dealing with two equations is much easier than dealing with the original six.

Solving Eqs. (7.39) and (7.40) means that we need to find the minima of the two-dimensional surface $F(N, t'_r, t''_r)$, defined in the plane of the real, t'_r , and the imaginary, t''_r , return times:

$$F(N, t'_r, t''_r) \equiv [F_1(N, t'_r, t''_r)]^2 + [F_2(N, t'_r, t''_r)]^2 = 0 . \quad (7.41)$$

These minima can be easily found numerically using the gradient method. The advantage of using $F(N, t'_r, t''_r)$ is the ability to visualize the solutions: by simply plotting the surface given by Eq. (7.41), see Figure 7.3, one can examine the positions of the minima versus the harmonic number N .

If we restrict our analysis to those solutions that lie within the same cycle of the laser field as the moment of ionization, $\Re(t_i)$, we will find two stationary solutions for each harmonic number N . These solutions are discussed in detail in the next section. They correspond to two families of quantum orbits, called the “short” and the “long” trajectories. The trajectories merge for the largest possible return energies, that is, near the cutoff of the harmonic spectrum.

There are also solutions that lie outside the laser cycle during which the electron was “born” into the continuum. These “superlong” trajectories describe second, third, and higher-order returns of the electron to the origin. In typical experimental conditions, their contribution to the high harmonic emission is negligible thanks to the macroscopic effects – very long trajectories do not phase match well (see, e.g., [25]). Only very recently, the experiments of A. Zair *et al.* [29] have been able to clearly resolve the contribution of these trajectories, and even identify their interference with the contribution from the long and the short trajectories.

The stationary phase method for the integral over the return time t breaks down when these two stationary points merge and the second derivative of the action with respect to the return time is equal to zero, $\partial^2 S / \partial t^2 = 0$. At this point, one needs to replace the standard saddle point method with the regularization procedure, discussed in Appendix 7.12.

Outside the cutoff region, and up to a global phase factor, the saddle point method yields the following expression for the harmonic dipole Eqs. (7.24) and (7.25):

$$\begin{aligned} D(N\omega) = & \sum_{j=1}^{4M} \left[\frac{2\pi}{i S''_{t_i, t_i}} \right]^{\frac{1}{2}} \left[\frac{2\pi}{i S''_{t_r, t_r}} \right]^{\frac{1}{2}} \frac{(2\pi)^{3/2}}{\sqrt{\det(i S''_{p_s, p_s})}} \\ & \times d^*(p_s + A(t_r^{(j)})) e^{-i S(p_s, t_r^{(j)}, t_i^{(j)})} \Upsilon(p_s + A(t_i)) e^{i N\omega t_r^{(j)}}, \end{aligned} \quad (7.42)$$

where the Hessian $\det(i S''_{p_s, p_s})$ appears due to the multidimensional nature of the integral over p . The sum runs over all stationary points j for M periods of the laser light, and the corresponding ionization and recombination times are labeled with the superscript j . Since there are two trajectories for each half-cycle of the laser field, that is, for each ionization “burst,” and since there are $2M$ ionization bursts for M laser cycles, the number of stationary points is $4M$. The length gauge SFA presents a good approximation for short-range potentials [30]. However, it misses polarization, the Stark shift and the depletion of the bound state, which can be introduced into Eq. (7.42) if necessary.

Note that expression Eq. (7.42) *cannot* be directly ported to long-range potentials. Indeed, in the long-range Coulomb potential the ground state has a different radial structure (compare Eqs. (7.55) and (7.56) below) and $\Upsilon(p_s + A(t_i))$ is singular exactly at the saddle point $[p_s + A(t_i)]^2/2 + \text{IP} = 0$. As a consequence, the saddle point calculations should be modified, (see, e.g., [21, 31]) to accommodate for the presence of such a singularity. Once the singularity is treated correctly [21, 31], the result is still incomplete and unsatisfactory, because the long-range potential also affects the structure of the continuum states, which cannot be accurately represented by the Volkov states. A consistent treatment of long-range effects including modifications of both bound and continuum states can be found in [28, 32]. A practical recipe for incorporating the effects of the Coulomb potential is discussed in the next section and in the Outlook section (Section 7.9).

7.5

Analysis of the Complex Trajectories

Let us now show how the above method of finding the saddle points works for a linearly polarized laser field $F = F_0 \cos(\omega t)$, which corresponds to the vector potential $A = -A_0 \sin(\omega t)$. We shall introduce the dimensionless variables $p_1 = \Re(p_{s,\parallel})/A_0$, $p_2 = \Im(p_{s,\parallel})/A_0$, $\phi_i = \omega t_i = \phi'_i + i\phi''_i$, $\phi_r = \omega t_r = \phi'_r + i\phi''_r$, $\gamma^2 = IP/(2U_p)$, $\gamma_N^2 = (N\omega - IP)/(2Up)$.

In terms of these variables, Eqs. (7.39) and (7.40) for the linearly polarized field yield:

$$\begin{aligned} F_1 &= p_1(\phi'_r - \phi'_i) - p_2(\phi''_r - \phi''_i) - \cos(\phi'_i) \cosh(\phi''_i) \\ &\quad + \cosh(\phi''_r) \cos(\phi'_r) = 0, \end{aligned} \quad (7.43)$$

$$\begin{aligned} F_2 &= p_1(\phi''_r - \phi''_i) + p_2(\phi'_r - \phi'_i) + \sin(\phi'_i) \sinh(\phi''_i) \\ &\quad - \sinh(\phi''_r) \sin(\phi'_r) = 0. \end{aligned} \quad (7.44)$$

The real and the imaginary parts of Eq. (7.38) allow us to express the real, p_1 , and the imaginary, p_2 , components of the canonical momentum via the real and the imaginary parts of the return time (for above-threshold harmonics):

$$p_1 = \cosh(\phi''_r) \sin(\phi'_r) + \gamma_N, \quad (7.45)$$

$$p_2 = \sinh(\phi''_r) \cos(\phi'_r). \quad (7.46)$$

The real and the imaginary parts of Eq. (7.36),

$$p_1 = \cosh(\phi''_i) \sin(\phi'_i), \quad (7.47)$$

$$p_2 + \gamma = \sinh(\phi''_i) \cos(\phi'_i), \quad (7.48)$$

allow us to express the real, ϕ'_i , and the imaginary, ϕ''_i , ionization times via p_1 and p_2 :

$$\phi'_i = \arcsin \left(\sqrt{\frac{(P - D)}{2}} \right), \quad (7.49)$$

$$\phi''_i = \text{arcosh} \left(\sqrt{\frac{(P + D)}{2}} \right), \quad (7.50)$$

where

$$\begin{aligned} P &= p_1^2 + \tilde{\gamma}^2 + 1, \\ D &= \sqrt{P^2 - 4p_1^2}, \\ \tilde{\gamma} &= \gamma + p_2. \end{aligned} \quad (7.51)$$

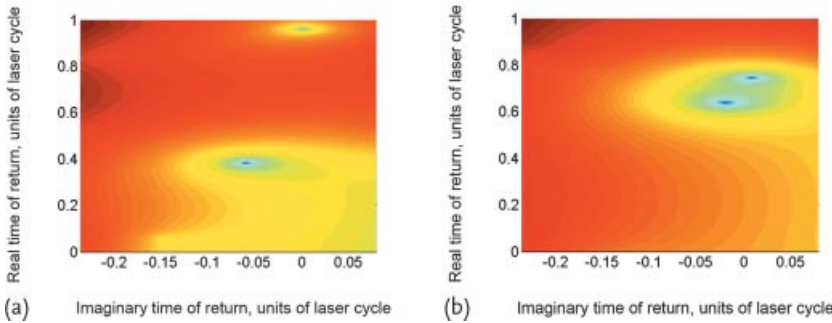


Figure 7.3 Surface in Eq. (7.41) for IP = 15.6 eV, $I = 1.3 \times 10^{14} \text{ W/cm}^2$, $\hbar\omega = 1.5 \text{ eV}$. $N = 11$ (a); two minima corresponding to short ($\phi'_r \sim 0.4$) and to long ($\phi'_r \sim 1$) tra-

jectories, respectively. $N = 27$ (b); the two minima corresponding to short and to long trajectories are merging together.

Now we can use our recipe:

- Pick a grid of values ϕ'_r, ϕ''_r in the complex plane of the return times ϕ_r .
- Pick a point ϕ'_r, ϕ''_r and calculate p_1, p_2 using Eqs. (7.45) and (7.46) and ϕ'_i, ϕ''_i using Eqs. (7.49) and (7.50).
- Substitute $p_1, p_2, \phi'_i, \phi''_i$ into Eqs. (7.43) and (7.44).
- Plot the function $F \equiv F_1^2 + F_2^2$ in the plane of the real and the imaginary return times.
- Look for the minima, see Figure 7.3.

Instead of reading out the solutions from the graph, one can find the minima using the gradient method. An alternative algorithm using the same ideas is described in Appendix 7.13.

The imaginary and the real return times (Figure 7.4b) define the integration contour in the complex plane: only along this contour the energy of return and there-

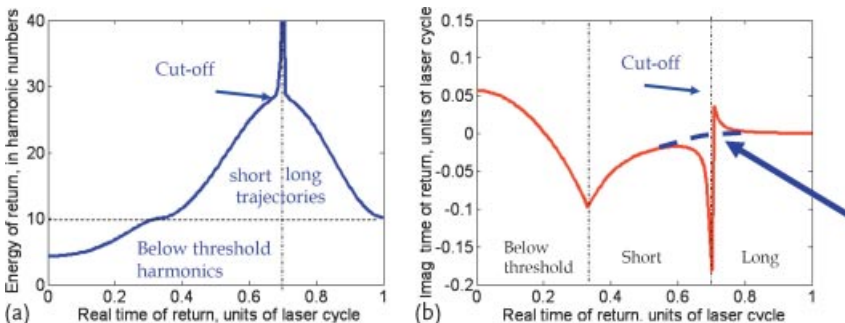


Figure 7.4 Emission energy, $E(t_r) + \text{IP} = N\omega$, vs. real time of return for IP = 15.6 eV, $I = 1.3 \times 10^{14} \text{ W/cm}^2$ (a). Imaginary time of return vs. real time of return (b). The solution

diverges in the cutoff region. The thick blue line schematically shows the desired outcome of the regularization procedure.

fore the energy of the emitted photon are real. This energy is shown in Figure 7.4a vs. the real component of the return time for typical experimental conditions.

The cutoff (maximal energy) corresponds to about $3.17 U_p + 1.32 \text{IP}$, see [23]. The extra 0.32IP comes from the extra kinetic energy the returning electron accumulates between the exit point from the barrier and the origin (see also Section 7.7). There are two different trajectories returning at different times that lead to the same recollision energy. Those returning earlier correspond to shorter excursion and are called “short trajectories,” those returning later are called “long trajectories” as they correspond to larger excursions and longer travel times.

Fortunately for attosecond imaging, the contributions of the long and short trajectories to the harmonic emission separate in the macroscopic response: the harmonic light diverges differently for those trajectories, and thus the signals coming from short and long trajectories can be collected separately. As a result, each harmonic N can be associated with a particular time delay between ionization and recombination, $t'_r - t'_i$, and therefore each harmonic takes a snapshot of the recombining system at a particular moment of time. This time-energy mapping, see [11, 12, 33], is the basis for attosecond time resolution in high harmonic spectroscopy.

As mentioned in the previous section, the stationary phase (saddle point) method for the integral over return times t breaks down near the cutoff, where the two stationary points (short and long trajectories) begin to coalesce and the second derivative of the phase S with respect to the return time is equal to zero, $\partial^2 S / \partial t^2 = 0$. The regularization of the solutions in the cutoff region is discussed in Appendix 7.12. Here, we shall proceed with the analysis of the stationary phase equations and turn to the ionization times.

The concept of ionization time together with the semiclassical (trajectory) perspective on ionization was first introduced by V. Popov and co-workers (PTT theory, see [34–37]). Just like in the Lewenstein model described above, the concept of trajectories arises from the application of the saddle point method to the integral describing ionization,³⁾

$$a_{\text{ion}}(\mathbf{p}, T) = -i \int_0^T dt' e^{-iS(\mathbf{p}, T, t')} \Upsilon(\mathbf{p} + A(t')) . \quad (7.52)$$

Here the upper limit of the integral in the action $S(\mathbf{p}, T, t')$ Eq. (7.21) is the real time T , at which the liberated photoelectron is observed (detected), function $\Upsilon(\mathbf{p} + A(t'))$ (see Eq. (7.23)) contains the Fourier transform of the bound state wavefunction. The saddle point method applied to Eq. (7.52) yields the ionization

3) Equation (7.52) corresponds to the length gauge SFA result for ionization. Equation (7.52) also results from the PPT approach under the approximation that the field-free ground state is substituted by the laser-dressed bound wavefunction. Thus, the PPT approach allows one to identify the approximations in Eq. (7.52) for short-range potentials. The SFA is inaccurate because the Volkov states are not sufficiently accurate even for short-range potentials.

amplitude,

$$a_{\text{ion}}(\mathbf{p}, T) = \left[\frac{2\pi}{i S''_{t_i, t_i}} \right]^{1/2} e^{-i S(\mathbf{p}, T, t_i)} \Upsilon(\mathbf{p} + A(t_i)) , \quad (7.53)$$

where t_i is the complex saddle point given by the condition

$$\frac{[\mathbf{p} + A(t_i)]^2}{2} + \text{IP} = 0 . \quad (7.54)$$

The saddle point method selects specific moments of time t_i when ionization occurs. At these times the instantaneous electron energy $[\mathbf{p} + A(t_i)]^2/2$ is equal to the energy of the ground state and therefore the instantaneous momentum of the electron hits the pole of the bound state wavefunction in momentum space. In the vicinity of the pole, the wavefunction in momentum space is determined by the asymptotic part of the wavefunction in coordinate space. Thus, in contrast to one-photon ionization, which probes the bound wave function near the core, the strong-field ionization probes the asymptotic part of the bound wavefunction:

$$\langle \mathbf{r} | g \rangle \simeq C_{kl} \kappa^{3/2} \frac{e^{-\kappa r}}{\kappa r} Y_{lm} \left(\frac{\mathbf{r}}{r} \right) . \quad (7.55)$$

Equation (7.55) restricts our analysis to short-range potentials (see [28] for a consistent analytical treatment of strong-field ionization from a long-range (Coulomb potential), $\kappa = \sqrt{2\text{IP}}$, C_{kl} is a constant, and $Y_{lm}(\mathbf{r}/r)$ reflects the angular structure of the bound state. For a Coulomb potential $-Q/r$, the asymptotic expression Eq. (7.55) must be multiplied by $(\kappa r)^{Q/\kappa}$:

$$\langle \mathbf{r} | g \rangle \simeq C_{kl} \kappa^{3/2} \frac{e^{-\kappa r}}{\kappa r} (\kappa r)^{Q/\kappa} Y_{lm} \left(\frac{\mathbf{r}}{r} \right) . \quad (7.56)$$

Evaluating the Fourier transform of Eq. (7.55) we obtain an explicit expression for $\Upsilon(\mathbf{p})$ (see [34]):

$$\Upsilon(\mathbf{p}) = \left(\frac{2\kappa}{\pi} \right)^{1/2} C_{kl} Y_{lm} \left(\frac{\mathbf{p}}{p} \right) . \quad (7.57)$$

Evaluation of the spherical function $Y_{lm}(\mathbf{p}/p)$ at the pole $p = \pm i\kappa$ yields (see [34] and also [38, 39] for circularly polarized fields)

$$Y_{lm} \left(\frac{\mathbf{p}}{p} \right) |_{p=\pm i\kappa} = C_{lm} \left(\frac{\pm p_\perp}{\kappa} \right)^m e^{im\phi_p} , \quad (7.58)$$

$$C_{lm} = \frac{1}{2^{|m|} |m|!} \sqrt{\frac{(2l+1)(l+|m|)!}{4\pi(l-|m|)!}} , \quad (7.59)$$

where p_\perp is the electron transverse momentum at the detector and ϕ_p is the azimuthal angle of the electron momentum at the detector. Taking into account that

$S''_{t_i, t_i} = (\mathbf{p} + \mathbf{A}(t_i)) \mathbf{A}'(t_i)$ can be written as

$$i S''_{t_i, t_i} = \mu \kappa F(t_i) , \quad (7.60)$$

$$\mu = -\text{sign}(F(t_i)) , \quad (7.61)$$

we obtain the final expression for the amplitude of a single ionization burst at complex time $t_i(\mathbf{p})$, specified by the final momentum of the electron \mathbf{p} :

$$a_{\text{ion}}(\mathbf{p}) = 2C \sqrt{\frac{1}{\mu F(t_i)}} \left(\mu \frac{p_\perp}{\kappa} \right)^m e^{-i S(\mathbf{p}, T, t_i(\mathbf{p}))} e^{im\phi_p} , \quad (7.62)$$

$$C = C_{lm} C_{kl} . \quad (7.63)$$

Note that both the real and the imaginary component of $t_i(\mathbf{p})$ depend on laser parameters. Therefore, the dependence of the preexponential factor (prefactor) in $a_{\text{ion}}(\mathbf{p})$ on the laser field is not simply $F^{-1/2}$, as illustrated below for ionization at the maximum of the laser cycle. Indeed, the subcycle dynamics in the prefactor is much slower than in the exponent, thus one can also use a simpler expression for S''_{t_i, t_i} , corresponding to its value at the maximum of the laser field [34]:

$$i S''_{t_i, t_i} = -\frac{\kappa^2}{\omega} \frac{\sqrt{1+\gamma^2}}{\gamma} . \quad (7.64)$$

Omitting the subcycle dynamics in the prefactor, we obtain a simpler expression for the amplitude of a single ionization burst at time $t_i(\mathbf{p})$, consistent with the one derived by [34]:

$$a_{\text{ion}}(\mathbf{p}) = 2C \left[\frac{-\gamma \omega}{\kappa \sqrt{1+\gamma^2}} \right]^{1/2} \left(\frac{\mu p_\perp}{\kappa} \right)^m e^{-i S(\mathbf{p}, T, t_i(\mathbf{p})) + im\phi_p} . \quad (7.65)$$

At the same level of approximation, that is, neglecting the subcycle dynamics in the prefactor, the effects of the Coulomb potential are incorporated by simply adding the factor $(2\kappa^3/F)^{Q/\kappa}$:

$$a_{\text{ion}}(\mathbf{p}) = 2C \left(\frac{2\kappa^3}{F} \right)^{\frac{Q}{\kappa}} \left[\frac{-\gamma \omega}{\kappa \sqrt{1+\gamma^2}} \right]^{\frac{1}{2}} \left(\frac{\mu p_\perp}{\kappa} \right)^m e^{-i S(\mathbf{p}, T, t_i(\mathbf{p})) + im\phi_p} . \quad (7.66)$$

The subcycle Coulomb effects are derived in [28]. Note that in the rigorous analysis within the analytical R-matrix (ARM) approach, which consistently treats the Coulomb effects both in bound and continuum states [28, 32], the pole in $\Upsilon(\mathbf{p} + \mathbf{A}(t_i))$ does not appear because the radial integration is removed due to the use of the Bloch operator [40]. Therefore, it removes all technical aspects and additional terms associated with the presence and the strength of the pole.

Note that the expression for the induced dipole, Eq. (7.42), contains terms that look very much like the ionization amplitude Eq. (7.53). This observation is important, as it suggests the connection of the harmonic response to ionization, as in the simple man model. However, the story is more subtle: the stationary momenta \mathbf{p}_s in the harmonic dipole are complex-valued, while here they are real observable quantities.

The integral Eq. (7.52) has been extensively studied by Keldysh, Popov, Perelomov, Terentév, and many others. The semiclassical picture in [34–37], enabled by the application of the saddle point method, shows that strong-field ionization can be understood as tunneling through the oscillating barrier created by the laser field. The tunneling picture clarifies the sensitivity of strong-field ionization to the asymptotic “tail” of the bound wavefunction (see Eqs. (7.55) and (7.56)), since it is this asymptotic part that “leaks” through the barrier. The modulus of the ionization amplitude is associated with the imaginary part of the action S in Eqs. (7.53), (7.62), (7.65), (7.66). This imaginary part is only accumulated from t_i to t'_i , since in the photoionization problem the canonical momentum registered at the detector is real and the integration over time also proceeds along the real time axis between t'_i and the observation time t .

This is why the complex saddle point t_i is associated with the time at which the electron enters the classically forbidden region – the tunneling barrier. The real part of the complex saddle point t'_i , after which changes to the ionization amplitude stop,⁴⁾ is associated with the time of exit from the classically forbidden “under-the-barrier” region. The same reasoning can be extended to the ionization times arising within the semiclassical picture of harmonic generation, see Figure 7.5. However, the ionization times in high harmonic generation are somewhat different due to the fact that \mathbf{p}_s is complex-valued. In the next section we will consider the connection between these two times.

The imaginary ionization time defines the ionization probability. Since the imaginary component of the ionization time is larger for short trajectories, these trajectories have a lower chance of being launched, compared to the long ones. The range over which the real part of the ionization time changes within the quarter-cycle defines the duration of the “ionization window”. Typically, for a $\lambda \simeq 800$ nm driving laser field and a laser intensity of $I \sim 10^{14}$ W/cm², the ionization times (their real part) are spread within ~ 250 as around the instantaneous maximum of the laser field (see Figure 7.5). Thus, strong-field ionization is an intrinsic attosecond process. Note that the quantum “ionization window” is shorter than the classical one (see Figure 7.1), as according to the classical simple man picture ionization happens at any phase of the laser field.

Figure 7.6 shows the saddle point solutions.

In photoionization, the electron canonical momentum is always real, since it is the observable registered at the detector. In contrast, in harmonic generation the observable registered at the detector is the emitted photon, and hence it is the pho-

4) Rigorously, this statement is only true for short-range potentials. Long-range electron-core interactions lead to additional modifications of the ionization amplitude after t'_i [28, 41].

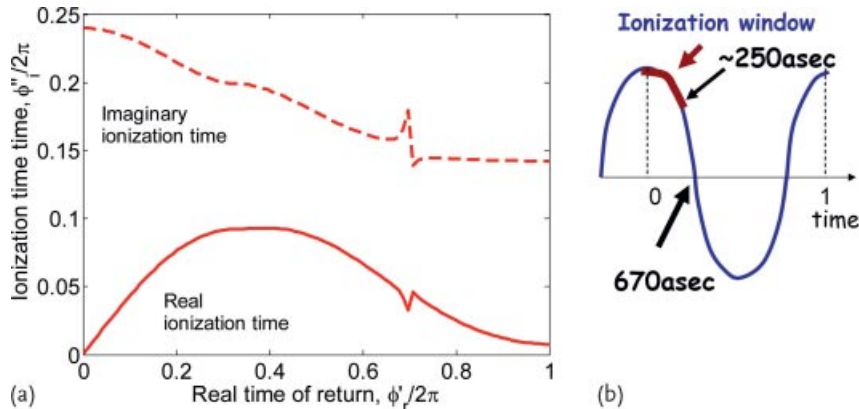


Figure 7.5 Real and imaginary ionization times vs. real return time for $IP = 15.6 \text{ eV}$, $I = 1.3 \cdot 10^{14} \text{ W/cm}^2$, $\hbar\omega = 1.5 \text{ eV}$ (a). Cartoon illustrating the ionization window (b).

Ionization occurs around the field maximum within an approximately 250 as time window (corresponding to the maximum value of the real ionization time).

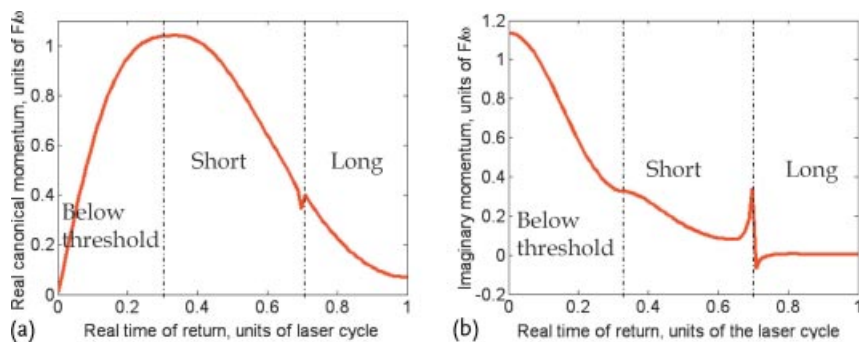


Figure 7.6 Real canonical momentum vs. real return time for $IP = 15.6 \text{ eV}$, $I = 1.3 \cdot 10^{14} \text{ W/cm}^2$, $\hbar\omega = 1.5 \text{ eV}$ (a). Imaginary canonical momentum vs. real return time (b).

ton energy that must be real. As a result, the electron canonical momenta in HHG are complex. Electrons on long trajectories have a very small imaginary canonical momentum. Therefore, it is a very good approximation to associate long trajectories with photoelectrons. Note that the maximum of the real canonical momentum is about $p_{\max} \simeq A_0$. In the photoelectron perspective p_{\max} corresponds to an energy of $2U_p$ at the detector – the cutoff energy for the so-called direct photoelectrons, that is, those that have not substantially changed their momentum after ionization due to re-encounter with the core.

The imaginary part of the canonical momentum can be quite large for short trajectories. The complex-valued solutions, not only for the ionization times, but also for the recombination times and the electron canonical momenta, challenge our understanding of the underlying physical picture of harmonic generation. If the first step of high harmonic generation is ionization, then why do these liberated

electrons have complex canonical momenta? Does this mean that these electrons have not been ionized? Can we factorize the harmonic dipole into ionization, propagation and recombination? The next section explores this opportunity.

7.6

Factorization of the HHG Dipole: Simple Man on a Complex Plane

Having derived the analytical expressions for the HHG dipole, can we identify the simple man model in it, within the consistent quantum approach? To do this, we need to factorize the harmonic dipole into the three steps: ionization, propagation and recombination. That is, we have to rewrite the dipole as a product of the ionization amplitude, the propagation amplitude and the recombination amplitude.

Such factorization of the harmonic dipole is not just curiosity driven. It is important for extending the modeling of harmonic emission to complex systems. Once the three steps are identified, the respective amplitudes can be imported from different approaches, tailored to calculate specifically ionization or recombination in complex systems.

The factorization of the harmonic dipole runs into two types of problems: technical and conceptual. The technical problems arise from the fact that the original three-step (simple man) model is formulated in the time domain. The three processes – ionization, propagation and recombination – are the sequence of subsequent time-correlated events. The harmonic spectrum formally corresponds to the harmonic dipole in the frequency domain, where the three processes become entangled: recall the contribution of different quantum trajectories to the same photon energy. Thus, rigorous factorization in the frequency domain is only possible in the cutoff region, where short and long solutions merge, see [42].⁵⁾

The conceptual problem is due to the complex canonical momentum of the electron responsible for HHG. Ionization in terms of creating photoelectrons with real canonical momenta does not appear to fit into the HHG picture. Can we build an alternative model of HHG based entirely on photoelectrons, that is, those electrons which are indeed ionized at the first step?

Let us address these issues step by step, starting with the factorization of the harmonic dipole in the frequency domain [42, 44, 45] and the time domain [24]. The former involves the factorization of Eq. (7.25), the latter factorizes Eq. (7.24).

5) Note that the quantitative rescattering theory (see [43]) postulates that one can factor out the recombination step in the frequency domain harmonic dipole. This postulate is supported by the results of numerical simulations demonstrating approximate factorization in the cutoff region, see [44].

7.6.1

Factorization of the HHG Dipole in the Frequency Domain

To rewrite the harmonic dipole in the semifactorized form, we can take Eq. (7.42) and split the action integral S that enters the phase of this expression into the following three time intervals: from t_i to t'_i , from t'_i to t'_r , and from t'_r to t_r (see Figure 7.2). Then we can identify the group of terms that looks like the ionization amplitude similar to that given by Eq. (7.53),

$$a_{\text{ion}}(\mathbf{p}_s, t_i) = \left[\frac{2\pi}{i S''_{t_i, t_i}} \right]^{1/2} e^{-i S(\mathbf{p}_s, t'_i, t_i)} \Upsilon(\mathbf{p}_s + A(t_i)) . \quad (7.67)$$

The ionization amplitude is associated with the first time interval, from t_i to t'_i , and only the part of the action integral from t_i to the real time axis $t'_i = \Re(t_i)$ enters this amplitude. For a short-range potential (neglecting the subcycle effects in the prefactor), we find:

$$a_{\text{ion}}(\mathbf{p}_s) = 2C \sqrt{\frac{-\tilde{\gamma}\omega}{\kappa\sqrt{1+\tilde{\gamma}^2}}} \left(\frac{\mathbf{p}_{s\perp}}{\kappa} \right)^m e^{-i S(\mathbf{p}_s, T, t_i) + im\phi_{ps}} . \quad (7.68)$$

Constant C is specified in Eq. (7.63). The momentum \mathbf{p}_s is given by the full set of saddle point conditions for t_i , t_r , and \mathbf{p}_s :

$$\begin{aligned} \frac{[\mathbf{p}_s + A(t_i)]^2}{2} + \text{IP} &= 0 , \\ \int_{t_i}^{t_r} [\mathbf{p}_s + A(t')] dt' &= 0 , \\ \frac{[\mathbf{p}_s + A(t_r)]^2}{2} + \text{IP} &= N\omega . \end{aligned} \quad (7.69)$$

Note that t_i in HHG and t_i in ionization are different. That is why we use γ and \mathbf{p} in Eq. (7.65), whereas we use $\tilde{\gamma}$ (see Eq. (7.51)) and \mathbf{p}_s in Eq. (7.68). If the imaginary part of \mathbf{p}_s is equal to zero, then $\tilde{\gamma} = \gamma$. For the Coulomb potential (neglecting the subcycle effects in the prefactor), we find:

$$a_{\text{ion}}(\mathbf{p}_s) = 2C \left(\frac{2\kappa^3}{F} \right)^{\frac{Q}{\kappa}} \sqrt{\frac{-\tilde{\gamma}\omega}{\kappa\sqrt{1+\tilde{\gamma}^2}}} \left(\frac{\mathbf{p}_{s\perp}}{\kappa} \right)^m e^{-i S(\mathbf{p}_s, T, t_i) + im\phi_{ps}} . \quad (7.70)$$

Now consider the next time interval, from t'_i to t'_r . The prefactor arising from saddle point integration over the electron momenta \mathbf{p} leads to the term

$$\frac{(2\pi)^{3/2}}{\sqrt{\det(i S''_{\mathbf{p}_s, \mathbf{p}_s})}} = \frac{(2\pi)^{3/2}}{(i(t_r - t_i))^{3/2}} . \quad (7.71)$$

This term describes the free spreading of the electron wave packet between t_i and t_r . Thus, we associate the following group of terms with the propagation amplitude:

$$a_{\text{prop}}(\mathbf{p}_s, t_r, t_i) = \frac{(2\pi)^{3/2}}{(i(t_r - t_i))^{3/2}} e^{-iS(\mathbf{p}_s, t'_r, t'_i)} . \quad (7.72)$$

Note that the denominator includes the complex-valued times t_i and t_r .

Finally, the recombination amplitude is represented by the recombination matrix element $\mathbf{d}^*(\mathbf{p}_s + A(t_r))$ and can be associated with the following group of terms:

$$a_{\text{rec}}(\mathbf{p}_s, t_i) = \left[\frac{2\pi}{i S''_{t_r, t_r}} \right]^{1/2} e^{-iS(\mathbf{p}_s, t_r, t'_r) + iN\omega t_r} \mathbf{d}^*(\mathbf{p}_s + A(t_r)) , \quad (7.73)$$

where $S''_{t_r, t_r} = -\sqrt{2(N\omega - \text{IP})}F(t_r)$ for a linearly polarized field. As a result, the total dipole is formally written as

$$D(N\omega) = \sum_{j=1}^{4M} a_{\text{rec}}(\mathbf{p}_s, t_r^{(j)}) a_{\text{prop}}(\mathbf{p}_s, t_r^{(j)}, t_i^{(j)}) a_{\text{ion}}(\mathbf{p}_s, t_i^{(j)}) , \quad (7.74)$$

where the index j labels the saddle points. However, in contrast to photoelectrons, the electrons involved in HHG have complex canonical momenta \mathbf{p}_s . Therefore, the imaginary part of the action is accumulated not only “under the barrier,” from t_i to t'_i , but also all the way between t'_i and t_r . Thus, factoring out ionization as the first step of HHG is not that convincing. Similarly, the recombination step involves not only the recombination dipole, but also the possible change in the amplitude due to the imaginary contribution to the action between t'_r and t_r . Thus, while we can formally associate several groups of terms in the harmonic dipole Eq. (7.74) with amplitudes of ionization, propagation, and recombination, the complex-valued electron momenta make such identification somewhat tenuous.

An additional point to note is that the three amplitudes are also entangled due to the sum over the different saddle points in Eq. (7.74). Even if we only consider contributions of the two most important trajectories, short and long, the sum entangles their contributions and also mixes up the contributions from different half-cycles. Importantly, a finite pulse duration leads to a different mapping between the given harmonic number and the ionization-recombination times for each half-cycle.

A practical approach to factorization realized in the so-called quantitative rescattering theory [43] is to assume that $a_{\text{rec}}(\mathbf{p}_s(N), t_r^{(j)}(N)) = a_{\text{rec}}(N\omega)$ for all j , yielding:

$$D(N\omega) = a_{\text{rec}}(N\omega) \sum_{j=1}^{4M} a_{\text{prop}}(\mathbf{p}_s, t_r^{(j)}, t_i^{(j)}) a_{\text{ion}}(\mathbf{p}_s, t_i^{(j)}) . \quad (7.75)$$

This approximation breaks down in the following cases:

- 1) In two-color orthogonally polarized fields [46]. In this case more than two trajectories returning at different angles can map into the same return energy [46]. Such trajectories must correspond to different recombination dipoles for different angles, violating Eq. (7.75).

- 2) In the vicinity of the structural minimum of the recombination matrix element, or when the phase of the matrix element changes rapidly [47, 48].
- 3) When the subcycle dynamics associated with the electron interaction with the core potential cannot be neglected.

These technical problems can be remedied by looking at the dipole in the time domain.

7.6.2

Factorization of the HHG Dipole in the Time Domain

There are several advantages of using the time-domain dipole. For starters, if we do not perform the Fourier transform analytically, the time t_r no longer has to be complex. With the Fourier integral performed using a standard FFT routine, we can keep t_r on the real time axis. The number of saddle point conditions is also conveniently reduced to two (one of them, for the momentum \mathbf{p}_s , is in general three-dimensional)

$$\begin{aligned} \frac{[\mathbf{p}_s + A(t_i)]^2}{2} + \text{IP} &= 0, \\ \int_{t_i}^{t_r} [\mathbf{p}_s + A(t')] dt' &= 0, \end{aligned} \quad (7.76)$$

with t_r being the parameter, instead of the harmonic number N .

In the time domain, it is natural to sort the contributions to the induced dipole according to the corresponding ionization bursts. Then, for each half-cycle j , there is a single ionization burst j at time $t_i^{(j)}$ that contributes to the induced dipole as a function of the real return time t_r , see Figure 7.5a. After saddle point integration, this contribution is:

$$\begin{aligned} D^{(j)}(t_r) &= i \left[\frac{2\pi}{i S''_{t_i^{(j)}, t_i^{(j)}}} \right]^{1/2} \frac{(2\pi)^{3/2}}{\sqrt{\det(i S''_{\mathbf{p}_s, \mathbf{p}_s})}} \\ &\times \mathbf{d}^*(\mathbf{p}_s + A(t_r)) e^{-i S(\mathbf{p}, t_r, t_i^{(j)})} \Upsilon(\mathbf{p}_s + A(t_i^{(j)})), \\ S(\mathbf{p}_s, t_r, t_i) &\equiv \frac{1}{2} \int_{t_i}^{t_r} [\mathbf{p}_s + A(\tau)]^2 d\tau + \text{IP}(t_r - t_i), \end{aligned} \quad (7.77)$$

with $\det(i S''_{\mathbf{p}_s, \mathbf{p}_s}) = [i(t_r - t_i^{(j)})]^{3/2}$ (see also Eq. (7.71)). Just as in the frequency domain, up to a global phase factor the dipole can be written as a product of three amplitudes:

$$D^{(j)}(t_r) = a_{\text{rec}}(\mathbf{p}_s, t_r) a_{\text{prop}}(\mathbf{p}_s, t_r, t_i^{(j)}) a_{\text{ion}}(\mathbf{p}_s, t_i^{(j)}). \quad (7.78)$$

The ionization and the propagation amplitudes entering this expression are given by Eqs. (7.67) and (7.72). The recombination amplitude is simply equal to the

recombination matrix element $\mathbf{d}^*(\mathbf{p}_s + A(t_r))$, as we have not performed the Fourier transform yet. Equation (7.78) is the natural mathematical formulation of the three-step model, which is intrinsically subcycle.

If we ignore multiple returns, that is, very long trajectories, then for each t_r there is only one ionization burst to deal with. As opposed to the frequency domain, the contributions of the long and the short trajectories from this ionization burst are not yet mixed – they are separated in time. This is very convenient if you need to look at the contribution of only the short, or only the long trajectories: it is straightforward to add a time-domain filter that would filter out the unwanted contributions. Essentially, this would correspond to making a window Fourier transform of the time-domain harmonic dipole. The inclusion of the contribution of multiple returns is rarely required for typical experimental conditions.

To model the full $\mathbf{D}(t_r)$ one needs to model ionization, recombination and propagation separately for each half-cycle, and then collect the contributions from each half-cycle (each ionization burst):

$$\mathbf{D}(t_r) = \sum_j \mathbf{D}^{(j)}(t_r). \quad (7.79)$$

To obtain the harmonic spectrum, we have to perform the Fourier transform, which is convenient to do numerically using a FFT routine. There are two possible approaches to implement the Fourier transform.

Integration along Lewenstein's contour In this approach, the Fourier transform is performed along the time contour in the complex plane $t_r = t'_r + i t''_r$. In this case the argument of the recombination dipole $\mathbf{p}_s + A(t_r)$ remains real and so does the recollision energy $E_{\text{rec}}(t_r)$. Since it is difficult to *numerically* perform an integration along a complex contour

$$\mathbf{D}(N\omega) = \int dt_r e^{-N\omega t''_r} \mathbf{D}(t_r) e^{iN\omega t'_r}, \quad (7.80)$$

one can use variable substitution and integrate over the real return times t'_r :

$$\mathbf{D}(N\omega) = \int dt'_r \left[\frac{dt_r}{dt'_r} e^{-[E_{\text{rec}}(t_r) + \text{IP}]t''_r} \right] \mathbf{D}(t'_r) e^{iN\omega t'_r}, \quad (7.81)$$

$$N\omega = E_{\text{rec}}(t_r) + \text{IP}, \quad (7.82)$$

$$E_{\text{rec}}(t_r) = \frac{[\mathbf{p}_s + A(t_r)]^2}{2}. \quad (7.83)$$

The derivative in the square bracket is associated with the variable substitution.

Note that Eq. (7.81) contains one approximation: the term $e^{-(N\omega)t''_r}$ is modified according to the energy conservation $N\omega = E_{\text{rec}}(t_r) + \text{IP}$. However, the integration of Eq. (7.81) is not very convenient due to the additional effort associated with the need to avoid the divergence of dt_r/dt'_r in the cutoff region (see Figure 7.4).

HHG dipole on the real time axis To keep things simple, one can keep the half-cycle harmonic dipole on the real time axis:

$$\mathbf{D}^{(j)}(t) = \mathbf{a}_{\text{rec}}(\mathbf{p}_s, t) \mathbf{a}_{\text{prop}}(\mathbf{p}_s, t, t_i^{(j)}) \mathbf{a}_{\text{ion}}(\mathbf{p}_s, t_i^{(j)}) , \quad (7.84)$$

where the saddle points \mathbf{p}_s and $t_i^{(j)}$ are given by Eq. (7.76) and the index j labels different laser half-cycles.

In this “real-time axis” approach, the return time t is a parameter: we have to find t_i and \mathbf{p}_s for each t . This can be done using a procedure similar to that described in the previous section, only simpler. Specifically, we introduce the dimensionless variables $\phi = \omega t$ and $p/(F/\omega) = p_1 + i p_2$. For a linearly polarized field $p_{s,\perp} = 0$. For each real ϕ we use Eqs. (7.43) and (7.44) with $\phi_r' = 0$ and $\phi_r' \equiv \phi$:

$$F_1(\phi) = p_1(\phi - \phi_i') + p_2\phi_i'' - \cos(\phi_i') \cosh(\phi_i'') + \cos(\phi) = 0 , \quad (7.85)$$

$$F_2(\phi) = -p_1\phi_i'' + p_2(\phi - \phi_i') + \sin(\phi_i') \sinh(\phi_i'') = 0 . \quad (7.86)$$

We can now use Eqs. (7.47) and (7.48) to express p_1 and p_2 in terms of ϕ_i' and ϕ_i'' . Then, we build the surface $F(\phi) = F_1^2 + F_2^2$ for each ϕ . Next, we find the minima on this surface. Alternatively, we can use p_1 and p_2 as our variables, expressing ϕ_i' and ϕ_i'' via p_1, p_2 , then the minima on the surface $F_1^2 + F_2^2$ will yield the real, p_1 , and the imaginary, p_2 , components of the canonical momentum, and then Eqs. (7.49) and (7.50) yield the corresponding ionization times.

In this approach the divergence at the cutoff is avoided, since the divergence occurs in the complex plane of the return times when calculating the Fourier transform analytically using the saddle point method. The price to pay is that the recombination dipole has to be taken at the complex arguments $\mathbf{p}_s + A(t)$ and the recollision energy $E_{\text{rec}}(t)$ has an imaginary part. In practice, one can use the real part of the recollision energy as the argument of the recombination dipole. If one wants to avoid this approximation, one has to extend the recombination dipoles into the complex plane of the electron momenta.

Thus, one can formally factorize the harmonic dipole in the time domain, overcoming the technical problems associated with the factorization. However, one has to keep in mind that the ionization amplitude has to be modified to include complex canonical momenta and slightly different ionization times. Fortunately, this does not lead to changes in angular factors, because $\Upsilon_n(\mathbf{p}_s + A(t_i))$ remains the same. Indeed, both \mathbf{p}_s and t_i are different in the case of HHG and ionization, but the term $\mathbf{p}_s + A(t_i) = i\mu\kappa$ (see Eq. (7.61)) is the same in both cases. The changes appear in the phase $S(\mathbf{p}_s, t_r, t_i)$ and the subcycle core effects, that is, everywhere where \mathbf{p}_s and t_i contribute separately.

The conceptual problem associated with understanding the physical meaning of the complex electron momenta, especially in the context of the “ionization step,” still remains. The next section shows how, and to what extent, this problem can be circumvented. It introduces the photoelectron model of HHG, where the electron canonical momentum is restricted to the real axis.

7.7

The Photoelectron Model of HHG: The Improved Simple Man

In the standard simple man model, the electron motion between ionization and recombination is modeled using classical trajectories. Naturally, the electron velocity, the ionization time, and the recombination time are all real-valued quantities. In the quantum description, the rigorous approach based on the saddle point method leads to trajectories with complex-valued momenta and complex-valued ionization and recombination times. The presence of complex canonical momenta makes it difficult to identify the ionization step.

The complex-valued canonical momenta and recombination times arise from the requirement that the electron returns exactly to its original position. Since the tunneling electron accumulates an imaginary displacement during its motion in the classically forbidden region, the complex-valued momenta and return times must compensate for this displacement.

This section shows that if we relax the return condition and neglect the imaginary displacement between t_i and its real part $\Re(t_i)$, we can obtain the same recollision energy for real-valued canonical momenta and for real-valued return times. We shall call this approach the *photoelectron model*, since it allows one to incorporate standard strong-field ionization concepts in a natural manner. The ionization amplitude would then correspond to creating an electron with a real-valued canonical momentum, and the imaginary part of the action integral would only be accumulated between t_i and $\Re(t_i)$.

In the classical model, one assumes that the electron trajectory is launched at the real “time of birth” t_B with zero instantaneous velocity. The electron instantaneous momentum at t_B can be written as $k(t_B) = p + A(t_B) = 0$, where the canonical momentum p is a constant of motion (neglecting the core potential). The link between t_B and p , $p = -A(t_B)$, links t_B via $[p + A(t_i)]^2 = -2\text{IP}$ to the complex-valued ionization time t_i . In particular, for a linearly polarized laser field we have $[A(t_{i,ph}) - A(t_B)]^2 = -2\text{IP}$. Note that this $t_{i,ph}$ is in general different from the ionization time t_i introduced in the previous section, since now the electron canonical momentum is forced to be real. The notation $t_{i,ph}$ stresses that this ionization time corresponds to photoelectrons, that is, to electrons with real canonical momenta. Figure 7.7 shows the mapping between the time of birth and the complex time $t_{i,ph}$.

The photoelectron exits the tunneling barrier at the real time, $\Re(t_{i,ph})$, and since $\Re(t_{i,ph})$ turns out to be smaller than t_B , the electron velocity at $\Re(t_{i,ph})$ is directed towards the core. It gradually decreases until becoming equal to zero at t_B . The difference between $\Re(t_{i,ph})$ and t_B is small near the peak of the oscillating electric field, but increases as the field approaches zero. While the times t_B are always spread within one quarter-cycle, as in the classical model, the times $\Re(t_{i,ph})$ are limited to a shorter fraction of the quarter-cycle, see Figure 7.7.

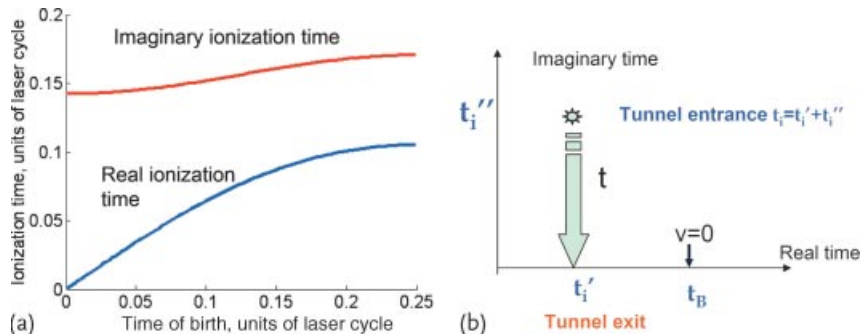


Figure 7.7 Complex ionization time for photoelectrons $t_{i,\text{ph}}$ vs. time of birth for $\text{IP} = 15.6 \text{ eV}$, $I = 1.3 \times 10^{14} \text{ W/cm}^2$, $\hbar\omega = 1.5 \text{ eV}$ (a). Cartoon illustrating the connection between $t_{i,\text{ph}}$ and t_B (b): the elec-

tron exits the barrier with a negative velocity $v(t_{i,\text{ph}}) = k(t_{i,\text{ph}})$ (directed towards the core). Its velocity gradually decreases and becomes zero at the classical ionization time ($v(t_B) = k(t_B) = 0$) – the time of birth t_B .

We now turn to the classical return time t_R . In the original classical model, it is defined by the condition

$$\int_{t_B}^{t_R} [p + A(\tau)] d\tau = \int_{t_B}^{t_R} [-A(t_B) + A(\tau)] d\tau = 0. \quad (7.87)$$

However, since the electron is already offset from the origin at t_B ,

$$\Delta z = \int_{t_{i,\text{ph}}}^{t_B} [A(\tau) - A(t_B)] d\tau, \quad (7.88)$$

it does not return to the origin at t_R , see Figure 7.8.

The energy $E(t_R) = [A(t_R) - A(t_B)]^2/2$ in the classical model is shown in Figure 7.8b, with the cutoff at $3.17 U_p + \text{IP}$. This cutoff is lower than in the quantum treatment, precisely because the electron has not yet returned to the core. The extra 0.32 IP in the quantum cutoff law, $3.17 U_p + 1.32 \text{ IP}$, is due to the extra energy accumulated by the electron while covering the extra distance Δz .⁶⁾

Can we improve these results if we allow the photoelectrons to travel a bit longer and allow them to return to the core? Why do not we continue to monitor the electron trajectory at times $t > t_R$ and register their energy at the time of return to the origin $t_{r,\text{ph}}$, ignoring whatever imaginary displacement they might have? There is just one problem with this plan: not all trajectories return to the core since we have limited the canonical momentum $p_{\text{ph}} = -A(t_B)$ to be no more than A_0 . With this in mind, we shall take the energy at the closest approach to the origin as the

6) Interestingly, if one defines the experimental cutoff using the classical model, then the classical time-energy mapping is very similar to the quantum: t_R is very close to the real part of t_r . Since in the experiment the intensity is rarely known exactly, it is very difficult to differentiate between the classical (red) and the quantum (blue) return energies in Figure 7.8.

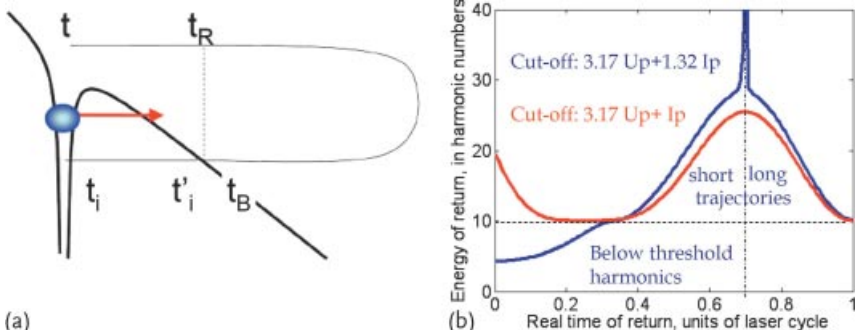


Figure 7.8 Physical picture of high harmonic generation in coordinate space and the meaning of different times (a). The electron enters the barrier at a complex time t_i and exits the barrier at the real time $t'_i = \Re t_i$. Its velocity goes through zero at a (later) time t_B . At the moment t_R the electron returns to the

position it had at t_B , and at the moment t it returns to the origin. The blue curve shows the electron return energy at the moment t in the Lewenstein model, while the red curve shows the electron return energy in the classical three-step model (b).

return energy. We shall call this an improved three-step model or *the photoelectron model*.

The model implies the neglect of the imaginary displacement and the minimization of the real displacement between $t_{i,\text{ph}}$ and $t_{r,\text{ph}}$. The imaginary displacement has to be neglected since we do not have imaginary canonical momenta and imaginary return times to cover for it.

The photon energy resulting from the photoelectron model is $E_{\text{rec}}^{\text{ph}}(t) + \text{IP} = dS/dt_{r,\text{ph}}$, where $S(p_{\text{ph}}, t_{r,\text{ph}}, t_{i,\text{ph}})$ is given by Eq. (7.21). It is in excellent agreement with the quantum photon energy (see Figure 7.9a) for all those trajectories for which the real part of the electron displacement from the origin passes through zero. This is the case for the long trajectories and for most of the short trajectories, except for the shortest ones. These latter ones are “born” at the end of the ion-

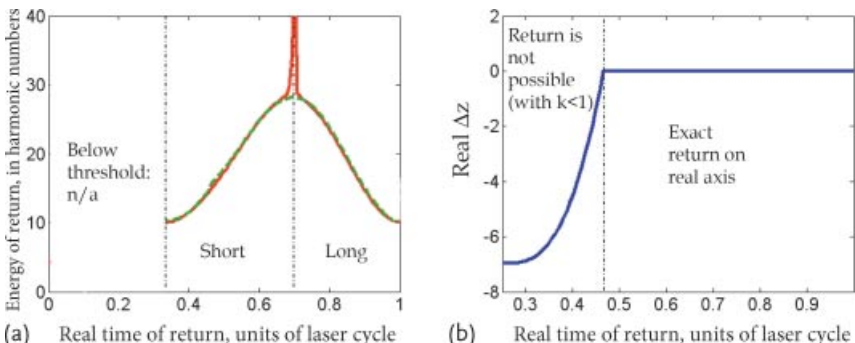


Figure 7.9 Energy of return for the Lewenstein model (red) and for the photoelectron model (green) vs. real return time for $\text{IP} = 15.6 \text{ eV}$, $I = 1.3 \times 10^{14} \text{ W/cm}^2$, $\hbar\omega = 1.5 \text{ eV}$ (a). Real part of the electron displacement in the photoelectron model (b).

ization window and contribute to the lowest harmonics, just above the ionization threshold.

For short trajectories, the electron is decelerated by the laser field while returning to the core. Therefore, it needs a sufficiently high drift momentum to reach the origin. Since we have limited the canonical momentum $p = -A(t_B)$ below A_0 , the shortest trajectories cannot quite make it to the core. For them, the time $t_{r,ph}$ corresponds to the closest approach to the core. A nonzero real displacement yields a deviation of the approximate action $S(p_{ph}, t_{r,ph}, t_{i,ph})$ from the real part of the exact action defined in the previous section, see Figure 7.9b.

The action in this model is reproduced very well, since it is the time integral from the photon energy. Once the electron return energy is well reproduced, so is the action, even if the end points t'_r , t'_i are shifted.

From the mathematical perspective, the photoelectron model implies that when we perform the integrals, we expand the action not at the exact saddle point, but in its vicinity. In particular, we shift the center of the expansion for the canonical momentum from the complex plane to the real axis. The error introduced in the integral by this procedure is minimized if the new expansion point lies within the saddle point region of the exact complex saddle point of the multidimensional integral. Thus, the difference $\Delta p = p_q - p_{ph}$ between the stationary point solution for quantum orbits p_q and the canonical momentum in the improved three-step model p_{ph} should be less than the size of the stationary point region: $|\Delta p| < |\partial^2 S / \partial p^2|^{-1/2} = (t_r - t_i)^{1/2}$. We can estimate $|\Delta p|$ as $|\Delta p| = |\Delta z| / (t_r - t_i)$, where $|\Delta z|$ includes the neglected imaginary displacement. This estimate yields $|\Delta z| < (t_r - t_i)^{1/2}$.

Figure 7.10a illustrates this condition for typical experimental parameters ($\omega = 0.057$ a.u., IP = 15.6 eV, $I = 1.3 \times 10^{14}$ W/cm²): the improved three-step model cannot be applied for very short trajectories returning earlier than $\omega t_{r,ph}/2\pi = 0.36$ or for harmonics lower than $N = 11$. Thus, for this particular set of parameters, all

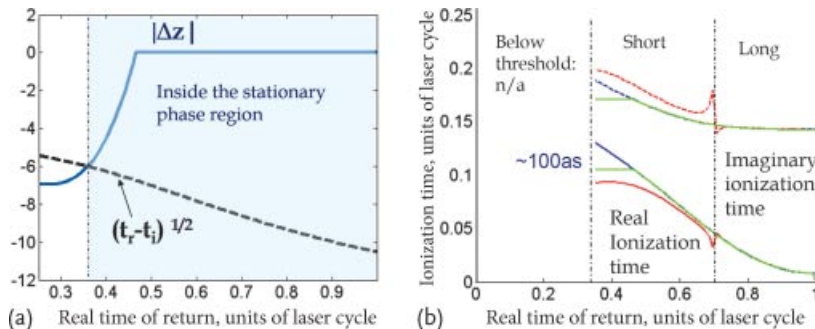


Figure 7.10 Applicability region of the photoelectron model (a). The condition $|\Delta z| < (t_r - t_i)^{1/2}$ specifies the region of return times (filled) where the photoelectron model can be used. The calculation is shown for IP = 15.6 eV, $I = 1.3 \times 10^{14}$ W/cm²,

$\hbar\omega = 1.5$ eV. Real and imaginary ionization times for the Lewenstein model (red), the photoelectron model with canonical momentum less than A_0 (green), and for the canonical momentum not limited by this condition (blue) (b).

above-threshold harmonics are within the applicability conditions of the improved three-step model.

Figure 7.10b compares the ionization times resulting from the Lewenstein model and the photoelectron model of HHG. The ionization times coincide for the long trajectories. In this sense, the long trajectories indeed correspond to photoelectrons. The difference between the ionization times for the short trajectories is associated with the presence of imaginary canonical momenta in the Lewenstein model. For the shortest trajectories, the difference in the real ionization times is about 100 as for the chosen laser parameters: the ionization window is wider for the photoelectron model. As for the imaginary component of the ionization times, they are smaller in the photoelectron model. Therefore, short trajectories are less suppressed in this model than in the full Lewenstein model.

Mathematically, implementing the photoelectron model requires only one approximation – relaxing the return condition. Note that the requirement of perfect return to the origin is an *artifact* of neglecting the size of the ground state in the saddle point analysis. If we take into account the size of the ground state, then the return condition will naturally be relaxed: to be able to recombine, the electron has to return to the core within the size of the ground state. From this perspective, the extension of the Lewenstein model to real systems, including molecules, should go hand in hand with relaxing the return condition for its real part.

Measurement of ionization times might allow one to differentiate between these two models and to pin down the nature of the electron trajectories responsible for HHG. A particularly interesting question is whether the complex momenta are an artifact of the δ -like initial state, or are indeed relevant for real systems.

The accuracy of the first measurement [33] was sufficient to distinguish between t_B and t'_i , but not high enough to distinguish delays between t'_i (red curve, Figure 7.10b) and $t'_{i,ph}$ (green curve, Figure 7.10b).

7.8

The Multichannel Model of HHG: Tackling Multielectron Systems

In multielectron systems, there are multiple ways of energy sharing between the liberated electron and the ion. The ion can be left in its ground or in one of its excited electronic states. These options are referred to as different ionization channels. Multiple ionization channels lead to multiple HHG channels: the returning electron can recombine with the ion in its ground or in one of its excited states.

Multiple HHG channels present different pathways connecting the same initial and final state – the ground state of the neutral system – via different intermediate electronic states of the ion. Thus, high harmonic emission in multielectron systems results from multichannel interference, see [13], that is, the interference of the harmonic light emitted in each channel. This interference naturally records multielectron dynamics excited upon ionization and probed by recombination, see [13]. How important are these multiple channels? How hard is it to excite the ion during strong-field ionization?

Strong-field ionization is exponentially sensitive to the ionization potential IP, suggesting that after ionization the molecular ion is typically left in its ground electronic state. In the Hartree–Fock picture, this corresponds to electron removal from the highest occupied molecular orbital (HOMO). However, multiple ionization channels can be very important in molecules due to the geometry of the molecular orbitals and the proximity of the excited electronic states in the ion to the ground state.

The formalism described above, in the Sections 7.1–7.7, is essentially a single-channel picture of HHG. It can be extended to multiple channels.

First, we introduce the Hamiltonian of an N -electron neutral molecule interacting with a laser field:

$$\begin{aligned} H^N &= T_e^N + V_C^N + V_{ee}^N + V_L^N , \\ V_C^N &= - \sum_m \sum_{i=1}^N \frac{Q_m}{|\mathbf{R}_m - \mathbf{r}_i|} , \\ V_{ee}^N &= \sum_{i \neq j}^N \frac{1}{|\mathbf{r}_i - \mathbf{r}_j|} , \\ V_L^N &= - \sum_i \mathbf{F}(t) \cdot \mathbf{d}_i = \sum_i \mathbf{F}(t) \cdot \mathbf{r}_i . \end{aligned} \quad (7.89)$$

Here, the nuclei are frozen at their equilibrium positions \mathbf{R}_m , the index m enumerates the nuclei with charges Q_m , the superscript N indicates the number of electrons involved, T_e^N is the electron kinetic energy operator, V_C^N describes the Coulomb potential of the nuclei, V_{ee}^N describes the electron–electron interaction, and V_L^N describes the interaction with the laser field. Hats on top of operators are omitted.

We will also use the Hamiltonian of the ion in the laser field, $H^{(N-1)}$, and the Hamiltonian of an electron interacting with the laser field, the nuclei, and the $(N-1)$ electrons of the ion, $H^e = H^N - H^{(N-1)}$.

The Schrödinger equation for the N -electron wavefunction of the molecule, initially in its ground electronic state $\Psi_g^N(\mathbf{r})$, is

$$\begin{aligned} i \frac{\partial}{\partial t} \Psi^N(\mathbf{r}, t) &= H^N \Psi^N(\mathbf{r}, t) , \\ \Psi^N(\mathbf{r}, t = t_0) &= \Psi_g^N(\mathbf{r}) . \end{aligned} \quad (7.90)$$

Similar to the single-electron case, its exact solution can be written as

$$|\Psi^N(t)\rangle = -i \int_{t_0}^t dt' U^N(t, t') V_L^N(t') U_0^N(t', t_0) \Psi_g^N(\mathbf{r}) + U_0^N(t, t_0) |\Psi_g^N\rangle . \quad (7.91)$$

Here the U_0^N and U^N are the N -electron propagators. The former is determined by

$$i \frac{\partial U_0^N}{\partial t} = H_0^N U_0^N , \quad (7.92)$$

$$U^N(t_0, t_0) = 1 , \quad (7.93)$$

where H_0^N is the field-free Hamiltonian of the molecule: $H_0^N = H^N - V_L^N$. The latter is the full propagator determined by $i\partial U^N/\partial t = H^N U^N$.

The harmonic dipole reads

$$\begin{aligned} D(t) = & -i \langle U_0^N(t, t_0) \Psi_g^N(\mathbf{r}) | \mathbf{d} | \int_{t_0}^t dt' U^N(t, t') \\ & \times V_L^N(t') U_0^N(t', t_0) \Psi_g^N(\mathbf{r}) \rangle + \text{c.c.} \end{aligned} \quad (7.94)$$

Just as in the one-electron case (Eq. (7.13)), propagation without the laser field is simple as long as the energy E_g and the wavefunction of the initial state of the neutral molecule or atom are known:

$$U_0^N(t', t_0) \Psi_g^N(\mathbf{r}) = e^{-i E_g(t' - t_0)} \Psi_g^N(\mathbf{r}) . \quad (7.95)$$

Finding the full propagator $U^N(t, t')$ is just as hard as solving the multielectron TDSE.

To simplify the analysis, we will make the following two approximations. First, we shall neglect the correlations between the electrons in the ion and the liberated electron after ionization. In this case, the full propagator factorizes into two independent parts, describing the evolution of the continuum electron and the evolution of the ion in the laser field between ionization and recombination: $U^N(t, t') \simeq U^{(N-1)}(t, t') U^e(t, t')$. Second, we will derive the results for short-range potentials, just like we did in the single-electron case considered above: $U^e(t, t') \simeq U_V^e(t, t')$, and supply the corrections due to Coulomb effects.

One can improve upon these two approximations by including the electron-electron correlations during ionization perturbatively [49], and by using the eikonal-Volkov states [50] for the continuum electron instead of the plane wave Volkov states. The eikonal-Volkov states include the laser field fully, the interaction of the continuum electron with the core in the eikonal approximation, and also take into account the interplay between these two interactions (the so-called Coulomb-laser coupling [51]).

A consistent approach, which includes both electron-electron correlations and long-range effects in strong-field ionization can be developed within the time-dependent analytical R-matrix (ARM) method [52]. This method (1) splits the configuration space into the inner and outer region and uses quantum chemistry in the inner region, (2) uses the eikonal-Volkov propagation in the outer region [50], and (3) uses the Bloch operator [40] to match the solutions in the two regions.

Moreover, if we can factorize the dipole response into the usual steps – ionization, propagation, recombination, we can think of improving each of the three steps

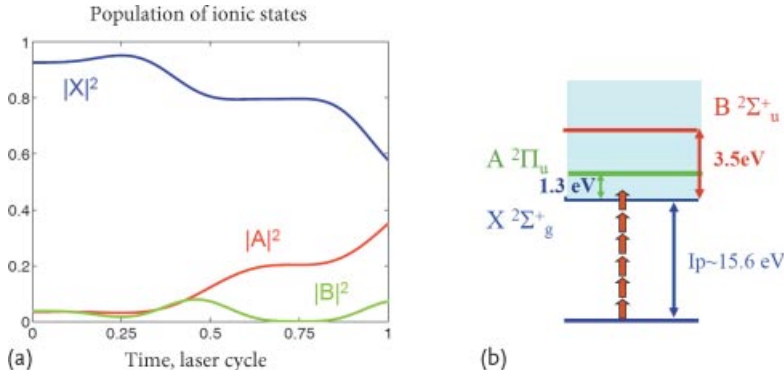


Figure 7.11 Subcycle dynamics in the N₂⁺ ion aligned at $\theta = 50^\circ$ to the laser field polarization: populations of the field-free ionic states X (blue), A (red), and B (green) in a $I = 0.8 \times 10^{14} \text{ W/cm}^2$, 800 nm laser field (a). Electronic states of the N₂⁺ ion (b).

separately, for example, by using improved ionization and recombination amplitudes that include the electron–electron correlation beyond the perturbation theory.

Just like in the one-electron formalism considered above, we will introduce the identity resolved on the momentum states of the continuum electron, but now we also have to include the electronic states of the ion,⁷⁾

$$I = \int d\mathbf{p} \sum_n \mathbb{A} |n^{(N-1)} \otimes \mathbf{p}_t^n\rangle \langle n^{(N-1)} \otimes \mathbf{p}_t^n| \mathbb{A}, \quad (7.96)$$

where \mathbb{A} denotes the antisymmetrizing operator.

The harmonic dipole becomes

$$\begin{aligned} D(t) = & -i (\Psi_g^N |d| \int_{t_0}^t dt' e^{iE_g(t-t')} \int d\mathbf{p} U^{(N-1)}(t, t') |n^{(N-1)}\rangle \\ & \times U_V^e(t, t') |\mathbf{p}_{t'}^n\rangle \langle \mathbf{p}_{t'}^n | n^{(N-1)} | V_L^N(t') | \Psi_g^N \rangle + \text{c.c.} \end{aligned} \quad (7.97)$$

Note a crucial change compared to the single-channel case (Eq. (7.18)): the appearance of the laser-induced dynamics between the bound states of the ion, described by the propagator $U^{(N-1)}(t, t') |n^{(N-1)}\rangle$. These dynamics can be calculated if the dipole couplings, d_{mn} , between all essential states, as well as their eigenenergies E_n , are known.

Consider, for example, the case of an N₂ molecule with three essential states in the N₂⁺ ion, denoted as X, A and B, see Figure 7.11. The time-dependent transition amplitudes $a_{mn}(t, t')$ between the state $n^{(N-1)}$ populated at the moment t' and the state $m^{(N-1)}$ at the moment t are given by $a_{mn}(t, t') = \langle m^{(N-1)} | U^{(N-1)}(t, t') | n^{(N-1)} \rangle$.

7) Here we use the field-free states of the ion. If the limited amount of basis states is used, then one should try to find the optimal “laser-dressed” basis.

It is a solution of the following system of differential equations:

$$\frac{d(A^{(n)})}{dt} = [\mathbf{H} + \mathbf{V}(t)] A^{(n)}, \quad (7.98)$$

where, for our three ionic states, the Hamiltonian of the ion is

$$\mathbf{H} = \begin{pmatrix} E_1 & 0 & 0 \\ 0 & E_2 & 0 \\ 0 & 0 & E_3 \end{pmatrix},$$

with the energies E_n of the three states. The interaction between these three states is described by the matrix of the laser-induced couplings, $V_{mn}(t) = -\mathbf{d}_{mn} \cdot \mathbf{F}(t)$, that is

$$\mathbf{V}(t) = \begin{pmatrix} 0 & V_{12}(t) & V_{13}(t) \\ V_{21}(t) & 0 & V_{23}(t) \\ V_{31}(t) & V_{32}(t) & 0 \end{pmatrix}.$$

Finally,

$$A^{(n)} = \begin{pmatrix} a_{1n}(t, t') \\ a_{2n}(t, t') \\ a_{3n}(t, t') \end{pmatrix}$$

is the vector describing the population amplitudes of all essential ionic states, starting from the state $n^{(N-1)}$ at time t' .

Let us introduce channel-specific Dyson orbitals $\Psi_n^D(\mathbf{r}) \equiv \sqrt{N} \langle n^{(N-1)} | \Psi_g^N(\mathbf{r}) \rangle$. These are the overlaps between the N -electron wavefunction of the ground state of the neutral and the $(N-1)$ -electron wavefunction of the ionic state $|n^{(N-1)}\rangle$. In the Hartree–Fock picture they coincide with the Hartree–Fock orbitals. Let us assume that the dipole operator that starts ionization at the moment t' in Eq. (7.97) acts only on the electron that will be liberated (i.e., we neglect the exchange-like effects in ionization). In this case, the multielectron dipole $\mathbf{D}^{(mn)}$, which corresponds to leaving the ion in the state $n^{(N-1)}$ after ionization and then recombination with the ion in the state $m^{(N-1)}$, can be rewritten in a form very similar to the one-electron case (Eq. (7.24)):

$$\begin{aligned} \mathbf{D}^{(mn)}(t) &= i \int_{t_0}^t dt' \int d\mathbf{p} \mathbf{d}_m^*(\mathbf{p} + \mathbf{A}(t)) a_{mn}(t, t') e^{-i S_n(\mathbf{p}, t, t')} \\ &\times \mathbf{F}(t') \mathbf{d}_n(\mathbf{p} + \mathbf{A}(t')) , \end{aligned} \quad (7.99)$$

$$\mathbf{d}_n(\mathbf{p} + \mathbf{A}(t)) = \langle \mathbf{p} + \mathbf{A}(t) | \mathbf{d} | \Psi_n^D \rangle ,$$

$$\mathbf{d}_m(\mathbf{p} + \mathbf{A}(t)) = \langle \mathbf{p} + \mathbf{A}(t) | \langle n^{(N-1)} | \mathbf{d} | \Psi_g^N \rangle ,$$

$$S_n(\mathbf{p}, t, t') = \frac{1}{2} \int_{t'}^t [\mathbf{p} + \mathbf{A}(\tau)]^2 d\tau + I_{\mathbf{p}, n}(t - t').$$

This expression is remarkably similar to a one-electron dipole (7.24). The transformation similar to (7.22) is also valid in this case, yielding

$$\mathbf{D}^{(mn)}(t) = i \int_0^t dt' \int d\mathbf{p} d_m^*(\mathbf{p} + A(t)) a_{mn}(t, t') e^{-iS(\mathbf{p}, t, t')} \Upsilon_n(\mathbf{p} + A(t')) , \quad (7.100)$$

$$\Upsilon_n(\mathbf{p} + A(t)) = \left[\frac{[\mathbf{p} + A(t)]^2}{2} + I_{p,n} \right] \langle \mathbf{p} + A(t) | \Psi_n^D \rangle ,$$

where $I_{p,n}$ is the ionization potential to the state n of the ion and the matrix $a_{mn}(t, t')$ is calculated while setting E_n to zero.

The total harmonic signal results from the coherent superposition of the dipoles $\mathbf{D}^{(mn)}$ associated with each ionization-recombination channel:

$$\mathbf{D}(t) = \sum_{m,n} \mathbf{D}^{(mn)}(t) . \quad (7.101)$$

Substantial subcycle transitions, such as those shown in Figure 7.11 for the N_2^+ ion in typical experimental conditions, have a crucial impact on the harmonic radiation. They lead to the appearance of the cross-channels in HHG (the off-diagonal elements $\mathbf{D}^{(mn)}$ for $m \neq n$ in Eq. (7.101)) since the state of the ion changes between the ionization and the recombination, see Figure 7.12. These channels can indeed be substantial in high harmonic generation, as is the case for N_2 molecules, see [53], as illustrated in Figure 7.11.

In the recent literature on high harmonic generation one can often come across a rather loose language, which refers to different ionization and recombination channels as associated with different Hartree–Fock molecular orbitals. This language

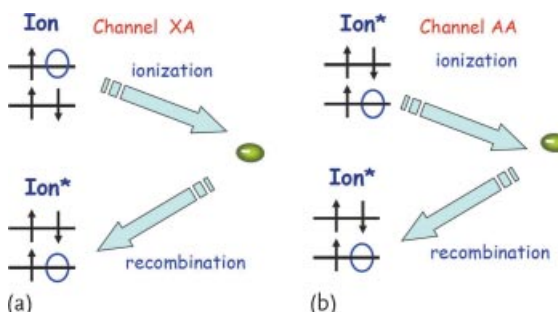


Figure 7.12 (a) Cross-channel in HHG associated with ionization from and recombination to different orbitals. This channel is due to real excitations induced by the laser field

between ionization and recombination. (b) Diagonal channel in HHG associated with ionization from and recombination to the same orbital.

should not be taken literally as a statement on the applicability of the Hartree–Fock picture and on the physical reality of the Hartree–Fock orbitals as observable physical quantities. Loosely speaking, removing an electron from the highest occupied molecular orbital (HOMO) creates the ion in the ground state. Removing an electron from one of the lower lying orbitals (e.g., HOMO-1, HOMO-2) creates the ion in one of its excited states. Thus, the reference to the orbitals should only be understood as a language for describing ionization and recombination channels associated with different multielectron states of the ion – and those are physically relevant and observable. In the orbital language, electron removal from an orbital creates a hole in this orbital. The laser-induced dynamics in the ion, moves the hole between the orbitals in the time window between ionization and recombination, see Figure 7.12.

Application of the saddle point method in each channel leads to the following half-cycle dipole for the given ionization-recombination channel:

$$\mathbf{D}^{(j,mn)}(t) = \mathbf{a}_{\text{rec}}^m(\mathbf{p}_s, t) \mathbf{a}_{\text{prop}}^{mn}(\mathbf{p}_s, t, t_i^{(j)}) \mathbf{a}_{\text{ion}}^n(\mathbf{p}_s, t_i^{(j)}), \quad (7.102)$$

$$\mathbf{a}_{\text{ion}}^n(\mathbf{p}_s, t_i) = \left[\frac{2\pi}{S''_{t_i, t_i}} \right]^{1/2} e^{-i S(\mathbf{p}_s, t_i^{(j)}, t_i^{(j)})} \Upsilon_n(\mathbf{p}_s + \mathbf{A}(t_i^{(j)})), \quad (7.103)$$

$$\mathbf{a}_{\text{prop}}^{mn}(\mathbf{p}_s, t, t_i) = \frac{(2\pi)^{3/2}}{(t - t_i)^{3/2}} e^{-i S(\mathbf{p}_s, t, t_i^{(j)})} \mathbf{a}_{mn}(t, t_i^{(j)}), \quad (7.104)$$

$$\mathbf{a}_{\text{rec}}^m = \mathbf{d}_m^*(\mathbf{p}_s + \mathbf{A}(t)). \quad (7.105)$$

Neglecting the subcycle dynamics in the prefactor of $\mathbf{a}_{\text{ion}}^n(\mathbf{p}_s, t_i)$, we can substitute Eq. (7.103) by the following expression, which includes the Coulomb effects in ionization (to learn about sub-cycle Coulomb effects, see [28, 32, 42]):

$$\mathbf{a}_{\text{ion}}^n(\mathbf{p}_s, t_i) = 2 \left(\frac{2\kappa^3}{F} \right)^{\frac{Q}{\kappa}} \sqrt{\frac{-\tilde{\gamma}\omega}{\kappa\sqrt{1+\tilde{\gamma}^2}}} e^{-i S(\mathbf{p}_s, t_i', t_i)} \Upsilon_n(\mathbf{p}_s + \mathbf{A}(t_i)). \quad (7.106)$$

A term similar to Υ_n also arises within the time-dependent analytical R-matrix approach, applied to multichannel strong-field ionization [52]. However, in [52] the radial integration is removed due to the use of the Bloch operator. Thus, in [52] the pole in Υ_n does not arise, even when the long-range potential is taken into account. Function $\Upsilon_n(\mathbf{p}_s + \mathbf{A}(t_i))$ encodes the angular structure of the Dyson orbital in the asymptotic region, which is more complex than the one arising in the asymptotic of the atomic wavefunction (7.56), leading to Eq. (7.58). The simple expressions for the asymptotic of the Dyson orbital for small molecules can be found in [54].

Here, we have considered the harmonic dipole on the real time axis. Note that the propagation amplitude is modified compared to the one in the one-electron case (Eq. (7.72)) to include the laser-induced dynamics in the ion $\mathbf{a}_{mn}(t)$. The full dipole for each ionization-recombination channel is the sum over the different half-cycles

and the harmonic spectrum results from the FFT of the full dipole $D_{mn}(N\omega)$:

$$D^{(mn)}(t) = \sum_j D^{(j,mn)}(t), \quad (7.107)$$

$$D^{(mn)}(N\omega) = \int dt D^{(mn)}(t) e^{iN\omega t}. \quad (7.108)$$

The complete harmonic response is obtained by adding coherently the contributions of all ionization-recombination channels.

7.9

Outlook

Having factorized the dipole, we can use improved amplitudes for each step. These are the key components of the current theoretical work in high harmonic spectroscopy of molecules.

Improving ionization Improved ionization amplitudes can be taken from semianalytical and/or numerical approaches. The task is to define the function $\Upsilon(\mathbf{p} + \mathbf{A}(t))$ for a realistic system and include long-range and polarization [55] effects. For example, one can use the results of [54], where the ionization amplitude is represented as:

$$\tilde{a}_{\text{ion}}^n(\mathbf{p}_s, t_i) = \mathbb{R}_{\text{Im}}(\text{IP}, F) e^{-iS(\mathbf{p}_s, t'_i, t_i)}. \quad (7.109)$$

The exponent describes the subcycle dynamics of strong-field ionization, that is, it is the same as for the atomic case and a short-range potential. The prefactor $\mathbb{R}_{\text{Im}}(\text{IP}, F)$ accounts for the influence of the core potential and the shape of the initial state on the ionization rate. For atoms, this prefactor has been derived in the seminal papers of Perelomov, Popov and Terentev (see [34–37]) and improved in [56]. A simple recipe for incorporating their results into the subcycle ionization amplitudes can be found in [57] correction for the pre-factor R in molecules is discussed in [54]. Fully consistent treatment of long-range, polarization and orbital effects can be developed within the time-dependent analytical R-matrix (ARM) approach, see [28, 52].

Improving propagation In addition to the dynamics in the molecular ion, that is the laser-induced transitions between different ionic states, the second most important modification of the propagation amplitudes is the incorporation of possible transverse nodal structure in the continuum wave packets. The nodal planes in the continuum wave packet arise during tunneling from bound states. For example, in the CO₂ molecule, the HOMO and the corresponding Dyson orbital have nodal planes parallel and perpendicular to the molecular axis. Consequently, in the

case of tunnel ionization with the molecular axis aligned parallel to the polarization of the ionizing field, the nodal plane will not only reduce the ionization rate, but will also be imprinted on the shape of the electronic wave packet that emerges after ionization. Propagation between ionization and recombination will lead to the spreading of the wave packet, but it will not remove the presence of the node as the wave packet returns to the core [13, 47, 58]. Clearly, this aspect of propagation is important for the recombination amplitude.

Consider, for example, ionization from a state with angular momentum $L = 1$. Its projection on the laser polarization is either $L_z = 0$ (no nodal plane along the electric field) or $L_z = \pm 1$ (nodal plane along the electric field). After tunneling, in the plane orthogonal to the laser polarization, in the momentum space the continuum wave packets are proportional to $(p_{\perp}/\kappa)^m$, (see Eq. (7.62) or (7.66)):

$$\begin{aligned}\Psi_{L_z=0}(p_{\perp}) &\propto e^{-\frac{p_{\perp}^2}{2}\tau}, \\ \Psi_{L_z=1}(p_{\perp}) &\propto \frac{p_{\perp}}{\kappa} e^{i\phi_p} e^{-\frac{p_{\perp}^2}{2}\tau},\end{aligned}\quad (7.110)$$

where $\tau = \Im(t_i)$ is the imaginary part of t_i , $\kappa = \sqrt{2IP}$, and ϕ_p is the angle between p_{\perp} and the x axis. As we can see, the presence of the nodal plane for $L_z = \pm 1$ leads to the additional term p_{\perp}/κ . We now propagate these wave packets until the recombination time t_r . Fourier transforming back into the coordinate space, in the plane orthogonal to the laser polarization, we get

$$\begin{aligned}\Psi_{L_z=0}(\rho) &\propto e^{-\frac{\rho^2}{2(t_r-t_i)}} \\ \Psi_{L_z=1}(\rho) &\propto \frac{\rho}{\kappa(t_r-t_i)} e^{i\phi} e^{-\frac{\rho^2}{2(t_r-t_i)}}\end{aligned}\quad (7.111)$$

where ρ is the transverse radial coordinate and ϕ is the angle between the radial vector and the x axis. Recalling that $x = \rho \cos \phi$, we see that if we combine the $L_z = \pm 1$ states to form the real-valued spherical harmonic p_x , the presence of the nodal plane effectively changes the dipole operator \mathbf{d} to $\mathbf{d} \cdot \mathbf{x}/(\kappa(t_r - t_i))$. In [13, 47, 58] such modifications of recombination operators have been used to account for the appearance of nodal planes.

In most experiments with molecular HHG to date, the alignment distribution is rather broad. Even if the molecular ensemble is, on average, aligned parallel to the laser polarization, for most molecules the characteristic alignment angle would be sufficiently different from that associated with the nodal plane. In this case, the relative importance of the nodal planes in recombination is reduced. However, for well-aligned molecular ensembles this would become a significant factor.

Improving recombination The recombination step can be significantly improved beyond the SFA, if one uses the recombination dipoles $\mathbf{d}_m^*(\mathbf{p}_s + \mathbf{A}(t))$ calculated using *ab initio* approaches. For example, the quantitative rescattering theory (see [59]) relies on using the Schwinger variational method to calculate the field-free

recombination matrix elements. Alternatively, one can use the R-matrix approach (see [60, 61]). Both allow one to incorporate the full complexity of the recombination process, including the channel coupling due to the electron–electron correlation and automatically include the exchange effects in recombination [55, 62, 63]. The drawback of these methods, at the moment, is the absence of the laser field in the calculations of the recombination amplitudes. This approximation breaks down in the case of a sharply structured continuum [48], common for many molecules. The impact of the IR field on such continuum states has been recently demonstrated experimentally [64], substantiating the prediction of [48]. In the approach described in [13], the eikonal-Volkov approximation for the continuum states was used to obtain improved dipoles in the single-channel approximation with exchange. The eikonal-Volkov approximation fully includes the interaction of the continuum electron with the laser field, but the interaction with the core potential is only included in the eikonal approximation, and the correlation-induced channel coupling is neglected. Improving the recombination amplitudes to account for all these effects – the channel coupling due to the electron–electron correlation, the core potential, and the laser field, is one of the key theoretical challenges today.

With each of the three steps in the harmonic response improved, the original SFA-based theory turns from purely qualitative into more realistic. The separation of the three steps, crucial for our ability to improve each of them separately, benefits from the high intensity of the driving field and the large oscillation amplitude of the active electron. The high field intensity also lies at the heart of the main difficulties in building an adequate theoretical description. Nevertheless, the effort is worth the investment: the combination of attosecond temporal and angstrom spatial resolution is extremely valuable. High harmonic spectroscopy appears to be well suited for tracking the multielectron dynamics induced by the ionization process.

It is very attractive to replace the ionization step induced by the IR field with the one-photon ionization induced by a controlled attosecond XUV pulse, phase locked to the strong IR field (see [65]). The latter would drive the continuum electron. Such an arrangement should allow one to move from dealing with outer valence electrons to dealing with inner valence and deeper lying electrons. This appears to be an exciting regime for tracking the hole dynamics [66] initiated by inner valence or deeper ionization. Importantly, for deeply bound orbitals, the effect of the IR driving field on the core rearrangement and the hole dynamics should be substantially less than for the outer valence electrons.

High harmonic spectroscopy helps to record the relative phases between different ionization channels, which provide information about electron rearrangement during ionization and define the initial conditions for the hole migration both in the inner valence [66] and outer valence [13] shells. These initial conditions are sensitive to the frequency, intensity and duration of the ionizing pulse, opening opportunities for controlling hole migration and, possibly, related chemical reactions [67].

Acknowledgements

We are grateful to Maria Richter for reading the manuscript and suggesting many important corrections, Szczepan Chelkowski and Thomas Schultz for useful comments, and Felipe Morales for his help in preparing the manuscript. We thank Pascal Salières and Alfred Maquet for encouraging us to undertake this project. Finally, we acknowledge the stimulating atmosphere of the KITPC workshop “Attosecond Science – Exploring and Controlling Matter on Its Natural Time Scale” in Beijing, where the seeds of this chapter were planted.

7.10

Appendix A: Supplementary Derivations

In this section we prove that the transformation in Eq. (7.22)

$$\int_{t_0}^t dt' e^{-iS(\mathbf{p}, t, t')} F(t') d(\mathbf{p} + A(t')) = \int_{t_0}^t dt' e^{-iS(\mathbf{p}, t, t')} \Upsilon(\mathbf{p} + A(t')) , \quad (7.112)$$

$$\Upsilon(\mathbf{p} + A(t')) = \left[\frac{(\mathbf{p} + A(t'))^2}{2} + \text{IP} \right] \langle \mathbf{p} + A(t') | g \rangle , \quad (7.113)$$

is applicable to the case of high harmonic generation. By definition

$$\int_{t_0}^t dt' e^{-iS(\mathbf{p}, t, t')} F(t') d(\mathbf{p} + A(t')) \equiv e^{-i\text{IP}t} \int_{t_0}^t dt' \langle \Psi_p^V(t'; t) | -V_L | g(t') \rangle . \quad (7.114)$$

Adding and subtracting the kinetic energy operator $\widehat{\mathbf{p}}^2/2$ [21, 22] we obtain:

$$\begin{aligned} & \int_{t_0}^t dt' \langle \Psi_p^V(t'; t) | -\frac{\widehat{\mathbf{p}}^2}{2} - V_L + \frac{\widehat{\mathbf{p}}^2}{2} | g(t') \rangle \\ &= \int_{t_0}^t dt' \left\{ i \frac{\langle \partial \Psi_p^V(t'; t) |}{\partial t'} | g(t') \rangle + \left[\frac{(\mathbf{p} + A(t'))^2}{2} \right] \langle \Psi_p^V(t'; t) | g(t') \rangle \right\} . \end{aligned} \quad (7.115)$$

Here we have used that $-i(\partial \Psi_p^V(t'; t))/\partial t' = [\widehat{\mathbf{p}^2}/2 + V_L](\Psi_p^V(t'; t))$. Integrating by parts the first term in Eq. (7.115) we obtain:

$$\begin{aligned} & \int_{t_0}^t dt' i \frac{\partial \Psi_p^V(t'; t)}{\partial t'} |g(t')\rangle \\ &= -i \int_{t_0}^t dt' \langle \Psi_p^V(t'; t) | \frac{\partial |g(t')\rangle}{\partial t'} + \langle \Psi_p^V(t'; t) | g(t') \rangle |_{t_0}^t . \end{aligned} \quad (7.116)$$

The transformation Eq. (7.112) can be recovered using $i\partial|g(t')\rangle/\partial t' = -iP|g(t')\rangle$ and taking into account that the boundary term $\langle \Psi_p^V(t'; t) | g(t') \rangle |_{t_0}^t$ does not contribute to the high harmonic dipole. Indeed the contribution of the boundary term to high harmonic dipole is:

$$\int d\mathbf{p} d^* (\mathbf{p} + A(t)) \left[\langle \Psi_p^V(t; t) | g(t) \rangle - \langle \Psi_p^V(t_0; t) | g(t_0) \rangle \right] \quad (7.117)$$

$$= \int d\mathbf{p} \langle g(t) | \hat{\mathbf{d}} | \Psi_p^V(t; t) \rangle \langle \Psi_p^V(t; t) | g(t) \rangle \quad (7.118)$$

$$- \int d\mathbf{p} \langle g(t) | \hat{\mathbf{d}} | \Psi_p^V(t; t) \rangle \langle \Psi_p^V(t_0; t) | g(t_0) \rangle . \quad (7.119)$$

The term Eq. (7.118) is equal to zero, the term Eq. (7.119) tends to zero when $t_0 \rightarrow -\infty$. Indeed,

$$\int d\mathbf{p} \langle g(t) | \hat{\mathbf{d}} | \Psi_p^V(t; t) \rangle \langle \Psi_p^V(t; t) | g(t) \rangle = \langle g(t) | \hat{\mathbf{d}} | g(t) \rangle = 0 , \quad (7.120)$$

while the second term Eq. (7.119) is:

$$\begin{aligned} & \int d\mathbf{p} \langle g(t) | \hat{\mathbf{d}} | \Psi_p^V(t; t) \rangle \langle \Psi_p^V(0; t) | g(0) \rangle \\ &= \int d\mathbf{p} e^{-i\frac{1}{2} \int_{t_0}^t d\tau [\mathbf{p} + A(\tau)]^2} \langle g(t) | \hat{\mathbf{d}} | \mathbf{p} + A(t) \rangle \langle \mathbf{p} | g(0) \rangle . \end{aligned} \quad (7.121)$$

This term corresponds to the projection of the ground state onto the basis of plane waves at $t_0 \rightarrow -\infty$ followed by recombination of the resulting oscillating wave packet back to the ground state at time t . Spreading of the free-electron wave packet over infinite time $(t - t_0) \rightarrow +\infty$ makes this projection negligible.

7.11

Appendix B: The Saddle Point Method

The saddle point method is one of the key techniques in the analytical strong-field theory. It is an asymptotic method, which allows one to analytically evaluate the integrals from highly oscillating functions, such as the integral in Eq. (7.19).

7.11.1

Integrals on the Real Axis

How would one calculate the following integral,

$$I = \int_a^b f(x) e^{\lambda h(x)} dx \quad (7.122)$$

for some smooth functions $f(x)$ and $h(x)$, without knowing much about them, or if they look ugly and complicated? All we know is that they are real-valued functions on the real axis x .

In general, one could think that there is not much one can do. Fortunately, this is not the case if the positive and real λ is large, $\lambda \gg 1$ – then, the integral can be calculated.

7.11.1.1 Contribution of the End Points

The first idea that comes to my mind when looking at such an integral is to try integration by parts. This approach works just fine under certain circumstances, see below. The first stumbling block meets you right at the gate: how does one integrate by parts if both $h(x)$ and $f(x)$ are unknown?

The trick is simple:

$$\begin{aligned} I &= \int_a^b f(x) e^{\lambda h(x)} dx \\ &= \int_a^b dx \frac{f(x)}{\lambda h'(x)} \lambda h'(x) e^{\lambda h(x)} \\ &= \frac{1}{\lambda} \frac{f(x)}{h'(x)} e^{\lambda h(x)} \Big|_a^b - \frac{1}{\lambda} \int_a^b dx e^{\lambda h(x)} \left[\frac{d}{dx} \left(\frac{f(x)}{h'(x)} \right) \right]. \end{aligned} \quad (7.123)$$

We started with an integral that did not have a small parameter $1/\lambda$ in front. Now we have two terms: the first comes from the contributions at the end points. The second term is another integral, now with a small parameter in front. Dealing with it in the same way as with the original integral, we will get terms proportional to $1/\lambda^2$, and so on.

Thus, we conclude that the main contribution to the integral comes from the end points, and is given by the first term:

$$\begin{aligned} I &= \int_a^b f(x) e^{\lambda h(x)} dx \\ &= \frac{1}{\lambda} \left[\frac{f(b)}{h'(b)} e^{\lambda h(b)} - \frac{f(a)}{h'(a)} e^{\lambda h(a)} \right] + O(\lambda^{-2}). \end{aligned} \quad (7.124)$$

This result is applicable unless there is a problem with the second term in Eq. (7.123) – the integral

$$-\frac{1}{\lambda} \int_a^b dx e^{\lambda h(x)} \left[\frac{d}{dx} \left(\frac{f(x)}{h'(x)} \right) \right]. \quad (7.125)$$

The problem arises if $h'(x) = 0$ somewhere between the two end points of the integral. What do we do then? Obviously, the points where $[f(x)/h'(x)]$ diverges can bring major contributions to the integral.

Given that $\lambda \gg 1$, the way the exponential function changes between a and b is most important. The first possibility is $h' \neq 0$ in the integration interval. Then, the integral is accumulated at the end points, and the end point where $h(x)$ is larger dominates. In general, for an exponential function $e^{\lambda h(x)}$ the main contribution to the integral will come from the region where it reaches its maximum value – and hence where $h'(x) = 0$.

Suppose that, somewhere between a and b , the derivative $h' = 0$. If the function $h(x)$ has a minimum, the contribution of this minimum will not be competitive with the contributions from the end points (remember that λ is large and positive). But if it has a maximum, then the main contribution to the integral comes from the region near the maximum. The way to handle this situation is described in the next section.

7.11.1.2 The Laplace Method

Let us consider an integral from a function $f(x)$ shown in Figure 7.13. The function is bell-shaped, has a maximum at the point x_0 , where its first derivative is, of course, equal to zero, and quickly falls off to each side of x_0 .

Back-of-the-envelope evaluation of this integral is very simple – all we need is to find the effective width Δx of the bell-shaped curve, and then the integral is

$$I = \int_{-\infty}^{\infty} f(x) dx = f(x_0) \Delta x. \quad (7.126)$$

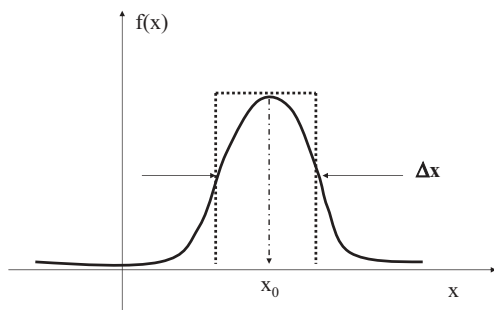


Figure 7.13 Integral from a bell-shaped curve with a maximum at x_0 and a width of Δx .

Let us first try some simple estimates of the width Δx . In order to do it, we expand $f(x)$ around x_0 in a Taylor series, remembering that the first derivative is zero at this point:

$$f(x) \approx f(x_0) + \frac{1}{2} f''(x_0)(x - x_0)^2 = f(x_0) - \frac{1}{2} |f''(x_0)|(x - x_0)^2. \quad (7.127)$$

We have explicitly used the fact that the second derivative at the local maximum is negative.

A potential candidate for the width Δx is the full width at half maximum (FWHM). The half-width $\Delta x/2$ at each side is given by

$$f(x_0) - \frac{1}{2} |f''(x_0)| \left(\frac{\Delta x}{2} \right)^2 = \frac{f(x_0)}{2}. \quad (7.128)$$

This gives us $\Delta x = \sqrt{4f_0/|f''|}$.

A more accurate calculation of the required width comes from the following trick, which will also smoothly bring us into the saddle point method

$$I = \int f(x) dx = \int e^{\ln f(x)} dx. \quad (7.129)$$

This transformation allows us to reduce the integral to a familiar Gaussian form. We proceed by expanding $\ln f(x)$ in a Taylor series, remembering that $f'(x_0) = 0$ and $f''(x_0) = -|f''(x_0)|$:

$$I = \int e^{\ln f(x)} dx \simeq \int e^{\ln f(x_0) - \frac{|f''(x_0)|}{f(x_0)} \frac{(x-x_0)^2}{2}} dx. \quad (7.130)$$

Recalling that the integral from a Gaussian is

$$\int_{-\infty}^{\infty} e^{-ax^2} dx = \sqrt{\frac{\pi}{a}}, \quad (7.131)$$

and setting the limits of our integral to $\pm\infty$, we get the final answer

$$I = f(x_0) \sqrt{2\pi \frac{f(x_0)}{|f''(x_0)|}}. \quad (7.132)$$

As you can see, the width Δx turned out to be pretty close to the FWHM.

7.11.1.3 Saddle Point Method: The Steepest Descent in a Complex Plane

We now move to the *saddle point method* which is used for integrals of complex-valued functions,

$$I = \int_C e^{\lambda f(z)} dz. \quad (7.133)$$

where λ is large and positive, and the rest is hidden in $f(z)$. The integral is to be taken over a contour C , and the only good thing about this contour is that its ends, somewhere far away from the place of action, and its ends do not contribute to the value of the integral.

There are assumed to be no poles, so that we are allowed to deform the contour C as we wish. The key to the steepest descent is a clever modification of the integration contour.

First, note that a complex function $f(z)$ has a real part and an imaginary part, $f(z) = u(z) + iv(z) \equiv u(x, y) + iv(x, y)$, where x and y are the real and the imaginary parts of z , $z = x + iy$.

Let us now look at the integral more closely and recall the previous section, where the integration was based on expanding the function around a maximum and reducing the integrand to a Gaussian. In our case we have a function $\exp(\lambda u + i\lambda v)$ that changes its absolute value very rapidly due to the λu part. It also oscillates rapidly due to the λv part. The trick of the steepest descent is to modify the contour of integration in such a way that it will go through a place where the real part u climbs to a maximum along the contour and then quickly falls, while the imaginary part v stays constant along the same contour, freezing any fast oscillations.

It may not be obvious that such a modification of the contour is possible. But it is.

We start in a manner entirely analogous to the previous section. Let us assume that the function $f(z)$ has a zero derivative at the point $z_0 = x_0, y_0$, where x_0 and y_0 are coordinates in the complex plane; the point z_0 lies somewhere between the left and the right ends of the contour C .

If $f_z(z_0) = 0$, then both the real and the imaginary parts of f must have zero derivatives there:

$$u_x = v_x = 0, \quad v_y = u_y = 0. \quad (7.134)$$

Thus, not only at z_0 does the absolute magnitude of our function go through an extremum, but also the oscillating part is stationary. Another important observation is that the gradients of the two functions, ∇u and ∇v , are always orthogonal to each other:

$$\nabla v \cdot \nabla u = u_x v_x + u_y v_y = 0. \quad (7.135)$$

This is the consequence of the Cauchy–Riemann conditions:

$$u_x = v_y, \quad v_x = -u_y. \quad (7.136)$$

The gradient points in the direction in which the function changes. If we move along the gradient of u , following the path of its steepest rise and fall through the point z_0 , we are also moving orthogonal to the gradient of v . Thus, v will stay constant, and fast oscillations are frozen. We see that the desired modification of the contour is indeed possible.

How should the landscape of $u(x, y)$ look like? Due to the same Cauchy–Riemann conditions the functions u and v can only have *saddle points* at z_0 :

$$u_{xx} + u_{yy} = 0, \quad v_{xx} + v_{yy} = 0. \quad (7.137)$$

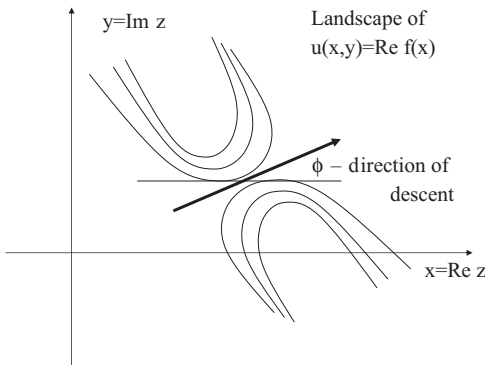


Figure 7.14 Saddle point method. The landscape of $u(x, y) = \Re f(z)$ around the point z_0 where $f' = 0$.

Real mountain peaks, which go down in all directions, only happen at singularities, and we decided that there would be no singularities in $f(z)$.

Therefore, the landscape of the function u around the point z_0 must look something like that shown in Figure 7.14.

All we have to do now is to find the correct path of the *steepest descent through the saddle point*, such that u will rise as quickly as possible as we approach the saddle point and then decrease as quickly as possible as we leave the saddle point. The Cauchy–Riemann conditions promise us that, while we are at it, v will stay constant.

Let us expand $f(z)$ in a Taylor series around z_0 , remembering that $f'(z_0) = 0$:

$$f(z) \approx f(z_0) + \frac{1}{2} f''(z_0)(z - z_0)^2. \quad (7.138)$$

Of course, $f''(z_0)$ is a complex number, which we will denote as $f''(z_0) = \alpha \exp(i\theta)$. If our path traverses the saddle point at some angle ϕ , then $z - z_0 = \rho \exp(i\phi)$ and

$$\frac{1}{2} f''(z_0)(z - z_0)^2 = \frac{1}{2} \alpha \rho^2 e^{i(\theta+2\phi)}. \quad (7.139)$$

Now, the trick is to choose the angle ϕ properly – we set

$$e^{i(\theta+2\phi)} = -1 \quad (7.140)$$

and keep the angle ϕ given by the above condition fixed, changing only ρ , so that $dz = d(z - z_0) = \exp(i\phi)d\rho$.

If we do this, the integral along such a path will look like

$$I = e^{\lambda f(z_0)} e^{i\phi} \int_{C'} e^{-\lambda \alpha \frac{\rho^2}{2}} d\rho, \quad (7.141)$$

where the deformed contour C' is going through the saddle point as a straight line at an angle ϕ . Note that, indeed, there are no oscillations along such path, and the real integrand decays as a Gaussian.

The integration limits are now extended to plus and minus infinity and the integral is done:

$$I = e^{\lambda f(z_0)} e^{i\phi} \sqrt{\frac{2\pi}{\lambda\alpha}}. \quad (7.142)$$

Recall that $\alpha \equiv |f''(z_0)|$.

At this point we are almost done, but three important remarks are still in order.

First, there is ambiguity in the definition of the direction ϕ from $\exp(i(\theta + 2\phi)) = -1$. Indeed, the total angle $\theta + 2\phi$ could be both plus and minus π . Thus, formally, without looking at the landscape shown in Figure 7.14, we have a choice of two ϕ :

$$\phi_1 = -\frac{\theta}{2} + \frac{\pi}{2}, \quad \phi_2 = -\frac{\theta}{2} - \frac{\pi}{2}. \quad (7.143)$$

The whole idea of the method is to choose such a direction that you never have to cross the “mountains” in the landscapes of $u(x, y)$ and $v(x, y)$. You should choose the direction (deforming the contour C) that takes you from the valley, through the saddle point, into another valley. Otherwise, you will also have to include the contributions of the “mountains” into the integral. Usually, it is the first choice that works, but one should take a look at the landscape and check. The wrong option will go in an obviously wrong way, crossing into the tops of the mountains rather than staying all the way in the valley and smoothly climbing to the saddle. We shall see an example of it in the next section.

Second, if there are several saddle points, that is, $f(z)$ has many points where its derivative is zero, the integral will be the sum of the contributions from all these points. Then the individual phases ϕ for each saddle point become very important.

Third, there is a modification of the prefactor when dealing with multidimensional integrals:

$$I = \int_C e^{\lambda f(z)} dz, \quad (7.144)$$

$$I \simeq \left(\frac{2\pi}{\lambda}\right)^{n/2} e^{\lambda f(z_0)} \frac{1}{\sqrt{-f_{zz}(z_0)}}, \quad (7.145)$$

where f_{zz} is the Hessian matrix (the matrix of the second derivatives of the function f).

7.11.2

Stationary Phase Method

The stationary phase method is a simple application of the saddle point method to a function with a purely imaginary phase,

$$I = \int g(x) e^{i\lambda f(x)} dx, \quad (7.146)$$

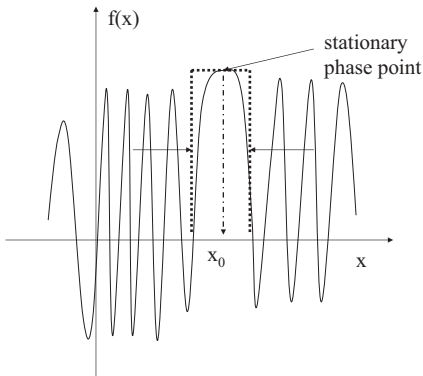


Figure 7.15 Stationary phase method. The integral comes from the area where the integrand does not oscillate as much.

where $g(x)$ is a benign, very slowly changing function which does not do much – just makes sure that the integrand goes to zero at infinity. The constant λ is again real and positive, the integral is supposed to be performed along the real axis and the function $f(x)$ is purely real on the real axis. Intuitively, it is clear that if the function $\exp(i\lambda f(x))$ is oscillating very quickly, its integral averages to zero unless there are some points where the oscillations freeze. These areas are the regions where the phase of the oscillation, $f(x)$, stays nearly constant, that is, areas around the point where the derivative turns to zero, $f' = 0$, see Figure 7.15.

The problem can be turned into that studied in the previous section. Again, suppose that the derivative $f' = 0$ at some point x_0 . We use the same Taylor expansion around this point and denote $x - x_0$ as, say, ξ . The integral is approximated as

$$I = g(x_0) e^{i\lambda f(x_0)} \int e^{i\lambda f''(x_0) \frac{\xi^2}{2}} d\xi \quad (7.147)$$

and we will assume that $f'' = \alpha > 0$ (f is a real-valued function and x_0 is on the real axis, hence f'' is real). The case $f'' < 0$ is handled in an identical manner.

Calculation of the integral

$$\int e^{i\lambda \alpha \frac{\xi^2}{2}} d\xi \quad (7.148)$$

follows the exact prescription of the saddle point method. The phase θ of the second derivative (see previous section) is $\theta = \pi/2$ (i.e., $i\alpha = \alpha \exp(i\pi/2)$) and the contour of integration has to be turned at an angle ϕ to the real axis, such that $\theta + 2\phi = \pm\pi$. This yields the two possible choices of ϕ : $\phi = +\pi/4$ and $\phi = -3\pi/4$. The answer for the integral is:

$$I = g(x_0) e^{i\lambda f(x_0)} \sqrt{\frac{2\pi}{\alpha\lambda}} e^{i\phi}. \quad (7.149)$$

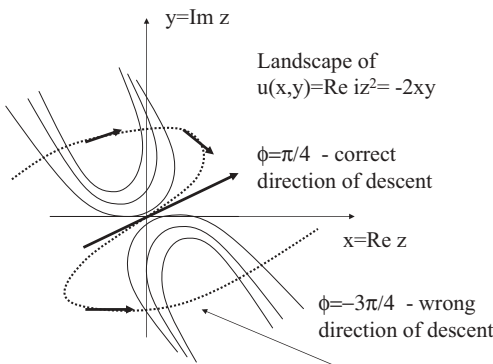


Figure 7.16 Stationary phase method. Correct and incorrect paths of the steepest descent for $f(z) = iz^2$.

To find the correct choice of ϕ , one has to look at the landscape of $u(x, y) = \Re(iz^2) = -2xy$. The landscape is shown in Figure 7.16. The correct choice is obviously the first one, $\phi = +\pi/4$, the second would mean that the contour has to be deformed as shown in Figure 7.16 with the dashed line, going through high mountains on the way to the saddle to cross it in the opposite direction of $\phi = -3\pi/4$.

So, the final answer is

$$I = g(x_0) e^{i\lambda f(x_0)} \sqrt{\frac{2\pi}{\alpha\lambda}} e^{i\pi/4}. \quad (7.150)$$

7.12

Appendix C: Treating the Cutoff Region: Regularization of Divergent Stationary Phase Solutions

In this section we briefly outline the idea of the so-called uniform approximation – one of the approaches for handling the merging stationary points. The regularization involves two steps. First, we need to find a specific real return time $t_r = t_{r0}$ and the associated $t_i = t_{i0}$, $p_s = p_{s0}$, such that $\partial^2 S(t_{r0}, t_{i0}, p_{s0})/\partial t^2 = 0$. In practice, one can simply pick the real return time corresponding to the cutoff energy. The next step requires the expansion of the total action in Eq. (7.21) around $t = t_{r0}$ in a Taylor series up to the third order,

$$S(t, t_{i0}, p_{s0}) = S(t_{r0}) + (t - t_{r0}) S'_{tt} + \frac{(t - t_{r0})^2}{2} S''_{tt} + \frac{(t - t_{r0})^3}{6} S'''_{ttt}, \quad (7.151)$$

where all the derivatives of $S(t, t_{i0}, p_{s0})$ are taken at t_{r0} (and the second derivative is equal to zero). Finally, one substitutes the expansion Eq. (7.151) into the harmonic

dipole,

$$D(N\omega) \propto \int_{-\infty}^{\infty} dt e^{iN\omega t} e^{-iS(t, t_{i0}, p_{s0}) + iN\omega t} + \text{c.c.}, \quad (7.152)$$

and uses the Airy function,

$$\int_{-\infty}^{\infty} dt \cos(at^3 \pm xt) \equiv \frac{\pi}{(3a)^{1/3}} Ai\left[\frac{\pm x}{(3a)^{1/3}}\right]. \quad (7.153)$$

Now we introduce the “cutoff harmonic number” N_0 and the distance from the cutoff $N = N - N_0$:

$$N_0\omega = E_{\text{rec}}(t_{r0}) + \text{IP}, \quad (7.154)$$

here $E_{\text{rec}}(t_{r0}) = p_{s0} + A(t_{r0})$ is the recollision energy at time t_{r0} , and N_0 does not have to be an integer. The dipole near the cutoff is expressed via the Airy function,

$$\int_{-\infty}^{\infty} dt e^{iN\omega t} e^{-iS(t, t_{i0}, p_{s0}) + iN\omega t} + \text{c.c.} = \int_{-\infty}^{\infty} d\xi \cos\left(\frac{\chi}{6}\xi^3 \pm \Delta N\omega\xi\right), \quad (7.155)$$

so that

$$D(N\omega) \propto \frac{2\pi}{\left(\frac{\chi}{2}\right)^{1/3}} Ai\left[\frac{\Delta N\omega}{\left(\frac{\chi}{2}\right)^{1/3}}\right], \quad (7.156)$$

where $\chi \equiv -S''_{tt}(t_{r0})$ and can be estimated as $\chi \cong v(t_{r0})F_0\omega$, given that $F'_t(\chi) \cong F_0\omega$ and $F(\chi) \cong 0$. Using the asymptotic expansion of the Airy functions, we obtain simple expressions for the dipole just before and after the cutoff. Before the cutoff of the harmonic spectra (for $\Delta N < 0$), the dipole oscillates, $Ai \sim \cos(-(\Delta N\omega)^{3/2}(8/9\chi)^{1/2})$, after the cutoff, the harmonic dipole exponentially decreases, $Ai \sim \exp(-(\Delta N\omega)^{3/2}(8/9\chi)^{1/2})$. The oscillations of the harmonic dipole before the cutoff are due to the interference of the short and the long trajectories.

7.13

Appendix D: Finding Saddle Points for the Lewenstein Model

In Sections 7.4 and 7.5 we have described how one can find all saddle point solutions in the Lewenstein model for a fixed harmonic number N . Here we present an alternative and equivalent approach of finding the saddle point solutions. In this approach, we solve Eqs. (7.36)–(7.38). This alternative can be used in all cases, but is particularly convenient if the Fourier transform is performed numerically. The

idea is to solve Eqs. (7.36)–(7.38) “forward,” that is, to fix the grid of real recombination times and then find all the other remaining saddle point solutions and the corresponding harmonic number N . The recombination condition Eq. (7.38) ($p_{s,\parallel} = p' + i p''$) can be rewritten as follows:

$$(\Delta p' + i \Delta p'')^2 = 2(N\omega - \text{IP}), \quad (7.157)$$

$$\Delta p' \equiv p' - A_0 \sin(\phi'_r) \cosh(\phi''_r), \quad (7.158)$$

$$\Delta p'' \equiv p'' - A_0 \sinh(\phi''_r) \cos(\phi'_r), \quad (7.159)$$

yielding

$$(\Delta p')^2 - (\Delta p'')^2 + 2i\Delta p' \Delta p'' = 2(N\omega - \text{IP}). \quad (7.160)$$

Since the right-hand side of this equation is real, we obtain that $\Delta p' \Delta p'' = 0$. For above-threshold harmonics ($N\omega - \text{IP} > 0$) and $\Delta p' \neq 0$, $\Delta p'' = 0$. For below-threshold harmonics ($N\omega - \text{IP} < 0$) and $\Delta p' = 0$, $\Delta p'' \neq 0$. Separating the imaginary and the real parts in Eqs. (7.36) and (7.37), we obtain the four equations quoted in the main text, see Eqs. (7.43), (7.44), (7.47) and (7.48). Supplementing these equations for above-threshold harmonics with $\Delta p'' = 0$ yields

$$p_2 = \sinh(\phi''_r) \cos(\phi'_r), \quad (7.161)$$

and for below-threshold harmonics with $\Delta p' = 0$, yielding

$$p_1 = \sin(\phi'_r) \cosh(\phi''_r), \quad (7.162)$$

we obtain five equations.

Above-threshold harmonics For each fixed ϕ'_r we use Eqs. (7.47) and (7.48) to express ϕ''_i , ϕ''_i via p_2 and p_1 and then we use Eq. (7.161) to exclude p_2 and substitute $\phi'_i(p_1, \phi''_r)$, $\phi''_i(p_1, \phi''_r)$ and $p_2(p_1, \phi''_r)$ into Eqs. (7.43) and (7.44). Using the gradient method, we can now find the minima of the function $F = F_1^2 + F_2^2$ in the plane of p_1 and ϕ''_r for each fixed ϕ'_r . The minima define the saddle point solutions for p_1 and ϕ''_r . Knowing p_1 and ϕ''_r , we find ϕ'_i , ϕ''_i , p_2 from Eqs. (7.47), (7.48) and (7.161). Finally, the corresponding harmonic number can be calculated from $(\Delta p')^2 = 2(N\omega - \text{IP})$, yielding $N\omega = A_0^2(p_1 - \sin \phi'_r \cosh \phi''_r)^2/2 + \text{IP}$. Naturally, the harmonic number defined this way does not have to be an integer.

Below-threshold harmonics The procedure for below-threshold harmonics is essentially the same. For each fixed ϕ'_r , we use the Eqs. (7.47) and (7.48) to express ϕ'_i , ϕ''_i via p_2 and p_1 and then we use Eq. (7.162) to exclude p_1 and substitute $\phi'_i(p_2, \phi''_r)$, $\phi''_i(p_2, \phi''_r)$ and $p_1(p_2, \phi''_r)$ into Eqs. (7.43) and (7.44). Using the gradient method, we can now find the minima of the function $F = F_1^2 + F_2^2$ in the plane of p_2 and ϕ''_r for each fixed ϕ'_r . The minima define the saddle point solutions for p_2 and ϕ''_r . Knowing p_2 and ϕ''_r we find ϕ'_i , ϕ''_i , p_1 from Eqs. (7.47), (7.48),

and (7.162). Finally, the corresponding harmonic number can be calculated from $(\Delta p'')^2 = 2(\text{IP} - N\omega)$, yielding $N\omega = \text{IP} - A_0^2(p_2 - \sinh \phi_r'' \cos \phi_r')^2/2$.

In this method, it is convenient to determine the return time ϕ_{tr}' corresponding to the threshold harmonic number $N_t = \text{IP}/\omega$. This can be done easily, since, at the threshold, $p_2 = \sinh(\phi_r'') \cos(\phi_r')$ and $p_1 = \sin(\phi_r') \cosh(\phi_r'')$. Thus, we can use these equations together with Eqs. (7.47) and (7.48) to express ϕ_i' , ϕ_i'' via ϕ_r' and ϕ_r'' and then use Eqs. (7.43) and (7.44) to find a minimum of the function $F = F_1^2 + F_2^2$ in the plane of ϕ_r' and ϕ_r'' , representing the threshold values of ϕ_r' and ϕ_r'' . Once the threshold value ϕ_{tr}' of ϕ_r' is known, one can separately implement the procedures described above for below, $\phi_r' < \phi_{\text{tr}}'$, and above, $\phi_r' > \phi_{\text{tr}}'$, threshold harmonics.

References

- 1 Corkum, P.B. (1993) Plasma perspective on strong field multiphoton ionization. *Phys. Rev. Lett.*, **71**, 1994.
- 2 Krause, J.L., Schafer, K.J., and Kulander, K.C. (1992) High-order harmonic generation from atoms and ions in the high intensity regime. *Phys. Rev. Lett.*, **68**, 3535.
- 3 Brunel, F. (1987) Not-so-resonant, resonant absorption. *Phys. Rev. Lett.*, **59**, 52.
- 4 Brunel, F. (1990) Harmonic generation due to plasma effects in a gas undergoing multiphoton ionization in the high-intensity limit. *J. Opt. Soc. Am. B*, **7**, 521.
- 5 Corkum, P.B., Burnett, N.H., and Brunel, F. (1989) Above-threshold ionization in the long-wavelength limit. *Phys. Rev. Lett.*, **62**, 1259.
- 6 Kuchiev, M.Y. (1987) Atomic antenna. *Sov. Phys. JETP Lett.*, **45**, 319.
- 7 Kulander, K., Krause, J.L., and Schafer, K.J. (1993) *NATO ASI Series*, Plenum Press, New York and London.
- 8 Schafer, K.J., Yang, B., DiMauro, L.F., and Kulander, K.C. (1993) Above threshold ionization beyond the high harmonic cutoff. *Phys. Rev. Lett.*, **70**, 1599.
- 9 Gallagher, T. (1988) Above-threshold ionization in low-frequency limit. *Phys. Rev. Lett.*, **61**, 2304.
- 10 Krausz, F. and Ivanov, F. (2009) Attosecond physics. *Rev. Mod. Phys.*, **81**, 163.
- 11 Lein, M. (2005) Attosecond probing of vibrational dynamics with high-harmonic generation. *Phys. Rev. Lett.*, **94**, 053004.
- 12 Baker, S., Robinson, J.S., Haworth, C.A., Teng, H., Smith, R.A., Chirila, C.C., Lein, M., Tisch, J.W.G., and Marangos, J.P. (2006) Probing proton dynamics in molecules on an attosecond time scale. *Science*, **312**, 424.
- 13 Smirnova, O., Mairesse, Y., Patchkovskii, S., Dudovich, N., Villeneuve, D., Corkum, P., and Ivanov, M.Y. (2009) High harmonic interferometry of multi-electron dynamics in molecules. *Nature*, **460**, 972.
- 14 Haessler, S., Caillat, J., Boutu, W., Giovanetti-Texeira, C., Ruchon, T., Auguste, T., Diveki, Z., Breger, P., Maquet, A., Carre, B., Taieb, R., and Salieres, P. (2010) Attosecond imaging of molecular electronic wavepackets. *Nat. Phys.*, **6**, 200.
- 15 Gaarde, M.B., Tate, J.L., and Schafer, K.J. (2008) Macroscopic aspects of attosecond pulse generation. *J. Phys. B*, **41**, 132001.
- 16 Huillier, A. and Balcou, P. (1993) High-order harmonic generation in rare gases with a 1-ps 1053-nm laser. *Phys. Rev. Lett.*, **70**, 774.
- 17 Macklin, J.J., Kmetec, J.D., and Gordon, C.L. (1993) High-order harmonic generation using intense femtosecond pulses. *Phys. Rev. Lett.*, **70**, 766.

- 18** Krause, J.L., Schafer, K.J., and Kulander, K.C. (1992) High-order harmonic generation from atoms and ions in the high intensity regime. *Phys. Rev. Lett.*, **68**, 3535.
- 19** Grynberg, G., Aspect, A., and Fabre, C. (2010) *Introduction to Quantum Optics: From the Semi-classical Approach to Quantized Light*, Cambridge University Press.
- 20** Smirnova, O., Spanner, M., and Ivanov, M. (2007) Anatomy of strong field ionization ii: to dress or not to dress? *J. Mod. Opt.*, **54**, 1019.
- 21** Gribakin, G.F. and Kuchiev, M.Y. (1997) Multiphoton detachment of electrons from negative ions. *Phys. Rev. A*, **55**, 3760.
- 22** Becker, W., Grasbon, F., Kopold, R., Milosevic, D.B., Paulus, G.G., and Walther, H. (2002) Above-threshold ionization: From classical features to quantum effects. *Adv. At. Mol. Opt. Phys.*, **48**, 36.
- 23** Lewenstein, M., Balcou, P., Ivanov, M.Y., L'Huillier, A., and Corkum, P.B. (1994) Theory of high-harmonic generation by low-frequency laser fields. *Phys. Rev. A*, **49**, 2117.
- 24** Ivanov, M.Y., Brabec, T., and Burnett, N. (1996) Coulomb corrections and polarization effects in high-intensity high-harmonic emission. *Phys. Rev. A*, **54**, 742–745.
- 25** Salieres, P., Carré, B., Le Deroff, L., Grasbon, F., Paulus, G.G., Walther, H., Kopold, R., Becker, W., Milosevic, D.B., Sanpera, A., and Lewenstein, M. (2001) Feynman's path-integral approach for intense-laser-atom interactions. *Science*, **292**, 902.
- 26** Kopold, R., Becker, W., and Milosevic, D.B. (2002) Quantum orbits: a space-time picture of intense-laser-induced processes in atoms. *J. Mod. Opt.*, **49**, 1362.
- 27** Becker, W., Grasbon, F., Kopold, R., B., M.D., Paulus, G.G., and Walther, H. (2002) Above-threshold ionization: from classical features to quantum effects. *Adv. At. Mol. Opt. Phys.*, **48**, 35.
- 28** Torlina, L. and Smirnova, O. (2012) Time-dependent analytical *R*-matrix approach for strong-field dynamics. I. One-electron systems. *Phys. Rev. A*, **86**, 043408.
- 29** Zair, A., Holler, M., Guandalini, A., Schapper, F., Biegert, J., Gallmann, L., Keller, U., Wyatt, A.S., Monmayrant, A., Walmsley, I.A., Cormier, E., Auguste, T., Caumes, J.P., and Salières, P. (2008) Quantum path interferences in high-order harmonic generation. *Phys. Rev. Lett.*, **100**, 143902.
- 30** Frolov, M.V., Manakov, N.L., Pronin, E.A., and Starace, A.F. (2003) Model-independent quantum approach for intense laser detachment of a weakly bound electron. *Phys. Rev. Lett.*, **91**, 053003.
- 31** Keldysh, L.V. (1965) Ionization in the field of a strong electromagnetic wave. *Sov. Phys. JETP*, **20**, 1307.
- 32** Kaushal, J. and Smirnova, O. (2013) Non-adiabatic coulomb effects in strong field ionisation in circularly polarised laser fields. I: Ionisation rates. *Phys. Rev. A*, **88** (1), 013421.
- 33** Shafir, D., Soifer, H., Bruner, B.D., Dagan, M., Mairesse, Y., Patchkovskii, S., Ivanov, M.Y., Smirnova, O., and Dudovich, N. (2012) Resolving the time when an electron exits a tunnelling barrier. *Nature*, **485**, 343.
- 34** Perelomov, A.M., Popov, V.S., and Terent'ev, M.V. (1966) *Sov. Phys. JETP*, **23**, 924.
- 35** Perelomov, A.M., Popov, V.S., and Terent'ev, M.V. (1967) *Sov. Phys. JETP*, **24**, 207.
- 36** Perelomov, A.M. and Popov, V.S. (1967) *Sov. Phys. JETP*, **25**, 336.
- 37** Popov, V.S., Kuznetsov, V.P., and Perelomov, A.M. (1968) *Sov. Phys. JETP*, **26**, 222.
- 38** Barth, I. and Smirnova, O. (2011) Non-adiabatic tunneling in circularly polarized laser fields: Physical picture and calculations. *Phys. Rev. A*, **84**, 063415.
- 39** Barth, I. and Smirnova, O. (2013) Non-adiabatic tunneling in circularly polarized laser fields. II: Derivation of formulas. *Phys. Rev. A*, **87**, 013433.
- 40** Bloch, C. (1957) Une formulation unifiee de la theorie des reactions nucleaires. *Nucl. Phys.*, **4**, 503.

- 41** Torlina, L., Kaushal, J., and Smirnova, O. (2013) Time-resolving electron-core dynamics during strong field ionization in circularly polarized fields, arXiv preprint arXiv:1308.1348.
- 42** Frolov, M.V., Manakov, N.L., Sarantseva, T.S., Emelin, M.Y., Ryabikin, M.Y., and Starace, A.F. (2009) Analytic description of the high-energy plateau in harmonic generation by atoms: Can the harmonic power increase with increasing laser wavelengths? *Phys. Rev. Lett.*, **102**, 243901.
- 43** Le, A.T., Lucchese, R.R., Tonzani, S., Morishita, T., and Lin, C.D. (2009) Quantitative rescattering theory for high-order harmonic generation from molecules. *Phys. Rev. A*, **80**, 013401.
- 44** Morishita, T., Le, A.T., Chen, Z., and Lin, C.D. (2008) Accurate retrieval of structural information from laser-induced photoelectron and high-order harmonic spectra by few-cycle laser pulses. *Phys. Rev. Lett.*, **100**, 013903.
- 45** Kuchiev, M.Y. and Ostrovsky, V.N. (1999) Quantum theory of high harmonic generation as a three-step process. *Phys. Rev. A*, **60**, 3111.
- 46** Morales, F., Barth, I., Serbinenko, V., Patchkovskii, S., and Smirnova, O. (2012) Shaping polarization of attosecond pulses via laser control of electron and hole dynamics. *J. Mod. Opt.*, **59**, 1303.
- 47** Smirnova, O., Patchkovskii, S., Mairesse, Y., Dudovich, N., and Ivanov, M.Y. (2009) Strong-field control and spectroscopy of attosecond electron-hole dynamics in molecules. *Proc. Natl. Acad. Sci. (PNAS)*, **106**, 16556.
- 48** Patchkovskii, S., Smirnova, O., and Spanner, M. (2012) Attosecond control of electron correlations in one-photon ionization and recombination. *J. Phys. B*, **45**, 131002.
- 49** Walters, Z.B. and Smirnova, O. (2010) Attosecond correlation dynamics during electron tunnelling from molecules. *J. Phys. B*, **43**, 161002.
- 50** Smirnova, O., Spanner, M., and Ivanov, M. (2008) Analytical solutions for strong field-driven atomic and molecular one- and two-electron continua and applica-
- tions to strong-field problems. *Phys. Rev. A*, **77**, 033407.
- 51** Smirnova, O., Mouritzen, A.S., Patchkovskii, S., and Ivanov, M.Y. (2007) Coulomb-laser coupling in laser-assisted photoionization and molecular tomography. *J. Phys. B*, **40**, F197.
- 52** Torlina, L., Ivanov, M., Walters, Z.B., and Smirnova, O. (2012) Time-dependent analytical *R*-matrix approach for strong-field dynamics. II. many-electron systems. *Phys. Rev. A*, **86**, 043409.
- 53** Mairesse, Y., Higuet, J., Dudovich, N., Shafir, D., Fabre, B., Mével, E., Constant, E., Patchkovskii, S., Walters, Z., Ivanov, M.Y., and Smirnova, O. (2010) High harmonic spectroscopy of multichannel dynamics in strong-field ionization. *Phys. Rev. Lett.*, **104**, 213601.
- 54** Murray, R., Spanner, M., Patchkovskii, S., and Ivanov, M.Y. (2011) Tunnel ionization of molecules and orbital imaging. *Phys. Rev. Lett.*, **106**, 173001.
- 55** Sukiasyan, S., Patchkovskii, S., Smirnova, O., Brabec, T., and Ivanov, M.Y. (2010) Exchange and polarization effect in high-order harmonic imaging of molecular structures. *Phys. Rev. A*, **82**, 043414.
- 56** Popruzhenko, S.V., Mur, V.D., Popov, V.S., and Bauer, D. (2008) Strong field ionization rate for arbitrary laser frequencies. *Phys. Rev. Lett.*, **101**, 193003.
- 57** Yudin, G.L. and Ivanov, M.Y. (2001) Nonadiabatic tunnel ionization: Looking inside a laser cycle. *Phys. Rev. A*, **64**, 013409.
- 58** Smirnova, O., Patchkovskii, S., Mairesse, Y., Dudovich, N., Villeneuve, D., Corkum, P., and Ivanov, M.Y. (2009) Attosecond circular dichroism spectroscopy of polyatomic molecules. *Phys. Rev. Lett.*, **102**, 063601.
- 59** Lin, C.D., Le, A.T., Chen, Z., Morishita, T., and Lucchese, R. (2010) Strong-field rescattering physics — self-imaging of a molecule by its own electrons. *J. Phys. B*, **43**, 122001.
- 60** Harvey, A. and Tennyson, J. (2009) The *R*-matrix method for attosecond spectroscopy. *J. Phys. B*, **42**, 095101.
- 61** Harvey, A.G., Morales, F., and Smirnova, O. (2012) The *R*-matrix method for attosecond spectroscopy. *Theory of*

- Electron-Molecule Collisions for Astrophysics, Biophysics and Low Temperature Plasmas: Opportunities and Challenges*, 106, 16.
- 62** Gordon, A. and Santra, R. (2006) Three-step model for high-harmonic generation in many-electron systems. *Phys. Rev. Lett.*, **96**, 073906.
- 63** Patchkovskii, S., Zhao, Z., Brabec, T., and Villeneuve, D.M. (2006) High harmonic generation and molecular orbital tomography in multielectron systems: beyond the single active electron approximation. *Phys. Rev. Lett.*, **97**, 123003.
- 64** Ott, C., Kaldun, A., Raith, P., Meyer, K., Laux, M., Evers, J., Keitel, C.H., Greene, C.H., and Pfeiffer, T. (2013)
- Lorentz meets Fano spectral line shapes: A universal phase and its laser control. *Science*, **340**, 716–720.
- 65** Schafer, K., Gaarde, M.B., A., H., J., B., and Keller, U. (2004) Strong field quantum path control using attosecond pulse trains. *Phys. Rev. Lett.*, **92**, 023003.
- 66** Lunnenmann, S., Kuleff, A., and Cederbaum, L. (2008) Ultrafast charge migration in 2-phenylethyl-*n,n*-dimethylamine. *Chem. Phys. Lett.*, **450**, 232.
- 67** Weinkauf, R., Schlag, E., Martinez, T., and Levine, R.D. (1997) Nonstationary electronic states and site-selective reactivity. *J. Phys. Chem. A*, **101**, 7702.

8**Time-Dependent Schrödinger Equation**

Armin Scrinzi

Solving the time-dependent Schrödinger equation (TDSE) for typical problems in attosecond physics usually requires numerical approaches. A notable exception is the case when Keldysh-type approximations are valid, like in the strong-field approximation (SFA) discussed elsewhere in this book (see Chapter 6). When moderately strong IR laser fields with intensities $\gtrsim 10^{14} \text{ W/cm}^2$ are involved, numerical solutions of the TDSE are far from trivial. Before devising any elaborate numerical model, one therefore must carefully consider the reasons for such an enterprise. In particular, as for the basic processes in attosecond physics – high harmonic spectra and photoelectron emission – rather clear physical pictures have emerged, mostly based on SFA and the recollision idea (see Chapters 6, 7 and 10). The need to go beyond those simple models arises when we want to verify them. For example, recollision describes the generation of very high harmonics with amazing accuracy, but is utterly unable to correctly reproduce lower harmonics. In this case the limitations of the model are well understood, however in other cases, model limitations are less obvious and need to be checked numerically. We can also turn the sequence of reasoning around and perform “numerical experiments” from which we gain physical insight. The most striking result of this kind is the numerical observation of the $\text{IP} + 3.2 U_p$ high harmonic cutoff in numerical simulations by Kulander and Krause [1] and its ingenious explanation by the recollision model by Corkum [2]. Similarly, we routinely use realistic descriptions or simplifying models, for example, with restricted dimensionality, to study possible mechanisms in ultrafast electronic dynamics. A second very important reason to numerically solve the TDSE is to get the numbers right: all models necessarily are approximate, yet experimentalists need to rely on data from theory, for example, ionization rates, or they need to interpret details of photoelectron spectra. Neither can be reliably deduced from simplifying models. Of course, ultimately, we would like to fully reproduce experimental findings by theory to make sure all relevant mechanisms are included. This is in general very hard to achieve considering the complexity of a typical attosecond experiment. Here, in addition to the quantum mechanical effects captured in the TDSE, macroscopic effects also play a role, such as propagation of harmonics or space-charge; also experimental uncertainties, for example, about the exact pulse profiles or target densities, must be taken into account.

Once the need to solve the TDSE is established, there is a broad range of techniques available and several specific features of the TDSE for laser-matter interactions must be taken into account. In this chapter, we will review several approaches to numerically solving the TDSE for atomic and molecular systems in strong laser fields.

8.1

Atoms and Molecules in Laser Fields

The atomic and molecular dimensions of typically ~ 0.1 nm are small as compared to wavelengths between some 10 nm and several micrometers. This justifies the use of the dipole-approximation for all calculations. Further, we will treat the fields classically, as we are usually dealing with very large photon numbers where fluctuations of photon number and quantum phase can be neglected. Using length gauge, the TDSE for a single electron moving in the potential of fixed nuclei $V(\mathbf{r})$ and experiencing a dipole interaction with the field $\mathcal{E}(t)$ is

$$i \frac{d}{dt} \Psi_l(\mathbf{r}, t) = \left\{ -\frac{1}{2} \Delta + V(\mathbf{r}) - \mathbf{r} \cdot \mathcal{E}(t) \right\} \Psi_l(\mathbf{r}, t). \quad (8.1)$$

Here, and throughout, we use atomic units with $m_e = \hbar = e = 1$, where m_e is the electron mass, and e is the (positive) proton charge. Atomic units for other quantities are summarized in Table 8.1.

An alternative representation of the TDSE is the velocity gauge form

$$i \frac{d}{dt} \Psi_v(\mathbf{r}, t) = \left\{ \frac{1}{2} [-i \nabla - A(t)]^2 + V(\mathbf{r}) \right\} \Psi_v(\mathbf{r}, t), \quad (8.2)$$

with

$$A(t) = - \int_{-\infty}^t dt' \mathcal{E}(t'). \quad (8.3)$$

Table 8.1 A few important quantities for the description of laser-atom interactions and their relation to atomic units (au): $m_e = \hbar = e = 1$. Vacuum polarizability and speed of light are denoted by ϵ_0 and c , respectively.

Unit	Definition	Numerical value
Length	$a_0 = [(4\pi\epsilon_0)\hbar^2]/(m_e e^2)$	0.052 917 nm
Energy	$2R\gamma = e^2/[(4\pi\epsilon_0)a_0]$	27.211 eV
Velocity	$v_0 = e^2/[(4\pi\epsilon_0)\hbar c]$	$c/137.035$
Time	$\tau_0 = a_0/v_0$	24.188×10^{-18} s
Field strength	$\mathcal{E}_0 = e^2/[(4\pi\epsilon_0)a_0^2]$	5.1422×10^{11} V/m
Intensity	$I_0 = \mathcal{E}_0^2/2$	$3.509\,44 \times 10^{16}$ W/cm ²
Wavelength at $2R\gamma$	$2\pi a_0 \alpha$	45.563 nm
Optical cycle at 800 nm	800 nm/c	110.32 au

Note that $A(t)$ is just the laser vector potential in the Coulomb gauge, where a factor e/c is absorbed into the definition. The term $\sim A(t)^2$ in (8.2) is often omitted, as it only leads to an additional time-dependent, but space-independent phase $\exp[-i \int_{-\infty}^t A^2(t') dt'/2]$ on the wavefunction, with no effect on observables. Note further that, as no laser pulse can have a zero-frequency component, A before and after the pulse must be equal

$$0 = - \int_{-\infty}^{\infty} dt' \mathcal{E}(t') = A(\infty) - A(-\infty). \quad (8.4)$$

Often, the dipole field is written as the product of an envelop and a carrier $\mathcal{E}(t) = \mathcal{E}_0(t) \cos(\omega t + \phi_{\text{CEO}})$. For very short pulses, condition (8.4) can be easily violated, which may lead to artifacts, for example, create spurious dependencies on the carrier envelope phase ϕ_{CEO} . When needed, such artifacts can be rigorously excluded, by defining the pulse shape in terms of the vector potential

$$A(t) = -\frac{\mathcal{E}_0(t)}{\omega} \sin(\omega t + \phi_{\text{CEO}}), \quad (8.5)$$

with $A(\infty) = A(-\infty) = 0$ and deriving the field from it as $\mathcal{E}(t) = -d/dt A(t)$.

The velocity gauge form of the TDSE (8.2) is related to the length form (8.1) by the simple unitary transformation of the wavefunction

$$\Psi_v(\mathbf{r}, t) = e^{i A(t) \cdot \mathbf{r}} \Psi_l(\mathbf{r}, t). \quad (8.6)$$

The two forms are obviously completely equivalent on a mathematical level, however, they can have quite different numerical properties, as the gauge transformation imprints a space-dependent phase on the wavefunction: numerically, a less oscillatory solution is easier to approximate. For example, in polar coordinates, velocity gauge usually requires fewer partial waves and is therefore to be preferred [3]. Note, that this is a very technical, coordinate-dependent statement: in linear polarization and cylinder coordinates, there is essentially no computational advantage of either gauge.

In atomic units, $A(t)$ can be interpreted as the momentum given to a free electron by the field up to time t . The gauge transform then corresponds to a time-dependent boost in momentum space by $A(t)$. Similarly, the so-called Kramers–Henneberger frame of reference is a time-dependent shift in *position* space by $\alpha(t) = \int_{-\infty}^t dt' A(t')$, that is, a frame of reference moving with the electron, where the nucleus instead of the electron appears to oscillate with the field. As the rapidly moving singularity of the Coulomb potential causes many numerical difficulties, the Kramers–Henneberger frame is rarely used in direct solutions of the TDSE [4].

8.2

Solving the TDSE

For solving the TDSE of systems in laser fields, all techniques available for general quantum dynamics are applied. For discretization, one uses grids with finite

difference representation of the differential operator [5, 6], discrete-variable (DVR) [7, 8] and pseudo-spectral methods [9], local basis sets, like finite elements and B-splines [3, 10, 11], essential state approaches [12], time-dependent CI [13], and multiconfiguration time-dependent Hartree–Fock [14]. Unfortunately, time-dependent density functional theory (TDDFT) has so far not been able to produce satisfactory results, except very close to the ground state [15, 16]. TDDFT appears to produce similar artifacts as single-configuration time-dependent Hartree–Fock, whose inapplicability was recognized when it was first tried in the late 1980s [17].

Before discussing a few of these approaches in more detail, we give a very general outline of numerical methods for the TDSE.

8.2.1

Discretization of the TDSE

For numerically solving the TDSE, we need to discretize the wavefunction Ψ , that is, parameterize it by a finite set of complex numbers $c = (c_1, c_2, \dots, c_N)$ and find the dynamical equations for c .

Discretization on a grid means that we identify c_i with the wavefunction value at some point q_i in space $c_i(t) := \Psi(q_i, t)$. Cartesian coordinates $q = (x, y, z)$ are often used, but grid methods can be formulated for any coordinate system. DVR methods use the base points of some quadrature rule for the q_i [18]. In grid methods, TDSE is reduced to a system of coupled ordinary differential equations for the c_i

$$i \frac{d}{dt} c_i(t) = - \sum_{j=1}^N \mathbf{D}_{ij} c_j(t) + V(q_i) c_i , \quad i = 1, 2, \dots, N , \quad (8.7)$$

where the matrix \mathbf{D} approximates the second derivative on the grid. Grid methods are “local,” that is, determining the time-derivative $d/dt c_i$ requires only a few neighboring c_i . For the second-order finite difference scheme, the action of the second derivative operator at one site involves only the nearest neighbors to its left and its right. In matrix language, matrix \mathbf{D} is narrowly banded. Grids can be adapted to the particular problem by coordinate transformation and nonequidistant choice of the grid points. Grid methods scale very well to massively parallel computers, which has boosted their importance in recent years.

The second large class of methods uses expansions into basis functions

$$|\Psi(t)\rangle \approx \sum_{i=1}^N |i\rangle c_i(t) , \quad (8.8)$$

where the basis $\{|1\rangle, |2\rangle, \dots, |N\rangle\}$ should be complete in the limit $N \rightarrow \infty$. The dynamical equations take the general form

$$i \frac{d}{dt} \sum_{j=1}^N \mathbf{S}_{ij} c_j = \sum_{j=1}^N \mathbf{H}(t)_{ij} c_j , \quad i = 1, 2, \dots, N , \quad (8.9)$$

with the overlap and Hamiltonian matrices

$$\mathbf{S}_{ij} := \langle i|j \rangle, \quad \mathbf{H}(t)_{ij} := \langle i|H(t)|j \rangle. \quad (8.10)$$

For solving, the equation is brought to the standard form in matrix-vector notation

$$i \frac{d}{dt} \mathbf{c} = \mathbf{S}^{-1} \mathbf{H}(t) \mathbf{c}. \quad (8.11)$$

Due to their compactness, basis methods have produced many of the early numerical results for strong-field phenomena [19, 20] and are still in use. However, they do not scale well to large N : in general, they are highly nonlocal, that is, the time-derivative $i d/dt c_i$ depends on *all* other c_j . Mathematically, this is still a good deal, as smartly chosen basis sets can be exceedingly more accurate than grid approximations with the same number of coefficients c_i . Technically, full matrices can cause big problems: they require large storage and, in the case of parallel computing, communication between all computer nodes is needed at every time step. In addition, a frequent problem of global basis functions is ill-conditioning of the matrix \mathbf{S} , which prevents the numerically accurate computation of \mathbf{S}^{-1} and sets an effective limit to the maximal basis size. Gaussian basis sets and Slater-type basis sets ($\sim r^n \exp(-\alpha r)$) are most strongly affected by ill-conditioning problems.

A special class of basis functions are the eigenstates of some time-independent operator. In that case, one speaks of a pseudo-spectral method. We may choose eigenstates of the field-free Hamiltonian [13, 21], which allows selection of the basis functions within some preset energy range. One will usually need to determine the basis itself by numerical methods before solving the TDSE. This approach allows highly efficient solutions for \mathbf{c} , if the time-*independent* problem can be solved efficiently. Note, however, that a rather dense set of functions must be selected in the continuous spectrum, if spatial reflections are to be avoided (see also the remarks on effective box size below). Another pseudo-spectral basis are plane waves, that is, eigenstates of the momentum operator \mathbf{p} , which is equivalent to working in the \mathbf{p} -(*momentum*-)space [9] rather than \mathbf{r} -space.

The use of basis sets has the general advantage that one can easily build known behavior of the solution into the basis, which further speeds up convergence. This may be the behavior near a singularity, exponential tails, well-defined oscillatory behavior, or specific symmetries like rotational, reflection, or exchange symmetry.

An intermediate discretization strategy between grids and basis sets are found in local basis sets, which unite locality, numerical stability, and high flexibility of grid methods with the rapid convergence and the possibility to build desired properties into the basis. Strictly speaking, they are basis sets in their own right, with the special condition that each basis function $|i\rangle$ is spatially localized and overlaps with only a few neighbors. The order of the local basis set is given by the number of overlapping neighbor basis functions and can range from one (similar to the lowest-order finite difference method) to all functions. The latter would be the limiting case of a global basis. With the correct choice of local basis sets, exponential convergence with the order of the basis can be achieved (see, e.g., [22]). The general

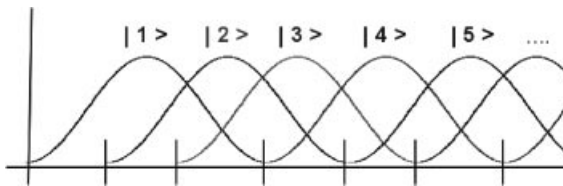


Figure 8.1 The first few B-spline basis functions $|1\rangle, |2\rangle, \dots$ on an interval starting from 0.

form of the dynamical equations for a local basis is the same as (8.11), but the matrices \mathbf{S} and $\mathbf{H}(t)$ are banded in the one-dimensional case and generally sparse for more than one dimension. As a rule, \mathbf{S} is well conditioned and the whole scheme is numerically robust.

A very transparent example of a local basis are B-splines, which are polynomials where each function is restricted to its own compact support (Figure 8.1). The order of the polynomials is related to the number p of overlapping neighbors. The \mathbf{S} and \mathbf{H} matrices for the B-spline basis are banded with bandwidth $2p + 1$ (Figure 8.2). B-splines of order five and higher are used as an auxiliary basis by several groups in attosecond and strong-field physics [13, 23–25]. Mathematically speaking, B-splines are a scheme to obtain piecewise polynomial approximations to the solution.

Other examples of local basis methods are wavelets (not used in the field at the time of writing) and finite elements, which will be discussed below in some detail.

In real applications, grids, global, and local bases are often combined. If any preference for rotational symmetry is given, like in laser-atom interaction up to moderate intensities, polar coordinates are the coordinate system of choice, where

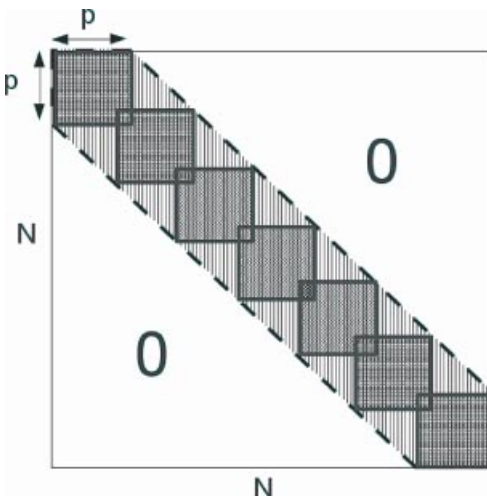


Figure 8.2 Banded matrix structure for N B-splines of order p (dashed line, hatched area). Squares show the matrix structure for finite element bases of 7 elements, each with p

functions on each element. The overlapping corners belong to the continuously connected boundary functions of neighboring elements.

approximate angular symmetries are well represented using spherical harmonics: this is the case of partial wave expansions, that is, writing

$$\Psi(\mathbf{r}) = \sum_{lm} Y_{lm}(\hat{\mathbf{r}}) \chi_{lm}(r), \quad (8.12)$$

where $Y_{lm}(\hat{\mathbf{r}})$ denote the spherical harmonics on the unit sphere. For discretization of the radial functions $\chi_{lm}(r)$, the methods mentioned above have been implemented by different groups.

8.2.2

Finite Elements

Finite elements are mathematically, and in computational practice, very similar to B-splines. However, they are not restricted to polynomials, but can be built combining any set of sufficiently linearly independent functions. We now elaborate in some detail on how to setup the TDSE in a finite element basis.

We follow the implementation strategy laid out in [22] and [26]: each coordinate axis is divided into N elements $[x_{n-1}, x_n]$, $n = 1, \dots, N$, see Figure 8.3. On each element with number n , we choose a set of p_n linearly independent functions $f_i^{(n)}$, $i = 1, \dots, p_n$ that can be transformed such that all functions are $= 0$ at x_{n-1} and x_n , except for the first and last functions, which have values $= 1$ at the lower and upper element boundaries, respectively:

$$\begin{aligned} f_i^{(n)}(x_{n-1}) &= f_i^{(n)}(x_n) = 0, \\ \text{except } f_1^{(n)}(x_{n-1}) &= f_{p_n}^{(n)}(x_n) = 1. \end{aligned} \quad (8.13)$$

We will call p_n the “rank” of the finite element. In principle any set of functions that obeys (8.13) can be used in a finite element scheme. In practice, we use real-valued polynomials which, for enhancing numerical stability, we transform to

$$\int_{x_{n-1}}^{x_n} f_i^{(n)}(x) f_j^{(n)}(x) dx = m_i^{(n)} \delta_{ij} \quad \forall (i, j) \neq (1, p_n), (p_n, 1), \quad (8.14)$$

with normalization constants $m_i^{(n)}$.

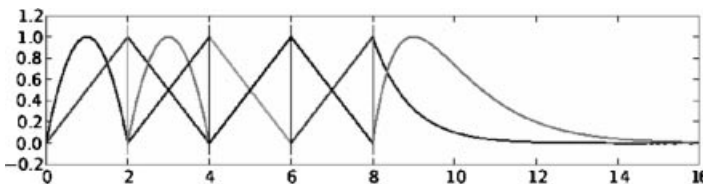


Figure 8.3 Finite element discretization combining 5 elements with different discretizations: polynomials up to degree 2 in the first two elements, then degree 1, and polynomials $\times \exp(-x)$ on the last *infinite* element $[8, \infty)$.

$$\begin{pmatrix} \ddots & \vdots & \vdots & \vdots & \vdots \\ \ddots & H_{p_{n-1}-1 p_{n-1}}^{(n-1)} & 0 & 0 & 0 \\ \dots & H_{p_{n-1} p_{n-1}}^{(n-1)} + H_{11}^{(n)} & \dots & H_n^{(n)} & 0 \\ 0 & H_{21}^{(n)} & \ddots & H_{2p_n}^{(n)} & 0 \\ \vdots & \vdots & \ddots & \vdots & \vdots \\ 0 & H_{p_n-1 1}^{(n)} & \dots & H_{p_n-1 p_n}^{(n)} & 0 \\ 0 & H_{p_n 1}^{(n)} & \dots & H_{p_n p_n}^{(n)} + H_{11}^{(n+1)} & H_{12}^{(n+1)} \\ 0 & 0 & 0 & H_{21}^{(n+1)} & \ddots \\ \vdots & \vdots & \vdots & \vdots & \ddots \end{pmatrix}$$

Figure 8.4 Placement of the element-wise block $H_{ij}^{(n)}$ in the overall Hamiltonian matrix \mathbf{H} .

For the element functions (8.13) Dirichlet boundary conditions are implemented by omitting the first and last functions $f_1^{(1)}$ and $f_{p_N}^{(N)}$ on the first and last elements of the simulation box, respectively. On the leftmost and rightmost intervals, we may also use polynomials times an exponential $e^{\pm\alpha x}$ with + and - signs on the intervals $(-\infty, x_1]$ and $[x_{N-1}, \infty)$, respectively. The conditions on the end element functions are

$$\begin{aligned} f_i^{(1)}(x_1) &= 0 \quad \text{except} \quad f_{p_1}^{(1)}(x_1) = 1 \\ f_i^{(N)}(x_{N-1}) &= 0 \quad \text{except} \quad f_1^{(N)}(x_{N-1}) = 1 . \end{aligned} \quad (8.15)$$

The exponent α can be optimized for a specific physical situation.

The finite element ansatz for the total wavefunction is

$$\Psi(x, t) = \sum_{n=1}^N \sum_{i=1}^{p_n} c_i^{(n)}(t) f_i^{(n)}(x) . \quad (8.16)$$

By construction of the $f_i^{(n)}$ of (8.13), continuity across element boundaries is assured by demanding

$$c_{p_{n-1}}^{(n-1)} = c_1^{(n)} , \quad n = 2, \dots, N . \quad (8.17)$$

Element-wise overlap and Hamiltonian matrices are

$$S_{ij}^{(n)} = \int_{x_{n-1}}^{x_n} J(x) \left[f_i^{(n)}(x) \right]^* f_j^{(n)}(x) dx \quad (8.18)$$

$$H_{ij}^{(n)} = \int_{x_{n-1}}^{x_n} J(x) \left[f_i^{(n)}(x) \right]^* H(t) f_j^{(n)}(x) dx , \quad (8.19)$$

where $J(x)$ denotes the Jacobian function for integration over x . The element-wise matrices are added into the overall discretized matrices \mathbf{H} and \mathbf{S} , such that the last row and column of each element-wise matrix overlaps with the first row and column of the following element (see Figure 8.4), which is equivalent to setting the corresponding coefficients equal, (8.17). As always in finite element methods, continuity of the first *derivative* does not need to be imposed (see [22] for a more detailed discussion). The total dimension of \mathbf{H} and \mathbf{S} is $M \times M$ with $M = \sum_{n=1}^N p_n - N - 1$.

8.2.3

Scaling with Laser Parameters

The numerical effort for solving the TDSE scales very unfavorably with laser wavelength. The reason can be easily explained. Assume that during its evolution, the wavefunction reaches maximal momentum P_{\max} and a maximal distance X_{\max} . If we want to avoid unphysical reflections from the grid boundaries, any discretization grid must extend to at least X_{\max} . At the same time, for resolving all wavefunction momenta up to P_{\max} , we need a grid spacing of at most

$$\Delta X \leq 2\pi \frac{\hbar}{P_{\max}} . \quad (8.20)$$

As a rule of thumb, the total number of grid points needed will be the classical phase space volume covered by the solution divided by $2\pi\hbar$. This applies in the ideal case of a perfect representation of the differential operators on the grid (e.g., by discrete Fourier transform), which is equivalent to using a global basis of plane waves and doing all integrals exactly in that basis. This rule of thumb sets a lower limit for any discretization. In practice, usually many more discretization points are needed. For example, low-order finite difference schemes miss that limit by a factor ~ 10 , depending on the accuracy requirements for the solution. Global and local basis sets can perform much better.

Note that this estimate applies only when we have no further structural knowledge of our solution. In reality, the solution may not cover the rectangle $P_{\max} \times X_{\max}$ evenly, but there may be a strong correlation between momentum and position. A trivial example for such a case is single-photon ionization by a long pulse: while the electron remains in the bound state, it is located near the nucleus but covers a broad range of momenta. After single-photon ionization, the wavefunction rapidly spreads over the whole space, but it covers a very narrow range of momenta. Actually, we know that we have a good approximation for the wavefunction of the process by just two parameters: c_0 , the amplitude of the initial state, and c_k the amplitude of the scattering solution at the final photoelectron energy. All we need is a simple perturbative formula for c_0 and c_k .

In strong-field IR ionization, we have no such insight: a wide range of photoelectron momenta from 0 to P_{\max} ($\sim \sqrt{2 \times 10 U_p}$ with $U_p = \mathcal{E}_{\text{peak}}^2 / 4\omega^2$) is gene-

rated with sizable amplitudes in the whole range. At the near-IR wavelength of $\lambda = 800 \text{ nm}$ (corresponding to photon energy $\omega = 0.057 \text{ au}$) and peak intensity $I = 2 \times 10^{14} \text{ W/cm}^2$ (resulting in $\mathcal{E}_{\text{peak}} = 0.075 \text{ au}$), we have $P_{\text{max}} \approx 2.9 \text{ au}$. As a single field oscillation takes $\sim 110 \text{ au}$ (cf. Table. 8.1), these fast electrons travel to a distance of $X_{\text{max}} = 2.9 \times 110 \approx 300 \text{ au}$. To correctly describe the motion for only a single optical cycle, we need at least $N = 300 \times 2.9/2\pi \approx 140$ coefficients c_i . We readily see that this number scales as $\mathcal{E}_{\text{peak}}^2 \times \lambda^3$, and this is only considering a single spatial dimension. In three dimensions and with linear polarization, the momenta in the perpendicular direction also grow as $\sim P_{\perp,\text{max}} \propto \lambda$ due to elastic scattering from the nucleus and the wavefunctions grow to dimensions $\sim X_{\perp,\text{max}} \propto \lambda^2$, leading to a scaling $\sim \lambda^6$. Only the cylindrical symmetry for linear polarization saves us from worse. This extremely unfavorable scaling of the problem size with laser wavelength is the reason why one sees far fewer calculations at $\lambda = 800 \text{ nm}$ compared to $\lambda = 400 \text{ nm}$: such calculations are 64 times as hard. Here we have taken into consideration only the spatial discretization. In addition, pulse duration and with it the time interval over which we need to solve the equations also tends to grow linearly with λ .

If, unlike the trivial example of single-photon ionization, we cannot exploit extra information about the wavefunction, there is no way of escaping this basic scaling. This scaling appears in momentum space as well as in configuration space, it appears with grids as well as with basis functions. However, we *do* have valuable additional knowledge about our solution at large distances: the wavefunction behaves like a wave packet of Volkov solutions (see Chapter 6) except for, possibly, the long-range action of the Coulomb potential. Once we know the amplitudes in the wave packet, we can predict its further evolution. Unfortunately, it is not easy to exploit that knowledge. One approach that capitalizes on that fact is “time-dependent coordinate scaling,” introduced for IR photoionization problems in [27] and [25]. In that approach, the coordinate space is allowed to expand with the evolution of the wave packet. At the same time, the predictable phase oscillations due to the free time-evolution are extracted from the wavefunction. The number of discretization points can be kept approximately constant while the grid expands, as the wavefunction becomes increasingly smooth. Yet another way of taking advantage of the known asymptotic time-evolution, the “time-dependent surface flux” (t-SURFF) method [28], will be briefly introduced below.

8.3 Time Propagation

Like in the case of spatial discretization, a wide range of standard methods are used for integrating the systems of ordinary differential equations (8.11): explicit and implicit Runge–Kutta schemes, predictor-corrector schemes [25], Krylov subspace methods [8, 29], and split step methods. We present a brief summary of the most wide-spread of these methods.

8.3.1

Runge–Kutta Methods

A single Runge–Kutta time-step is made as

$$c(t + \Delta t) = \Delta t \sum_{j=1}^s (\beta_j k_j), \quad (8.21)$$

where

$$k_j = \mathbf{S}^{-1} \mathbf{H}(t + \gamma_j \Delta t) \left[c(t) + \sum_{i=1}^s \alpha_{ji} k_i \right]. \quad (8.22)$$

The Runge–Kutta method is fully defined by the coefficients α_{ji} , β_j and γ_j . The error in a single step is $\sim (\Delta t)^{p+1}$. A large variety of Runge–Kutta methods with different s and p are available, described by their “Butcher tableaus,” see Figure 8.2.

There is an important distinction between “explicit” Runge–Kutta methods, which are subjected to the constraint $\alpha_{ji} = 0$ for $i \geq j$, and “implicit” methods without such a constraint. Explicit methods have the great technical advantage that for constructing any k_i , we only need the k_j , $j < i$ that have been constructed in the preceding steps. For time-independent Hamiltonians, the solution $c(t + \Delta t)$ is just a linear combination of vectors $(\mathbf{S}^{-1}\mathbf{H})^j c(t)$, $j = 0, \dots, s$, the “Krylov” vectors. When \mathbf{H} is time-dependent, products of $\mathbf{H}(t_i)$ at different times $t_i = t + \gamma_i \Delta t$ are taken.

In implicit methods, on the other hand, the k_j are only given by an implicit equation and must be obtained as the solution of a usually large linear system of equations. In practice, this can be achieved by using standard iterative linear equation solvers.

Table 8.2 gives the Butcher tableaus of two frequently used Runge–Kutta methods: probably most popular is the “classical” explicit Runge–Kutta scheme with $s = 4$ and $p = 4$. This only requires keeping a single additional vector in memory, which can be an advantage for very large systems. It is also the highest order where we can have $p = s$. A frequently used implicit Runge–Kutta method with consistency order $p = 2$ is the Crank–Nicholson method, which for the TDSE can

Table 8.2 General Butcher tableau of a Runge–Kutta method (left) and tableaus of the classical fourth-order Runge–Kutta method (center) and the Crank–Nicolson method (right).

γ_1	α_{11}	α_{12}	\dots	α_{1s}						
γ_2	α_{21}	\ddots		\vdots	0	0	0	0	0	
\vdots	\vdots		\ddots	\vdots	1/2	1/2	0	0	0	
γ_s	α_{s1}	\dots	\dots	α_{ss}	1	0	1/2	0	0	0
	β_1	β_2	\dots	β_s		1/6	1/3	1/3	1/6	1/2

be written as

$$c(t + \Delta t) = \left[\mathbf{H} \left(t + \frac{\Delta t}{2} \right) + i\mathbf{S} \right]^{-1} \left[\mathbf{H} \left(t + \frac{\Delta t}{2} \right) - i\mathbf{S} \right] c(t). \quad (8.23)$$

Its application is particularly efficient, when the matrices \mathbf{H} and \mathbf{S} are narrowly banded, as is often the case in low-order finite difference methods. The low consistency order, however, makes it costly to achieve high accuracies in the time propagation.

8.3.1.1 Discretization and Stability

In spite of their more complex implementation, implicit methods can be of advantage, as all implicit Runge–Kutta methods are unconditionally stable, that is, small errors remain small. In contrast, all explicit Runge–Kutta methods become unstable for large step sizes Δt , meaning that small errors are amplified exponentially. For the TDSE, the maximal Δt for stable solutions is inversely proportional to the maximal energy E_{\max} in the discretization. If that energy is related to the maximal energy that we are interested in, the corresponding step size is acceptable: our solution will have physically relevant time-structure, for example, quantum beats, on the scale Δt . Unfortunately, it is not always easy to adjust the discretization such that only the relevant energies are represented. In a grid discretization with spacing Δx , peak energy grows like $E_{\max} \sim (2\pi/\Delta x)^2$. Over-ambitiously fine discretizations lead to dramatic slowdown of explicit solvers and even to breakdown of the calculation. Near the nucleus, large kinetic energies require small grid spacing Δx , but actually, the kinetic energies are compensated by a large negative potential energy. However, if the same spacing is used at large distances, there is no potential to compensate the kinetic energy and E_{\max} rises to high values. Locally adjusted discretization, like variable grids, not only reduce the total number of discretization points, they also allow larger time steps Δt , if an explicit method is used.

8.3.2

Krylov Subspace Methods

When the laser field oscillations, and therefore the time-dependence of $H(t)$, are slow compared to the internal time scale (which is governed by the relevant energy range of the field-free system) approximations with constant Hamiltonian $H(t_0)$ for some $t_0 \in [t, t + \Delta t]$ can be efficient, for example,

$$c(t + \Delta t) \approx e^{-i\Delta t \mathbf{S}^{-1} H(t + \Delta t/2)} c(t). \quad (8.24)$$

Note that the Crank–Nicolson method could be understood as one particular, non-polynomial approximation to the exponential up to second order. Any *polynomial* approximation of the exponential leads to a Krylov subspace method, where the right-hand side of (8.24) is replaced by a linear combination of the Krylov vectors $(\mathbf{S}^{-1}\mathbf{H})^j c(t)$. The short iterative Lanczos method [30] used in [8] and the Arnoldi scheme used in [29] both fall into that category. For constant Hamiltonians, also the

explicit Runge–Kutta methods are reduced to particular variants of Krylov subspace methods.

8.3.3

Split-Step Methods

A special form of exponentiation can be used, when the Hamiltonian can be split into two parts $\mathbf{H} = \mathbf{A} + \mathbf{B}$ and exponentials for the two operators \mathbf{A} and \mathbf{B} can be formed easily:

$$e^{-i\Delta t \mathbf{H}} = e^{-i\Delta t \mathbf{A}/2} e^{-i\Delta t \mathbf{B}} e^{-i\Delta t \mathbf{A}/2} + \mathcal{O}(\Delta t^3), \quad (8.25)$$

where the error also depends on the commutator $[\mathbf{A}, \mathbf{B}]$. The exponentials can be calculated by bringing the matrices to diagonal form. The most common application of the split-step idea is when we have a discretization on an equidistant grid. In this case the potential is simply a multiplication operator, that is, a diagonal matrix which can be directly exponentiated. The transition to the momentum representation, where kinetic energy and velocity gauge field-interaction are diagonal, can be done by Fast Fourier Transform (FFT) with an operations count $\sim N \log(N)$. The favorable operations count is the key to efficient use of the split step method. Unfortunately, FFT is tied to the use of equidistant grids and Cartesian coordinates.

A different version of the split step method was introduced in [21], where the Hamiltonian is split into the field-free Hamiltonian H_0 and time-dependent dipole interaction. The transformation between the diagonal representations of the two operator parts can be done efficiently as H_0 can be decomposed into moderate size angular momentum blocks.

8.4

Absorption of Outgoing Flux

For many observables, we do not need to know the complete wavefunction: ionization can be determined from the residual population of well-localized bound states, high harmonics are only created from wavefunction parts near the nucleus, and in favorable circumstances even photoelectron spectra can be calculated without ever computing the wavefunction at large distances. However, for all these processes it is important to avoid contamination of the wavefunction by electron flux that is reflected from the artificial boundaries of the simulation volume.

The most obvious method for keeping the wavefunction from reaching the box boundary is multiplying it at preset times t_i by a differentiably smooth mask function $\Psi(\mathbf{r}, t_i) \rightarrow M(\mathbf{r})\Psi(\mathbf{r}, t_i)$ with the properties

$$M(\mathbf{r}) = \begin{cases} 1 & \text{for } |\mathbf{r}| < R_{\max} - A \\ 0 & \text{for } |\mathbf{r}| = R_{\max} \end{cases}, \quad (8.26)$$

where R_{\max} designates the simulation volume boundary and A is the “absorption range.” Closely related are complex absorbing potentials (CAPs), where one adds to the Hamiltonian a potential $V_{\text{CAP}}(\mathbf{r})$ with a negative imaginary component for $|\mathbf{r}| > R_{\max} - A$. Closer inspection shows that strictly imaginary V_{CAP} can be interpreted as a differential version of absorption by mask. Choosing particular shapes for $M(\mathbf{r})$ or $V_{\text{CAP}}(\mathbf{r})$ allows tuning the absorption to particular physical situations. However, fundamentally, no finite range of A can fully suppress reflections and in practice it is difficult to suppress reflection to levels below $\sim 10^{-3}$ for photoionization processes.

In a recent publication [26] it was shown that for the velocity gauge TDSE (8.2) absorption to machine precision 10^{-14} can be achieved by a technique dubbed “infinite range exterior complex scaling” (irECS) using only very few (~ 20) discretization points in the absorption range. irECS is based on the time-honored technique of exterior complex scaling (for an extensive discussion and literature see [22]), where the coordinates beyond the “scaling radius” R_0 are continued into the complex plane

$$\mathbf{r} \rightarrow \begin{cases} \mathbf{r} & \text{for } |\mathbf{r}| < R_0 \\ \left[R_0 + e^{i\phi}(|\mathbf{r}| - R_0) \right] \frac{\mathbf{r}}{|\mathbf{r}|} & \text{else} \end{cases}. \quad (8.27)$$

R_0 can be chosen anywhere, including $R_0 = 0$ and the scaling angle ϕ can be anywhere in the interval $(0, \pi/4)$. The coordinate transformation induces an analytical continuation of velocity gauge Hamiltonian $H_v(t)$ (8.2) to a complex scaled Hamiltonian $H_\phi(t)$, for which the exterior complex scaled wavefunction $\Psi_\phi(t)$ is obtained according to

$$i \frac{d}{dt} \Psi_\phi(t) = H_\phi(t) \Psi_\phi(t). \quad (8.28)$$

It was found in [26] that

$$\Psi_v(\mathbf{r}, t) \equiv \Psi_\phi(\mathbf{r}, t) \quad \text{for } |\mathbf{r}| < R_0. \quad (8.29)$$

Rigorous mathematical proof for this fact is absent, but the numerical evidence with its accuracies of 10^{-14} is overwhelming. Note that this is by no means a trivial fact, as, for example, it does not hold for the length gauge TDSE (8.1).

In the infinite range $[R_0, \infty)$, $\Psi_\phi(t)$ becomes exponentially damped and can be well approximated by a few basis functions of the form $r^m \exp(-\alpha r)$, $m = 1, \dots, M$. It was found in [26] that scaling angles $\phi \sim 0.6$ are most efficient with complete absorption for $\alpha = 0.4$ and only $M \approx 20$.

8.4.1

Absorption for a One-Dimensional TDSE

As an example, we show the absorption by irECS for the simple, one-dimensional TDSE

$$i \frac{d}{dt} \Psi(x, t) = \left\{ \frac{1}{2}[-i\partial_x - A(t)]^2 - \frac{1}{\sqrt{x^2 + 2}} \right\} \Psi(x, t) \quad (8.30)$$

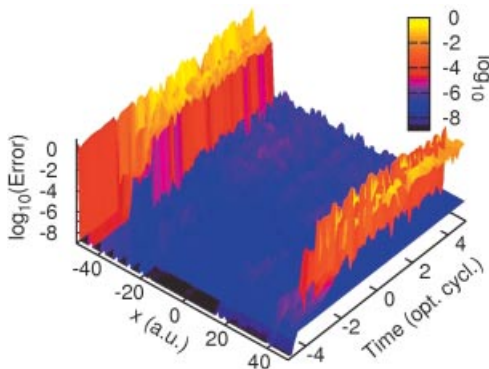


Figure 8.5 Evolution of the relative error $|\Psi_\theta(x) - \Psi(x)|/|\Psi(x)|$ during a 10-cycle pulse. The denominator is averaged over 5 grid points to avoid spurious spikes. For the pulse parameters and discretization (see text). The sharp rise of error marks the boundaries

of the inner region. A plane is drawn at error level 10^{-7} ; only a few error peaks in the inner region are above 10^{-6} . Away from the center, relative errors are enhanced initially as the wavefunction is nearly zero. (Copyright 2010 by The American Physical Society [26].)

with the vector potential

$$A(t) = \frac{\mathcal{E}}{\omega} \cos^2\left(\frac{t\omega}{20}\right) \sin(\omega t) \quad (8.31)$$

with a total pulse duration of 10 optical cycles. A more extensive discussion of this and other applications of irECS can be found in [26]. We choose $\omega = 0.06$ (~ 760 nm) and a peak field of $\mathcal{E} = 0.0755$ au corresponding to 2×10^{14} W/cm². For avoiding reflections in the unscaled TDSE, we had to use a box size of $[x_1, x_{N-1}] = [-1180, 1180]$ with a total of $M = 4801$ discretization points distributed over 120 finite elements with constant rank $p_n \equiv 41$. At both ends, infinite elements $x_0 = -\infty$ and $x_N = \infty$ were added with exponent $\alpha = 0.5$.

For comparison, we computed the irECS wavefunction $\Psi_\theta(x, t)$ with parameters $\theta = 0.5$ and $R_0 = 40$ and finite elements that up to R_0 are the same as in the unscaled calculation. In the scaled ranges on either end of the axis, we use infinite elements $(\infty, -R_0]$ and $[R_0, \infty)$ with $p_1 = p_N = 41$ and exponent $\alpha = 0.5$, resulting in a total of 301 discretization points. Here, no attempt was made to minimize the number of coefficients used for absorption.

Figure 8.5 shows the relative difference of the unscaled and complex scaled solutions

$$\Delta\Psi = \frac{|\Psi_\theta(x, t) - \Psi(x, t)|}{|\Psi(x, t)|}. \quad (8.32)$$

In the unscaled region the agreement is $\sim 10^{-7}$ throughout the time propagation, with only a few places where the error increases to $\sim 10^{-6}$. The error control of the Runge–Kutta scheme used is based on a measure of the square-integral of the wavefunction. The overlap error, in fact, remains on the level of 10^{-14} , that is, full machine precision.

That high of accuracies will rarely be needed, but they can be achieved with a total of only 321 discretization points, out of which only 80 are used for absorption. This must be compared to the 4801 points needed without absorption. A comparison with standard complex absorbing potentials shows that with much larger efforts, only moderate accuracies of 10^{-5} for the square of the wavefunction, or $\gtrsim 10^{-3}$ for the amplitude can be reached. Inaccuracies on that level will compromise results for delicate observables, like photoelectron spectra.

8.5

Observables

Once we have obtained an accurate approximation to the wavefunction $\Psi(\mathbf{r}, t)$, we can extract the main experimental observables: ionization, excitation, harmonic response, and photoelectron spectra. The list is in order of increasing difficulty.

8.5.1

Ionization and Excitation

If the complete bound state spectrum of the field-free system is known, ionization is simply the probability of finding the system not in a bound state after the pulse is over. Let $|n\rangle$ denote the bound states of the field-free system, then the total ionization yield is

$$Y_{\text{ion}} = 1 - \sum_n \langle \Psi(T) | n \rangle \langle n | \Psi(T) \rangle := 1 - \langle \Psi(T) | P_b | \Psi(T) \rangle, \quad (8.33)$$

where T is any time *after the end of the pulse*. The rightmost term defines the projector onto all bound states P_b . We can also model the definition of ionization by how it is measured in experiment: let the system evolve for a long time and then measure the percentage of the system that does not have their electrons attached, without reference to any eigenstates. Computationally, this means that we choose a sufficiently large area around the system and define the ionization yield as the probability for the electron to be outside this area. Let $\theta_R(\mathbf{r})$ be the function

$$\theta_R(\mathbf{r}) = \begin{cases} 1 & \text{for } |\mathbf{r}| < R \\ 0 & \text{else} \end{cases} \quad (8.34)$$

then

$$Y_{\text{ion}} \approx 1 - \langle \Psi(T) | \theta_R | \Psi(T) \rangle. \quad (8.35)$$

The area diameter R must be chosen large enough to accommodate all relevant bound states and the time T must be long after the end of the pulse to let slow, unbound electrons move beyond R . An approximate size of the bound state region R can be obtained by estimating the maximal extension of the bound states as

$R \gtrsim 1/\sqrt{2|E_{\min}|}$, where $|E_{\min}|$ is the smallest binding energy in the system. Clearly, if Rydberg states with large spatial extension get excited, we may need to use very large R and wait for long times T .

Computing the probability of excitation into a single bound state is simple: given the bound state wavefunction $|n\rangle$, the yield in that state is

$$Y_n = \langle \Psi(T) | n \rangle \langle n | \Psi(T) \rangle . \quad (8.36)$$

8.5.1.1 Ionization Rates

For defining an ionization rate, we must be able to tell which fraction $Y_{\text{ion}}(t)$ of the electrons is unbound at any moment in time. The rate then simply would be $\Gamma(t) = d/dt Y_{\text{ion}}(t)/Y_{\text{ion}}(t)$. Unfortunately, this idea is hard to apply in many attosecond experiments of interest. The difficulty is not due to numerical problems in solving the TDSE, but it is related to the very concept of ionization: ionization is not defined as an instantaneous process, but it is only defined in the limit of large times.

Our habit of thinking in terms of ionization rates is mostly derived from perturbative processes, where we can justifiably assume that the system is in some state that gets slowly depleted, but is not significantly distorted. Unfortunately, this is not the situation in most present day attosecond experiments. In fact, it is not possible to define an instantaneous photoionization rate in general terms, as we cannot decide, in general, whether an electron is “bound” or “detached” *while a field is present*.

What is measured in the experiment is the arrival of some charged particle, a long time after it has left the vicinity of the atom or molecule. The time of measurement is related to the particle momentum, not to its time of release. If we were to define $Y_{\text{ion}}(t)$ as in (8.35), we would observe a strong dependence of the rates on R . So what about defining the yield by projecting onto some bound or quasi-bound states? If we pick the bound states of the field-free Hamiltonian, we will in general see severe artifacts. There are significant polarization effects that distort the wavefunction and create temporary virtual population in the continuum, which later adiabatically relapses into bound states (see Figure 8.6). In addition to just “polarization,” we may also think of “true” detachment and recapture lat-

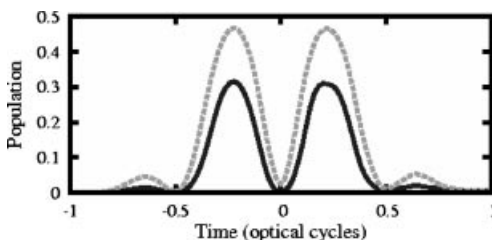


Figure 8.6 Nonbound content $\langle \Psi(t) | (1 - P) | \Psi(t) \rangle$ (solid line) and nonground state content $\langle \Psi(t) | (1 - |0\rangle\langle 0|) | \Psi(t) \rangle$ (gray dashed) of the hydrogen wavefunction in an 800 nm single-cycle laser pulse with peak-

intensity 10^{14} W/cm^2 . More than 50% of the ground state polarization involves virtual continuum states. Almost all population relapses into the ground state after the end of the pulse.

er during the pulse, which, in general, leads to the population of excited states. The situation can only be saved, if we can define some “adiabatic” time-dependent Hamiltonian, whose eigenstates at a fixed time describe polarization, and if excitation is unimportant. Such adiabatic states may be the eigenstates in the presence of a static electric field. However, such states will always have a finite probability for tunneling, which must be suppressed, for example, by truncating the basis at the end of the tunneling barrier. If we can find such an adiabatic Hamiltonian $H_a(t)$ with an adiabatic eigenstate

$$H_a(t)\Phi_a(t) = W_a(t)\Phi_a(t) \quad (8.37)$$

and initial condition $\Phi_a(t = -\infty) = \Psi(t = -\infty)$, then we can define the instantaneous yield

$$Y_{\text{ion}}(t) \approx 1 - \langle \Psi(t) | \Phi_a(t) \rangle \langle \Phi_a(t) | \Psi(t) \rangle. \quad (8.38)$$

This is the case for weak, slowly varying fields. Note that “weak” and “slowly varying” relates to the binding forces and characteristic time scales of the state to be ionized. The same field that is weak and slow for the ground state, can be already strong and fast for the first excited state of a system.

At the time of writing, these conceptual problems remain unresolved. It may be that we need to abandon the idea of “ionization at some time t ” and interpret attosecond experiments more in terms of the actual measurement setup. A discussion of various “adiabatic states” and their limitations for strong-field ionization problems can be found in [31].

8.5.2

Harmonic Response

When the laser pulse propagates through a medium, the medium responds by the polarization of individual atoms or molecules and radiates a field proportional to the acceleration of the dipole moment

$$\frac{d^2}{dt^2} \mathbf{d}(t) = \frac{d^2}{dt^2} \langle \Psi(t) | \mathbf{r} | \Psi(t) \rangle. \quad (8.39)$$

Using the TDSE, we can write this response also in velocity form

$$\frac{d^2}{dt^2} \mathbf{d}(t) = \frac{d}{dt} \langle \Psi(t) | i[H(t), \mathbf{r}] | \Psi(t) \rangle \quad (8.40)$$

and acceleration form

$$\frac{d^2}{dt^2} \mathbf{d}(t) = \langle \Psi(t) | -[H(t), [H(t), \mathbf{r}]] | \Psi(t) \rangle + \langle \Psi(t) | i \left[\frac{dH(t)}{dt}, \mathbf{r} \right] | \Psi(t) \rangle. \quad (8.41)$$

For our Hamiltonians (8.1) and (8.2), the commutators and the derivative $dH(t)/dt$ are easy to evaluate. In length gauge, we obtain

$$[H(t), \mathbf{r}] = -\frac{1}{2}[\nabla \cdot \nabla, \mathbf{r}] = -\frac{1}{2}\nabla \quad (8.42)$$

and

$$-[H(t), \nabla] = \nabla V(\mathbf{r}) + \mathcal{E}(t) , \quad \left[\frac{d H(t)}{dt}, \mathbf{r} \right] = 0 . \quad (8.43)$$

The direct evaluation of the dipole acceleration using (8.43) is best suited for numerical calculations, because contributions to the matrix elements dominantly come from small distances $|\mathbf{r}|$, where usually also the numerical solution is most accurate. This advantage far outweighs the little extra programming effort for computing matrix elements of the gradient of the potential.

The harmonic power spectrum is then obtained as the modulus square of the Fourier transform of $d^2\mathbf{d}(t)/dt^2$ over a sufficiently large time interval $[-T_0, T]$. A note of caution is needed here: excited states formed in response to the laser will keep ringing indefinitely, as radiative decay is not part of our TDSE. Propagating to long times T invariably produces spikes in the spectrum at the system's excitation energies. In some cases, radiative decay rates may be added "by hand," that is, adding small imaginary parts to the excited state energies. In practice this may be difficult and not required: it is simpler to terminate the signal at not too large times T . Note that this turn-off should be done smoothly, as a sudden turnoff generates a broad spurious spectrum. The interval for smooth turn-off must be larger than the period for the lowest frequency we want to resolve.

8.5.3

Photoelectron Spectra

Photoelectron spectra are certainly the hardest observable to compute. This has two reasons: first of all, while for ionization and high harmonics we only need to know the wavefunction at small distances, for photoelectron spectra we need information from the complete wavefunction. The resulting large expansion of the simulation volume requires very large computational resources. Secondly, even when we do know the complete wavefunction after the end of the pulse, we also need the asymptotic spectral information about the system at large times and distances for the extraction spectra.

As for the ionization yield, time information can be obtained by solving the stationary problem. Let $|\mathbf{k}\rangle$ be an eigenfunction of $H(T)$ with asymptotic momentum \mathbf{k} . Then the photoelectron yield at that momentum will be

$$Y_{\mathbf{k}} = |\langle \Psi(T) | \mathbf{k} \rangle|^2 , \quad (8.44)$$

assuming δ -normalization $\langle \mathbf{k} | \mathbf{k}' \rangle = \delta^{(3)}(\mathbf{k} - \mathbf{k}')$. However, for any system except hydrogen-like atoms, obtaining a large set of $|\mathbf{k}\rangle$ is a formidable task in itself.

If only energy spectra are needed, the \mathbf{k} do not need to be evaluated. The yield integrated over all states with energy E can be formally computed as

$$Y_E = \langle \Psi(T) | \delta(H_0 - E) | \Psi(T) \rangle \quad (8.45)$$

where the δ -function of the field-free Hamiltonian H_0 is defined through its spectral representation. Numerical approximations to the δ -function can be obtained

in different ways. One way is to use the approximation $\delta(x) \approx \epsilon/(x^2 + \epsilon^2)$ with $x = H_0 - E$, for which a linear system of equations needs to be solved. Note, however, that the resolution is limited by ϵ , which cannot be smaller than the separation of discretized continuum states. Using too small ϵ produces severe discretization artifacts.

A very powerful way to evaluate (8.45) is by the exterior complex scaling method discussed above. It is based on the rigorous identity

$$\Im \left[\lim_{\epsilon \downarrow 0} \langle \Psi(T) | (H_0 - E - i\epsilon)^{-1} | \Psi(T) \rangle \right] = \langle \Psi(T) | \pi \delta(H_0 - E) | \Psi(T) \rangle . \quad (8.46)$$

One finds that the resolvent matrix element on the left-hand side can be evaluated for the complex scaled Hamiltonian H_ϕ replacing H_0 , if the scaling radius R_0 is chosen outside the simulation volume used for $\Psi(T)$:

$$\langle \Psi(T) | (H_0 - E - i\epsilon)^{-1} | \Psi(T) \rangle = \langle \Psi(T) | (H_\phi - E - i\epsilon)^{-1} | \Psi(T) \rangle . \quad (8.47)$$

The advantage is that the complex scaled H_ϕ has no real-valued continuum eigenvalues (see discussion in [22]) and for the right-hand side of (8.47), $\epsilon \rightarrow 0$ can be taken without producing any numerical artifacts [32, 33].

Alternatively, if the asymptotic form $|\mathbf{k}\rangle_a$ of the scattering states is known, one can perform the spectral decomposition only to parts of the wavefunction outside some finite volume. For that, like for Y_{ion} , one must propagate to times T large enough such that the continuum parts have left a finite region defined by $\theta_R(\mathbf{r})$ (cf. (8.34)). For high-energy electrons, this may be at short times after the pulse. Then

$$Y_{\mathbf{k}} = |\langle \Psi(T) | 1 - \theta_R | \mathbf{k} \rangle_a|^2 . \quad (8.48)$$

This approach is used in many cases, especially to determine double ionization [8, 34]. Note, however, that for two electrons even the asymptotic form $|\mathbf{k}_1, \mathbf{k}_2\rangle_a$ of the two-electron scattering function cannot be given in closed form. The merits of various approximations to $|\mathbf{k}_1, \mathbf{k}_2\rangle_a$ are being discussed intensively.

Even when the exact scattering solutions are available, the methods described so far require us to know the complete wavefunction $\Psi(T)$ at the end of the pulse, requiring a great number of discretization coefficients c_i . But, if we know asymptotic time-dependent scattering wavefunctions $|\mathbf{k}, t\rangle_a$ with the same time dependence and asymptotics as the solutions of the full time-dependent problem, the problem size can be greatly reduced. For our problem, we have the Volkov solutions with exactly this property. This is the basis for the time-dependent surface flux (t-SURFF) method [28]. There we only need to keep $\Psi(\mathbf{r}, t)$ in the comparatively small region defined by θ_R and can absorb it outside. The photoelectron amplitude of (8.48) can be written as the time-integral

$$\langle \Psi(T) | 1 - \theta_R | \mathbf{k}, T \rangle_a = - \int_{-\infty}^T dt \langle \Psi(t) | i[H(t), \theta_R] | \mathbf{k}, t \rangle_a , \quad (8.49)$$

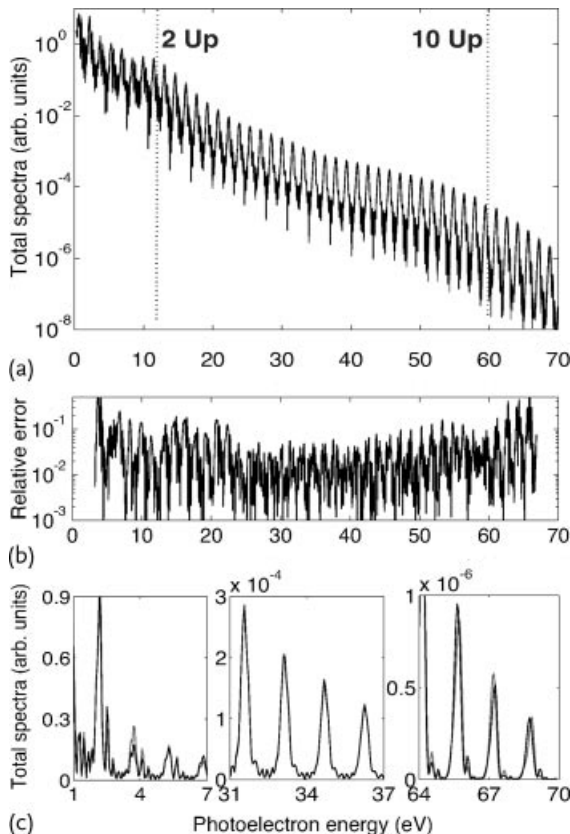


Figure 8.7 Photoelectron energy spectra for the hydrogen atom (a) obtained with surface radius $R = 110$ (black) and $R = 140$ (gray). On the log scale, the two lines are barely distinguishable. Also shown is the estimate of

the relative error by comparing the two spectra (b). Blow-up of the spectra from part (a) on a linear scale (c). (Copyright 1998 by The American Physical Society [28].)

which has nonzero contributions only on the surface $|r| = R$. A detailed discussion of this approach can be found in [28].

As one application, we show the photoelectron spectrum emitted from a hydrogen atom exposed to a 800 nm pulse with peak intensity 10^{14} W/cm^2 , \cos^2 pulse shape, and a duration of 40 optical cycles. In a real calculation, a three-dimensional box with radius ~ 9000 au would be needed to avoid reflection of the $10 U_p \sim 60$ eV electrons from the box boundaries before the end of the pulse after 40 optical cycles ≈ 4400 au. The radial coordinate must be discretized by ~ 3000 points to be able to represent the momenta ~ 2 au corresponding to $10 U_p$. In contrast, for the calculation of spectra by (8.49), as shown in Figure 8.7, we need only a box size of 110 au and ~ 200 discretization points and obtain $\sim 5\%$ accuracy for the spectrum up to $10 U_p$. Only at lower energies, the errors are larger because Coulomb scattering is not correctly taken into account beyond the box boundary (a detailed explanation is given in [28]).

8.6

Two-Electron Systems

The discretization methods outlined above can be directly extended to two-electron problems, however the problem size squares: instead of a three-dimensional problem, we are dealing with a six-dimensional one. If we were able to solve the single-electron problem with a few thousand discretization coefficients, solving the two-electron problem on the same level of accuracy will require some 10 million coefficients. Clearly, we quickly reach the limits of feasibility.

8.6.1

Very Large-Scale Grid-Based Approaches

The only project to date that fully solves the strong-field two-electron problem at optical and infrared wavelength is a supercomputing approach. The approach was first introduced in 1996 [35], with application to the helium atom. It uses an expansion with respect to the electron coordinates \mathbf{r}_1 and \mathbf{r}_2 . The angular degrees of freedom are discretized by angular eigenfunctions $|l_1, l_2, L\rangle$, while the radial functions $f_{l_1, l_2, L}$ on the r_1, r_2 -plane are grid-discretized [34]

$$\Psi(r_1, \theta_1, \phi_1, r_2, \theta_2, \phi_2) = \mathcal{A} \sum_{L, l_1, l_2} |l_1, l_2, L\rangle f_{l_1, l_2, L}(r_1, r_2), \quad (8.50)$$

where \mathcal{A} indicates anti-symmetrization. Note that in linear polarization, the M -component of total angular momentum is conserved and the problem reduces to “only” five dimensions. Differential operators are implemented by the finite difference method and an Arnoldi scheme is used for time propagation. In a heroic effort, the approach was pushed also to the 780 nm wavelength. For this, a maximum of 3800 angular factors and up to 1000 au were used for each radius [34], resulting in hundreds of millions linear coefficients. The approach was extended also to the hydrogen molecule [36]. One remarkable numerical finding is a cutoff in the two-electron photoelectron spectrum produced by a 390 nm pulse [37], see Figure 8.8.

A similar approach of very high numerical quality, which uses a finite element DVR grid with about 600 grid points on each radial coordinate, was applied in the shorter wavelength regime [8].

Also the t-SURF method has been extended to the two-particle case [38], which may finally allow a full calculation of double-ionization in IR fields with acceptable computational effort.

8.6.2

Basis and Pseudospectral Approaches

Clearly, even at shorter wavelengths, full discretization of the problem takes us very close to the limits of present day computers. For specific situations, basis set approaches can produce quite accurate results with moderate effort. The three-body

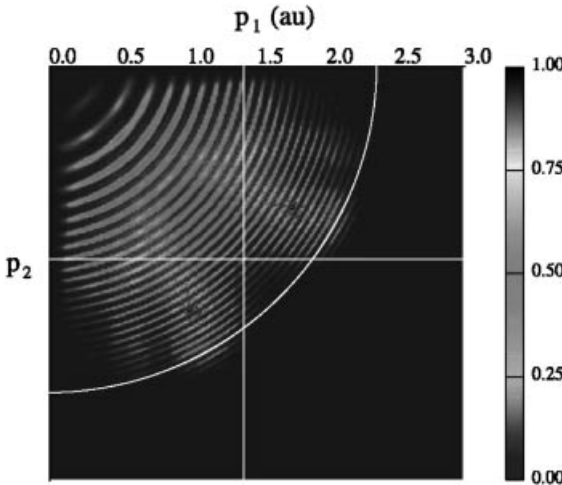


Figure 8.8 Joint-probability distribution in momentum space of doubly ionizing electrons at the end of a seven-period pulse with a wavelength of 390 nm and an intensity of 10^{15} W/cm^2 . Along the vertical line, elec-

tron 1 is constrained to kinetic energy $1.9U_p$. Along the white circular arc, total kinetic energy equals $5.3U_p$. (Copyright 2006 by The American Physical Society [37].)

Coulomb problem is special, as it allows the use of various coordinate systems for which very compact discretization is possible. Early benchmark calculations for ionization, and single- and double-excitation of helium [20] combine Euler angles, interparticle coordinates $r_1, r_2, r_3 = |\mathbf{r}_1 - \mathbf{r}_2|$, complex scaling, and an explicitly correlated basis of Slater-type functions

$$|i\rangle = r_1^{m_i} r_2^{n_i} r_3^{k_i} \exp(-\alpha r_1 - \beta r_2). \quad (8.51)$$

For this basis, absorption was performed by complex scaling with $R_0 = 0$.

Figure 8.9 shows excitation and ionization of helium by a short, intense pulse at photon energies from 0.2 au (wavelength $\sim 230 \text{ nm}$) to 1.2 au (wavelength $\sim 30 \text{ nm}$). The total ionization yield is defined as

$$Y_{\text{ion}} = 1 - \sum_i |\langle \Phi_{i,\theta}^*(\mathbf{r}_1, \mathbf{r}_2) | \Psi_\theta(\mathbf{r}_1, \mathbf{r}_2; t = \infty) \rangle|^2, \quad (8.52)$$

where $\Phi_{i,\theta}$ is the bound state eigenfunction of the complex scaled atomic Hamiltonian

$$H_{0,\theta} \Phi_{i,\theta} = E_i \Phi_{i,\theta}. \quad (8.53)$$

Within the same approach, highly accurate ionization rates for helium were computed [39] that cover field strengths deep into the regime where the barrier for electron binding is suppressed by the field (see Table 8.3). While the ADK type formula for static fields is confirmed in the tunneling regime, there is no reliable analytic

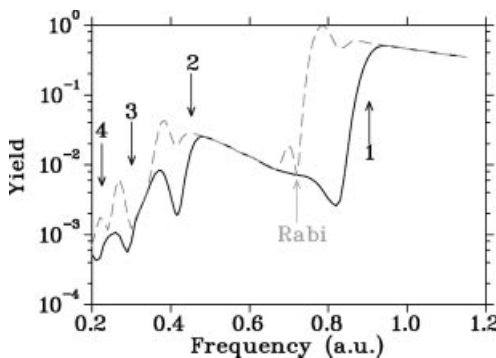


Figure 8.9 Excitation and ionization of He by a \cos^2 -shaped pulse of duration 3.8 fs and peak intensity $2.97 \times 10^{14} \text{ W/cm}^2$, as a function of frequency. Shown is the ionization (solid line) and ionization plus bound state

excitation (dashed line). The arrows labeled by $n = 1, 2, 3$, and 4 indicate n -photon ionization thresholds. The dip at frequency 0.72 is due to a Rabi oscillation. (Copyright 1998 by The American Physical Society [20].)

Table 8.3 Field ionization rates from the ground state of the helium atom in atomic units. The numerical data is accurate to at least two digits. (Copyright 1999 by The American Physical Society [39].)

E	w	E	w	E	w
0.08	0.463×10^{-7}	0.28	0.266×10^{-1}	0.48	0.164
0.09	0.509×10^{-6}	0.29	0.309×10^{-1}	0.49	0.174
0.10	0.288×10^{-5}	0.30	0.356×10^{-1}	0.50	0.183
0.11	0.115×10^{-4}	0.31	0.405×10^{-1}	0.55	0.233
0.12	0.362×10^{-4}	0.32	0.458×10^{-1}	0.60	0.287
0.13	0.943×10^{-4}	0.33	0.513×10^{-1}	0.65	0.345
0.14	0.212×10^{-3}	0.34	0.572×10^{-1}	0.70	0.406
0.15	0.423×10^{-3}	0.35	0.633×10^{-1}	0.75	0.470
0.16	0.768×10^{-3}	0.36	0.696×10^{-1}	0.80	0.536
0.17	0.129×10^{-2}	0.37	0.763×10^{-1}	0.85	0.604
0.18	0.203×10^{-2}	0.38	0.832×10^{-1}	0.90	0.673
0.19	0.302×10^{-2}	0.39	0.903×10^{-1}	0.95	0.744
0.20	0.431×10^{-2}	0.40	0.977×10^{-1}	1.00	0.818
0.21	0.590×10^{-2}	0.41	0.105	1.10	0.97
0.22	0.783×10^{-2}	0.42	0.113	1.20	1.13
0.23	0.101×10^{-1}	0.43	0.121	1.30	1.29
0.24	0.127×10^{-1}	0.44	0.129	1.40	1.45
0.25	0.157×10^{-1}	0.45	0.138	1.50	1.61
0.26	0.190×10^{-1}	0.46	0.146	1.60	1.77
0.27	0.226×10^{-1}	0.47	0.155	1.70	1.92

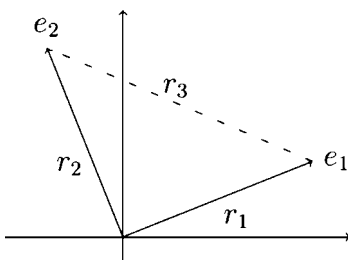


Figure 8.10 Interparticle coordinates r_1, r_2, r_3

formula available beyond barrier suppression. Also, note that these are results for *static* electric fields. For typical laser pulses, the quasi-static description of ionization is often not applicable, see also the discussion in Section 8.5.1.1.

Another efficient representation is in “perimetric coordinates”

$$u = -r_1 + r_2 + r_3$$

$$v = r_1 - r_2 + r_3$$

$$w = r_1 + r_2 - r_3 ,$$

with Sturmian functions for discretization [40]. These coordinates are technically convenient, as all integrals are easy to compute and matrices can be made sparse (interparticle coordinates shown in Figure 8.10).

Special coordinates can also be used for the H_2 molecule or any diatomic system with fixed nuclei. The prolate-spheroidal coordinates (see Figure 8.11) allow collapsing the Coulomb singularities at the two protons into a single point in coordinate space, which constitutes a significant advantage for discretization. The complexity of the resulting Schrödinger equation is not much larger than for helium. Of course, with laser fields not parallel to the molecular axis, the cylindrical symmetry is lost and one has to deal with a truly six-dimensional problem. Using this approach, benchmark results for ionization of H_2 were produced [41].

Special coordinate systems can give good results for specific two-electron situations. Neither interparticle nor perimetric coordinates are well suited to describe important processes like single ionization. In addition, these coordinates cannot be extended beyond two-electron systems. Therefore, single-electron coordinates, using pseudo-spectral representations with respect to the single-electron operators, have been also used for two-electron systems [23, 24]. To control the growth of problems size, pseudo-spectral discretizations (cf. Section 8.2.1) with respect to the single-electron operators are used in that approach.

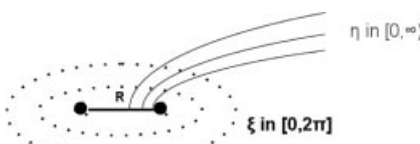


Figure 8.11 Prolate-spheroidal coordinates for diatomic molecules. Points in the plane are defined by the intersection of an ellipsis ξ with a hyperbola η ; both have their foci on the nuclei.

8.7

Few-Electron Systems

The problem size grows exponentially with the number of particles. From the discussion above, it is obvious that computation of strong-field effects involving more than two electrons requires severe approximations and new methods. Fortunately, we are hardly ever interested in more than two *unbound* electrons. Bound states, even if somewhat distorted, are much easier to compute than the violent motion of unbound electrons in a strong field. In fact, all few-electron calculations to date admit only a single continuum electron. This is dictated by the sheer size of the problem. Also, most attosecond experiments aim at understanding electronic dynamics *inside* the atom or molecule, with the photoelectron serving as the messenger telling us about the inner dynamics.

“Essential states” type of approaches select a basis of ground, singly, and doubly excited states that, we believe, participate in the reaction. It is possible to give one electron the freedom to become ionized, and solve the TDSE in this strongly constrained basis. This closely models our conventional idea of “internal” electron dynamics. The complexity of the calculation does not much exceed a single-electron calculation. Where applicable, this provides the most transparent and efficient way of solving the TDSE.

The next step of approximation, which is less biased by physical intuition, is given in time-dependent configuration-interaction methods (TDCI). These can be understood as pseudo-spectral methods for the few-electron case, where (approximate) eigenstates of the neutral or ionic few-electron system are used, including pseudo-continuum states of the important ionization channels. If we want to distinguish TDCI from essential state methods, we can do so by the basis constraint: the states are selected by energy, symmetry consideration, and possibly by the continuum channels included, not by an *a priori* idea of the physical process. In the limit of infinitely many states, these methods become exact. In practice, such calculations remain far from a regime where one can simply observe convergence of the method with respect to all parameters of the constraint. Good physical intuition is also needed in these methods.

A key problem for any bound state-based approximation is the importance of virtual continuum states in strong fields. Even when, after the end of the pulse, all population relapses into bound states, the correct description of intermediate dynamics, like polarization, may require the inclusion of continuum states. This was discussed in the section about ionization rates Section 8.5.1.1. We do not know the role of continuum states in advance and it is difficult to include them into an already large calculation. In view of this fact, it is unfortunate that the (in principle) *ab initio* method time-dependent TDDFT appears not to be applicable for strong-field phenomena: studies of very simple systems where comparison with exact results is possible, have shown failure of TDDFT [15, 42]. The reason for this failure is not fully understood, but it may be related to the difficulty of representing excited states in DFT.

Time-dependent Hartree–Fock (TDHF) is another approximate method that was applied to strong-field phenomena. The only, but severe, bias of TDHF is that the few-electron wavefunction is written as a single determinant of time-dependent single-electron functions

$$\Psi(q_1, \dots, q_M; t) \approx \mathcal{A} \left[\prod_{j=1}^M \Phi_j(q_j; t) \right], \quad (8.54)$$

where \mathcal{A} again indicates anti-symmetrization and spin is included as part of the coordinates $q_j = (\mathbf{r}_j, s_j)$. The orbitals $\Phi_j(q; t)$ are optimized by some minimal principle, whose exact choice is not essential for the method. The usual choice is the so-called Dirac–Frenkel variational principle, which is local in time. Any minimal principle leads to a set of M coupled nonlinear Schrödinger equations for the $\Phi_j(q; t)$. This particular method has no problem to model the virtually excited continuum states arising in polarization processes, as the single-electron wavefunctions are fully flexible. Unfortunately, it soon became clear that TDHF cannot work as soon as significant ionization occurs in a strong-field process [17]. Hartree–Fock methods approximate the wavefunction as a single determinant. This can work well for the ground state $\Phi_0(q_1, q_2)$, and also for an ionized state $\Phi_i(q_1, q_2)$, of a two electron system

$$\Phi_0(q_1, q_2) \approx \mathcal{A}[\phi_a(q_1)\phi_a(q_2)], \quad \Phi_i(q_1, q_2) \approx \mathcal{A}[\phi_i(q_1)\phi_c(q_2)]. \quad (8.55)$$

However, there is no single determinant that can approximate a superposition of two determinants

$$c_0(t)\mathcal{A}[\phi_a(q_1)\phi_a(q_2)] + c_i(t)\mathcal{A}[\phi_i(q_1)\phi_c(q_2)] \not\approx \mathcal{A}[\xi(q_1)\eta(q_2)], \quad (8.56)$$

when both determinants contribute on a comparable level $|c_0| \sim |c_i|$.

8.7.1

MCTDHF: Multiconfiguration Time-Dependent Hartree–Fock

The left-hand side of (8.56) indicates an obvious extension from single- to multideterminant or “multiconfiguration time-dependent Hartree–Fock” (MCTDHF). Taking a few (this may also mean a few thousand) determinants, one can hope to obtain a good approximation of the solution. In this method, the single-particle functions can be highly accurate and no significant truncations of the single-particle Hilbert space must be made. This allows, in particular, to fully include the single-electron response to the external field. The only constraint is the total number of determinants, which limits the amount of “correlation” that is included in the calculation.

The MCTDHF Ansatz for an f -particle wavefunction is a linear combination of determinants of N single-particle functions $\phi_j(q, t)$

$$\Psi_{\text{MCTDHF}}(q_1, \dots, q_f; t) = \frac{1}{\sqrt{f!}} \sum_{j_1 \dots j_f=1}^N B_{j_1 \dots j_f}(t) \phi_{j_1}(q_1; t) \dots \phi_{j_f}(q_f; t), \quad (8.57)$$

where $q = (\mathbf{r}, s)$ combine the spatial coordinates and spin. Anti-symmetric determinant character is ensured by demanding anti-symmetry of the $B_{j_1 \dots j_f}(t)$ under exchange of any two of its indices. It is important to note that both, the expansion coefficients $B_{j_1 \dots j_f}(t)$ and the single-particle functions $\phi_{j_f}(q_f; t)$ are time dependent and evolve according to dynamical equations of the form

$$i \frac{d}{dt} B_{j_1 \dots j_f} = \sum_{k_1 \dots k_f} \langle \phi_{j_1} \dots \phi_{j_f} | H | \phi_{k_1} \dots \phi_{k_f} \rangle B_{k_1 \dots k_f} \quad (8.58)$$

$$i \frac{d}{dt} \phi_j = (1 - P) \sum_k \sum_l (\rho^{-1})_{jl} \overline{H}_{lk}[\mathbf{B}, \boldsymbol{\phi}] \phi_k. \quad (8.59)$$

Here, ρ_{jl} denotes the single-particle reduced density matrix

$$\rho_{jl} = \sum_{j_2 \dots j_f=1}^N B_{j_1 j_2 \dots j_f}^* B_{l j_2 \dots j_f} \quad (8.60)$$

and $\overline{H}_{lk}[\mathbf{B}, \boldsymbol{\phi}]$ is a matrix of mean field operators that itself depends on all $\boldsymbol{\phi} = (\phi_1, \dots, \phi_N)$ and $B_{j_1 \dots j_f}$. P is the projector onto the space spanned by the time-dependent orbitals $\phi_j(q; t)$,

$$P = \sum_{j=1}^N |\phi_j\rangle \langle \phi_j|. \quad (8.61)$$

The spatial part of the single-particle functions $\phi_j(q)$ can be discretized by any of the methods discussed above, in our implementation [14], we use finite elements with

$$\phi(q, t) = \sum_{i=1}^Q |s\rangle |i\rangle c_i(t). \quad (8.62)$$

A more detailed discussion of the method can be found in [14, 43].

The method can be efficient, because the time-evolution of the single-particle functions ϕ_n follows the evolution of the multiparticle system: in a sense, the $\phi_j(q, t)$ form an optimally self-adaptive time-dependent basis. The price to pay for self-adaptivity is the nonlinearity brought into the evolution equations (8.58) and (8.59) by the density $\rho[\mathbf{B}]$, the projector $P[\boldsymbol{\phi}]$ and the mean field operators $\overline{H}_{lk}[\mathbf{B}, \boldsymbol{\phi}]$.

It is easy to see that, if the number of discretization coefficients $c_i(t)$ equals the total number of single-particle functions $Q = N$, the projector in (8.59) becomes zero ($1 - P = 0$). In this case there is no time-evolution of the ϕ_j and MCTDHF reduces to an ordinary basis set calculation with antisymmetrized linear coefficients $B_{j_1\dots j_f}$. We see that the method is asymptotically exact, but that limit requires $\binom{Q}{f} \sim Q^f$ coefficients $B_{j_1\dots j_f}$, generally an absurdly large number.

Note that the number of expansion coefficients $B_{j_1\dots j_f}$ grows rapidly with the number of orbital as $\binom{N}{f}$. The method is only useful, when $N = 10$ to 30 single-particle functions are sufficient. The number of determinants needed is related to the correlation in the system, that is, just how far the solutions is from a single-determinant, Hartree–Fock wavefunction. Limiting the number of $B_{j_1\dots j_f}$ to a few thousand means that we can describe moderately correlated few-electron systems. This case is of interest in attosecond physics: we want to describe processes that involve a few (2–4) active electrons in the valence shell of some atom or molecule. When we speak about these individual electrons as being in single-particle “states,” we implicitly use the Hartree–Fock picture. If we want to form useful physical pictures, the investigated dynamics of the system should not be too far from this situation. MCTDHF offers a practical computational scheme for those cases.

Time-evolution of the single-particle function allows correct inclusion of polarization, as discussed above. We will show now that polarization of core electrons can dramatically change the harmonic response of few-electron systems [43].

8.7.2

Dynamical Multielectron Effects in High Harmonic Generation

“Molecular orbital tomography” [44] tries to extract information about some single-electron part of the wavefunction from a high harmonic signal. For the original illustration in [44], the Hartree–Fock HOMO was used, but the exact nature of the orbital is not important: the high harmonic response is actually a true *multielectron effect* [43]. For a mathematical description, we start by obtaining the high harmonic response for a diatomic model molecule with four active electrons in a potential of the form

$$V(\mathbf{r}) = V_1 \left(\left| \mathbf{r} - \frac{\mathbf{R}}{2} \right| \right) + V_1 \left(\left| \mathbf{r} + \frac{\mathbf{R}}{2} \right| \right), \quad (8.63)$$

with the potential for one nucleus being

$$V_1(r) = \frac{Z}{r} + \alpha \frac{e^{-\beta r}}{r}. \quad (8.64)$$

The charge Z on each nucleus is equal to half the number of active electrons and the internuclear distance is $|\mathbf{R}| = 2.8$. The screening parameters α and β have been adjusted such as to yield an ionization potential $IP = 0.58$ (the same as N_2). The active electrons are in two doubly occupied orbitals with gerade and ungerade symmetry and Hartree–Fock energies of -0.781 (gerade) and -0.595 (ungerade), composing a fairly realistic molecular model. High harmonic spectra for an 800 nm

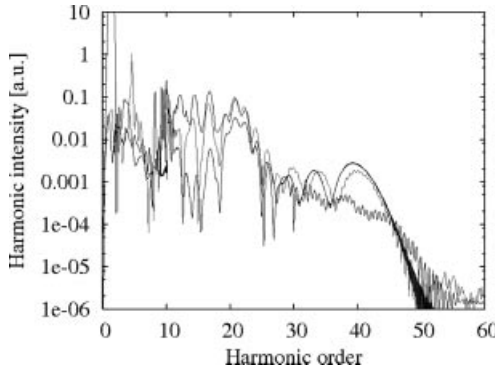


Figure 8.12 Comparison of harmonic spectra obtained with four active electron (lowest yield at high harmonic orders), in the SFA (highest) and from a single active electron TDSE (slight-

ly below SFA). The few-electron calculation differs qualitatively from the single-electron results. (From [43].)

single-cycle infrared laser pulse with peak intensity $3 \times 10^{14} \text{ W/cm}^2$ and linear polarization parallel to the molecular axis were calculated by MCTDHF. Convergence was checked by using up to $N = 8$ orbitals.

Surprisingly, one finds very large discrepancies between the four-electron numerical result and the strong-field approximation (see Figure 8.12). The discrepancy is not only in magnitude, but in the peak structure of the highest harmonics: while SFA shows pronounced peaks, the four-electron calculation has a rather broad, featureless high harmonic spectrum. In contrast, using the same techniques for two-electron systems (atom or molecule) gave good agreement of the numerical result and SFA. Solutions of the single-electron TDSE using various models always give results close to the SFA.

The energy dependence and phases contain the main information for extracting structural information from high harmonics, therefore it is essential to understand the reason for the discrepancy between SFA and MCTDHF calculations. Including the exchange corrections, as proposed in [45], changes the harmonic amplitudes but has only a small effect on the energy dependence of the response. Note that these corrections only appear when at least two different spatial orbitals are involved, as in the four active electron calculation.

The discrepancy is actually due to a truly multielectron effect and this effect is dynamical, that is, cannot be deduced from the field-free structure. To show this, we compute the time-dependent ionic wavefunction $\Psi_+(t)$ with three active electrons. Due to the stronger binding, the amplitude of the ionic harmonic response is two orders of magnitude smaller than that of the neutral. Using $\Psi_+(t)$, we define the static and dynamic time-dependent “Dyson orbitals” as

$$|\phi_D^{\text{stat}}(q; t)\rangle = 2\langle\Psi_+(0)|\Psi_0(t)\rangle \quad (8.65)$$

and

$$|\phi_D^{\text{dyn}}(q; t)\rangle = 2\langle\Psi_+(t)|\Psi_0(t)\rangle . \quad (8.66)$$

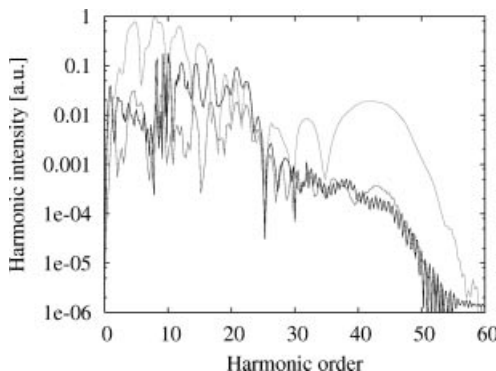


Figure 8.13 Comparison of harmonic spectra obtained by MCTDHF (wiggly line, lowest yield) and from the static (8.66) (highest yield) and dynamic (8.66) Dyson orbitals (near MCTDHF). (Reproduced from [43].)

In Figure 8.13, the high harmonic responses for ϕ_D^{stat} and ϕ_D^{dyn} are compared to the MCTDHF result. Surprisingly, although there is almost no harmonic response of the ion, the dynamic Dyson response is very close to the four active electron response. The static Dyson response, in turn, is very similar to the SFA and single active electron responses. This shows that the harmonic response is a collective effect of the motion of several atoms in the laser field. Note that, although we can easily obtain ϕ_D^{dyn} from $\Psi_0(t)$ and $\Psi_+(t)$, we cannot give single-particle equations for the time-evolution of ϕ_D^{dyn} , as it invariably includes exchange effects. As observed in [45], these effects are strong. If they are time-dependent, they will modify the frequency dependence of the high harmonics. Similar findings were reported later in [46].

8.8 Nuclear Motion

The inclusion of nuclear motion adds further challenges to numerical calculations, beyond the simple fact that we add more degrees of freedom. The reason lies in the strong correlation of electronic and nuclear motion: most of the electronic wavefunction just follows the nuclear motion. Even when we treat the nuclei classically, the Coulomb-singularities of the nuclear potentials move with time and require adjustment of the discretization for the electronic degrees of freedom. In addition, the scientifically most interesting processes in nuclear-electronic dynamics, such as deexcitation through conical intersections [47] or control of branching into different dissociation channels, are inherently quantum-mechanical in nature. This limits the usefulness of classical simulations.

The Born–Oppenheimer approximation of molecular physics uses the strong correlation to its advantage by assuming that the electrons adiabatically follow the nuclear motion. The multisurface Born–Oppenheimer approach relaxes this as-

sumption and becomes exact in the limit of infinitely many surfaces: when a sufficiently large number of Born–Oppenheimer potentials are used and couplings between the corresponding excited electronic states near avoided crossings and by the laser field, are included, electronic and nuclear motion can be approximated to any accuracy. This is just one particular time-dependent, complete, and hopefully efficient basis for discretizing the TDSE.

Here we want to present the principles of the methods, but we refer to [10] for a more detailed discussion. The TDSE for a diatomic molecule is

$$i \frac{d}{dt} \Psi(\mathbf{r}, R, t) = H(\mathbf{r}, R, t) \Psi(\mathbf{r}, R, t), \quad (8.67)$$

where all electronic coordinates are summarized as \mathbf{r} . By using only the interparticle *distance* R , but no angles, we indicate that rotations of the molecular axis were neglected in the calculation. On the field-free part of the Hamiltonian, the usual Born–Oppenheimer procedure is applied, that is, the kinetic energy of the nuclei is split off:

$$H_0(\mathbf{r}, R) = T(R) + H_e(\mathbf{r}, R), \quad T(R) := -\frac{1}{2M} \frac{1}{R} \partial_R^2 R, \quad (8.68)$$

where M is the reduced mass of nuclear relative motion. The eigenfunctions of the electronic Hamiltonian form a complete basis for any fixed R

$$H_e(\mathbf{r}, R) \Phi_s(\mathbf{r}, R) = E_s(R) \Phi_s(\mathbf{r}, R). \quad (8.69)$$

A B-spline representation is used for the radial parts of $\Phi_s(\mathbf{r}, R)$. Note that for completeness, *all* eigenfunctions, bound, single continuum, and multiple continuum states must be included. Very important is a suitable truncation of the basis according to energy, symmetries, and expected physical mechanisms. Considering physical mechanisms, it was found that doubly excited resonances, which are resonant states in the single continuum, play an important role in H_2 laser dissociation [48].

In [10], the nuclear part of the wavefunction is expanded in a time-independent basis of vibrational nuclear functions $\chi_\nu^{(s)}(R)$, which is computed for each potential energy curve $E_s(R)$ as

$$[T(R) + E_s(R)] \chi_\nu^{(s)}(R) = W_\nu \chi_\nu^{(s)}(R), \quad (8.70)$$

where ν labels bound as well as continuous functions. That differs from the usual time-dependent Born–Oppenheimer method, where no intermediate spectral eigenfunctions of nuclear motion are calculated, but rather the time-dependent equation for the nuclear motion is computed on a grid.

In a somewhat simplifying notation, the ansatz for the total wavefunction in [10] is

$$\Psi(\mathbf{r}, R, t) = \sum_\nu \sum_s C_\nu^{(s)}(t) \chi_\nu^{(s)}(R) \Phi_s(\mathbf{r}, R). \quad (8.71)$$

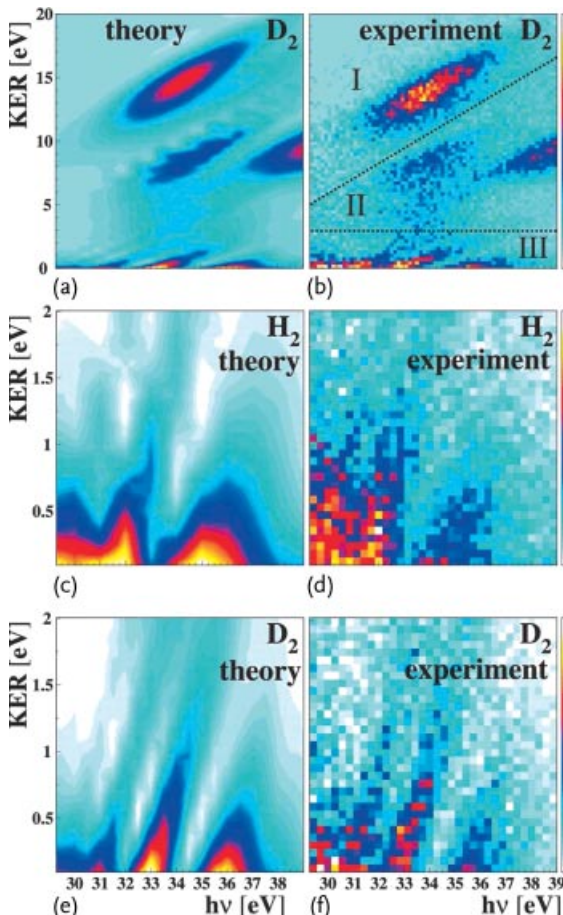


Figure 8.14 Kinetic energy release (KER) as a function of photon energy for dissociative ionization of H_2 and D_2 (8.1). Theory (a) and experiment (b) for D_2 . Regions I, II, and III show three distinct clusters of data formed by

photoionization. Magnification of the low-KER region of (a) and (b) for H_2 (c, d), and D_2 (e, f); theory (a–c) and experiment (e, f). (Figure reproduced from [48].)

All labels cover discrete (bound) as well as continuous (scattering) parts of the spectrum and s must correctly label symmetries and degeneracies of the electronic states [10]. Using the terminology of Section 8.2.1, we see that the method is a rather complex version of a pseudo-spectral approach.

The ansatz (8.71) does not fully define the approach. When inserting it into the full TDSE, $\partial_{\mathbf{R}}$ -dependent terms appear that are neglected in the Born–Oppenheimer approximation. These terms are particularly important near “avoided crossings,” that is, when potential energy surfaces get close to each other. In the continuum, there is an infinite number of such avoided crossings. To cope with this situation the “diabatic representation” was used in [10], implying that this type

of transition at avoided crossings to and from continuum states can be neglected. The interaction with the laser field occurs primarily through the electrons and the direct action of the laser field on the nuclei is neglected because of the large nuclear mass.

This approach has delivered the most impressive results on doubly differential electron and nuclear dissociation spectra. As an example, Figure 8.14 shows the kinetic energy release for dissociative ionization of H₂ and D₂ [48]. The reader will hardly be surprised that these are among the largest numerical calculations in the field so far.

References

- 1 Kulander, K.C., Schafer, K.J., and Krause, J.L. (1993) Dynamics of short-pulse excitation, ionization and harmonic conversion. *Proc. Workshop, Super Intense Laser Atom Physics (SILAP) III*, edited by B. Piraux (Plenum, New York).
- 2 Corkum, P.B. (1993) Plasma perspective on strong-field multiphoton ionization. *Phys. Rev. Lett.*, **71**, 1994.
- 3 Cormier, E. and Lambropoulos, P. (1996) Optimal gauge and gauge invariance in nonperturbative time-dependent calculation of above-threshold ionization. *J. Phys. B*, **29** (9), 1667–1680.
- 4 Telnov, D.A. and Chu, S.I. (2009) Above-threshold-ionization spectra from the core region of a time-dependent wave packet: An ab initio time-dependent approach. *Phys. Rev. A*, **79** (4), 043421.
- 5 Müller, H.G. (1999) An efficient propagation scheme for the time-dependent Schrödinger equation in the velocity gauge. *Laser Phys.*, **9**, 138.
- 6 Bauer, D. and Koval, P. (2006) Qprop: A Schrödinger-solver for intense laser-atom interaction. *Comp. Phys. Comm.*, **174** (5), 396–421.
- 7 Morishita, T., Chen, Z., Watanabe, S., and Lin, C.D. (2007) Two-dimensional electron momentum spectra of argon ionized by short intense lasers: Comparison of theory with experiment. *Phys. Rev. A*, **75**, 023407.
- 8 Feist, J., Nagele, S., Pazourek, R., Persson, E., Schneider, B.I., Collins, L.A., and Burgdörfer, J. (2008) Nonsequential two-photon double ionization of helium. *Phys. Rev. A*, **77** (4), 043420, doi:10.1103/PhysRevA.77.043420.
- 9 Zhou, Z. and Chu, S.I. (2011) Precision calculation of above-threshold multiphoton ionization in intense short-wavelength laser fields: The momentum-space approach and time-dependent generalized pseudospectral method. *Phys. Rev. A*, **83** (1), 013405.
- 10 Sanz-Vicario, J.L., Bachau, H., and Martín, F. (2006) Time-dependent theoretical description of molecular autoionization produced by femtosecond xuv laser pulses. *Phys. Rev. A*, **73**, 033410.
- 11 Bachau, H., Cormier, E., Declava, P., Hansen, J., and Martin, F. (2001) Applications of B-splines in atomic and molecular physics. *Rep. Prog. Phys.*, **64** (12), 1815–1943.
- 12 Nicolaides, C.A. and Piagios, N.A. (2001) State-specific approach and computation of resonance states: Identification and properties of the lowest $^2P^o$ and 2D triply excited states of He⁻. *Phys. Rev. A*, **64**, 052505.
- 13 Awasthi, M., Vanne, Y., and Saenz, A. (2005) Non-perturbative solution of the time-dependent Schrodinger equation describing H₂ in intense short laser pulses. *J. Phys. B*, **38** (22), 3973–3985.
- 14 Caillat, J., Zanghellini, J., Kitzler, M., Koch, O., Kreuzer, W., and Scrinzi, A. (2005) Correlated multielectron systems in strong laser fields – an mctdhf approach. *Phys. Rev. A*, **71**, 012712.
- 15 Veniard, V., Taieb, R., and Maquet, A. (2003) Photoionization of atoms using

- time-dependent density functional theory. *Laser Phys.*, **13**, 465.
- 16** Maitra, N.T., Burke, K., and Woodward, C. (2002) Memory in time-dependent density functional theory. *Phys. Rev. Lett.*, **89**, 023002.
- 17** Kulander, K.C. (1987) Time-dependent Hartree–Fock theory of multiphoton ionization: Helium. *Phys. Rev. A*, **36**, 2726.
- 18** Lill, J., Parker, G., and Light, J. (1982) Discrete variable representation and sudden models in quantum scattering theory. *Chem. Phys. Lett.*, **89** (6), 483–489.
- 19** Pont, M., Proulx, D., and Shakeshaft, R. (1991) Numerical integration of the time-dependent Schrödinger equation for an atom in a radiation field. *Phys. Rev. A*, **44** (7), 4486–4492.
- 20** Scrinzi, A. and Piraux, B. (1998) Two-electron atoms in short intense laser pulses. *Phys. Rev. A*, **58**, 1310.
- 21** Tong, X.M. and Chu, S.I. (1997) Theoretical study of multiple high-order harmonic generation by intense ultrashort pulsed laser fields: A new generalized pseudospectral time-dependent method. *Chem. Phys.*, **217** (2–3), 119–130, doi: 10.1016/S0301-0104(97)00063-3, <http://www.sciencedirect.com/science/article/pii/S0301010497000633>, dynamics of Driven Quantum Systems.
- 22** Scrinzi, A. and Elander, N. (1993) A finite element implementation of exterior complex scaling. *J. Chem. Phys.*, **98**, 3866.
- 23** Zhang, J. and Lambropoulos, P. (1996) Time-dependent calculation of photo-electron spectra in Mg involving multiple continua. *Phys. Rev. Lett.*, **77** (11), 2186–2189.
- 24** Hasbani, R., Cormier, E., and Bachau, H. (2000) Resonant and non-resonant ionization of helium by XUV ultrashort and intense laser pulses. *J. Phys. B*, **33** (11), 2101–2116.
- 25** Hamido, A., Eiglsperger, J., Madronero, J., Mota-Furtado, F., O’Mahony, P., Frapiccini, A.L., and Piraux, B. (2011) Time scaling with efficient time-propagation techniques for atoms and molecules in pulsed radia-
- tion fields. *Phys. Rev. A*, **84** (1), doi:10.1103/PhysRevA.84.013422.
- 26** Scrinzi, A. (2010) Infinite-range exterior complex scaling as a perfect absorber in time-dependent problems. *Phys. Rev. A*, **81** (5), 053845.
- 27** Sidky, E.Y. and Esry, B.D. (2000) Boundary-free propagation with the time-dependent Schrödinger equation. *Phys. Rev. Lett.*, **85** (24), 5086–5089, doi:10.1103/PhysRevLett.85.5086.
- 28** Tao, L. and Scrinzi, A. (2012) Photo-electron momentum spectra from minimal volumes: the time-dependent surface flux method. *New J. Phys.*, **14** (1), 013021.
- 29** Smyth, E., Parker, J., and Taylor, K. (1998) Numerical integration of the time-dependent Schrödinger equation for laser-driven helium. *Comp. Phys. Comm.*, **114** (1–3), 1–14.
- 30** Park, T.J. and Light, J.C. (1986) Unitary quantum time evolution by iterative lanczos reduction. *J. Chem. Phys.*, **85** (10), 5870.
- 31** Yakovlev, V., Korbmann, M., and Scrinzi, A. (2013) Dressed bound states for attosecond dynamics in strong laser fields. *Chem. Phys.*, **414**, 26.
- 32** Putz, V., Ede, C., and Scrinzi, A. (2007) Photoabsorption of quantum dots in quantum wells with a strong electric bias field. *Phys. Rev. B*, **76**, 035318.
- 33** Morales, F., Martin, F., Horner, D.A., Rescigno, T.N., and McCurdy, C.W. (2009) Two-photon double ionization of H₂ at 30 eV using exterior complex scaling. *J. Phys. B*, **42** (13).
- 34** Taylor, K., Parker, J., Meharg, K., and Dundas, D. (2003) Laser-driven helium at 780 nm. *Eur. Phys. J. D*, **26** (1), 67–71.
- 35** Parker, J., Taylor, K., Clark, C., and Blodgett-Ford, S. (1996) Intense-field multiphoton ionization of a two-electron atom. *J. Phys. B*, **29** (2), L33–L42.
- 36** Taylor, K., Parker, J., Dundas, D., Meharg, K., Moore, L., and McCann, J. (2003) Laser-driven helium, H₂⁺ and H₂. *J. Modern Opt.*, **50** (3–4), 401–422, doi:10.1080/09500340308233539.
- 37** Parker, J.S., Doherty, B.J.S., Taylor, K.T., Schultz, K.D., Blaga, C.I., and DiMaurro, L.F. (2006) High-energy cutoff in

- the spectrum of strong-field nonsequential double ionization. *Phys. Rev. Lett.*, **96** (13), 133001.
- 38** Scrinzi, A. (2012) t-SURFF: fully differential two-electron photo-emission spectra. *New J. Phys.*, **14** (8), 085008.
- 39** Scrinzi, A., Geissler, M., and Brabec, T. (1999) Ionization above the coulomb barrier. *Phys. Rev. Lett.*, **83**, 706–709.
- 40** Yang, B., Pont, M., Shakeshaft, R., van Duijn, E., and Piraux, B. (1997) Description of a two-electron atom or ion in an ac field using interparticle coordinates, with an application to H^- . *Phys. Rev. A*, **56** (6), 4946–4959, doi:10.1103/PhysRevA.56.4946.
- 41** Saenz, A. (2002) Behavior of molecular hydrogen exposed to strong DC, AC, or low-frequency laser fields. I. bond softening and enhanced ionization. *Phys. Rev. A*, **66**, 63407.
- 42** Rohringer, N., Peter, S., and Burgdörfer, J. (2006) Calculating state-to-state transition probabilities within time-dependent density-functional theory. *Phys. Rev. A*, **74**, 042512.
- 43** Jordan, G. and Scrinzi, A. (2008) Core-polarization effects in molecular high harmonic generation. *New J. Phys.*, **10**, 25035.
- 44** Itatani, J., Levesque, J., Zeidler, D., Niikura, H., Pepin, H., Kieffer, J.C., Corkum, P.B., and Villeneuve, D.M. (2004) Tomographic imaging of molecular orbitals. *Nature*, **432** (7019), 867–871.
- 45** Patchkovskii, S., Zhao, Z., Brabec, T., and Villeneuve, D.M. (2006) High harmonic generation and molecular orbital tomography in multielectron systems: Beyond the single active electron approximation. *Phys. Rev. Lett.*, **97** (12), 123003, doi:10.1103/PhysRevLett.97.123003, <http://link.aps.org/abstract/PRL/v97/e123003>.
- 46** Sukiasyan, S., McDonald, C., Deste-fani, C., Ivanov, M.Y., and Brabec, T. (2009) Multielectron correlation in high-harmonic generation: A 2D model analysis. *Phys. Rev. Lett.*, **102** (22).
- 47** Geppert, D. and de Vivie-Riedle, R. (2005) Reaction velocity control by manipulating the momentum of a nuclear wavepacket with phase-sensitive optimal control theory. *Chem. Phys. Lett.*, **404** (4–6), 289–295.
- 48** Martin, F., Fernández, J., Havermeier, T., Foucar, L., Weber, T., Kreidi, K., Schoeffler, M., Schmidt, L., Jahnke, T., Jagutzki, O., Czasch, A., Benis, E.P., Osipov, T., Landers, A.L., Belkacem, A., Prior, M.H., Schmidt-Boecking, H., Cocke, C.L., and Doerner, R. (2007) Single photon-induced symmetry breaking of H^2 dissociation. *Science*, **315** (5812), 629–633.

9**Angular Distributions in Molecular Photoionization**

Robert R. Lucchese and Danielle Dowek

Photoelectron angular distributions (PADs) in molecular photoionization can provide detailed information about the geometry of a molecule, the initial electronic state and the electronic state of the product molecular ion. In general, the molecular frame photoelectron angular distribution (MFPAD) can be a function of four angles for linearly and circularly polarized light and five angles for elliptically polarized light. In this chapter, we show how, for dipole transitions, these multidimensional distributions can be reduced to a limited number of one-dimensional functions. PADs must be determined relative to the molecular frame of reference and we consider experimental distributions that can be obtained with post-ionization analysis of the molecular frame orientation, using coincidence detection of the photoelectron and at least one ionic fragment. We also consider concurrent orientation, where a multiphoton process modifies the alignment of the molecule, helping the analysis of the PAD. And finally, we consider the form of the PAD when the molecule is preoriented, as can be achieved with impulsive alignment by intense infrared lasers.

9.1**Introduction**

The ionization of molecules by absorption of light is significantly different from absorption where the final state is a bound state. In the case of ionization, the continuous nature of the final state leads to a lack of quantization for the total energy of the system. The infinite degeneracy of the continuum allows ejection of the photoelectron in any direction relative to the molecular frame (MF), that is, in any direction in the coordinate system of the molecule. The differential cross-section for this photoemission process is the molecular frame photoelectron angular distribution (MFPAD). This observable results from the coherent superposition of all partial waves contributing to the continuum electronic wavefunction: it therefore provides a very sensitive probe of the potentials and interactions governing the quantum dynamics of the emitted photoelectrons. In molecules, the MFPAD is a function of

the molecular frame electron emission direction, as well as the relative orientation of the light polarization axis to the molecular frame. Dill recognized that the measurement of the MFPAD provides the maximum information available from a one-photon photoionization experiment and he derived the first general expression for their description [1]. More than fifteen years after this theoretical statement, pioneering experiments resolved MFPADs experimentally: Golovin *et al.* observed PADs in valence shell ionization of O₂ [2] and Shigemasa *et al.* in K-shell ionization of N₂ [3]. Since then, molecular frame photoemission has been determined for one-photon photoionization induced by valence and inner valence shell [4]–[16] or inner shell [17]–[33] excitation of a number of mainly diatomic or linear molecules, thereby probing fundamental processes such as electronic correlation [11], circular dichroism in molecular frame photoemission [8, 11, 16, 20, 24], quantum interferences [14, 15, 26] (which may induce symmetry breaking in dissociative ionization of symmetric molecules [12, 16, 27, 31, 32]), core hole localization, and entanglement [28, 29].

When there is no information about the orientation of a molecule, the only quantities that can be measured in photoionization, at a given energy are the total photoionization cross-section and the photoelectron asymmetry parameter. The latter describes the photoelectron angular distribution (PAD) relative to the polarization direction of linearly polarized light or the propagation of circularly polarized light [34]:

$$\frac{d\sigma}{d\Omega} = \frac{\sigma}{4\pi} [1 + \beta P_2(\cos \theta)] , \quad (9.1)$$

where θ is the angle between the polarization axis of the light and the emission direction of the photoelectron. Given that the angular distribution in Eq. (9.1) has been averaged over all orientations of the molecule, it contains limited information about the MFPAD.

To extract more information about the MFPAD of isolated molecules, there are three general experimental approaches. The first approach is to consider dissociative photoionization (DPI) by coincident detection of the photoelectron and at least one fragment. In the simple case of a diatomic molecule, and by using the axial recoil approximation [35, 36], the recoil direction of the atomic fragment ion gives the direction of the molecular axis at the time of ionization. Together with the measured direction of photoelectron emission and the known orientation of the light polarization, the MFPAD can be directly measured [2]. Such a measurement constitutes a *post-orientation*, that is, the orientation of the molecule is determined after the ionization event. The main limitation of this approach is that only dissociative states of the molecular ion can be studied and the lifetime of the dissociative state must be short with respect to rotation and geometry changes (in the case of polyatomic molecules). For nonlinear molecules, when only two fragments are produced, the orientation about the recoil axis cannot be observed, so that only the recoil frame angular distribution (RFPAD) can be observed and not the full MFPAD. When the axial recoil approximation breaks down, one cannot directly measure the MFPAD, but only the RFPAD since the recoil direction then no

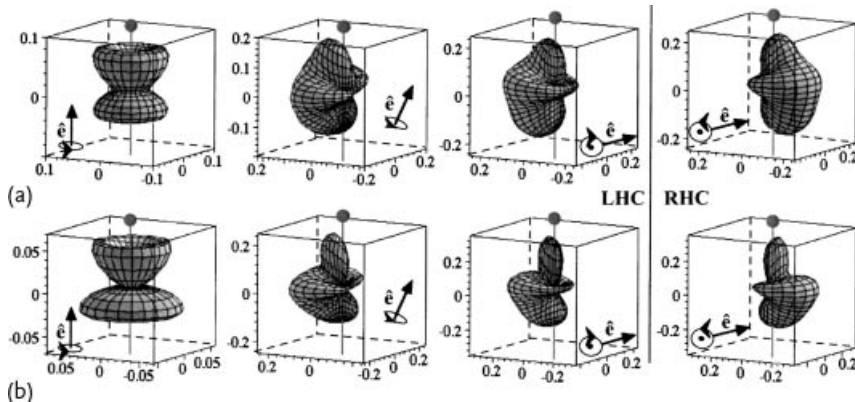


Figure 9.1 MFPADs for photoionization of NO from [11], as described in the text. The arrows indicate the propagation axis of circularly polarized light. The experimental (a) and computed (b) parallel, magic angle, and perpendicular MFPADs are shown for left-hand

circularly (LHC) polarized light (from left to right in first three columns); the perpendicular MFPAD for right-hand circularly (RHC) polarized light is shown for comparison (last column).

longer corresponds to the original molecular orientation. A detailed discussion of both experimental and theoretical aspects of the post-alignment approach has been presented elsewhere [37].

A second approach to obtain MFPAD information is *concurrent orientation*. By this, we mean the alignment, which occurs in $n + 1$ multiphoton ionization. Here, the first n photons involve transitions to bound states. Such transitions usually show an alignment dependence, therefore the last photon leads to ionization of a partially aligned sample. In this case the first n photons provide a partial orientation of the molecule. In combination with a coincidence measurement of a dissociative ionization fragment, it is possible to obtain additional information about the MFPAD beyond what is available from a measured one-photon RFPAD [38] for a nonlinear molecule. The multiphoton ionization process can also provide information about the photoionization of excited states, which is otherwise difficult to obtain.

Finally, it is possible to employ *pre-orientation* of a molecular target and study photoionization under field-free conditions [39–41] after impulsive alignment using short infrared laser pulses [42–44]. Here we will consider the form of the measured photoelectron angular distributions in each of these cases and consider the connection to the underlying complex-valued photoionization dipole matrix elements. Some of these issues have also been discussed in an earlier review of photoelectron angular distributions [45].

In general, the molecular frame photoelectron angular distribution can be a function of four angles for linearly and circularly polarized light and five angles for elliptically polarized light. In this chapter, we show how these many-dimensional distributions can be reduced to a limited number of one-dimensional functions for dipole transitions. For example, in Figure 9.1 we give the computed and measured

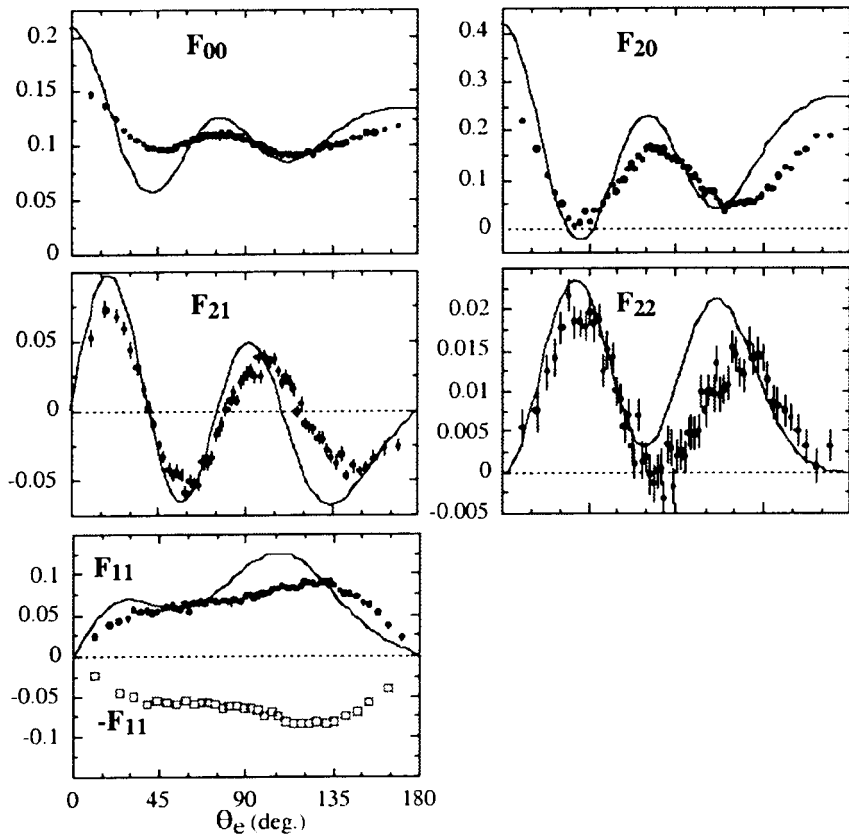


Figure 9.2 Experimental and computed one-dimensional functions that describe the MFPAD for the photoionization of NO as given in Figure 1 from [11].

MFPAD for ionization of NO leading to the $c^3\Pi$ state of NO^+ , measured using coincidence detection of the photoelectron and N^+ fragment ion after irradiation with circularly polarized light at a photon energy of 23.65 eV [11]. In Figure 9.2, we give the corresponding five one-dimensional functions, which can be used to determine the MFPAD for any orientation of the field in the molecular frame. These one-dimensional functions can be useful for analysis of experimental data, as well as for the comparison of computed and measured data. The ability to make accurate predictions of MFPADs can be very useful since comparisons between computed and measured MFPADs can then be used to determine the structure and electronic state of the molecule that is ionized. We will give a brief survey of the theoretical methods that can be used to compute such angular distributions.

There are several mechanisms by which a measured MFPAD can be used to determine the structure of a molecular system. The MFPAD contains information both about the initial state, and its geometry dependence, as well as the final continuum state of the photoelectron [46]. At low energy, features in the scattering con-

tinuum, such as shape resonances, will dramatically change the MFPAD and are sensitive to the geometry of the system [47]. At high energy, when the wavelength of the photoelectron becomes comparable to the interatomic distances, interference effects such as the Cohen–Fano interference [48, 49] will reveal information about molecular structure.

9.2

One-Photon Photoionization in the Molecular Frame

The differential cross-section, $T_{i,f}$, for one-photon photoionization in the molecular frame (MF) is proportional to the absolute square of the transition matrix elements giving

$$T_{i,f} = \frac{4\pi^2 E}{c} I_{i,f} I_{i,f}^*, \quad (9.2)$$

where E is the photon energy and c is the speed of light. In the dipole approximation, the photoionization matrix element, $I_{i,f}$, can be written in the form

$$I_{i,f} = \left\langle \Psi_i | \mathbf{r} \cdot \mathbf{A} | \Psi_{f,k}^{(-)} \right\rangle, \quad (9.3)$$

where Ψ_i is the wavefunction representing the initial unionized state, $\Psi_{f,k}^{(-)}$ is the ionized final state with the continuum electron leaving the system with asymptotic momentum \hat{k} , and \mathbf{A} is the field. The MFPAD can then be written as

$$T_{i,f} = \frac{4\pi^2 E}{c} \left| \left\langle \Psi_i | \mathbf{r} \cdot \mathbf{A} | \Psi_{f,k}^{(-)} \right\rangle \right|^2. \quad (9.4)$$

For light of arbitrary elliptical polarization within the rotating wave approximation (RWA) [50] and in the dipole approximation, the field can be represented by

$$\mathbf{A} = \hat{\mathbf{x}}_{\text{FF}} \cos \lambda + \hat{\mathbf{y}}_{\text{FF}} \sin \lambda \exp(i\delta), \quad (9.5)$$

where the light is propagating in the z direction in the field frame (FF), also commonly referred to as the laboratory frame, that is, in the $\hat{\mathbf{z}}_{\text{FF}}$ direction, and where $\hat{\mathbf{x}}_{\text{FF}}$, $\hat{\mathbf{y}}_{\text{FF}}$, and $\hat{\mathbf{z}}_{\text{FF}}$ form a mutually orthogonal set of vectors. The parameters λ and δ are related to the Stokes parameters by [51]

$$\begin{aligned} s_0 &= 1 \\ s_1 &= \cos(2\lambda) \\ s_2 &= \sin(2\lambda) \cos(\delta) \\ s_3 &= \sin(2\lambda) \sin(\delta). \end{aligned} \quad (9.6)$$

Then the dipole operator can be written as

$$\mathbf{r} \cdot \mathbf{A} = (\mathbf{r} \cdot \hat{\mathbf{x}}_{\text{FF}}) \cos \lambda + (\mathbf{r} \cdot \hat{\mathbf{y}}_{\text{FF}}) \sin \lambda \exp(i\delta). \quad (9.7)$$

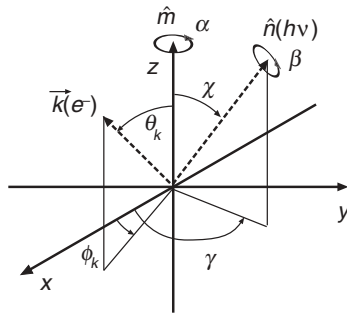


Figure 9.3 Schematic of the angles and directions used to describe the MFPAID distributions. In the schematics, the molecular axis is assumed to be in the \hat{z} direction, \hat{n} is either the direction of light propagation for elliptically polarized light or the direction of polarization for linearly polarized light, and

the photoelectron is emitted in direction \hat{k} . The angle α represents the rotation of the molecule about the z axis and, for elliptically polarized light, the angle β represents the rotation of the \hat{x}_{FF} direction away from the plane containing the z axis and the \hat{n} vector.

In the case of linearly polarized light, Eq. (9.7) can be simplified, so that Eq. (9.3) becomes

$$I_{i,f}^{(\text{LP})} = \left\langle \Psi_i | \mathbf{r} \cdot \mathbf{n} | \Psi_{f,k}^{(-)} \right\rangle , \quad (9.8)$$

where \hat{n} is the direction of the linear polarization. Defining the spherical tensor operator e_μ as

$$e_\mu = r Y_{1,\mu} (\theta_e, \phi_e) \sqrt{\frac{4\pi}{3}} = \begin{cases} z & \text{for } \mu = 0 \\ -\frac{x+iy}{\sqrt{2}} & \text{for } \mu = 1 \\ \frac{x-iy}{\sqrt{2}} & \text{for } \mu = -1 \end{cases} \quad (9.9)$$

and writing the partial-wave expansion of the ionized state as [52]

$$\Psi_{f,k}^{(-)}(\mathbf{r}) = \sqrt{\frac{2}{\pi}} \sum_{l,m} i^l \Psi_{f,l,m}^{(-)}(\mathbf{r}) Y_{lm}^*(\theta_k, \phi_k) , \quad (9.10)$$

where the angles (θ_k, ϕ_k) define the direction of emission of the photoelectron in the MF as illustrated in Figure 9.3, the complex-valued partial-wave dipole matrix elements can then be given by

$$I_{l,m,\mu}^{(i,f)} = \sqrt{\frac{2}{\pi}} i^l \left\langle \Psi_i | e_\mu | \Psi_{f,l,m}^{(-)}(\mathbf{r}) \right\rangle , \quad (9.11)$$

so that the dipole matrix element for linearly polarized light, defined in Eq. (9.8), can be written in a partial-wave expanded form as

$$I_{i,f} = \sum_{l,m,\mu} \sqrt{\frac{4\pi}{3}} I_{l,m,\mu}^{(i,f)} Y_{lm}^*(\theta_k, \phi_k) Y_{l,\mu}^*(\chi_{\text{LP}}, \gamma_{\text{LP}}) . \quad (9.12)$$

In the case of arbitrary polarization, the field can be expressed using A_{\pm} , defined as

$$A_{\pm} = \cos \lambda \pm i \sin \lambda \exp(i\delta) \quad (9.13)$$

so that the interaction operator can be written as

$$\mathbf{r} \cdot \mathbf{A} = \frac{1}{\sqrt{2}} \left[A_+ \sum_{\mu=-1}^1 e_{\mu} D_{\mu,-1}^{(1)}(\gamma, \chi, \beta) - A_- \sum_{\mu=-1}^1 e_{\mu} D_{\mu,1}^{(1)}(\gamma, \chi, \beta) \right] \quad (9.14)$$

where $D_{M,M'}^{(J)}(\gamma, \chi, \beta)$ are the rotation matrices and (γ, χ, β) are the Euler angles that rotate the molecular frame into the field frame [53].

Using this notation, the dipole matrix element given in Eq. (9.3) can be written in a partial-wave expanded form as

$$I_{i,f} = \sum_{l,m,\mu} I_{lm\mu} Y_{lm}^*(\theta_k, \phi_k) \frac{1}{\sqrt{2}} \left[A_+ D_{\mu,-1}^{(1)}(\gamma, \chi, \beta) - A_- D_{\mu,1}^{(1)}(\gamma, \chi, \beta) \right]. \quad (9.15)$$

In the case of linearly polarized light or circularly polarized light, Eqs. (9.12) and (9.15) can be combined into a single form

$$I_{i,f}^{(\mu_0)} = \sum_{l,m,\mu} I_{lm\mu} Y_{lm}^*(\theta_k, \phi_k) D_{\mu,-\mu_0}^{(1)}(\gamma, \chi, \beta). \quad (9.16)$$

Applying Eq. (9.16) to linearly polarized light, we take $\mu_0 = 0$, $\gamma = \gamma_{LP}$, $\chi = \chi_{LP}$, and $\beta = 0$, where (χ_{LP}, γ_{LP}) gives the direction of polarization in the molecular frame. For circularly polarized light, $\mu_0 = -s_3$ so that for left-hand circularly polarized light we have $\mu_0 = 1$ and (χ, γ) gives the direction of propagation of the light.

The MFPAD $T_{i,f}$, as given in Eq. (9.4), is then, *a priori*, a function of five angles: the electron emission direction in the MF (θ_k, ϕ_k) and the (γ, χ, β) Euler angles that rotate the molecular frame into the field frame. The differential cross-section can be written in terms of a set of one-dimensional functions $F_{N,\nu}^{(L)}(\theta_k)$ multiplied by low-order functions of the other angles [9]. The $F_{N,\nu}^{(L)}(\theta_k)$ functions contain all the dynamical information and they can be expanded as

$$F_{N,\nu}^{(L)}(\theta_k) = \frac{L!(-1)^{L+N+\frac{|N+\nu|+N+\nu}{2}}}{2\pi} \frac{i^L}{1 + \delta_{N,0}} \left[\frac{(L-N)!}{(L+N)!} \right]^{\frac{1}{2}} \times \sum_{L'} \left[\frac{(L'-|N+\nu|)!}{(L'+|N+\nu|)!} \right]^{\frac{1}{2}} P_{L'}^{|N+\nu|}(\cos \theta_k) G_{L',L,N,\nu}, \quad (9.17)$$

where the $G_{L',L,N,\nu}$ terms are defined as combinations of products of the partial-wave dipole matrix elements:

$$\begin{aligned} G_{L',L,N,\nu} = & \frac{4\pi^2 E}{c} \sum_{l,l',m,\mu} (-1)^{N+m+\mu+1} I_{l,m,\mu} (I_{l',m+N+\nu,\mu-N})^* \\ & \times [(2l+1)(2l'+1)]^{\frac{1}{2}} \langle 1, 1, \mu, N-\mu | L, N \rangle \langle 1, 1, 1, -1 | L, 0 \rangle \\ & \times \langle l, l', m, -(m+N+\nu) | L', -(N+\nu) \rangle \langle l, l', 0, 0 | L', 0 \rangle , \end{aligned} \quad (9.18)$$

and the $\langle l_1, l_2, m_1, m_2 | L, M \rangle$ are the usual Clebsch–Gordon coefficients. The three indices, L , N , and ν , which define the $F_{N,\nu}^{(L)}(\theta_k)$ functions, are constrained by the geometry of the system and the assumptions made in deriving Eq. (9.17). Thus, in the one-photon dipole approximation, L comes from the expansion of the square of the field, so that it satisfies $0 \leq L \leq 2$, as can be seen in the Clebsch–Gordon coefficients in Eq. (9.18). Likewise, N is constrained by L such that $0 \leq N \leq L$. Note that the $F_{N,\nu}^{(L)}(\theta_k)$ have been defined so that only nonnegative values of N are used. In principle, the range for L' needed in Eq. (9.17) is $0 \leq L' \leq \infty$. However, in practice, the maximum value of L' needed is limited by the size of the molecular system, represented by the radius R_{\max} , and by the momentum of the photoelectron, p . Thus, the maximum value of l needed to describe the asymptotic state of the continuum electron in Eq. (9.10) can be estimated from $\hbar L_{\max} = R_{\max} \times p$, leading to the range of L' being given by $0 \leq L' \leq 2L_{\max}$. Finally, the index ν is connected to the amount of asymptotic angular momentum about the \hat{z} axis in the molecular frame. As can be seen in Eq. (9.18), the range of ν is constrained by the values of L' and N leading to the constraint $-L' - 2 \leq \nu \leq L'$. Then the practical limits on ν are given by $-2L_{\max} - 2 \leq \nu \leq 2L_{\max}$. For systems that have a smaller moment of inertia about the \hat{z} axis, as compared to the other two axes, that is, for prolate molecules, the practical limits on the range of ν may be much smaller in absolute magnitude.

With the definition of the $F_{N,\nu}^{(L)}$ functions given in Eq. (9.17), we obtain the following expression $T_{i,f}$ for the differential cross-section in the molecular frame [11, 54]

$$\begin{aligned} T_{i,f}(\theta_k, \phi_k, \gamma, \chi, \beta) = & \sum_{\nu} \operatorname{Re} \left(\exp(i\nu\gamma) \left\{ F_{0,\nu}^{(0)}(\theta_k) \exp[i\nu(\phi_k - \gamma)] \right. \right. \\ & + \sum_{N=0}^1 i s_3 F_{N,\nu}^{(1)}(\theta_k) P_1^N(\cos \chi) \exp[i(N+\nu)(\phi_k - \gamma)] \\ & + \sum_{N=0}^2 F_{N,\nu}^{(2)}(\theta_k) \left[-\frac{1}{2} P_2^N(\cos \chi) + t_1(\beta) Q_N^+(\chi) - i t_2(\beta) Q_N^-(\chi) \right] \\ & \left. \left. \times \exp[i(N+\nu)(\phi_k - \gamma)] \right\} \right) , \end{aligned} \quad (9.19)$$

where t_1 and t_2 are defined by

$$\begin{aligned} t_1(\beta) &= s_1 \cos(2\beta) - s_2 \sin(2\beta) \\ t_2(\beta) &= s_1 \sin(2\beta) + s_2 \cos(2\beta) \end{aligned} \quad (9.20)$$

and the $Q_N^\pm(\chi)$ are defined as

$$\begin{aligned} Q_N^\pm(\chi) &= \frac{3}{(2-N)!} \left\{ (-1)^N \left[\cos\left(\frac{\chi}{2}\right) \right]^{2+N} \left[\sin\left(\frac{\chi}{2}\right) \right]^{2-N} \right. \\ &\quad \left. \pm \left[\cos\left(\frac{\chi}{2}\right) \right]^{2-N} \left[\sin\left(\frac{\chi}{2}\right) \right]^{2+N} \right\}. \end{aligned} \quad (9.21)$$

If the molecule under consideration has a reflection symmetry plane containing the z axis, the $F_{N,\nu}^{(L)}$ are real valued functions, which leads to further simplification of the expansion. In particular, using the phase convention for the associated Legendre polynomials as given in [55], Eq. (9.19) can then be written as

$$\begin{aligned} T_{i,f}(\theta_k, \phi_k, \gamma, \chi, \beta) &= \sum_\nu \left(F_{0,\nu}^{(0)}(\theta_k) \cos(\nu \phi_k) \right. \\ &\quad - \sum_{N=0}^1 s_3 F_{N,\nu}^{(1)}(\theta_k) P_1^N(\cos \chi) \sin[N(\phi_k - \gamma) + \nu \phi_k] \\ &\quad + \sum_{N=0}^2 F_{N,\nu}^{(2)}(\theta_k) \left\{ \left[-\frac{1}{2} P_2^N(\cos \chi) + t_1(\beta) Q_N^+(\chi) \right] \right. \\ &\quad \times \cos[N(\phi_k - \gamma) + \nu \phi_k] \\ &\quad \left. \left. + t_2(\beta) Q_N^-(\chi) \sin[N(\phi_k - \gamma) + \nu \phi_k] \right\} \right). \end{aligned} \quad (9.22)$$

Analyzing the multidimensional $T_{i,f}$ differential cross-section in the molecular frame according to the general expression given in Eq. (9.22), where the dependence on χ , γ , and ϕ_k is only through low-order trigonometric functions, enables us to determine the one-dimensional functions $F_{N,\nu}^{(L)}(\theta_k)$ giving access to the dipole matrix elements, their magnitudes and phases, as well as the Stokes parameters characterizing the ionizing light. Equation (9.22) can be simplified for particular choices of the polarization of the light. For *linearly polarized light*, we have

$$\begin{aligned} T_{i,f}^{\text{LP}}(\theta_k, \phi_k, \chi_{\text{LP}}, \gamma_{\text{LP}}) &= \sum_\nu \sum_{L=0,2} \sum_{N=0}^L F_{N,\nu}^{(L)}(\theta_k) P_L^N(\cos \chi_{\text{LP}}) \\ &\quad \times \cos[N(\phi_k - \gamma_{\text{LP}}) + \nu \phi_k] \end{aligned} \quad (9.23)$$

and for *circularly polarized light*

$$\begin{aligned}
 T_{i,f}^{\text{CP}}(\theta_k, \phi_k, \chi, \gamma) = & \sum_v \left\{ F_{0,v}^{(0)}(\theta_k) \cos(\nu \phi_k) \right. \\
 & \pm \sum_{N=0}^1 F_{N,v}^{(1)}(\theta_k) P_1^N(\cos \chi) \sin[N(\phi_k - \gamma) + \nu \phi_k] \\
 & \left. - \frac{1}{2} \sum_{N=0}^2 F_{N,v}^{(2)}(\theta_k) P_2^N(\cos \chi) \cos[N(\phi_k - \gamma) + \nu \phi_k] \right\}
 \end{aligned} \tag{9.24}$$

where the upper sign is for left-handed circularly polarized light or helicity of +1.

9.3

Methods for Computing Cross-Sections

Any method capable of computing photoionization matrix elements [56] given in Eq. (9.3) can be used to study MFPADs. By extension, any method that can compute electron–molecular ion scattering wavefunctions can, in principle, be used to compute photoionization matrix elements. In addition to computing the electronic wavefunctions, one must also consider how to treat the vibrational motion in the photoionization process. When explicit treatment of the nuclear motion is needed, one can usually employ the Born–Oppenheimer approximation and compute the photoionization matrix elements at a series of different geometries, with the final matrix elements being obtained as integrals of the fixed-nuclei results integrated with the product of the appropriate vibrational wavefunctions. In the context of electron–molecule collisions, this is also known as the Chase approximation [57]. An alternative, the simpler fixed-nuclei approximation, is to compute the cross-section only at a single geometry, usually the equilibrium geometry of the initial state. For transitions involving bound vibrational states, the fixed-nuclei approximation is usually adequate, unless there is a scattering resonance that is sensitive to the geometry [58] or one is interested in specific vibrational cross-sections [59].

One common approach for computing the photoionization matrix elements is to separately compute the wavefunctions for the initial and final electronic state, as found in Eq. (9.3), at a particular geometry. Then, the appropriate dipole matrix integral is computed using the explicit functions for the initial and final states. The initial state, Ψ_i , can be treated with traditional Hartree–Fock (HF) or configuration interaction (CI) methods appropriate for such a bound state wavefunction. The final state, $\Psi_{f,k}^{(-)}$, must be treated differently, since the final state is part of the continuum and the wavefunction does not go to zero when one of the electrons is far from the molecule. Instead, the appropriate boundary condition for the ionized state has a flux of electrons leaving the system with asymptotic momentum k . The final state is often expanded in terms of a close-coupling expansion, that is, a finite sum of products of $N - 1$ electron target states, Φ_p , times one-electron continuum

functions, $\Psi_{p,k}^{(-)}$. In some formulations, additional purely bound N electron terms, $\Psi_q^{(b)}$, are also added to the expansion, leading to the form

$$\Psi_{f,k}^{(-)} = \sum_{p=1}^{N_c} A(\phi_p \Psi_{p,k}^{(-)}) + \sum_{q=1}^{N_b} \Psi_q^{(b)} \quad (9.25)$$

where A is the antisymmetrization operator. Such an expansion can be characterized by the number of terms included in the expansions and the form of the target states used in the expansion. Thus, one can have single-channel (SC) and multichannel (MC) expansions, depending on the value of N_c as given in Eq. (9.25). Additionally, if the target states are described using single-configuration state functions where the orbitals are the same as in an initial state Hartree–Fock calculation, then this is referred to as a frozen-core Hartree–Fock calculation (FCHF) [52]. Alternatively, one can use some type of CI wavefunction in the target states.

The close-coupling approach has been extensively used to study molecular photoionization within the multichannel Schwinger configuration interaction (MC-SCI) method [60–62]. Two additional methods based on the wavefunction expansion given in Eq. (9.25) have been extensively applied to electron–molecule collisions but have been only applied to electron–molecular ion collisions in a limited number of cases: the complex Kohn variational method [63], and the R -matrix method [64]. Numerical solutions of the close-coupling equations have also been obtained using methods based on B spline basis sets [65].

One of the difficulties with direct wavefunction-based approach is that the initial and final states are computed using separate calculations. A balanced treatment of these two parts of the calculation cannot be uniquely defined. An alternative approach for obtaining photoionization cross-sections is to use linear-response theories of electronic structure theory. In general, response theories for the electronic structure of a molecule solve the appropriate equations for the response of the electronic wavefunction to an oscillating external field. The simplest linear response theory for molecular calculations assumes that the wavefunction of the unperturbed state is represented by a HF wavefunction. With this assumption, the resulting equations are usually referred to as the random phase approximation (RPA), or as the time-dependent Hartree–Fock (TDHF) approximation [66, 67].

Beyond traditional *ab initio* type methods, molecular photoionization can be treated using density functional theory (DFT) formulations. The simplest application of the DFT uses a form of the one-electron Kohn–Sham (KS) Hamiltonian to describe the one-electron continuum states [68]. A more accurate DFT method for treating molecular photoionization is based on the time-dependent density functional theory (TDDFT) method [69]. This approach is the DFT analog of the RPA method discussed above since it is based on the linear response of a HF like wavefunction to a slowly time-varying external electric field.

One of the first computational methods that was used to study molecular photoionization is the multiple scattering method (MSM) [70]. This approach assumes a very simplified electron–molecule interaction potential for which the corresponding scattering equation can be easily solved. This approach has been applied to many photoionization systems with significant success in describing nonresonant

scattering and various one-electron resonances. The advantage of this approach is that it can be applied to large systems without significant computational effort.

Of the methods for computing molecular photoionization matrix elements mentioned above, most have been used to compute MFPADs. Here, we will give a representative publication for each approach. The MCSCF method has been used for many studies. One particularly interesting study considered the valence ionization of NO, where the effects of using different close-coupling expansion on the MFPAD were considered in some detail [11]. The simpler SC type calculations have also been used to study MFPADs in C1s ionization of CO₂ [22]. The complex Kohn method has also been used to study the MFPADs in C1s ionization of CO₂ [71]. The TDDFT method was used to study the full MFPAD of H₂O [33]. The RPA was used to study the inner shell ionization of N₂ [21]. MSM was used to study the RFPADs of valence ionization of CH₃F and CH₃Cl [7]. The B spline method has been used to study PADs in both single and double ionization of H₂ [27, 72]. Finally, although the R-matrix method has not yet been applied to MFPAD type calculations, promising results on the total photoionization cross-sections of N₂ and NO [73] indicate that this could also be a good approach for computing MFPADs.

Beyond molecular photoionization, similar theoretical techniques can be used to study electron continuum processes encountered in high-field physics. Such processes include high harmonic generation and rescattering phenomena [74, 75].

9.4

Post-orientation MFPADs

The most extensively employed experimental method for studying MFPADs uses dissociative ionization and coincidence detection of the ejected photoelectron and one or more of the molecular fragments produced in the ionization event. This approach then constitutes a post-orientation method, since the orientation is only determined after the ionization has occurred. The direct analysis of such measured angle resolved coincidence data is possible when the axial recoil approximation is valid. In the axial recoil approximation one assumes that the direction of the fragments produced in dissociative ionization is the same as the orientation of the bond that breaks at the time of the ionization process [35, 36]. Thus, for linear molecules in the axial recoil approximation, the recoil direction is taken to be the same as the *z* axis in the molecular frame.

9.4.1

MFPADs for Linear Molecules in the Axial Recoil Approximation

For linear molecules, we can modify the expressions of the MFPADs in Eqs. (9.22)–(9.24) to explicitly include the effects of degeneracy in the initial and final ion states. That is, we must sum over all degenerate final states and average over the degenerate initial states. Here, we will not include spin-orbit interactions, in which case the degenerate electronic states can be identified by the angular momentum about

the molecular axis. We will write M_i for the electronic angular momentum about the molecular axis of the initial state, which has a degeneracy of g_i , and M_f for the corresponding angular momentum of the ion state. Thus, for an electronic Π state, the values for M will be ± 1 and $g = 2$. With the sum and average over degenerate states in linear molecules, the only nonzero terms remaining in the MFPAD as given in Eq. (9.19) are those with $\nu = 0$. Therefore, the number of $F_{N,\nu}^{(L)}$ functions describing the MF differential cross-section is reduced to 4 and 5 for linearly and elliptically polarized light, respectively, and the $G_{L',L,N,0}$ can be written in terms of the partial-wave dipole matrix elements as

$$\begin{aligned} G_{L',L,N,0} = & \frac{4\pi^2 E}{g_i c} \sum_{M_i, M_f} \sum_{l, l', m, \mu} (-1)^{N+m+\mu+1} I_{l m \mu}^{(M_i, M_f)} \left[I_{l', m+N, \mu-N}^{(M_i, M_f)} \right]^* \\ & \times [(2l+1)(2l'+1)]^{\frac{1}{2}} \langle 1, 1, \mu, N-\mu | L, N \rangle \langle 1, 1, 1, -1 | L, 0 \rangle \\ & \times \langle l, l', m, -(m+N) | L', -N \rangle \langle l, l', 0, 0 | L', 0 \rangle . \end{aligned} \quad (9.26)$$

The corresponding differential cross-sections can then be obtained from Eqs. (9.22)–(9.24) by limiting the sums to include only $\nu = 0$ terms, thus leading to explicit equations for the MFPADs as presented previously for linear molecular systems for ionization by linearly [9], circularly [10], and elliptically [11] polarized light, respectively. It is noteworthy that, out of the five $F_{N,0}^{(L)}$ functions containing the information extracted from a photoionization experiment performed with elliptically polarized light, four are identical to those obtained from an experiment using linearly polarized light. Therefore, a single measurement using elliptically (or circularly) polarized light results in a complete experiment. $F_{1,0}^{(1)}$ is the additional function obtained when the incoming light has a nonzero helicity and characterizes the molecular frame circular dichroism [8, 11, 16, 20, 24]. It constitutes a sensitive probe of the relative phases of the partial-wave dipole matrix elements describing the parallel and perpendicular components of the photoionization transition, which involve molecular states of different symmetries in the ionization continuum. Considering the issue of the experimental determination of MFPADs, we also stress that once the set of $F_{N,0}^{(L)}$ functions is obtained from the measured angular distribution $T(\chi, \gamma, \theta_k, \phi_k)$, based on the general form of Eqs. (9.22)–(9.24), one is able to plot the $T(\theta_k, \phi_k)$ MFPADs for any well-defined orientation χ of the molecular axis with respect to the polarization axis of linearly polarized light, or the propagation axis of circularly polarized light and is performed by inserting the chosen orientation in Eqs. (9.23) or (9.24), and taking advantage of the statistics of the complete set of data. (Note that in the previously published equations [11] for elliptically polarized light, expressions involving β had the wrong sign in front of this angle.) For the PI of linear molecules from an initial neutral state of Σ^+ symmetry to an ionic state of the same Σ^+ symmetry, which is often met in K-shell ionization of diatomic molecules such as CO or N₂, the number of independent $F_{N,0}^{(L)}$ functions reduces further to 3 for linearly polarized light [76] and to 4 for elliptically polarized light. The same is true for a $\Sigma^- \rightarrow \Sigma^-$ transition.

9.4.2

MFPADs for Nonlinear Molecules in the Axial Recoil Approximation

We now turn to nonlinear molecules. When only two fragments are produced in the dissociative ionization process, there remains an unobserved angle in the experiment, namely the orientation of the molecule about the recoil direction. In Figure 9.3, this angle is denoted by the angle α and the z axis is coincident with the recoil axis. In the axial recoil approximation, z is the axis defined by the bond that breaks in the photoionization reaction at the moment of ionization. The observed PAD relative to the recoil direction is then the *recoil frame* photoelectron angular distribution (RFPAD). To obtain the RFPAD from computed matrix elements, one must average over different orientations of the molecule, which can be obtained by a rotation about the recoil axis. Introducing the orientation of a molecule about the recoil axis, as parameterized by the angle α in Figure 9.3, into Eq. (9.19) gives

$$\begin{aligned} T_{i,f}(\theta_k, \phi_k, \gamma, \chi, \beta, \alpha) = & \sum_{\nu} \operatorname{Re} \left(\exp[i\nu(\gamma - \alpha)] \left\{ F_{0,\nu}^{(0)}(\theta_k) \exp[i\nu(\phi_k - \gamma)] \right. \right. \\ & + \sum_{N=0}^1 i s_3 F_{N,\nu}^{(1)}(\theta_k) P_1^N(\cos \chi) \exp[i(N+\nu)(\phi_k - \gamma)] \\ & + \sum_{N=0}^2 F_{N,\nu}^{(2)}(\theta_k) \left[-\frac{1}{2} P_2^N(\cos \chi) + t_1(\beta) Q_N^+(\chi) - i t_2(\beta) Q_N^-(\chi) \right] \\ & \left. \times \exp[i(N+\nu)(\phi_k - \gamma)] \right\} . \end{aligned} \quad (9.27)$$

Then, averaging over α using

$$T_{i,f}^{(\text{RF})}(\theta_k, \phi_k, \gamma, \chi, \beta) = \frac{1}{2\pi} \int_0^{2\pi} T_{i,f}(\theta_k, \phi_k, \gamma, \chi, \beta, \alpha) d\alpha , \quad (9.28)$$

leads to all terms with $\nu \neq 0$ averaging to zero. This gives the following expression for the RFPAD:

$$\begin{aligned} T_{i,f}^{(\text{RF})}(\theta_k, \phi_k, \gamma, \chi, \beta) & = \operatorname{Re} \left\{ F_{0,0}^{(0)}(\theta_k) + \sum_{N=0}^1 i s_3 F_{N,0}^{(1)}(\theta_k) \right. \\ & \times P_1^N(\cos \chi) \exp[iN(\phi_k - \gamma)] \\ & + \sum_{N=0}^2 F_{N,0}^{(2)}(\theta_k) \left[-\frac{1}{2} P_2^N(\cos \chi) + t_1(\beta) Q_N^+(\chi) - i t_2(\beta) Q_N^-(\chi) \right] \\ & \left. \times \exp[iN(\phi_k - \gamma)] \right\} . \end{aligned} \quad (9.29)$$

For molecules that have a reflection symmetry plane that contains the recoil axis, this equation leads to

$$\begin{aligned}
 T_{i,f}^{(\text{RF})} & (\theta_k, \phi_k, \gamma, \chi, \beta) \\
 &= F_{0,0}^{(0)}(\theta_k) - \sum_{N=0}^1 s_3 F_{N,0}^{(1)}(\theta_k) \times P_1^N(\cos \chi) \sin[N(\phi_k - \gamma)] \\
 &\quad + \sum_{N=0}^2 F_{N,0}^{(2)}(\theta_k) \left\{ \left[-\frac{1}{2} P_2^N(\cos \chi) + t_1(\beta) Q_N^+(\chi) \right] \cos[N(\phi_k - \gamma)] \right. \\
 &\quad \left. + t_2(\beta) Q_N^-(\chi) \sin[N(\phi_k - \gamma)] \right\}, \tag{9.30}
 \end{aligned}$$

which has the same form as Eq. (9.22), and, by extension, to Eqs. (9.23) and (9.24) for linearly and circularly polarized light, with the restriction that $\nu = 0$. The functional form of the RFPAD is therefore identical to that obtained for the MFPAD of a linear molecule [9–11]. This same functional form can be obtained for a more general choice of recoil axis in achiral molecules, as long as one averages the RFPAD over pairs of axes that are connected by a reflection through a symmetry plane of the molecule.

Additionally, one can distinguish two cases of RFPADs based on the relationship between the recoil axis and a rotation symmetry axis of the molecule. First, if the recoil axis is parallel to a symmetry axis of the molecule, then the matrix elements for parallel and perpendicular transitions relative to the recoil axis will be distinct, leading to a closer connection between the MFPAD and RFPAD.

Second, we consider the case where the recoil direction differs from a symmetry axis. The matrix elements $I_{lm\mu}$ are then usually computed in an initial reference frame that is not simply related to the recoil frame, but where the recoil frame is obtained from the initial frame by a rotation through a second set of Euler angles $(\alpha_R, \beta_R, \gamma_R)$. One finds that Eq. (9.17) can be used if $G_{L',L,N,\nu}$ is replaced by $G_{L',L,N,\nu}^{(\alpha_R, \beta_R, \gamma_R)}$, which is characteristic of the geometry of the dissociation process and is defined by [77]

$$\begin{aligned}
 G_{L',L,N,\nu}^{(\alpha_R, \beta_R, \gamma_R)} &= \sum_{J,N',\nu'} G_{L',L,N',\nu''} \left(\frac{2J+1}{2L'+1} \right) \langle J, L, \nu, N | L', N + \nu \rangle \\
 &\quad \times \langle J, L, \nu', N' | L', N' + \nu' \rangle \left[D_{\nu',\nu}^{(J)}(\alpha_R, \beta_R, \gamma_R) \right]^*. \tag{9.31}
 \end{aligned}$$

Dissociative photoionization of the $\text{C}_{2\nu}\text{NO}_2$ molecule into $(\text{NO}^+ + \text{O} + e)$ is an example where this formalism has been applied [77]. In this case, the RFPAD averaging always mixes at least two different transition dipole symmetry directions, that is, x with y , x with z , or y with z , making it more difficult to extract the underlying MFPAD from an observed RFPAD.

9.4.3

Breakdown of the Axial Recoil Approximation Due to Rotation

When the axial recoil approximation is not valid and the molecule breaks into only two fragments, the measured post-orientation PAD corresponds to an RFPAD that is not the same as the MFPAD. The axial recoil approximation can fail for two reasons: either the dissociative state has a lifetime that is long as compared to rotation, or nuclear vibrational motion before dissociation affects the recoil direction. In both cases, the recoil direction is not the same as the original orientation of the bond that breaks. For diatomic molecules, the axial recoil approximation will only break down when the molecule has time to rotate before the dissociation. If the dissociation can be modeled as a unimolecular process with lifetime τ then one obtains the functional form of the differential cross-section $T_{i,f}$ for diatomic molecules and, more generally, for linear molecules. Here, the $F_{N,0}^{(L)}$ are modified to include the effects of rotation that occurs before dissociation, leading to [10]

$$F_{N,\nu}^{(L,\tau)}(\theta_k) = \frac{1}{Q(T)} \sum_{J,J',J''} F_{N,0}^{(L,J,J',J'')}(\theta_k) \exp\left[\frac{-B'' J'' (J'' + 1)}{kT}\right] \times \frac{(2J'' + 1)}{1 + i \frac{\tau B'}{\hbar} [J'(J' + 1) - J(J + 1)]}, \quad (9.32)$$

where we have assumed a thermal distribution of initial rotational states with temperature T , with rotational partition function $Q(T)$, an initial state rotational constant B'' and final state rotational constant B' . The rotational state-specific $F_{N,0}^{(L,J,J',J'')}(\theta_k)$ are then defined in terms of rotational state-specific $G_{L',L,N,0}^{(J,J',J'')}$, using the relationship given in Eq. (9.17) between F and G , which is defined in terms of rotational state-specific dipole matrix elements using, in analogy to Eq. (9.26),

$$G_{L',L,N,0}^{(J,J',J'')} = \frac{4\pi^2 E}{g_i c} \sum_{M_i, M_f} \sum_{l, l', m, \mu} (-1)^{N+m+\mu+1} I_{l,m,\mu}^{(J',M_f,J'',M_i)} \left[I_{l',m+N,\mu-N}^{(J,M_f,J'',M_i)} \right]^* \times [(2l+1)(2l'+1)]^{\frac{1}{2}} \langle 1, 1, \mu, N-\mu | L, N \rangle \langle 1, 1, 1, -1 | L, 0 \rangle \times \langle l, l', m, -(m+N) | L', -N \rangle \langle l, l', 0, 0 | L', 0 \rangle, \quad (9.33)$$

where the rotational state-specific dipole matrix elements are defined as

$$I_{l,m,\mu}^{(J,M_f,J'',M_i)} = \sum_{m',\mu'} I_{l,m',\mu'}^{(M_i,M_f)} (-1)^{m+\mu+M_f+M_i} \frac{2J+1}{2J''+1} \times \sum_K \langle K, J, m+\mu, M_f | J'', m+\mu+M_f \rangle \times \langle K, J, M_i-M_f, M_f | J'', M_i \rangle \langle l, 1, m, \mu | K, m+\mu \rangle \times \langle l, 1, m', \mu' | K, M_i-M_f \rangle. \quad (9.34)$$

9.4.4

Breakdown of the Axial Recoil Approximation Due to Vibrational Motion

For polyatomic molecules, motion of the nuclei between the moment of ionization and fragmentation can change the geometry of the molecule, leading to changed bond angles, rearrangement, or isomerization. This can lead to a recoil direction that is different from the axis of the breaking bond at the time of ionization, thus the axial recoil approximation can fail. In particular, for linear polyatomic molecules, molecular bending before dissociation can lead to a breakdown of the axial recoil approximation. In this case, the situation becomes comparable to the case of DPI of a nonlinear molecule, when the recoil direction differs from a symmetry axis, as discussed above. If the angle between the initial direction of the molecular axis and the recoil direction is β_R , where β_R is the same angle as in Eq. (9.31), one obtains the $F_{N,0}^{(L,\beta_R)}(\theta_k)$ that include the effects of the bending motion and are given by Eq. (9.17). Here, $G_{L',L,N',0}$, as defined in Eq. (9.18), has been replaced by the related $G_{L',L,N',0}^{(\beta_R)}$, which is defined by [78]

$$G_{L',L,N,0}^{(\beta_R)} = \sum_{J,N'} \langle L', L, N, -N | J, 0 \rangle \langle L', L, N', -N' | J, 0 \rangle \\ \times P_J^0(\cos \beta_R) (-1)^{N'-N} G_{L',L,N',0}. \quad (9.35)$$

9.4.5

Electron Frame Photoelectron Angular Distributions

When the RFPAD only contains the $F_{N,0}^{(L)}$ functions with $\nu = 0$, (as for example for linearly polarized light) and assuming that a 4π collection of photoelectrons and recoil ions is achieved experimentally, it is easy to determine the four functions $F_{N,0}^{(L)}$ with a very good accuracy by a fit of the experimental data to the equation

$$T_{i,f}^{(\text{LP})} = \sum_{L=0,2} \sum_{N=0}^L F_{N,0}^{(L)}(\theta_k) P_L^N(\cos \chi_{\text{LP}}) \cos[N(\phi_k - \gamma_{\text{LP}})]. \quad (9.36)$$

This is equivalent to a (χ, ϕ) 2D Fourier transform of the measured distribution [9, 10]. Alternatively, four pairs of values of χ_{LP} and $(\phi_k - \gamma_k)$ [79] constitute the minimum number of fixed space directions at which the $I(\theta_k)$ distribution must be measured to give access to the four $F_{N,0}^{(L)}$ functions. Using a coincidence dissociative ionization experiment to determine the MFPAD with the detection at a few fixed molecular axes orientations relative to the field therefore requires the measurement of photoelectrons at a range of angles relative to the light polarization. Depending on the experimental geometry and detection schemes, it may be advantageous to instead use detection in the electron frame (EF). In this case [80]

$$T_{i,f}^{(\text{LP}, \text{EF})} = \sum_{L=0,2} \sum_{N=0}^L F_{N,0}^{(L,\text{EF})}(\theta_k) P_L^N(\cos \chi_{\text{EF}}) \cos[N(\phi_{\text{EF}} - \gamma_{\text{EF}})] \quad (9.37)$$

where θ_k is the same polar angle between the direction of emission of the photo-electron and the recoil axis, χ_{EF} is the angle between the direction of the field polarization and the direction of emission of the photoelectron, ϕ_{EF} is the azimuthal angle of the recoil axis in the electron frame and γ_{EF} is the azimuthal angle of the polarization direction in the electron frame. In this frame, one can determine the electron frame photoelectron angular distribution (EFPAD) by detecting the photo-electrons at a few orientations relative to the field orientation, while measuring the full angular range of ionic fragment emission. Once the $F_{N,0}^{(L,\text{EF})}(\theta_k)$ functions have been determined, a simple rotation recovers the molecular frame (MF) functions $F_{N,0}^{(L,\text{MF})}(\theta_k)$ [81],

$$F_{N,0}^{(L,\text{MF})}(\theta_k) = \sum_{N'} \left[\frac{(L-N)!(L+N')!}{(L+N)!(L-N')!} \right]^{\frac{1}{2}} \frac{(-1)^{N'}}{1 + \delta_{N,0}} \\ \times \left[d_{-N,-N'}^{(L)}(\theta_k) + (-1)^N d_{N,-N'}^{(L)}(\theta_k) \right] F_{N,0}^{(L,\text{EF})}(\theta_k). \quad (9.38)$$

9.5

MFPADs from Concurrent Orientation in Multiphoton Ionization

Photoelectron angular distributions in multiphoton ionization can differ from single-photon ionization in a number of ways, depending on the nature of the multiphoton process and the observables measured. We will limit the discussion here to the consideration of the case where the multiphoton process can be viewed as an $n+1$ process, where all ionization events proceed through the same final bound state. In the considered case, the bound state is reached by the absorption of n photons, with the final photon leading to ionization. The absorption of the first n photons can lead to a distribution of excited molecules that is no longer isotropic. Ionization then occurs from a partially oriented sample. If the photoelectrons are detected relative to the polarization axis, more information is obtained about the MFPAD than can be gleaned from an experiment with randomly oriented molecules. However, if the molecule is ionized to a dissociative state and the photoelectron and one of the fragments are detected in coincidence, the amount of information available is more than that available from a simple RFPAD and approaches that of the full MFPAD for a nonlinear system. The multiphoton ionization will also yield information about the ionization dynamics of excited states, which are not easily obtained from traditional one-photon experiments. In this section, we will consider the MFPAD information available in multiphoton coincidence experiments.

For a single bound-to-bound transition between two states Ψ_i and Ψ_f in the RWA, the matrix element needed to obtain the angular dependence of the transition in the molecular frame can be written in terms of the transition dipole t_{if} defined as

$$t_{if} = \langle \Psi_i | x | \Psi_f \rangle \hat{x} + \langle \Psi_i | y | \Psi_f \rangle \hat{y} + \langle \Psi_i | z | \Psi_f \rangle \hat{z}. \quad (9.39)$$

Then, for the field as given in Eq. (9.5) the transition amplitude matrix element

$$I_{if} = \langle \Psi_i | \mathbf{r} \cdot \mathbf{A} | \Psi_f \rangle \quad (9.40)$$

is given by

$$\mathbf{t}_{if} = \mathbf{t}_{if} \cdot \mathbf{A}. \quad (9.41)$$

In the dipole approximation, in analogy to Eq. (9.7) we have for general elliptical polarization

$$\mathbf{t}_{if} = (\mathbf{t}_{if} \cdot \hat{\mathbf{x}}_{\text{FF}}) \cos \lambda + (\mathbf{t}_{if} \cdot \hat{\mathbf{y}}_{\text{FF}}) \sin \lambda \exp(i\delta). \quad (9.42)$$

The transition dipole \mathbf{t}_{if} can be written in terms of a spherical polar vector with angles (θ_{if}, ϕ_{if}) in the molecular frame, so that in the recoil frame we have

$$\begin{aligned} \mathbf{t}_{if} &= t_{if} [\sin \theta_{if} \cos(\phi_{if} + \alpha) \hat{\mathbf{x}}_{\text{RF}} \\ &\quad + \sin \theta_{if} \sin(\phi_{if} + \alpha) \hat{\mathbf{y}}_{\text{RF}} + \cos \theta_{if} \hat{\mathbf{z}}_{\text{RF}}] . \end{aligned} \quad (9.43)$$

Following the work of Dixon and others [82]–[86], the one-color $n + 1$ -photon absorption amplitude in the lowest order of perturbation theory and within the RWA has the form

$$\begin{aligned} J_{if}^{(n+1)} &= \sum_{k_1} \sum_{k_2} \cdots \sum_{k_{n-1}} \frac{\langle \Psi_i | \mathbf{r} \cdot \mathbf{A} | \psi_{k_1} \rangle \left\{ \prod_{j=2}^n \langle \psi_{k_{j-1}} | \mathbf{r} \cdot \mathbf{A} | \psi_{k_j} \rangle \right\} \langle \psi_{k_n} | \mathbf{r} \cdot \mathbf{A} | \Psi_f \rangle}{\prod_{j=1}^n (\Delta E_{k_j i} - j h\nu + i\Gamma_{k_j})}, \end{aligned} \quad (9.44)$$

where the intermediate states ψ_k have a homogeneous half-width of Γ_k and an energy E_k higher than the energy E_i of the initial state by $\Delta E_{k i} = E_k - E_i$. In general, such a transition can have a very complicated angular dependence if different pathways contribute to the transition. In order to simplify the discussion, we will assume that there is a single set of real states, $\psi_1, \psi_2, \dots, \psi_n$ that are nearly resonant in the n -photon process, so that the transition intensity can be written in terms of the square of the matrix element $I_{if}^{(n+1)}$ defined as

$$I_{if}^{(n+1)} = \langle \Psi_i | \mathbf{r} \cdot \mathbf{A} | \psi_1 \rangle \left\{ \prod_{k=2}^n \langle \psi_{k-1} | \mathbf{r} \cdot \mathbf{A} | \psi_k \rangle \right\} \langle \psi_n | \mathbf{r} \cdot \mathbf{A} | \Psi_f \rangle. \quad (9.45)$$

This formalism has been applied, for example, to analyze the recoil anisotropy for four-photon-induced dissociation of the C_2vNO_2 molecule, leading to the $(\text{NO}^+, \text{O}^-)$ ion pair formation [87]. Alternatively, if the first n transitions are bound-to-bound and the $n + 1$ transition is into the continuum, from Eqs. (9.3), (9.7), and (9.41) one obtains

$$\begin{aligned} I_{if}^{(n+1)} &= (\mathbf{t}_{i,1} \cdot \mathbf{A}) \left\{ \prod_{k=2}^n \mathbf{t}_{k-1,k} \cdot \mathbf{A} \right\} \\ &\quad \times \left\langle \psi_n | (\mathbf{r} \cdot \hat{\mathbf{x}}_{\text{FF}}) \cos \lambda + (\mathbf{r} \cdot \hat{\mathbf{y}}_{\text{FF}}) \sin \lambda \exp(i\delta) | \Psi_{f,k}^{(-)} \right\rangle. \end{aligned} \quad (9.46)$$

As before, this can be given a compact form if the light is linearly polarized or circularly polarized, as in Eq. (9.16)

$$\begin{aligned} I_{if}^{(n+1,\mu_0)} &= (\mathbf{t}_{i,1} \cdot \mathbf{A}) \left\{ \prod_{k=2}^n \mathbf{t}_{k-1,k} \cdot \mathbf{A} \right\} \\ &\times \sum_{l,m,\mu} I_{lm\mu}^{(n,f)} Y_{lm}^*(\theta_k, \phi_k - \alpha) D_{\mu,-\mu_0}^{(1)}(\gamma - \alpha, \chi, \beta). \end{aligned} \quad (9.47)$$

Now the final cross-section for ionization is proportional to the square of the amplitude, so that we have

$$T_{if}^{(n+1)} = I_{if}^{(n+1)} \left[I_{if}^{(n+1)} \right]^*. \quad (9.48)$$

Assuming that all ionization occurs through the same n th bound state, the cross-section can then be factored into a bound-to-bound part of the form

$$T_{i,n} = |\mathbf{t}_{i,1} \cdot \mathbf{A}|^2 \left\{ \prod_{k=2}^n |\mathbf{t}_{k-1,k} \cdot \mathbf{A}|^2 \right\} \quad (9.49)$$

and the bound to continuum term of the form

$$T_{n,f} = \left| \langle \psi_n | (\mathbf{r} \cdot \hat{\mathbf{x}}_{FF}) \cos \lambda + (\mathbf{r} \cdot \hat{\mathbf{y}}_{FF}) \sin \lambda \exp(i\delta) | \Psi_{f,k}^{(-)} \rangle \right|^2, \quad (9.50)$$

so that the full cross-section is given by

$$T_{if}^{(n+1)} = T_{i,n} T_{n,f}. \quad (9.51)$$

To obtain an expression for the $n + 1$ photon RFPAD, we explicitly factor out the orientation dependence about the recoil axis in the bound-to-bound part of the transition probability, $T_{i,n}$, to give

$$T_{i,n} = \sum_{\nu=-2n}^{2n} H_{\nu}^{(\lambda,\delta)}(\chi, \beta) \exp[-i\nu(\gamma - \alpha)]. \quad (9.52)$$

The function $T_{i,n}$ can be evaluated for many different pathways of the bound-to-bound part of the process, however, if we make the same single pathway assumption as we did above, we obtain Eq. (9.49). Combining Eq. (9.27) with Eq. (9.52) we obtain the MFPAD given in Eq. (9.51) as

$$\begin{aligned} T_{if}^{(n+1,RF)} &= \sum_{\nu=-2n}^{2n} \operatorname{Re} \left\{ H_{\nu}^{(\lambda,\delta)}(\chi, \beta) \left[F_{0,\nu}^{(0)}(\theta_k) \exp[i\nu(\phi_k - \gamma)] \right. \right. \\ &+ \sum_{N=0}^1 i s_3 F_{N,\nu}^{(1)}(\theta_k) P_1^N(\cos \chi) \exp[i(N+\nu)(\phi_k - \gamma)] \\ &+ \sum_{N=0}^2 F_{N,\nu}^{(2)}(\theta_k) \left\{ -\frac{1}{2} P_2^N(\cos \chi) + \left[t_1 Q_N^+(\chi) - i t_2 Q_N^-(\chi) \right] \right\} \\ &\times \left. \left. \exp[i(N+\nu)(\phi_k - \gamma)] \right] \right\}. \end{aligned} \quad (9.53)$$

This can again be simplified for circularly polarized light to be

$$\begin{aligned} T_{fi}^{(n+1,\text{CPRF})} = & \sum_{\nu=-2n}^{2n} \operatorname{Re} \left\{ H_{\nu}^{(\lambda,\delta)}(\chi) \left[F_{0,\nu}^{(0)}(\theta_k) \exp[i\nu(\phi_k - \gamma)] \right. \right. \\ & \mp i \sum_{N=0}^1 F_{N,\nu}^{(1)}(\theta_k) P_1^N(\cos \chi) \exp[i(N+\nu)(\phi_k - \gamma)] \\ & \left. \left. - \frac{1}{2} \sum_{N=0}^2 F_{N,\nu}^{(2)}(\theta_k) P_2^N(\cos \chi) \exp[i(N+\nu)(\phi_k - \gamma)] \right] \right\} \end{aligned} \quad (9.54)$$

and for linearly polarized light to

$$\begin{aligned} T_{fi}^{(n+1,\text{LPRF})} = & \sum_{\nu=-2n}^{2n} \operatorname{Re} \left\{ H_{\nu}^{(\text{LP})}(\chi_{\text{LP}}) \sum_{L=0,2} \sum_{N=0}^L F_{N,\nu}^{(L)}(\theta_k) P_L^N(\cos \chi_{\text{LP}}) \right. \\ & \times \exp[i(\nu + N)(\phi_k - \gamma_{\text{LP}})] \left. \right\} \end{aligned} \quad (9.55)$$

where the one-dimensional $F_{N,\nu}^{(L)}$ are those defined by Eqs. (9.17) and (9.18) and where the dipole matrix elements used in Eq. (9.18) are the $I_{l,m,\mu}^{(n,f)}$ as found in Eq. (9.47). If the recoil axis contains a reflection plane of symmetry and if we define the rotation about the recoil axis (the angle α in Figure 9.3) relative to the symmetry plane, then $H_{\nu}^{(n,\lambda,\delta)}(\chi, \beta)$ and $F_{N,\nu}^{(L)}(\theta_k)$ will be real valued and Eq. (9.53) will be simplified. In this case, and with linearly polarized light, Eq. (9.55) will reduce to

$$\begin{aligned} T_{fi}^{(n+1,\text{LPRF})} = & \sum_{\nu=-2n}^{2n} H_{\nu}^{(n,\text{LP})}(\chi_{\text{LP}}) \\ & \times \sum_{L=0,2} \sum_{N=0}^L F_{N,\nu}^{(L)}(\theta_k) P_L^N(\cos \chi_{\text{LP}}) \cos[(\nu + N)(\phi_k - \gamma_{\text{LP}})] \end{aligned} \quad (9.56)$$

and for left/right circularly polarized light we have

$$\begin{aligned} T_{fi}^{(n+1,\text{CPRF})} = & \sum_{\nu=-2n}^{2n} H_{\nu}^{(n,\lambda,\delta)}(\chi) \left[F_{0,\nu}^{(0)}(\theta_k) \cos[\nu(\phi_k - \gamma)] \right. \\ & \pm \sum_{N=0}^1 F_{N,\nu}^{(1)}(\theta_k) P_1^N(\cos \chi) \sin[(N+\nu)(\phi_k - \gamma)] \\ & \left. - \frac{1}{2} \sum_{N=0}^2 F_{N,\nu}^{(2)}(\theta_k) P_2^N(\cos \chi) \cos[(N+\nu)(\phi_k - \gamma)] \right]. \end{aligned} \quad (9.57)$$

We can see that, in the multiphoton case, a finite number of the one-dimensional $F_{N,\nu}^{(L)}$ functions are needed to describe the full multiphoton RFPAD. There will be at most $24n + 6$ one-dimensional functions, where n is the number of bound-to-bound transitions involved. We note, however, that the number of such functions is significantly increased over the one-photon photoionization case where $n = 0$, therefore appropriate strategies must be developed for the data analysis. We can also see that the multiphoton RFPAD can provide access to a subset of the full set of $F_{N,\nu}^{(L)}$ functions needed to evaluate the MFPAD for a general nonlinear polyatomic molecule as used in Eq. (9.19).

9.6

Pre-orientation or Alignment, Impulsive Alignment

One method for producing preoriented molecules is impulsive nonadiabatic laser alignment [42–44]. With a short infrared laser pulse, it is possible to form a rotational wave packet that has alignment recurrences at fixed time intervals after the aligning pulse. If the photoionization event occurs at one of the recurrences (or anti-recurrences), then the PAD can be obtained by an average over appropriate angular distributions of the molecules [39–41]. This approach for obtaining MFPAD information can be applied to any ionization process, since it does not depend on the ion state being a dissociative state, as in the case of post-orientation discussed above.

If one uses a linearly polarized alignment laser, then the distribution of orientations of the molecules at the time of ionization will have a cylindrical symmetry about the direction of the laser polarization, which can be described as

$$\rho(\chi_{\text{OF}}) = \sum_K c_K P_K (\cos \chi_{\text{OF}}) \quad (9.58)$$

where χ_{OF} is the angle between the MF z axis and the polarization direction of the aligning laser. Then it is possible to show that the orientation-frame photoelectron angular distribution (OFPAD) $T_{i,f}^{(\rho)}(\Omega_K, \hat{S}_{\text{OF}})$ can be obtained using Eq. (9.29) where \hat{S}_{OF} are the Euler angles that describe the elliptical light polarization in the orientation frame (OF), $\hat{\Omega}_K$ gives the direction of emission of the photoelectron in the OF and where the $F_{N,0}^{(L)}$ are defined using Eq. (9.17). The $G_{L',L,N,0}^{(\rho)}$ are defined by

$$\begin{aligned} G_{L',L,N,0}^{(\rho)} = & \frac{4\pi^2 E}{c} \sum_K c_K \frac{[4\pi(2L'+1)]^{\frac{1}{2}}}{2K+1} \sum_{\substack{l,m,n,\mu,\nu,j \\ l',m',\mu',j'}} (-1)^{-N-1-(m+\mu)} I_{lm\mu} I_{l',m',\mu'}^* \\ & \times \langle l, 1, n, \nu | J, n + \nu \rangle \langle l, 1, m, \mu | J, m + \mu \rangle \langle l', 1, N + n, \nu - N | J', n + \nu \rangle \\ & \times \langle l', 1, m', \mu' | J', m + \mu \rangle \langle 1, 1, \nu, N - \nu | L, N \rangle \langle 1, 1, 1, -1 | L, 0 \rangle \\ & \times \langle l, l', 0, 0 | L', 0 \rangle \langle l, l', -n, N + n | L', N \rangle \langle J, J', -(n + \nu), n + \nu | K, 0 \rangle \\ & \times \langle J, J', -(m + \mu), m + \mu | K, 0 \rangle . \end{aligned} \quad (9.59)$$

When the molecule has a plane of symmetry that contains the molecular axis, the $F_{N,0}^{(L)}$ are real valued and the expressions for the OFPAD then simplify to be equivalent to those given in Eqs. (9.22)–(9.24) with $\nu = 0$. This formalism has not been previously applied, although the equivalent result has been obtained by a numerical averaging of the MFPAD over a measured molecular orientation distribution [41].

9.7 Conclusions

We have considered a variety of forms for the MFPAD. In its most general form for a nonlinear molecular system, the MFPAD can be written in harmonic expansions relative to the field orientation and as a function of the azimuthal angle of the photoelectron direction relative to the molecular axis. This leads to a sequence of one-dimensional $F_{N,\nu}^{(L)}(\theta_k)$ functions of the angle between the MF z axis and the direction of emission of the photoelectron. These functions provide access to the complex-valued partial-wave dipole matrix elements, which are the basic dynamical parameters for describing the photoionization process. For one-photon transitions in a number of cases for linear molecules and for polyatomic molecules when the molecular orientation is averaged over an unobserved azimuthal angle, the sum over $F_{N,\nu}^{(L)}$ functions can be reduced to only a few terms. This approach can be used to describe the PADs for post-orientation, concurrent orientation, multiphoton ionization, and pre-orientation. With further development of both the theoretical and experimental tools, the MFPADs should become a useful tool for studying both electronic and nuclear dynamics in molecular systems.

Acknowledgements

The authors gratefully acknowledge the support of the CNRS through the PICS France-USA CNRS contract. RRL acknowledges the support of the Robert A. Welch Foundation (Houston, Texas) under grant A-1020 and the support of the Chemical Sciences, Geosciences and Biosciences Division, Office of Basic Energy Sciences, Office of Science, U.S. Department of Energy and the CNRS for a three-month invited researcher position.

References

- 1** Dill, D. (1976) Fixed-molecule photoelectron angular distributions. *J. Chem. Phys.*, **65**, 1130–1133.
- 2** Golovin, A.V., Cherepkov, N.A., and Kuznetsov, V.V. (1992) Photoionization of oriented molecules in a gas-phase. *Z. Phys. D*, **24**, 371–375.
- 3** Shigemasa, E., Adachi, J., Oura, M., and Yagishita, A. (1995) Angular distributions of $1s\sigma$ photoelectrons from fixed-in-space N_2 molecules. *Phys. Rev. Lett.*, **74**, 359–362.
- 4** Downie, P. and Powis, I. (1999) Molecular-frame photoelectron angu-

- lar distributions from oriented CF_3I molecules. *Phys. Rev. Lett.*, **82**, 2864–2867.
- 5** Eland, J.H.D., Takahashi, M., and Hikosaka, Y. (2000) Photoelectron-fragment ion correlations and fixed molecule photoelectron angular distributions from velocity imaging coincidence experiments. *Faraday Discuss.*, **115**, 119–126.
- 6** Lafosse, A., Lebech, M., Brenot, J.C., Guyon, P.M., Jagutzki, O., Spielberger, L., Vervloet, M., Houver, J.C., and Dowek, D. (2000) Vector correlations in dissociative photoionization of diatomic molecules in the VUV range: Strong anisotropies in electron emission from spatially oriented NO molecules. *Phys. Rev. Lett.*, **84**, 5987–5990.
- 7** Hikosaka, Y., Eland, J.H.D., Watson, T.M., and Powis, I. (2001) Molecule frame photoelectron angular distributions from oriented methyl chloride and methyl fluoride molecules. *J. Chem. Phys.*, **115**, 4593–4603.
- 8** Gessner, O., Hikosaka, Y., Zimmermann, B., Hempelmann, A., Lucchese, R.R., Eland, J.H.D., Guyon, P.-M., and Becker, U. (2002) $4\sigma^{-1}$ Inner valence photoionization dynamics of NO derived from photoelectron–photoion angular correlations. *Phys. Rev. Lett.*, **88**, 193002.
- 9** Lucchese, R.R., Lafosse, A., Brenot, J.C., Guyon, P.M., Houver, J.C., Lebech, M., Raseev, G., and Dowek, D. (2002) Polar and azimuthal dependence of the molecular frame photoelectron angular distributions of spatially oriented linear molecules. *Phys. Rev. A*, **65**, 020702.
- 10** Lafosse, A., Brenot, J.C., Guyon, P.M., Houver, J.C., Golovin, A.V., Lebech, M., Dowek, D., Lin, P., and Lucchese, R.R. (2002) Vector correlations in dissociative photoionization of O_2 in the 20–28 eV range. II. Polar and azimuthal dependence of the molecular frame photoelectron angular distribution. *J. Chem. Phys.*, **117**, 8368–8384.
- 11** Lebech, M., Houver, J.C., Lafosse, A., Dowek, D., Alcaraz, C., Nahon, L., and Lucchese, R.R. (2003) Complete description of linear molecule photoionization achieved by vector correlations using the light of a single circular polarization. *J. Chem. Phys.*, **118**, 9653–9663.
- 12** Lafosse, A., Lebech, M., Brenot, J.C., Guyon, P.M., Spielberger, L., Jagutzki, O., Houver, J.C., and Dowek, D. (2003) Molecular frame photoelectron angular distributions in dissociative photoionization of H_2 in the region of the Q_1 and Q_2 doubly excited states. *J. Phys. B*, **36**, 4683–4702.
- 13** Dowek, D., Lebech, M., Houver, J.C., and Lucchese, R.R. (2004) Photoemission in the molecular frame using the vector correlation approach: from valence to inner-valence shell ionization. *J. Electron. Spectrosc. Relat. Phenom.*, **141**, 211–227.
- 14** Kugeler, O., Prümper, G., Hentges, R., Viehhaus, J., Rolles, D., Becker, U., Marburger, S., and Hergenhahn, U. (2004) Intramolecular electron scattering and electron transfer following autoionization in dissociating molecules. *Phys. Rev. Lett.*, **93**, 033002.
- 15** Lebech, M., Houver, J.C., Dowek, D., and Lucchese, R.R. (2006) Molecular frame photoelectron emission in the presence of autoionizing resonances. *Phys. Rev. Lett.*, **96**, 073001.
- 16** Dowek, D., Pérez-Torres, J.F., Picard, Y.J., Billaud, P., Elkharrat, C., Houver, J.C., Sanz-Vicario, J.L., and Martín, F. (2010) Circular dichroism in photoionization of H_2 . *Phys. Rev. Lett.*, **104**, 233003.
- 17** Heiser, F., Gessner, O., Viehhaus, J., Wieliczek, K., Hentges, R., and Becker, U. (1997) Demonstration of strong forward-backward asymmetry in $\text{C}1s$ photoelectron angular distributions from oriented CO molecules. *Phys. Rev. Lett.*, **79**, 2435–2437.
- 18** Cherepkov, N.A., Raseev, G., Adachi, J., Hikosaka, Y., Ito, K., Motoki, S., Sano, M., Soejima, K., and Yagishita, A. (2000) K-shell photoionization of CO: II. determination of dipole matrix elements and phase differences. *J. Phys. B*, **33**, 4213–4236.
- 19** Landers, A., Weber, T., Ali, I., Cassimi, A., Hattass, M., Jagutzki, O., Nauert, A., Osipov, T., Staudte, A., Prior, M.,

- Schmidt-Böcking, H., Cocke, C., and Dörner, R. (2001) Photoelectron diffraction mapping: Molecules illuminated from within. *Phys. Rev. Lett.*, **87**, 013002.
- 20** Jahnke, T., Weber, T., Landers, A., Knapp, A., Schössler, S., Nickles, J., Kammer, S., Jagutzki, O., Schmidt, L., Czasch, A., Osipov, T., Arenholz, E., Young, A., Díez Muñoz, R., Rolles, D., García de Abajo, F., Fadley, C., Van Hove, M., Semenov, S., Cherepkov, N., Rösch, J., Prior, M., Schmidt-Böcking, H., Cocke, C., and Dörner, R. (2002) Circular dichroism in K-shell ionization from fixed-in-space CO and N₂ molecules. *Phys. Rev. Lett.*, **88**, 073002.
- 21** Motoki, S., Adachi, J., Ito, K., Ishii, K., Soejima, K., Yagishita, A., Semenov, S.K., and Cherepkov, N.A. (2002) Direct probe of the shape resonance mechanism in 2σ_g-shell photoionization of the N₂ molecule. *Phys. Rev. Lett.*, **88**, 063003.
- 22** Saito, N., Ueda, K., Fanis, A.D., Kubozuka, K., Machida, M., Koyano, I., Dorner, R., Czasch, A., Schmidt, L., Cassimi, A., Wang, K., Zimmermann, B., and McKoy, V. (2005) Molecular frame photoelectron angular distribution for oxygen 1s photoemission from CO₂ molecules. *J. Phys. B*, **38**, L277–L284.
- 23** Adachi, J., Ito, K., Yoshii, H., Yamazaki, M., Yagishita, A., Stener, M., and Declerva, P. (2007) Site-specific photoemission dynamics of N₂O molecules probed by fixed-molecule core-level photoelectron angular distributions. *J. Phys. B* **40**, 29–47.
- 24** Li, W.B., Montuoro, R., Houver, J.C., Journel, L., Haouas, A., Simon, M., Lucchese, R.R., and Dowek, D. (2007) Photoemission in the NO molecular frame induced by soft-X-ray elliptically polarized light above the N(1s)⁻¹ and O(1s)⁻¹ ionization thresholds. *Phys. Rev. A*, **75**, 052718.
- 25** Fukuzawa, H., Liu, X.J., Montuoro, R., Lucchese, R.R., Morishita, Y., Saito, N., Kato, M., Suzuki, I.H., Tamenori, Y., Teranishi, T., Lischke, T., Prümper, G., and Ueda, K. (2008) Nitrogen K-shell photoelectron angular distribution from NO molecules in the molecular frame. *J. Phys. B*, **41**, 045102.
- 26** Akoury, D., Kreidi, K., Jahnke, T., Weber, T., Staudte, A., Schöffler, M., Neumann, N., Titze, J., Schmidt, L.P.H., Czasch, A., Jagutzki, O., Fraga, R.A.C., Grisenti, R.E., Muñoz, R.D., Cherepkov, N.A., Semenov, S.K., Ranitovic, P., Cocke, C.L., Osipov, T., Adaniya, H., Thompson, J.C., Prior, M.H., Belkacem, A., Landers, A.L., Schmidt-Böcking, H., and Dörner, R. (2007) The simplest double slit: interference and entanglement in double photoionization of H₂. *Science*, **318**, 949–952.
- 27** Martin, F., Fernandez, J., Havermeier, T., Foucar, L., Weber, T., Kreidi, K., Schöffler, M., Schmidt, L., Jahnke, T., Jagutzki, O., Czasch, A., Benis, E.P., Osipov, T., Landers, A.L., Belkacem, A., Prior, M.H., Schmidt-Böcking, H., Cocke, C.L., and Dorner, R. (2007) Single photon-induced symmetry breaking of H₂ dissociation. *Science*, **315**, 629–633.
- 28** Rolles, D., Braune, M., Cvejanovic, S., Gessner, O., Hentges, R., Korica, S., Langer, B., Lischke, T., Prümper, G., Reinköster, A., Viehhaus, J., Zimmermann, B., McKoy, V., and Becker, U. (2005) Isotope-induced partial localization of core electrons in the homonuclear molecule N₂. *Nature*, **437**, 711–715.
- 29** Schöffler, M.S., Titze, J., Petridis, N., Jahnke, T., Cole, K., Schmidt, L.P.H., Czasch, A., Akoury, D., Jagutzki, O., Williams, J.B., Cherepkov, N.A., Semenov, S.K., McCurdy, C.W., Rescigno, T.N., Cocke, C.L., Osipov, T., Lee, S., Prior, M.H., Belkacem, A., Landers, A.L., Schmidt-Böcking, H., Weber, T., and Dörner, R. (2008) Ultrafast probing of core hole localization in N₂. *Science*, **320**, 920–923.
- 30** Rolles, D., Prümper, G., Fukuzawa, H., Liu, X.J., Pešia, Z., Fink, R., Grum-Grzhimailo, A., Dumitriu, I., Berrah, N., and Ueda, K. (2008) Molecular-frame angular distributions of resonant CO:C(1s) Auger electrons. *Phys. Rev. Lett.*, **101**, 263002.
- 31** Liu, X.J., Fukuzawa, H., Teranishi, T., De Fanis, A., Takahashi, M., Yoshida, H., Cassimi, A., Czasch, A., Schmidt, L., Dorner, R., Wang, K., Zimmermann, B., McKoy, V., Koyano, I., Saito, N., and

- Ueda, K. (2008) Breakdown of the Two-Step Model in K-shell photoemission and subsequent decay probed by the molecular-frame photoelectron angular distributions of CO₂. *Phys. Rev. Lett.*, **101**, 083001.
- 32** Sturm, F.P., Schöffler, M., Lee, S., Osipov, T., Neumann, N., Kim, H.K., Kirschner, S., Rudek, B., Williams, J.B., Daughhetee, J.D., Cocke, C.L., Ueda, K., Landers, A.L., Weber, T., Prior, M.H., Belkacem, A., and Dorner, R. (2009) Photoelectron and Auger-electron angular distributions of fixed-in-space CO₂. *Phys. Rev. A*, **80**, 032506.
- 33** Yamazaki, M., Adachi, J.-I., Teramoto, T., Yagishita, A., Stener, M., and Declava, P. (2009) 3D mapping of photoemission from a single oriented H₂O molecule. *J. Phys. B*, **42**, 051001.
- 34** Tully, J.C., Berry, R.S., and Dalton, B.J. (1968) Angular distribution of molecular photoelectrons. *Phys. Rev.*, **176**, 95–105.
- 35** Zare, R.N. (1967) Dissociation of H₂⁺ by electron impact: calculated angular distribution. *J. Chem. Phys.*, **47**, 204–215.
- 36** Zare, R.N. (1972) Photoejection dynamics. *Molec. Photochem.*, **4**, 1–37.
- 37** Dowek, D. and Lucchese, R.R. (2011) Photoionization dynamics: photoemission in the molecular frame of small molecules ionized by linearly and elliptically polarized light, in *Dynamical Processes in Atomic and Molecular Physics*, (ed. G. Ogu), Bentham, Bussum, Netherlands, pp. 57–95.
- 38** Vredenborg, A., Roeterdink, W.G., and Janssen, M.H. (2008) Femtosecond time-resolved photoelectron–photoion coincidence imaging of multiphoton multichannel photodynamics in NO₂. *J. Chem. Phys.*, **128**, 204311.
- 39** Thomann, I., Lock, R., Sharma, V., Gagnon, E., Pratt, S.T., Kapteyn, H.C., Murnane, M.M., and Li, W. (2008) Direct measurement of the angular dependence of the single-photon ionization of aligned N₂ and CO₂. *J. Phys. Chem. A*, **112**, 9382–9386.
- 40** Bisgaard, C.Z., Clarkin, O.J., Wu, G., Lee, A.M.D., Gessner, O., Hayden, C.C., and Stolow, A. (2009) Time-resolved molecular frame dynamics of fixed-in-space CS₂ molecules. *Science*, **323**, 1464–1468.
- 41** Rouzee, A., Kelkensberg, F., Siu, W.K., Gademann, G., Lucchese, R., and Vrakking, M.J.J. (2012) Photoelectron kinetic and angular distributions for the ionization of aligned molecules using a HHG source. *J. Phys. B*, **45**, 074016.
- 42** Rosca-Pruna, F. and Vrakking, M.J.J. (2001) Experimental observation of revival structures in picosecond laser-induced alignment of I₂. *Phys. Rev. Lett.*, **87**.
- 43** Ghafur, O., Rouzee, A., Gijsbertsen, A., Siu, W.K., Stolte, S., and Vrakking, M.J.J. (2009) Impulsive orientation and alignment of quantum-state-selected NO molecules. *Nat. Phys.*, **5**, 289–293.
- 44** Stapelfeldt, H. and Seideman, T. (2003) Colloquium: Aligning molecules with strong laser pulses. *Rev. Mod. Phys.*, **75**, 543.
- 45** Reid, K.L. (2003) Photoelectron angular distributions. *Ann. Rev. Phys. Chem.*, **54**, 397–424.
- 46** Lucchese, R.R. (2004) A simple model of molecular frame photoelectron angular distributions. *J. Electron. Spectrosc. Relat. Phenom.*, **141**, 201–210.
- 47** Piancastelli, M.N. (1999) The never-ending story of shape resonances. *J. Electron. Spectrosc. Relat. Phenom.*, **100**, 167–190.
- 48** Cohen, H.D. and Fano, U. (1966) Interference in the photo-ionization of molecules. *Phys. Rev.*, **150**, 30–33.
- 49** Fernandez, J., Fojon, O., Palacios, A., and Martin, F. (2007) Interferences from fast electron emission in molecular photoionization. *Phys. Rev. Lett.*, **98**, 043005.
- 50** Tannor, D.J. (2007) *Introduction to Quantum Mechanics, A Time-Dependent Perspective*, University Science Books, Sausalito, CA.
- 51** Born, M. and Wolf, E. (1999) *Principles of optics*, Cambridge University Press, Cambridge.
- 52** Lucchese, R.R., Raseev, G., and McKoy, V. (1982) Studies of differential and total photoionization cross sections of molecular nitrogen. *Phys. Rev. A*, **25**, 2572–2587.
- 53** Zare, R.N. (1988) *Angular Momentum*, Wiley, New York.

- 54** Lucchese, R.R., Carey, R., Elkharrat, C., Houver, J.C., and Dowek, D. (2008) Molecular frame and recoil frame angular distributions in dissociative photoionization of small molecules. *J. Phys.: Conf. Ser.*, **141**, 012009.
- 55** Messiah, A. (1961) *Quantum Mechanics*, North-Holland, New York.
- 56** Lucchese, R.R. (2005) Molecular Photoionization, in *Encyclopedia of Computational Chemistry*, (ed. P.V.R. Schleyer), Wiley, Chichester, England, doi: 10.1002/0470845015.cn0096.
- 57** Chase, D.M. (1956) Adiabatic approximation for scattering processes. *Phys. Rev.*, **104**, 838–842.
- 58** Raseev, G., Le Rouzo, H., and Lefebvre-Brion, H. (1980) Partial photoionization cross section and photoelectron angular distribution for the $X^2 \Sigma_g^+$ state of N_2^+ in the static-exchange approximation. *J. Chem. Phys.*, **72**, 5701–5709.
- 59** Poliakoff, E.D. and Lucchese, R.R. (2006) Evolution of photoelectron-vibrational coupling with molecular complexity. *Phys. Scr.*, **74**, C71.
- 60** Lucchese, R.R., Takatsuka, K., and McKoy, V. (1986) Applications of the Schwinger variational principle to electron-molecule collisions and molecular photoionization. *Phys. Rep.*, **131**, 147–221.
- 61** Stratmann, R.E. and Lucchese, R.R. (1995) A graphical unitary group approach to study multiplet specific multichannel electron correlation effects in the photoionization of O_2 . *J. Chem. Phys.*, **102**, 8493–8505.
- 62** Stratmann, R.E., Zurales, R.W., and Lucchese, R.R. (1996) Multiplet-specific multichannel electron–correlation effects in the photoionization of NO . *J. Chem. Phys.*, **104**, 8989–9000.
- 63** Orel, A.E. and Rescigno, T.N. (1997) Photoionization of ammonia. *Chem. Phys. Lett.*, **269**, 222–226.
- 64** Rabadan, I. and Tennyson, J. (1996) R-matrix calculation of the bound and continuum states of the $e^- - NO^+$ system. *J. Phys. B*, **29**, 3747–3761.
- 65** Bachau, H., Cormier, E., Decleva, P., Hansen, J.E., and Martin, F. (2001) Applications of B-splines in atomic and molecular physics. *Rep. Prog. Phys.*, **64**, 1815–1942.
- 66** McCurdy Jr., C.W., Rescigno, T.N., Yeager, D.L., and McKoy, V. (1977) The Equations of Motion Method: An Approach to the Dynamical Properties of Atoms and Molecules, in *Methods of Electronic Structure Theory*, vol. 3 (ed. H.F. Schaefer), Plenum Press, New York, pp. 339–386.
- 67** Williams, G.R.J. and Langhoff, P.W. (1979) Photoabsorption in H_2O : Stieltjes–Tchebycheff calculations in the time-dependent Hartree–Fock approximation. *Chem. Phys. Lett.*, **60**, 201–207.
- 68** Venuti, M., Sterner, M., and Decleva, P. (1998) Valence photoionization of C_6H_6 by the B-spline one-centre expansion density functional method. *Chem. Phys.*, **234**, 95–109.
- 69** Stener, M. and Decleva, P. (2000) Time-dependent density functional calculations of molecular photoionization cross sections: N_2 and PH_3 . *J. Chem. Phys.*, **112**, 10871–10879.
- 70** Dehmer, J.L. and Dill, D. (1978) The continuum multiple-scattering approach to the electron–molecule scattering and molecular photoionization, in *Electron-Molecule and Photon-Molecule Collisions* (eds T. Rescigno, V. McKoy, B. Schneider), Plenum, New York, pp. 225–265.
- 71** Miyabe, S., McCurdy, C.W., Orel, A.E., and Rescigno, T.N. (2009) Theoretical study of asymmetric molecular-frame photoelectron angular distributions for $C1s$ photoejection from CO_2 . *Phys. Rev. A*, **79**, 053401.
- 72** Vanroose, W., Martin, F., Rescigno, T.N., and McCurdy, C.W. (2005) Complete photo-induced breakup of the H_2 molecule as a probe of molecular electron correlation. *Science*, **310**, 1787–1789.
- 73** Tashiro, M. (2010) Application of the R-matrix method to photoionization of molecules. *J. Chem. Phys.*, **132**, 134306.
- 74** Lin, C.D., Le, A.-T., Chen, Z., Morishita, T., and Lucchese, R. (2010) Strong-field rescattering physics – self-imaging of a molecule by its own electrons. *J. Phys. B*, **43**, 122001.

- 75** Okunishi, M., Niikura, H., Lucchese, R., Morishita, T., and Ueda, K. (2011) Extracting electron-ion differential scattering cross sections for partially aligned molecules by laser-induced rescattering photoelectron spectroscopy. *Phys. Rev. Lett.*, **106**, 063001.
- 76** Semenov, S.K. and Cherepkov, N.A. (2009) On the simplest presentation of the molecular frame photoelectron angular distributions for core levels. *J. Phys. B*, **42**, 085101.
- 77** Toffoli, D., Lucchese, R.R., Lebech, M., Houver, J.C., and Dowek, D. (2007) Molecular frame and recoil frame photoelectron angular distributions from dissociative photoionization of NO₂. *J. Chem. Phys.*, **126**, 054307.
- 78** Lebech, M., Houver, J.C., Dowek, D., and Lucchese, R.R. (2004) Dissociative photoionization of N₂O in the region of the N₂O⁺ (B^2) state studied by ion-electron velocity vector correlation. *J. Chem. Phys.*, **120**, 8226–8240.
- 79** Lucchese, R.R., Montuoro, R., Grum-Grzhimailo, A.N., Liu, X.-J., Prumper, G., Morishita, Y., Saito, N., and Ueda, K. (2007) Projection methods for the analysis of molecular-frame photoelectron angular distributions. I: Minimal parameterizations in the dipole limit. *J. Electron. Spectrosc. Relat. Phenom.*, **155**, 95–99.
- 80** Liu, X.-J., Lucchese, R.R., Grum-Grzhimailo, A.N., Morishita, Y., Saito, N., Prumper, G., and Ueda, K. (2007) Molecular-frame photoelectron and electron-frame photoion angular distributions and their interrelation. *J. Phys. B*, **40**, 485–496.
- 81** Prümper, G., Rolles, D., Fukuzawa, H., Liu, X.J., Pesic, Z., Dumitriu, I., Lucchese, R.R., Ueda, K., and Berrah, N. (2008) Measurements of molecular-frame Auger electron angular distributions at the CO C1s⁻¹2π* resonance with high energy resolution. *J. Phys. B*, **41**, 215101.
- 82** Dixon, R.N. (2005) Recoil anisotropy following multiphoton dissociation via near-resonant intermediate states. *J. Chem. Phys.*, **122**, 194302–194313.
- 83** Dixon, R.N., Bayley, J.M., and Ashfold, M.N.R. (1984) The rotational structure of three-photon resonances of polyatomic molecules. *J. Chem. Phys.*, **84**, 21–34.
- 84** Nieman, G.C. (1981) Vibronic intensities and rotational line strength factors for the three-photon absorption spectrum of ammonia. *J. Chem. Phys.*, **75**, 584–595.
- 85** Andrews, D.L. (1982) The theory of double-beam three-photon absorption. *J. Chem. Phys.*, **77**, 2831–2835.
- 86** Bray, R.G. and Hochstrasser, R.M. (1976) Two-photon absorption by rotating diatomic molecules. *Mol. Phys.*, **31**, 1199–1211.
- 87** Elkhattar, C., Picard, Y.J., Billaud, P., Cornaggia, C., Garzella, D., Perdriz, M., Houver, J.C., Lucchese, R.R., and Dowek, D. (2010) Ion pair formation in multiphoton excitation of NO₂ using linearly and circularly polarized femtosecond light pulses: kinetic energy distribution and fragment recoil anisotropy. *J. Phys. Chem. A*, **114**, 9902–9918.

Part Three

High Harmonic Generation and Attosecond Pulses

10

High-Order Harmonic Generation and Attosecond Light Pulses: An Introduction

Anne L'Huillier

This chapter describes how the understanding of high-order harmonic generation (HHG) and the generation of attosecond pulses progressed since the first experiments, which were performed at the end of the 1980s. The text describes how the ideas arose, as perceived by the author of this chapter. It is neither a detailed and comprehensive review nor a documented historical background.

10.1

Early Work, 1987–1993

Somewhat surprisingly, HHG was not discovered in the nonlinear optics community, but by scientists interested in the response of atoms to intense laser fields. In nonlinear optics, the general (and quite reasonable) understanding was that high-order processes are less probable than low-order processes. Consequently, on a not so successful route toward vacuum ultraviolet light, researchers used ultraviolet radiation in order to start with VUV photons. At the same time, a lot of progress in laser technology allowed scientists to focus radiation at very high intensities, reaching 10^{13} – 10^{15} W/cm². Atoms, when exposed to such intense radiation, get ionized by absorbing several photons. Above-threshold-ionization and multiple-ionization were observed as unexpected results of such experiments.

One experimental idea was to detect fluorescence emitted by excited atoms or ions that were produced during strong field excitation. To this end, the pressure of sample atoms in the interaction chamber had to be increased: gas jets were installed, and photon detectors were placed along the laser propagation axis. First results for HHG from VUV radiation were obtained by Rhodes and his co-workers, using a 248-nm excimer laser with high laser intensity [1]. Strong fluorescence was seen from Ar, Kr and Xe ions, together with high harmonics up to the 17th harmonic in Ne. Shortly afterward, high-order harmonics were observed in Xe, Kr and Ar using a 30-ps Nd:YAG laser (1064 nm) [2]. The HHG spectra exhibited a characteristic behavior, with a rapid intensity decrease for the first orders, a plateau from the seventh harmonic up to a very high order (e.g., the 29th in Ar) and an abrupt cutoff.

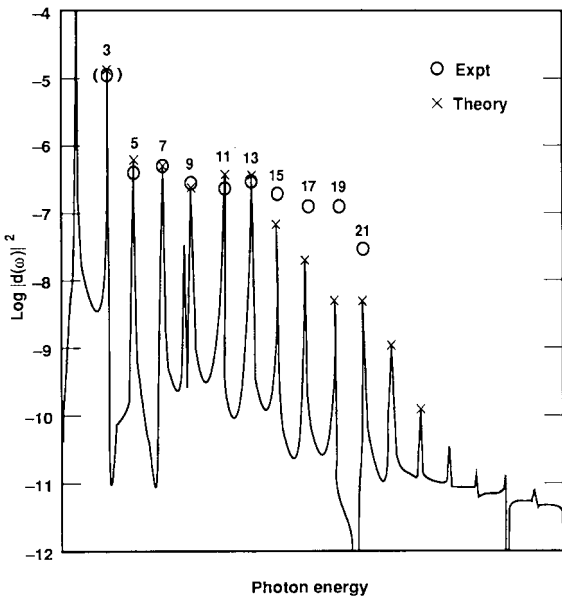


Figure 10.1 Experimental results from [2] in Xe and theoretical calculations (from [3]).

Theorists succeeded in reproducing the experimental results by numerically solving the time-dependent Schrödinger equation for a single active electron, considering only the single atom response.

$$i\hbar \frac{\partial \Psi}{\partial t} = \frac{\hbar^2}{2m} \nabla^2 \Psi + (V(r) + eE \cdot r) \Psi , \quad (10.1)$$

where $\Psi(t)$ is the time-dependent wavefunction and $E(t)$ the electric field. The induced electric dipole moment is then

$$d(t) = \langle \Psi | e\mathbf{r} | \Psi \rangle ,$$

with Fourier components giving the harmonic strengths. Figure 10.1 shows a comparison between the experimental results of [2] in Xe and the numerical results from [3]. The good agreement between experiment and theory led to the question of phase matching effects on the harmonic spectrum. Early calculations [4] of the signal emitted by an ensemble of emitters

$$S \approx \left| \int_V P(\mathbf{r}, t) e^{-i\Delta k \cdot \mathbf{r}} d\mathbf{r} \right|^2$$

with

$$P(\mathbf{r}, t) = N(\mathbf{r}, t) d(\mathbf{r}, t) , \quad \Delta k = k_q - qk_1 ,$$

showed that in this highly nonperturbative regime, phase matching should not differ significantly from one order to the next, at least in the plateau region. P is

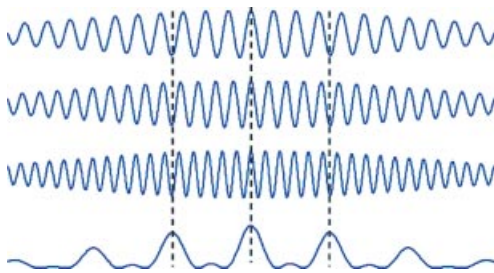


Figure 10.2 Illustration of the phase locking of harmonics (top three traces) leading to attosecond pulses (bottom trace).

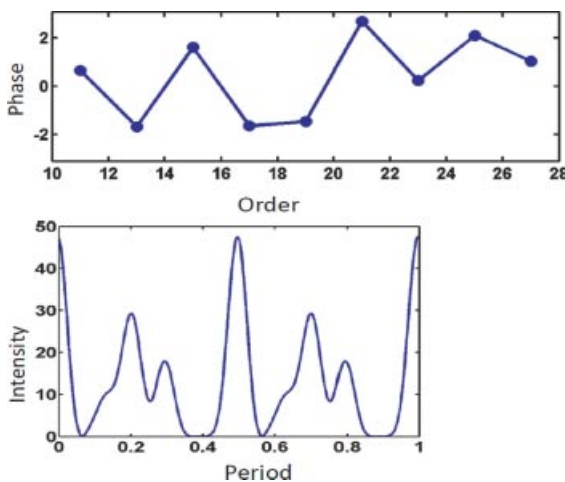


Figure 10.3 In early work, the phase locking was hidden by interferences (see [4]).

the laser-induced polarization in the medium, N is the atomic density and Δk is the wave vector mismatch.

The question whether the light generated by HHG could lead to attosecond pulses was almost immediately raised by several physicists, and was discussed in the literature [5, 6]. A necessary condition for attosecond pulses is that the harmonics must be phase locked (see Figure 10.2). Unfortunately, the early single atom results did not show a locked HHG phase, but rather a random behavior (Figure 10.3).

10.2

Three-Step Model, 1993–1994

Research in HHG made a giant leap in 1993, when the first HHG spectra [7, 8] were obtained with high-power short-pulse lasers using the chirped pulse amplification technique [9]. At the same time, a simple physical picture of the HHG process was proposed [10, 11]. According to this model, the electron tunnels through

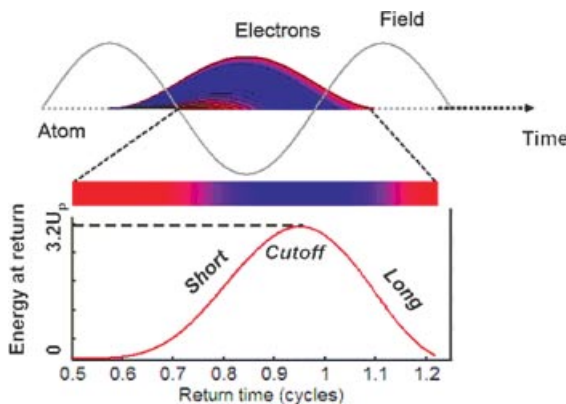


Figure 10.4 Electron trajectories in the three-step model. Color denotes the recollision energy (highest energy in blue).

the Coulomb energy barrier, which is suppressed by the presence of the linearly polarized laser electric field. The electron then undergoes classical oscillations in the laser field. The influence of the Coulomb force from the nucleus is practically negligible at this time. If the electron comes back to the vicinity of the nucleus, it may recombine back to the ground state, thus producing a photon with energy IP (the ionization potential) plus the kinetic energy acquired during the oscillatory motion. The corresponding electron trajectories are shown in Figure 10.4, the color indicating the kinetic energy acquired by the electron when it returns. The trajectories are obtained by solving the Newton equation

$$m \frac{d^2 r}{dt^2} = -e E ,$$

assuming that the electrons are born with zero velocity at $t = 0$. The energy of emitted HHG photons is then simply

$$E_{\text{ph}} = \frac{1}{2} m v^2 + \text{IP} ,$$

where IP is the ionization energy. This simple classical calculation allows us to understand the cutoff behavior at

$$E_{\text{cutoff}} = \text{IP} + 3.17 U_p ,$$

with the ponderomotive energy

$$U_p = \frac{e^2 E^2}{4 m \omega^2} .$$

It also shows the existence of two classes of trajectories (short and long) with different return times, and with opposite energy versus time variation (positive and negative).

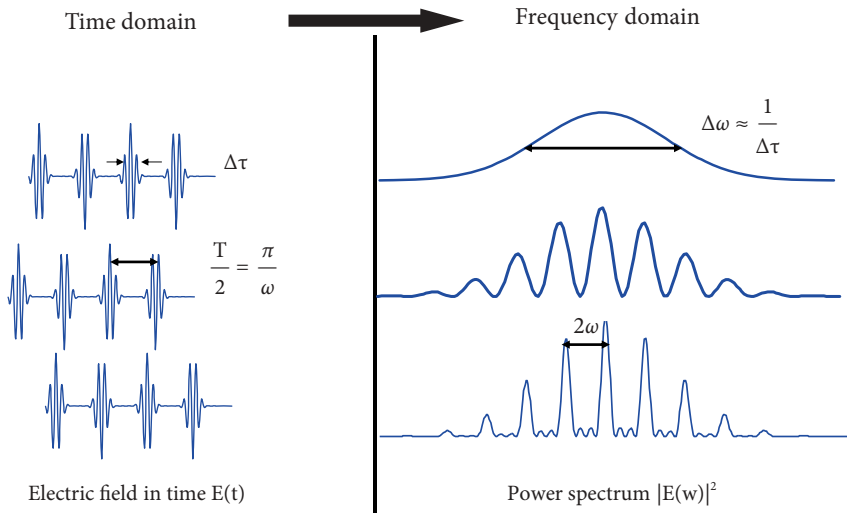


Figure 10.5 Interferences between successive attosecond pulses lead to a spectrum of odd harmonics with a plateau and a cutoff.

Recollision, and therefore emission of a short (attosecond) pulse of energetic photons, occurs every half-laser cycle. The interference of attosecond pulses emitted with *opposite* signs every half-laser cycle leads to a spectrum of *odd* harmonics of the fundamental frequency, as shown in Figure 10.5. The number of pulses in the train, as well as the variation of the pulse-to-pulse spacing, determines the bandwidth and chirp of the individual harmonics [12]. The extent of the plateau reflects the bandwidth of the individual attosecond pulses. In addition, low-order harmonics are created via conventional “below-threshold” multiphoton processes, leading to decreasing rather than increasing harmonic intensities for the first orders (cf. Figure 10.1).

Shortly afterward, Lewenstein and co-workers developed the strong field approximation (SFA) [13], based on a quasi-classical approximation, which gave a firm ground to the three-step model and allowed scientists to perform systematic single-

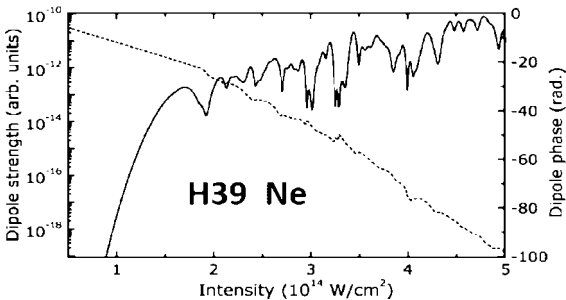


Figure 10.6 Dipole strength and phase for the 39th harmonic in Ne, calculated using the SFA.

atom calculations. The dipole strength and phase of the 39th harmonic in Ne, calculated using the SFA, is shown in Figure 10.6. The irregular behavior at intensities higher than $1.5 \times 10^{14} \text{ W cm}^{-2}$ is due to the interferences between the short and long trajectories. An interesting consequence of the SFA was the discovery of the rapid phase decrease with intensity, owing to the influence of the long trajectory [14].

10.3

Trajectories and Phase Matching, 1995–2000

During the last years of the previous century, high harmonics were studied in detail and characterized in both, the spatial and temporal domain. The existence of trajectories with different temporal and spatial behaviors was experimentally demonstrated [15]. Theoretical methods were developed to disentangle the two trajectories analytically within the SFA [16], or numerically from the results of the TDSE [17]. Figure 10.7a shows calculations for the 19th harmonic in Ar, obtained by solving the saddle-point equations within the SFA. Remarkably, the phase at high intensity, corresponding to the plateau region, varies linearly. The accumulated phase during the trajectory can be written as

$$\Phi \approx -\alpha_q^{\text{traj}} I ,$$

with a positive coefficient α dependent on the process order and trajectory. The variation of α with order is shown in Figure 10.7b. The value of α determines, to a large extent, the spatial and spectral properties of the emitted harmonic field,

$$E(\mathbf{r}, t) = A(\mathbf{r}, t) e^{iq\omega t + i\alpha_q^{\text{traj}} I(\mathbf{r}, t)} ,$$

where ω is the laser frequency and A is a slowly varying amplitude factor. The far-field profile strongly depends on the radial phase variation of the laser intensity (times the α coefficient) in the equation above, while the spectral properties

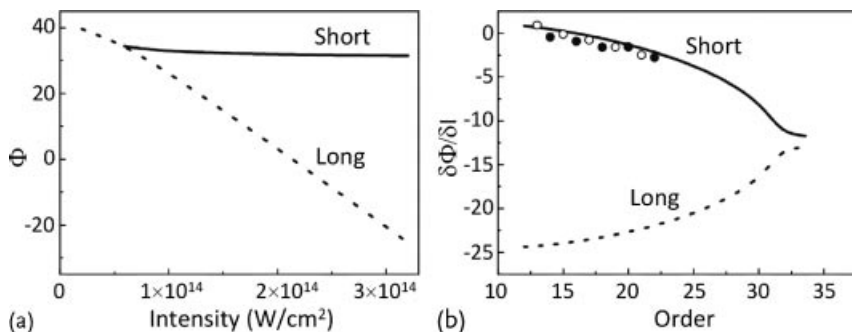


Figure 10.7 Phase of the dipole moment generated in Ar as a function of intensity (a). Derivative of the phase with respect to intensity as a function of harmonic order (b) (from [17]).

(chirp and spectral bandwidth) reflect the temporal intensity variation. The harmonic field from the short trajectory is well collimated and spectrally narrow, while that from the long trajectory is divergent and strongly negatively chirped. Assuming Gaussian profiles for the laser and harmonic beams, with radius w_0 and w_q and a laser peak intensity equal to I_0 , it is possible to estimate the divergence with the following expression [18]:

$$\theta = \frac{2}{q\omega w_q} \sqrt{1 + 4 \left[\alpha_q^{\text{traj}} \right]^2 I_0^2 \frac{w_q^4}{w_0^4}}.$$

The chirp coefficient b , defined as the slope of the frequency variation as a function of time, can be calculated in a similar fashion. For a Gaussian pulse with width at half maximum τ , the chirp coefficient is

$$b = \frac{\partial \Omega}{\partial t} = -\alpha_q^{\text{traj}} I_0 \frac{4 \ln 2}{\tau^2}.$$

Figure 10.8 presents experimental measurements of the 15th harmonic, generated in xenon. The 15th harmonic is observed in the far field (see Figure 10.8a). The two spatial regions (a central collimated area and a more divergent ring) correspond to emission due to the short- and long-trajectory contribution, respectively. Two harmonic sources are created using a Michelson interferometer, with one of the arms slightly misaligned. On the left, the two pulses are temporally overlapped. On the right, they are delayed by 15 fs. The presence of interference fringes indicates that

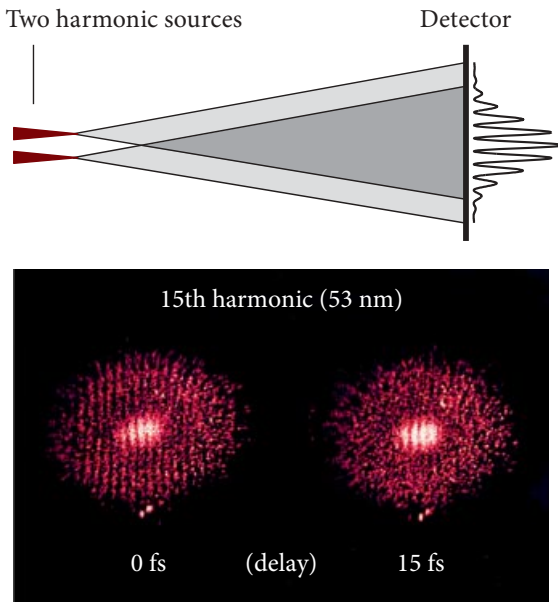


Figure 10.8 Far field profile and temporal coherence measurement of the 15th harmonic generated in xenon (see [15]).

Table 10.1 Contributions to the wave vector mismatch Δk . The table gives the mathematical expression, sign, and the relevant properties determining the magnitude of Δk . z denotes the propagation axis.

Wave vector mismatch	Expression	Sign	Property
Δk_a	$q\omega/(2\varepsilon_0 c) N[\alpha_{\text{pol}}(q\omega) - \alpha_{\text{pol}}(\omega)]$	—	$\propto N$
Δk_{fe}	$qe^2/(2\varepsilon_0 cm\omega) N_{\text{fe}}$	+	$\propto N, t, f(I)$
Δk_{foc}	$\approx q/z_0$	+	
Δk_{traj}	$\alpha_q^{\text{traj}} \partial I / \partial z$	—sign(z)	$\propto l, t, \text{traj}$

the two harmonic pulses (see Figure 10.8a) are mutually coherent. The temporal coherence is shorter than 15 fs for the long trajectory contribution, leading to a blurring of the fringe pattern on the outer ring of the profile (on the right).

These results indicated the necessity of considering separately the two trajectory contributions in the phase matching relation,

$$\Delta k = \Delta k_a + \Delta k_{\text{fe}} + \Delta k_{\text{foc}} + \Delta k_{\text{traj}} = 0 ,$$

where Δk is the difference in wavenumbers at the harmonic and fundamental frequency. The different Δk contributions are those of neutral atom dispersion, the dispersion due to free electrons, the effect of the focusing geometry on the fundamental, and finally the phase derivative of the polarization field. Different terms and their properties are indicated in Table 10.1. The wave vector mismatch due to neutral dispersion involves the difference between the atomic polarizabilities at the harmonic and fundamental frequencies. Above the ionization threshold, this term is always negative (see Figure 10.9). The wave vector mismatch due to the free electrons is strongly nonlinear and depends on the laser intensity and on the pulse duration. This strong contribution only allows harmonic emission for a small degree of ionization (a small percentage). It is also responsible for transient phase matching [20]. The geometrical effect due to focusing does not depend on the pressure, therefore leading to a pressure dependence deviating from N^2 , even when phase matching is realized. Finally, if the dipole phase is antisymmetric (contrary to the other contributions), this leads to different phase matching conditions on either sides of the focus. It is also important to consider the effect of the imaginary part of the polarizability (see Figure 10.9), which leads to absorption of the generated radiation and thus limits the conversion efficiency.

Phase matching can be achieved in different ways, depending on factors such as pressure, focusing, and whether the short or long trajectories are of interest. Often, phase matching is realized at a given laser intensity, and therefore at a given time within the laser pulse envelope. In general, the short and long trajectory contributions are not both phase-matched under the same conditions. Therefore, the generation of “clean” attosecond light pulses (one per half-laser cycle) is possible when considering the response of the macroscopic medium [21]. Numerical simu-

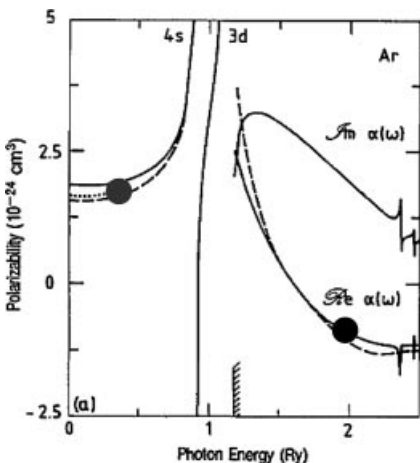


Figure 10.9 Polarizability as a function of photon energy. The neutral dispersion depends on the difference between two points indicated in the figure (from [19]).

lations confirmed this result and even showed that single attosecond pulses could be generated when a short fundamental pulse is used [22].

A number of experimental studies measured the pulse duration of the harmonics [23, 24]. These studies relied on electron spectroscopy, using laser-assisted photoionization. The sideband peaks, due to absorption of a harmonic photon and a laser photon, are measured as a function of delay between the harmonic and the laser pulses and this cross-correlation measurement allows us to determine the duration of the harmonic pulses. As shown below, this experimental development turned out to be a precursor to the first attosecond measurements.

In parallel to these characterization studies, experiments were performed using shorter and shorter laser pulses, thus following progress in laser technology [25, 26]. This led to an important increase in the energy range accessible by HHG, with experiments reaching the water window, as well as orders over 200. Also, first applications of high harmonics for atomic and molecular spectroscopy and surface physics were demonstrated [27]. However, the perspective to detect attosecond pulses experimentally seemed remote, because autocorrelation techniques were difficult to implement.

10.4 Attosecond Pulses 2001

At the end of the last century, it was believed that attosecond pulses could be created via HHG, but the route to an experimental demonstration seemed quite tough. A European network “ATTO” was proposed and granted with the aim to “bring attosecond physics into experimental reality.” The proposed methods were auto-

correlation, inspired by pioneering experiments in Japan [28] with femtosecond resolution, or streaking by a low-frequency field.

Ultimately, the successful methods [29, 30], both published during 2001, were based upon cross-correlation of the harmonic light with the infrared radiation used for the HHG. The cross-correlation uses photoionization of an atomic gas in the presence of the infrared field, analyzed by electron spectroscopy. The RABITT (reconstruction of attosecond bursts by interference of two-photon transitions, see Figure 10.10) technique leads to distinct harmonic peaks and is well suited to the measurement of attosecond pulses in a pulse train [29]. The intensity of the IR field is weak enough that perturbation theory remains valid. Absorption or emission of an IR laser photon can occur together with absorption of an HHG photon and leads to the creation of sidebands. Each sideband can be reached by two quantum paths. An oscillation of the sidebands is due to interference between the quantum paths. The variation of the oscillation phase with energy is directly related to the group delay of the attosecond pulses, through the formula

$$\tau_a = \frac{\partial\phi_{q+1}}{2\omega} = \frac{\varphi_{q+2} - \varphi_q}{2\omega}.$$

In this expression, $\partial\phi_{q+1}$ denotes the phase of the oscillation of sideband $q + 1$, while ϕ_q is the phase of the q th harmonic field [31, 32]. This formula neglects the effect of two-photon ionization, which is usually small. Extracting time delays in photoionization with this technique (or with streaking techniques) has recently become an active research area in attosecond science [33, 34].

The “streaking” technique is well suited for the characterization of single attosecond pulses with a broad spectrum. The intensity of the IR laser field must be large enough to modulate the electron spectrum depending on the laser-XUV delay. Figure 10.11 presents the first result and Figure 10.12 more recent ones using different detection geometries [35, 36].

Interestingly, both methods were discovered more or less accidentally. Originally, the goal of the experiments was to perform a cross-correlation, on a femtosecond timescale, between the harmonics and the generating laser pulse. The observed oscillations, which were not expected, gave access to the attosecond timescale, by interferometry in the RABITT case, and by phase gating in the streaking technique.

10.5

Conclusion

During the last decade, attosecond science has progressed considerably, from the first observation of HHG, to ever more detailed physics experiments. The range and control of HHG has been increased by using multicolor fields as well as by longer wavelengths, in the mid-IR region (see Chapter 10). Applications have been developed in many physics areas, as witnessed by the content of this book (see Chapters 12–14, and 17).

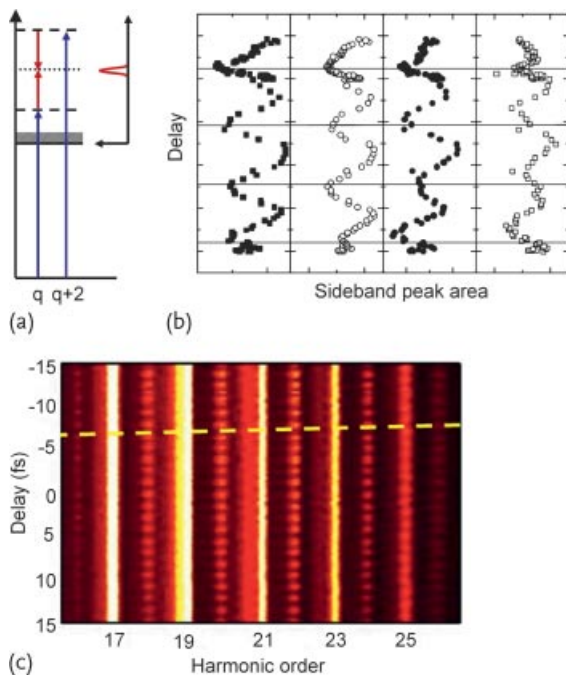


Figure 10.10 RABITT technique, from [29, 32]. Two quantum paths via harmonics q and $q + 2$ lead to the same sideband frequency (a) and interfere. Interference leads to oscillatory behavior as a function of time-delay between HHG and IR pulse (b, c).

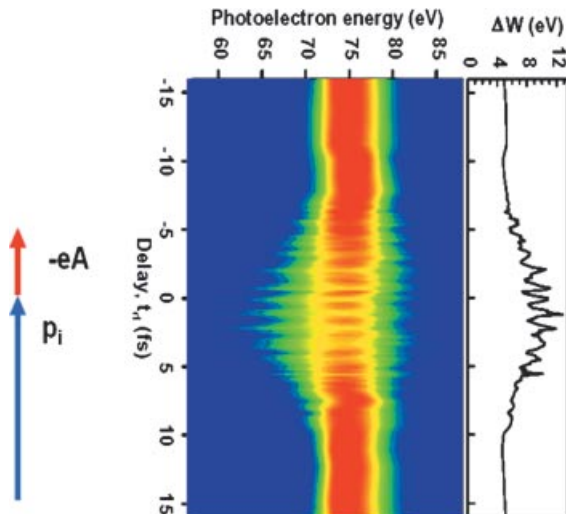


Figure 10.11 First measurement using the streaking technique [30].

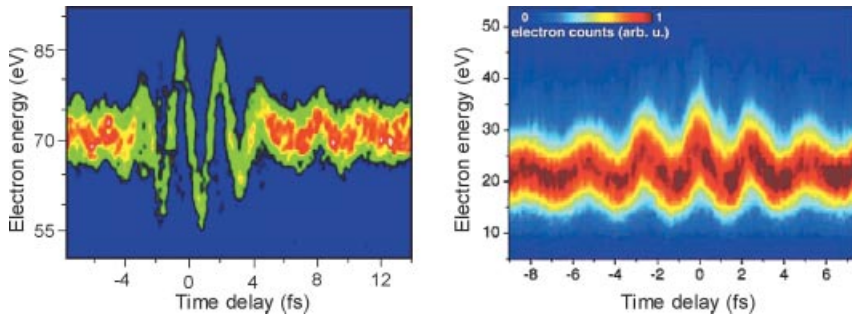


Figure 10.12 Streak traces in Ne [35] and Ar [36], using the polarization gating technique.

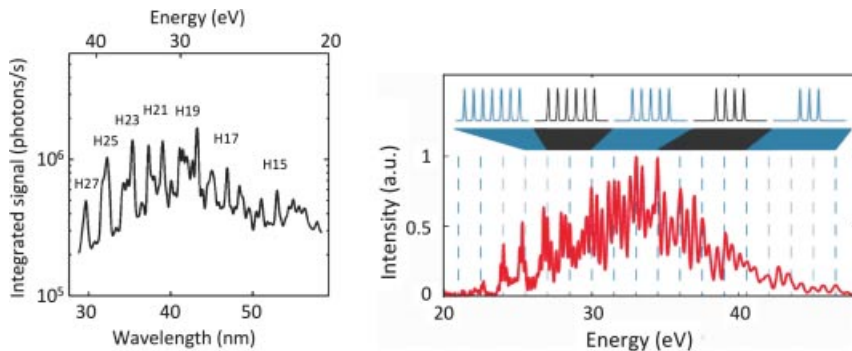


Figure 10.13 Harmonic spectra showing an interference structure superposed to the harmonics (see [37, 38]).

Does this mean that we should consider the physics of high-order harmonics, which led to attosecond pulses, as well understood and controlled? Obviously not, the field continuously surprises us with new developments. We show, for example (and for fun), two recent harmonic spectra in Figure 10.13, where the harmonic peaks disappear under a forest of extra peaks [37, 38]. The additional peaks are interpreted in two different ways. In Figure 10.13a, the experiment was performed in argon with a low energy per pulse ($7\text{ }\mu\text{J}$) 100-kHz 45-fs Ti:S laser, using a tight focusing geometry [38]. The observed structures are interpreted as phase matching (Maker) fringes for the long trajectory. Figure 10.13b has been observed with two color pulses (fundamental and second harmonics) with a carrier-envelope-phase (CEP) stabilized few-cycle laser. Here, the additional structure is assigned to interferences between attosecond pulses in the train, leading to “secondary maxima” between the main odd and even harmonic peaks [37].

Acknowledgment

The author wants to thank many students, postdocs, and colleagues who have participated to increasing the understanding of the harmonic generation process dur-

ing the last 25 years. This work has been supported by the Marie Curie Initial Training Network ATTOFEL, the European Research Council through the advanced grant ALMA, the Knut and Alice Wallenberg Foundation and the Swedish Research Council.

References

- 1 McPherson, A., Gibson, G., Jara, H., Johann, U., Luk, T.S., McIntyre, I., Boyer, K., and Rhodes, C.K. (1987) Studies of multiphoton production of vacuum-ultraviolet radiation in the rare gases. *J. Opt. Soc. Am. B*, **4**, 595.
- 2 Ferray, M., L'Huillier, A., Li, X.F., Lompré, L.A., Mainfray, G., and Manus, C. (1988) Multiple-harmonic conversion of 1064 nm radiation in rare gases. *J. Phys. B*, **21**, 31.
- 3 Kulander, K.C. and Shore, B.W. (1989) Calculations of multiple harmonic conversion of 1064-nm radiation in Xe. *Phys. Rev. Lett.*, **62**, 524.
- 4 L'Huillier, A., Schafer, K.J., and Kulander, K.C. (1991) High order harmonic generation in xenon at 1064 nm: the role of phase matching. *Phys. Rev. Lett.*, **66**, 2200.
- 5 Farkas, G. and Toth, C. (1992) Proposal for attosecond light pulse generation using laser induced multiple-harmonic conversion processes in rare gases. *Phys. Lett. A*, **168**, 447.
- 6 Harris, S.E., Macklin, J.J., and Hänsch, T.W. (1993) Atomic scale temporal structure inherent to high-order harmonic generation. *Opt. Commun.*, **100**, 487.
- 7 L'Huillier, A. and Balcou, P. (1993) High-order harmonic generation in rare gases with an intense short-pulse laser. *Phys. Rev. Lett.*, **70**, 774.
- 8 Macklin, J.J., Kmetec, J.D., Gordon, C.L.II.I. (1993) High-order harmonic generation using intense femtosecond pulses. *Phys. Rev. Lett.*, **70**, 766.
- 9 Strickland, D. and Mourou, G. (1985) Compression of amplified chirped optical pulses. *Opt. Comm.*, **56**, 219.
- 10 Schafer, K.J., Yang, B., DiMauro, L.F., Kulander, K.C. (1993) Above threshold ionization beyond the high harmonic cutoff, *Phys. Rev. Lett.* **70**, 1599; see also Krause, J.L., Schafer K.J., and Kulander, K.C. (1992), High-order harmonic generation from atoms and ions in the high intensity regime. *Phys. Rev. Lett.*, **68**, 3535.
- 11 Corkum, P.B. (1993) Plasma perspective on strong-field multiphoton ionization. *Phys. Rev. Lett.*, **71**, 1994.
- 12 Mauritsson, J., López-Martens, R., Johnsson, P., Kornelis, W., Biegert, J., Keller, U., Gaarde, M.B., K.J. Schafer, and L'Huillier, A. (2004) Measurement and control of the frequency chirp rate of high-order harmonics. *Phys. Rev. A*, **70**, 021801(R).
- 13 Lewenstein, M., Balcou, P., Ivanov, Y.M., L'Huillier, A., and Corkum, P. (1994) Theory of high-order harmonic generation by low-frequency laser fields. *Phys. Rev. A*, **49**, 2117.
- 14 Lewenstein, M., Salières, P., and L'Huillier, A. (1995) Phase of the atomic polarisation in high-order harmonic generation. *Phys. Rev. A*, **52**, 4747.
- 15 Bellini, M., Tozzi, A., Gaarde, M.B., Delfin, C., Hänsch, T.W., L'Huillier, A., and Wahlström, C.G. (1998) Temporal coherence of ultrashort high-order harmonic pulses. *Phys. Rev. Lett.*, **81**, 297.
- 16 Gaarde, M.B. and Schafer, K.J. (2002) Quantum path distributions for high-order harmonics in rare gas atoms. *Phys. Rev. A*, **65**, R031406.
- 17 Varjú, K., Mairesse, Y., Carré, B., Gaarde, M.B., Johnsson, P., Kazamias, S., López-Martens, R., Mauritsson, J., Schafer, K.J., Balcou, P., L'Huillier, A., and Salières, P. (2005) Frequency chirp of harmonic and attosecond pulses. *J. Mod. Opt.*, **52**, 379.
- 18 He, X., Miranda, M., Schwenke, J., Guibaud, O., Rakowski, R., Heyl, C., Georgiadou, E., Persson, A., Gaarde, M.B., and L'Huillier, A. (2009) Spatial and spectral properties of the high-order har-

- monic emission in argon for seeding applications. *Phys. Rev. A*, **79**, 063829.
- 19** L'Huillier, A., Li, X.F., and Lompré, L.A. (1990) Propagation effects in high-order harmonic generation in rare gases. *J. Opt. Soc. Am. B*, **7**, 529.
- 20** Kazamias, S., Douillet, D., Weihe, F., Valentin, C., Rousse, A., Sebban, S., Grillon, G., Augé, F., Hulin, D., and Balcou, P. (2003) Global optimization of high harmonic generation. *Phys. Rev. Lett.*, **90**, 193901.
- 21** Antoine, P., L'Huillier, A., and Lewenstein, M. (1996) Attosecond pulse trains using high-order harmonics. *Phys. Rev. Lett.*, **77**, 1234.
- 22** Christov, I.P., Murnane, M.M., and Kapteyn, H.C. (1997) High harmonic generation of attosecond pulses in the 'singlecycle' regime. *Phys. Rev. Lett.*, **78**, 1251–1254.
- 23** Glover, T.E., Schoenlein, R.W., Chin, A.H., and Shank, C.V. (1996) Observation of Laser Assisted Photoelectric Effect and Femtosecond High Order Harmonic Radiation. *Phys. Rev. Lett.*, **76**, 2468.
- 24** Schins, J.M., Breger, P., Agostini, P., Constantinescu, R.C., Muller, H.G., Bouhal, A., Grillon, G., Antonetti, A., and Mysyrowicz, A. (1996) Cross-correlation measurements of femtosecond extreme-ultraviolet high-order harmonics. *JOSA B*, **13**, 197.
- 25** Chang, Z., Rundquist, A., Wang, H., Murnane, M.M., and Kapteyn, H.C. (1997) Generation of coherent soft X-rays at 2.7 nm using high harmonics. *Phys. Rev. Lett.*, **79**, 2967.
- 26** Spielmann, C., Burnett, N., Sartania, S., Koppitsch, R., Schnurer, M., Kan, C., Lenzner, M., Wobrauschek, P., and Krausz, F. (1997) Generation of coherent X-rays in the water window using 5-femtosecond laser pulses. *Science*, **278**, 661.
- 27** L'Huillier, A., Johansson, A., Norin, J., Mauritsson, J., and Wahlström, C.-G. (2003) Applications of high-order harmonics. *Eur. Phys. J. D*, **26**, 91 and refs therein.
- 28** Kobayashi, Y., Sekikawa, T., Nabekawa, Y., and Watanabe, S. (1998) 27-fs extreme ultraviolet pulse generation by high-order harmonics. *Opt. Lett.*, **23**, 64.
- 29** Paul, P.M., Toma, E.S., Breger, P., Mullet, G., Augé, F., and Balcou, P. (2001) Observation of a train of attosecond pulses from high harmonic generation. *Science*, **292**, 1689–1692.
- 30** Hentschel, M., Kienberger, R., Spielmann, C., Reider, G.A., Milosevic, N., Brabec, T., Corkum, P.B., Heinze, U., Drescher, M., and Krausz, F. (2001) Attosecond metrology. *Nature*, **414**, 509–513.
- 31** Varjú, K., Johnsson, P., López-Martens, R., Remetter, T., Gustafsson, E., L'Huillier, A., Mauritsson, J., Gaarde, M.B., Schafer, K.J., Erny, C., Sola, I., Zaïr, A., Constant, E., Cormier, E., and Mével, E. (2005) Experimental studies of Attosecond Pulse Trains. *Laser Phys.*, **15**, 888.
- 32** Mairesse, Y., De Bohan, A., Frasin-ski, L.J., Merdji, H., Dinu, L.C., Monchicourt, P., Bréger, P., Kovacev, M., Taieb, R., Carré, B., Muller, H.G., Agostini, P., and Salieres, P. (2003) Attosecond synchronization of high-harmonic soft X-rays. *Science*, **302**, 1540.
- 33** Schultze, M., Fieß, M., Karpowicz, N., Gagnon, J., Korbman, M., Hofstetter, M., Neppl, S., Cavalieri, A.L., Komninos, Y., Mercouris, T., Nicolaides, C.A., Pazzourek, R., Nagele, S., Feist, J., Burgdörfer, J., Azzeer, A.M., Ernststorfer, R., Kienberger, R., Kleineberg, U., Goulielmakis, E., Krausz, F., and Yakovlev, V.S. (2010) Delay in Photoemission. *Science*, **328**, 1658.
- 34** Klünder, K., Dahlström, J.M., Gisselbrecht, M., Fordell, T., Swoboda, M., Guénöt, D., Johnsson, P., Caillat, J., Mauritsson, J., Maquet, A., Taieb, R., and L'Huillier, A. (2011) Probing single-photon ionization on the attosecond time scale. *Phys. Rev. Lett.*, **106**, 143002.
- 35** Goulielmakis, E., Uiberacker, M., Kienberger, R., Baltuska, A., Yakovlev, V., Scrinzi, A., Westerwalbesloh, T., Kleineberg, U., Heinze, U., Drescher, M., and Krausz, F. (2004) Direct measurement of light waves. *Science*, **305**, 1267.

- 36** Sansone, G., Benedetti, E., Calegari, F., Vozzi, C., Avaldi, L., Flammini, R., Poletto, L., Villoresi, P., Altucci, C., Velotta, R., Stagira, S., De Silvestri, S., and Nisoli, M. (2006) Isolated single-cycle attosecond pulses. *Science*, **314**, 443.
- 37** Mansten, E., Dahlström, J.M., Mauritsson, J., Ruchon, T., L'Huillier, A., Tate, J., Gaarde, M.B., Eckle, P., Guandalini, A., Holler, M., Schapper, F., Gallmann, L., and Keller, U. (2009) Spectral signature of short attosecond pulse trains. *Phys. Rev. Lett.*, **102**, 083002.
- 38** Heyl, C.M., Gündde, J., Höfer, U., and L'Huillier, A. (2011) Spectrally-Resolved Maker fringes in High-Order Harmonic Generation. *Phys. Rev. Lett.*, **107**, 033903.

11**Strong-Field Interactions at Long Wavelengths**

*Manuel Kremer, Cosmin I. Blaga, Anthony D. DiChiara, Stephen B. Schoun,
Pierre Agostini, and Louis F. DiMauro*

The interaction of short and intense laser pulses with matter can cause highly nonlinear effects. One such effect is high-harmonic generation (HHG), which offers a method to develop compact extreme ultraviolet (EUV) radiation sources with pulse durations on the attosecond ($1 \text{ as} = 10^{-18} \text{ s}$) timescale (see e.g., [1, 2]). The physics behind HHG can be described by a sequence of strong-field ionization and re-collision occurring in atoms and molecules that are exposed to intense, linearly polarized laser light. This sequence can be modeled in three distinct steps [3, 4]: (i) strong field ionization, followed by (ii) motion in the laser field, and by (iii) electron-ion collisions that can be observed through (in)elastic scattering channels and recombination. Recombination is the process leading to HHG. Each step is affected by the choice of laser wavelength. In general, the use of long wavelength lasers offers benefits, both, toward understanding how an atom ionizes and toward improving the characteristics of HHG. The Ohio State University (OSU) group has led a substantial effort investigating the benefits and drawbacks of driving HHG with long-wavelength lasers. The systematic study of wavelength-dependent strong-field ionization leads to a robust understanding of the mechanistic (single-atom) aspects of HHG and opens the door to optimize strong-field processes for future applications.

In this chapter, we will discuss all strong-field processes relevant to HHG, from tunnel ionization to classical electron dynamics and basic scattering physics. The chapter briefly illustrates the theoretical background and then gives an overview of the mid-infrared (mid-IR) sources operated at OSU and a short description of the new attosecond beamline. The relevance of long-wavelength drivers for strong-field and attosecond physics will be shown by means of two exemplary and recent experiments – the reconstruction of elastic differential cross sections from photoelectron angular distributions and the generation and characterization of high-harmonic radiation with mid-IR lasers.

11.1

Theoretical Background

11.1.1

Keldysh Picture of Ionization in Strong Fields

The route to generating attosecond pulses lies in the interaction of a dilute atomic or molecular vapor with a strong laser field where the magnitude of the field is typically on the order of a few 10^{10} V/m. Such large fields strongly distort the Coulomb field between nuclei and electrons (Figure 11.1). However, the field magnitude does not solely determine the ionization mechanism. Our current understanding of strong-field ionization is largely based on the work of Keldysh from 1964 [6]. Prior to Keldysh's argument, the ionization of atoms with ionization energies I_P greater than the laser photon energy was considered as a multiphoton ionization process, caused by simultaneous absorption of N photons ($N\hbar\omega \geq I_P$) as illustrated in Figure 11.1a. Multiphoton ionization was treated by time-dependent perturbation theory [7–9]. However, early experiments [10] performed with a Q-switched ruby laser ($\lambda = 694.3$ nm) at high intensities found that ionization rates depended exponentially on laser intensity I , contrary to the power law (I^N) predicted by perturbation theory. Keldysh suggested a tunneling mechanism that correctly predicted an exponential dependence. Tunnel ionization occurs when the strong electric field of the laser suppresses the Coulomb field of the atom as illustrated in Figure 11.1b, so that a bound electron wave packet has a finite probability of escaping into the classically forbidden region.

In Keldysh's theory, the transition from multiphoton to tunnel ionization is gauged by an adiabaticity parameter γ (also “Keldysh parameter”) that approximates when the periodic motion of the field is static to an electron crossing the barrier. The parameter γ is given by the ratio between the laser field frequency ω_L and the tunneling frequency $\omega_T = 2\pi/\tau_T$ and reads

$$\gamma = \frac{\omega_L}{\omega_T} = \sqrt{\frac{I_P}{2U_P}},$$

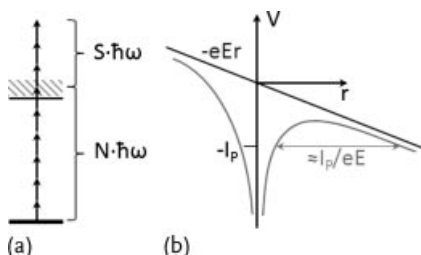


Figure 11.1 Strong field ionization mechanisms. (a) Multiphoton ionization: N Photons are required for ionization, but S additional photons are absorbed (above threshold ion-

ization, ATI [5]). (b) Tunnel ionization: The strong external field distorts the Coulomb potential and facilitates tunnel ionization.

with τ_T being the tunneling time. Atomic units are used throughout unless noted otherwise. U_P is the ponderomotive potential, that is, the cycle-averaged kinetic energy of a free electron in a laser field given by

$$U_P = \frac{E^2}{4\omega^2},$$

with the electric field amplitude E . For $\gamma \gg 1$ (high frequencies and/or low intensities), ionization is viewed as a multiphoton process. Therefore, tunnel ionization becomes important when the field intensity or the laser wavelength increase. However, depletion of the ground state sets an upper limit to the maximum field and motivates the use of long-wavelength sources and lower fields. The experiments we discuss in this chapter are carried out in the limiting case of tunnel ionization, $\gamma < 0.5$.

For long wavelength, γ becomes small and the tunneling regime is preferred because U_P is larger. As we will see, this provides access to higher frequency photons, shorter attosecond pulses, and more energetic electron wave packets in the HHG process. When the condition for tunnel ionization is satisfied, a simple and intuitive description for HHG emerges; a great deal of what happens after the wave packet emerges from the barrier can be explained with simple Newtonian dynamics.

11.1.2

Classical Perspectives on Postionization Dynamics

Because the electron wave packet formed by tunnel ionization is released into the strong laser field, the final detected energy spectra are not direct measurements of ionization energies, but rather reflect the energy of the electrons at the end of the laser field. In 1987, van Linden van der Heuvell and Muller [11] introduced the simple man model, based on a classical treatment for the postionization dynamics of the electron. The model predicts that if the electrons are born with zero kinetic energy, the photoelectron energy spectra have a cutoff at $2U_P$. Later experiments found, however, that linearly polarized fields produce photoelectron spectra extending well beyond the $2U_P$ cutoff. The detected yield of these high-energy electrons was nearly constant, forming a so-called plateau, as opposed to the exponential decay of the more abundant low-energy electrons. This radically different behavior was explained in 1993 [3, 4], when the re-scattering model was introduced. According to the model, photoelectrons quivering in the laser field might revisit the parent ion, upon which recombination or scattering could occur. The first of these possibilities is at the core of HHG, while the latter is at the heart of electron diffraction (elastic scattering) and nonsequential double or multiple ionization (inelastic scattering). Results from experiments on the first two of these processes – high-harmonic generation and elastic electron scattering – are subject of this chapter and will be discussed in detail below.

After an electron is released into the continuum, it experiences a net force determined by the combined field of the laser and the parent ion. This Hamiltonian is

given by

$$H = \frac{(\mathbf{p} - \mathbf{A})^2}{2} - \frac{1}{r},$$

where \mathbf{p} is the mechanical momentum, \mathbf{A} is the vector potential and r is the electron–core distance. Especially at long laser wavelengths, the ponderomotive energy is much larger than the binding potential of the ion and we assume that the Coulombic term can be neglected. Consequently, the generalized momentum $\mathbf{P} = \mathbf{p} - \mathbf{A}$ is a constant of motion and analytic solutions for the motion of a wave packet can be found. To illustrate the power of the classical approximation, we will show below how elastic differential cross sections (DCS) can be extracted from strong-field photoelectron spectra recorded in the tunneling limit.

11.1.3

High-Harmonic Generation

The complete characterization of any form of electromagnetic radiation requires knowledge of both, the spectral amplitude and phase (see Chapter 2). However, it is technically not feasible to measure these two quantities for ultrafast laser pulses in real time, but it is mathematically equivalent to measure them in the frequency domain. The frequency spectrum consists of equally spaced peaks – the odd-order harmonics – separated by twice the photon energy with amplitudes that drop significantly after the first few orders before remaining almost constant up to a characteristic cutoff frequency.

There are various ways to measure the amplitudes in the frequency spectrum, for example, by directly detecting the photons with an XUV spectrometer or by detecting the photoelectron emission spectrum resulting from ionizing an atomic or molecular target in an imaging spectrometer.

Measuring the spectral phase of high-harmonic radiation, however, is much more involved than measuring the high-harmonic spectrum. We will describe and discuss the results of two alternative methods used in our laboratory to measure the phase. We are thereby able to completely characterize our high-harmonic laser pulses.

11.1.4

Wavelength Scaling of High-Harmonic Cutoff and Attochirp

Two critical quantities relevant to understanding the science of HHG are the high-energy cutoff, as well as the temporal shift in recombination times for individual harmonics. The high-energy cutoff defines the highest occurring photon energy while the temporal shift is commonly interpreted as an attosecond group delay dispersion, also known as attochirp (here referred to as β). Both of them depend on the driving-laser wavelength. While the single-atom harmonic cutoff is given by $IP + 3.17 U_p$ and scales quadratically with the wavelength (it is only linear in inten-

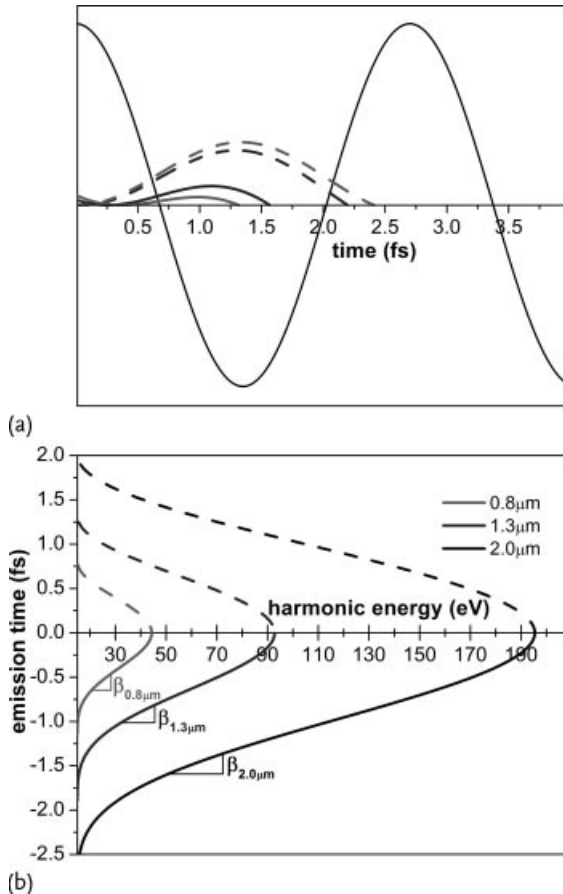


Figure 11.2 Classical model predictions.
(a) Two exemplary sets of electron trajectories (dark and light gray) that lead to the same harmonic energy. Plotted are the short (solid line) and the long (dashed line) trajectories in a $0.8 \mu\text{m}$ (period $\approx 2.7 \text{ fs}$) laser field. (b) Energy of the emitted harmonics in dependence

of their emission times for the wavelength $0.8, 1.3$, and $2.0 \mu\text{m}$. Again, the solid lines represent short and the dashed lines long trajectories. The attochirp β is given by the derivative of the corresponding curves and is significantly reduced for longer wavelength.

sity), the attochirp is expected to be $\propto \lambda^{-1}$ [12]. Classical Newtonian calculations show that within a single optical cycle, every recollision energy can be reached by two pathways: The short and the long trajectories as depicted in Figure 11.2a. By plotting the electron return time or the photon emission times versus the corresponding harmonic energy, the attochirp is given by the derivative of the curve (see Figure 11.2b). It can be seen that, for a given class of trajectories (short or long), the attochirp is almost constant, that is, the spectral phase is nearly quadratic. As is shown in Figure 11.2b, the gradients of the short and the long trajectories have opposite signs, for example, they are positively or negatively chirped, respectively.

There are basically two different approaches to reduce the attochirp: (i) increasing the peak intensity and (ii) using a longer wavelength. The first approach uses the fact that the cutoff energy is proportional to the laser intensity and increasing the intensity would lead to a smaller derivative of the curves shown in Figure 11.2b and, thus, a reduced attochirp. However, as already mentioned, the intensity cannot be increased arbitrarily as this leads to a depletion of the ground state. The second method, that is using longer driving wavelength, is more promising. Since the laser period is proportional to λ and the cutoff energy to λ^2 , their ratio scales as λ^{-1} . Increasing the wavelength at a constant intensity avoids the problems of depletion and opens the route for the creation of shorter attosecond bursts centered at higher photon energies [13]. Besides these microscopic single-atom considerations, the attochirp can also be reduced, or partially compensated, by propagating the pulses through a suitable dispersive medium [14–16].

Due to the existence of attochirp, there is a maximum spectral bandwidth for the shortest possible pulse. The pulse duration is proportional to $\sqrt{1 + \beta^2 B^4}/B$, where B is the bandwidth. The first term results from the time–frequency Fourier relationship and the second from the attochirp. By restricting the bandwidth to $B = 1/\sqrt{\beta}$, the shortest pulse duration is obtained and has a value of $\sqrt{2\beta}$, that is, scales as $1/\sqrt{\lambda}$. Beyond that point, dispersion dominates and the pulse broadens [12]. We will revisit this point later when measurements are presented.

11.1.5

In-situ and RABBITT Technique

Measuring the chirp of attosecond light pulses only recently became feasible [17]. Conventional complete-characterization schemes for ultrashort femtosecond laser pulses are all based on a convolution of the pulse, either with itself, or with a known reference pulse in a nonlinear device. The most successful of these methods are FROG [18] and SPIDER [19] and it was shown that the FROG technique can be, at least for low-order harmonics, extended to UV femtosecond pulses by using two-photon ionization as a nonlinear device [20–22]. The extension of these schemes into the XUV and soft X-ray regime, as, for example, proposed by Muller for the SPIDER method [23], is experimentally challenging. Both methods require pulse replicas. As there exist no beam splitters for those wavelengths, such pulse replicas are difficult to obtain. Also, all eligible nonlinear materials are strongly absorbing in this spectral range. One solution is using the so-called RABBITT (reconstruction of attosecond beating by interference of two-photon transitions) method [14, 23], which is based on two-photon, two-color ionization of rare-gas atoms. Here, the harmonic radiation interferes with a small fraction of the generation beam. Without the presence of the IR field (sometimes also called the dressing beam), the photoelectron spectrum consists of a number of peaks separated by twice the fundamental frequency ω_L (odd-order harmonic comb). By adding the IR field, stimulated emission and absorption becomes possible resulting in sidebands located between the harmonics as schematically shown in Figure 11.3. The amplitude of these sidebands oscillates when the subcycle delay between the IR and the XUV

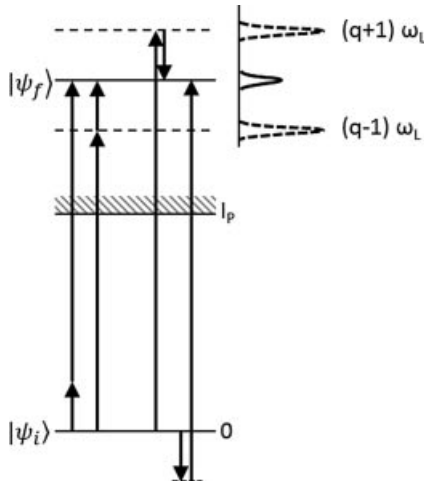


Figure 11.3 Energy level diagram of the RABBITT method. Stimulated emission and absorption of one IR photon leads to sidebands between the odd-order harmonic peaks.

beam is scanned. This is due to interference between the different quantum paths. It can be shown (see, e.g., [1, 24]) that the transition from the initial state $|\Psi_i\rangle$ to the final state $|\Psi_f\rangle$ includes an oscillatory term given by

$$A_f \cos \left[2\omega_L \tau + \varphi_{q-1} - \varphi_{q+1} - \Delta\varphi_{\text{atomic}}^f \right].$$

The amplitudes A_f are proportional to the product of the intensities of the IR and XUV fields and the corresponding bound-free and free-free matrix elements. Recording this sideband oscillation gives access to the phase difference between two consecutive harmonics $\varphi_{q-1} - \varphi_{q+1}$. The so-called atomic phase $\Delta\varphi_{\text{atomic}}^f$ in the above equation is the intrinsic phase of the matrix elements for above-threshold, two-photon ionization and can, at least for suitable target atoms, be calculated with high precision [25].

Besides RABBITT, there exists an experimentally much simpler way to obtain information about the spectral phase of attosecond pulse trains (APTs): In 2006, Du-dovich *et al.* introduced the $\omega - 2\omega$ method, an all-optical scheme to measure the attochirp of an attosecond pulse train [26]. This method is based on high-harmonic generation in a two-color driving field (e.g., the fundamental and its second harmonic). Such a field breaks the centrosymmetry of the generation process and leads to the creation of even-order harmonics. It is easy to see that the amplitude of these even-order harmonics depends on the relative phase of the two colors. Scanning the subcycle delay between the two fields thus leads to oscillations in the even-order harmonics, while the strength of the odd-order harmonics remains unaffected. By comparing these oscillations with semiclassical model calculations, the emission times of the even-order harmonics can be retrieved and, by interpolation, those of the APT. For a sufficiently weak second harmonic field, the emission times correspond to the unperturbed ones. Importantly, this method allows measurement of

the *in-situ* spectral phase independent of any dispersive elements (e.g., metal filters) and is thus well suited for comparison with theory. The RABBITT method, on the other hand, measures the attochirp on target, which is an important quantity if the high harmonics are used for applications.

Both, the $\omega - 2\omega$ and the RABBITT method, have been used at OSU to measure the attochirp of high harmonics created by mid-IR drivers. The corresponding results will be discussed later in this chapter.

11.2

Mid-IR Sources and Beamlines at OSU

This section gives a short overview on the mid-IR laser systems currently used at OSU as well as the newly completed attosecond beamline.

11.2.1

2- μm Source

Femtosecond laser pulses emitted from a broadband Ti:sapphire oscillator (Venteon Pulse 1 by Venteon Femtosecond Laser Technologies) are stretched to 250 ps and amplified in two home-build amplification stages. The first stage is a regenerative amplifier, which increases the pulse energy up to 1.8 mJ, before a multipass amplifier boosts it to about 6.5 mJ at a repetition rate of 1 kHz. The use of a regenerative preamplifier leads to the advantage that only a low number of passes are required in the multipass section (two passes in our system). We thereby obtain high pulse energies with highly improved beam profiles and M^2 values close to 1.

After the amplified pulses are compressed to about 50 fs, they are sent into a commercial high-energy optical parametric amplifier (OPA) (HE-TOPAS, Light Conversion). A small amount of the incoming beam is used to generate a broadband spectrum via superfluorescence. A narrow portion of the broadened spectrum then acts as a seed for the remaining 800-nm Ti:sapphire pulse in a β -barium borate (BBO) nonlinear crystal. After six amplification stages, 550- μJ pulses at 2 μm are available. The amount of dispersive optical materials in the OPA is small and the pulse duration remains almost constant during the conversion process. As the parametric amplifier splits one 800-nm photon into two lower-energy photons, conservation of energy implies that 850 μJ of 1.3- μm radiation is also generated.

Experiments on HHG presented below have been carried out by using the described 2- μm source. At the moment, the Ti:sapphire amplification stage is undergoing modifications to increase the output power from 6.5 to about 10 mJ, leading to significantly higher mid-IR pulse energies while the other pulse parameters will remain the same.

11.2.2

3.6- μ m Source

The generation of wavelengths between 3.2 and 3.9 μ m is done by difference frequency generation (DFG) in a nonlinear potassium titanyl arsenate (KTA) crystal. The pump pulses are 100 fs, 3.2-mJ Ti:sapphire pulses with a center wavelength of 0.816 μ m. As signal pulses, we use 16-ps pulses at 1.053 μ m with 0.8-mJ pulse energy. The Ti:sapphire amplifier system is almost identical to the one of the 2- μ m laser system, while the 1.053- μ m pulses are created by a home-build Nd:YLF regenerative amplifier [27]. Both beams are sent into the 2.5-mm long KTA crystal in a nearly collinear geometry, which allows a spatial separation of the idler beam. The high damage threshold of KTA [28] and the good transparency in the wavelength range between 0.3 and 5 μ m [29] make KTA well suited for the generation of mid-IR laser pulses. By slightly tuning the phase-matching conditions, the idler wavelength can be tuned between 3.2 and 3.9 μ m.

One unique aspect of the DFG system at OSU is that the 0.816 and the 1.053- μ m pulses are produced by two independent laser systems. In order to create a DFG signal, their repetition rates must be locked. Therefore, the cavity lengths of the two oscillators are electronically referenced to an external electronic oscillator [30].

11.2.3

OSU Attosecond Beamline

Most of the results on HHG presented in this chapter have been obtained by optically detecting the high-harmonic photons with a Hettrick spectrometer [31], in combination with a thermo-electrically cooled back-illuminated X-ray camera (Andor). These studies demonstrated the effective creation of high-harmonic radiation with long-wavelength driving pulses and fathomed the optimal experimental conditions, such as target gas pressure, focus geometry, or gas nozzle type.

A new attosecond beamline was designed, built and commissioned at OSU to broaden the range of experimental investigations, in particular toward applications of mid-IR pulses in molecular orbital tomography [32, 33] or investigations of time-resolved core-level and multielectron dynamics [2]. The beamline consists of a HHG source and X-ray optics chambers. The source chamber allows different focusing geometries, beam separation, and beam manipulation, while the differentially pumped X-ray optics chamber contains X-ray filtering, recombination, and focusing optics. A 750-mm focal length, 5° grazing incidence, toroidal mirror, operating in a $2f$ - $2f$ geometry and located in the X-ray optics chamber, defines the interaction region in the end-station. The end-station is a 2π magnetic bottle electron energy spectrometer (MBES) [34]. A schematic drawing of the beamline and the MBES is shown in Figure 11.4.

With the new beamline, it is possible to fully characterize the created high harmonics. For this, we simultaneously measure the amplitude of the generated high-harmonic radiation (by detecting the photoelectrons created by ionizing the target gas), and the attochirp (by applying the RABBITT technique).

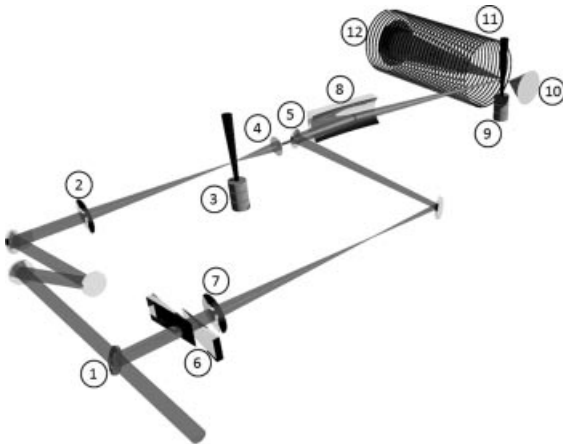


Figure 11.4 Sketch of the attosecond beamline. The labels stand for (1) beam splitter, (2) focusing lens to generate harmonics, (3) generation gas target, (4) metal filter, (5) recombination mirror, (6) glass wedges

for delay scans, (7) focusing lens to match divergence, (8) toroidal mirror, (9) detection gas jet, (10) cone-shaped permanent magnet, (11) magnetic bottle solenoid coils, and (12) microchannel plate detector.

Besides the attosecond beamline, our group operates time-of-flight spectrometers for the detection of ions or electrons in strong-field ionization experiments, as well as a high-resolution electron–ion-coincidence spectrometer. The experimental investigations on the transition from the multiphoton ionization regime to the deep tunneling regime, which will be presented in the next section, were carried out using these devices.

11.3

Strong-Field Ionization: The Single-Atom Response

Classical simulations of the postionization dynamics show a maximum kinetic energy of $2U_p$ for electrons that leave the vicinity of the ion directly and up to $10U_p$ when the electron undergoes elastic backscattering at the ion. These values are valid for electrons that are born with zero kinetic energy and are connected to the birth phase, that is, the phase of the laser field at which they are promoted in the continuum. This last statement holds well for the tunneling regime [35], but breaks down in the multiphoton regime, since the lifetime of the multiphoton transition is comparable with the duration of the laser period. Therefore, one expects the $2U_p$ and $10U_p$ cutoff to be absent at $\gamma \gg 1$ and visible at $\gamma \ll 1$. In the case of argon, the two regimes have been interrogated by changing the wavelength of the driving fields and the results are presented in Figure 11.5. Indeed, the $2U_p$ cutoff is missing at $0.8\text{ }\mu\text{m}$, whereas at longer wavelengths it is clearly visible. Furthermore, at longer wavelengths, the ATI peaks are washed-out, another clear indication of the transition into the tunneling regime. The theoretical curves (gray lines

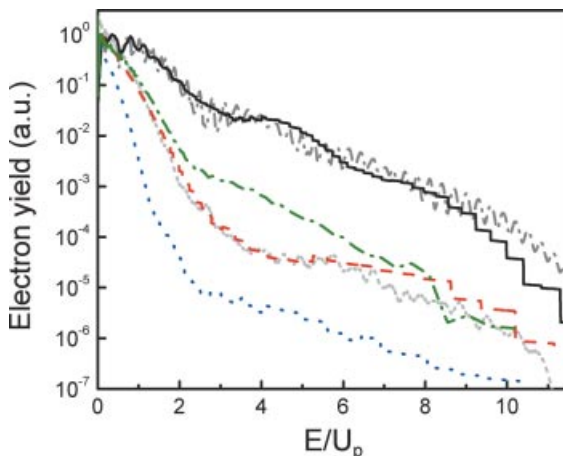


Figure 11.5 Comparison of photoelectron energy distributions from argon for different wavelengths at constant intensity. Excitation at $0.8\text{ }\mu\text{m}$ (black line), $1.3\text{ }\mu\text{m}$ (green line), $2\text{ }\mu\text{m}$ (red line), and $3.6\text{ }\mu\text{m}$ (blue line) at an intensity of 0.08 PW/cm^2 . For this intensity, U_p is approximately 5, 13, 30, and 100 eV for

wavelengths of 0.8 , 1.3 , 2 , and $3.6\text{ }\mu\text{m}$, respectively. Also shown are the TDSE calculations at $0.8\text{ }\mu\text{m}$ (dark-gray line) and $2\text{ }\mu\text{m}$ (light-gray line). The agreement between experiment and theory is very good and reproduces the loss of resonant structure at the longer wavelengths.

in Figure 11.5), obtained from numerically solving the Schrödinger equation in the single active electron approximation, accurately reproduce the experimental results for 0.8 and $2.0\text{ }\mu\text{m}$. Finally, the ponderomotive energies at long wavelengths are in excess of 100 eV . This last observation is important for single-electron diffraction: for probing intermolecular distances it is necessary to produce returning electron wave packets with associated de Broglie wavelengths on the order of the molecular bond lengths [36].

The approximations introduced above, that is, zero electron kinetic energy when born and classical treatment of the dynamics after ionization by neglecting the Coulomb field, allow us to reconstruct the history of detected electrons and therefore to extract relative elastic differential cross sections (DCS) for electron–ion collisions from photoelectron angular distributions. Following the recipe of Okunishi *et al.* [37], Figure 11.6 presents the extracted DCS in the case of argon, irradiated with $2.0\text{ }\mu\text{m}$, 50-fs pulses (open circles). Remarkably, we find excellent agreement with results obtained via well-established gas phase electron diffraction on neutral argon atoms [38] (solid squares). Apparently, when the electron revisits its parent ion with large enough kinetic energy, the long-range Coulombic tail of the ionic potential plays only a minor role in determining the observed electron yield at large scattering angles. For molecular targets, this short range nature of the interaction offers hope that laser driven electron diffraction at long wavelengths could become a valuable tool for extracting structural information, especially since the presence of the laser field guarantees temporal resolutions on the femtosecond timescale as the time the electron spends in the continuum is less than one optical cycle.

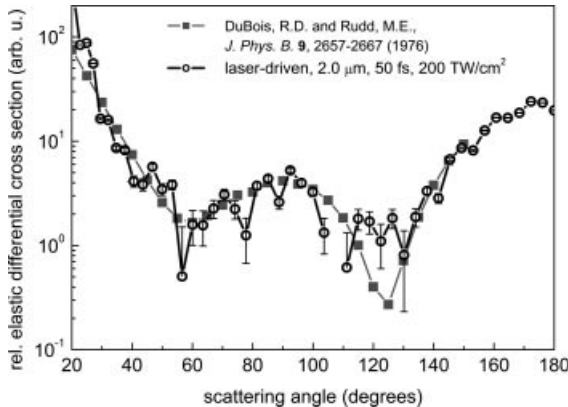


Figure 11.6 Extraction of relative elastic differential cross sections of argon from photo-electron angular distributions. The excellent agreement between the laser-driven electron + Ar ion collision (open circles) with the electron + neutral argon collision (solid squares) shows the short range nature of the particle interaction.

11.4

High-Harmonic Generation

Complete characterization of an attosecond pulse train requires knowledge of both, spectral phase and power spectrum of the high harmonics. Two important quantities of high-harmonic radiation, the maximum photon energy and the attochirp, scale favorably with the wavelength. Therefore, ultrafast mid-IR driving pulses have the potential to produce attosecond bursts with higher carrier frequencies and with shorter pulse durations than conventional 0.8-μm Ti:sapphire-based sources. In this section, we show results from experiments carried out recently at OSU with 2 μm, 50-fs laser pulses. First, the cutoff extension as well as the achievable yield of high harmonics is discussed before results from attochirp measurements are presented.

11.4.1

Harmonic Cutoff and Harmonic Yield

The exact position of the high-harmonic cutoff is difficult to determine in experiments as well as in numerical simulations. The most obvious reason is that there exists no *sharp* cutoff, but the harmonic spectrum drops off rather slowly at high energies. Another uncertainty is the position where the cutoff should be expected. As already mentioned, the theoretical single-atom response predicts the position to be at $\text{IP} + 3.17 U_p$. However, under experimental conditions, macroscopic phase-matching and pulse-propagation effects occur in the neutral and partially ionized gas (see, e.g., [39, 40]). These effects are due to the different refractive indices between the fundamental and the harmonics, absorption, defocussing or geometrical

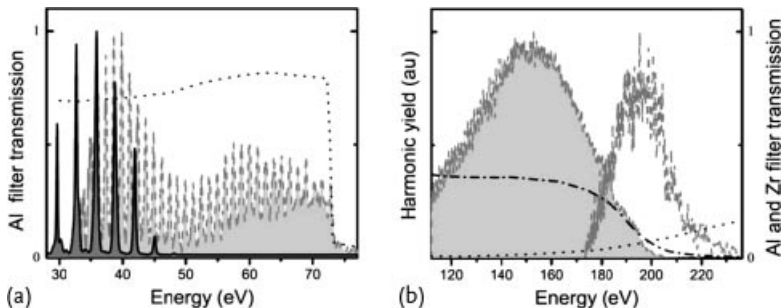


Figure 11.7 High harmonics from long drivers. (a) High-harmonic spectra produced in argon from 0.8 μm (solid line, dark shaded area) and from 2.0 μm (dashed line, light shaded area) driving pulses and measured through a 0.15- μm thick aluminum filter. (b) Harmonics from the 2.0- μm driver measured through a 0.3- μm thick zirconium filter (dashed line, shaded area) and through the second aluminum transmission window

(dash-dotted line, unfilled area). The theoretical transmission curves of the metal filters are shown in (a) for aluminum (dotted line) and in (b) for zirconium (dash-dotted line) and aluminum (dotted line). Both measurements have been performed at a laser intensity of 0.18 PW/cm 2 . Reprinted figure with permission from Colosimo *et al.*, *Nat. Phys.* **4**, 386, 2008. Copyright (2008) by Nature Publishing Group.

(Gouy) phase shift. As a result, not only the conversion efficiency and the harmonic yield is lowered, but also the cutoff is affected [41].

Early measurements [42] demonstrated that the use of mid-IR driving laser fields extends the harmonic comb significantly toward higher energies. This behavior was later quantified by Colosimo *et al.* [43]. In the following, we are going to discuss their results. Figure 11.7 shows a comparison between high harmonics generated with 0.8 μm (Figure 11.7a, dark shaded area) and with 2 μm (Figure 11.7a, light shaded area and Figure 11.7b). To block the fundamental light and the low-order harmonics, thin aluminum (Figure 11.7a) and zirconium (Figure 11.7b) metal filters have been used. Their characteristic transmission curves are plotted in the corresponding figures. The 2- μm driving laser produces a much denser frequency comb of odd-order harmonics (due to the smaller fundamental photon energy $\hbar\omega_{2\,\mu\text{m}} = 0.62$ eV), which extends beyond the sharp aluminum L-edge at 72.5 eV, while the harmonics generated by the 0.8- μm laser drop off at around 45 eV. To measure the complete spectrum, the Al filter was replaced by a Zr filter which is transparent for higher photon energies up to about 200 eV. As can be seen in Figure 11.7b, the harmonics extend over the whole zirconium energy window. The actual cutoff was found to be at ≈ 220 eV by using a second transmission window in the aluminum filter [43, 44].

The demonstrated availability of much higher photon energies and, consequently, a reduced de Broglie wavelength [45], opens the road for applications such as molecular orbital tomography [32, 33]. However, from an experimental point of view, not only the photon energy range, but also the photon flux (i.e., the photon yield) is an important quantity. Based on numerical single-atom calculations of the time-dependent Schrödinger equation (TDSE), the high harmonic yield at constant

intensity (integrated over the power spectrum) is predicted to be $\propto \lambda^{-5.5 \pm 0.5}$ [46]. A recent experiment [47], where phase-matching effects were minimized, confirmed this prediction and found a scaling of $\lambda^{-6.3 \pm 1.1}$ for Krypton at wavelength between 0.8 and 1.85 μm . Experiments at OSU were carried out to confirm the wavelength-scaling, but under identical experimental conditions the harmonic yield from argon at 2 μm was found to be approximately 1000 times lower than at 0.8 μm . The harmonic yield was considered in a spectral range, where both driving pulses create harmonics (35–50 eV). In our experiment, we kept the focusing conditions, gas parameters, and the laser intensity fixed and the yield was predicted to decrease by a factor of ≈ 150 when changing the wavelength from 0.8 to 2 μm . However, macroscopic phase-matching effects and destructive interference can significantly reduce the idealized single-atom response. Theory predicts in this case an even more unfortunate scaling of $\lambda^{-10.2 \pm 0.2}$ [13], but it is known that satisfying phase-matching conditions at longer wavelength requires higher target densities [48]. Consequently, by independently optimizing the target densities for the 0.8 and the 2- μm drivers for maximum yield, the ratio 2/0.8 μm increased from 1/1000 to 1/85 [43]. Furthermore, it is surely legitimate to expect that by fully optimizing the HHG process at a mid-IR wavelength, that is, by choosing favorable gas densities and focusing geometries, the photon yield can be significantly increased. In general, good phase-matching conditions are more difficult to achieve at longer wavelength; even by placing the focus before the gas jet, the short trajectories are not selected as efficiently as at a wavelength of 0.8 μm [13]. HHG in gas-filled waveguides seems to be a promising approach to overcome these experimental difficulties [40, 49].

11.4.2

Attochirp

We already discussed the expectation of reduced attochirp of high-harmonic radiation created by long-wavelength fundamental fields as compared to 0.8- μm drivers. In 2009, Dudovich's $\omega - 2\omega$ method was adopted by Doumy *et al.* [12] for the first comprehensive experimental study on the attochirp scaling law.

11.4.3

In-situ Phase Measurement

The experiments at OSU [12] have been performed by using 0.8, 1.3, and 2.0- μm driving fields, in combination with the Hettrick spectrometer described above. The experimental setup is schematically shown in Figure 11.8. The required weak second harmonic field was created by a 300- μm thick BBO, which was tuned out of its phase-matching angle. A number of birefringent calcite plates were used to compensate for the different group velocities in air and in glass to ensure temporal overlap in the target gas jet. The different polarizations of the two beams were rotated onto a common axis by a zero-order half-wave plate and the subcycle delay was controlled by a pair of fused silica glass wedges. High-target densities in the

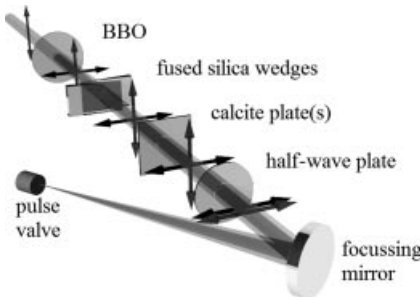


Figure 11.8 Experimental setup of the *in-situ* phase measurement. The polarizations of the two beams are represented by the gray (fundamental) and the black (second harmonic) arrows.

generation medium have been achieved with a pulsed gas valve in a 2-mm long, 1-mm diameter channel.

As can be seen in Figure 11.2b, in order to extract the attochirp, one of the two trajectories needs to be selected. Experimentally, this can be achieved by placing the laser focus before the gas jet and by spatial filtering with the small acceptance angle of the spectrometer [50, 51]. Placing the focus before the jet leads to smaller phase variations of the fundamental beam, which prefers phase matching of the short trajectory. Furthermore, as the divergence of the long trajectory is larger, significant parts of it can be blocked with an iris or a small acceptance angle.

Two typical harmonic spectra obtained from xenon at an intensity of 21 TW/cm^2 at $2.0 \mu\text{m}$ are shown in Figure 11.9a. The solid (dotted) line was recorded at a delay that maximizes (minimizes) the even-order harmonics. Figure 11.9b shows a full subcycle delay scan where the photon yield is plotted as a function of harmonic order and delay between the two colors. From this data, the relative phase that maximizes each even-order harmonic φ_{\max} can be extracted. To calculate the attochirp, it is necessary to find the correspondence between φ_{\max} and the emission time for each harmonic. In [26], it is suggested to use the semiclassical model to calculate φ_{\max} and fit it to the experimental values by adjusting an additive constant. The latter is the unknown offset of the relative phase between the two colors. Note that this analysis is only valid in the plateau region where harmonic generation can be described by a re-collision process.

The attochirp was reconstructed from a series of measurements at different intensities and wavelength and the result is shown in Figure 11.10. The product of attochirp β and intensity I is plotted in order to eliminate the influence of the different peak intensities on the chirp. The plot shows results from argon obtained with $0.8 \mu\text{m}$, 80 TW/cm^2 , $1.3 \mu\text{m}$, 38 TW/cm^2 , and $2.0 \mu\text{m}$, 71 TW/cm^2 pulses as well as the data from Figure 11.9 obtained in xenon with $2.0 \mu\text{m}$, 21 TW/cm^2 pulses. The solid line represents the predicted λ^{-1} scaling. Clearly, the reconstructed attochirp is in excellent agreement with the theoretical expectation and significantly lower for longer fundamental wavelength. In fact, it is reduced from 41.5 as/eV at $0.8 \mu\text{m}$ to 21.5 as/eV at $2.0 \mu\text{m}$. However, if one is aiming for the shortest attosecond pulse duration, one has to restrict the bandwidth as using too large a bandwidth will re-

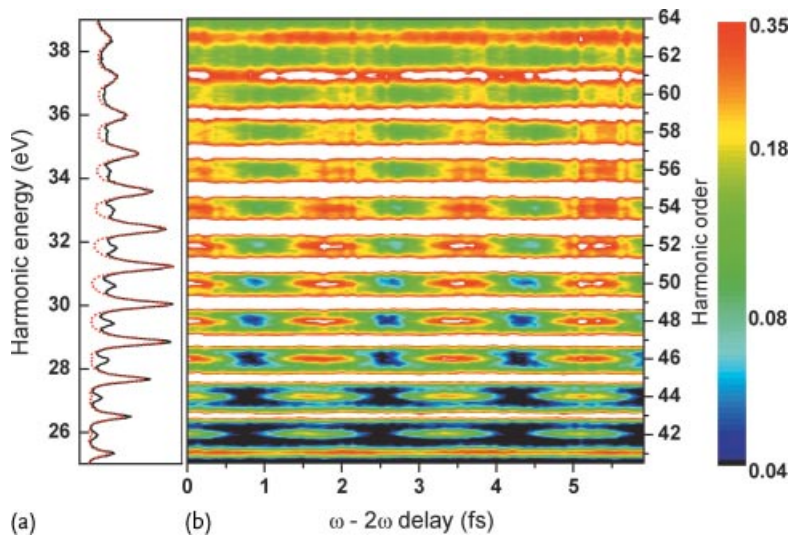


Figure 11.9 *In situ* phase measurement. (a) Two typical harmonic spectra for delays maximizing (solid line) and minimizing (dotted line) the even harmonics. (b) Result of a $\omega - 2\omega$ scan obtained in xenon at $2.0 \mu\text{m}$ with an intensity of $21 \text{ TW}/\text{cm}^2$. The even-order harmonics oscillate with four times the fundamental frequency.

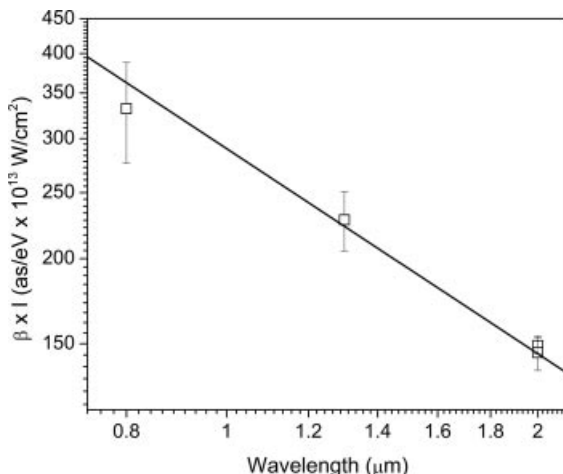


Figure 11.10 Product of attochirp β and intensity I as a function of wavelength. The product is plotted in order to eliminate the influence of different peak intensities from the individual measurements. The solid line shows the expected λ^{-1} scaling.

sult in a temporally broadened pulse. By restricting the bandwidth to its optimal value, the measured attochirp supports pulses of a 250-as duration with the $0.8\text{-}\mu\text{m}$ driver (12.5 eV of bandwidth) and of 180 as with the $2.0\text{-}\mu\text{m}$ fundamental field (20 eV of bandwidth).

The $\omega - 2\omega$ method is well suited for, but also restricted to, studies concerning the high-harmonic generation process itself. However, for many applications it is not desirable to know the spectral phase in the generation medium, but knowing it at the position where the APT is focused onto a target. This is particularly useful for assessing pulse shortening techniques that use the negative group delay dispersion of metal filters (see e.g., [52]) or specially designed XUV chirped mirrors [53]. For such cases, the RABBITT technique can be applied to measure the attochirp at target.

11.4.4 RABBITT Method

To the best of our knowledge, the first example for a full subcycle RABBITT scan from a 2.0- μm driving laser is shown in Figure 11.11a, with sideband orders ranging from 50 to 120. As an aluminum filter was used to block the fundamental light after the generation process, the spectrum is restricted to below ≈ 72.5 eV. The sideband oscillations are clearly visible and the reconstructed phase differences are shown in Figure 11.11b. The RABBITT measurement yields the spectral phase at the target gas rather than where the harmonics are generated. Therefore the extra dispersion caused by the metal filter and the generation gas (argon) must be taken into account to characterize the attochirp [17]. Actually, the filter dispersion, or more precisely its group delay dispersion, when negative as in aluminum, can be used to compensate for the positive attochirp of the high harmonics and thus to produce shorter pulses [15]. Please note that the oscillations of the odd-order harmonics in Figure 11.11a are due to a high intensity in the dressing beam, leading to three-photon, three-color ionization.

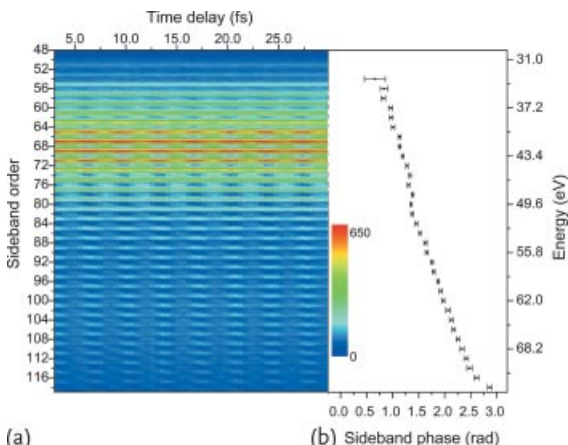


Figure 11.11 RABBITT phase measurement. (a) Full subcycle delay scan with 2.0 μm , 50-fs laser pulses. Note that both, even and odd order harmonics, show oscillations (see the text). (b) Reconstructed phase of the even-order harmonics.

11.5

Conclusions and Future Perspectives

We demonstrated how the rapidly developing technology for ultrafast long-wavelength laser pulses can be used to test fundamental scaling laws and to explore new regimes of strong-field physics up to the classical limit. Tuning the wavelength offers unique opportunities to continuously tune interactions from the multiphoton to the tunneling regime. As the ionization dynamics of atoms or molecules in strong laser fields are independent from the field parameters (as long as γ is kept constant), a much broader class of targets will become accessible. In this spirit, we like to point out that long-wavelength lasers are not only invaluable tools to explore fundamental questions in strong-field physics, but they also promise to become even more relevant for applications.

Very recently [33], the applicability of long-wavelength pulses for gaining structural information from high-harmonic radiation with the molecular orbital tomography method [32] was demonstrated. Long-wavelength drivers are also expected to open the road for the coherent imaging of more complex and chemically relevant molecules. A similar impact can be expected for molecular structure determination by laser-induced electron diffraction [36, 54].

Acknowledgments

The work was supported by the US Department of Energy, Basic Energy Sciences and the National Science Foundation. LFD acknowledges support from the Dr. Edward and Sylvia Hagenlocker chair.

References

- 1 Agostini, P. and DiMauro, L.F. (2004) The physics of attosecond light pulses. *Rep. Prog. Phys.*, **67**, 813–855.
- 2 Corkum, P.B. and Krausz, F. (2007) Attosecond science. *Nat. Phys.*, **3**, 381–387.
- 3 Schafer, K.J., Yang, B., DiMauro, L.F., and Kulander, K.C. (1993) Above threshold ionization beyond the high harmonic cutoff. *Phys. Rev. Lett.*, **70**, 1599–1602.
- 4 Corkum, P.B. (1993) Plasma perspective on strong field multiphoton ionization. *Phys. Rev. Lett.*, **71**, 1994–1997.
- 5 Agostini, P., Fabre, F., Mainfray, G., Petitte, G., and Rahman, N.K. (1979) Free-free Transitions Following Six-Photon Ionization of Xenon Atoms. *Phys. Rev. Lett.*, **42**, 1127–1130.
- 6 Keldysh, L.V. (1964) Ionization in the field of a strong electromagnetic wave. *Sov. Phys. JETP*, **20**, 1945–1950.
- 7 Göppert-Mayer, M. (1931) Über Elementarakte mit zwei Quantensprüngen. *Ann. Phys.*, **401**, 273–294.
- 8 Zernik, W. (1964) Two-photon ionization of atomic hydrogen. *Phys. Rev.*, **135**, A51–A57.
- 9 Gold, A. and Bebb, H.B. (1966) Multiphoton ionization of hydrogen and rare-gas atoms. *Phys. Rev.*, **143**, 1–24.
- 10 Damon, E.K. and Tomlinson, R.G. (1963) Observation of Ionization of Gases by a Ruby Laser. *Appl. Opt.*, **2**, 546–547.

- 11 van Linden van der Heuvell, H.B. and Muller, H.G. (1987) Limiting cases of excess-photon ionization. *Multiphoton Processes*, (eds. S.J. Smith and P.L. Knight), Cambridge University Press, pp. 25–34.
- 12 Doumy, G., Wheeler, J., Roedig, C., Chirla, R., Agostini, P., and DiMauro, L.F. (2009) Attosecond Synchronization of High-Order Harmonics from Mid-infrared Drivers. *Phys. Rev. Lett.*, **102**, 093002.
- 13 Jin, C., Le, A.-T., and Lin, C.D. (2011) Medium propagation effects in high-order harmonic generation of Ar and N₂. *Phys. Rev. A*, **83**, 023411.
- 14 Mairesse, Y., de Bohan, A., Frasin-ski, L.J., Merdji, H., Dinu, L.C., Monchicourt, P., Breger, P., Kovaèev, M., Taïeb, R., Carré, B., Muller, H.G., Agostini, P., and Salières, P. (2003) Attosecond Synchronization of High Harmonic Soft X-rays. *Science*, **302**, 1540–1543.
- 15 López-Martens, R., Varjú, K., Johnsson, P., Mauritsson, J., Mairesse, Y., Salières, P., Gaarde, M.B., Schafer, K.J., Persson, A., Svanberg, S., Wahlström, C.-G., and L'Huilier, A. (2005) Amplitude and Phase Control of Attosecond Light Pulses. *Phys. Rev. Lett.*, **94**, 033001.
- 16 Gustafsson, E., Ruchon, T., Swoboda, M., Remetter, T., Pourtal, E., López-Martens, R., Balcou, Ph., and L'Huilier, A. (2007) Broadband attosecond pulse shaping. *Opt. Lett.*, **32**, 1353–1356.
- 17 Dinu, L.C., Muller, H.G., Kazamias, S., Mullot, G., Augé, F., Balcou, Ph., Paul, P.M., Kovaèev, M., Breger, P., and Agostini, P. (2003) Measurement of the Subcycle Timing of Attosecond XUV Bursts in High-Harmonic Generation. *Phys. Rev. Lett.*, **91**, 063901.
- 18 Trebino, R., DeLong, K.W., Fittinghoff, D.N., Sweetser, J.N., Krumbügel, M.A., Richman, B.A., and Kane, D.J. (1997) Measuring ultrashort laser pulses in the time-frequency domain using frequency-resolved optical gating. *Rev. Sci. Instrum.*, **68**, 3277.
- 19 Walmsley, I.A., and Trebino, R. (1999) Measuring fast pulses with slow detectors. *Opt. Photonics News*, **7**, 23–29.
- 20 Norin, J., Mauritsson, J., Johansson, A., Raarup, M.K., Buil, S., Persson, A., Dühr, O., Gaarde, M.B., Schafer, K.J., Keller, U., Wahlström, C.-G., and L'Huilier, A. (2002) Time-frequency characterization of femtosecond extreme ultraviolet pulses. *Phys. Rev. Lett.*, **88**, 193902.
- 21 Sekikawa, T., Katsura, T., Miura, S., and Watanabe, S. (2002) Measurement of the intensity-dependent atomic dipole phase of a high harmonic by frequency-resolved optical gating. *Phys. Rev. Lett.*, **88**, 193902.
- 22 Power, E.P., March, A.M., Catoire, F., Sistrunk, E., Krushelnick, K., Agostini, P., and DiMauro, L.F. (2010) XFROG phase measurement of threshold harmonics in a Keldysh-scaled system. *Nat. Photonics*, **4**, 352–356.
- 23 Muller, H.G. (2002) Reconstruction of attosecond harmonic beating by interference of two-photon transitions. *Appl. Phys. B*, **74**, S17–S21.
- 24 Varjú, K., Johnsson, P., López-Martens, R., Remetter, T., Gustafsson, E., Mauritsson, J., Gaarde, M.B., Schafer, K.J., Erny, Ch., Sola, I., Zaïr, A., Constant, E., Cormier, E., Mével, E., and L'Huilier, A. (2005) Experimental studies of attosecond pulse trains. *Laser Phys.*, **15**, 888–898.
- 25 Toma, E.S. and Muller, H.G. (2002) Calculation of matrix elements for mixed extreme-ultraviolet-infrared two-photon above-threshold ionization of argon. *J. Phys. B*, **35**, 3435–3442.
- 26 Dudovich, N., Smirnova, O., Levesque, J., Mairesse, Y., Ivanov, M.Y., Villeneuve, D.M., and Corkum, P.B. (2006) Measuring and controlling the birth of attosecond XUV pulses. *Nat. Phys.*, **2**, 781–786.
- 27 Saeed, M., Kim, D., and DiMauro, L.F. (1990) Optimization and Characterization of a High-Repetition Rate, High-Powered Nd:YLF Regenerative Amplifier. *Appl. Opt.*, **29**, 1752–1757.
- 28 Cussat-Blanc, S., Ivanov, A., Lupinski, D., and Freysz, E. (2000) KTiOPO₄, KTiOAsO₄, KnbO₃ crystals for mid-infrared femtosecond optical parametric amplifiers. *Appl. Phys. B*, **70**, S247–S252.

- 29** Hansson, G., Karlsson, H., Wang, Shun-hua, and Laurell, F. (2000) Transmission measurements in KTP and isomorphic compounds. *Appl. Opt.*, **39**, 5058–5069.
- 30** Rodwell, M.J.W., Bloom, D.M., and Weingarten, K.J. (1989) Subpicosecond Laser Timing Stabilization. *IEEE J. Quantum Electron.*, **25**, 817–827.
- 31** Hettrick, M.C. (1984) Aberrations of varied line-space grazing incidence gratings in converging light beams. *Appl. Opt.*, **23**, 3221–3235.
- 32** Itatani, J., Levesque, J., Zeidler, D., Niikura, H., Pépin, H., Kieffer, J.C., Corkum, P.B., and Villeneuve, D.M. (2004) Tomographic imaging of molecular orbitals. *Nature*, **432**, 867–871.
- 33** Vozzi, C., Negro, M., Calegari, F., Sansone, G., Nisoli, M., De Silvestri, S., and Stagira, S. (2011) Generalized molecular orbital tomography. *Nat. Phys.*, **7**, 822–826.
- 34** Kruit, P., and Read, F.H., (1983) Magnetic field paralleliser for 2π electron-spectrometer and electron-image magnifier. *J. Phys. E*, **16**, 313.
- 35** Bisgaard, C.Z., and Madsen, L.B. (2004) Tunneling ionization of atoms. *Am. J. Phys.*, **72**, 249.
- 36** Xu, J., Chen, Z., Le, A.-T., and Lin, C.D. (2010) Self-imaging of molecules from diffraction spectra by laser-induced rescattering electrons. *Phys. Rev. A*, **82**, 033403.
- 37** Okunishi, M., Morishita, T., Prümper, G., Shimada, K., Lin, C.D., Watanabe, S., and Ueda, K. (2008) Experimental retrieval of target structure information from laser-induced rescattered photo-electron momentum distributions. *Phys. Rev. Lett.*, **100**, 143001.
- 38** DuBois, R.D., and Rudd, M.E. (1976) Differential cross sections for elastic scattering of electrons from argon, neon, nitrogen and carbon monoxide. *J. Phys. B*, **9**, 2657–2667.
- 39** Constant, E., Garzella, D., Breger, P., Mével, E., Dorrer, Ch., Le Blanc, C., Salin, F., and Agostini, P. (1999) Optimizing high harmonic generation in absorbing gases: Model and experiment. *Phys. Rev. Lett.*, **82**, 1668–1671.
- 40** Chen, M.-C., Arpin, P., Popmintchev, T., Gerrity, M., Zhang, B., Seaberg, M., Popmintchev, D., Murnane, M.M., and Kapteyn, H.C. (2010) Bright, coherent ultrafast soft X-ray harmonics spanning the water window from tabletop light sources. *Phys. Rev. Lett.*, **105**, 173901.
- 41** L'Huillier, A., Lewenstein, M., Salières, P., Balcou, Ph., Ivanov, M.Y., Larsson, J., and Wahlström, C.G. (1993) High-order harmonic-generation cutoff. *Phys. Rev. A*, **48**, R3433–R3436.
- 42** Shan, B., and Chang, Z. (2001) Dramatic extension of the high-order harmonic cutoff by using a long-wavelength driving field. *Phys. Rev. A*, **65**, 011804(R).
- 43** Colosimo, P., Doumy, G., Blaga, C.I., Wheeler, J., Hauri, C., Catoire, F., Tate, J., Chirla, R., March, A.M., Paulus, G.G., Muller, H.G., Agostini, P., and DiMauro, L.F. (2008) Scaling strong-field interactions towards the classical limit. *Nat. Phys.*, **4**, 386.
- 44** Agostini, P. and DiMauro, L.F. (2008) Atoms in high intensity mid-infrared pulses. *Contemp. Phys.*, **49**, 179–197.
- 45** Le, V.-H., Le, A.-T., Xie, R.-H., and Lin, C.D. (2007) Theoretical analysis of dynamic chemical imaging with lasers using high-order harmonic generation. *Phys. Rev. A*, **76**, 013414.
- 46** Tate, J., Auguste, T., Muller, H.G., Salières, P., Agostini, P., and DiMauro, L.F. (2007) Scaling of wave-packet dynamics in an intense midinfrared field. *Phys. Rev. Lett.*, **98**, 013901.
- 47** Shiner, A.D., Trallero-Herrero, C., Kajumba, N., Bandulet, H.-C., Comtois, D., Légaré, F., Giguère, M., Kieffer, J.-C., Corkum, P.B., and Villeneuve, D.M. (2009) Wavelength scaling of high harmonic generation efficiency. *Phys. Rev. Lett.*, **103**, 073902.
- 48** Popmintchev, T., Chen, M.-C., Cohen, O., Grisham, M.E., Rocca, J.J., Murnane, M.M., and Kapteyn, H.C. (2008) Extended phase matching of high harmonics driven by mid-infrared light. *Opt. Lett.*, **33**, 2128–2130.
- 49** Popmintchev, T., Chen, M.-C., Arpin, P., Murnane, M.M., and Kapteyn, H.C. (2010) The attosecond nonlinear optics

- of bright coherent X-ray generation. *Nat. Photonics*, **4**, 822–832.
- 50 Antoine, P., L'Huillier, A., and Lewenstein, M. (1996) Attosecond pulse trains using high-order harmonics. *Phys. Rev. Lett.*, **77**, 1234.
- 51 Mairesse, Y., de Bohan, A., Frasin-ski, L.J., Merdji, H., Dinu, L.C., Monchicourt, P., Breger, P., Kovaèev, M., Auguste, T., Carré, B., Muller, H.G., Agostini, P., and Salières, P. (2004) Optimization of attosecond pulse generation. *Phys. Rev. Lett.*, **93**, 163901.
- 52 Kim, K.T., Kim, C.M., Baik, M.-G., Umesh, G., and Nam, C.H. (2004) Single sub-50-attosecond pulse generation from chirp-compensated harmonic radiation using material dispersion. *Phys. Rev. A*, **69**, 051805(R).
- 53 Morlens, A.-S., Balcou, P., Zeitoun, P., Valentin, C., Laude, V., and Kazamias, S. (2005) Compression of attosecond harmonic pulses by extreme-ultraviolet chirped mirrors. *Opt. Lett.*, **30**, 1554.
- 54 Zuo, T., Bandrauk, A.D., and Corkum, P.B. (1996) Laser-induced electron diffraction: A new tool for probing ultrafast molecular dynamics. *Chem. Phys. Lett.*, **295**, 313–320.
- 55 Dubietis, A., Jonusauskas, G., and Piskarskas, A. (1992) Powerful femtosecond pulse generation by chirped and stretched pulse parametric amplification in BBO crystal. *Opt. Commun.*, **88**, 437.
- 56 Adachi, S., Ishii, H., Hanai, T., Ishnii, N., Kosuge, A., and Watanabe, S. (2007) 1.5 mJ, 6.4 fs parametric chirped-pulse amplification system at 1 kHz. *Opt. Lett.*, **32**, 2487.
- 57 Blaga, C.I., Xu, J., DiChiara, A.D., Sistrunk, E., Zhang, K., Agostini, P., Miller, T.A., DiMauro, L.F., Lin, C.D. (2012) Imaging ultrafast molecular dynamics with laser-induced electron diffraction. *Nature*, **483**, 194.
- 58 Xu, J., Blaga, C.I., DiChiara, A.D., Sistrunk, E., Zhang, K., Chen, Z., Le, A.-T., Morishita, T., Lin, C.D., Agostini, P., and DiMauro, L.F. (2012) Laser-induced electron diffraction for probing rare gas atoms. *Phys. Rev. Lett.*, **109**, 233002.

12

Attosecond Dynamics in Atoms

Giuseppe Sansone, Francesca Calegari, Matteo Lucchini, and Mauro Nisoli

12.1

Introduction

The energy spacing among electronic levels determines the timescale for the dynamics in single and multielectron systems. The basic principles of quantum mechanics state that an eigenstate $|\psi_j^0\rangle$ of the time independent Hamiltonian \hat{H} with energy E_j , evolves in time through a phase factor according to the relation

$$|\psi_j(t)\rangle = \exp\left(-i\frac{\hat{H}t}{\hbar}\right)|\psi_j^0\rangle = \exp\left(-i\frac{E_j t}{\hbar}\right)|\psi_j^0\rangle, \quad (12.1)$$

where \hbar is the reduced Planck constant. The state $|\psi_j(t)\rangle$ represents a stationary state in the sense that the expectation value T of a generic observable associated to the operator \hat{T} does not depend on time:

$$T = \langle \hat{T} \rangle = \langle \psi(t) | \hat{T} | \psi(t) \rangle = \langle \psi_j^0 | \hat{T} | \psi_j^0 \rangle. \quad (12.2)$$

Dynamics occur when the state of the system is given by a superposition of stationary states:

$$|\psi_j(t)\rangle = \sum_{j=1}^n a_j \exp\left[-\frac{i E_j t}{\hbar}\right] |\psi_j^0\rangle. \quad (12.3)$$

where a_j are normalization coefficients. In this case the expectation value T depends on time according to the relation

$$\begin{aligned} T &= \langle \psi(t) | \hat{T} | \psi(t) \rangle = \sum_{i=1}^n \sum_{j=1}^n a_i^* a_j \exp\left[\frac{i(E_i - E_j)t}{\hbar}\right] \langle \psi_i^0 | \hat{T} | \psi_j^0 \rangle \\ &= \sum_{i=1}^n |a_i|^2 T_{ii} + \sum_{i,j=1; i \neq j}^n a_i^* a_j \exp\left[\frac{i(E_i - E_j)t}{\hbar}\right] T_{ij}, \end{aligned} \quad (12.4)$$

where $T_{ii} = \langle \psi_i^0 | \hat{T} | \psi_i^0 \rangle$ and $T_{ij} = \langle \psi_i^0 | \hat{T} | \psi_j^0 \rangle$. The expectation value evolves on a timescale that is given by the inverse of the energy spacing ($E_i - E_j$); the larger is the difference in energy, the faster will be the time evolution and the dynamics of the system. For core and valence electronic levels, such a difference is on the order of tens of electron volt or fractions of an electron volt, leading to dynamics in the attosecond or few femtosecond domains, respectively. These basic considerations indicate that the attosecond regime is the natural timescale for the electronic motion. In the following, we will consider different superpositions of energy eigenstates in atoms and will analyze the induced dynamics in terms of the energy difference between the levels. In Section 12.2, the hydrogen atom will be analyzed to introduce an example for the superposition of electronic states. In Section 12.3, the two-electron helium atom will be discussed. Different phenomena (imaging of electronic wave packets, two-photon double ionization (TPDI), autoionization) will be discussed. Particular attention will be focused on the role played by electron correlation, that is, by the electron–electron interaction in the unfolding of the electronic dynamics. In Section 12.4, the typical processes of multielectron systems will be considered. Particular attention will be devoted to phenomena arising in highly excited neutral or ionic states, such as excitation of shake-up states (Section 12.4.1), Fano resonances (Section 12.4.3), single, and cascaded Auger decay (Sections 12.4.4 and 12.4.6).

12.2

Single-Electron Atom: Hydrogen

In this section we will discuss a tutorial example to illustrate the basic properties of the dynamics in a single-electron system. We consider the coherent superposition of the two lowest lying eigenstates of the hydrogen Hamiltonian the $|\psi_{1s}\rangle$ and $|\psi_{2s}\rangle$, whose representation in the space is given by [1]

$$\begin{aligned}\psi_{1s}(\mathbf{r}) &= \langle \mathbf{r} | \psi_{1s} \rangle = \frac{1}{\sqrt{\pi} a_0^{3/2}} \exp\left(-\frac{r}{a_0}\right) \\ \psi_{2s}(\mathbf{r}) &= \langle \mathbf{r} | \psi_{2s} \rangle = \frac{1}{2\sqrt{2\pi} a_0^{3/2}} \left(1 - \frac{r}{2a_0}\right) \exp\left(-\frac{r}{2a_0}\right),\end{aligned}\quad (12.5)$$

where r indicates the radial distance and a_0 is the Bohr radius. The representation of the two eigenstates in momentum space is given by

$$\begin{aligned}\phi_{1s}(\mathbf{p}) &= \langle \mathbf{p} | \phi_{1s} \rangle = \left(\frac{2}{p_0}\right)^{(3/2)} \frac{1}{\pi} \frac{1}{[(p/p_0)^2 + 1]^2} \\ \phi_{2s}(\mathbf{p}) &= \langle \mathbf{p} | \phi_{2s} \rangle = \frac{16}{\pi(p_0)^{3/2}} \frac{4(p/p_0)^2 - 1}{[4(p/p_0)^2 + 1]^3},\end{aligned}\quad (12.6)$$

where p_0 is the atomic unit of momentum. The coherent superposition of the two states with equal amplitude will be given by

$$|\psi(t)\rangle = \frac{1}{\sqrt{2}}|\psi_{1s}\rangle \exp\left(-i E_{1s} \frac{t}{\hbar}\right) + \frac{1}{\sqrt{2}}|\psi_{2s}\rangle \exp\left(-i E_{2s} \frac{t}{\hbar}\right) \quad (12.7)$$

with $E_{1s} = -0.5 E_{au}$ and $E_{2s} = -(1/8) E_{au}$, where E_{au} is the atomic unit of energy. We can analyze the radial ($P(r, t)$) and radial momentum ($P(p, t)$) density distributions as a function of time according to the definitions:

$$\begin{aligned} P(r, t) &= \int \sin \theta d\theta d\phi r^2 |\langle \mathbf{r} | \psi(t) \rangle|^2 = 4\pi r^2 |\psi(\mathbf{r}, t)|^2 \\ &= 2\pi r^2 \left[\psi_{1s}^2(\mathbf{r}) + \psi_{2s}^2(\mathbf{r}) + 2\psi_{1s}(\mathbf{r})\psi_{2s}(\mathbf{r}) \cos\left[(E_{2s} - E_{1s}) \frac{t}{\hbar}\right] \right] \\ P(p, t) &= \int \sin \theta_p d\theta_p d\phi_p p^2 |\langle \mathbf{p} | \psi(t) \rangle|^2 = 4\pi p^2 |\phi(\mathbf{p}, t)|^2 \\ &= 2\pi p^2 \left[\phi_{1s}^2(\mathbf{p}) + \phi_{2s}^2(\mathbf{p}) + 2\phi_{1s}(\mathbf{p})\phi_{2s}(\mathbf{p}) \cos\left[(E_{2s} - E_{1s}) \frac{t}{\hbar}\right] \right]. \end{aligned} \quad (12.8)$$

The density distributions $P(r, t)$ and $P(p, t)$ are reported in Figures 12.1 and 12.2,

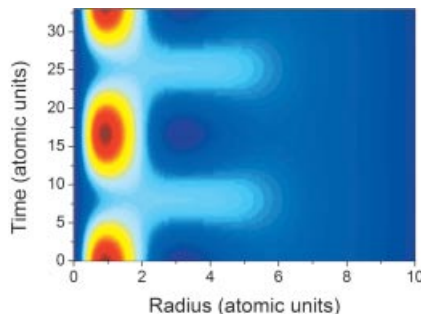


Figure 12.1 Radial density distribution $P(r, t)$ as a function of time.

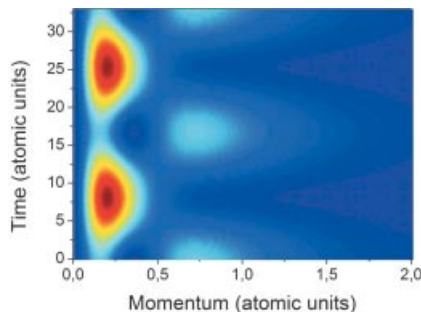


Figure 12.2 Radial momentum density distribution $P(p, t)$ as a function of time.

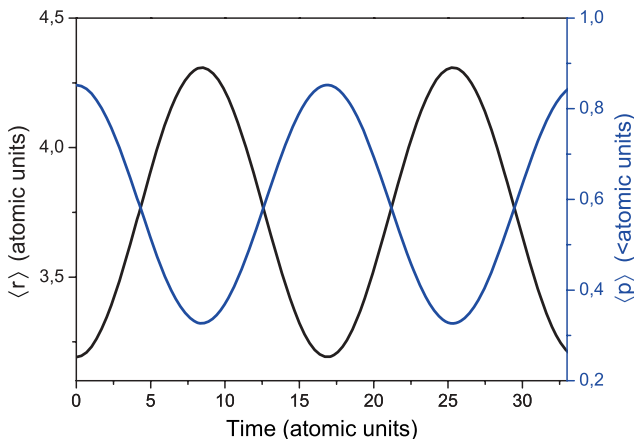


Figure 12.3 Time evolution of the mean values $\langle r \rangle$ (black solid line) and $\langle p \rangle$ (blue solid line).

respectively, which indicate a clear periodic motion with a period T :

$$T = \frac{2\pi\hbar}{E_{2s} - E_{1s}} = 402 \text{ as} . \quad (12.9)$$

The periodic changes indicate that the localization in space and in momentum of the electronic wave packet changes with time. It can be easily observed that the radial and momentum distributions oscillated out of phase according to the uncertainty principle. This is clearly shown in Figure 12.3, which reports the mean value of r and p according to the relations

$$\langle r(t) \rangle = \int_0^{+\infty} 4\pi r^3 |\psi(r, t)|^2 dr \quad (12.10)$$

$$\langle p(t) \rangle = \int_0^{+\infty} 4\pi p^3 |\phi(p, t)|^2 dr . \quad (12.11)$$

Scrinzi *et al.* [2] proposed an experiment to excite and to image the “breathing” motion of the coherent superposition of the 1s and 2s states. They suggested to populate the 2s state using an (ultraviolet) UV pulse resonant with the 1s – 2p transition. Using an intense static field, it is then possible to transfer population from the 2p to the 2s state, realizing the 1s – 2s superposition. A short attosecond pulse could then be used to ionize the excited atom and to measure the ionization yield as a function of the relative delay between the two pulses. Indeed, due to the oscillation of the wave packet, the ionization probability changes in time as shown in Figure 12.4; in particular, it can be observed that the ionization yield oscillates in phase with the mean value of p . The relation between these properties can be understood in terms of a classical mechanism; the power absorption is related to the

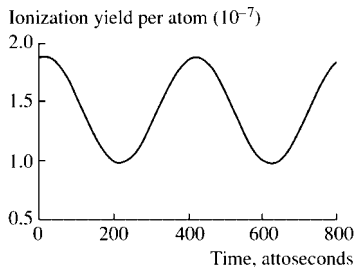


Figure 12.4 Oscillation of the ionization probability in hydrogen (adapted from [2]).

force F due to the interaction between the external electric field of the attosecond pulse and the electron by the relation

$$W = \mathbf{F} \cdot \mathbf{v} = \mathbf{F} \cdot \left(\frac{\mathbf{p}}{m} \right), \quad (12.12)$$

where m is the electron mass. Therefore the absorption is larger when the momentum p is large, corresponding to an electronic wave packet localized around the nucleus. In spite of its simple description, the excitation and the imaging of this wave packet has not yet been performed.

12.3

Two-Electron Atom: Helium

Helium represents a benchmark for the investigation of attosecond and few-femtosecond dynamics and it has already been used in a number of experiments [3–5]. Several theoretical investigations have focused on the role played by electron correlation in the ultrafast dynamics taking place in helium [6–11]. A coherent superposition of states in helium can be written (in the space representation) as

$$\begin{aligned} \psi(\mathbf{r}_1, \mathbf{r}_2, t) = & \sum_{i,j} a_{i,j}(t) \psi_{i,j}(\mathbf{r}_1, \mathbf{r}_2) + \sum_i \int d^3 p b_{i,p}(t) \psi_{i,p}(\mathbf{r}_1, \mathbf{r}_2) \\ & + \iint d^3 p d^3 p' b_{p,p'}(t) \psi_{p,p'}(\mathbf{r}_1, \mathbf{r}_2). \end{aligned} \quad (12.13)$$

The first, second, and third terms on the right-hand side of Eq. (12.13) represent a wave packet with two bound electrons, with one bound electron and one electron in the continuum, and with two electrons in the continuum, respectively. The bound and continuum states are eigenstates of a two-electron Hamiltonian (atomic units):

$$\hat{H} = -\frac{1}{2} \nabla_{\mathbf{r}_1}^2 - \frac{1}{2} \nabla_{\mathbf{r}_2}^2 - \frac{2}{r_1} - \frac{2}{r_2} + \frac{1}{r_{12}}. \quad (12.14)$$

Because of the interaction term between the electron ($1/r_{12}$), the two-electron wavefunction $\psi(\mathbf{r}_1, \mathbf{r}_2)$ cannot be expressed as the product of single-particle orbitals

$\psi(\mathbf{r}_1)$, and $\psi(\mathbf{r}_2)$. In the central field approximation, leading to the Hartree–Fock orbital, the interaction term is replaced by the mean field experienced by the electron due to the presence of the other electron. In this way, it is still possible to write the wavefunction as a product of single-particle orbitals. The electron interaction is taken into account only to some extent and the wavefunction obtained as product of single-electron orbitals is not an exact eigenstate of the Hamiltonian \hat{H} . In the following, we will discuss two situations where electron correlation beyond the Hartree–Fock approximation plays a relevant role.

12.3.1

Electronic Wave Packets

The large bandwidth of the attosecond pulses allows us to create complex wave packets by shaping either the phase and/or the spectrum of the excitation pulse. In the experiment of Mauritsson *et al.* [4], a coherent wave packet characterized by bound and continuum components was created using an isolated attosecond pulse centered around the ionization threshold of helium. Spectral components below the ionization threshold can excite the atom to an np state, whereas spectral components above the ionization threshold can lead to ionization with the emission of an electron with momentum \mathbf{p} . Therefore the electronic wave packet can be described by the following relation (the index 1s for the wavefunction has been omitted for simplicity):

$$\begin{aligned}\psi(\mathbf{r}_1, \mathbf{r}_2, t) = & \sum_n a_{np}(t) \exp\left(-i\varphi_{np} - i\frac{E_{np}t}{\hbar}\right) \psi_{np}(\mathbf{r}_1, \mathbf{r}_2) \\ & + \int d^3 p b_p(t) \psi_p(\mathbf{r}_1, \mathbf{r}_2).\end{aligned}\quad (12.15)$$

The bound components of the electronic wave packet can be completely characterized by using a synchronized ultrashort IR pulse that promotes part of the bound wave packet into the continuum. A complete characterization requires the measurement of the energies of the state E_{np} , the amplitudes a_{np} , and the initial phases φ_{np} . Mauritsson *et al.* [4] suggested to acquire the photoelectron spectra created by the interference between an electron wave packet whose evolution is “known” and the electron wave packet to be characterized, in order to retrieve this information. In this respect, the technique represents an extension of holographic concepts to electron wave packets. Usually, holography is used for the reconstruction of a coherent light beam from the interference pattern (holographic pattern) created by the coherent superposition between a reference beam and an object beam.

The interference pattern presents characteristic features as shown in Figure 12.5, which reports the result of a time-dependent Schrödinger equation (TDSE), using a single active electron approach, for different delays between the excitation with an extreme ultraviolet (XUV) pulse and the infrared (IR) probe. Around the region of temporal overlap of the pump–probe pulses, the photoelectron spectra show a

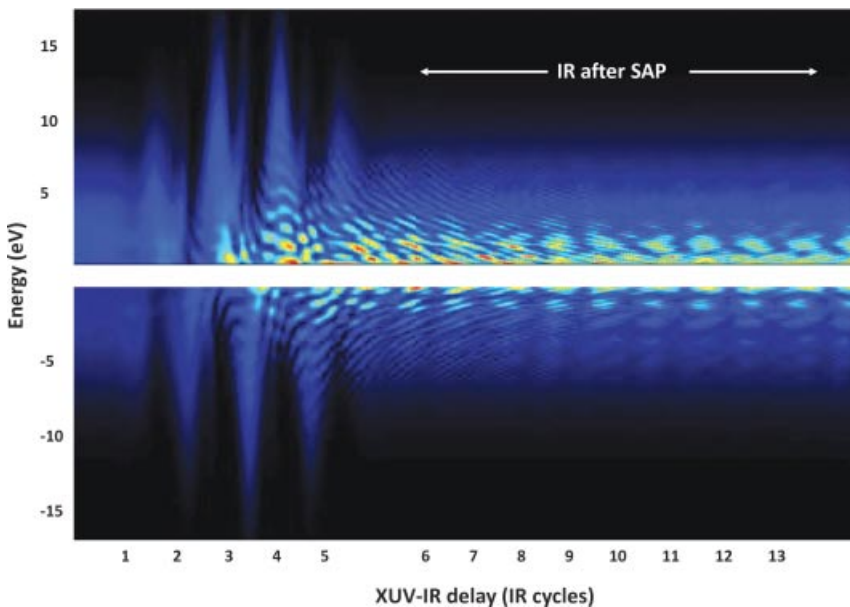
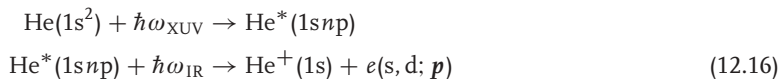


Figure 12.5 TDSE simulation of the photoelectron spectra emitted by an XUV isolated attosecond pulse and a single cycle IR pulse (courtesy of Dr. J. Mauritsson).

periodic oscillation due to the additional momentum transferred from the IR pulse to the electrons emitted by the isolated attosecond pulse. For positive time delays (i.e., the IR pulse arrives after the XUV pulse), the photoelectron spectra are characterized by a series of interference fringes, whose energy spacing decreases with increasing time delay, and by a periodic oscillation of the signal that reflects a quantum beat (QB) in the photoionization yield. The different origin of the structures can be better understood by considering the Fourier transform along the delay axis, as shown in Figure 12.6. This plot is characterized by structure tilted by 45° due to the interference between two ionization paths:



and



The term $e(p; \mathbf{p})$ indicates that the electron, due to the absorption of a single XUV photon, is emitted with momentum \mathbf{p} in a p-like wave. On the other hand, the term $e(s, d; \mathbf{p})$ indicates that, after absorption of one XUV and one IR photon, the

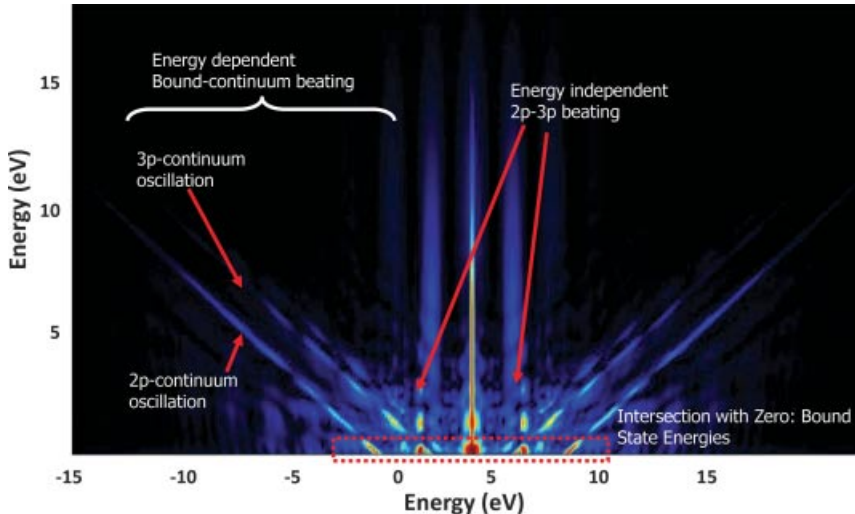
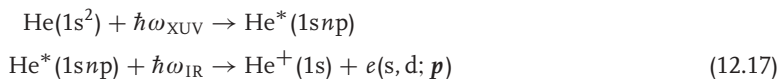
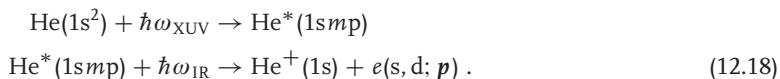


Figure 12.6 Fourier analysis of the photoelectron spectra shown in Figure 12.5 (courtesy of Dr. J. Mauritsson).

electron is emitted in a s- or d-like wave. The vertical lines in Figure 12.6 correspond to quantum beats among bound components of the wave packets ionized by the IR field according to the relation



and



After excitation with the XUV pulse, the wave packet evolution is controlled by the Hamiltonian $H_{\text{tot}} = H + \mathbf{r} \cdot \mathbf{E}_L$ including a dipole term taking into account the interaction with the IR field \mathbf{E}_L . The observation of an electron characterized by momentum \mathbf{p} is then given by

$$M_p = \langle \mathbf{p} | \psi(t) \rangle = \langle \mathbf{p} | U_{\text{tot}} \psi \rangle \simeq \langle \mathbf{p} | U_L U_0 \psi \rangle , \quad (12.19)$$

where U_{tot} , U_0 , and U_L represent the evolution operators associated to the total Hamiltonian $\hat{H} + \mathbf{r} \cdot \mathbf{E}_L$, the field free Hamiltonian H , and the dipole term $\mathbf{r} \cdot \mathbf{E}_L$, respectively. It is important to point out that this schematization is valid only if the IR pulse arrives after the XUV pulse.

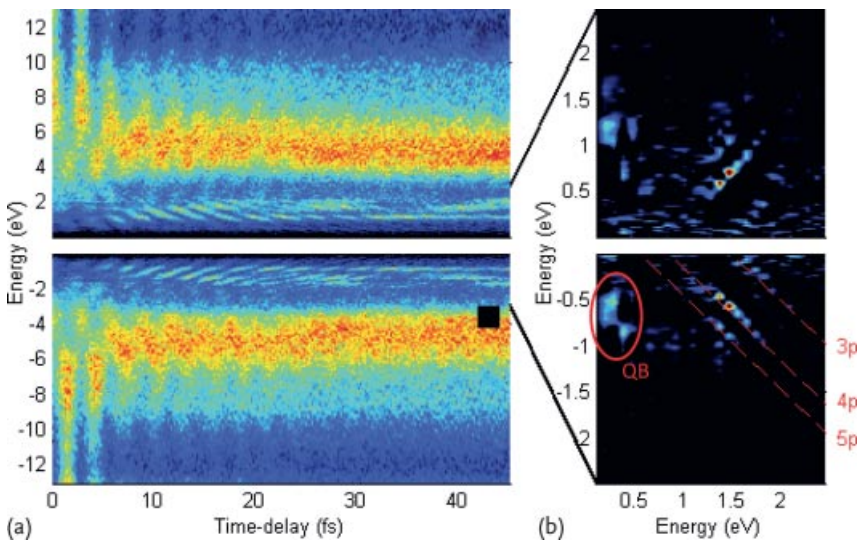


Figure 12.7 Evolution of He photoelectron spectra as a function of the relative delay between the XUV isolated attosecond pulse and the IR few-cycle pulse (a). Fourier analysis of

the photoelectron spectra (b). Reprinted with permission from [4]. Copyright (2010) by the American Physical Society.

Following the approach developed in [12], it is possible to express the final transition to the state of momentum \mathbf{p} as

$$\begin{aligned} |M_p|^2 = & a_{p^2} + \sum_n b_{p,np}^2 a_{np}^2 \\ & + 2 \sum_n a_p b_{p,np} a_{np} \cos[\Phi_{p,np} - (E_p - E_{np})\tau] \\ & + 2 \sum_{n < m} b_{p,np} b_{p,mp} a_{np} a_{mp} \cos[\Phi_{mp,np} - (E_{mp} - E_{np})\tau], \end{aligned} \quad (12.20)$$

where the term $\Phi_{p,np}$ contains the terms due to the Volkov phase and the dipole phases involved in the transition from the ground state to the continuum ψ_p and in the transition first from the ground state to the bound state ψ_{np} and then to the continuum ψ_p . Similarly, the phase $\Phi_{mp,np}$ is related to the phase difference between the path from the ground state to the continuum ψ_p , through the bound states ψ_{mp} and ψ_{np} . The coefficient $b_{p,np}$ describes the amplitude of the matrix elements associated with the transitions among the states ψ_{np} and ψ_p . Finally, E_{np} , E_{mp} , and E_p indicate the energies of the bound states ψ_{np} , ψ_{mp} and of the continuum state ψ_p , respectively.

The first and second term on the right-hand side of Eq. (12.20) correspond to direct ionization to the p states by the XUV and ionization by the combination of the IR and XUV field, respectively. The third term corresponds to an interference term between direct ionization to a p state and ionization by the IR field of a bound state $|np\rangle$ excited by the XUV pulse. Finally, the fourth term corresponds to the

interference between two bound states, excited by the XUV (ψ_{np} and ψ_{mp}) and ionized by the IR field. The two distinct interference patterns are characterized by a different evolution as a function of the delay τ and of the observation energy E_p . Indeed Eq. (12.20) indicates that the equi-phase surfaces in the (τ, E) plane are given for the third term by the relation

$$\cos[\Phi_{p,np} - (E_p - E_{np})\tau] = \text{const.} \Rightarrow \tau \propto \frac{1}{(E_p - E_{np})} \quad (12.21)$$

and are represented by hyperbola. The onset of such lines can be recognized in Figure 12.7a at low energies and for positive time delays. For the fourth term of Eq. (12.20), the corresponding relation is

$$\cos[\Phi_{mp,np} - (E_{mp} - E_{np})\tau] = \text{const.} \Rightarrow \tau \propto \frac{1}{(E_{mp} - E_{np})}. \quad (12.22)$$

These surfaces do not depend on the energy E_p and are represented by lines parallel to the energy axes and can be recognized in the time domain as oscillations of the photoelectron yield (longer time delays visible in Figure 12.5).

It is important to observe that the characterization of the angular distribution of the photoelectrons allows us to distinguish between the two interference terms (bound–continuum and bound–bound). Indeed, the two ionization channels are characterized by the absorption of a different number of photons: the direct channel involves the absorption of a single XUV photon, leading to the emission of an electron in a p ($l = 1$) state; on the other hand, the indirect channel requires the absorption of one XUV photon and one IR photon (or more, depending on the IR intensity), leading to emission of an electron in an s ($l = 0$) or d state ($l = 2$). These contributions can be distinguished by applying decomposition in Legendre polynomials according to the relation

$$F(E, \theta, t) = \sum_{j=0}^{L_{\max}} \beta_j(E, t) P_j(\cos \theta), \quad (12.23)$$

where $P_j(\cos \theta)$ is the Legendre polynomial of j -order, β_j is an expansion coefficient and L_{\max} is the maximum angular component of the ionized wave packet. The Legendre analysis of the experimental data is shown in Figure 12.8, which reports the coefficients $\beta_1(E, t)$ and $\beta_2(E, t)$ of the Legendre polynomial expansion and the corresponding Fourier analysis.

The analysis indicates that the angular information allows us to separate the contributions of the different interference patterns contributing to the photoelectron spectra. In the Fourier domain, the different interference terms are associated with different structures (vertical or tilted lines), as shown in Figure 12.8d and f.

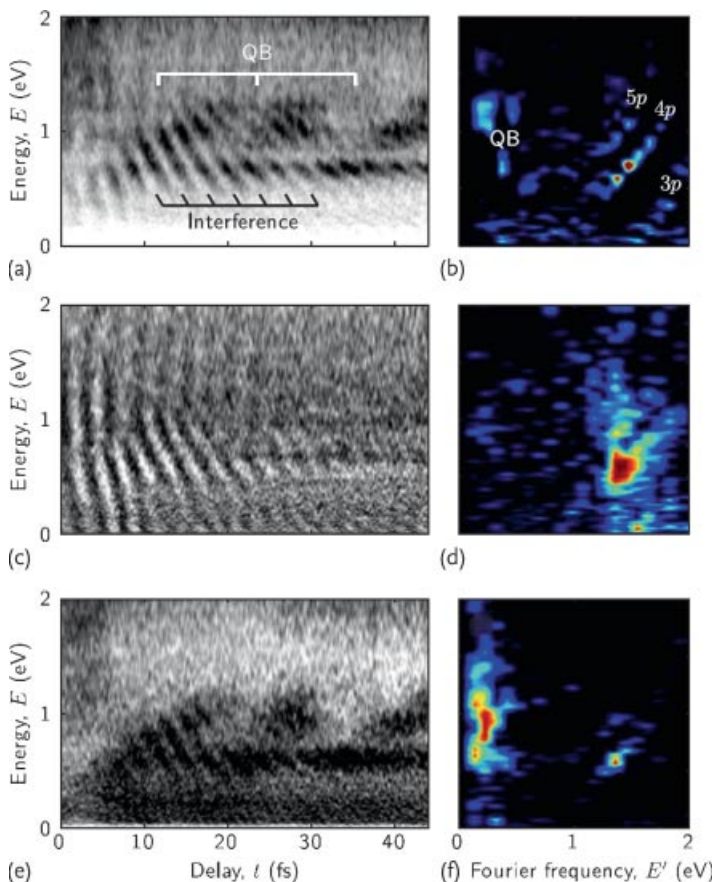


Figure 12.8 Legendre polynomial analysis of the photoelectron spectra shown in Figure 12.7a with the corresponding Fourier analysis (b). Coefficients $\beta_1(E, t)$ (c) and

$\beta_2(E, t)$ (e) of the expansion (12.23) and their corresponding Fourier analysis (d) and (f). Reprinted with permission from [4]. Copyright (2010) by the American Physical Society.

12.3.2

Autoionization: Fano Profile

The autoionization process is an ionization mechanism in which an initially electronic excited atom releases its excess energy by emitting an electron into the continuum while a second electron decays to a lower energy state. The autoionization mechanism is due to the interaction between electrons in the excited state and is ubiquitous in nature. This mechanism was recognized for the first time in helium by analyzing the dependence of the impact ionization cross section on the energy of the incoming electron. Early measurements revealed the presence of resonances that were interpreted by Fano as the result of the interference between two ioniza-

tion pathways. Such resonances also characterize the photoionization process of helium. The two mechanisms are schematically summarized in Figure 12.9a and b:

- 1) absorption of an XUV photon and emission of an electron into the continuum with an energy $E = \hbar\omega - \text{IP}$.
- 2) absorption of an XUV photon that leads to population of a doubly excited state, which decays with a time constant T . The interaction between the two electrons can lead to the emission of one electron into the continuum with the same energy E , while the second electron reoccupies the original 1s orbital. The total photoelectron spectrum measured is given by the coherent superposition of these two paths due to a mixing of two different electronic configurations (configuration interaction) and present a typical shape named Fano resonance [13]. The initial interpretation of Fano assumed a wavefunction given by

$$\psi(\mathbf{r}_1, \mathbf{r}_2, t) = a(t)\psi(\mathbf{r}_1, \mathbf{r}_2) + \int d^3 p b_p(t)\psi_p(\mathbf{r}_1, \mathbf{r}_2), \quad (12.24)$$

where $\psi(\mathbf{r}_1, \mathbf{r}_2)$ and $\psi_p(\mathbf{r}_1, \mathbf{r}_2)$ are Hartree–Fock orbitals (configurations). The term $a(t)\psi(\mathbf{r}_1, \mathbf{r}_2)$ represents the doubly excited state (2s2p), while the integral $\int d^3 p b_p(t)\psi_p(\mathbf{r}_1, \mathbf{r}_2)$ describes the fraction of the wavefunction characterized by one electron in the continuum and one electron in the bound state (1s). The coefficient $a(t)$ decreases in time due to the autoionization process. Because of the interaction term $1/r_{12}$, the Hartree–Fock orbitals are not orthogonal and a coupling between the bound and the continuum state exists according to the relation:

$$V_E = \langle \psi_{2s2p}(\mathbf{r}_1, \mathbf{r}_2) | H | \psi_p(\mathbf{r}_1, \mathbf{r}_2) \rangle. \quad (12.25)$$

The coupling term V_E describes the strength of the interaction between the two configurations and determines the linewidth Γ of the resonance and the decay timescale T according to the equations

$$\Gamma = \pi |V_E|^2 \quad (12.26)$$

and

$$T = \frac{1}{\Gamma}. \quad (12.27)$$

The photoionization cross section is characterized by a shape resonance according to the relation

$$F(\epsilon) = \frac{(q + \epsilon)^2}{1 + \epsilon^2}, \quad (12.28)$$

where q is the Fano parameter and ϵ is the reduced energy given by the relation

$$\epsilon = \frac{E - E_{\text{res}}}{\frac{\Gamma}{2}}, \quad (12.29)$$

where E_{res} is the resonant absorption energy. A few examples of Fano profiles for different q parameters are shown in Figure 12.9b. It is important to observe that the profile of the resonance is governed by the q parameter; in particular for $q \rightarrow +\infty$, the Fano profile reduces to a Lorentzian profile. Due to the typical linewidth of the resonances, the autoionization times can range from few tens of attoseconds up to few femtoseconds.

The time evolution of the Fano resonance was analyzed by Mercouris *et al.* [14] for helium, Choi and Lin [12] for beryllium and by Wickenhauser *et al.* for Dy [15]. In particular, they studied how the resonance profile changes in time after the interaction of the XUV field with the atom. Different approaches were suggested for the time-resolved investigation of Fano resonances, including attosecond streaking spectroscopy [15] of the emitted photoelectron wave packet and XUV-pump XUV-probe approaches [12]. Recently, the first approach was implemented to resolve in time the autoionization of the Fano resonance excited in He by absorption of XUV light around 60.1 eV [16]. A streaking of the electronic wave packet was performed using a synchronized intense IR field. The autoionization process leads to the emission of an electron with energy around 35.5 eV, as shown in Figure 12.10a. When the emission takes place in the presence of an IR field, single (multiple) IR-photon absorption or emission redistributes the electron signal in two additional sidebands (SB1 and SB2), leading to a decrease of the signal in the autoionization band (AI), as shown in Figure 12.10b. This figure reports the AI signal as a function of the relative delay between the isolated attosecond and the IR pulses. For longer time delays, the autoionization process has time to occur and the signal in the AI increases while the sidebands decrease. Fitting the temporal evolution of the AI signal with a Lorentzian, a time constant of $T = 17$ fs was estimated in agreement with spectral measurements of the linewidth of the Fano resonance.

12.3.3

Two-Photon Double Ionization

Experimental investigations of the TPDI process on the subfemtosecond timescale have not been performed so far because of the lack of intense attosecond pulses. Theoretical studies, however, have analyzed in deep detail the correlated dynamics originating from the absorption of two XUV photons, suggesting possible approaches to characterize the motion of the two-electron wave packet. Depending on the energy of the XUV radiation, electron correlation can lead to different photoionization mechanisms. Considering that the first and second ionization potential of helium are $I_{\text{p}1} = 24.6$ eV and $I_{\text{p}2} = 54.4$ eV, respectively, two photon-energy ranges can be identified for the generation of doubly ionized helium (He^{2+}).

(i) $39.5 \text{ eV} \leq \hbar\omega \leq 54.4 \text{ eV}$

Generation of He^{2+} is possible only if two photons are absorbed simultaneously by the electrons according to the relation



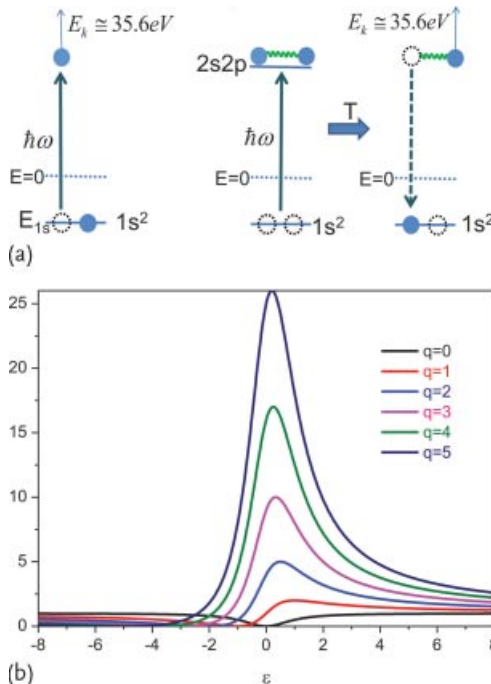


Figure 12.9 (Schematic view of the autoionization process in helium using an XUV photon $\hbar\omega = 60.1$ eV. (a) Direct photoionization path with emission of an electron with an energy $E = 35.6$ eV and excitation of a

doubly excited state that decays with a time constant T emitting an electron with an energy $E = 35.6$ eV. (b) Fano profile according to Eq. (12.28) for different values of the q parameter.

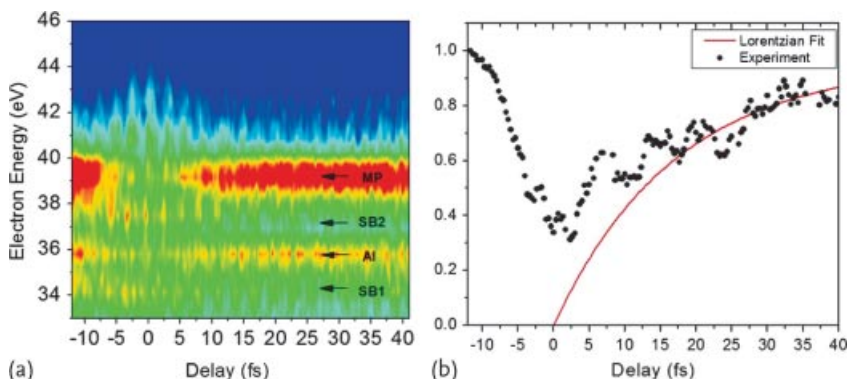


Figure 12.10 Time-resolved measurement of autoionization in He around the Fano resonance (from [16]). (a) Photoelectron spectra as a function of the delay time between the isolated attosecond and the intense 800-nm IR laser pulse. For negative time delays, the IR pulse precedes the attosecond pulse. AI: electron signal corresponding to the autoioniza-

tion resonance, SB1-2: sidebands generated by the emission/absorption of an IR-photon by the autoionizing electronic wave packet. (b) Time-dependent photoelectron signal near 35.5 eV. The red line corresponds to an assumed lifetime of 17 fs. Reprinted with permission from [16]. Copyright (2010) by the American Physical Society.

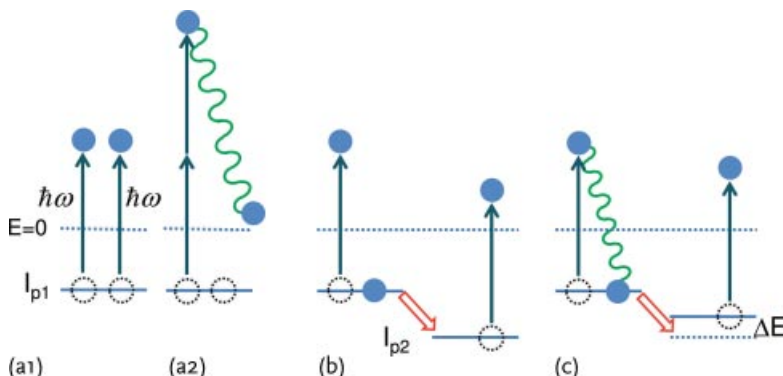


Figure 12.11 Schematic view of double ionization induced by absorption of two XUV photons $\hbar\omega$. NS-TPDI described by independent interaction of the two electrons with the external field (a1) or by interaction of a single electron with the external field and involving electron correlation (shown as a green line) (a2). S-TPDI described by independent inter-

action of the electrons with the external field at different time instants (b). S-TPDI characterized by electron correlation leading to the population of shake-up states (c). I_{p1} and I_{p2} are the first and second ionization potential, respectively. ΔE is the energy difference between the shake-up state and the ionic ground state.

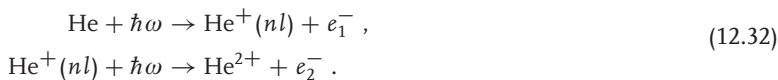
where $\hbar\omega$ is the photon energy and e_1^- and e_2^- indicate the two photoionized electrons. This mechanism is usually referred to as nonsequential two-photon double ionization (NS-TPDI) and can be described by two different pictures, as schematically shown in Figure 12.11a1 and a2. The two electrons adsorb separately two photons and are emitted into the continuum (Figure 12.11a1). This process can be described by an independent particle picture and does not imply electron correlation. On the other hand, a single electron can absorb two photons (Figure 12.11a2) and give part of the energy to the second electron that is emitted at the same time. This mechanism cannot be described by an independent particle model and it is based on the interaction between electrons.

(ii) $\hbar\omega \geq 54.4$ eV

In this energy range, besides the NS-TPDI mechanism, two additional pathways can lead to the formation of He^{2+} :



and



The first mechanism (see Figure 12.11b) represents a sequential process in which a first photon ejects one electron, leaving the ion in the ground state $\text{He}^+(1s)$. At a later time, a second photon is absorbed by the bound electron

leading to a second ionization event. This process can be understood in an independent particle picture and does not require electron correlation. The second mechanism (see Figure 12.11c) is analogous but the intermediate ionic state is an excited state, characterized by quantum numbers (n,l). The process can be interpreted as a sequential process; however electron correlation plays a role as the first electron leaving the atom can exchange energy with the ionic core, promoting the second electron to an unoccupied electronic state (shake-up state). These two mechanisms are usually called sequential two-photon double ionization (S-TPDI). It should be pointed out that for photon energy $\hbar\omega \geq I_{p1} + I_{p2} = 79.0$ eV, a mechanism for double ionization based on the absorption of a single XUV photon opens up. The process of single photon double ionization requires electron correlation, but will not be further discussed.

The signature of S-TPDI and NS-TPDI was investigated in the probability energy distributions for the two electrons emitted by an intense attosecond pulse with central energy $\hbar\omega = 91.45$ eV and different pulse durations Δt , as shown in Figure 12.12a–c [7].

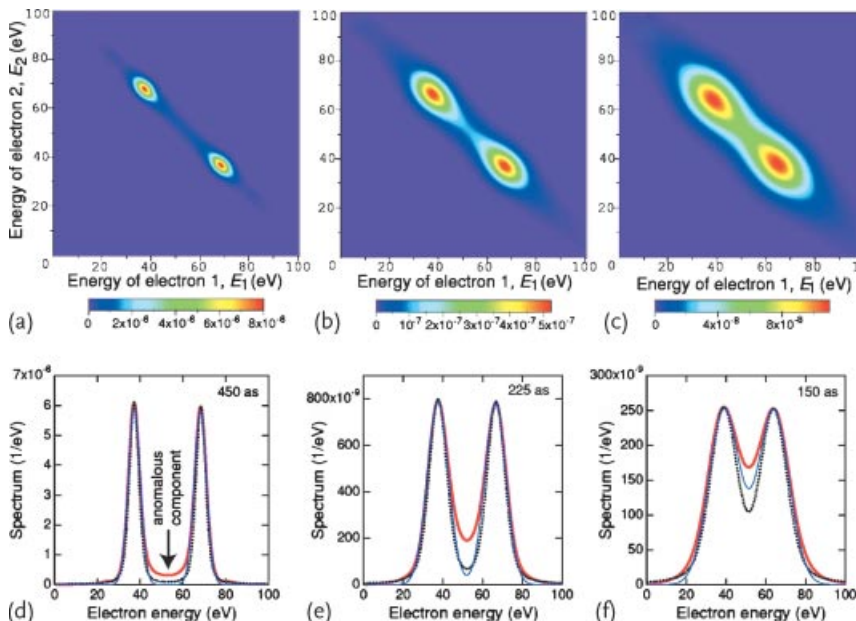


Figure 12.12 Probability distribution for the two electron energies E_1 and E_2 emitted by two-photon double ionization (a–c); integration of the two-electron energy distribution over E_2 (red thick solid line), electron energy distribution based on an independent-particle model considering the Gaussian profile of the

attosecond pulse (blue thin solid line) and the absorption profile of a single electron (black thin dotted lines) (d–f), for the three different pulse durations Δt : 450 as (a,d), 225 as (b,e) and 150 as (c,f). Reprinted with permission from [7]. Copyright (2005) by the American Physical Society.

For a pulse duration of $\Delta t = 450$ as (see Figure 12.12a), two strong contributions can be observed around $E_1 = 66.9$ eV and $E_2 = 37.1$ eV, corresponding to a sequential process in which the first electron is emitted with an energy $E_1 = \hbar\omega - I_{p1}$ and the second one is ejected at a later time with an energy $E_2 = \hbar\omega - I_{p2}$. Besides these two main peaks, other peaks at energies of $E_{s1} = 25$ eV and $E_{s2} = 80$ eV are present (barely visible in Figure 12.12a). These peaks correspond to a sequential ionization mechanism with excitation of a 2s or a 2p shake-up state, according to the relation $E_{s1} = \hbar\omega - I_{p1} - \Delta E$ and $E_{s2} = \hbar\omega - I_{p1} + \Delta E$, where ΔE indicates the energy difference between the ionic ground state and the shake-up state. The contribution of such a mechanism was also reported in Fig. 1 of [8].

The region between the two main peaks is characterized by a contribution that has been referred to as “anomalous” component in [7]. The relevance of this component increases upon reducing the pulse duration. This is shown in Figure 12.12b and c, which display the two-electron energies for $\Delta t = 225$ as and $\Delta t = 150$ as, respectively. The increase of the anomalous component cannot be completely attributed to the larger pulse bandwidth associated to shorter attosecond pulses as shown in Figure 12.12d–f. These figures report the integration of the two-electron energy distributions over the energy E_2 (red line) and the results of two independent particle models reflecting the Gaussian profile of the attosecond pulses (black line) and the absorption profile of the helium electrons (blue line). Neither models can fit the behavior of the anomalous component, leading to the conclusion that the central part cannot be explained in the framework of an independent particle approach.

The origin of this contribution has been discussed in several publications and different mechanisms have been suggested. Parker *et al.* [6] have attributed this component to a nonsequential double above threshold ionization process (NS-DATI), in which the two electrons absorb simultaneously two photons and exchange energy while escaping the atom. Ishikawa *et al.* [7] argued that the anomalous component can be attributed to a sequential process and investigated two mechanisms involving electron correlation in the final or intermediate state:

- 1) Postionization energy exchange (PIEE): The second electron leaves the ion when the first one is still in the proximity of the ion. In the continuum, the two electrons can exchange energy by Coulomb interaction.
- 2) Second ionization during core relaxation (SICR): When the first electron is emitted, the ion is in a nonstationary state that can relax to the ionic ground state on a timescale determined by the difference between the two ionization potentials, $\hbar/(I_{p2} - I_{p1}) = 22$ as. The anomalous component can be attributed to ionization of the second electron during relaxation of the ionic core.

Considering the timescale for the core relaxation, it is clear that the distinction between NS-TPDI and S-TPDI has to be revisited when discussing photoionization induced by attosecond pulses. Indeed, the sequential mechanism is based on the assumption that the ion, after ejection of the first electron, can relax to a stationary state before the second electron is emitted. In the case of ionization by an attosecond pulse, the first electron is still close to the ion when the second electron is

emitted and an unambiguous temporal distinction of the two ionization events is not straightforward. Therefore, sequential and nonsequential mechanisms do not represent the most suitable physical picture to describe the TPDI in the attosecond domain. In this context it is more appropriate to distinguish between features that can be interpreted in an independent particle picture and components that imply the relevance of the electron correlation. In particular, more physical understanding can be gained by identifying in which way the correlated electronic motion plays a key role.

Feist *et al.* [10] distinguished three different types of electron correlation:

- 1) correlation in the ground state due to the Coulomb interaction in the helium atom;
- 2) correlation in the intermediate state, corresponding to the relaxation of the ionic core when the first electron is being ionized;
- 3) correlation in the final state, corresponding to the exchange of energy between the two electrons in the continuum.

It must be noted that no sharp boundaries between these three situations can be drawn. Nevertheless, their introduction allows us to deepen our physical understanding of the process.

Ishikawa *et al.* [7] attributed the origin of the anomalous component mainly to the SICR process, fitting the correlated energy distributions for different pulse durations. Such a conclusion indicated that correlation in the intermediate state plays the most relevant role in explaining this component. The contribution of the PIEE (therefore correlation in the final state) cannot be, however, completely ruled out.

Barna *et al.* [8] analyzed the single electron angular distribution $P(\theta)$ to identify the contributions of the different mechanisms to the TPDI. The photoelectron angular distribution can be expressed as

$$\frac{d\sigma}{d\Omega} = \frac{\sigma_0}{4\pi} [1 + \beta P_2(\cos \theta) + \gamma P_4(\cos \theta)], \quad (12.33)$$

where σ_0 is the total cross section, $P_{2,4}$ are the Legendre polynomials, and β and γ are the second-order ($k = 2$) and fourth-order ($k = 4$) anisotropy parameters, respectively. The coefficient β can take values between -1 and 2 ; a value of $\beta = 2$ indicates a dipole transition given by the interaction of a single electron with the external field. The coefficient γ indicates the presence of a quadrupole component that can only arise from electron correlation. For the peaks shown in Figure 12.12a, the angular distribution resembles that of a Hertz dipole that characterizes the interaction of a single electron with an external field (see Figure 12.13a). Deviations from the independent-particle model indicate the presence of correlation effects. For the angular distribution corresponding to the peaks, β is at least an order of magnitude larger than γ and is close to the maximum value of 2 ; for such peaks, the double-ionization process can be understood in terms of an independent-particle model. On the other hand, for the anomalous component, β and γ have comparable values, leading to a superposition of dipole and quadrupole contributions (as shown in Figure 12.13b), and indicating the relevance of electron correlation. The presence of the quadrupole component can be used to identify whether electron

correlation affects the initial (both electrons are in a bound state), the intermediate (one electron is in a continuum state and the other is bound), or the final state (both electrons are in the continuum) of the two-electron dynamics. The two-electron wavefunction can be written in the configuration interaction form as

$$|\Psi\rangle = \sum_{n,j} a_s^{(n,j)} |s^n\rangle |s^j\rangle + \sum_{n,j} a_p^{(n,j)} |p^n\rangle |p^j\rangle + \sum_{n,j} a_d^{(n,j)} |d^n\rangle |d^j\rangle + \dots \quad (12.34)$$

Electron correlation in the initial state leads to the presence of non-*s* orbitals contributing to the ground state. A quadrupole component requires a contribution to the final state characterized by a total angular momentum $L_f = 2$ as $k = 2L_f$. This condition can be realized by a combination of single particle momentum orbitals in the finale state l_f and l'_f such that $(l_f, l'_f) \in \{(s_f, d_f), (p_f, p_f), (d_f, d_f)\}$. The last configuration is negligible for the intensities used in the simulations. The peaks are dominated by the (p_f, p_f) configurations, while the anomalous component is dominated by the (s_f, d_f) component.

This final configuration can be reached along two pathways involving absorption of two XUV photons:

$$\begin{aligned} s_i &\xrightarrow{\hbar\omega} s_f; s_i \xrightarrow{\hbar\omega} p \xrightarrow{\hbar\omega} d_f, \\ p_i &\xrightarrow{\hbar\omega} s_f; p_i \xrightarrow{\hbar\omega} d_f. \end{aligned} \quad (12.35)$$

While the first mechanism can be realized from the dominant configuration of the ground state (s_i, s_i) , the second one requires the contribution of a configuration (p_i, p_i) to the ground-state wavefunction and is only possible considering electron correlation in the initial state. Barna and co-workers [8] have verified that the anomalous component is reduced by an order of magnitude when the contribution of the initial configuration (p_i, p_i) is switched off. This indicates that correlation in the initial state may be more relevant than in the final state. The conclusion that electron correlation between the two outgoing electrons may play only a secondary role in the process is consistent with the observation of Ishikawa and co-workers [7] that PIEE is only a secondary effect with respect to SICR. On the other hand, second ionization during core relaxation points toward correlation in the intermediate state, whereas the conclusion of Barna and co-workers indicates that initial state correlation could be more relevant. These conclusions indicate that the interpretation of the different features of the TPDI process is still under discussion. Theoretical simulations will strongly benefit by comparison with experimental two-electron angular distributions that could be measured using the intense attosecond light sources available in the near future.

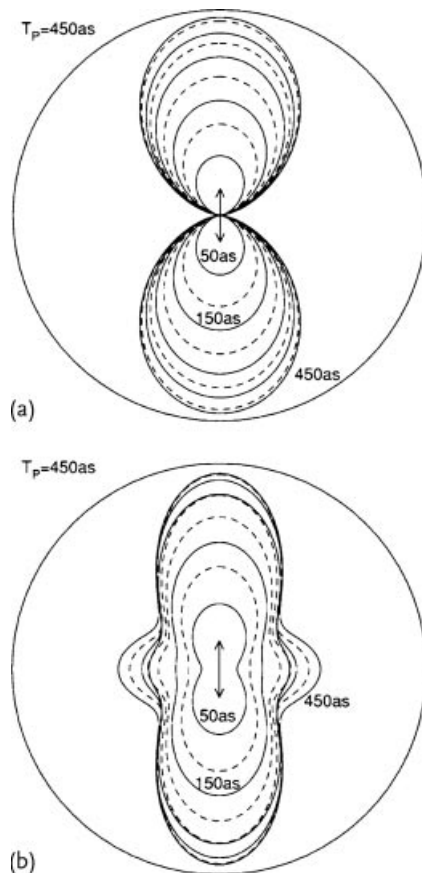


Figure 12.13 The angular distribution of the electrons emitted by an attosecond pulse with duration of 450 as for an energy of $E = 37 \text{ eV}$ (a) and $E = 52 \text{ eV}$ (b). The solid and dashed lines indicate surface of con-

stant intensities at times 50 to 450 as in steps of 50 as. Reprinted with permission from [8]. Copyright (2006) by the American Physical Society.

12.4 Multielectron Systems

Several experiments have been performed on multielectron systems, investigating the ultrafast response to an external electric field in the XUV or X-ray region. These experiments focused on studying how the absorption of an XUV photon that creates a hole in the inner-valence or core shells, leads to an electronic rearrangement on a few femtosecond or subfemtosecond timescale. Excitation of shake-up states and relaxation dynamics, such as single core hole Auger decay and autoionization, are among the most intriguing processes driven by electron correlation that have been investigated in real time. In Table 12.1, a few of the most relevant experiments have been summarized. In the following section, we will discuss the main

experimental conclusions of the studies reported in Table 12.1, pointing out how the attosecond or few-femtosecond dynamics has been characterized.

12.4.1

Neon: Dynamics of Shake-Up States

The basic understanding of the photoionization process relies on a single active electron picture: an electron adsorbs a sufficient number of photons from the external field in order to overcome the Coulomb barrier, given by the nucleus and the other electrons, and it is emitted into the continuum. This oversimplified picture does not consider that the total electron wave packet interacts with the external field and that electron correlation can cause a different redistribution of the energy during the process. An example is given by the excitation of shake-up states during the photoionization process: an electron is emitted in the continuum by an external field and during its way out of the atom, it exchanges energy with a second electron (or several electrons) that is (are) raised to an unoccupied excited state of the ion. This mechanism was already introduced discussing the TPDI in helium (see Section 12.3) and is responsible for the observation of the side energy peaks in Figure 12.12a. The characterization of the population of shake-up states can be used to infer information about the electron correlation involved in the photoionization process. Such states can eventually decay to higher binding energy ions by Auger decay, as will be discussed in Section 12.4.4.

Uiberacker *et al.* [17] characterized the time evolution of the shake-up states created in the photoionization of neon with an isolated attosecond pulse centered at 91 eV. As shown in Figure 12.14a, Ne^+ ion can be created in the states $2p^{-1}$, $2s^{-1}$, or in a shake-up state $2p^{-2}(nl)$ by single XUV photon absorption. The interaction of the IR field with the Ne^+ ion can lead to ionization of the shake-up states, leading to an increase of the yield of Ne^{2+} ions with respect to the yield associated with single XUV photon double ionization. The population of the shake-up states can be monitored by varying the delay between the XUV and IR pulses for different in-

Table 12.1 Attosecond dynamics in multielectron systems: Examples of experiments performed on atoms (first column) using isolated attosecond pulses or intense X-ray pulses.

Process	Spectroscopy	Reference
Neon	Shake-up states	Tunneling spectroscopy [17]
$1s^2 2s^2 2p^6$	Delay in photoemission	Attosecond streaking [18]
Argon	Fano resonance	Transient absorption spectroscopy [19]
$(\text{Ne})3s^2 3p^6$		
Krypton	Auger decay	Attosecond streaking [20]
$(\text{Ar})3d^{10} 4s^2 4p^6$	Hole oscillation	Transient absorption spectroscopy [21]
Xenon	Cascaded Auger decay	Ion chronoscopy [22]
$(\text{Kr})4d^{10} 5s^2 5p^6$	Autoionization	XUV-pump/XUV-probe [23]

tensities of the IR pulse, in order to disentangle the contributions of the different shake-up states to the formation of doubly ionized neon. In the dipole approximation, the IR field distorts the Coulomb potential experienced by the atom or the ion and creates a barrier through which the electron can escape. Depending on the time required by the electron to tunnel through the potential barrier, the strong field photoionization process can be better described in terms of a multiphoton process or as a tunneling process. The fundamental parameter for distinguishing the different regimes is the so-called Keldysh parameter given by

$$\gamma = \frac{t_{\text{tun}}}{T_0}, \quad (12.36)$$

where t_{tun} is the time required for the electron wave packet to tunnel through the potential barrier and T_0 is the optical period. For $\gamma \ll 1$, the tunneling time is much shorter than the semi-optical period; in this condition, the ionization process is described in terms of tunneling ionization and the photoelectron wave-packet emission is confined around the peaks of the electric field. For $\gamma \gg 1$, the tunneling time is longer than the electric field period and the ionization process is described in terms of absorption of several photons (multiphoton ionization) in order to overcome the ionization potential IP. Considering the length L of the potential barrier created by the IR field:

$$L = \frac{I_p}{E} \quad (12.37)$$

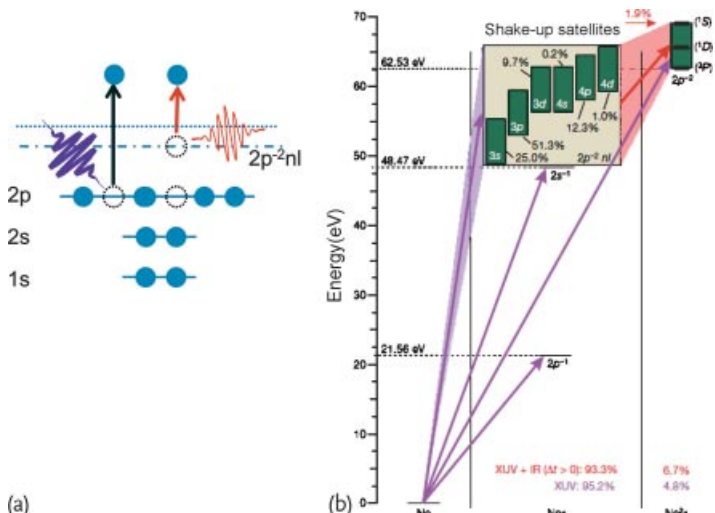


Figure 12.14 Schematic view of the excitation of shake-up states $2p^{-2}nl$ during photoionization of a $2p$ electron. (a) The IR field can ionize these states leading to the formation of Ne^{2+} . (b) Population of the $2p^{-2}nl$ states and population of singly and doubly charged

ions Ne^+ and Ne^{2+} by the interaction with the XUV pulse only and with the XUV and IR pulses. Reprinted by permission from Macmillan Publishers Ltd: Nature ([17]). Copyright 2007.

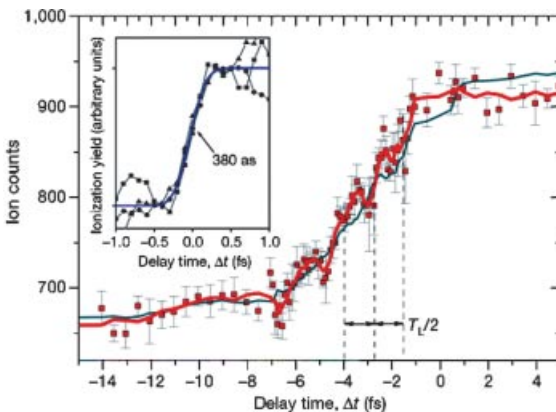


Figure 12.15 Ne^{2+} -ion yield as a function of the delay between the attosecond pump pulse and the IR probe. The inset shows that the increase of ion yield is confined by the

tunneling process on few hundreds of attosecond. Reprinted by permission from Macmillan Publishers Ltd: Nature ([17]). Copyright 2007.

and that the time required to tunnel through this barrier is

$$t_{\text{tun}} = \frac{L}{v} = \frac{I_p}{E\nu} = \frac{I_p}{E\sqrt{2I_p}} \quad (12.38)$$

the following expression can be derived for the Keldysh parameter:

$$\gamma \propto \sqrt{\frac{I_p}{2U_p}} \quad (12.39)$$

where E is the electric field, v is the electron's velocity, and $U_p = E^2/(4\omega^2)$ is the ponderomotive potential of the IR field. Equation (12.39) indicates that a transition from multiphoton to the tunneling regime can occur in the same laser field intensity, if states with different ionization potentials are ionized. This situation is shown in Figure 12.14b, which reports the energy levels and the ionization rates for different shake-up states of neon populated by single XUV-photon absorption. Due to the low ionization potential, the higher lying shake-up state $2p^{-2}4p$ is expected to be ionized at low electric field intensity where the multiphoton mechanism dominates; in this condition, the ionization process is expected to follow the envelope of the laser pulse. On the other hand, for lower lying states (such as the $2p^{-2}3p$ and $2p^{-2}3s$ states), ionization is confined close to the peak of the electric field and is expected to occur in the tunneling regime. In the latter case, the ionization should be characterized by sharp increases around the peak of the IR electric field.

In the experiment, the yield of doubly charged ions Ne^{2+} was measured as a function of the relative delay between the IR and the XUV field. The intensity of the IR field was limited to $(7 \pm 1) \times 10^{13} \text{ W/cm}^2$ to avoid double ionization by the IR field alone. The effect of the IR field is an enhancement of the Ne^{2+} yield, corresponding to about 40% of the yield released by the XUV pulse alone when

the delay between the two pulses approaches zero. This indicates that the IR pulse ionizes species that have been formed in the interaction with the XUV field. The experimental points (see Figure 12.15) show an initial smooth increase at large negative delays associated to depletion of the $2p^{-2}4p$ state (relative population of 12%) and $2p^{-2}3d$ state (relative population of 10%). Just before the time overlap, a rapid increase of the yield is due to the depletion of the strongly populated shake-up states $2p^{-2}3p$ ($\sim 50\%$) and $2p^{-2}3s$ ($\sim 25\%$). The increase of the yield proceeds in few steps on a timescale of few hundreds of attosecond; these steps represent the first experimental evidence, in the time domain, of an attosecond tunneling ionization process and clearly demonstrate that the bound electron is released in the form of attosecond wave packets. Ion chronoscopy could be a very powerful technique to characterize the dynamics of transient electronic excited states (such as shake-up states) with a time resolution of few hundreds of attoseconds, only limited by the rise time of the ion yield. This is shown in the inset of Figure 12.15, which presents the evolution of the Ne^{2+} around the time overlap between the XUV and IR pulse. An application of this technique in xenon will be presented in Section 12.4.6.

12.4.2

Neon: Delay in Photoemission

Photoionization from different atomic levels can occur due to the large photon energy bandwidth associated to isolated attosecond pulses. Such an experiment was performed by Schultzze *et al.* [18], using an isolated attosecond pulse with a central energy of 106 eV to ionize electrons from the 2s and the 2p levels of neon; due to the pulse bandwidth (14 eV), photoelectrons emitted by the two levels are well-separated in energy. By applying an intense, synchronized IR pulse, the emission time of the electronic wave packet can be mapped into the momentum shift of the electronic distribution according to the attosecond streak camera principle [25, 26]. In particular the authors demonstrated that the emission from the 2p level is delayed by $\Delta t = 20.5$ as with respect to the emission time from the 2s level (see Figure 12.16). The delay in the photoemission corresponds to the atomic phase, that is, the phase $\varphi(p)$ of the matrix element $D(p)$ that describes, in the dipole approximation, the transition from a bound state of the N electrons wavefunction $|\psi(t)\rangle$ to a continuum state $|p\rangle$ (a state in which $N - 1$ electrons are bound and one electron with momentum p is measured):

$$D(p) = \langle p | r | \psi(t) \rangle = |D(p)| e^{i\varphi(p)}. \quad (12.40)$$

The relevance of this phase term in attosecond physics and, more generally, its relevance in the photoionization process was already recognized in pioneering works on attosecond science, where this term was derived from theoretical models [27]. The experimental observations indicate the possibility to characterize the phase $\varphi(p)$ using the current attosecond streaking technique, as clearly demonstrated in some subsequent publications [28].

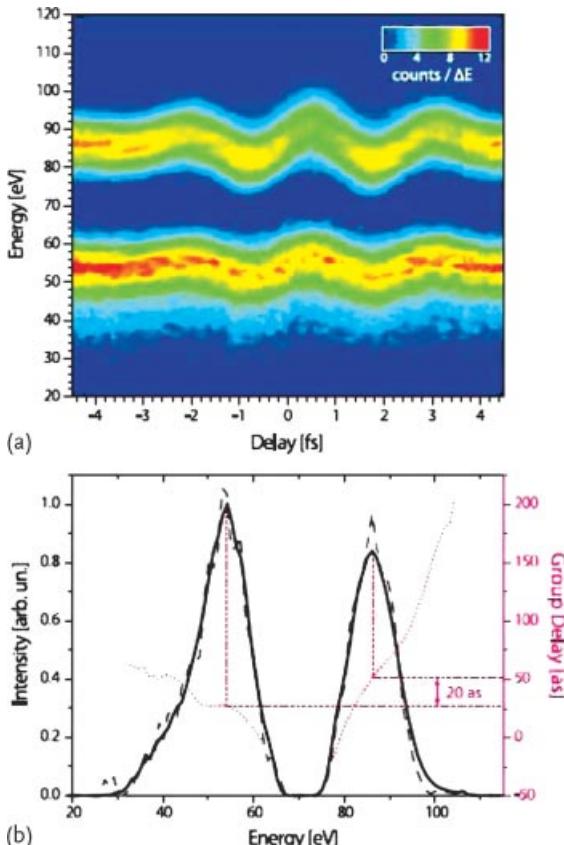


Figure 12.16 (a) Attosecond streaking photoelectron distributions emitted by the 2s and 2p levels of neon as a function of the relative delay between the XUV and IR pulse. (b) Measured (black solid line) and reconstructed (gray dashed line) photoelectron wave packets. The group delays of the retrieved wave packet (red dotted line) indicate a mean delay difference of 20 as (b).

So far, the quantitative agreement between the observed delay and theoretical models is not completely satisfactory and clearly indicates the relevance of electronic correlation effects for a complete description of the atomic wavefunction. The authors compared the outcomes of the TDSE in the single active electron approximation, the Coulomb–Volkov approximation, and more refined models including multielectron correlation such as a state-specific expansion approach. Even though these models turn out to be in qualitatively agreement with the experimental observation (the photo ionization from the 2p shell is delayed with respect to the one from the 2s), they do not offer proper agreement with the experiment as the estimated delay of 5 as is three standard deviations smaller than the measured one. The discrepancy clearly indicates that our understanding and our capability of modeling multielectron correlation effects is still far from being complete and

that subtle effects leading to attosecond time delays cannot yet be satisfactorily described. In this contest, the experimental data will represent a benchmark for more sophisticated and advanced models, including electron correlations.

Further investigations regarding the delay in the photoemission process could answer the question whether an “absolute” time delay in the photoionization process may occur, that is, a delay between the interaction of the XUV pulse with the atomic system and the release of the electronic wave packet. This question is of paramount relevance for the further development of attosecond science, as neglecting such a delay would introduce a systematic error in the determination of the trigger time of the electronic reaction, preventing a correct temporal tracking of the subsequent dynamics. However, the characterization of such a delay may be extremely elusive: as attosecond pulses already represent the shortest events that can be generated by mankind, it would not be possible to sample this delay as performed in usual pump–probe experiments. A possible solution, as outlined by the authors, would be to perform a two-color photoionization (XUV and intense IR) experiment in Helium, as in this case multielectron theory allows us to solve “exactly” the Schrödinger equation without neglecting terms related to the electron correlation. The comparison between theory and experiment could allow for the characterization of the time delay occurring in the photoionization process, opening the way for a more precise definition of the origin of the time arrow in electronic reactions in atoms and molecules. However, the time resolution achieved experimentally so far is mainly limited by the poor signal to noise ratio due to the low cross section of photoionization in helium. Improved experimental setups (larger collection solid angle for the photoelectrons, larger gas density, or higher repetition rate laser systems) should allow us to overcome these limitations in the near future. It is important to point out that such an “absolute” time delay has been neglected so far; however with the latest advances in attosecond science, and with the possibility to synthesize pulses approaching the atomic unit of time ($1 \text{ au} = 24 \text{ as}$), the answer to this question becomes a key point for pushing our understanding of ultrafast dynamics down to the few attosecond limit.

12.4.3

Argon: Fano Resonance

The autoionization process discussed in Section 12.3.2 is ubiquitous in nature and occurs when an excited states is embedded in a continuum of states. In 2010, Wang *et al.* [19] reported on the control of the decay of autoionizing states in argon by using an intense IR field. The autoionizing levels $3s3p^64p$, $3s3p^65p$ and $3s3p^66p$ were excited using an isolated attosecond pulse (see Figure 12.17c). The interaction of the IR field can couple these states to states in the continuum (nonresonant coupling) or to other autoionizing states (resonant coupling) as shown in Figure 12.18. In the first case, the absorption of one or more IR photons leads to a coupling between the autoionizing levels and the Ar^{*+} ($3s3p^6\epsilon l$) with a reduction in the lifetime of the decaying states. In the second case the state $3s3p^64p$ can be coupled to the $3s3p^64d$ state by the IR photon, inducing Rabi oscillations between the two

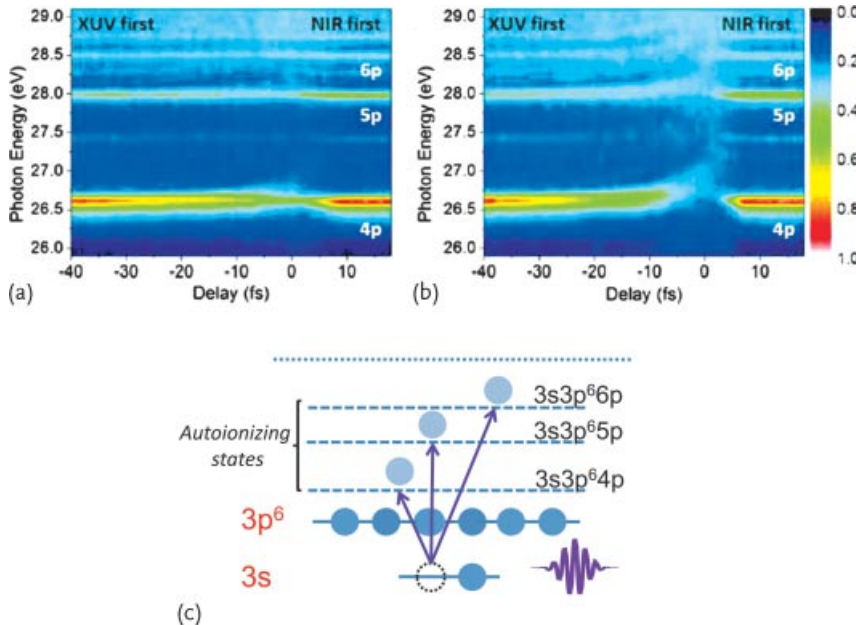


Figure 12.17 Transient absorption spectra measured for an IR intensity of $I = 5 \times 10^{11} \text{ W/cm}^2$ (a) and $I = 10^{12} \text{ W/cm}^2$ (b). Autoionizing states populated by the XUV

photon absorption (c). Reprinted with permission from [19]. Copyright (2010) by the American Physical Society.

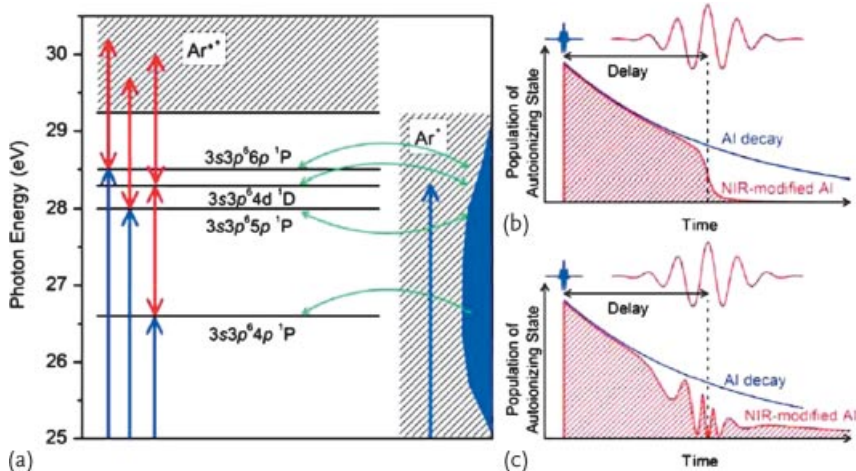


Figure 12.18 (a) Energy levels and IR-induced couplings between the autoionizing manifold $3s3p^6np$ and $3s3p^64d$ and the ground and excited states of Ar^+ . (b) Coupling between the manifold and the continuum of states determines a reduction of the population of the

autoionizing states. (c) Coupling between the manifold and the autoionizing state $3s3p^64d$ determines a Rabi oscillation of the population of the autoionizing states. Reprinted with permission from [19]. Copyright (2010) by the American Physical Society.

states. This will determine a symmetric splitting of the energy levels that will be modified by the decay of both states to the continuum, leading to a final asymmetric profile.

The control of the autoionization mechanism was observed by monitoring the XUV light of the isolated attosecond pulse through a gas cell filled with argon. In Figure 12.17a and b, the variation of the XUV light for different delays between the XUV and the IR pulses is reported for two different IR intensities. The IR determines a broadening of the linewidth of the autoionization channel and also a splitting of the levels. The effect is more relevant for the higher IR intensity.

12.4.4

Krypton: Auger Decay

The process of Auger decay can be regarded as an autoionization process driven by electron correlation similar to the one described in Section 12.3.2 for Helium. The initial step for the Auger mechanism is usually the photoionization of an inner valence or core electron, creating an ion in an excited state. Energy exchange driven by electron correlation, that is, the coupling due to configuration interaction between the singly ionized excited states and the doubly ionized states of the continuum, can lead to the emission of an electron while a second one decays to a lower energy state (the inner-valence or core vacancy). This mechanism is the dominant one in several electronic configurations; for core hole vacancy the decay time can be as short as few femtoseconds or even in the attosecond domain.

Before the availability of isolated attosecond pulses, the Auger mechanism was investigated using synchrotron sources by analyzing the Auger electron emitted in the decay process. Such experiments, however, could deliver only time integrated information and the lifetime of the Auger level was inferred by the linewidth of the Auger electron peak. This method, does not allow to gain any physical insight in complex de-excitation mechanisms, as in the case of cascaded Auger processes; in this case only resolving the transient population of the excited states in time allows us to track the decay path. The new possibilities offered by attosecond pulses will be highlighted discussing an example of time-resolved cascaded Auger decay in xenon in Section 12.4.6.

The first time-resolved investigation of an Auger process was reported in a pioneering work by Drescher *et al.* in 2002 [20]. Using a 90-eV isolated attosecond pulse, an M-shell (3d) core vacancy was created as shown in Figure 12.19a; this hole is expected to decay with a lifetime τ of a few femtoseconds by Auger decay of a 4s electron filling the vacancy, while a 4p electron is emitted into the continuum (see Figure 12.19b). The emission of the Auger electrons can be sampled in time by using a synchronized IR field. For very short time decay (τ well below the IR optical cycle T_0), the Auger electron will experience a momentum shift given by the instantaneous vector potential of the IR field according to the attosecond streak camera principle [25, 26]. On the other hand, for a long decay time (τ longer than the IR optical cycle T_0), the electron wave packet can absorb or emit IR photons leading to the formation of sidebands of the main photoelectron line. By analyz-

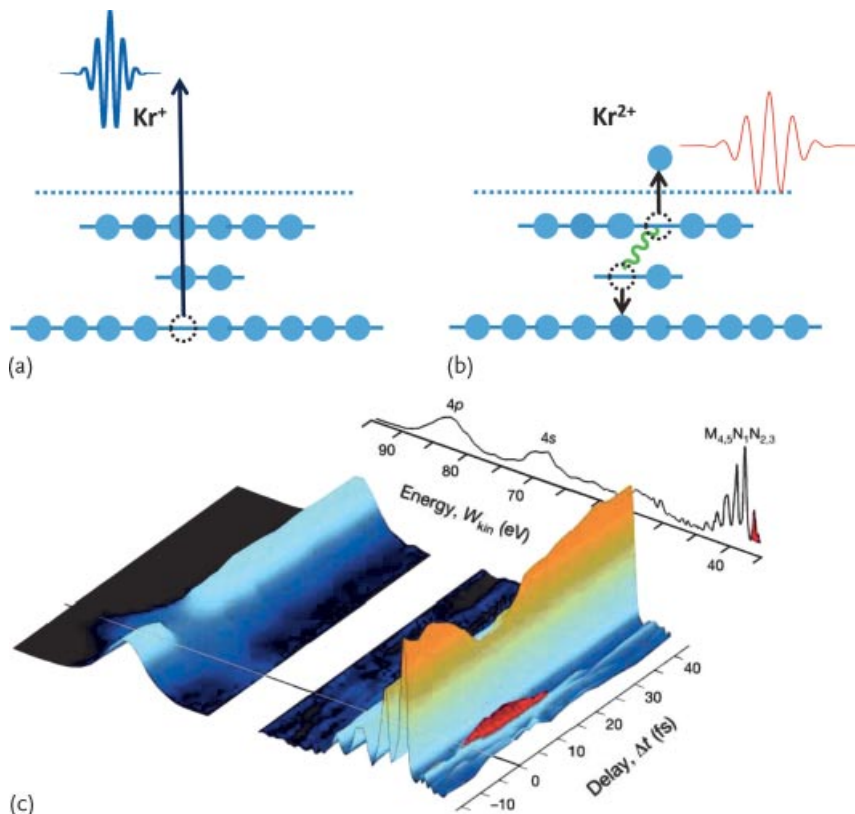


Figure 12.19 Photoionization of a 3d shell by single XUV absorption (a) and generation of Kr²⁺ by Auger decay (b). Photoelectron spectrum as a function of the relative delay

between the XUV and IR pulse (c). Reprinted by permission from Macmillan Publishers Ltd: Nature ([20]). Copyright 2002.

ing the time evolution of the sidebands signals as a function of the relative delay between the XUV and IR pulses, the decay time can be inferred. The photoelectron spectra measured in the experiment is shown in Figure 12.19c. The peaks 4p and 4s indicate the electrons emitted directly by the two different atomic orbitals. These peaks are not shifted by the IR field, since the carrier-envelope phase of the IR pulses was not stabilized; in this condition, the main effect of the IR pulse is to broaden the photoelectron distribution. The electron peaks corresponding to the Auger lines are visible and sidebands of these lines appear close to the temporal overlap between the XUV and IR pulses. The duration of the sidebands signal represents a cross-correlation between the XUV and IR pulses and the Auger decay time. From this measurement, a time constant $\tau = 7$ fs was estimated, in good agreement with previous estimations based on spectral measurements.

12.4.5

Krypton: Charge Oscillation

In Section 12.2, it has been shown that the coherent superposition of two eigenstates ($1s$ and $2s$) in hydrogen leads to a periodic oscillation of the electron density that influences the absorption probability of an external XUV photon. The coherent excitation and the imaging of such a charge oscillation require short pulses (in the few femtosecond or attosecond domain) due to the energy spacing of the valence electronic levels. The first experimental demonstration of such a charge oscillation was reported by Goulielmakis *et al.* [21] in Kr^+ ions. A coherent superposition of states was created in the ion by an intense near-single-cycle IR pulse that ionized one valence electron, leaving the ion in a coherent superposition of the $4p_{j=3/2}^{-1}$ ($m_j = -3/2, -1/2, 1/2, 3/2$) and $4p_{j=1/2}^{-1}$ ($m_j = -1/2, 1/2$) manifolds, where j indicates the total angular momentum and m_j is the projection of the total angular momentum along the quantization axis z (see Figure 12.20a). Strong field ionization is confined to the peaks of the instantaneous electric field and, for each oscillation maximum, an electronic wave packet is launched into the system, evolving with a period of $T = 6.2 \text{ fs}$ (corresponding to a spin-orbit splitting of $\Delta E_{\text{so}} = 0.67 \text{ eV}$). Due to the oscillation of the electric field, in each half-optical cycle a hole wave packet is launched in the $4p$ shell with a phase difference with respect to the previous one of about $\Delta\varphi = 4\pi$, imposed by the time between the

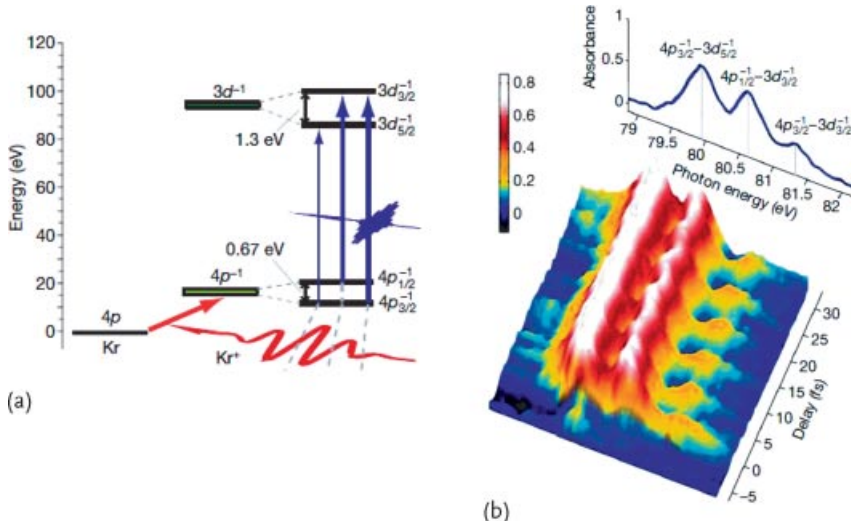


Figure 12.20 Relevant energy levels for Kr and Kr^+ . The single-cycle IR pulse creates a coherent superposition of the $4p_{j=3/2}^{-1}$ and $4p_{j=1/2}^{-1}$ manifolds. The XUV pulse promotes these states to the $3d_{3/2}^{-1}$ excited ionic state (a). Transmitted XUV spectrum for different time

delays (b). The modulation in the absorption are due to the hole oscillation in the valence shell of Kr^+ . Reprinted by permission from Macmillan Publishers Ltd: Nature ([21]). Copyright 2010.

two electric field maxima (~ 1.25 fs). The use of a near-single cycle pulse allows us to confine the excitation to few half-optical cycles, thus ensuring that the total hole wave packet is almost in phase.

Imaging of the hole motion was accomplished by exploiting the modulation of the absorption properties related to hole motion, as discussed in Section 12.2. In this case, a broadband attosecond pulse, centered around 80 eV, can excite the ion to the $3d_{3/2}^{-1}$ state, creating a core-electron vacancy according to the two paths: $4p_{3/2}^{-1} \rightarrow 3d_{3/2}^{-1}$ and $4p_{1/2}^{-1} \rightarrow 3d_{3/2}^{-1}$. Depending on the relative phase between the $4p_{3/2}^{-1}$ and $4p_{1/2}^{-1}$ states, constructive or destructive interference in the population of the excited state can occur, leading to a delay-dependent modulation of the absorption of XUV light. The delay between the near-single-cycle and the attosecond pulse was varied in a range of few femtoseconds around the temporal overlap and the XUV spectra were analyzed using an XUV spectrometer. The spectra clearly reveal an absorption structure when the IR arrives before the XUV light, with an evolution dependent on the time delay as shown in Figure 12.20b. The oscillation in the absorption lines is due to the hole motion in the valence shell and allows us to reconstruct the time evolution of the electron density distribution.

12.4.6

Xenon: Cascaded Auger Decay

Photoexcitation of xenon using XUV radiation around 90 eV leads to the generation of multiply charged ions up to Xe^{3+} . The ionization of a core electron can lead to a cascade of Auger decays with the formation of Xe^{3+} . The formation of transient states of singly and doubly ionized Xe ions was traced in time using the ion chronoscopy approach discussed in Section 12.4.1 and by measuring the charge-state ion yields by delaying the IR pulse with respect to the exciting isolated attosecond pulse. In the two-color photoionization process, charge states up to Xe^{4+} were observed. The temporal evolution of the population of the ion states is shown in Figure 12.21a and b. The figures show the evolution for the transient population of the Xe^{4+} and Xe^{3+} ions, respectively. The interaction with the 90-eV photon field leads to the emission of a core electron, leaving a core vacancy that can be filled by an Auger decay process A_1 , as shown in Figure 12.21c. This leads to the formation of Xe^{2+} . The formation of these ions is required for the observation of higher charge states ions Xe^{3+} (that can be formed by a second Auger decay A_2 or by IR-photoionization) and for the observation of ions Xe^{4+} by direct IR double-photoionization of the Xe^{2+} population. Figure 12.21b and c indicates that the background of the population of Xe^{3+} is the result of the cascaded Auger decays A_1 and A_2 . The Auger decay A_1 can also populate long-lived Xe^{2+} states that can be ionized by the IR field, explaining the increase of the Xe^{3+} signal close to the temporal overlap between the XUV and IR pulses. The rise time of the population depends on the convolution between the decay time τ_{A1} of the first Auger process and the IR-induced ionization of the Xe^{2+} level. From the rise time, the decay time of A_1 could be estimated to be $\tau_{A1} = 6.0$ fs.

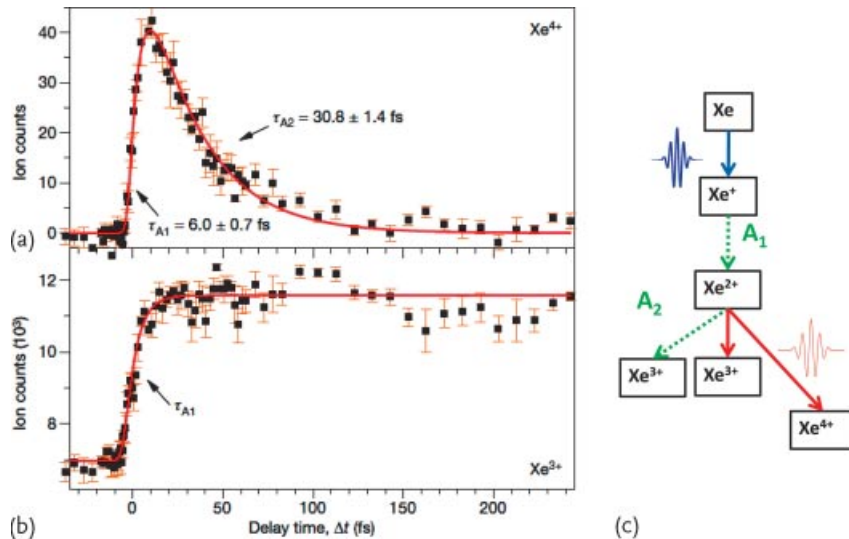


Figure 12.21 Transient population of Xe^{4+} (a) and Xe^{3+} (b). Sequence of XUV photoionization, cascaded Auger decays (A_1 and A_2) and single and double-IR photoionization lead-

ing to the formation of highly charged Xe^{4+} (c). Reprinted by permission from Macmillan Publishers Ltd: Nature ([17]. Copyright 2007.

Charge states higher than Xe^{3+} cannot be created directly by the XUV, as the energy required for the formation of Xe^{4+} is larger than the XUV photon energy. In the presence of the IR pulse, however, formation of Xe^{4+} was observed with the time evolution shown in Figure 12.21a. The signal presents a fast rise time, followed by a longer decay time. The formation of the Xe^{4+} takes place through double IR-ionization of Xe^{2+} ions, which are populated by the Auger decay A_1 of Xe^{+} and that can eventually decay (A_2) to Xe^{3+} ions. The rise and fall times of the signal, therefore reflects the times τ_{A1} and τ_{A2} associated to the two Auger processes. Quantitative analysis leads to the estimation of $\tau_{A1} = 6.0 \text{ fs}$ for the first Auger process, in agreement with the value obtained by the analysis of the Xe^{3+} population and $\tau_{A2} = 30.8 \text{ fs}$ for the second Auger process.

Acknowledgment

G.S. acknowledge financial support from the Ateneo italo-tedesco (Programma-Vigoni 2007–2009), from the Alexander von Humboldt Foundation (Project “Tirinto”) and from the Italian Ministry of Research (FIRB RBID08CRXK). All the authors acknowledges financial support from the European Research Council (ERC-Elyche, No. 227355) and the Marie Curie Research Training Network ATTOFEL. Discussions with J. Mauritsson and M. Vrakking are gratefully acknowledged.

References

- 1 Bransden, B. and Joachain, C. (2000) *Quantum mechanics*, Prentice Hall, <http://books.google.com/books?id=K9f3F0EGACgC>.
- 2 Scrinzi, A., Geissler, M., and Brabec, T. (2001) Techniques for attosecond pulse detection and the observation of electronic quantum motion. *Laser Phys.*, **11**, 169.
- 3 Johnsson, P., Mauritsson, J., Remetter, T., L'Huillier, A., and Schafer, K.J. (2007) Attosecond control of ionization by wave-packet interference. *Phys. Rev. Lett.*, **99**, 233001.
- 4 Mauritsson, J., Remetter, T., Swoboda, M., Klunder, K., L'Huillier, A., Schafer, K.J., Ghafur, O., Kelkensberg, F., Siu, W., Johnsson, P., Vrakking, M.J.J., Znakovskaya, I., Uphues, T., Zherebtsov, S., Kling, M.F., Lepine, F., Benedetti, E., Ferrari, F., Sansone, G., and Nisoli, M. (2010) Attosecond electron spectroscopy using a novel interferometric pump-probe technique. *Phys. Rev. Lett.*, **105**, 053001.
- 5 Ranitovic, P., Tong, X.M., Gramkow, B., De, S., DePaola, B., Singh, K.P., Cao, W., Magrakvelidze, M., Ray, D., Bocharova, I., Mashiko, H., Sandhu, A., Gagnon, E., Murnane, M.M., Kapteyn, H., Litvinyuk, I., and Cocke, C.L. (2010) IR-assisted ionization of helium by attosecond extreme ultraviolet radiation. *New J. Phys.*, **12**, 013008.
- 6 Parker, J., Moore, L., Meharg, K., Dundas, D., and Taylor, K. (2001) Double-electron above threshold ionization of helium. *J. Phys. B*, **34**, L69–L78.
- 7 Ishikawa, K. and Midorikawa, K. (2005) Above-threshold double ionization of helium with attosecond intense soft X-ray pulses. *Phys. Rev. A*, **72**, 013407.
- 8 Barna, I., Wang, J., and Burgdörfer, J. (2006) Angular distribution in two-photon double ionization of helium by intense attosecond soft-X-ray pulses. *Phys. Rev. A*, **73**, 023402.
- 9 Feist, J., Nagele, S., Pazourek, R., Persson, E., Schneider, B.I., Collins, L.A., and Burgdörfer, J. (2008) Nonsequential two-photon double ionization of helium. *Phys. Rev. A*, **77**, 043420.
- 10 Feist, J., Nagele, S., Pazourek, R., Persson, E., Schneider, B.I., Collins, L.A., and Burgdörfer, J. (2009) Probing electron correlation via attosecond XUV pulses in the two-photon double ionization of helium. *Phys. Rev. Lett.*, **103**, 063002.
- 11 Pazourek, R., Feist, J., Nagele, S., Persson, E., Schneider, B.I., Collins, L.A., and Burgdörfer, J. (2011) Universal features in sequential and nonsequential two-photon double ionization of helium. *Phys. Rev. A*, **83**, 053418.
- 12 Choi, N.N., Jiang, T.F., Morishita, T., Lee, M.H., and Lin, C.D. (2010) Theory of probing attosecond electron wave packets via two-path interference of angle-resolved photoelectrons. *Phys. Rev. A*, **82**, 013409.
- 13 Fano, U. (1961) Effects of configuration interaction on intensities and phase shifts. *Phys. Rev.*, **124**, 1866–1878.
- 14 Mercouris, T., Komninos, Y., and Nicolaides, C.A. (2007) Time-dependent formation of the profile of the He $2s2p^1p^0$ state excited by a short laser pulse. *Phys. Rev. A*, **75**, 013407.
- 15 Wickenhauser, M., Burgdörfer, J., Krausz, F., and Drescher, M. (2005) Time resolved Fano resonances. *Phys. Rev. Lett.*, **94**, 023 002.
- 16 Gilbertson, S., Chini, M., Feng, X., Khan, S., Wu, Y., and Chang, Z. (2010) Monitoring and controlling the electron dynamics in helium with isolated attosecond pulses. *Phys. Rev. Lett.*, **105** (26), 263003.
- 17 Uiberacker, M., Uphues, T., Schultze, M., Verhoef, A.J., Yakovlev, V., Kling, M.F., Rauschenberger, J., Kabachnik, N.M., Schröder, H., Lezius, M., Kompa, K.L., Müller, H.G., Vrakking, M.J.J., Hendel, S., Kleineberg, U., Heinzmann, U., Drescher, M., and Krausz, F. (2007) Attosecond real-time observation of electron tunnelling in atoms. *Nature*, **446**, 627–632.
- 18 Schultze, M., Fieß, M., Karpowicz, N., Gagnon, J., Korbman, M., Hofstetter, M., Neppl, S., Cavalieri, A.L., Komninos,

- Y., Mercouris, T., Nicolaides, C.A., Pazzourek, R., Nagel, S., Feist, J., Burgdörfer, J., Azzeer, A.M., Ernstoffer, R., Kienberger, R., Kleineberg, U., Goulielmakis, E., Krausz, F., and Yakovlev, V.S. (2010) Delay in photoemission. *Science*, **328**, 1658–1662.
- 19** Wang, H., Chini, M., Chen, S., Zhang, C.H., He, F., Cheng, Y., Wu, Y., Thumm, U., and Chang, Z. (2010) Attosecond time-resolved autoionization of argon. *Phys. Rev. Lett.*, **105**, 143002.
- 20** Drescher, M., Hentschel, M., Kienberger, R., Uiberacker, M., Yakovlev, V., Scrinzi, A., Westerwalbesloh, T., Kleineberg, U., Heinzmann, U., and Krausz, F. (2002) Time-resolved atomic inner-shell spectroscopy. *Nature*, **419**, 803–807.
- 21** Goulielmakis, E., Loh, Z.H., Wirth, A., Santra, R., Rohringer, N., Yakovlev, V.S., Zherebtsov, S., Pfeifer, T., Azzeer, A.M., Kling, M.F., Leone, S.R., and Krausz, F. (2010) Real-time observation of valence electron motion. *Nature*, **466**, 739–743.
- 22** Uphues, T., Schultze, M., Kling, M.F., Uiberacker, M., Hendel, S., Heinzmann, U., Kabachnik, N.M., and Drescher, M. (2008) Ion-charge-state chronoscopy of cascaded atomic Auger decay. *New J. Phys.*, **10**, 025009.
- 23** Skantzakis, E., Tzallas, P., Kruse, J.E., Kalpouzos, C., Faucher, O., Tsakiris, G.D., and Charalambidis, D. (2010) Tracking autoionizing-wave-packet dynamics at the 1-fs temporal scale. *Phys. Rev. Lett.*, **105**, 043902.
- 24** Galayda, J.N., Arthur, J., Ratner, D.F., and White, W.E. (2010) X-ray free-electron lasers – present and future capabilities. *J. Opt. Soc. Am. B*, **27**, B106–B118.
- 25** Itatani, J., Quéré, F., Yudin, G.L., Ivanov, M.Y., Krausz, F., and Corkum, P.B. (2002) Attosecond streak camera. *Phys. Rev. Lett.*, **88**, 173903.
- 26** Kitzler, M., Milosevic, N., Scrinzi, A., Krausz, F., and Brabec, T. (2002) Quantum theory of attosecond XUV pulse measurement by laser dressed photoionization. *Phys. Rev. Lett.*, **88**, 173904.
- 27** Paul, P., Toma, E., Breger, P., Mullot, G., Auge, F., Balcou, P., Muller, H., and Agostini, P. (2001) Observation of a train of attosecond pulses from high harmonic generation. *Science*, **292**, 1689–1692.
- 28** Yakovlev, V.S., Gagnon, J., Karpowicz, N., and Krausz, F. (2010) Attosecond streaking enables the measurement of quantum phase. *Phys. Rev. Lett.*, **105**, 073001.

13

Application of Attosecond Pulses to Molecules

Franck Lépine

13.1

Attosecond Dynamics in Molecules

Understanding of electronic structure, atomic rearrangement, and dynamical processes in molecules is based, to a large extent, on the study of light–matter interaction. Compared to single atoms, molecules bring an additional complexity due to their nuclear degree-of-freedom, as well as through the existence of chemical bonds that strongly depend on the exchange–correlation interaction and spin configuration. From the point of view of an electron, a molecule can be considered as a complex landscape on which the electron exists in a static state or dynamically evolves. During many molecular reactions, this landscape is very slowly changing compared to the typical timescale at which the electron is moving. This leads to the well-known Born–Oppenheimer approximation that allows us to consider the nuclear and electronic degrees of freedom separately. This also leads to the common representation of molecular potential energy curves that describe the various electronic states of a molecule. Molecules vibrate, nuclei re-arrange, and molecular structure changes on the femtosecond timescale. As a consequence, the motion of the nuclei has been probed in many experiments using femtosecond pulses, allowing, for instance the investigation of dissociation, molecular vibration, or rotation [1]. Recently, time-resolved photoelectron spectroscopy experiments managed to observe, in real time, the modification of molecular orbitals along a dissociation process [2]. Therefore, femtosecond pulses are obviously valuable tools for studying dynamics in molecules.

With the birth of the methods to generate subfemtosecond, or attosecond, pulses, the question arose of how these light pulses can help us to understand atoms, molecules, or condensed matters [3]. Since the attosecond timescale is the timescale of the electronic motion on the atomic length scale, the answer to this question is clear in the case of atoms (see Chapter 12). In this chapter, we would like to discuss the point of view of molecular science. We might naively argue that the attosecond timescale is only important for purely electronic motion and consequently does not play any role in chemical reactions that are mainly

concerned by nuclei that react on a much longer timescale. Therefore, we could conclude that molecules or chemistry are not concerned by attosecond physics. In fact, this assumption happens to be essentially wrong and attosecond molecular physics or chemistry, will certainly be one of the most fascinating developments that will arise in the coming years. The importance of attosecond pulses to study molecules is related to the crucial role that is played by the exchange–correlation term in the many-body Hamiltonian, in the creation of chemical bonds, and in the electronic configuration of a molecule. The importance of attosecond pulses is also related to the possibility to control the charge localization in molecules. We can foresee that the possibility to create new electronic configurations from which new chemical processes can be initiated, will be considered as the first step toward attosecond chemistry. In the following, we will discuss several examples from the emerging field of attosecond molecular science that demonstrate the importance of attosecond pulses to investigate fundamental properties of molecules.

The attosecond timescale is the natural unit of time to characterize the motion of electrons. In a classical picture of the 1s electron orbital in hydrogen atom, one radian of the electron roundtrip time takes 24 as. When one considers the electron as a quantum object, this intuitive image of an electron circulating around the nucleus breaks apart. In fact, quantum mechanics taught us that electrons in atoms exist as discrete states that are eigenvectors of the Hamiltonian of the system. The energy of these states corresponds to the associated eigenvalues. In quantum mechanics, the electron in the ground atomic state is described by a stationary probability wave. As a consequence, there is no electronic motion. This counter intuitive description was questioned in the early days of quantum physics. Soon the quantum picture and classical intuition were merged with each other thanks to the correspondence principle and the Ehrenfest's theorem, which connects classical motion and quantum observables. As a direct consequence, this means that classical motion rises from the coherent superposition of eigenstates (that can either be part of a discrete or a continuum basis). The concept of quantum wave packets is therefore crucial in electron dynamics. This was illustrated in the field of Rydberg physics that deals with electrons in highly excited states for which electronic motion is relatively slow (typically moving on the femtosecond or picosecond timescale). In a sense, attosecond science can be considered as an extension of this research field to the case of faster electrons and rapid mechanisms.

Attosecond physics aims at probing extremely fast events, which naturally concern low mass particles such as electrons. However, the motion of hydrogen atoms might also play an important role in such dynamics since the typical timescale for its vibrational motion is only a few femtoseconds. Simply speaking, in a molecule, the timescale of any electron dynamics depends on the particle velocity and how much it has to travel before a remarkable event occurs and raises our interest. In general, electrons interact over long distances and react to Coulomb interactions and to the Pauli exclusion principle, which makes the electron dynamics subtle and sometimes counter intuitive. In very large molecules, charge transfer over the whole molecular skeleton is usually a slow process, which extends to much longer timescales than a few femtoseconds. As a consequence, attosecond science will deal

with processes that occur on atomic-scale distances, or with high-velocity particles. In molecules, this means that attosecond physics is a perfect tool to study, electron exchange–correlation effects (for instance in Auger decay), charge transfer (electron or hole propagation), non-Born–Oppenheimer dynamics, and possibly local proton motion (such as ultrafast isomerization following ionization). In addition, attosecond is also the timescale of the electric field oscillation in a visible (or short wavelength) laser pulse. Therefore, attosecond pulses also offer the possibility to study “in-pulse” dynamics (transient processes), which could help us to study the properties of a molecule that is dressed by the photon field.

Consequently, attosecond physics might offer powerful tools to investigate very fundamental mechanisms and model systems, but we can also anticipate applications in chemistry, catalysis, molecular electronics, biomolecules, photosynthesis, plasmonics, molecular logic, energy flow in large molecules and so on . . .

In the first part of this chapter, we will discuss experimental results obtained with state-of-the-art IR femtosecond–XUV attosecond pump–probe schemes. In the second part, we will discuss theoretical investigations concerning attosecond electron dynamics in small or large molecular systems. We will finally discuss general perspectives in the field of attosecond molecular science.

13.2

State-of-the-Art Experiments Using Attosecond Pulses

While pump–probe experiments on the femtosecond or picosecond timescale are widely used in the molecular physics community, the extension of this concept to the attosecond timescale is still emerging. So far, no experiment exists where an attosecond pump pulse is followed by an attosecond probe pulse simply because the high-harmonic generation (HHG) is a low-efficiency process and attosecond pulses are most of the time, weakly intense pulses. However, with rapid instrumental developments, such experiment will certainly be available in the near future. Until now, every attosecond physics experiment that uses attosecond pulses, is based on the utilization of an infrared femtosecond pulse that is synchronized with one attosecond pulse (or a sequence of attosecond pulses). In these experiments, the key idea is that the synchronization of the pulses occurs on the attosecond timescale, meaning that the time variation of the femtosecond light electric field is fixed and serves as a “clock” for a time-resolved experiment. Two kinds of experiments can be distinguished. The first one relies on the creation of a sequence of pulses (or attosecond pulse train: APT) that is created via HHG from an intense multicycle femtosecond pulse. In that situation, one attosecond pulse is generated at each half cycle, at the same periodic optimum of the IR laser field. Combining the APT and a second IR femtosecond pulse, it is experimentally possible to change the phase between the XUV pulse train and the IR pulse. In a second protocol, a more complex experimental setup allows the generation of a single attosecond pulse. This requires the utilization of a carrier envelop phase (CEP) stabilized pulse (see Chapter 4) and, for instance, the so-called polarization gate technique that permits the

isolation of a single electron recombination event. Here, the attosecond pulse is synchronized on the attosecond timescale with a short few-cycle CEP stabilized pulse (typically a 7-fs pulse). Therefore, the time-resolution results from the well-defined phase between the IR electric field and the attosecond pulse. In both cases, the attosecond pulse can be used either as a pump or as a probe.

Attosecond pulses can be generated and propagated only if the period of the light is shorter than one femtosecond, which consequently brings attosecond pulse to the XUV domain and therefore to the high-photon energy range. As a direct consequence, in attosecond experiments ionization, core excitation, or dissociation of molecules usually occurs. This determines the type of spectroscopy that we can use. The most obvious choice for the study of electron dynamics is certainly electron spectroscopy. However, this is not always the most relevant choice, partially because of the presence of the strong IR field that influences the asymptotic electron momentum distribution.

13.2.1

Ion Spectroscopy

13.2.1.1 Attosecond Molecular Coulomb Explosion: Nonlinear XUV Interaction with a Molecule

The APT autocorrelation technique proposed by Midorikawa *et al.* [4] aimed at probing the nonlinear interaction between XUV light and small molecules. In that experiment, a dual APT was used to induce the fragmentation of a molecule with a two-photon transition in the XUV domain that brings the system above the threshold of the Coulomb explosion channel. The ion fragments were detected with a time-of-flight spectrometer and the fragment yield was recorded for various delays between the two APTs. A complex periodic variation of the yields was measured and analyzed by Fourier transformation. An application of this technique to carbon dioxide molecule is shown in [5]. The analysis of the Fourier components of the pump–probe trace of CO_2^{2+} , C^+ , and CO^+ yields revealed the combination of harmonics involved in the double ionization and dissociation of the molecule. This technique is particularly relevant to free-electron laser experiments in which a high-XUV photon flux can be used to photoionize and dissociate a molecule. The attosecond molecular Coulomb explosion technique provides information on the two-photon absorption cross section in the XUV domain, which is a quantity that is difficult to measure. It also carries information on the electronic structure of the molecule.

13.2.1.2 Electron Localization on the Attosecond Timescale

CEP stabilized pulses have a perfectly defined electric field with respect to the envelope of the laser pulse. Since the pulses are short (few femtoseconds), they contain only a few optical oscillations. Consequently, the phase stabilization can generate an asymmetric light electric field that breaks the inversion symmetry of the interaction. Application of such pulses to molecular physics was demonstrated in a

seminal experiment by Kling *et al.* [6], who controlled electron localization during the dissociation of a deuterium molecule by changing the CEP phase. The neutral molecule was ionized within the laser pulse and as a result, started to dissociate. During the dissociation, the removed electron was accelerated back to the molecule by the strong light electric field, it collided with the parent ion and lead to the population of repulsive states. The molecular dissociation occurred during the interaction with the laser, which induced a time-dependent modification of the molecular potential energy surfaces that eventually guided the final molecular wavefunction. Changing the CEP phase allowed to modify this wavefunction and to influence the asymptotic localization of the remaining electron on one or the other nucleus. Interestingly, this process depends on the attosecond electron dynamics in the laser field.

A time-resolved investigation of attosecond electron localization in a molecule has been achieved by Sansone *et al.* [7]. This pioneering experiment was performed on H₂ and D₂ molecules and used a two-color attosecond pump–probe configuration. A single attosecond pulse ionized the neutral diatomic molecule. The attosecond wave packet created during this process evolved on the dissociative molecular potential energy surfaces. In a usual dissociation of H₂, the asymptotic result of the photoreaction leads to an equal distribution of charge on both nuclei. In fact, the remaining electron is located on both nuclei when the wavefunction collapses, giving 50% chance to measure the remaining electron bounded to one or the other proton. In this experiment, a second CEP controlled laser pulse was used to modify the molecular potential energy surfaces during the dissociation process. The IR pulse created a time-dependent coherent superposition of bound (1s σ_g) and dissociative (2p σ_u) states. This coherent superposition of states is classically equivalent to an oscillatory motion of the electron along the molecular axis. During the dissociation, the nuclei part while the remaining electron alternatively channels between the two nuclei under the influence of the IR pulse. Asymptotically, the remaining electron is not equally localized on the two nuclei. The final wavefunction leads a higher probability to obtain a localized electron on either one or the other nucleus depending on the delay between the two pulses. The localization of the particle is measured through the asymmetry of the asymptotic ion velocity distribution with respect to the laser polarization (Figure 13.1). We observe that this asymmetry oscillates with the delay between the pulses and the amplitude of this oscillation decays after a few femtoseconds. Interestingly, this decay could serve as a direct measurement of the laser-induced electron channelling efficiency. It decreases when the distance between the nuclei increases.

This description in terms of two “dressed” potential energy surfaces, gives a simple and intuitive understanding of the attosecond electron localization. However, this single active electron picture is incomplete because the attosecond XUV photoexcitation is not selective and also leads to doubly excited states that relax to dissociative states via autoionization. In that case, the localization arises from the interference between two quantum decay paths of the doubly excited states: autoionization leads to 1s σ_g and single IR photon ionization to 2p σ_u . A more accurate theoretical description requires a more complex description. This was developed

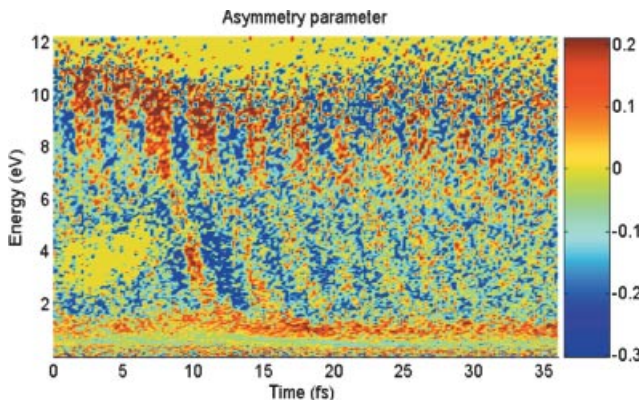


Figure 13.1 Evolution of the ion signal asymmetry with respect to the laser polarization, as a function of the ion kinetic energy, when the delay between a single attosecond pulse and a CEP controlled IR femtosecond pulse is changed. Clear oscillations are observed and show the control of electron localization

on the nuclei. This is explained in terms of time-dependent coupling between potential energy surfaces. The amplitude of the oscillation vanishes with time due to the decrease of the efficiency of light-induced channeling of the electron from one to the other nucleus [7].

for H₂ by solving the time-dependent Schrödinger equation using a close-coupling method that describes the fully correlated electro-nuclear motion.

To conclude, this experiment addresses several crucial questions in attosecond molecular physics. What is the typical timescale of multistate interactions and how do multielectronic states relax? How do nonadiabatic dynamics occur in molecules? How does the interplay between the light and nuclear or electronic degrees of freedom determine the photophysical process? How does electron tunneling occur between nuclei? Importantly, it also shows that attosecond pulses can be used to modify the final output of a photo-induced reaction by acting directly on the electrons. In this experiment, the charge localization was controlled after a single or many-electron excitation. Obviously, such mechanisms are highly interesting if they can be identified in more complex molecular systems.

13.2.1.3 Attosecond Control of Dissociative Ionization

Another pioneering experiment was performed on the dissociative ionization of diatomic molecules (H₂ and D₂). In that case, the combination of an APT and an IR femtosecond pulse [8] was used. In that experiment, it was possible to control the dissociative states of the molecule using mildly strong IR light and an APT. Modulation of the fragment kinetic energy distribution of ions for various ionic states was monitored as a function of the delay between the APT and the IR femtosecond pulse (see Figure 13.2). The interpretation of this result relied on a Rabbit-like excitation scheme, in which the continua corresponding to the 1sσ_g and 2pσ_u states

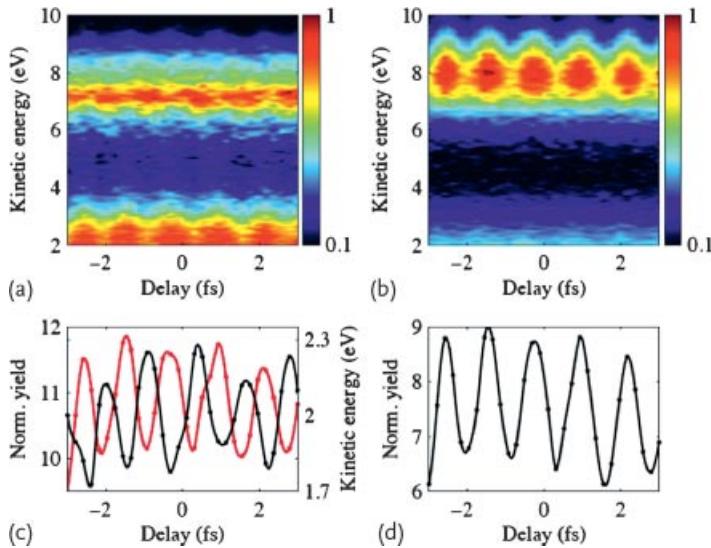


Figure 13.2 Evolution of the ion kinetic energy as a function of delay between the APT and the IR femtosecond pulse. An oscillation of the yield in each dissociation channel is observed. The result for two different IR inten-

sities is presented. It shows that out-of-phase and in-phase oscillations can be obtained. The oscillations are explained in terms of coupling between two continua (from [8]).

were coherently coupled by XUV + IR photons. This reconstruction of attosecond beating by interference of two-photon transitions (RABITT)-induced process is very similar to a multipath coherent control scheme and it certainly paves the way to attosecond coherent control experiments.

The possibility to extend such experiment to more complex molecular systems is an important issue. However, the photoexcitation of a large system with a high density of electronic states with a broadband laser pulse makes it very challenging to define a relevant excitation scheme. However, it has been shown that such control can already be attained for simple (H_2) or more complex multielectronic systems (O_2) [9]. Future investigations of this type require a full description of the electro-nuclear wave packet dynamics evolving along many dissociative channels. This is especially challenging for most of the time-dependent many body theories.

The ion spectroscopy experiments previously discussed gave very striking results that illustrate the importance of nuclear degrees of freedom in attosecond science. We can state that nuclear motion is able to retain the information of the electron dynamics that occur on the subfemtosecond timescale, which is, *a priori*, not trivial. In fact, the most obvious tool to study electrons is certainly electron spectroscopy. In the following, we will discuss experimental results based on the measurement of electron momentum distribution.

13.2.2

Electron Spectroscopy**13.2.2.1 Atomic Phase and Time/Scattering Phase Relation**

To access attosecond dynamics, several experimental protocols using phase locked IR/XUV pulses have been developed. A very fruitful approach is based on measurement of the electron kinetic energy spectrum. In the following, we will briefly discuss so-called streaking and RABITT measurements (see Chapters 2 and 4). In such experiments, the attosecond photoionization occurs at a certain phase of the IR field. The streaking measurement relies on the changes of the measured final electron kinetic momentum, depending on the instant of creation of the electronic wave packet in the IR field. In fact, the streaking technique measures the acceleration of the electron by the electric field of the IR light. By changing the delay between the attosecond pulse and the short femtosecond IR pulse, the electron acquires different final momenta. Therefore, we observe variations of the maximum electron kinetic energy that map the vector potential of the IR pulse. This method can be used to characterize the laser pulse itself. More recently, it was applied to study core relaxation in atoms and surfaces by measuring phase differences between streaking traces from different states. In these experiments, the streaking is used as a probe of the processes induced by the attosecond XUV pump pulse.

Streaking experiments are also possible with an APT and can serve for electron wave packet reconstruction [10]. It is important to point out that APT offers the possibility to obtain high temporal and spectral resolution, which is not directly attainable with the broad bandwidth of a single attosecond pulse. An APT consists of a frequency comb formed by a combination of odd harmonics of the fundamental light. This energy resolution is crucial for RABITT measurements [11]. In RABITT, an APT ionizes a gas phase sample. As a consequence, a series of peaks is observed in the electron kinetic energy spectrum, with each peak corresponding to the ionization by different harmonics. By adding an IR field, we observe additional peaks in the spectrum (called sidebands) at the energy of 1 XUV photon + 1 IR photon. The oscillator strength leading to this signal is a coherent superposition of several quantum paths, where a single XUV photon is absorbed and one or more IR photons are either absorbed or emitted. The intensity of the sidebands depends on the phase difference between the harmonics, plus an additional phase that is intrinsic to the ionization process itself, generally called “atomic phase.” By changing the delay between the APT and the IR field, the intensity of each sideband oscillates and the harmonic and atomic phases can be recovered from the phase difference between these oscillations. The measurement of the phases between harmonics is used to reconstruct the train of attosecond pulses. Additionally, it was recently realized that the atomic phase carries important information on the photoexcitation and photoemission process itself.

13.2.2.2 Delay in Photoemission in Molecules

Recently, attosecond streaking and RABITT electron spectroscopy was used to measure atomic phases. It is known that the energy variation of the phase can be related to a time difference, this relation defines the “Wigner time.” The atomic phase is the sum of two terms, the Coulomb phase that corresponds to the phase accumulated by the electron in the Coulomb field and the scattering phase itself. As a consequence, the phase measurements performed with streaking can allow us to measure the Wigner time that is, in our case, the time that an electron takes to reach the ionization continuum following the ionization by a XUV photon. In a recent publication, the streaking technique was applied to measure variation in photoemission time in neon atoms [12]. The authors observed a relative time delay of 20 fs in the photoemission from the 2s state respect to the emission from the 2p atomic state. A careful interpretation of this type of measurement showed the importance of the “dressing” IR field, which induces an additional time delay in the measurement [13].

An example of the phase analysis, applied to the ionization of nitrogen molecules, was proposed by Haessler *et al.* [14]. The authors observed a phase variation around a resonance that lies in the continuum. This resonance corresponds to a B-state, which autoionizes to the A or X-state of the ion (see Figure 13.3). The phase vari-

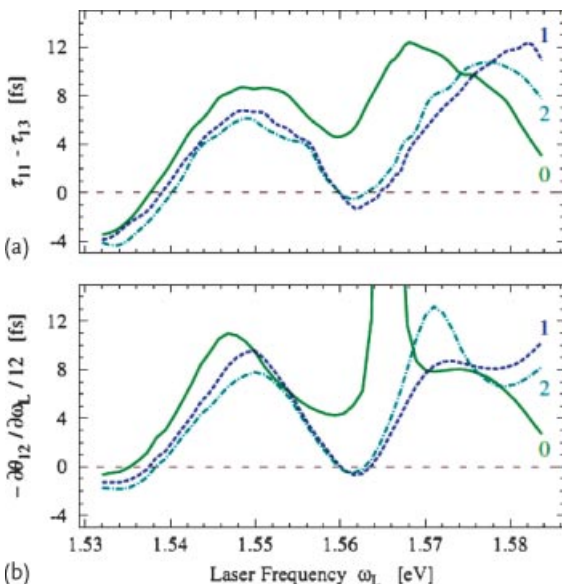


Figure 13.3 Using RABITT measurements, Haessler *et al.* showed that phase variations around an autoionizing resonance of the nitrogen molecule. The phase differences between two ionization channels, for various

vibrational states, are directly related to ionization delays. This demonstrates the sensitivity of the method to study molecular potential energy surfaces and time-resolved autoionization processes (from [14]).

ations for the various vibrational states involved are measured with the RABITT method, and “molecular phases” are disentangled from the harmonic phases using a perfectly characterized APT. The analysis of the phase variation leads to a direct measurement of the difference in the time of electron release for the two ionization channels associated with the A, X states [15]. It is very interesting to notice that this time varies for all the vibrational states involved, which makes the measurement extremely sensitive to the exact potential energy surfaces. This result already taught us that the phase measurement, based on streaking or RABITT, is applicable to molecular species. In general, it allows the direct measurement of the photoemission time, which is certainly a very powerful observable to probe electron correlation and the details of molecular potential energy surfaces.

13.2.3

Photo Absorption

One of the oldest spectroscopic approaches used in physics is the measurement of photon loss (absorption spectroscopy, based on Beer’s law). It remains a very important tool in physics. Absorption measurement characterizes the dipole (or multipole) transitions and the imaginary part of the polarizability of the states involved. In attosecond science, it has been used to investigate “in-pulse” processes called transient phenomena.

Contrary to attosecond streaking or RABITT electron spectroscopy, attosecond transient absorption spectroscopy uses the attosecond pulse as a probe of the mechanisms that are induced by an IR femtosecond pulse. During the interaction between an atom and a relatively strong laser field, a coherent superposition of states is created. The corresponding dynamics can be probed on the attosecond timescale. The states involved are described in terms of a density matrix, in [16] the authors used transient absorption to measure the corresponding density matrix elements for Krypton ionic states that are produced during the interaction with a moderately strong IR field. Thereby, the population and the coherence of these states are explicitly determined, giving access to the full quantum mechanical electronic motion in Kr atoms. The same technique was used to measure interference of transient bound states in He that are prepared by one harmonic of the attosecond pulse train. The absorption efficiency for each harmonic oscillates with the delay between the APT and the IR field. The phase difference between these oscillations carries information on the optical response and electron interferences on the attosecond timescale [17].

Although not yet applied to polyatomic species, this promising approach could be used in molecular physics to investigate coherence and electronic motion in molecular systems and therefore to enlighten the role of multiple electrons and of nuclear motion in coherence loss during electron transport.

13.3**Theoretical Work**

In recent years, an increasing number of published theoretical works that aims at studying attosecond dynamics in molecules appeared in the literature. The methods that are used are based on time-dependent approaches and use either models or *ab-initio* calculations. The key concept in this theoretical work is the creation of a coherent superposition of states (for instance with different symmetries). Depending on the angular or radial character of the states that compose the electronic wave packet, it is possible to generate a time-dependent localization of the electrons in complex molecules. Such light-induced mechanisms are possible by using the propensity rules in photoexcitation. Therefore, the calculations consider molecules that are fixed in space and the direction of the light polarization, with respect to the molecular axis, is used as a “knob” to design a specific wave packet. Another very important example concerns the propagation of a hole after the ultrafast removal of an electron from a molecule.

We will first discuss electron dynamics in molecules for cases where no nuclear motion is taken into account. This is certainly relevant on the attosecond timescales. However, the role of the nuclear degrees of freedom should not be dismissed, as we have shown in the previous experimental results. This is especially true because our observables can be based on dissociation processes. Moreover, our experimental observations are always macroscopic, which means that the measurement occurs at a much later time than the mechanism itself. Therefore, long timescale dynamics can always be important. Finally, the link between attosecond dynamics and dynamics that occur at later delays (nuclear dynamics) is crucial if one wishes to use attosecond pulses to study chemical processes or life related phenomena. Therefore, a more complete approach is compulsory even if computationally very demanding. In the following, we discuss some examples of theoretical investigations that surely pave the way to future applications of attosecond pulses.

13.3.1**Electron Dynamics in Small Molecules**

A number of investigations consider electron dynamics in small molecules following the interaction with a short laser pulse. These investigations are explicitly (or implicitly) referring to the use of CEP stabilized pulses.

Remacle *et al.* investigated complex electron dynamics in LiH [18] and Li hybrides [19]. The coherent superposition of several electronic states can be built to generate a specific electronic motion that can be either translational or rotational with respect to the molecular axis. The symmetry of the states that compose the electronic wave packet, determine the symmetry of the motion. While linear motion is created by superposition of Σ states, a combination of Σ and Π states leads to rotational electronic motion. Interestingly, a transition between adiabatic and nonadiabatic dynamics is observed when the light intensity is increased (see Figure 13.4). These results provide insights for future experiments that could use UV

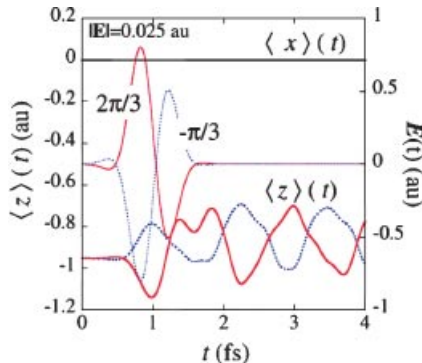


Figure 13.4 LiH interacts with a short light pulse. The electronic response shows a time-dependent variation of the dipole, related to the electron dynamics in the molecule. De-

pending on the CEP phase and light intensity, the dynamics change and can create a situation where nonadiabatic evolution is observed (from [18]).

CEP stabilized pulses, nevertheless, the question remains on how this dynamics could be probed in real time with a second short laser pulse.

A hint to answer this question is given by Bandrauk *et al.* [20], who showed how electron dynamics can be probed in H_2^+ ions using electron spectroscopy. Unlike most of the current attosecond experiments, the method proposed in this article does not require a strong femtosecond laser field. It is shown that information on electronic motion in the molecule is encoded in the photoelectron spectrum that is generated by the interaction with an X-ray pulse. In that protocol, a first short pulse creates a superposition of two bound electronic states of different symmetry, Σ_g and Σ_u , thanks to a resonant excitation with a photon energy that matches the energy difference between the two states. A second pulse, with a wavelength lying in the X-ray domain, ionizes the molecule. If this last pulse is shorter than the period of the electronic motion, the two components of the electron kinetic energy spectrum associated with the two electronic states, overlap in momentum space. This leads to a two-center interference effect that creates an asymmetry in the electron momentum distribution (see Figure 13.5). This asymmetry is a direct observable of the electron motion in the molecule. This theoretical work provides a very good example of a possible pump–probe experiment, where electron motion is observed on the attosecond timescale in a molecule.

13.3.2

Electron Dynamics in Large Molecules

The use of CEP stable pulses to create electron dynamics was also investigated for larger molecules. Let us mention two examples that use either circularly or linearly polarized light.

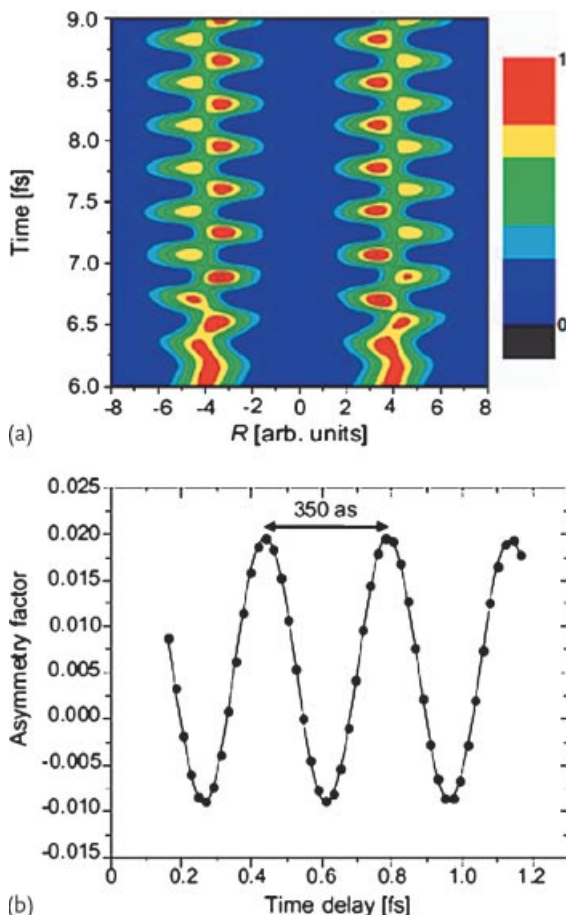


Figure 13.5 The coherent superposition of two electronic states, generated by a broad UV pulse, leads to attosecond electron dynamics that can be probed by time-dependent photoelectron spectroscopy using a second X-ray pulse. Periodic asymmetry is observed and characterizes the electron motion in the molecule (from [20]).

13.3.2.1 Ring Currents Generated in Mg-Porphyrin

Barth *et al.* [21] studied how to generate ring currents in a planar Mg-porphyrin molecule, fixed in space. In this approach, circularly polarized UV light is used (see Figure 13.6). Thanks to a selective excitation, the laser pulse can induce a superposition of quasidegenerate angular momentum states that leads to an intense circular electron current in the molecule. This current is 100 times stronger than any current produced by a macroscopic magnetic field. This photoinduced electron current generates a local magnetic field of 0.159 T, which can have direct applications in molecular electronics.

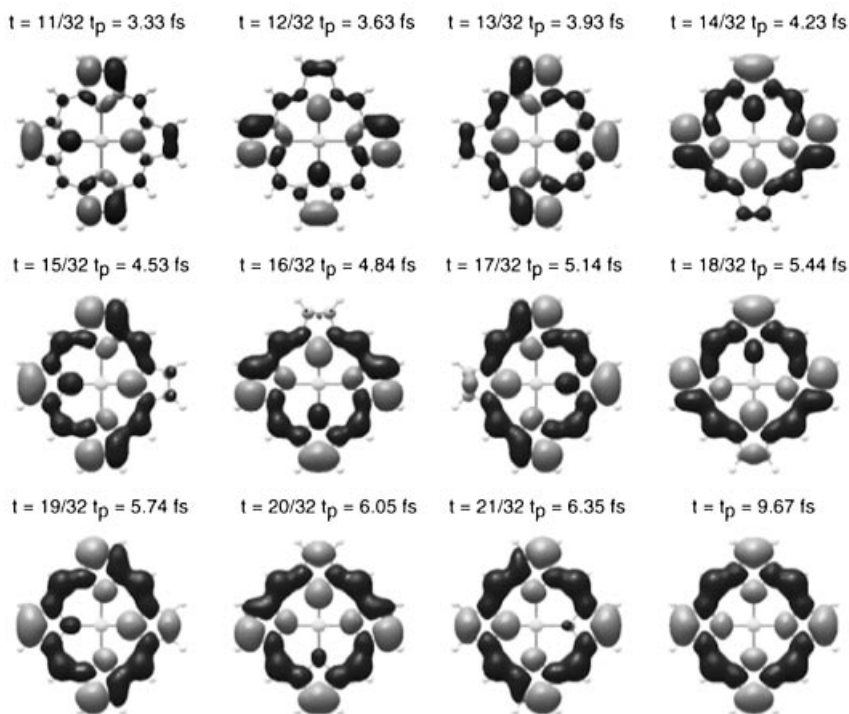


Figure 13.6 Electron rotational motion in the circular Mg-porphyrin molecule can be generated using a circularly polarized, CEP stable short pulse. The intense spinning electron

current evolves on the attosecond timescale and can generate magnetic field that might find applications in molecular electronics (from [21]).

13.3.2.2 ABCU Stereo Electron Dynamics

A similar investigation has been proposed by Mignolet *et al.* [22], who studied the photoinduced electron dynamics in the polyatomic molecule azabicyclo[3.3.3]undecane, ABCU, using a time-dependent multielectron approach. The proposed protocol is using CEP stabilized pulses in the UV or IR domain. There again, the key idea is to excite a coherent superposition of electronic states with specific symmetries, which leads to a time-dependent variation of the electron density that exhibits an evolution of the electron localization in the neutral molecule on the attosecond timescale. In order to create such a superposition and to generate a specific wave packet, the crucial parameter is the direction of the light polarization with respect to the molecular axis. A superposition of A-states or mixed A and E-states is created when the light polarization is aligned along one or the other molecular axis. As expected, the coherent superposition of molecular states still evolves after the laser pulse is turned off and quantum beating is observed through the oscillations of the dipole. In these results, nuclei are fixed and no other relaxation processes, which would produce decoherence of the electronic wave packet, are taken into account.

13.3.2.3 Hole Migration Following Photoionization in Molecular Chains and Peptides

The previous examples considered the creation of a coherent superposition of electron excited states that induce rapid variations of the electron density in the neutral molecule. Another, ultrafast charge dynamics that is driven by exchange-correlation was recently investigated. It considers the dynamics of a hole that is created after prompt removal of an electron from a neutral molecule. This electron ejection can be induced by photoionization with an ultrashort pulse. An example for a theoretical description of a hole migration process was given by Breidbach and Cederbaum [23]. They demonstrated the existence of universal attosecond hole dynamics as a response to the ultrafast ionization from a neutral molecule. After the electron ejection, the ion is left in a nonstationary state that can be described as a coherent superposition of one-particle orbitals that are eigenstates of the ion. They observed that similar dynamics occur during the first 50 as, after the ionization of the 2p state of a Kr atom, the $1\pi_u$ orbital of the CO₂ molecule and even for the $3\pi_u$ orbital of N-methylacetamide (see Figure 13.7). This effect is caused by the exchange–correlation potential that maintains electrons away from each other. This interaction induces a re-arrangement of the electronic density when one electron is removed. The universal character of this response comes from the fact that the density rearrangement is induced by a large number of weakly populated deep holes that collectively contribute to the process. The process is a signature of the averaged multielectron interaction and therefore only requires a sufficiently large number of electrons in the system. Another universal phenomenon was studied by Kuleff *et al.* [24], who showed that hole transport was accompanied by characteristic light emission, associated with the oscillation of the charge in the molecule. In general, IR light is emitted and, in the case of ultrafast ionization, there is also strong UV emission. This provides an experimental observable to identify hole transport phenomena in a variety of molecules.

A general description of ultrafast charge migration driven by electron exchange–correlation was given by Cederbaum *et al.* [25] who treated the problem of hole

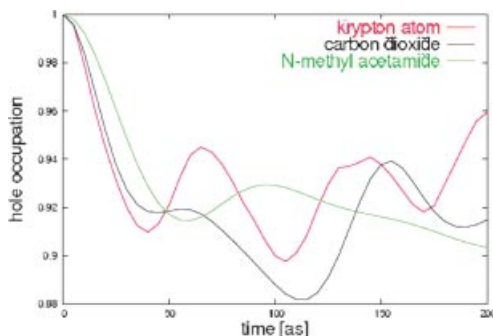


Figure 13.7 Ultrafast removal of an electron from a molecule (or an atom) is followed by the attosecond re-shaping of the exchange–correlation hole density within 50 as. This process is generally expected for any sufficiently large multielectronic system (from [23]).

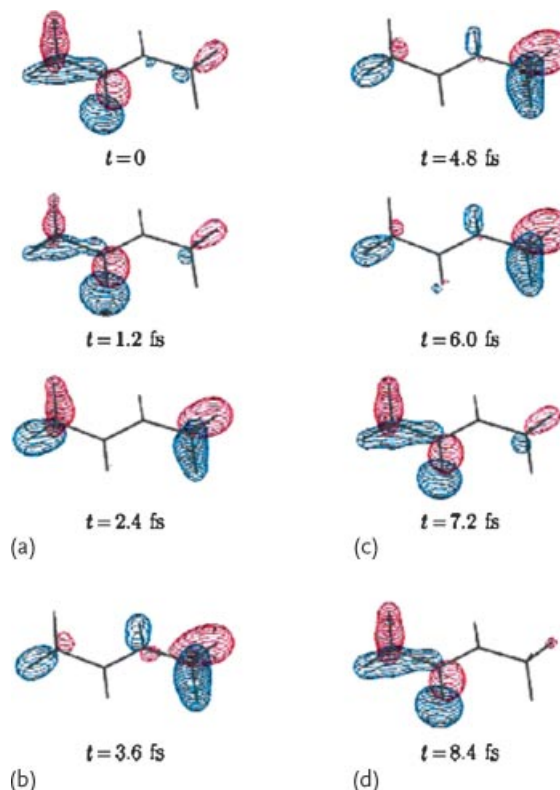


Figure 13.8 The ultrafast photoionization of *N*-methyl acetamide is followed by an ultrafast hole propagation that moves the charge density from one end of the molecule to the other. The timescale for this evolution spans from

attoseconds to few femtoseconds and could be probed by electron spectroscopy. Such dynamics is determined by the exchange–correlation potential.

propagation after prompt electron ejection in a general case. The coherent superposition of states formed after the removal of one electron, requires specific symmetry and energy spacing to induce an ultrafast hole prior to any nuclear motion. Hole propagation was investigated in linear molecules and it was shown that hole propagation can be entirely driven by exchange–correlation effects and does not require nuclear dynamics. A theoretical investigation was performed on a linear molecule, *N*-methylacetamide [26], which demonstrated an ultrafast hole propagation from one end to the other end of the molecule within a few femtoseconds (see Figure 13.8). It is especially interesting to notice that the calculated electron spectrum showed a signature and the role that is played by the correlation through appearance of satellite peaks, paving the way to experimental realization. A similar effect was shown for the amino acid glycine, for which they have investigated the role of isomers on the timescale of the charge motion [27]. The hole propagation driven by correlation is a purely electronic mechanism and is certainly an

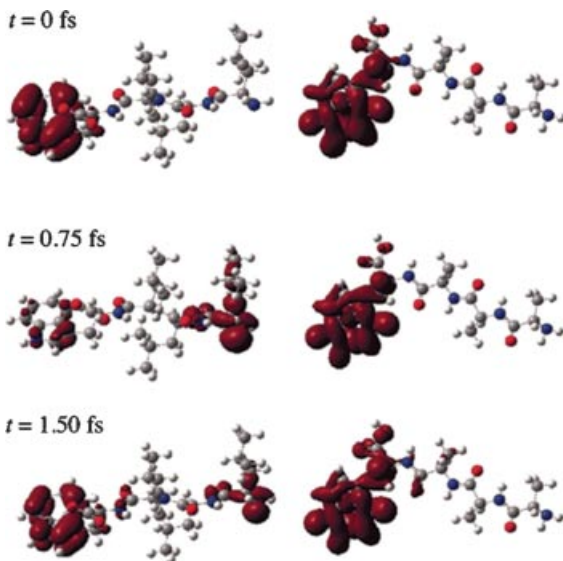


Figure 13.9 Hole dynamics driven by pure exchange–correlation effects was investigated theoretically in a tetrapeptide. The dynamics strongly depend on the peptide sequence and the energy of the removed electron (from [28]).

example of how attosecond physics might offer opportunities for new chemistry on the subfemtosecond timescale. However, the importance of conformer geometry demonstrates that nuclear structure is intimately correlated with electronic dynamics.

Another important example for attosecond dynamics in molecules, was given by Remacle *et al.*, who studied hole migration in a small peptide following prompt ionization [28]. The theoretical description is based on the self consistent field approximation. In that approximation, the HOMO of the neutral is defined as a linear combination of the orbitals of the cation. As a consequence, the removal of the electron in the HOMO leads to time-dependent hole localization in the cation, as discussed in the previous examples. Importantly, the timescale of the charge propagation and its localization was shown to depend strongly on the chosen peptide sequence, but also on the binding energy of the ionized orbital. In the case of TrpLeu₃ the HOMO and HOMO-1 have π character and are located on the chromophore (Trp), on one end of the peptide. Ultrafast removal of the HOMO electron leads to a nonstationary hole that propagates from one end to the other end of the peptide within less than 1 fs (see Figure 13.9). Very fast dynamics are also observed in TrpAla₃ and hole migration occurs within 10 fs. In both cases, attosecond pulses would offer a perfect tool to observe such charge dynamics. The authors have also discussed changes in the orbital energies that are directly accessible by photoelectron spectroscopy. This result is especially fascinating, as it gives a practical example of the connection between attosecond dynamics and biomolecules and proposes a possible experiment to test theoretical predictions.

13.3.2.4 Electro-Nuclear Dynamics

In the results mentioned so far, the electron dynamics is assumed to occur on a very short timescale, prior to any nuclear motion. In the calculations, nuclei are considered as frozen, which considerably simplifies the theoretical investigations. In a more general case, it is relevant to address the role of nonadiabatic couplings and electro-nuclear dynamics. An example of such dynamics is given by Kanno *et al.* [29] who have investigated the nonadiabatic couplings between electronic and vibration degrees of freedom in the chiral aromatic molecule 2,5-dichloropyrazine. In that molecule, electron dynamics is induced by photoexcitation, with a linearly polarized UV pulse, of quasidegenerate 1B_u -states (with a small gap energy of 0.44 eV). After photoexcitation, the π electrons rotate along the ring on the attosecond timescale (see Figure 13.10). The dynamics is controlled by the orientation of the molecule with respect to the light polarization, which modifies the phase difference between states in the wave packet. Either a clockwise or counterclockwise motion can be produced. The nonadiabatic coupling consists in the interaction between the electronic wave packet and the Ag vibrational mode. It is shown that this coupling induces a modification of the electron rotational motion. While the population of the electronic state evolves, the vibrational nuclear motion is activated. The analysis of the vibrational modes at play shows a clear evidence for the direction

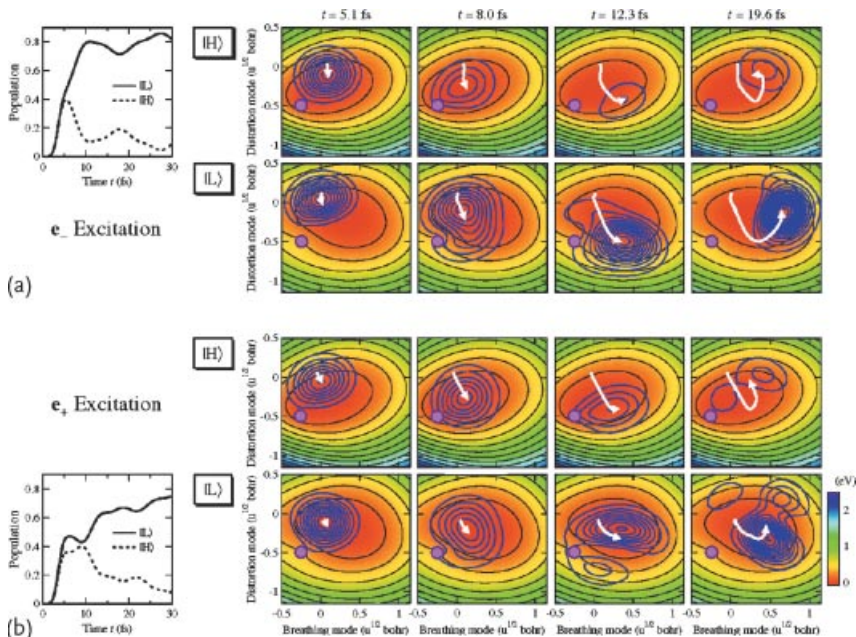


Figure 13.10 Evolution of the population of quasidegenerated states in the case of (a) the clockwise and (b) counterclockwise (b) excitation. The time-dependent evolution of the

wave packet is shown, electron motion is coupled to an Ag vibrational mode that leads to the evolution of the population in the L and H states (from [29]).

of the electron motion on the attosecond timescale. In that example, mechanisms occurring at a long delay time (vibration) preserve a striking signature of the electron motion on the attosecond timescale. This signature is due to the nonadiabatic couplings between electrons and nuclei.

13.4 Perspectives

We have shown several experimental and theoretical examples of attosecond dynamics in molecules. In the following, we would like discuss some important issues that could influence future experiments using attosecond pulses. First, we will discuss the problem of fixing molecules in space, as we have shown that this is crucial for the design of electron wave packets. In a second part, we will discuss experiments performed in the frequency domain at synchrotron facilities that revealed important questions in molecular physics.

13.4.1 Molecular Alignment and Orientation

Compared to atomic or solid state physics, the investigation of isolated molecules with attosecond light pulses may require control over the molecular orientation in space. This has a crucial importance in experiments where specific electron dynamics is created. The interaction between a molecule and a light pulse strongly depends on the relative alignment between the molecule and the light polarization. As discussed before, this determines the nature of accessible excited states through quantum selection rules. Unfortunately, in the gas phase, molecules are randomly aligned and the interaction with linearly polarized light leads to a superposition of signals from all the possible molecular orientations. In order to improve our control of the light/molecule interaction recent work aimed at developing strategies for aligning the molecules in space. One of the most popular methods is based on the creation of a rotational wave packet via Raman stimulated excitation, using a short light pulse. The coherent excitation of rotational states leads to a time-dependent wave packet that periodically de-phases and re-phases. A striking consequence is that, at a well-defined time delays after the instant of excitation, the molecular sample becomes aligned with respect to the polarization axis of the light. This is called “field free molecular alignment,” as it provides a macroscopic ensemble of molecules that are aligned and fixed in space with respect to the laboratory frame (see Figure 13.11) in the absence of the light pulse. While this approach has been widely applied to di-atomic or small molecules [30], such a strategy can also be extended to 3D alignment in which the three molecular axis are fixed in space, or even to molecular orientation by using an experimental protocol based on hexapole state selection or a half-cycle pulse [31].

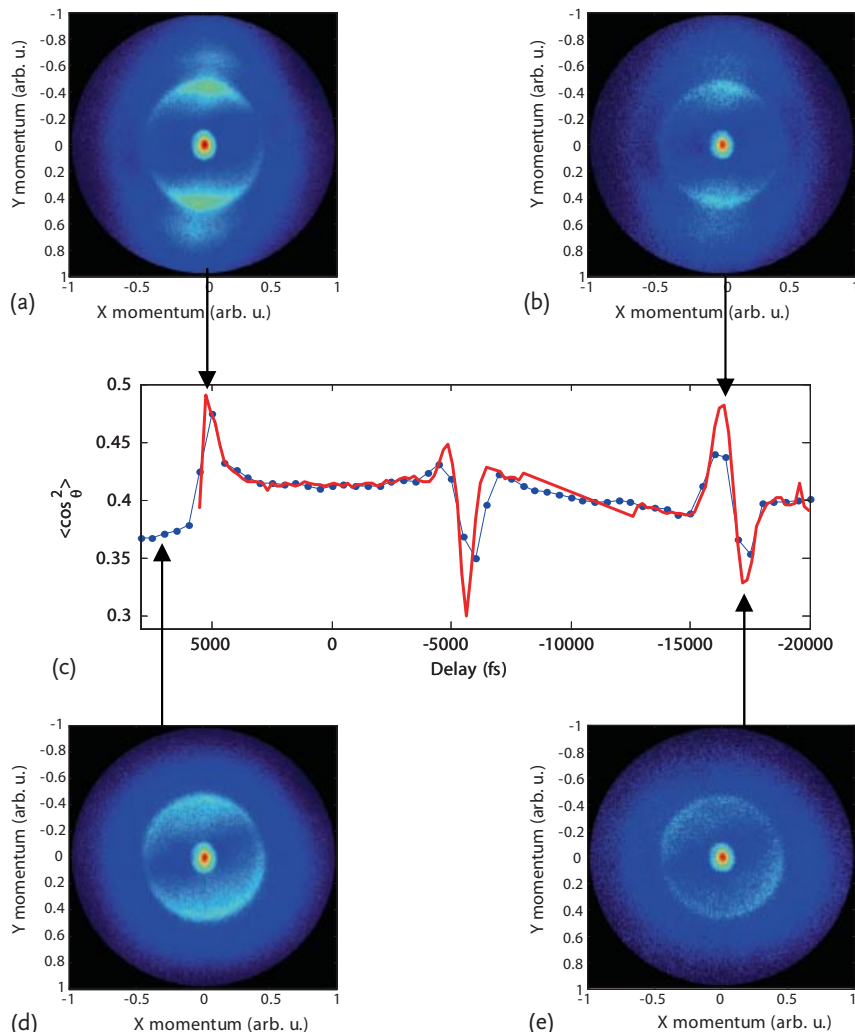


Figure 13.11 Periodically aligned molecular samples can be created by inducing a rotational wave packet. The aligned molecules can be observed by measuring the ion angular distribution formed in a fast dissociation

process. In the displayed example, the time-dependent alignment of CO₂ molecules was probed by dissociation with short XUV pulses at the free-electron laser FLASH (from [30]).

13.4.2

Electron Delocalization between DNA Group Junction

Several experiments demonstrated possible applications of attosecond pulses to study electron dynamics in a complex molecular environment. There is a natural connection between attosecond science and experiments performed at synchrotrons as both experimental approaches rely on excitation with high-energy

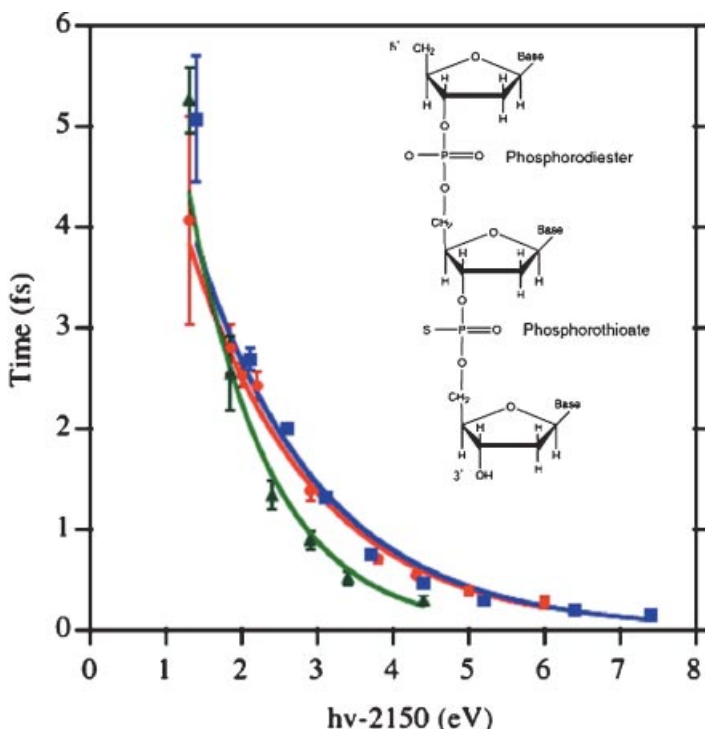


Figure 13.12 Core–hole clock spectroscopy was used to study electron delocalization in periodic and aperiodic DNA. Delocalization was shown to occur on a subfemtosecond timescale. This indicates that charge transfer

depends strongly of the organization of the DNA structure and might occur through the phosphate groups instead of π – π couplings in stacking (from [32]).

photons. For instance, an increasingly popular X-ray absorption technique named “core–hole clock” spectroscopy has pointed out new mechanisms that occur on the attosecond timescale. We will discuss two examples in the following.

Sekiguchi *et al.* [32] studied electron transport along phosphate backbone sites in DNA, using core hole clock spectroscopy. For genomic DNA, the periodic structure shows a delocalized electronic state despite the presence of the insulator sugar groups. On the contrary for an antisense DNA aperiodic backbone, the electronic states are localized. Ultrafast electron delocalization occurs for wet DNA within 740 as but even faster (< 300 as) charge transport is observed for aperiodic single-stranded phosphothioate Guanine decamers. The energy dependence of the delocalization time seems to have a nontrivial evolution (see Figure 13.12). This result demonstrates that charges in DNA do not only migrate through π – π couplings of nucleobases as it is commonly admitted, but can also efficiently propagate through the phosphate backbone. The measurements of electron delocalization and charge transport in DNA is of prior importance to understand the mechanisms responsible for recognition and repair in DNA. The observation in real time of this process is certainly crucial in biomolecular physics.

13.4.3

Similar Dynamics in Water and Ice

The same spectroscopy technique was used to study the initial steps of electron delocalization in liquid water and ice [33]. The spectroscopy shows that an excess electron propagates through the conduction band of the organized H-bond network within 500 as. This mechanism precedes the electron trapping and solvation dynamics, leading to a solvated electron state. While electron solvation has been experimentally explored using pump–probe techniques, the early stage dynamics could be probed time dependently with attosecond pulses. Such an experiment will reveal the complete electron dynamics and, especially, the transition stages between propagation, localization and solvation.

13.4.4

More

Beyond the few examples discussed in this chapter, there are many other problems that attosecond pulses can potentially address. Certainly, electron transport in complex molecular structures appears as a general case where ultrafast electron dynamics is important. We can foresee that such a dynamics will be probed at any molecular interfaces. Charge transport also plays a central role in light harvesting phenomena. The collective electron excitation (plasmon) is not only observed in nanoparticles but also in small clusters, fullerenes and related molecular structures. The plasmon dynamics could be investigated in real time, which would permit to understand how a many electron coherent excitation builds up and how it decays. Let us also mention recent research in nanomagnetism that addressed the attosecond dynamics of the coupling between spin and electromagnetic field [34]. This process could also be investigated in complex molecular samples with relevance in spintronics. As we mentioned in the introduction, not only electrons can travel on the attosecond timescale, protons can also react within few femtoseconds. For instance ultrafast isomerization of CH₄ following ionization, was measured with HHG [35]. Although, these experiments are preliminary we can anticipate that local proton motion could be observed in real time, and this could be very important to investigate mechanisms driven by Van der Waals forces (responsible for the stable configurations of proteins).

13.5

Conclusion

The use of attosecond pulses to investigate the properties of molecules is an emerging field of photophysics. So far, only few experiments used attosecond pulses to probe molecular ultrafast dynamical processes in real time. It is fascinating that these early results already challenge the many-body theories, meaning that attosecond molecular science already addresses nontrivial questions beyond the proof-of-

principle stage. Indeed, attosecond timescale experiments address the fundamental timescale where electron, nuclei, and light start to interact. This also means that usual approximations, such as Born–Oppenheimer or the mean-field theories might be invalidated at this scale. Beyond the first experiments, there are several important future developments in attosecond molecular physics could follow. For instance, attosecond coherent control strategies could be used to control dissociation or ionization on the electronic timescale. This will require a very detailed description of the molecular states, couplings and electron correlations effects. The development of attosecond chemistry could have the goal of observing and controlling processes also in large molecular systems. This certainly requires to bridge ultrashort and long timescales and to account for, dissipation, stochastic effects and nuclear dynamics. Progresses in molecular attosecond physics are also linked to the new experimental development of tunable CEP stable sources or HHG sources, high-repetition rate lasers and high-intensity HHG sources. In parallel, molecular orbital reconstruction based on HHG has been developed very rapidly, and information on the dynamics can also be extracted using the relation between recollision time and energy of the harmonics. The extension of this powerful technique to a pump–probe experiment, where the evolution of the molecular orbitals can be followed in real time and real space, during a reaction, could be accessible in the future. The observables that we can use are certainly electrons, ions but also absorption or emission of photons that all can retain the memory of processes that occur on the subfemtosecond timescale. Attosecond molecular physics is still at its infancy but offers very broad possible applications for future.

References

- 1 Hertel, I.V., and Radloff, W. (2006) Ultrafast dynamics in isolated molecules and molecular clusters. *Rep. Prog. Phys.*, **69**, 1897–2003.
- 2 Wernet, Ph., Odelius, M., Godehusen, K., Gaudin, J., Schwarzkopf, J., and Eberhardt, W. (2009) Real-Time Evolution of the Valence Electronic Structure in a Dissociating Molecule. *Phys. Rev. Lett.*, **103**, 013001.
- 3 Krausz, F., and Ivanov, M. (2009) Attosecond physics. *Rev. Mod. Phys.*, **81**, 163–234.
- 4 Okino, T., Yamanouchi, K., Shimizu, T., Furusawa, K., Hasegawa, H., Nabekawa, Y., and Midorikawa, K. (2006) Attosecond molecular Coulomb explosion. *Chem. Phys. Lett.*, **432**, 68–73.
- 5 Okino, T., Yamanouchi, K., Shimizu, T., Ma, R., Nabekawa, Y., and Midorikawa, K. (2008) Attosecond nonlinear Fourier transformation spectroscopy of CO₂ in extreme ultraviolet wavelength region. *J. Chem. Phys.*, **129**, 161103.
- 6 Kling, M.F., Siedschlag, Ch., Verhoef, A. J., Khan, J.I., Schultze, M., Uphues, T., Ni, Y., Uiberacker, M., Drescher, M., Krausz, F., and Vrakking, M.J.J. (2006) Control of electron localization in molecular dissociation. *Science*, **312**, 246–248.
- 7 Sansone, G., Kelkensberg, F., Pérez-Torres, J.F., Morales, F., Kling, M.F., Siu, W., Ghafur, O., Johnsson, P., Swoboda, M., Benedetti, E., Ferrari, F., Lépine, F., Sanz-Vicario, J.L., Zherebtsov, S., Znakovskaya, I., L’Huillier, A., Ivanov, M.Y., Nisoli, M., Martín, F., and Vrakking, M.J.J. (2010) Electron localization following attosecond molecular photoionization. *Nature*, **465**, 763–766.
- 8 Kelkensberg, F., Siu, W., Pérez-Torres, J.F., Morales, F., Gademan, G., Rouzée,

- A., Johnson, P., Lucchini, M., Calegari, F., Martín, F. and Vrakking, M.J.J. (2011) Attosecond Control in Photoionization of Hydrogen Molecules. *Phys. Rev. Lett.*, **107**, 043002.
- 9** Siu, W., Kelkensberg, F., Gademann, G., Rouzee, A., Johnsson, P., Dowek, D., Lucchini, M., Calegari, F., De Giovannini, U., Rubio, A., Lucchesi, R., Kono, H., Lepine, F., and Vrakking, M. J. J. (2011) Attosecond control of dissociative ionization of O₂ molecules, *Phys. Rev. A*, **84**, 063412.
- 10** Remetter, T., Jonhsson, P., Varjù, K., Mauritsson, J., Ni, Y. F., Lépine, F., Kling, M., Khan, J., Lopez-Martens, R., Schafer, K. J., Vrakking, M.J.J., and L'Huillier, A. (2006) Attosecond electron wave packet interferometry. *Nat. Phys.*, **2**, 323–326.
- 11** Paul, P.M., Toma, E.S., Breger, P., Mullot, G., Augé, F., Balcou, Ph., Muller, H.G., and Agostini, P. (2001) Observation of a train of attosecond pulses from high harmonic generation. *Science*, **292**, 1689–1692.
- 12** Schultze, M., Fieß, M., Karpowicz, N., Gagnon, J., Korbman, M., Hofstetter, M., Neppl, S., Cavalieri, A.L., Komninos, Y., Mercouris, Th., Nicolaides, C.A., Pażourek, R., Nagel, S., Feist, J., Burgdörfer, J., Azzeer, A. M., Ernstorfer, R., Kienberger, R., Kleineberg, U., Goulielmakis, E., Krausz, F., and Yakovlev, V.S. (2010) Delay in photoemission. *Science*, **328**, 1658–1662.
- 13** Klündter, K., Dahlström, J.M., Gisselbrecht, M., Fordell, T., Swoboda, M., Guénöt, D., Johnsson, P., Caillat, J., Mauritsson, J., Maquet, A., Taïeb, R., and L'Huillier, A. (2011) Probing single-photon ionization on the attosecond time scale. *Phys. Rev. Lett.*, **106**, 143002.
- 14** Haessler, S., Fabre, B., Higuet, J., Caillat, J., Ruchon, T., Breger, P., Carré, B., Constant, E., Maquet A., Mével E., Salières P., Taïeb R., and Mairesse Y. (2009) Phase-resolved attosecond near-threshold photoionization of molecular nitrogen. *Phys. Rev. A*, **80**, 011404.
- 15** Caillat, J., Maquet, A., Haessler, S., Fabre, B., Ruchon, T., Salières, P., Mairesse, Y., and Taïeb, R. (2011) Attosecond re-solved electron release in two-color near-threshold photoionization of N₂. *Phys. Rev. Lett.*, **106**, 093002.
- 16** Goulielmakis, E., Loh, Z., Wirth, A., Santra, R., Rohringer, N., Yakovlev, V. S., Zherebtsov, S., Pfeifer, T., Azzeer, A. M., Kling, M. F., Leone, S. R., and Krausz, F. (2010) Real-time observation of valence electron motion *Nature*, **466**, 739–743.
- 17** Holler, M., Schapper, F., Gallmann, L., and Keller, U. (2011), Attosecond electron wave-packet interference observed by transient absorption. *Phys. Rev. Lett.* **106**, 123601.
- 18** Remacle, F., Nest, M., and Levine, R. D. (2007). Laser steered ultrafast quantum dynamics of electrons in LiH. *Phys. Rev. Lett.*, **99**, 183902.
- 19** Remacle, F., Kienberger, R., Krausz, F., and Levine, R.D. (2007). On the feasibility of an ultrafast purely electronic re-organization in lithium hydride. *Chem. Phys.*, **338**, 342–347.
- 20** Bandrauk, A., Chelkowski, A.D.S., and Nguyen, H.S. (2004) Attosecond localization of electrons in molecules. *Int. J. Quantum Chem.*, **100**, 834–844.
- 21** Barth, I., Shigeta, Y., and Yagi, K. (2006) Unidirectional electronic ring current driven by a few cycle circularly polarized laser pulse: Quantum model simulations for Mg-porphyrin. *J. Am. Chem. Soc.*, **128**, 7043–7049.
- 22** Mignolet, B., Gijsbertsen, A., Vrakking, M.J.J., Levine, R.D., and Remacle, F. (2011) Stereocontrol of attosecond time-scale electron dynamics in ABCU using ultrafast laser pulses: a computational study. *Phys. Chem. Chem. Phys.*, **13**, 8331–8344
- 23** Breidbach, J., and Cederbaum, L.S. (2005) Universal attosecond response to the removal of an electron. *Phys. Rev. Lett.*, **94**, 033901.
- 24** Kuleff, A., and Cederbaum, L.S. (2011) Radiation generated by the ultrafast migration of a positive charge following the ionization of a molecular system. *Phys. Rev. Lett.*, **106**, 053001.
- 25** Cederbaum, L.S., and Zobeley, J. (1999) Ultrafast charge migration by electron correlation. *Chem. Phys. Lett.*, **307**, 205–210.

- 26 Hennig, H., Breidbach, J. and Cederbaum, L.S., (2005) Electron correlation as the driving force for charge transfer: Charge migration following ionization in *N*-methyl acetamide. *J. Phys. Chem. A*, **109**, 409–414.
- 27 Kuleff, A.I., and Cederbaum, L.S. (2007) Charge migration in different conformers of glycine: The role of nuclear geometry. *Chem. Phys.* **338**, 320–328.
- 28 Remacle, F., Levine, R.D. (2006) An electronic time scale in chemistry. *Proc. Natl. Acad. Sci. USA*, **103**, 6793–6798.
- 29 Kanno, M., Kono, H., Fujimura, Y., and Lin, S. H. (2010) Non-adiabatic response model of laser-induced ultrafast π -electron rotations in chiral aromatic molecules. *Phys. Rev. Lett.*, **104**, 108302.
- 30 Johnsson, P., Rouzée, A., Siu, W., Huismans, Y., Lépine, F., Marchenko, T., Dusterer, S., Tavella, F., Stojanovic, N., Azima, A., Treusch, R., Kling, M., and Vrakking, M. (2009) Field-free molecular alignment probed by the free electron laser in Hamburg (FLASH). *J. Phys. B*, **42**, 134017.
- 31 Ghafur, O., Rouzée, A., Gijsbertsen, A., Siu, W., Stolte, S., and Vrakking, M. (2009) Impulsive orientation and alignment of quantum-state-selected NO molecules. *Nat. Phys.*, **5**, 289–293.
- 32 Ikeura-Sekiguchi, H., and Sekiguchi, T. (2007) Attosecond electron delocalization in the conduction band through the phosphate backbone of genomic DNA. *Phys. Rev. Lett.*, **99**, 228102.
- 33 Nordlund, D., Ogasawara, H., Bluhm, H., Takahashi, O., Odelius, M., Nagasono, M., Petterson, L.G.M., and Nilsson, A. (2007) Probing the electron delocalization in liquid water and ice at attosecond time scales. *Phys. Rev. Lett.*, **99**, 217406.
- 34 Bigot, J.-Y., Vomir, M., and Beaurepaire, E. (2009) Coherent ultrafast magnetism induced by femtosecond laser pulses. *Nat. Phys.*, **5**, 515–520.
- 35 Baker, S., Robinson, J.S., Haworth, C.A., Teng, H., Smith, R.A., Chirila, C.C., Lein, M., Tisch, J.W.G., and Marangos, J.P. (2006) Probing proton dynamics in molecules on an attosecond time scale. *Science*, **312**, 424–427.

14

Attosecond Nanophysics

*Frederik Süssmann, Sarah L. Stebbings, Sergey Zherebtsov, Soo Hoon Chew,
Mark I. Stockman, Eckart Rühl, Ulf Kleineberg, Thomas Fennel, and Matthias F. Kling*

14.1

Introduction

Ultrafast control of electronic motion in isolated atoms with light fields has led to the birth of attosecond pulses [1, 2]. Waveform-controlled, optical, few-cycle laser pulses are powerful tools to steer electrons on subfemtosecond timescales and have been successfully applied to control the electron emission from atoms [3] and the electron localization in molecules [4]. The realization of a similar level of control of the electron motion in nanocircuits has the potential to revolutionize modern electronics by enabling significantly higher computation and communication speeds [5, 6].

Worldwide communication relies on optical fiber networks. Data encoding and decoding, however, involves the transformation of photon-based information within the optical fibers to electronic information and vice versa and is thus the current bottleneck for ultrafast communication and information processing. Lightwave-controlled nanocircuits (lightwave nanoelectronics) [7] are expected to reach petahertz operating frequencies which would remove the bottleneck in conventional communication technology by enabling all-optical data processing and communication. The key challenges on the way to lightwave nanoelectronics are (1) the control of electrodynamics in nanostructured materials on subcycle timescales and (2) the ability to monitor the resulting currents in nanostructured circuits with attosecond time and nanometer spatial resolution [6, 8–11]. The development and utilization of attosecond metrologies for the control and observation of ultrafast electron dynamics in nanosystems is therefore an issue with far-reaching implication. This chapter discusses selected key concepts and fundamental experiments in this area of attosecond nanophotonics.

The central objective of attosecond nanophotonics is the utilization of the widely tunable optical properties of nanostructured materials. This idea, which has a long history, might be illustrated best by the special optical phenomena arising from small nanoparticles. Without deeper insight, already the makers of color-stained glass church windows in the middle ages used the properties of metallic nanopar-

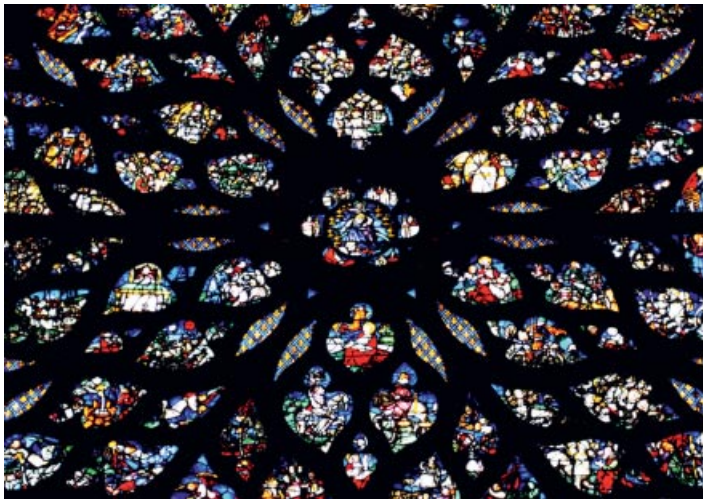


Figure 14.1 Plasmonic colors as evident from the stained glass windows of the Sainte-Chapelle in Paris. Picture credit: M.F. Kling.

ticles to their advantage. A vibrant red color was achieved by adding gold dust to the glass melt. The origin of this effect is understood today: if nanoparticles are exposed to visible light, the free-moving conduction electrons are displaced by the light's electric field to form *plasmons*. Since the structure is small, the electrons do not move very far, but are driven back by the electrostatic forces which build up through the excursion of the negative electron cloud with respect to the positively charged atoms in the much heavier nanoparticle. This way, the electrons move collectively in synchronized coherent oscillations. Such oscillations have particle characteristics and are called *surface plasmons*. The red color of old church windows is due to scattering and absorption of part of the visible light by the gold nanoparticles, which is converted into plasmons. The residual transmitted light shines in the complementary colors (see e.g. Figure 14.1 for one of the windows of the Sainte-Chapelle in Paris).

In more detail, the optical properties of nanomaterials are determined by the interaction of external electromagnetic radiation with the material [12]. Surface plasmons can either be confined to a single nanoparticle as localized surface plasmons (LSP), Figure 14.2a, or propagate along metal–dielectric interfaces as surface plasmon polaritons (SPP), Figure 14.2b [12, 13]. In both cases, energy from the external electromagnetic field can be localized beyond the diffraction limit onto nanometer scales [7].

The strong optical response of metallic nanoparticles in the presence of an external field depends on the material, composition [14], shape [15], configuration [16], and local environment [17, 18]. The progress in the field of nanophotonics has been fueled by advances in fabrication techniques such as lithography (see [16]) and chemical synthesis (see [19]). These techniques have allowed the precise and reproducible fabrication of single nanoparticles and nanoparticle arrays including

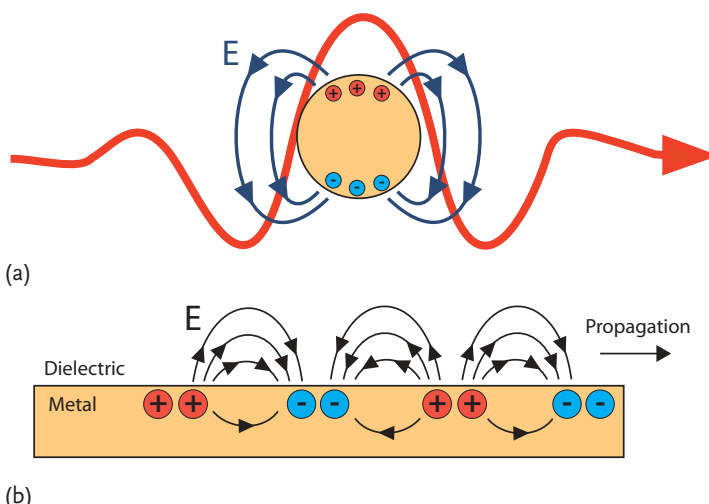


Figure 14.2 (a) Field configurations of a localized surface plasmon (LSP) of a metal nanosphere in an external light field. (b) Sketch of a travelling surface plasmon polariton (SPP).

solid metallic nanospheres, nanocages, hollow particles, and composites. The high sensitivity of the optical response of nanostructures to their configuration and environment has led to a variety of novel spectroscopic applications [20], reaching the detection level of single molecules in methods such as scanning near-field microscopy (SNOM) and surface-enhanced Raman scattering (SERS). For reviews on these techniques see [21].

The spectral properties of plasmons as a function of particle size, shape, and dielectric properties are reasonably understood for many nanoparticles and can be predicted well theoretically by solving the classical Maxwell equations [13, 22]. However, the subcycle dynamics of collective electronic excitations (i.e., how they are formed and how the phase coherence is lost) has not been directly measured. The dephasing time of a nanolocalized plasmon is in the range of 5–100 fs across the plasmonic spectrum. The dephasing time T_2 of a plasmon can be expressed by (see e.g. [23, 24])

$$\frac{1}{T_2} = \frac{1}{2T_1} + \frac{1}{T^*} . \quad (14.1)$$

T^* is the time for a pure dephasing, that is, a loss of the fixed phase relationship between individual electrons in the collective dynamics. Possible decay mechanisms for the pure dephasing include scattering and inhomogeneous phase velocities caused by broadband excitation and/or local inhomogeneities of the nanoparticle. T_1 is the time for the creation of electron–hole pairs and the decay by the emission of photons (radiative decay). The former production of electron–hole pairs includes intraband and interband excitations [24]. The latter depends on the coupling strength to the far field being governed mostly by the antenna shape and size. Figure 14.3 depicts the dominant dephasing processes occurring after the excitation

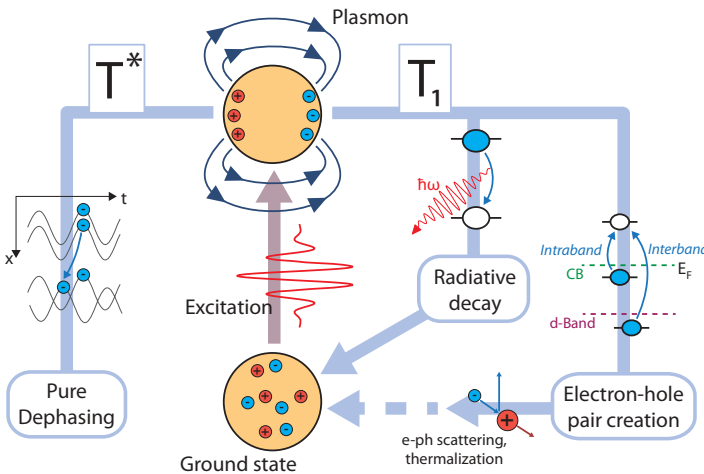


Figure 14.3 Dynamics following the excitation of localized surface plasmons by a few-cycle laser field. See text for details.

of a surface plasmon. The figure also shows the last step in the decay of plasmons resulting from electron–phonon coupling. Despite considerable efforts to not only infer the dephasing times from spectroscopic measurements but also measure them by time-resolved methods (see e.g. [25] and references therein), studies so far have been mostly limited by the use of laser pulses on the order of the plasmon decay times, making the analysis of the obtained signals challenging. It is highly desirable to utilize much shorter, attosecond pulses in such measurements to elucidate the decay mechanisms in detail.

Most importantly, collective electron motion in nanoplasmatic systems unfolds on extremely short, attosecond timescales, as defined by the inverse spectral bandwidth of the plasmonic resonant region. Theoretical results have predicted that local optical fields in disordered nanostructured systems (clusters, composites, and rough surfaces) will experience giant fluctuations on attosecond temporal and nanometer spatial scales [9]. It was shown that the electric field and photoemission are enhanced by a factor of several hundred [26] at such *hot spots*. Until now, the attosecond dynamics of nanoplasmatic fields have not been directly observed with simultaneous attosecond temporal and nanometer spatial resolution. Hence, an experimental study of those ultrafast and nanolocalized plasmonic field dynamics is of particular importance.

Furthermore, the interaction with strong external fields may induce nonlinear behavior and transitions in the electronic properties of nanomaterials on attosecond timescales (see e.g. [6, 27, 28]). These fast processes can now be uncovered with available attosecond tools, such as few-cycle optical and attosecond extreme ultraviolet (XUV) pulses [9] giving birth to the rapidly developing field of attosecond nanophysics.

In this chapter, we will highlight work on the subcycle control and probing of collective electron motion. The chapter begins with the topic of lightwave control

of the electron emission and acceleration in dielectric nanospheres as a showcase example for the control of nonresonant electron motion in nanostructures. As an example for the direct time-resolved probing of resonant collective electron motion the spectral interferometry technique is introduced for few-nm Na clusters, which allows the extraction of information on temporal dynamics with subfemtosecond resolution up to highly nonlinear laser excitation. As one of the most promising techniques to achieve attosecond temporal resolution in the probing the collective electron dynamics of larger nanosystems, we will introduce nanoplasmonic streaking, which allows the real-time observation of the fastest plasmon dynamics. Nanometer spatial resolution can be achieved simultaneously by implementing the attosecond nanoscope (ATN), which is based on a combination of attosecond nanoplasmonic streaking and photoemission electron microscopy (PEEM). We will introduce this technique and describe the progress and challenges toward its experimental implementation. Finally, we will outline recent experimental and theoretical progress on the generation of XUV light at MHz repetition rates by high-harmonic radiation using nanoplasmonic field enhancement in nanostructures.

14.2

Attosecond Light-Field Control of Electron Emission and Acceleration from Nanoparticles

Carrier-envelope phase stabilized laser pulses provide a well-defined electric field and provide an ideal tool for manipulating collective electron motion. They allow unique spatiotemporal control of local electric fields on nanometer spatial and attosecond temporal scales. Developments in femtosecond laser technology culminated in the generation of laser pulses of only a few optical cycles duration [29, 30], where the electric field waveform can be described as

$$E_{\text{las}}(t) = E_{\text{env}}(t) \cos(\omega_0 t + \varphi_{\text{CE}}) , \quad (14.2)$$

where $E_{\text{env}}(t)$ is the real-valued amplitude envelope, ω_0 the angular frequency of the carrier wave, and φ_{CE} the carrier-envelope phase (CEP). The evolution of the electric field $E_{\text{las}}(t)$ of such ultrashort laser pulses can be controlled with subfemtosecond precision by the CEP.

A first demonstration of the CEP-control of electron emission and acceleration from nanostructures was recently reported by Zherebtsov *et al.* [10, 31] for SiO₂ nanoparticles followed by its implementation for tungsten nanotips [11, 32]. The results of the study on SiO₂ nanoparticles are highlighted below. The wide spectral response of the dielectric material allows for an effective use of the full bandwidth of ultrashort pulses. The large work function of the material makes it possible to realize tunneling ionization conditions with relatively low ionization yields up to high intensities, enabling the probing of the dielectric response with only limited interaction between free carriers.

14.2.1

Imaging of the Electron Emission from Isolated Nanoparticles

The laser-induced electron emission from isolated nanoparticles was studied using a beam of nanoparticles, thus every laser shot interacts with a fresh sample. Ultrafast processes resulting from the interaction of the laser with the particles can therefore be studied even up to conditions where the particles Coulomb explode after exposure to the laser pulse. Using few-cycle pulses allows us to restrict laser the interaction with the particles to a few femtoseconds and separates the laser-induced electron emission and acceleration from any electronic and nuclear dynamics taking place on longer timescales [33, 34].

The electron emission from the nanoparticles was recorded via velocity-map imaging (VMI) schematically presented in Figure 14.4a. SiO_2 nanoparticles were prepared by wet chemical techniques yielding a narrow particle size and shape distribution [35, 36]. The nanoparticles were introduced into the gas phase by aerosol techniques and prepared into a focused beam by applying aerodynamic focusing [37, 38]. CEP stabilized 5 fs laser pulses centered at a wavelength of 720 nm were generated as described in [39] and focused onto the nanoparticle beam. The emitted electrons were projected onto a microchannel plate (MCP)/phosphor screen assembly by the ion optics of the VMI spectrometer and the resulting images were recorded by a CCD camera. To reconstruct the 3D momentum distribution of the electron emission from the recorded 2D projection, an iterative inversion procedure was used [40]. Above-threshold ionization (ATI) in Xe was measured at the same laser parameters as for the nanoparticles in order to derive the laser intensity in the interaction region.

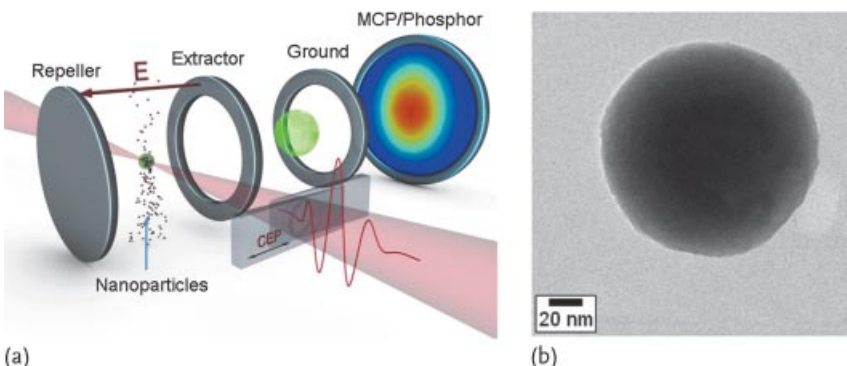


Figure 14.4 (a) Schematic diagram of the velocity-map imaging (VMI) of the electron emission from isolated nanoparticles in few-cycle laser fields. The VMI spectrometer consists of the ion optics (repeller, extractor, and ground plate) and an MCP/phosphor screen detector. The CEP of the phase sta-

lized laser pulses was adjusted with a pair of glass wedges. The polarization of the laser field was in the plane of the detector. (b) High-resolution transmission electron microscope (HRTEM) image of a SiO_2 nanoparticle. After [10].

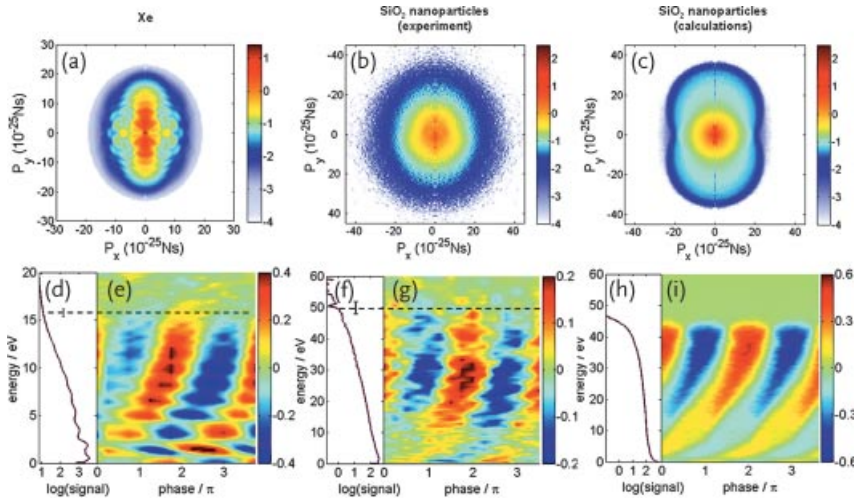


Figure 14.5 Electron emission from Xe and SiO₂ nanoparticles. (a) Momentum map of photoelectrons from Xe (log color scale) at an intensity of $1.9 \times 10^{13} \text{ W/cm}^2$ averaged over the CEP with the laser polarization along the p_y -axis. (d) Electron kinetic energy spectrum obtained from angular integration over 50° (full opening angle) along the laser polarization axis. (e) Asymmetry of the electron emission from Xe as a function of the electron kinetic energy and phase. (b) Photoelectron momentum map (log color scale), (f) electron kinetic energy spectrum, and (g) asymmetry

map measured in SiO₂ nanoparticles at the same conditions as for Xe. The electron energy cutoffs are indicated by the dashed lines, the vertical bars indicate the uncertainty in the cutoff energy. Results of the theoretical calculations: (c) Photoelectron momentum map, (h) electron kinetic energy spectrum, and (i) asymmetry map calculated for a SiO₂ nanosphere of 100 nm diameter (log color scale) at an intensity of $2 \times 10^{13} \text{ W/cm}^2$ and averaged over the phase and the focal intensity distribution. After [10].

Figure 14.5a shows a typical cross section of the momentum distribution ($p_z = 0$ plane) of the ATI of Xe atoms (averaged over all CEP values). The polarization axis of the laser is along the p_y -axis. Two principal mechanisms contribute to the ATI signal: (1) most of the electrons leave the atom directly with kinetic energies up to 2–3 eV, and (2) a much smaller fraction of the electrons return to the parent ion and (re)scatter [41, 42], here acquiring kinetic energies of up to about 16 eV. The cutoff for the rescattered electrons in the classical limit is $10 U_p$, where $U_p = e^2 E_{\text{env}}^2 / (4m\omega_0^2)$ is the ponderomotive potential of an electron in the laser field, e is the elementary charge, and m is the electron mass. Figure 14.5b shows the momentum distribution of the electrons emitted from (109 ± 6) nm diameter SiO₂ nanoparticles measured at the same laser parameters. The angular distribution is more isotropic as compared to Xe, and the corresponding photoelectron spectrum extends up to much higher kinetic energies of about 50 eV (cf. Figure 14.5f).

The waveform of a few-cycle laser pulse critically depends on the temporal offset between the carrier wave and the pulse envelope and offers a possibility to control

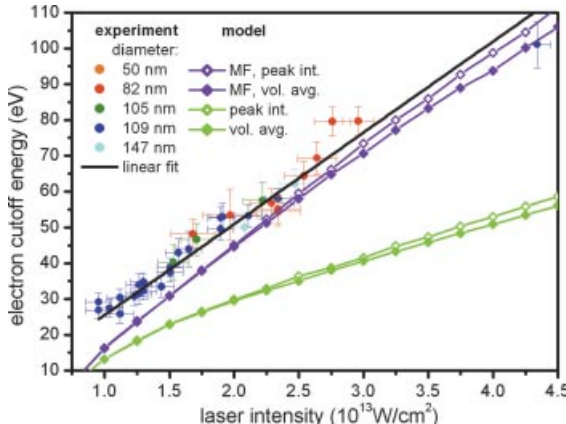


Figure 14.6 Dependence of the cutoffs in the electron emission spectra from SiO_2 nanoparticles on laser intensity. The experimental results for nanoparticles of different sizes are represented by circles of different colors as indicated in the legend. The experimental data are fitted by a linear function (black solid line) with a slope of $53.0 \pm 0.6 U_p$. The cutoffs predicted for SiO_2 nanoparticles of 100 nm diameter by the simulations with the laser and polarization fields only (green lines) and sim-

ulations including the mean field (MF) created by free charges (purple lines). For both types of curves open diamonds correspond to single (peak) laser intensity calculations and filled diamonds correspond to volume averaged (vol. avg.) data. The error bars were determined from the uncertainties in the electron cut-off energies from Xe and SiO_2 nanoparticles similar to the error bars given in Figure 14.5. After [10].

the electron emission directions by the CEP [43]. The directional electron emission can be represented by the asymmetry parameter

$$A(W, \varphi_{\text{CE}}) = \frac{P_{\text{up}}(W, \varphi_{\text{CE}}) - P_{\text{down}}(W, \varphi_{\text{CE}})}{P_{\text{up}}(W, \varphi_{\text{CE}}) + P_{\text{down}}(W, \varphi_{\text{CE}})} \quad (14.3)$$

for the electron kinetic energy W and carrier-envelope phase φ_{CE} , where $P_{\text{up}}(W, \varphi_{\text{CE}})$ and $P_{\text{down}}(W, \varphi_{\text{CE}})$ are the angle integrated electron yields in the up (positive p_y momentum) and down (negative p_y momentum) directions. Figure 14.5e and g shows $A(W, \varphi_{\text{CE}})$ for Xe and SiO_2 , respectively. Periodic oscillations of the asymmetry parameter with CEP are present in the energy range up to the cutoff of asymmetry at (15.7 ± 0.5) eV for Xe and (49.6 ± 3.0) eV for SiO_2 (corresponding to $(54.1 \pm 4.4) U_p$), in good agreement with the spectral cutoffs. From the cutoff in the Xe data a laser pulse intensity of $(1.9 \pm 0.1) \times 10^{13} \text{ W/cm}^2$ is derived by comparison to the semiclassical cutoff formula of $10.007 U_p + 0.538 \text{ IP}$, where IP is the ionization potential of Xe [44] and verified by comparison to time-dependent Schrödinger equation calculations (see [10]). The energy-dependent slopes in the asymmetry map of Xe are similar to what was previously observed in atoms [45]. For SiO_2 nanospheres the slopes are steeper and the asymmetry oscillations cover a broad energy range up to the cutoff energy with the largest asymmetry amplitude occurring above 10 eV. Laser-driven acceleration of these high-energy electrons is supported by the observation of a significant CEP-dependence of the directional

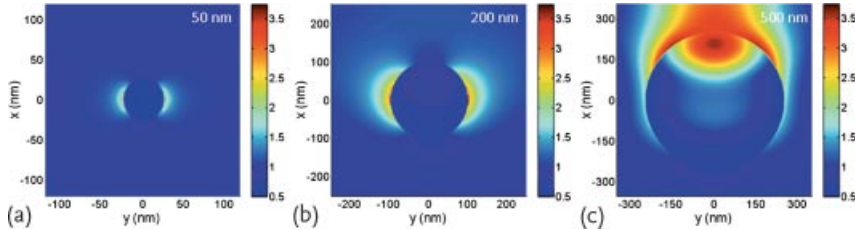


Figure 14.7 Electric field distribution in SiO_2 nanoparticles of different sizes for irradiation with 5 fs laser pulses as calculated by FDTD simulations. Maximum field intensity (relative to the laser peak intensity) in the $z = 0$ plane for the incident pulse propagating in the x -direction and polarized along the y -axis. After [10].

emission and by the fact that the asymmetry maxima versus CEP shift with energy. Because of the latter effect and the nearly linear scaling of the energy cutoff with intensity as analyzed below, electron evaporation due to asymmetric heating of the nanoparticles can be excluded as the origin of these energetic electrons.

The intensity dependence of the cutoff values in the kinetic energy spectra measured for nanoparticles of different sizes are displayed in Figure 14.6. The cutoff energy shows a nearly linear dependence on laser intensity with an average cutoff value of $(53.0 \pm 0.6) U_p$ as obtained from a linear fit (black solid line in Figure 14.6). No significant dependence of the electron cutoff energy on the particle size is observed within the experimental error bars. The results of finite difference time domain (FDTD) calculations (Figure 14.7) indicate that only for spheres with diameters exceeding 200 nm the field distribution inside the particles and the dielectric near-field enhancement close to the surface become substantially distorted by propagation effects, explaining in part the size-independence in the experimental data for smaller particles.

14.2.2

Microscopic Analysis of the Electron Emission

To model the nanoparticle ionization dynamics and the electron emission processes a quasiclassical, trajectory-based Monte Carlo approach was used. The electron emission from the nanoparticle surface and the subsequent, classical electron propagation is considered to be driven by the effective field produced by the laser pulse, the nanoparticle polarization, and free charges, that is, previously liberated electrons and residual ions at the surface of the nanoparticle. Under the dipole approximation for the near field and neglecting the nonlinear terms and dynamical changes in the dielectric response of the nanoparticle, the combined potential of the laser field E_{las} and the induced polarization of the dielectric sphere with relative permittivity ϵ is

$$\Phi^{\text{sphere}}(\mathbf{r}, t) = \begin{cases} -E_{\text{las}}(t) \left(1 - \frac{\epsilon-1}{\epsilon+2} \frac{R^3}{r^3}\right) y & r \geq R \\ -E_{\text{las}}(t) \left(\frac{3}{\epsilon+2}\right) y & r < R \end{cases} \quad (14.4)$$

and the effective potential is $\Phi^{\text{eff}}(\mathbf{r}, t) = \Phi^{\text{sphere}}(\mathbf{r}, t) + \Phi^{\text{free}}(\mathbf{r}, t)$, where Φ^{free} is the Coulomb potential produced by the free charges. This potential creates the additional electric mean field (MF) acting on each free electron. Tunnel ionization of atoms at the surface of the nanoparticle was approximated by the ADK ionization rates where the ionization potential of atomic Si (8.1 eV) was used. After appearing at the tunnel exit, the electron was propagated on a classical trajectory via $\ddot{\mathbf{r}} = e/m\nabla\Phi^{\text{eff}}(\mathbf{r}, t)$. Interference effects were neglected as the phase relations between different electron trajectories are nearly random in systems with many active electrons. If electron trajectories re-penetrated the nanoparticle, elastic electron-ion scattering was evaluated via Monte Carlo sampling assuming an isotropic cross section and a constant mean-free path $\lambda_{\text{mfp}} = 1 \text{ nm}$, similar to the effective attenuation length in SiO_2 [46]. A sufficiently large number of trajectories ($\sim 10^6$) were propagated simultaneously within a statistical ensemble for evaluating the Coulomb mean-field Φ^{free} term and the electron spectra.

The momentum map, energy spectrum, and asymmetry map calculated for parameters close to the experiment are presented in Figure 14.5c, h, and i. The model reproduces the main experimental features, with a smooth spectrum, a phase-dependent, high-energy component, and asymmetry slopes similar to the experiment. The disappearance of the asymmetry oscillations with CEP around 47 eV coincides well with the energy cutoff (Figure 14.5h and i), and is in good agreement with the experiment. The increased isotropic distribution in the experimental momentum map can likely be attributed to additional scattering effects, for example, due to a finite surface roughness of the experimental nanoparticles (Figure 14.4b), which are not accounted for in the modeling.

For a closer analysis of the physics described by the model, Figure 14.8 compares results from simulations with the laser and polarization fields alone (Figure 14.8a) to simulations with the full potential (Figure 14.8b). For the laser and polarization

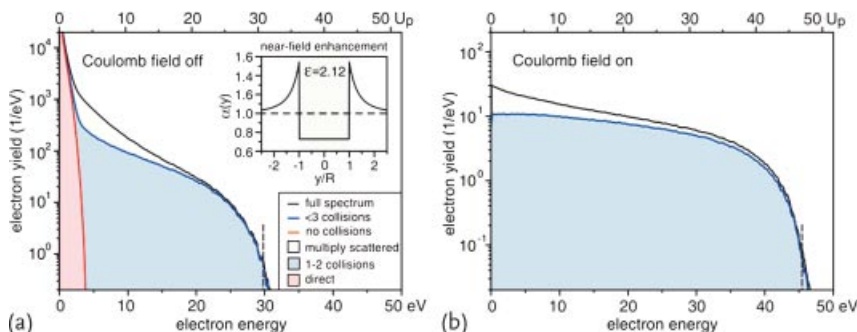


Figure 14.8 Electron emission from a SiO_2 nanosphere (diameter: 100 nm) calculated for excitation with 5 fs pulses at 720 nm and $I_0 = 2 \times 10^{13} \text{ W/cm}^2$. (a) Simulation with laser and polarization field. (b) Simulation with the full potential, including the free charge Φ^{free} . The CEP-averaged electron en-

ergy spectra (black) in (a) and (b) are given together with partial energy spectra (red, blue) from trajectories with a certain number of collisions (as indicated). The inset in (a) shows the y -dependent dielectric field enhancement $\alpha(y)$. After [10].

field alone, the CEP-averaged electron energy spectrum (Figure 14.8a, black line) exhibits a pronounced peak at low electron energies and a plateau-like extension to high energies. Partial energy spectra from trajectories with only a certain number of collisions show that direct electrons (red shaded area) produce the low energy feature and backscattered electrons (one or two collisions, blue shaded area) are dominant in the high-energy region, similar to atomic high-order ATI. The cut-offs of direct and backscattered electrons are at about 4 and $30 U_p$, in fair agreement with the modified classical atomic cutoffs $2\alpha^2 U_p = 4.47 U_p$ for direct and $10\alpha^2 U_p = 23.72 U_p$ for rescattered electrons ($2 U_p$ and $10 U_p$ in the atomic case), where $\alpha \approx 1.54$ is the field enhancement factor at the poles of the nanoparticle (cf. inset of Figure 14.8a). The roughly 30% higher backscattering cutoff in our model reflects that electrons are ejected with an initial displacement to the residual ion, that is, at the tunnel exit, which is neglected in the classical $10 U_p$ cutoff law. However, the simulations with the laser and polarization field alone predict an overly strong signal from direct electrons at low energies as well as energy cutoffs well below the experimental values. These discrepancies are almost fully resolved when taking into account the Coulomb field generated by liberated electrons and residual ions at the surface of the nanoparticle. In this case the direct electron emission is suppressed and the backscattering plateau extends up to $47 U_p$, close to the experimental values (Figure 14.8b). Moreover, the intensity-dependent energy cutoffs show slopes similar to the experimental data (Figure 14.6). The increase in the cut-off energy can be attributed to two main processes: (1) the trapping field created by the positive ions at the surface relaxes the birth-time requirements for rescattering electrons that result in higher return energies, (2) Coulomb repulsion of the created electron cloud provides additional acceleration.

Figure 14.9 compares typical fast trajectories from simulations both with and without the Coulomb term Φ^{free} (red vs. green curves). In the first case, the optimum trajectory (launched about 0.4 fs after the field maximum) recollides with a kinetic energy of about 12 eV near the zero crossing of the laser, and escapes after backscattering with a final energy of 31 eV. When including the Coulomb field Φ^{free} , the trajectory starts almost at the field maximum and recollides with a kinetic energy of 23 eV, reflecting the effect of the attractive short-range trapping field. This return energy corresponds to $\sim 23 U_p$ (blue ellipse in Figure 14.9), about $20 U_p$ higher than the classical return energy in atomic gas. After backscattering and when the laser pulse has ceased, the trajectory including the Coulomb field has a kinetic energy roughly 10 eV higher, see inset of Figure 14.9. A further energy gain of about 5 eV observed at later times results from space-charge repulsion in the escaping electron cloud, similar to an electronic Coulomb explosion.

The electron acceleration in SiO_2 nanoparticles occurs via a novel mechanism, where the emitted electrons are accelerated by the combined action of the dielectrically enhanced near field and the surface-trapping potential produced by the previously released electrons and residual ions. A similar acceleration process and its CEP control might be expected for other materials, including semiconductor and metal nanoparticles. Nurturing this expectation, high-energy electron emission observed recently in medium-sized Ag clusters was also ascribed to a rescattering

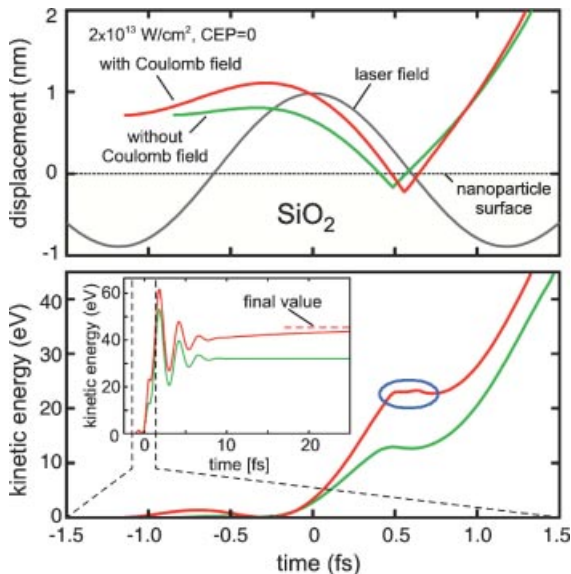


Figure 14.9 Evolution of the displacement and the kinetic energy of typical fast trajectories. The green curves correspond to simulations with the laser and the polarization field alone whereas the red curves show results

from full calculations including the Coulomb field Φ^{free} . The blue ellipse on the red curve in the lower panel indicates the energy gained at the moment, when the electron recollides with the nanoparticle surface. After [10].

process, where electrons are driven through the cluster by the plasmon-enhanced polarization field [47].

Lightwave nanoelectronics ultimately requires control of nanoscopic currents in surface assembled nanostructures. This sets a limit for the maximum intensity of the driving laser field, which must be kept sufficiently low to avoid damage to the assembled nanostructures. A first step into this direction was the demonstration of CEP-controlled electron emission and acceleration from tungsten nanotips [11]. In the experiment by Krüger *et al.*, few-cycle pulses from a Ti:Sapphire oscillator were focused onto a sharp metal nanotip of 10–20 nm radius [11]. Featureless spectra were observed for cosine-type laser pulses ($\varphi_{\text{CE}} = 0$), when the electrons were emitted within a single subcycle interval at the maximum of the laser field. For sine-type laser pulses ($\varphi_{\text{CE}} = \pi/2$) spectral interference was observed, indicating that electrons were emitted within at least two time intervals within the pulse and accelerated to the same final energy.

CEP-dependent electron acceleration up to keV energies by locally enhanced evanescent fields of laser-induced SPPs has been predicted for thin metal films [48, 49]. The absence of a significant CEP dependence of electron spectra recently recorded from the metal film [50] was attributed to the nanoscale surface roughness of the sample randomizing the electron trajectories. The smearing of the CEP effects can be minimized in future experiment with atomically flat metal films.

Alternatively, experiments implementing nanometer-resolved electron detection could overcome this obstacle.

14.3

Few-Cycle Pump-Probe Analysis of Cluster Plasmons

The previous section has discussed collective electron dynamics in nanoparticles excited by nonresonant near-infrared few-cycle laser fields and the resulting modification of the release and acceleration of electrons via the buildup of polarization-induced near-fields. We now discuss a method for direct tracing of the short-time plasmonic response of nanosystems by spectral interferometry with few-cycle pulses that was recently reported by Köhn *et al.* [51]. Below we introduce the working principle in terms of a simplified oscillator model and study the time-domain imaging of plasmon oscillations and the ionization-induced increase of the plasmon lifetime in few-nm-sized Na clusters as a computational example. For the following clusters were chosen as a model system that is well-known from strong field experiments and that can be described fully microscopically. The interferometric analysis with few-cycle pulses is, of course, applicable to other plasmonic nanosystems as well.

Clusters in intense near-infrared (NIR) laser pulses are known for their extremely high absorption of light due to the interaction of the laser field with a dense nanoplasma [52]. A key mechanism behind strong absorption and the resulting emission of fast electrons and highly charged energetic ions is resonant excitation of the cluster Mie plasmon, for recent reviews see [53, 54]. The plasmon frequency in metallic as well as preionized clusters from other materials is typically well above the laser frequency in early stages of the interaction. Noting the density dependence of the plasmon frequency in a spherical metallic drop $\omega_{\text{Mie}} = \sqrt{e\rho_i/(3\varepsilon_0 m)}$, with ρ_i as the ion background charge density and ε_0 as the vacuum permittivity, resonant plasmon excitation requires a certain cluster expansion (timescale of nuclear motion) induced by laser-driven ionization and heating. Such a sequence of ionization, expansion, and resonant excitation may be realized with sufficiently long pulses or by appropriate pump–probe excitation [55, 56]. Though resonant plasmon enhancement is typical in strong-field laser-cluster experiments, its direct time-domain analysis has not been achieved yet. Such analysis is, however, important to advance the understanding of collective electronic processes in intense laser fields and their signatures in the electron and ion emission [57–59].

14.3.1

Basics of Spectral Interferometry

Using the electric field of a few-cycle laser pulse in the notation of Eq. (14.2), the field of a pulse pair with equal CEP reads

$$E_{\text{tot}}(t) = E_{\text{las}}(t) + E_{\text{las}}(t - \Delta t), \quad (14.5)$$

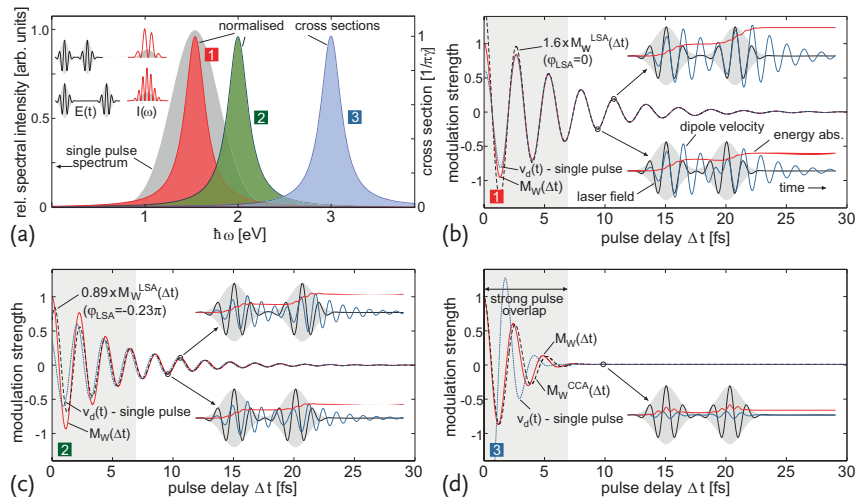


Figure 14.10 Spectral interferometry results with Gaussian 3 fs FWHM pulses ($\hbar\omega_0 = 1.54$ eV) for three Lorentz oscillator settings. (a) single pulse spectral intensity (gray) and normalized absorption cross sections for $\omega_{\text{res}} = \omega_0$, $1.3\omega_0$, and $2\omega_0$ (red, green, blue) for $\gamma^{-1} = 5$ fs lifetime; insets show electric field evolutions (black) and resulting spectral intensity distributions (red) for different delays; (b–d) delay-dependent

modulation signals $M_w(\Delta t)$ (red) compared to results in linear spectrum approximation or constant cross section approximation; corresponding φ_{LSA} values as indicated; dashed blue curves show the pump-only dipole velocity signal $v_d(t)$; insets depict evolutions of the laser field (black), dipole velocity (blue), and absorbed energy (red) for indicated delays. After [51].

where Δt is the pulse delay. Now we consider the energy absorption of a weakly damped oscillator resulting from excitation with the pulse pair, which has the form

$$W_{\text{abs}}(\Delta t) = \frac{\gamma}{\pi} \int_{-\infty}^{\infty} \frac{[1 + \cos(\omega \Delta t)] |E_{\text{env}}(\omega - \omega_0)|^2 / 2\pi}{(\omega_{\text{res}} - \omega)^2 + \gamma^2} d\omega , \quad (14.6)$$

where ω_{res} and γ are the resonance frequency and spectral width (inverse lifetime) of the oscillator and $E_{\text{env}}(\omega) = \int_{-\infty}^{\infty} E_{\text{env}}(t) \exp(i\omega t) dt$ is the envelope in the frequency domain. The nominator of the integrand is the spectral intensity of the pulse pair, containing the single pulse spectrum $I_{\text{las}}(\omega) = |E_{\text{env}}(\omega - \omega_0)|^2 / 4\pi$ times a spectral modulation with $2[1 + \cos(\omega \Delta t)]$. This tunable interference of the spectral intensity (cf. insets of Figure 14.10a) is the key feature of spectral interferometry. The absorbed energy $W(\Delta t)$ in Eq. (14.6) will now be considered for two approximations.

Linear Spectrum Approximation (LSA)

For an oscillator resonance inside the laser spectrum, $I_{\text{las}}(\omega)$ can be linearized around ω_{res} by $I_{\text{las}}^{\text{LSA}}(\omega) = \alpha + (\omega - \omega_{\text{res}})\beta$ with $\alpha = I_{\text{las}}(\omega_{\text{res}})$ and $\beta = \partial I_{\text{las}}(\omega)/\partial\omega|_{\omega=\omega_{\text{res}}}$. The integral in Eq. (14.6) becomes

$$W_{\text{abs}}^{\text{LSA}}(\Delta t) = 2\alpha \left(1 + \sqrt{1 + c_{\text{LSA}}^2} \cos(\omega_{\text{res}}\Delta t + \varphi_{\text{LSA}}) \exp(-\gamma \Delta t) \right) \quad (14.7)$$

with $c_{\text{LSA}} = \tan \varphi_{\text{LSA}} = \beta\gamma/\alpha$. For a resonance at the maximum of $I_{\text{las}}(\omega)$, that is, for $\beta = 0$, this linear spectrum approximation (LSA) reduces further to

$$W_{\text{abs}}^{\text{LSA}}(\Delta t) = 2\alpha(1 + \cos(\omega_{\text{res}}\Delta t) \exp(-\gamma \Delta t)) \quad (14.8)$$

The delay-dependent absorption contains a static offset and a damped periodic oscillation with the eigenfrequency and lifetime of the oscillator. For CEP = 0, the modulation provides a direct time-domain image of the dipole velocity of the oscillator after the first pulse. Besides a phase shift φ_{LSA} and a scaled modulation amplitude (both known for a given laser spectrum), the plasmonic motion can be extracted even for a resonance located in the wings of the laser spectrum ($\beta \neq 0$), cf. Eq. (14.7).

Constant Cross-Section Approximation

The second limiting case is fully off-resonant excitation (ω_{res} outside the laser spectrum). Approximating the cross section by $\sigma_0 = \sigma(\omega_0)$ yields the constant cross-section approximation (CCA)

$$\begin{aligned} W_{\text{abs}}^{\text{CCA}} &= 2\sigma_0 \int_{-\infty}^{\infty} (1 + \cos(\omega\Delta t)) I_{\text{las}}(\omega) d\omega \\ &= \sigma_0 [2F_0 + A_{\text{env}}(\Delta t) \cos \omega_0 \Delta t], \end{aligned} \quad (14.9)$$

with the single pulse fluence $F_0 = 1/2 \int_{-\infty}^{\infty} E_{\text{env}}^2(t) dt$, the envelope autocorrelation $A_{\text{env}}(\Delta t) = \int_{-\infty}^{\infty} E_{\text{env}}(t) E_{\text{env}}(t - \Delta t) dt$, and the total fluence in square brackets. Hence, for nonresonant excitation, the absorption is proportional to the field fluence.

14.3.2

Oscillator Model Results for Excitation with Gaussian Pulses

For a Gaussian envelope $E_{\text{env}}(t) = \hat{E} \exp(-t^2/\tau_g^2)$ with field amplitude \hat{E} and pulse width τ_g , the LSA parameter is found as $c_{\text{LSA}} = \tan \varphi_{\text{LSA}} = -\tau_g^2 \gamma (\omega_{\text{res}} - \omega_0)$, cf. Eq. (14.7). The full width at half maximum (FWHM) of the intensity is related by $\tau_{\text{fwhm}} = \tau_g \sqrt{2 \ln 2}$. Excitation with pulses for CEP = 0 ($\tau_{\text{fwhm}} = 3 \text{ fs}, 800 \text{ nm}$) will now be considered for three oscillator configurations with resonances $\omega_{\text{res}} = \omega_0$, $1.3\omega_0$, and $2\omega_0$. A damping constant of $\hbar\gamma = 0.13 \text{ eV}$ (lifetime $\tau_{\text{res}} = 5 \text{ fs}$) is as-

sumed. These examples reflect (1) fully resonant, (2) near-resonance, and (3) non-resonant excitation. Normalized cross sections are shown Figure 14.10a in relation to the single pulse spectrum. The delay-dependent absorption can be measured by a dimensionless modulation

$$M_W(\Delta t) = \frac{W(\Delta t)}{W} (\Delta t' \gg \tau_{\text{res}}) - 1 \quad (14.10)$$

which is unity for $\Delta t = 0$ and zero for pulse delays much larger than the oscillator lifetime. The modulation signal $M_W^{\text{LSA}}(\Delta t)$ and $M_W^{\text{CCA}}(\Delta t)$ for the approximated energy absorptions in Eq. (14.7) or Eq. (14.9) are defined analogously. In Figure 14.10b–d, the evolutions of $M_W(\Delta t)$ (solid red curves) are shown in relation to the applicable approximation $M_W^{\text{LSA}}(\Delta t)$ or $M_W^{\text{CCA}}(\Delta t)$ (dashed, approximation as indicated).

For the fully resonant and the near-resonant scenario (Figure 14.10b and c), the predictions of the linear spectrum approximation $M_W^{\text{LSA}}(\Delta t)$ (rescaled in amplitude as indicated) are in good agreement with $M_W(\Delta t)$ and show damped oscillations with high contrast. A closer comparison of the rescaled $M_W^{\text{LSA}}(\Delta t)$ signals with $M_W(\Delta t)$ shows that the modulations appear in phase with the oscillator frequency and decay rate for $\Delta t > 6$ fs, that is, outside the pulse overlap.

For selected delays, time-domain evolutions of the laser field, dipole velocity, and absorbed energy are sketched as insets, providing a direct image of the dynamics being mapped into the modulation signals. Focusing on the upper time-domain plot in Figure 14.10b, a resonant dipole oscillation is excited by the pump pulse, that is, the dipole velocity and the laser field are in phase. For the chosen delay, the probe pulse arrives in phase with the dipole velocity (constructive interference) and the oscillator motion can be strongly amplified, resulting in a high-energy gain from the probe pulse due to coherent superposition of remaining coherent pump-induced plasmon motion. The lower illustration shows destructive interference, where the probe pulse stops and reverses the oscillator motion. Here the net energy gain from the probe is substantially reduced. The oscillation of the modulation parameter thus reflects the alternation of amplification and suppression of energy absorption from the probe pulse due to the residual oscillator motion. In turn, the decrease of the modulation amplitude with delay indicates the decay of the pump-pulse-induced oscillator motion.

In the resonant scenario in Figure 14.10b, the modulation signals directly image the pump-induced motion of the oscillator. This can be inferred from the close-to-perfect agreement of $M_W(\Delta t)$ and the rescaled $M_W^{\text{LSA}}(\Delta t)$ with the dipole velocity $v_d(t)$ for pump-only excitation (blue dashed curve in Figure 14.10b). Outside the pulse overlap region, signals are in phase and show the same relative amplitude evolution.

A set of time-domain examples for the near-resonance scenario is shown in Figure 14.10c (see insets), with trends and modulation effects similar to the fully resonant case. The modulation signals (Figure 14.10c) are now phase shifted to the pump-induced dipole velocity by a small phase offset of the order of φ_{LSA} . However, even for detunings as large as the width of the pulse spectrum as in our example,

the phase effect is small and may be neglected to the first order. The modulation signal still yields a reasonable image of the dipole velocity and the oscillator motion can be retrieved.

Finally, for the nonresonant scenario in Figure 14.10d there remains no notable excitation after the pump pulse. The modulation parameter $M_W(\Delta t)$ almost exclusively images the trivial interference-induced fluence variations (interferometric autocorrelation) of the two pulses at small delays, as can be inferred from comparison to the $M_W^{CCA}(\Delta t)$ data, cf. Eq. (14.9). This behavior allows identification of a nonresonant scenario.

14.3.3

Spectral Interferometry Analysis of Plasmons in Small Sodium Clusters

We now apply semiclassical Vlasov simulations to calculate the excitation of pre-expanded Na_{147} clusters by a pair of intense 3 fs few-cycle pulses with $\text{CEP} = 0$ at 800 nm. Details of the computational approach are described elsewhere [51]. To prepare resonant conditions, the ionic frame of the ground state is artificially expanded by a factor of 1.55 such that the plasmon is nearly resonant with an 800 nm laser field. To analyze the collective electron motion we begin with an inspection of selected time-domain results, see Figure 14.11a,b.

The two scenarios in Figure 14.11a and b corresponds to pump-only excitation with intensities $I_0 = 10^{12}$ and 10^{13} W/cm^2 , respectively. In both cases, strong plasmon oscillations are excited, as is reflected in the oscillations of the dipole velocity after the end of the laser pulse. The eigenfrequencies determined from damped oscillator fits are very similar ($\hbar\omega_{\text{res}} \approx 1.6 \text{ eV}$) for both intensities.

Most interestingly, for the more intense pump pulse, the plasmon oscillations exhibits a substantially longer lifetime of $\tau_{\text{res}} = 7.7 \text{ fs}$ over the result for the lower intensity scenario of 2.8 fs, which is a nonlinear effect of the excitation process. This behavior can be understood by considering the higher cluster ionization achieved with the stronger pulse, see the relative ionization (red curves) in Figure 14.11a and b. For the higher intensity, the remaining electron cloud is confined to a volume smaller than the ionic frame of the cluster (compare 3D plots in Figure 14.11a and b). When oscillating with a not-too-large amplitude, the electron cloud traverses only the inner cluster region where the ion background potential is nearly harmonic. This effectively reduces plasmon dephasing by interactions with the anharmonic surface potential. Hence, the nonlinear effect yields an intensity-dependent reduction of the plasmon lifetime.

Having outlined the main physics of the test cases, we now apply the spectral interferometry analysis. Therefore, the cluster response for pump–probe excitation is calculated for systematic delay-scans. Modulation signals are given for the total absorption $M_W(\Delta t)$ and ionization $M_Q(\Delta t)$ as a function of pulse delay, see Figure 14.11c and d. The modulation parameters show strong oscillations well beyond the pulse autocorrelation. Focusing on the region outside the pulse overlap, a nearly perfect mapping of the pump-pulse-induced dipole velocity into the modulation signals is observed, that is, $M_W(\Delta t) \approx M_Q(\Delta t) \propto v_d(t)$, where $v_d(t)$ is the corre-

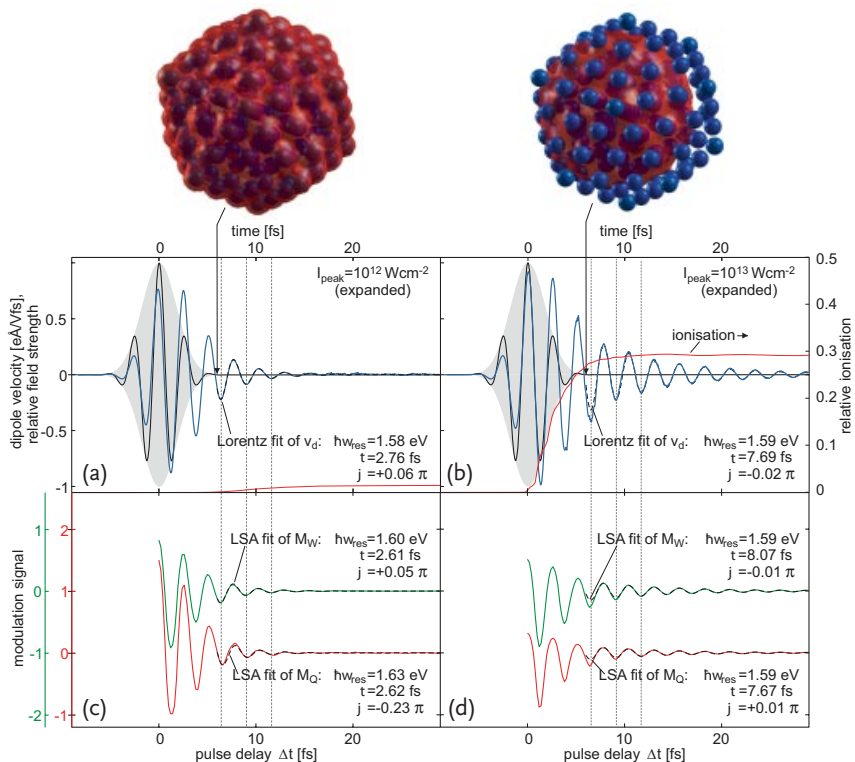


Figure 14.11 Plasmon dynamics and spectral interferometry analysis of Na_{147} under intense 3 fs FWHM few-cycle pulses at $\hbar\omega_0 = 1.54 \text{ eV}$ as calculated within the semiclassical Vlasov approach (cluster configurations and laser peak intensities as indicated). (a,b) Time-evolutions of the laser field, dipole velocity (relative to the peak field amplitude) and

cluster ionization for pump-only excitation; Lorentz fits of the dipole velocity for $t > 6 \text{ fs}$; (c,d) delay scans of the modulation signals of the absorption and cluster ionization [$M_W(\Delta t)$, $M_Q(\Delta t)$] and corresponding LSA fits. After [51]

sponding dipole velocity for pump-only excitation. In particular, different lifetimes are clearly resolved and the damped oscillator fits of the dipole signals and the LSA fits of $M_W(\Delta t)$, $M_Q(\Delta t)$ yield frequencies and lifetimes that agree within a small percentage. The extracted phase offsets are close to zero, as expected for fully resonant excitation. The modulation signals can be well described by the fit functions, except for short delays in the high-intensity scenario, where deviations due to nonlinearities can be found in the delay range $\Delta t = 7 \dots 9 \text{ fs}$, see Figure 14.11d.

These results support that nonlinear spectral interferometry with few-cycle pulses opens up an avenue toward imaging of strong-field-induced plasmons in metal clusters with subfs time resolution. In addition, as the to-be-scanned delay window can be as narrow as a few tens of fs, our approach is expected to provide valuable insights into the time-evolution of plasmonic properties in expanding clusters, which would be of great interest for nanoplasma science.

14.4

Measurements of Plasmonic Fields with Attosecond Time Resolution

It has been shown in the previous section for the case of spectral interferometry that the analysis of photoemitted electrons is a valuable tool for investigating plasmonic motion on ultrashort timescales. A different technique is inelastic scattering of high energy (200 keV) electrons, which has been used by Barwick *et al.* to image evanescent fields of carbon nanotubes excited by a femtosecond laser pulse [60]. In their case, the interaction with the plasmonic field leads to absorption and emission of photon quanta by the electron. From a classical point of view this process is equivalent to the acceleration and deceleration of the electron in the plasmonic field. The time resolution of such an approach is so far limited to several tens-hundreds of femtoseconds, as determined from the duration of the electron pulses [61]. Here, we will highlight an approach that might enable the measurements of the local field oscillations with attosecond time resolution. For a true subcycle measurement of plasmonic field oscillations the probe process has to be confined to a time significantly shorter than the field oscillation period. Such subcycle resolved information may thus give very detailed insight into the plasmon dynamics, including the build-up and decay processes as well as any nonlinear effects.

The attosecond streaking technique [62] is one of the most successful approaches to fully characterize attosecond light pulses, few-cycle laser fields, and to measure ultrafast electron dynamics in gases [63–65] and from surfaces [66, 67]. In attosecond streaking, electrons are photoemitted by an attosecond XUV pulse in the presence of a strong optical driving pulse, which accelerates or decelerates emitted electrons depending on their emission time with respect to the phase of the optical field. The technique permits to reconstruct the laser electric field from the measured photoelectron spectra by for example, time-of-flight (TOF) spectroscopy.

In the classical picture, the change in the final drift velocity of the electron (photoemitted at time t_e) is proportional to the vector potential $v_f(t_e) \propto A(t_e) = \int_{t_e}^{t_\infty} E(t) dt$ [62, 68]. From the obtained streaking spectrograms, the light field as well as the XUV pulse properties can be retrieved with high accuracy [5, 69]. This section discusses the implementation of the attosecond streaking technique for the real-time probing of plasmonic systems via attosecond nanoplasmonic streaking (APS) spectroscopy. We will furthermore describe the principal idea and the progress toward the implementation of APS spectroscopy with spatial electron imaging via the attosecond nanoscope.

14.4.1

Attosecond Nanoplasmonic Streaking

Attosecond nanoplasmonic streaking is a two-color pump–probe technique (Figure 14.12). First, plasmonic oscillations are excited by a few-cycle near-infrared (NIR) laser pulse (the pump pulse). In the second step, an attosecond XUV pulse (the probe pulse) will emit photoelectrons from the material. A photoemitted electron released at time t_e with an initial velocity v_0 will be accelerated in the plas-

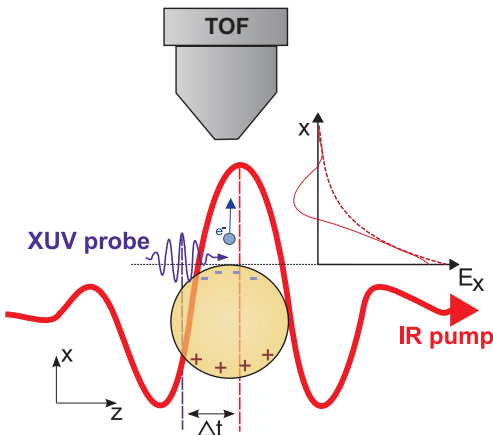


Figure 14.12 Principle of nanoplasmonic streaking. The driving NIR laser pulse excites plasmonic oscillations. The attosecond probe pulse with variable time delay emits

electrons from the nanoparticle, which will be accelerated in the local electric field. The energy-resolved detection is achieved with a time-of-flight (TOF) spectrometer.

monic near-field $E(r, t)$. The final shift in velocity can be expressed classically by the equation of motion

$$v_f(t_e) = v_0 - \int_{t_e}^{\infty} dt \frac{E(r, t)e}{m}. \quad (14.11)$$

By measuring the shift in kinetic energy as a function of the delay between pump and probe pulses, the plasmonic field evolution can be mapped onto the photoelectron spectra.

The absorption of XUV photons can result in the release of electrons from bands with a binding energy smaller than the photon energy, where the highest energy electrons will have a kinetic energy of

$$W_{\text{kin}} = \hbar\omega_{\text{XUV}} - W_f. \quad (14.12)$$

Here ω_{XUV} is the XUV angular frequency and W_f is the work function of the sample. This will lead to an energy spectrum of the photoelectrons that show distinct features of the band structure of the material. The penetration depth of the XUV radiation into solid metals is on the order of some tens of nanometers [70]. The free mean path of high-energetic electrons with a kinetic energy of about 100 eV, however, is only some Ångstroms [71]. As a consequence, only photoelectrons that are created close to sample surface are able to leave the sample without being inelastically scattered. This is advantageous for nanoplasmonic streaking, as the electron escape time from that layer is on the same order as the XUV pulse length. If additional electrons from deeper within the sample would be emitted, the additional travel time would result in the lowering of the temporal resolution. In addition to unscattered electrons the photoelectron spectrum will show contributions from lower

states. These secondary electrons typically lead to a pronounced tail in the photo-electron spectrum at low kinetic energies, which arises from inelastic collisions and Auger decay [72, 73]. For nanoplasmonic streaking the unscattered electrons are of highest interest as their emission time is confined to a short (attosecond) time window.

14.4.2

The Regimes of APS Spectroscopy

The most important difference of APS spectroscopy as compared to conventional attosecond streaking experiments performed on atoms is that the plasmon field $E(\mathbf{r}, t)$ is strongly localized at the nanoparticle's surface. Especially for more complex geometries, the electric near-field can show complicated structure and has to be evaluated using numerical computations such as the finite difference time domain (FDTD) or finite element (FEM) method. It is obvious that the streaking process governed by Eq. (14.11) will result in a quite different outcome depending on the exact plasmonic field geometry and the trajectory of the photoelectron through these fields defined by its initial conditions.

For an easier understanding, we will now derive a simplified expression for $E(\mathbf{r}, t)$. For a single plasmonic resonance, the temporal envelope can be characterized by an exponential decay of the plasmon due to electron scattering and radiation damping [24]. The spatial decay of the near-field of an isolated nanoparticle or nanofeature of a surface-assembled nanostructure can be approximated by a multipole expansion. The dipolar term $\sim 1/r^3$ is typically dominating already at short distances from the sample [74]. For sufficiently simple particle geometries, the spatial decay into free space along the normal to the surface can be well approximated by an exponential function. We will here consider electrons emitted parallel to the plasmonic field. For sufficiently high-field enhancement, where the laser field can be neglected, the resulting electric field acting on the photoelectrons includes two exponential decaying terms in addition to the oscillating time dependence:

$$E(x, t) = E_p \exp\left(\frac{-t}{T_2}\right) \exp\left(\frac{-x(t)}{\chi}\right) \cos(\omega_{\text{res}} t + \varphi). \quad (14.13)$$

Here E_p is the maximum field strength at the surface and ω_{res} is the angular frequency of the plasmon oscillation, while T_2 and χ are the temporal and spatial decay constants, respectively. This equation can be further simplified, if we assume a weak enough electric field compared to the electron energy. This implies that the change in velocity by acceleration in the electric field is small with respect to its initial value $\Delta v_0 \ll v_0$ and (for times $t \geq t_e$) the distance to the sample surface approximated by $x(t) \approx v_0(t - t_e)$. Equation (14.13) can be written as

$$E(x, t) = E_p \exp\left(\left[\frac{-t}{T_2} + \frac{-(t - t_e)v_0}{\chi}\right]\right) \cos(\omega_{\text{res}} t + \varphi). \quad (14.14)$$

Essential parameters for the regime of attosecond nanoplasmonic streaking is the relation between the electron energy W_{kin} , the plasmon frequency $\omega_{\text{res}} = 2\pi T_{\text{res}}^{-1}$

and the spatial extent of the plasmonic field χ . These quantities will define the interaction between electron and near-field and therefore determine the streaking spectra. Generally, one can distinguish between two limiting regimes. First, for an interaction much shorter in time than the period of the plasmonic oscillation, the instantaneous electric field probing regime is entered. With respect to Eq. (14.14), this is equivalent to $T_{\text{res}}^{-1} \ll v_0 \chi^{-1}$, as usually $T_2 > T_{\text{res}}$. On the other end, the ponderomotive streaking regime is reached, if the plasmonic oscillations have already decayed before the electron has left the near-field region. This regime is equivalent to $T_2^{-1} \gg v_0 \chi^{-1}$, representing a much shorter plasmon lifetime than electron travel time. For the calculations shown below for spherical metal nanoparticles, nanoplasmonic streaking often takes place in an intermediate region between these two extreme regimes. To characterize the streaking process quantitatively, the phase shift $\Delta\phi_s$ between the electric near-field oscillations and the streaked waveform can be employed. This phase shift will vary between the instantaneous and ponderomotive regime from $\Delta\phi_s = 0$ to $\pi/2$.

With the simplifications made above, the electrons' equation of motion is integrable. Introducing an effective decay time $\tau_s = \chi/v_0$, the shift in velocity as a function of emission time can be expressed by

$$\begin{aligned}\Delta v(t_e) = & -\frac{e E_p}{m} \frac{T_2 \tau_s}{(T_2 + \tau_s)^2 + T_2^2 \tau_s^2 \omega_{\text{res}}^2} \exp\left(-\frac{t_e}{T_2}\right) \\ & \times [(T_2 + \tau_s) \cos(\omega_{\text{res}} t_e + \varphi) - T_2 \tau_s \omega_{\text{res}} \sin(\omega_{\text{res}} t_e + \varphi)].\end{aligned}\quad (14.15)$$

From this expression, we can see that the absolute change in final drift velocity is decreasing for higher plasmon frequencies. The interplay between T_2 , τ_s and ω_{res} defines the streaking regime [76]. The phase shift $\Delta\phi_s$ is given by

$$\Delta\phi_s = \arctan\left(\frac{T_2 \tau_s \omega_{\text{res}}}{T_2 + \tau_s}\right). \quad (14.16)$$

Figure 14.13c shows the phase shift $\Delta\phi_s$ as a function of electron energy and spatial decay length for a fixed decay time of $T_2 = 10$ fs. As can be seen in Eq. (14.15), besides the oscillatory terms, the temporal envelope is still given by $\exp(-t_e/T_2)$. Consequently, the exponential decay constant T_2 of the plasmonic field oscillation can directly be recovered from the streaking spectra (see Figure 14.13b).

14.4.3

APS Spectroscopy of Collective Electron Dynamics in Isolated Nanoparticles

We will now turn to the implementation of APS spectroscopy on isolated, spherical metal nanoparticles. As already shown in the previous section, the streaking amplitude as well as the phase shift is heavily dependent on the exact trajectory of a photoelectron. Additionally, the contrast in the streaking spectrograms can be reduced if the sample has large areas without noticeable field enhancement [75]. Numerical

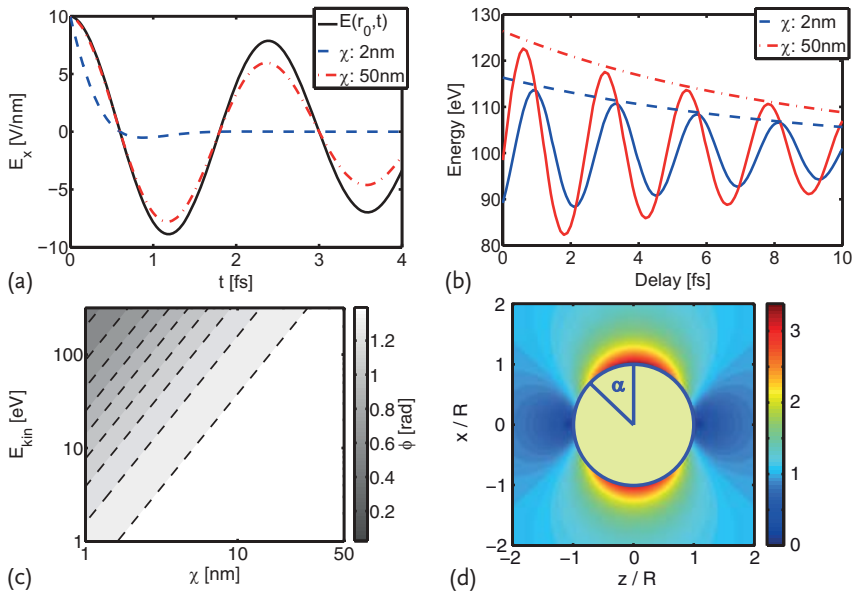


Figure 14.13 (a) Calculated acceleration fields for different spatial decay parameters. The electron energy is 100 eV, $E_p = 10^{10} \text{ V/m}$ and $T_2 = 100 \text{ fs}$. (b) Simulated streaking spectra for the same parameters as in (a).

(c) Map of phase shift as a function of spatial decay length and electron energy for $T_2 = 10 \text{ fs}$. (d) Field enhancement profile for a Au nanosphere of radius 50 nm (cut through $\gamma = 0$). After [75, 76].

studies have tested the feasibility of such an integrated measurement using either isolated nanospheres [75] or nanopatterned surface structures [9, 77]. A numerical study on isolated gold nanospheres by Süßmann *et al.* showed the dependence of the resulting streaking spectrograms on the electron emission position on the sphere [75]. Spherical particles show an inhomogeneous field enhancement profile (see Figure 14.13d). A large phase-shift and small amplitude is observed in the streaking spectrogram if the emission occurs at the sides of the sphere. This is due to the fact that those electrons initially experience weak or even opposite electric fields after liberation. The smallest streaking amplitude is observed for $\alpha = 90^\circ$. As examples, Figure 14.14a,b show streaking spectra for different emission positions α (with α being the angle with respect to the pole of the sphere as illustrated in Figure 14.13d). The sphere diameters are 10 and 100 nm, the electron kinetic energy is 100 eV and the pulse length is 5 fs (FWHM of a Gaussian envelope) at an intensity of 10^{12} W/cm^2 . To see the influence of these retardation effects on the streaking spectrograms, a large number of trajectories were computed with their relative probabilities determined by the emission position, the XUV pulse spectral bandwidth and pulse length. Figure 14.14c and d shows these simulated streaking spectrograms for the two sphere sizes. The retardation effects are more pronounced for the larger sphere size and results in a stronger blurring of the streaking spectrogram.

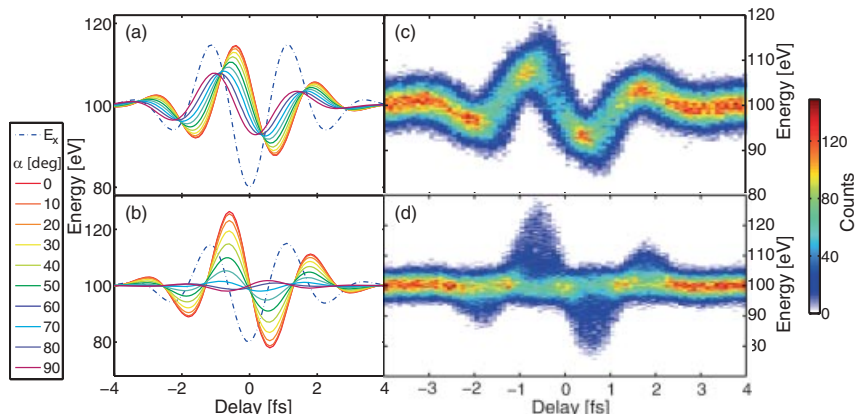


Figure 14.14 Streaking spectrograms for different emission positions from (a) 10 nm Au spheres and (b) 100 nm Au spheres. (c), (d) Simulated streaking spectrogram composed of 1.5×10^5 electrons for 10 nm and 100 nm sphere diameter. After [75].

Similar results were shown for coupled systems on a substrate [77], where the streaking process from the gap region of a coupled antenna was simulated. The results show that, due to the high homogeneity of the field enhancement within the gap region, averaging over electron emission positions yields clear streaking spectrograms predominantly in the ponderomotive regime [77]. For either approach nanoplasmonic streaking seems to be achievable, but the reconstruction of the near-fields remains a challenge. The envelope can be easily identified (see Eq. (14.15)) and should give good results for the lifetime of the oscillation. The resonance frequency can also be easily obtained given sufficient temporal resolution. The spatiotemporal properties of the subcycle evolutions of the nanoplasmonic field will, due to the retardation effects, in most cases require comparison of the measured data with numerical simulations for an exact recovery of the waveform.

14.4.4

Attosecond Nanoscope

Combining the described nanoplasmonic streaking technique with ultrahigh, nanometer spatial resolution is highly desirable for measurements on surface assembled nanostructures.

Photoemission electron microscopy (PEEM) has been successfully applied for the imaging of plasmonic fields with femtosecond time resolution [78, 79]. Experiments on plasmonic systems usually employ two-photon-photoemission (2PPE), where two photons (typically in the UV region) are utilized to photoemit an electron from a nanostructured sample (see, e.g. [80]). This results in a nonlinear dependence of the local photocurrent on the local surface field strength $j \sim |E|^4$ and as a consequence plasmonic near-fields can be efficiently imaged. Phase-resolved measurements are able to trace propagation effects of traveling SPPs and monitor

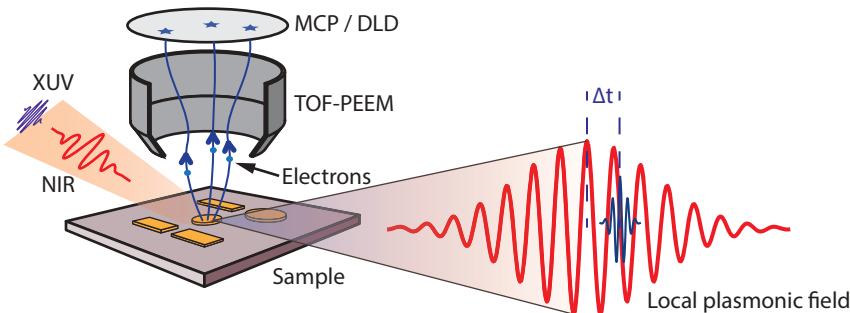


Figure 14.15 Principle of the attosecond nanoscope (ATN). A short NIR pulse induces plasmonic oscillations which are probed by a time-delayed attosecond XUV pulse. The streaked photoelectrons are imaged with a time-of-flight PEEM (TOF-PEEM), where their

time-of-flight and position are detected by a MCP/delay-line detector. Streaking spectrograms for each image point can be measured by scanning the delay between the pump and probe pulses.

the build-up and decay of SPPs [80]. Furthermore, coherent control of femtosecond laser pulses can be exploited to spatially control the excitation of plasmons [81].

Stockman *et al.* proposed to combine PEEM and attosecond nanoplasmonic streaking for the noninvasive, direct probing of nanoplasmonic fields with nanometer spatial and attosecond temporal resolution [9]. The principle of the attosecond nanoscope (ATN) is shown in Figure 14.15. A short infrared laser pulse excites the collective electron dynamics on a nanostructured surface and then a time-delayed attosecond XUV pulse emits photoelectrons from the surface. These electrons are accelerated in the plasmonic near-fields as described in the previous section. But unlike before, now the detector is a PEEM, which enables the imaging of photoelectrons from the sample surface with nanometer resolution. A recently developed time-of-flight PEEM (TOF-PEEM) allows (in addition to the measurement of their emission position) the measurement of electron kinetic energy spectra [82]. By scanning the delay between the NIR pump and XUV probe pulses, a streaking spectrogram is obtained for each image point on the TOF-PEEM, representing a small volume on the sample surface. From these spectrograms, the local field oscillations for each image point can be reconstructed.

The study by Stockman *et al.* focused on the instantaneous regime of nanoplasmonic streaking [9, 83]. Simulations showed that on a rough silver surface (see Figure 14.16a), hot spots with field enhancement factors of $Q = 30$ and a spatial extension of a few nanometers are expected [9]. These hot spots are so small that the electron escape time is much smaller than the period of the plasmonic oscillation ($\tau_s \ll T_{\text{res}}$). This results in a direct mapping of the instantaneous local electrostatic potential $\Phi(\mathbf{r}, t_e)$ onto the streaking spectrogram.

Results of the calculations by Stockman *et al.* [9, 83] for the nanostructure in Figure 14.16a are shown in Figure 14.16b. An attosecond XUV pulse at 90 eV with a pulse duration of 170 as was employed. The XUV pulse is synchronized with a few-cycle optical field 5 fs in duration for the excitation of the nanosystem and both are focused onto the sample. Due to their large kinetic energy and short emission

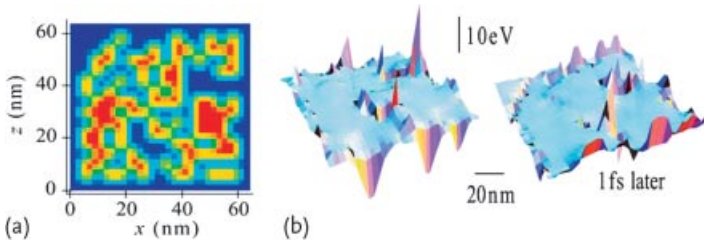


Figure 14.16 (a) Ag nanostructure employed in the calculations. (b) Snapshots of streaking spectrograms for two time delays between a few-cycle excitation pulse and attosecond XUV probe pulse. After [83].

time, the XUV-emitted valence band photoelectrons escape from the nanosized regions of local electric field enhancement within a fraction of the oscillation period of the driven plasmonic field. These photoelectrons are accelerated or decelerated by the local plasmonic field, which defines their energy. The imaging using the XUV-emitted photoelectrons by an energy-resolving PEEM probes the electrical field potential at the surface as a function of the XUV-pulse incidence time and emission position with ultrahigh resolution. The spatial resolution is defined by the aberrations of the TOF-PEEM electron optics. Lin *et al.* have achieved 25 nm spatial resolution with a recently developed TOF-PEEM in threshold photoemission mode using UV excitation [82]. The temporal resolution is determined by the duration of the attosecond pulse and the time-of-flight of the photoelectrons through the local-field region, which can be on the order of (a few) hundred attoseconds. As an example, Figure 14.16b shows two snapshots of the spatially resolved spectrograms for different near-infrared (NIR) pump–XUV probe delay times of 66.45 and 67.60 fs on the left and right, respectively [83]. Streaking amplitudes of up to about 10 eV were obtained for an NIR intensity of 10 GW/cm^2 , where the direct streaking of the electrons by the external NIR field can be neglected. These theoretical results demonstrate the potential of ATN for the direct, noninvasive spatiotemporal probing of collective electron motion. Accordingly, the implementation of the ATN has a huge potential to boost the development of lightwave electronics.

14.4.5

Experimental Implementation of the Attosecond Nanoscope

For the successful implementation of the attosecond nanoscope several aspects have to be considered. When using a PEEM in conjunction with pulsed lasers, space charge effects will limit the maximum number of electrons that can be emitted per laser shot [84]. The emitted electrons will repel each other on their way through the electron optics causing a blurring of the image and spectral shifts. With respect to space charge effects it is important to note that the PEEM optics itself is energy selective. Contrast apertures must be inserted in the back focal plane of the objective lens [73] to obtain high-spatial resolution [82]. These apertures reduce the acceptance angle for the photoelectrons with respect to their lateral momentum

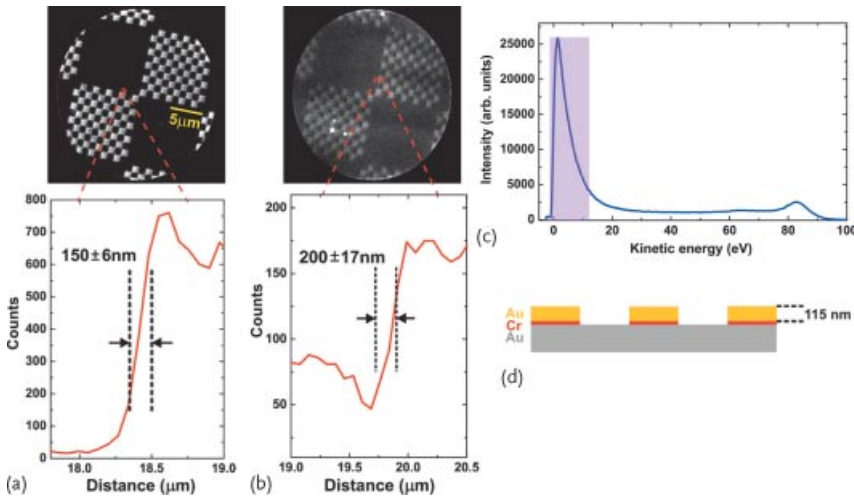


Figure 14.17 (a) UV-PEEM image of Au squares illuminated by an Hg arc lamp with an exposure time of 2 min. Intensity profile extracted from the region marked on the image gives a spatial resolution of 150 nm. (b) XUV-PEEM image illuminated by attosecond XUV pulses under the same conditions with an exposure time of 1.5 h. Intensity profile extracted

from the region marked on the image gives a spatial resolution of 200 nm. (c) Full energy spectrum of XUV excited photoelectrons integrated over the whole Au sample area (secondary electron emission peak marked by the purple region). (d) Sample geometry. After [87].

component. Consequently, the transmission decreases with higher photoelectron energy, which may according to Watts *et al.* [85] be expressed by

$$T = \frac{1}{1 + W_a/C}, \quad (14.17)$$

where C is dependent on the PEEM geometry and W_a is the photoelectron energy. The interplay of space charge effects and transmission poses constraints on the maximum applicable XUV intensity [86, 87]. Another challenge of using a TOF-PEEM is the compensation for chromatic aberration, as the electron spectrum to be imaged has a spectral width of at least several electron volts originating from the broadband XUV excitation with an attosecond source [87]. In recent experiments these difficulties could be confirmed: Chew *et al.* tested the imaging capabilities of a TOF-PEEM with attosecond XUV pulses centered at 93 eV [87] and Mikkelsen *et al.* explored photoemission electron microscopy in conjunction with attosecond pulse trains [86]. In both studies, the XUV pulses were produced at a repetition rate of 1 kHz.

Figure 14.17 shows results from the study by Chew *et al.* [87]. Here, an isolated attosecond pulse is spectrally selected from the cutoff region of the XUV spectrum produced by a few-cycle NIR pulse by applying a Zr/Si₃N₄ filter in combination with a multilayer mirror (for more details on the setup, see [87]). The TOF-PEEM is equipped with an MCP/delay-line detector (DLD) providing temporal and spatial information about the recorded photoelectrons. Figure 14.17a and b shows a

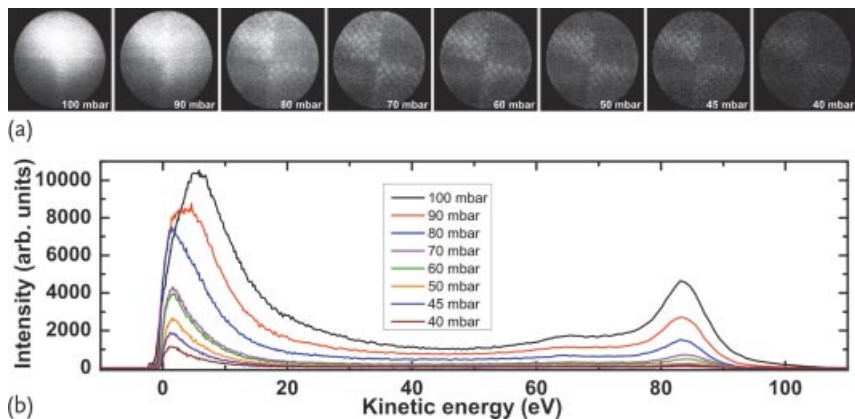


Figure 14.18 (a) TOF-PEEM images excited with XUV light at different HHG target gas pressures (100, 90, 80, 70, 60, 50, 45, 40 mbar). (b) Electron kinetic energy spectra of XUV emitted photoelectrons at different HHG target gas pressures in mbar. After [87].

comparison between images obtained from an Hg lamp and an attosecond XUV illumination of the chess-board nanostructured Au sample shown in Figure 14.17d. The spatial resolution may be determined by the image quality of a nanostructure edge (as shown in the lower part of Figure 14.17a and b) and is very similar for both light sources. It should be noted, however, that a small contrast aperture was used and the XUV image is mainly composed of low energy, secondary electrons, as is evident in the measured, spatially integrated kinetic energy spectrum shown in Figure 14.17c. Nevertheless, a peak between 80 and 90 eV indicates the successful recording of high-energy electrons from the direct XUV-emission of electrons from the Au Fermi edge, which have been considered in the theoretical proposal for the ATN [9] and were crucial for reaching the instantaneous streaking regime.

Due to space charge effects, the achievable PEEM image quality can strongly depend on the incident XUV fluence and the photoelectron energy. Figure 14.18 shows energy-integrated TOF-PEEM images (consisting largely of secondary electrons) acquired for different XUV fluences (here, the target pressure in high-harmonic generation was varied to alter the XUV fluence). For single-photon photoemission, the number of photoelectrons is proportional to the XUV fluence and for a sufficiently low XUV fluence, space charge effects can be avoided. A similar conclusion was reached by Mikkelsen *et al.* [86], who used trains of 30 eV XUV pulses to image a nanostructured Au film [86] with a conventional PEEM without time-of-flight. A TOF-PEEM allows for the distinction between the otherwise dominating secondary photoelectrons and the direct photoelectrons (see Figure 14.18b). Chew *et al.* found in their studies that predominantly the secondary electrons are affected by the build-up of space charge (as observed by spectral broadening) while the direct electrons are not affected [87]. Unfortunately, so far, the use of the contrast apertures in the TOF-PEEM, together with a repetition rate of 1 kHz, limited the count rates for the direct electrons such that the spatial and energy-resolved

detection of direct electrons would take too long to realistically perform a pump-probe imaging experiment using just these electrons. The implementation of the ATN will therefore benefit largely from the use of high-repetition rate attosecond XUV sources. Motivated by this and other applications, such sources are being developed (see next section for a nanoplasmonic approach to the realization of MHz rate XUV sources).

14.5

Nanoplasmonic Field-Enhanced XUV Generation

High-harmonic generation is a highly nonlinear process between a medium (e.g. a rare gas) and an intense femtosecond laser field [88, 89]. In order to achieve the necessary, high intensity of a few-cycle driving pulse for attosecond XUV generation ($> 10^{13} \text{ W/cm}^2$ for Xe as a target [90]), typically amplified laser systems are employed operating at kHz repetition rates [39, 91, 92]. Motivated by various applications of high-repetition rate XUV sources (high-resolution spectroscopy [93, 94] and time-resolved measurements [87]) various approaches have been followed for the generation of XUV pulses at (up to) MHz rates.

One approach is to directly generate XUV light from amplified femtosecond MHz laser systems (see e.g. [95]). Another approach is to seed a passive enhancement cavity with the output from a femtosecond MHz oscillator (see e.g. [93]). Despite impressive progress concerning the circulating power in such cavities [96], such systems are hard to stabilize and the outcoupling of the XUV light remains a challenge to their more widespread application [96].

An alternative approach, introduced by Kim *et al.* in 2008 is to employ nanoplasmonic field enhancement for the generation of XUV pulses (nano-HHG) at MHz repetition rates [97]. The production of XUV light is based on the near-field within the gap of Au bow-tie nanoantennas (see Figure 14.19), arranged in an array on a thin sapphire substrate, which is back-illuminated by a 10 fs pulse

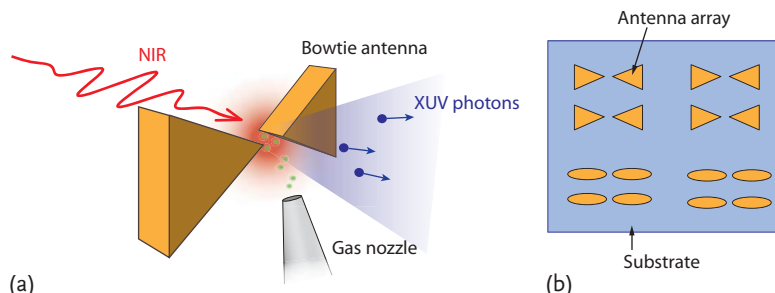


Figure 14.19 (a) Principle of nanoplasmonic high-harmonic generation. Noble gas atoms are inserted into the gap region of a nanoplasmonic antenna. These antennas are illuminated by a short resonant NIR laser pulse. Due to

the field enhancement the HHG process can take place in the antenna gap region. (b) The samples are placed on a transparent substrate (sapphire in [97]). Various geometries can be used.

from a Ti:sapphire laser oscillator. The incident laser intensity of approximately 10^{11} W/cm^2 was increased by plasmonic field enhancement and reached sufficient strength to generate harmonic radiation in Ar, which was injected between the bow-ties. Kim *et al.* claim the generation of XUV light with photon energies between 11 to 26 eV at the full repetition rate of the Ti:sapphire oscillator of 75 MHz [97]. The interpretation of these results was recently challenged by Sivis *et al.*, who only observed an enhancement of multiphoton and strong-field fluorescence in bow-tie nanoantennas [98]. Kim *et al.* claim that the local rare gas pressures that were realized at the bow-tie nanostructures are responsible for the different observations [99, 100]. Further studies will be required to resolve this dispute and clarify the importance of coherent versus incoherent XUV emission from such nanostructures. An alternative approach to the nanoplasmonic field-enhanced XUV generation at MHz repetition rates was recently presented by Park *et al.*, who employed nanostructured waveguides and demonstrated the generation of XUV light up to 70 eV at an incident laser intensity of about $5 \times 10^{11} \text{ W/cm}^2$ [100, 101].

The temporal properties of XUV pulses generated via nanoplasmonic field enhancement have not yet been studied. In the discussion below we will neglect incoherent processes and show how for metallic nanoellipsoids the temporal evolution of the near-field within the gap of a coupled nanoantenna is influenced by the antenna geometry, and how this approach can be extended to the generation of isolated attosecond pulses.

14.5.1

Tailoring of Nanoplasmonic Field Enhancement for HHG

In contrast to traditional XUV sources where the generation process is driven directly by the electric field waveform of the laser, nanoplasmonic-field-enhanced HHG has an additional degree of complexity due to the local plasmonic fields. This provides the opportunity to optimize both the laser parameters and the nanostructure configuration in order to tailor the resulting XUV pulses. In the computations described below and outlined in [102] coupled ellipsoids were used instead of bow-tie antennas. These antennas can be produced in large quantities by chemical synthesis [103] and in aligned arrays on surfaces (see, e.g. [104]), so that the fabrication of such arrays with small separation between the ellipsoids can be achieved more easily when compared to the lithography techniques used to produce other configurations such as bow-tie nanostructures [16].

Important from an experimental point of view is the damage threshold of the sample. The scattering processes of hot electrons will first equilibrate the temperature of the electron gas, which will then heat the lattice by electron–phonon scattering. If the fluence of the laser is too high, the nanostructure can potentially melt [105]. The reported damage threshold of Au nanostructures is on the order of 10^{11} W/cm^2 maximum peak intensity [106]. For the realization of HHG in noble gases such as Xe and Ar, it is necessary that the field enhancement is at least 30–40 [97].

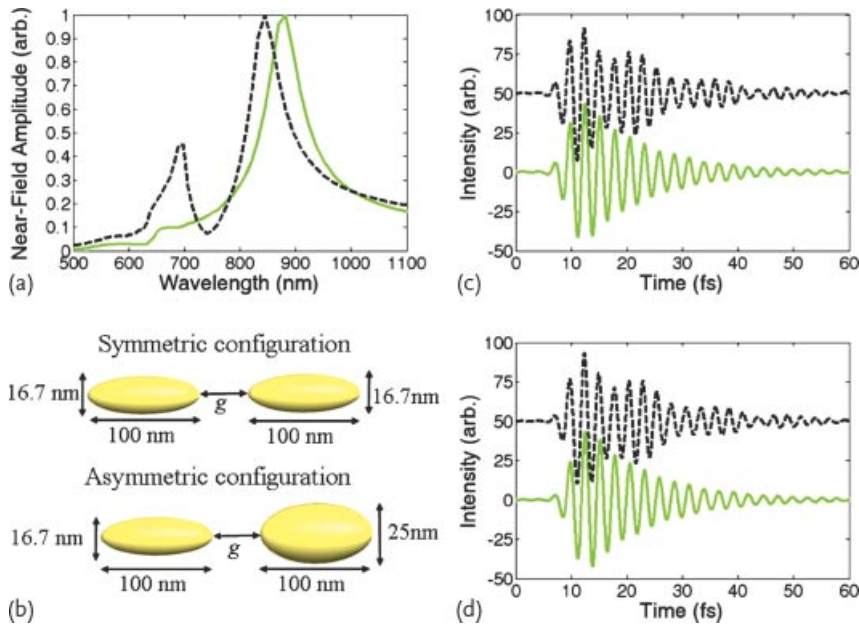


Figure 14.20 Results showing (a) the near-field amplitude (normalized to 1), (b) dimensions of the coupled nanostructures and the enhanced plasmonic fields for a

carrier-envelope phase of (c) $\varphi_{CE} = 0$ and (d) $\varphi_{CE} = \pi/2$ for the symmetric (solid green line) and asymmetric (dashed black lines) configurations, respectively. After [102].

In the described calculations, the peak intensity of an 800 nm laser with a pulse duration of 3.5 fs is $1 \times 10^{11} \text{ W/cm}^2$. Symmetric and asymmetric configurations of coupled ellipsoids were considered (with the geometries shown in Figure 14.20b). In both cases the enhanced plasmonic fields were calculated at the center of the $g = 5 \text{ nm}$ gap between the ellipsoids using the FDTD technique. For details on the computations, see [102]. In addition to the nanostructure configuration, the CEP of the few-cycle driving laser field is expected to offer an additional and important degree of control over the response of the localized plasmonic field enhancement [79, 107]. The corresponding plasmonic field responses were determined for the symmetric and asymmetric ellipsoid configurations with CEPs, $\varphi_{CE} = 0$ and $\pi/2$. The results are shown in Figure 14.20.

Isolated, attosecond XUV pulses can be obtained via HHG by a number of well-established techniques (see e.g. [45]) including the application of few-cycle laser pulses with well-defined electric fields in combination with spectral filtering of the XUV light from the cutoff region [29]. This technique has led to the generation of the shortest isolated XUV pulses to date of only 80 as duration [30]. The near-field amplitudes of the symmetric and asymmetric configurations are shown in Figure 14.20a. Both spectra exhibit one dominant peak at 882 and 845 nm for the symmetric and asymmetric configurations respectively, and are both intentionally slightly off-resonant with the central wavelength of the driving laser field to facilitate a faster plasmonic response.

The reduced spatial symmetry in the asymmetric configuration results in the appearance of a secondary peak centered at approximately 698 nm. The effect of symmetry has a straightforward physical interpretation. For the center-symmetric systems, there are two longitudinal surface plasmon modes: these are modes of the dipole of the individual ellipsoids directed along the axis of symmetry. Using parity arguments, these can be described as symmetric and anti-symmetric (or even and odd, respectively) [102]. The even mode, where the dipoles of both ellipsoids oscillate in phase, is bright and strongly red-shifted due to opposite charges facing one another across the gap, which reduces the electrostatic energy. With the odd mode, however, it is the like charges that are separated across the gap resulting in a blue-shift. Figure 14.20c and d shows the enhanced plasmonic fields for the symmetric and asymmetric structures and CEPs of $\varphi_{CE} = 0$ and $\varphi_{CE} = \pi/2$, respectively. The maximum amplitudes for the symmetric and asymmetric configurations were found to be similar with 43.5 and 43.3, corresponding to intensities of 1.89×10^{14} and 1.88×10^{14} W/cm², respectively, which is sufficient for HHG from Ar.

Although the maximum field enhancement is very similar for both nanostructure configurations, the decay of the plasmonic field differs: the symmetric structure shows a long, smooth exponential decay with a time constant of about 10.2 fs. For the asymmetric structure, the subsequent decay is strongly modulated, which can be attributed to the beating pattern between the two different modes within the structure. Although not immediately obvious, the subtle effect of the CEP causes a shift in the phase of the oscillations of the enhanced plasmonic fields shown in Figure 14.20c and d. As shown in the following section, both the CEP and the nanostructure configuration have a profound effect on the resulting high-harmonic spectra and the production of single and multiple, subfemtosecond XUV pulses.

14.5.2

Generation of Single Attosecond XUV Pulses in Nano-HHG

The enhanced plasmonic fields calculated in the previous section were used to determine the corresponding high-harmonic spectra by employing the single-active electron model [108]. The results are shown in Figure 14.21.

The high-harmonic spectra, Figure 14.21a and c, display a number of common features. All spectra show a series of peaks corresponding to the odd harmonics of the driving laser field. For example, the dominant peak centered at 1.55 eV is the photon energy of the laser with the two subsequent peaks at 4.65 and 7.75 eV corresponding to the third and fifth harmonics. There is an extended region from 17 to 58 eV where the odd harmonics are of a similar intensity, before falling off rapidly with photon energy. These correspond to the plateau and cutoff regions of the high-harmonic spectra, respectively. While for the current parameters, the plateau region remains largely independent of the CEP and nanostructure configuration, the cutoff region displays a strong dependence on both of these variables. The cutoff with the highest energy XUV photon, W_{max} , is given classically by

$$W_{max} = 3.17 U_p + IP , \quad (14.18)$$

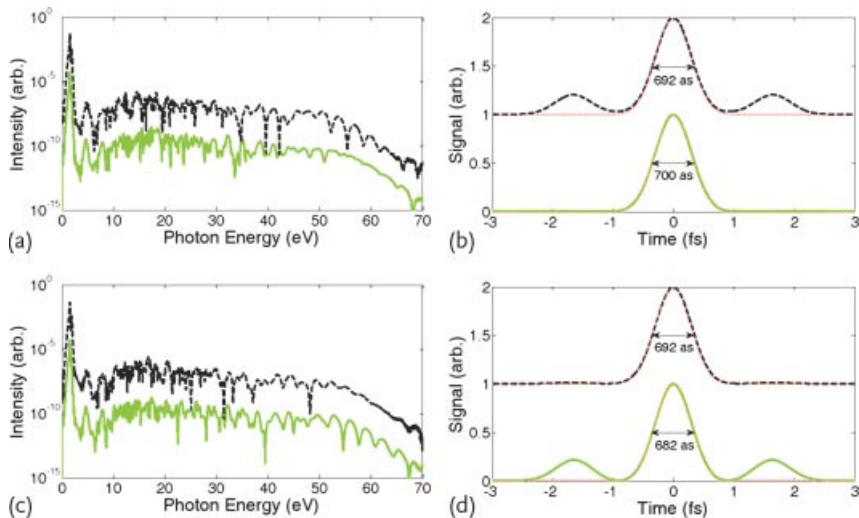


Figure 14.21 High-harmonic spectra calculated from the enhanced plasmonic fields for symmetric (solid green lines) and asymmetric (dashed black lines) nanostructure configurations for a CEP of (a) $\varphi_{CE} = 0$ and (b) $\varphi_{CE} = \pi/2$. Also shown are the corresponding temporal pulse profiles following

spectral filtering within the cutoff region of the high-harmonic spectra for a CEP of (c) $\varphi_{CE} = 0$ and (d) $\varphi_{CE} = \pi/2$. The dotted red lines indicate a Gaussian fit to the temporal profiles and the FWHMs are also indicated. After [102].

where IP is the ionization potential of the atom (or molecule) and U_p is the ponderomotive potential of the electron within the field.

As both the symmetric and asymmetric configurations had near-identical enhancements and therefore, effective intensities, their high-harmonic spectra show equal cutoff energies of 68 eV. However, as can be seen in Figure 14.21a and c, the behavior within the cutoff region varies depending upon the configuration and CEP. To examine potential temporal XUV pulse profiles resulting from the spectral selection of a portion of the cutoff region a Gaussian filter of FWHM = 5 nm centered at 60 eV was used. The filtered spectral data were subsequently Fourier transformed to obtain the temporal pulse profiles shown in Figure 14.21c and d. The CEP is found to have a significant impact on whether single or multiple XUV pulses are produced within the cutoff region. The CEP will affect the phase of the plasmonic field, which in turn determines whether multiple electron trajectories contribute to HHG or only one. The production of attosecond pulse trains or single attosecond pulses is correspondingly indicated by either a modulated or a smooth spectrum, respectively. As can be seen from Figure 14.21b and d, single XUV pulses are predicted from the symmetric and asymmetric configurations for CEPs $\varphi_{CE} = 0$ and $\pi/2$, respectively. We can conclude from these results that a suitable tailoring of the nanostructure configuration and CEP of the incident laser field can enable the generation of isolated attosecond XUV pulses in nano-HHG.

Note that these conclusions are drawn on the basis of the simple modeling of the nano-HHG process in [102], which did not include spatially dependent fields during the electron excursion. Such improved computations were recently performed by various authors [109–112]. The accurate prediction of the absolute phases of plasmonic fields remains a challenge for future theoretical work, which shall be compared to experimental studies expected to emerge in the very near future.

14.6

Conclusions and Outlook

The control of the collective electronic response of nanostructured materials with the waveform of a laser field is one of the first experimental achievements in this emerging field of attosecond nanophysics. In the first studies employing few-cycle pulses on dielectric nanoparticles [10] and metal nanotips [11] the carrier-envelope phase has been shown to be a crucial parameter for the control of the electron emission and electron acceleration from these nanostructures.

Future studies may employ synthesized light fields spanning over several octaves [113], which could provide full control over collective electron motion on the nanoscale. The lightwave control of electron motion in nanostructures is an important part of the development of lightwave (nano)electronics. Existing experimental approaches employing CEP-stabilized few-cycle laser fields will in the near future be complemented by those utilizing attosecond XUV pulses providing access to attosecond temporal resolution. This will give unprecedented, novel insight into the collective electron dynamics for dielectric, semiconductor, and metal nanostructures and will enable us to explore in detail how plasmons are formed and decay on a subcycle timescale. We have introduced three concepts for the time-resolved measurement of plasmonic fields: (1) spectral interferometry as shown for the example of metallic clusters, (2) attosecond nanoplasmonic streaking, and (3) the attosecond nanoscope. It is likely that more concepts will be developed in the near future. At present, the theoretical development is ahead of experimental implementation, but significant progress has already been made implementing, for example, the ATN [82, 86, 87].

We expect that the theoretically developed concepts, when put into practice, to give novel insight into field-dependent phase transitions in nanomaterials and the generation of coherent light via the emission, acceleration and recombination of electrons from nanostructures or in the enhanced local fields near nanostructures. As was shown in [10, 31], even for moderate field intensities dielectric nanoparticles show new, field-dependent effects on an ultrafast timescale. These results were collected at laser intensities where the dielectric response of the medium is still linear. Extension of the experiments toward higher laser intensities might lead to a regime where the instantaneous medium response is highly nonlinear in nature and exhibits novel properties. Time-dependent density-functional theory calculations for SiO₂ have predicted the optical breakdown of this dielectric at about 10¹⁵ W/cm² [114]. Dielectric nanofilms can metalize in strong adiabatic and

nonadiabatic fields without optical breakdown [27, 115]. Recent experimental and theoretical work elucidated that these field-induced changes in the optical and electronic properties of a dielectric follow the electric field [28]. Furthermore, a laser field with controlled waveform enabled ultrafast switching of a dielectric from an insulating to a conducting state within an optical cycle [6]. Such nonlinear behavior of nanomaterials in strong, ultrashort laser fields may be utilized to realize a nanometer sized, light-controlled field-effect transistor (FET) providing one of the building blocks for lightwave (nano)electronics.

The integration of attosecond science and nanotechnology will yield unprecedented insight into collective, multielectron behavior, where the information contained in a time-resolved experiment may significantly exceed what can be obtained by other (time-integrated) means.

Acknowledgement

We acknowledge the invaluable contributions of our collaborators and co-workers to the experimental and theoretical work contained in this book chapter. We thank Markus Raschke for fruitful discussions on the topic of this chapter. We are grateful for support by the European Union via the ATTOFEL network, the BMBF via the network PhoNa and the DFG via SPP 1391 and SFB 652, the Emmy–Noether and Heisenberg programs, the North-German Supercomputing Alliance, and the Cluster of Excellence: Munich Center for Advanced Photonics. SLS acknowledges support by a stipend from the Alexander von Humboldt foundation.

References

- 1 Paul, P.M., Toma, E.S., Bregerl, P., Mullet, G., Augé, F., Balcoul, P., Muller, H.G., and Agostini, P. (2001) Observation of a train of attosecond pulses from high harmonic generation. *Science*, **292**, 1689–1692.
- 2 Hentschel, M., Kienberger, R., Spielmann, C., Reider, G.A., Milosevic, N., Brabec, T., Corkum, P., Heinzmann, U., Drescher, M., and Krausz, F. (2001) Attosecond metrology. *Nature*, **414**, 509–513.
- 3 Paulus, G.G., Lindner, F., Walther, H., Baltuška, A., Goulielmakis, E., Lezius, M., and Krausz, F. (2003) Measurement of the phase of few-cycle laser pulses. *Phys. Rev. Lett.*, **91**, 253004.
- 4 Kling, M.F., Siedschlag, C., Verhoef, A.J., Khan, J.I., Schultze, M., Uphues, T., Ni, Y., Uiberacker, M., Drescher, M., Krausz, F., and Vrakking, M.J.J. (2006) Control of electron localization in molecular dissociation. *Science*, **312**, 246–248.
- 5 Krausz, F. and Ivanov, M. (2009) Attosecond physics. *Rev. Mod. Phys.*, **81**, 163–234.
- 6 Schiffrian, A., Paasch-Colberg, T., Karpowicz, N., Apalkov, V., Gerster, D., Mühlbrandt, S., Korbman, M., Reichert, J., Schultze, M., Holzner, S., Barth, J., Kienberger, R., Ernstorfer, R., Yakovlev, V., Stockman, M., and Krausz, F. (2013) Optical field-induced current in dielectrics. *Nature*, **493**, 70.
- 7 Gramotnev, D.K. and Bozhevolnyi, S.I. (2010) Plasmonics beyond the diffraction limit. *Nat. Photonics*, **4**, 83–91.
- 8 Goulielmakis, E., Yakovlev, V.S., Cavaliere, A., Uiberacker, M., Pervak, V., Apolonski, A., Kienberger, R., and Krausz, F. (2013) Attosecond control of electron dynamics in molecules. *Nature*, **493**, 70.

- Kleineberg, U., and Krausz, F. (2007) Attosecond control and measurement: lightwave electronics. *Science*, **317**, 769–775.
- 9** Stockman, M.I., Kling, M.F., Kleineberg, U., and Krausz, F. (2007) Attosecond nanoplasmonic-field microscope. *Nat. Photonics*, **1**, 539–544.
- 10** Zherebtsov, S., Fennel, T., Plenge, J., Antonsson, E., Znakovskaya, I., Wirth, A., Herrwerth, O., Süßmann, F., Peltz, C., Ahmad, I., Trushin, S.A., Pervak, V., Karsch, S., Vrakking, M.J.J., Langer, B., Graf, C., Stockman, M., Krausz, F., Rühl, E., and Kling, M.F. (2011) Controlled near-field enhanced electron acceleration from dielectric nanospheres with intense few-cycle laser fields. *Nat. Phys.*, **7**, 656–662.
- 11** Krüger, M., Schenk, M., and Hommelhoff, P. (2011) Attosecond control of electrons emitted from a nanoscale metal tip. *Nature*, **475**, 78–81.
- 12** Garcia, M.A. (2011) Surface plasmons in metallic nanoparticles: fundamentals and applications. *J. Phys. D*, **44**, 283001.
- 13** Maier, S. (2007) *Plasmonics: Fundamentals and Applications*, Springer, New York.
- 14** West, J.L. and Hales, N.J. (2003) Engineered nanomaterials for biophotonics applications: Improving sensing, imaging and therapeutics. *Ann. Rev. Biomed. Eng.*, **5**, 285–292.
- 15** Murray, W.A. (2007) Plasmonic materials. *Adv. Mat.*, **19**, 3771–3782.
- 16** Weber-Bargioni, A., Schwartzberg, A., Schmidt, M., Harteneck, B., Ogletree, D.F., Schuck, P.J., and Cabrini, S. (2010) Functional plasmonic antenna scanning probes fabricated by induced-deposition mask lithography. *Nanotechnology*, **21**, 065306.
- 17** Mock, J.J., Smith, D.R., and Schultz, S. (2003) Local refractive index dependence of plasmon resonance spectra from individual nanoparticles. *Nano Lett.*, **3**, 485–491.
- 18** Homola, J., Yee, S.S., and Gauglitz, G. (1999) Surface plasmon resonance sensors: review. *Sens. Actuators B*, **54**, 3–15.
- 19** Lu, X., Rycenga, M., Skrabalak, S.E., Wiley, B., and Xia, Y. (2009) Chemical synthesis of novel plasmonic nanoparticles. *Annu. Rev. Phys. Chem.*, **60**, 167–192.
- 20** Halas, N.J. (2010) Plasmonics: an emerging field fostered by nano letters. *Nano Lett.*, **10**, 3816–3822.
- 21** Willets, K.A. and Van Duyne, R.P. (2007) Localized surface plasmon resonance spectroscopy and sensing. *Annu. Rev. Phys. Chem.*, **58**, 267–297.
- 22** Bohren, C. (1983) *Absorption and scattering of light by small particles*, John Wiley & Sons, Inc., New York.
- 23** Lamprecht, B., Leitner, A., and Aussenegg, F.R. (1999) Few-femtosecond plasmon dephasing of a single metallic nanostructure from optical response function reconstruction by interferometric frequency resolved optical gating. *Appl. Phys. B*, **68**, 419–423.
- 24** Sönnichsen, C., Franzl, T., Wilk, T., von Plessen, G., Feldmann, J., Wilson, O., and Mulvaney, P. (2002) Drastic reduction of plasmon damping in gold nanorods. *Phys. Rev. Lett.*, **88**, 077402.
- 25** Anderson, A., Deryckx, K.S., Xu, X.G., Steinmeyer, G., and Raschke, M.B. (2010) Few-femtosecond plasmon dephasing of a single metallic nanostructure from optical response function reconstruction by interferometric frequency resolved optical gating. *Nano Lett.*, **10**, 2519–2524.
- 26** Stockman, M.I. and Hewageegana, P. (2005) Nanolocalized nonlinear electron photoemission under coherent control. *Nano Lett.*, **5**, 2325–2329.
- 27** Durach, M., Rusina, A., Kling, M.F., and Stockman, M.I. (2011) Predicted ultrafast dynamic metallization of dielectric nanofilms by strong single-cycle optical fields. *Phys. Rev. Lett.*, **107**, 086602.
- 28** Schultzze, M., Bothschafter, E., Sommer, A., Holzner, S., Schweinberger, W., Fiess, M., Hofstetter, M., Kienberger, R., Apalkov, V., Yakovlev, V., Stockman, M., and Krausz, F. (2013) Controlling dielectrics with the electric field of light. *Nature*, **493**, 75.
- 29** Baltuska, A., Udem, T., Uiberacker, M., Hentschel, M., Goulielmakis, E., Gohle, C., Holzwarth, R., Yakovlev, V., Scrinzi,

- A., Hänsch, T., and Krausz, F. (2003) Attosecond control of electronic processes by intense light fields. *Nature*, **421**, 611–615.
- 30** Goulielmakis, E., Schultze, M., Hofstetter, M., Yakovlev, V.S., Gagnon, J., Uiberacker, M., Aquila, A.L., Gullikson, E.M., Attwood, D.T., Kienberger, R., Krausz, F., and Kleineberg, U. (2008) Single-cycle nonlinear optics. *Science*, **320**, 1614–1617.
- 31** Zherebtsov, S., Süßmann, F., Peltz, C., Plenge, J., Betsch, K., Znakovskaya, I., Alnaser, A., Johnson, N., Kübel, M., Horn, A., Mondes, V., Graf, C., Trushin, S., Azzeer, A., Vrakking, M., Paulus, G., Krausz, F., Rühl, E., Fenner, T., and Kling, M. (2012) Carrier-envelope phase-tagged imaging of the controlled electron acceleration from SiO₂ nanospheres in intense few-cycle laser fields. *New J. Phys.*, **14**, 075010.
- 32** Wachter, G., Lemell, C., Burgdörfer, J., Schenk, M., Krüger, M., and Hommelhoff, P. (2012) Electron rescattering at metal nanotips induced by ultrashort pulses. *Phys. Rev. B*, **86**, 035402.
- 33** Skopalová, E., El-Taha, Y.C., Zair, A., Hohenberger, M., Springate, E., Tisch, J.W.G., Smith, R.A., and Marangos, J.P. (2010) Pulse-length dependence of the anisotropy of laser-driven cluster explosions: Transition to the impulsive regime for pulses approaching the few-cycle limit. *Phys. Rev. Lett.*, **104**, 203401.
- 34** Mathur, D. and Rajgara, F.A. (2010) Communication: Ionization and coulomb explosion of xenon clusters by intense, few-cycle laser pulses. *J. Chem. Phys.*, **133**, 061101.
- 35** Philipse, A.P. (1988) Quantitative aspects of the growth of (charged) silica spheres. *Colloid & Polymer Science*, **266**, 1174–1180.
- 36** Blaaderen, A.V., Geest, J.V., and Vrij, A. (1992) Monodisperse colloidal silica spheres from tetraalkoxysilanes: Particle formation and growth mechanism. *J. Coll. Inter. Sci.*, **154**, 481–501.
- 37** Shu, J., Wilson, K.R., Ahmed, M., Leone, S.R., Graf, C., and Rühl, E. (2006) Elastic light scattering from nanoparticles by monochromatic vacuum-ultraviolet radiation. *J. Chem. Phys.*, **124**, 034707.
- 38** Bresch, H., Wassermann, B., Langer, B., Graf, C., Flesch, R., Becker, U., Osterreicher, B., Leisner, T., and Ruhl, E. (2008) Elastic light scattering from free sub-micron particles in the soft X-ray regime. *Faraday Discuss.*, **137**, 389–402.
- 39** Schultze, M., Wirth, A., Grguras, I., Uiberacker, M., Uphues, T., Verhoeft, A.J., Gagnon, J., Hofstetter, M., Kleineberg, U., Goulielmakis, E., and Krausz, F. (2011) State-of-the-art attosecond metrology. *J. Electron. Spectrosc. Relat. Phenom.*, **184**, 68–77.
- 40** Vrakking, M.J.J. (2001) An iterative procedure for the inversion of two-dimensional ion/photoelectron imaging experiments. *Rev. Sci. Instr.*, **72** (11), 4084–4089.
- 41** Yang, B., Schafer, K.J., Walker, B., Kuhlander, K.C., Agostini, P., and DiMauro, L.F. (1993) Intensity-dependent scattering rings in high order above-threshold ionization. *Phys. Rev. Lett.*, **71**, 3770–3773.
- 42** Paulus, G.G., Nicklich, W., Xu, H., Lambropoulos, P., and Walther, H. (1994) Plateau in above threshold ionization spectra. *Phys. Rev. Lett.*, **72**, 2851–2854.
- 43** Paulus, G., Grasbon, F., Walther, H., Villoresi, P., Nisoli, M., Stagira, S., Priori, E., and De Silvestri, S. (2001) Absolute-phase phenomena in photoionization with few-cycle laser pulses. *Nature*, **414**, 182–184.
- 44** Busuladžić, M., Gazibegović-Busuladžić, A., and Milošević, D. (2006) High-order above-threshold ionization in a laser field: Influence of the ionization potential on the high-energy cutoff. *Laser Phys.*, **16**, 289–293.
- 45** Kling, M.F., Rauschenberger, J., Verhoeft, A.J., Hasović, E., Uphues, T., Milošević, D.B., Muller, H.G., and Vrakking, M.J.J. (2008) Imaging of carrier-envelope phase effects in above-threshold ionization with intense few-cycle laser fields. *New J. Phys.*, **10**, 025024.
- 46** Suzuki, M., Ando, H., Higashi, Y., Takenaka, H., Shimada, H., Matsubayashi, N., Imamura, M., Kurosawa, S., Tanu-

- ma, S., and Powell, C.J. (2000) Experimental determination of electron effective attenuation lengths in silicon dioxide thin films using synchrotron radiation i. data analysis and comparisons. *Surf. Interface Anal.*, **29**, 330–335.
- 47** Fennel, T., Döppner, T., Passig, J., Schaal, C., Tiggesbäumer, J., and Meiwes-Broer, K.H. (2007) Plasmon-enhanced electron acceleration in intense laser metal-cluster interactions. *Phys. Rev. Lett.*, **98**, 143401.
- 48** Zawadzka, J., Jaroszynski, D.A., Carey, J., and Wynne, K. (2001) Evanescent-wave acceleration of ultrashort electron pulses. *Appl. Phys. Lett.*, **79**, 2130–2132.
- 49** Irvine, S.E., Dechant, A., and Elezzabi, A.Y. (2004) Generation of 0.4-keV femtosecond electron pulses using impulsively excited surface plasmons. *Phys. Rev. Lett.*, **93**, 184801.
- 50** Racz, P., Irvine, S., Lenner, M., Mitrofanov, A., Baltuska, A., Elezzabi, A.Y., and Dombi, P. (2011) Strong-field plasmonic electron acceleration with few-cycle, phase-stabilized laser pulses. *Appl. Phys. Lett.*, **98**, 111116.
- 51** Koehn, J. and Fennel, T. (2011) Time-resolved analysis of strong-field induced plasmon oscillations in metal clusters by spectral interferometry with few-cycle laser fields. *Phys. Chem. Chem. Phys.*, **13**, 8747–8754.
- 52** Ditmire, T., Smith, R.A., Tisch, J.W.G., and Hutchinson, M.H.R. (1997) High intensity laser absorption by gases of atomic clusters. *Phys. Rev. Lett.*, **78**, 3121–3124.
- 53** Saalmann, U., Siedschlag, C., and Rost, J.M. (2006) Mechanisms of cluster ionization in strong laser pulses. *J. Phys. B*, **39**, R39.
- 54** Fennel, T., Meiwes-Broer, K.H., Tiggesbäumer, J., Reinhard, P.G., Dinh, P.M., and Suraud, E. (2010) Laser-driven nonlinear cluster dynamics. *Rev. Mod. Phys.*, **82**, 1793.
- 55** Döppner, T., Fennel, T., Radcliffe, P., Tiggesbäumer, J., and Meiwes-Broer, K.H. (2006) Ion and electron emission from silver nanoparticles in intense laser fields. *Phys. Rev. A*, **73**, 031202(R).
- 56** Zweiback, J., Ditmire, T., and Perry, M.D. (1999) Femtosecond time-resolved studies of the dynamics of noble-gas cluster explosions. *Phys. Rev. A*, **59**, R3166–R3169.
- 57** Fennel, T., Döppner, T., Passig, J., Schaal, C., Tiggesbäumer, J., and Meiwes-Broer, K.H. (2007) Plasmon-enhanced electron acceleration in intense laser metal-cluster interactions. *Phys. Rev. Lett.*, **98**, 143401.
- 58** Skopalová, E., Zaří, Y.C.E.T.A., Hohenberger, M., Springate, E., Tisch, J.W.G., Smith, R.A., and Marangos, J.P. (2010) Pulse-length dependence of the anisotropy of laser-driven cluster explosions: transition to the impulsive regime for pulses approaching the few-cycle limit. *Phys. Rev. Lett.*, **104**, 203401.
- 59** Mathur, D. and Rajgara, F.A. (2010) Ionization and coulomb explosion of xenon clusters by intense, few-cycle laser pulses. *J. Chem. Phys.*, **133**, 061101.
- 60** Barwick, B., Flannigan, D.J., and Zewail, A.H. (2009) Photon-induced near-field electron microscopy. *Nature*, **462**, 902–906.
- 61** Baum, P. and Zewail, A.H. (2007) Attosecond electron pulses for 4D diffraction and microscopy. *PNAS*, **104**, 18409–18414.
- 62** Itatani, J., Quéré, F., Yudin, G.L., Ivanov, M.Y., Krausz, F., and Corkum, P.B. (2002) Attosecond streak camera. *Phys. Rev. Lett.*, **88**, 173903.
- 63** Kienberger, R., Goulielmakis, E., Uiberacker, M., Baltuska, A., Yakovlev, V., Bammer, F., Scrinzi, A., Westerwalbesloh, T., Kleineberg, U., Heinemann, U., Drescher, M., and Krausz, F. (2004) Atomic transient recorder. *Nature*, **427**, 817–821.
- 64** Schultze, M., Fiess, M., Karpowicz, N., Gagnon, J., Korbman, M., Hofstetter, M., Neppl, S., Cavalieri, A.L., Komninos, Y., Mercouris, T., Nicolaides, C.A., Pazzourek, R., Nagele, S., Feist, J., Burgdörfer, J., Azzeer, A.M., Ernstorfer, R., Kienberger, R., Kleineberg, U., Goulielmakis, E., Krausz, F., and Yakovlev, V.S. (2010) Delay in photoemission. *Science*, **328**, 1658–1662.

- 65** Goulielmakis, E., Loh, Z.H., Wirth, A., Santra, R., Rohringer, N., Yakovlev, V.S., Zherebstov, S., Pfeifer, T., Azzeer, A.M., Kling, M.F., Leone, S.R., and Krausz, F. (2010) Real-time observation of valence electron motion. *Nature*, **466**, 739–743.
- 66** Cavalieri, A.L., Müller, N., Uphues, T., Yakovlev, V.S., Baltuska, A., Horvath, B., Schmidt, B., Blümel, L., Holzwarth, R., Hendel, S., Drescher, M., Kleineberg, U., Echenique, P.M., Kienberger, R., Krausz, F., and Heinzmann, U. (2007) Attosecond spectroscopy in condensed matter. *Nature*, **449**, 1029–1032.
- 67** Neppl, S., Ernstorfer, R., Bothschafter, E., Cavalieri, A., Menzel, D., Barth, J., Krausz, F., Kienberger, R., and Feulner, P. (2012) Attosecond time-resolved photoemission from core and valence states of magnesium. *Phys. Rev. Lett.*, **109**, 087401.
- 68** Goulielmakis, E., Uiberacker, M., Kienberger, R., Baltuska, A., Yakovlev, V., Scrinzi, A., Westerwalbesloh, T., Kleineberg, U., Heinzmann, U., Drescher, M., and Krausz, F. (2004) Direct measurement of light waves. *Science*, **305**, 1267–1269.
- 69** Gagnon, J. and Yakovlev, V.S. (2009) The robustness of attosecond streaking measurements. *Opt. Exp.*, **17**, 17678.
- 70** Henke, B.L., Gullikson, E.M., and Davis, J.C. (1993) X-ray interactions: photoabsorption, scattering, transmission, and reflection at $E = 50\text{--}30\,000\text{ eV}$, $z = 1\text{--}92$. *At. Data Nucl. Data Tab.*, **54**, 181–342.
- 71** Tanuma, S., Powell, C.J., and Penn, D.R. (1991) Calculations of electron inelastic mean free paths. II. data for 27 elements over the 50–2000 eV range. *Surf. Interface Anal.*, **17**, 911–926.
- 72** Schneider, C.M. (2006) Soft X-Ray photoelectron Emission-Microscopy (X-PEEM), in *Neutron and X-ray Spectroscopy* (eds F. Hippert *et al.*), Springer-Verlag, Berlin/Heidelberg, pp. 271–295.
- 73** Feng, J. and Scholl, A. (2007) Photoemission electron microscopy (PEEM), in *Science of Microscopy* (eds P.W. Hawkes and J.C.H. Spence), Springer, New York, pp. 657–695.
- 74** Jain, P.K. and El-Sayed, M.A. (2010) Plasmonic coupling in noble metal nanostructures. *Chem. Phys. Lett.*, **487**, 153–164.
- 75** Süßmann, F. and Kling, M.F. (2011) Attosecond nanoplasmonic streaking of localized fields near metal nanospheres. *Phys. Rev. B*, **84**, 121406(R).
- 76** Süßmann, F. and Kling, M.F. (2011) Attosecond measurement of petahertz plasmonic near-fields. *Proc. SPIE*, **8096**, 80961C.
- 77** Skopalová, E., Lei, D.Y., Witting, T., Arrell, C., Frank, F., Sonnenaud, Y., Maier, S.A., Tisch, J.W.G., and Marangos, J.P. (2011) Numerical simulation of attosecond nanoplasmonic streaking. *New J. Phys.*, **13**, 083003.
- 78** Meyer zu Heringdorf, F.J., Chelaru, L., Möllenbeck, S., Thien, D., and Horn-von Hoegen, M. (2007) Femtosecond photoemission microscopy. *Surf. Sci.*, **601**, 4700–4705.
- 79** Bauer, M., Wiemann, C., Lange, J., Bayer, D., Rohmer, M., and Aeschlimann, M. (2007) Phase propagation of localized surface plasmons probed by time-resolved photoemission electron microscopy. *Appl. Phys. A*, **88**, 473–480.
- 80** Kubo, A., Onda, K., Petek, H., Sun, Z., Jung, Y.S., and Kim, H.K. (2005) Femtosecond imaging of surface plasmon dynamics in a nanostructured silver film. *Nano Lett.*, **5**, 1123–1127.
- 81** Aeschlimann, M., Bauer, M., Bayer, D., Brixner, T., Javier, F., de Abajo, G., Pfeiffer, W., Rohmer, M., Spindler, C., and Steeb, F. (2007) Ultrafast nanoplasmonics under coherent control. *Nature*, **446**, 301–304.
- 82** Lin, J., Weber, N., Wirth, A., Chew, S.H., Escher, M., Merkel, M., Kling, M.F., Stockman, M.I., Krausz, F., and Kleineberg, U. (2009) Time of flight-photoemission electron microscope for ultrahigh spatiotemporal probing of nanoplasmonic optical fields. *J. Phys.: Condens. Matter*, **21**, 314005.
- 83** Stockman, M.I. (2008) Ultrafast nanoplasmonics under coherent control. *New J. Phys.*, **10**, 025031.
- 84** Buckanie, N.M., Göhre, J., Zhou, P., von der Linde, D., Horn-von Hoegen,

- M., and Meyer zu Heringdorf, F.J. (2009) Space charge effects in photoemission electron microscopy using amplified femtosecond laser pulses. *J. Phys.: Condens. Matter*, **21**, 314003.
- 85** Watts, R.N., Liang, S., Levine, Z.H., Luatoro, T.B., Polack, F., and Scheinfein, M.R. (1997) A transmission X-ray microscope based on secondary-electron imaging. *Rev. Sci. Instr.*, **68**, 3464.
- 86** Mikkelsen, A., Schwenke, J., Fordell, T., Luo, G., Kluender, K., Hilner, E., Anttu, N., Zakharov, A.A., Lundgren, E., Mauritsson, J., Andersen, J.N., Xu, H.Q., and L'Huillier, A. (2009) Photoemission electron microscopy using extreme ultraviolet attosecond pulse trains. *Rev. Sci. Instr.*, **80**, 123703.
- 87** Chew, S.H., Süßmann, F., Späth, C.K., Wirth, A., Schmidt, J., Zherebtsov, S., Guggenmos, A., Oelsner, A., Weber, N., Kapaldo, J., Gliserin, A., Stockman, M.I., Kling, M.F., and Kleineberg, U. (2012) Time-of-flight photoelectron emission microscopy on plasmonic structures using attosecond XUV pulses. *Appl. Phys. Lett.*, **100**, 051904.
- 88** Corkum, P.B. (1993) Plasma perspective on strong field multiphoton ionization. *Phys. Rev. Letts.*, **71**, 1994–1997.
- 89** Lewenstein, M., Balcou, P., Ivanov, M.Y., L'Huillier, A., and Corkum, P.B. (1994) Theory of high-harmonic generation by low-frequency laser fields. *Phys. Rev. A.*, **49**, 2117–2132.
- 90** Lompré, L.A., L'Huillier, A., Ferray, M., Monot, P., Mainfray, G., and Manus, C. (1990) High-order harmonic generation in xenon: intensity and propagation effects. *J. Opt. Soc. B*, **7**, 754.
- 91** Fieß, M., Schultze, M., Goulielmakis, E., Dennhardt, B., Gagnon, J., Hofstetter, M., Kienberger, R., and Krausz, F. (2010) Versatile apparatus for attosecond metrology and spectroscopy. *Rev. Sci. Instr.*, **81**, 093103.
- 92** Magerl, E., Nepli, S., Cavalieri, A.L., Botschäfer, F.M., Stanislawski, M., Uphues, T., Hofstetter, M., Kleineberg, U., Barth, J.V., Menzel, D., Krausz, F., Ernststorfer, R., Kienberger, R., and Feulner, P. (2011) A flexible apparatus for attosecond photoelectron spectroscopy of solids and surfaces. *Rev. Sci. Instr.*, **82**, 063104.
- 93** Ozawa, A., Rauschenberger, J., Gohle, C., Herrmann, M., Walker, D.R., Pervak, V., Fernandez, A., Graf, R., Apolonski, A., Holzwarth, R., Krausz, F., Hänsch, T.W., and Udem, T. (2008) High harmonic frequency combs for high resolution spectroscopy. *Phys. Rev. Lett.*, **100**, 253901.
- 94** Kandula, D.Z., Gohle, C., Pinkert, T.J., Ubachs, W., and Eikema, K.S.E. (2010) Extreme ultraviolet frequency comb metrology. *Phys. Rev. Lett.*, **105**, 063001.
- 95** Vernaleken, A., Weitenberg, J., Satarius, T., Russbueldt, P., Schneider, W., Stebbings, S.L., Kling, M.F., Hommelhoff, P., Hoffmann, H.D., Poprawe, R., Krausz, F., Hänsch, T.W., and Udem, T. (2011) Single-pass high-harmonic generation at 20.8 MHz repetition rate. *Opt. Lett.*, **36**, 3428–3430.
- 96** Pupeza, I., Eidam, T., Rauschenberger, J., Bernhardt, B., Ozawa, A., Fill, E., Apolonski, A., Udem, T., Limpert, J., Alahmed, Z.A., Azzeer, A.M., Tünnermann, A., Hänsch, T.W., and Krausz, F. (2011) Power scaling of a high-repetition-rate enhancement cavity. *Opt. Lett.*, **35**, 2052–2054.
- 97** Kim, S., Jin, J., Kim, Y.J., Park, I.Y., Kim, Y., and Kim, S.W. (2008) High-harmonic generation by resonant plasmon field enhancement. *Nature*, **453**, 757–760.
- 98** Sivis, M., Duwe, M., Abel, B., and Rogers, C. (2012) Nanostructure-based high harmonic generation revisited: predominance of field-enhanced atomic line emission. *Nature*, **485**, E1–E2.
- 99** Kim, S., Jin, J., Kim, Y., Park, I., Kim, Y., and Kim, S. (2012) Kim *et al.* reply. *Nature*, **485**, E2–E3.
- 100** Park, I., Choi, J., Lee, D., Han, S., Kim, S., and Kim, S. (2013) Generation of euv radiation by plasmonic field enhancement using nano-structured bowties and funnel-waveguides. *Ann. Phys.*, **525**, 87.
- 101** Park, I., Kim, S., Choi, J., Lee, D., Kim, Y., Kling, M., Stockman, M., and Kim, S. (2011) Plasmonic generation of ultra-short extreme-ultraviolet light pulses. *Nat. Photonics*, **5**, 677.

- 102** Stebbings, S.L., Süßmann, F., Yang, Y.Y., Scrinzi, A., Durach, M., Rusina, A., Stockman, M.I., and Kling, M.F. (2011) Generation of isolated attosecond extreme ultraviolet pulses employing nanoplasmnic field enhancement: optimization of coupled ellipsoids. *New J. Phys.*, **13**, 073010.
- 103** Jana, N.R., Gearheart, L., and Murphy, C.J. (2001) Wet chemical synthesis of high aspect ratio cylindrical gold nanorods. *J. Phys. Chem. B*, **105**, 4065–4067.
- 104** Penninkhof, J.J., Graf, C., van Dillen, T., Vrerdenberg, A.M., van Blaaderen, A., and Polman, A. (2005) Angle-dependent extinction of anisotropic silica/Au core/shell colloids made via ion irradiation. *Adv. Mat.*, **17**, 1484–1488.
- 105** Zijlstra, P., Chon, J.W.M., and Gu, M. (2009) White light scattering spectroscopy and electron microscopy of laser induced melting in single gold nanorods. *Phys. Chem. Chem. Phys.*, **11**, 5915.
- 106** Plech, A., Kotaidis, V., Lorenc, M., and Boneberg, J. (2005) Femtosecond laser near-field ablation from gold nanoparticles. *Nat. Phys.*, **2**, 44–47.
- 107** Stockman, M.I. and Hewageegana, P. (2007) Absolute phase effect in ultrafast optical responses of metal nanostructures. *Appl. Phys. A*, **89**, 247–250.
- 108** Schafer, K.J., Tang, B., DiMauro, L.F., and Kulander, K.C. (1993) Above Threshold Ionization Beyond the High Harmonic Cutoff. *Phys. Rev. Lett.*, **70**, 1599–1602.
- 109** Husakou, A., Kelkensberg, F., Herrmann, J., and Vrakking, M. (2011) Polarization gating and circularly-polarized high harmonic generation using plasmonic enhancement in metal nanostructures. *Opt. Exp.*, **19**, 25346.
- 110** Yavuz, I., Bleeda, E., Altun, Z., and Topcu, T. (2012) Generation of a broadband XUV continuum in high-order-harmonic generation by spatially inhomogeneous fields. *Phys. Rev. A*, **85**, 013416.
- 111** Ciappina, M., Biegert, J., Quidant, R., and Lewenstein, M. (2012) High-order-harmonic generation from inhomogeneous fields. *Phys. Rev. A*, **85**, 033828.
- 112** B. Fetic, K.K. and Milosevic, D. High-order-harmonic generation by a spatially inhomogeneous field. *Ann. Phys.*, published online, doi:10.1002/andp.201200184.
- 113** Wirth, A., Hassan, M.T., Grguraš, I., Gagnon, J., Moulet, A., Luu, T., Pabst, S., Santra, R., Alahmed, Z., Azzeer, A., Yakovlev, V., Pervak, V., Krausz, F., and Goulielmakis, E. (2011) Synthesized light transients. *Science*, **334**, 195–200.
- 114** Otobe, T., Yabana, K., and Iwata, J.I. (2009) First-principles calculation of the electron dynamics in crystalline SiO₂. *J. Phys. Condens. Matter*, **21**, 064224.
- 115** Durach, M., Rusina, A., Kling, M.F., and Stockman, M.I. (2010) Metallization of nanofilms in strong adiabatic electric fields. *Phys. Rev. Lett.*, **105**, 086803.

Part Four

Ultra Intense X-Ray Free Electron Laser Experiments

15

Strong-Field Interactions at EUV and X-Ray Wavelengths

Artem Rudenko

15.1

Introduction

The invention of lasers in the beginning of the 1960s revolutionized optical science and technology and created the tools for a new era of research. Nowadays, laser applications include precision processing of materials, testing of ultrahigh-speed semiconductor devices, data storage and retrieval, for example, in CD-players, data transmission through optical fibers, and sophisticated surgical treatment in neurology and ophthalmology. In the field of science and analytics, it is almost impossible to imagine modern spectroscopy without laser light sources. Lasers have a unique ability to concentrate enormous amount of energy in a very small spatial region and in a very short time interval. State-of-the-art laser systems therefore permit the study of light-matter interactions at unprecedentedly high intensities and field strengths (up to, or even exceeding, the field experienced by an electron in a hydrogen atom). Such systems provide experimental tools for time-resolved measurements on extremely short timescales.

One major motivation for modern laser physics is the dream to “film” chemical reactions in real time. The timescale of chemical reactions is defined by the motion of atoms in the reacting molecules. Despite the development of fast stroboscopic photography techniques in the 1930s, the microsecond exposure times of cameras were still orders of magnitude too slow to obtain snapshots of molecular motion that occurs on the picosecond (ps) rotational and femtosecond (fs) vibrational timescales. With the rapid evolution of laser technology in the early 1980s, laser systems with subpicosecond pulse duration became routinely available and provided experimental tools for achieving this long-sought goal. A key experimental approach is the “pump–probe technique,” where a first (pump) laser pulse initiates a process of interest, for example launches a molecular reaction, and a second (probe) pulse arrives after a well-defined time delay to sample (“photograph”) the evolution of molecular structure in time. To employ this technique, the effective duration of the pump and probe pulses (i.e., the “exposure time”) has to be shorter than the timescale of the process of interest. With femtosecond pulses, the dynam-

ics of numerous photo-induced processes, ranging from bond-breaking in simple diatomic molecules to intramolecular rearrangement in large organic and biological complexes, became accessible to experimental investigation. This opened an entirely new field of *femtochemistry* [1], and a pioneer of the field, A. Zewail, was awarded the Nobel Prize in chemistry in 1999.

Amazing progress was achieved over the last decades in time-resolved imaging of light-induced molecular reactions. But the employed optical femtosecond lasers soon showed their fundamental limitations for spatial and temporal resolution. Both limitations originate from the wavelength range of the light sources. Since the laser wavelength typically lies in the range of a few hundred nanometers to a few micrometers, subnanometer spatial resolution (the scale required to trace atomic motion in a reaction) cannot be achieved by a direct optical probe scheme. Therefore, typical femtochemistry experiments employ indirect probe methods based, for example, on absorption of light, laser-induced fluorescence, action mass spectrometry, or a variety of ionization-based schemes (such as ion time-of-flight measurements, photoelectron spectroscopy, Coulomb explosion imaging, etc.). The wavelength also determines the length of one optical cycle, which is ~ 1 fs for ultraviolet (UV) and few femtoseconds for infrared (IR) light. The optical cycle is the ultimate limit for the pump and probe pulse duration and, thus, for the time resolution achievable.

A quest for subnanometer spatial and subfemtosecond temporal resolution began at the end of the twentieth century and led to the development of short-pulsed, short wavelength radiation sources in the extreme ultraviolet (EUV) or X-ray domain.¹⁾ Angstrom spatial resolution can nowadays be routinely achieved in X-ray crystallography at synchrotrons, which represent one of the most advanced tools for the imaging of static matter [2]. Beginning with the pioneering work of von Laue, Bragg and many others in the beginning of the twentieth century, the field of X-ray diffraction developed into a routine, yet indispensable technique for structure determination in a broad range of disciplines. X-ray diffraction created the basis for most of our current knowledge about structure in fields from biology to condensed matter physics, and is an almost exclusive tool for the analysis of macromolecular structure [3]. Thus, the idea to exploit a similar approach for obtaining time-resolved snapshots of evolving molecular structure is appealing. The realization of this idea, however, requires X-ray pulses with femtosecond or subfemtosecond duration. These kinds of pulses became available very recently, provided either by high-order harmonic generation (HHG) with optical or IR lasers, or by fourth-generation accelerator-based sources, the so-called free-electron lasers (FELs).

Beyond the vision of time-resolved structure analysis, the availability of ultrafast and intense X-ray pulses might also resolve two fundamental problems of state-of-the-art X-ray imaging, namely, the issue of radiation damage [4] and the necessity to crystallize samples. If the imaging pulse is intense enough to provide a reasonable diffraction pattern (i.e., enough scattered photons) within its ultrashort duration,

1) Although there is no universally recognized convention, we will refer to the wavelengths from 124 to 10 nm as “extreme ultraviolet,” and to shorter wavelengths as “X-rays.”

then the imaging process can be faster than any light-induced structural change of the sample [5]. Within this “diffraction before destruction” scheme, the radiation dose delivered to the sample can be increased by many orders of magnitude compared to conventional X-ray crystallography, enabling diffractive imaging of nanoscale crystals [6–8] or even single particles [9, 10].

Most novel imaging schemes with short-wavelength light sources, both time-resolved and static, require high radiation intensity. The coherent diffractive imaging concept mentioned above requires the scattering of a huge number of X-ray photons in the sample within a very short time. Time-resolved pump–probe schemes, ultimately aiming for subfemtosecond temporal resolution, typically require photoabsorption from both the pump and the probe pulses, that is, would rely on (at least) a two-photon process. Thus, the prerequisite for the development of these imaging techniques is a basic understanding of nonlinear light–matter interactions in the high-frequency, short wavelength regime.

This chapter provides an overview of recent experimental studies, which investigated nonlinear interactions of intense, short, high-frequency light pulses with atoms and molecules. Section 2.1 offers a discussion of “strong field” terminology, followed by a brief description of available light sources and basic experimental techniques in Sections 15.2.2 and 15.2.3. Section 15.3 addresses experiments on nonlinear ionization of atoms and molecules in the EUV regime, starting with a very basic two-photon reaction, single ionization of He (Section 15.3.1). The discussion of double and multiple ionization follows in Sections 15.3.2 and 15.3.3. The consideration of molecular dynamics under intense EUV pulses is presented in Section 15.3.4. Section 15.4 deals with EUV–pump/EUV–probe experiments, with an emphasis on the multiphoton nature of this time-resolved technique. Finally, Section 15.5 discusses experiments on multiple ionization of atoms and molecules by intense, ultrafast X-ray pulses.

15.2 Experimental Background

15.2.1 What Is a “Strong” Field?

The importance of nonlinear light-induced reactions was recognized immediately after the practical realization of a laser. At that time, the lowest order nonlinear process, the simultaneous absorption of two photons by an atom, was already discussed by Göppert-Mayer [11]. The first experimental evidence for this phenomenon was provided by Hughes and Grabner in radio frequency absorption spectra of molecular RbF [12]. The realistic perspective for the development of intense optical laser light sources stimulated theoretical studies on nonlinear light–matter interactions. Already in 1964, the pioneering work of Keldysh [13] and a series of related papers [14–16] established basic concepts for our understanding of strong-field-induced phenomena. This work postulated conditions for the

applicability of the “multiphoton” or the quasistatic “field” description of nonlinear optical processes. According to Keldysh, the nonlinear interaction (e.g., ionization) can be gauged depending on the value of the so-called adiabaticity parameter $\gamma = \sqrt{IP/2U_p}$ [13], nowadays known as the Keldysh parameter. (Here, IP is the ionization potential, $U_p = I/4\omega^2$ the ponderomotive potential, I is the light intensity, and ω its frequency; atomic units are used throughout, if not stated otherwise.) The Keldysh parameter reflects the ratio of the tunneling time, that is, the average time the electron needs to tunnel out of an atom through the potential barrier suppressed by the external field, to the duration of the laser field cycle. For $\gamma \gg 1$, the interaction can be better understood as discretized multiphoton ionization, while for $\gamma \ll 1$ it is best described in terms of field ionization. Although this simple classification has a limited range of applicability and should not be considered as a universal criterion [17–19], the Keldysh parameter proved to be useful and instructive for the practical treatment of nonlinear light induced phenomena.

Until very recently, studies of nonlinear light-induced processes have been restricted to the optical and infrared domain, where γ is typically close to or smaller than 1. In the first decade of the twenty-first century, the rapid development of laser-based HHG [20–23] and accelerator-based FEL [24–28] light sources enabled the generation of intense, ultrashort EUV or even X-ray pulses. Those, in turn, extended experiments on multiphoton nonlinear interactions toward much shorter wavelengths [29–48]. Due to the fundamental nature of multiphoton processes, and also in view of practical applications, enormous theoretical interest focused on the description of few-photon, few-electron interactions for simple atomic and molecular systems in this energy range (see [49–69] for an incomplete selection of recent publications). Most of the high-frequency nonlinear interactions can be reasonably described within low-order perturbation theory [70, 71].

For EUV and X-ray radiation, where the photon energy $\hbar\omega$ approaches or even exceeds the ionization potential, the concept of tunneling and the physical meaning of the Keldysh parameter are less clear. In those cases, the Keldysh parameter becomes inappropriate for gauging nonlinear interactions [17–19]. A more general judgment about “strong-field” effects beyond the perturbative limit is possible by comparing the ponderomotive potential U_p to the photon energy. U_p represents the cycle-averaged energy of a free electron (or a nearly free electron, for example, in a high Rydberg state) oscillating in the light field. Nonperturbative, “strong-field” behavior can be expected when U_p approaches or exceeds $\hbar\omega$. Typical values of U_p , corresponding to one atomic unit of the field strength, are shown in Table 15.1 for different wavelengths. As can be seen from the table, much higher intensities are needed for nonperturbative effects in the EUV and X-ray domains as compared to the optical or infrared regime.

Ponderomotive effects might already become important for X-ray wavelengths when U_p reaches tens of eV, approaching binding energies of valence electrons, that is, at intensities considerably lower than those estimated from the condition $U_p = \hbar\omega$ in Table 15.1. But such intensities have not yet been realized in experiments; the highest demonstrated intensities up to now were $\sim 10^{16} \text{ W/cm}^2$ for the EUV [37, 72] and $\sim 10^{18} \text{ W/cm}^2$ [73, 74] for the X-ray domain.

Table 15.1 Ponderomotive energies U_p corresponding to one atomic unit of the field strength ($E = 1 \text{ a.u.} = 5.14 \times 10^9 \text{ V/cm}$; $I = 3.52 \times 10^{16} \text{ W/cm}^2$) and intensities I for which the condition $U_p = \hbar\omega$ is fulfilled, calculated for exemplary IR, EUV and X-ray wavelengths.

Wavelength λ (nm)	Photon energy $\hbar\omega$ (eV)	U_p for $E = 1 \text{ a.u.}$ (eV) ($I = 3.52 \times 10^{16} \text{ W/cm}^2$)	Intensity I for which $U_p = \hbar\omega$ (W/cm^2)
800	1.55	2095.1	2.6×10^{13}
20	62	1.31	1.67×10^{18}
1.0	1240	0.0033	1.33×10^{22}

Therefore, most of the processes discussed in this chapter can be considered as multiphoton phenomena and can be reasonably described within the low-order perturbation theory. Nevertheless, already under the intensities available now, one might encounter a very high degree of nonlinearity: the number of photons absorbed by a single atom can be as high as 19 for the X-ray [75] and 50 for the EUV [37] domain. For the latter case, there is an ongoing debate on whether these observations can be explained within the perturbative treatment [37, 71, 76–79].

15.2.2

Basic Parameters of Intense High-Frequency Radiation Sources

The discussion above brings us to the characteristics of currently available light sources. In the last decades of the twentieth century, atomic, molecular, and optical physics greatly benefited from the development of third-generation synchrotron radiation facilities. These facilities delivered high average radiation flux tunable in a very broad energy range from the UV to X-ray domain [80]. However, experiments performed with synchrotron light were restricted to linear processes, that is, to one-photon absorption processes. Nonlinear phenomena at photon energies of tens of eV or higher became accessible in the beginning of the twenty-first century with the development of intense, laser-like, short-pulsed radiation sources. All of the observations considered here are based on those novel light sources and were carried out using HHG-based or FEL sources. Although considerable progress was achieved toward realization of plasma-based soft X-ray lasers [81, 82], up to now their temporal and coherent properties [82] (see also Chapter 5) have prevented studies of nonlinear reactions.

Figure 15.1 depicts the peak brilliance of different light sources as a function of their photon energy. The peak brilliance denotes the number of photons per second, per unit source size, within one unit of solid angle and 0.1% bandwidth, measured at the peak of the radiation pulse). In the photon energy range considered in this chapter (EUV to X-rays), FELs are by far the most brilliant sources currently available. Covering an enormous bandwidth from 10 eV to more than 10 keV, these machines provide one billion times higher brilliance and orders of magnitude shorter pulses as compared to the third-generation synchrotrons. Therefore, most of the experimental data on intense light-matter interactions presented here stem

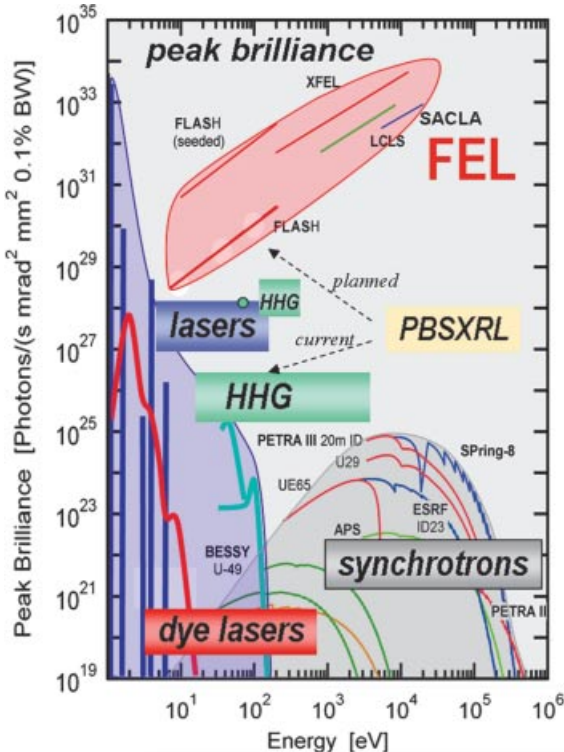


Figure 15.1 Peak brilliance of various FEL facilities as compared to state-of-the-art synchrotrons and optical lasers including high-harmonic sources (HHG). PBSXRL – plasma-based soft X-ray laser. The upper HHG point corresponds to the setup described in [83].

from FEL facilities. Nevertheless, it should be noted that the most intense HHG-based sources deliver pulses intense enough to induce nonlinear processes and several important early experiments were performed using this approach [29, 30].

Table 15.2 summarizes the essential parameters of several FEL and HHG-based sources. For the latter, several examples for experimental arrangements delivering maximal numbers of photons in a given energy range are included. The repetition rate of those examples is limited to 10 Hz; typical repetition rates of HHG experiments lie in the kHz regime, defined by the properties of the driving IR lasers, but such experiments deliver lower photon numbers. Even though these sources are inferior to FELs in terms of photon numbers, especially for X-ray frequencies, they are readily available in many laboratories worldwide, and are capable of delivering pulses shorter than 100 as. This short pulse duration potentially provides experimental tools for time-resolved imaging of electronic motion in atoms via EUV pump–EUV probe experiments. With the rapid development of laser technology, μ J energies per pulse are expected to become routinely available at EUV frequencies [22, 23, 83] and the photon energy range will be extended into the soft X-ray regime [84, 85].

Table 15.2 Parameters of FEL and HHG-based radiation sources. For the FEL facilities, not all of the characteristics listed in the table can be achieved simultaneously. For FELs, the photon energy range indicates the region in which the particular machine can operate; for the HHG

Light source	Photon energy range (eV)	Photons/pulse	Pulse duration (fs)	Repetition rate (Hz)
FLASH ^{a)}	0.028–0.31	10^{12} – 10^{13}	30–300	up to 1000 ^{e)}
SCSS ^{b)}	20–24.8	10^{12} – 10^{13}	30–100	20
LCLS ^{c)}	0.45–10.0	10^{12} – 10^{13}	3–300	120
SACLA ^{d)}	4.5–19.5	up to $\sim 5 \times 10^{11}$	10–30	20
European XFEL (design)	280–24 800	10^{12} – 10^{14}	2–100	up to 27 000 ^{e)}
HHG [83]	16.8–29.1	3×10^{12}	~ 30	10
HHG [84]	280–520	6×10^7	40	10
HHG [86]	~ 16 –23	3×10^{10}	~ 0.5	10

a) Free-Electron LASer in Hamburg

b) SPring 8 Compact SASE Source

c) LINAC Coherent Light Source

d) SPring 8 Angstrom Compact free-electron LASer. SASE stands for “self-amplified spontaneous emission”

e) These facilities deliver radiation in pulse trains generated at 10 Hz repetition rate and containing up to 100 (FLASH) or 2700 (XFEL design) pulses per train.

15.2.3

Detection Systems

Experimental studies of nonlinear interactions in the EUV and X-ray domain often require completely new designs of experimental end stations and particle detection systems. Since two or more photons have to be absorbed, these experiments need high peak intensities (typically $> 10^{12} \text{ W/cm}^2$) on target, corresponding to huge numbers of photons per pulse (up to $\sim 10^{12}$ – 10^{13} at FLASH and LCLS). However, the photon energy typically lies well above the relevant ionization potentials and single-photon ionization occurs with probabilities that exceed those for nonlinear processes by orders of magnitude. This creates a large linear background contribution to the signal. The signal to noise ratio is reduced because the (nonlinear) reactions of interest can be triggered only in the focal region, whereas single photon ionization can occur all along the trace of the beam through the reaction chamber. For yield measurements, this issue can be partly resolved by increasing the target density. For differential measurements (e.g., energy- or angle-resolved detection), space charge effects and particle detector limitations often restrict the effective target densities to $< 10^{10}$ – $10^{11} \text{ particles/cm}^3$, leading to a very low observation rate for the nonlinear events of interest.

sources it gives the limits of the photon spectrum measured in a given setup. In the latter case, the indicated pulse energies/photon numbers are given for the whole generated spectrum.

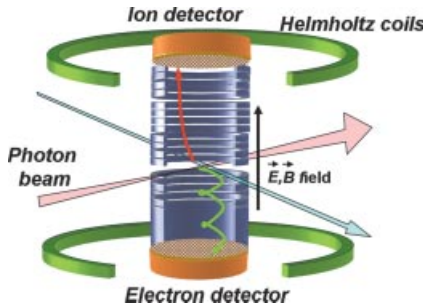


Figure 15.2 Sketch of a reaction microscope spectrometer.

A large variety of methods obtain spectroscopic information about ions and electrons emitted from an atomic or molecular target after the interaction with intense EUV/X-ray pulses. The list ranges from standard ion time-of-flight (TOF) spectrometers equipped with high count-rate particle detectors or arrays of electron TOF spectrometers placed around the interaction region [87] to very efficient magnetic bottle spectrometers [88] that can record single-shot electron spectra with high resolution and sophisticated multiparticle ion-electron imaging spectrometers [89–91]. Some of these advanced imaging systems will be briefly discussed below.

Velocity map imaging (VMI) spectrometers allow the measurement of kinetic energy and angular distributions for electrons or ions with high count rates [92, 93]. A static electric field is generated by two electrodes (repeller and extractor) and projects charged particles, onto a large-area microchannel plate (MCP) detector. A phosphor screen in combination with a fast CCD camera records the 2D image, which directly reflects the 2D momentum distribution in the detector plane (for details see [94]). The 3D momentum distribution is reconstructed from the measured 2D projection using a mathematical inversion procedure. In the case of ion detection, a sub- μ s electrical gate can be applied to the MCP to collect momentum images of mass selected ions.

The coincident detection of multiple ions and electrons becomes possible with a multiparticle imaging spectrometer (“reaction microscope,” REMI [95]). REMI measures the 3D momentum vectors of all charged fragments [89]. This technique is based on the cold-target recoil ion momentum spectroscopy (COLTRIMS) [96, 97], combined with electron imaging [98]. As sketched in Figure 15.2, the photon beam is focused onto a collimated supersonic gas jet ($\sim 10^{10}$ particles/cm $^{-2}$) in the center of an ultrahigh vacuum chamber ($\sim 10^{-11}$ mbar). Ions and electrons are guided by weak electric (1–50 V/cm) and strong magnetic (10 G) fields, applied along the spectrometer axis, onto two position-sensitive and multihit capable MCP detectors. The detectors are equipped with delay line-anodes allowing one to resolve the hit position and time for each particle. REMI achieves close to 4π solid-angle detection for low-energy particles. Initial momentum vectors can be reconstructed from the measured arrival position and time on the detector. REMI allows highly differential and even kinematically complete measurements [43, 89, 95, 99].

Recently it was demonstrated that the VMI and REMI approaches can be combined in order to perform coincidence measurements for somewhat higher fragment energies [91, 100, 101]. Here, the double-sided VMI-type focusing spectrometer is designed to focus ions and electrons in opposite directions onto two time- and position-sensitive delay line detectors, similar to REMI. As a further extension, a combination of a “reaction microscope” or VMI with two large area X-ray CCD detectors was used for experiments at LCLS in the “CFEL-ASG Multi-Purpose” (CAMP) instrument enabling the detection of charged particles in coincidence with scattered or fluorescent photons from the target [91].

15.3

Atoms and Molecules under Intense EUV Light

15.3.1

Two-Photon Single Ionization of Helium

Two-photon single ionization (TPSI) represents the most basic example of a nonlinear light-induced process. Its simplest realization would be TPSI of a hydrogen atom. However, the production of atomic hydrogen targets is experimentally difficult and TPSI of He became the fundamental test grounds for our understanding of this basic nonlinear process. TPSI also plays an important role for modern ultrafast science and is extensively used as a nonlinear signal for the characterization of femtosecond or attosecond EUV light sources ([102–105], see also Section 15.4.1).

Low-order perturbation theory predicts the yield of ions Y produced by direct n -photon absorption to be proportional to the n th power of light intensity [70, 106]:

$$Y = \sigma_n I^n, \quad (15.1)$$

where σ_n is a generalized n -photon cross section. For nonresonant TPSI of He (see Figure 15.3a) below saturation intensities, one would expect the quadratic intensity dependence of the ion yield. Figure 15.3b shows the measured intensity dependence of the He^+ yield produced by SCSS EUV FEL pulses at 20.45-eV photon energy. The experimental data indeed manifest a slope of 2 (within the experimental uncertainty) for the intensity-dependent yield curve confirming the nonlinear origin of the signal.

The quadratic intensity dependence was considered as primary evidence for two-photon absorption in many early TPSI experiments [102–104, 107]. However, because of saturation effects, possible intermediate resonant states, and the second harmonic of the EUV radiation often present in the beam (and varying with the primary beam intensity), the measured slope can significantly deviate from 2, sometimes leading to a serious controversy in the interpretation of experimental data [108, 109]. Photoelectron energy spectra [104] provide complementary information of the TPSI reaction. However, absorption of two photons at the fundamental wavelength or one photon at the second harmonic would lead to the

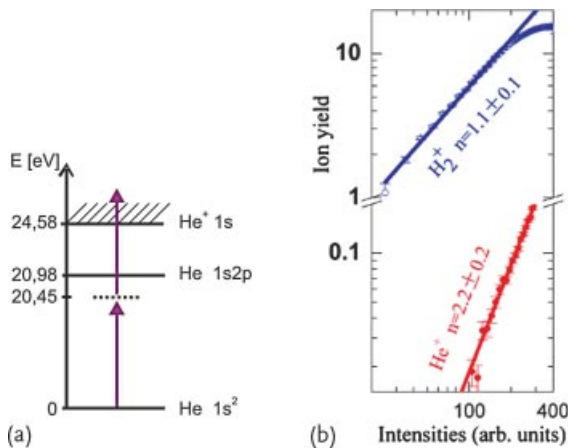


Figure 15.3 (a) Schematic illustration of the TP SI process. The dashed line depicts a virtual intermediate state. (b) Intensity-dependent yields of He^+ (two-photon transition) and H_2^+ (one-photon reaction, residual gas contribution) at 20.45-eV photon energy. The maximum intensity is $\sim 10^{14} \text{ W/cm}^2$.

same photoelectron energy. Thus, the most unambiguous characterization of TP-SI can be achieved if not only the energies but also the emission angles of the created photoelectrons are measured, that is, a fully differential measurement is performed.

The results of such differential measurements are presented in Figure 15.4. Here, momentum vectors for the photoelectrons and the He^+ ion were measured (Figure 15.4a). Since the two absorbed photons carry negligibly small momenta, the final-state ion recoil momentum is coupled with the momentum of the electron. We can therefore apply the momentum conservation law to extract the electron momenta and angular distribution from the measured ion data. The result is shown

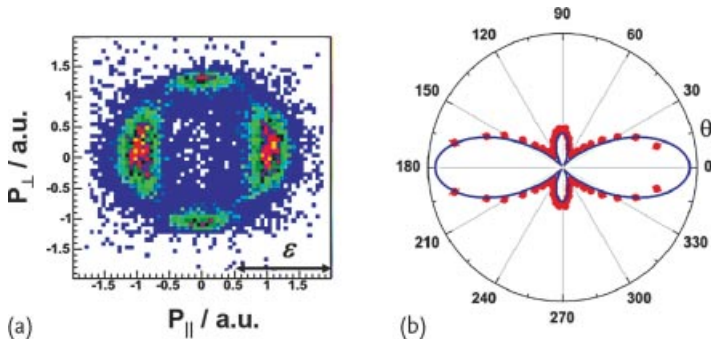


Figure 15.4 (a) Recoil-ion momentum distribution for single ionization of He by 20.45-eV SC-SS photons. ϵ indicates the FEL polarization axis. (b) Electron angular distribution for single ionization of He, extracted from the data presented in (a). Solid line: TDSE calculation [110].

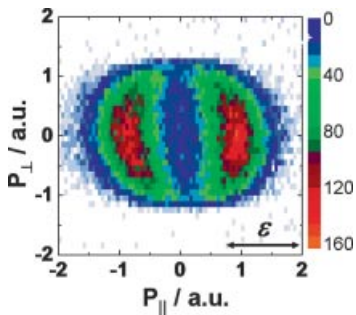


Figure 15.5 Recoil-ion momentum distribution for single ionization of He by 44-eV FLASH photons. The arrow indicates the direction of the FEL polarization.

in Figure 15.4b. In both Figure 15.4a and b, a lobe perpendicular to the polarization direction is discernible. This lobe is absent in Figure 15.5, where the He^+ ion momentum distribution produced by one-photon absorption is displayed. This nondipole contribution arises from the superposition of s- and d-wave emission and unambiguously proves that He^+ is formed in a two-photon transition. The observed angular distribution is well reproduced by a calculation with the full-dimensional time-dependent Schrödinger equation [110, 111].

For TPSI, the electron angular distribution is given by [112]:

$$\frac{d\sigma(E)}{d\Omega} = \frac{\sigma(E)}{4\pi} \left(1 + \beta_2^{2+}(E) P_2 \cos \theta_2 + \beta_4^{2+}(E) P_4 \cos \theta_2 \right), \quad (15.2)$$

where E denotes the photon energy, $\sigma(E)$ the partial photoionization cross section, θ the electron emission angle with respect to the FEL polarization direction, P_2 the second, and P_4 the fourth-order Legendre polynomials; β_2 and β_4 represent the anisotropy parameters associated with respective Legendre polynomials. A fit to the experimental data in Figure 15.4b reveals values of $\beta_2 = 1.01 \pm 0.014$ and $\beta_4 = 1.42 \pm 0.016$, in good agreement with the theoretical predictions at this photon energy. For a given photon energy, these parameters can be linked to the phase shift between s and d partial waves [110].

As can be seen from the sketch in Figure 15.3a, TPSI is a nonresonant second-order process at a photon energy of 20.45 eV (note that the spectral width of the SCSS pulses does not reach the $1s2p$ state at 20.98 eV [26, 105]). Therefore, TPSI offers a perfect tool for the temporal characterization of the EUV pulse via second-order autocorrelation, which will be discussed in Section 15.4.1. For the resonance-enhanced TPSI the dynamics is more complicated, defined by the competition of resonant and nonresonant contributions. The observables of the ionization process, in particular the photoelectron angular distribution, might thus depend not only on the wavelength of radiation but also on its pulse duration [111].

15.3.2

Few-Photon Double Ionization of Helium and Neon

15.3.2.1 Direct and Sequential Channels in EUV Double Ionization

The most basic nonlinear light-matter reaction involving more than one electron is two-photon double ionization (TPDI) of the He atom. Due to its fundamental nature, this process has received enormous theoretical attention (see, e.g., [49–51, 53–57, 62–68, 113–117]) as soon as the possibility of its experimental realization appeared on the horizon. Surprisingly, the calculated total cross sections for TPDI of He (σ_{TPDI}) vary over more than one order of magnitude [66], even for moderate intensities where second-order perturbative approaches are expected to be valid. Two measurements of σ_{TPDI} were recently performed for photon energies of 41.8[29, 30] and 42.8 eV [36], employing HHG and FLASH radiation, respectively. The measurements did not resolve the problem of conflicting theoretical predictions, mainly due to the fact that neither the experimental pulse profile nor the pulse duration was precisely known. The estimated experimental intensity therefore exhibits relatively large error bars and the experiment can not discriminate between different theoretical predictions.

Two channels are usually distinguished in TPDI. As illustrated in Figure 15.6, “sequential double ionization” (SDI) is allowed if the photon energy $\hbar\omega$ is larger than the ionization potential IP^+ of the singly charged ion. It is usually seen as proceeding sequentially in time, with two independent photo absorption events, one by the atom and one by the singly charged ion. The direct, or “nonsequential double ionization” (NSDI) is the only possible process at lower photon energies ($\text{IP}^+ > \hbar\omega$, but $2\hbar\omega > \text{IP}^+ + \text{IP}$, with IP and IP^+ being the ionization potentials of the neutral and the ion, respectively) NSDI requires the “instantaneous” absorption of two photons through an intermediate virtual state (“vs” in Figure 15.6) and is considered to be a highly correlated process, with a smooth energy partition between the two electrons at lower photon energies. When approaching the border for sequential ionization at $\text{IP}^+ = \hbar\omega$, distinct features are predicted. In principle, also sequential mechanisms can be considered at these photon energies. However, the second ionization step would require direct two-photon absorption by the singly charged ion and SDI thereby becomes a stepwise three-photon process. This

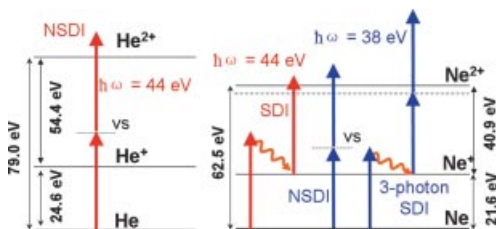


Figure 15.6 Schematic of direct and sequential ionization of He and Ne at 38 and 44 eV, and of the relevant energy levels. VS: virtual state. The dashed line indicates an intermediate excited state in Ne^+ .

is expected to become a dominant channel at intensities higher than those needed for direct TPDI [36, 38, 59, 117].

Since the ratio of direct or sequential channels is determined by the relation between photon energy and atomic structure (ionization potentials), considerable theoretical efforts extended calculations for EUV double ionization to other rare gas atoms, for example, Ne [52, 58–61, 69], and Ar [52, 60, 118]. Ne is often a more convenient experimental target than He [38, 39, 43] and provides a good model for the qualitative understanding of ionization mechanisms.

As discussed in Section 15.3.1, low-order perturbation theory predicts the yield of ions to be proportional to I^n , where I is the radiation intensity and n is the number of absorbed photons. Experiments on He mentioned above [29, 30, 36] revealed the dominance of the two-photon NSDI channel at light intensities up to 10^{14} W/cm^2 , reflected in the linear intensity dependence of the double-to-single ionization ratio. This is equivalent to a quadratic intensity dependence of the doubly charged ion yield if single ionization is not saturated. However, for example, the double ionization of Ne at 42.8 eV, where sequential TPDI is energetically allowed, displayed the same intensity dependence (see Figure 15.7a) [36]. In the same work, the $\text{Ne}^{2+}/\text{Ne}^{+}$ ratio was presented for 38.8 eV, where sequential TPDI is energetically forbidden. The ratio exhibited a quadratic intensity dependence, indicating that three photons are involved in the ionization process. However, as shown in Figure 15.7b (for 38.4 eV and at somewhat lower intensities, [38]), a nearly quadratic intensity dependence of the Ne^{2+} yield has been observed up to intensities of $\sim 6 \times 10^{12} \text{ W/cm}^2$, the lowest value used in [36], and a dependence of $I^{2.6}$ was found at higher intensities. This most likely reflects a transition from two-photon NSDI to three-photon SDI [117]. From this assessment, one can clearly conclude that, as was previously realized for the single-photon [119] and the strong-field (multiphoton) [99] regimes, measurements of the total cross sections alone do not allow definite conclusions about the physical mechanisms underlying few-electron ionization dynamics, and differential data are required for further insights.

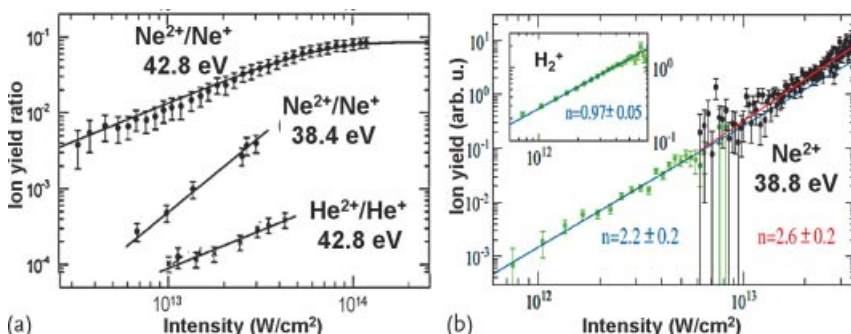


Figure 15.7 (a) Intensity-dependent ratio of the doubly to singly charged ion yield. The data are taken at photon energies of 38.4 and 42.8 eV, as indicated in the figure (from [36]). (b) Intensity-dependent yield of Ne^{2+} ions

measured at 44 eV. The inset shows the intensity dependence of the H_2^+ yield (produced by one-photon absorption), measured under the same conditions to confirm the linearity of the intensity scale [38].

15.3.2.2 Recoil Ion Momentum Distribution for Double Ionization of Helium and Neon

Figure 15.8 depicts the first differential data for TPDI of He: the recoil ion momentum distribution of doubly charged ions. In contrast to single ionization (Figures 15.4 and 15.5), where momentum conservation requires the ion momentum distribution to balance the electron momentum, for double ionization the ion momentum reflects the sum of momenta for both emitted electrons:

$$P_{\text{ion}} = - \sum P_{\text{el}} \left(\sum P_{\text{photons}} \approx 0 \right) . \quad (15.3)$$

Momentum distributions of the He^{2+} ions in Figure 15.8 were obtained at photon energies of $\hbar\omega = 44 \text{ eV}$ (a) and 52 eV (b). The data are shown in the plane defined by the jet propagation direction and the spectrometer axis, and are integrated over the third momentum component parallel to the FEL beam propagation. The FEL intensity was estimated as $I \approx 10^{14} \text{ W/cm}^2$.

The distribution in Figure 15.8a displays a distinct maximum at the origin and the majority of events lie well within the circle marking the maximum He^{2+} momentum upon two-photon absorption. This maximum momentum can only be reached if both electrons are emitted in the same direction with equal energies. This behavior clearly differs from the momentum spectra obtained for single ionization (Figure 15.5), as well as those for double-ionization induced by a single photon with similar energy above the threshold (see [119]): the latter cases manifest a pronounced dipole-like shape. Since, for double ionization, the momentum of the doubly charged ion is balanced by the sum of the momenta of both emitted electrons, the dominance of the events with very low ion momenta indicates that the two electrons are preferentially emitted back-to-back into opposite hemispheres and with similar energies. The electrons thus largely compensate the momenta of each other. This is in striking contrast with the observation for single-photon double ionization, where back-to-back emission along the polarization direction is forbidden by the dipole selection rules. Since this limitation is lifted for the case of

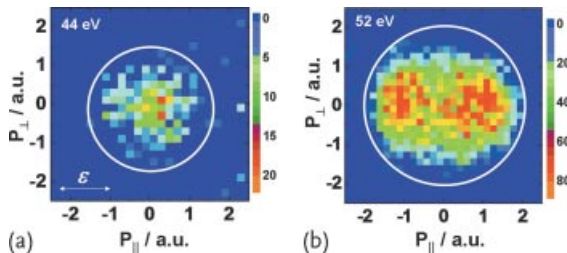


Figure 15.8 Recoil-ion momentum distributions for double ionization of He at 44 (a) and 52 eV (b). The arrow indicates the direction of the FLASH polarization. P_{\parallel} denotes the momentum component parallel and P_{\perp}

– perpendicular to the polarization direction. The data are integrated over the third momentum component (parallel to the FLASH beam propagation).

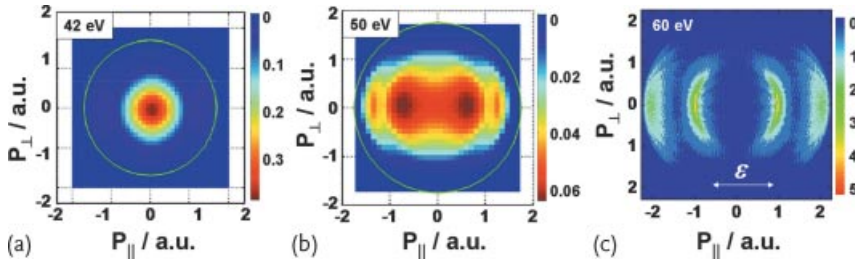


Figure 15.9 Calculated recoil-ion momentum distributions for double ionization of He at 42 eV (a), 50 eV (b) and 60 eV (c). Circles in (a,b) mark the maximum possible He^{2+} momentum after two-photon absorption. (a) and (b) from [63]. (c) from [39].

TPDI, the qualitative difference between the ion momentum distributions can be readily understood.

In contrast to the data of Figure 15.8a, the spectrum at 52 eV (Figure 15.8b) exhibits two maxima at longitudinal momenta close to $\pm 1 \text{ a.u.}$. This is in good qualitative agreement with recent theoretical predictions illustrated in Figure 15.9. According to a series of calculations [51, 56, 57, 63–65, 68, 116], a change of the energy distribution shape between both electrons should be expected. As discussed in the literature, for example, in [63] for photon energies of 40–45 eV, equal energy sharing between both emitted electrons is required to overcome the attraction of the nucleus and to promote both electrons into the continuum (see Figure 15.9a). As the photon energy approaches the SDI threshold (54.4 eV), the asymmetric energy sharing starts to dominate. It should be noted that, even though this general trend can be clearly seen in multiple calculations, different theoretical approaches predict significantly different energy sharing at specific photon energies. In the case of asymmetric energy sharing, both electrons are still preferentially emitted back to back, but one of them receives most of the excess energy. This leads to a maximum signal at nonzero momentum values in the total ion recoil momentum (Figures 15.8b and 15.9b). The momentum distribution has been considered as a signature of the SDI via a virtual intermediate state and was dubbed “virtual sequential ionization” [51, 56, 57]. Indeed, the theoretically predicted signal starts to resemble the one predicted for photon energies above the SDI threshold as shown in Figure 15.9c (taken from [39]).

The fine structure of the “virtual sequential ionization” contribution in TPDI of He at 50–52 eV differs in various calculations, sometimes exhibiting four maxima (see Figure 15.9b) [56, 57, 63, 69]. Unfortunately, the momentum resolution of the present experiments (limited, among other factors, by space charge effects) does not allow one to reliably discriminate between these theoretical predictions. Factors defining the experimental resolution, its convolution with the outcome of the calculations as well as the comparison to results from various theoretical approaches are described in detail in [120]. In the future, with increased repetition rates for microbunches at FLASH, space charge effects might be significantly reduced and fully differential cross sections might be measured as ultimate benchmark for theory.

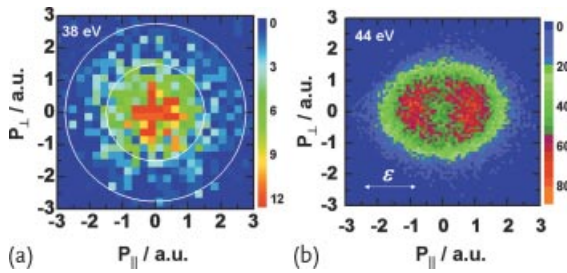


Figure 15.10 Same as Figure 15.8, but for Ne at 38.8 eV (a) and 44 eV (b). The inner and outer circles in (a) indicate the maximum possible Ne^{2+} momentum after two- and three-photon absorption, respectively.

Within the available photon energy range and limited FLASH beamtime, experiments on SDI of He could not be performed yet. However, this channel has been studied in detail for Ne. Figure 15.10 displays ion recoil momentum distributions for double ionization of Ne at 38 (a) and 44 eV (b). As apparent from the sketch presented in Figure 15.6, the sequential regime for TPDI is reached for Ne at a photon energy of 44 eV. This is reflected in the observed momentum spectrum (Figure 15.10b), which exhibits a ring-like structure, corresponding to the intuitive expectations for sequential TPDI. Here, the two electrons are emitted independently along the polarization direction, one from the neutral atom and one from the ground state of the singly charged ion. Each electron exhibits a dipole-like shape in its momentum distribution. The recoil spectrum of the doubly charged ion should then reflect the convolution of these two dipole structures. For He, we would expect a clear two-ring structure with outer and inner rings on both sides: this reflects the situation where the electrons either go into the same or opposite hemispheres (see Figure 15.9c). For Ne, this structure is smeared out due to several factors: (i) there are different electron energies in the continuum (depending on the final state of the doubly charged ion, see Figure 15.11); (ii) the emission patterns of the two electrons are different, with a β -parameter of the second between 0 and 0.5, that is, close to isotropic emission [52]; (iii) the experimental momentum resolution achievable for Ne is lower as compared to He because the internal gas-jet temperature is higher, resulting in a broadening of the spectrum ($\Delta p \sim 0.7$ a.u., see [39, 120]).

Figure 15.10a displays the momentum distribution of Ne^{2+} ions obtained at a photon energy of $\hbar\omega = 38.8$ eV (at intensities $I \geq 2 \times 10^{13} \text{ W/cm}^2$, where doubly charged ion yields showed a $I^{2.6}$ intensity dependence). Here, sequential TPDI is energetically forbidden, and the recoil-ion momentum spectrum clearly resembles the pattern observed in Figure 15.8a for He. This indicates the dominance of the direct TPDI channel and dominating back-to-back electron emission. However, in contrast to Figure 15.8a, where essentially all events show momenta well below the maximum sum-momentum of both electrons, a noticeable amount of counts in Figure 15.10a lie outside this expected maximum momentum (depicted as a circle). The contribution of a three-photon channel, though not dominating, is therefore not negligible under these experimental conditions. This qualitatively

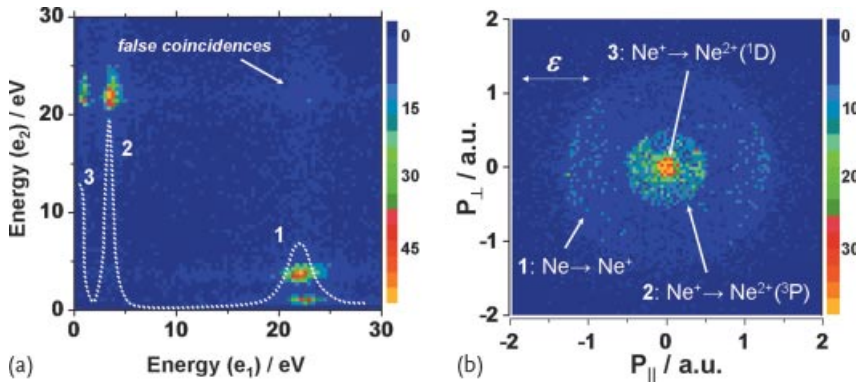


Figure 15.11 (a) Coincident two-electron energy spectrum for TPDI of Ne, interacting with 44-eV FLASH photons. The dashed line shows the electron energy spectrum. (b) 2D momentum distribution of electrons for the

same reaction. The numbers in both panels mark electrons from the first (1) and second (2, 3) sequential ionization steps. (2) and (3) correspond to the Ne^{2+} ion left in the ${}^3\text{P}$ and ${}^1\text{D}$ states, respectively (from [89]).

agrees with the observed slope of the intensity-dependent Ne^{2+} yield, which lies between 2 and 3, as observed in Figure 15.7 [38]. According to some theoretical predictions, the transition between two-photon direct and three-photon sequential mechanisms should occur at a well-defined intensity [59, 117]. The observation of nonnegligible contributions from both channels might thus seem surprising. One possible reason for this, as well as for somewhat different slopes of the Ne^{2+} yield curves observed in [36, 38], originates from the role of the intermediate resonance for the second step in the sequential channel. There are a number of excited states in the Ne^+ ion between 38 and 39 eV. Ionization caused by different parts of the rather broad (and fluctuating) FEL pulse spectrum may proceed via different pathways, enhanced by a resonance with the excited states. This effect can also explain the lowering of the slope in the intensity-dependent ion yield curve (note that measurements [36, 38] have been performed at slightly different photon energies).

15.3.2.3 Sequential TPDI of Ne at 44 eV: A Kinematically Complete Experiment

Difficulties with the separation of different contributing pathways, as discussed in the previous subsection, would be readily resolved if coincident electron spectra were available. Unfortunately, because of low cross sections and experimental difficulties outlined in Section 15.2.3, no fully differential data could be acquired under conditions where direct TPDI dominates. However, fully differential data were obtained for sequential TPDI of Ne at 44 eV [43] and shed new light on this seemingly simple process.

SDI is characterized by several features [121]: first, the electrons are considered to be emitted independent of each other. Second, whenever sequential TPDI is energetically allowed, it is expected to dominate the total cross section. Third, the predicted photoelectron spectrum is characterized by two lines, defined by the energy conservation law and the two ionization potentials. While the latter two expecta-

tions are in line with the results of recent, more elaborate calculations [65, 122], the former has been questioned and angular correlation between the emitted electrons was predicted [60], pointing to a more complex nature of the process.

In Figures 15.11–15.13, we present electron spectra for SDI of Ne at 44 eV. Note that all electrons measured here are detected in coincidence with Ne^{2+} ions and, thus, fulfill the momentum conservation condition (Eq. (15.3)). Figure 15.11a displays the coincident two-electron energy distribution, integrated over all emission angles (with the dotted line showing the integrated energy spectrum). Apart from a small contribution from false coincidences (indicated by the arrow), the correlated energy spectrum consists of four distinct peaks, symmetric with respect to the main diagonal. For each pair of peaks, the energy of the electron from the first ionization step is centered at 22.5 eV (peak 1), which is identical to the measured energy of electrons from single ionization. The second electron either emerges with a kinetic energy of about 3 eV (peak 2), or with nearly zero energy (peak 3), indicating that the Ne^{2+} ion is left in the $^3P_{0,1,2}$ state (40.9 eV above the Ne^+ ground state; the triplet fine structure is not resolved), or in the 1D_2 state (44.1 eV). The 1S_0 final state (47.1 eV) is energetically not accessible for sequential TPDI. The contributions from direct TPDI, which would be distributed along the lines parallel to the second diagonal [64, 65], cannot be observed in the spectrum.

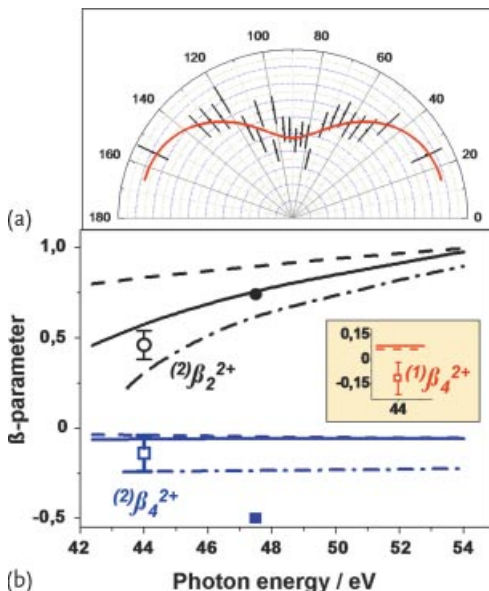


Figure 15.12 (a) Measured (full circles) and fitted (solid red line) angular distribution of the second-step electrons in TPDI of Ne at 44 eV. (b) Measured and calculated angular asymmetry parameters $(2)\beta_2^{2+}$ (black) and $(2)\beta_4^{2+}$ (blue) as a function of the photon energy. Inset (red): $(1)\beta_4^{2+}$ -parameter for the

electrons from the first step of TPDI. Open symbols: experiment [43]; full symbols: experiment [124]; solid lines: multiconfiguration Hartree–Fock calculation [43, 60]; dashed lines: multiconfiguration Dirac–Fock calculation [43, 60]; dashed-dotted lines: Hartree–Fock calculation [52].

Figure 15.11b displays the 2D momentum distribution of the electrons originating from double ionization. Three dominant structures (marked by the arrows) correspond to the different electron energies of Figure 15.11a. The outer ring (Eq. (15.1)) corresponds to the 22.5-eV electrons from the first ionization step, the middle ring (Eq. (15.2)) reflects electrons with ~ 3 eV energy from the second step leading to the 3P final state of Ne^{2+} , and the spot close to zero (Eq. (15.3)) originates from low-energy electrons emitted in the second step, corresponding to the 1D final state.

From the measured momenta for each final state, we reconstructed their emission angular distributions (see, e.g., Figure 15.12a for the second electron emitted with the Ne^{2+} left in the 3P state) and extracted angular asymmetry parameters (β) from fits (e.g., the full red line in Figure 15.12a). The asymmetry parameters contain β_2 and β_4 parameters, as expected theoretically for a two-photon process

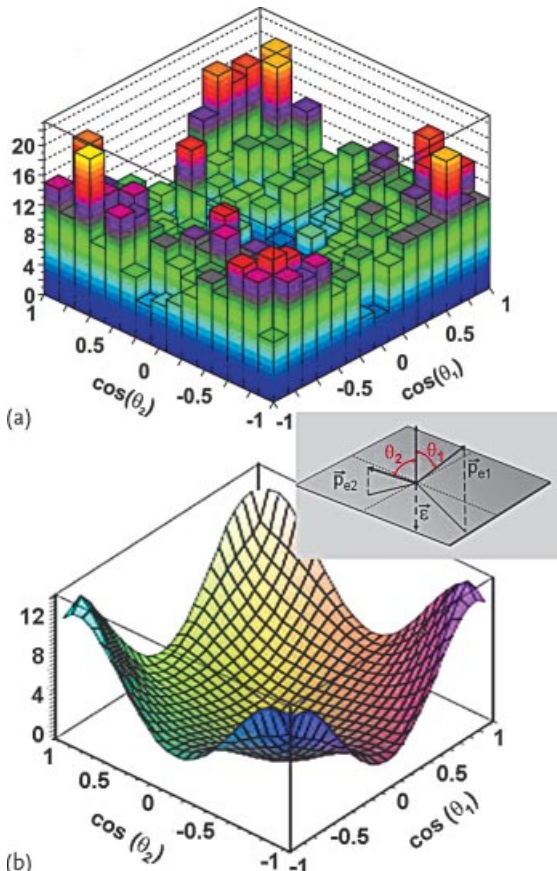


Figure 15.13 Experimental (a) and theoretical (b) probability density distribution of two emitted electrons as a function of $(\cos(\theta_1), \cos(\theta_2))$, where θ is the emission angle with respect to the FLASH polarization direction. Inset: sketch of the experimental geometry. From [43].

(see Eq. (15.2)). The resulting angular parameters β obtained for the electrons from the first step (${}^{(1)}\beta$) and the second step (${}^{(1)}\beta$) are presented in Figure 15.12b. Again, only the events where the Ne^{2+} ion is left in the 3P final state are included.

In Figure 15.12b, the experimental β -values (open symbols) are compared with theoretical predictions. The solid and dashed lines represent results of multiconfigurational Hartree–Fock (MCHF) and Dirac–Fock (MCDF) calculations [43, 60]. For a direct comparison, the theoretical results were averaged over the unresolved ${}^3P_{0,1,2}$ final states of the Ne^{2+} ion (see [60]). The predicted state-selective ${}^{(1)}\beta_2^{2+}$ parameters considerably deviate from each other. Our experimental value lies much closer to the MCHF result, which is slightly above the upper limit of the experimental error. Noticeably, recent calculations by Kheifets [52] (shown as a dashed–dotted line in Figure 15.12b) predict an even lower value, thus placing our experimental point exactly in-between these two theoretical curves. A similar behavior can be observed for the ${}^{(1)}\beta_4^{2+}$ parameter. Here, both MCHF and MCDF calculations yield almost identical values, again lying at the upper limit of the experimental error bar, whereas the results of [52] are close to the lower one.

Figure 15.12b also shows ${}^{(1)}\beta_2^{2+}$ and ${}^{(1)}\beta_4^{2+}$ parameters, obtained in the noncoincident experiment of Braune *et al.* at 47.5 eV [123] (full symbols without error bars). The ${}^{(1)}\beta_2^{2+}$ value agrees well with the prediction of the MCHF calculation, and, accounting for the expected wavelengths dependence, also with our experimental result. The value for ${}^{(1)}\beta_4^{2+}$ is much lower than all three theoretical values. Correspondingly, it also considerably differs from the value obtained in the coincidence experiment described above.

The coincidence scheme allows one not only to measure the electron angular distribution for the second ionization step, but also for the first step (which is not feasible in noncoincident photoelectron spectroscopy because these electrons have the same energy as those from single ionization). Since, according to the theoretical expectations [60], both electrons in sequential TPDI are not emitted independently, effects related to double-ionization might be imprinted in the angular distribution of the electrons emitted in the first step. The electron angular momenta of these electrons should then differ from those obtained for pure single ionization. Up to now, we have considered the electron angular distribution for the second ionization step independently. However, as discussed in [60, 124], one might expect angular correlation between the electrons, mainly as a consequence of the polarization of the intermediate ionic state. In order to explore this, we plot in Figure 15.13a the measured emission angle of the first electron θ_1 versus that of the second electron θ_2 and compare it with the theoretical (MCDF) angular correlation function (Figure 15.13b). One observes a similar pattern in theory and experiment. A slight but significant asymmetry in the theoretical data reveals an angular correlation, but cannot be clearly identified in the experimental results with statistical significance. However, some difference reflected in the nonzero value of the β_4 parameter for the first step (${}^{(1)}\beta_4^{2+}$), slightly outside the statistical error bar can be observed (${}^{(1)}\beta_4^{2+} = -0.12 \pm 0.11$, red data point in the inset of Figure 15.12b). Analysis of this effect in the framework of the MCHF and MCDF approaches [43] yields nonzero values of ${}^{(1)}\beta_4^{2+} = 0.08$ and ${}^{(1)}\beta_4^{2+} = 0.06$, respectively (red full and dashed lines

in the inset of Figure 15.12b). Thus, even though the observed deviations from zero are weak, we did find a discrepancy between theory and experiment beyond the statistical experimental error.

Modifications of the angular distribution for the first step electrons compared to single ionization raise a very general question concerning the nature of sequential TPDI: it appears counterintuitive that the second electron, which might be emitted much later within the FEL pulse duration, influences the emission characteristics of the first electron. This brings us back to the conclusion stated in the initial paper on the subject [121], which claimed that “there is no way of distinguishing sequential from simultaneous” processes, that is, that the timing of the electron emission cannot be resolved from the experimental observables.

15.3.3

Multiple Ionization of Atoms

Under intense EUV light, more than two electrons can be released from an atomic target. The general mechanism of multiple ionization attracts considerable interest because this is the dominant process when intense high-frequency radiation interacts with matter. To induce multiple ionization, few or many EUV photons need to be absorbed. (The regime of inner-shell ionization, which routinely produces more than one electron per absorbed photon becomes accessible only at high photon energies and will be considered in Section 15.5.) Therefore central questions concern the characteristic timescales for multiphoton absorption and whether the final charge state is reached by direct multiphoton absorption, or by sequential stripping of electrons via intermediate states (see e.g., [31, 37, 44, 47, 59]). As in the case of double ionization, the issue could be addressed experimentally by collecting differential data. However, coincident measurements for these few-electron nonlinear reactions are very difficult because of low signal-to-noise ratio (see Section 15.2.3). Noncoincident photoelectron spectroscopy (also quite challenging) can yield valuable information only for sequential channels. To the best of our knowledge, only one differential measurement in this regime has been reported so far (angle-resolved photoelectron spectroscopy of sequential three-photon triple ionization of Ne by 90.5-eV FLASH photons [125]). Recoil ion momentum spectra do not provide as much information as for single or double ionization because they reflect the sum momenta of several emitted electrons emitted into different directions.

Due to the experimental limitations described above, the most common observable for studying multiphoton multiple ionization of atoms at EUV wavelengths is the intensity-dependent ion yield. As discussed in Section 15.3.1 its slope in double-logarithmic representation yields information about the number of photons involved (Eq. (15.1)). For sequential multiphoton processes, which proceed via long-lived intermediate states, the yield may diverge from the expected I^n dependence. First, since lifetimes of the intermediate states are typically larger than the pulse duration, the yield does not depend on the latter, that is, it is defined by the pulse fluence (pulse energy per unit area) and not by its intensity. Second,

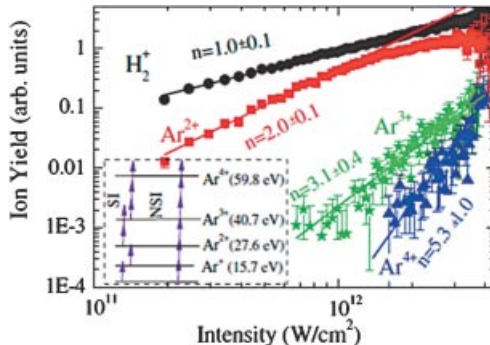


Figure 15.14 Ion yield of $\text{Ar}^{(1-4)+}$ and H_2^+ as a function of FLASH intensity at 28-eV photon energy. An energy scheme relevant for multiple ionization of Ar is plotted in the inset. The number of arrows indicate the photo-

ton numbers absorbed from the initial state to the respective final ionic state. The numbers in parenthesis are the first four ionization potentials of Ar. SI and NSI: sequential and nonsequential ionization. From [44].

since the total transition probability is given by the convolution of the probabilities for all intermediate steps, every saturated step reduces the apparent value of n in the intensity-dependent yield curve as compared to the actual number of absorbed photons. Thus, it is sometimes claimed that this slope for the sequential process is given by the number of photons involved in the last step [31].

Figure 15.14 displays intensity-dependent yields of Ar^{n+} ($n = 1-4$) ions, measured at FLASH with 28-eV photon energy. The inset of the figure sketches two possible scenarios for reaching the highest charge state observed. The quadratic intensity dependence ($n = 2$) is observed for double ionization. However, both sequential and direct TPDI are energetically allowed and we cannot distinguish between these channels on the basis of this observation (as discussed in Section 15.3.2.1). For triple and quadruple ionization, the slopes are consistent with a minimum of three or six photons required to reach the respective final states. This points toward the dominance of nonsequential channels (direct for Ar^{3+} , and likely a two-step channel for Ar^{4+}). The data do not offer unambiguous evidence, since saturation of the first ionization steps might reduce the determined slopes.

Most studies of intensity-dependent ion yields for few-photon, few-electron reactions in the sequential regime revealed slopes lower than the minimum number of photons needed to reach corresponding charge states [31, 47]. Figure 15.15 presents the example of neon ionization, where all measured ionization processes manifest the full number of photons required to reach the final ionic state. The yields of $\text{Ne}^{(1-3)+}$ ions, measured at the SCSS EUV FEL at 24.3-eV photon energy, are shown as a function of the FEL intensity. At this photon energy one photon is required to ionize a neutral neon atom, two photons to ionize the singly charged ion, and three photons to ionize Ne^{2+} to Ne^{3+} . The measured slopes for Ne^{1+} , Ne^{2+} and Ne^{3+} ion yields fit perfectly to this scheme, showing slopes of 1, 3 and 6, respectively. Thus, triple ionization of neon at this photon energy proceeds via three sequential steps, involving one-, two-, and three-photon absorption.

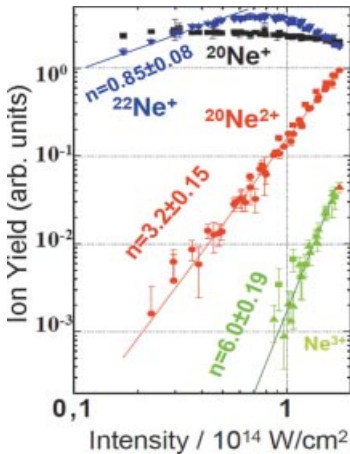


Figure 15.15 Measured yields of $\text{Ne}^{(1-3)+}$ ions as a function of SCSS intensity at 24.3 eV photon energy. For Ne^{1+} , the yield of both ^{20}Ne and ^{22}Ne isotopes, are shown.

Because of the severe detector saturation at the arrival time of ^{20}Ne ions, $^{22}\text{Ne}^+$ yield was used to determine the slope of the intensity-dependent curve for single ionization.

15.3.4

EUV-Induced Fragmentation of Simple Molecules

For molecules, the absorption of a few EUV photons resulting in the ejection of two or more electrons typically leads to further disintegration (dissociation, Coulomb explosion) of the created molecular ions. Therefore, apart from electron–electron correlation, one needs to consider specific molecular issues, such as the role of nuclear motion on the timescale of the EUV pulse and the coupling between electronic and nuclear degrees of freedom. FEL pulse durations currently range from few to few hundred fs and match the characteristic timescale of atomic motion in molecules. This leads to very rich dynamics and creates multiple possibilities to study light-induced molecular reactions. Every two- or multiphoton absorption process in the EUV or X-ray domain essentially corresponds to a pump–probe measurement, where the first absorbed photon creates a molecular wave packet (typically in a highly excited or ionic state, possibly bound or dissociating). The following photoabsorption step probes the wave packet on the timescale of the pulse [126]. Following the first experimental evidence of two-photon molecular ionization obtained at FLASH [33] and SCSS [40], a lot of effort was devoted to disentangle different multiple molecular ionization pathways, in particular those proceeding via direct and sequential few-photon absorption [44–46, 48, 127].

15.3.4.1 Direct and Sequential Two-Photon Double Ionization of D_2

A fundamental test ground for studies of the interactions of light with molecular systems is the hydrogen (or deuterium) molecule. Hydrogen is the only molecular system that is readily accessible by theory. Beautiful kinematically complete experiments on single-photon induced double ionization have been reported re-

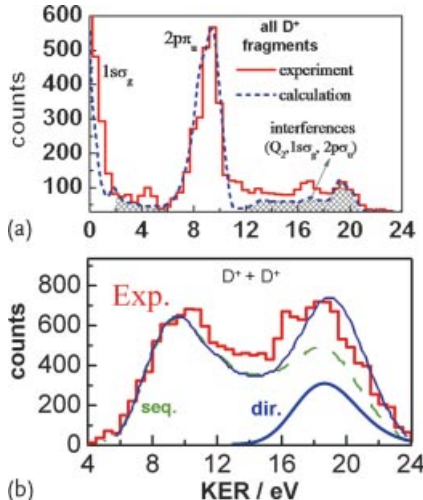


Figure 15.16 (a) KER spectrum of noncoincident D^+ fragments at 38-eV photon energy, taken under an emission angle of $90^\circ \pm 5^\circ$ with respect to the light polarization axis. (b) KER spectrum measured for coincident $D^+ + D^+$ pairs, in comparison with theory (see text).

cently, addressing some fundamental aspects of quantum mechanics [128, 129]. The possibility of multiphoton absorption adds a new dimension to these studies. The pulse durations of the novel FEL sources match characteristic timescales of vibrational motion and of fast dissociation in these simple molecular systems, giving intriguing insight into few-photon-induced fragmentation.

Here, we consider fragmentation of the D_2 molecule, irradiated by intense FLASH pulses at $\hbar\omega = 38$ eV, and trace the mechanisms of TPDI. Similar to the atomic case, there are two basic TPDI pathways: direct and sequential. For the latter channel, the photons are assumed to be absorbed via an intermediate stationary state of the ion (assumed to be the $1s\sigma_g$ ground state of D_2^+ , which is populated with a probability of about 95% in the first absorption step). Sequential ionization therefore occurs in two steps, which might be separated in time, whereas both photons are absorbed simultaneously through a virtual intermediate state in the case of direct ionization. This implies that TPDI occurs close to the equilibrium internuclear distance (R) of the neutral molecule. The signature of both TPDI pathways can be expected in the kinetic energy release (KER) spectra of the Coulomb exploding doubly charged molecule. The KER is related to the internuclear distance R due to repulsion of two positively charged protons (deuterons).

To gain insight into the various processes that might occur upon absorption of the first photon, we plot the KER spectrum for noncoincident D^+ fragments in Figure 15.16a. These fragments are formed via dissociative channels of D_2^+ . Only fragments emitted perpendicular to the polarization direction ($\theta = 90^\circ \pm 5^\circ$) are considered here. For comparison, we also show theoretical *ab initio* results obtained using the time-dependent method developed in [130].

The experimental data are in excellent agreement with the *ab initio* calculations and with previous measurements for one-photon single ionization [131]. All rel-

event fragmentation pathways, namely ground-state dissociation (maximum at $E_{KER} = 0$), dissociation via the $2p\pi_u$ channel ($E_{KER} \approx 9$ eV), as well as contributions and interferences involving the decay of doubly excited (Q2) states [129], are well resolved (Figure 15.16a).

The KER spectrum for coincident $D^+ + D^+$ fragments integrated over all emission angles is shown in Figure 15.16b. Two bands are visible in the experimental data. The high-energy band at 18 eV corresponds to a Franck–Condon transition from the molecular ground state to the repulsive Coulomb state. Such a high KER is expected for direct TPDI. However, sequential ionization with a very short time gap between both absorption steps or with absorption of the second photon when the ionic wave packet reaches its inner turning point may also contribute to this band. The low KER region, however, is only accessible via sequential ionization. This allows a quantitative separation of both pathways with the help of theory. Advanced many-particle quantum calculations by Martin *et al.* (included in [48]) deliver absolute cross sections for the sequential part along with relative KER distributions for direct TPDI. By comparison with the experiment, both pathways can be disentangled. Moreover, first conclusions on the relative importance of both processes can be obtained. Thus, coincident KER spectra encode the time between sequential ionization steps. This provides a basis for an experimental concept sometimes referred to as “molecular clock” [132].

15.3.4.2 Multiple Ionization and Fragmentation of N_2 Molecules

The ionization and fragmentation of a nitrogen molecule exposed to intense FEL pulses offers an example of a multielectron process with a large variety of possible fragmentation pathways. N_2 is a simple few-electron diatomic system, and its interaction with light has been studied extensively, both experimentally and theoretically. A wealth of data was reported for single-photon interactions (see, e.g., general examples [133–137], fragmentation by intense laser fields [138, 139], two-color time-resolved studies [140], and high-resolution electron impact coincidence measurements [141]). Recently, experiments on multiple ionization of N_2 by few EUV photons were performed at FLASH and SCSS. Total ionization cross sections [33, 34], time-of-flight spectra [40], as well as energy and angular distributions [44–46] of the ionic fragments have been reported for different fragmentation pathways.

Figure 15.17 shows a sketch of the potential energy curves of N_2 that can be reached by few-photon absorption from the N_2 ground state. Figure 15.18 displays a photo-ion–photo-ion-coincidence (PIPICO) spectrum measured at FLASH at a photon energy of 44 eV. Here, the TOF spectrum of the first detected ionic fragment is plotted as a function of the TOF of the second. True coincident events, resulting from three different Coulomb explosion channels ($N_2^{2+} \rightarrow N^+ + N^+$, $N_2^{3+} \rightarrow N^2+ + N^+$ and $N_2^{4+} \rightarrow N^2+ + N^{2+}$), can be identified as hyperbolic lines and obey momentum conservation. False coincidences (fragments originating from two different molecules) appear as diffuse background. Based on the measured ion kinetic energies, we can separate different channels of N_2 fragmentation.

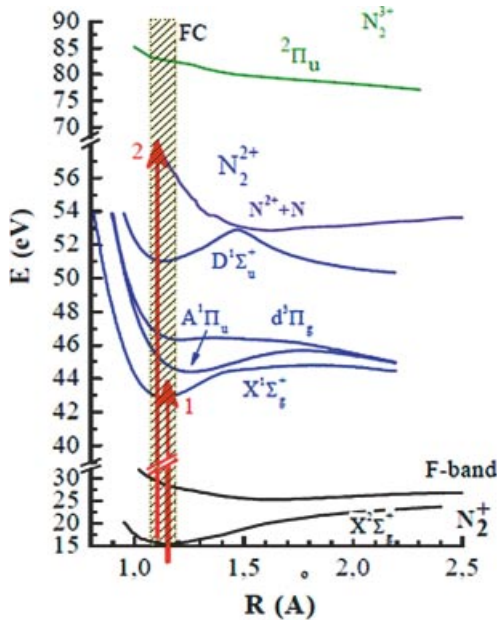


Figure 15.17 Sketch of the relevant potential energy curves of the N_2 molecule as a function of the internuclear distance R . Arrows 1 and 2 denote the states accessible by one 44-eV photon from the ground state of the neutral and the singly charged molecule, respectively.

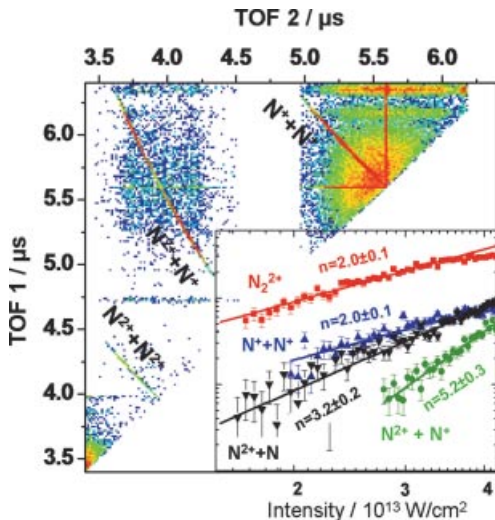


Figure 15.18 Photo-ion–photo-ion coincidence spectrum measured for N_2 fragmentation at 44 eV. The time-of-flight of the first ion is plotted versus the time-of-flight of the

second. Overlay: ion yields as a function of the FEL intensity I for the same experiment. The symbols and solid lines depict experimental data and fits, respectively.

The number of photons involved in the fragmentation process is revealed via the intensity-dependent yield for the particular pathway. Similar to the data in Figures 15.3b, 15.7b, and 15.14, the linearity of the intensity scale was ensured by inspecting the H_2^+ ion yield (not shown here), originating from single-photon ionization with a slope of 1 in a double-logarithmic representation (see also [38, 44, 45]).

The result of this analysis is presented in the inset of Figure 15.18. Surprisingly, the slopes of the yield curves indicate that several pathways require more photons than expected based on the energy of the final states. Dissociative molecular dications $\text{N}_2^{2+} \rightarrow \text{N}^+ + \text{N}^+$, but also bound doubly charged molecular ions N_2^{2+} ($X^1\Sigma_g^+$), are predominantly created by two-photon absorption. This can be easily understood for the dissociative states $A^1\Pi_u$, $d^3\Pi_g$, and $D^1\Sigma_u^+$, since none of them can be populated via a one-photon absorption. But the situation is different for the $X^1\Sigma_g^+$ state (43 eV above the neutral N_2 ground state), which is energetically accessible by one 44-eV photon (see Figure 15.17). An exceedingly small one-photon cross section close to the single-photon double ionization threshold is the most likely explanation. Sequential two-photon double ionization involving, for example, excited states of N_2^+ is expected to have comparatively larger cross sections [44]. The asymmetric dissociative dication channel ($\text{N}_2^{2+} \rightarrow \text{N}^2+ + \text{N}$) is dominated by three-photon absorption, even though only two photons would suffice to reach the final state. Here, a one-photon threshold for the $(\gamma, 2e)$ reaction has been established recently at 55 eV, with a cross section of only $5 \times 10^{-21} \text{ cm}^2$ at $\sim 10 \text{ eV}$ excess energy [136]. At 44 eV, this excess energy is just reachable by two-photon SDI via the bound N_2^+ states or dissociative F band. Those states are predominantly populated via single-photon absorption [140], such that the cross section for the $(2\gamma, 2e)$ pathway is intuitively expected to be small. The dominance of the three-photon channel does therefore not seem unreasonable. Certainly surprising, however, is that as much as five photons need to be absorbed for the creation of dissociating N_2^{3+} ions, even though, according to the potential curves given in [142], two photons would be enough for nonsequential triple ionization and three would allow to reach this final state via the sequential pathway.

Further insight into the fragmentation dynamics can be gained from the angular distribution of the detected ionic fragments. In Figure 15.19 we present the measured angular distribution as a function of KER for all N^+ fragments. Non-coincident dissociating fragments (predominantly created by one-photon absorption) preferentially emerge along the FEL polarization axis (Figure 15.19a). Ions from the Coulomb explosion produced by two-photon absorption ($\text{N}^+ + \text{N}^+$ coincidences, Figure 15.19b) exhibit a clear maximum in the perpendicular direction for the $A^1\Pi_u$ and $d^3\Pi_g$ final states and only the fragments in the $D^1\Sigma_u^+$ state are predominantly ejected along the laser electric field. The FEL pulse duration is much shorter than the rotational period of the molecule and we thus found strong evidences that the $A^1\Pi_u$ and $d^3\Pi_g$ states cannot be created via the dissociating F - or H -bands by absorption of a second photon. Both states are most likely reached through bound N_2^+ states.

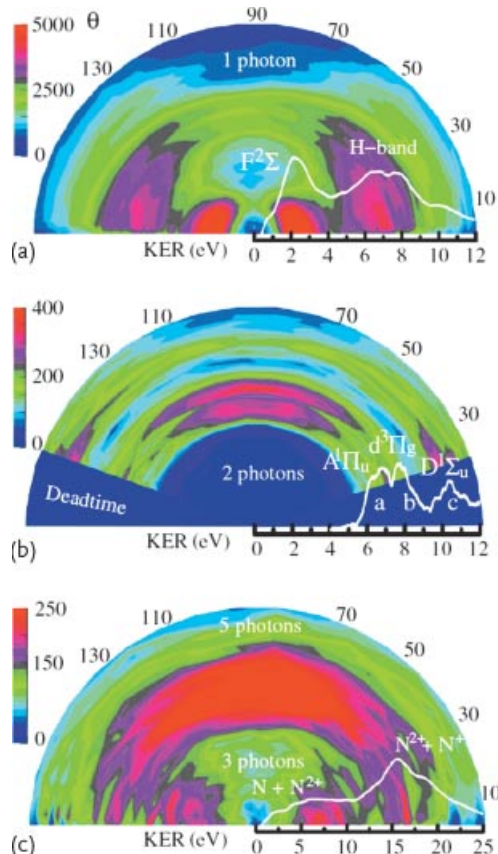


Figure 15.19 Polar density plots of ion angular distribution and KER for various fragmentation channels. θ denotes the angle with respect to the FEL polarization axis (horizontal) and the radius represents the KER. The

curve overlays display the KER spectra integrated over all fragment emission angles. (a) Noncoincident N^+ fragments. (b) $N^+ + N^+$ coincidences. (c) Noncoincident N_2^+ ions. From [45].

Considering the angular distribution of the N_2^+ fragments in Figure 15.19c, we observe low-energy ions emerging along the FEL polarization axis. These mostly result from the $N_2^{2+} \rightarrow N_2^+(^2P) + N(^4S)$ dissociation channel. This pathway can therefore proceed via both dissociative and bound intermediate states of N_2^+ . Fragments with $KER > 10$ eV originating from the $N_2^+ + N^+$ channel are emitted preferentially in the perpendicular direction. This pathway, involving in total five photons as discussed above, does therefore not proceed through the dissociating F - or H -bands of N_2^+ , but rather via the bound states of the singly charged ion and via one of the bound or dissociating states of N_2^{2+} (with the exclusion of the $D^1\Sigma_u^+$ state, which decays along the FEL polarization axis). The above constraints on the possible intermediate states involved in the production of highly charged fragments will become crucial for the understanding of time-dependent N_2 dynamics discussed in Section 15.4.2.2.

15.4

EUV Pump–EUV Probe Experiments

The ultrashort pulse duration of EUV or X-ray FELs and HHG-light sources creates unprecedented possibilities for time-resolved imaging of fundamental light-induced reactions on fs or even subfemtosecond timescales [126, 143]. As a consequence, a variety of experimental techniques for EUV/X-ray as well as IR/EUV/X-ray pump–probe measurements have been developed. Since this chapter deals with nonlinear interactions, we will focus here on one-color EUV (X-ray) pump–probe experiments, which necessarily involve at least two photoabsorption steps (the pump and the probe). This configuration is particularly important, since it has a potential for dynamic measurements with attosecond time resolution. All HHG-based isolated attosecond light pulses are generated at EUV frequencies and, thus, attosecond pump/attosecond probe schemes currently imply an EUV pump/EUV probe experiment. It should be noted that existing isolated attosecond pulses rarely contain enough photons for pump–probe measurements, although promising results in this direction have been recently reported [86]. At FELs, the FEL pump/FEL probe scheme offers a time resolution that is superior to laser-FEL experiments because it is not subject to jitter between the stochastic SASE FEL pulse and a synchronized external laser [126].

15.4.1

Split-and-Delay Arrangements and Characterization of the EUV Pulses

A variety of split-and-delay units, based on geometrical (or wavefront) pulse segmentation, have been brought into operation for HHG setups and at FEL facilities. Usually, one of two approaches was used. The first technique relies on a grazing incidence Mach–Zehnder geometry [144, 145] that offers an almost photon-energy independent transmission (between 50 and 70%) in a broad photon energy range. The second approach uses a back-reflecting focusing mirror, which is physically separated into two parts for pulse-pair creation [146]. The time delay between both pulses is adjustable, with a typical resolution $< 1 \text{ fs}$, by moving one half-mirror with respect to the other along the FEL beam axis by means of a high-precision piezo-stage. Figure 15.20 depicts an example of the split-mirror arrangement used at FLASH and SCSS in combination with a “reaction microscope” setup [89, 105, 146].

These types of split and delay units have been widely employed for temporal characterization of HHG and FEL pulses via second or higher order autocorrelation measurements. The second-order autocorrelation spectrum is given by

$$I(\Delta t) = \int |(E(t) + E(t + \Delta t))^2|^2 dt , \quad (15.4)$$

where I is the signal strength and E is the electric field strength. One of the most common nonlinear signals employed for these measurements is TPSI of He, as considered in Section 15.3.1 [102–105]. The choice is based on the relative simplicity of the TPSI process, both in terms of experimental requirements and in-

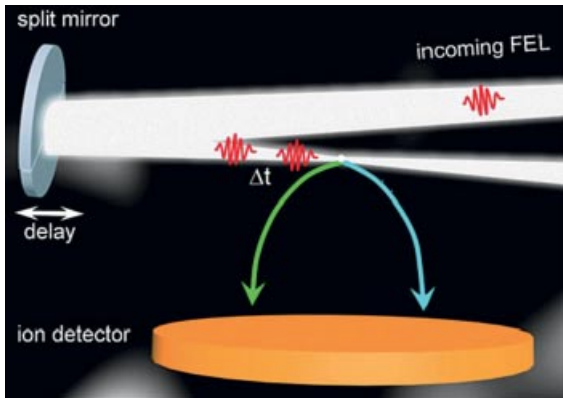


Figure 15.20 Schematic of an EUV/EUV experimental pump–probe setup with split-mirror stage and the ion-detection part of the reaction microscope.

terpretation of the results. Figure 15.21a shows an autocorrelation trace measured at the SCSS with 20.45-eV photon energy and using the split-mirror experimental setup as shown in Figure 15.20. The autocorrelation trace exhibits a broad maximum with ~ 40 fs-FWHM, superimposed with a narrow peak (~ 10 fs-FWHM) at zero delay time. As follows from FEL theory [147] and from the partial coherence model [148] (and corresponding to direct observations in the spectral domain [26]), each individual FEL pulse comprises several subpulses (or modes) [145–150]. Each subpulse is intrinsically coherent, giving rise to a sharp spike in the autocorrelation spectrum at zero delay, whose width is a measure of the subpulse duration or the coherence time. The underlying broader contribution can be attributed to the temporal width of the pulse envelope averaged over many fluctuating FEL pulses. From the data we extract a coherence time of ~ 8 fs and an average pulse dura-

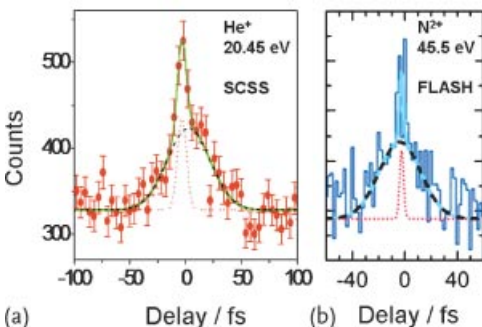


Figure 15.21 (a) Experimental second-order autocorrelation spectrum measured at SCSS. The yield of He^+ ions (same signal as in Figure 15.4) is shown as a function of the pump–probe delay. (b) Experimental autocorrelation trace measured with the N_2^+ fragments

($22 \text{ eV} < E_{\text{KER}} < 40 \text{ eV}$). In both (a) and (b), the solid line represents a sum of two Gaussians with FWHM of 40 and 8 fs in (a), and 40 and 5 fs in (b). The dashed and dotted lines correspond to the broad and narrow Gaussian, respectively.

tion of 28 ± 3 fs-FWHM, much shorter than the 100–150 fs expected from electron bunch length measurements. The comparison with a statistical pulse shape model (partial coherence model, PCM [148] also suggested a 6 fs tilt of the FEL pulse-front across the 10-mm beam diameter [105].

Figure 15.21b shows the autocorrelation trace obtained with the same experimental setup at FLASH, using 45.5-eV photon energy and employing N₂ multiple ionization to generate a nonlinear signal. Although the shape due to the pulse structure is convoluted with some molecular dynamics, the same essential features can be observed. We extract a pulse duration of 40 ± 10 fs and a coherence time of 5 ± 1 fs, in good agreement with other autocorrelation tests [41, 144, 150] and interferometric measurements [145].

15.4.2

Nuclear Wave Packet Imaging in Diatomic Molecules

15.4.2.1 Vibrational Wave Packet Motion in D₂⁺

Figure 15.22 shows the results of a proof-of-principle experiment [151] on one of the simplest molecular systems, the deuterium molecular ion. As sketched in Figure 15.22a, a first EUV photon at 38 eV removes one electron from a D₂ molecule, creating a bound D₂⁺ molecular ion. With about 95% probability, the 1sσ_g ground state of D₂⁺ is populated and a coherent vibrational nuclear wave packet is created. The wave packet oscillates with a period characteristic for the ionic ground-state potential energy surface (PES). The EUV probe pulse removes the second electron, causing Coulomb explosion of the D₂²⁺ molecule with a kinetic energy release of the D⁺ fragment proportional to 1/R.

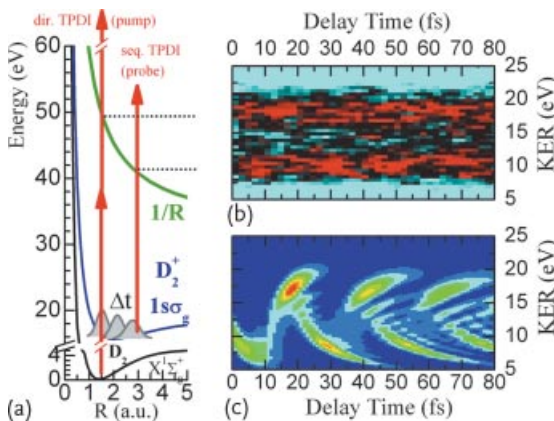


Figure 15.22 (a) Sketch of the pump–probe scheme with the pump photon launching a nuclear wave packet in the 1sσ_g state of D₂⁺ and the second photon probing it by ionizing the cation to the repulsive PES of the dication.

The molecule can undergo direct TPDI as indicated, causing background signal that was subtracted in the evaluation the data; (b) experimental KER versus the delay time between the pump and probe; (c) theory. From [126].

The KER spectrum as a function of the delay time is shown in Figure 15.22b and extends from 7 to 23 eV. The data comprehensively visualize the ultrafast vibrational motion in the ground state of the D_2^+ molecule. Two pronounced horizontal bands around $E_{KER} \cong 18$ and 10 eV can be attributed to ionization of D_2^+ at the inner or outer classical turning points. Projections for kinetic energy release (KER) related to the inner and outer turning points allowed us to extract the time the molecule needs for a complete vibrational period. The measured value of 22 ± 4 fs is in good agreement with the theoretical prediction shown in Figure 15.22c. For the theoretical treatment, the time-dependent Schrödinger equation (TDSE) was solved separately for the two ionization steps, using 10-fs cosine-square-shaped XUV pulses. Single ionization by the pump pulse ($D_2 \rightarrow D_2^+$) was treated without essential approximations by including all electronic and vibrational (dissociative) degrees of freedom (see [151]).

The nuclear wave packet can be ionized at any R from the inner to the outer turning point. We might ask whether the ionization probability is R -independent. In the present case, the experimental results indicate (within the error bars) an R -independent ionization probability. This is in slight disagreement with a theoretical calculation predicting a distinct dependence of the D_2^+ ionization probability on the internuclear distance [48, 151]. Details about the R -dependent ionization probability of the D_2^+ molecular ion are discussed in [151].

It might come as a surprise that the ultrafast nuclear motion, with a round trip time of around 22 fs, can be observed at all with SASE pulses that have an FWHM of ~ 40 fs. But [152] showed that a time resolution on the order of the 5 ± 1 -fs coherence length of the pulses can be reached in jitter-free measurements. Even though the fine structure of the wave packet motion as predicted by theory (Figure 15.22c) is washed out, the salient features survive and can be extracted.

15.4.2.2 Dissociation Dynamics of the N_2 Molecule

The wave packet motion in N_2^+ and N_2^{2+} molecular ions, excited by 38 and 46-eV photons at FLASH, was investigated in similar manner as that of D_2 [89, 153]. Here, the decay dynamics of a variety of metastable PES in the N_2^{2+} dication is observed by probing the dissociating molecule via inspecting $N^+ + N^+$, $N^{2+} + N^+$ and $N^{2+} + N^{2+}$ Coulomb exploding fragments in coincidence (see Figures 15.18 and 15.19). The main features in delay-dependent KER data are reproduced by a classical model [153] and are shown in Figure 15.23. Again, the nuclear wave packet motion in several intermediate states was observed along the entire reaction coordinate, from the intermediate bound metastable state, populated via the Frank-Condon transition at the ground state N_2 equilibrium internuclear distance, to the dissociated atoms.

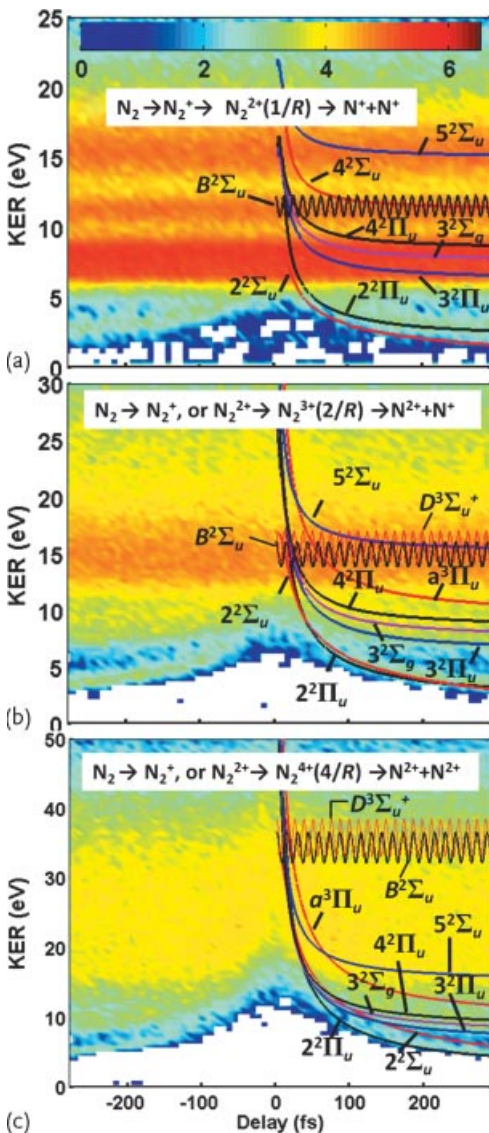


Figure 15.23 Measured KER spectra as a function of pump–probe delay and compared with classically calculated KER curves, $K(\tau)$, for different break-up channels: (a) $N^+ + N^+$, (b) $N^{2+} + N^+$, and (c) $N^{2+} + N^{2+}$. The

classical calculations were performed for the dissociative: $2^2\Sigma_u$, $2^2\Pi_u$, $3^2\Pi_u$, $3^2\Sigma_g$, $4^2\Pi_u$, $4^2\Sigma_u$, $5^2\Sigma_u$ and the bound $B^2\Sigma_u^+$ states of N^{2+} ; and the dissociative $a^3\Pi_u$ and bound $D^3\Sigma_u^+$ states of N_2^{2+} . From [153].

15.4.3

Isomerization Dynamics of Acetylene Cations

Tracing of chemical reactions along an entire reaction coordinate with femtosecond time resolution is one new research area created by the availability of ultra-short EUV and X-ray light sources. Of particular interest are isomerization reactions, which are ubiquitous in functional biological systems, for example, in vision or photosynthesis. A first study of isomerization was performed for acetylene cations [154].

As schematically depicted in Figure 15.24, the linear ($D_{\infty h}$) acetylene cation $[HC=HC]^+$ undergoes isomerization with a proton moving from one side of the molecule to the other, forming the nonlinear (C_{2v}) vinylidene $[H_2CC]^+$. Isomerization occurs via a concerted bending mode that bends both hydrogen atoms out of the acetylene molecular axis. Through absorption of a 38-eV photon, the $A^2\Sigma_g^+$ excited ionic state is formed (Figure 15.24a). Earlier photoelectron spectroscopy indicated ultrafast relaxation of this state within 51 fs [154]. Neither absorption nor emission bands of the dipole-allowed transition to the $X^2\Pi_u$ ground state have been observed, nor can the state dissociate into $H^+ + C_2H$ or $H + C_2H^+$ final channels due to the existence of high potential energy barriers. An effective redistribution of energy via isomerization or vibronic coupling was suggested by theory (see [154]) but, lacking conclusive time-dependent measurements, the ultimate reason for the ultrafast decay of the state remained under intense debate.

Upon pumping of the C_2H_2 by the first 38-eV FEL photon, isomerization of the acetylene $A^2\Sigma_g^+$ state might proceed to the vinylidene \tilde{X}^2B_1 or \tilde{A}^2B_2 states, both are nearly degenerate with the acetylene excited state. The occurrence of isomerization is probed as a function of time by absorption of a second photon. The second absorption event creates the dication as depicted in Figure 15.24b. If isomeriza-

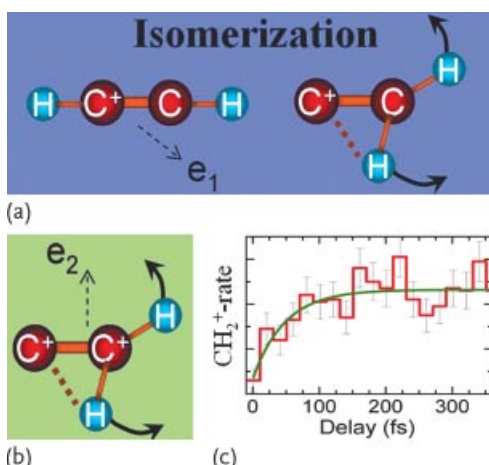


Figure 15.24 (a,b) Schematic of acetylene–vinylidene isomerization. (c) Yield of the $CH_2^+ + C^+$ coincident fragments as a function of the pump–probe delay. From [126].

tion has taken place, Coulomb explosion into the $\text{C}^+ + \text{CH}_2^+$ fragments will occur and offers conclusive evidence for the process [154]. By recording the yield of the respective fragments in coincidence and as a function of the pump–probe delay (Figure 15.24c), the isomerization time was measured to be 52 ± 15 fs. For the analysis, a kinetic energy release window of $5.8 \text{ eV} < \text{KER} < 8 \text{ eV}$ was used. The observation provides clear evidence for the existence of a fast, nonradiative decay channel, which was postulated 40 years ago by Herzberg [155].

These experiments give a first glimpse of molecular dynamics studies with intense, short-pulse EUV radiation, in combination with many-particle fragment-imaging spectrometers. Using EUV pump pulses produced by splitting FEL or HHG beams provides efficient access to highly excited metastable states and, due to the intrinsic time stability between the two pulses, enables few femtoseconds or even attosecond time resolution.

15.5

Experiments in the X-Ray Domain

As detailed in Chapters 5 and 17 of this book, there is strong motivation to bring intense short-pulsed accelerator- and HHG-based radiation sources into the sub-nanometer wavelength regime. This development is to a large extent driven by the vision of single-shot high-resolution imaging of biological objects [5, 156]. The first source of this type was realized in 2009 with the startup of the LCLS, the world's first X-ray FEL. First years of LCLS operations triggered tremendous scientific activity in a very broad range of disciplines, ranging from chemistry and biology to material science and matter under extreme conditions. The common theme of all these studies is the interaction of intense ultrafast X-rays with building blocks of matter. Therefore, understanding the response of individual atoms and small molecules to intense X-ray pulses is considered essential for most applications. Many early LCLS experiments addressed this topic.

Even before the LCLS became operational, a lot of progress in this direction had been achieved at the FLASH facility in Hamburg, where available photon energies reached the water window [25]. Several experiments on nonlinear ionization were performed in the transition region between the EUV and X-ray domains, addressing inner-shell electrons of heavy rare gas atoms [37, 76, 77, 157]. Among them was the surprising observation of a very high degree of ionization in Xe (up to Xe^{21+}), at intensities of $\sim 10^{16} \text{ W/cm}^2$. This process requires the absorption of up to fifty 93-eV photons [37]. The result triggered a lot of discussions on the nature of light–matter interactions in the regime of superintense fields and X-ray frequencies. One controversial question, which is still not completely clarified, is whether the observed behavior can be explained within the perturbative picture [37, 71, 76–79]. Even though the ponderomotive energy at these parameters remains small as compared to the photon energy; it was argued that nonperturbative effects or a collective electron response might be responsible for the unexpectedly high level of ionization [76–78].

The experiments [37, 76, 77] were performed in the transition regime between EUV radiation, addressing valence electrons, and X-rays, interacting predominantly with the inner-shell electrons. For Xe at $h\omega \sim 100$ eV, the first one or two photons interact primarily with $4d$ electrons, resulting in double or multiple ionization via Auger decays. Later, photons can be absorbed sequentially, releasing valence electrons until the valence ionization potential becomes larger than the photon energy (this occurs for Xe^{7+}). To reach higher charge states, direct multiphoton absorption steps are required. Thus, reaching Xe^{21+} at this photon energy involves a complicated sequence of inner-shell, single-photon valence shell, and multiphoton transitions.

15.5.1

Multiple Ionization of Heavy Atoms: Role of Resonant Excitations

In contrast to the EUV regime discussed above, first experiments performed at LCLS showed that multiphoton multiple-ionization of atoms at X-ray frequencies proceeds predominantly via a sequence of single-photon absorption steps. For atomic Ne [73] and molecular N₂ [158, 159], the measured data were in good agreement with theory based on sequential single-photon absorption [160]. It was shown that all electrons from these light elements can be stripped, provided the photon energy is larger than the ionization potential of all intermediate ionic ground states. With intense LCLS pulses, several novel effects were observed. These include double core hole creation, where a second photon is absorbed by the atomic inner shell before the first vacancy relaxes via Auger decay [73, 161–164], or frustrated X-ray absorption because of efficient inner-shell depletion [73, 158]. The contribution from direct (“nonsequential”) two-photon absorption was found to be very small [165, 166].

First measurements on a heavier rare gas atom, for example, Xe at 1500 eV revealed a surprisingly high degree of ionization [75] (similar to the experiment [37] at FLASH). As illustrated in Figure 15.25, charge states as high as Xe^{36+} were produced. The theoretical model based on the sequential ionization scheme, which was very successful for lighter elements, predicts Xe^{27+} as the highest accessible charge state [75, 167, 168]. This is in good agreement with intuitive expectations, since the ionization potential of Xe^{27+} exceeds the photon energy. Interestingly, while the model fails for 1500-eV photon energy, it provides good agreement with experimental data at 2000 eV (see Figure 15.25) as well as at 850 eV [169]. Detailed comparison of the experimental data with theory at two different photon energies indicates that highly charged ionic states at 1.5 keV are produced via resonant pathways, as schematically illustrated in Figure 15.26. These resonances, which occur in highly charged xenon ions produced during the course of a single femtosecond X-ray pulse, are not included in the simulation [75, 167, 168]. The latter account for bound-free transitions. Inclusion of the bound-bound (resonant) transitions is beyond the current computational limits [167].

As the binding energy of the xenon M-shell ($n = 3$) electrons surpasses the 1.5-keV photon energy for charge states higher than Xe^{18+} , direct single-photon

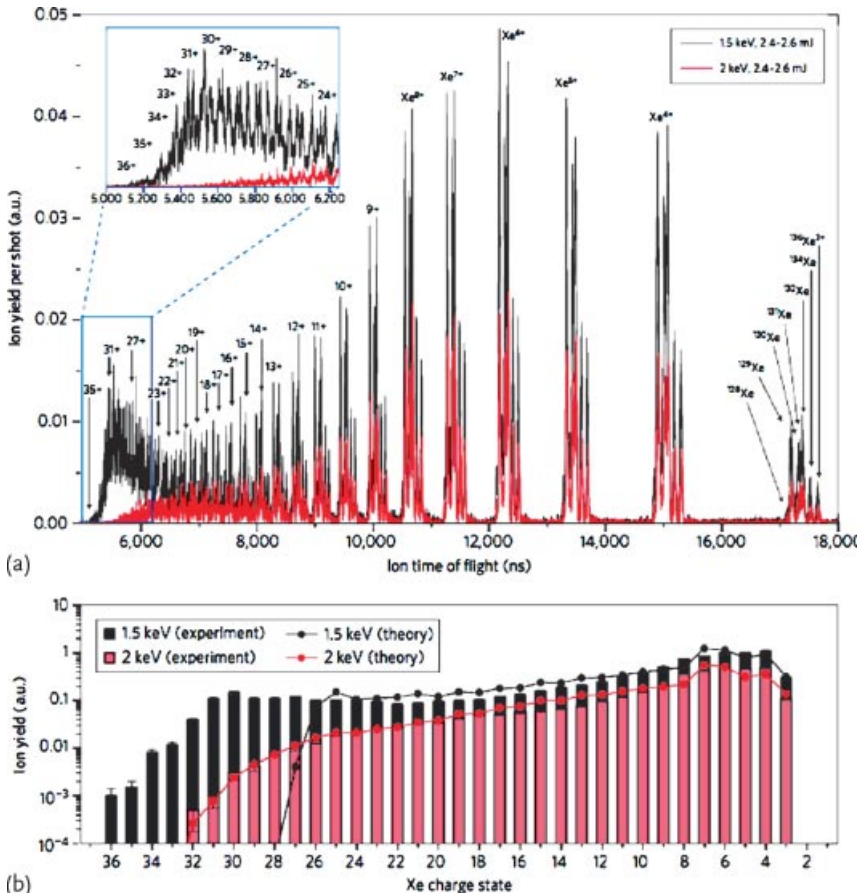


Figure 15.25 Comparison of experimental and simulated xenon charge state yields for 80-fs LCLS pulses. (a) Xenon ion TOF spectra at photon energies of 1.5 keV (black) and 2.0 keV (red) for 2.4–2.6 mJ pulse energy. (b) Experimental xenon charge state distribution extracted from (a) (bars) after deconvolution of overlapping charge states and comparison

to theory (circles with lines) calculated for an 80-fs X-ray pulse with a pulse energy of 2.5 mJ and integrated over the interaction volume. The theoretical charge state distributions are scaled such that the total ion yield integrated over all charge states agrees with the total ion yield in the experiment. From [75].

ionization (left blue arrow in Figure 15.26) from this shell is no longer possible. However, the electrons can still be resonantly excited into densely spaced Rydberg states and unoccupied valence orbitals (red arrows). Based on the calculated cross sections [75], we expect resonant excitations to occur for any given charge state above the resonance threshold, which excites several electrons into Rydberg states. The multiply excited states can then be ionized by Auger decay and other auto-ionizing transitions mediated by electron–electron interaction (green arrows).

Ionization of a Rydberg electron by absorption of another photon is unlikely: calculations indicate that the corresponding photoionization cross sections are very

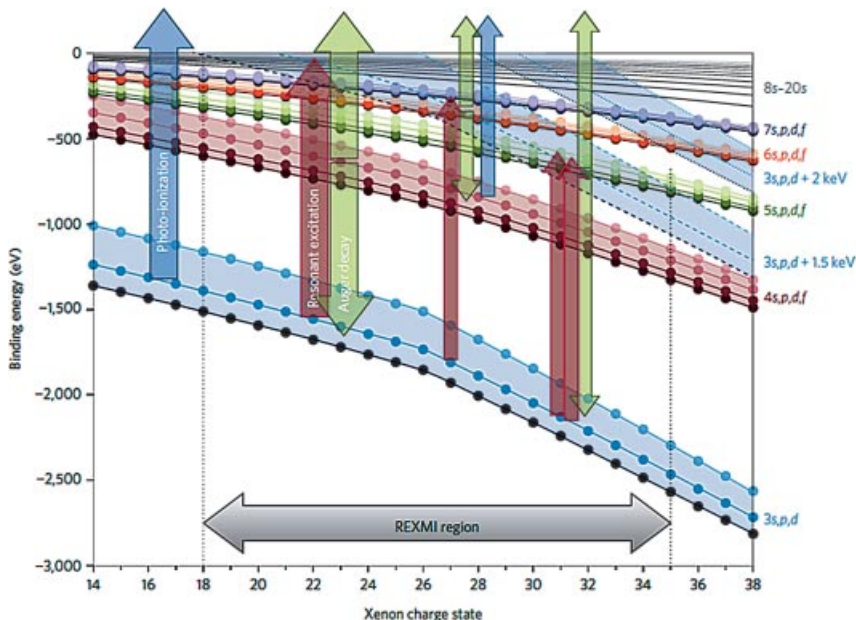


Figure 15.26 Ground-state binding energies for M-, N-, and O-shell electrons in xenon for charge states between Xe^{14+} and Xe^{38+} . The arrows denote schematic ionization pathways. Unoccupied orbitals are shown explicitly up to 7f, but densely spaced Rydberg orbitals (gray lines) cover the entire energy range up to the continuum. To illustrate the occurrence of resonances at a photon energy of 1.5 keV, lines parallel to the 3s, 3p, and 3d binding energies shifted by 1.5 keV are drawn as blue dashed lines. For charge states between Xe^{19+} and Xe^{35+} , they intersect with the binding energies of various outer orbitals; hence the possibility of resonant transitions from the M shell to those outer shells. Below this REXMI region, M-shell photoelectrons can be created by direct single-photon ionization (left blue

arrow). For charge states higher than Xe^{18+} , 3s, 3p and/or 3d electrons can be resonantly excited into unoccupied valence orbitals (red arrows). The resulting M-shell holes are refilled by Auger decay (green arrows, left). Electrons excited into outer orbitals can undergo Auger decay or other autoionizing transitions involving other outer-shell electrons (green arrows, middle and right), especially if multiply excited states are created (red arrows, right). In some cases, Auger decay may also lead to other core-excited states, which can be ionized by a second X-ray photon (blue arrow, right). At a photon energy of 2.0 keV, resonances can only occur for charge states Xe^{29+} and higher, as shown by the dotted blue lines representing the 3s, 3p, and 3d binding energies shifted by 2.0 keV. From [75].

small. However, Auger decay and autoionization of these core-excited states efficiently deplete the outer shells and refill the lower lying levels, thus continuously fuelling the resonance-enabled X-ray multiple ionization (REXMI) pathway. (Note that the effectiveness of fast Auger and autoionization decay processes of hollow atoms has also been observed experimentally [170].) In even higher charge states, direct photoionization (right blue arrow, Figure 15.26) of excited intermediate states reached via Auger decay, becomes increasingly efficient; the binding energy of electrons in the $n = 4$ shell approaches 1.5 keV for increasing ionic charge. Finally, for charge states above Xe^{35+} , the photon energy is no longer sufficient

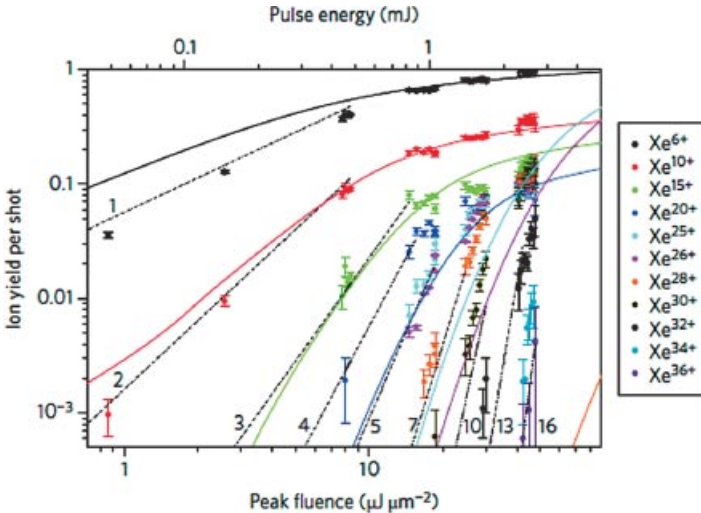


Figure 15.27 Xenon ion yield for selected charge states at 1.5-keV photon energy as a function of X-ray fluence. To correct for gas detector nonlinearities at LCLS pulse energies below 1 mJ, the gas detector readings were

recalibrated using a linear ion signal (H^+ ions created from residual gas). Calculated ion yields (without inclusion of REXMI) are shown as solid lines [75].

to excite resonant transitions from the M shell, which agrees with the observed cut-off in the experimental charge-state spectrum at Xe^{36+} . The resonant nature of multiphoton absorption in Xe at 1500 eV is also confirmed by the simultaneously measured fluorescence spectra [75].

In this context, it should be noted that REXMI pathways would also be accessible for a photon energy of 2.0 keV, but starting at much higher charge states ($q \geq 29$) when the M-shell ionization potential begins to exceed 2.0 keV (Figure 15.26). However, even for the highest peak fluence in our experiment, charge states with $q \geq 29$ are populated only with low probability [75]. Therefore, REXMI does not play a significant role in our 2.0-keV data, although it should become important at 2.0-keV photon energy if higher peak fluences are available and charge states with $q \geq 29$ can be efficiently created. In general, this effect is very similar to resonance-enhanced ionization observed in the EUV domain (see, e.g., [118, 171, 172]). However, the very broad range of charge states accessible, along with the broad spectrum of the LCLS, opens multiple resonance channels within the same X-ray pulse.

In Figure 15.27, the measured yields of several exemplary Xe charge states are shown as a function of the LCLS pulse energy or pulse fluence. Under these conditions, ionization is a sequential process and these variables offer more information than the pulse intensity (see Section 15.3.3). As the pulse duration was not changed in the course of this experiment, intensity-dependent experiments would yield the same results. From the slopes in the double-logarithmic plot in Figure 15.27, we can conclude that the highest charge states are produced by the absorption of more

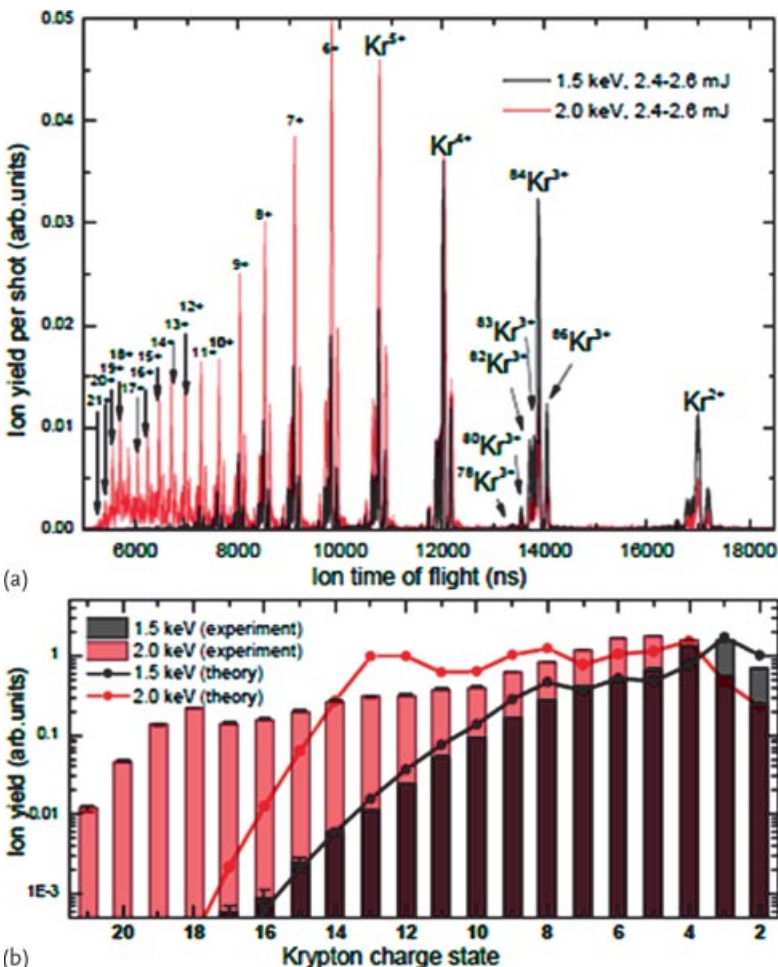


Figure 15.28 (a) Krypton time-of-flight spectra measured at LCLS at photon energies above (2 keV, red) and below (1.5 keV, black) the L-edge. The pulses have a nominal pulse duration of 80 fs and 2.4–2.6-mJ pulse energy. (b) Experimental krypton charge state distribu-

tion extracted from (a) (bars) and comparison to theory (circles with lines). The theoretical charge state distributions are scaled such that the total ion yield, integrated over all charge states, agrees with the total ion yield in the experiment. From [173].

than ten 1.5-keV photons. It should be noted that the presence of intermediate resonances may lead to slopes that are smaller than the number of absorbed photons (e.g., if the transitions are saturated) and the values derived from Figure 15.27 only represent a lower limit. The slopes are, however, in good agreement with energetic considerations based on the minimum ionization energy (that is, the sum of all ground-state ionization energies) that is required to reach a given charge state. For Xe²⁶⁺, this sum of all ground-state ionization energies is 9.2 keV, for Xe³⁰⁺ it is 15.9 keV and for Xe³⁶⁺ it is 28.6 keV. This corresponds to the absorption of

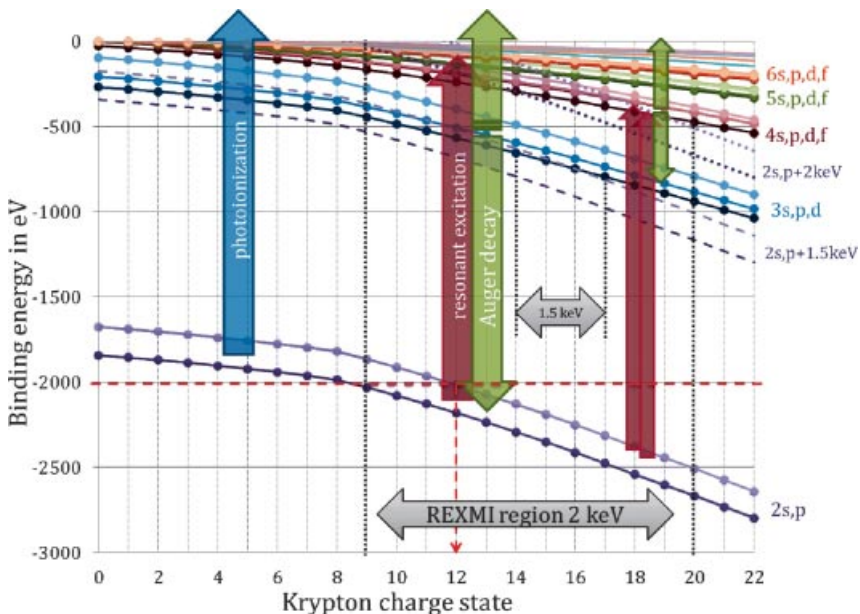


Figure 15.29 Ground-state binding energies for electrons in the L-, M-, and N-shells in krypton ions of charge state up to Kr^{22+} , together with schematic ionization pathways: direct photoionization is depicted as blue arrows, resonant transitions as red arrows, and Auger decay as green arrows. To illustrate the occurrence of resonances at a photon energy of 2 keV (1.5 keV), lines parallel to the 2s and 2p binding energies shifted by 2 keV

(1.5 keV) are drawn as purple dotted (dashed) lines. For charge states between Kr^{9+} and Kr^{20+} , the dotted lines intersect with the binding energies of valence or Rydberg orbitals; hence resonant transitions from the L-shell to outer shells are possible at 2-keV photon energy. For 1.5-keV photon energy, the region of energetically accessible and electric-dipole-allowed resonances is limited to Kr^{14+} to Kr^{17+} . From [173].

at least 7, 11, and 19 photons of 1.5 keV. These numbers emphasize the dramatic enhancement of ionization as a result of the REXMI mechanism, which opens the ionization channels beyond Xe^{28+} and more than doubles the energy that can be absorbed per atom as compared to our expectations without accounting for resonant excitations.

REXMI is expected to be a general phenomenon for X-ray ionization of heavy atoms. Its signatures have also been observed in Kr L-shell ionization [173]. Figure 15.28 shows the measured and calculated charge state distributions for multiple ionization of Kr by intense 80-fs LCLS pulses at 1.5 and 2-keV photon energies. The relation between theory and experiment here is reversed compared to the Xe data in Figure 15.25. Namely, the measured charged state distribution at 1.5 eV is in good agreement with the predictions of the model [167, 168], whereas the theory strongly underestimates the highest charge states at 2-keV photon energy. This behavior can be readily understood within the REXMI picture (see Figure 15.29): at 1.5 keV, the photon energy is below the L-edge of Kr, such that mostly M-shell electrons are ionized. As can be seen from Figure 15.29, resonant bound-bound transi-

tions are expected to play only a minor role under these conditions. Therefore, the model [167, 168] describes the experimental results reasonably well (Figure 15.28b). At 2 keV, above the Kr L-edge, resonant excitations (wide red arrow in Figure 15.29) from the L-shell lead into Rydberg orbitals. The resonant channels open up after the direct ionization of the L-shell electrons becomes inaccessible, at the charge state Kr^{9+} for the 2s and at Kr^{12+} for the 2p orbitals. In order to illustrate where resonant transitions are energetically accessible, purple dotted (dashed) lines are drawn in Figure 15.29 parallel to the 2s and 2p binding energies, but shifted by 2 keV (1.5 keV). After resonant excitation, the resulting L-shell vacancies are filled via Auger decay. Thus, resonant excitations significantly enhance photoionization levels at 2-keV photon energy, explaining the large discrepancy between theory and experiment.

As discussed in [75, 173], REXMI can significantly enhance the amount of energy absorbed per high-Z atom. This might have serious implications for local radiation damage in coherent diffractive imaging [174] (see also Chapter 17), if the photon energy can drive REXMI processes. In particular, this can be important in the vicinity of high-Z impurities [175], (e.g., S, Fe, or Se atoms often contained in biological samples), which might lead to the appearance of “hot spots” in the diffraction pattern because of the local charge redistribution. This effect is considered in the next section.

15.5.2

Multiphoton Ionization of Molecules Containing High-Z Atoms

Since most envisaged applications of intense, ultrafast X-rays deal with extended polyatomic systems, the role of the environment in multiple ionization of individual atoms becomes an important issue. A first step in this direction can be made by comparing the ionization dynamics of an isolated atom with that of an atom in the presence of molecular partners. In Figure 15.30, the ionization of an isolated Kr atom is compared to the ionization of a small polyatomic molecule containing an embedded Se atom (CH_3SeH , methylselenol, see Figure 15.30a). Kr and Se have similar electronic structure and similar photoabsorption cross sections at 2 keV, the photon energy that was used for this experiment [176]. The photoabsorption cross section of Se is more than 50 times higher than that of the rest of the molecule. X-rays are therefore almost exclusively absorbed by the Se atom. Note that the highest charge state of Kr observed in Figure 15.30c (16+) is significantly lower than that given in Figure 15.28, due to a considerably lower pulse energy in the \sim 5-fs pulses used here. No effects of frustrated absorption were found for Kr ionization by 80 and 5-fs pulses [173].

Here it should be noted that the LCLS pulse duration quoted throughout this chapter are the “nominal” values defined from the length of the electron bunch. Therefore, they only provide a rough estimate of the actual temporal width of the X-ray pulse. For longer pulses, dedicated pulse duration measurements [177] suggested that the actual X-ray pulse might be considerably shorter than these nominal values (cf. also Section 15.4.1). This appears plausible, since the electron bunch

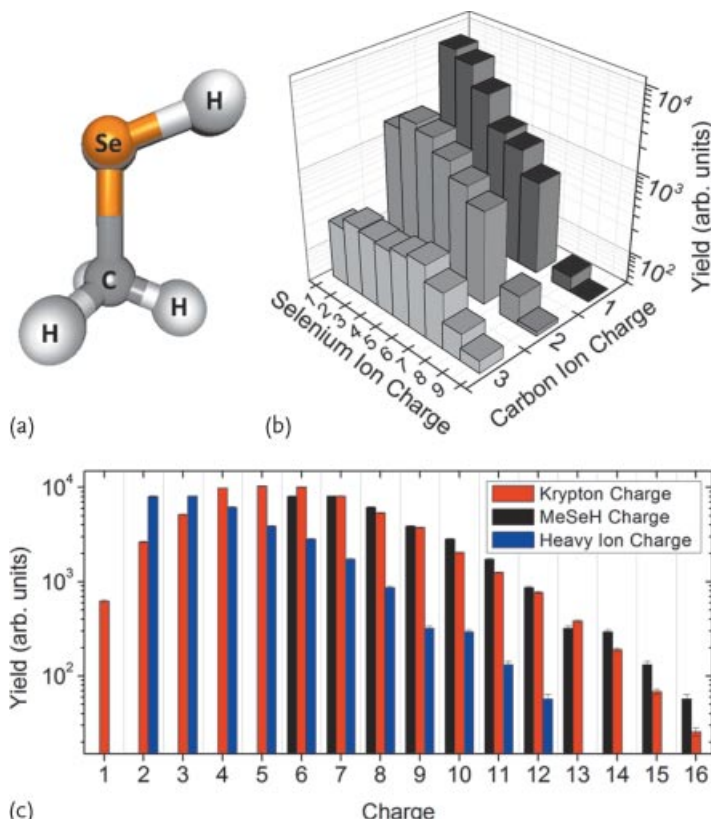


Figure 15.30 (a) Structure of the methylselenol molecule. (b) Measured yield of coincident Se and C ion pairs for different final charge states. (c) Sum charge induced on the molecule compared to the charge state distribution observed in Kr under the same

conditions. The heavy ion charge represents the sum of Se and C charges measured in coincidence, whereas CH_3SeH charge denotes the total charge of the molecule assuming that four H^+ ions were produced. From [176].

length should give an upper limit for the X-ray pulse duration. For the ultrashort (sub-10-fs) pulses used in [176] the simulations from the measured bunch parameters suggest that the X-ray pulse might be as short as a few femtoseconds [178], in a reasonable agreement with recent THz streaking measurements (A.L. Cavalieri and R. Kienberger: Investigation of the time structure of LCLS's few fs X-ray pulses, unpublished results, 2013).

Figure 15.30b depicts the measured charge state distribution of Se and C ions detected in coincidence. Considering only selenium and carbon ions, the highest charge state combination observed with statistical significance is $\text{Se}^{9+} + \text{C}^{3+}$. Although proton fragments were detected as well, they were not used for the determination of the total charge state of the molecule: typically more than one proton is ejected, and the total detection efficiency becomes very low for coincidences of more than three particles. Therefore, in order to estimate the total charge, we

assume that all hydrogen fragments are charged, which is well justified for higher charge states [179], but might overestimate the total charge for lower charge states. The estimated total charge for the methylselenol molecule is shown in Figure 15.30c in comparison with the charge state distribution measured for the Kr atom under identical experimental conditions. The results in Figure 15.30c show that the charge on the Se atom is much lower than that on Kr, but the total charge induced on the molecule (up to 16+) is very similar to the atomic case. The charge initially localized on the heavy Se atom is efficiently redistributed to its molecular partners [176].

The dominant ionization mechanism in the X-ray regime is core-shell photoionization, followed by Auger decay (except for K-shell ionization of heavy atoms, where fluorescent decay dominates). For Se or Kr, a vacancy in the L-shell causes multiple ionization via an Auger cascade. The first relaxation step with the highest probability is an “intra atomic” LMM Auger decay (hole lifetime ~ 500 as) in the Se atom, producing mainly 3d (less likely 3p) vacancies [180]. It is followed by a decay of these M-shell vacancies involving the valence electrons of Se and their neighbors (MVV Auger), which occurs on an ~ 10 -fs timescale [180]. The latter step causes a considerable portion of the total charge to be distributed over all molecular constituents, even though the initial inner-shell photoabsorption and the first Auger decay are very likely to be localized on the Se atom.

More insight into the charge rearrangement and nuclear dynamics upon multiple inner-shell ionization can be obtained by examining the measured kinetic energies of the ionic fragments (Figure 15.31). In Figure 15.31a–c, the measured KERs of selenium ions (a), carbon ions (b), and protons (c), detected in coincidence, are presented for three different charge state combinations. In all cases, we observe a broad energy distribution with a KER maximum shifting toward higher energies with increasing total charge state. To relate these results to the molecular geometry, we performed a simple simulation of the molecular Coulomb explosion (CE), assuming instantaneous removal of the electrons at the neutral ground-state equilibrium bond lengths and angles. The results of the simulation are shown as vertical lines in Figure 15.31a–c.

For the lowest charge state ($\text{Se}^+ + \text{C}^+$), the simulated energies of carbon and selenium ions fit well to the maximum of the KER, whereas they increasingly overestimate the experimental results for higher charge states. The simulated proton energies are much larger than the measured ones for all charge states. The considerable discrepancy between the measured KERs and simulated CE energies for higher charge states is a direct indication for the motion of the nuclei on the timescale of multiple ionization. Low charge states are predominantly produced by single photon absorption, upon ultrafast core-vacancy decay. In this case, the final charge state is reached before nuclear motion occurred, resulting in kinetic energies of the heavy ions that are in reasonable agreement with the simulation. The lightest ionic fragments, that is, protons, are considerably displaced even within this very short time (in 1 fs, a proton with one atomic unit of kinetic energy (27.2 eV) moves about 3.5 Å, that is, more than a bond length per fs). Therefore, the protons never

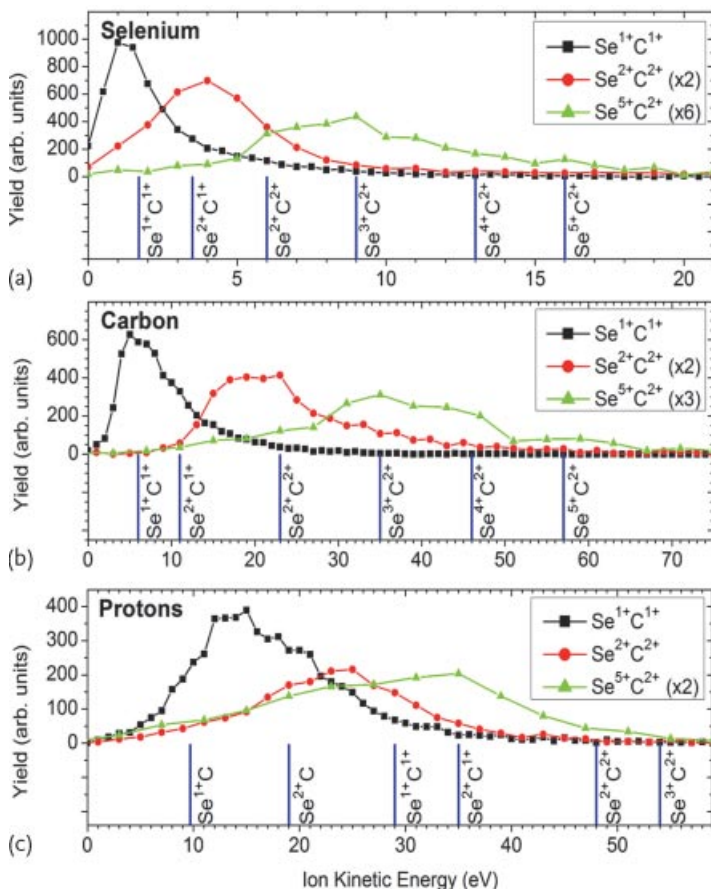


Figure 15.31 The kinetic energy distributions of Se, C, and H ions for three different fragmentation channels. The vertical blue lines indicate simulated energies for given charge states assuming the equilibrium geometry of the neutral molecule [176].

exhibit the simulated CE energies corresponding to the equilibrium internuclear distances R_{eq} (Figure 15.31c).

In general, the production of higher charge states involves sequential absorption of two or more photons with a femtosecond-scale time delay between the absorption steps. Each absorption triggers new Auger cascades. However, the removal of the first few electrons can already trigger the dissociation of the molecule [181]. By the time the final charge state is reached, the bond lengths have significantly increased. This leads to lower Coulomb repulsion energies for a given charge state combination and, thus, larger deviations from the CE model (as can be clearly observed in Figure 15.31). These deviations indicate that the bond length can increase by more than 50% within the timescale of multiple ionization, that is, within the time defined by the ultrashort pulse duration ($\sim 5 \text{ fs}$) and the lifetime of the Auger processes leading to the final charge state of the molecule. These data provide a

quantitative estimate of the radiation damage induced by an X-ray pulse on such a small molecule.

15.6

Summary and Outlook

Free-electron lasers, along with high-harmonics based femtosecond and attosecond sources, opened a new era for the study of light–matter interactions, expanding nonlinear physics and time-resolved measurements into the EUV and X-ray domain. Isolated attosecond pulses from HHG in gas targets, with pulse durations shorter than 100 as, are nowadays available in a few laboratories world-wide (see, [22, 23, 86, 182–184] and Chapters 10 and 12) and intensities approach the range needed for attosecond pump–attosecond probe experiments [86]. In parallel, HHG driven by mid-infrared lasers at few micron wavelength allowed the generation of rather intense kV X-ray pulses in the lab (see [84] and [85]). Intense femtosecond or attosecond pulses can be generated by HHG using the plasma mirror approach [185–187]. There are also promising developments in the field of plasma-based soft X-ray lasers, with a realistic perspective to reach mJ-scale for a lab-based femtosecond source [82] (see also Chapter 5). On top of this, FLASH, SCSS, SACLA, and LCLS continue their operation with optimized performance (e.g., FLASH reaching the effective repetition rate of 1 kHz, self-seeding demonstrated at LCLS, etc.). The first seeded EUV FEL is FERMI at Elettra and has been successfully commissioned [188]. The multikilohertz European XFEL, as well as XFEL facilities in Switzerland, China, and Korea are currently being built, as well as the next-generation machines FLASH 2 and LCLS 2. Thus, the superior properties of the novel light sources open up exciting research possibilities for ultrafast EUV and X-ray science and the rapidly increasing availability of these facilities makes experiments much more systematic and reproducible.

Numerous questions concerning basic few-photon reactions still need to be answered. One important example is the paradigm reaction of direct two-photon double ionization of He, where controversy remains despite more than hundred theoretical papers published within last two decades. No kinematically complete experimental data have been reported for this reaction, (in fact, no data beyond ion yields and momentum distributions) . With rapidly increasing repetition rates of intense EUV sources, this experiment might become feasible in the nearest future. The controversy regarding Xe^{21+} production at 90 eV [37] is yet to be resolved, with alternative explanations being put forward [71, 76–79]. In the X-ray domain, experiments on a simple system have been performed and there are growing demands for systems with an increasing degree of complexity. It remains to be established whether the same level of understanding can be reached for complex systems. On the other hand, the theory of intense X-ray–matter interaction has received enormous experimental input over the last few years and now tries to deliver the increasing level of detail required for the future, more elaborate experiments. In particular, some well-established quantum optics concepts are being revisited in

the X-ray domain, with the most prominent example being the LCLS-driven X-ray laser [189].

The success of early coherent diffractive imaging experiments at LCLS gave birth to a new field of femtosecond nanocrystallography, which already came from the proof-of-principle experiments [6–8] to real biological applications [190]. On the other hand, the enormous intensities needed for high-resolution single particle imaging are yet to be realized. When such intensities (higher than $\sim 10^{20} \text{ W/cm}^2$) will become routinely available (e.g., in the 100 nm focus of the Coherent X-ray Imaging end station at LCLS), there will be another important call for basic atomic and molecular experiments: one might need to revisit basic mechanisms of X-ray interactions with matter approaching the real “strong field” regime. Dedicated radiation damage studies will be required on rather large objects serving as targets for imaging schemes [7, 174], as well as on simple systems aiming to highlight individual atom dynamics as a response to the ultraintense X-ray field [176].

Numerous opportunities emerged for time-resolved experiments. As a direct continuation of the measurements described in Section 15.4, several ongoing and proposed projects aim at investigating other structural rearrangement reactions. Among those are isomerization processes (e.g., in haloethanes), ring-closure and -opening reactions in allene cations or in 1,3-cyclohexadiene, tracing ultrafast charge rearrangement in dissociating sulfur- or iodine-containing molecules upon core-shell photoabsorption, as well as watching the interatomic Coulombic decay of Ne dimers, predicted to occur on a 90-fs timescale [191]. In this contribution, only EUV-pump–EUV-probe schemes have been considered. However, numerous other pump–probe arrangements, mainly in two-color configuration, have been realized (see, e.g., reviews [126, 192, 193] for an incomplete selection of FEL and HHG-based experiments). Some HHG-based experiments featured $\sim 20\text{-as}$ time resolution [194]. At FLASH and LCLS, significant efforts have been undertaken to overcome the time jitter between the FEL pulses and a synchronized external laser [195–198]. In addition, two different types of split mirrors and delay units for X-rays are being developed, and first X-ray pump, X-ray probe experiments have been performed (R. Coffee: Time-resolved Auger relaxation via transient X-ray bleaching in O₂, unpublished results, 2013). The breadths and the mere number of projects underline the huge potential of EUV and X-ray experiments and, in particular, of pump–probe experiments appreciated by the ultrafast and strong field science community.

Acknowledgments

Most of the experiments reported here were supported by the Max Planck Society within the Max-Planck Advanced Study Group (ASG) at the Center for Free Electron Laser Science (CFEL) in Hamburg, Germany. This work would not have been possible without the sustained and enthusiastic support by the DESY, SCSS, and LCLS accelerator teams and beam line scientists. Parts of this research were carried out at the Linac Coherent Light Source (LCLS) at the SLAC National Accelerator Labo-

ratory. LCLS is an Office of Science User Facility operated for the US Department of Energy Office of Science by Stanford University. The author acknowledges the support from Chemical Sciences, Geosciences, and Biosciences Division, Office of Basic Energy Sciences, Office of Science, US Department of Energy.

References

- 1 Zewail, A.H. (2000) Femtochemistry: Atomic-scale dynamics of the chemical bond. *J. Phys. Chem. A*, **104** (24), 5660–5694.
- 2 Drenth, J. (1999) *Principles of Protein X-ray Crystallography*, Springer, New York.
- 3 Rupp, B. (2009) *Biomolecular Crystallography: Principles, Practice and Application to Structural Biology*, Garland Science, New York.
- 4 Breedlov Jr., J.R. and Trammell, G.T. (1970) Molecular microscopy – fundamental limitations. *Science*, **170** (3964), 1310–1313.
- 5 Neutze, R., Wouts, R., van der Spoel, D., Weckert, E., and Hajdu, J. (2000) Potential for biomolecular imaging with femtosecond X-ray pulses. *Nature*, **406** (6797), 752–757.
- 6 Chapman, H.N., Fromme, P., Barty, A., White, T.A., Kirian, R.A., Aquila, A., Hunter, M.S., Schulz, J., DePonte, D.P., Weierstall, U., Doak, R.B., Maia, F., Martin, A.V., Schlichting, I., Lomb, L., Coppola, N., Shoeman, R.L., Epp, S.W., Hartmann, R., Rolles, D., Rudenko, A., Foucar, L., Kimmel, N., Weidenspointner, G., Holl, P., Liang, M.N., Barthelmess, M., Caleman, C., Boutet, S., Bogan, M.J., Krzywinski, J., Bostedt, C., Bajt, S., Gumprecht, L., Rudek, B., Erk, B., Schmidt, C., Homke, A., Reich, C., Pietschner, D., Struder, L., Hauser, G., Gorke, H., Ullrich, J., Herrmann, S., Schaller, G., Schopper, F., Soltau, H., Kuhnle, K.U., Messerschmidt, M., Bozek, J.D., Hau-Riege, S.P., Frank, M., Hampton, C.Y., Sierra, R.G., Starodub, D., Williams, G.J., Hajdu, J., Timneanu, N., Seibert, M.M., Andreasson, J., Rocker, A., Jonsson, O., Svenda, M., Stern, S., Nass, K., Andritschke, R., Schroter, C.D., Krasniqi, F., Bott, M., Schmidt, K.E., Wang, X.Y., Grotjohann, I., Holton, J.M., Barends, T.R.M., Neutze, R., Marchesini, S., Fromme, R., Schorb, S., Rupp, D., Adolph, M., Gorkhover, T., Andersson, I., Hirsemann, H., Potdevin, G., Graafsma, H., Nilsson, B., and Spence, J.C.H. (2011) Femtosecond X-ray protein nanocrystallography. *Nature*, **470** (7332), 73–77.
- 7 Barty, A., Caleman, C., Aquila, A., Timneanu, N., Lomb, L., White, T.A., Andreasson, J., Arnlund, D., Bajt, S., Barends, T.R.M., Barthelmess, M., Bogan, M.J., Bostedt, C., Bozek, J.D., Coffee, R., Coppola, N., Davidsson, J., DePonte, D.P., Doak, R.B., Ekeberg, T., Elser, V., Epp, S.W., Erk, B., Fleckenstein, H., Foucar, L., Fromme, P., Graafsma, H., Gumprecht, L., Hajdu, J., Hampton, C.Y., Hartmann, R., Hartmann, A., Hauser, G., Hirsemann, H., Holl, P., Hunter, M.S., Johansson, L., Kassemeyer, S., Kimmel, N., Kirian, R.A., Liang, M.N., Maia, F., Malmerberg, E., Marchesini, S., Martin, A.V., Nass, K., Neutze, R., Reich, C., Rolles, D., Rudek, B., Rudenko, A., Scott, H., Schlichting, I., Schulz, J., Seibert, M.M., Shoeman, R.L., Sierra, R.G., Soltau, H., Spence, J.C.H., Stellato, F., Stern, S., Struder, L., Ullrich, J., Wang, X., Weidenspointner, G., Weierstall, U., Wunderer, C.B., and Chapman, H.N. (2012) Self-terminating diffraction gates femtosecond X-ray nanocrystallography measurements. *Nat. Photonics*, **6** (1), 35–40.
- 8 Boutet, S., Lomb, L., Williams, G.J., Barends, T.R.M., Aquila, A., Doak, R.B., Weierstall, U., DePonte, D.P., Steinbrenner, J., Shoeman, R.L., Messerschmidt, M., Barty, A., White, T.A., Kassemeyer, S., Kirian, R.A., Seibert, M.M., Montanez, P.A., Kenney, C., Herbst, R., Hart,

- P., Pines, J., Haller, G., Gruner, S.M., Philipp, H.T., Tate, M.W., Hromalik, M., Koerner, L.J., van Bakel, N., Morse, J., Ghosalves, W., Arnlund, D., Bogan, M.J., Caleman, C., Fromme, R., Hampton, C.Y., Hunter, M.S., Johansson, L.C., Katona, G., Kupitz, C., Liang, M.N., Martin, A.V., Nass, K., Redecke, L., Stellato, F., Timneanu, N., Wang, D.J., Zatsepin, N.A., Schafer, D., Defever, J., Neutze, R., Fromme, P., Spence, J.C.H., Chapman, H.N., and Schlichting, I. (2012) High-resolution protein structure determination by serial femtosecond crystallography. *Science*, **337** (6092), 362–364.
- 9** Seibert, M.M., Ekeberg, T., Maia, F.R.N.C., Svenda, M., Andreasson, J., Joensson, O., Odic, D., Iwan, B., Rocker, A., Westphal, D., Hantke, M., DePonte, D.P., Barty, A., Schulz, J., Gumprecht, L., Coppola, N., Aquila, A., Liang, M., White, T.A., Martin, A., Caleman, C., Stern, S., Abergel, C., Seltzer, V., Claverie, J.-M., Bostedt, C., Bozek, J.D., Boutet, S., Miahnahri, A.A., Messerschmidt, M., Krzywinski, J., Williams, G., Hodgson, K.O., Bogan, M.J., Hampton, C.Y., Sierra, R.G., Starodub, D., Andersson, I., Bajt, S., Barthelmess, M., Spence, J.C.H., Fromme, P., Weierstall, U., Kirian, R., Hunter, M., Doak, R.B., Marchesini, S., Hau-Riege, S.P., Frank, M., Shoeman, R.L., Lomb, L., Epp, S.W., Hartmann, R., Rolles, D., Rudenko, A., Schmidt, C., Foucar, L., Kimmel, N., Holl, P., Rudek, B., Erk, B., Hoemke, A., Reich, C., Pietschner, D., Weidenspointner, G., Strueder, L., Hauser, G., Gorke, H., Ullrich, J., Schlichting, I., Herrmann, S., Schaller, G., Schopper, F., Soltau, H., Kuehnle, K.-U., Andritschke, R., Schroeter, C.-D., Krasniqi, F., Bott, M., Schorb, S., Rupp, D., Adolph, M., Gorkhover, T., Hirsemann, H., Potdevin, G., Graafsma, H., Nilsson, B., Chapman, H.N., and Hajdu, J. (2011) Single mimivirus particles intercepted and imaged with an X-ray laser. *Nature*, **470** (7332), 78–81.
- 10** Loh, N.D., Hampton, C.Y., Martin, A.V., Starodub, D., Sierra, R.G., Barty, A., Aquila, A., Schulz, J., Lomb, L., Steinbrenner, J., Shoeman, R.L., Kassemeyer, S., Bostedt, C., Bozek, J., Epp, S.W., Erk, B., Hartmann, R., Rolles, D., Rudenko, A., Rudek, B., Foucar, L., Kimmel, N., Weidenspointner, G., Hauser, G., Holl, P., Pedersoli, E., Liang, M., Hunter, M.M., Gumprecht, L., Coppola, N., Wunderer, C., Graafsma, H., Maia, F., Ekeberg, T., Hantke, M., Fleckenstein, H., Hirsemann, H., Nass, K., White, T.A., Tobias, H.J., Farquar, G.R., Benner, W.H., Hau-Riege, S.P., Reich, C., Hartmann, A., Soltau, H., Marchesini, S., Bajt, S., Barthelmess, M., Bucksbaum, P., Hodgson, K.O., Struder, L., Ullrich, J., Frank, M., Schlichting, I., Chapman, H.N., and Bogan, M.J. (2012) Fractal morphology, imaging and mass spectrometry of single aerosol particles in flight. *Nature*, **486** (7404), 513–517.
- 11** Göppert-Mayer, M. (1931) Über Elementarakte mit zwei Quantensprüngen. *Ann. Phys.*, **9**, 273–294.
- 12** Hughes, V. and Grabner, L. (1950) The radiofrequency spectrum of Rb₈₅F and Rb₈₇F by the electric resonance method. *Phys. Rev.*, **79** (2), 314–322.
- 13** Keldysh, L.V. (1965) Ionization in field of a strong electromagnetic wave. *Sov. Phys. JETP*, **20** (5), 1307.
- 14** Perelomov, A.M., Popov, V.S., and Terentiev, M.V. (1966) Ionization of atoms in an alternating electric field 1. *Sov. Phys. JETP*, **23**, 924.
- 15** Perelomov, A.M., Popov, V.S., and Terentiev, M.V. (1966) Ionization of atoms in an alternating electric field 2. *Sov. Phys. JETP*, **24**, 207.
- 16** Nikishov, A.I. and Ritus, V.I. (1964) Quantum processes in the field of a plane electromagnetic wave and in a constant field. *Sov. Phys. JETP*, **19** (2), 529–541.
- 17** Reiss, H.R. (2008) Limits on tunneling theories of strong-field ionization. *Phys. Rev. Lett.*, **101** (4), 043002.
- 18** Reiss, H.R. (2010) Unsuitability of the Keldysh parameter for laser fields. *Phys. Rev. A*, **82** (2), 023418.
- 19** Topcu, T. and Robicheaux, F. (2012) Dichotomy between tunneling and multiphoton ionization in atomic photoionization: Keldysh parameter gamma ver-

- sus scaled frequency. *Phys. Rev. A*, **86** (5), 053407.
- 20** Agostini, P. and DiMauro, L.F. (2004) The physics of attosecond light pulses. *Rep. Progr. Phys.*, **67** (6), 813–855.
- 21** Krausz, F. and Ivanov, M. (2009) Attosecond physics. *Rev. Mod. Phys.*, **81** (1), 163–234.
- 22** Midorikawa, K. (2011) High-order harmonic generation and attosecond science. *Jpn. J. Appl. Phys.*, **50** (9), 090001.
- 23** Sansone, G., Poletto, L., and Nisoli, M. (2011) High-energy attosecond light sources. *Nat. Photonics*, **5** (11), 656–664.
- 24** Feldhaus, J., Arthur, J., and Hastings, J.B. (2005) X-ray free-electron lasers. *J. Phys. B*, **38** (9), S799–S819.
- 25** Ackermann, W., Asova, G., Ayvazyan, V., Azima, A., Baboi, N., Baehr, J., Balandin, V., Beutner, B., Brandt, A., Bolzmann, A., Brinkmann, R., Brovko, O.I., Castellano, M., Castro, P., Catani, L., Chiadroni, E., Choroba, S., Cianchi, A., Costello, J.T., Cubaynes, D., Dardis, J., Decking, W., Delsim-Hashemi, H., Delserieys, A., Di Pirro, G., Dohlus, M., Duesterer, S., Eckhardt, A., Edwards, H.T., Faatz, B., Feldhaus, J., Floettmann, K., Frisch, J., Froehlich, L., Garvey, T., Gensch, U., Gerth, C., Goerler, M., Golubeva, N., Grabosch, H.J., Grecki, M., Grimm, O., Hacker, K., Hahn, U., Han, J.H., Honkavaara, K., Hott, T., Huening, M., Ivanisenko, Y., Jaeschke, E., Jalmuzna, W., Jezynski, T., Kammering, R., Katalev, V., Kavanagh, K., Kennedy, E.T., Khodyachykh, S., Klose, K., Kocharyan, V., Koerfer, M., Kollewe, M., Koprek, W., Korepanov, S., Kostin, D., Krassilnikov, M., Kube, G., Kuhlmann, M., Lewis, C.L.S., Lilje, L., Limberg, T., Lipka, D., Loehl, F., Luna, H., Luong, M., Martins, M., Meyer, M., Michelato, P., Miltchev, V., Moeller, W.D., Monaco, L., Mueller, W.F.O., Napieralski, A., Napol, O., Nicolosi, P., Noelle, D., Nunez, T., Oppelt, A., Paganin, C., Paparella, R., Pchalek, N., Pedregosa-Gutierrez, J., Petersen, B., Petrosyan, B., Petrosyan, G., Petrosyan, L., Pflueger, J., Ploenjes, E., Poletto, L., Pozniak, K., Prat, E., Proch, D., Pucyk, P., Radcliffe, P., Redlin, H., Rehlich, K., Richter, M., Roehrs, M., Roensch, J., Romanik, R., Ross, M., Rossbach, J., Rybnikov, V., Sachwitz, M., Saldin, E.L., Sandner, W., Schlarb, H., Schmidt, B., Schmitz, M., Schmueser, P., Schneider, J.R., Schneidmiller, E.A., Schnepf, S., Schreiber, S., Seidel, M., Sertore, D., Shabunov, A.V., Simon, C., Simrock, S., Sombrowski, E., Sorokin, A.A., Spanknebel, P., Spesyvtsev, R., Staykov, L., Steffen, B., Stephan, F., Stulle, F., Thom, H., Tiedtke, K., Tischer, M., Toleikis, S., Treusch, R., Trines, D., Tsakov, I., Vogel, E., Weiland, T., Weise, H., Wellhoeffer, M., Wendt, M., Will, I., Winter, A., Wittenburg, K., Wurth, W., Yeates, P., Yurkov, M.V., Zagorodnov, I., and Zapfe, K. (2007) Operation of a free-electron laser from the extreme ultraviolet to the water window. *Nat. Photonics*, **1** (6), 336–342.
- 26** Shintake, T., Tanaka, H., Hara, T., Tanaka, T., Togawa, K., Yabashi, M., Otake, Y., Asano, Y., Bizen, T., Fukui, T., Goto, S., Higashiya, A., Hiroto, T., Hosoda, N., Inagaki, T., Inoue, S., Ishii, M., Kim, Y., Kimura, H., Kitamura, M., Kobayashi, T., Maesaka, H., Masuda, T., Matsui, S., Matsushita, T., Marechal, X., Nagasono, M., Ohashi, H., Ohata, T., Ohshima, T., Onoe, K., Shirasawa, K., Takagi, T., Takahashi, S., Takeuchi, M., Tamasaku, K., Tanaka, R., Tanaka, Y., Tanikawa, T., Togashi, T., Wu, S., Yamashita, A., Yanagida, K., Zhang, C., Kitamura, H., and Ishikawa, T. (2008) A compact free-electron laser for generating coherent radiation in the extreme ultraviolet region. *Nat. Photonics*, **2** (9), 555–559.
- 27** Ishikawa, T., Aoyagi, H., Asaka, T., Asano, Y., Azumi, N., Bizen, T., Ego, H., Fukami, K., Fukui, T., Furukawa, Y., Goto, S., Hanaki, H., Hara, T., Hasegawa, T., Hatsui, T., Higashiya, A., Hiroto, T., Hosoda, N., Ishii, M., Inagaki, T., Inubushi, Y., Itoga, T., Joti, Y., Kago, M., Kameshima, T., Kimura, H., Kirihara, Y., Kiyomichi, A., Kobayashi, T., Kondo, C., Kudo, T., Maesaka, H., Marechal, X.M., Masuda, T., Matsubara, S., Matsumoto, T., Matsushita, T., Matsui, S., Nagasono, M., Nariyama, N., Ohashi, H., Ohata, T., Ohshima, T., Ono, S., Otake, Y., Saji, C., Sakurai, T., Sato, T., Sawada,

- K., Seike, T., Shirasawa, K., Sugimoto, T., Suzuki, S., Takahashi, S., Takebe, H., Takeshita, K., Tamasaku, K., Tanaka, H., Tanaka, R., Tanaka, T., Togashi, T., Togawa, K., Tokuhisa, A., Tomizawa, H., Tono, K., Wu, S., Yabashi, M., Yamaga, M., Yamashita, A., Yanagida, K., Zhang, C., Shintake, T., Kitamura, H., and Kumagai, N. (2012) A compact X-ray free-electron laser emitting in the sub-angstrom region. *Nat. Photonics*, **6** (8), 540–544.
- 28** Emma, P., Akre, R., Arthur, J., Bionta, R., Bostedt, C., Bozek, J., Brachmann, A., Bucksbaum, P., Coffee, R., Decker, F.J., Ding, Y., Dowell, D., Edstrom, S., Fisher, A., Frisch, J., Gilevich, S., Hastings, J., Hays, G., Hering, P., Huang, Z., Iverson, R., Loos, H., Messerschmidt, M., Miahnahri, A., Moeller, S., Nuhn, H.D., Pile, G., Ratner, D., Rzepiela, J., Schultz, D., Smith, T., Stefan, P., Tompkins, H., Turner, J., Welch, J., White, W., Wu, J., Yocky, G., and Galayda, J. (2010) First lasing and operation of an angstrom-wavelength free-electron laser. *Nat. Photonics*, **4** (9), 641–647.
- 29** Nabekawa, Y., Hasegawa, H., Takahashi, E.J., and Midorikawa, K. (2005) Production of doubly charged helium ions by two-photon absorption of an intense sub-10-fs soft X-ray pulse at 42 eV photon energy. *Phys. Rev. Lett.*, **94** (4), 043001.
- 30** Hasegawa, H., Takahashi, E.J., Nabekawa, Y., Ishikawa, K.L., and Midorikawa, K. (2005) Multiphoton ionization of He by using intense high-order harmonics in the soft-X-ray region. *Phys. Rev. A*, **71** (2), 023407.
- 31** Wabnitz, H., de Castro, A.R.B., Gurtler, P., Laermann, T., Laasch, W., Schulz, J., and Moller, T. (2005) Multiple ionization of rare gas atoms irradiated with intense VUV radiation. *Phys. Rev. Lett.*, **94** (2), 023001.
- 32** Benis, E.P., Charalambidis, D., Kitsopoulos, T.N., Tsakiris, G.D., and Tzallas, P. (2006) Two-photon double ionization of rare gases by a superposition of harmonics. *Phys. Rev. A*, **74** (5), 051402 (R).
- 33** Sorokin, A.A., Bobashev, S.V., Tiedtke, K., and Richter, M. (2006) Multi-photon ionization of molecular nitrogen by femtosecond soft X-ray FEL pulses. *J. Phys. B*, **39** (14), L299–L304.
- 34** Foehlisch, A., Nagasono, M., Deppe, M., Suljoti, E., Hennies, F., Pietzsch, A., and Wurth, W. (2007) High-brilliance free-electron-laser photoionization of N₂: Ground-state depletion and radiation-field-induced modifications. *Phys. Rev. A*, **76** (1), 013411.
- 35** Nagasono, M., Suljoti, E., Pietzsch, A., Hennies, F., Wellhoefer, M., Hoeft, J.-T., Martins, M., Wurth, W., Treusch, R., Feldhaus, J., Schneider, J.R., and Foehlisch, A. (2007) Resonant two-photon absorption of extreme-ultraviolet free-electron-laser radiation in helium. *Phys. Rev. A*, **75** (5), 051406 (R).
- 36** Sorokin, A.A., Wellhoefer, M., Bobashev, S.V., Tiedtke, K., and Richter, M. (2007) X-ray-laser interaction with matter and the role of multiphoton ionization: Free-electron-laser studies on neon and helium. *Phys. Rev. A*, **75** (5), 051402 (R).
- 37** Sorokin, A.A., Bobashev, S.V., Feigl, T., Tiedtke, K., Wabnitz, H., and Richter, M. (2007) Photoelectric effect at ultra-high intensities. *Phys. Rev. Lett.*, **99** (21), 213002.
- 38** Moshammer, R., Jiang, Y.H., Foucar, L., Rudenko, A., Ergler, T., Schroeter, C.D., Luedemann, S., Zrost, K., Fischer, D., Titze, J., Jahnke, T., Schoeffler, M., Weber, T., Doerner, R., Zouros, T.J.M., Dorn, A., Ferger, T., Kuehnel, K.U., Duesterer, S., Treusch, R., Radcliffe, P., Ploenjes, E., and Ullrich, J. (2007) Few-photon multiple ionization of Ne and Ar by strong free-electron-laser pulses. *Phys. Rev. Lett.*, **98** (20) 203001.
- 39** Rudenko, A., Foucar, L., Kurka, M., Ergler, T., Kuehnel, K.U., Jiang, Y.H., Voitkiv, A., Najjari, B., Kheifets, A., Luedemann, S., Havermeier, T., Smolarski, M., Schoessler, S., Cole, K., Schoeffler, M., Doerner, R., Duesterer, S., Li, W., Keitel, B., Treusch, R., Gesch, M., Schroeter, C.D., Moshammer, R., and Ullrich, J. (2008) Recoil-ion momentum distributions for two-photon double ionization of He and Ne by 44 eV

- free-electron laser radiation. *Phys. Rev. Lett.*, **101** (7), 073003.
- 40** Sato, T., Okino, T., Yamanouchi, K., Yagishita, A., Kannari, F., Yamakawa, K., Midorikawa, K., Nakano, H., Yabashi, M., Nagasono, M., and Ishikawa, T. (2008) Dissociative two-photon ionization of N₂ in extreme ultraviolet by intense self-amplified spontaneous emission free electron laser light. *Appl. Phys. Lett.*, **92** (15), 154103.
- 41** Mitzner, R., Sorokin, A.A., Siemer, B., Roling, S., Rutkowski, M., Zacharias, H., Neeb, M., Noll, T., Siewert, F., Eberhardt, W., Richter, M., Juranic, P., Tiedtke, K., and Feldhaus, J. (2009) Direct autocorrelation of soft-X-ray free-electron-laser pulses by time-resolved two-photon double ionization of He. *Phys. Rev. A*, **80** (2), 025402.
- 42** Hikosaka, Y., Fushitani, M., Matsuda, A., Tseng, C.M., Hishikawa, A., Shigemasa, E., Nagasono, M., Tono, K., Togashi, T., Ohashi, H., Kimura, H., Senba, Y., Yabashi, M., and Ishikawa, T. (2010) Multiphoton double ionization of Ar in intense extreme ultraviolet laser fields studied by shot-by-shot photoelectron spectroscopy. *Phys. Rev. Lett.*, **105** (13), 133001.
- 43** Kurka, M., Rudenko, A., Foucar, L., Kuehnle, K.U., Jiang, Y.H., Ergler, T., Havermeier, T., Smolarski, M., Schoessl, S., Cole, K., Schoeffler, M., Doerner, R., Gensch, M., Duesterer, S., Treusch, R., Fritzsche, S., Grum-Grzhimailo, A.N., Gryzlova, E.V., Kabachnik, N.M., Schroeter, C.D., Moshammer, R., and Ullrich, J. (2009) Two-photon double ionization of Ne by free-electron laser radiation: a kinematically complete experiment. *J. Phys. B*, **42** (14), 141002.
- 44** Jiang, Y.H., Rudenko, A., Kurka, M., Kuehnle, K.U., Foucar, L., Ergler, T., Luedemann, S., Zrost, K., Ferger, T., Fischer, D., Dorn, A., Titze, J., Jahnke, T., Schoeffler, M., Schoessl, S., Havermeier, T., Smolarski, M., Cole, K., Doerner, R., Zouros, T.J.M., Duesterer, S., Treusch, R., Gensch, M., Schroeter, C.D., Moshammer, R., and Ullrich, J. (2009) EUV-photon-induced multiple ioniza-
- tion and fragmentation dynamics: from atoms to molecules. *J. Phys. B*, **42** (13), 134012.
- 45** Jiang, Y.H., Rudenko, A., Kurka, M., Kuehnle, K.U., Ergler, T., Foucar, L., Schoeffler, M., Schoessl, S., Havermeier, T., Smolarski, M., Cole, K., Doerner, R., Duesterer, S., Treusch, R., Gensch, M., Schroeter, C.D., Moshammer, R., and Ullrich, J. (2009) Few-photon multiple ionization of N₂ by extreme ultraviolet free-electron laser radiation. *Phys. Rev. Lett.*, **102** (12), 123002.
- 46** Fukuzawa, H., Motomura, K., Liu, X.J., Prumper, G., Okunishi, M., Ueda, K., Saito, N., Iwayama, H., Nagaya, K., Yao, M., Nagasono, M., Higashiya, A., Yabashi, M., Ishikawa, T., Ohashi, H., and Kimura, H. (2009) Ion momentum spectroscopy of N₂ and O₂ molecules irradiated by EUV free-electron laser pulses. *J. Phys. B*, **42** (18), 181001.
- 47** Motomura, K., Fukuzawa, H., Foucar, L., Liu, X.J., Prumper, G., Ueda, K., Saito, N., Iwayama, H., Nagaya, K., Murakami, H., Yao, M., Belkacem, A., Nagasono, M., Higashiya, A., Yabashi, M., Ishikawa, T., Ohashi, H., and Kimura, H. (2009) Multiple ionization of atomic argon irradiated by EUV free-electron laser pulses at 62 nm: evidence of sequential electron strip. *J. Phys. B*, **42** (22), 221003.
- 48** Jiang, Y.H., Rudenko, A., Perez-Torres, J.F., Herrwerth, O., Foucar, L., Kurka, M., Kuehnle, K.U., Toppin, M., Plesiat, E., Morales, F., Martin, F., Lezius, M., Kling, M.F., Jahnke, T., Doerner, R., Sanz-Vicario, J.L., van Tilborg, J., Belkacem, A., Schulz, M., Ueda, K., Zouros, T.J.M., Duesterer, S., Treusch, R., Schroeter, C.D., Moshammer, R., and Ullrich, J. (2010) Investigating two-photon double ionization of D₂ by XUV-pump-XUV-probe experiments. *Phys. Rev. A*, **81** (5), 021401 (R).
- 49** Foumouo, E., Kamta, G.L., Edah, G., and Piroux, B. (2006) Theory of multiphoton single and double ionization of two-electron atomic systems driven by short-wavelength electric fields: An ab initio treatment. *Phys. Rev. A*, **74** (6), 063409.

- 50** Shakeshaft, R. (2007) Two-photon single and double ionization of helium. *Phys. Rev. A*, **76** (6), 063405.
- 51** Horner, D.A., Morales, F., Rescigno, T.N., Martin, F., and McCurdy, C.W. (2007) Two-photon double ionization of helium above and below the threshold for sequential ionization. *Phys. Rev. A*, **76** (3), 030701(R).
- 52** Kheifets, A.S. (2007) Sequential two-photon double ionization of noble gas atoms. *J. Phys. B*, **40** (22), F313–F318.
- 53** Nikolopoulos, L.A.A. and Lambropoulos, P. (2007) Time-dependent theory of double ionization of helium under XUV radiation. *J. Phys. B*, **40** (7), 1347–1357.
- 54** Ivanov, I.A., and Kheifets, A.S. (2007) Two-photon double ionization of helium in the region of photon energies 42–50 eV. *Phys. Rev. A*, **75** (3), 033411.
- 55** Kheifets, A.S., Ivanov, A.I., and Bray, I. (2007) Different escape modes in two-photon double ionization of helium. *Phys. Rev. A*, **75** (2), 024702.
- 56** Horner, D.A., Rescigno, T.N., and McCurdy, C.W. (2008) Decoding sequential versus nonsequential two-photon double ionization of helium using nuclear recoil. *Phys. Rev. A*, **77** (3), 030703(R).
- 57** Horner, D.A., McCurdy, C.W., and Rescigno, T.N. (2008) Triple differential cross sections and nuclear recoil in two-photon double ionization of helium. *Phys. Rev. A*, **78** (4), 043416.
- 58** Hamonou, L., van der Hart, H.W., Dunseath, K.M., and Terao-Dunseath, M. (2008) Two-photon emission of a 2p electron from Ne^+ and consequences for sequential double ionization of Ne. *J. Phys. B*, **41** (1), 015603.
- 59** Makris, M.G. and Lambropoulos, P. (2008) Theoretical interpretation of multiphoton ionization of neon by soft-X-ray intense radiation. *Phys. Rev. A*, **77** (2), 023401.
- 60** Fritzsche, S., Grum-Grzhimailo, A.N., Gryzlova, E.V., and Kabachnik, N.M. (2008) Angular distributions and angular correlations in sequential two-photon double ionization of atoms. *J. Phys. B*, **41** (16), 165601.
- 61** Kheifets, A.S. (2009) Photoelectron angular correlation pattern in sequential two-photon double ionization of neon. *J. Phys. B*, **42** (13), 134016.
- 62** Lambropoulos, P. and Nikolopoulos, L.A.A. (2008) Angular distributions in double ionization of helium under XUV sub-femtosecond radiation. *New J. Phys.*, **10**, 025012.
- 63** Foumouo, E., Antoine, P., Piraux, B., Malegat, L., Bachau, H., and Shakeshaft, R. (2008) Evidence for highly correlated electron dynamics in two-photon double ionization of helium. *J. Phys. B*, **41** (5), 051001.
- 64** Feist, J., Nagele, S., Pazourek, R., Persson, E., Schneider, B.I., Collins, L.A., and Burgdoerfer, J. (2008) Nonsequential two-photon double ionization of helium. *Phys. Rev. A*, **77** (4), 043420.
- 65** Guan, X., Bartschat, K., and Schneider, B.I. (2008) Dynamics of two-photon double ionization of helium in short intense XUV laser pulses. *Phys. Rev. A*, **77** (4), 043421.
- 66** Antoine, P., Foumouo, E., and Piraux, B. (2008) Two-photon double ionization of helium: An experimental lower bound of the total cross section. *Phys. Rev. A*, **78** (2), 023415.
- 67** Feist, J., Pazourek, R., Nagele, S., Persson, E., Schneider, B.I., Collins, L.A., and Burgdoerfer, J. (2009) Electron correlation in two-photon double ionization of helium from attosecond to XFEL pulses. *J. Phys. B*, **42** (13), 134014.
- 68** Horner, D.A., Rescigno, T.N., and McCurdy, C.W. (2010) Nuclear recoil cross sections from time-dependent studies of two-photon double ionization of helium. *Phys. Rev. A*, **81** (2), 023410.
- 69** Hamonou, L., Lysaght, M.A., and van der Hart, H.W. (2010) Influence of autoionizing states on the pulse-length dependence of strong-field Ne^+ photoionization at 38.4 eV. *J. Phys. B*, **43** (4), 045601.
- 70** Delone, N.B., Krainov, V.P. (2000) *Multiphoton Processes in Atoms*, Springer, Berlin.
- 71** Makris, M.G., Lambropoulos, P., and Mihelic, A. (2009) Theory of multiphoton multielectron ionization of xenon under strong 93-eV radiation. *Phys. Rev. Lett.*, **102** (3), 033002.

- 72** Nagler, B., Zastrau, U., Faustlin, R.R., Vinko, S.M., Whitcher, T., Nelson, A.J., Sobierajski, R., Krzywinski, J., Chalupsky, J., Abreu, E., Bajt, S., Bornath, T., Burian, T., Chapman, H., Cihelka, J., Doppner, T., Duesterer, S., Dzelzainis, T., Fajardo, M., Forster, E., Fortmann, C., Galtier, E., Glenzer, S.H., Gode, S., Greggori, G., Hajkova, V., Heimann, P., Juha, L., Jurek, M., Khattak, F.Y., Khorsand, A.R., Klinger, D., Kozlova, M., Laermann, T., Lee, H.J., Lee, R.W., Meiweis-Broer, K.H., Mercere, P., Murphy, W.J., Przystawik, A., Redmer, R., Reinholz, H., Riley, D., Ropke, G., Rosmej, F., Saksl, K., Schott, R., Thiele, R., Tiggesbaumker, J., Toleikis, S., Tschentscher, T., Uschmann, I., Vollmer, H.J., and Wark, J.S. (2009) Turning solid aluminiun transparent by intense soft X-ray photoionization. *Nat. Phys.*, **5** (9), 693–696.
- 73** Young, L., Kanter, E.P., Kraessig, B., Li, Y., March, A.M., Pratt, S.T., Santra, R., Southworth, S.H., Rohringer, N., Di-Mauro, L.F., Doumy, G., Roedig, C.A., Berrah, N., Fang, L., Hoener, M., Bucksbaum, P.H., Cryan, J.P., Ghimire, S., Glownia, J.M., Reis, D.A., Bozek, J.D., Bostedt, C., and Messerschmidt, M. (2010) Femtosecond electronic response of atoms to ultra-intense X-rays. *Nature*, **466** (7302), 56–66.
- 74** Vinko, S.M., Cricosta, O., Cho, B.I., Engelhorn, K., Chung, H.K., Brown, C.R.D., Burian, T., Chalupsky, J., Falcone, R.W., Graves, C., Hajkova, V., Higginbotham, A., Juha, L., Krzywinski, J., Lee, H.J., Messerschmidt, M., Murphy, C.D., Ping, Y., Scherz, A., Schlotter, W., Toleikis, S., Turner, J.J., Vysin, L., Wang, T., Wu, B., Zastrau, U., Zhu, D., Lee, R.W., Heimann, P.A., Nagler, B., and Wark, J.S. (2012) Creation and diagnosis of a solid-density plasma with an X-ray free-electron laser. *Nature*, **482** (7383), 59–75.
- 75** Rudek, B., Son, S.K., Foucar, L., Epp, S.W., Erk, B., Hartmann, R., Adolph, M., Andritschke, R., Aquila, A., Berrah, N., Bostedt, C., Bozek, J., Coppola, N., Filsinger, F., Gorke, H., Gorkhov, T., Graafsma, H., Gumprecht, L., Hartmann, A., Hauser, G., Herrmann, S., Hirsemann, H., Holl, P., Homke, A., Journel, L., Kaiser, C., Kimmel, N., Krasnaniqi, F., Kuhnel, K.U., Matysek, M., Messerschmidt, M., Miesner, D., Moller, T., Moshammer, R., Nagaya, K., Nilsson, B., Potdevin, G., Pietschner, D., Reich, C., Rupp, D., Schaller, G., Schlichting, I., Schmidt, C., Schopper, F., Schorb, S., Schroter, C.D., Schulz, J., Simon, M., Soltau, H., Struder, L., Ueda, K., Weidenspointner, G., Santra, R., Ullrich, J., Rudenko, A., and Rolles, D. (2012) Ultra-efficient ionization of heavy atoms by intense X-ray free-electron laser pulses. *Nat. Photonics*, **6** (12), 857–864.
- 76** Richter, M., Amusia, M.Y., Bobashev, S.V., Feigl, T., Juranic, P.N., Martins, M., Sorokin, A.A., and Tiedtke, K. (2009) Extreme ultraviolet laser excites atomic giant resonance. *Phys. Rev. Lett.*, **102** (16), 163002.
- 77** Richter, M., Bobashev, S.V., Sorokin, A.A., and Tiedtke, K. (2010) Multiphoton ionization of atoms with soft X-ray pulses. *J. Phys. B*, **43** (19), 194005.
- 78** Richter, M. (2011) Atomic plasma excitations in the field of a soft X-ray laser. *J. Phys. B*, **44** (7), 075601.
- 79** Popruzhenko, S.V., Mur, V.D., Popov, V.S., and Bauer, D. (2008) Strong field ionization rate for arbitrary laser frequencies. *Phys. Rev. Lett.*, **101** (19), 193003.
- 80** Bilderback, D.H., Elleaume, P., and Weckert, E. (2005) Review of third and next generation synchrotron light sources. *J. Phys. B*, **38** (9), S773–S797.
- 81** Zeitoun, P., Faivre, G., Sebban, S., Moczek, T., Hallou, A., Fajardo, M., Aubert, D., Balcou, P., Burgi, F., Douillet, D., Kazamias, S., de Lacheze-Murel, G., Lefrou, T., le Pape, S., Mercere, P., Merdji, H., Morlens, A.S., Rousseau, J.P., and Valentin, C. (2004) A high-intensity highly coherent soft X-ray femtosecond laser seeded by a high harmonic beam. *Nature*, **431** (7007), 426–429.
- 82** Oliva, E., Fajardo, M., Li, L., Pittman, M., Le, T.T.T., Gautier, J., Lambert, G., Velarde, P., Ros, D., Sebban, S., and Zeitoun, P. (2012) A proposal for multi-tens of GW fully coherent femtosecond

- soft X-ray lasers. *Nat. Photonics*, **6** (11), 764–767.
- 83** Takahashi, E., Nabekawa, Y., and Midorikawa, K. (2002) Generation of 10- μ coherent extreme-ultraviolet light by use of high-order harmonics. *Opt. Lett.*, **27** (21), 1920–1922.
- 84** Chen, M.C., Arpin, P., Popmintchev, T., Gerrity, M., Zhang, B., Seaberg, M., Popmintchev, D., Murnane, M.M., and Kapteyn, H.C. (2010) Bright, coherent, ultrafast soft X-ray harmonics spanning the water window from a tabletop light source. *Phys. Rev. Lett.*, **105** (17), 173901.
- 85** Popmintchev, T., Chen, M.C., Popmintchev, D., Arpin, P., Brown, S., Alisauskas, S., Andriukaitis, G., Balciunas, T., Mucke, O.D., Pugzlys, A., Baltuska, A., Shim, B., Schrauth, S.E., Gaeta, A., Hernandez-Garcia, C., Plaja, L., Becker, A., Jaron-Becker, A., Murnane, M.M., and Kapteyn, H.C. (2012) Bright coherent ultrahigh harmonics in the keV X-ray regime from mid-infrared femtosecond lasers. *Science*, **336** (6086), 1287–1291.
- 86** Tzallas, P., Skantzakis, E., Nikolopoulos, L.A.A., Tsakiris, G.D., and Charalambidis, D. (2011) Extreme-ultraviolet pump-probe studies of one-femtosecond-scale electron dynamics. *Nat. Phys.*, **7** (10), 781–784.
- 87** Bozek, J.D. (2009) AMO instrumentation for the LCLS X-ray FEL. *Eur. Phys. J. – Spec. Top.*, **169**, 129–132.
- 88** Meyer, M., Costello, J.T., Duesterer, S., Li, W.B., and Radcliffe, P. (2010) Two-colour experiments in the gas phase. *J. Phys. B*, **43** (19), 194006.
- 89** Rudenko, A., Jiang, Y.H., Kurka, M., Kuhnel, K.U., Foucar, L., Herrwerth, O., Lezius, M., Kling, M.F., Schroeter, C.D., Moshammer, R., and Ullrich, J. (2010) Exploring few-photon, few-electron reactions at FLASH: from ion yield and momentum measurements to time-resolved and kinematically complete experiments. *J. Phys. B*, **43** (19), 194004.
- 90** Motomura, K., Foucar, L., Czasch, A., Saito, N., Jagutzki, O., Schmidt-Boecking, H., Doerner, R., Liu, X.J., Fukuzawa, H., Pruemper, G., Ueda, K., Okunishi, M., Shimada, K., Harada, T., Toyoda, M., Yanagihara, M., Yamamoto, M., Iwayama, H., Nagaya, K., Yao, M., Rudenko, A., Ullrich, J., Nagasano, M., Higashiyama, A., Yabashi, M., Ishikawa, T., Ohashi, H., and Kimura, H. (2009) Multi-coincidence ion detection system for EUV-FEL fragmentation experiments at SPring-8. *Nucl. Instrum. Meth. A*, **606** (3), 770–773.
- 91** Strueder, L., Eppa, S., Rolles, D., Hartmann, R., Holl, P., Lutz, G., Soltau, H., Eckart, R., Reich, C., Heinzinger, K., Thamm, C., Rudenko, A., Krasniqi, F., Kuehnel, K.-U., Bauer, C., Schroeter, C.-D., Moshammer, R., Techert, S., Miessner, D., Porro, M., Haelker, O., Meidinger, N., Kimmel, N., Andritschke, R., Schopper, F., Weidenspointner, G., Ziegler, A., Pietschner, D., Herrmann, S., Pietsch, U., Walenta, A., Leitenberger, W., Bostedt, C., Moeller, T., Rupp, D., Adolph, M., Graafsma, H., Hirsemann, H., Gaertner, K., Richter, R., Foucar, L., Shoeman, R.L., Schlichting, I., and Ullrich, J. (2010) Large-format, high-speed, X-ray pnCCDs combined with electron and ion imaging spectrometers in a multipurpose chamber for experiments at 4th generation light sources. *Nucl. Instrum. Meth. A*, **614** (3), 483–496.
- 92** Johnsson, P., Rouzee, A., Siu, W., Huismans, Y., Lepine, F., Marchenko, T., Duesterer, S., Tavella, F., Stojanovic, N., Redlin, H., Azima, A., and Vrakking, M.J.J. (2010) Characterization of a two-color pump-probe setup at FLASH using a velocity map imaging spectrometer. *Opt. Lett.*, **35** (24), 4163–4165.
- 93** Johnsson, P., Rouzee, A., Siu, W., Huismans, Y., Lepine, F., Marchenko, T., Dusterer, S., Tavella, F., Stojanovic, N., Azima, A., Treusch, R., Kling, M.F., and Vrakking, M.J.J. (2009) Field-free molecular alignment probed by the free electron laser in Hamburg (FLASH). *J. Phys. B*, **42** (13), 134017.
- 94** Eppink, A. and Parker, D.H. (1997) Velocity map imaging of ions and electrons using electrostatic lenses: Application in photoelectron and photofragment ion imaging of molecular oxygen. *Rev. Sci. Instrum.*, **68** (9), 3477–3484.
- 95** Ullrich, J., Moshammer, R., Dorn, A., Dorner, R., Schmidt, L.P.H., and

- Schniidt-Bocking, H. (2003) Recoil-ion and electron momentum spectroscopy: reaction-microscopes. *Rep. Progr. Phys.*, **66** (9), 1463–1545.
- 96** Ullrich, J., Moshammer, R., Dorner, R., Jagutzki, O., Mergel, V., Schmidt-Bocking, H., and Spielberger, L. (1997) Recoil-ion momentum spectroscopy. *J. Phys. B*, **30** (13), 2917–2974.
- 97** Dörner, R., Mergel, V., Jagutzki, O., Spielberger, L., Ullrich, J., Moshammer, R., and Schmidt-Bocking, H. (2000) Cold Target Recoil Ion Momentum Spectroscopy: a “momentum microscope” to view atomic collision dynamics. *Phys. Rep.*, **330** (2–3), 95–192.
- 98** Moshammer, R., Unverzagt, M., Schmitt, W., Ullrich, J., and Schmidt-Bocking, H. (1996) A 4π recoil-ion electron momentum analyzer: A high-resolution “microscope” for the investigation of the dynamics of atomic, molecular and nuclear reactions. *Nucl. Instrum. Meth. B*, **108** (4), 425–445.
- 99** de Jesus, V.L.B., Rudenko, A., Feuerstein, B., Zrost, K., Schroter, C.D., Moshammer, R., and Ullrich, J. (2004) Reaction microscopes applied to study atomic and molecular fragmentation in intense laser fields: non-sequential double ionization of helium. *J. Electron. Spectrosc. Relat. Phenom.*, **141** (2–3), 127–142.
- 100** Vredenborg, A., Roeterdink, W.G., and Janssen, M.H.M. (2008) A photoelectron-photoion coincidence imaging apparatus for femtosecond time-resolved molecular dynamics with electron time-of-flight resolution of 18 ps and energy resolution 3.5%. *Rev. Sci. Instrum.*, **79** (6), 063108.
- 101** Vredenborg, A., Lehmann, C.S., Irimia, D., Roeterdink, W.G., and Janssen, M.H.M. (2011) The reaction microscope: Imaging and pulse shaping control in photodynamics. *Chem. Phys. Chem.*, **12** (8), 1459–1473.
- 102** Kobayashi, Y., Sekikawa, T., Nabekawa, Y., and Watanabe, S. (1998) 27-fs extreme ultraviolet pulse generation by high-order harmonics. *Opt. Lett.*, **23** (1), 64–66.
- 103** Tzallas, P., Charalambidis, D., Papadogiannis, N.A., Witte, K., and Tsakiris, G.D. (2003) Direct observation of attosecond light bunching. *Nature*, **426** (6964), 267–271.
- 104** Benis, E.P., Tzallas, P., Nikolopoulos, L.A.A., Kovacev, M., Kalpouzos, C., Charalambidis, D., and Tsakiris, G.D. (2006) Frequency-resolved photoelectron spectra of two-photon ionization of He by an attosecond pulse train. *New J. Phys.*, **8**, 92.
- 105** Moshammer, R., Pfeifer, T., Rudenko, A., Jiang, Y.H., Foucar, L., Kurka, M., Kuehnel, K.U., Schroeter, C.D., Ullrich, J., Herrwerth, O., Kling, M.F., Liu, X.J., Motomura, K., Fukuzawa, H., Yamada, A., Ueda, K., Ishikawa, K.L., Nagaya, K., Iwayama, H., Sugishima, A., Mizoguchi, Y., Yase, S., Yao, M., Saito, N., Belkacem, A., Nagasano, M., Higashiya, A., Yabashi, M., Ishikawa, T., Ohashi, H., Kimura, H., and Togashi, T. (2011) Second-order autocorrelation of XUV FEL pulses via time resolved two-photon single ionization of He. *Opt. Express*, **19** (22), 21698–21706.
- 106** Saenz, A. and Lambropoulos, P. (1999) Theoretical two-, three- and four-photon ionization cross sections of helium in the XUV range. *J. Phys. B*, **32** (23), 5629–5637.
- 107** Papadogiannis, N.A., Nikolopoulos, L.A.A., Charalambidis, D., Tsakiris, G.D., Tzallas, P., and Witte, K. (2003) Two-photon ionization of he through a superposition of higher harmonics. *Phys. Rev. Lett.*, **90** (13), 133902.
- 108** Laermann, T., de Castro, A.R.B., Gurtler, P., Laasch, W., Schulz, J., Wabnitz, H., and Moller, T. (2005) Photoionization of helium atoms irradiated with intense vacuum ultraviolet free-electron laser light. Part I. Experimental study of multiphoton and single-photon processes. *Phys. Rev. A*, **72** (2), 023409.
- 109** Charalambidis, D., Tzallas, P., Papadogiannis, N.A., Nikolopoulos, L.A.A., Benis, E.P., and Tsakiris, G.D. (2006) Comment on “Photoionization of helium atoms irradiated with intense vacuum ultraviolet free-electron laser light. Part I. Experimental study of multiphoton

- and single-photon processes." *Phys. Rev. A*, **74** (3), 037401.
- 110** Ishikawa, K.L., Kawazura, Y., and Ueda, K. (2010) Two-photon ionization of atoms by ultrashort laser pulses. *J. Mod. Opt.*, **57** (11), 999–1007.
- 111** Ishikawa, K.L. and Ueda, K. (2012) Competition of resonant and nonresonant paths in resonance-enhanced two-photon single ionization of He by an ultrashort extreme-ultraviolet pulse. *Phys. Rev. Lett.*, **108** (3), 033003.
- 112** Smith, S.J. and Leuchs, G. (1988) Angular correlation in multiphoton ionization of atoms. *Adv. At. Mol. Phys.*, **24**, 157–221.
- 113** Nikolopoulos, L.A.A. and Lambropoulos, P. (2001) Multichannel theory of two-photon single and double ionization of helium. *J. Phys. B*, **34** (4), 545–564.
- 114** Colgan, J. and Pindzola, M.S. (2002) Core-excited resonance enhancement in the two-photon complete fragmentation of helium. *Phys. Rev. Lett.*, **88** (17), 173002.
- 115** Feng, L. and van der Hart, H.W. (2003) Two-photon double ionization of He. *J. Phys. B*, **36** (1), L1–L7.
- 116** Hu, S.X., Colgan, J., and Collins, L.A. (2005) Triple-differential cross-sections for two-photon double ionization of He near threshold. *J. Phys. B*, **38** (1), L35–L45.
- 117** Lambropoulos, P., Nikolopoulos, L.A.A., and Makris, M.G. (2005) Signatures of direct double ionization under XUV radiation. *Phys. Rev. A*, **72** (1), 013410.
- 118** Gryzlova, E.V., Ma, R., Fukuzawa, H., Motomura, K., Yamada, A., Ueda, K., Grum-Grzhimailo, A.N., Kabachnik, N.M., Strakhova, S.I., Rouzee, A., Hundermark, A., Vrakking, M.J.J., Johnsson, P., Nagaya, K., Yase, S., Mizoguchi, Y., Yao, M., Nagasano, M., Tono, K., Togashi, T., Senba, Y., Ohashi, H., Yabashi, M., and Ishikawa, T. (2011) Doubly resonant three-photon double ionization of Ar atoms induced by an EUV free-electron laser. *Phys. Rev. A*, **84** (6), 063405.
- 119** Bräuning, H., Dörner, R., Cocke, C.L., Krassig, B., Kheifets, A.S., Bray, I., Brauning-Demain, A., Carnes, K., Dreuil, S., Mergel, V., Richard, P., Ullrich, J., and Schmidt-Bocking, H. (1998) Absolute triple differential cross sections for photo-double ionization of helium – experiment and theory. *J. Phys. B*, **31** (23), 5149–5160.
- 120** Kurka, M., Feist, J., Horner, D.A., Rudenko, A., Jiang, Y.H., Kuehnel, K.U., Foucar, L., Rescigno, T.N., McCurdy, C.W., Pazourek, R., Nagele, S., Schulz, M., Herrwerth, O., Lezius, M., Kling, M.F., Schoeffler, M., Belkacem, A., Duesterer, S., Treusch, R., Schneider, B.I., Collins, L.A., Burgdoerfer, J., Schroeter, C.D., Moshammer, R., and Ullrich, J. (2010) Differential cross sections for non-sequential double ionization of He by 52 eV photons from the Free Electron Laser in Hamburg, FLASH. *New J. Phys.*, **12**, 073035.
- 121** Bachau, H. and Lambropoulos, P. (1991) Theory of the photoelectron-spectrum in double ionization through 2-photon absorption from He. *Phys. Rev. A*, **44** (1), R9–R12.
- 122** Laulan, S. and Bachau, H. (2003) Correlation effects in two-photon single and double ionization of helium. *Phys. Rev. A*, **68** (1), 013409.
- 123** Braune, M., Reinkoster, A., Viehaus, J., Lohmann, B., and Becker, U. (2007) Photoelectron spectroscopy of rare gas atoms following multi-photon ionization by FEL radiation, 25th Int. Conf. At. Electron. Photonic Collis., Freiburg, Germany, Fr034.
- 124** Gryzlova, E.V., Grum-Grzhimailo, A.N., Fritzsch, S., and Kabachnik, N.M. (2010) Angular correlations between two electrons emitted in the sequential two-photon double ionization of atoms. *J. Phys. B*, **43** (22), 225602.
- 125** Rouzee, A., Johnsson, P., Gryzlova, E.V., Fukuzawa, H., Yamada, A., Siu, W., Huismans, Y., Louis, E., Bijkerk, F., Holland, D.M.P., Grum-Grzhimailo, A.N., Kabachnik, N.M., Vrakking, M.J.J., and Ueda, K. (2011) Angle-resolved photoelectron spectroscopy of sequential three-photon triple ionization of neon at 90.5 eV photon energy. *Phys. Rev. A*, **83** (3), 031401 (R).

- 126** Ullrich, J., Rudenko, A., and Moshammer, R. (2012) Free-electron lasers: New avenues in molecular physics and photochemistry. *Annu. Rev. Phys. Chem.*, **63**, 635–660.
- 127** Yamada, A., Fukuzawa, H., Motomura, K., Liu, X.J., Foucar, L., Kurka, M., Okunishi, M., Ueda, K., Saito, N., Iwayama, H., Nagaya, K., Sugishima, A., Murakami, H., Yao, M., Rudenko, A., Kuehnel, K.U., Ullrich, J., Feifel, R., Czasch, A., Doerner, R., Nagasono, M., Higashiyama, A., Yabashi, M., Ishikawa, T., Ohashi, H., Kimura, H., and Togashi, T. (2010) Ion-ion coincidence studies on multiple ionizations of N_2 and O_2 molecules irradiated by extreme ultraviolet free-electron laser pulses. *J. Chem. Phys.*, **132** (20), 204305.
- 128** Akoury, D., Kreidi, K., Jahnke, T., Weber, T., Staudte, A., Schoeffler, M., Neumann, N., Titze, J., Schmidt, L.P.H., Czasch, A., Jagutzki, O., Costa Fraga, R.A., Grisenti, R.E., Diez Muino, R., Cherepkov, N.A., Semenov, S.K., Ranitovic, P., Cocke, C.L., Osipov, T., Adaniya, H., Thompson, J.C., Prior, M.H., Belkacem, A., Landers, A.L., Schmidt-Boecking, H., and Doerner, R. (2007) The simplest double slit: Interference and entanglement in double photoionization of H_2 . *Science*, **318** (5852), 949–952.
- 129** Martin, F., Fernandez, J., Havermeier, T., Foucar, L., Weber, T., Kreidi, K., Schoeffler, M., Schmidt, L., Jahnke, T., Jagutzki, O., Czasch, A., Benis, E.P., Osipov, T., Landers, A.L., Belkacem, A., Prior, M.H., Schmidt-Boecking, H., Cocke, C.L., and Doerner, R. (2007) Single photon-induced symmetry breaking of H_2 dissociation. *Science*, **315** (5812), 629–633.
- 130** Sanz-Vicario, J.L., Bachau, H., and Martin, F. (2006) Time-dependent theoretical description of molecular autoionization produced by femtosecond XUV laser pulses. *Phys. Rev. A*, **73** (3), 033410.
- 131** Ito, K., Hall, R.I., and Ukai, M. (1996) Dissociative photoionization of H_2 and D_2 in the energy region of 25–45 eV. *J. Chem. Phys.*, **104** (21), 8449–8457.
- 132** Niikura, H., Legare, F., Hasbani, R., Bandrauk, A.D., Ivanov, M.Y., Villeneuve, D.M., and Corkum, P.B. (2002) Sub-laser-cycle electron pulses for probing molecular dynamics. *Nature*, **417** (6892), 917–922.
- 133** Schoeffler, M.S., Titze, J., Petridis, N., Jahnke, T., Cole, K., Schmidt, L.P.H., Czasch, A., Akoury, D., Jagutzki, O., Williams, J.B., Cherepkov, N.A., Semenov, S.K., McCurdy, C.W., Rescigno, T.N., Cocke, C.L., Osipov, T., Lee, S., Prior, M.H., Belkacem, A., Landers, A.L., Schmidt-Boecking, H., Weber, T., and Doerner, R. (2008) Ultrafast probing of core hole localization in N_2 . *Science*, **320** (5878), 920–923.
- 134** Ahmad, M., Lablanquie, P., Penent, F., Lambourne, J.G., Hall, R.I., and D'Eland, J.H. (2006) Structure and fragmentation dynamics of N_2^{2+} ions in double photoionization experiments. *J. Phys. B*, **39** (17), 3599–3616.
- 135** Reddish, T.J., Colgan, J., Bolognesi, P., Avaldi, L., Gisselbrecht, M., Lavallee, M., Pindzola, M.S., and Huetz, A. (2008) Physical interpretation of the “Kinetic Energy Release” effect in the double photoionization of H_2 . *Phys. Rev. Lett.*, **100** (19), 193001.
- 136** Franceschi, P., Ascenzi, D., Tosi, P., Thissen, R., Zabka, J., Roithova, J., Rickerts, C.L., De Simone, M., and Coreno, M. (2007) Dissociative double photoionization of N_2 using synchrotron radiation: Appearance energy of the N^{2+} dication. *J. Chem. Phys.*, **126** (13), 134310.
- 137** Rolles, D., Braune, M., Cvejanovic, S., Gessner, O., Hentges, R., Korica, S., Langer, B., Lischke, T., Prumper, G., Reinkoster, A., Viehaus, J., Zimmermann, B.R., McKoy, V., and Becker, U. (2005) Isotope-induced partial localization of core electrons in the homonuclear molecule N_2 . *Nature*, **437** (7059), 711–715.
- 138** Eremina, E., Liu, X., Rottke, H., Sandner, W., Schatzel, M.G., Dreischuh, A., Paulus, G.G., Walther, H., Moshammer, R., and Ullrich, J. (2004) Influence of molecular structure on double ionization of N_2 and O_2 by high intensity ultrashort laser pulses. *Phys. Rev. Lett.*, **92** (17), 173001.

- 139** Zeidler, D., Staudte, A., Bardon, A.B., Villeneuve, D.M., Dorner, R. and Corkum, P.B. (2005) Controlling attosecond double ionization dynamics via molecular alignment. *Phys. Rev. Lett.*, **95** (20), 203003.
- 140** Gagnon, E., Ranitovic, P., Tong, X.-M., Cocke, C.L., Murnane, M.M., Kapteyn, H.C., and Sandhu, A.S. (2007) Soft X-ray-driven femtosecond molecular dynamics. *Science*, **317** (5843), 1374–1378.
- 141** Lundqvist, M., Edvardsson, D., Baltzer, P., and Wannberg, B. (1996) Doppler-free kinetic energy release spectrum of N_2^{2+} . *J. Phys. B*, **29** (8), 1489–1499.
- 142** Bandrauk, A.D., Musaev, D.G., and Morokuma, K. (1999) Electronic states of the triply charged molecular ion N_2^{3+} and laser-induced Coulomb explosion. *Phys. Rev. A*, **59** (6), 4309–4315.
- 143** Kling, M.F. and Vrakking, M.J.J. (2008) Attosecond electron dynamics. *Annu. Rev. Phys. Chem.*, **59**, 463–492.
- 144** Sorgenfrei, F., Schlotter, W.F., Beeck, T., Nagasono, M., Gieschen, S., Meyer, H., Foehlisch, A., Beye, M., and Wurth, W. (2010) The extreme ultraviolet split and femtosecond delay unit at the plane grating monochromator beamline PG2 at FLASH. *Rev. Sci. Instrum.*, **81** (4), 043107.
- 145** Mitzner, R., Siemer, B., Neeb, M., Noll, T., Siewert, F., Roling, S., Rutkowski, M., Sorokin, A.A., Richter, M., Juranic, P., Tiedtke, K., Feldhaus, J., Eberhardt, W., and Zacharias, H. (2008) Spatio-temporal coherence of free electron laser pulses in the soft X-ray regime. *Opt. Express*, **16** (24), 19909–19919.
- 146** Jiang, Y.H., Pfeifer, T., Rudenko, A., Herrwerth, O., Foucar, L., Kurka, M., Kuehnel, K.U., Lezius, M., Kling, M.F., Liu, X., Ueda, K., Duesterer, S., Treusch, R., Schroeter, C.D., Moshammer, R., and Ullrich, J. (2010) Temporal coherence effects in multiple ionization of N_2 via XUV pump-probe autocorrelation. *Phys. Rev. A*, **82** (4), 041403 (R).
- 147** Saldin, E., Schneidmiller, E., and Yurkov, M. (2000) The Physics of Free Electron Lasers, Springer, Heidelberg.
- 148** Pfeifer, T., Jiang, Y., Duesterer, S., Moshammer, R., and Ullrich, J. (2010) Partial-coherence method to model experimental free-electron laser pulse statistics. *Opt. Lett.*, **35** (20), 3441–3443.
- 149** Fruehling, U., Wieland, M., Gensch, M., Gebert, T., Schuette, B., Krikunova, M., Kalms, R., Budzyn, F., Grimm, O., Rossbach, J., Ploenjes, E. and Drescher, M. (2009) Single-shot terahertz-field-driven X-ray streak camera. *Nat. Photonics*, **3** (9), 523–528.
- 150** Schlotter, W.F., Sorgenfrei, F., Beeck, T., Beye, M., Gieschen, S., Meyer, H., Nagasano, M., Foehlisch, A., and Wurth, W. (2010) Longitudinal coherence measurements of an extreme-ultraviolet free-electron laser. *Opt. Lett.*, **35** (3), 372–374.
- 151** Jiang, Y.H., Rudenko, A., Perez-Torres, J.F., Herrwerth, O., Foucar, L., Kurka, M., Kuehnel, K.U., Toppin, M., Plesiat, E., Morales, F., Martin, F., Lezius, M., Kling, M.F., Jahnke, T., Doerner, R., Sanz-Vicario, J.L., van Tilborg, J., Belkacem, A., Schulz, M., Ueda, K., Zouros, T.J.M., Duesterer, S., Treusch, R., Schroeter, C.D., Moshammer, R., and Ullrich, J. (2010) Investigating two-photon double ionization of D_2 by XUV-pump-XUV-probe experiments. *Phys. Rev. A*, **81** (5), 051402 (R).
- 152** Meyer, K., Ott, C., Raith, P., Kaldun, A., Jiang, Y.H., Senftleben, A., Kurka, M., Moshammer, R., Ullrich, J., and Pfeifer, T. (2012) Noisy optical pulses enhance the temporal resolution of pump-probe spectroscopy. *Phys. Rev. Lett.*, **108** (9), 098302.
- 153** Magrakvelidze, M., Herrwerth, O., Jiang, Y.H., Rudenko, A., Kurka, M., Foucar, L., Kuhnel, K.U., Kubel, M., Johnson, N.G., Schroter, C.D., Dusterer, S., Treusch, R., Lezius, M., Ben-Itzhak, I., Moshammer, R., Ullrich, J., Kling, M.F., and Thumm, U. (2012) Tracing nuclear-wave-packet dynamics in singly and doubly charged states of N_2 and O_2 with XUV-pump-XUV-probe experiments. *Phys. Rev. A*, **86** (1), 013415.
- 154** Jiang, Y.H., Rudenko, A., Herrwerth, O., Foucar, L., Kurka, M., Kuhnel, K.U., Lezius, M., Kling, M.F., van Tilborg, J., Belkacem, A., Ueda, K., Dusterer, S.,

- Treusch, R., Schroter, C.D., Moshammer, R., and Ullrich, J. (2010) Ultrafast extreme ultraviolet induced isomerization of acetylene cations. *Phys. Rev. Lett.*, **105** (26), 263002.
- 155** Herzberg, G. (1971) Spectra and structures of molecular ions. *Q. Rev.*, **25** (2), 201.
- 156** Spence, J.C.H., Weierstall, U., and Chapman, H.N. (2012) X-ray lasers for structural and dynamic biology. *Rep. Prog. Phys.*, **75** (10), 102601.
- 157** Richardson, V., Costello, J.T., Cubaynes, D., Dusterer, S., Feldhaus, J., van der Hart, H.W., Juranic, P., Li, W.B., Meyer, M., Richter, M., Sorokin, A.A., and Tiedke, K. (2010) Two-photon inner-shell ionization in the extreme ultraviolet. *Phys. Rev. Lett.*, **105** (1), 013001.
- 158** Hoener, M., Fang, L., Kornilov, O., Gessner, O., Pratt, S.T., Guehr, M., Kanter, E.P., Blaga, C., Bostedt, C., Bozek, J.D., Bucksbaum, P.H., Buth, C., Chen, M., Coffee, R., Cryan, J., DiMauro, L.F., Glownia, M., Hosler, E., Kukk, E., Leone, S.R., McFarland, B., Messerschmidt, M., Murphy, B., Petrovic, V., Rollés, D., and Berrah, N. (2010) Ultraintense X-ray induced ionization, dissociation, and frustrated absorption in molecular nitrogen. *Phys. Rev. Lett.*, **104** (25), 083005.
- 159** Fang, L., Osipov, T., Murphy, B., Tarantelli, F., Kukk, E., Cryan, J.P., Glownia, M., Bucksbaum, P.H., Coffee, R.N., Chen, M., Buth, C., and Berrah, N. (2012) Multiphoton ionization as a clock to reveal molecular dynamics with intense short X-ray free electron laser pulses. *Phys. Rev. Lett.*, **109** (26), 263001.
- 160** Rohringer, N. and Santra, R. (2007) X-ray nonlinear optical processes using a self-amplified spontaneous emission free-electron laser. *Phys. Rev. A*, **76** (3), 033416.
- 161** Fang, L., Hoener, M., Gessner, O., Tarantelli, F., Pratt, S.T., Kornilov, O., Buth, C., Guehr, M., Kanter, E.P., Bostedt, C., Bozek, J.D., Bucksbaum, P.H., Chen, M., Coffee, R., Cryan, J., Glownia, M., Kukk, E., Leone, S.R., and Berrah, N. (2010) Double core-hole production in N₂: Beating the Auger clock. *Phys. Rev. Lett.*, **105** (8), 083005.
- 162** Cryan, J.P., Glownia, J.M., Andreasson, J., Belkacem, A., Berrah, N., Blaga, C.I., Bostedt, C., Bozek, J., Buth, C., DiMauro, L.F., Fang, L., Gessner, O., Guehr, M., Hajdu, J., Hertlein, M.P., Hoener, M., Kornilov, O., Marangos, J.P., March, A.M., McFarland, B.K., Merdji, H., Petrovic, V.S., Raman, C., Ray, D., Reis, D., Tarantelli, F., Trigo, M., White, J.L., White, W., Young, L., Bucksbaum, P.H., and Coffee, R.N. (2010) Auger electron angular distribution of double core-hole states in the molecular reference frame. *Phys. Rev. Lett.*, **105** (8), 083004.
- 163** Berrah, N., Fang, L., Murphy, B., Osipov, T., Ueda, K., Kukk, E., Feifel, R., van der Meulen, P., Salén, P., Schmidt, H.T., Thomas, R.D., Larsson, M., Richter, R., Prince, K.C., Bozek, J.D., Bostedt, C., Wada, S.-I., Piancastelli, M.N., Tashiro, M., and Ehara, M. (2011) Double-core-hole spectroscopy for chemical analysis with an intense X-ray femtosecond laser. *Proc. Natl. Acad. Sci. USA*, **108** (41), 16912–16915.
- 164** Salén, P., van der Meulen, P., Schmidt, H.T., Thomas, R.D., Larsson, M., Feifel, R., Piancastelli, M.N., Fang, L., Murphy, B., Osipov, T., Berrah, N., Kukk, E., Ueda, K., Bozek, J.D., Bostedt, C., Wada, S., Richter, R., Feyer, V., and Prince, K.C. (2012) Experimental verification of the chemical sensitivity of two-site double core-hole states formed by an X-ray free-electron laser. *Phys. Rev. Lett.*, **108** (19), 153003.
- 165** Doumy, G., Roedig, C., Son, S.K., Blaga, C.I., DiChiara, A.D., Santra, R., Berrah, N., Bostedt, C., Bozek, J.D., Bucksbaum, P.H., Cryan, J.P., Fang, L., Ghimire, S., Glownia, J.M., Hoener, M., Kanter, E.P., Kraessig, B., Kuebel, M., Messerschmidt, M., Paulus, G.G., Reis, D.A., Rohringer, N., Young, L., Agostini, P., and DiMauro, L.F. (2011) Nonlinear atomic response to intense ultrashort X-rays. *Phys. Rev. Lett.*, **106** (8), 083002.
- 166** Sytcheva, A., Pabst, S., Son, S.-K., and Santra, R. (2012) Enhanced nonlinear response of Ne⁸⁺ to intense ultrafast X-rays. *Phys. Rev. A*, **85** (2), 023414.

- 167** Son, S.K. and Santra, R. (2011) XATOM – an integrated toolkit for X-ray and atomic physics, CFEL Report, vol. 1, DESY, pp. 304.
- 168** Son, S.-K. and Santra, R. (2012) Monte Carlo calculation of ion, electron, and photon spectra of xenon atoms in X-ray free-electron laser pulses. *Phys. Rev. A*, **85** (6), 063415.
- 169** Thomas, H., Helal, A., Hoffmann, K., Kandadai, N., Keto, J., Andreasson, J., Iwan, B., Seibert, M., Timneanu, N., Hajdu, J., Adolph, M., Gorkhover, T., Rupp, D., Schorb, S., Moeller, T., Doumy, G., DiMauro, L.F., Hoener, M., Murphy, B., Berrah, N., Messerschmidt, M., Bozek, J., Bostedt, C., and Ditmire, T. (2012) Explosions of xenon clusters in ultraintense femtosecond X-ray pulses from the LCLS free electron laser. *Phys. Rev. Lett.*, **108** (13), 133401.
- 170** Martin, S., Bredy, R., Bernard, J., Desesquelles, J., and Chen, L. (2002) Very fast hollow-atom decay processes in Xe^{30+} - C_{60} collisions. *Phys. Rev. Lett.*, **89** (18), 183401.
- 171** Fukuzawa, H., Gryzlova, E.V., Motomura, K., Yamada, A., Ueda, K., Grum-Grzhimailo, A.N., Strakhova, S.I., Nagaya, K., Sugishima, A., Mizoguchi, Y., Iwayama, H., Yao, M., Saito, N., Piseri, P., Mazza, T., Devetta, M., Coreno, M., Nagasono, M., Tono, K., Yabashi, M., Ishikawa, T., Ohashi, H., Kimura, H., Togashi, T., and Senba, Y. (2010) Photoelectron spectroscopy of sequential three-photon double ionization of Ar irradiated by EUV free-electron laser pulses. *J. Phys. B*, **43** (11), 111001.
- 172** Miyauchi, N., Adachi, J., Yagishita, A., Sako, T., Koike, F., Sato, T., Iwasaki, A., Okino, T., Yamanouchi, K., Midorikawa, K., Yamakawa, K., Kannari, F., Nakano, H., Nagasono, M., Tono, K., Yabashi, M., Ishikawa, T., Togashi, T., Ohashi, H., Kimura, H., and Senba, Y. (2011) Three-photon double ionization of Ar studied by photoelectron spectroscopy using an extreme ultraviolet free-electron laser: Manifestation of resonance states of an intermediate Ar^+ ion. *J. Phys. B*, **44** (7), 071001.
- 173** Rudek, B., Rolles, D., Son, S.K., Foucar, L., Erk, B., Epp, S., Boll, R., Anielski, D., Bostedt, C., Schorb, S., Coffee, R., Bozek, J., Trippel, S., Marchenko, T., Simon, M., Christensen, L., De, S., Wada, S.i., Ueda, K., Schlichting, I., Santra, R., Ullrich, J., and Rudenko, A. (2013) Resonance-enhanced multiple ionization of krypton at an X-ray free-electron laser. *Phys. Rev. A*, **87** (2), 023413.
- 174** Lomb, L., Barends, T.R.M., Kassemeyer, S., Aquila, A., Epp, S.W., Erk, B., Foucar, L., Hartmann, R., Rudek, B., Rolles, D., Rudenko, A., Shoeman, R.L., Andreasson, J., Bajt, S., Barthelmess, M., Barty, A., Bogan, M.J., Bostedt, C., Bozek, J.D., Caleman, C., Coffee, R., Coppola, N., DePonte, D.P., Doak, R.B., Ekeberg, T., Fleckenstein, H., Fromme, P., Gebhardt, M., Graafsma, H., Gumprecht, L., Hampton, C.Y., Hartmann, A., Hauser, G., Hirsemann, H., Holl, P., Holton, J.M., Hunter, M.S., Kabsch, W., Kimmel, N., Kirian, R.A., Liang, M.N., Maia, F., Meinhart, A., Marchesini, S., Martin, A.V., Nass, K., Reich, C., Schulz, J., Seibert, M.M., Sierra, R., Soltau, H., Spence, J.C.H., Steinbrener, J., Stellato, F., Stern, S., Timneanu, N., Wang, X.Y., Weidenspointner, G., Weierstall, U., White, T.A., Wunderer, C., Chapman, H.N., Ullrich, J., Struder, L., and Schlichting, I. (2011) Radiation damage in protein serial femtosecond crystallography using an X-ray free-electron laser. *Phys. Rev. B*, **84** (21), 021411.
- 175** Jurek, Z. and Faigel, G. (2009) The effect of inhomogeneities on single-molecule imaging by hard XFEL pulses. *Eur. Phys. Lett.*, **86** (6), 68003.
- 176** Erk, B., Rolles, D., Foucar, L., Rudek, B., Epp, S.W., Cryle, M., Bostedt, C., Schorb, S., Bozek, J., Rouzee, A., Hundertmark, A., Marchenko, T., Simon, M., Filsinger, F., Christensen, L., De, S., Trippel, S., Kupper, J., Stapelfeldt, H., Wada, S., Ueda, K., Swiggers, M., Messerschmidt, M., Schroter, C.D., Moshammer, R., Schlichting, I., Ullrich, J., and Rudenko, A. (2013) Ultrafast charge rearrangement and nuclear dynamics upon inner-shell multiple ion-

- ization of small polyatomic molecules. *Phys. Rev. Lett.*, **110** (5), 053003.
- 177** Duesterer, S., Radcliffe, P., Bostedt, C., Bozek, J., Cavalieri, A.L., Coffee, R., Costello, J.T., Cubaynes, D., DiMaurro, L.F., Ding, Y., Doumy, G., Gruener, F., Helml, W., Schweinberger, W., Kienberger, R., Maier, A.R., Messerschmidt, M., Richardson, V., Roedig, C., Tschentscher, T., and Meyer, M. (2011) Femtosecond X-ray pulse length characterization at the Linac Coherent Light Source free-electron laser. *New J. Phys.*, **13**, 093024.
- 178** Ding, Y., Brachmann, A., Decker, F.J., Dowell, D., Emma, P., Frisch, J., Gilevich, S., Hays, G., Hering, P., Huang, Z., Iverson, R., Loos, H., Miahnahri, A., Nuhn, H.D., Ratner, D., Turner, J., Welch, J., White, W., and Wu, J. (2009) Measurements and simulations of ultralow emittance and ultrashort electron beams in the Linac coherent light source. *Phys. Rev. Lett.*, **102** (25), 254801.
- 179** Shigemasa, E., Ueda, K., Sato, Y., Yagishita, A., Maezawa, H., Sasaki, T., Ukai, M., and Hayaishi, T. (1990) Ionic fragmentation of SiH₄ following the K-shell excitation. *Phys. Scr.*, **41** (1), 67–70.
- 180** Campbell, J.L. and Papp, T. (2001) Widths of the atomic K-N7 levels. *At. Data Nucl. Data Tabl.*, **77** (1), 1–56.
- 181** Simon, M., Lavallee, M., Meyer, M., and Morin, P. (1996) Multicoincidence mass spectrometry of core excited molecules. *J. Electron. Spectrosc. Relat. Phenom.*, **79**, 401–406.
- 182** Sola, I.J., Mevel, E., Elouga, L., Constant, E., Strelkov, V., Poletto, L., Villoresi, P., Benedetti, E., Caumes, J.P., Stagira, S., Vozzi, C., Sansone, G., and Nisoli, M. (2006) Controlling attosecond electron dynamics by phase-stabilized polarization gating. *Nat. Phys.*, **2** (5), 319–322.
- 183** Schultze, M., Goulielmakis, E., Uiberacker, M., Hofstetter, M., Kim, J., Kim, D., Krausz, F., and Kleineberg, U. (2007) Powerful 170-attosecond XUV pulses generated with few-cycle laser pulses and broadband multilayer optics. *New J. Phys.*, **9**, 243.
- 184** Gilbertson, S., Chini, M., Feng, X.M., Khan, S., Wu, Y., and Chang, Z.H. (2010) Monitoring and controlling the electron dynamics in helium with isolated attosecond pulses. *Phys. Rev. Lett.*, **105** (26), 263003.
- 185** Thaury, C., Quere, F., Geindre, J.P., Levy, A., Ceccotti, T., Monot, P., Bougeard, M., Reau, F., D’Oliveira, P., Audebert, P., Marjoribanks, R. and Martin, P.H. (2007) Plasma mirrors for ultrahigh-intensity optics. *Nat. Phys.*, **3** (6), 424–429.
- 186** Teubner, U., and Gibbon, P. (2009) High-order harmonics from laser-irradiated plasma surfaces. *Rev. Mod. Phys.*, **81** (2), 445–479.
- 187** Wheeler, J.A., Borot, A., Monchoce, S., Vincenti, H., Ricci, A., Malvache, A., Lopez-Martens, R., and Quere, F. (2012) Attosecond lighthouses from plasma mirrors. *Nat. Photonics*, **6** (12), 828–832.
- 188** Allaria, E., Appio, R., Badano, L., Barletta, W.A., Bassanese, S., Biedron, S.G., Borga, A., Busetto, E., Castronovo, D., Cinquegrana, P., Cleva, S., Cocco, D., Cornacchia, M., Craievich, P., Cudin, I., D’Auria, G., Dal Forno, M., Danailov, M.B., De Monte, R., De Ninno, G., Delgiusto, P., Demidovich, A., Di Mitri, S., Diviacco, B., Fabris, A., Fabris, R., Fawley, W., Ferianis, M., Ferrari, E., Ferry, S., Froehlich, L., Furlan, P., Gaio, G., Gelmetti, F., Giannessi, L., Giannini, M., Gobessi, R., Ivanov, R., Karantzoulis, E., Lonza, M., Lutman, A., Mahieu, B., Milloch, M., Milton, S.V., Musardo, M., Nikolov, I., Noe, S., Parmigiani, F., Penico, G., Petronio, M., Pivetta, L., Predonzani, M., Rossi, F., Rumiz, L., Salom, A., Scafuri, C., Serpico, C., Sigalotti, P., Spampinati, S., Spezzani, C., Svandrik, M., Svetina, C., Tazzari, S., Trovo, M., Umer, R., Vascotto, A., Veronese, M., Visintini, R., Zaccaria, M., Zangrandi, D., and Zangrandi, M. (2012) Highly coherent and stable pulses from the FERMI seeded free-electron laser in the extreme ultraviolet. *Nat. Photonics*, **6** (10), 699–704.
- 189** Rohringer, N., Ryan, D., London, R.A., Purvis, M., Albert, F., Dunn, J., Bozek, J.D., Bostedt, C., Graf, A., Hill, R., Haurie, S.P., and Rocca, J.J. (2012) Atomic inner-shell X-ray laser at 1.46 nanome-

- tres pumped by an X-ray free-electron laser. *Nature*, **481** (7382), 488–491.
- 190** Redecke, L., Nass, K., DePonte, D.P., White, T.A., Rehders, D., Barty, A., Stellato, F., Liang, M.N., Barends, T.R.M., Boutet, S., Williams, G.J., Messerschmidt, M., Seibert, M.M., Aquila, A., Arnlund, D., Bajt, S., Barth, T., Bogan, M.J., Caleman, C., Chao, T.C., Doak, R.B., Fleckenstein, H., Frank, M., Fromme, R., Galli, L., Grotjohann, I., Hunter, M.S., Johansson, L.C., Kassemeyer, S., Katona, G., Kirian, R.A., Koopmann, R., Kupitz, C., Lomb, L., Martin, A.V., Mogk, S., Neutze, R., Shoeman, R.L., Steinbrener, J., Timneanu, N., Wang, D.J., Weierstall, U., Zatsepina, N.A., Spence, J.C.H., Fromme, P., Schlichting, I., Duszenko, M., Betzel, C., and Chapman, H.N. (2013) Natively inhibited trypanosoma brucei Cathepsin B structure determined by using an X-ray laser. *Science*, **339** (6116), 227–230.
- 191** Vaval, N. and Cederbaum, L.S. (2007) Ab initio lifetimes in the interatomic Coulombic decay of neon clusters computed with propagators. *J. Chem. Phys.*, **126** (16), 164110.
- 192** Berrah, N., Bozek, J., Costello, J.T., Duesterer, S., Fang, L., Feldhaus, J., Fukuzawa, H., Hoener, M., Jiang, Y.H., Johnsson, P., Kennedy, E.T., Meyer, M., Moshammer, R., Radcliffe, P., Richter, M., Rouzee, A., Rudenko, A., Sorokin, A.A., Tiedtke, K., Ueda, K., Ullrich, J., and Vrakking, M.J.J. (2010) Non-linear processes in the interaction of atoms and molecules with intense EUV and X-ray fields from SASE free electron lasers (FELs). *J. Mod. Opt.*, **57** (12), 1015–1040.
- 193** Gallmann, L., Cirelli, C., and Keller, U. (2012) Attosecond science: Recent highlights and future trends. in *Annu. Rev. Phys. Chem.* (eds M.A. Johnson and T.J. Martinez), **63**, 447–469.
- 194** Schultze, M., Fiess, M., Karpowicz, N., Gagnon, J., Korbman, M., Hofstetter, M., Neppl, S., Cavalieri, A.L., Komninos, Y., Mercouris, T., Nicolaides, C.A., Pazzourek, R., Nagele, S., Feist, J., Burgdorfer, J., Azzeer, A.M., Ernststorfer, R., Kienberger, R., Kleineberg, U., Goulielmakis, E., Krausz, F., and Yakovlev, V.S. (2010) Delay in photoemission. *Science*, **328** (5986), 1658–1662.
- 195** Maltezopoulos, T., Cunovic, S., Wieland, M., Beye, M., Azima, A., Redlin, H., Krikunova, M., Kalms, R., Fruhling, U., Budzyn, F., Wurth, W., Fohlis, A., and Drescher, M. (2008) Single-shot timing measurement of extreme-ultraviolet free-electron laser pulses. *New J. Phys.*, **10**, 033026.
- 196** Gahl, C., Azima, A., Beye, M., Deppe, M., Doebrich, K., Hasslinger, U., Henries, F., Melnikov, A., Nagasano, M., Pietzsch, A., Wolf, M., Wurth, W., and Foehlisch, A. (2008) A femtosecond X-ray/optical cross-correlator. *Nat. Photonics*, **2** (3), 165–169.
- 197** Schorbs, S., Gorkhover, T., Cryan, J.P., Glownia, J.M., Bionta, M.R., Coffee, R.N., Erk, B., Boll, R., Schmidt, C., Rolles, D., Rudenko, A., Rouzee, A., Swiggers, M., Carron, S., Castagna, J.C., Bozek, J.D., Messerschmidt, M., Schlotter, W.F., and Bostedt, C. (2012) X-ray-optical cross-correlator for gas-phase experiments at the Linac Coherent Light Source free-electron laser. *Appl. Phys. Lett.*, **100** (12), 121107.
- 198** Beye, M., Krupin, O., Hays, G., Reid, A.H., Rupp, D., de Jong, S., Lee, S., Lee, W.S., Chuang, Y.D., Coffee, R., Cryan, J.P., Glownia, J.M., Fohlis, A., Holmes, M.R., Fry, A.R., White, W.E., Bostedt, C., Scherz, A.O., Durr, H.A., and Schlotter, W.F. (2012) X-ray pulse preserving single-shot optical cross-correlation method for improved experimental temporal resolution. *Appl. Phys. Lett.*, **100** (12), 121108.

16

Ulaintense X-Ray Interactions at the Linac Coherent Light Source

Linda Young

16.1

Introduction

Ulaintense, tunable X-ray pulses recently available from the LCLS, the world's first hard X-ray free electron laser, increase the intensity and fluence available in a single X-ray pulse up to a billion-fold over that typically available at synchrotron facilities. As a result the LCLS has provided a unique opportunity to investigate nonlinear phenomena at short wavelengths. After an introduction to basic X-ray processes, we review initial experiments at the LCLS that establish basic principles of X-ray interactions with matter at intensities approaching 10^{18} W/cm^2 at wavelengths down to 0.6 nm. Throughout the chapter interactions with neon atoms are discussed. Neon is taken as a prototypical example as it is a second row element with sufficient complexity to display basic inner-shell processes, Auger decay, radiative relaxation, and shakeup excitation and ionization. The complexity of inner-shell processes induced in molecules is briefly discussed. Nonresonant processes that selectively address inner- and outer-shell electrons and X-ray-laser-driven resonant processes, such as Rabi flopping of inner-shell electrons, are discussed. The first use of the LCLS for laser-pump/X-ray probe studies of molecular dynamics is discussed. Characterization of LCLS pulse properties, pulse energy, duration, profile, jitter, focus is described, as this knowledge is critical for predictive theoretical models. Finally, an outlook presents prospects for generating a fully coherent X-ray pulse via self-seeding techniques, a matter of considerable impact for atomic physics and imaging experiments.

The first laser was built in 1960 by Ted Maiman at Hughes Research Laboratory [1]. It consisted of a flashlamp-pumped 1-cm ruby rod with silvered end faces that exhibited stimulated emission at 6943 Å. Visible lasers and their applications have since become widely appreciated and are commonly found in everyday appliances. However, long-wavelength visible lasers can not be used to fabricate objects at the nanoscale, interrogate matter on the atomic scale, or for high-resolution metrology and microscopy. Envisioning such applications, scientists have long dreamt of producing an X-ray laser. Early proposals dating from the 1960s suggested schemes to

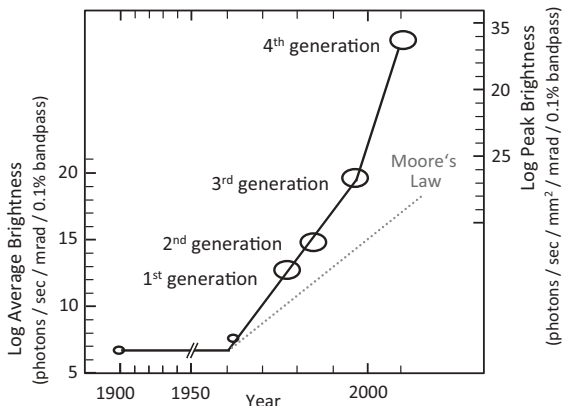


Figure 16.1 Peak X-ray brilliance as a function of time [16]. Steep slope starting in the 1960s is due to the utilization of synchrotron radiation. The last point at 2010 is a result of the SASE X-ray FELs.

produce population inversion based upon collisional recombination [2], photoionization [3], and electron impact excitation [4–6]. Since then, soft X-ray lasing has been achieved at large-scale tabletop installations, for example, using a laser-heated plasma [7], and more recently using smaller scale capillary discharge devices [8] and optical-laser-pumped soft X-ray lasers [9, 10]. These remarkable tabletop soft X-ray lasers have reached sub-10 nm wavelengths with pulse energies at the millijoule level. However, because they operate on specific transitions in highly ionized atoms, they do not yet provide the wide tunability or general accessibility of short-wavelength accelerator-based free-electron laser (FEL) facilities which have come to life within the past decade (for a recent review see [11]). Most notably, the free-electron laser facility in Hamburg, now named FLASH, has undergone a continual upgrade [12–15] from observed laser action at $\sim 1000 \text{ \AA}$ [12] to current operations down to 40 \AA .

The first *hard* X-ray free-electron laser, the LCLS at SLAC, lased at 1.5 \AA in April 2009 [17], coming to life in a scientific environment fertilized by the earlier work at FLASH. This X-ray FEL, first proposed in 1992 [18], uses the last 1 km of the SLAC linear accelerator to send a relativistic electron beam of up to 14 GeV through an $\sim 100\text{-m}$ undulator array [19] where self-amplified spontaneous emission (SASE) [20–22] produces quasi-coherent X-ray radiation. The hard X-ray radiation pulses produced by SASE FELs have duration on the femtosecond timescale, a pulse energy on the millijoule level, and a bandwidth of $\sim 0.5\%$. The radiation therefore offers roughly a billion-fold gain in peak brightness over that of synchrotron radiation (see Figure 16.1). Wide tunability of photon energy is accomplished by changing the electron beam energy, and the LCLS has demonstrated lasing from ~ 26 to 1.2 \AA (480–10 000 eV). The enormous potential of X-ray FELs was recognized early on and there are multiple large scale projects planned or in operation, for example, SACLA in Japan [23], which demonstrated lasing at 1 \AA in June 2011, and the European XFEL [24] scheduled to come online in 2014, FERMI

at Elettra in Trieste, the SwissFEL, the PAL XFEL and others [25]. The properties of individual SASE X-ray pulses from these X-ray FEL facilities are comparable, though the pulse repetition rate differs. The unprecedented peak brilliance of the X-ray FEL facilities makes them unique in the world for studying short-wavelength nonlinear phenomena, as described in this chapter, and for novel applications such as biomolecule imaging [26]. Indeed, focused LCLS SASE pulses have an extremely high fluence concentrated in a single pulse $\sim 10^{13}$ X-ray photons/ μm^2 , or the equivalent of $10^5/\text{\AA}^2$. This may be compared to the nominal dose at which damage occurs for biological samples $200/\text{\AA}^2$ [26, 27]. Corresponding damage may be suppressed on the short femtosecond timescale relevant for X-ray FEL pulses. The broad energy tunability and short pulse duration down to a few femtoseconds [28, 29] of these X-ray FELs therefore promise molecular movies with atomic-scale time and spatial resolution.

16.1.1

Comparison of Ultrafast, Ultraintense Optical, and X-Ray Lasers

It is interesting to compare the evolution of optical lasers with that of X-ray light sources. The experimental realization of SASE FELs led to a dramatic increase in X-ray intensity. The increase mirrors the development of the optical laser intensity

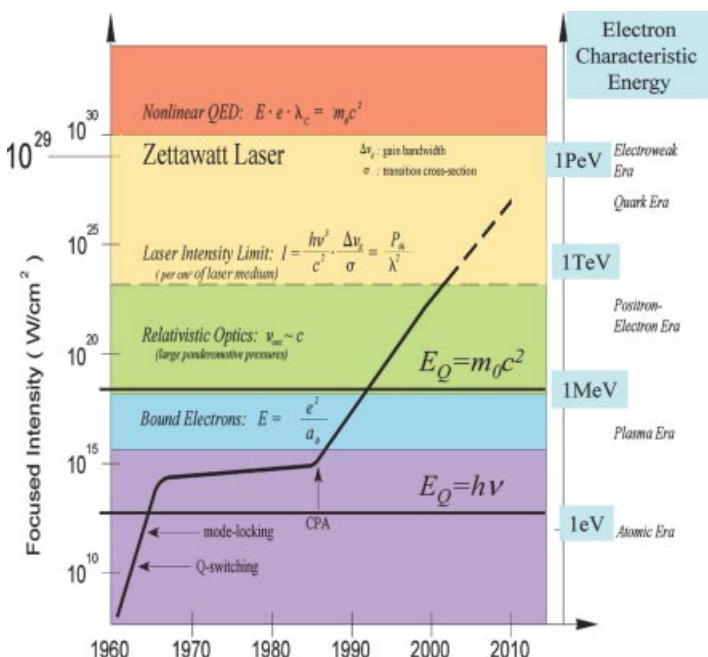


Figure 16.2 Focused optical laser intensity as a function of time. The steep slope in the 1960s stems from utilization of nonlinear optical effects and the steep slope in the

mid-1980s reflects developments resulting from chirped pulse amplification methodology. Adapted from [30] (Copyright (2007) by the American Physical Society.)

Table 16.1 Intense optical lasers vs X-ray FELs.

	Ti:sapphire	LCLS
Photon energy	1.5 eV	800 eV
Pulse energy	1 mJ	1 mJ
Photons per pulse	5×10^{15}	10^{13}
Pulse duration	30 fs	100 fs
Focused spot size	1 μm	1 μm
Flux	$5 \times 10^{35} \text{ cm}^{-2} \text{ s}^{-1}$	$10^{33} \text{ cm}^{-2} \text{ s}^{-1}$
Intensity	10^{17} W/cm^2	10^{17} W/cm^2
Period	2.7 fs	2 as
Number of cycles	11	40 000
Ponderomotive energy U_p	6000 eV	25 meV
Displacement α	53 nm	0.000 16 nm

after the discovery of chirped pulse amplification in 1985 [31]. Figure 16.2 shows the focused optical laser intensity as a function of time. More than two decades ago optical laser intensities reached a magnitude where the laser electric field equals that binding the electron in a hydrogen atom ($51 \text{ V}/\text{\AA}$). Optical lasers with this intensity can give rise to coherent X-ray pulses. Because of the strong electric field of the optical laser, and its low frequency, it is possible for an outer electron to tunnel through the suppressed Coulomb barrier that occurs every half cycle of the laser. The ratio of the optical frequency to the tunneling frequency is given by the Keldysh parameter γ [32] ($\gamma^2 = W_b/2U_p$ where $U_p = I_0/4\omega_0^2$ is the ponderomotive energy, I_0 and ω_0 are the intensity and frequency of the laser and W_b is the binding energy of the tunneling electron – all quantities in atomic units). After the electron is freed, it is accelerated in the laser field to a displacement of $\alpha = E/\omega_0^2$ and, upon field reversal, is driven back to the residual ion from which it originated. There the electron may recombine with the parent ion to produce a series of high-order odd harmonics [33–36] that can reach X-ray wavelengths in the water window [37, 38] (for comprehensive reviews see [39–42]). The distinguishing characteristic of strong-field interactions of atoms with optical lasers is the dominance of field-driven electron motion – as characterized by the large ponderomotive energies.

The interaction with strong-field X-ray pulses, as produced by present X-ray FELs, is quite different. Table 16.1 compares nominal parameters of a common ultrafast optical laser (Ti:sapphire, 1.55 eV) used to produce high-harmonic radiation in the X-ray regime with those of the LCLS X-ray FEL operating at 15 \AA (800 eV). In both cases, the pulse energy is 1 mJ and the focal spot size is on the order of 1 μm . For the Ti:sapphire laser, these parameters create a ponderomotive energy of

6000 eV, whereas the value for the LCLS operating at 800 eV is only 25 meV.¹⁾ As a consequence, the displacement is large for the optical laser, but minuscule for the X-ray laser. Thus, laser-driven electron dynamics does not play an appreciable role in X-ray/atom interactions. Another qualitative difference between the two 1-mJ lasers is that the 30-fs optical laser pulse contains only ~ 10 cycles, whereas the 100-fs X-ray pulse contains $\sim 40\,000$ cycles. Thus the X-ray field appears as a quasi-continuous wave to a target atom. It is important to remember that the SASE X-ray pulses are not longitudinally coherent because the lasing starts from noise, leading to a chaotic and spiky temporal profile. Additional details on the properties of the SASE-LCLS pulses are described later in Section 16.4. As such, every LCLS pulse is different and spiky, both in the temporal and spectral domains. The coherence time within the LCLS SASE pulse is predicted to be a few hundred attoseconds and is given by $t_c = \sqrt{\pi}/\sigma_\omega$, where σ_ω is the rms SASE bandwidth [22]. However, even a few hundred attosecond spike within a 100-fs SASE pulse duration contains hundreds to thousands of X-ray periods and few-cycle laser-driven phenomena are not prevalent – interactions with LCLS SASE pulses are dominated by well-known X-ray/matter interactions.

16.1.2

X-Ray Atom Interactions

The dominant X-ray interactions with matter are illustrated in Figure 16.3 for the prototypical second row element neon – the subject of intense investigations discussed later in this chapter. The second row is of particular interest for biology. Comparable to carbon, nitrogen and oxygen, the binding energy of the 1s electron in neon is below 1 keV, producing a sharp jump in photoabsorption at the K-edge, ~ 870 eV. In the regime of interest for current X-ray FELs, below ~ 20 keV, the photoelectric effect, σ_{photo} dominates the other two photo processes of note, coherent (σ_{coh}), and incoherent (σ_{inc}) scattering. The coherent scattering cross section, albeit small, is of considerable importance, as elastic scattering is the basis for structure determination: for ordered materials by crystallography and for disordered material by coherent diffractive imaging [43]. The corresponding diffraction experiments are discussed in Chapter 17. The ratio of the photoelectric to the coherent scattering cross section is thus an important figure of merit for understanding X-ray-induced damage in systems. Note that incoherent Compton scattering, another inelastic process that ionizes matter, dominates at higher X-ray energies.

Photoionization dominates X-ray interactions up to 20 keV, so let us examine this process in more detail for neon [45]. The photoionization cross section is proportional to an overlap integral of the initial bound state wave function with the outgoing continuum wave weighted by r . For photoionization of a 1s electron the cross section is given by $\sigma_{1s} = (8\pi^2/3)\alpha E_{\text{ph}} R_{e\text{p},1s}^2$, where α is the fine structure

¹⁾ The parameters calculated for the Ti:sapphire laser are purely calculations and unlikely to be realized when attempting to generate high harmonics as tunnel ionization occurs well-before the extreme intensities of 10^{17} W/cm².

constant, E_{ph} is the photon energy, and $R_{\epsilon p,1s} = \langle R_{\epsilon p} | r | R_{1s} \rangle$. The binding energies for 2s, 2p_{1/2}, and 2p_{3/2} electrons are 48.5, 21.7 and 21.6 eV, respectively [46]. Thus, for photon energies above these binding energies, multiple continua are present. The photoionization cross sections for these subshells as a function of energy [47] are shown in Figure 16.4. Clearly, the kinetic energy of the photoelectrons may be used to distinguish ejection from the different subshells, $E_{e,\text{kin}}(\epsilon l) = E_{\text{ph}} - E_{\text{nl}}$.

Photoelectron angular distributions may be used, in addition to the kinetic energy, to distinguish ionization mechanisms. The photoelectron angular distribution, in the dipole approximation, is given by

$$\frac{d\sigma}{d\Omega} = \frac{\sigma}{4\pi}[1 + \beta P_2 \cos(\vartheta)] . \quad (16.1)$$

Here σ is the photoionization cross section, $P_2 = (3 \cos^2(\vartheta) - 1)/2$ is the second Legendre polynomial, and ϑ is the angle between the electric field vector of the photon field and the direction of photoelectron ejection. The 1s and 2s photoelectrons exhibit a particularly simple $\cos^2(\vartheta)$ angular distribution, that is, $\beta_{1s} = \beta_{2s} = 2$. The 2p photoelectron angular distribution is more complex with outgoing s and d waves that interfere with a phase shift of Δ [45]

$$\beta_{2p} = \frac{2R_{\epsilon d,2p}^2 - 4R_{\epsilon d,2p}R_{\epsilon s,2p}\cos\Delta}{R_{\epsilon s,2p}^2 + 2R_{\epsilon d,2p}^2} . \quad (16.2)$$

One may eliminate contributions from s electrons by detection at $\vartheta = 90^\circ$. In addition, one may obtain an angle-independent measure of the photoionization

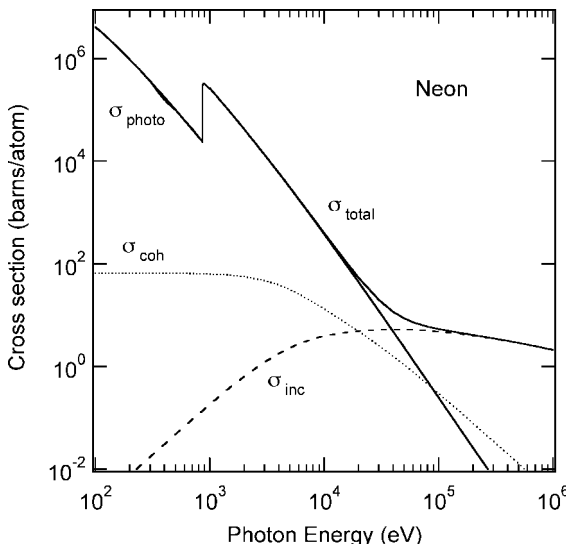


Figure 16.3 Photon interactions with neon. Cross sections for photoabsorption (σ_{photo}), coherent scattering (σ_{coh}) and incoherent (Compton) scattering (σ_{inc}) are shown as a function of photon energy. Data from [44].

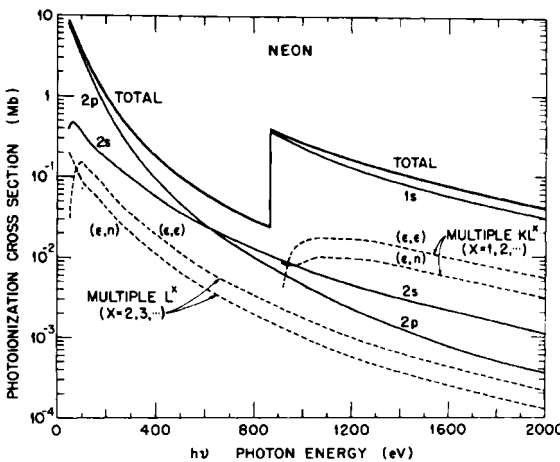


Figure 16.4 Total and partial subshell photoionization cross sections for neon. Reprinted with permission from [47]. Copyright (1974) by the American Physical Society.

cross section by detecting at the magic angle, 54.7° , where $P_2 \cos(\vartheta) = 0$. Energy and angular distributions may be readily used to distinguish photoionization from different subshells.

Understanding photoionization is only the first step in understanding the atomic response. If the photon energy is high enough to eject a 1s electron, the residual hole can be filled either by radiative or Auger processes at a rate given by $\Gamma(1s) = \Gamma_R(1s) + \Gamma_A(1s)$. Radiative processes, governed by the dipole operator, involve a parity change and are subject to selection rules for the total angular momentum ($\Delta J = \pm 1.0$ and $J = 0 \leftrightarrow 0$ is forbidden). Conversely, Auger processes are mediated by the Coulomb interaction, involve no parity change and have selection rules of $\Delta L = \Delta S = \Delta M_L = \Delta M_S = 0$. Auger processes are labeled according to the holes in the initial photo ionized state and in the final state after decay, for example, $K - L_{2,3}L_{2,3}$ is the process that starts with a K hole and ends with two holes in the 2p shell. The radiative rate scales with the atomic number as Z^4 , so at high Z the radiative branch dominates. At about $Z = 32$ the radiative and Auger rates are equal for refilling a 1s hole. In neon, $Z = 10$, Auger decay dominates the refilling of the 1s hole with a branching ratio of 0.984 [48]. The calculation of Auger rates is a complex many body problem; for the Auger decay of neon [1s] a number of methods have been employed [49–51].

Auger electrons are distinguishable from photoelectrons in two ways. First, photoelectron kinetic energies disperse 1 : 1 with the incident photon energy via $E_{e,kin}(\epsilon l) = E_{ph} - E_{nl}$, whereas the kinetic energy of Auger electrons is independent of the incident photon energy. Second, Auger electrons have angular distributions distinct from photoelectrons. Within a two-step model, the angular distribution of Auger electrons can be characterized by $\beta_A = \mathcal{A}_{20}\alpha_2$, where \mathcal{A}_{20} is the *alignment* parameter characterizing the ion formed by photoionization and α_2 characterizes the Auger process [45, 52]. For the Auger electrons coming from a K-shell vacancy

in neon, the alignment parameter $A_{20} = 0$ and $K\text{-}LL$ Auger electrons are expected to be isotropic.

16.2

Atomic and Molecular Response to Ultraintense X-Ray Pulses

Given the extreme fluence and intensity at short wavelengths provided by the world's first hard X-ray free electron laser it is imperative to understand the response of matter to such unprecedented conditions. Such an understanding will provide a firm foundation for all future applications and motivated initial experiments in atomic neon [53]. The application that has captured the imagination of the wider community is one proposed in 2000 by Hajdu and collaborators: the use of an ultrashort, ultraintense X-ray pulse can image a biomolecule without the need for crystallization [26]. This proposal specified a fluence of 3×10^{12} X-ray photons at 12 keV in a 100-nm spot within a pulse of approximately 10-fs duration, leading to a calculated intensity of 10^{22} W/cm². The now-familiar pictures of the Coulomb explosion of a lysozyme molecule during X-ray irradiation show minimal displacement of nuclei within 10 fs, but significant disintegration within 50 fs. However, even prior to the movement of nuclei, the molecule is damaged due to photoionization and rearrangement of the electrons. The localization of electrons, in particular the contracted inner-shell electrons, is crucial for diffraction imaging experiments. It is that movement of inner-shell electrons that we seek to understand and control using ultraintense X-ray pulses.

In the following sections, we discuss early experiments at the LCLS at intensities approaching 10^{18} W/cm² designed to elucidate the nature of the atomic and molecular response to X-rays at these extreme conditions. In Section 16.2.1, we discuss nonresonant X-ray processes where the photon energies are far removed from resonant structures. In Section 16.2.2, we focus on resonant X-ray processes where the cross section can be several orders of magnitude greater than that for nonresonant interactions and thus may permit the observation of phenomena such as Rabi cycling of inner-shell electrons. In Section 16.3, we describe the first laser-pump/X-ray probe experiment at the LCLS. In Section 16.4, we describe characterization of LCLS pulses based upon two-color atomic/molecular interactions. In Section 16.5, we present an outlook, summarizing briefly our current understanding of intense X-ray interactions, their impact on the X-ray imaging of complex species and the route to fully coherent X-ray pulses from FEL, which will benefit a wide community of researchers. We also refer the reader to two recent review articles that cover some of the same material [54, 55].

The experiments described here were carried out in the atomic, molecular and optical (AMO) endstation in the high-field physics chamber [56] where the tightest focus of the soft X-ray LCLS beam is obtained. Beamline optics was simulated by [57]. LCLS beams are focused by a Kirkpatrick–Baez mirror pair to spot sizes of approaching 1 μm to intercept an atomic/molecular beam in the interaction region

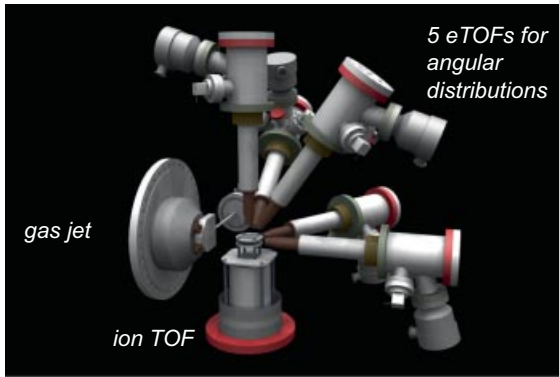


Figure 16.5 High-field physics chamber in the AMO end station. Five high-resolution electron time-of-flight spectrometers and a Wiley-McLaren ion spectrometer view the interaction region where focused LCLS pulses intercept a pulsed atomic/molecular beam. Using a coordinate system with z representing the

X-ray propagation axis and x the polarization axis, there are three electron spectrometers in the $x-y$ plane, one each along x , y and one at the magic angle 54.7° . Two out-of-plane spectrometers complete the array. Figure courtesy by J. Bozek and C. Bostedt.

viewed by five high-resolution electron time-of-flight spectrometers [58] and one ion time-of-flight spectrometer as shown schematically in Figure 16.5.

16.2.1

Nonresonant High-Intensity X-Ray Phenomena

Atoms

The simplest approach to understanding nonresonant X-ray phenomena at ultrahigh intensities is to irradiate a well-known target, in the case of the first experiment at the LCLS, the neon atom [53]. Neon, in addition to being well studied [47, 59–63] has a 1s-binding energy of 870 eV, conveniently located in the initial tuning range of the LCLS, as shown in Figure 16.3. The X-ray interaction can therefore be tuned from “peeling” the outer- to “coring” the inner-shell electrons [64].

The experiments were preceded by theoretical predictions by Rohringer and Santra [65]. Even though the focused intensity of the X-ray FEL during these early experiments approached 10^{18} W/cm^2 , perturbation theory is largely adequate at these short wavelengths near 10 \AA . Therefore, Rohringer and Santra used a rate equation model to predict the charge state distribution when neon was irradiated with nominal X-ray pulses from the LCLS containing 10^{13} photons in 100 fs, focused to a range of spot diameters ($0.3\text{--}5 \mu\text{m}$). The chaotic temporal profile of the LCLS pulses was included explicitly using an assumed coherence time of a few femtoseconds. The predictions were averaged over an ensemble of 10 000 random pulses to best simulate experimental observables.

The experimental results [53] firmly established sequential single-photon absorption as the dominant mechanism of X-ray atom interaction at intensities up to

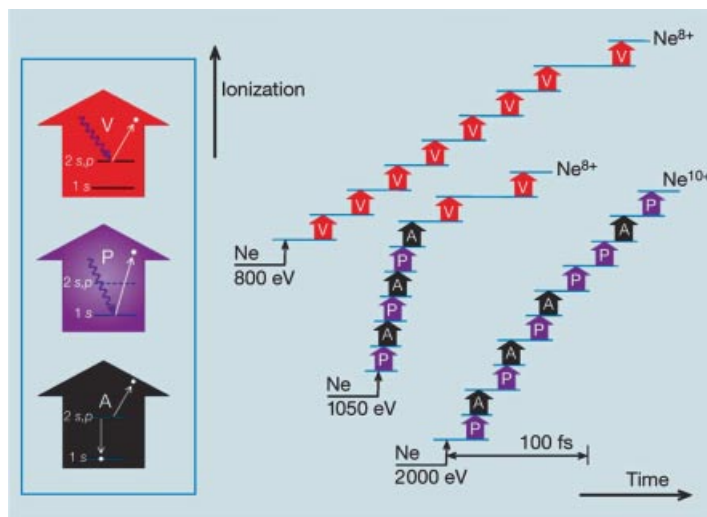


Figure 16.6 High-intensity X-ray–atom interaction mechanisms observed in neon. Ionization occurs via valence-shell photoionization (V) or inner-shell photoionization (P) and subsequent Auger ionization (A). From [53].

10^{18} W/cm². Three photon energies, 800, 1050, and 2000 eV were carefully selected to access three regimes, respectively: below the inner-shell ionization threshold, above the energetic threshold to produce hollow neon and above all thresholds for all charge states of neon. Ion charge state distributions, as well as electron energy and electron angular distributions were observed as a function of pulse duration and pulse energy at each photon energy. The observed ionization mechanisms are shown graphically in Figure 16.6, where three types of electrons are shown – V for valence ionization, P for inner-shell photoionization, and A for Auger ionization. The electrons were easily distinguished by their kinetic energies and angular distributions using the five strategically placed high-resolution electron time-of-flight spectrometers [58]. The corresponding ion charge state distributions for given pulse parameters were determined using Wiley–McLaren ion time-of-flight techniques and these were compared to theoretical predictions using the rate equation approach [65].

Beyond establishing the dominant interaction mechanism at high-X-ray intensities, this experiment further highlighted the power, and dangers, of these high-fluence X-ray pulses. From Figure 16.6, one can see that multiphoton absorption is the rule, not the exception for pulses containing 10^{13} X-ray photons focused to focal diameters of $\sim 1\text{ }\mu\text{m}$. Within the LCLS pulse duration, it is obvious that the target is changing dramatically, that is, going from a 10-electron atom to a naked ion, within 100 fs. The concept of the X-ray pulse being a gentle, nonperturbing probe of a sample, the basis of most synchrotron-based X-ray studies, is simply not applicable at these intensities and fluences.

A third general observation was that of intensity-induced X-ray transparency. This general phenomenon occurs when hollow atoms (empty 1s shell) are formed

during the ionization process. Hollow atoms are easily formed by high-fluence, ultrashort X-ray pulses which can eject both 1s electrons prior to Auger decay (2.4 fs for Ne). Since 1s electrons carry most of the absorption strength, their absence induces transparency in the atom. Two counter-intuitive features associated with this observation are noted: first, the induced transparency was dependent on the pulse durations which ranged between the nominal values of 80 and 300 fs (for the electron beam) at constant fluence. Second, the shorter, more intense pulse caused less damage. The first observation was initially puzzling. However, as one accesses higher charge states during the course of the pulse, the inner-shell decay lifetimes progressively lengthen. For example, ground state Ne^{7+} cannot Auger decay. The observation of induced transparency (also observed in molecules and there termed “frustrated absorption” [66]) suggested that X-ray-induced damage is decreased at higher intensity (equivalent to shorter pulse duration at constant fluence) and that the ratio of elastic scattering relative to absorption, so important for imaging applications, would be enhanced. An interest to quantify this effect led to the development of a general purpose code, XATOM, that tracks electron dynamics during the course of irradiation with an FEL pulse [67].

These straightforward observations on neon atoms combined with theory also provide information on the pulse characteristics of the LCLS [53]. Comparisons of both the observed hollow-atom yield and the intensity-induced transparency with theoretical predictions indicated strongly that the pulse durations of the X-rays are shorter than those of the electron beam in the FEL. These indirect pulse duration measurements were subsequently corroborated by independent measurements [68] as discussed later in this chapter. The well-characterized ion-charge-state distribution for valence ionization also gives a reliable measure of the pulse fluence. (Since there are no Auger decays to provide an internal clock in valence ionization, there is no pulse duration dependence for ion charge state yield.)

A class of phenomena, the “direct” two-photon X-ray absorption, analogous to early investigations of nonlinear interactions of intense optical fields with matter [69], has not yet been discussed. In fact, a search for two-photon, one-electron ionization was the topic of study for the second experiment at the LCLS [70] and previously the subject of theoretical study [71]. One might consider starting with neutral neon as the target and irradiating with photon energies below the 1s threshold (870 eV), where direct two-photon one-electron ionization will create a 1s vacancy. Then the observation of the Auger decay should be a clean signature of direct two-photon absorption, since 1s vacancy formation is energetically forbidden in a one-photon process. However, due to competing channels, for example, valence ionization which produces copious electrons of similar energies, this simple approach was not successful. It was found that a helium-like neon target (Ne^{8+}) offered a cleaner measurement. With high-fluence pulses, Ne^{8+} is readily produced via sequential single-photon absorption. By tuning the X-ray energy above (1225 eV) and below (1110 eV) the K-shell threshold for ionization of Ne^{8+} (1196 eV), it was possible to distinguish one- versus two-photon production of Ne^{9+} . Above the threshold, a linear dependence between the photon number and the Ne^{9+} ion yield was observed, whereas below the threshold a quadratic

dependence was observed. With improved theoretical modeling, taking into account shake-off and incorporating two-photon absorption cross sections, $\sigma^{(2)}$, the two-photon mechanisms, either sequential single-photon absorption proceeding through valence ionization of transiently excited Ne^{7+} , or direct two-photon ionization of the ground state Ne^{8+} , could be assessed relative to one another. The observations could be modeled only after the two-photon absorption cross section, $\sigma^{(2)}$, at 1110 eV was enhanced over that given in [71] by two to three orders of magnitude. A potential reason for an enhanced $\sigma^{(2)}$ is the existence of a $|1s^1 4p\rangle$ state at 1127 eV which is near resonant with the below-threshold photon energy of 1110 eV. Of course, the investigation of nonlinear effects such as two-photon absorption requires extreme care to remove/measure harmonic content (second and third harmonics) contained in the incident LCLS beam [72].

16.2.1.1 Molecules

Just as in atoms, the mechanism of intense X-ray interaction with molecules was investigated early on [66, 73]. In atoms, the prototypical target was neon; for molecules, detailed studies were conducted on nitrogen, N_2 . Because the 1s-binding energy for nitrogen is 410 eV, in these early studies the photon energy could not be tuned low enough for selective outer-shell ionization and the interactions observed in N_2 were nonresonant and above the K-shell threshold. The phenomena observed were similar to those observed in atoms, for example, copious hollow atom formation [73] and intensity-induced transparency or “frustrated absorption” in the terminology of [66]. In these studies of frustrated absorption in N_2 , irradiation at constant fluence and variable pulse duration showed a decrease in the average charge state for shorter pulses – down to the sub-10 fs level, where Auger decay cannot occur within the pulse.

In molecules, a distinction relative to atoms is that multiple core holes may be formed on different atomic sites. Such inner-shell double vacancies are calculated to be much more sensitive to local chemical environment than the inner-shell single vacancies used in standard X-ray photoelectron spectroscopy [74, 75]. Double vacancies may be formed on a single site (ssDCH: single-site double core hole) or on two sites (tsDCH: two-site double core hole). The energetic shifts for ssDCH are significantly greater than those for tsDCH, thus the observation of ssDCH is significantly simpler [73].

16.2.2

Resonant High-Intensity X-Ray Phenomena

The previous section dealt with interactions of atoms and high-intensity X-rays in regimes far removed from resonances. However, resonant cross sections can exceed nonresonant photoionization cross sections by many orders of magnitude. (The importance of resonances as potential enhancers of nonlinear processes was described in the previous section.) Once again, we make use of the neon atom as a prototypical example. We consider the energy region near the K-edge where a textbook Rydberg series $1s \rightarrow 3p, 4p \dots$ is visible, as shown in Figure 16.7. The

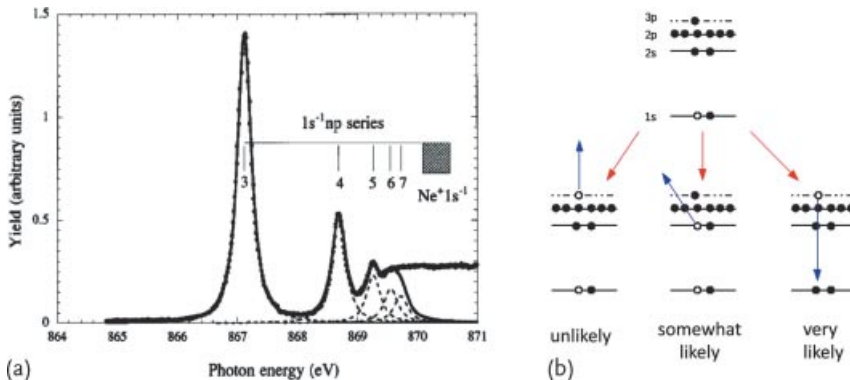


Figure 16.7 (a) Experimental high-resolution X-ray absorption spectrum of neon near the K-edge. The resonances are broadened by the 2.4 fs natural lifetime of a 1s vacancy in neon, which corresponds to a 0.27 eV Lorentzian width. From [63]. (b) Propensity for various photoabsorption processes when the photon energy is tuned to the $1s \rightarrow 3p$ resonance.

Following the excitation of the 1s electron to the $1s^{-1}3p$ resonance state as shown at the top, the most likely photoabsorption process is stimulated emission. Ejection of the other outer-shell electrons (such as the 2s or the 3p), to the continuum is much less probable due to the extremely large $1s^{-1}3p$ resonance cross section.

$1s \rightarrow 3p$ resonance, ~ 1.5 Mb, stands far above the typical valence photoabsorption cross section at 860 eV of ~ 10 kb. The width of the resonance is controlled by the lifetime of the 1s vacancy, 2.4 fs, which is primarily governed by Auger relaxation.

The similarity of the neon absorption spectrum to that of a hydrogen atom, combined with the strength of the resonance, suggests that a strong enough X-ray field might exert control over inner-shell electron dynamics. For a simple control sequence, a strong monochromatic X-ray field could excite a 1s electron to the 3p state and then stimulate emission back to the 1s state, that is, drive Rabi cycling [76, 77]. Rabi cycling would offer a way to alter the natural X-ray decay process, that is, to inhibit Auger decay and thereby X-ray damage. A simple back-of-the-envelope estimate suggests that Rabi flopping may be possible at presently available X-ray intensities; the dipole matrix element for the $1s \rightarrow 3p$ transition is 0.01 atomic units (a.u.). With a field strength of $E = 6.3$ au ($I = 1.8 \times 10^{18}$ W/cm 2), the Rabi flopping rate, $\mu E/\hbar$, equals the Auger decay rate (0.01 au). The earlier discussion emphasized complications due to competing processes. Therefore, it is useful to examine the propensities for various photoabsorption processes when sitting on a resonance, as is shown in Figure 16.7b. It is clear that stimulated emission is the dominant photoinduced process under resonant excitation conditions and that the primary competing channel is Auger decay.

Unfortunately, the properties of present-day XFELs, based on SASE [21] are not ideal for quantum control experiments. The lack of longitudinal (temporal) coherence prevents the direct observation of Rabi cycling, even in an isolated two-level system. The current situation is not unlike early research with intense optical lasers, where the effects of a strong stochastic field on atomic transitions were considered more than 30 years ago [78, 79]. In anticipation of XFELs, theoreticians have

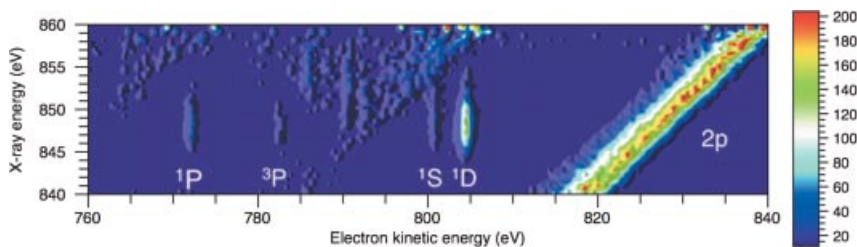


Figure 16.8 Electron emission from neon (observed at 90° from the X-ray polarization axis) produced by LCLS pulses (nominally 0.3 mJ, 8.5 fs) focused to $1 \times 2 \mu\text{m}^2$. X-ray photon en-

ergies were corrected on a shot-by-shot basis using electron beam energies. Reprinted with permission from [82]. Copyright (2011) by the American Physical Society.

considered the effects of strong field excitation of inner-shell resonances [80, 81]. The incoherent nature of the SASE excitation pulse of current XFELs causes the mean times between excitation and stimulated emission to fluctuate.

For the Ne $1s \rightarrow 3p$ transition, theoretical estimates of the resonant Auger process at high intensity [80] used a simplified two-level model, which neglects photoabsorption from valence electrons and AC stark shifts from other levels. Models using incoherent LCLS pulses of 230-fs duration found that a time domain measurement would be difficult, but an energy domain signature of Rabi flopping would be observable as broadening of the resonant Auger line shape. A single-shot spectrum shows spiky structure, due to the coherence spikes within a LCLS pulse and cannot be compared with the model. However, the spectrum averaged over 10 000 shots produces a resonant Auger profile that is broadened at high intensity. The observation of this intensity-induced broadening was the target of experimental investigation [82].

Although the theoretical calculations [80] were done for the Ne $1s \rightarrow 3p$ transition, the experiment [82] was actually performed on the Ne $1s \rightarrow 2p$ transition. The experimental choice facilitated theory and experiment because the $1s-2p$ resonance is better isolated (more than 70 natural linewidths separated from the $1s-3p$) giving freedom from lineshape distortion [83]. The chosen transition is also stronger by a factor of 30, decreasing the intensity requirements for Rabi cycling. The only experimental drawback is the lack of a $2p$ hole in the ground state of neon. However, a single SASE FEL pulse can be used both to prepare the desired target, singly ionized neon containing a $2p$ hole, and to drive the $1s \rightarrow 2p$ transition. Further, by using a relatively short pulse, one can prevent complicating ionization pathways and obtain a relatively clean spectrum. The experimental search for Rabi flopping then consists of (1) producing the $1s-2p$ resonance, (2) driving it with the remainder of the high-intensity SASE pulse, and (3) comparing the driven resonant Auger line shape with the off-resonant Auger line shape.

The unveiling of the originally “hidden” $1s-2p$ resonance, using a single SASE pulse as both pump and probe, is shown in Figure 16.8. Here, the electron kinetic energy is displayed versus the incident X-ray energy. Only single photon processes occur in X-ray experiments at synchrotrons. At energies below the K-threshold for neon only a single photon would be absorbed, giving rise to valence ionization and

thus a single diagonal photoelectron line (labeled 2p). However, with high-fluence FEL pulses, a second photon can be readily absorbed when the photon energy is tuned to the 1s–2p resonance. This resonant photoabsorption creates a 1s hole. The hole can be refilled by an Auger electron leading to vertical Auger lines, corresponding to different final states in the doubly charged ion. It is important to note that these Auger cascades are triggered at photon energies substantially below the threshold for 1s-electron ejection (870 eV). The propensity of high-fluence femtosecond FEL pulses to alter the target, combined with the power of hidden giant resonances reveals challenges in using FELs [82]. Calculations at a simple Hartree–Fock–Slater level can easily misplace resonances by 10 eV or more, and these resonances can be many orders of magnitude larger than the background nonresonant cross section; hence simple theoretical approaches may be insufficient for the interpretation of FEL spectroscopic data.

Rabi flopping on the 1s–2p resonance was confirmed by carefully comparing the line shape of the ^1D Auger line under on- and off-resonance conditions. The difference between the resonance line shapes was small but clear. Reasons for the small effect include intensity averaging over the focal volume, lower intensity than initially expected, and the temporal chaoticity of the beam. In this experiment, one must first prepare the 2p hole and then drive a 1s electron to and from the 2p hole – all with 10–20-fs pulse containing a spiky structure! Calculations show that for a Gaussian pulse, the Rabi flopping, and modification of the resonant Auger lineshape would be significantly more visible [82]. Simple schemes to produce longitudinally coherent pulses by self-seeding have been proposed [84] and are currently being implemented at the LCLS. These will be discussed in Section 16.5.

16.3

Ultrafast X-Ray Probes of Dynamics

The ultraintense nature of LCLS pulses is coupled to a second unique property, the ultrafast timescale – down to sub-10 fs. Other sources of subpicosecond X-ray pulses exist, for example, tabletop high-harmonic generation and synchrotron-based slicing sources do not possess the unique combination of ultrafast timescale, tunability and pulse energy present in LCLS pulses. This powerful probe can be used to capture snapshots of molecules in action and represents the first step toward the dream of molecular movies.

A first use of the LCLS as an ultrafast X-ray probe of dynamical processes was reported by Cryan *et al.* [85]. His study used a Ti:sapphire laser to generate an ensemble of transiently aligned N_2 molecules. The alignment, created as a rotational wave packet, recurs on a picosecond timescale and the X-ray pulse was timed to probe the aligned ensemble. This methodology delivers dynamical information relative to the fixed molecular frame. Coupled with the high intensity of the LCLS pulses, this presents a unique opportunity to investigate double-core–hole Auger electron dynamics in the molecular frame, without the usual complication of rotational averaging. The two beams were overlapped collinearly in the high-field physics cham-

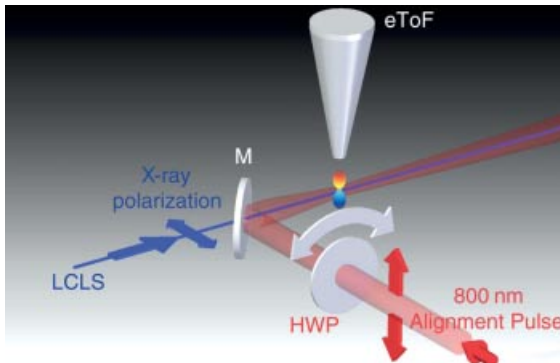


Figure 16.9 Experimental setup for laser-pump/X-ray probe measurements of aligned molecules. X-ray and laser pulses propagate collinearly through the high-field-physics chamber as shown in Figure 16.5. A half-wave

plate rotates the polarization of the nonresonant alignment laser. Reprinted with permission from [85]. Copyright (2010) by the American Physical Society.

ber and the molecular axis was rotated with the polarization of the alignment laser, as shown in Figure 16.9. After overcoming technical hurdles associated with spatial and temporal overlap, the experiment revealed a slightly anisotropic distribution of Auger emission from ssDCH molecules, with a maximal yield along the molecular axis. The experiment further emphasized the difficulty of using tsDCH spectroscopy, as these features appear in a congested spectral regime. Nevertheless, the ability to use aligned molecules under field-free conditions for experiments with X-ray FELs is an important advance for AMO physics; it can lead to an understanding of dynamics in the molecular frame, and for coherent X-ray imaging [26, 86] it can reduce difficulties associated with orientational averaging.

16.4

Characterization of LCLS Pulses

Characterizing the properties of SASE X-ray FEL pulses (energy, duration, timing jitter, temporal profile, focus) is a great technical challenge. Knowledge of these properties is key to the interpretation of experimental data and to the development of predictive theories. Obtaining these properties in a nondestructive manner, as is possible with a dilute gas phase target where the X-ray beam passes virtually untouched, is a widely appreciated goal. Several diagnostics investigated early rely on phenomena associated with strong-field laser-based AMO experiments, such as ionization processes in the presence of a laser field or impulsive molecular alignment. Considerable efforts have been made to quantify the pulse energy [88] using X-ray-induced ultraviolet emission in gaseous nitrogen. At the LCLS, these nitrogen-gas-based detectors are placed downstream of the undulator and upstream of optics that deliver the FEL radiation to one of six endstations. The pulse

energy measured using these gas detectors is, of course, reduced by optical reflections or monochromatization. Nevertheless, the gas detector value is a valuable measure of LCLS performance.

Characterization of the X-ray pulse duration is still a work in progress. The X-ray pulse duration is an enormously flexible parameter and can be varied either by changing the bunch compression of the electron beam (70–300 fs) [89], or by lowering the electron bunch charge from the nominal 250 to 20 pC (to produce sub-10-fs pulse durations) [28]. Development of a noninvasive technique to provide knowledge of the pulse duration on a shot-by-shot basis would be extremely valuable. For X-ray pulse lengths greater than 40 fs, cross-correlation between an optical laser and the X-ray pulses using laser-assisted Auger decay (LAAD) in a gaseous target [90] can fulfill this need [68]. In this scheme, Auger electrons are released into a multicycle laser field of energy $h\nu$, where they exchange energy with the optical laser field. This energy exchange requires relatively modest optical laser fields, $\leq 10^{12} \text{ W/cm}^2$, to produce satellite electron lines. The satellite lines are displaced by the energy of the optical laser, $h\nu$, from the normal “diagram” Auger line. The LAAD spectra reflect four parameters: the pulse duration and intensity of the optical laser, the pulse duration of the X-ray laser and the temporal overlap between the optical and X-ray laser pulses. In order to perform cross-correlation on a shot-by-shot basis, a large solid-angle magnetic bottle spectrometer was used. The magnetic bottle spectrometer had only modest energy resolution (0.4%, 3 eV) so that adjacent sidebands could not be resolved. Nevertheless, through modeling of the LAAD spectra produced by 1000 eV X-ray pulses incident on neon gas in the presence of an 800-nm, 10^{12} W/cm^2 , 100 fs dressing field, it was possible to extract X-ray FWHM pulse durations of $\tau_{\text{X-ray}} = 40 \pm 20(120 \pm 20)$ fs that correspond to FWHM electron bunch durations of $\tau_{\text{el}} = 75(175)$ fs with a FWHM jitter of 140 ± 20 fs. The finding that the X-ray pulse duration is substantially shorter than that of the electron beam is in agreement with indirect measurements made earlier [53]. Simulations of the electron and X-ray temporal profiles are shown in Figure 16.10. The work demonstrated the feasibility of this noninvasive method for characterization of the pulse duration and jitter of the LCLS beam with respect to an optical laser. With the careful selection of target atoms and Auger transitions the method can be generally applicable.

For shorter X-ray pulses on the few-femtosecond scale, where $\tau_{\text{X-ray}}$ is comparable to the period of the dressing laser, the LAAD sideband technique is inadequate. In this case, a long-wavelength laser can streak the photoelectrons, chosen such that the X-ray pulse duration lies safely within a half period, as has been widely used in characterization of tabletop attosecond, XUV sources [42, 91, 92]. Extensive efforts have been made at the LCLS to measure sub-10 fs pulses, though, as of the writing of this chapter, no official publication has appeared. The predicted pulse profile, containing a few hundred attosecond spikes over an envelope of 100-fs duration, is difficult to map in the temporal domain.

Characterization of the time-jitter between the LCLS pulse and a secondary optical laser is important to advance the use of X-rays as an ultrafast probe of dynamical phenomena. The earliest characterization of optical/X-ray jitter [93] was done in

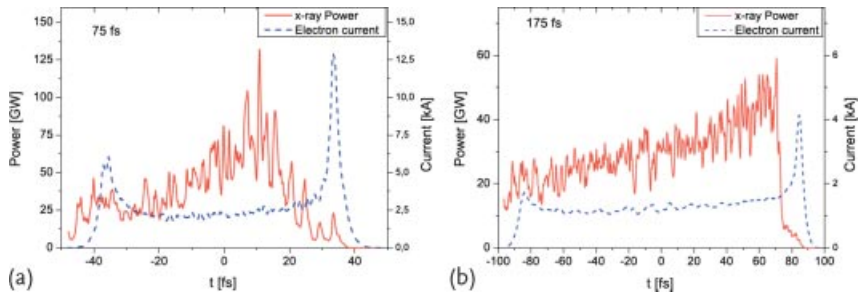


Figure 16.10 Simulations of FEL pulses for electron pulse durations of $\tau_{el} = 75$ and 175 fs using the GENESIS code [87]. For details see [68].

conjunction with the experiment probing Auger decay of aligned N₂ molecules [85]. In contrast to the LAAD or streaking approach, where electron spectroscopy was employed, this experiment relied on ion spectroscopy: transient molecular alignment features were resolved in ion-fragmentation spectra. The width of the alignment features required that the optical and X-ray pulses synchronize to better than 400 fs. A slot in the ion time-of-flight spectrometer allowed a clear distinction of the X-ray-induced fragmentation patterns associated with molecules aligned or anti-aligned relative to the spectrometer axis. Correlation of these X-ray-induced ion-fragments with an electron beam arrival time monitor, located in the accelerator complex, revealed a timing synchronization between the optical and X-ray pulses of approximately 280 fs (FWHM) [93]. To take full advantage of the ultrashort X-ray pulses from LCLS, it is clear that improved timing and synchronization tools must be developed.

16.5 Outlook

Science at the LCLS is thriving during this exciting period and we, the researchers, are on a steep learning curve. Fundamental interactions of SASE X-ray pulses with matter in the high-intensity regime up to 10^{18} W/cm² and for photon energies up to 2000 eV have been investigated and a framework of understanding has been established [53, 66, 73]. The dominant mechanism of interaction is sequential single photon absorption, which, for high-fluence pulses from LCLS, results in multiphoton absorption within a single pulse. The existence of resonances that may be revealed during this multiphoton process presents both dangers and opportunities. The danger lies in unforeseen giant resonances that, when excited, unleash damaging Auger cascades. The opportunities are that such giant resonances can be used to enhance the normally weak X-ray–atom interaction and provide a route to quantum control of inner-shell electrons. Attempts to control of inner-shell dynamics are in the beginning stages [82] and would be much enhanced by X-ray pulses with temporal coherence, for example, near transform-limited pulses that can be achieved by seeding [84]. An alternate scheme to temporally coherent X-ray pulses,

that is, an atomic neon X-ray laser pumped by the LCLS [94], has been developed by Rohringer and colleagues [95].

Considerable effort has been devoted to the control of atomic and molecular processes using ultrafast laser technology to manipulate valence electrons [39, 96, 97]. The active control of inner-shell electron processes is basically unexplored. There is potential for wide-ranging applications: for example, inhibition of Auger decay could suppress X-ray radiation damage [98] and modification of inner-shell electronic structure can alter nuclear lifetimes dominated by internal conversion [99] or electron capture decay [100]. The absence of research in this field is due to the ultrafast nature of inner-shell decay and the lack of a suitably intense radiation source to selectively address inner-shell electron motion on the relevant timescale. Fully coherent tunable, polarized X-ray pulses, as potentially available from seeded FELs, are critical to advance this field.

Seeding of the LCLS using the Geloni scheme [84] is currently an ongoing project at the LCLS. A single-crystal diamond monochromator, to selectively delay a small bandpass $\Delta E/E = 10^{-4}$ of X-rays, is deployed after the initial undulator stages have produced SASE radiation of bandwidth $\Delta E/E \sim 10^{-3}$. At the same point in the undulator hall, the electron beam is chicaned using a set of magnetic structures to overlap the delayed, narrow bandpass X-ray pulse in the remainder of the undulator hall. This seeding scheme is expected to produce, in the low bunch charge mode (20 pC), a 100 GW, fully coherent pulse containing 4×10^{11} photons in a pulse with duration of 5 fs (FWHM) at 0.15 nm. While there are limitations to this initial implementation (limited tuning range (~ 0.14 – 0.16 nm) and operation only in the low bunch charge mode), this is a major step toward fully coherent FEL pulses. The advantages for AMO experiments, for example, control of inner-shell electrons, are clear, but there are also clear advantages for experiments that simply use monochromatic radiation. Currently there is a 100% intensity variation for LCLS SASE pulses that pass a standard two-crystal silicon monochromator of bandpass $\Delta E/E = 10^{-4}$. Even worse, the most probable intensity is zero, since the likelihood of an energy spike in the SASE pulse overlapping the monochromator bandpass is small. In a seeded LCLS beam such intensity fluctuation should be reduced as the pulses, after the monochromator, proceed through the remainder of the undulator hall and are amplified to saturation. With reduced intensity fluctuations on a monochromatic beam, unwanted nonlinear effects for ultrafast X-ray probes can be better accounted for. Experimentalists eagerly await the tests of these first hard X-ray seeding experiments at the LCLS.

Imaging of biomolecules, though not discussed here in detail (see Chapter 17), continues to be a prime motivation for X-ray FEL development. Already some notable successes have been achieved using the soft X-ray pulses to image nanocrystals of photosystem I [101] and a single intact mimi virus [86]. In the case of the photosystem I nanocrystal experiment, the concept of “diffract and destroy” was validated on crystals of submicron dimensions, that is, on crystals too small to be routinely imaged at synchrotrons. The orientation problem for nanocrystals is solved *in situ* by capturing both small and wide angle scattering patterns. The radiation damage that occurs within a single pulse appears manageable for nanocrystals – and Coulomb explosion is not an issue as the loss of periodic order terminates

the scattering into Bragg peaks. For the single mimi virus imaging, this experiment demonstrated the potential for single shot imaging of nonperiodic objects on a virus of 0.75 μm diameter, too large for full 3D reconstruction by cryo-electron microscopy. Both of these stunning achievements were enabled by the design, construction, and operation of the CAMP instrument, comprised of large-format, high-speed, X-ray pnCCDs combined with electron and ion imaging spectrometers in a multipurpose chamber [102].

However, challenges in bioimaging remain. The reported results for nanocrystals do not yet achieve atomic resolution due to the long wavelength of soft X-ray radiation – so results from hard X-ray imaging experiments are eagerly anticipated. To acquire enough statistics for a 3D reconstruction, approximately 3 million images were required, and the hit rate to assure fidelity was typically less than 50%. So an efficient throughput mechanism for the hard X-ray experiments, where the focus will be 100 nm rather than a few microns, will be challenging. This is especially true if the nanocrystals are difficult to manufacture. For noncrystalline objects, the dream of reconstructing structure via a series of single shot coherent diffraction images remains an outstanding challenge. The resolution obtained using 0.69-nm (1.8-keV) radiation was 32 nm. The reconstructed image is only two-dimensional at present and some limitations were encountered due to the lack of dynamic range in the detector. In both cases, it appears that atomic resolution structure determination requires the terawatt level FEL output – a goal that, according to simulations, can be reached using a seeded beam and a 200-m tapered undulator, as tentatively planned for the LCLS-II project.

While considerable effort has been devoted to the control of atomic and molecular processes using ultrafast laser technology to manipulate valence electrons [39, 96, 97], active control of inner-shell electron processes is unexplored. The exploration of wide-ranging applications, for example, inhibition of Auger decay [98] and modification of inner-shell electronic structure [99, 100], will surely continue as the FEL radiation sources reach maturity.

Acknowledgments

I thank my colleagues at Argonne National Laboratory, particularly Steve Southworth, Elliot Kanter, and Bertold Krässig for many years of collaboration that enabled the design and implementation of the first experiments at the LCLS. I am indebted to Robin Santra for many fruitful discussions and theoretical support for these initial experiments. Lou DiMauro, Nora Berrah, and Phil Bucksbaum were critical colleagues in a large team effort that brought the AMO high-field physics chamber to life together with the indispensable contributions of John Bozek and Christoph Bostedt. Of course, the LCLS accelerator physicists played the most important role in bringing this remarkable machine alive and, in particular, I thank Paul Emma, Zhirong Huang, Jo Frisch, and Franz Josef Decker for insightful discussions during beam times that helped us operate the LCLS in its flexibility to our experimental needs. This work was supported by the Chemical Sciences, Geo-

sciences, and Biosciences Division of the Office of Basic Energy Sciences, Office of Science, US Department of Energy (DE-AC02-06CH11357). The LCLS is funded by the US Department of Energy's Office of Basic Energy Sciences.

References

- 1 Maiman, T.H. (1960) Stimulated optical radiation in ruby. *Nature*, **187**, 493–494.
- 2 Gudzenko, G.A. and Shelepin, L.A. (1964) *Sov. Phys. JETP*, **18**, 998.
- 3 Duguay, M.A. and Rentzepis, P.M. (1967) *Appl. Phys. Lett.*, **10**, 350.
- 4 Molchanov, A.G. (1972) *Sov. Phys. Usp.*, **15**, 124.
- 5 Elton, R. (1975) *Appl. Opt.*, **14**, 97.
- 6 Zherikin, A., Koshelev, K.N., and V. S. Letokhov, V. (1976) *Appl. Opt.*, **6**, 82.
- 7 Matthews, D.L., Hagelstein, P.L., Rosen, M.D., Eckart, M.J., Ceglio, N.M., Hazi, A.U., Medecki, H., MacGowan, B.J., Trebes, J.E., Whitten, B.L., Campbell, E.M., Hatcher, C.W., Hawryluk, A.M., Kauffman, R.L., Pleasance, L.D., Rambach, G., Scofield, J.H., Stone, G., and Weaver, T.A. (1985) Demonstration of a soft X-ray amplifier. *Phys. Rev. Lett.*, **54** (2), 110–113, doi:10.1103/PhysRevLett.54.110.
- 8 Rocca, J., Shlyaptsev, V., Tomasel, F., Cortazar, O., Hartshorn, D., and Chilla, J. (1994) Demonstration of a discharge pumped table-top soft-X-ray laser. *Phys. Rev. Lett.*, **73** (16), 2192–2195.
- 9 Rocca, J. (1999) Table-top soft X-ray lasers. *Rev. Sci. Instrum.*, **70** (10), 3799–3827.
- 10 Furch, F.J., Reagan, B.A., Luther, B.M., Curtis, A.H., Meehan, S.P., and Rocca, J.J. (2009) Demonstration of an all-diode-pumped soft X-ray laser. *Opt. Lett.*, **34** (21), 3352–3354.
- 11 Barletta, W.A., Bisognano, J., Corlett, J.N., Emma, P., Huang, Z., Kim, K.J., Lindberg, R., Murphy, J.B., Neil, G.R., Nguyen, D.C., Pellegrini, C., Rimmer, R.A., Sannibale, F., Stupakov, G., Walker, R.P., and Zholents, A.A. (2010) Free electron lasers: Present status and future challenges. *Nucl. Instrum. Methods Phys. Res.*, **618** (1-3), 69–96.
- 12 Andruszkow, J., Aune, B., Ayvazyan, V., Baboi, N., Bakker, R., Balakin, V., Barni, D., Bazhan, A., Bernard, M., Bosotti, A., Bourdon, J.C., Brefeld, W., Brinkmann, R., Buhler, S., Carneiro, J.P., Castellano, M., Castro, P., Catani, L., Chel, S., Cho, Y., Choroba, S., Colby, E.R., Decking, W., Den Hartog, P., Desmons, M., Dohlus, M., Edwards, D., Edwards, H.T., Faatz, B., Feldhaus, J., Ferrario, M., Fitch, M.J., Flöttmann, K., Fouaidy, M., Gamp, A., Garvey, T., Gerth, C., Geitz, M., Gluskin, E., Gretschko, V., Hahn, U., Hartung, W.H., Hubert, D., Hüning, M., Ischebek, R., Jablonka, M., Joly, J.M., Juillard, M., Junquera, T., Jurkiewicz, P., Kabel, A., Kahl, J., Kaiser, H., Kamps, T., Katelev, V.V., Kirchgessner, J.L., Körfer, M., Kravchuk, L., Kreps, G., Krzywinski, J., Lokajczyk, T., Lange, R., Leblond, B., Leenen, M., Lesrel, J., Liepe, M., Liero, A., Limberg, T., Lorenz, R., Hua, L.H., Hai, L.F., Magne, C., Maslov, M., Materlik, G., Matheisen, A., Menzel, J., Michelato, P., Möller, W.D., Mosnier, A., Müller, U.C., Napoly, O., Novokhatski, A., Omeich, M., Padamsee, H.S., Paganini, C., Peters, F., Petersen, B., Pierini, P., Pfütger, J., Piot, P., Phung Ngoc, B., Plucinski, L., Proch, D., Rehlich, K., Reiche, S., Reschke, D., Reyzi, I., Rosenzweig, J., Rossbach, J., Roth, S., Saldin, E.L., Sandner, W., Sanok, Z., Schlarb, H., Schmidt, G., Schmüser, P., Schneider, J.R., Schneidmiller, E.A., Schreiber, H.J., Schreiber, S., Schütt, P., Sekutowicz, J., Serafini, L., Sertore, D., Setzer, S., Simrock, S., Sonntag, B., Sparr, B., Stephan, F., Sytchev, V.A., Tazzari, S., Tazzioli, F., Tigner, M., Timm, M., Tonutti, M., Trakhtenberg, E., Treusch, R., Trines, D., Verzilov, V., Vielitz, T., Vogel, V., Walter, G.v., Wanzenberg, R., Weiland, T., Weise, H., Weisend, J., Wendt, M., Werner, M., White, M.M., Will, I., Wolff,

- S., Yurkov, M.V., Zapfe, K., Zhogolev, P., and Zhou, F. (2000) First observation of self-amplified spontaneous emission in a free-electron laser at 109 nm wavelength. *Phys. Rev. Lett.*, **85**, 3825–3829.
- 13** Ayvazyan, V., Baboi, N., Bohnet, I., Brinkmann, R., Castellano, M., Castro, P., Catani, L., Choroba, S., Cianchi, A., Dohlus, M., Edwards, H.T., Faatz, B., Fateev, A.A., Feldhaus, J., Flöttmann, K., Gamp, A., Garvey, T., Genz, H., Gerth, C., Gretschko, V., Grigoryan, B., Hahn, U., Hessler, C., Honkavaara, K., Hüning, M., Ischebeck, R., Jablonka, M., Kamps, T., Körfer, M., Krassilnikov, M., Krzywinski, J., Liepe, M., Liero, A., Limberg, T., Loos, H., Luong, M., Magne, C., Menzel, J., Michelato, P., Minty, M., Müller, U.C., Nölle, D., Novokhatski, A., Pagani, C., Peters, F., Pflüger, J., Piot, P., Plucinski, L., Rehlich, K., Reyzl, I., Richter, A., Rossbach, J., Saldin, E.L., Sandner, W., Schlarb, H., Schmidt, G., Schmüser, P., Schneider, J.R., Schneidmiller, E.A., Schreiber, H.J., Schreiber, S., Sertore, D., Setzer, S., Simrock, S., Sobierajski, R., Sonntag, B., Steeg, B., Stephan, F., Sytchev, K.P., Tiedtke, K., Tonutti, M., Treusch, R., Trines, D., Türke, D., Verzilov, V., Wanzenberg, R., Weiland, T., Weise, H., Wendt, M., Will, I., Wolff, S., Wittenburg, K., Yurkov, M.V., and Zapfe, K. (2002) Generation of GW radiation pulses from a VUV free-electron laser operating in the femtosecond regime. *Phys. Rev. Lett.*, **88**, 104802, doi:10.1103/PhysRevLett.88.104802.
- 14** Ackermann, W., Asova, G., Ayvazyan, V., Azima, A., Baboi, N., Baehr, J., Balandin, V., Beutner, B., Brandt, A., Bolzmann, A., Brinkmann, R., Brovko, O.I., Castellano, M., Castro, P., Catani, L., Chiadroni, E., Choroba, S., Cianchi, A., Costello, J.T., Cubaynes, D., Dardis, J., Decking, W., Delsim-Hashemi, H., Delseries, A., Di Pirro, G., Dohlus, M., Duesterer, S., Eckhardt, A., Edwards, H.T., Faatz, B., Feldhaus, J., Flöttmann, K., Frisch, J., Froehlich, L., Garvey, T., Gensch, U., Gerth, C., Goerler, M., Golubeva, N., Grabosch, H.J., Grecki, M., Grimm, O., Hacker, K., Hahn, U., Han, J.H., Honkavaara, K., Hott, T., Huening, M., Ivanisenko, Y., Jaeschke, E., Jalmuzna, W., Jezynski, T., Kammerling, R., Katalev, V., Kavanagh, K., Kennedy, E.T., Khodyachykh, S., Klose, K., Kocharyan, V., Koerfer, M., Kollewe, M., Koprek, W., Korepanov, S., Kostin, D., Krassilnikov, M., Kube, G., Kuhlmann, M., Lewis, C.L.S., Lilje, L., Limberg, T., Lipka, D., Loehl, F., Luna, H., Luong, M., Martins, M., Meyer, M., Michelato, P., Miltchev, V., Moeller, W.D., Monaco, L., Mueller, W.F.O., Napieralski, O., Napolys, O., Nicolosi, P., Noelle, D., Nunez, T., Oppelt, A., Pagani, C., Paparella, R., Pchalek, N., Pedregosa-Gutierrez, J., Petersen, B., Petrosyan, B., Petrosyan, G., Petrosyan, L., Pflueger, J., Ploenjes, E., Poletto, L., Pozniak, K., Prat, E., Proch, D., Pucyk, P., Radcliffe, P., Redlin, H., Rehlich, K., Richter, M., Roehrs, M., Roensch, J., Romaniuk, R., Ross, M., Rossbach, J., Rybnikov, V., Sachwitz, M., Saldin, E.L., Sandner, W., Schlarb, H., Schmidt, B., Schmitz, M., Schmueser, P., Schneider, J.R., Schneidmiller, E.A., Schnepf, S., Schreiber, S., Seidel, M., Sertore, D., Shabunov, A.V., Simon, C., Simrock, S., Sombrowski, E., Sorokin, A.A., Spanknebel, P., Spesvtsev, R., Staykov, L., Steffen, B., Stephan, F., Stulle, F., Thom, H., Tiedtke, K., Tischer, M., Toleikis, S., Treusch, R., Trines, D., Tsakov, I., Vogel, E., Weiland, T., Weise, H., Wellhoeffer, M., Wendt, M., Will, I., Winter, A., Wittenburg, K., Wurth, W., Yeates, P., Yurkov, M.V., Zagorodnov, I., and Zapfe, K. (2007) Operation of a free-electron laser from the extreme ultraviolet to the water window. *Nat. Photonics*, **1** (6), 336–342.
- 15** Tiedtke, K., Azima, A., von Bargen, N., Bittner, L., Bonfigt, S., Duesterer, S., Faatz, B., Fruehling, U., Gensch, M., Gerth, C., Guerassimova, N., Hahn, U., Hans, T., Hesse, M., Honkavaar, K., Jastrow, U., Juranic, P., Kapitzki, S., Keitel, B., Kracht, T., Kuhlmann, M., Li, W.B., Martins, M., Nunez, T., Ploenjes, E., Redlin, H., Saldin, E.L., Schneidmiller, E.A., Schneider, J.R., Schreiber, S., Stojanovic, N., Tavella, F., Toleikis, S., Treusch, R., Weigelt, H., Wellhoefer, M., Wabnitz, H., Yurkov, M.V., and

- Feldhaus, J. (2009) The soft X-ray free-electron laser FLASH at DESY: beam-lines, diagnostics and end-stations. *New J. Phys.*, **11**, 023029, doi:10.1088/1367-2630/11/2/023029.
- 16** Moncton, D. Private communication.
- 17** Emma, P., Akre, R., Arthur, J., Bionta, R., Bostedt, C., Bozek, J., Brachmann, A., Bucksbaum, P., Coffee, R., Decker, F.J., Ding, Y., Dowell, D., Edstrom, S., Fisher, A., Frisch, J., Gilevich, S., Hastings, J., Hays, G., Hering, P., Huang, Z., Iverson, R., Loos, H., Messerschmidt, M., Miahnahri, A., Moeller, S., Nuhn, H.D., Pile, G., Ratner, D., Rzepiela, J., Schultz, D., Smith, T., Stefan, P., Tompkins, H., Turner, J., Welch, J., White, W., Wu, J., Yocky, G., and Galayda, J. (2010) First lasing and operation of an angstrom-wavelength free-electron laser. *Nat. Photonics*, **4** (9), 641–647.
- 18** Pellegrini, C. (1992) 4 to 0.1 nm FEL based on the SLAC linac. *Workshop on 4th Generation Light Sources SSRL-Report-92/02*, (eds M. Cornacchia and H. Winick), pp. 364–375.
- 19** Arthur, J. et al. (2002) Linac coherent light source (LCLS) conceptual design report, *Tech. Rep. SLAC-R-593*, SLAC.
- 20** Kondratenko, A.M. and Saldin, E.L. (1980) Generation of coherent radiation by a relativistic electron beam in an undulator. *Part. Accel.*, **10**, 207–216.
- 21** Bonifacio, R., Pellegrini, C., and Narducci, L.M. (1984) Collective instabilities and high-gain regime in a free-electron laser. *Opt. Comm.*, **50** (6), 373–378.
- 22** Huang, Z. and Kim, K.J. (2007) Review of X-ray free-electron laser theory. *Phys. Rev. ST Accel. Beams*, **10**, 034801, doi:10.1103/PhysRevSTAB.10.034801.
- 23** Tanaka, T. and Shintake, T. (2005) SCSS X-FEL conceptual design report, *Tech. Rep.*, SPring-8, Riken, Japan.
- 24** Altarelli, M., Brinkmann, R., Chergui, M., Decking, W., Dobson, B., Düsterer, S., Grübel, G., Graeff, W., Graafsma, H., Hajdu, J., Marangos, J., Pflüger, J., Redlin, H., Riley, D., Robinson, I., Rossbach, J., Tiedtke, A.S.K., Tschentscher, T., Vartaniants, I., Wabnitz, H., Weisse, H., Wichmann, R., Witte, K., Wolf, A., Wulff, M., and Yurkov, M. (2006) The European X-ray free-electron laser, technical design report, *Tech. Rep. DESY 2006-097*, DESY, Notkestrasse 85, 22607 Hamburg.
- 25** McNeil, B.W.J. and Thompson, N.R. (2010) X-ray free-electron lasers. *Nat. Photonics*, **4**, 814–821.
- 26** Neutze, R., Wouts, R., van der Spoel, D., Weckert, E., and Hajdu, J. (2000) Potential for biomolecular imaging with femtosecond X-ray pulses. *Nature*, **406**, 752–757.
- 27** Henderson, R. (1995) The potential and limitations of neutrons, electrons and X-rays for atomic resolution microscopy of unstained biological molecules. *Q. Rev. Biophys.*, **28**, 171–193.
- 28** Ding, Y., Brachmann, A., Decker, F.J., Dowell, D., Emma, P., Frisch, J., Gilevich, S., Hays, G., Hering, P., Huang, Z., Iverson, R., Loos, H., Miahnahri, A., Nuhn, H.D., Ratner, D., Turner, J., Welch, J., White, W., and Wu, J. (2009) Measurements and simulations of ultralow emittance and ultrashort electron beams in the linac coherent light source. *Phys. Rev. Lett.*, **102**, 254801, doi:10.1103/PhysRevLett.102.254801.
- 29** Emma, P., Bane, K., Cornacchia, M., Huang, Z., Schlarb, H., Stupakov, G., and Walz, D. (2004) Femtosecond and subfemtosecond X-ray pulses from a self-amplified spontaneous-emission based free-electron laser. *Phys. Rev. Lett.*, **92**, 074801, doi:10.1103/PhysRevLett.92.074801.
- 30** Mourou, G.A., Tajima, T., and Bulanov, S.V. (2006) Optics in the relativistic regime. *Rev. Mod. Phys.*, **78**, 309–371, doi:10.1103/RevModPhys.78.309.
- 31** Strickland, D. and Mourou, G. (1985) Compression of amplified chirped optical pulses. *Opt. Comm.*, **56** (3), 219–221.
- 32** Keldysh, L.V. (1965) *Sov. Phys. JETP*, **20**, 1307.
- 33** McPherson, A., Gibson, G., Jara, H., Johann, U., Luk, T.S., McIntyre, I.A., Boyer, K., and Rhodes, C.K. (1987) Studies of multiphoton production of vacuum-ultraviolet radiation in the rare gases. *J. Opt. Soc. Am. B*, **4** (4), 595–601, doi:10.1364/JOSAB.4.000595.

- 34** Krause, J.L., Schafer, K.J., and Kulander, K.C. (1992) High-order harmonic generation from atoms and ions in the high intensity regime. *Phys. Rev. Lett.*, **68**, 3535–3538, doi:10.1103/PhysRevLett.68.3535.
- 35** Corkum, P.B. (1993) Plasma perspective on strong field multiphoton ionization. *Phys. Rev. Lett.*, **71**, 1994–1997, doi:10.1103/PhysRevLett.71.1994.
- 36** Lewenstein, M., Balcou, P., Ivanov, M.Y., L'Huillier, A., and Corkum, P.B. (1994) Theory of high-harmonic generation by low-frequency laser fields. *Phys. Rev. A*, **49**, 2117–2132, doi:10.1103/PhysRevA.49.2117.
- 37** Chang, Z., Rundquist, A., Wang, H., Murnane, M.M., and Kapteyn, H.C. (1997) Generation of coherent soft x rays at 2.7 nm using high harmonics. *Phys. Rev. Lett.*, **79**, 2967–2970, doi:10.1103/PhysRevLett.79.2967.
- 38** Spielmann, C., Burnett, N., Sartania, S., Koppitsch, R., Schnürer, M., Kan, C., Lenzner, M., Wobrauscheck, P., and Krausz, F. (1997) Generation of coherent X-rays in the water window using 5-femtosecond laser pulses. *Science*, **278**, 661–664.
- 39** Brabec, T. and Krausz, F. (2000) Intense few-cycle laser fields: Frontiers of nonlinear optics. *Rev. Mod. Phys.*, **72** (2), 545–591, doi:10.1103/RevModPhys.72.545.
- 40** Agostini, P. and DiMauro, L.F. (2004) The physics of attosecond light pulses. *Rep. Progr. Phys.*, **67** (6), 813.
- 41** Pfeifer, T., Spielmann, C., and Gerber, G. (2006) Femtosecond X-ray science. *Rep. Progr. Phys.*, **69** (2), 443–505.
- 42** Krausz, F. and Ivanov, M. (2009) Attosecond physics. *Rev. Mod. Phys.*, **81** (1), 163–234, doi:10.1103/RevModPhys.81.163.
- 43** Miao, J., Charalambous, P., Kirz, J., and Sayre, D. (1999) Extending the methodology of X-ray crystallography to allow imaging of micrometre-sized non-crystalline specimens. *Nature*, **400**, 342–344.
- 44** Veigle, W.J. (1973) Photon cross sections from 0.1 keV to 1 meV for elements $z = 1$ to $z = 94$. *At. Data Nucl. Data Tables*, **5** (1), 51–111.
- 45** Schmidt, V. (1997) *Electron Spectrometry of Atoms using Synchrotron Radiation*, Cambridge University Press.
- 46** Thomson, A. et al. (2009) *X-ray Data Booklet*, Lawrence Berkeley National Laboratory, Berkeley.
- 47** Wuilleumier, F. and Krause, M.O. (1974) Photoionization of neon between 100 and 2000 eV: Single and multiple processes, angular distributions, and sub-shell cross sections. *Phys. Rev. A*, **10**, 242–258, doi:10.1103/PhysRevA.10.242.
- 48** Krause, M.O. (1979) Atomic radiative and radiationless yields for k and l shells. *J. Phys. Chem. Ref. Data*, **8**, 307.
- 49** Kelly, H.P. (1975) k auger rates calculated for Ne^+ . *Phys. Rev. A*, **11**, 556–565, doi:10.1103/PhysRevA.11.556.
- 50** Bhalla, C.P., Folland, N.O., and Hein, M.A. (1973) Theoretical k -shell auger rates, transition energies, and fluorescence yields for multiply ionized neon. *Phys. Rev. A*, **8**, 649–657, doi:10.1103/PhysRevA.8.649.
- 51** Chen, M.H. (1991) Auger transition rates and fluorescence yields for the double-K-hole state. *Phys. Rev. A*, **44**, 239–242, doi:10.1103/PhysRevA.44.239.
- 52** Berezhko, E.G. and Kabachnik, N.M. (1977) Theoretical study of inner-shell alignment of atoms in electron impact ionisation: angular distribution and polarisation of X-rays and auger electrons. *J. Phys. B*, **10**, 2467–2477.
- 53** Young, L., Kanter, E.P., Krässig, B., March, A.M., Pratt, S.T., Santra, R., Southworth, S., Rohringer, N., DiMauro, L.F., Doumy, G., Roedig, C.A., Berrah, N., Fang, L., Hoener, M., Bucksbaum, P.H., Cryan, J.P., Ghimire, S., Glownia, J.M., Reis, D.A., Bozek, J.D., Bostedt, C., and Messerschmidt, M. (2010) Femtosecond electronic response of atoms to ultra-intense X-rays. *Nature*, **466**, 56–61.
- 54** Marangos, J.P. (2011) Introduction to the new science with X-ray free electron lasers. *Contemp. Phys.*, **52** (6), 551–569.
- 55** Bucksbaum, P.H., Coffee, R., and Berrah, N. (2011) The first atomic and molecular experiments at the linac coherent light source X-ray free electron laser, in *Advances in Atomic, Molecular, and Optical Physics*, Vol 60 (eds E. Ari-

- mondo, P. Berman, and C. Lin), Academic Press, pp. 239–289.
- 56** Bozek, J.D. (2009) *Eur. Phys. J. – Special Top.*, **169**, 129–132.
- 57** Barty, A., Soufli, R., McCarville, T., Baker, S.L., Pivovaroff, M.J., Stefan, P., and Bionta, R. (2009) Predicting the coherent X-ray wavefront focal properties at the linac coherent light source (LCLS) X-ray free electron laser. *Opt. Express*, **17** (18), 15508–15519.
- 58** Hemmers, O., Whitfield, S., Glans, P., Wang, H., Lindle, D., Wehlitz, R., and Sellin, I. (1998) High-resolution electron time-of-flight apparatus for the soft X-ray region. *Rev. Sci. Instrum.*, **69** (11), 3809–3817.
- 59** Krause, M.O., Vestal, M.L., Johnston, W.H., and Carlson, T.A. (1964) Readjustment of the neon atom ionized in the k shell by x rays. *Phys. Rev.*, **133**, A385–A390, doi:10.1103/PhysRev.133.A385.
- 60** Saito, N. and Suzuki, I.H. (1992) Multiple photoionization of Ne in the k-shell ionization region. *Phys. Scr.*, **45**, 253–256.
- 61** Kanngießer, B., Jainz, M., Brünken, S., Benten, W., Gerth, C., Godehusen, K., Tiedtke, K., van Kampen, P., Tuttay, A., Zimmermann, P., Demekhin, V.F., and Kochur, A.G. (2000) Simultaneous determination of radiative and nonradiative decay channels in the neon K shell. *Phys. Rev. A*, **62**, 014702, doi:10.1103/PhysRevA.62.014702.
- 62** Southworth, S.H., Kanter, E.P., Krässig, B., Young, L., Armen, G.B., Levin, J.C., Ederer, D.L., and Chen, M.H. (2003) Double K-shell photoionization of neon. *Phys. Rev. A*, **67**, 062712, doi:10.1103/PhysRevA.67.062712.
- 63** Coreno, M., Avaldi, L., Camilloni, R., Prince, K.C., de Simone, M., Karvonen, J., Colle, R., and Simonucci, S. (1999) Measurement and ab initio calculation of the Ne photoabsorption spectrum in the region of the k edge. *Phys. Rev. A*, **59**, 2494–2497, doi:10.1103/PhysRevA.59.2494.
- 64** Wark, J. (2010) Atomic physics X-ray laser peels and cores atoms. *Nature*, **466** (7302), 35–36.
- 65** Rohringer, N. and Santra, R. (2007) X-ray nonlinear optical processes using a self-amplified spontaneous emission free-electron laser. *Phys. Rev. A*, **76** (3), 033416, doi:10.1103/PhysRevA.76.033416.
- 66** Hoener, M., Fang, L., Kornilov, O., Gessner, O., Pratt, S.T., Gühr, M., Kanter, E.P., Blaga, C., Bostedt, C., Bozek, J.D., Bucksbaum, P.H., Buth, C., Chen, M., Coffee, R., Cryan, J., DiMauro, L., Glownia, M., Hosler, E., Kukk, E., Leone, S.R., McFarland, B., Messerschmidt, M., Murphy, B., Petrovic, V., Rolles, D., and Berrah, N. (2010) Ultraintense X-ray induced ionization, dissociation, and frustrated absorption in molecular nitrogen. *Phys. Rev. Lett.*, **104** (25), 253002, doi:10.1103/PhysRevLett.104.253002.
- 67** Son, S.K., Young, L., and Santra, R. (2011) Impact of hollow-atom formation on coherent X-ray scattering at high intensity. *Phys. Rev. A*, **83** (3), 033402.
- 68** Düsterer, S., Radcliffe, P., Bostedt, C., Bozek, J., Cavalieri, A.L., Coffee, R., Costello, J.T., Cubaynes, D., DiMauro, L.F., Ding, Y., Doumy, G., Grüner, F., Helml, W., Schweinberger, W., Kienberger, R., Maier, A.R., Messerschmidt, M., Richardson, V., Roedig, C., Tschentscher, T., and Meyer, M. (2011) Femtosecond X-ray pulse length characterization at the linac coherent light source free-electron laser. *New J. Phys.*, **13** (9), 093024.
- 69** Franken, P. and Ward, J. (1963) Optical harmonics and nonlinear phenomena. *Rev. Modern Phys.*, **35**, 23–39.
- 70** Doumy, G., Roedig, C., Son, S.K., Blaga, C.I., DiChiara, A.D., Santra, R., Berrah, N., Bostedt, C., Bozek, J.D., Bucksbaum, P.H., Cryan, J.P., Fang, L., Ghimire, S., Glownia, J.M., Hoener, M., Kanter, E.P., Krässig, B., Kuebel, M., Messerschmidt, M., Paulus, G.G., Reis, D.A., Rohringer, N., Young, L., Agostini, P., and DiMauro, L.F. (2011) Nonlinear atomic response to intense ultrashort x rays. *Phys. Rev. Lett.*, **106** (8), 083002, doi:10.1103/PhysRevLett.106.083002.
- 71** Novikov, S. and Hopersky, A. (2002) Two-photon knocking-out of two electrons of

- the 1s(2)-shell of the neon atom. *J. Phys. B*, **35** (15), L339–L343.
- 72** Ratner, D., Brachmann, A., Decker, F.J., Ding, Y., Dowell, D., Emma, P., Fisher, A., Frisch, J., Gilevich, S., Huang, Z., Hering, P., Iverson, R., Krzywinski, J., Loos, H., Messerschmidt, M., Nuhn, H.D., Smith, T., Turner, J., Welch, J., White, W., and Wu, J. (2011) Second and third harmonic measurements at the linac coherent light source. *Phys. Rev. Special Top.–Accel.*, **14** (6), 060701.
- 73** Fang, L., Hoener, M., Gessner, O., Tarantelli, F., Pratt, S.T., Kornilov, O., Buth, C., Gühr, M., Kanter, E.P., Bostedt, C., Bozek, J.D., Bucksbaum, P.H., Chen, M., Coffee, R., Cryan, J., Glownia, M., Kukk, E., Leone, S.R., and Berrah, N. (2010) Double core-hole production in N₂: Beating the Auger clock. *Phys. Rev. Lett.*, **105** (8), 083005, doi:10.1103/PhysRevLett.105.083005.
- 74** Cederbaum, L.S., Tarantelli, F., Sgamellotti, A., and Schirmer, J. (1986) On double vacancies in the core. *J. Chem. Phys.*, **85** (11), 6513–6523.
- 75** Santra, R., Kryzhevci, N.V., and Cederbaum, L.S. (2009) X-ray two-photon photoelectron spectroscopy: A theoretical study of inner-shell spectra of the organic para-aminophenol molecule. *Phys. Rev. Lett.*, **103** (1), 013002.
- 76** Rabi, I.I. (1937) Space quantization in a gyrating magnetic field. *Phys. Rev.*, **51** (8), 652–654, doi:10.1103/PhysRev.51.652.
- 77** Rabi, I.I., Zacharias, J.R., Millman, S., and Kusch, P. (1938) A new method of measuring nuclear magnetic moment. *Phys. Rev.*, **53** (4), 318, doi:10.1103/PhysRev.53.318.
- 78** Georges, A.T., Lambropoulos, P., and Zoller, P. (1979) Saturation and Stark splitting of resonant transitions in strong chaotic fields of arbitrary bandwidth. *Phys. Rev. Lett.*, **42** (24), 1609–1613, doi:10.1103/PhysRevLett.42.1609.
- 79** Georges, A.T. and Lambropoulos, P. (1979) Saturation and Stark splitting of an atomic transition in a stochastic field. *Phys. Rev. A*, **20** (3), 991, doi:10.1103/PhysRevA.20.991.
- 80** Rohringer, N. and Santra, R. (2008) Resonant Auger effect at high X-ray intensity. *Phys. Rev. A*, **77** (5), 053404, doi:10.1103/PhysRevA.77.053404.
- 81** Liu, J.C., Sun, Y.P., Wang, C.K., Ågren, H., and Gel'mukhanov, F. (2010) Auger effect in the presence of strong X-ray pulses. *Phys. Rev. A*, **81** (4), 043412, doi:10.1103/PhysRevA.81.043412.
- 82** Kanter, E.P., Krässig, B., Li, Y., March, A.M., Ho, P., Rohringer, N., Santra, R., Southworth, S.H., DiMauro, L.F., Doumy, G., Roedig, C.A., Berrah, N., Fang, L., Hoener, M., Bucksbaum, P.H., Ghimire, S., Reis, D.A., Bozek, J.D., Bostedt, C., Messerschmidt, M., and Young, L. (2011) Unveiling and driving hidden resonances with high-fluence, high-intensity X-ray pulses. *Phys. Rev. Lett.*, **107**, 233001.
- 83** Aksela, S., Kukk, E., Aksela, H., and Svensson, S. (1995) Experimental verification of the line-shape distortion in resonance Auger spectra. *Phys. Rev. Lett.*, **74** (15), 2917–2920, doi:10.1103/PhysRevLett.74.2917.
- 84** Geloni, G., Kocharyan, V., and Saldin, E. (2010) Scheme for generation of highly monochromatic X-rays from a baseline XFEL undulator. *ArXiv e-prints*.
- 85** Cryan, J.P., Glownia, J.M., Andreasson, J., Belkacem, A., Berrah, N., Blaga, C.I., Bostedt, C., Bozek, J., Buth, C., DiMauro, L.F., Fang, L., Gessner, O., Guehr, M., Hajdu, J., Hertlein, M.P., Hoener, M., Kornilov, O., Marangos, J.P., March, A.M., McFarland, B.K., Merdji, H., Petrović, V.S., Raman, C., Ray, D., Reis, D., Tarantelli, F., Trigo, M., White, J.L., White, W., Young, L., Bucksbaum, P.H., and Coffee, R.N. (2010) Auger electron angular distribution of double core-hole states in the molecular reference frame. *Phys. Rev. Lett.*, **105** (8), 083004, doi:10.1103/PhysRevLett.105.083004.
- 86** Seibert, M.M., Ekeberg, T., Maia, F.R.N.C., Svenda, M., Andreasson, J., Joensson, O., Odic, D., Iwan, B., Rocker, A., Westphal, D., Hantke, M., DePonte, D.P., Barty, A., Schulz, J., Gumprecht, L., Coppola, N., Aquila, A., Liang, M., White, T.A., Martin, A., Caleman, C., Stern, S., Abergel, C., Seltzer, V., Claver-

- ie, J.M., Bostedt, C., Bozek, J.D., Boutet, S., Miahnahri, A.A., Messerschmidt, M., Krzywinski, J., Williams, G., Hodgson, K.O., Bogan, M.J., Hampton, C.Y., Sierra, R.G., Starodub, D., Andersson, I., Bajt, S., Barthelmess, M., Spence, J.C.H., Fromme, P., Weierstall, U., Kirian, R., Hunter, M., Doak, R.B., Marchesini, S., Hau-Riege, S.P., Frank, M., Shoeman, R.L., Lomb, L., Epp, S.W., Hartmann, R., Rolles, D., Rudenko, A., Schmidt, C., Foucar, L., Kimmel, N., Holl, P., Rudek, B., Erk, B., Hoemke, A., Reich, C., Pietschner, D., Weidenspointner, G., Strueder, L., Hauser, G., Gorke, H., Ullrich, J., Schlichting, I., Herrmann, S., Schaller, G., Schopper, F., Soltau, H., Kuehnel, K.U., Andritschke, R., Schroeter, C.D., Krasnqi, F., Bott, M., Schorb, S., Rupp, D., Adolph, M., Gorkhover, T., Hirsemann, H., Potdevin, G., Graafsma, H., Nilsson, B., Chapman, H.N., and Hajdu, J. (2011) Single mimivirus particles intercepted and imaged with an X-ray laser. *Nature*, **470** (7332), 78–U86.
- 87** Reiche, S. (1999) Genesis 1.3: a fully 3d time-dependent fel simulation code. *Nucl. Instrum. Methods Phys. Res. Sect. A*, **429** (1-3), 243–248
- 88** Hau-Riege, S.P., Bionta, R.M., Ryutov, D.D., London, R.A., Ables, E., Kishiyama, K.I., Shen, S., McKernan, M.A., McMahon, D.H., Messerschmidt, M., Krzywinski, J., Stefan, P., Turner, J., and Ziaja, B. (2010) Near-ultraviolet luminescence of N₂ irradiated by short X-ray pulses. *Phys. Rev. Lett.*, **105** (4), 043003, doi:10.1103/PhysRevLett.105.043003.
- 89** Emma, P., Akre, R., Arthur, J., Bionta, R., Bostedt, C., Bozek, J., Brachmann, A., Bucksbaum, P., Coffee, R., Decker, F.J., Ding, Y., Dowell, D., Edstrom, S., Fisher, A., Frisch, J., Gilevich, S., Hastings, J., Hays, G., Hering, P., Huang, Z., Iverson, R., Loos, H., Messerschmidt, M., Miahnahri, A., Moeller, S., Nuhn, H.D., Pile, G., Ratner, D., Rzepiela, J., Schultz, D., Smith, T., Stefan, P., Tompkins, H., Turner, J., Welch, J., White, W., Wu, J., Yocky, G., and Galayda, J. (2010) First lasing and operation of an Ångstrom-wavelength free-electron laser. *Nat. Photonics*, **4**, 641–647, doi:10.1038/nphoton.2010.176.
- 90** Schins, J.M., Breger, P., Agostini, P., Constantinescu, R.C., Muller, H.G., Grillon, G., Antonetti, A., and Mysyrowicz, A. (1994) *Phys. Rev. Lett.*, **73**, 2180.
- 91** Drescher, M., Hentschel, M., Kienberger, R., Tempea, G., Spielmann, C., Reiher, G.A., Corkum, P.B., and Krausz, F. (2001) *Science*, **291**, 1923.
- 92** Kienberger, R., Goulielmakis, E., Uiberacker, M., Baltuska, A., Yakovlev, V., Hammer, F., Scrinzi, A., Westerwalbesloh, T., Kleineberg, U., Heinzenmann, U., Drescher, M., and Krausz, F. (2004) Atomic transient recorder. *Nature*, **427** (6977), 817–821.
- 93** Glownia, J.M., Cryan, J., Andreasson, J., Belkacem, A., Berrah, N., Blaga, C.I., Bostedt, C., Bozek, J., DiMauro, L.F., Fang, L., Frisch, J., Gessner, O., Gühr, M., Hajdu, J., Hertlein, M.P., Hoener, M., Huang, G., Kornilov, O., Marangos, J.P., March, A.M., McFarland, B.K., Merdji, H., Petrovic, V.S., Raman, C., Ray, D., Reis, D.A., Trigo, M., White, J.L., White, W., Wilcox, R., Young, L., Coffee, R.N., and Bucksbaum, P.H. (2010) Time-resolved pump-probe experiments at the LCLS. *Opt. Express*, **18** (17), 17620–17630.
- 94** Rohringer, N. and London, R. (2009) Atomic inner-shell X-ray laser pumped by an X-ray free-electron laser. *Phys. Rev. A*, **80** (1), 013809, doi:10.1103/PhysRevA.80.013809.
- 95** Rohringer, N. (2012) Atomic inner-shell X-ray laser at 1.46 nm pumped by an X-ray free-electron laser. *Nature*, **481**, 488.
- 96** Warren, W.S., Rabitz, H., and Dahlfeh, M. (1993) Coherent control of quantum dynamics: The dream is alive. *Science*, **259** (5101), 1581–1589, doi:10.1126/science.259.5101.1581.
- 97** Weiner, A.M. (2000) Femtosecond pulse shaping using spatial light modulators. *Rev. Sci. Instrum.*, **71** (5), 1929–1960, doi:10.1063/1.1150614.
- 98** Hau-Riege, S.P., London, R.A., and Szoke, A. (2004) Dynamics of biological molecules irradiated by short X-ray

- pulses. *Phys. Rev. E*, **69** (5), 051906, doi:10.1103/PhysRevE.69.051906.
- 99** Phillips, W.R., Ahmad, I., Banes, D.W., Glagola, B.G., Henning, W., Kutschera, W., Rehm, K.E., Schiffer, J.P., and Wang, T.F. (1989) Charge-state dependence of nuclear lifetimes. *Phys. Rev. Lett.*, **62** (9), 1025–1028, doi:10.1103/PhysRevLett.62.1025.
- 100** Litvinov, Y.A., Bosch, F., Geissel, H., Kurcewicz, J., Patyk, Z., Winckler, N., Batist, L., Beckert, K., Boutin, D., Brandau, C., Chen, L., Dimopoulou, C., Fabian, B., Faestermann, T., Fragner, A., Grigorenko, L., Haettner, E., Hess, S., Kienle, P., Knöbel, R., Kozhuharov, C., Litvinov, S.A., Maier, L., Mazzocco, M., Montes, F., Münzenberg, G., Musumarra, A., Nociforo, C., Nolden, F., Pfützner, M., Plaß, W.R., Prochazka, A., Reda, R., Reuschl, R., Scheidenberger, C., Steck, M., Stöhlker, T., Torigov, S., Trassinelli, M., Sun, B., Weick, H., and Winkler, M. (2007) Measurement of the β^+ and orbital electron-capture decay rates in fully ionized, hydrogenlike, and heliumlike ^{140}Pr ions. *Phys. Rev. Lett.*, **99** (26), 262501, doi:10.1103/PhysRevLett.99.262501.
- 101** Chapman, H.N., Fromme, P., Barty, A., White, T.A., Kirian, R.A., Aquila, A., Hunter, M.S., Schulz, J., DePonte, D.P., Weierstall, U., Doak, R.B., Maria, F.R.N.C., Martin, A.V., Schlichting, I., Lomb, L., Coppola, N., Shoeman, R.L., Epp, S.W., Hartmann, R., Rolles, D., Rudenko, A., Foucar, L., Kimmel, N., Weidenspointner, G., Holl, P., Liang, M., Barthelmess, M., Caleman, C., Boutet, S., Bogan, M.J., Krzywinski, J., Bostedt, C., Bajt, S., Gumprecht, L., Rudek, B., Erk, B., Schmidt, C., Hoemke, A., Reich, C., Pietschner, D., Strueder, L., Hauser, G., Gorke, H., Ullrich, J., Herrmann, S., Schaller, G., Schopper, F., Soltau, H., Kuehnel, K.U., Messerschmidt, M., Bozek, J.D., Hau-Riege, S.P., Frank, M., Hampton, C.Y., Sierra, R.G., Starodub, D., Williams, G.J., Hajdu, J., Timneanu, N., Seibert, M.M., Andreasson, J., Rocker, A., Joensson, O., Svenda, M., Stern, S., Nass, K., Andritschke, R., Schroeter, C.D., Krasniqi, F., Bott, M., Schmidt, K.E., Wang, X., Grotjohann, I., Holton, J.M., Barends, T.R.M., Neutze, R., Marchesini, S., Fromme, R., Schorb, S., Rupp, D., Adolph, M., Gorkhover, T., Andersson, I., Hirsemann, H., Potdevin, G., Graafsma, H., Nilsson, B., and Spence, J.C.H. (2011) Femtosecond X-ray protein nanocrystallography. *Nature*, **470** (7332), 73–U81, doi:10.1038/nature09750.
- 102** Strueder, L., Epp, S., Rolles, D., Hartmann, R., Holl, P., Lutz, G., Soltau, H., Eckart, R., Reich, C., Heinzinger, K., Thamm, C., Rudenko, A., Krasniqi, F., Kuehnel, K.U., Bauer, C., Schroeter, C.D., Moshammer, R., Techert, S., Miessner, D., Porro, M., Haelker, O., Meidinger, N., Kimmel, N., Andritschke, R., Schopper, F., Weidenspointner, G., Ziegler, A., Pietschner, D., Herrmann, S., Pietsch, U., Walenta, A., Leitenberger, W., Bostedt, C., Moeller, T., Rupp, D., Adolph, M., Graafsma, H., Hirsemann, H., Gaertner, K., Richter, R., Foucar, L., Shoeman, R.L., Schlichting, I., and Ullrich, J. (2010) Large-format, high-speed, X-ray pnCCDs combined with electron and ion imaging spectrometers in a multipurpose chamber for experiments at 4th generation light sources. *Nucl. Instrum. Phys. Res. Sect. A*, **614** (3), 483–496.

17

Coherent Diffractive Imaging

Willem Boutu, Bertrand Carré, and Hamed Merdji

17.1

Introduction

The connection between the protein structure and protein function is one central topic in modern biology. Knowledge of the protein sequence and composition is not enough: the three-dimensional structure is a crucial parameter to enable the protein function. X-ray crystallography has already provided us with the full 3D conformation of hundreds of macroproteins, but its limitations are increasingly obvious: The big protein crystals necessary for X-ray crystallography are often not available and crystallization turned into a serious bottleneck for structure determination. Smaller crystals (nanocrystals) are easier to produce, but, as we will see later, the X-ray dose required to measure a high-quality signal is too large and the small crystal is damaged before the diffraction signal can be collected. (With a larger crystal the dose is spread over many replicas of the protein. The molecular dose is consequently reduced). Alternative imaging techniques, allowing to reach Angström spatial resolution, are needed. Third-generation synchrotron sources provide us with high-brilliance beams at Angström wavelength; hence one could consider duplicating traditional microscopy techniques to image the sample under study directly. High-quality optics is required for this approach. Soft X-ray zone plates have been developed, for example. However, the maximal spatial resolution is limited by the outermost period of the zone plate [1]. Nowadays, the most advanced zone plates have an outermost zone width of 15.1 nm, hence offering a spatial resolution down to approx. 12 nm [2]. Those results are very interesting, but atomic resolution seems to be out of reach. Moreover, the diffraction efficiency of such state-of-the-art zone plates is very low (less than a percent). To acquire good images, they must be accumulated over a long time or very high-radiation doses are required, the latter which is often forbidden by the sample tolerance. As we will see in this chapter, coherent diffractive imaging (CDI) of hard X-ray free-electron laser radiation has the potential to allow such an experiment [3, 4].

Reaching the atomic spatial resolution is not the only reason to use CDI with EUV or X-ray light. In this energy domain, the penetration depth of radiation is

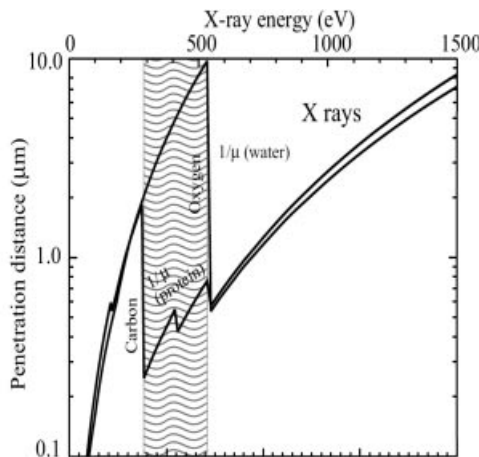


Figure 17.1 Penetration depth of carbon and oxygen with respect to the X-ray photon energy. The gray area represents the water window, where the contrast is maximized for biological samples. Taken from [5].

very large, allowing the study of the inside of thick or buried samples. This is a great advantage compared to electron imaging, which offers very good spatial resolution but is limited to thin samples (around 100 nm). Figure 17.1 represents the penetration distance of carbon and oxygen for soft X-ray radiation. Penetration depth tends to increase with the photon energy and already reaches around 10 μm at 1.5 keV. The figure also shows that going for hard X-ray is not always necessary. Carbon is the main component of biological samples, while water (and therefore oxygen) is a source of background signal. The so-called water window, between the carbon and oxygen absorption K-edges (at respectively 284 and 530 eV) offers the highest contrast for organic material imaging, because carbon will absorb, while water is transparent.

Whatever the energy domain selected, CDI is a lensless imaging technique, where the objective optics are replaced by an algorithm running on a computer. The idea behind coherent diffractive imaging comes from Sayre [6]. He stated that if a diffraction pattern from a crystal was sufficiently oversampled, the phase problem could be solved, that is, the unknown phase of the diffraction pattern, which is necessary to achieve the reconstruction of the sample image, can be determined. He later extended the approach to noncrystalline objects [7, 8]. The first experimental demonstration of the technique was provided by Miao and co-workers in 1999 [9]. Since then, multiple applications, as well as improvements of the technique, have been published.

Thanks to the absence of an imaging lens, the spatial resolution of coherent diffractive imaging is, theoretically, only limited by the wavelength. Although CDI can be used at visible wavelengths, we will restrict the following examples and applications to the UV and X-ray domains. Section 17.2 presents different approaches to demonstrate the basic equation of CDI, that is, that the coherent field diffracted

by a sample is, in the far field, equal to the sample Fourier transform. Section 17.3 examines the requirements regarding the light properties and the experimental setup, and presents the expected resolution of corresponding experiments. In the following sections, we concentrate on two commonly used techniques of coherent diffractive imaging, using either iterative phasing algorithms (Section 17.4) or holographic schemes (Section 17.5).

17.2

Far-Field Diffraction

The far-field diffraction pattern of a scatterer is its Fourier transform. The main goal of this section is not to re-demonstrate this relation, any good optics book can help you through that. Our idea is to review different approximations used, as they will constrain the experimental design. Those constraints will determine the requirements on the light source properties, on the distances involved and on the detector characteristics. The relevant optics can be considered from several points of view, which we will review briefly.

17.2.1

Optical Point of View

In this section, we consider a plane wave going through a *2D thin sample*. An object is considered to be thin if its thickness e is smaller than the depth of focus of the imaging setup [10]:

$$e < \frac{\lambda}{2NA^2}, \quad (17.1)$$

where NA is the numerical aperture of the system.

Just behind the sample, the electromagnetic field will propagate in free space. This propagating field is a solution of Maxwell's equations. As we are not sensitive to polarization, we can use the scalar form, known as the Helmholtz equation:

$$\nabla^2 \Psi(\mathbf{r}) + k^2 \Psi(\mathbf{r}) = 0, \quad (17.2)$$

where, dropping the time dependence, $\Psi(\mathbf{r})$ is the electromagnetic field. In a typical coherent diffractive imaging experiment, the detector will be put at a distance Z from the sample (see Figure 17.2) and will be perpendicular to the beam propagation direction. This suggests for the separation of the transverse (x and y) and

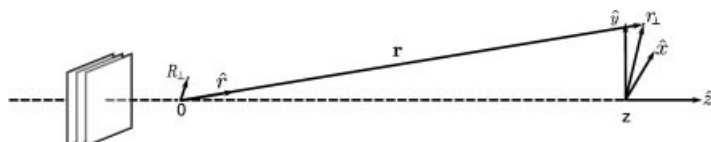


Figure 17.2 Illustration of an incident plane wave scattered by an object.

parallel (z) components of the field. Taking the Fourier transform of Eq. (17.2) only in the perpendicular plane, we get

$$(-\mathbf{q}_\perp^2 + \partial_z^2 + k^2)\tilde{\Psi}(\mathbf{q}_\perp; z) = 0, \quad (17.3)$$

where $\tilde{\Psi}(\mathbf{q}_\perp; z)$ denotes the $\Psi(\mathbf{r})$ Fourier transform. The general solution of Eq. (17.3) has the following form:

$$\tilde{\Psi}(\mathbf{q}_\perp; z) = \tilde{\Psi}^+(\mathbf{q}_\perp)e^{i\kappa z} + \tilde{\Psi}^-(\mathbf{q}_\perp)e^{-i\kappa z}, \quad (17.4)$$

where $\kappa = \sqrt{k^2 - \mathbf{q}_\perp^2}$ and $\tilde{\Psi}^\pm(\mathbf{q}_\perp)$ are two independent functions, representing the fields propagating in the forward and backward directions. In usual experimental conditions, there is no backward propagating field, so $\tilde{\Psi}^-(\mathbf{q}_\perp)$ can be set to zero.

Taking the wave at the exit of the sample Ψ_0 as an initial condition, the scattered field at any position z can be written as

$$\Psi(\mathbf{r}_\perp; z) = \mathcal{F}^{-1}[\tilde{\Psi}_0(\mathbf{q}_\perp)e^{i\kappa z}]. \quad (17.5)$$

Under the *paraxial approximation*, the diffracted angles are small and one assumes that $\tilde{\Psi}(\mathbf{q}_\perp)$ is nonnegligible only when $|\mathbf{q}_\perp| \ll k$. One can then expand κ to the first nonzero order in \mathbf{q}_\perp and Eq. (17.5) becomes

$$\Psi(\mathbf{r}_\perp; z) = \mathcal{F}^{-1}\left[\tilde{\Psi}_0(\mathbf{q}_\perp)\exp\left(i\kappa z\left(1 - \frac{\mathbf{q}_\perp^2}{2k^2}\right)\right)\right]. \quad (17.6)$$

If $(f * g) = \int f(x')g(x - x')dx'$ is the convolution operation, the following useful relation can be formulated:

$$f * g = \sqrt{2\pi}\mathcal{F}^{-1}(\mathcal{F}(f)\mathcal{F}(g)). \quad (17.7)$$

Using relation (17.7), Eq. (17.6) becomes

$$\Psi(\mathbf{r}_\perp; z) = \frac{1}{\sqrt{2\pi}}\Psi_0(\mathbf{r}_\perp) * P_z(\mathbf{r}_\perp), \quad (17.8)$$

where P_z is the Fresnel propagator, $P_z(\mathbf{r}_\perp) = -ik/z \exp[ikz[(1 + \mathbf{r}_\perp^2)/(2z^2)]]$. Choosing \mathbf{R}_\perp as variable in the sample plane ($z = 0$, see Figure 17.2), Eq. (17.8) can be developed as

$$\Psi(\mathbf{r}_\perp; z) = \frac{-ik}{2\pi z}e^{ikz}\int d\mathbf{R}_\perp \Psi_0(\mathbf{R}_\perp; 0) \exp\left[i\frac{k(\mathbf{r}_\perp - \mathbf{R}_\perp)^2}{2z}\right]. \quad (17.9)$$

After expanding the square term, this integral can be written as a Fourier transform if we identify \mathbf{q}_\perp with $k\mathbf{r}_\perp/z$. Omitting some phase terms, we obtain

$$\Psi(\mathbf{r}_\perp; z) = \mathcal{F}\left[\Psi_0(\mathbf{R}_\perp) \exp\left(i\frac{k\mathbf{R}_\perp^2}{2z}\right)\right] \Big|_{\mathbf{q}_\perp = k\mathbf{r}_\perp/z}. \quad (17.10)$$

Usually, in a coherent diffraction imaging experiment, the object's transmission is equal to zero except in a finite region of space ($\Psi(\mathbf{R}_\perp)$ has a support). The phase modulation, due to the last exponential term in Eq. (17.10), is then maximal along the edges of the support. If a is the typical sample dimension, then this phase is small for

$$f = \frac{a^2}{\lambda z} \ll 1 , \quad (17.11)$$

where f is called the Fresnel number. If that condition is true, then the *Fraunhofer approximation* says that the phase term can be neglected. This is the case in the far field, that is, for $z \gg a^2/\lambda$. Equation (17.10) then becomes

$$\Psi\left(\mathbf{r}_\perp; z \gg \frac{a^2}{\lambda}\right) = \mathcal{F}[\Psi_0(\mathbf{R}_\perp)] . \quad (17.12)$$

This is a key equation in CDI: *in the far field, the diffractive field is equal to the Fourier transform of the exit wave after the sample.*

17.2.2

Born Approximation

We now consider the case when the propagation does not happen in free space. Equation (17.2) can be rewritten as

$$\nabla^2 \Psi(\mathbf{r}) + k^2 n^2 \Psi(\mathbf{r}) = 0 , \quad (17.13)$$

which can be reformulated using the scattering potential $F = 1/(4\pi)k^2(n^2(\mathbf{r}) - 1)$:

$$\nabla^2 \Psi(\mathbf{r}) + k^2 \Psi(\mathbf{r}) = -4\pi F(\mathbf{r}) \Psi(\mathbf{r}) . \quad (17.14)$$

In X-ray domains, interactions are very weak. Hence, we can adopt a perturbative method to solve Eq. (17.14). If we expand the field $\Psi(\mathbf{r})$ as the Born series

$$\Psi(\mathbf{r}) = \Psi^{(0)}(\mathbf{r}) + \Psi^{(1)}(\mathbf{r}) + \dots \quad (17.15)$$

the zeroth order $\Psi^{(0)}$ is a solution to Eq. (17.2) and higher terms follow:

$$\nabla^2 \Psi^{(n)}(\mathbf{r}) + k^2 \Psi^{(n)}(\mathbf{r}) = -4\pi F(\mathbf{r}) \Psi^{(n-1)}(\mathbf{r}) . \quad (17.16)$$

Intuitively, the wave $\Psi^{(1)}$ is the scattered field resulting from the interaction of $\Psi^{(0)}$ with the sample scattering potential, $\Psi^{(2)}$ is the scattering amplitude due to $\Psi^{(1)}$, and so on.

Equation (17.14) can be solved using the Green function [11]. Considering that the incident wave is a plane wave, $\Psi^{(0)}(\mathbf{r}) = \Psi_0 \exp(i k \hat{z} \cdot \mathbf{r})$, the scattered field can be written as

$$\Psi(\mathbf{r}) = \Psi_0 e^{ik\hat{z}\cdot\mathbf{r}} + \int_{\Omega} F(\mathbf{R}_\perp) \Psi(\mathbf{R}_\perp) \frac{e^{ik|\mathbf{r}-\mathbf{R}_\perp|}}{|\mathbf{r}-\mathbf{R}_\perp|} d^3 R_\perp \quad (17.17)$$

with Ω being the object volume. Under the *Fraunhofer approximation*, $|\mathbf{r}| \gg \mathbf{R}_\perp$, and $|\mathbf{r} - \mathbf{R}_\perp|$ rewrites as

$$|\mathbf{r} - \mathbf{R}_\perp| \approx |\mathbf{r}| - \mathbf{R}_\perp \cdot \hat{\mathbf{r}}. \quad (17.18)$$

Equation (17.17) can be simplified as

$$\Psi(\mathbf{r}) = \Psi_0 e^{ik\hat{z} \cdot \mathbf{r}} + \frac{e^{ik|\mathbf{r}|}}{|\mathbf{r}|} \int_{\Omega} F(\mathbf{R}_\perp) \Psi(\mathbf{R}_\perp) e^{ik\mathbf{R}_\perp \cdot \hat{\mathbf{r}}} d^3 \mathbf{R}_\perp. \quad (17.19)$$

As we just remarked, the scattering cross section is very weak, hence we can consider only the first-order perturbation, $\Psi = \Psi^{(0)} + \Psi^{(1)}$: because of the weakness of the interaction, photons can only be scattered once. This is known as *the first Born approximation*. Replacing $\Psi(\mathbf{R}_\perp)$ by $\Psi^{(0)}(\mathbf{r})$, Eq. (17.19) reads as

$$\Psi(\mathbf{r}) = \Psi_0 e^{ik\hat{z} \cdot \mathbf{r}} + \Psi_0 \frac{e^{ik|\mathbf{r}|}}{|\mathbf{r}|} \int_{\Omega} F(\mathbf{R}_\perp) e^{-ik\mathbf{R}_\perp \cdot (\hat{\mathbf{r}} - \hat{z})} d^3 \mathbf{R}_\perp. \quad (17.20)$$

In an experiment one has to remove the direct beam after the sample, as the diffraction efficiency is very low. This is required to avoid saturation or even destruction of the detector. Equation (17.20) reduces then to the Fourier transform of the scattering factor. This result is similar to Eq. (17.12) and the result obtained in the previous section. The Born approximation supposes that $\Psi^{(1)} \ll \Psi^{(0)}$, which in turn implies that the object has to be optically thin (but there is no restriction on two-dimensional objects).

17.2.3 Resolution

Figure 17.3 represents the actual layout of a CDI experiment. The detector is placed in the far field at a distance Z from the sample. It is made of N^2 pixels of size Δr^2 . The system numerical aperture NA can then be defined as $NA = n \sin \theta_{\max}$. In the paraxial approximation, and because the refractive index is equal to one, $NA \approx N\Delta r/(2Z)$.

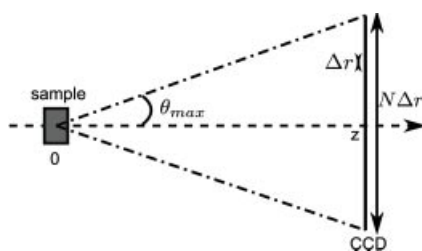
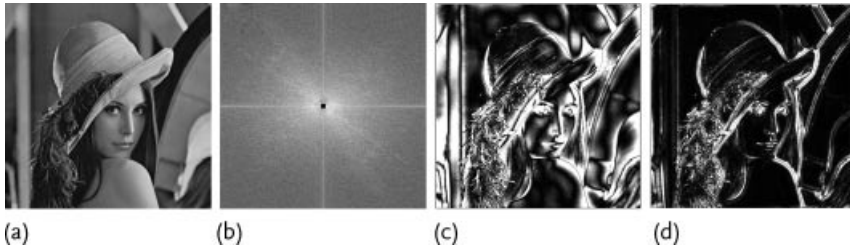


Figure 17.3 Experimental geometry.



(a)

(b)

(c)

(d)

Figure 17.4 (a) Sample. (b) Modulus square of the sample Fourier transform, with a beam block removing the central data. (c) Inverse Fourier transform of (b) (the phase information from the Fourier transform was kept). (d) Same as (c) after low pass filtering of the data, on the same color scale.

Let us call r_t the transverse resolution (usually, we consider the half-period transverse resolution). The maximum angle θ_{\max} can be written as

$$\theta_{\max} \approx \sin \theta_{\max} = \frac{\lambda}{2r_t} \quad (17.21)$$

or

$$\theta_{\max} \approx \tan \theta_{\max} = \frac{N\Delta r}{2Z} . \quad (17.22)$$

Hence, we determine the theoretically possible transverse resolution

$$r_t = \frac{\lambda Z}{N\Delta r} . \quad (17.23)$$

However, the resolution is usually worse when working with real data. A consideration of Eq. (17.20) provides a good example of the difficulties and limitations of this definition. For example, the use of a beam block to stop the intense direct beam removes the low-frequency data from the measurements. This is illustrated in Figure 17.4. We calculated the Fourier transform of sample (a), removing the central pixels to simulate a beam stop (the modulus square of the result is presented in Figure 17.4b). The inverse Fourier transform results in Figure 17.4c shows that the few missing frequencies significantly affect the reconstruction. One way around this is to apply a low-pass filter on the data before the inverse Fourier transform. This removes the slow variations in the reconstruction (Figure 17.4d). When accumulation is possible, it might be better to generate a full diffraction pattern by adding several datasets, obtained using short and long acquisition times. The former can be taken without a beam block, and only the central part of the diffraction pattern will be recorded with sufficient signal-to-noise ratio (SNR). The latter, using a beam block, will be used for the wide diffraction angles. That way, the full dynamics of the signal can be recorded, without loss of information, despite the limited dynamic range of the detector. Another solution is to subtract the least constrained modes from the reconstruction [12].

The longitudinal resolution r_l is equal to the depth of focus, hence

$$r_l = \frac{\lambda}{2NA^2} . \quad (17.24)$$

Consequently, the longitudinal resolution reads as

$$n = \frac{2\lambda Z^2}{(N\Delta r)^2}. \quad (17.25)$$

17.2.4

Comments on the Approximations

Let us comment here on the different approximations made in Sections 17.2.1 and 17.2.2 and their implications for an actual experiment.

- Paraxial approximation. This is the small-angle approximation. Under this condition, the arc of the Ewald sphere can be considered as a straight line, in the detector plane.
- Fraunhofer approximation. This is the far-field approximation. The Fresnel number $f = a^2/(\lambda z)$ is smaller than one, that is, $z \gg a^2/\lambda$, with a being a typical dimension of the object. This condition sets some constraints on the experimental layout: depending on the wavelength and the size of the object under study, there is a minimum distance between the detector and the object. This has to be balanced by the signal detection efficiency: if the detector is placed too far away from the object, the number of photons detected per pixel might be too low to ensure a good SNR. Taking the example of Ravasio *et al.* [13], their object size is around 2 μm, the wavelength is 32 nm and the distance from sample to CCD is around 2 cm. The Fresnel number f is then equal to 6×10^{-3} , well below one.
- Thin sample. Several different notions can be used here. In both previous cases, the object under study was considered to be optically thin. An object optical thickness can be defined as $|k \delta n_{\perp}|$ where:

$$\delta n_{\perp}(R_{\perp}) = \int (n(R_{\perp}; z) - 1) dz. \quad (17.26)$$

An object is optically thin if $|k \delta n_{\perp}| \ll 1$. A basic interpretation of this is that there will be no multiple scattering effect.

The approximation used in Section 17.2.1 is more restrictive. It considers an object to be thin when the thickness is smaller than the depth of focus. As CDI aims at reaching high-spatial resolutions, the depth of focus becomes very small. If condition (17.1) is not fulfilled, 3D imaging has to be considered, and 2D views can be obtained from 2D projections of the 3D reconstruction. Trying to reconstruct directly the 2D projection from a single view will result in an image with defocusing artifacts. Once a reconstruction is obtained at a given position in Z , it is possible to propagate it using the Fresnel propagation equation, hence bringing different parts of the image under focus. But this is not equivalent to 3D imaging: for complicated samples, the different images will be difficult to interpret [10].

17.3

Source Requirements

According to Eq. (17.12), CDI is, in principle, experimentally easy: one just has to shine light on a unknown sample, to record the far-field diffraction pattern, and to invert the data by Fourier transform. The great advantage, as we already stated, is that no imaging optics are needed. To increase the photon flux on the sample, the beam can be focused. A basic experimental setup is shown in Figure 17.5. As we will see in the following sections, the crucial aspects of the setup are the relation between the detector pixel size, the sample size and the distance between the detector and the sample (see Section 17.4.1). The source of radiation used to perform the experiment must also fulfill some specific requirements. In this section, we will go through the main requirements to see how one can work with a real and nonperfect source. In the last part of the section, we will briefly compare the main sources used so far in the UV/X-ray domain. Of course, other sources can be used, such as X-ray lasers [14] or lasers (when working at visible wavelengths).

17.3.1

Coherence

Coherent diffractive imaging, as stated in its name, requires a highly coherent beam. Two kinds of coherence will be discussed here, the transverse coherence in the plane perpendicular to the propagation direction, and the temporal, or longitudinal, coherence in the propagation direction.

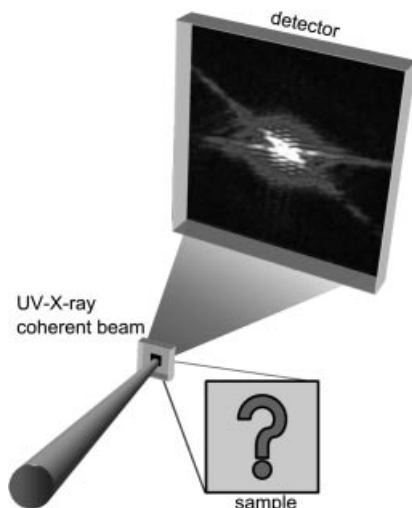


Figure 17.5 Scheme of a coherent diffractive imaging setup.

17.3.1.1 Transverse Coherence

The transverse coherence length gives the width of the area over which the radiation shows a clear phase relationship. For diffractive imaging, this coherence length has to be as large as, or larger than, the size of the sample under study. More detailed considerations showed that the transverse coherent length of the source has to be about twice the transverse dimension of the object [15]. Williams *et al.* showed that even slight perturbances of the coherence are enough to prevent the convergence of reconstruction algorithms, and consequently to prevent the object reconstruction [16].

UV or X-ray free-electron lasers (see [17] for instance) and high-order harmonics [18, 19] have very good spatial properties. For commonly used samples, they can be considered as fully coherent and the mentioned condition is always met. Synchrotrons, thanks to their high-photon flux and the relatively large amount of facilities available, represent the most commonly used source for CDI experiments. But synchrotron radiation is not spatially coherent. However, it is possible to generate a partially coherent beam from a synchrotron source using an aperture. According to the van Cittert–Zernike theorem, the illumination within the half-radius of the Airy pattern from a pinhole can be considered as coherent. If the sample fits under this area, coherent diffractive imaging is feasible.

However, there are techniques to work with a partially coherent source. Williams *et al.* proposed to use illumination with a curved wavefront. Fresnel diffraction gives better convergence properties and makes the algorithms more robust to partial convergence, as the solution to the phase problem is then unique [16]. Whitehead *et al.* decomposed their partially coherent source as a multimodal field with mutually incoherent modes and modified the reconstruction algorithm accordingly [20]. Experimentally, they performed a coherent diffractive imaging experiment at a synchrotron, with the slit either open (low coherence) or closed (high coherence). Figure 17.6 shows their results. The diffraction pattern shown here (Figure 17.6a) was

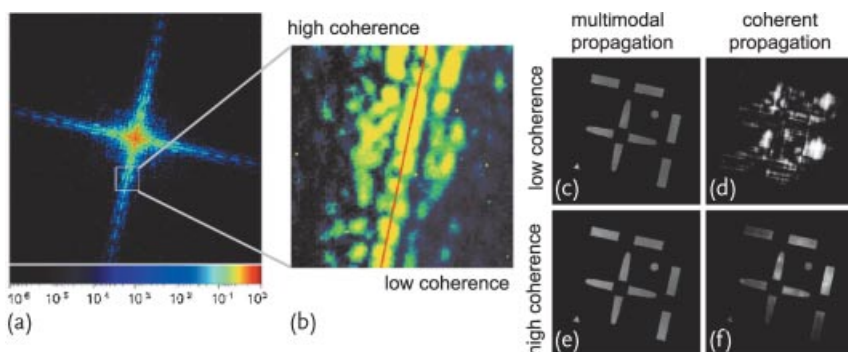


Figure 17.6 Effect of partial coherence on coherent diffractive imaging. (a) Diffraction pattern, acquired with a high-coherence illumination. (b) Detail of the diffraction pattern, taken with a high-coherence beam on the left

side of the line and a low-coherence beam on the right side. Reconstruction of the sample from low (c,d) or high (e,f) coherence beam using a modified (c,e) or usual (d,f) algorithm. Taken from [20].

taken with the high-coherence beam. The inset represents a detail of the pattern, with high coherence on the left side of the line and low coherence on the right hand. The loss of contrast is clearly visible. The four images on the right represent four reconstructions of the sample, using four different conditions. Using the multimodal approach, they were able to image the object even in the low-coherence case, while usual phasing algorithms failed. This technique requires, however, that the beam coherence properties have been completely characterized, which is not always feasible.

17.3.1.2 Longitudinal Coherence

The longitudinal coherence length is the length over which two wavefronts with wavelengths differing by $\Delta\lambda$ are dephased by π . Using Figure 17.7a, it can be evaluated as

$$L_{coh} \approx \frac{\lambda^2}{2\Delta\lambda} . \quad (17.27)$$

Figure 17.7b gives the required condition for the coherence length to allow coherent diffractive imaging. At the maximum diffraction angle, for a sample size a , we get

$$L_{coh} > \frac{a}{2 \sin \theta} . \quad (17.28)$$

Combining Eqs. (17.27) and (17.28), we get

$$\frac{\lambda}{\Delta\lambda} \geq \frac{a}{2r_t} . \quad (17.29)$$

Equation (17.29) gives a relationship between the spectral bandwidth $\lambda/\Delta\lambda$, the size of the object and the (best possible) spatial resolution r_t . Synchrotrons usually offer high-spectral purity, thanks to monochromators, with $\Delta\lambda/\lambda$ up to the 10^{-4} range. This is not the case with high-order harmonic sources. If only one given harmonic order is selected, for example, by using a multilayer coated mirror, $\Delta\lambda/\lambda$ is in the 10^{-2} range. This is sufficient for coherent diffractive imaging experiment. But if multiple orders are used, either in order to achieve attosecond time resolution or to increase the photon number on the sample, $\Delta\lambda/\lambda$ is on the order of

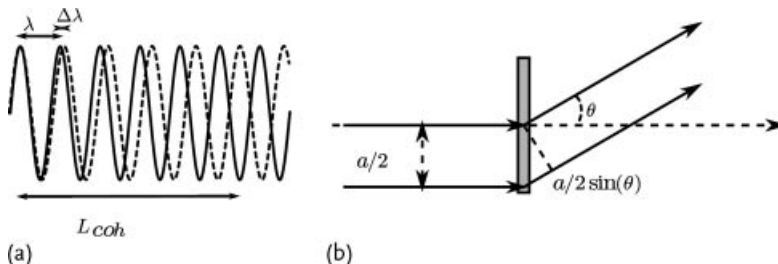


Figure 17.7 (a) Illustration of the longitudinal coherence length L_{coh} . (b) Path length difference at maximum diffraction angle.

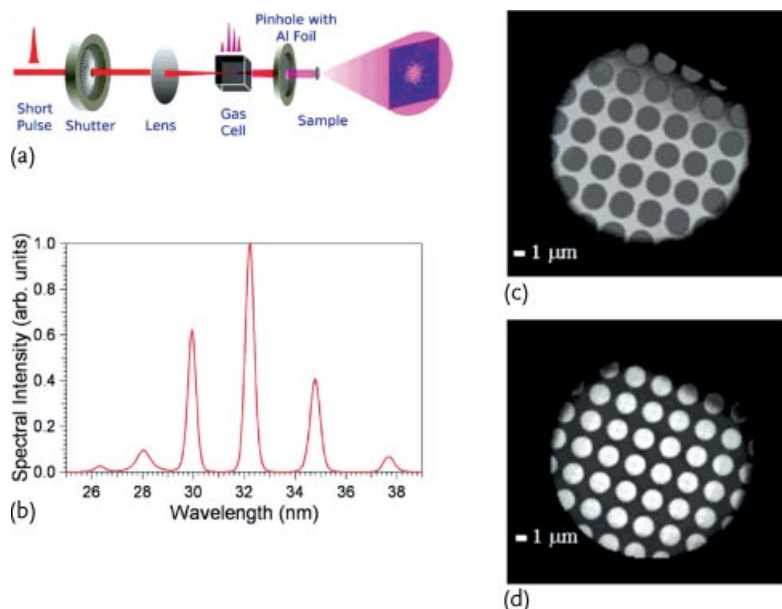


Figure 17.8 (a) Experimental setup for coherent diffractive imaging with multiple harmonic orders. (b) Harmonic comb used in the experiment. (c) Scanning electron microscope image of the sample. (d) Reconstruction of the sample from the diffraction data. Taken from [21].

unity. However, this lack of longitudinal coherence can also be taken into account in the analysis. For instance, Chen *et al.* used a modified phasing algorithm to invert diffraction data taken with several harmonic orders [21]. Figure 17.8a and b represents the experimental setup they used. A simple aluminum filter selected six consecutive harmonic orders, generated in argon. Thanks to this configuration; they estimated that the acquisition time was reduced by a factor of 16 compared to acquisition with the single most intense harmonic. Figure 17.8c shows an electron microscope image of the sample, and Figure 17.8d its reconstruction by the modified algorithm, with a spatial resolution of 165 ± 5 nm for a wavelength of about 35 nm.

17.3.2

Signal-to-Noise Ratio

Figure 17.9 is illustrating another limitation of working with real data. On this diffraction pattern, acquired with a high-harmonic source in Saclay, signal is visible up to q values of $8.9 \mu\text{m}^{-1}$, corresponding to a spatial resolution of 56 nm. However, after reconstruction, the actual spatial resolution, evaluated by the phase-retrieval transfer function (PRTF) (see Section 17.4.3.1), is limited to 78 nm. This is due to the fact that, at large diffraction angles, the number of photons per pixel is too low. Moreover, this weak signal is buried in the noise. The actual spatial resolution is limited by the SNR.

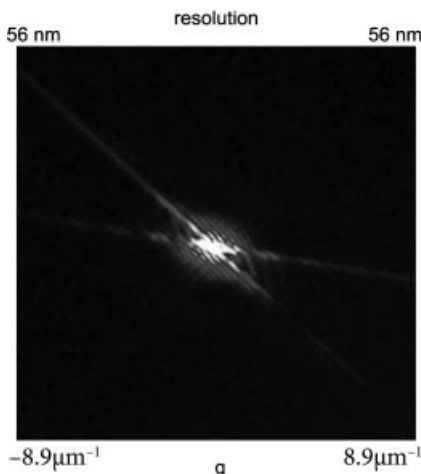


Figure 17.9 Experimental diffraction data (log scale).

Sources of noise are well known, some of them being unavoidable. Noise can be due to the experimental setup. For instance, XUV CCD cameras are extremely sensitive to infrared light. When working with high-order harmonic, or in an infrared-pump/XUV probe setup, the detector has to be shielded from all IR photons. The detector itself can be a source for noise: readout noise of a CCD camera cannot be avoided. When working with hard X-rays, hybrid-pixel detectors offer a noiseless readout and are able to detect single photons, but they work only in the keV range. However, photon noise can be minimized, as it scales with the square root of the number of photons: increasing the flux or increasing the pixel size (by hardware binning of the CCD for instance) will increase the SNR. Another path to improve the spatial resolution is to use postexperiment image processing and statistical tools.

17.3.3

Dose

We just mentioned that increasing the photon flux was a way to increase the SNR, hence improving the spatial resolution. But there is an upper limit to the radiation dose a sample can receive. This limit is especially severe for biological samples. The dose, measured in Gray (Gy), is defined as the absorbed energy divided by the mass:

$$\text{Dose} = \frac{\text{absorbed energy}}{\text{mass}} = \frac{\mu N_0 E}{\rho A} \quad (17.30)$$

with μ being the absorption coefficient, N_0 the number of photons per unit area A , ρ the material density and E the photon energy. The maximum dose depends on the desired spatial resolution. While a relatively low dose of 2×10^7 Gy will destroy the atomic order in a protein crystal [22], higher doses on the order of 10^{10} Gy

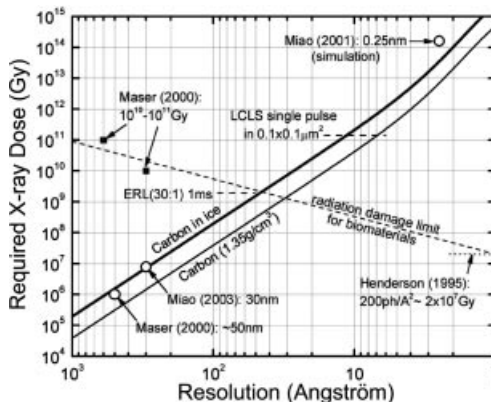


Figure 17.10 Required dose to achieve a desired spatial resolution for 8-keV photons, for either biological samples in vacuum (the “carbon” line) or frozen samples (the “carbon in ice” line). The dashed line represents the radiation damage limit. Some points taken from the literature are marked. Taken from [24].

can be tolerated in frozen cells to generate lower resolution images [23]. Those two points are represented in Figure 17.10 and linked with a dashed line: radiation doses above this line cannot, *a priori*, be used for imaging biological object. The limit is higher, but still exists, for inorganic materials. Knowing the scattering cross section of a sample and the minimum SNR required for coherent diffractive imaging (usually, the Rose criterion is used, which states that a SNR of at least 5 is needed to recognize a feature above the background), it is possible to calculate the minimum dose needed to achieve a desired spatial resolution (see, e.g., [25]). An example of such a calculation is reported in Figure 17.10 [24]. The thick black line represents the dose needed when working with a frozen biological sample, the thin black line is the same for a sample in vacuum. Frozen cells can bear higher doses.

According to Figure 17.10, the best spatial resolution one could reach using coherent diffractive imaging is around 5 nm. Those calculations were performed for 8-keV radiation, but using a shorter wavelength would not change the result by much. Atomic resolution seems to be out of reach. In crystallography, the radiation damage problem is avoided by spreading the dose over many replicas of the same protein in the crystal. When studying isolated protein by coherent diffractive imaging, a proposed solution is to use many copies of the protein, sent within a jet into the X-ray beam path, one at a time. Accumulating signal for many copies should give a good SNR. A problem with the molecular jet concept is that the molecules fall into the beam path with random orientation. To circumvent this problem, the molecules could be aligned or oriented before interaction with the X-ray pulse [26]. Another possibility is to classify different diffraction patterns into classes of orientations. All the patterns are then assembled to create a full three-dimensional set, which can be inverted to reconstruct the sample structure in real space [27–30].

Another possibility to break the 5-nm barrier is offered by free-electron lasers. This can be explained by looking at the damage mechanisms. Depending on the

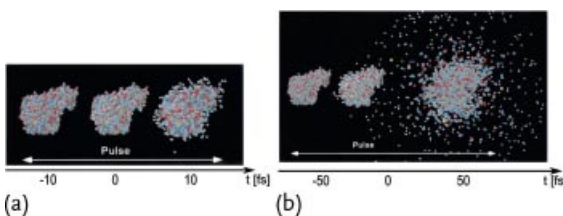


Figure 17.11 Explosion of a macroprotein induced by radiation damage. The molecule was exposed to the same number of photons in a (a) 10-fs or a (b) 50-fs pulse. Taken from [33].

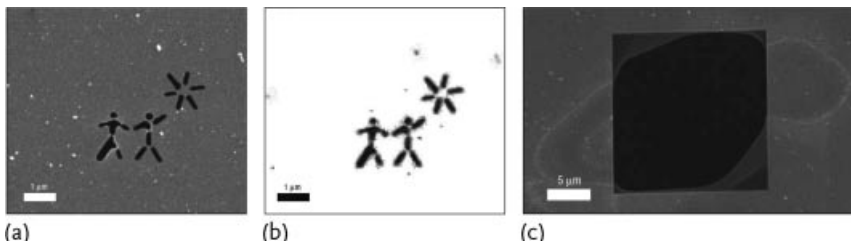


Figure 17.12 Coherent diffractive imaging experiment performed at FLASH ($\lambda = 32 \text{ nm}$). (a) Scanning electron microscope image of the sample. (b) Reconstruction of the object.

(c) Scanning electron microscope image of the sample after exposure to a single FLASH pulse. Taken from [32].

photon energy, different processes will be involved. At X-ray wavelengths, ionization plays the major role. Inner shell electrons, ionized by the radiation, will leave the molecule. Vacancies will be subsequently filled by relaxation through Auger processes, releasing more electrons from the molecule. At the beginning of the pulse, the electrons simply leave, leaving a net positive charge. The accumulating positive charges will eventually trap lower energy electrons in the sample. For strong XFEL light pulses, this happens in a few femtoseconds. At a longer timescale (on the order of 10 fs), Coulomb explosion of the sample due to electrostatic forces will occur [31]. Calculations have shown that a sample exposed to an X-ray pulse with few femtoseconds duration will explode only after the pulse has passed through it. The photons are consequently diffracted by an unperturbed sample, and coherent diffractive imaging is possible. This is illustrated in Figure 17.11. When exposed to a 50-fs long pulse, the disintegration of the molecule happens before the end of the pulse, preventing diffractive imaging. For shorter pulses of 10 fs or less, the changes in the molecular structure between the beginning and the end of the pulse are minor. Chapman *et al.* showed that diffraction imaging before the onset of radiation damage was indeed possible at the FLASH free-electron laser (Figure 17.12) [32]. In spite of the destruction of the sample by the UV pulse (Figure 17.12c), they could invert the diffraction pattern and reconstruct the sample image (Figure 17.12b).

Table 17.1 Comparison of light sources for coherent diffractive imaging.

Sources	Synchrotron	FEL	HHG
Pros	High brilliance	High brilliance	Spatially coherent
	High repetition rate	Short pulse duration	Short pulse duration
	Longitudinal coherence	VUV to hard X-ray	Synchronized with lasers
	VUV to hard X-ray	Spatially coherent	Table-top, affordable
Cons	No spatial coherence	Start on noise	VUV only
	Low flux after pinhole	Temporal jitter	Low efficiency
	No temporal resolution	Destroys the sample	
	Big and expensive	Big and expensive	
Future	Slicing (temporal jitter!)	Seeding with laser HHG	Reach water window

17.3.4

Different XUV Sources Comparison

Table 17.1 summarizes different characteristics of the three main sources of UV/X-ray radiation used for coherent diffractive imaging, namely synchrotrons, free-electron lasers, and high-order laser harmonics. As one can see, each has its own advantages and disadvantages. The choice of source should therefore be adapted to the desired application.

17.4

Solving the Phase Problem

As demonstrated in Section 17.2 (e.g., Eq. (17.12)), the far-field diffraction pattern of a sample is its Fourier transform. However, detectors in the UV-X-ray range can only record the intensity of the field, and not its phase. Inverting the experimental data by a simple inverse Fourier transform is therefore not possible. This is called the *phase problem*. Thankfully, techniques exist to either retrieve the spatial phase, which is the subject of this section, or to encode the phase directly in the diffraction pattern, as we will see in Section 17.5.

17.4.1

Oversampling Method

17.4.1.1 Oversampling Ratio

Before trying to solve the phase problem one has to ask whether or not it is solvable. One necessary condition is that the number of unknown variables is smaller or equal to the number of equations. If the detector has $N \times N$ pixels, the latter, equal to the number of measured amplitudes, is equal to N^2 . Consider a sample made of $n \times n$ pixels. Because of its complex value (usually, a sample has a given

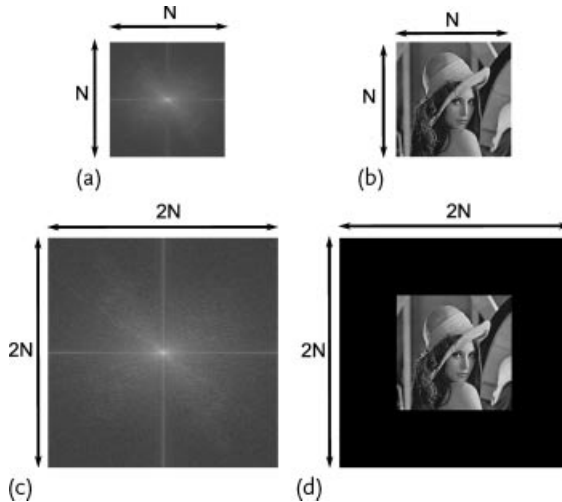


Figure 17.13 Illustration of the oversampling. (a) and (b) A N^2 object and its Fourier transform. (c) and (d): same Fourier transform, but sampled over $(2N)^2$ pixels. The sample has the same support (N^2 pixels) and is embedded in a $(2N)^2$ area.

absorption, which is related to the imaginary part of the refractive index), the number of unknowns is equal to $2n^2$. Defining the *oversampling ratio* σ as the number of measured amplitudes over the number of pixels in the real space [34], one gets

$$\sigma = \frac{N^2}{n^2} \geq 2 . \quad (17.31)$$

This means that the number of unknown variables has to be reduced by a factor at least equal to two. To that goal, one can use a *finite* and *isolated* object embedded in an otherwise empty space (which is usually the case in experiments). To fulfil the requirement of Eq. (17.31), the object support (that is, the area where it has a nonzero value) has to be smaller than half the size of the field of view, as illustrated by Figure 17.13. Test objects used in the literature are often real objects, that is, pure transmission objects. The number of unknown variables is consequently reduced by 2. But due to Friedel symmetry, the object Fourier transform is symmetric, and so is the measured diffraction pattern. The number of equations is then also reduced by two, and the sample oversampling condition applies.

Another point of view on oversampling is given by the Nyquist–Shannon theorem. This theorem states that a signal can be completely reconstructed if the sampling frequency is at least twice the highest frequency of the signal. Suppose that the object has a size $n \times n$, with a pixel size (in the real space) Δr . The minimum signal period in the Fourier space is then equal to $1/(n\Delta r)$. If this object is embedded in a $N \times N$ sample, the sampling period in reciprocal space is equal to $1/(N\Delta r)$. The Nyquist–Shannon theorem then implies that $n/N \geq 1/2$. This condition restricts the object size less than Eq. (17.31).

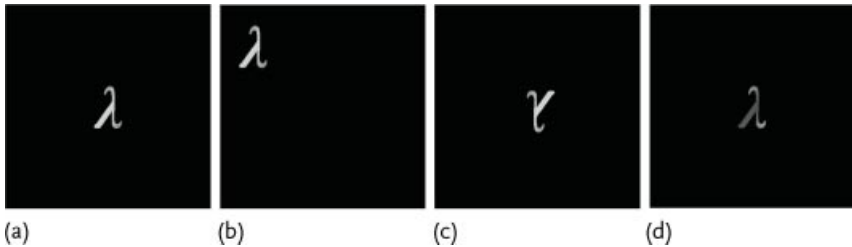


Figure 17.14 All displayed objects have the same Fourier transform intensity. If (a) is the object (the hue scale represent the phase, the brightness the amplitude), (b) is just a translation of the object, (c) the inverted object and (d) differs from (a) by a global phase shift.

The oversampling condition is true, whatever the object dimension. Therefore, in principle, oversampling the diffraction pattern by the factor of 2 in each dimension is not necessary [35]. A minimum sampling ratio of $\sqrt{2}$ for 2D and $\sqrt[3]{2}$ for 3D objects has been shown to be enough by simulations [34]. An oversampling ratio higher than two does not give any additional information, but up to a certain point it can help the convergence of the phasing algorithms [35].

17.4.1.2 Uniqueness of the Solution

Respecting the oversampling condition guarantees that the phase problem can be solved, but not that a unique solution exists. For 1D objects this is never the case and the problem cannot be solved. Thankfully, for objects with higher dimensionality, the solution is almost always unique (see, e.g., [36]). In this regard, we can already mention some trivial cases, which are not among the pathological cases of nonuniqueness, but which will pose a problem to the reconstruction algorithms. All the objects presented in Figure 17.14 have the same Fourier transform intensity. Therefore, reconstruction algorithms will need additional input to discriminate one solution. The problem posed by the central symmetry of the object (Figure 17.14c) is known as the twin image problem in holography.

17.4.2

Basics on Iterative Phasing Algorithms

17.4.2.1 Constraints

Solving the phase problem when the oversampling conditions are fulfilled does not require any *a priori* knowledge about the sample. The analysis is based on the measured diffraction pattern, that is, the square of the amplitude of the sample Fourier transform. In real space, we know that the object is isolated, that is, that it fits inside a support – but we usually have no information about this support. The first step is hence to find additional constraints, and finding a tighter support is usually enough. A first approximation of the support can be found using the measured diffraction pattern. Indeed, an object, whatever it is, fits under its autocorrelation, which is the inverse Fourier transform of the measured data (Figure 17.15):

$$\mathcal{A}\Psi_0 = \Psi_0 \otimes \Psi_0 = \mathcal{F}^{-1} [|\mathcal{F}(\Psi_0)|^2]. \quad (17.32)$$

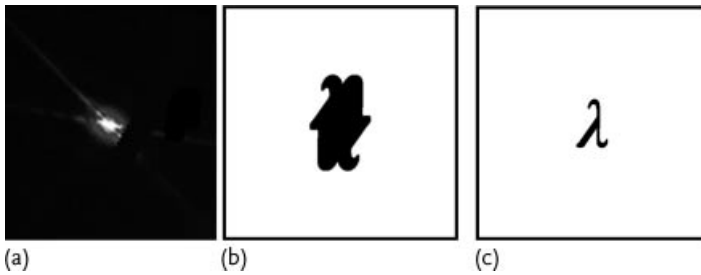


Figure 17.15 (a) Experimental diffraction pattern (same as Figure 17.9). (b) Fourier transform of (a) (with a saturated vertical scale). (c) Object corresponding to (a). (b) is clearly the autocorrelation of (c).

But as can be seen in Figure 17.15b, the inverted object also fits under the autocorrelation. Moreover, different objects can have the same autocorrelation. However, a number of techniques have been developed to further restrict the support starting from the autocorrelation (see, e.g., [37]).

Having a tight support helps achieving fast convergence. A theoretical method for support determination usually gives a good first approximation, but it is usually still too large. Marchesini *et al.* proposed an empirical method, called the Shrinkwrap method [38]. The phase-retrieval algorithm starts from a “loose” support, found by the technique we just mentioned for instance, and after a certain number of iterations tightens the support accordingly to the last partial sample reconstruction. This can of course be done several times during the reconstruction process. The method has already been used for experimental reconstruction (see, e.g., [10]).

17.4.2.2 Error Reduction Algorithm

A phase-retrieval algorithm will try to retrieve the spatial phase of the diffracted field using the constraints mentioned in the previous section, namely (i) the measured diffraction intensity (constraint in the Fourier space) and (ii) the support finite size (constraint in the real space). Starting from a usually random guess, it projects it alternatively onto each constraint set, using a Fourier transform between each projection to switch from one space to the other. An error metric is used after each iteration to evaluate the accuracy of the reconstruction, which is usually good enough after a few thousand iterations.

The error reduction algorithm, introduced by Gerchberg and Saxton [39], is easy to implement and can be used to illustrate the phase-retrieval algorithms principle. It uses two projectors, one in the real space and one in the Fourier space. The first one can be written as

$$P_S \rho(\mathbf{r}) = \begin{cases} \rho(\mathbf{r}) & \text{if } \mathbf{r} \in \text{support} \\ 0 & \text{otherwise} \end{cases}, \quad (17.33)$$

which means that for a given reconstruction $\rho(\mathbf{r})$, for all the \mathbf{r} outside the support, $\rho(\mathbf{r})$ is set to zero. The second projector can be expressed as follows:

$$\tilde{P}_F \tilde{\rho}(\mathbf{q}) = \sqrt{I(\mathbf{q})} e^{i\phi(\mathbf{q})}, \quad (17.34)$$

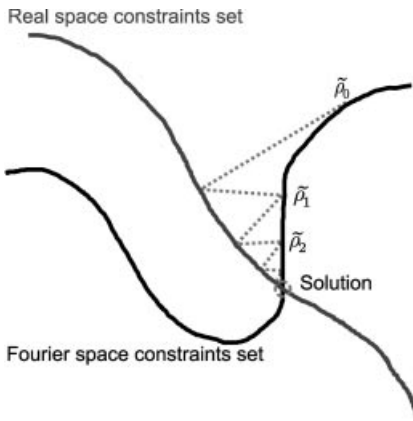


Figure 17.16 Principle of a phase-retrieval algorithm.

which means that the amplitudes of the Fourier transform of a given reconstruction are replaced by the measured data points, while its phase is kept unchanged (here, $\tilde{\rho}$ is the Fourier transform of ρ) the whole algorithm can thus be written as

$$\rho_{n+1}(\mathbf{r}) = P_S P_F \rho_n(\mathbf{r}) \text{ where } P_F = \mathcal{F}^{-1}(\tilde{P}_F) \mathcal{F}. \quad (17.35)$$

The first step is usually to assign an arbitrary spatial phase to the measured diffraction pattern, giving $\tilde{\rho}_0$. After a few thousand iterations, the algorithm converges (Figure 17.16). The main problem with the error-reduction algorithm is that it can easily be trapped at a local minimum.

17.4.2.3 Other Projectors and Algorithms

To help the convergence of the algorithms, everything that is known about the sample can help. Indeed, the algorithms aim at reconstructing a sample transmission, which is a physical problem. Hence, known physical properties of the object can be used to improve the real space projector. Here are some examples:

- Positivity: The object is real, that is, it is a pure transmission object.

$$P_S \rho(\mathbf{r}) = \begin{cases} |\rho(\mathbf{r})| & \text{if } \mathbf{r} \in \text{support} \\ 0 & \text{otherwise} \end{cases} \quad (17.36)$$

- Absorption cannot be negative.

$$P_S \rho(\mathbf{r}) = \begin{cases} \Im(\rho(\mathbf{r})) \geq 0 & \text{if } \mathbf{r} \in \text{support} \\ 0 & \text{otherwise} \end{cases} \quad (17.37)$$

- Pure phase object:

$$P_S \rho(\mathbf{r}) = \begin{cases} \rho_0(\mathbf{r}) e^{i\phi(\mathbf{r})} & \text{if } \mathbf{r} \in \text{support} \\ 0 & \text{otherwise.} \end{cases} \quad (17.38)$$

Likewise, physical considerations can be taken into account when defining the Fourier space projector:

- Missing data:

$$\tilde{P}_F \tilde{\rho}(\mathbf{q}) = \begin{cases} \sqrt{I(\mathbf{q})} e^{i\phi(\mathbf{q})} & \text{if } I(\mathbf{q}) \text{ is measured} \\ 0 & \text{otherwise.} \end{cases} \quad (17.39)$$

Those are just a few examples, more sophisticated projectors can of course be designed.

The error-reduction algorithm is only one example among many others. A good comparison between the most popular algorithms can be found in [40]. Fienup introduced the hybrid input output (HIO) algorithm in the late seventies, which introduced nonlinear feedback to avoid local minima [41, 42]. HIO is one of the most popular algorithms, usually used in an alternating scheme with the error-reduction algorithm, which is supposed to speed up the convergence. Other common algorithms are the relaxed average alternating reflector (RAAR) [43] and the difference map [44].

17.4.3

Implementations of Phase Retrieval Algorithms

17.4.3.1 Back to Spatial Resolution

A phase retrieval algorithm stops iterating when a predefined error function goes below an arbitrary set value. But the actual spatial resolution of the reconstructed object is difficult to evaluate. The resolution definition given by Eq. (17.23) cannot really be used here, because the resolution has to be estimated from the reconstructed image. Usually, the resolution is quite different from the theoretical resolution limit (see Figure 17.9 and the associated comment). Because different definitions for the resolution can be used, it is sometimes difficult to compare results from the literature. However, the PRTF becomes increasingly common [12, 32]. PRTF is based on the assumption that several reconstructions are produced for one experimental diffraction pattern. Each reconstruction uses a different random set of spatial phases for the phase-retrieval algorithm starting step. The PRTF is then defined as

$$\text{PRTF}(q) = \frac{\langle |\mathcal{F}(\rho(\mathbf{r}))| \rangle}{\sqrt{I_{\text{measured}}(q)}}, \quad (17.40)$$

where the averaging is done over multiple reconstructions. This relation gives a degree of confidence that the phases were retrieved: if so, the values add in phase, otherwise the average tends toward zero. The half-period resolution is defined as the value where the PRTF drops below $1/e$ (see Figure 17.17).

17.4.3.2 A Few Examples

Since the first experimental demonstration of CDI in 1999 by Miao *et al.* [9], this research activity has gained in popularity. Publication deals with a multitude of

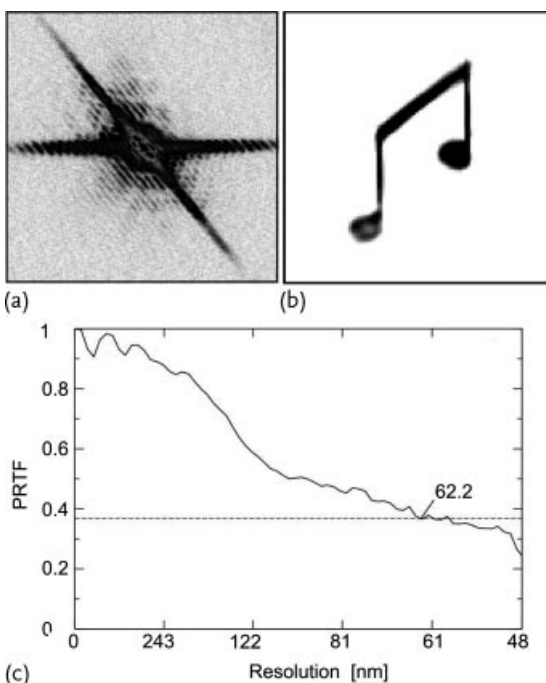


Figure 17.17 Illustration of the spatial resolution estimation from the PRTF. (a) Diffraction pattern. (b) Reconstruction of the object. (c) PRTF function of the reconstruction, giving a half-period resolution of 62 nm. Taken from [13].

issues, from experimental improvements to biological applications, from 3D imaging to time resolved experiments. The following list of examples is far from exhaustive, but it illustrates the variety of the work currently performed.

Figure 17.18 represents the first image reconstruction from experimental data. Their sample (Figure 17.18a) was a collection of 100-nm gold dots, deposited on a silicon nitride membrane. The experiment was performed at the National Synchrotron Light Source, at $\lambda = 1.7$ nm, with an exposure time of 15 min. A modified HIO algorithm leads to the image reconstruction (Figure 17.18c), after 1000 itera-

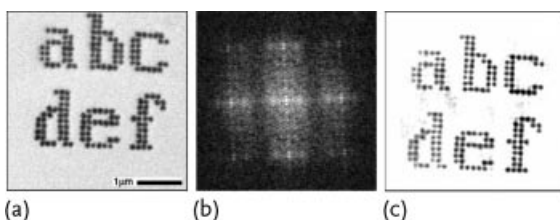


Figure 17.18 The first experimental X-ray coherent diffractive imaging experiment. (a) SEM image of the sample. (b) Diffraction pattern, on a log scale. (c) Reconstruction of the sample. Taken from [9].

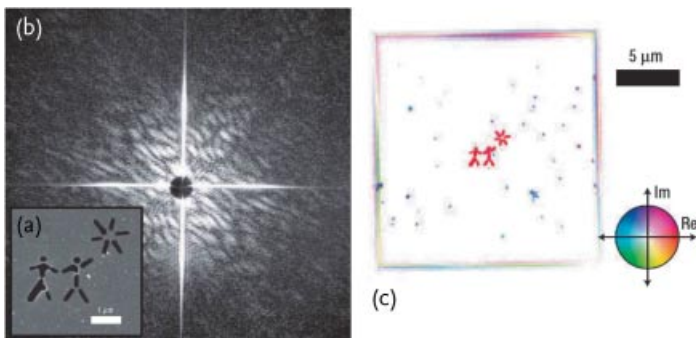


Figure 17.19 The first experimental X-ray coherent diffractive imaging experiment using a free-electron laser. (a) SEM image of the sample. (b) Diffraction pattern. (c) Reconstruction of the sample. Taken from [32].

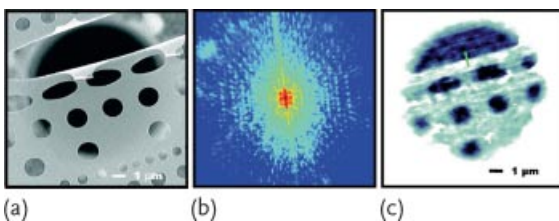


Figure 17.20 The first experimental X-ray coherent diffractive imaging experiment using HHG. (a) SEM image of the sample. (b) Diffraction pattern, on a log scale. (c) Reconstruction of the sample. Taken from [46].

tions. As mentioned in Section 17.3.4, other XUV sources can be used to perform coherent diffractive imaging experiments. Figures 17.19 and 17.20 are the first published results using a free-electron laser at $\lambda = 32$ nm and a high-order harmonic source at 29 nm. The experiment using the FLASH free-electron laser is a single shot measurement. The sample was a silicon nitride membrane patterned with a focused ion beam. The shrinkwrap technique was used to improve the support for the reconstruction. Figure 17.19c is an average over 250 reconstructions (3000 to 4000 iterations each) and presents a resolution of 62 nm. For the HHG experiment, Sanberg *et al.* used a 40 μm thick carbon foil with holes of various sizes. The exposition was 2 h long. The reconstruction was performed with the Guided HIO algorithm [45] and achieved a 214-nm spatial resolution.

Multiple experiments on biological samples have since been performed [12, 47–52]. Figure 17.21 represents some examples, showing that imaging small (top) and large (bottom left) cells is possible, as well as resolving finer structure, for example, in chromosomes (bottom right). Because of the high-penetration power of the used wavelength, the inside of the cells is visible, and inner structures can be identified. Figure 17.21a also demonstrates that single shot imaging is feasible with a free-electron laser even for biological samples, which are more sensitive to radiations.

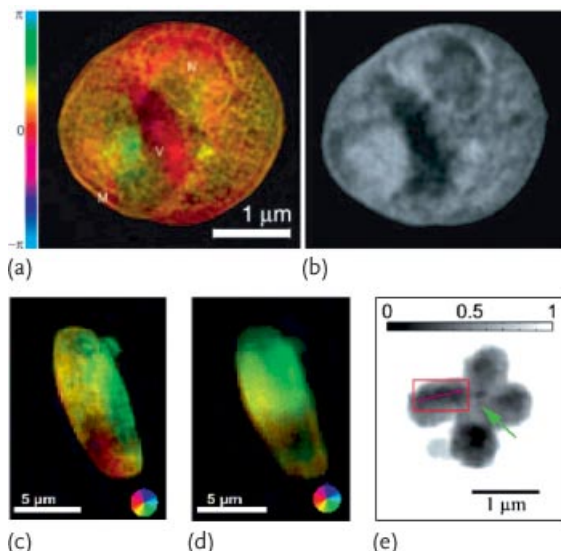


Figure 17.21 (a,b) Image of a freeze-dried yeast cell ((a) CDI reconstruction from ALS data ($\lambda = 1.66 \text{ nm}$), (b) from scanning transmission X-ray microscope). The letters identify cell parts. Taken from [12]. (c,d) Reconstruc-

tions of a diatom (unicellular algae) at FLASH ($\lambda = 8 \text{ nm}$). (c) 1500 shots accumulation. (d) Single shot image. Taken from [51]. (e) Reconstruction of a human chromosome (at SPring-8, $\lambda = 0.25 \text{ nm}$). Taken from [49].

Three-dimensional imaging is more challenging experimentally as well as numerically. The data acquisition procedure is very time consuming, the sample has to be rotated using fine steps to achieve a good spatial resolution. Two different approaches can be used to invert the diffraction patterns and reconstruct the image. The 3D pyramid image in Figure 17.22a was obtained by inverting directly the 3D data set in Fourier space, obtained by assembling together multiple diffraction patterns acquired for each orientation [10]. Chapman *et al.* took one measurement for every angular degree, with a 73-s acquisition time per orientation. The shrinkwrap technique, with a HIO and a RAAR algorithm was applied on this 3D data set to obtain a 3D image with a spatial resolution of 10 to 50 nm. Another approach was used in the result presented in Figure 17.22b [50]: Jiang *et al.* measured diffraction patterns for 25 different orientations (with an exposure time of $2000 \times 0.5 \text{ s}$ plus $80 \times 50 \text{ s}$ per orientation). They then used the guided HIO [45] to reconstruct the 25 different 2D projections, which they assembled in a 3D image using a tomographic technique. Numerous other 3D imaging examples can be found (e.g., [53, 54]). Raines *et al.* proposed another method, which they called ankylography, to achieve 3D imaging from a single orientation of the sample under some specific experimental conditions [55]. Ptychography is another technique based on coherent diffractive imaging developed for extended objects, larger than the beam size (in which case the object is not an isolated object) [56]. The idea is to scan the object with the beam, taking a diffraction pattern at each position. If each spot overlaps with its neighbors, the information is highly re-

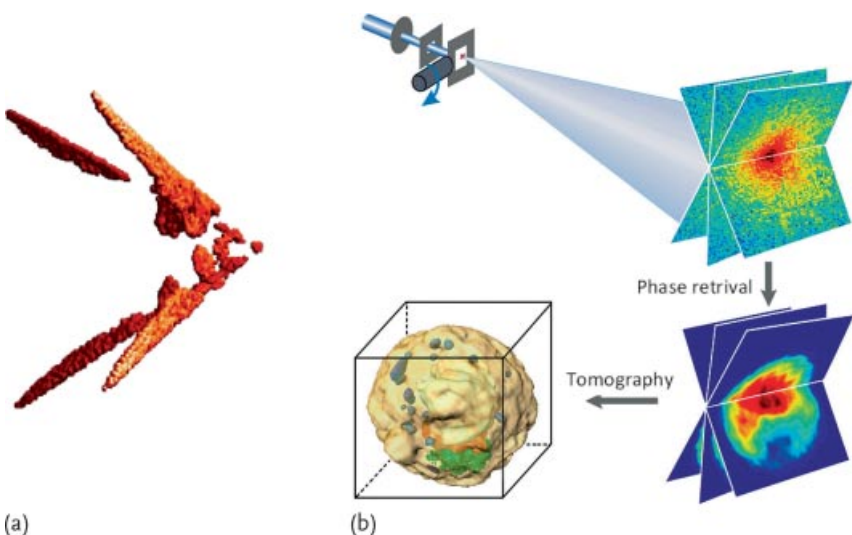


Figure 17.22 (a) 3D reconstruction of a pyramid of silicon nitride membrane, covered by 50-nm gold spheres. Experiment performed at the ALS ($\lambda = 1.65 \text{ nm}$). Taken from [10]. (b)

3D reconstruction of a yeast spore cell. Experiment performed at the SPring-8 synchrotron source ($\lambda = 0.25 \text{ nm}$). Taken from [50].

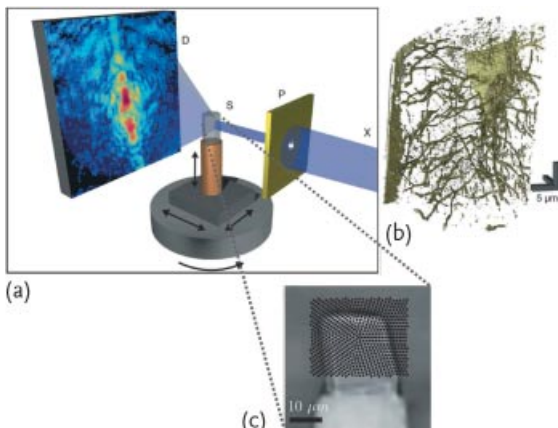


Figure 17.23 (a) Ptychography experimental set up, (c) projection image of a mouse bone with the scanning points superimposed. (b) 3D rendering of the tomographic reconstruction, showing an inner structure of the bone. Taken from [56].

dundant and both the sample and the beam properties can be recovered. An example is presented in Figure 17.23. Of course, this kind of measurement is even more demanding experimentally: the example shown here required a set of 704 scan points for each of the 180 sample orientations. The total exposure time was 36 h.

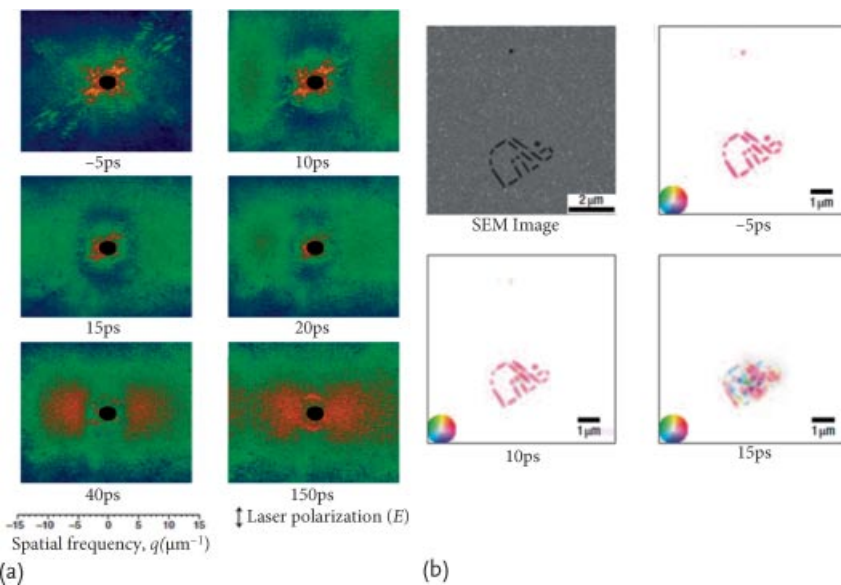


Figure 17.24 Time-resolved CDI of a patterned silicon nitride sample at the moment of destruction by picosecond laser ablation. (a) Evolution of the diffraction pattern with pump–probe delay. (b) Evolution of the sample reconstruction with pump–probe delay. Taken from [57].

One advantage of the high-order harmonics sources, and to a lesser extent of free-electron lasers (cf. 17.1) is a short pulse duration that allows time-resolved experiments. The difficulty with FELs is that they need to be synchronized with a pump laser. The temporal jitter from imperfect synchronization lowers the temporal resolution. An early experiment at FLASH FEL [57] used a picosecond laser to ablate a sample made of a silicon nitride membrane, patterned with a focused ion beam. In a pump–probe scheme, using new, but identical samples for each delay, the destruction of the object could be observed in real time by imaging the process with picosecond resolution. The result is presented in Figure 17.24. Single shot measurements are mandatory if perfectly identical samples are not available. Free-electron lasers offer the required properties for such single shot measurements (contrary to synchrotrons). High-order harmonics sources also demonstrated the ability to perform single shot coherent diffraction experiments [13]. Because they are naturally synchronized with the generating ultrafast laser, their femtosecond or even attosecond pulse duration should soon lead to time resolved results with subpicosecond time resolution.

17.5 Holography

Oversampling and phase-retrieval algorithms are one way to solve the phase problem and reconstruct a sample image from its far-field diffraction pattern. This technique is efficient and has already provided beautiful results, but it suffers from some drawbacks. The algorithms can be complicated and requires significant computation time for 3D image reconstruction. When the data are noisy, convergence is difficult to achieve. Also, sophisticated algorithms depend on parameters that have optimum values which are problem dependent: finding the right parameter values for each reconstruction is time consuming. However it is possible to encode directly the sample phase information in the diffraction pattern using holographic techniques. Here, we describe two such techniques: Fourier transform holography (FTH) first and secondly a holography technique using extending references.

17.5.1 Fourier Transform Holography

Fourier transform holography uses interferences between the field scattered by the sample and the field of a reference to encode phase information. In the first X-ray FTH experiment [58], McNulty and co-workers used the first-order focus of a zone plate to generate the reference beam, while the zero order was illuminating the sample. In later experiments, the reference was usually produced by a small aperture in the vicinity of the sample (see [59] for instance). In order to explain the principle of FTH, let us take this latter example, using a sample as shown in Figure 17.25. The sample is labeled ρ , and contains two components: the object itself, o (here a letter h patterned in a silicon nitride membrane), and the references, r (two holes were used here). The experimental setup and parameters are the same as for coherent diffractive imaging (Figure 17.5, [13]). The recorded diffraction pattern in the far field, which is called a *hologram* in holography, presents additional fringes due to the interferences between the scattered fields from the object and the references. It can be written as

$$\text{Hologram} = |\mathcal{F}(\rho)|^2 = |\mathcal{F}(o) + \mathcal{F}(r)|^2 . \quad (17.41)$$

Denoting the object and reference Fourier transforms as O and R , Eq. (17.41) becomes

$$\text{Hologram} = |O|^2 + |R|^2 + OR^* + O^*R . \quad (17.42)$$

If we take the inverse Fourier transform of Eq. (17.42), we get the sample autocorrelation (see Eq. (17.32)), which can be written as

$$\mathcal{F}^{-1}(\text{Hologram}) = \rho \otimes \rho = o \otimes o + r \otimes r + o \otimes r + r \otimes o . \quad (17.43)$$

The first two terms in Eq. (17.43) represent the object and reference autocorrelations. The other two terms represent cross-correlations between object and reference. If the reference is small enough to be considered as a Dirac function, the

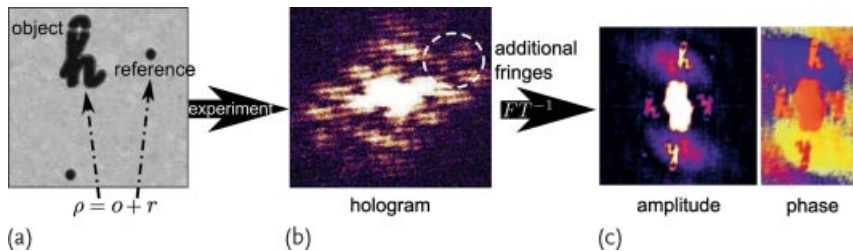


Figure 17.25 Fourier transform holography: the sample contains the object o and one (or more) references r , close to it (a). The diffraction pattern, called the hologram, shows fringes due to the interferences be-

tween the different diffracted fields (b). The reconstructed image shows four object images corresponding to the object-reference cross-correlations (c).

inverse Fourier transform of the hologram directly gives the object reconstruction (and its twin image). An example is given in Figure 17.25. In the reconstruction, the bright central part is the superposition of object and reference autocorrelations. Four object images “ h ” can be recognized. The two images on the top and bottom come from the vertically displaced reference (they are one reconstruction and its central symmetric), while the other two come from the horizontally displaced reference. Finally, only two independent reconstructions are achieved, one for each reference pinhole. The reconstruction principle works for complex object. In the example shown in Figure 17.25, the sample was a pure transmission object and in this simple case the phase is flat.

17.5.1.1 Limitations

The main limitation of FTH is apparent in Eq. (17.43). To reconstruct the object directly from the hologram by inverse Fourier transform, we supposed that the reference could be approximated by a Dirac function. If the reference is larger, the reconstruction will actually give the cross-correlation between the object and the reference, thus reducing the spatial resolution. This is illustrated in Figure 17.26a: the reference pinhole is large and the object reconstruction is blurred. However, this is an interference experiment. To ensure a fringe visibility, the intensities of the fields going through the object and the reference have to be similar, which implies

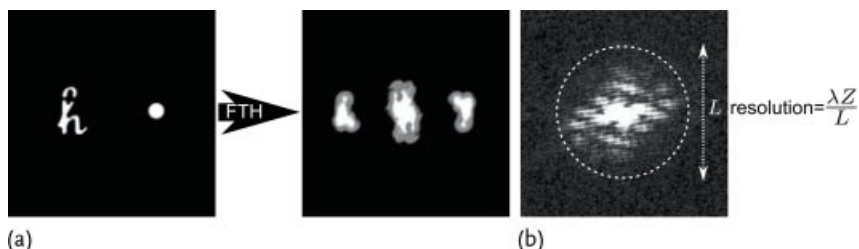


Figure 17.26 (a) Effect of a large reference on the spatial resolution. (b) Relationship between diffraction angle and spatial resolution.

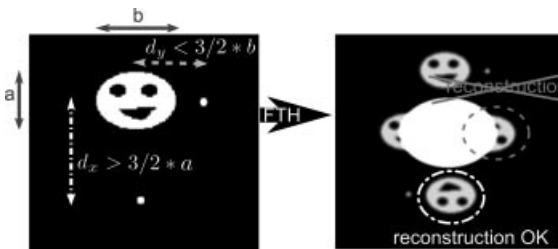


Figure 17.27 Holographic separation condition. The object has a size $a \times b$. The distance d_y between the object and one reference is too short, so the object reconstruction by that ref-

erence is overlapping with the autocorrelation terms. Distance d_x with the second reference is large enough to separate the object reconstruction from autocorrelation terms.

that the reference has to be large. Moreover, enlarging the reference increases the SNR at large diffraction angles, which in turn implies that the spatial resolution will be better (see Figure 17.26b).

Another drawback of FTH lies in the experimental requirements. The sample needs to be designed carefully. Figure 17.27 illustrates a case, when the distance between the object and the reference is too small and the object reconstruction overlaps with the autocorrelation terms. This is called the holographic separation condition. The direct consequence of this condition is that fields with higher spatial coherence are required: the coherence length needs to be larger than the distance between the object and the reference, not just larger than the object as in pure coherent diffractive imaging.

17.5.1.2 Applications

Fourier transform holography has been used with lasers in the visible regime for some time now, but its first meaningful applications with UV or X-ray sources are more recent. Mc Nulty *et al.*, as we already mentioned, performed a FTH experiment in 1992 but without a pinhole or a small scatterer for the reference [58]. An experiment with reference was performed in 2004 by Eisebitt and co-workers (see Figure 17.28) [59]. They used FTH to image magnetic domains in a Co/Pt multilayer film, working at the cobalt L edge ($\lambda = 1.59$ nm). Since then, many experiments

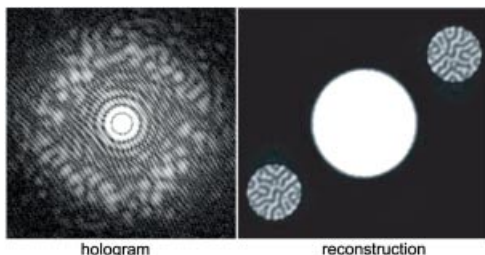


Figure 17.28 FTH imaging of magnetic domains in CO/Pt multilayer films. The black and white domains in the object reconstruction represent the two orientations of domains. The reference size was 100 nm and the spatial resolution 50 nm ($\lambda = 1.59$ nm). Taken from [59].

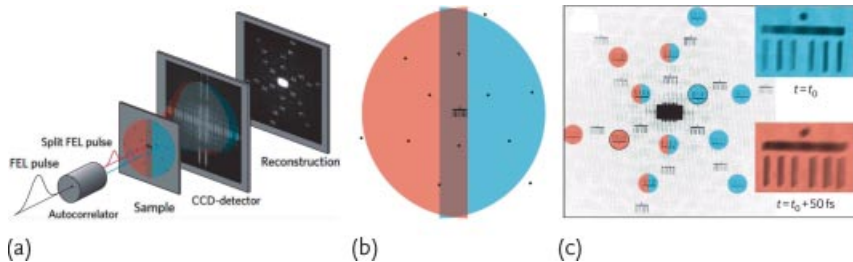


Figure 17.29 (a) Experimental setup, with two spatially separated and time delayed pulses, represented in red and blue. (b) Sample illumination: the object at the center is illuminated by both red and blue pulses, while

most of the references see only one pulse. (c) Hologram and object reconstructions. Reconstructions marked in red are due to a reference illuminated only by the red pulse. Taken from [64].

imaged magnetic domains, not only mostly at the same Co edge [60–62], but also at higher wavelength (at the cobalt M edge). Imaging of biological samples was also published [63]. Gnüther and co-workers proposed a clever way, by using multiple references hit by delayed pulses (while both pulses are superimposed on the object) to perform time resolved sequential imaging (Figure 17.29) [64].

In parallel, a lot of effort was invested to overcome FTH limitations. FTH can be combined with iterative algorithms: FTH can be the first step, producing a tight support for the phase-retrieval algorithm [65]. But there is no clear demonstration that this can really improve the spatial resolution. As we already mentioned, the problem lies in the size of the reference. If the reference is large but perfectly known, its exact shape can however be deconvoluted from the reconstruction, and so its size is less a limitation [66]. Tackling the problem from the other side, one can use a small-sized reference, in order to achieve a good spatial resolution, and add several of them (see, e.g., [67]). As shown in Figure 17.30, the reconstruction from a single small reference can be so noisy that the object is not visible. But when all the reconstructions from five different reference holes are summed coherently, a good quality reconstruction of the object is obtained. However the holographic

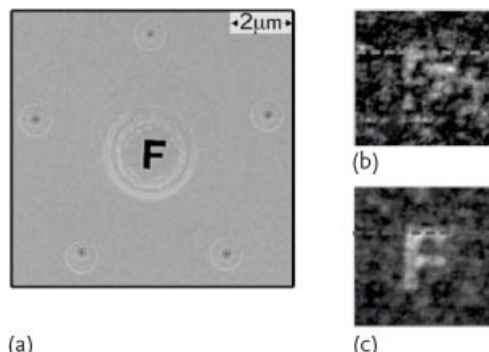


Figure 17.30 (a) Sample, with one object (the “F” letter) and five point-like references. (b) Reconstruction from one single reference. (c) Coherent sum of the five reconstructions. Taken from [67].

separation condition has to be fulfilled for every reference, which can complicate the layout. Marchesini and co-workers pushed this approach to the extreme, using a uniformly redundant array: a special procedure can then be used to decode the hologram [68].

17.5.2 HERALDO

Holography with extended reference by autocorrelation linear differential operation (HERALDO) was proposed by Guizar Sicairos and Fienup [69, 70], based on an idea of Podorov and co-workers [71]. HERALDO uses extended references to maximize the fringe contrast but does not require a perfect knowledge of the reference. More precisely, it used the edges of extended objects as the references and combine a differential operator with the reference shape to provide a direct reconstruction procedure.

17.5.2.1 HERALDO Principle

The idea behind the HERALDO technique is summarized in Figure 17.31: the slit r , parallel to the \hat{x} axis, delivers two point-like Dirac functions after derivation along \hat{x} . Applying the correct differential operator associated to a given reference, a single-point reference can be reconstructed. This adds one step as compared to FTH reconstruction, as can be seen in Figure 17.32. The hologram is first inverse Fourier transformed (this is the same step as in FTH). The object is still convoluted with the reference and, consequently, no spatial resolution is apparent at this point. The differential operator associated with the reference is then applied. In the example, one reconstruction of the object appears at each extremity of the reference slit. Compared to Eq. (17.43), the HERALDO procedure can be written as

$$\frac{d}{d\hat{x}}(\rho \otimes \rho) = C + \frac{d}{d\hat{x}}(o \otimes r) + \frac{d}{d\hat{x}}(r \otimes o), \quad (17.44)$$

where C stands for the autocorrelation terms. Hence

$$\frac{d}{d\hat{x}}(\rho \otimes \rho) = C + (-o) \otimes \frac{d}{d\hat{x}}(r) + \frac{d}{d\hat{x}}(r) \otimes o \quad (17.45)$$

$$\frac{d}{d\hat{x}}(\rho \otimes \rho) = C - o_{(x+a)} + o_{(x+b)} \quad (17.46)$$

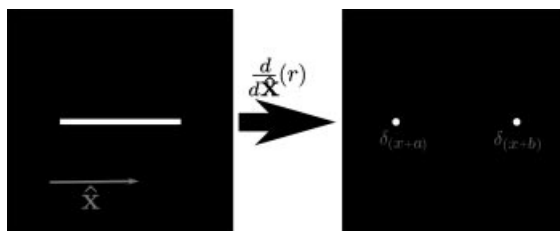


Figure 17.31 A extended slit can be transformed into two single-point references by derivation along the slit direction.

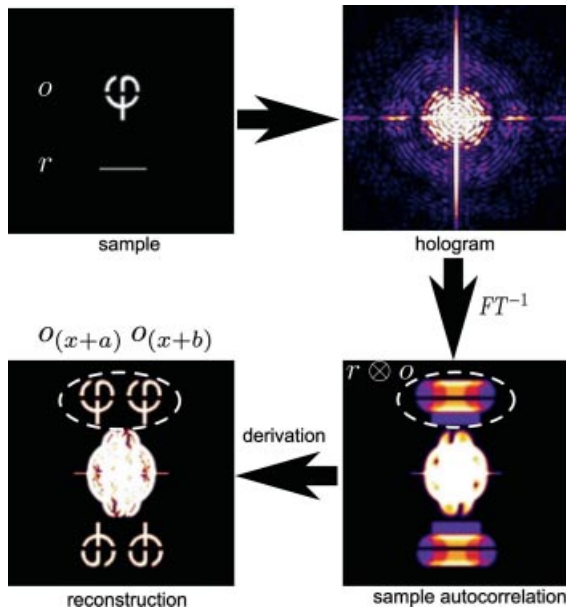


Figure 17.32 HERALDO reconstruction procedure: the field diffracted by the sample (object + extended reference) gives an hologram.

After inverse Fourier transform, the linear dif-

ferential operator is applied to the sample autocorrelation, and gives a direct reconstruction of the object.

as $d/(d\hat{x})(r)$ is a Dirac function centered on the reference extremity. It is worth noting that the exact orientation of the reference does not have to be known: it can be found analyzing the main diffraction direction in the hologram. The shape of the extended reference can be more complicated than a simple slit: the reference can consist of triangles, squares, or other shapes. In those cases, it may be necessary to combine two or more differential operators along different directions, transforming the sharp edge of a triangle into a point, for instance. The technique has also been extended to the case of crossing wires, which may be easier to manufacture for small-scale samples [72].

17.5.2.2 Limitations and Advantages

The spatial resolution in a HERALDO experiment is not limited by the size of the reference, but the quality of the edges is nevertheless a limiting factor. If the reference derivative is not a point-like function, Eq. (17.45) shows that the reconstruction process will degrade the resolution.

Another difficulty comes from the holographic separation condition. Designing a sample with an extended reference adds additional constraints in the reference size and position [69]. This also means that the coherence requirement on the source is more stringent. Also, the reference should be tailored to match the object under study. Although this is not difficult when patterning objects and references on a membrane, this may be more difficult for other kinds of samples. The use of carbon

nanotubes as references was proposed to achieve better resolution [73]. However, in the case of macroprotein imaging, bringing the reference at the right distance from the object seems to be rather difficult. Experiments may need to rely on luck, sending both the object and the reference into the X-ray beam path using molecular jets and hoping that, for some shots, the distance would be right.

It is difficult to compare different techniques, but from preliminary results obtained with our HHG source, HERALDO seems to be less sensitive to noise than iterative algorithms [74]. Moreover, we found that for 1- μm objects, using a 32-nm HHG source to perform diffractive imaging experiments, iterative algorithms could not invert the diffraction patterns in the single shot regime, while HERALDO, with various reference shapes, succeeded.

17.5.2.3 Applications

Experiments using the HERALDO technique have been performed, with several different radiation sources: synchrotrons [72, 75], free-electron lasers [76], and HHG sources [73]. Figures 17.33 and 17.34 show two of those results. The first illustrates the use of a nontrivial reference shape (a triangle). The diffraction pattern (Figure 17.33b) is dominated by the diffraction from the edges of the reference, but signal from the object itself is also visible. The triangular reference gives three independent reconstructions, each obtained after applying two differential operators per reference. The three reconstructions can be added coherently to increase the spatial resolution. The second example, performed with a HHG source, is a single laser shot measurement: we demonstrated a 110-nm spatial resolution ($\lambda = 32 \text{ nm}$) and 20-fs temporal resolution. Time-resolved experiments become possible with real time data analysis, thanks to the direct image reconstruction. Figure 17.35 shows a sample with two large square references. The spacing between the references and the object, as well as the size of the squares, are dictated by the holographic separation condition. After applying the reconstruction procedure,

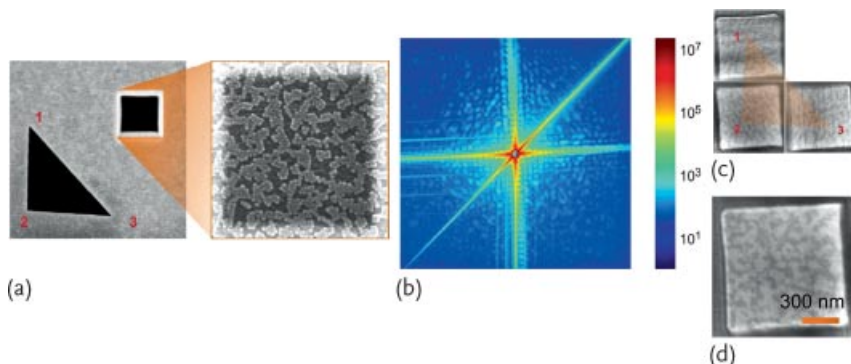


Figure 17.33 (a) SEM image of the sample. The triangle is the reference, and the squares, made of 18-nm iron nanocubes, is the object. (b) Diffraction pattern, on a log scale, taken at the Stanford Synchrotron Light Source

($\lambda = 1.76 \text{ nm}$). (c) Individual reconstruction from each corner of the reference. (d) Coherent sum of the reconstructions, providing 16-nm resolution. Taken from [75].

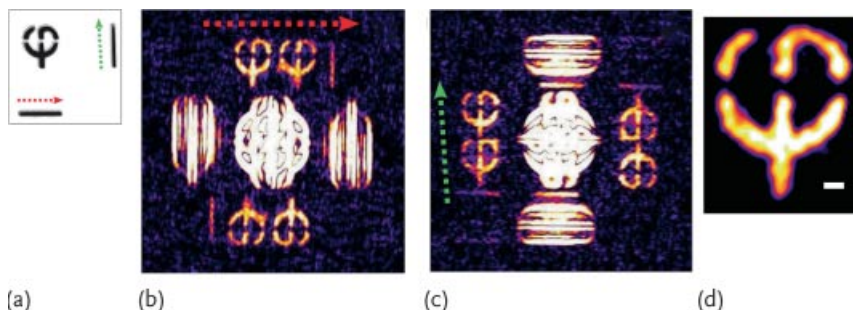


Figure 17.34 (a) SEM image of the sample. Two perpendicular slits were used as references. (c) and (d) Reconstructions from the horizontal and vertical slits, respectively. Two

independents images are obtained per reconstruction, one at each slit extremity. (d) Coherent sum of the reconstructions, providing 110-nm resolution. Taken from [73].

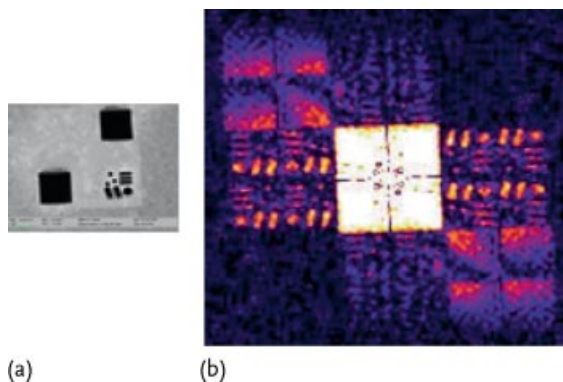


Figure 17.35 (a) SEM image of the sample. Two large squares were used as references. The object and the squares are each 1- μm wide. (b) Reconstruction of the object. The inverse Fourier transform of the diffraction

pattern was differentiated along both, the vertical and the horizontal axis. Eight independent reconstructions are visible, with their twin images.

eight different reconstructions of the object are obtained, one for each corner of the either reference. One of the two references was badly illuminated, which explains why some of the reconstructions show reduced contrast. Nevertheless, adding coherently the eight reconstructions should result in a good spatial resolution.

17.6 Conclusions

UV-X-ray CDI is a promising imaging technique, which will soon give access to both the ultrasmall (nanometer or Angström) and the ultrafast (femtosecond) scales. CDI is based on the far-field diffraction theory, stating that the far-field diffraction pattern of a sample is its Fourier transform. However, because detec-

tors, such as CCD cameras, register only the intensity of the field, oversampling of the diffraction pattern is necessary to solve the phase problem and to reconstruct the sample image. Thanks to very powerful iterative algorithms, 3D imaging of isolated objects is now possible. The phase problem can also be solved using experimental tricks to encode the phase into the diffraction pattern. We discussed FTH, with or without extended references. Other kinds of holography are, of course, applicable, for example, in-line holography. We deliberately did not compare the resolution achieved by holography and iterative algorithms. Such a comparison is not easy, and maybe even impossible. The choice of experimental method is strongly problem dependent. Holography data are easier to analyze, but the resolution is limited by the reference size and/or quality. Nanocrystals or carbon nanotubes can be used, but reaching atomic-scale spatial resolution seems difficult. On the other hand, we saw that HERALDO was more efficient than iterative algorithms for image retrieval in the case of single shot imaging with a low-photon flux.

As we mentioned in the introduction, one goal of CDI is to perform protein imaging, in order to reveal three-dimensional protein structure. A first step toward this end has been reached at the hard X-ray free-electron laser LCLS in the beginning of

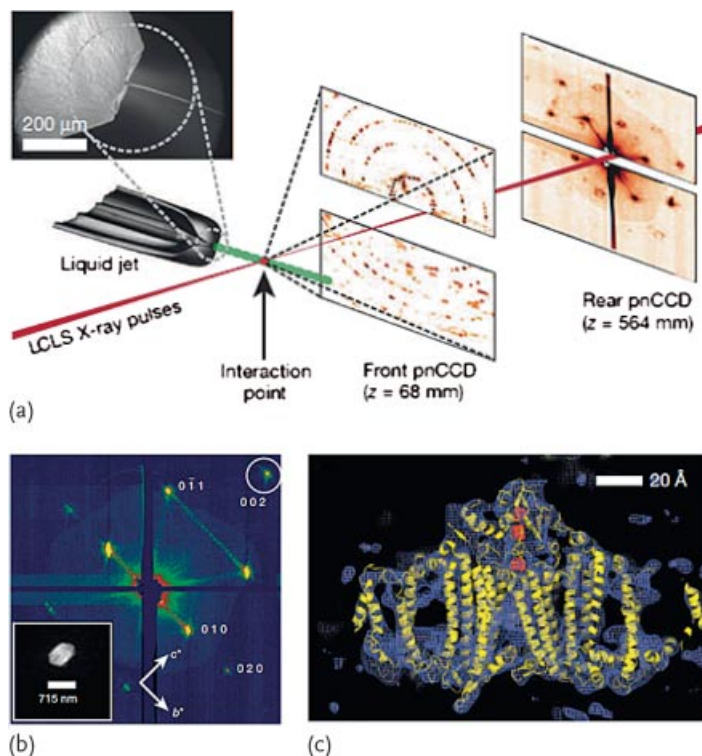


Figure 17.36 (a) Experimental setup for protein nanocrystal imaging. (b) Low angle diffraction pattern on a log scale. The inset shows the reconstruction of the corresponding nanocrystal. (c) Electron density map of the protein complex. See [4] for details.

2011 [4]. The authors were able to resolve the structure of photosystem I, with 8.5-Å resolution, by the investigation of nanocrystals. Nanocrystals are easier to manufacture as compare to the larger crystals traditionally used in crystallography. Figure 17.36 shows their experimental setup and main results. Individual nanocrystals, suspended in a liquid jet, cross the X-ray beam path ($\lambda = 1.8 \text{ keV} = 0.69 \text{ nm}$). Two detectors, at a short distance (for large angle diffraction) and farther away (for small-angle diffraction) recorded more than 3 000 000 diffraction patterns. After sorting the data to account for random crystal orientations, they were able to reconstruct the shape of the nanocrystals (bottom left) but also the electron density map for the protein complex (bottom right). A newer experiment at the same facility resolved the structure of a cysteine protease with 2.1-Å resolution by analyzing some 300 000 diffraction images from microcrystals [77].

References

- 1 Chao, W., Kim, J., Rekawa, S., Fischer, P., and Anderson, E.H. (2009) Demonstration of 12 nm resolution fresnel zone plate lens based soft X-ray microscopy. *Opt. Express*, **17** (20), 17669–17677.
- 2 Chao, W., Harteneck, B.D., Liddle, J.A., Anderson, E.H., and Attwood, D.T. (2005) Soft X-ray microscopy at a spatial resolution better than 15 nm. *Nature*, **435**, 1210–1213.
- 3 Gaffney, K.J. and Chapman, H.N. (2007) Imaging atomic structure and dynamics with ultrafast X-ray scattering. *Science*, **316** (5830), 1444–1448.
- 4 Chapman, H.N., Fromme, P., Barty, A., White, T.A., Kirian, R.A., Aquila, A., Hunter, M.S., Schulz, J., DePonte, D.P., Weierstall, U., Doak, R.B., Miao, F.R.N.C., Martin, A.V., Schlichting, I., Lomb, L., Coppola, N., Shoeman, R.L., Epp, S.W., Hartmann, R., Rolles, D., Rudenko, A., Foucar, L., Kimmel, N., Weidenspointner, G., Holl, P., Liang, M., Barthelmess, M., Caleman, C., Boutet, S., Bogan, M.J., Krzywinski, J., Bostedt, C., Bajt, S., Gumprecht, L., Rudek, B., Erk, B., Schmidt, C., Homke, A., Reich, C., Pietschner, D., Struder, L., Hauser, G., Gorke, H., Ullrich, J., Herrmann, S., Schaller, G., Schopper, F., Soltau, H., Kuhnel, K.U., Messerschmidt, M., Bozek, J.D., Hau-Riege, S.P., Frank, M., Hampton, C.Y., Sierra, R.G., Starodub, D., Williams, G.J., Hajdu, J., Timneanu, N., Seibert, M.M., Andreasson, J., Rocker, A., Jonsson, O., Svenda, M., Stern, S., Nass, K., Andritschke, R., Schroter, C.D., Krasniqi, F., Bott, M., Schmidt, K.E., Wang, X., Grotjohann, I., Holton, J.M., Barends, T.R.M., Neutze, R., Marchesini, S., Fromme, R., Schorb, S., Rupp, D., Adolph, M., Gorkhover, T., Andersson, I., Hirsemann, H., Potdevin, G., Graafsma, H., Nilsson, B., and Spence, J.C.H. (2011) Femtosecond X-ray protein nanocrystallography. *Nature*, **470**, 73–77.
- 5 Kirz, J., Jacobsen, C., and Howells, M. (1995) Soft X-ray microscopes and their biological applications. *Q. Rev. Biophys.*, **28**, 33–130.
- 6 Sayre, D. (1952) Some implications of a theorem due to Shannon. *Acta Crystallogr.*, **5** (6), 843.
- 7 Sayre, D. (1980) *Prospects for long-wavelength X-ray microscopy and diffraction*, Springer-Verlag, Berlin, in: Imaging Processes and Coherence in Physics, pp. 229–235.
- 8 Sayre, D., Chapman, H.N., and Miao, J. (1998) On the Extendibility of X-ray Crystallography to Noncrystals. *Acta Crystallogr. Sect. A*, **54** (2), 232–239.
- 9 Miao, J., Charalambous, P., Kirz, J., and Sayre, D. (1999) Extending the methodology of X-ray crystallography to allow imaging of micrometre-sized

- non-crystalline specimens. *Nature*, **400**, 342–344.
- 10 Chapman, H.N., Barty, A., Marchesini, S., Noy, A., Hau-Riege, S.P., Cui, C., Howells, M.R., Rosen, R., He, H., Spence, J.C.H., Weierstall, U., Beetz, T., Jacobsen, C., and Shapiro, D. (2006) High-resolution ab initio three-dimensional X-ray diffraction microscopy. *J. Opt. Soc. Am. A*, **23** (5), 1179–1200.
- 11 Born, M. and Wolf, E. (1989) *Principles of Optics*, Pergamon Press, 6th edn.
- 12 Shapiro, D., Thibault, P., Beetz, T., Elser, V., Howells, M., Jacobsen, C., Kirz, J., Lima, E., Miao, H., Neiman, A.M., and Sayre, D. (2005) Biological imaging by soft X-ray diffraction microscopy. *Proc. Natl. Acad. Sci. USA*, **102** (43), 15343–15346.
- 13 Ravasio, A., Gauthier, D., Maia, F.R.N.C., Billon, M., Caumes, J.P., Garzella, D., Géléoc, M., Gobert, O., Hergott, J.F., Penna, A.M., Perez, H., Carré, B., Bourhis, E., Gierak, J., Madouri, A., Mailly, D., Schiedt, B., Fajardo, M., Gautier, J., Zeitoun, P., Bucksbaum, P.H., Hajdu, J., and Merdji, H. (2009) Single-shot diffractive imaging with a table-top femtosecond soft X-ray laser-harmonics source. *Phys. Rev. Lett.*, **103**, 028104.
- 14 Kim, H.T., Kim, I.J., Kim, C.M., Jeong, T.M., Yu, T.J., Lee, S.K., Sung, J.H., Yoon, J.W., Yun, H., Jeon, S.C., Choi, I.W., and Lee, J. (2011) Single-shot nanometer-scale holographic imaging with laser-driven X-ray laser. *Appl. Phys. Lett.*, **98** (12), 121105.
- 15 Spence, J.C.H., Weierstall, U., and Howells, M. (2004) Coherence and sampling requirements for diffractive imaging. *Ultramicroscopy*, **101** (2-4), 149–152.
- 16 Williams, G.J., Quiney, H.M., Peele, A.G., and Nugent, K.A. (2007) Coherent diffractive imaging and partial coherence. *Phys. Rev. B*, **75** (10), 104102.
- 17 Singer, A., Vartanyants, I.A., Kuhlmann, M., Duesterer, S., Treusch, R., and Feldhaus, J. (2008) Transverse-coherence properties of the free-electron-laser FLASH at DESY. *Phys. Rev. Lett.*, **101** (25), 254801.
- 18 Ditzmire, T., Gumbrell, E.T., Smith, R.A., Tisch, J.W.G., Meyerhofer, D.D., and Hutchinson, M.H.R. (1996) Spatial coherence measurement of soft X-ray radiation produced by high order harmonic generation. *Phys. Rev. Lett.*, **77** (23), 4756–4759.
- 19 Le Déroff, L., Salières, P., Carré, B., Joyeux, D., and Phalippou, D. (2000) Measurement of the degree of spatial coherence of high-order harmonics using a Fresnel-mirror interferometer. *Phys. Rev. A*, **61** (4), 043802.
- 20 Whitehead, L.W., Williams, G.J., Quiney, H.M., Vine, D.J., Dilanian, R.A., Flewett, S., Nugent, K.A., Peele, A.G., Balaur, E., and McNulty, I. (2009) Diffractive imaging using partially coherent x rays. *Phys. Rev. Lett.*, **103** (24), 243902.
- 21 Chen, B., Dilanian, R.A., Teichmann, S., Abbey, B., Peele, A.G., Williams, G.J., Hannaford, P., Van Dao, L., Quiney, H.M., and Nugent, K.A. (2009) Multiple wavelength diffractive imaging. *Phys. Rev. A*, **79** (2), 023809.
- 22 Henderson, R. (1995) The potential and limitations of neutrons, electrons and X-rays for atomic resolution microscopy of unstained biological molecules. *Q. Rev. Biophys.*, **28**, 171–193.
- 23 Maser, Osanna, Wang, Jacobsen, Kirz, Spector, Winn, and Tennant (2000) Soft X-ray microscopy with a cryo scanning transmission X-ray microscope: I. instrumentation, imaging and spectroscopy. *J. Microsc.*, **197** (1), 68–79.
- 24 Shen, Q., Bazarov, I., and Thibault, P. (2004) Diffractive imaging of nonperiodic materials with future coherent X-ray sources. *J. Synchrotron Radiat.*, **11** (5), 432–438.
- 25 Howells, M., Beetz, T., Chapman, H., Cui, C., Holton, J., Jacobsen, C., Kirz, J., Lima, E., Marchesini, S., Miao, H., Sayre, D., Shapiro, D., Spence, J., and Starodub, D. (2009) An assessment of the resolution limitation due to radiation-damage in X-ray diffraction microscopy. *J. Electron Spectrosc. Relat. Phenom.*, **170** (1-3), 4–12.
- 26 Larsen, J., Hald, K., Bjerre, N., and Stapelfeldt, H. (2000) Three dimensional alignment of molecules using

- elliptically polarized laser fields. *Phys. Rev. Lett.*, **85** (12), 2470.
- 27** Huldt, G., Szoke, A., and Hajdu, J. (2003) Diffraction imaging of single particles and biomolecules. *J. Struct. Biol.*, **144** (1-2), 219–227.
- 28** Hau-Riege, S.P., London, R.A., Huldt, G., and Chapman, H.N. (2005) Pulse requirements for X-ray diffraction imaging of single biological molecules. *Phys. Rev. E*, **71** (6), 061919.
- 29** Loh, N.T.D. and Elser, V. (2009) Reconstruction algorithm for single-particle diffraction imaging experiments. *Phys. Rev. E*, **80** (2), 026705.
- 30** Loh, N.D., Bogan, M.J., Elser, V., Barto, A., Boutet, S., Bajt, S., Hajdu, J., Ekeberg, T., Maia, F.R.N.C., Schulz, J., Seibert, M.M., Iwan, B., Timneanu, N., Marchesini, S., Schlichting, I., Shoeman, R.L., Lomb, L., Frank, M., Liang, M., and Chapman, H.N. (2010) Cryptotomography: Reconstructing 3D Fourier intensities from randomly oriented single-shot diffraction patterns. *Phys. Rev. Lett.*, **104** (22), 225501.
- 31** Hau-Riege, S.P., London, R.A., and Szoke, A. (2004) Dynamics of biological molecules irradiated by short X-ray pulses. *Phys. Rev. E*, **69** (5), 051906.
- 32** Chapman, H.N., Barto, A., Bogan, M.J., Boutet, S., Frank, M., Hau-Riege, S.P., Marchesini, S., Woods, B.W., Bajt, S., Benner, W.H., London, R.A., Plonjes, E., Kuhlmann, M., Treusch, R., Dusterer, S., Tschentscher, T., Schneider, J.R., Spiller, E., Moller, T., Bostedt, C., Hoener, M., Shapiro, D.A., Hodgson, K.O., van der Spoel, D., Burmeister, F., Bergh, M., Caleman, C., Huldt, G., Seibert, M.M., Maia, F.R.N.C., Lee, R.W., Szoke, A., Timneanu, N., and Hajdu, J. (2006) Femtosecond diffractive imaging with a soft-X-ray free-electron laser. *Nat. Phys.*, **2** (12), 839–843.
- 33** Neutze, R., Wouts, R., van der Spoel, D., Weckert, E., and Hajdu, J. (2000) Potential for biomolecular imaging with femtosecond X-ray pulses. *Nature*, **406**, 752–757.
- 34** Miao, J., Sayre, D., and Chapman, H.N. (1998) Phase retrieval from the magnitude of the fourier transforms of nonperiodic objects. *J. Opt. Soc. Am. A*, **15** (6), 1662–1669.
- 35** Miao, J., Ishikawa, T., Anderson, E.H., and Hodgson, K.O. (2003) Phase retrieval of diffraction patterns from non-crystalline samples using the oversampling method. *Phys. Rev. B*, **67** (17), 174104.
- 36** Bates, R. (1982) Fourier phase problems are uniquely solvable in more than one dimension. I: Underlying theory. *Optik*, **61**, 247–262.
- 37** Crimmins, T.R., Fienup, J.R., and Thelen, B.J. (1990) Improved bounds on object support from autocorrelation support and application to phase retrieval. *J. Opt. Soc. Am. A*, **7** (1), 3–13.
- 38** Marchesini, S., He, H., Chapman, H.N., Hau-Riege, S.P., Noy, A., Howells, M.R., Weierstall, U., and Spence, J.C.H. (2003) X-ray image reconstruction from a diffraction pattern alone. *Phys. Rev. B*, **68** (14), 140101.
- 39** Gerchberg, R. and Saxton, W. (1972) A practical algorithm for the determination of phase from image and diffraction plane pictures. *Optik*, **35**, 237–246.
- 40** Marchesini, S. (2007) Invited article: A unified evaluation of iterative projection algorithms for phase retrieval. *Rev. Sci. Instrum.*, **78** (1), 011301.
- 41** Fienup, J.R. (1978) Reconstruction of an object from the modulus of its Fourier transform. *Opt. Lett.*, **3** (1), 27–29.
- 42** Fienup, J.R. (1982) Phase retrieval algorithms: a comparison. *Appl. Opt.*, **21** (15), 2758–2769.
- 43** Russel Luke, D. (2005) Relaxed averaged alternating reflections for diffraction imaging. *Inverse Probl.*, **21**, 37–50.
- 44** Elser, V. (2003) Phase retrieval by iterated projections. *J. Opt. Soc. Am. A*, **20**, 40–55.
- 45** Chen, C.C., Miao, J., Wang, C.W., and Lee, T.K. (2007) Application of optimization technique to noncrystalline X-ray diffraction microscopy: Guided hybrid input-output method. *Phys. Rev. B*, **76** (6), 064113.
- 46** Sandberg, R.L., Paul, A., Raymondson, D.A., Hädrich, S., Gaudiosi, D.M., Holtzman, J., Tobey, R.I., Cohen, O., Murane, M.M., Kapteyn, H.C., Song, C.,

- Miao, J., Liu, Y., and Salmassi, F. (2007) Lensless diffractive imaging using tabletop coherent high-harmonic soft-X-ray beams. *Phys. Rev. Lett.*, **99** (9), 098103.
- 47** Miao, J., Hodgson, K.O., Ishikawa, T., Larabell, C.A., LeGros, M.A., and Nishino, Y. (2003) Imaging whole Escherichia coli bacteria by using single-particle X-ray diffraction. *Proc. Natl. Acad. Sci. USA*, **100** (1), 110–112.
- 48** Huang, X., Nelson, J., Kirz, J., Lima, E., Marchesini, S., Miao, H., Neiman, A.M., Shapiro, D., Steinbrener, J., Stewart, A., Turner, J.J., and Jacobsen, C. (2009) Soft X-ray diffraction microscopy of a frozen hydrated yeast cell. *Phys. Rev. Lett.*, **103** (19), 198101.
- 49** Nishino, Y., Takahashi, Y., Imamoto, N., Ishikawa, T., and Maeshima, K. (2009) Three-dimensional visualization of a human chromosome using coherent X-ray diffraction. *Phys. Rev. Lett.*, **102** (1), 018101.
- 50** Jiang, H., Song, C., Chen, C.C., Xu, R., Raines, K.S., Fahimian, B.P., Lu, C.H., Lee, T.K., Nakashima, A., Urano, J., Ishikawa, T., Tamanoi, F., and Miao, J. (2010) Quantitative 3D imaging of whole, unstained cells by using X-ray diffraction microscopy. *Proc. Natl. Acad. Sci. USA*, **107** (25), 11234–11239.
- 51** Mancuso, A.P., Gorniak, T., Staier, F., Yefanov, O.M., Barth, R., Christophis, C., Reime, B., Gulden, J., Singer, A., Pettit, M.E., Nisius, T., Wilhein, T., Gutt, C., Grübel, G., Guerassimova, N., Treusch, R., Feldhaus, J., Eisebitt, S., Weckert, E., Grunze, M., Rosenhahn, A., and Vartanyants, I.A. (2010) Coherent imaging of biological samples with femtosecond pulses at the free-electron laser FLASH. *New J. Phys.*, **12** (3), 035003.
- 52** Seibert, M.M., Ekeberg, T., Maia, F.R.N.C., Svenda, M., Andreasson, J., Jonsson, O., Odic, D., Iwan, B., Rocker, A., Westphal, D., Hantke, M., DePonte, D.P., Barty, A., Schulz, J., Gumprecht, L., Coppola, N., Aquila, A., Liang, M., White, T.A., Martin, A., Caleman, C., Stern, S., Abbergel, C., Seltzer, V., Claverie, J.M., Bostedt, C., Bozek, J.D., Boutet, S., Miahnahri, A.A., Messerschmidt, M., Krzywinski, J., Williams, G., Hodgson, K.O., Bogan, M.J., Hampton, C.Y., Sierra, R.G., Starodub, D., Andersson, I., Bajt, S., Barthelmess, M., Spence, J.C.H., Fromme, P., Weierstall, U., Kirian, R., Hunter, M., Doak, R.B., Marchesini, S., Hau-Riege, S.P., Frank, M., Shoeman, R.L., Lomb, L., Epp, S.W., Hartmann, R., Rolles, D., Rudenko, A., Schmidt, C., Foucar, L., Kimmel, N., Holl, P., Rudek, B., Erk, B., Homke, A., Reich, C., Pietschner, D., Weidenspointner, G., Struder, L., Hauser, G., Gorke, H., Ullrich, J., Schlichting, I., Herrmann, S., Schaller, G., Schopper, F., Soltau, H., Kuhnel, K.U., Andritschke, R., Schroter, C.D., Krasniqi, F., Bott, M., Schorb, S., Rupp, D., Adolph, M., Gorkhover, T., Hirsemann, H., Potdevin, G., Graafsma, H., Nilsson, B., Chapman, H.N., and Hajdu, J. (2011) Single mimivirus particles intercepted and imaged with an X-ray laser. *Nature*, **470**, 78–81.
- 53** Miao, J., Ishikawa, T., Johnson, B., Anderson, E.H., Lai, B., and Hodgson, K.O. (2002) High resolution 3d X-ray diffraction microscopy. *Phys. Rev. Lett.*, **89** (8), 088303.
- 54** Diaz, A., Mocuta, C., Stangl, J., Mandl, B., David, C., Vila-Comamala, J., Chamard, V., Metzger, T.H., and Bauer, G. (2009) Coherent diffraction imaging of a single epitaxial InAs nanowire using a focused X-ray beam. *Phys. Rev. B*, **79** (12), 125324.
- 55** Raines, K.S., Salha, S., Sandberg, R.L., Jiang, H., Rodriguez, J.A., Fahimian, B.P., Kapteyn, H.C., Du, J., and Miao, J. (2009) Three-dimensional structure determination from a single view. *Nature*, **463**, 214–218.
- 56** Dierolf, M., Menzel, A., Thibault, P., Schneider, P., Kewish, C.M., Wepf, R., Bunk, O., and Pfeiffer, F. (2010) Ptychographic X-ray computed tomography at the nanoscale. *Nature*, **467**, 436–439.
- 57** Barty, A., Boutet, S., Bogan, M.J., Hau-Riege, S., Marchesini, S., Sokolowski-Tinten, K., Stojanovic, N., Tobey, R., Ehrke, H., Cavalleri, A., Dusterer, S., Frank, M., Bajt, S., Woods, B.W., Seibert, M.M., Hajdu, J., Treusch, R., and Chapman, H.N. (2008) Ultrafast single-

- shot diffraction imaging of nanoscale dynamics. *Nat. Photonics*, **2**, 415–419.
- 58** McNulty, I., Kirz, J., Jacobsen, C., Anderson, E.H., Howells, M.R., and Kern, D.P. (1992) High-resolution imaging by Fourier transform X-ray holography. *Science*, **256** (5059), 1009–1012.
- 59** Eisebitt, S., Lörigen, M., Eberhardt, W., Lüning, J., Andrews, S., and Stöhr, J. (2004) Scalable approach for lensless imaging at X-ray wavelengths. *Appl. Phys. Lett.*, **84** (17), 3373–3375.
- 60** Hellwig, O., Eisebitt, S., Eberhardt, W., Schlotter, W.F., Lüning, J., and Stöhr, J. (2006) Magnetic imaging with soft X-ray spectroholography. *J. Appl. Phys.*, **99** (8), 081307.
- 61** Scherz, A., Schlotter, W.F., Chen, K., Rick, R., Stöhr, J., Lüning, J., McNulty, I., Günther, C., Radu, F., Eberhardt, W., Hellwig, O., and Eisebitt, S. (2007) Phase imaging of magnetic nanostructures using resonant soft X-ray holography. *Phys. Rev. B*, **76** (21), 214410.
- 62** Stickler, D., Frömter, R., Stillrich, H., Menk, C., Tieg, C., Streit-Nierobisch, S., Sprung, M., Gutt, C., Stadler, L.M., Leupold, O., Grübel, G., and Oepen, H.P. (2010) Soft X-ray holographic microscopy. *Appl. Phys. Lett.*, **96** (4), 042501.
- 63** Guehrs, E., Günther, C.M., Könnecke, R., Pfau, B., and Eisebitt, S. (2009) Holographic soft X-ray omni-microscopy of biological specimens. *Opt. Express*, **17** (8), 6710–6720.
- 64** Gunther, C.M., Pfau, B., Mitzner, R., Siemer, B., Roling, S., Zacharias, H., Kutz, O., Rudolph, I., Schondelmaier, D., Treusch, R., and Eisebitt, S. (2011) Sequential femtosecond X-ray imaging. *Nat. Photonics*, **5**, 99–102.
- 65** Stadler, L.M., Gutt, C., Autenrieth, T., Leupold, O., Rehbein, S., Chushkin, Y., and Grübel, G. (2008) Hard x ray holographic diffraction imaging. *Phys. Rev. Lett.*, **100** (24), 245503.
- 66** He, H., Weierstall, U., Spence, J.C.H., Howells, M., Padmore, H.A., Marchesini, S., and Chapman, H.N. (2004) Use of extended and prepared reference objects in experimental Fourier transform X-ray holography. *Appl. Phys. Lett.*, **85** (13), 2454–2456.
- 67** Schlotter, W.F., Rick, R., Chen, K., Scherz, A., Stöhr, J., Lüning, J., Eisebitt, S., Günther, C., Eberhardt, W., Hellwig, O., and McNulty, I. (2006) Multiple reference fourier transform holography with soft x rays. *Appl. Phys. Lett.*, **89** (16), 163112.
- 68** Marchesini, S., Boutet, S., Sakdinawat, A.E., Bogan, M.J., Bajt, S., Barty, A., Chapman, H.N., Frank, M., Hau-Riege, S.P., Szoke, A., Cui, C., Shapiro, D.A., Howells, M.R., Spence, J.C.H., Shaevitz, J.W., Lee, J.Y., Hajdu, J., and Seibert, M.M. (2008) Massively parallel X-ray holography. *Nat. Photonics*, **2**, 560–563.
- 69** Guizar-Sicairos, M. and Fienup, J.R. (2007) Holography with extended reference by autocorrelation linear differential operation. *Opt. Express*, **15** (26), 17592–17612.
- 70** Guizar-Sicairos, M. and Fienup, J.R. (2008) Direct image reconstruction from a Fourier intensity pattern using heraldo. *Opt. Lett.*, **33** (22), 2668–2670.
- 71** Podorov, S.G., Pavlov, K.M., and Paganin, D.M. (2007) A non-iterative reconstruction method for direct and unambiguous coherent diffractive imaging. *Opt. Express*, **15** (16), 9954–9962.
- 72** Guizar-Sicairos, M., Zhu, D., Fienup, J.R., Wu, B., Scherz, A., and Stöhr, J. (2010) Holographic X-ray image reconstruction through the application of differential and integral operators. *Opt. Lett.*, **35** (7), 928–930.
- 73** Gauthier, D., Guizar-Sicairos, M., Ge, X., Boutu, W., Carré, B., Fienup, J.R., and Merdji, H. (2010) Single-shot femtosecond X-ray holography using extended references. *Phys. Rev. Lett.*, **105** (9), 093901.
- 74** Merdji, H. (2012) Private communication.
- 75** Zhu, D., Guizar-Sicairos, M., Wu, B., Scherz, A., Acremann, Y., Tyliszczak, T., Fischer, P., Friedenberger, N., Ollefs, K., Farle, M., Fienup, J.R., and Stöhr, J. (2010) High-resolution X-ray lensless imaging by differential holographic encoding. *Phys. Rev. Lett.*, **105** (4), 043901.
- 76** Nishino, Y., Tanaka, Y., Okada, M., Okaya, M., Uozaki, Y., Nozaki, K., Yabashi, M., Nagasano, M., Tono, K.,

- Kimura, H., Ohashi, H., Matsui, S., Ishikawa, T., and Matsubara, E. (2010) Femtosecond snapshot holography with extended reference using extreme ultraviolet free-electron laser. *Appl. Phys. Express*, **3** (10), 102701.
- 77 Redecke, L., Nass, K., DePonte, D.P., White, T.A., Rehders, D., Barty, A., Stellato, F., Liang, M., Barends, T.R., Boutet, S., Williams, G.J., Messerschmidt, M., Seibert, M.M., Aquila, A., Arnlund, D., Bajt, S., Barth, T., Bogan, M.J., Caleman, C., Chao, T.C., Doak, R.B., Fleckenstein, H., Frank, M., Fromme, R., Galli, L., Grotjohann, I., Hunter, M.S., Johansson, L.C., Kassmeyer, S., Katona, G., Kirian, R.A., Koopmann, R., Kupitz, C., Lomb, L., Martin, A.V., Mogk, S., Neutze, R., Shoeman, R.L., Steinbrener, J., Timneanu, N., Wang, D., Weierstall, U., Zatsepin, N.A., Spence, J.C.H., Fromme, P., Schlichting, I., Duszenko, M., Betzel, C., and Chapman, H.N. (2013) Natively inhibited trypanosoma brucei cathepsin b structure determined by using an X-ray laser. *Science*, **339**, 227–230.

Index

Symbols

- 1/f noise, 101
- 2DSI, 73
- 2PE, 444
- N-methylacetamide
 - electron hole migration, 410

A

- ABCU
 - from 2 µm NIR radiation, 408
- Above-threshold ionization, 426
- Above-threshold ionization (ATI), 121, 191
- AD, 47
- Adiabaticity parameter
 - in Kr, 340
- Alignment of molecules, 413
- Amplified self-emission, 138
- Amplified spontaneous emission, 55
- Angular dispersion (AD), 47
- Angular distribution
 - measurement, 297
 - measurement by velocity map imaging, 472
- APS, 439
- ARAGNEE, 71
- Argon
 - autoionization, 386
 - Fano resonance, 386
 - multiple ionization, 486
- ASE, 138
- ATI, 121, 191, 426
- Attosecond nanophotonics, 421
- Attosecond nanoplasmonic streaking, 439
 - collective electron dynamics, 442
- Attosecond nanoscope, 444
- Attosecond pulse train
 - Attosecond pulses, 331, 421
 - autocorelation, 398

attosecond pulses

- from nanoparticles, 452

Attosecond streaking technique, 439

Auger cascade, 543

Auger decay, 380

- cascaded Auger decay, 391
- Krypton, 388
- xenon, 391

Auger ionization

- of neon, 542

Autocorrelation, 75

- field autocorrelation, 53
- intensity autocorrelation, 54
- interferometric autocorrelation, 53
- second-order autocorrelation, 53

Autoionization

- argon, 386
- autoionization times in helium, 373
- helium, 371
- krypton, 388
- xenon, 391

Azabicyclo[3.3.3]undecane

- electron dynamics, 408

B

Basis functions, 260

Born approximation, 561

Born–Oppenheimer approximation, 287

Broadband frequency conversion, 23

C

Carbon dioxide

- electron hole migration, 409
- pump–probe experiment, 398

Carrier envelope offset (CEO), 44

Carrier envelope phase

- control of electron emission, 425
- control of hydrogen dissociation, 399

- Carrier envelope phase (CEP), 21, 44, 45, 95, 96, 334, 397, 425
 - amplifier stabilization, 123
 - closed-loop noise analysis, 103
 - feedback stabilization, 110
 - feed-forward stabilization, 114
 - in amplifiers, 115
 - in oscillators, 104
 - noise, 100
 - open-loop noise analysis, 101
 - oscillator stabilization, 110
- Carrier envelope phase detection, 107
 - 0-f CEP stabilization, 128
 - above-threshold ionization (ATI), 121
 - common-path interferometer, 109
 - f-2f interferometer, 107, 119
 - half-cycle cutoff in high harmonic spectra, 123
 - Michelson interferometer, 109
 - multiphoton-induced surface photoemission, 122
 - quantum interferences in semiconductors, 109
 - spectrally and spatially resolved interferometry, 110
 - terahertz-emission spectroscopy, 122
- CCA, 435
- CEO, 44
- CEP, 44, 45, 95, 334, 397, 425
- charge oscillation
 - krypton, 390
- Chirped pulse amplification (CPA), 22, 25, 26, 116
- Chromatic aberration, 48
- Cluster plasmons, 433
- Cold-target recoil ion momentum spectroscopy (COLTRIMS)
 - in Xe, 472
- COLTRIMS
 - electron dynamics, 472
- Constant cross-section approximation, 435
- CPA, 22, 25, 26, 116
- Cross-correlation, 55
 - with X-rays, 545
- Cross-phase modulation (XPM), 62
- D**
- Delayed photoemission, 384
- Deuterium
 - two-photon double ionization, 487
- DFG, 127, 128
- Difference frequency generation (DFG), 127, 128
- Discrete-variable grid, 260, 278
- Dissociative ionization
 - of hydrogen, 290
- Dissociative photoionization (DPI), 294
- Double ionization
 - helium, 373
 - nonsequential double above threshold ionization, 377
 - nonsequential two-photon double ionization, 375
 - postionization energy exchange, 377
 - second ionization during core relaxation, 377
 - sequential two-photon double ionization, 376
- DPI, 294
- Dressed potential energy surfaces
 - high-energy cutoff, 399
- DVR, 260
- E**
- Effective range theory, 198
- Ehrenfest theorem, 396
- Eigenstates of helium, 365
- Eigenstates of hydrogen, 362
- Electron complex canonical momenta, 220
- Electron correlation, 378
- Electron dynamics, 397
 - coupled to nuclear dynamics, 412
 - hole migration, 409
 - in ABCU, 408
 - in lithium hydride, 405
 - in Mg-porphyrin, 407
 - in the DNA backbone, 415
 - in water and ice, 416
- Electron dynamics in hydrogen
 - in Xe, 406
- Electron emission
 - control by carrier envelope phase, 425
 - from nanoparticles, 426
 - from SiO₂ nanoparticles, 427
- Electron hole migration
 - in N-methylacetamide, 410
 - in a peptide, 411
 - in carbon dioxide, 397, 409
 - in glycine, 410
- Electron localization
 - hydrogen, 398
- Electron ponderomotive energy
 - in Xe, 341
 - post-orientation in linear molecules, 326
- Electron recollision, 325
- Electron tunneling, 219

- Electron wavefunction
 – asymptotic part, 217
- Electron-electron correlation, 233
- Electron-hole dynamics, 237, 240
- Electronic potential curve, 39, 40
- Electronic wave packet, 366
- Electrooptic sampling (EOS), 55
- EOS, 55
- Exit point in electron tunneling, 210
- Experimental observables
 – modeling by TDSE, 272
 – TDSE modeling of harmonic response, 274
 – TDSE modeling of ionization, 272
 – TDSE modeling of photoelectron spectra, 275
- F**
- Factorization of the high harmonic dipole, 221
- Fano resonance
 – argon, 386
 – helium, 371
- FDTD, 441
- FEL, 530
- FEM, 441
- Few-cycle pulses, 20, 22, 23, 425
- Fiber amplifier, 26
- Field-enhanced XUV generation, 449
- Finite difference time domain, 441
- Finite element, 441
- Finite element basis functions, 263
- FLASH, 530
- Fourier transform spectroscopy (FTS), 53
- Fraunhofer approximation, 564
- Free-electron laser
 – brilliance, 469
 – pulse parameters, 470
- Free-electron laser (FEL), 530
 – pulse parameters, 470
- Frequency-resolved optical gating (FROG), 55
 – FROG-CRAB, 80
 – GRENOUILLE, 59
 – polarization grating FROG, 56
 – principle component generalized projection algorithm, 57
 – reconstruction algorithm, 57
 – second harmonic FROG, 56
 – third harmonic FROG, 56
 – transient grating FROG, 56
- FROG, 55
- FTS, 53
- G**
- Gaussian laser profile, 139
- GD, 44
- GDD, 44
- Glycine
 – electron–hole migration, 410
- GRENOUILLE, 59
- Group delay (GD), 44
- Group delay dispersion (GDD), 44
- Group velocity, 21
- H**
- Hamilton–Jacobi equation, 186
- Helium
 – autoionization, 371
 – double ionization, 373
 – eigenstates, 365
 – Fano resonance, 371
 – shake-up states, 376
 – TDSE modeling of ionization, 279
 – two-photon double ionization, 476
 – two-photon ionization, 473
- HERALDO, 587
- HHG, 74
 – high-order harmonic generation, 323
- High harmonic dipole
 – factorization in the frequency domain, 222
 – factorization in the time domain, 224
 – for one-electron systems, 209
- High harmonic generation
 – cutoff energy, 203, 212, 216, 250
 – electron propagation, 223, 238
 – electron propagation with Coulomb correction, 217
 – electron recombination, 223, 239
 – ionization time, 210, 214
 – laser-induced dynamics in the ion, 234
 – multielectron effects, 285
 – multielectron model, 231
 – one-electron system, 205
 – plasmon field enhanced, 450
 – pulse parameters, 470
 – recombination time, 210, 214
 – saddle point method, 209
 – semiclassical description, 195
 – the simple man model, 203
- High-energy oscillators, 23
- Highest occupied molecular orbital (HOMO), 232
- High-harmonic generation
 – electron trajectories, 328
 – energy range, 331
 – from 2 μm NIR radiation, 346, 352
 – from 3.6 μm IR radiation, 347, 352

- from 243 nm VUV radiation, 323
- from 800 nm radiation, 352
- from 1064 nm Nd
 - YAG radiation, 323
- high-energy cutoff, 326, 342, 350
- in Ar, 323, 328, 334
- in Kr, 323
- in Ne, 323, 332
- in Xe, 323, 329
- pulse duration, 331
- pulse parameters, 470
- short and long trajectories, 326, 343
- three step model, 325
- Hole migration
 - RABITT, 409
- Hollow atoms, 538
- Holography, 583
- HOMO, 232
- Hydrodynamic modeling of plasma, 141
- Hydrogen
 - dissociative ionization, 400
 - eigenstates, 362
 - electron dynamics, 406
 - electron localization, 398
- Hydrogen atom
 - photoelectron spectrum, 277
- Hydrogen molecule
 - dissociative ionization, 290
 - TDSE modeling of ionization, 281
- I**
- index
 - SFA, see strong field approximation, 327
- Index REMI
 - reaction microscope, 472
- Infinite range exterior complex scaling
 - (irECS), 270
- Interferometry, 63
 - 2DSI, 73
 - ARAIGNEE, 71
 - long crystal SPIDER, 71
 - multiple spectral shearing interferometry, 68
 - SEA-SPIDER, 67
 - Spectral interferometry, 63
 - Spectral phase interferometry, 64
 - SPIDER, 64
 - SPIRIT, 73
- Ion chronoscopy
 - neon, 384
 - xenon, 391
- Ion momentum distribution
 - double ionization of helium and neon, 478
- Ionization
 - double ionization of helium and neon, 478
 - modeling by TDSE, 272
 - multiple ionization of argon, 486
 - multiple ionization of neon, 486
 - nonsequential double ionization, 476
 - sequential double ionization, 476
 - sequential two-photon double ionization of neon, 481
 - two-photon double ionization of helium, 476
 - two-photon double ionization of neon, 480
 - two-photon single ionization of helium, 473
- Ionization time, 210, 214, 219
 - measurement of ionization times, 231
- irECS, 270
- K**
- Keldysh parameter, 382
 - from 243 nm VUV radiation, 468
 - in Ar, 340
- Keldysh theory of tunnel ionization
 - high-order harmonic generation, 340
- KER, 488
- Kerr lens mode-locking (KLM), 21
- Kinetic energy
 - measurement by COLTRIMS, 472
 - measurement by velocity map imaging, 472
- kinetic energy release, 488
- KLM, 21
- Kramers–Henneberger frame of reference, 259
- Krypton
 - Auger decay, 388
 - charge oscillation, 390
- L**
- LAAD, 545
- Laser
 - average power, 24, 25
 - broadband frequency conversion, 19, 23
 - few-cycle pulses, 20, 22, 23, 425
 - group velocity, 21
 - high-energy oscillators, 23
 - intensity regimes, 531
 - interaction with atoms and molecules, 258
 - mode-locking, 21
 - phase velocity, 21
 - Pulse duration, 22

- THz pulses, 22
- Ti:sapphire laser, 20
- Ti:sapphire laser parameters, 532
- XUV pulses, 22
- Laser amplifiers, 25
 - CEP in amplifiers, 115
 - CEP stabilization, 123
 - chirped pulse amplification, 25, 26
 - fiber amplifier, 26
 - multipass amplifier, 26
 - parametric amplifier, 27
 - plasma-based soft X-ray amplifier, 137
 - regenerative amplifier, 26
- Laser gain media, 105
 - Cr:ZnSe, 22
 - sesquioxide, 24
 - tungstate, 24
 - Yb:KLuW, 24
 - Yb:KYW, 24
 - Yb:Lu₂O₃, 24
- Laser oscillators, 20
 - CEP in oscillators, 106
 - CEP stabilization, 110
- Laser pulse characterization
 - attosecond spectral shearing interferometry, 77
 - attosecond streak camera, 78
 - autocorrelation, 53
 - chronocyclic tomography, 60
 - cross-correlation, 55
 - electrooptic sampling, 55
 - FROG, 55, 344
 - FROG-CRAB, 80
 - GRENOUILLE, 59
 - long crystal SPIDER, 71
 - multiple spectral shearing interferometry, 68
 - PROOF, 81
 - RABITT, 79, 332, 344, 355
 - SEA-SPIDER, 67
 - spectral interferometry, 63
 - SPIDER, 64, 344
 - X-SPIDER, 80
 - XUV autocorrelation, 75
 - XUV chronocyclic tomography, 78
 - XUV interferometry, 81
 - XUV pulses, 73
 - XUV SPIDER, 81
- laser-assisted Auger decay (LAAD), 545
- Laser-induced dynamics in the ion, 234
- LCLS, 530
- Length gauge, 181, 205
- Linac Coherent Light Source (LCLS), 530
- Linear spectrum approximation, 435
- Lithium hydride
 - electron dynamics, 405
- Local basis functions, 261
- Lorentzian laser profile, 139
- LSA, 435
- M**
- magnetic bottle electron energy spectrometer
 - pulse duration, 347
- Maxwell wave equation, 43
- MBES
 - in Xe, 347
- Mean field, 430
- MF, 430
- MFPAD, 293
- Mg-porphyrin
 - electron dynamics, 407
- Michelson interferometer, 109
- Mode-locking, 21
- Molecular Coulomb explosion
 - in Ar, 398
- Molecular fragmentation
 - of deuterium, by EUV pulses, 487
 - of nitrogen, by EUV pulses, 489
- Molecular frame photoelectron angular distribution (MFPAD), 293
- Multielectron model to describe HHG, 231
- Multipass amplifier, 26
- N**
- Nanoparticles
 - control of electron emission, 426
- Nanoplasma, 433
- Neon
 - Auger process, 542
 - multiple ionization, 486
 - nonresonant multiple ionization, 537
 - photoionization cross-section, 533
 - resonant multiple ionization, 540
 - sequential photon absorption, 537
 - sequential two-photon double ionization, 481
 - shake-up states, 381
 - two-photon double ionization, 480
 - two-photon ionization, 539
 - X-ray interaction, 533
- Nitrogen
 - delay in photoionization, 403
 - EUV ionization and fragmentation, 489
 - nonresonant multiple ionization, 540
- Nodal planes in molecular orbitals, 238
- nonlinear optical parametric amplification (NOPA), 28

- Nonsequential double above threshold ionization (NS-DATI), 377
- Nonsequential double ionization
 - coupled to nuclear dynamics, 476
- Nonsequential two-photon double ionization (NS-TPDI), 375
- NOPA, 20, 28
- NS-DATI, 377
- NSDI
 - in a peptide, 476
- NS-TPDI, 375
- Nyquist–Shannon theorem, 573

- O**
- One-electron system
 - high harmonic dipole, 209
 - high harmonic generation, 205
- OPA, 28
- OPCPA, 28, 118
- optical parametric amplification (OPA), 28
- optical parametric chirped pulse amplification (OPCPA), 28

- P**
- PAD, 293
- Parametric amplifier, 27
 - carrier envelope phase stabilization, 126
- Paraxial approximation, 564
- PCGPA, 57
- PEC, 39, 40
- PEEM, 444
- Peptide
 - electron hole migration, 411
- Periodically poled nonlinear crystals (PPLN), 109
- PES, 77
- PFT, 47
- Phase retrieval by omega oscillation filtering, 81
- Phase-locked loop (PLL), 110
- Photoelectron angular distribution (PAD), 293
 - concurrent orientation, 310
 - molecular orientation, 294
 - one-photon photoionization, 297
 - orientation by alignment, 314
 - photoionization cross-sections, 302
 - postorientation in linear molecules, 304
 - postorientation in nonlinear molecules, 306
- Photoelectron emission microscopy
 - imaging of plasmonic fields, 444
- Photoelectron spectroscopy
 - IR-XUV ionization of helium, 369
- TDSE simulation, 366
- velocity map imaging, 426
- Photoelectron spectroscopy (PES), 77
- Photoelectron spectrum
 - hydrogen atom, 277
- Photoionization cross-sections, 302
- Photoionization delay
 - nitrogen, 403
- PIEE, 377
- Pink noise, 101
- Plasma X-ray amplifier, 137
 - Bloch–Maxwell model, 149
 - chirped pulse amplification, 157, 163
 - gain and saturation fluence, 143
 - hydrodynamic modeling, 141
 - multistage amplifier, 156, 168
 - spatial profile, 145, 158
 - temporal profile, 151, 158
- Plasmons, 422
 - attosecond experiments, 439
 - field-enhanced XUV generation, 449
 - in clusters, 433
- PLL, 110
- Poles in dipole matrix elements, 212
- Ponderomotive energies
 - in Ar, 469
- Ponderomotive potential, 383
- Postionization dynamics
 - classical model, 341
 - classical model, see simple man model, 341
- Postionization energy exchange (PIEE), 377
- Potential energy curve (PEC), 39, 40
- Power spectra density (PSD), 100
- PPLN, 109
- PPT theory, 198, 216
- Principle component generalized projection algorithm (PCGPA), 57
- PROOF, 81
- PSD, 100
- Pulse front tilt (PFT), 47
- Pulse parameters of X-ray sources
 - electron localization, 470
- Pulse-shaping, 366
- Pump–probe experiment
 - carbon dioxide, 398
- Pump–probe spectroscopy, 40

- Q**
- Quantitative rescattering theory, 198

- R**
- RABITT, 79, 332
 - nitrogen photoionization, 403

- Reaction microscope (REMI)
 – in lithium hydride, 472
- Recombination time, 210, 214
- Regenerative amplifier, 20, 26
- Runge–Kutta methods, 267
- S**
- Saddle point methods, 209, 242
 – approximation, 190, 213
 – divergence in saddle point solutions, 251
 – finding the saddle points, 214
 – saddle point solutions, 219
- Sampling theorem, 45
- SASE, 530
- SD, 56
- SDI
 – electron hole migration, 476
- Second ionization during core relaxation (SICR), 377
- Second-order harmonic generation (SHG), 56
- Self-amplified spontaneous emission (SASE), 530
- Self-diffraction (SD), 56
- Self-phase modulation (SPM), 22, 62
- Semiconductor saturable absorber (SESAM), 24
- Sequential double ionization (SDI), 481
 – in glycine, 476
- Sequential ionization
 – of deuterium, 488
- Sequential two-photon double ionization (S-TPDI), 376
- SESAM, 24
- SFA, 76, 179
- Shake-up states
 – helium, 376
 – neon, 381
- SHG, 56
- SICR, 377
- Signal-to-noise ratio
 – in X-ray diffraction, 568
- Signal-to-noise ratio (SNR)
 – in autocorrelation, 54
- Simple man model
 – three step model, 341
- Single active electron approximation, 181
 – model high harmonic generation, 205
- Singular value decomposition (SVD), 58
- SiO₂ nanoparticles
 – effective field, 429
 – electron emission, 427
- SNR, 54, 568
- Sonography, 60
- Space-time coupling (STC), 46, 50
- Spatial chirp, 48
- Spectral interferometry
 – basics, 433
 – sodium nanoparticles, 437
- Spectral shearing interferometry, 64
- Spectrography, 55
- SPIDER, 64
 – SEA-SPIDER, 67
- SPIRIT, 73
- SPM, 62
- SSI, 64
- STC, 46, 50
- S-TPDI, 376
- Strong field approximation
 – orientation by alignment, 327
- Strong field interactions, 339
- Strong fields, 467
- Strong-field approximation (SFA), 76, 184, 186
 – comparison with time-dependent Hartree–Fock, 286
 – limits of the SFA, 188
 – transition amplitudes, 187
- Strong-field ionization, 219, 232, 238
 – electron correlation effects, 233
- Strong-field ionization of Ar
 – energy range, 348
- Strong-field S-matrix, 184
- SVD, 58
- T**
- Tabletop X-ray lasers, 135
- TADPOLE, 64
- TAS, 39
- TBP, 45
- TDCI, 282
- TDHF, 283
- TDSE, 81, 179, 257
- TG, 56
- The simple man model, 203
- THG, 56
- Third-order harmonic generation (THG), 56
- Three-step model, 341
- THz pulses, 22
- Ti:sapphire laser, 20
- Time-bandwidth product (TBP), 45
- Time-dependent configuration-interaction (TDCI), 282
- Time-dependent Hartree–Fock (TDHF), 283
 – comparison with the strong-field approximation, 286
 – multiconfiguration TDHF, 283

- Time-dependent Schrödinger equation (TDSE), 81, 179, 181, 366
 - basis functions, 257, 260
 - discretization of the TDSE, 260
 - few-electron systems, 282
 - finite element basis functions, 263
 - formal solution, 182
 - grid boundary, 265, 269
 - grid methods, 260
 - helium, 278
 - hydrogen molecule, 278
 - length gauge, 258
 - local basis functions, 261
 - modeling harmonic response, 274
 - modeling ionization, 272
 - modeling of observables, 272
 - modeling of photoelectron spectra, 275
 - nuclear motion, 287
 - pseudo-spectral approach, 278
 - Runge–Kutta time propagation, 267
 - single active electron, 324
 - split Hamiltonian, 269
 - strong-field approximation, 184
 - time propagation, 266
 - two electron systems, 278
 - velocity gauge, 258
 - Volkov propagator, 185
- Time-dependent surface flux (t-SURFF), 276
- Time-resolved fluorescence spectroscopy (TRFS), 39
- Time-resolved spectroscopy (TRS), 39, 40
- TPDI, 362
 - in carbon dioxide, 476
- TPSI
 - from 2 μm NIR radiation, 473
- TRA, 39
- Transient absorption spectroscopy (TAS), 39
- Transient grating (TG), 56
- TRFS, 39
- TRS, 39
- t-SURFF, 276
- Tunnel ionization
 - from 243 nm VUV radiation, 340
- Tunneling time, 193
- Two photon absorption
 - high-order harmonic generation, 467
- Two-photon double ionization
 - helium, 476
 - neon, 480
 - nonsequential, 375
 - of helium, 476
 - positionization energy exchange, 377
 - second ionization during core relaxation, 377
 - sequential process in neon, 481
 - sequential TPDI, 376, 377
- Two-photon double ionization (TPDI), 373
- Two-photon double ionization of deuterium, 487
- Two-photon ionization
 - helium, 473
- Two-photon single ionization
 - of helium, 473
- Two-photon-photoemission, 444
- V**
- Velocity gauge, 181
- Velocity map imaging, 426
 - with X-rays, 472
- VER Molecular alignment, 413
- VMI
 - seevelocity map imaging, 426
- Volkov function, 207
- Volkov propagator, 184, 276
- W**
- Wave equation, 43
- Wavepacket
 - electronic wave packet, 366
- White noise, 101
- Wigner distribution, 41, 46
- X**
- Xenon
 - above-threshold ionization, 427
 - Auger decay, 391
- XPM, 62
- X-ray
 - Auger process in neon, 542
 - brilliance of synchrotrons and FELs, 530
 - characterization of LCLS pulses, 544
 - cross-correlation, 545
 - induced transparency, 538
 - interaction with neon, 533
 - LCLS pulse parameters, 532
 - light sources, 469
 - nonresonant multiple ionization of neon, 537
 - nonresonant multiple ionization of nitrogen, 540
 - Rabi cycling, 541
 - radiation dose, 569
 - resonant multiple ionization of neon, 540
 - streaking, 545
 - two-photon ionization, 539
 - ultrafast X-ray probe, 543

- X-ray diffraction
 - before sample destruction, 557, 571
 - Born approximation, 561
 - far-field diffraction, 559
 - iterative phase retrieval, 574, 577
 - nanocrystal structure analysis, 592
 - of biological samples, 579
 - phase retrieval, 557, 572, 577
 - protein imaging, 592
 - Resolution, 562, 570, 577
 - signal-to-noise ratio, 557, 568
 - source requirements, 565
 - with XFEL pulses, 578
- X-ray gratings, 165
 - conical diffraction grating, 166
- X-ray holography, 583
 - HERALDO, 587
 - of Co/Pt magnetic domains, 585
 - of iron nanotubes, 589
 - time resolved sequential imaging, 586
- X-SPIDER, 80
- XUV photoionization, 75
- XUV pulses, 22
- XUV simplified chronocyclic tomography (XUV-SCT), 78
- XUV sources, 572
- XUV-SCT, 78

Y

- Yb-doped laser, 20